Digitized by Arya Samaj Foundation Chennai and eGangotri

PRAMANA

VOL. 28
1987

Digitized by Arya Samaj Foundation Chennai and eGangotri

CC-0. In Public Domain. Gurukul Kangri Collection, Haridwar

G. K. U.
Hardwar

Digitized by Arya Samaj Foundation Chennai and eGangotri

111940

CC-0. In Public Domain. Gurukul Kangri Collection, Haridwar

Digitized by Arya Samaj Foundation Chennai and eGangotri

CC-0. In Public Domain. Gurukul Kangri Collection, Haridwar

Digitized by Arya Samaj Foundation Chennai and eGangotri

CC-0. In Public Domain. Gurukul Kangri Collection, Haridwar

Digitized by Arya Samaj Foundation Chennai and eGangotri

Pramāṇa

journal of physics

Volume 28, January–June 1987

CONTENTS

S:18
111940 L

Mathematical Physics

Implementation and comparative study of random sequences for nonlinear least square data fitting
Tapas Bandyopadhyay and P K Sarkar 97–108

Quantum Mechanics

Semiclassical approximation for relativistic potentials *J Thakur* 1–8

The generalized Pauli-Lubanski vector for massless spinning particles in arbitrary space-time dimensions *M V Atre* 233–239

Equivalent potentials for a nonsymmetric non-local interaction
G C Sett, U Laha and B Talukdar 325–334

General Relativity, Gravitation and Cosmology

Kerr-Newman metric in deSitter background
L K Patel, Sharda S Koppar and P V Bhatt 109–115

Nonsingular cosmological models with torsion determined by vacuum polarization of quantum fields *I L Buchbinder and S D Odintsov* 241–245

Statistical Physics

On the short-time behaviour of quantum unstable systems
V J Menon 335–341

Thermodynamic properties of molecular fluid mixtures of hard ellipsoids *A K Singh, U N Singh and S K Sinha* 343–354

Local quantum statistics in arbitrary curved space-time
P Pronin and I Kulikov 355–359

Microscopic theory of soliton propagation in a mixture of two boson fluid films *A C Biswas* 361–366

Interpolation model for molecular reorientation in gases and liquids
S K Deb and A K Sood 367–378

CC-0. In Public Domain. Gurukul Kangri Collection, Haridwar

Digitized by Arya Samaj Foundation Chennai and eGangotri

Particle Physics

Superconformal transformations of the $N = 2$, $D = 4$, SSYM
Mayank R Mehta 9–14

Tree-level breaking of SU (2) × U(1) in general SUGRA theories
Anjan S Joshipura, A Mukherjee and Sanjeev K Soni 15–22

Phenomenological structure functions and Gribov-Lipatov relation
D K Choudhury and A K Misra 23–34

Slope parameter and scaling of differential cross-section of Λ-p scattering *J K Mohapatra, S Mohanty and S N Nayak* 35–39

Analytic representation for ^{3}He form factors
K N Agrawalla and M K Parida 117–130

Relativistic effects on meson spectra
S P Misra, S Naik and A R Panda 131–158

Production of tachyons and antiparticles in extended manifolds of general relativity *A P Trofimenko and V S Gurin* 379–386

Chou-Yang model and predictions for high-energy pion-deuteron scattering *Sunachand Patel and M K Parida* 607–616

Equivalence of stochastic quantization to field theories from supersymmetry *S Chaturvedi, A K Kapoor and V Srinivasan* 617–619

Supersymmetric $SU_C(4) \times SU_L(2) \times SU_R(2)$ and spontaneous breakdown of symmetries *B Bhuyan and B B Deo* 621–632

Relativistic extension of the Hohenberg-Kohn theorem *S N Datta* 633–639

Nuclear Physics

Heavy-ion fusion cross-section calculations in classical microscopic equations of motion approach *S S Godre and Y R Waghmare* 41–44

Off-shell variation in the binding energy of triton *Md. Yasin* 247–256

Density of nucleons in heavy nuclei *Nazakat Ullah* 641–644

Calculation of geometrical coupling coefficients for the hyperspherical harmonics approach *Tapan K Das and Tushar Baran De* 645–651

Instrumentation

Design studies of a 100 MeV proton linear accelerator
P Singh, R Mythili and M G Betigeri 257–267

Atomic and Molecular Physics

Theoretical study of ^{14}N pure quadrupole resonance in amino acids
B V R R K Murty, G Krishna Kishore, D Krishna Rao and G Satyanandam 45–50

CC-0. In Public Domain. Gurukul Kangri Collection, Haridwar

Digitized by Arya Samaj Foundation Chennai and eGangotri

On the direct determination of constrained pure state one-electron density matrices: II. A modified algorithm and its applications
Kalyan K Das, Priyotosh Khan and Sankar P Bhattacharyya 51–58

Isotope shift studies in the spectrum of boron monosulphide
Sheila Gopal and G Lakshminarayana 159–165

Electron impact excitation of hydrogen and helium in Coulomb-projected Born methods *C S Singh and D K Rai* 167–179

Modification in high energy higher order Born approximation
K Suja and H S Desai 387–397

Quenching of excitations in an impure molecular crystal
S Priyadarshy and S N Datta 653–660

Optics

Kramers-Kronig type of dispersion relation in nonlinear optics
P Sen and P K Sen 661–667

Spectroscopy

Transient excited singlet state absorption in Rhodamine 6G
Putcha Venkateswarlu, M C George, Yerneni V Rao, H Jagannath, G Chakrapani and A Miahnahri 59–71

Plasma Physics

Near perpendicular propagation of ion cyclotron modes in a deuterium-hydrogen-oxygen fusion plasma *Chandu Venugopal* 181–193

Weak electron acoustic double layers in a multicomponent plasma
K S Goswami and S Bujarbarua 399–408

Condensed Matter Physics

Precise lattice parameter measurements in CsCl-Br solid solutions between room temperature and 90°K by powder x-ray diffraction
V Ganesan and K S Girirajan 73–79

X-ray diffraction and colour centre studies on RbCl-RbBr mixed crystals
K Srinivas, Mohd. Ateequddin and D B Sirdeshmukh 81–86

Temperature invariance of S_0-parameter of polymers
B K Sharma and R R Reddy 195–203

Collective excitation modes in the intermediate and superconducting states of doped and undoped indium and lead
V V Joshi and K D Chaudhuri 205–215

A three-body force shell model calculation of Schottky defect formation energies of ionic crystals with CsCl structure
V Mishra, S P Sanyal and R K Singh 217–228

CC-0. In Public Domain. Gurukul Kangri Collection, Haridwar

Digitized by Arya Samaj Foundation Chennai and eGangotri

The dielectric constant of the binary liquid system *n*.heptane + methanol near its critical temperature
Y Jayalaxmi, S Guha, V C Vani and E S R Gopal 269–275

Effects of various ambient-aging processes in chopped and non-chopped optical films *K Vijaya, R K Puri and R N Karekar* 277–285

Phonon dispersion curves of transition metals using modified general tensor force model *Satish Kumar Mahna* 287–292

Photoacoustic determination of energy band gap of semiconductors
R S Ram, Om Prakash and A N Pandey 293–297

Stabilization of valence fluctuations in the cerium solid by the time-dependent collision approach *Ratan Lal* 299–310

Refinement of twinned crystal data
Sandhya Bhakay-Tamhane and A Sequeira 409–413

Precession photography of fibres: Prediction of patterns
M Sundaramoorthy 415–424

Electronic contribution to electric field gradient in dilute alloys
K V K Nair and N V Nair 669–673

X-ray electrical conductivity, magnetic and infra-red studies of the system $CO_{2-x}Ge_{1-x}Fe_{2x}O_4$ *Prabha Nathwani and V S Darshane* 675–688

Unified study of alkaline earth metal *Suratna Das and A Sarkar* 689–697

Rapid Communications

High-temperature superconductivity in the 100 K region in perovskite-related oxides of the Ln-Ba-Cu-O (Ln = Y or La) system
P Ganguly, A K Raychaudhuri, K Sreedhar and C N R Rao L229–L231

Flexoelectric origin of oblique-roll electrohydrodynamic instability in nematics *N V Madhusudana, V A Raghunathan and K R Sumathy* L311–L316

Electron-fluctuating distortion interaction in the new high T_c superconductors *R Jagadish and K P Sinha* L317–L319

Identification of the high-temperature superconducting phase in the Y-Ba-Cu-O system as the pervoskite $YBa_2Cu_3O_{7\pm\delta}$
P Ganguly, R A Mohan Ram, K Sreedhar and C N R Rao L321–L323

An 'EPR' study of $YBa_2Cu_3O_7$ and related high temperature superconductors *S V Bhat, P Ganguly and C N R Rao* L425–L427

A Lagrangian basis for Ashtekar's reformulation of canonical gravity
Joseph Samuel L429–L432

Constraint on unstable photino mass from a superlight gravitino
Tanmoy Bhattacharya and Probir Roy L699–L704

CC-0. In Public Domain. Gurukul Kangri Collection, Haridwar

Digitized by Arya Samaj Foundation Chennai and eGangotri

Observation of inverse a.c. Josephson effect in bulk Y-Ba-Cu-O possessing high T_c
A K Gupta, S K Agarwal, B Jayaram, Anurag Gupta and A V Narlikar L705–L708

Endothermic quasicrystalline-to-crystalline phase transition in Al_6CuMg_4 *M K Sanyal, V C Sahni and G K Dey* L709–L712

Electro-magnetic response of a single phase Y-Ba-Cu-O compound superconducting in the 90 K range
V Nagarajan, P L Paulose, A K Grover, S K Dhar and E V Sampathkumaran L713–L719

Comments

Existence of quantum soliton for ϕ^6-like field theories in 1+1 dimensions *C N Kumar and B K Parida* 87–93

Some remarks on the finiteness of soliton mass
R K Kaul and R Rajaraman L95–L96

Erratum 605

Special issue on Indo-Soviet Conference on Low Temperature Physics
Foreword 433
High pressure techniques at low temperatures
S Ramaseshan, G Parthasarathy and E S R Gopal 435–469

Low temperature elastic behaviour of As-Sb-Se and Ge-Sb-Se glasses
E S R Gopal, T S Mukundan, J Philip and S Sathish 471–482

Electromagnetic generation of ultrasound in metals at low temperatures
A N Vasil'ev and Yu P Gaidukov 483–488

Phonon drag effect in three- and two-dimensional electron systems
N V Zavaritsky 489–501

Low temperature resistance fluctuation in disordered conductors
N Kumar 503–508

Resistivity of metallic systems with a strong dynamic disorder
V F Gantmakher, G I Kulesko and V M Teplinsky 509–516

Josephson voltage standard at National Physical Laboratory, New Delhi
A K Gupta, N S Natarajan, V S Tomar, N D Kataria, V K Batra, A V Narlikar and K Chandra 517–527

Transformation kinetics of A-15 superconductors formed by solid state reactions *A V Narlikar* 529–545

Disorder in superconductors — a study on $Cu_2Mo_6S_8$ *P Chaddah* 547–553

Structural instability and superconductivity in niobium-titanium alloys
T S Radhakrishnan 555–564

CC-0. In Public Domain. Gurukul Kangri Collection, Haridwar

Digitized by Arya Samaj Foundation Chennai and eGangotri

Theoretical studies on magnetic superconductors
R Jagadish and K P Sinha 565–571

Phase transition studies of paramagnetic crystals at low temperatures
S K Dutta Roy and B Ghosh 573–581

Nuclear magnetic resonance studies in rare earth ternary phosphides
R Vijayaraghavan 583–587

Abstracts

Layered structure of superfluid ^{4}He at supercritical motion
L P Pitaevskii 589

Study of the two-domain processing structure in the superfluid ^{3}He-B
A S Borovik-Romanov, Yu M Bunkov, V V Dmitriev, Yu M Mukharsky and I A Fomin 590

Roughening (faceting) transitions on the helium crystal-superfluid interface
A V Babkin, K O Keshishev, D B Kopeliovich and A Ya Parshin 591

Quantum interference of electrons in disordered metals
B Yu V Sharvin 592

Residual conductance fluctuations of tiny disordered conductors
B L Altshuler, D E Khmel'nitskii and B Z Spivak 593

Experimental study of resistivity of metallic materials with dynamic disorder *V F Gantmakher, G I Kulesko and V M Teplinsky* 594

Nonstationary phenomena in Si MOSFET's in the quantum Hall effects regime *V M Pudalov, S G Semenchinsky and V S Edel'man* 595

Electron fluid and quasiparticles in the quantum Hall effect
V L Pokrovsky and A L Talapov 596

Unusual superconductivity and its physical properties *L P Gor'kov* 597

Superconductivity of the twinning plane *I N Khlustikov* 598

Investigations of UBe_{13} of other compounds of Be and U in normal and superconductive states *N E Alekseevskii* 599

Disordered magnets *M V Feigel'man* 600

Spin waves in paramagnetic Boltzmann gases *E P Bashkin* 601

Magnetic properties and peculiarity of magnetic states in dilute antiferromagnets $Mn_{1-x}Zn_xF_2$ *A N Bazhan and S V Petrov* 602

Periodic density redistribution of parametrically excited spin waves in an antiferromagnet *A I Smirnov* 603

Frozen photoconductivity in PbTe films
I P Krylov and Ya B Pojarkov 604

CC-0. In Public Domain. Gurukul Kangri Collection, Haridwar

Digitized by Arya Samaj Foundation Chennai and eGangotri

Pramāṇa

journal of physics

Notes on the preparation of papers

Authors wishing to have papers published in Pramāṇa should send them to Editorial Office.

Three copies of the paper must be submitted.
The submission of a paper will be held to imply that it represents the results of original research not previously published; that it is not under consideration for publication elsewhere; and that if accepted for Pramāṇa it will not be published elsewhere. Papers should not normally exceed 8000 words.

Typescript:

Papers must be written clearly and concisely in English, the preferred spelling being that of the Concise Oxford Dictionary. They must be typed double spaced with ample margin on all sides on white bond paper, 292 × 210 mm. This also applies to the abstract, tables, figure captions, and the list of references which are to be typed on separate sheets.

Title page:

The first page must bear (*a*) the title of the paper; (*b*) the initials and names of the authors; (*c*) the name and address of the institution where the work was carried out; (*d*) the permanent or present addresses of the authors, if different from (*c*); and (*e*) the American Physical Society classification number for the manuscript. A copy of the APS classification scheme can be obtained from the Academy. Authors should suggest an abbreviated running title of not more than 50 letters and spaces. Title must be specific and should contain words useful for indexing.

Abstract:

All papers must have an abstract of not more than 200 words of the significant results reported in the paper.

Keywords:

Between 3 and 6 keywords must be provided for indexing and information retrieval services.

List of Symbols:

Authors should attach to the manuscript a complete list of symbols identified typographically, not mathematically. This list will not appear in print, but it is essential in order to avoid costly corrections at the proof stage.

The Text:

The paper must be divided into sections starting preferably with 'Introduction' and ending with 'Conclusions'. The main sections should be numbered 1, 2, 3, etc. and subsections 2.1., 2.2, etc.

References:

References should be cited in the text by author and year, not by number. If there are more than two authors, reference should be to the first author followed by *et al* in the text, but names of all authors must be given in the list of references at the end. References at the end of the paper

CC-0. In Public Domain. Gurukul Kangri Collection, Haridwar

Digitized by Arya Samaj Foundation Chennai and eGangotri

should be listed alphabetically by authors' names, followed by initials, year of publication, name of the journal (abbreviated in the standard form, as in *Chemical Abstracts*), volume number, and number of the first page. References to book should include: name(s) of author(s), initials, year of publication, title of the book, edition if not the first, initials and name(s) of editor(s) if any, preceded by ed(s), place of publication, publisher, and chapter or pages referred to. References to thesis must include the year, the title of the thesis, the degree for which submitted and the university.

Mathematical Material:

Equations must be clearly written, each on its own line, well away from the text. All equations must be numbered consecutively in arabic numerals with the number in parentheses near the right hand margin. Indices or superscripts must be indicated in pencil with a √ sign and subscripts with a ^ sign; 'oh' and 'zero', K, *k*, and kappa, 'ell' and one, etc., must be clearly distinguished. Authors must indicate wherever special characters (Greek, German, script, scalar, vector, tensor, matrix, etc.) are required. All other letters will be set in italic types. Vectors must be underlined by a wavy line and tensors by two wavy lines. The SI system of units and symbols is recommended.

Figures:

All figures, including photographs which must be glossy prints, should be numbered consecutively in arabic numerals in the order of occurrence in the text. Figure captions must be typed on a separate sheet.

Line drawings must be in Indian ink on good quality tracing paper or white card of the same size as the text paper or smaller. Curves should be drawn sufficiently thick to permit reduction to one half or even one third of the original size. The axes must be about 0·3 mm thick and the curves 0·6 mm thick.

Tables:

All tables must be numbered consecutively in arabic numerals in the order of appearance in the text. The tables should be self-contained and have a descriptive title. Column headings of tables should be brief. Extensive tables will be reproduced photographically and should therefore be typed carefully and in the exact format desired. Footnotes to the tables, if any, should be identified by superscript letters and placed at the bottom of the page containing the table.

Footnotes:

Footnotes to the text should be avoided if possible but when necessary should be numbered consecutively, and typed on a separate sheet.

Appendices:

All appendices should be numbered consecutively in arabic numerals.

Proofs:

Normally two sets of page-proofs are sent to authors for correction along with a reprint order form and one set of corrected proof should be returned to the editorial office within two days of receipt. If the corrected proof is not received within a reasonable number of days, it will be presumed that the authors have no corrections to make.

The articles are typeset by computer photocomposition and printed by offset process. While this process is neat, it makes corrections at the proof stage very difficult and expensive. Addition or deletion of a letter, a word or a sentence in the proof means resetting the whole line or para and sometimes a few pages. Authors are therefore requested to indicate only typographical or composing errors. Fresh corrections which are absolutely essential and unavoidable can be indicated but will be charged to the authors at actuals.

Reprints:

50 reprints of each article will be supplied free of charge.

CC-0. In Public Domain. Gurukul Kangri Collection, Haridwar

Digitized by Arya Samaj Foundation Chennai and eGangotri

Papers accepted for forthcoming issues

Substitutional effect on superconducting transition of Y-Ba-Cu-O.....
.....*S K Agarwal, B Jayaram, A Gupta and A V Narlikar*

Phase dependent superconductivity in the Y-Ba-Cu-O system .....
.....*Om Prakash, N Venkataramani, S N Bhatia, R Aiyar, R Walia and C M Srivastava*

Adler-Bardeen theorem in path integral formulation.....
.....*Satish D Joglekar and Anuradha Misra*

Hypersensitive and forbidden transitions of trivalent europium ion in $Tb_{1.8}\ Eu_{0.2}\ (MoO_4)_3$ single crystal.....*S Sheik Saleem and T K K Srinivasan*

Dielectric polarization of the solutions of nitrotoluene and cyclohexane.....
.....*M Sliwinska-Bartkowiak, B Szurkowski and T Hilczer*

Rotational analysis of $A^1\ \Pi - X^1\ \Sigma^+$ bands of $P^{14}N$ and $P^{15}N$: perturbation studies in the $A^1\ \Pi$ state.....*P Saraswathy and G Krishnamurty*

Laser photoacoustic spectroscopy of iodine molecule: Single and two photon absorptions.....*Putcha Venkateswarlu, G Chakrapani, M C George, Y V Rao and C Okvfor*

Effective medium in dispersed systems..*R N Pande, D R Chaudhary and F Gori*

Shock Hugoniot calculations and melting in Pb.....
.....*B K Godwal, S K Sikka and R Chidambaram*

Finite Larmor radius and Hall effects on thermal instability of a compressible plasma.....*R C Sharma and J N Misra*

Wave reflection from inhomogeneous media at normal incidence.....
.....*Philip D'Souza*

Fluctuations in $^{12}C + ^{24}Mg$ elastic and inelastic scattering.....
.....*B Ghosh and R Singh*

Confinement models for gluons.....*S B Khadkikar and P C Vinod Kumar*

Electrical second harmonic generation by $(Pb_x - Ba_{1-x})\ TiO_3$ and $(Pb_x - Sr_{1-x})\ TiO_3$ in the autostabilized state.....*V M Jamadar, T A Patil and S H Chavan*

On the valence instability in $CeAl_2$.....*T G Ramesh and W B Holzapfel*

Holographic grating Ebert spectrograph.....*N C Das and M V R K Murty*

A search for colour Van der Waals interaction.....
.....*C V K Baba, V M Datar and A Roy*

Theoretical evaluation of the probability of success of the quasi-anomalous method.....*K Chinnakali, S Parthasarathy and N Elango*

CC-0. In Public Domain. Gurukul Kangri Collection, Haridwar

Digitized by Arya Samaj Foundation Chennai and eGangotri

CC-0. In Public Domain. Gurukul Kangri Collection, Haridwar

Digitized by Arya Samaj Foundation Chennai and eGangotri

Pramāṇa – J. Phys., Vol. 28, No. 1, January 1987, pp. 1–8. © Printed in India.

Semiclassical approximation for relativistic potentials

J THAKUR
Department of Physics, Patna University, Patna 800005, India

MS received 17 May 1986; revised 30 September 1986

Abstract. We consider the application of semiclassical approximation to relativistic potentials for massless particles where the kinetic energy is a nontrivial, nonlocal operator. Quantization rules are derived for an arbitrary confining potential and compared to some exact results for S-waves. These results admit of a partial generalization to small l values.

Keywords. Semiclassical approximation; relativistic potentials; massless particles; quantization.

PACS Nos 03·65; 03·30

1. Introduction

The problem of bound states of relativistic systems is a matter of great and varied interest. Such systems ought to be described by field theoretic methods such as the Bethe-Salpeter equation, but the solution, and its interpretation, is simple only for instantaneous kernels in which case it is equivalent to a potential model. Such a potential description can now be formulated quite generally (Rohrlich 1979; Thakur J (to be published)) but the problems associated with centre of mass motion is most simply accounted for in the case of two equal mass particles. In that case one is left with an internal Hamiltonian (in the CM frame)

$$h = 2(m^2 + \mathbf{p}^2)^{1/2} + 2V, \tag{1}$$

where $2V$ is the interaction potential which will henceforth be considered to be local and central. The eigenvalues of this Hamiltonian operator are the masses of the composite system. This operator reduces to the familiar non-relativistic (NR) Hamiltonian for large m, but, for a relativistic system, the mass of the constituents may be much smaller than the masses of the composite system. This is particularly true for the excited states in a confining potential and in this sense relevant to meson spectroscopy even if the quark mass which ought to be inserted in the above expression turns out to be much larger than the current quark mass estimate of a few MeV for the u and d quarks, and a few hundred MeV for the strange quarks. Also we have objects like gluebails whose constituents are massless. For these reasons, and for mathematical simplicity, we were led to consider the massless limit ($m = 0$) of (1).

We shall work in the semiclassical approximation where NR analogy suggests the following form for the wavefunction.

CC-0. In Public Domain. Gurukul Kangri Collection, Haridwar

Digitized by Arya Samaj Foundation Chennai and eGangotri

$$\psi = \exp\left[\frac{i}{\hbar}\sigma_0(\mathbf{r}) + \sigma_1(\mathbf{r}) + O(\hbar)\right]. \tag{2}$$

Then, the eigenvalue equation

$$h\psi = M\psi, \tag{3}$$

is equivalent to

$$h(\nabla\sigma_0, \mathbf{r}) = M, \tag{4a}$$

$$\frac{1}{2}\nabla\cdot\frac{\partial h}{\partial\nabla\sigma_0} + \nabla\sigma_1\cdot\frac{\partial h}{\partial\nabla\sigma_0} = 0. \tag{4b}$$

But this method is practically useless for confining potentials for σ_0 turns out to be real both in the allowed and forbidden region and, furthermore, σ_1 turns out to be nearly constant so that the wavefunctions appear to be unnormalizable. For this reason it is desirable to give an alternative derivation of the quantization rules which we shall do below. We shall first consider in §2 the quantization rules for S waves and then give a partial generalization in §3 valid for nonzero angular momentum. Our conclusion is briefly stated in §4.

2. Quantization rules for $l = 0$

Dividing the Hamiltonian by 2, we are led to consider the eigenvalue equation

$$p\psi + V(r)\psi = \lambda\psi. \tag{5}$$

The operator p is best defined in momentum space. Let $\phi(p)$ be the unnormalized wavefunction in momentum space, so that ignoring irrelevant factors

$$r\psi(r) = S(r) = \int_0^\infty p\phi(p)\sin pr\,\mathrm{d}p, \tag{6}$$

and the eigenvalue equation reads

$$\int_0^\infty p[p\phi(p)]\sin pr\,\mathrm{d}p - [\lambda - V(r)]\,S(r) = 0. \tag{7}$$

Defining $$C(r) = \int_0^\infty p\phi(p)\cos pr\,\mathrm{d}p, \tag{8}$$

equation (7) can be written as

$$-\frac{\mathrm{d}C}{\mathrm{d}r} - (\lambda - V(r))\,S(r) = 0. \tag{9}$$

In the equation above $C(r)$ is determined if $S(r)$ is known for $C(r)$ is the cosine transform of $p\phi(p)$ which, by Fourier inversion theorem, is the sine transform of $S(r)$. It is, therefore, a genuine and well-posed equation for a single function $S(r)$. But the point of transition to (9) is that we can treat $C(r)$ and $S(r)$ as independent functions, more

CC-0. In Public Domain. Gurukul Kangri Collection, Haridwar

Digitized by Arya Samaj Foundation Chennai and eGangotri

precisely, as the real and imaginary parts of a complex valued function of r. Thus we observe that (9) is the real part of the equation

$$-\frac{dE}{dr}+i(\lambda-V(r))E(r)=-if(r), \tag{10}$$

for some real $f(r)$ which may depend on λ. (Here $E(r)=C(r)+i\,S(r)$.) The occurrence of the arbitrary function $f(r)$ which may depend on λ is related to the fact that (10) is a much more general equation than (7). It is, in fact, a pair of real linear differential equations for *two* independent functions $C(r)$ and $S(r)$. All trace of the inherent interdependence of $S(r)$ and $C(r)$ via (6) and (8) has been lost. The solutions of (10) form a much larger class among which, however, we may find the solutions of (7). Now, it is easy to solve (10) for $E(r)$ in terms of $f(r)$ and obtain the general solution for the wavefunction $S(r)$. It is

$$S(r)=C\sin[\Phi(r)+\alpha]+\int_0^r dr' f(r')\cos[\Phi(r)-\Phi(r')], \tag{11}$$

where

$$\Phi(r)=\int_0^r(\lambda-V(r'))\,dr'. \tag{12}$$

As a solution of (7), this is merely a representation since it contains the arbitrary function $f(r)$ which may even depend on λ. Nevertheless, it is useful for us because we shall see that the wavefunction and the eigenvalues are independent of $f(r)$ in the approximation in which it is regarded as slowly varying. Keeping $f(r)$ undetermined for the present, we notice that the wavefunction vanishes as $r\to\infty$ if (and only if)

$$C=-\int_0^\infty f(r)\sin(\Phi(r)+\alpha)\,dr, \tag{13}$$

and

$$0=\int_0^\infty f(r)\cos(\Phi(r)+\alpha)\,dr. \tag{14}$$

The last equation would determine λ if $f(r)$ and α were known. If the potential is bounded at the origin then the form of the wavefunction near $r=0$ requires $\alpha=0$ and we shall assume this unless otherwise stated. $f(r)$ can be determined, in principle, for it satisfies an integral equation by virtue of the fact that $S(r)$ and $C(r)$ (which is obtained from the same solution of (10)) are related to each other via (6) and (8) being the sine and cosine transform of one and the same function $p\phi(p)$. Explicitly, this integral equation is

$$\int_0^\infty dr' f(r')\int_0^{r'} dr\sin(\Phi(r)-\Phi(r')+pr)=0, \tag{15}$$

but solving this exactly is clearly a hopeless task. Rather we notice that with

$$S(r)=-\int_r^\infty f(r')\cos(\Phi(r)-\Phi(r'))\,dr', \tag{16}$$

in view of (11), (13) and (14), we have

CC-0. In Public Domain. Gurukul Kangri Collection, Haridwar

Digitized by Arya Samaj Foundation Chennai and eGangotri

$$S''(r) = -(\Phi'(r))^2 S(r) + \Phi''(r)C(r) + f'(r), \tag{17}$$

where $C(r)$ is derived from the same solution of (10) and is obtained by replacing cosine by minus sine in (16). Equation (17) is apparently an inhomogeneous one, but it is important to note that if we had a true solution of (5) or (7), then this will uniquely determine the form of $f(r)$ in (10). But the point of the representation (16) is that we can assume $f(r)$ to be slowly varying and, in fact, set $f(r) = -1$ (for convenience). In the allowed region, we expect $S(r)$ and $C(r)$ to have the same order of magnitude, so for *constant* $\Phi'(r)$, $S(r)$ will be an eigenfunction of (5) for we can *formally* represent the operator p by $(-d^2/dr^2)^{1/2}$ and an eigenfunction of a positive Hermitean operator A is also an eigenfunction of $(A)^{1/2}$. From this, we can infer that for large λ and for slowly varying potentials, for which the second term above may be neglected in comparison to the first, $S(r)$ will be an approximate solution of (5). Actually, as we shall show below, the second term includes the dominant term taking account of the variation of the potential in (5). The presence of this term is, in fact, essential for obtaining a normalizable solution. At large distances the wavefunction $S(r)$ has the form

$$S(r) \to \frac{V'(r)}{(V(r)-\lambda)^3}, \tag{18}$$

and the wavefunction is square integrable for all confining potentials. The quantization rule can be obtained from (14). The integral can be evaluated by the method of stationary phase and is dominated by contributions from around the turning point r_0 defined by $V(r_0) = \lambda$. We use the standard formula

$$\int_0^\infty \cos \Phi(r)\, dr \cong \left(\frac{2\pi}{V'(r_0)}\right)^{1/2} \cos\left(\Phi(r_0) - \frac{\pi}{4}\right), \tag{19}$$

derived in the stationary phase approximation by expanding the integrand about the turning point. Equating this to zero, we get

$$\int_0^{r_0} (\lambda - V(r))\, dr = (n + \tfrac{3}{4})\pi. \tag{20}$$

These results can be compared to some exact results. For the simple potential $V(r) = r^2$, the eigenvalue equation can be solved in momentum space. The eigenfunctions are the Airy functions which we shall write in this case as

$$p\phi(p) = \int_0^\infty \cos\left(\int_0^u V(w)\, dw + (p-\lambda)u\right) du, \tag{21}$$

and the eigenvalue is determined from the condition that this vanish at $p = 0$

$$0 = \int_0^\infty \cos\left(\int_0^u V(w)\, dw - \lambda u\right) du, \tag{22}$$

and agrees exactly with (14) for $\alpha = 0$. More generally, we can solve exactly the eigenvalue equation for any potential $V(r)$ which is a polynomial in r^2 of degree n, say. The resulting differential equation of order $2n$ is of the Laplace type (Spain and Smith 1970) and has exactly n solutions which vanish as $p \to \infty$ and (21) is one of them. The

CC-0. In Public Domain. Gurukul Kangri Collection, Haridwar

Digitized by Arya Samaj Foundation Chennai and eGangotri

general solution is a linear combination of those and the eigenvalues are determined from the condition that the wave function ($p\phi(p)$) and its first $n-1$ even order derivatives vanish at the origin $p = 0$ as required by the Hermiticity of the Hamiltonian. An analysis of these equations shows that although (21) differs from the true wavefunction significantly for $p \to \infty$, it is the true wavefunction to within terms which are suppressed by some power of λ at $p = 0$ and (22) is the correct eigenvalue equation in the same sense (i.e. correct to $O(\lambda^{-\beta})$ for some $\beta > 0$.) The correct asymptotic behaviour of the wavefunction in coordinate space for the polynomial potential turns out to be r^{-2n-3} which agrees with (18) for $n = 1$. For $n = 2$, the coefficient of the leading term (r^{-7}) is suppressed by some power of λ and the dominant term appears to be r^{-9} in agreement with (18) and this probably is true generally.

These comparisons make it plausible that $f(r) =$ constant represents a reasonable approximation to the true wavefunction in (16). We shall now show directly that this is a well-defined semiclassical approximation by identifying and isolating terms whose neglect, with *a priori* justification, leads to this choice. First, we note that the eigenvalue equation (5) can also be written in the "squared version" as

$$p^2\psi + [p, V(r)]\psi - (\lambda - V(r))^2\psi = 0, \tag{23}$$

which is like a Schrödinger equation with a complex, energy-dependent, non-local potential. Because of the wrong sign of the real part of the potential, normalizable solutions exist only because of the strong absorption provided by the purely imaginary second term. We can use the identity (see Appendix)

$$[p, V(r)] = \frac{-i}{2}(\nabla V\cdot\hat{p} + \hat{p}\cdot\nabla V) + \tfrac{1}{4}[p, [\hat{p}_\alpha, [\hat{p}_\alpha, V(r)]]], \tag{24}$$

where $\hat{p} = \mathbf{p}/p$ (and $\hat{p}_\alpha$ are its components). Dimensional estimates show that the last term is $O(1/n^2)$ relative to the terms to be retained and may be neglected. (The method of obtaining these and other estimates is explained in the Appendix). The identity

$$\hat{p} = \hat{r}(\hat{r}\cdot\hat{p}) - \frac{\hat{r}}{r}\times\frac{1}{p}\mathbf{L}, \tag{25}$$

then shows that to a relative accuracy of $O(l/n)$ we can identify $[p, V(r)] \cong -iV'(r)$. This term is already included in (17), the effect of $-i$ being the change of the wave function $S(r)$ to $C(r)$. Equation (23) thus reduces to (17) when the triple commutator (which must be small in the classical limit for slowly varying potentials) is neglected, the operator $\hat{p}$ is replaced by the operator $\hat{r}$ for S-waves and the effect of $-i$ in the term which depends on the derivative of the potential is taken into account by changing the sine wave into cosine wave ($S(r)$ to $C(r)$). The approximation is thus physically justified. Equation (23) can also be used to generalize the above solutions to potentials which are unbounded at the origin. For this it is necessary to get a solution of (23) directly out to some distance where the singularity has been tamed. After that we take the approximate solution (11) with the phase shift α taken from the exact solution of the singular part. Because of this (20) is modified by a term α on the left. α can also be estimated in various ways if an exact solution is not available.

CC-0. In Public Domain. Gurukul Kangri Collection, Haridwar

Digitized by Arya Samaj Foundation Chennai and eGangotri

3. Generalization to non-zero angular momentum

The case $l \neq 0$ is fundamentally different from the S-wave case in that the Hamilton–Jacobi equation (4a) shows that σ_0 becomes imaginary in some region around the turning point before becoming real again. This implies the existence of a potential barrier in that region. The height and the width of this barrier depend on l and vanish with it. For that reason, we can hope to extend the above formalism to non-zero l at least where l can be considered small in some sense. For $l \neq 0$ the eigenvalue equation is a generalization of (7)

$$\int_0^\infty p(p\phi(p))\, f_l(pr)\, \mathrm{d}p = (\lambda - V(r)) \int_0^\infty p\phi(p)\, f_l(pr)\mathrm{d}p, \tag{26}$$

where $f_l(x) = xj_l(x)$, $(g_l(x) = -xn_l(x))$ are the spherical Bessel functions multiplied by $x(-x)$. For large r this equation is identical with (7) except for an unimportant phase shift. Thus although a direct representation on the lines of (11) is not possible, we can attempt a representation by analogy:

$$S_l(r) = r\psi_l(r) = f_l(\Phi(r)) \int_r^\infty g_l'(\Phi(r'))\, f(r')\, \mathrm{d}r' + g_l(\Phi(r)) \int_0^r f_l'(\Phi(r'))\, f(r')\, \mathrm{d}r', \tag{27}$$

subject to the condition

$$\int_0^\infty f_l'(\Phi(r))\, f(r)\, \mathrm{d}r = 0, \tag{28}$$

(prime on a function denotes differentiation with respect to its argument). The function $f(r)$ must vanish sufficiently rapidly as $r \to 0$ so that the integrals converge and in analogy with the $l = 0$ case, we expect that $f(r) \to 1$ at large distances, but otherwise it is not determined. A simple interpolating form for $f(r)$ is

$$f(r) = x^{l+1}/(1 + x^{l+1}), \tag{29}$$

where $x = |\Phi(r)|$. Direct differentiation gives

$$-S_l + \frac{l(l+1)}{r^2} S_l = (\Phi')^2 S_l - \Phi'' C_l - \frac{l(l+1)}{r^2}\left[\left(\frac{r\Phi'(r)}{\Phi(r)}\right)^2 - 1\right] S_l - f'(r), \tag{30}$$

where C_l which is the generalization of $C(r)$ is obtained by replacing f_l, g_l by f_l', g_l' in front of the integrals in (27).The various terms in this equation should be compared to the exact equation (23) which is valid for all angular momenta. The second term on the right of (30) is the analogue of the second term in (23) and is obtained from it by the same steps as for S-waves (neglect of triple commutator, changing $\hat{p}$ to $\hat{r}$ and $-iS_l(r)$ to $C_l(r)$). This is justified only for small angular momenta. The last term is apparently an inhomogeneous term but with the chosen form of $f(r)$ it corresponds to a short-ranged potential singular (like r^{-1}) at the origin but contributing a phase shift which is $O(\lambda^{-1})$ and hence negligible. The most dangerous term is the third term on the right of (30). It is

CC-0. In Public Domain. Gurukul Kangri Collection, Haridwar

Digitized by Arya Samaj Foundation Chennai and eGangotri

bounded if the potential $V(r) \sim r^2$ near the origin and has the relative magnitude $l(l+1)\lambda^{-2-(2/n)}$ compared to the first term if $V(r) \sim r^n$ at large distances. On the other hand if $V(r) \sim r^\beta$ with $0 < \beta < 2$ near the origin, then this term is unbounded at the origin and contributes a phase shift $O(l(l+1)/\lambda^2)$ if cut off at some distance ~ 1. If these are negligible, then (27) is the approximate semi-classical eigenfunction that we require. Evaluating (28) by the method of stationary phase in which case the integral is dominated by contributions from around the turning point r_0 given by $V(r_0) = \lambda$ where we may write $f(r) \approx 1$ and use the asymptotic form of Bessel functions appropriate for $l \ll \Phi(r_0)$, we get the quantization rule

$$\int_0^{r_0} (\lambda - V(r))\, \mathrm{d}r = (n + \tfrac{1}{2}l + \tfrac{3}{4})\pi\,, \tag{31}$$

which differs in this limit from (20) exactly by the phase shift produced by the centrifugal potential as compared to the $l = 0$ case. There are no exact results in this case but (31) agrees with the result of the application of ordinary WKB approximation in momentum space to the potential $V(r) = r^2$ for the limiting case $l \ll n$ relevant here. The opposite case $l \gtrsim n$, in particular the case $l \gg n$ (circular orbits) is excluded from the domain of validity of (31).

Since $\Phi(r)$ has a positive maximum at $r = r_0$ and then a continuous decrease to $-\infty$ for confining potentials, it vanishes at some point far out in the classically forbidden region. This leads to a singularity of the approximate wavefunction there for $l \neq 0$. It is not possible by this method to have globally smooth wavefunctions which lead to correct eigenvalues. The best choice for wavefunction appears to be one which corresponds to the redefinition

$$\Phi(r) = \int_0^r |\lambda - V(r')|\, \mathrm{d}r', \tag{32}$$

in (25) but this leads to an error of $O(1)$ in the eigenvalues (31) because it corresponds to a wavefunction which is not sufficiently smooth around the turning point.

4. Conclusion

It appears possible to apply semiclassical approximation to relativistic potentials, despite the fact that for confining potentials the equivalent Schrödinger potential is negative unbounded as displayed in (23). The final result as given in (20) and (31) is extremely simple but is valid only for $0 \lesssim l \ll n$ and therefore excludes the case of circular orbits. A result that appears to be valid in both limiting cases is the expected one

$$\int \left((\lambda - V(r))^2 - \frac{(l+\frac{1}{2})^2}{r^2} \right)^{1/2} \mathrm{d}r = (n + \tfrac{1}{2})\pi, \tag{33}$$

with limits being determined by the classical turning points. Equation (33) is reasonable for large l (circular orbits) in which limit the potential barrier referred to earlier may be considered to extend to infinity producing an NR-like situation. Whether the formula also holds generally in the semiclassical approximation is not known in the absence of

CC-0. In Public Domain. Gurukul Kangri Collection, Haridwar

Digitized by Arya Samaj Foundation Chennai and eGangotri

any proof. A proof of the formula (33) can also help us to deduce the formula for the general case ($m \neq 0$) covered by (1).

Appendix A

The identity (24) is derived as follows. Writing $p = \hat{p}\cdot\mathbf{p} = \mathbf{p}\cdot\hat{p} = \frac{1}{2}(\hat{p}\cdot\mathbf{p} + \mathbf{p}\cdot\hat{p})$, we find

$$[p, V(r)] = -\frac{i}{2}(\nabla V\cdot\hat{p} + \hat{p}\cdot\nabla V) + \tfrac{1}{2}\mathbf{p}\cdot[\hat{p}, V(r)] + \tfrac{1}{2}[\hat{p}, V(r)]\cdot\mathbf{p}\cdot \tag{A.1}$$

But we have the identity $\hat{p}\cdot[\hat{p}\cdot f(r)] + [\hat{p}, f(r)]\cdot\hat{p} = 0$ since $\hat{p}^2 = 1$ and hence commutes with everything. From this we find

$$\tfrac{1}{2}\mathbf{p}\cdot[\hat{p}, V(r)] = \tfrac{1}{4}p[\hat{p}_\alpha, [\hat{p}_\alpha, V(r)]], \tag{A.2}$$

and (24) then follows. Equation (25) follows from the identity

$$\mathbf{r}\times(\mathbf{r}\times\mathbf{p}) = \mathbf{r}(\mathbf{r}\cdot\mathbf{p}) - r^2\mathbf{p}. \tag{A.3}$$

In the text we have given estimates for various quantities. The principle behind this is the following. Terms which are bounded are estimated by evaluating them near the turning point. For instance, we estimate the triple commutator in (24) to have the magnitude $\sim V'''(r)/p^2$. Noting that $rp \sim n$ because of the quantization condition, we estimate the triple commutator to have the relative magnitude $O(1/n^2)$ with respect to the term $\sim V'(r)$ retained in (24). When terms which are unbounded occur in the equation, their influence cannot be estimated by this method. Now the singularity can occur only at the origin, so its influence can be estimated by the method mentioned at the end of §2. For example, the term $f'(r)$ in (30) is equivalent to a short-ranged potential with a r^{-1} singularity at the origin. Near the origin, (30) is like a Schrödinger equation with λ acting as the wavenumber. We can therefore estimate the phase shifts by methods familiar in NR quantum mechanics. This leads to the estimate $O(\lambda^{-1})$ for the phase shift which can, therefore, be neglected.

References

Rohrlich F 1979 *Ann. Phys. NY* **117** 292
Spain B and Smith M G 1970 *Functions of mathematical physics* (London: Van Nostrand Reinhold)
Thakur J 1978 *Pramana–J. Phys.* **27** 731

CC-0. In Public Domain. Gurukul Kangri Collection, Haridwar

Digitized by Arya Samaj Foundation Chennai and eGangotri

Pramāṇa – J. Phys., Vol. 28, No. 1, January 1987, pp. 9–14. © Printed in India.

Superconformal transformations of the $N = 2$, $D = 4$, SSYM

MAYANK R MEHTA

Department of Physics, Indian Institute of Science, Bangalore 560012, India

MS received 24 July 1986

Abstract. We obtain the superconformal transformation laws for the $N = 2$, $D = 4$ SSYM. The transformations involve Yang-Mills fields and the corresponding field strength tensor is not constrained to be self antidual. We explicitly demonstrate the closure of the superconformal algebra.

Keywords. Extended supersymmetry; superconformal symmetry.

PACS No. 11·30

Supersymmetric theories have an important property that some of the perturbative ultraviolet divergences due to bosons and fermions cancel each other. Extended supersymmetric theories have more than one supersymmetry. Such theories have even better ultraviolet behaviour than $N = 1$ SUSY (supersymmetric) theory. For example, the SSYM (supersymmetric Yang-Mills theory) with two generators ($N = 2$) of SUSY is believed to be finite beyond one loop, (Grisaru and Siegel 1982 and Howe *et al* 1983) and $N = 4$ SSYM is believed to be finite to all orders in perturbation (Mandelstam 1983; Howe *et al* 1983; Brink *et al* 1983; Salam *et al* 1983). Classical SSYM theories are conformally invariant and hence are also superconformally invariant. The $N = 2$ superconformal algebra is known (Sohnius 1985), a representation of which was found by Dondi and Sohnius (1974). However, that representation involved only self antidual, antisymmetric tensor field, and no Yang-Mills gauge fields. In the following we obtain a representation of the $N = 2$ superconformal algebra which involves Yang-Mills fields and the corresponding field strength tensor is not restricted to be self antidual.

The $N = 2$ superconformal algebra in $3 + 1$ dimensions contains fifteen generators of the usual conformal group corresponding to four translations P_μ, six rotations $M_{\mu\nu}$, one dilatation D, and four conformal boosts K_μ. In addition there are four four-component Majorana fermionic generators (Sohnius 1985), or equivalently four two-component Weyl fermions and their hermitian conjugates. These are SUSY generators $Q_{i\alpha}$ and $\bar{Q}_i^{\dot{\alpha}}$; and superconformal generators $S_{i\alpha}$ and $\bar{S}_i^{\dot{\alpha}}$ with $i = 1, 2$—and, the Weyl spinor indices are α and $\dot{\alpha}$. In this Weyl representation $Q_{i\alpha}$'s can be rotated into each other under global SU(2) transformations. The generators of this SU(2) will be represented by traceless part of B_i^j. Further, the algebra also involves the chiral charge R, which is represented by 2 (trace B_i^j). In four-component notation these charges can be combined into a Dirac SUSY charge and a Dirac superconformal charge,

$$Q = \begin{pmatrix} Q_{1\alpha} \\ i\bar{Q}^{2\dot{\alpha}} \end{pmatrix} \quad \text{and} \quad S = \begin{pmatrix} iS_\alpha^2 \\ \bar{S}_1^{\dot{\alpha}} \end{pmatrix}. \tag{1}$$

CC-0. In Public Domain. Gurukul Kangri Collection, Haridwar

Digitized by Arya Samaj Foundation Chennai and eGangotri

(Alternatively these charges can be combined, to form two four-component Majorana supercharges and two four-component Majorana superconformal charges. However, these will mix under SO(2) instead of SU(2).)

The conformal algebra is well known and is given by:

$$
\begin{aligned}
&[M_{\mu\nu}, M_{\rho\sigma}] = i(g_{\nu\rho}M_{\mu\sigma} - g_{\mu\rho}M_{\nu\sigma} - g_{\nu\sigma}M_{\mu\rho} + g_{\mu\sigma}M_{\nu\rho}),\\
&[P_\mu, M_{\rho\sigma}] = i(g_{\mu\rho}P_\sigma - g_{\mu\sigma}P_\rho), \quad [K_\mu, M_{\rho\sigma}] = i(g_{\mu\rho}K_\sigma - g_{\mu\sigma}K_\rho),\\
&[D, M_{\mu\nu}] = [P_\mu, P_\nu] = [K_\mu, K_\nu] = 0,\\
&[P_\mu, D] = iP_\mu, \quad [K_\mu, D] = -iK_\mu,\\
&[P_\mu, K_\nu] = 2i(g_{\mu\nu}D - M_{\mu\nu}).
\end{aligned}
\tag{2}
$$

The supersymmetrized version of this algebra with two supersymmetries (in four-component Dirac notation) also includes (Sohnius 1985)

$$
\begin{aligned}
&[Q, M_{\mu\nu}] = i\Sigma_{\mu\nu}Q, \quad [S, M_{\mu\nu}] = i\Sigma_{\mu\nu}S,\\
&[Q, D] = iQ/2, \quad [S, D] = -iS/2,\\
&[Q, P_\mu] = 0, \quad [S, P_\mu] = \gamma_\mu Q,\\
&[Q, K_\mu] = \gamma_\mu S, \quad [S, K_\mu] = 0,\\
&[Q, R] = \gamma_5 Q, \quad [S, R] = -\gamma_5 S,\\
&[R, M_{\mu\nu}] = [R, P_\mu] = [R, K_\mu] = [R, D] = 0,\\
&\{Q, \overline{Q}\} = 2\gamma^\mu P_\mu,\\
&\{S, \overline{S}\} = 2\gamma_\mu K^\mu.
\end{aligned}
\tag{3a}
$$

To see the appearance of the global SU(2) generators we write the fermionic charges in two-component Weyl representation, $Q_{i\alpha}$, $\overline{Q}_i^{\dot\alpha}$, $S_{i\alpha}$, $\overline{S}_i^{\dot\alpha}$, in terms of which we have

$$
\begin{aligned}
&\{Q_{i\alpha}, S^{j\beta}\} = 2i\,\delta_i^j(D + \sigma^{\mu\nu}M_{\mu\nu})_\alpha^\beta - 4B_i^j\,\delta_\alpha^\beta,\\
&[Q_i, B_j^k] = \delta_i^k Q_j - \tfrac{1}{4}(\delta_j^k)Q_i,\\
&[\overline{Q}^i, B_j^k] = -\delta_j^i\,\overline{Q}^k + \tfrac{1}{4}(\delta_j^k)\overline{Q}^i,\\
&[B_i^j, B_k^l] = \delta_i^l B_k^j - \tfrac{1}{4}(\delta_k^j)B_i^l,\\
&(B_i^j)^\dagger = B_j^i.
\end{aligned}
\tag{3b}
$$

The traceless parts of B_i^j are the global SU(2) generators and $2\,\mathrm{Tr}(B_i^j) = R$ is the chiral charge. And $(\sigma_\mu)_{\alpha\dot\beta} = (\sigma_0, \sigma_i)_{\alpha\dot\beta}$, $(\overline{\sigma}_\mu)^{\dot\alpha\beta} = (\sigma_0, -\sigma_i)^{\dot\alpha\beta}$, with $\sigma_{\mu\nu} = (1/4)\,[\sigma_\mu, \overline{\sigma}_\nu]$, in terms of which the usual 4×4 Dirac matrices are, $\gamma_\mu = \begin{pmatrix} 0 & \sigma_\mu \\ \overline{\sigma}_\mu & 0 \end{pmatrix}$, $\gamma_5 = i\gamma_0\gamma_1\gamma_2\gamma_3$ and $\Sigma_{\mu\nu} = \frac{1}{4}[\gamma_\mu, \gamma_\nu] = \begin{pmatrix} \sigma_{\mu\nu} & 0 \\ 0 & \overline{\sigma}_{\mu\nu} \end{pmatrix}$.

A representation of the algebra

Let us discuss a representation of this algebra (equations (2) and (3)) involving Yang-

CC-0. In Public Domain. Gurukul Kangri Collection, Haridwar

Digitized by Arya Samaj Foundation Chennai and eGangotri

Mills gauge fields A_μ^a. In four dimensions a massless vector field has two degrees of freedom, and a Weyl fermion also has two degrees of freedom. To have $N = 2$ SSYM we must have two Weyl fermions (or equivalently a four-component Dirac spinor). To match the Bose-Fermi degrees of freedom the $N = 2$ multiplet should have two more bosonic degrees of freedom, which correspond to two scalars S^a and P^a. Thus the $N = 2$, SSYM field multiplet consists of an $N = 1$ gauge multiplet and an $N = 1$ chiral multiplet (Sohnius 1985).

Supersymmetry transformation properties of the scalar fields S^a and P^a, vector field A_μ^a and, Dirac spinor field λ^a have been obtained by dimensional reduction of $N = 1$ SSYM multiplet in six dimensions (Brink *et al* 1977). Those are as follows:

$$\begin{aligned}
&\delta_Q(\varepsilon)S^a = i[S, \bar{Q}\varepsilon + \bar{\varepsilon}Q] = i(\bar{\varepsilon}\lambda^a - \bar{\lambda}^a\varepsilon),\\
&\delta_Q(\varepsilon)P^a = (\bar{\varepsilon}\gamma_5\lambda^a - \lambda^a\gamma_5\bar{\varepsilon}),\\
&\delta_Q(\varepsilon)A_\mu^a = i(\bar{\varepsilon}\gamma_\mu\lambda^a - \bar{\lambda}^a\gamma_\mu\varepsilon),\\
&\delta_Q(\varepsilon)\lambda^a = [\Sigma_{\mu\nu}F^{\mu\nu a} + (\not{D}(i\gamma_5 P - S))^a - ig\gamma_5(P \times S)^a]\varepsilon,
\end{aligned} \tag{4}$$

where $(P \times S)^a = f^{abc}P^bS^c$ and, f^{abc} are the structure constants of the gauge group. The transformation parameter ε is a four-component, complex Grassman variable. The on shell $N = 2$ SSYM Lagrangian density is given by (Brink *et al* 1977):

$$\begin{aligned}
L = {} & (-1/4)F_{\mu\nu}^a F^{\mu\nu a} + (1/2)D_\mu S^a D^\mu S^a + (1/2)D_\mu P^a D^\mu P^a + i\bar{\lambda}^a(\not{D}\lambda)^a\\
& + ig\bar{\lambda} \times \lambda \cdot S + g\bar{\lambda}\gamma_5 \times \lambda \cdot P - (g^2/2)(P \times S)^2.
\end{aligned} \tag{5}$$

To obtain the $N = 2$ superconformal transformation laws, consider the following set of equation (3a):

$$[Q, K_\mu] = \gamma_\mu S \Rightarrow [\gamma_\mu Q, K^\mu] = 4S.$$

For a generic field X^a,

$$4[X^a, S] = [X^a, [\gamma^\mu Q, K_\mu]] = -[[X^a, \gamma^\mu Q], K_\mu] + [[X^a, K_\mu], \gamma^\mu Q], \tag{6}$$

where the conformal transformation property of X^a is given by

$$[X^a, K_\mu] = i[2x_\mu x \cdot \partial - x^2\partial_\mu + 2x_\mu d + x^\nu \Omega_{\mu\nu}]X^a \tag{7}$$

with mass dimension $d = 1$ for bosons and $d = 3/2$ for fermions; and the proper Lorentz transformation matrices $\Omega_{\mu\nu}$ are given by

$$\begin{aligned}
&\Omega_{\mu\nu}P^a = 0, \quad \Omega_{\mu\nu}S^a = 0,\\
&\Omega_{\mu\nu}^{\rho\sigma}A_\sigma^a = (g_\mu^\rho g_\nu^\sigma - g_\mu^\sigma g_\nu^\rho)A_\sigma^a,\\
&(\Omega_{\mu\nu})_{\alpha\beta}\lambda_\beta^a = (1/2)[\gamma_\mu, \gamma_\nu]_{\alpha\beta}\lambda_\beta^a.
\end{aligned} \tag{8}$$

Using these and the SUSY transformation laws, (6) can be evaluated. For example for a scalar field S^a

$$\begin{aligned}
4[S^a, \bar{\zeta}S] &= -[\bar{\zeta}\gamma^\mu\lambda^a, K_\mu] + i[[2x_\mu x \cdot \partial - x^2\partial_\mu + 2x_\mu]S^a, \bar{\zeta}\gamma^\mu Q]\\
&= -4i\bar{\zeta}x_\mu\gamma^\mu\lambda^a;
\end{aligned} \tag{9}$$

CC-0. In Public Domain. Gurukul Kangri Collection, Haridwar

Digitized by Arya Samaj Foundation Chennai and eGangotri

where $\bar{\zeta}$ is the transformation parameter, again a four component Grassman variable. Similarly $4[S^a, \bar{\zeta} S] = -4i\bar{\lambda}^a x_\mu \gamma^\mu \zeta$. Thus the superconformal transformation laws for the whole multiplet can be evaluated to be

$$\begin{aligned}
\delta_s(\zeta) S^a &= -(\bar{\zeta} x_\mu \gamma^\mu \lambda^a + \bar{\lambda}^a \gamma_\mu x^\mu \zeta), \\
\delta_s(\zeta) P^a &= i(\bar{\zeta} \not{x} \gamma_5 \lambda^a + \bar{\lambda}^a \gamma_5 \not{x} \zeta), \\
\delta_s(\zeta) A_\mu^a &= -(\bar{\zeta} \not{x} \gamma_\mu \lambda^a + \bar{\lambda}^a \gamma_\mu \not{x} \zeta), \\
\delta_s(\zeta) \lambda^a &= [\Sigma^{\mu\nu} F_{\mu\nu}^a + (\not{D}(i\gamma_5 P - S))^a - ig\gamma_5 (P \times S)^a](-i\not{x}\zeta) \\
&\quad + 2i(i\gamma_5 P^a + S^a)\zeta. \qquad (10)
\end{aligned}$$

Thus the superconformal transformation laws for bosons look similar to the SUSY transformation laws if we call $-i\not{x}\zeta$ as ε. However, for the fermion transformation, there is a term which contains ζ and not $\not{x}\zeta$. This is in contrast to $N = 1$ SSYM transformations where mere replacement of SUSY transformation parameter ζ by $-i\not{x}\zeta$ in SUSY transformations gives the superconformal transformation laws. The difference arises because $N = 2$ SSYM multiplet contains an $N = 1$ chiral multiplet also, and the superconformal transformation of the fermion belonging to the chiral multiplet will exhibit this extra piece.

It is instructive to study the closure of the transformation laws thus obtained. In particular let us study the commutator of superconformal transformations on scalar field S^a: (We will denote $-i\not{x}\zeta$ by η)

$$\begin{aligned}
[\delta_s(\zeta_1), \delta_s(\zeta_2)] S^a &= [2i\bar{\eta}_2(-\not{D} S)^a \zeta_1 - 2i\bar{\eta}_2(ig\gamma_5 (P \times S)^a \eta_1 \\
&\quad - 2(\bar{\eta}_2 \zeta_1 - \bar{\zeta}_2 \eta_1) S^a] \qquad (11) \\
&- \zeta_1 \leftrightarrow \zeta_2.
\end{aligned}$$

These terms can be rearranged as

$$\begin{aligned}
&2i(\bar{\zeta}_1 \gamma_\mu \zeta_2 - \bar{\zeta}_2 \gamma_\mu \zeta_1)[2x_\mu x \cdot \partial - x^2 \partial_\mu + 2x_\mu] S^a \\
&-2i\{S \times [\bar{\eta}_1 (\not{A} + i\gamma_5 P)\eta_2 - \bar{\eta}_2 (\not{A} + i\gamma_5 P)\eta_1]\}^a. \qquad (12)
\end{aligned}$$

The first term is the conformal transformation (6) of S^a, by an amount $(\bar{\zeta}_1 \gamma_\mu \zeta_2 - \bar{\zeta}_2 \gamma_\mu \zeta_1)$. The second term is a field-dependent Yang-Mills gauge transformation of S^a by an amount $(\bar{\eta}_1 (\not{A}^b + i\gamma_5 P^b)\eta_2 - \bar{\eta}_2 (\not{A}^b + i\gamma_5 P^b)\eta_1]$.

Thus the algebra closes only upto a field-dependent local gauge transformation. This is because we are in the Wess-Zumino gauge. The effect of the commutator of two superconformal transformations on other members of the multiplet can be evaluated in the same manner. For the fermion the proof of closure will also require the use of equations of motion, as implied by the Lagrangian (5), because we are working on shell. Thus for a generic field X^a the final result can be written as

$$\begin{aligned}
[\delta_s(\zeta_1), \delta_s(\zeta_2)] X^a &= 2[X^a, (\bar{\zeta}_1 \gamma_\mu \zeta_2 - \bar{\zeta}_2 \gamma_\mu \zeta_1) K^\mu + G^b \tilde{\Lambda}^b] \\
&\quad + \text{equations of motion}, \qquad (13)
\end{aligned}$$

where G^b is the generator of local gauge transformation, by an amount

$$\tilde{\Lambda}^b = \bar{\eta}_1 (\not{A}^b + i\gamma_5 P^b - S^b)\eta_2 - \bar{\eta}_2 (\not{A}^b + i\gamma_5 P^b - S^b)\eta_1. \qquad (14)$$

CC-0. In Public Domain. Gurukul Kangri Collection, Haridwar

Digitized by Arya Samaj Foundation Chennai and eGangotri

Similarly we can compute the commutator of SUSY transformation with superconformal transformation on different fields. As we can see from the algebra (3b), the right hand side will involve generators of global SU(2). The two-component Weyl fermions transform as doublet under these SU(2) rotations, and all the bosons are invariant. Thus to see the effect of global SU(2), the Dirac fermion λ^a, should be written in terms of two two-component Weyl spinors, λ_1^a and λ_2^a and similarly all the other anticommuting objects. Thus using,

$$Q = \begin{pmatrix} Q_{1\alpha} \\ i\bar{Q}^{2\dot{\alpha}} \end{pmatrix}, \quad S = \begin{pmatrix} iS^2 \\ \bar{S}_1 \end{pmatrix}, \quad \eta = \begin{pmatrix} \eta_1 \\ i\bar{\eta}^2 \end{pmatrix}, \quad \varepsilon = \begin{pmatrix} i\varepsilon^2 \\ \bar{\varepsilon}_1 \end{pmatrix} \quad \text{and} \quad \lambda^a = \begin{pmatrix} \lambda^{a2} \\ i\bar{\lambda}_1^a \end{pmatrix}.$$

$$[\delta_Q(\varepsilon), \delta_s(\zeta)] X^a = -[X^a, 2i[(\bar{\zeta}\Sigma_{\mu\nu}\varepsilon - \bar{\varepsilon}\Sigma_{\mu\nu}\zeta) M^{\mu\nu} + (\bar{\zeta}\varepsilon + \bar{\varepsilon}\zeta)D + G^b\tilde{\Lambda}'^b] - 4Y_j^i B_i^j] + \text{equations of motion}, \tag{15}$$

where $Y_j^i = \varepsilon^{i\alpha}\eta_{j\alpha} - \bar{\eta}_{\dot{\alpha}}^i\bar{\varepsilon}_j^{\dot{\alpha}}$ is the amount by which SU(2) rotation is performed. The field-dependent gauge transformation parameter is $\tilde{\Lambda}'^b$

$$\tilde{\Lambda}'^b = \bar{\varepsilon}(\not{A}^b + i\gamma_5 P^b - S^b)\eta - \bar{\eta}(\not{A}^b + i\gamma_5 P^b - S^b)\varepsilon. \tag{16}$$

The dilatation and Lorentz transformation of X^a are given by

$$[X^a, D] = i(x\cdot\partial + d)X^a \quad \text{and,}$$

$$[X^a, M_{\mu\nu}] = i(x_\mu\partial_\nu - x_\nu\partial_\mu)X^a + i\Omega_{\mu\nu}X^a \tag{17}$$

with $\Omega_{\mu\nu}$ as defined in equation (8). Further the fields transform under chiral charge $R = 2\mathrm{Tr}\,B_i^j$ as

$$[S^a, R] = iP^a, \quad [P^a, R] = -iS^a,$$

$$[A_\mu^a, R] = 0 \quad \text{and} \quad [\lambda^a, R] = \gamma_5(\lambda^a/2). \tag{18}$$

Thus we have obtained a representation for the $N = 2$ superconformal algebra, involving Yang-Mills fields, with the corresponding field strength unconstrained. This is in contrast with the earlier attempt where the representation involved only self anti-dual fields but no gauge field (Dondi and Sohnius 1974).

Acknowledgements

The author thanks Romesh Kaul for help at every stage of the work and, Martin Sohnius and R Rajaraman for discussions. A fellowship from CSIR, New Delhi is gratefully acknowledged.

References

Brink L, Schwarz J H and Scherk 1977 *J. Nucl. Phys.* **B121** 77
Brink L, Lindgren O and Nielson B E W 1983 *Phys. Lett.* **123** 323
Dondi P H and Sohnius M 1974 *Nucl. Phys.* **881** 317
Grisaru M T and Siegel W 1982 *Nucl. Phys.* **B201** 292
Howe P, Stelle K and West P 1983a *Phys. Lett.* **B124** 55

CC-0. In Public Domain. Gurukul Kangri Collection, Haridwar

Digitized by Arya Samaj Foundation Chennai and eGangotri

Howe P, Townsend P K and Stelle K 1983b *Nucl. Phys.* **B214** 519
Mandelstam S 1983 *Nucl. Phys.* **B213** 149
Salam A, Strathdee J and Namazie M A 1983 *Phys. Rev.* **D28** 1481
Sohnius M 1985 *Phys. Rep.* **128** 39

CC-0. In Public Domain. Gurukul Kangri Collection, Haridwar

Digitized by Arya Samaj Foundation Chennai and eGangotri

Pramāṇa – J. Phys., Vol. 28, No. 1, January 1987, pp. 15–22. © Printed in India.

Tree-level breaking of SU(2) × U(1) in general SUGRA theories

ANJAN S JOSHIPURA*, A MUKHERJEE and SANJEEV K SONI†

Department of Physics, Indian Institute of Technology, Kanpur 208 016, India
† Department of Physics and Astrophysics, University of Delhi, Delhi 110 007, India
* Present address: Institute of Mathematical Sciences, Madras 600 113, India
† Present address: Department of Physics, Khalsa College, New Delhi 110 007, India

MS received 3 June 1986; revised 3 October 1986

Abstract. It is shown that SU(2) × U(1) can be broken at the tree level, without the occurrence of global potential minima that break $U(1)_{e.m.}$, in supergravity models that are more general than those proposed by Nilles, Srednicki and Wyler. The study comprises an analysis of models with a general soft supersymmetry-breaking structure as well as those of the Hall-Lykken-Weinberg type.

Keywords. SU(2) × U(1) theory; supergravity; spontaneous symmetry breakdown.

PACS Nos 11·30; 11·15; 12·10; 04·50

1. Introduction

It is now realized# that the breaking of supersymmetry (SUSY) in local SUSY theory, via the super-Higgs effect, generates an effective theory capable of incorporating the spontaneous breakdown of electroweak symmetry. If matter is coupled 'minimally' (Ellis 1983) to supergravity (SUGRA) and if the Higgs sector consists only of SU(2)-doublet fields, then the said breakdown does not occur at the tree level of the effective theory below the Planck mass M_P. Radiative corrections can trigger the breaking (Alvarez Gaume *et al* 1983; Ellis *et al* 1983) if some of the Yukawa couplings are large: this typically requires a top quark with mass $\sim$ 45–50 GeV##.

The electroweak symmetry can be broken at the tree level itself if an SU(2) × U(1)-singlet superfield is present (Nilles *et al* 1983a). The singlet is known, however, (a) to destabilize the gauge hierarchy (Nilles *et al* 1983b; Labanas 1983) and (b) to induce global minima of the potential (Frere *et al* 1983) which spontaneously break the conservation of electric charge. Both these problems have been discussed in a special class of models proposed by Nilles *et al* (1983a), hereafter referred to as NSW. We point out in this paper that the above mentioned problem (b) does not exist in models more general than those of NSW. Coupled with the fact that there exists a way (Ferrara *et al* 1983) to solve problem (a), our observation makes tree-level breaking of SU(2) × U(1) a

---

* To whom correspondence should be addressed.

For a review and original references, Ellis (1983).

This is not an inescapable conclusion: SU(2) × U(1) breaking can also be driven with a light top quark in some models (Claudson *et al* 1983).

CC-0. In Public Domain. Gurukul Kangri Collection, Haridwar

Digitized by Arya Samaj Foundation Chennai and eGangotri

viable alternative for the construction of realistic models.

In §2 we review the problem of electric-charge-breaking minima and discuss its solution with a potential which has a general soft SUSY-breaking structure. Potentials of the Hall-Lykken-Weinberg (HLW) type are considered in §3, and it is argued that charge-conserving global minima probably exist in this case too. Appendix A gives details of minimization of an HLW potential.

2. Charge-preserving minima in general SUGRA theories

It is customary in a SUGRA theory to divide the spin-0 fields into two subsets: $S_A \sim (Z_i, Y_a)$. The 'hidden' fields Z_i acquire vacuum expectation values (VEV's) of $O(M_P)$, while Y_a are the ordinary fields. The scalar potential V at an energy scale M ($M = M_P/\sqrt{8\pi}$) is given by (Ellis 1983).

$$V = \exp(d/M^2)\left(d^{-1}_{AB}F^{\dagger}_{A}F_{B} - 3\frac{|W|^2}{M^2}\right) + \tfrac{1}{2}D^{\alpha}D^{\alpha}. \tag{1}$$

Here d is an arbitrary function of S_A and $S^{\dagger}_A$, and the super-potential W depends on S_A. Moreover,

$$d_{AB} = \frac{\partial^2 d}{\partial S_A \partial S^{\dagger}_B},$$

$$F_A = \frac{\partial W}{\partial S_A} + M^{-2}\frac{\partial d}{\partial S_A}W,$$

and

$$D^{\alpha} = \frac{\partial d}{\partial S_A}t^{\alpha}_{AB}S_B,$$

where (t^{α}) are generators of the internal-symmetry group.

The low energy ($\sim M_W$) limit of V can be derived by eliminating hidden fields as well as those having $O(M_{GUT})$ masses. Three cases can be distinguished:

(a) Here $d = S^{\dagger}_A S_A$, which brings the kinetic energy for scalars into the canonical form, and W is taken as the sum of separate terms involving hidden and ordinary fields respectively:

$$W(S_A) = f(Z_i) + \tilde{g}(Y_a). \tag{2}$$

If one neglects the presence of the GUT sector, the following effective potential is obtained at a scale $\sim M_W$ (Nilles *et al* 1983a)

$$V_{\text{eff}} = |g_a|^2 + m^2_{3/2}\,Y^{\dagger}_a Y_a + m_{3/2}\left[(A-3)g(Y_a) + Y_a\frac{\partial g}{\partial Y_a} + \text{c.c.}\right], \tag{3}$$

where $g = \tilde{g}\exp(\langle Z^{\dagger}_i Z_i\rangle/M^2)$, $g_a = \partial g/\partial Y_a$ and A is a numerical constant. The mass parameter $m_{3/2}$ coincides with the gravitino mass.

(b) If, in addition to the above, the superpotential $g(Y_a)$ is assumed to depend on GUT

CC-0. In Public Domain. Gurukul Kangri Collection, Haridwar

Digitized by Arya Samaj Foundation Chennai and eGangotri

fields, then after integrating out the latter one obtains the HLW potential (Hall *et al* 1983).

$$V_{\text{eff}} = \left|\frac{\partial g_{\text{eff}}}{\partial Y_m}\right|^2 + [m_{3/2}^2 g_3 + 2m_{3/2} g_2 + (4m_{3/2} - m'_{3/2})g_1 + \text{c.c.}] + m_{3/2}^2 |Y_m|^2 + \tfrac{1}{2} D^\alpha D^\alpha \tag{4}$$

$g_{\text{eff}} = g_3 + g_2 + g_1 + g_0$. In the above equation g_i is a homogeneous polynomial of degree i in the light fields Y_m, and $m'_{3/2}$ is a parameter of the same order of magnitude as $m_{3/2}$.

(c) Here W and d are taken to have the following most general allowed structure (Soni and Weldon 1983).

$$W = M^2 W_2(\xi_i) + M W_1(\xi_i) + W_0(Y_a, \xi_i), \tag{5a}$$

$$d = M^2 d_2(\xi_i, \xi_i^\dagger) + M d_1(\xi_i, \xi_i^\dagger) + d_0(\xi_i, \xi_i^\dagger, Y_a, Y_a^\dagger) \tag{5b}$$

with $$\left\langle \frac{\partial^2 d}{\partial Y_a \partial Y_b^\dagger} \right\rangle \equiv \frac{\partial^2 d_0(\langle \xi_i \rangle, \langle \xi_i^\dagger \rangle, Y_a, Y_a^\dagger)}{\partial Y_a \partial Y_b^\dagger} = \delta_{ab}, \qquad \xi_i \equiv Z_i/M.$$

The resulting V_{eff} describes a theory with SUSY broken softly by terms of the most general possible structure consistent with the absence of quadratic divergences.

$$V_{\text{eff}} = \left|\frac{\partial g}{\partial Y_a}\right|^2 + m_{3/2}^2 S_{ab} Y_a^\dagger Y_b + m_{3/2}(h(Y_a) + \text{c.c.}). \tag{6}$$

Here g and h are *a priori* independent cubic polynomials in the fields Y_a, depending on the form of W_0 and d_0, while S_{ab} is a numerical matrix. In the special case $d = Z^\dagger Z^\dagger$, S_{ab} reduces to the identity matrix.

The simplest V_{eff} of (3) can break SU(2) × U(1) at the tree level. Consider two Higgs doublets H, H' with hypercharges $+1/2$, $-1/2$, and a singlet Y, with the following g:

$$g = \lambda H H' Y + \tfrac{1}{3}\sigma Y^3. \tag{7}$$

We are led, through (3), to the following V_{eff}:

$$V_{\text{eff}} = |\lambda|^2(|H|^2 + |H'|^2)|Y|^2 + |\lambda H H' + \sigma Y^2|^2 + m_{3/2}^2(|H|^2 + |H'|^2 + |Y|^2) + m_{3/2} A(\lambda H H' Y + \tfrac{1}{3}\sigma Y^3 + \text{c.c}). \tag{8}$$

It is possible to minimize this V_{eff} exactly (Joshipura *et al* 1986), although only approximate minima are given in the literature (Ellis 1983; Nilles *et al* 1983a; Frere *et al* 1983). The global minimum occurs at

$$\langle H^0 \rangle = \langle H^{0\prime} \rangle = \lambda^{-1} m_{3/2} \left[\frac{A^2 \sigma'}{(1+2\sigma')^2} - 1\right]^{1/2}$$

$$\langle Y \rangle = \lambda^{-1} m_{3/2} \frac{A}{1+2\sigma'}, \tag{9}$$

CC-0. In Public Domain. Gurukul Kangri Collection, Haridwar

Digitized by Arya Samaj Foundation Chennai and eGangotri

where $H^0(H^{0\prime})$ is the neutral component of $H(H')$ and $\sigma' = \sigma/\lambda$ provided

$$|A| > \frac{2\sigma' + 1}{(\sigma')^{1/2}}.$$

Thus SU(2) × U(1) is broken at the tree level. The potential at the minimum is given by (Joshipura *et al* 1986)

$$V_{\min} = \lambda^{-2} m_{3/2}^4 \left[-\frac{2\sigma'}{3} \frac{A^4}{(1+2\sigma')^3} - \frac{A^2}{1+2\sigma'} - 1 \right]. \tag{10}$$

It was noticed by Frere *et al* (1983) that (9) no longer corresponds to a global minimum of the potential if quarks and leptons are included. Let us consider the following g in the presence of leptons:

$$g = \lambda H H' Y + \lambda_e L H' E^+ \tag{11}$$

with L, E^+ respectively corresponding to $SU(2)_L$ doublet and singlet fields. Substitution in (3) shows that the V_{eff} for this theory has a charge-breaking minimum corresponding to non-zero VEV's for E^+ and L^-. The value of the potential at this minimum is scaled by λ_e^{-2} (cf. (10)). Now λ_e is the Yukawa coupling which controls the mass of the electron and hence is expected to be small ($\sim 10^{-6}$). Thus unless λ is also chosen to be at least as small as λ_e the charge-breaking minimum lies lower than the charge-preserving one. In the former case, $U(1)_{\text{e.m.}}$ can be preserved at the cost of the existence of a charged fermion lighter than the electron, as implied by the Yukawa interaction corresponding to $\lambda H H' Y$.

In view of the above serious problem, we address ourselves to the following question: can one obtain an acceptable pattern of SU(2) × U(1) breaking if one goes beyond the simple models described by (3)? The answer, as we show below, is yes. As long as one uses the V_{eff} of (3), the problem persists, since the cubic SUSY-breaking terms are fixed once g is fixed. This restriction is a consequence of the simple form assumed for W (equation (2)). By starting with a more general expression for W as given in (5), one can obtain a V_{eff} (equation (6)) in which the cubic terms are not simply related to g. We take h in (6) to be independent of g and demonstrate that a choice of h exists for which the charge-preserving minimum becomes absolute.

Let us consider the following h in a model with leptons and Higgs fields:

$$h = \lambda' H H' Y + \lambda'_e L H' E^+. \tag{12}$$

Symmetry-breaking terms with this structure are not allowed in NSW or HLW potentials. They can be obtained, however, if W_0 in (5) is chosen to depend nontrivially on hidden fields. With g and h as given by (11) and (12), substitution in (6) yields

$$\begin{aligned} V_{\text{eff}} = {} & |\lambda|^2 |H'|^2 |Y|^2 + |\lambda H^0 Y + \lambda_e L^- E^+|^2 + |\lambda H^\dagger Y + \lambda_e L^0 E^+|^2 \\ & + |\lambda H H'|^2 + |\lambda_e L H'|^2 + |\lambda_e E^+|^2 H'^\dagger H' \\ & + m_{3/2}^2 (H'^\dagger H' + H^\dagger H + L^\dagger L + |E^+|^2 + |Y|^2) \\ & + m_{3/2} (\lambda' H H' Y + \lambda'_e L H' E^+ + \text{c.c.}) + \tfrac{1}{2} D^\alpha D^\alpha. \end{aligned} \tag{13}$$

CC-0. In Public Domain. Gurukul Kangri Collection, Haridwar

Digitized by Arya Samaj Foundation Chennai and eGangotri

We have dropped the Y^3 terms from g for simplicity. They are not expected to change the qualitative conclusions but need to be retained in general to get rid of an unwanted global U(1) symmetry.

It can be seen from (13) that all charged fields are forced to acquire vanishing vacuum expectation values if $|A'| \equiv |\lambda'_e/\lambda_e| < 3$. The charge-preserving solution can still exist if $|A| \equiv |\lambda'/\lambda| \geqslant 3$. V at this minimum is given by (Frere *et al* 1983).

$$\underset{\min}{V(1)} = -m_{3/2}^4/\lambda^2\,(\Delta^2(\Delta^2-1)); \quad \Delta = \tfrac{1}{4}[|A| + (|A|^2-8)^{1/2}]. \tag{14}$$

In the NSW case (corresponding to W_0 being independent of ξ_i) $|A'| = |A|$ and the charge-breaking solution must exist. In general by allowing nontrivial dependence on ξ_i in W_0 one can make $A' < 3$ even when $A > 3$ and avoid the charge-breaking minimum altogether.

Even when $A' > 3$ there exists a reasonable range of parameters for which the charge-breaking minimum lies higher. For $A' > 3$, $\langle L^- \rangle = \langle E^+ \rangle = \langle H^{0\prime} \rangle = (m_{3/2}/\lambda_e)\Delta'$ with all other VEV's vanishing corresponds to a minimum with

$$\underset{\min}{V(2)} = -\frac{m_{3/2}^4}{\lambda_e^2}\Delta'^2(\Delta'^2-1); \quad \Delta' = \tfrac{1}{4}[|A'| + (|A'|^2-8)^{1/2}]. \tag{15}$$

A suitable choice of A and A' can make $V_{\min}(2)$ higher than $V_{\min}(1)$. Consider for example $|A|, |A'| \gg 3$, then $V_{\min}(2) > V_{\min}(1)$ provided

$$\frac{(\lambda_e|A|^2)^2}{(\lambda|A'|^2)^2} > 1,$$

i.e. $$|\lambda'/\lambda'_e| > |\lambda/\lambda_e|.$$

With $\lambda/\lambda_e \sim 10^4$, this needs $\lambda'/\lambda'_e \approx 10^6$. This can be achieved by fine-tuning the coefficients in $W_0(Y_a, \xi_i)$. Such a fine tuning is technically natural.

3. Charge-preserving minima in HLW theories

By starting with a complicated W in (5), it is possible to avoid the spontaneous breaking of $U(1)_{e.m.}$. Nevertheless, a theory with the superpotential separable as in (2) is simpler and it would be nice if this were free of the problem. This may be the case if one considers the HLW potential containing nontrivial effects of superheavy fields in the low-energy sector.

Consider again the light sector consisting of H, H' and Y, and choose the following g_{eff}:

$$g_{\text{eff}} = \lambda HH'Y + mHH'. \tag{16}$$

This leads to the following V_{eff}:

$$\begin{aligned} V_{\text{eff}} = &\left|\lambda\left(Y+\frac{m}{\lambda}\right)\right|^2 (H'^\dagger H' + H^\dagger H) + |\lambda HH'|^2 \\ &+ m_{3/2}^2\,(H'^\dagger H' + H^\dagger H + |Y|^2) \\ &+ (m'_{3/2}\lambda HH'Y + 2m_{3/2}mHH' + \text{c.c.}) + \tfrac{1}{2}D^\alpha D^\alpha. \end{aligned} \tag{17}$$

CC-0. In Public Domain. Gurukul Kangri Collection, Haridwar

Digitized by Arya Samaj Foundation Chennai and eGangotri

The value of V_{eff} of (17) is not the most general which could have been constructed. However, this form of V_{eff} is expected to hold in a large class of models. For example, the quadratic and linear terms in Y in g_{eff} do not arise in the minimal SU(5) model (Ellis 1983) or in its extension (Ferrara *et al* 1983) which makes the gauge hierarchy stable at one loop. The Y^3 term will also be absent if it is absent in the original superpotential.

As shown in Appendix A, the SU(2) × U(1)-breaking minimum of V_{eff} can and must exist if $A(\equiv m'_{3/2}/m_{3/2})$ does not lie in the following range:

$$2\hat{m} - 1 - 2|\hat{m} - 1| < A < 1 + 2\hat{m} + 2|\hat{m} - 1|. \tag{18}$$

This inequality reduces to the well-known $|A| < 3$ when $\hat{m} \equiv m/m_{3/2} = 0$.

Even in the presence of leptons, the above charge-preserving minimum may continue to be the global minimum. This is plausible for the following reason: the inclusion of leptons adds a term $\lambda_e LH'E^+$ to g_{eff}. However, the presence of the mass term for HH' in g_{eff} spoils the inherent symmetric role of L and H existing in the NSW example. This symmetry was crucially responsible for leading to a global $U(1)_{\text{e.m.}}$-breaking minimum. It is easy to see that the point at which only L^-, E^+ and H'^0 acquire nonzero VEV's, as in the earlier example, is not even an extremum of V_{eff}. The complexity of the potential does not allow us to rule out the existence of other charge-breaking minima. It is, however, conceivable that a reasonable range of parameters A and m may exist for which charge-breaking minima do not exist but the $U(1)_{\text{e.m.}}$-preserving minimum does.

4. Conclusions

We have investigated the breaking of SU(2) × U(1) at the tree level in a wider class of SUGRA models than that studied by NSW. It appears that, for some choice of parameters in the theories, the absolute minimum of the potential corresponds to the desired breaking of SU(2) × U(1) down to $U(1)_{\text{e.m.}}$. The existence of charge-breaking absolute minima in NSW models has led to the belief that, in a realistic SUGRA theory, tree-level electroweak breaking is impossible. Our work shows that this need not be the case if we go beyond the NSW structure. Taken together with the fact that there exist ways (Ferrara *et al* 1983) to avoid the gauge hierarchy problem in the presence of light singlets, tree-level electroweak breaking appears to be a viable possibility.

In the last couple of years, many papers dealing with the question of the electroweak symmetry breaking have appeared (Ibanez *et al* 1985). Most authors except Derendinger and Savoy (1984) rule out symmetry breaking through singlets on the basis of the results of Frere *et al*. Moreover, none of these papers have considered the consequences of allowing a general (Soni and Weldon 1983) soft breaking of supersymmetry. Considering the open status of supergravity model building, our results are thus still of relevance in that they enlarge considerably the class of phenomenologically reasonable models. It remains for us to extend the model of § 2 to include a full set of fermions and to work out in detail the consequences for low energy ($\sim 10^2$ GeV) physics.

CC-0. In Public Domain. Gurukul Kangri Collection, Haridwar

Digitized by Arya Samaj Foundation Chennai and eGangotri

111940

Acknowledgements

This work was supported by the Council of Scientific and Industrial Research, New Delhi.

Appendix A

We consider here the minimization of the potential of equation (17). For the nonzero VEV's we write

$$\langle H_1^{0\prime} \rangle = \lambda^{-1} m_{3/2} a e^{i\alpha}, \quad \langle H_2^0 \rangle = \lambda^{-1} m_{3/2} v e^{i\omega},$$
$$\langle Y \rangle = \lambda^{-1} m_{3/2} y e^{i\eta} \tag{A1}$$

where a, v and y are chosen positive. The phases α, ω and η can be chosen as zero at the minimum without affecting the final conclusions.

With the above choices and definitions, V_{eff} takes a value V_0 given by

$$V_0 = \lambda^{-2} m_{3/2}^4 \hat{V}_0,$$

$$\hat{V}_0 = (y+\hat{m})^2(a^2+v^2) + v^2 a^2 + (a^2+v^2+y^2)$$
$$- 2av(AY + 2\hat{m}) + \tfrac{1}{2} D^\alpha D^\alpha \lambda^2 / m_{3/2}^4, \tag{A2}$$

where $\hat{m} = m/m_{3/2}$. It is easy to see that at an extremum

$$a = v.$$

This equality ensures that the D-terms vanish at an extremum of V_{eff}. The extremum conditions now take the form

$$v[(y+\hat{m})^2 + v^2 + 1 - (Ay + 2\hat{m})] = 0, \tag{A3a}$$

$$v^2(2y - A + 2\hat{m}) + y = 0. \tag{A3b}$$

We are interested in solutions that break $SU(2) \times U(1)$, so we discard the solution $v = y = 0$, and define a new constant $A' = A - 2m$. In terms of A', the extremum conditions are

$$v^2 + y^2 - A'y + (\hat{m} - 1)^2 = 0, \tag{A4a}$$

$$2v^2 y - A'v^2 + y = 0. \tag{A4b}$$

The value of V_{eff} at the extremum is given by

$$V_0 = -v^4 + y^2. \tag{A5}$$

Equations (A4) can be reduced to a single cubic equation. If we write

$$x = (y/A') - \tfrac{1}{2}$$

CC-0. In Public Domain. Gurukul Kangri Collection, Haridwar

Digitized by Arya Samaj Foundation Chennai and eGangotri

we can eliminate v from (A4), obtaining

$$0 = f(x) \equiv x^3 + \left[\frac{(\hat{m}-1)^2}{A'^2} - \frac{1}{2A'^2} - \frac{1}{2}\right]x - \frac{1}{4A'^2}. \tag{A6}$$

By (A4b), $v^2 = -(2x)^{-1}(x+\frac{1}{2})$. Thus, to get a real v, we must look for solutions with $-\frac{1}{2} < x < 0$.

The symmetry-breaking extremum will lie lower than the symmetric solution $v = y = 0$ if and only if the right side of (A5) is negative, i.e. $y^2 < v^4$. This yields

$$2|A'x_0| < 1, \tag{A7}$$

where x_0 is a solution of (A6). Equation (A7) has a solution in the range $-\frac{1}{2} < x_0 < 0$ provided $|A'| > 1$ and $f(-1/2|A'|) > 0$. Substitution in the definition of $f(x)$ yields the inequality

$$(|A'|-1)^2 > 4(\hat{m}-1)^2,$$

i.e. $$|A - 2\hat{m}| - 1 > 2(\hat{m}-1). \tag{A8}$$

This is equivalent to the restriction that A does not lie between $|2\hat{m}-1| - 2|\hat{m}-1|$ and $2\hat{m}+1+2|\hat{m}-1|$. Approximate values of v and y can be obtained by neglecting the cubic term in (A6). These are

$$y \approx \frac{A'}{2}\left[\frac{A'^2 - 2(\hat{m}-1)^2}{A'^2 + 1 - 2(\hat{m}-1)^2}\right],$$

$$v \approx \tfrac{1}{2}[A'^2 - 2(\hat{m}-1)^2].$$

In the large $|A'|$ limit, both y^2 and v^2 are proportional to A'^2.

References

Alvarez-Gaume L, Polchinski J and Wise M B 1983 *Nucl. Phys.* **B221** 495
Claudson M, Hall L J and Hinchcliffe I 1983 *Nucl. Phys.* **B228** 501
Derendinger J and Savoy C A 1984 *Nucl. Phys.* **B237** 307
Ellis J 1984 Supersymmetric GUTS, lectures delivered at Munich, September 1983, CERN Report TH 3802
Ellis J, Hagelin J S, Nanopoulos D V and Tamvakis K 1983 *Phys. Lett.* **B125** 275
Ferrara S, Nanopoulos D V and Savoy C A 1983 *Phys. Lett.* **B123** 214
Frere J M, Jones D R T and Raby S 1983 *Nucl. Phys.* **B222** 11
Hall L J, Lykken J and Weinberg S 1983 *Phys. Rev.* **D27** 2359
Ibanez L E, Lopez C and Munoz C 1985 *Nucl. Phys.* **B256** 218
Joshipura A S, Mukherjee A and Soni S K 1986 *Pramana – J. Phys.* **27** 4
Lahanas A B 1983 *Phys. Lett.* **B124** 341
Nilles H P, Srednicki M and Wyler D 1983a *Phys. Lett.* **B120** 346
Nilles H P, Srednicki M and Wyler D 1983b *Phys. Lett.* **B124** 337
Soni S K and Weldon H A 1983 *Phys. Lett.* **B126** 215

CC-0. In Public Domain. Gurukul Kangri Collection, Haridwar

Digitized by Arya Samaj Foundation Chennai and eGangotri

Pramāṇa – J. Phys., Vol. 28, No. 1, January 1987, pp. 23–34. © Printed in India.

Phenomenological structure functions and Gribov-Lipatov relation

D K CHOUDHURY and A K MISRA†

Department of Physics, †Department of Chemistry, University of Gauhati, Gauhati 781 014, India

MS received 27 September 1984; revised 29 September 1986

Abstract. We make an analysis of the Gribov-Lipatov relation using the phenomenological forms of the structure function F_2^{ep}. Our analysis indicate breakdown of the relation at PETRA energies. Plausible reasons of the breakdown of Gribov-Lipatov relation are discussed together with its phenomenological form.

Keywords. Gribov-Lipatov relation; structure function; scale breaking.

PACS Nos 13·65; 13·60

1. Introduction

The present paper deals with an analysis of Gribov-Lipatov relation (Gribov and Lipatov 1971; 1972) at high energies using the phenomenological forms of structure functions proposed by various authors (Perkins *et al* 1977; Karlinger and Sullivan 1978; Roy *et al* 1978) as alternatives to QCD structure (Buras and Gaemers 1978).

Phenomenological analysis of Gribov-Lipatov relation was done earlier by Gilman (1974) and Brandelik *et al* (1979) using the empirical structure functions of Miller *et al* (1972) and Riordan *et al* (1974) respectively. While Gilman (1974) observed approximate validity of the Gribov-Lipatov relation, Brandelik *et al* (1979) pointed out its violation. There was also an attempt to study scale-breaking patterns (Choudhury 1976; Choudhury and Vanryckghem 1978) assuming the validity of Gribov-Lipatov relation.

The parametrization of the phenomenological structure functions used by some of the authors (Perkins *et al* 1977; Karlinger and Sullivan 1978; Roy *et al* 1978) is essentially determined by low Q^2 data ($Q^2 \sim 15$–$20\,\text{GeV}^2$). We will therefore test their validity in the high Q^2 regime of EMC (Aubert *et al* 1981; Dress 1981) and CDHS (Wotschalk 1981) before using them in our analysis at high Q^2 PETRA data ($Q^2 \sim 900\,\text{GeV}^2$).

The inference of our analysis might be dependent on the form of low Q^2 structure functions used (Perkins *et al* 1977; Karlinger and Sullivan 1978; Roy *et al* 1978). Hence we will also use the parametrization from high Q^2 data of CDHS (Abramowicz *et al* 1983), EMC (Aubert *et al* 1981) and NA 10 (Betev *et al* 1985) to study the status of the Gribov-Lipatov relation. Low Q^2 region is generally assumed to have significant higher twist effect (Abbott *et al* 1980; Aubert *et al* 1981; Godbole and Roy 1982). We will comment on such a possibility in our analysis. Finally the plausible reasons of the

CC-0. In Public Domain. Gurukul Kangri Collection, Haridwar

Digitized by Arya Samaj Foundation Chennai and eGangotri

breakdown of Gribov-Lipatov relation will be discussed together with its phenomenological form.

2. Formalism

The Gribov-Lipatov relation (Gribov and Lipatov 1971; 1972) is defined as

$$F_2^{ep}(x,Q^2) = \frac{x}{\beta\sigma(e^+e^- \to \mu^+\mu^-)} \frac{d\sigma}{dx}(e^+e^- \to \overline{P}+X), \tag{1}$$

where β is the ratio of the momentum and energy of $\overline{P}$ and other variables have usual meanings.

In order to test the relation (1), one needs to know the theoretical structures of $F_2^{ep}(X,Q^2)$ and experimental information about $(d\sigma/dx)$ $(e^+e^- \to \overline{P}+X)$. In the scaling model, F_2^{ep} is a function of quark distribution V_u, V_d, ξ and ξ_c defined as

$$F_2^{ep}(x,Q^2) = x\left[\tfrac{4}{9}V_u(x) + \tfrac{1}{9}V_d(x) + \tfrac{4}{3}\xi(x) + \tfrac{8}{9}\xi_c(x)\right]. \tag{2}$$

Here V_u and V_d denote the valence contributions, ξ and ξ_c represent SU(3) symmetric and $c\bar{c}$ component of the sea respectively. These have been parametrized as (Berger and Phillips 1974):

$$\begin{aligned} V_u &= 0{\cdot}594x^{-1/2}(1-x^2)^3 + 0{\cdot}461x^{-1/2}(1-x^2)^5 + 0{\cdot}621x^{-1/2}(1-x^2)^7,\\ V_d &= 0{\cdot}072x^{-1/2}(1-x^2)^3 + 0{\cdot}206x^{-1/2}(1-x^2)^5 + 0{\cdot}621x^{-1/2}(1-x^2)^7,\\ \xi &= 0{\cdot}145x^{-1}(1-x)^9, \end{aligned} \tag{3}$$

using the SLAC data (Riordan *et al* 1974) on F_2^{ep} and F_2^{en}. By all evidence, the charm component ξ_c is strongly suppressed (Sivers 1976) at low Q^2 and is taken to be zero in conformity with common practice (Buras and Gaemers 1978). Equation (3) will be taken as the low Q^2 input in the scale-breaking models discussed below.

Let us now record the phenomenological scale-breaking models as F_2^{ep} to be studied later.

2.1 *PSS models*

Perkins *et al* (1977) have shown that scale-breaking in electron (muon) scattering on both proton and isoscalar target can be described in terms of a single form factor:

$$F_2(x,Q^2) = F_2(x,Q_0^2)\,(Q^2/Q_0^2)^{0\cdot25-x}, \tag{4}$$

where Q_0^2 is $3\,\mathrm{GeV}^2$.

With the same form factor, they were also able to describe the νP and νN data. Since these four processes correspond to different combinations of the valence and the sea quark distribution, the model amounts to assuming identical forms for V_u, V_d, ξ and ξ_c:

$$\begin{aligned} V_u(x,Q^2) &= V_u(x,Q_0^2)\,(Q^2/Q_0^2)^{0\cdot25-x},\\ V_d(x,Q^2) &= V_d(x,Q_0^2)\,(Q^2/Q_0^2)^{0\cdot25-x},\\ \xi(x,Q^2) &= \xi(x,Q_0^2)\,(Q^2/Q_0^2)^{0\cdot25-x},\\ \xi_c(x,Q^2) &= \xi_c(x,Q_0^2)\,(Q^2/Q_0^2)^{0\cdot25-x}. \end{aligned} \tag{5}$$

CC-0. In Public Domain. Gurukul Kangri Collection, Haridwar

Digitized by Arya Samaj Foundation Chennai and eGangotri

We shall use the parametrization of (3) for the low Q^2 input on the right hand side of (4). The variation of the effective Q^2 with x in the parametrization, (3) will be taken care of by re-expressing the above equation as (Roy *et al* 1978)

(i) *PSS(I)*:

$$V_{u,d}(x, Q^2) = V_{u,d}(x, Q_1^2(x)) \left(\frac{Q}{Q_1^2(x)}\right)^{0\cdot25-x}, \tag{6}$$

where $Q_1^2(x)$ is the average Q^2 for this parametrization for a given x given by (Roy *et al* 1978)

$$Q_1^2(x) \sim 13\cdot3x. \tag{7}$$

To check the sensitivity of the prediction of the Gribov-Lipatov relation on the latitude allowed by the ep data, we shall also use an alternative parametrization proposed by Roy *et al* (1978).

(ii) *PSS(II)*:

$$V_{u,d}(x, Q^2) = V_{u,d}(x, Q_1^2(x)) \left(\frac{Q^2}{Q_1^2(x)}\right)^{0\cdot075-0\cdot5x} \tag{8}$$

which is designed to mimic the QCD model (Buras and Gaemers 1978).

2.2 *KS models*

Karlinger and Sullivan (1978) considered two different parametrization of scale breaking in eN and μN scattering, one involving logarithmic type as suggested by asymptotic freedom and the other a power type, suggested by conventional re-normalizable field theory. These are given by

(i) *KS(I)*

$$F_2^{\log}(x, Q^2) = \left(1 + b(x)\frac{\ln(Q^2/Q_0^2)}{\ln(Q_0^2/\Lambda^2)}\right) F_2(x, Q_0^2), \tag{9}$$

with $Q_0^2 = 3\,\text{GeV}^2$, $\Lambda = 0\cdot4\,\text{GeV}^2$, $b(x) = b_0[1-(x/x_0)^\alpha]$, $x_0^{-1} = 4\cdot489$, $b_0 = 0\cdot804$ and $\alpha = 0\cdot6343$. It is to be noted that (9) is to be used recursively for high Q^2 range.

(ii) *KS(II)*

$$F_2^{\text{power}}(X, Q^2) = (Q^2/Q_0^2)^{f(x)} F_2(X, Q_0^2) \tag{10}$$

with $Q_0^2 = 3\,\text{GeV}^2$, $f(x) = a + bx + \varepsilon/x$, $a = 0\cdot21324$, $b = -0\cdot97955$ and $\varepsilon = 5\cdot9 \times 10^{-4}$.

2.3 *Effect of longitudinal cross-section*

We shall now consider the effect of non-zero longitudinal (σ_L) to transverse cross-section (σ_T) ratio

$$R = \frac{F_2}{xF_1} - 1. \tag{11}$$

CC-0. In Public Domain. Gurukul Kangri Collection, Haridwar

Digitized by Arya Samaj Foundation Chennai and eGangotri

This is incorporated simply by multiplying the left side of (1) by

$$\frac{1}{2}\left(\frac{3}{R+1}-1\right). \tag{12}$$

The modification of our results due to (12) will be shown for typical values $R = 0{\cdot}0$, 0·31 and 0·76.

3. Results

3.1 *Comparison of the phenomenological forms of the structure function in high Q^2 region*

In figure 1(a–d) we show the comparison with EMC data for a few representative x values $x = 0{\cdot}03$, 0·25, 0·45 and 0·65. In figures (2) and (3) the corresponding comparisons are made with the CDHS data. In figure 1, we observe that PSS(II) fits the overall data better than the other three forms of the structure function viz PSS(I), KS(I) and KS(II). A similar inference about PSS(II) can also be drawn even from figure 2 with high x CDHS data of $F_2^{\nu N}$. Figure 3 representing all the four models (KS I, KS II, PSS I and PSS II) for xF_3 does not however show such a definite trend. Hence PSS(II) may be preferred over other models of F_2^{ep} and $F_2^{\nu N}$ both in EMC and CDHS data but cannot be preferred over them in xF_3 CDHS data. We however note that it is F^{ep} that appear in our defining equation (1). We therefore select PSS(II) out of the four models to test it.

PSS(II) is still a phenomenological parametrization at low Q^2. There are high Q^2 parametrizations directly from EMC (Aubert *et al* 1981), CDHS (Abramowicz *et al* 1983) and NA 10 (Betev *et al* 1985) data. We will also test (1) with these high Q^2 parametrizations as well besides with PSS(II).

3.2 *Analysis of Gribov-Lipatov relation*

We now compare the predictions of the formalism with data for

$$\frac{x}{\beta\sigma(e^+e^-\to\mu^+\mu^-)}\frac{d\sigma}{dx}(e^+e^-\to\bar{P}+X).$$

To that end, we take data at the centre of mass energy $\sqrt{S} = 3{\cdot}74$, 4·72, 5·2 and 34·0 GeV from earlier results (Gilman 1974; Brandelik *et al* 1979; Mess and Wiik 1982; Wolf 1980; Jade Collaboration 1981).

In figure 4(a–d) we show the predictions of the models of F_2^{ep} defined as PSS(II). In the same figure we also show the predictions of the parametrizations given by EMC, CDHS and NA 10 graphs. Although the large x data at $\sqrt{S} = 3{\cdot}74$ GeV reported by Gilman (1974) give good agreement with the models under consideration, the rest of the data indicates break down of (1).

In fact the theoretical curves in general fall below the experimental values of

$$\frac{x}{\beta\sigma(e^+e^-\to\mu^+\mu^-)}\frac{d\sigma}{dx}(e^+e^-\to\bar{P}+X).$$

CC-0. In Public Domain. Gurukul Kangri Collection, Haridwar

Digitized by Arya Samaj Foundation Chennai and eGangotri

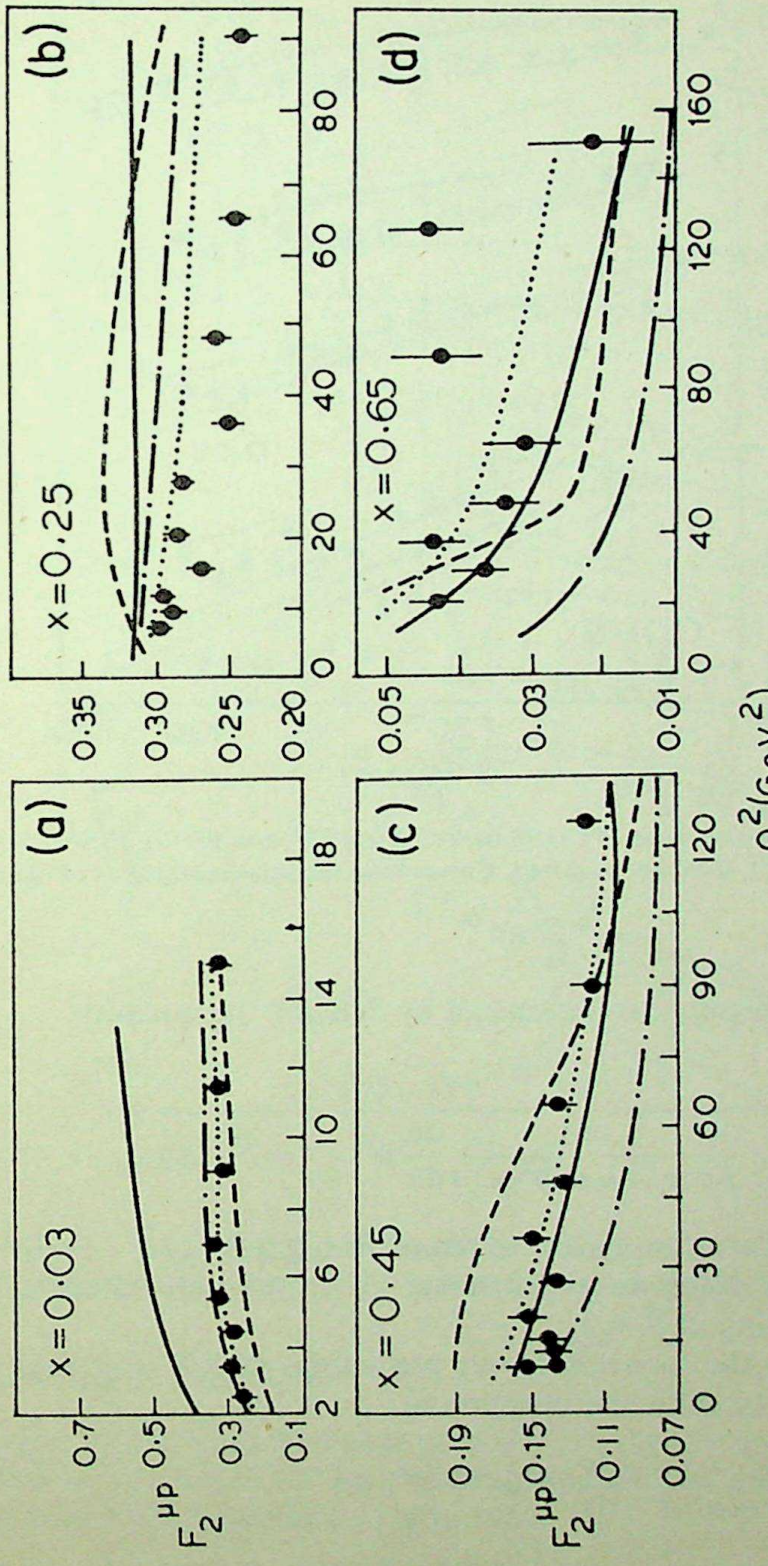

Figure 1(a–d). Comparison of EMC data $F_2^{\mu p}$ with phenomenological structure functions PSS(I) (continuous curve) PSS(II) (dotted curve), KS(I) (dashed curve) and KS(II) (dashed dot dashed curve) for x = 0·03, 0·25, 0·45 and 0·65 respectively.

CC-0. In Public Domain. Gurukul Kangri Collection, Haridwar

Digitized by Arya Samaj Foundation Chennai and eGangotri

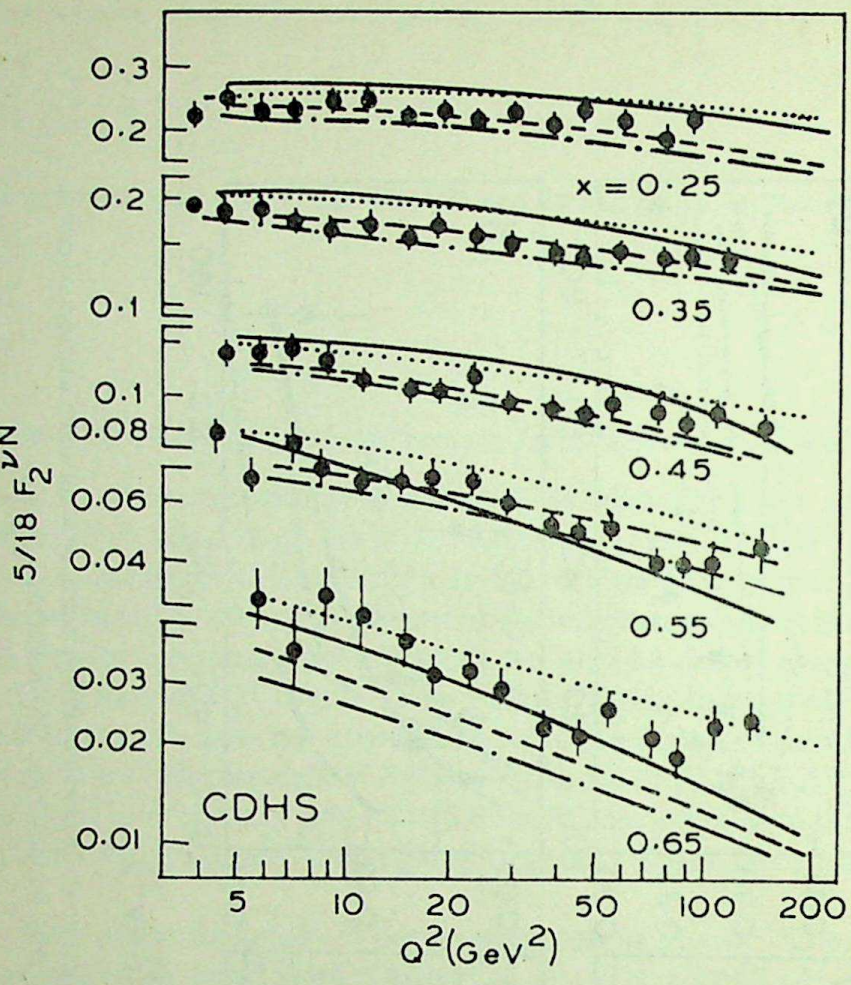

Figure 2. Comparison of CDHS data of (5/18) $F_2^{\nu N}$ with PSS(I), PSS(II), KS(I), KS(II) for $x = 0{\cdot}25$, 0·35, 0·45, 0·55 and 0·65. Curves have the same meaning as of figure 1.

Such an effect conveniently can be studied by defining the quantity

$$\bar{R}(x, Q^2) = \frac{F_2^{ep}(x, Q^2)}{\dfrac{x}{\beta\sigma(e^+e^- \to \mu^+\mu^-)}\dfrac{d\sigma}{dx}(e^+e^- \to \bar{P} + X)_{\text{expt}}}. \tag{13}$$

In figure 5(a–d) we evaluate typical values of $\bar{R}(x, Q^2)$ for $\sqrt{S} = 3{\cdot}65$, 4·42, 5·2 and 34·0 GeV respectively using an approximate QCD structure function (Buras and Gaemers 1978) resulting in $\bar{R} < 1$.

Let us now discuss the variation of our predictions with $R = (\sigma_L/\sigma_T)$.

In figure 6(a, b, c) we show the variation of

$$\frac{x}{\beta\sigma(e^+e^- \to \mu^+\mu^-)}\frac{d\sigma}{dx}(e^+e^- \to \bar{P} + X)$$

with R using PSS II as a typical model of F_2^{ep} and taking $R = 0{\cdot}0$, 0·31 and 0·76 at three typical energies $\sqrt{S} = 12$, 30 and 34 GeV. Figures 6(a, b, c) demonstrate that increase of R makes the disagreement between the data and Gribov-Lipatov relation (1) more prominent.

CC-0. In Public Domain. Gurukul Kangri Collection, Haridwar

Digitized by Arya Samaj Foundation Chennai and eGangotri

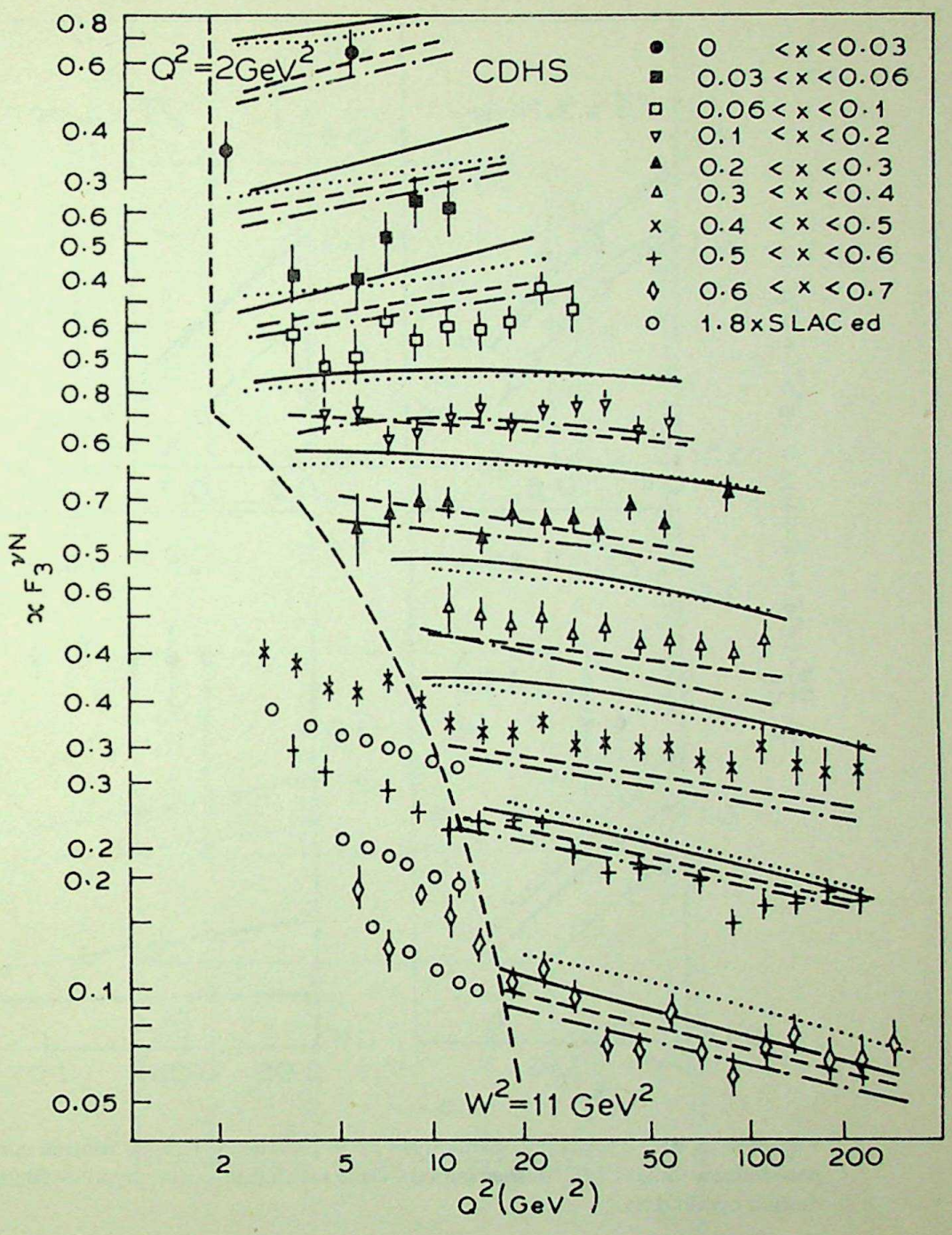

Figure 3. Comparison of $xF_3^{\nu N}$ from CDHS data with PSS(I), PSS(II), KS(I) and KS(II) for various ranges of x. Curves have the same meaning as of figure 1.

3.3 *Higher twist (HT) contribution*

In order to consider the effect of higher twist (H^T) in the low end of e^+e^- energy we assume the following form of the structure function (Abbott *et al* 1980; Abuert *et al* 1981; Bollini *et al* 1981; Godbole and Roy 1982)

$$F_2(x,Q^2) = F_2(x,Q^2)\left(1+\frac{\mu^2}{(1-x)Q^2}\right). \tag{14}$$

The effect of (14) is shown in figure 5(a–d).

CC-0. In Public Domain. Gurukul Kangri Collection, Haridwar

Digitized by Arya Samaj Foundation Chennai and eGangotri

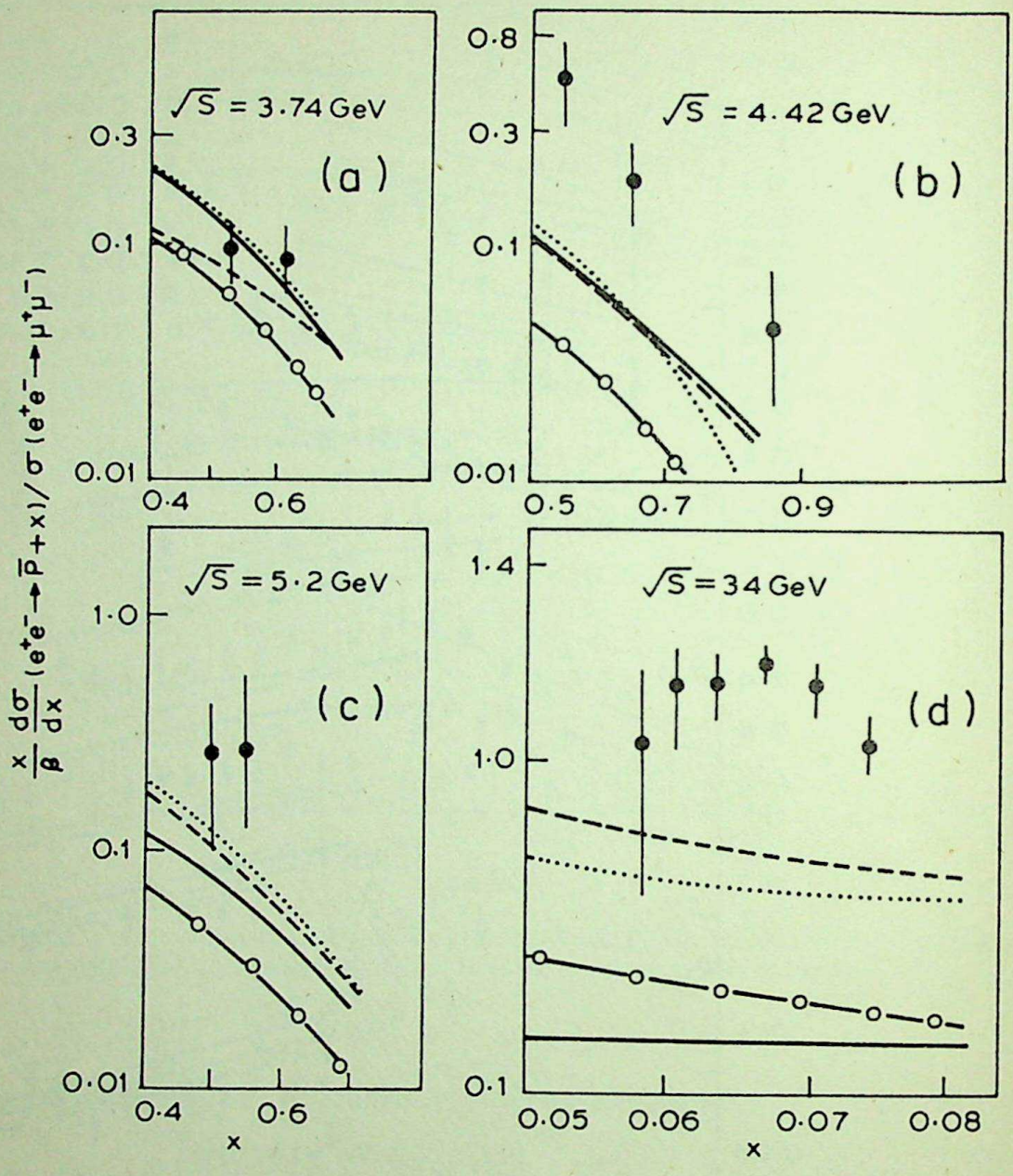

Figure 4 (a–d). Theoretical predictions at 34 GeV using PSS(II) (dotted curve) as well as parametrization of EMC (dashed curve) CDHS (continuous curve) and NA 10 (dashed crossed dashed curve) data.

A study of these figures shows that the higher twist effect enhances the value of $\bar{R}$ slightly, but not significant enough to alter the feature of breakdown of (1) as we have already obtained.

3.4 *Implication of violation of Gribov-Lipatov relation and its plausible significance*

Let us discuss the plausible theoretical significance of breakdown of Gribov-Lipatov relation (1).

The perturbative QCD gives this relation exactly as a result of leading logarithmic approximation for the case of single parton distribution (Konishi *et al* 1978; Dokshitzer 1977). However it is found (Kubota 1980; Floratas *et al* 1981) that even for single parton distribution, the next to leading logarithmic corrections in perturbative QCD

CC-0. In Public Domain. Gurukul Kangri Collection, Haridwar

Digitized by Arya Samaj Foundation Chennai and eGangotri

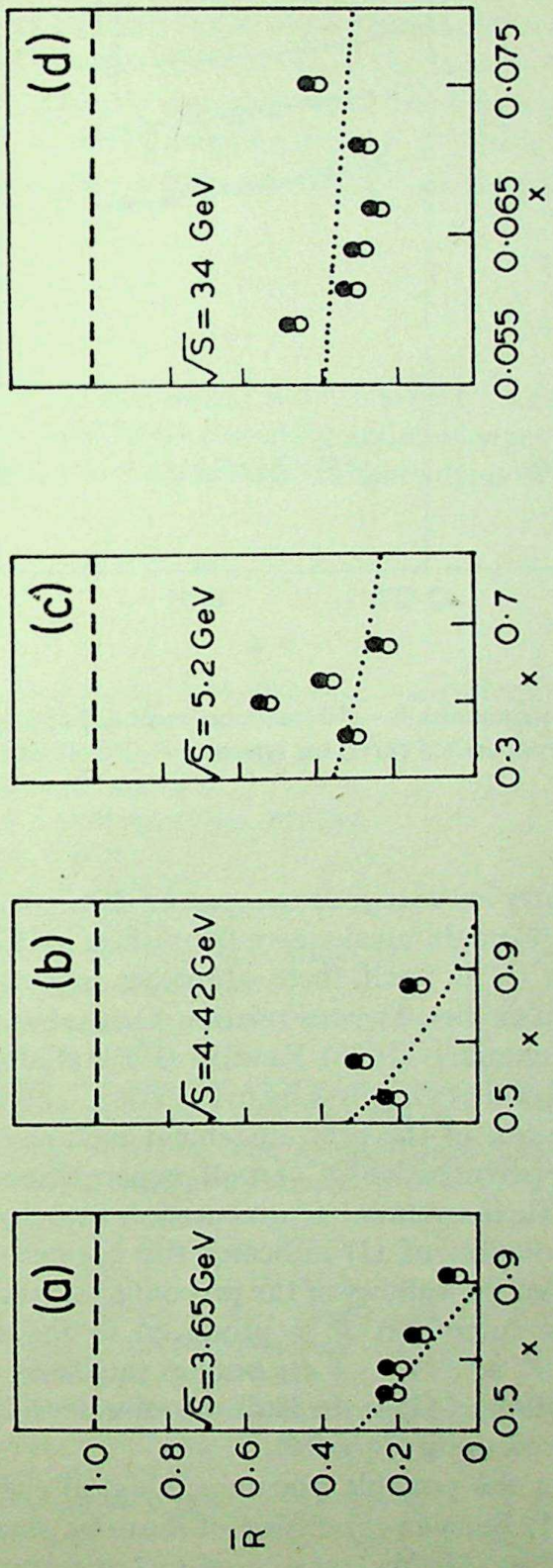

Figure 5(a–d). Values of $\bar{R}(x, Q^2)$ vs x for $\sqrt{S}$ = 3·65, 4·42, 5·2 and 34 GeV (open circle). Effects of higher twist are shown by closed circles. The dotted curve corresponds to the prediction of Kato *et al* (1983).

CC-0. In Public Domain. Gurukul Kangri Collection, Haridwar

Digitized by Arya Samaj Foundation Chennai and eGangotri

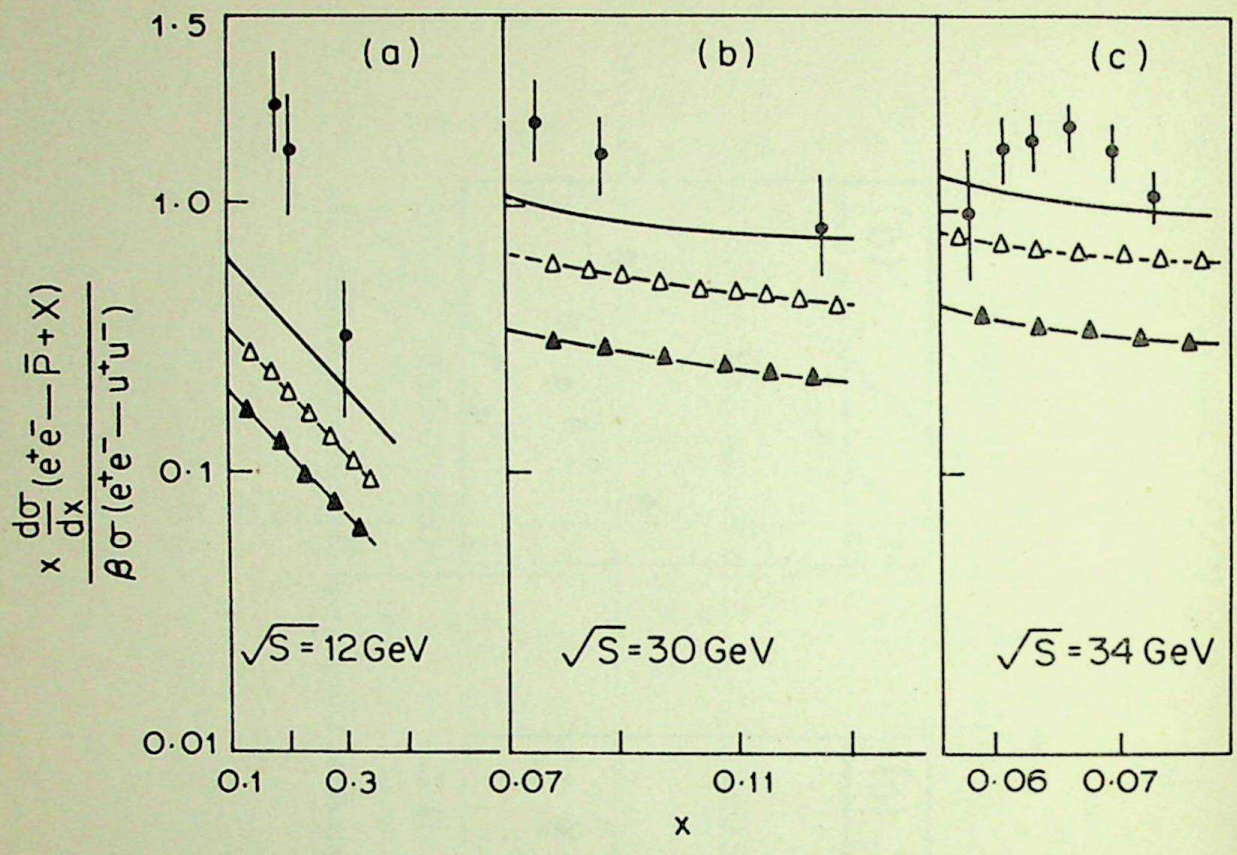

Figure 6(a–c). Variation with $R = 0{\cdot}0$ (continuous curve), 0·31 (dotted crossed dotted curve) and 0·76 (dashed cross dashed curve) for typical $\sqrt{S} = 12$, 30 and 34 GeV with PSS(II).

violates this relation. Similarly in the case of two-parton distribution which is required for hadronization, relation (1) might break down (Konishi *et al* 1978; Dokshitzer 1977).

Within the perturbative QCD itself there are other arguments as well on the implication of breakdown of Gribov-Lipatov relation. On the basis of pre-confinement hypothesis of Amati and Veneziano (1978), Kawabe (1981) studied the hadronization of quark jets and finds violation of Gribov-Lipatov relation. This is then interpreted as the evidence of the realization of the preconfinement picture. We note that in the preconfinement picture, the perturbative QCD itself prepares the colour singlet clusters with finite masses before their eventual fragmentation into hadrons. Thus within perturbative QCD, the violation of (1) indicates the presence of next to leading logarithmic correction and/or the validity of the preconfinement hypothesis. As $\bar{R} < 1$ invariably, one might also infer that $\bar{P}$ is produced in the sequential processes $e^+e^- \to h^+ + x$, $h^+ = \bar{\Lambda} \to \bar{P}$, $h^+ = \bar{\Sigma} \to \bar{P}$ etc besides the direct $(e^+e^- \to \gamma \to \bar{P} + x)$. Furthermore, massive violation of (1) at the hadronization level is perhaps the reason why $\bar{R}$ is so much away from unity ($\bar{R} \leqslant 0{\cdot}6$).

Let us now comment on the possible phenomenological expression of (13) as a measure of breakdown of (1). Such an expression of $\bar{R}$ can be obtained once the forms of the structure function $F_2^{\bar{p}p}$ and $(d\sigma/dx)$ $(e^+e^- \to \bar{p} + x)$ are known. Taking PSS (II) as the typical structure function and the renormalized distribution of Kato *et al* (1983) from Monte Carlo simulation, we plot $\bar{R}(x, Q^2)$ vs x for $\sqrt{S} = 3{\cdot}65$, 4·42, 5·2 and 34 GeV in figure 5(a–d) representing the gross feature.

CC-0. In Public Domain. Gurukul Kangri Collection, Haridwar

Digitized by Arya Samaj Foundation Chennai and eGangotri

4. Conclusion

To conclude, the Gribov-Lipatov relation breaks down within the present energy regime assuming the validity of the forms of the structure functions discussed in § 2. Such a breakdown was earlier pointed out by Brandelik *et al* (1979) using the empirical structure function of Riordan *et al* (1974). In the present work, we have confirmed its breakdown for higher energies using the recent models of structure function. Plausible reasons of its breakdown are discussed within QCD. Using a distribution given by Kato *et al* (1983) its gross feature is also represented phenomenologically.

Acknowledgements

Both of us are grateful to Professor G Wolf of DESY for assistance with recent data of e^+e^- physics. One of us (DKC) gratefully acknowledges financial support from the Department of Science, Technology and Environment of Government of Assam.

References

Abbott L F, Atwood W B and Barnett R M 1980 *Phys. Rev.* **D22** 582
Abramowicz H *et al* 1983 *Z. Phys.* **C17** 283
Amati D and Veneziano G 1979 *Phys. Lett.* **B83** 87
Aubert J J *et al* 1981 *Phys. Lett.* **B105** 315
Berger V and Phillips R J N 1974 *Nucl. Phys.* **B73** 269
Betev B *et al* 1985 *Z. Phys.* **C28** 15
Bollini D *et al* 1981 *Phys. Lett.* **B104** 403
Brandelik *et al* 1979 *Nucl. Phys.* **D148** 189
Buras A J and Gaemers K J F 1978 *Nucl. Phys.* **B132** 249
Choudhury D K 1976 *Nuovo Cimento* **A31** 669
Choudhury D K and Vanryckeghem L G F 1978 *Phys. Rev.* **D17** 1766
Dokshitser Yu L 1977 *Sov. Phys. JETP* **46** 641
Dress J 1981 *Proc. Int. Symp. on Lepton and Photon Interaction at High Energies*, Bonn (ed.) W Pfeil
Floratas E G, Lacoze R and Kounnas 1981 *Phys. Lett.* **B98** 89
Gilman 1974 *Proc. Int. Conf. (XVII) on High Energy Physics, London* (ed.) J P Smith (Rutherford Laboratory, Chilton, Did cot, Barkeshire, England)
Godbole R M and Roy D P 1982 *Z. Phys.* **C15** 39
Gribov V N and Lipatov L N 1971 *Phys. Lett.* **B37** 78
Gribov V N and Lipatov L N 1972 *Yad. Fiz.* **15** 781
Gribov V N and Lipatov L N 1972 *Sov. J. Nucl. Phys.* **15** 438
Jade Collaboration 1981 DESY 81/028 (unpublished)
Karlinger I and Sullivan J D 1978 *Phys. Rev.* **D18** 3202
Kato K, Munehisa T, Okada H and Shimizu Y 1983 The perturbative QCD and the e^+e^- single particle Inclusive Reaction, University of Tokyo preprint (UT-387)
Kawabe T 1981 *Prog. Theor. Phys.* **65** 1973
Konishi K, Ukaya A and Veneziano 1978 *Phys. Lett.* **B78** 24
Kubota T 1980 *Nucl. Phys.* **B165** 277
Mess K H and Wiik B H 1982 DESY 82/011 (unpublished)
Miller D H *et al* 1972 *Phys. Rev.* **D5** 528
Perkins D H, Schreiner P and Scott W C 1977 *Phys. Lett.* **B67** 347
Riordan E M, Bodek A and Coward D H 1974 *Phys. Lett.* **B52** 249
Roy D P, Paranjepe S, Pandita P N and Choudhury D K 1978 *Pramana–J. Phys.* **11** 619

CC-0. In Public Domain. Gurukul Kangri Collection, Haridwar

Digitized by Arya Samaj Foundation Chennai and eGangotri

Sivers D 1976 *Nucl. Phys.* **B106** 95
Wolf G 1980 DESY 80/85 (unpublished)
Wotschalk J 1981 *Proc. Int. Symp. on Lepton and Photon Interaction at High Energies* Bonn (ed.) W Pfeil

CC-0. In Public Domain. Gurukul Kangri Collection, Haridwar

Digitized by Arya Samaj Foundation Chennai and eGangotri

Pramāṇa – J. Phys., Vol. 28, No. 1, January 1987, pp. 35–39. © Printed in India.

Slope parameter and scaling of differential cross-section of Λ-p scattering

J K MOHAPATRA, S MOHANTY* and S N NAYAK**

Department of Physics, Regional College of Education, Bhubaneswar 751 007, India
* Department of Physics, Utkal University, Vani Vihar, Bhubaneswar 751 004, India
** Department of Physics, B. J. B. College, Bhubaneswar 751 014

MS received 1 January 1986; revised 29 August 1986

Abstract. The claim of Mohapatra and Maharana that $tb(s)$ is a better scaling variable than $t(\ln s)^2$ is put to test in the case of Λ-p scattering, after parametrizing $b(s)$ as $C_1 + C_2(\ln s)^\alpha$. It was observed that in this case the data also prefer an α value which is close to those obtained by Mohapatra and Maharana for other scattering processes.

Keywords. Λ-p scattering; slope parameter; scaling; unitarity bound.

PACS No. 13·75

1. Introduction

During the last decade, the scaling phenomenon has been qualitatively well established. Auberson *et al* (1971) were the first to investigate the scaling of scattering amplitude, $F(s, t)$. While studying the analytic properties of the Pomeranchuk-theorem-violating amplitudes in the high energy limit, they demonstrated that for a sequence $(s_n) \to \infty$ $\lim f(s_n, \tau(\ln s_n)^{-2})$ exists and is a nontrivial function of τ where $\tau = 1(\ln s)^2$, and $f(s, t) = F(s, t)/F(s, 0)$. Cornille and Simao (1971) extended the results of Auberson *et al* (1971) for other forward high energy behaviour of the scattering amplitude and arrived at similar conclusions regarding the scaling of $f(s, t)$. Auberson and Roy (1977) deduced the bounds on slope and curvature of the diffraction peak and further observed that $\tau = t(\ln s)^2$ can be chosen as a scaling variable. Thus in the recent past, there has been a general unanimity over the conclusion that $\tau = t(\ln s)^2$ is a good scaling variable and $b(s)$ is likely to grow as $(\ln s)^2$.

However, in a recent paper Mohapatra and Maharana (1983) demonstrated that the data of pp, $\bar{p}p$, $K^{\pm}p$, $\pi^{\pm}p$ scatterings perhaps do not favour such a conclusion. Through the analysis of data they claim that (i) if $b(s)$ is parametrized as $C_1 + C_2(\ln s)^\alpha$, then the data prefer an α value close to 1·25 instead of 2, and (ii) $tb(s)$ is a better scaling variable than $t(\ln s)^2$.

In this paper we have tried to test their claim by applying their method of analysis to Λp scattering. We are conscious of the fact that (a) data on Λp scattering are scanty because of the short lifetime (de Swart *et al* 1970) of Λ beam; (b) the available data are

* To whom all correspondence should be addressed.

CC-0. In Public Domain. Gurukul Kangri Collection, Haridwar

Digitized by Arya Samaj Foundation Chennai and eGangotri

in the incident momentum range of 0·13 GeV/c to 20 GeV/c only (Hauptman 1974); and (c) $(d\sigma/dt)(s, t)$ values are available only upto 6 GeV/c (Hauptman 1974). Though this momentum is not high enough to conclusively show the scaling of $(d\sigma/dt)(s, t)$ of Λp scattering, we assume that it is high enough to test the validity of the claim of Mohapatra and Maharana (1983).

The plan of the paper is as follows: In § 2 a brief summary of previous work is given as we are attempting to test the conclusions of the earlier work. Section 3 contains our analysis of data and conclusion.

2. Relevant previous work

Defining

$$f(s, t) = \frac{d\sigma}{dt}(s, t) \Big/ \frac{d\sigma}{dt}(s, 0) \tag{1}$$

and the slope and curvature, respectively, as

$$b(s) = \frac{d}{dt} f(s, t)_{t=0}, \tag{2}$$

$$c(s) = \frac{d^2}{dt^2} \ln f(s, t)_{t=0}. \tag{3}$$

Maharana (1978), using

$$w(s) = \ln \frac{s^2}{(d\sigma/dt)(s, 0)} \tag{4}$$

proved that if

$$b(s) \simeq [w(s)]^{\alpha} \tag{5}$$

for s large and all zeros, t_i, of $f(s, t)$ lie in a domain $\mathrm{Im}\, t_i < \varepsilon |t_i|^2$, ε being some s-dependent and arbitrarily small positive number and if

$$\tfrac{5}{4} \leqslant \alpha \leqslant 2, \tag{6}$$

then $\tau = tb(s)$ is a scaling variable.

This bound (equation (6)) is important for two reasons: (i) The upper bound for α is reminiscent of Froissart's bound and agrees well with the observation of Auberson and Roy (1977). (ii) The lower bound of α in (6) is of interest in the sense that if the data on various scattering processes favour this then one has to possibly take a second look at the earlier results on scaling and the Froissart's bound.

3. Analysis of data and conclusion

Keeping in view the findings of Mohapatra and Maharana (1983) we parametrized $b(s)$ as,

CC-0. In Public Domain. Gurukul Kangri Collection, Haridwar

Digitized by Arya Samaj Foundation Chennai and eGangotri

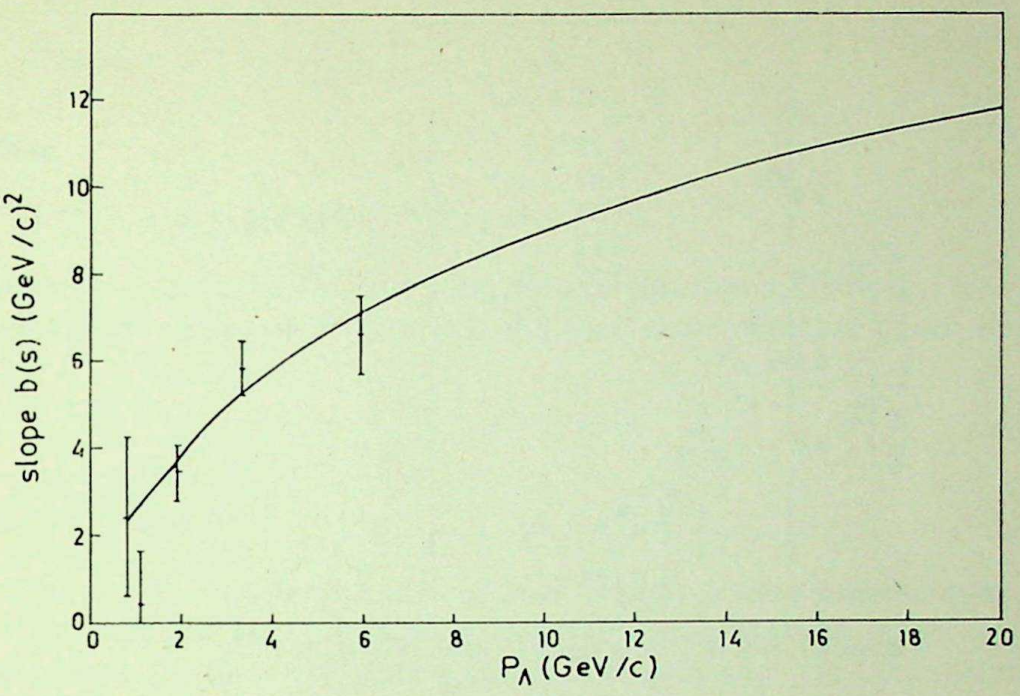

Figure 1. Fit for the slope parameter $b(s)$ and the extrapolated value of it for P_Λ value upto 20 GeV/c.

$$b(s) = C_1 + C_2 (\ln s)^\alpha \tag{7}$$

and made a least $-\chi^2$ fit to the data on $b(s)$ figure 1. For our best fit, the values of the parameters are

$$C_1 = 0{\cdot}64638, \quad C_2 = 0{\cdot}69443, \quad \text{and} \quad \alpha = 1{\cdot}35\ ^{+0{\cdot}035}_{-0{\cdot}047}.$$

Assuming that our theoretical curve for $b(s)$ faithfully represents the actual $b(s)$ for Λp scattering, we generated the data on $b(s)$ by extrapolating our theoretical curve to $P_\Lambda = 20$ GeV/c for future use. As, in this analysis, we have converged our interests on the value of α only, we have not searched for the allowed errors in C_1 and C_2. The α value clearly shows that α does not saturate to the unitarity bound, rather the data also favour a value close to the lower bound of α as observed by Mohapatra and Maharana (1983). Since the value of α is consistent with the condition (equation (6)) it satisfies the requirements of scaling. Hence $\tau = tb(s) = t(C_1 + C_2 (\ln s)^\alpha)$ should be the correct scaling variable instead of $\tau = t(\ln s)^2$. However, to test this claim of Mohapatra and Maharana (1983), we are handicapped in two ways. (i) Though data on $b(s)$ are now available upto a P_Λ value of 20 GeV/c, data on $(d\sigma/dt)(s, t)$ are available upto a P_Λ value of 6 GeV/c. (ii) There are no published numbers for the experimental values of $(d\sigma/dt)(s, 0)$. However, data (Hauptman 1974) are available on $|\rho|^2$ (upto 6 GeV/c) and σ_T, where ρ is the ratio of the real to imaginary part of the scattering amplitude. We would like to use them to our advantage and note that the scattering amplitude $f(q, \theta)$ is in general given by,

$$f(q, \theta) = a_1(q, \theta) + i a_2(q, \theta), \tag{8}$$

so that $$d\sigma/d\Omega = a_1^2(q, \theta) + a_2^2(q, \theta).$$

CC-0. In Public Domain. Gurukul Kangri Collection, Haridwar

Digitized by Arya Samaj Foundation Chennai and eGangotri

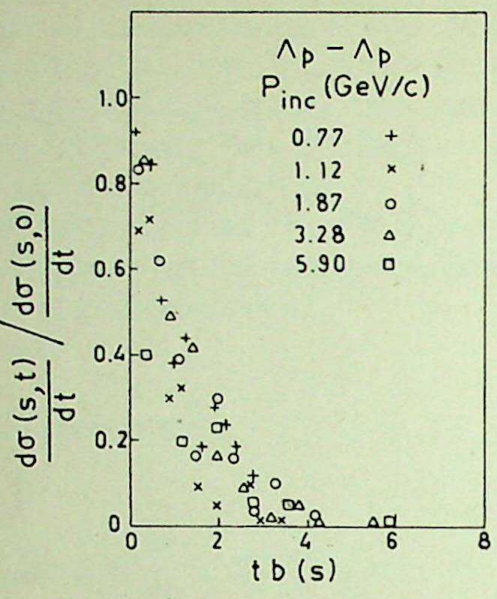

Figure 2. Plot of $\{[d\sigma(s, t)]/dt\}/\{[d\sigma(s, 0)]/dt\}$ vs $tb(s)$.

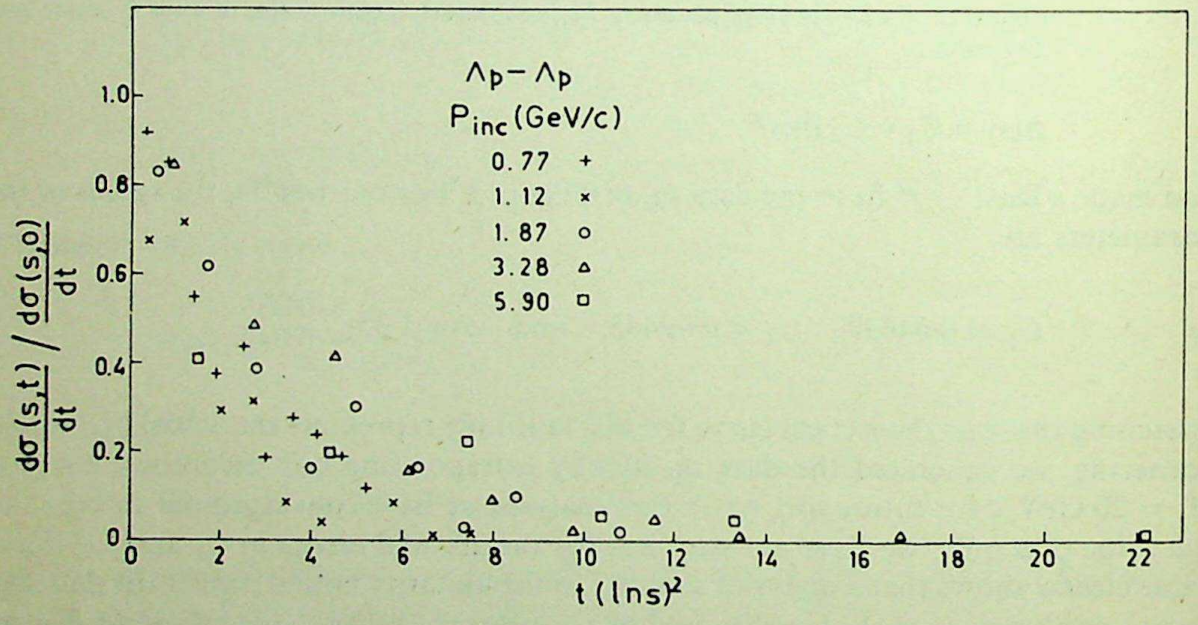

Figure 3. Plot of $\{[d\sigma(s, t)]/dt\}/\{[d\sigma(s, 0)]/dt\}$ vs $t(\ln s)^2$.

Using
$$\frac{d\sigma}{d\Omega} = \frac{d\sigma}{dt}\frac{dt}{d\Omega} = A\exp(bt)\frac{q^2}{\pi}. \tag{9}$$

We obtain,

$$a_1^2(q, 0) + a_2^2(q, 0) = A\frac{q^2}{\pi}. \tag{10}$$

From the optical theorem we get,

$$\sigma_T = \frac{4\pi}{q}\,\mathrm{Im}\, f(q, 0) = \frac{4\pi}{q}\, a_2(q, 0). \tag{11}$$

From (10) and (11) we obtain

CC-0. In Public Domain. Gurukul Kangri Collection, Haridwar

Digitized by Arya Samaj Foundation Chennai and eGangotri

$$a_1^2(q, 0) = q^2\left(\frac{A}{\pi} - \frac{\sigma_T^2}{16\pi^2}\right). \tag{12}$$

Then we have

$$|\rho(q)|^2 = a_1^2/a_2^2 = (16\pi A/\sigma_T^2) - 1 \tag{13}$$

where of course $A = (\mathrm{d}\sigma/\mathrm{d}t)(s, 0)$. Thus using the data (Hauptman 1974) on $|\rho(q)|^2$ and σ_T we computed the values of A from (13) and used these numbers as our data for $(\mathrm{d}\sigma/\mathrm{d}t)(s, 0)$.

In figures 2 and 3

$$\frac{\mathrm{d}\sigma}{\mathrm{d}t}(s, t)\Big/\frac{\mathrm{d}\sigma}{\mathrm{d}t}(s, 0)$$

versus $\tau = tb(s) = t(C_1 + C_2(\ln s)^\alpha)$ and $\tau = t(\ln s)^2$ is plotted upto a momentum range of 6 GeV/c. Since the scales in both the graphs are the same, a comparison of the spread in the data points (in the two figures) clearly indicates that the observations of Mohapatra and Maharana (1983) are correct. Also as $s \to \infty$

$$\tau \simeq C_2\, t(\ln s)^\alpha \tag{14}$$

and one is likely to think that $t(\ln s)^\alpha$ may be a good scaling variable. But this can only be tested when high energy data are available on Λp scattering. This present analysis revalidates the results of Mohapatra and Maharana (1983) that $t(C_1 + C_2(\ln s)^\alpha)$ and not $t(\ln s)^2$ could be the real scaling variable for all processes, although its universality can only be tested at energies for which $(\ln s)^\alpha$ will be comparable to C_1/C_2, and α does not necessarily saturate to the unitarity bound.

Acknowledgement

We are thankful to the Computer Centre, Utkal University, for the facilities extended to us.

References

Auberson G, Kinoshita T and Martin A 1971 *Phys. Rev.* **D3** 3185
Auberson G and Roy S M 1977 *Nucl. Phys.* **B117** 322
Cornille H and Simao F R A 1971 *Nuovo Cimento* **A5** 138
de Swart J J, Nagels M M, Rijken T A and Vehoeven P A 1970 Invited paper presented at the Ruhestein Meeting on low energy hadron interactions
Hauptman J M 1974 *An Experimental study of Lambda-proton interactions*, Ph.D. thesis, Lawrence Berkeley Laboratory, California
Maharana J 1978 *Commun. Math. Phys.* **58** 195
Mohapatra J K and Maharana J 1983 *Phys. Rev.* **D27** 130
Titchmarsh E C 1939 *The theory of functions* (London: Oxford University Press) 171

CC-0. In Public Domain. Gurukul Kangri Collection, Haridwar

Digitized by Arya Samaj Foundation Chennai and eGangotri

CC-0. In Public Domain. Gurukul Kangri Collection, Haridwar

Digitized by Arya Samaj Foundation Chennai and eGangotri

Pramāṇa – J. Phys., Vol. 28, No. 1, January 1987, pp. 41–44. © Printed in India.

Heavy-ion fusion cross-section calculations in classical microscopic equations of motion approach

S S GODRE and Y R WAGHMARE
Department of Physics, Indian Institute of Technology, Kanpur 208 016, India

MS received 30 September 1986

Abstract. Fusion cross-sections for $^{16}O + ^{16}O$ reaction earlier calculated in classical microscopic equations of motion approach, with Lennard-Jones form of *NN* interaction potential are overestimated compared to the experimental data at lower energies. This large deviation was attributed to possible breakdown of classical approximations at lower energies. The aim of this paper is to show that this discrepancy was rather due to certain assumptions made in the specification of initial conditions; in particular due to neglect of Coulomb interaction between the colliding ions at far off distances. Use of Lennard-Jones potential is also critically examined.

Keywords. Classical microscopic equations of motion approach; $^{16}O + ^{16}O$ reaction; fusion cross-section; Lennard-Jones potential; nucleon-nucleon potential.

PACS Nos 25·70; 24·10; 21·30

In recent years, classical microscopic equations of motion approach has been widely used to study heavy-ion reactions (Bodmer and Panos 1977, 1981; Bodmer *et al* 1980; Wilets *et al* 1977, 1978; Ramamurthy and Kataria 1978; Callaway *et al* 1979; Kitazoe *et al* 1981; Dixit *et al* 1983; Dixit *et al* 1985; Kiselev *et al* 1983; Kiselev 1985; Molitoris *et al* 1984; Vicentini *et al* 1985). In this approach, nucleons within the colliding nuclei are considered as classical point particles, interacting via an effective two-body interaction. Constants of the interaction are chosen so as to reproduce ground state characteristics of nuclei such as binding energies and root-mean-square (rms) radii. Collision dynamics is studied by computing trajectories of all the participating nucleons, by numerically integrating coupled classical equations of motion:

$$m\mathrm{d}^2\mathbf{r}_i/\mathrm{d}t^2 = -\nabla_i\left(\sum_{j\neq i} V_{ij}\right) \tag{1}$$

for different initial conditions of collision energies and impact parameters. Since all the translational degrees of freedom are explicitly included, dissipation of relative kinetic energy required for fusion and deep-inelastic collisions is naturally built-in in this approach without any additional assumptions of frictional forces (Birkelund *et al* 1979) or nuclear shape parametrizations (Schroder and Huizenga 1985).

Ramamurthy and Kataria (1978) studied $^{16}O + ^{16}O$ reaction with Lennard-Jones form of nucleon-nucleon potential

$$V(r_{ij}) = 4\varepsilon[(\sigma/r_{ij})^{12} - (\sigma/r_{ij})^{6}]. \tag{2}$$

CC-0. In Public Domain. Gurukul Kangri Collection, Haridwar

Digitized by Arya Samaj Foundation Chennai and eGangotri

It is found that most of the essential features of heavy-ion reactions at low energies (a few MeV/nucleon) such as fusion, deep-inelastic scattering and particle-exchange are adequately brought out in this approach. Dixit *et al* (1983, 1985) also used Lennard-Jones potential (equation (2)) and calculated fusion cross-sections for $^{16}O + ^{16}O$ (Dixit *et al* 1983) and $^{16}O + ^{40}Ca$ and $^{40}Ca + ^{40}Ca$ (Dixit *et al* 1985) reactions. Calculated fusion cross-sections qualitatively reproduced experimentally observed trend for fusion cross-sections as a function of centre of mass energy (NGO 1984). However, fusion cross-sections for all the above reactions are systematically overestimated at lower energies. This large deviation from experimental data was thought to be due to possible breakdown of classical approximations at projectile energies of the order of a few MeV/nucleons above the Coulomb barrier (Dixit *et al* 1983, 1985). The cause of this discrepancy in classical fusion cross-sections at low energies for $^{16}O + ^{16}O$ reaction is explained here and the use of Lennard-Jones potential for heavy-ion reactions is critically examined.

It is noted that, initially at $t = 0$ for collision the centres of mass of the colliding nuclei were placed at relatively large separation distance (about 20 fm) (see figure 3 of Dixit *et al* 1983) but assumed to be moving along straight line trajectories from far in the past, with initial velocities corresponding to given centre of mass collision energy and impact parameter. Thus, the repulsive effect of Coulomb interaction between the two ions was neglected for $t < 0$ at large separation distances. Coulomb potential between two ^{16}O ions separated by 20 fm is about 4·6 MeV; this though small compared to the highest energy ($E_{cm} = 67$ MeV), for which Dixit *et al* (1983) calculated fusion cross-section for $^{16}O + ^{16}O$ reaction, it cannot be neglected at lower energies. Due to this neglect of repulsive Coulomb interaction, trajectories with even higher impact parameters led to fusion of the colliding nuclei for given collision energy. This resulted in a very high value of fusion cross-section for $^{16}O + ^{16}O$ reaction at low energies. This effect is even more pronounced for reactions involving heavier ions in Dixit *et al* (1985).

Therefore, to illustrate the above effect, we recalculate fusion cross-sections for $^{16}O + ^{16}O$ reaction using the same two-body Lennard-Jones potential (equation (2)) and parameters ε and σ taken from Dixit *et al* (1983). Calculational details are also the same as in Dixit *et al* (1983) except that now initially at $t = 0$ for collision, the centres of mass of the colliding nuclei, separated by about 20 fm, are assumed to be moving along classical Coulomb trajectories the ions would have followed from far in the past with given collision energy and impact parameters. Thus calculated fusion cross-sections, averaged over 12 initial relative random orientations of the colliding nuclei, for $E_{cm} = 16{\cdot}7$, 37·6 and 66·8 MeV are shown in figure 1 (denoted by L1). Also shown in figure 1 (denoted by L1′) are fusion cross-sections calculated by neglecting Coulomb interaction for $t < 0$, as in Dixit *et al*'s calculations. It is clear from figure 1 that fusion cross-section with initially classical Coulomb trajectories (L1) is considerably reduced at lower energy compared to fusion cross-section with initially undeflected straight line trajectories (L1′). For higher energies the effect of Coulomb repulsion at large distances is reduced and since ions move in nearly straight line trajectories, fusion cross-section in both the cases do not show any appreciable difference at $E_{cm} = 66{\cdot}8$ MeV.

The parameters of potential L1 are listed in table 1 along with the calculated binding energy and rms radius of ^{16}O. Root-mean-square radius of ^{16}O obtained in the present calculation is slightly smaller than that obtained by Dixit *et al* (1983) (2·24 fm) for the same set of parameters. Because of this smaller size of the ions, fusion cross-sections

CC-0. In Public Domain. Gurukul Kangri Collection, Haridwar

Digitized by Arya Samaj Foundation Chennai and eGangotri

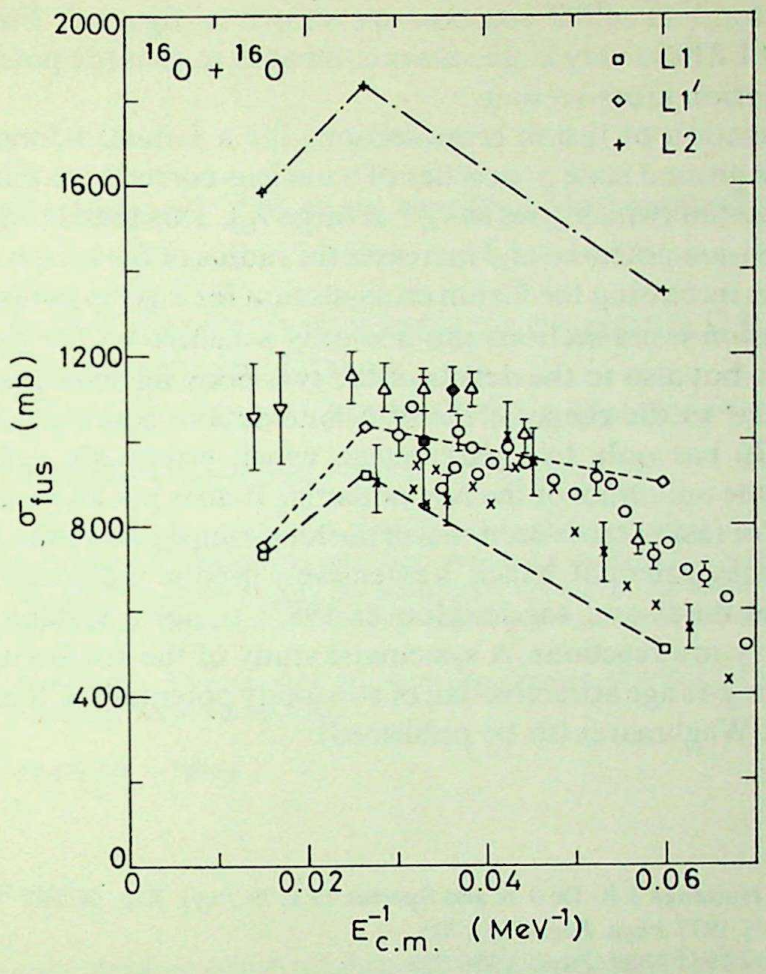

Figure 1. Calculated fusion cross-sections for $^{16}O + ^{16}O$ reaction: □—potential L1 and initially Coulomb trajectories; ◇—potential L1 and initially straight line trajectories (L1′); +—potential L2, which reproduces ground-state properties of ^{16}O. Calculated points with different potentials and initial conditions are connected to guide the eye. Experimental data: O—Tserruya *et al* (1978); X-Kover *et al* (1979); △—Fernandez *et al* (1978)◆—Cole *et al* (1980); ■—Weidinger *et al* (1976); ▽-Saint-Laurent *et al* (1979).

Table 1. Parameters of Lennard-Jones potential (equation (2)) and calculated binding energies and rms radii of ^{16}O.

	L1	L2	Experiment
ε(MeV)	2·20	2·72	—
σ(fm)	1·80	2·36	—
Binding energy (MeV)	− 96·8	− 127·6	− 127·6
RMS radius (fm)	2·12	2·73	2·73

with initially straight line trajectories (L1′) are slightly smaller than the corresponding fusion cross-sections obtained by Dixit *et al* (1983). However, rms radius obtained in both calculations is about 20% smaller than the experimental rms radius of ^{16}O. Consequently, fusion cross-sections with potential L1, and correct initial conditions, are also lower than the experimental fusion cross-sections. Therefore, we have readjusted the parameters of Lennard-Jones potential (equation (2)) such that, experimental binding energy and rms radius of ^{16}O are reproduced correctly. Parameters of this potential (called L2) are given in table 1 and the corresponding

CC-0. In Public Domain. Gurukul Kangri Collection, Haridwar

Digitized by Arya Samaj Foundation Chennai and eGangotri

fusion cross-sections for $^{16}O + ^{16}O$ reaction are shown in figure 1. Fusion cross-sections with potential L2 have very large values compared to that for potential L1, as well as experimental fusion cross-sections.

The above overestimation of fusion cross-sections for a Lennard-Jones potential (L2), which reproduces ground state properties of a nucleus correctly, is mainly due to its long-range attractive-tail (which goes as r_{ij}^{-6} at large r_{ij}). This tends to increase the attractive part of the ion-ion potential and increases the radius of the fusion barrier and decrease its height, thus increasing the fusion cross-section for a given collision energy. This indicates that fusion cross-sections are not only sensitive to the ground state properties of the nuclei but also to the details of the two-body nucleon-nucleon (NN) interaction, in particular to the range of the N-N interaction. Since, Lennard-Jones potential (equation (2)) has only two parameters, which essentially determine the position and depth of the minimum of the NN potential, it does not allow a systematic study of the sensitivity of fusion cross-sections on the long-range part of the interaction. Hence the Lennard-Jones potential, which is extensively used in molecular dynamical simulations of classical fluids and solids (Hoover 1983), is not a suitable two-body potential to study heavy-ion reactions. A systematic study of the sensitivity of fusion cross-sections on the long-range attractive-tail of two-body potentials will be presented elsewhere (Godre and Waghmare) (to be published).

References

Birkelund J R, Tubbs L E, Huizenga J R, De J N and Sperber D 1979 *Phys. Rep.* **56** 107

Bodmer A R and Panos C N 1977 *Phys. Rev.* **C17** 1700

Bodmer A R and Panos C N 1981 *Nucl. Phys.* **A356** 517

Bodmer A R, Panos C N and MacKellar A D 1980 *Phys. Rev.* **C22** 1025

Callaway D J E, Wilets L and Yariv Y 1979 *Nucl. Phys.* **A327** 250

Cole A J *et al* 1980 *Nucl. Phys.* **A341** 284

Dixit A N, Ramamurthy V S and Waghmare Y R 1983 *Pramana–J. Phys.* **20** 523

Dixit A N, Mani T K and Waghmare Y R 1985 *Proc. Natl. Acad. Sci.* **A55** 76

Fernandez B *et al* 1978 *Nucl. Phys.* **A306** 259

Godre S S and Waghmare Y R (to be published)

Hoover W G 1983 *Ann. Rev. Phys. Chem.* **34** 103

Kislev S M 1985 *Phys. Lett.* **B154** 247

Kislev S M and Pokrovskii Y E 1983 *Sov. J. Nucl. Phys.* **38** 46

Kitazoe Y, Yamamoto K and Sano M 1981 *Lett. Nuovo Cimento* **32** 337

Kover D G *et al* 1979 *Phys. Rev.* **C20** 1255

Molitoris J J, Hoffer J B, Kruse H and Stocker H 1984 *Phys. Rev. Lett.* **53** 899

NGO C 1984 *Il Nuovo Cimento* **A81** 47

Ramamurthy V S and Kataria S K 1978 *Pramana–J. Phys.* **11** 457

Saint-Laurent F *et al* 1979 *Nucl. Phys.* **A327** 517

Schroder W U and Huizenga J R 1985 *Treatise on heavy-ion science*, (ed) D A Bromley (New York: Plenum Press), Vol. 2, p. 115 and references therein

Tserruya I *et al* 1978 *Phys. Rev.* **C18** 1688

Vicentini A, Jacucci G and Pandharipande V R 1985 *Phys. Rev.* **C31** 1783

Weidinger A *et al* 1976 *Nucl. Phys.* **A263** 511

Wilets L, Henley E M, Kraft M and MacKellar A D 1977 *Nucl. Phys.* **A282** 341

Wilets L, Yariv Y and Chestnut R 1978 *Nucl. Phys.* **A327** 250

CC-0. In Public Domain. Gurukul Kangri Collection, Haridwar

Digitized by Arya Samaj Foundation Chennai and eGangotri

Pramāṇa – J. Phys., Vol. 28, No. 1, January 1987, pp. 45–50. © Printed in India.

Theoretical study of ^{14}N pure quadrupole resonance in amino acids

B V R R K MURTY, G KRISHNA KISHORE, D KRISHNA RAO and G SATYANANDAM

Department of Physics, Nagarjuna University, Nagarjuna Nagar 522 510, India

MS received 9 September 1985; revised 2 August 1986

Abstract. The theoretical hybridization model of Vega is adapted to the tetrahedral environment around the nitrogen nucleus in eleven amino acids to estimate the orbital occupation numbers using the experimental values of the quadrupole coupling constant and asymmetry parameter of ^{14}N quadrupole resonance and the results are discussed.

Keywords. Electric field gradient; quadrupole coupling constant; occupation number; hybrid orbitals; amino acids.

PACS No. 76·60

1. Introduction

The study of the nuclear quadrupole coupling constants (QCC) helps in calculating the electric field gradients (EFG) and also provides useful information about the concepts of chemical bonds like ionic character, occupation numbers, double bond character etc. The theoretical interpretation of QCC in terms of the chemical bonds was first given by Townes and Dailey (1949) and has been applied to N-heteroaromatics (Scrocco 1965), hydrazines and hydrazides (Sauer and Bray 1972), azines (Sauer *et al* 1972) and amino acids (Edmonds and Summers 1973). Later Vega (1974) proposed a theoretical model relating the EFG components, the electronic occupation numbers and degrees of hybridization in sp^3 tetrahedral configuration around the nitrogen nucleus, without recourse to the assumptions involved in Townes and Dailey theory. In the present work, the treatment proposed by Vega (1974) has been adapted to nitrogen resonance in various amino acids to calculate the occupation numbers of hybrid orbitals and the results are discussed.

2. Theory

To correlate the EFG components with the charge distribution in the molecule, Vega (1974) considered tetrahedral configuration around the resonating nucleus and assumed reflection symmetry for the two equivalent hybrids ϕ_1 and ϕ_2 with the occupation number a_1 which make an angle $2\theta(>\pi/2)$ with each other while the other two hybrids ϕ_3 and ϕ_4 with occupation numbers a_3 and a_4 lie in the symmetry plane as shown in figure 1. An orthogonal coordinate system $\xi\,\eta\,\zeta$ is chosen such that ζ-axis is perpendicular to the symmetry plane, η-axis bisecting the ϕ_1 and ϕ_2 orbits and ξ-axis

CC-0. In Public Domain. Gurukul Kangri Collection, Haridwar

Digitized by Arya Samaj Foundation Chennai and eGangotri

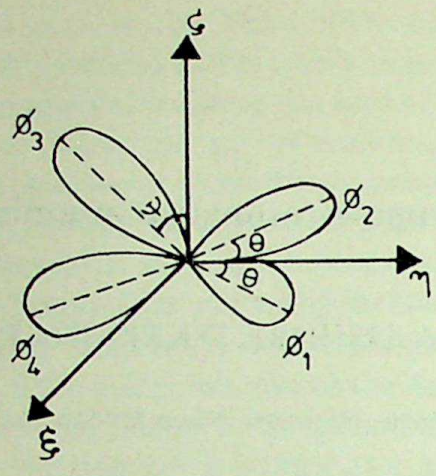

Figure 1. The chosen orthogonal coordinate system ($\xi\eta\zeta$) and the hybrid orbitals. (ϕ_1, ϕ_2, ϕ_3): hybrid orbitals. ($\xi\eta\zeta$): Chosen orthogonal coordinate system. θ is the angle made by the ϕ_1, ϕ_2 orbitals with η-axis. ψ is the angle made by ϕ_3 orbital with ζ-axis.

perpendicular to both the axes. Using the orthonormality relation of the hybrids and replacing each hybrid by a point charge along the hybrid direction at a unit distance from the resonating nucleus, the EFG tensor in $\xi\eta\zeta$ system can be expressed as (Vega 1974),

$$\begin{Vmatrix} 2C(3\sin^2\theta - 1) - 1 & 0 & 0 \\ 0 & 2C(2-3\sin^2\theta) + 3\sin^2\psi - 1 & 3\sin\psi\cos\psi \\ 0 & 3\sin\psi\cos\psi & 2 - 3\sin^2\psi - 2C \end{Vmatrix} \quad (1)$$

where $$C = \frac{1+\cot^2\theta}{2(1-\alpha^2\cot^2\theta)} \frac{a_1 - a_4}{a_3 - a_4},$$

and $$\alpha^2 = \frac{\tan^2\psi}{\sec^2\psi - \cot^2\theta}. \quad (2)$$

Here ψ is the angle made by ϕ_3 with ζ-axis. Thus the NQR parameters are written in terms of the reduced charge C and the resulting diagonalized EFG values may be called 'reduced' principal values V'_{ii} ($i = x, y, z$) which vary continuously with C. However, the assorted values V'_{jj} ($j = X, Y, Z$ the principal system) which have to satisfy the convention $|V'_{XX}| < |V'_{YY}| < |V'_{ZZ}|$ do not vary continuously. Further, C is a multiple valued function of η and cannot therefore be determined without further considerations such as electronegativity etc. Thus, if a proper solution for C is found, information on the relative occupation numbers can be sought from the experimental result for quadrupole coupling constant (e^2qQ) using the relation

$$e^2qQ = (1/2)e^2q_0Q(a_3 - a_4)(1 - \alpha^2\cot^2\theta)V'_{ZZ}, \quad (3)$$

where e^2q_0Q is the atomic coupling constant.

3. Method of calculation and results

In the present work, this theoretical model is applied to the nitrogen resonance in eleven amino acids namely, α-glycine (Jonsson and Kvick 1972), L-cysteine (Oughton and

CC-0. In Public Domain. Gurukul Kangri Collection, Haridwar

Digitized by Arya Samaj Foundation Chennai and eGangotri

Harrison 1959), β-glycine (Iitaka 1960), L-tyrosine (Frey *et al* 1973), L-alanine (Lehmann *et al* 1972), DL-alanine (Kitaigorodskii 1961), L-cysteine 2HCl with two ^{14}N resonances (Jones *et al* 1974), L-glutamic acid HCl (Sequeira *et al* 1972), DL-serine (Shoemaker *et al* 1953), L-tyrosine HCl (Frey *et al* 1973) and L-histidine (orthorhombic) (Madden *et al* 1972). The experimental values of quadrupole coupling constant and η at 77 K for all the compounds (Edmonds and Summers 1976; Hunt 1974; Hunt and Mackay 1976) are given in table 1.

In solid state, these amino acids are zwitter ions which have the general formula $N^+H_3 \cdot C(R)H \cdot COO^-$ where R is the side group which distinguishes the different amino acids. Here two of the three hydrogens attached to nitrogen form strong hydrogen bonds to the oxygen atoms of the neighbouring molecules and the third hydrogen takes part in a weaker bifurcated hydrogen bond (Jonsson and Kvick 1972) to the two neighbouring oxygen ions. Thus the system with three N–H bonds and the N–C bond is close to a tetrahedral configuration and possesses, to a good approximation, a plane of symmetry passing through the carbon atom, the nitrogen atom and the hydrogen in the bifurcated hydrogen bond.

For the sake of consistency, in all these compounds, the nearly equivalent N–H bonds are taken as ϕ_1 and ϕ_2, N–C bond as ϕ_3 and the other N–H bond as ϕ_4 orbital representation. Now by using the crystal structure data of all the eleven compounds, the reduced principal EFG components V'_{XX}, V'_{YY}, V'_{ZZ} are calculated as function of C according to tensor (1). It can be seen that there are several values for C corresponding to the experimental η, thereby requiring additional information for the correct choice of C.

Due to lack of experimental field gradient directions, the electronegativities of the orbitals are considered. As the electronegativities can be estimated from the bond distances, the trend of the calculated values for the four orbitals helps in fixing the correct region for the value of C and thereby arriving at a right solution. Thus the calculated values of C for all the compounds are given in table 1.

The relative occupation numbers are obtained from (3) taking the value of e^2q_0Q for nitrogen as $-11{\cdot}88$ MHz and subsequently from (2). The values of these relative occupation numbers and the angle (ξ) between the calculated Z axis and the N–C bond for all the compounds are incorporated in table 1.

4. Discussion

The present calculated values for occupation numbers in the cases of α-glycine, L-cysteine, L-tyrosine and L-histidine (orthorhombic) are in good agreement with those obtained by Edmonds and Summers (1973) as given in square brackets in table 1. Further the angle ξ of $7{\cdot}17°$ for α-glycine agrees well with their result of $8{\cdot}8°$ and of $10{\cdot}1°$ obtained by NMR data (Andersson *et al* 1968). As additional theoretical or experimental data on any of the compounds under study are not available, further comparison cannot be made.

For small values of η, the Z axis can be expected to be nearly parallel to the N–C bond such that the value of η will reflect the asymmetry about this direction. Thus the plot between η and the tilt angle (ξ) for the data in table 1 gave a linear relationship as

$$\eta = 3{\cdot}83 \sin \xi. \tag{4}$$

CC-0. In Public Domain. Gurukul Kangri Collection, Haridwar

Table 1. Experimental NQR data and the calculated results for the amino acids.*

Compound	Experimental e^2qQ (MHz)	η	C	$a_1 - a_4$	$a_3 - a_4$	ξ	$(\Delta\xi)$
α-glycine	1·249	0·501	−0·445	0·049	−0·107	7·17°	(+0·35°)
				[0·06]	[−0·10]	[8·76°]	
L-cysteine	1·220	0·475	0·285	−0·042	−0·191	6·94°	(+0·18°)
				[−0·05]	[−0·10]	[8·17°]	
β-glycine	1·317	0·440	−0·439	0·049	−0·118	7·47°	(−0·87°)
L-tyrosine	1·078	0·414	0·253	−0·036	−0·145	4·96°	(+1·24°)
				[−0·04]	[−0·09]	[6·8°]	
L-alanine	1·205	0·261	0·163	−0·025	−0·151	3·30°	(+0·61)
DL-alanine	1·243	0·245	−0·191	−0·024	−0·122	3·44°	(+0·22°)
L-cysteine 2HCl	1·167	0·151	0·112	−0·014	−0·168	2·47°	(−0·21°)
	1·160	0·094	0·072	−0·009	−0·163	1·62°	(−0·21°)
L-glutamicacid HCl	1·193	0·143	0·108	−0·015	−0·148	2·40°	(−0·26°)
DL-serine	1·217	0·118	0·108	−0·015	−0·135	1·32°	(+0·44°)
L-tyrosine HCl	0·977	0·113	0·080	−0·009	−0·118	1·83°	(−0·13°)
L-histidine (orthorhombic)	1·251	0·113	−0·095	0·012	−0·139	3·31°	(−1·61°)
				[0·01]	[−0·13]	[1·64°]	

* The values given in square brackets are taken from Edmonds and Summers (1973).

Digitized by Arya Samaj Foundation Chennai and eGangotri

CC-0. In Public Domain. Gurukul Kangri Collection, Haridwar

Digitized by Arya Samaj Foundation Chennai and eGangotri

Table 2. Reported values (Edmonds *et al* 1973; Edmonds and Summers 1973) in other compounds in the tetrahedral environment. The values in brackets are calculated from equations (4) and (5) of the present work.

	Experimental			
Compound	e^2qQ (MHz)	η	$a_1 - a_4$	ξ
Dimethyl ammonium chloride	1·261	0·964	0·12 (0·09)	27·7° (14·6°)
Diethyl ammonium chloride	1·059	0·925	0·10 (0·09)	24.4° (13·9°)
Methyl ammonium chloride	0·913	0·109	0·01 (0·01)	1·6° (1·6°)
Ethyl ammonium chloride	0·858	0·086	0·01 (0·01)	1·2° (1·3°)
L-proline	1·623	0·955	0·16 (0·09)	26·8° (14·4°)
Cysteine (A)	1·273	0·640	0·07 (0·06)	12·3° (9·6°)
Phenylalanine	1·354	0·630	0·08 (0·06)	12·0° (9·5°)
L-serine	1·215	0·184	0·02 (0·02)	2·6° (2·7°)
Cysteine (B)	1·195	0·130	0·01 (0·01)	1·9° (1·9°)
Cysteine HCl	1·223	0·120	0·01 (0·01)	1·7° (1·8°)

The best fit nature of equation (4) can be understood from the deviations given in table 1.

Further, in the model of Townes and Dailey (1949), the value of η is solely attributed to the difference between the N–H bond occupation numbers i.e. $|a_1 - a_4|$ arising out of the intramolecular or intermolecular hydrogen bonds. The variation of $|a_1 - a_4|$ with η in the present work is also found to be linear and is given by

$$\eta = 9{\cdot}908\,|a_1 - a_4|. \tag{5}$$

The application of the fitted equations (4) and (5) to other amino acids (Edmonds and Summers 1973) and compounds having tetrahedral environment (Edmonds *et al* 1973) to predict the values of ξ and $|a_1 - a_4|$ is fairly satisfactory for low values of η as can be seen from table 2.

The difference between the average electron occupation of an N–H bond and that of N–C bond i.e. $(a_3 - a_4) - (2/3)(a_1 - a_4)$ for the group of compounds under study is found to be nearly constant around an average value of 0·140 which is in good agreement with the value of 0·135 found by Edmonds and Summers (1973) for another group of amino acids given in table 2. Such an observation is also found in amines and amides (Lucken 1969).

Acknowledgements

The authors are indebted to the late Professor C R K Murty for helpful suggestions and discussions. Financial support from CSIR and DAE is gratefully acknowledged. Part of the work was presented at the Silver Jubilee Physics Symposium, BARC, Bombay, 1981.

CC-0. In Public Domain. Gurukul Kangri Collection, Haridwar

Digitized by Arya Samaj Foundation Chennai and eGangotri

References

Andersson L, Gourdji M, Guibe L and Proctor W S 1968 *C R. Acad. Sci. Paris* **B267** 803
Edmonds D T, Hunt M J and Mackay A L 1973 *J. Magn. Reson.* **9** 66
Edmonds D T and Summers C P 1973 *J. Magn. Reson.* **12** 134
Edmonds D T and Summers C P 1976 *Chem. Phys. Lett.* **41** 482
Frey M N, Koetzle T F, Lehmann M S and Hamilton W C 1973 *J. Chem. Phys.* **58** 2547
Hunt M J 1974 *J. Magn. Reson.* **15** 113
Hunt M J and Mackay A L 1976 *J. Magn. Reson.* **22** 295
Iitaka Y 1960 *Acta Crystallogr.* **13** 35
Jones D D, Bernal I, Frey M N and Koetzle T F 1974 *Acta Crystallogr.* **B30** 1220
Jonsson P G and Kvick A 1972 *Acta Crystallogr.* **B28** 1827
Kitaigorodskii A I 1961 *Organic chemical crystallography* (New York: Consultants Bureau)
Lehmann M S, Koetzle T F and Hamilton W C 1972 *J. Am. Chem. Soc.* **94** 2657
Lucken E A C 1969 *Nuclear quadrupole coupling constants* (New York: Academic Press)
Madden J J, Mc Gandy E L and Seeman N C 1972 *Acta Crystallogr.* **B28** 2377
Oughton B M and Harrison P M 1959 *Acta Crystallogr.* **12** 396
Sauer E G and Bray P J 1972 *J. Chem. Phys.* **56** 820, 2788
Sauer E G, Bray P J, Marino R A and Oja T 1972 *J. Chem. Phys.* **57** 3807
Scrocco E 1965 *Molec. Biophys.* 293
Sequeira A, Rajagopal H and Chidambaram R 1972 *Acta Crystallogr.* **B28** 2514
Shoemaker D P, Barieau R E, Donohue J and Chia-Silu L 1953 *Acta Crystallogr.* **6** 241
Townes C H and Dailey B P 1949 *J. Chem. Phys.* **17** 782
Vega S 1974 *J. Chem. Phys.* **60** 3884

CC-0. In Public Domain. Gurukul Kangri Collection, Haridwar

Digitized by Arya Samaj Foundation Chennai and eGangotri

Pramāṇa – J. Phys., Vol. 28, No. 1, January 1987, pp. 51–58. © Printed in India.

On the direct determination of constrained pure state one-electron density matrices: II. A modified algorithm and its applications

KALYAN K DAS, PRIYOTOSH KHAN† and
SANKAR P BHATTACHARYYA

Department of Physical Chemistry, Indian Association for the Cultivation of Science, Jadavpur, Calcutta 700032, India
†Department of Mathematics, Behala College, Parnasree, Calcutta 700062, India

MS received 2 June 1986; revised 25 September 1986

Abstract. An algorithm recently proposed by us for the direct determination of pure state one-electron density matrices (P) under externally imposed constraints has been remodelled. The modified algorithm is applied to the construction of ground state potential energy curve of lithium hydride molecule using *known* values of dipole moments of LiH at various internuclear distances as the *external* constraint. The equilibrium internuclear distances (R_e) is seen to be unaffected by the constraint, but the force constant improves remarkably. The relevant features of the constrained density vis-a-vis those of the unconstrained one are analyzed revealing some of the improved features of the constrained density.

Keywords. Direct density method; constrained variational calculations; penalty function method; constrained density method.

PACS No. 31·15

1. Introduction

One-electron density is a quantity of paramount importance in the understanding of molecules and their structural and chemical features (Bamzai and Deb 1981). The route to one-electron density, however, varies. It can be an experimental quantity or a theoretical one. Theoretically, the one-electron density $P(\mathbf{r})$ can be treated as a derived quantity obtained from an appropriate N-particle wave function or may be regarded as a directly obtainable quantity. Consequently, the mathematical problem of directly obtaining an N-representable one-electron (atomic or molecular) density has attracted considerable attention and has led to the development of density functional theories through the celebrated Hohenberg-Kohn theorem (Hohenberg and Kohn 1964) and the Kohn-Sham (Kohn and Sham 1965) variational principle. The time-dependent generalizations of density functional theory (DFT) too, have been suggested (Deb and Ghosh 1982; Bartolotti 1981).

Alternatively, one may also look for the one-electron density (OED) in a discrete orthonormal (say) basis. The corresponding quantity is the one-electron density matrix (OEDM) P. At the lowest level of approximation, the direct determination of the P matrix has been most generally tackled through methods based on first-order constrained variational procedure (McWeeny 1956, 1957). We (Das *et al* 1985) recently proposed a method for the direct determination of 'property'-constrained P matrix using the penalty-function scheme of handling equality (inequality) constraints. Unlike

CC-0. In Public Domain. Gurukul Kangri Collection, Haridwar

Digitized by Arya Samaj Foundation Chennai and eGangotri

an earlier attempt in this direction (Weinstein and Pauncz 1972), our algorithm is *not* a gradient biased one and uses a particular realization of the penalized-function procedure called the method of Morrison's Function (MF) (Morrison 1968). Our initial experiences with the algorithm (Das *et al* 1985) revealed certain difficulties: (i) the rate of convergence is slow for a given penalty weight factor; (ii) several penalty weight factors have to be used in general to improve convergence; (iii) the choice of several optimal weight factors entails significant computational labour and time; (iv) the problem is ill-conditioned for very small penalty weight factors, etc. To circumvent these difficulties (at least partially) we have recently proposed an alternative hybrid procedure (Das and Bhattacharyya 1986). The present paper deals with the details of a concrete application of this hybrid algorithm.

2. The problem

Accurate dipole moment function $\mu^0(R)$ of lithium hydride molecule in the ground state is known (Patridge Hary and Langhoff 1981). We propose to use $\mu^0(R)$ as the constraining observable at different internuclear distances and construct the constrained ground state potential energy curve of Li-H and try to answer the following questions:

(i) does the 'μ'-constraint affect the calculated equilibrium internuclear separation in the ground state?

(ii) does it modify the stretching force constant?

(iii) under the influence of the 'μ-constraint' what kind of reorganization takes palce in the OED with respect to the unconstrained HF density (UHFD).

3. The method

The details of the derivation can be found in one of our earlier communications (Das and Bhattacharyya 1986). In the present context, it therefore suffices to present the brief outline of the derivation which simultaneously serves to define the working equations.

Let P be the trial OEDM in an n-dimensional discrete orthonormal basis $\{\chi_i\}_{i=1,n}$ representing the ground state of a $2m$ electron closed-shell atom or molecule ($n \geqslant m$).

The N-presentability constraints on P demand that

$$P^2 = P, \tag{1}$$

$$P^\dagger = P, \tag{2}$$

and

$$\mathrm{Tr}\, P = m. \tag{3}$$

Conditions (1), (2) and (3) constitute what may be called pure state N-representability conditions. We impose additional property constraints on P which demand that

$$\mathrm{Tr}\,[P B_k] = b_k^0 \quad (k = 1, 2, \ldots q), \tag{4}$$

where B_k is the Hermitian matrix representing the kth observable in χ basis, the "known" value of the observable concerned being b_k^0. The constrained variational procedure can now be based on a functional E_{MC} where

CC-0. In Public Domain. Gurukul Kangri Collection, Haridwar

Digitized by Arya Samaj Foundation Chennai and eGangotri

$$E_{MC} = (E - E_L)^2 + \beta \,\mathrm{Tr}\,(P^2 - P)^2 + \sum_{k=1}^{q} \bar{\lambda}_k [\mathrm{Tr}\,(PB_k) - b_k^0], \tag{5}$$

where E_L is a lower bound to the constrained energy E, $\bar{\lambda}_k$'s are Lagrangian multipliers and β is an appropriate penalty weight factor. This functional leads to the following iterative scheme for the self-consistent determination of the constrained density (Das and Bhattacharyya 1986).

$$P_i \to P_{i+1} = 3P_i^2 - 2P_i^3 - \alpha(\tilde{E}_i - E_L^i) F_i - \sum_k \gamma_k^i B_k, \tag{6}$$

where $\alpha = 2/\beta$ and $\gamma_k^i = \bar{\lambda}_k^i/\beta$, F_i is the usual closed-shell HF matrix at the ith iteration, $\tilde{E}_i$ being the constrained energy at the same stage. The updating of E_L^i is accomplished by using

$$E_L^{i+1} = E_L^i + a[\mathrm{Tr}\,(A_i^\dagger A_i)]^{1/2} \qquad (0 < a \leqslant 1), \tag{7}$$

where

$$A_i = \alpha(\tilde{E}_i - E_L^i) F_i + (2P_i^3 - 3P_i^2 + P_i) + \sum_k \gamma_k^i B_k. \tag{8}$$

γ_k^i's are determinable through the solution of the following set of linear simultaneous equations:

$$V Y^i = D^i \ (Y \text{and } D \text{ are column vectors}) \tag{9}$$

where

$$V_{kl} = \mathrm{Tr}(B_k{}^\dagger B_l), \quad D_k^i = [\mathrm{Tr}\,(Q_i B_k) - b_k^0],$$
$$Y_k^i = \gamma_k^i \quad \text{and} \quad Q_i = 3P_i^2 - 2P_1^3 - \alpha(\tilde{E}_i - E_L^i) F_i. \tag{10}$$

We have assumed so far that our basis (χ) is orthonormal. It is quite straightforward to formulate the algorithm in a non-orthogonal basis ($\bar{\chi}$).

4. Results and discussion

4.1 *Methodological details*

The calculations have been carried out at the CNDO/2 level of approximations (Pople *et al* 1965; Pople and Segal 1965) to cut down computational costs. Since the dipole moment curves calculated at the HF level have qualitatively similar features whether calculated at the CNDO/2 or *ab-initio* (STO-3G) level the use of CNDO/2 suffices for test calculations. For the constrained calculations, the corresponding unconstrained P-matrix has been used as the input. The calculations have been carried out over a wide range of Li-H distance (R) viz from $R = 1{\cdot}5$ a.u. to $4{\cdot}0$ a.u. The iteration procedure was based on equation (6) and iterations were terminated when the object function(al) decreased below 10^{-6} (cf (6)) or equivalently, when $\mathrm{Tr}\,(A_i{}^\dagger A_i) < 10^{-6}$ condition was achieved. The Lagrangian multiplier $\bar{\lambda}_k$ (only one in the present example) was calculated at each step by using (9) and monitored along the iteration path. Care was taken to ensure that $\bar{\lambda}_k < 10^{-6}$ at convergence. The only penalty weight factor in the present

CC-0. In Public Domain. Gurukul Kangri Collection, Haridwar

Digitized by Arya Samaj Foundation Chennai and eGangotri

case is α (cf (6)). In all these calculations we started with α as small as 10^{-5} and increased it by a factor of 10 whenever the value of Morrison function(al) was reduced further by a factor of 10. Subsequently, when α was already 0·1, we slowed down the penalty enhancement rate further by a factor of 0·5 ensuring, however, that $\alpha \to 1$ as E_{MC} or $\mathrm{Tr}(A_i^\dagger A_i) \to 0$. This strategy has been found to ensure smooth convergence and was established through extensive model calculations. After the achievement of convergence the P matrix was diagonalized and its eigenvalues were examined as a further check on the Hartree-Fock N-representability of P.

The updating of the estimated lower bound to energy (E_L) was done by using the following equation (equation (7))

$$E_L^{i+1} = E_L^i + a[\mathrm{Tr}(A_i^\dagger A_i)]^{1/2},$$

with $a = -0{\cdot}0025$ to start with when $\mathrm{Tr}(A_i^\dagger A_i)$ was still large. After the iterations moved into a stable region and $\mathrm{Tr}(A_i^\dagger A_i)$ are started to fall off monotonically, the absolute value of a was slowly increased. Unless this is done, iterations tend to converge too slowly. The use of a negative value of a requires explanation. Since we use the unconstrained OEDM as the input and since the constrained energy is an upper bound to the unconstrained energy, we prefer to interpret E_L^i of (6) as an upperbound to E^i. This requires that $E_L^i > E^i$ and $E_L^i \to E^i$ from above as $\mathrm{Tr}(A_i^\dagger A_i) \to 0$. This can be ensured by choosing $a < 0$ in (7).

4.2 *μ-Constrained versus unconstrained potential energy curves*

The dipole moment function $\mu^0(R)$ of a diatomic molecule may be viewed as a continuous collective coordinate describing sharing of electron density between the atoms and also of any deformation of the same on the bonded atoms under the influence of its partner. Since $\mu^0(R)$ could be an experimental or accurate theoretical quantity, its use as the constraining collective variable has the advantage in that it has important effects of many-body interactions incorporated in it and conceivably therefore, the use of $\mu^0(R)$ as the constraining observable could succeed in inducing certain reorganizations in the unconstrained electron density representing many-body effects. Due to the constraint imposed E (constrained) $> E$ (unconstrained) at each R. The second order estimate of this energy difference ($\Delta E^2(R)$) (Byers Brown 1966) is given by

$$\Delta E(R) \approx \Delta E^2(R) = -|\Delta\mu(R)|^2/4E^2(R),$$

where

$$E^2 = \sum_i \langle\psi_0|e\cdot\mathbf{r}|\psi_i\rangle^2/(E_0 - E_i) \quad \text{and}$$

$$\Delta\mu(R) = \mu^0(R) - \mu(R),$$

$\mu(R)$ being the unconstrained value of μ^0. Since Li-H is a highly polarizable (soft) molecule, one expects it to have several low-lying excited states (ψ_i) that can mix with the ground state (ψ_0) under the $e\cdot\mathbf{r}$ perturbation making $E^2(R)$ rather large. This means that $\Delta E^2(R)$ should be a small quantity enabling one to enforce $\mu(R)$ constraint at a small sacrifice of energy.

Figures 1(a) and (b) present the unconstrained and the constrained potential energy curves of Li-H molecule respectively. At each R, the constrained energy is slightly above

CC-0. In Public Domain. Gurukul Kangri Collection, Haridwar

Digitized by Arya Samaj Foundation Chennai and eGangotri

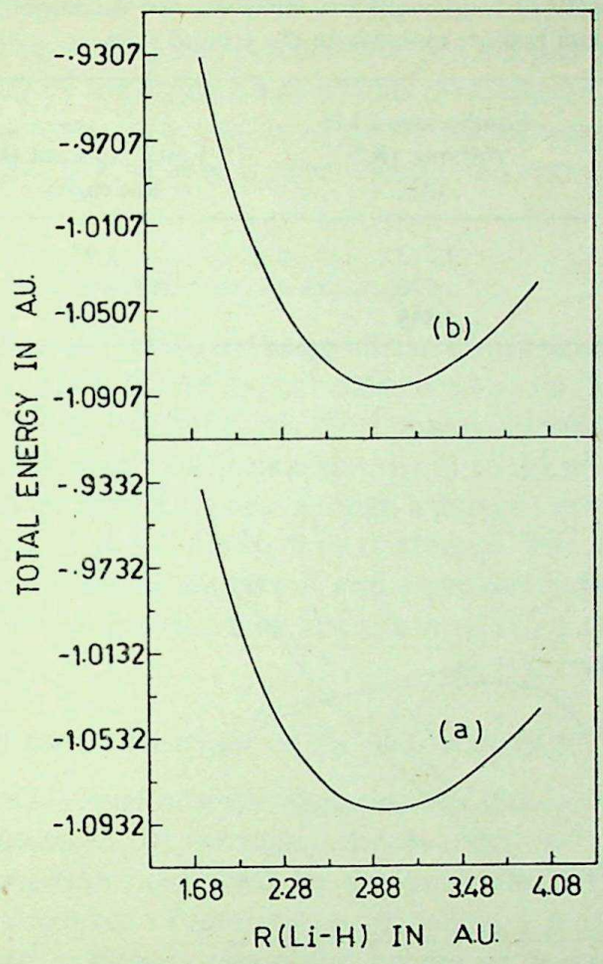

Figure 1. (a) Unconstrained ground state potential energy (PE) curve of lithium hydride molecule, (b) the constrained PE curve for the same.

its unconstrained counterpart as expected. 10^{-6} a.u $\leqslant \Delta E(R) \leqslant 10^{-2}$ a.u over the range of R studied, the minimum value of $\Delta E(R)$ occurring near $R = R_e$. The calculated R_e values and the force constants are reported in table 1 along with their experimental counterparts. The R_e values are virtually identical for the constrained and the unconstrained calculations. But the force constant (k_e) calculated from the constrained PE curve (figure 1(b)) is much smaller than the unconstrained value and is in quite good agreement with the experimental value. The fact that the μ-constraint does not affect R_e significantly can be easily explained by noting that $\Delta\mu(R)$ is rather small at and around R_e (see figures 2(a) and (a_0)) and is minimum at $R = R_e$. The appreciable reduction of the value of k_e from its HF value apparently shows that the "μ-constraint" has indirectly introduced certain many-body effects in the constrained density; for it is well known that the computed value of diatomic force constant is always significantly reduced from its HF value when the effects of doubly-excited configurations involving excitation of electron pairs into antibonding orbitals are included in the CI calculations.

4.3 *Constrained versus the unconstrained dipole moment curve*

Figure 2 (a_0) depicts the variation of μ calculated with the unconstrained OEDM (P_0), with R. Figure 2(a), on the other hand, displays the μ-R profile with μ calculated with the constrained OEDM(P_c). In practice, the μ-R profile in figure 2(a) virtually coincide with the known dipole moment curve. The two curves cross each other at around

CC-0. In Public Domain. Gurukul Kangri Collection, Haridwar

Digitized by Arya Samaj Foundation Chennai and eGangotri

Table 1. Results of constrained and unconstrained variational calculation on lithium hydride molecule in the ground state.

	Equilibrium Li-H distance (R_e) (Å)	Force constant (k_e) (mdyn/Å)
Unconstrained result	1·573	1·95
Constrained result	1·576	1·12
Experimental data[a]	1·595	1·03

[a] Herzberg (1950)

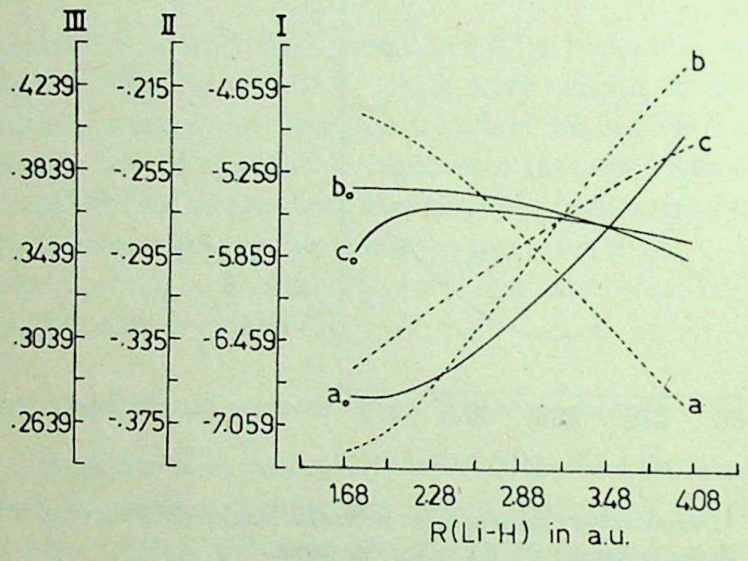

Figure 2. (a_0) Unconstrained ground state dipole moment function, (**a**) the constrained counterpart of a_0; (b_0) the net charge (q_H) on the H-atom of Li-H in the ground state shown as a function of the internuclear distance R in the unconstrained case; (**b**) the constrained q_H-R profile; (c_0) the R-dependence of the degree of sp mixing (P_{sp}) on the Li-atom in Li-H (ground state) in the unconstrained case, (**c**) the constrained $P_{sp} - R$ profile, curves (a, a_0) are drawn in scale (I), (b, b_0) in scale (II) while curves (c, c_0) are drawn in scale (III).

$R = R_e$ leading to fortuitously low $\Delta\mu$ values around $R = R_e$. Clearly, over the range of R studied, μ (unconstrained) does not have even the qualitatively correct features of the "actual" dipole moment curve. It is worth noting that the same unconstrained density, however, gives better energy estimates [figure 1(a)] showing that variationally determined energy may conceal errors in the corresponding wavefunction or one-electron density which are revealed only when some first order property is used for error calibration.

4.4 *Reorganization of electron density under the μ-constraint*

Figures 2(b_0) and (b) display the variation of the computed net charges on the hydrogen atom (q_H^0 or q_H^c) atom with the internuclear separation (R) in the unconstrained and the μ-constrained calculations. At shorter values of R, the effect of the μ-constraint is clearly seen to result in an increase of net electron density on the H-atom relative to what is observed in the unconstrained case (figure 2(b)). With the increase of R, the unconstrained calculations predict an increase of the net charge (negative) on H atom

CC-0. In Public Domain. Gurukul Kangri Collection, Haridwar

Digitized by Arya Samaj Foundation Chennai and eGangotri

suggesting that as $R \rightarrow \infty$, LiH is expected dissociate into a mixture of Li + H and $Li^+ + H^-$. The constrained calculations predict just the opposite behaviour indicating the possibility of the correct homopolar dissociation occurring as $R \rightarrow \infty$. The $q_H^c - R$ and $q_H^0 - R$ curves, however, cross each other around the equilibrium Li-H distance, revealing again that at $R = R_e$ the constrained and unconstrained results might agree accidentally.

4.5 *Effect of μ-constraint on sp mixing*

A substantial contribution to the net dipole moment of Li-H in the present model comes from the mixing of $2s$ and $2p_z$ orbitals on Li-atom (H has no p-function in the basis). Figures 2(c_0) and (c) display how the degree of sp mixing vary with R in the constrained and unconstrained calculations respectively. In the unconstrained case, the degree of sp mixing increases slowly, passes through a maximum and then decreases monotonically over the range of R (1·5 a.u to 4·5 a.u) studied. The μ-constraint is seen to reduce the degree of sp mixing at shorter R and increases it for larger internuclear separation relative to what is predicted by the unconstrained calculation.

4.6 *Effect of the μ-constraint on the shared density*

At the CNDO/2 level of approximation the diatomic overlap density does not make any contribution to the calculated dipole moment. Table 2 displays the net diatomic overlap population computed by the unconstrained and μ-constrained variational methods at a number of internuclear distances. From $R = 1{\cdot}75$ a.u to $R = 3{\cdot}0$ a.u, the diatomic overlap density computed by the μ-constrained variational calculations is smaller than the corresponding unconstrained quantity. At $R \simeq R_e$, they are almost equal and for $R > R_e$ the trend is reversed. The difference between the constrained and unconstrained Li-H overlap density shows that the μ-constraint could indirectly affect k_e.

Table 2. Comparison of constrained and unconstrained diatomic overlap population in the ground state of Li-H at various internuclear distance.

Internuclear separation (R in a.u)	Unconstrained variational result	Constrained variational result
1·75	1·3528	1·2882
2·00	1·3590	1·3034
2·25	1·3620	1·3186
2·50	1·3628	1·3322
2·75	1·3624	1·3440
3·00	1·3610	1·3538
3·25	1·3592	1·3632
3·50	1·3568	1·3714
3·75	1·3540	1·3782
4·00	1·3514	1·3840

CC-0. In Public Domain. Gurukul Kangri Collection, Haridwar

Digitized by Arya Samaj Foundation Chennai and eGangotri

5. Conclusions

The hybrid method of a direct constrained variational determination of electron density is quite practicable and the use of dipole moment function as constraint enables one to improve even the qualitative features of electron density, potential energy curves etc. We are trying to extend these calculations to the dissociation limit and construct energy map $E(R, \bar{\mu})$ describing total E as functions of two collective variables R and $\bar{\mu}$. As noted by Eichler (1981) standard HF calculations yield only the bottom of a valley with $E = E(R_e)$ and the corresponding dipole moment $\mu(R_e)$, leaving an otherwise barren landscape in the $(R, \bar{\mu})$ plane. A complete knowledge of the energy surfaces in the $(R, \bar{\mu})$ plane will surely yield valuable information on metastable species, nature of bonding etc. Although Eichler (1981) thought of these possibilities, he could not offer a very practicable means of doing the needed constrained variational calculations. Ours is certainly a modest step in this direction.

Acknowledgements

The authors would like to thank the Department of Science and Technology, Government of India, New Delhi for financial support.

References

Bamzai A S and Deb B M 1981 *Rev. Mod. Phys.* **53** 593
Bartolotti L J 1981 *Phys. Rev.* **A24** 1682
Byers Brown W 1966 *J. Chem. Phys.* **44** 567
Das K K, Khan P and Bhattacharyya S P 1985 *Pramana–J. Phys.* **25** 281 and references cited therein.
Das K K and Bhattacharyya S P 1986 *Chem. Phys. Lett.* **125** 225
Deb B M and Ghosh S K 1982 *J. Chem. Phys.* 77 342
Eichler J 1981 *Comm. Atom. Mol. Phys.* **10** 203
Herzberg G 1950 *Diatomic molecules* (Princeton: D Van Nostrand)
Hohenberg P and Kohn W 1964 *Phys. Rev.* **B136** 864
Kohn W and Sham L J 1965 *Phys. Rev.* **A140** 1133
McWeeny R 1956 *Proc. R. Soc.* (*London*) **A235** 496
McWeeny R 1957 *Proc. R. Soc.* (*London*) **A241** 239
Morrison D D 1968 *SIAM J. Numer. Anal.* **5** 83
Pople J A, Santry D P and Segal G A 1965 *J. Chem. Phys.* **43** S129
Pople J A and Segal G A 1965 *J. Chem. Phys.* **43** S136
Patridge Hary and Langhoff S R 1981 *J. Chem. Phys.* **74** 2361
Weinstein H and Pauncz R 1972 *Chem. Phys. Lett.* **14** 161

CC-0. In Public Domain. Gurukul Kangri Collection, Haridwar

Digitized by Arya Samaj Foundation Chennai and eGangotri

Pramāṇa – J. Phys., Vol. 28, No. 1, January 1987, pp. 59–71. © Printed in India.

Transient excited singlet state absorption in Rhodamine 6G*

PUTCHA VENKATESWARLU, M C GEORGE, YERNENI V RAO**, H JAGANNATH, G CHAKRAPANI† and A MIAHNAHRI

Department of Physics, Alabama A&M University, Normal, Alabama 35762, USA
* Research supported by Ballistic Missile Defence System Command
** A N R College, Gudivada 521 301, India (on leave)
† Department of Physics, Indian Institute of Technology, Kanpur 208 016, India (on leave)

MS received 21 August 1986

Abstract. Transient excited singlet state absorption (ESSA) has been studied in Rhodamine 6G in ethanol using a nitrogen laser and nitrogen laser-pumped dye laser. Broad absorption with several submaxima and possible shoulders, which represent the vibrational structure, has been observed in Rhodamine 6G in the region, 4175–4640 Å. The position of the lowest vibrational level of the first excited singlet state S_1 has been determined from the crossing point of the long and short wavelength spectral wings of absorption and fluorescence respectively. The energy level scheme of the molecule has been obtained with the help of the absorption and fluorescence spectra recorded. The observed structure in ESSA has been tentatively interpreted to be due to transitions from the different vibrational levels of S_1 to one or more vibrational levels of the upper singlet electronic state S_4.

Keywords. Rhodamine 6G; excited singlet state absorption; absorption spectra; fluorescence spectra.

PACS Nos 33·50; 33·10

1. Introduction

Laser dyes like Rhodamine 6G are a class of organic molecules which show lasing action under appropriate conditions of excitation. Dye lasers are among the most useful types of lasers because of their easy tunability, wavelength coverage and simplicity (Schafer 1983; Pavlopoulos and Hammond 1974; Sorokin *et al* 1967; Sorokin *et al* 1968; Shank 1975; Peterson 1979). Dyes can be used in solid, liquid or gaseous phase and their concentration and hence their absorption and gain can be readily controlled. Solutions of dyes are especially convenient for experimental studies. Different scintillators, coumarins, xanthines, oxazines and polymethines can be conveniently chosen to cover a wide range of the spectrum from 3200 Å to 13000 Å.

The ground electronic state of a dye molecule is in general a singlet state (Schafer 1983). The first excited singlet state is generally higher than the lowest triplet state. Dye molecules, when excited to the higher singlet states, relax by nonradiative interactions to the lowest excited singlet state S_1 in a short time of the order of picoseconds. This is the only state from which dye molecules have been observed to fluoresce, which, in most cases, have lifetimes of a few nanoseconds. Also this is the state from which the radiative transition that is directly responsible for laser action takes place under appropriate conditions of stimulation in all laser dye molecules.

Though singlet to triplet state inter-system transitions are generally forbidden, relaxation of molecules in the S_1 to the lowest triplet state T_1 is possible through

CC-0. In Public Domain. Gurukul Kangri Collection, Haridwar

Digitized by Arya Samaj Foundation Chennai and eGangotri

induced processes. This singlet $S_1 \rightarrow$ triplet T_1 decay will decrease the net available excited singlet state population for stimulated emission thus affecting the lasing efficiency of dyes, particularly in the CW mode of operation.

The other process which affects the lasing efficiency of dyes is the excited singlet state absorption (ESSA). As the state S_1 has a radiative lifetime which is longer than the non-radiative relaxation times of the higher excited singlet electronic states, dye molecules in the S_1 state can undergo absorptive transitions in addition to stimulated emissive transitions in the presence of a pump beam.

The study of these two processes is of great interest because of the widespread use of laser dyes. However, the present study concerns itself with the excited singlet state absorption which may be called transient absorption as the lifetime of the first excited singlet state is of the order of few nanoseconds.

Sahar and Wieder (1973) obtained excited singlet state absorption of Acridine Red in ethanol in the region, 20000–25000 cm^{-1} with a maximum at about 22800 cm^{-1} using nitrogen laser coupled with a tunable dye laser. Sahar and Wieder (1974) also reported cross-sections for excited state absorption of some of the laser dyes at the nitrogen laser wavelength of 3371 Å. Shah and Leheny (1974) and Leheny and Shah (1975) obtained ESSA in Cresyl violet perchlorate in methanol in the region, 2–2·9 eV with a maximum at 2·45 eV. These experiments demonstrated the influence of the excited state absorption at the pump wavelength on the pumping efficiency and at the probe laser wavelength on the gain per pass. Dolan and Goldschmidt (1976) reported absolute cross-section measurements on the ESSA of Rhodamine 6G in ethanol. They reported ESSA in the region, 2700–4650 Å with a maximum at 4400 Å and a sub-maximum at about 3950 Å. Sahar and Treves (1977) studied ESSA of a few dyes like Rhodamine 6G and Rhodamine B in ethanol using dual beam laser photolysis experiment in the nanosecond range. They reported excited state absorption with maxima at about 5300 Å and 5650 Å in Rhodamine 6G. Nitrogen laser and nitrogen laser-pumped dye laser were used in these studies.

In all the above experiments, transient ESSA spectra were observed to consist of broad maxima and the transitions involved were not identified except in Rhodamine 6G in which Sahar and Treves suggested that the ESSA obtained by them was due to $S_1 \rightarrow S_3$ transition.

The study of ESSA in Rhodamine 6G, α-NPO, POPOP and dimethyl POPOP has been undertaken recently in this laboratory. The spectra show broad absorption with a coarse structure consisting of a number of submaxima and shoulders.

As a comprehensive energy level scheme essential for the analysis of the observed ESSA is not available for any of these dyes in literature, absorption and fluorescence spectra of these molecules have been recorded as part of this work. The analysis of the absorption and fluorescence spectra yielded the energy level schemes needed and the excited singlet state absorption in each of the four dyes is sought to be analyzed on the basis of these energy level schemes. This paper deals with the results obtained in Rhodamine 6G in solution.

2. Experimental details

2.1 *Absorption and fluorescence spectra*

Absorption spectrum of Rhodamine 6G in ethanol has been recorded using Perkin-Elmer model 323 UV-Vis-NIR spectrophotometer in the region, 2000–7000 Å. The dye

CC-0. In Public Domain. Gurukul Kangri Collection, Haridwar

Digitized by Arya Samaj Foundation Chennai and eGangotri

was obtained from Kodak and was used without further purification. Also its fluorescence spectra excited by a mercury lamp and a nitrogen laser (3371 Å) have been recorded using the same spectrophotometer.

The laser source of fluorescence was a 1 MW pulsed nitrogen laser system (Molectron model UV24) with a pulse width of 8 nsec and a variable pulse repetition rate of 1–100 pps. Fluorescence from the dye cell was collected in a direction normal to that of the nitrogen laser beam and focussed on to the entrance slit of the spectrophotometer. The light output from the spectrophotometer was detected by a photomultiplier tube (Hamamatsu R928). The output signal current, after being amplified by a current amplifier (Keithley model 427), was fed to a boxcar integrator (EG&G PAR model 162) for signal processing and to an oscilloscope (Tektronix model 2465) for visual monitoring. The boxcar integrator and the oscilloscope were triggered by a synchronous trigger pulse from the nitrogen laser operated at 20 pps. The aperture delay of the integrator was so chosen as to permit the sampling of the current pulse at its peak. The aperture duration and the time constant of the integrator were so adjusted as to obtain optimum signal-to-noise ratio consistent with the spectral scan rate. The output of the boxcar integrator was recorded on the strip chart recorder.

2.2 *Excited singlet state absorption*

The experimental arrangement for recording the ESSA is shown in figure 1. The output of the 1 MW nitrogen laser (NL) was split into two beams of unequal intensity (75:25) using a beam splitter (BS). The stronger of these two beams was steered to pass through the dye solution in the absorption cell (AC) which results in populating the S_1 state as almost every absorbed photon will produce a molecule in that state. The absorption by the molecules in the S_1 state was probed by another beam obtained by pumping a dye laser with the other beam having 25% intensity of the nitrogen laser output. The dye laser beam was directed by using a suitable optical arrangement to cross the excited dye volume normal to the direction of the pump beam. An optical delay line (ODL) was used to adjust the delay between the pump and the probe pulses to an optimum value ($\sim$ 3 nsec). Since most of the pump beam gets absorbed within the first few millimeters of the dye solution, the probe beam was made to pass through the

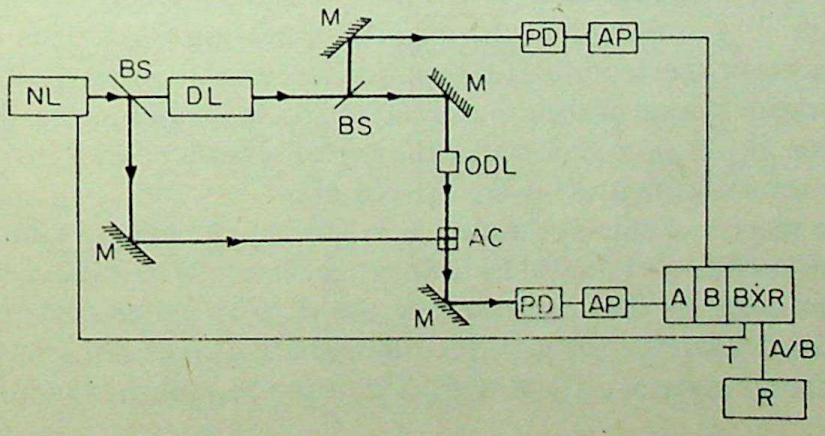

Figure 1. Schematic diagram of the experimental arrangement to study the excited singlet state absorption. AC, absorption cell; AP, amplifier; BS, beam splitter; BXR, box-car integrator; DL, dye laser; M, mirror; NL, nitrogen laser; ODL, optical delay line; PD, photo-diode detector; R, strip-chart recorder.

CC-0. In Public Domain. Gurukul Kangri Collection, Haridwar

Digitized by Arya Samaj Foundation Chennai and eGangotri

absorption cell close to its wall on which the pump beam was incident so as to ensure maximum possible interaction with the excited state population. To make the pumping more effective the pump beam was focussed on the dye solution in the absorption cell using a quartz cylindrical lens. The probe beam, after passing through the highest intensity region of the pump beam in the absorption cell, was detected by a photodetector (PD UDT model 10DP) and the signal, after being amplified by an amplifier (AP) was processed using a boxcar integrator (BXR). The detected signal A was normalized with respect to the input of the probe beam to take into account any possible fluctuations in the intensity of the probe beam. A second beam splitter (BS) reflected 4 % of the input beam which was detected by another photodetector (PD) and the output B of this detector was used for normalization. The normalized output A/B from the boxcar integrator was recorded on a strip chart recorder.

In the experiment, initially, the absorption cell was filled with pure solvent and the transmission curve was recorded by scanning the dye laser through the region of interest. The absorption cell was then filled with the dye solution and the experiment was repeated to obtain absorption, if any, due to the molecules in the ground state S_0. Next, the nitrogen laser beam was turned on so as to allow it to excite the molecules in the ground state to populate the first excited singlet state S_1 and the transmission curve was recorded to obtain the absorption due to the molecules in the S_1 state as well as the absorption, if any, due to the molecules in the S_0 state. This absorption was greater than that obtained in the absence of the pump beam.

The excited singlet state absorption extends over a considerable region of the spectrum. Since the tuning range of the dye laser with a single laser dye does not cover the whole region of interest, three different dyes have been used. These are Stilbene 420(4180–4300 Å), Coumarin 440(4250–4500 Å) and Coumarin 1(4430–4780 Å).

3. Results

3.1 *Rhodamine 6G*

3.1*a Absorption and fluorescence*: The absorption spectrum of Rhodamine 6G in ethanol (figure 2) shows maxima at (18605, 18810, 20140)*, 28660, (33840, 36220)*, 40420, 44730 and 49490 cm^{-1}. The strong absorption in the visible region extends from 17295–22725 cm^{-1} and shows a peak at 18810 cm^{-1} accompanied by two shoulders at 20140 and 18605 cm^{-1}. Assuming that the maxima appearing alone or in close lying groups in the absorption spectrum correspond to the vertical energies of excitation from the lowest vibrational level of the ground state S_0 to one or more vibrational levels of the different upper singlet electronic states, the energy levels labeled S_1, S_2, S_3, S_4 etc of Rhodamine 6G shown in figure 3, were arrived at.

The fluorescence spectra of this dye molecule excited by the mercury lamp (3125·7, 3650·2, 4046·6, 4358·4 and 5460·7 Å) and by the nitrogen laser (3370 Å) have been found to be identical. This suggests that regardless of the state to which they are initially excited, the dye molecules relax through fast nonradiative transitions to the lowest excited singlet electronic state S_1, where thermalization is established in a time much

---

* The wave numbers shown in parantheses correspond to a group of maxima or submaxima or shoulders lying close enough to one another to be considered as arising from a single electronic transition.

CC-0. In Public Domain. Gurukul Kangri Collection, Haridwar

Digitized by Arya Samaj Foundation Chennai and eGangotri

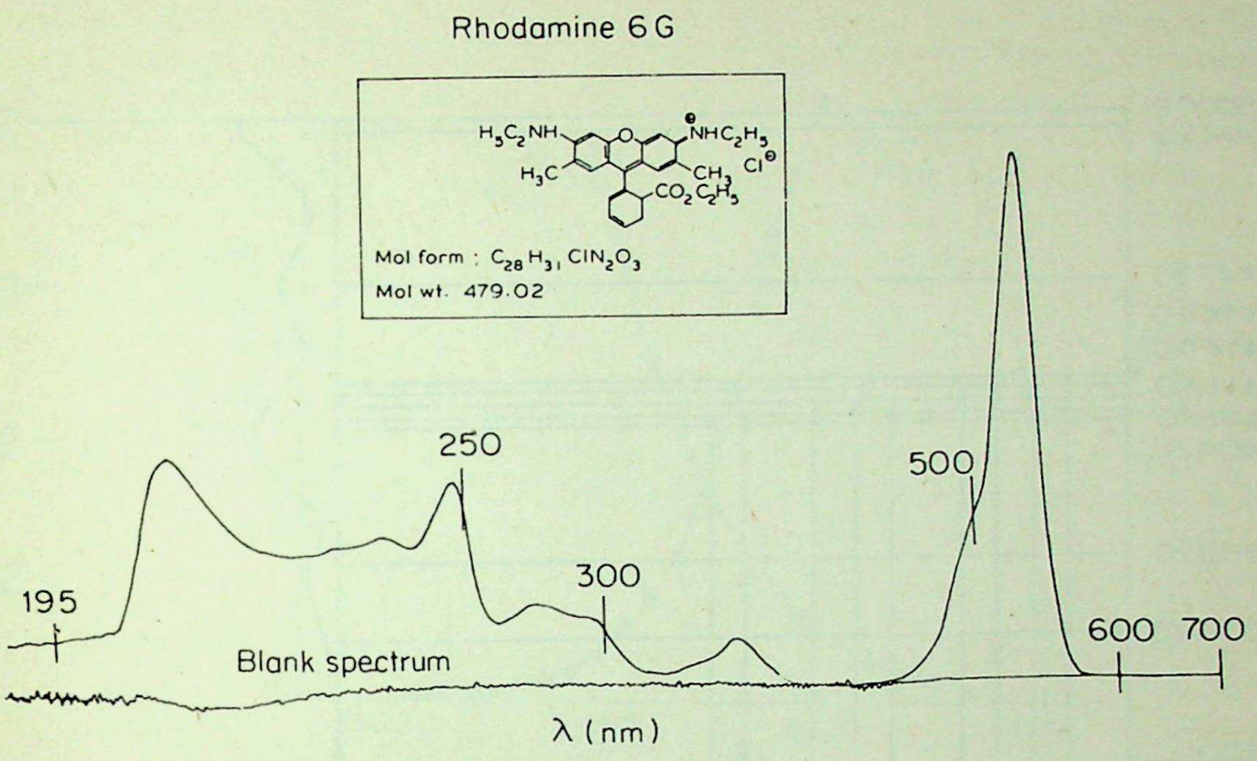

Figure 2. Absorption spectrum of Rhodamine 6G in ethanol.

shorter than the radiative lifetime of that state. The fluorescence spectrum in solution extends from 14425–18755 cm^{-1} with a maximum at 17635 cm^{-1} and a shoulder at 16710 cm^{-1}.

The fluorescence spectrum rises steeply on its short wavelength side while the absorption spectrum falls steeply on its long wavelength side. The short-wavelength edge of fluorescence is at 18755 cm^{-1} while the long-wavelength edge of absorption is at 17295 cm^{-1}. The normalized fluorescence $Q(\lambda)/Q_{max}$ and the normalized absorption $\varepsilon(\lambda)/\varepsilon_{max}$ spectral wings in the region, 17295–18755 cm^{-1} have been plotted in figure 4. They appear to be mirror images of each other resulting from a reflection in a plane passing through the point of intersection of these spectra, as is to be expected in the case of any dye molecule.

The point of intersection which is found to be 18110 cm^{-1}, represents the position of the lowest vibrational level of the excited singlet state S_1 above that of the ground state S_0 (Schafer 1983). This is shown accordingly in figure 3. Assuming that the fluorescence maximum at 17635 cm^{-1} and the shoulder at 16710 cm^{-1} arise as a result of transitions from the lowest vibrational level of the S_1 state at 18110 cm^{-1} to two different vibrational levels of the ground state, one obtains the levels at 475 and 1400 cm^{-1} shown in figure 3.

3.1*b Excited singlet state absorption:* The excited singlet state absorption of Rhodamine 6G in ethanol was recorded in the region 4175–4640 Å as described earlier. If I_0 is the incident intensity of the probe beam I the transmitted intensity through the solvent and I_2 and I_1 are respectively the transmitted probe beam intensities with and without the pump beam, then

$$I = I_0 \exp(-\alpha) L,$$
$$I_1 = I_0 \exp(-(\alpha + \sigma_g N) L)$$

CC-0. In Public Domain. Gurukul Kangri Collection, Haridwar

Digitized by Arya Samaj Foundation Chennai and eGangotri

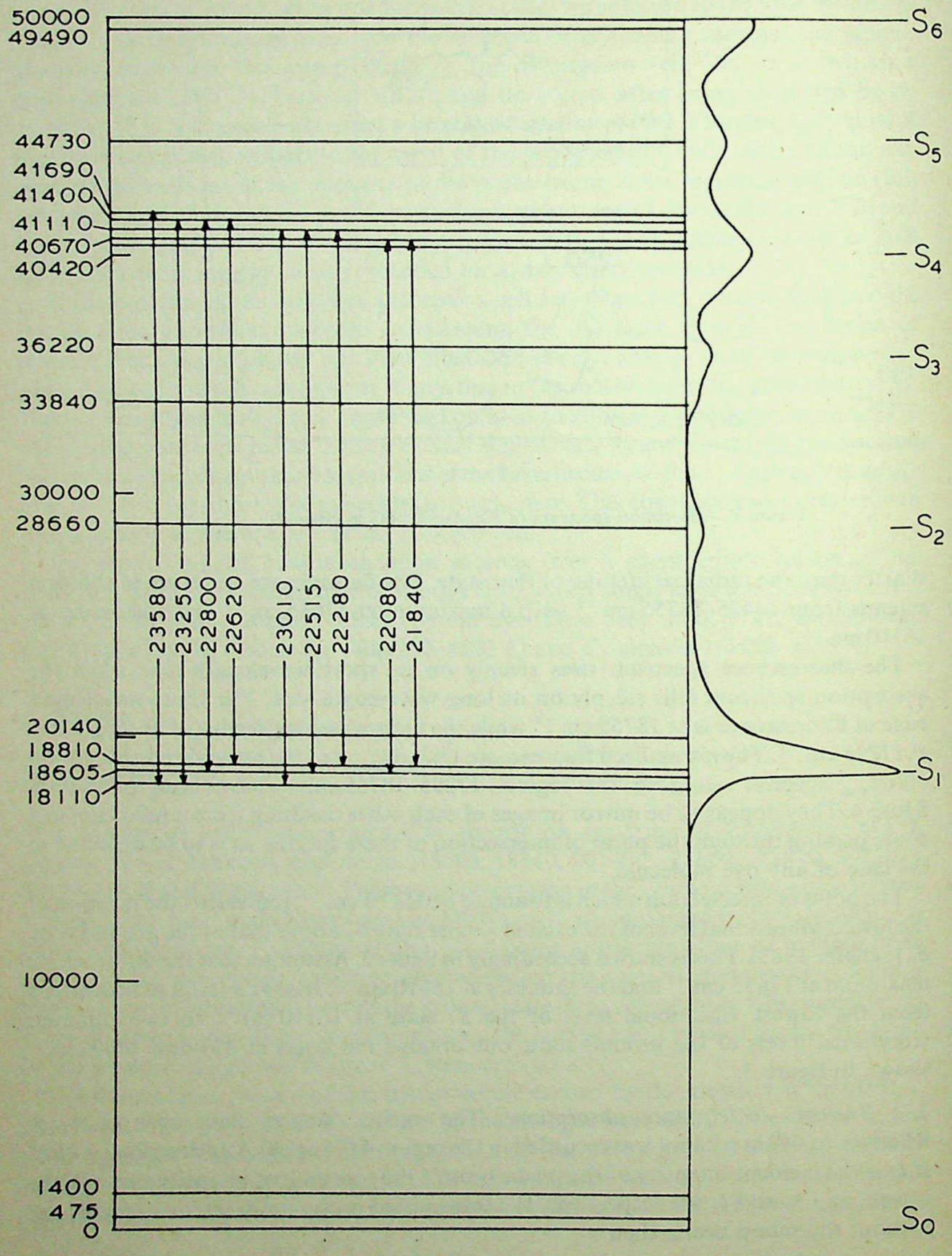

Figure 3. Energy level diagram of Rhodamine 6G.

CC-0. In Public Domain. Gurukul Kangri Collection, Haridwar

Digitized by Arya Samaj Foundation Chennai and eGangotri

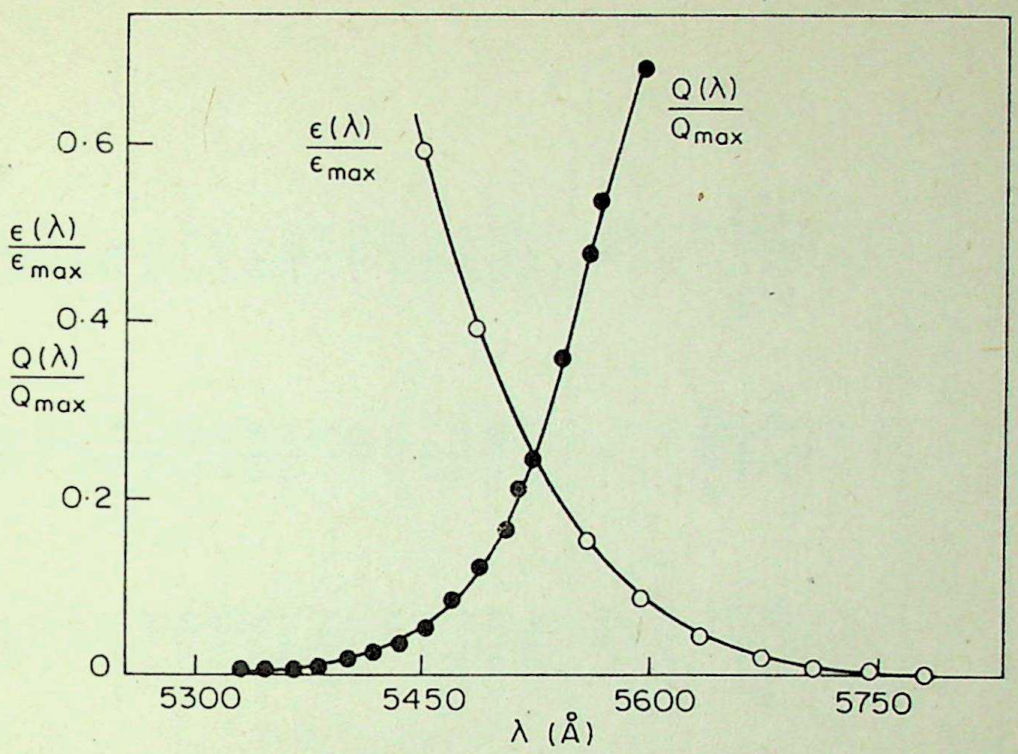

Figure 4. Absorption spectrum, $\varepsilon(\lambda)/\varepsilon_{max}$ and fluorescence spectrum $Q(\lambda)/Q_{max}$ of Rhodamine 6G.

and $$I_2 = I_0 \exp(-(\alpha + \sigma_g(N-n) + \sigma_e n)L),$$

where L is the absorption path length, α is the linear absorption coefficient of the pure solvent, σ_g and σ_e are respectively the cross-sections for absorption out of the ground and excited singlet states S_0 and S_1 of the solute molecules at the probe wavelength and N and n are respectively the total number of solute molecules per unit volume and the number of those lifted to the S_1 state by the pump beams which are encountered by the probe beam. In the expression for I_2 the effect of stimulated emission on n at the wavelength of the probe has been neglected.*

The ground state absorption parameter is given by

$$N((\sigma_g)_\lambda)L = \ln(I/I_0)_\lambda - \ln(I_1/I_0)_\lambda = \ln(I/I_1)_\lambda,$$

and the absorption cross-section relative to its maximum value,

$$(\sigma_g)_\lambda/(\sigma_g)_{max} = \ln(I/I_1)_\lambda/\ln(I/I_1)_{max}.$$

Similarly the relative differential absorption cross-section between the ground and the first excited singlet states S_0 and S_1 is given by

$$n(\sigma_e - \sigma_g)_\lambda L = \ln(I_1/I_0)_\lambda - \ln(I_2/I_0)_\lambda = \ln(I_1/I_2)_\lambda,$$

or

$$(\sigma_e - \sigma_g)_\lambda/(\sigma_e - \sigma_g)_{max} = \ln(I_1/I_2)_\lambda/\ln(I_1/I_2)_{max}.$$

* This assumption is valid in the region covered by the present study as there is no evidence of stimulated emission in this region.

CC-0. In Public Domain. Gurukul Kangri Collection, Haridwar

Table 1. Excited singlet state absorption in Rhodamine 6G ($6{\cdot}7 \times 10^{-4}$ M/l in ethanol) in the region, 4180–4640 Å.

Probe beam wavelength	Normalized transmitted probe beam intensity through			$\ln \frac{\text{column 2}}{\text{column 3}}$	$N(\sigma_g)_\lambda L$ after matching	$\frac{(\sigma_g)\lambda}{(\sigma_g)_{max}}$	$\ln \frac{\text{column 3}}{\text{column 4}}$	$\ln(\sigma_e - \sigma_g)_\lambda$ after matching	$\frac{(\sigma_e - \sigma_g)_\lambda}{(\sigma_e - \sigma_g)_{max}}$
	Pure solvent	Solution							
		without pump	with pump						
λ in Å	I/I_0	I_1/I_0	I_2/I_0	$= N(\sigma_g)_\lambda L$			$= n(\sigma_e - \sigma_g)_\lambda L$		
1	2	3	4	5	6	7	8	9	10
4180	5·60	2·80	2·50	0·693	0·552	0·175	0·113	0·090	0·481
4200	8·30	4·30	3·80	0·658	0·524	0·166	0·124	0·099	0·529
4220	10·00	5·40	4·70	0·616	0·491	0·155	0·139	0·111	0·594
4230	10·44	5·80	5·00	0·588	0·468	0·148	0·149	0·119	0·636
4240	10·80	6·00	5·15	0·588	0·468	0·148	0·153	0·122	0·652
4250	10·84	6·13	5·27	0·570	0·454	0·144	0·151	0·121	0·652
4255	11·06	6·12	5·26	0·592	0·471	0·149	0·151	0·121	0·647
4260	11·04	6·20	5·37	0·577	0·459	0·145	0·144	0·115	0·615
4265	10·98	6·17	5·27	0·576	0·458	0·145	0·158	0·126	0·674
4270	10·90	6·20	5·28	0·564	0·449	0·142	0·161	0·129	0·690
4280*	12·80	8·22	7·15	0·443	0·452	0·143	0·139	0·140	0·749
4290*	13·02	8·10	7·00	0·475	0·467	0·148	0·146	0·146	0·781
4300	13·30	8·10	6·97	0·496	0·496	0·157	0·150	0·148	0·791
4305	13·50	8·11	6·98	0·510	0·510	0·161	0·150	0·150	0·802
4310	13·68	8·13	6·96	0·520	0·520	0·165	0·155	0·155	0·829
4315	13·80	8·14	6·93	0·528	0·528	0·167	0·161	0·161	0·861
4320	13·80	8·16	6·90	0·525	0·525	0·166	0·168	0·168	0·898
4330	14·00	8·06	6·80	0·552	0·552	0·175	0·170	0·170	0·909
4340	14·00	7·96	6·65	0·565	0·565	0·179	0·180	0·180	0·963
4350	14·00	7·79	6·50	0·586	0·586	0·185	0·181	0·181	0·968

Digitized by Arya Samaj Foundation Chennai and eGangotri

CC-0. In Public Domain. Gurukul Kangri Collection, Haridwar

4360	14·00	7·52	6·28	0·621	0·621	0·196	0·180	0·180	0·963
4370	13·88	7·28	6·07	0·645	0·645	0·204	0·182	0·182	0·973
4380	13·80	7·04	5·84	0·673	0·673	0·213	0·187	0·187	1·000
4390	13·68	6·76	5·62	0·705	0·705	0·223	0·185	0·185	0·989
4440	13·60	6·50	5·46	0·738	0·738	0·233	0·174	0·174	0·930
4410	13·74	6·25	5·24	0·788	0·788	0·249	0·176	0·176	0·941
4420	13·60	6·00	5·02	0·818	0·818	0·259	0·178	0·178	0·952
4430	13·74	5·71	4·83	0·878	0·878	0·278	0·168	0·168	0·898
4435	13·74	5·60	4·72	0·898	0·898	0·284	0·171	0·171	0·914
4400	13·80	5·46	4·60	0·927	0·927	0·293	0·172	0·172	0·920
4450	13·98	5·20	4·40	0·989	0·989	0·313	0·167	0·167	0·893
4460	14·20	4·95	4·20	1·054	1·054	0·333	0·164	0·164	0·877
4470	14·36	4·66	4·00	1·125	1·125	0·356	0·153	0·153	0·818
4480*	14·60	4·40	3·80	1·199	1·195	0·378	0·147	0·150	0·802
4490*	14·90	4·18	3·60	1·271	1·271	0·402	0·149	0·150	0·802
4500*	15·20	3·90	3·40	1·360	1·365	0·432	0·137	0·136	0·727
4510	26·40	6·55	6·10	1·394	1·466	0·464	0·071	0·129	0·690
4520	26·90	6·00	5·65	1·500	1·577	0·499	0·060	0·109	0·583
4530	27·52	5·50	5·18	1·610	1·693	0·536	0·060	0·109	0·583
4540	27·85	5·00	4·75	1·717	1·805	0·571	0·051	0·093	0·497
4550	28·16	4·55	4·35	1·823	1·917	0·606	0·045	0·082	0·439
4560	28·65	4·04	3·88	1·959	2·060	0·652	0·041	0·075	0·401
4570	28·80	3·61	3·50	2·077	2·184	0·691	0·031	0·057	0·305
4580	28·95	3·23	3·13	2·193	2·306	0·730	0·032	0·058	0·310
4590	29·12	2·83	2·76	2·331	2·451	0·775	0·026	0·047	0.251
4600	29·30	2·50	2·45	2·461	2·587	0·818	0·020	0·036	0·193
4610	29·30	2·23	2·19	2·576	2·708	0·857	0·019	0·035	0·187
4620	29·30	1·92	1·90	2·725	2·865	0·906	0·011	0·020	0·107
4630	29·30	1·68	1·67	2·859	3·006	0·951	0·005	0·009	0·048
4640	29·30	1·45	1·45	3·006	3·161	1·000	0·000	0·000	0·000

* These are points in the overlap portions of two adjacent tuning ranges of the laser dyes and the corresponding absorption parameters given in columns 6 and 9 represent the average values of these quantities obtained after matching.

Digitized by Arya Samaj Foundation Chennai and eGangotri

CC-0. In Public Domain. Gurukul Kangri Collection, Haridwar

Digitized by Arya Samaj Foundation Chennai and eGangotri

The normalized transmitted probe beam intensities I/I_0, I_1/I_0 and I_2/I_0, the absorption parameters $N(\sigma_g)_\lambda L$ and $n(\sigma_e-\sigma_g)_\lambda L$ and the relative absorption cross-section $(\sigma_g)_\lambda/(\sigma_g)_{max}$ and the relative differential absorption cross-section $(\sigma_e-\sigma_g)_\lambda/(\sigma_e-\sigma_g)_{max}$ are given in table 1 for Rhodamine 6G at a concentration of $6{\cdot}7\times10^{-4}$ M/l in ethanol. As the calculated values of the absorption parameters in the overlapping portions of adjacent laser dye tuning ranges are found to vary the final values of these quantities over the complete region of study have been obtained by multiplying the calculated values in different tuning ranges by appropriate matching factors. The values of $(\sigma_g)_\lambda/(\sigma_g)_{max}$ and $(\sigma_e-\sigma_g)_\lambda/(\sigma_e-\sigma_g)_{max}$ are plotted against the probe wavelength in figure 5. It can be seen from the figure that the relative absorption cross-section of the ground state varies smoothly with wavelength whereas the relative differential absorption cross-section varies unevenly with wavelength showing a broad maximum with a number of submaxima and shoulders. It is therefore reasonable to assume that this uneven variation arises solely as a result of the variation of the excited singlet state absorption cross-section σ_e with the probe wavelength. Accordingly, in what follows, the six submaxima at 23580, 23250, 23010, 22800, 22620 and 22515 cm^{-1} and three possible shoulders at 22280, 22080 and 21840 cm^{-1} given in table 2 are treated as excited singlet state absorption features.

Excited singlet state absorption in Rhodamine 6G was studied earlier by different groups. Dolan and Goldschmidt (1976) studied the region, 3650–4750 Å and observed a maximum at 4400 Å and a submaximum around 4000 Å. Magde *et al* (1981) investigated the region, 3000–6500 Å and reported a submaximum at 5300 Å in addition to the two reported by Dolan and Goldschmidt. Sahar and Treves (1977) investigated the region, 4600–6150 Å and reported two maxima at 5300 Å and 5650 Å, which were confirmed by Falkenstein *et al* (1978). The different maxima in the excited singlet state absorption observed by these workers are included for comparison in table 2.

The six absorption submaxima and the three possible shoulders observed in the present experiments obviously represent the vibrational structure in the broad absorption band with the maximum at about 4400 Å reported earlier by other workers. It can be seen from the energy level diagram (figure 3) that all the submaxima and shoulders can be tentatively attributed to transitions from the first excited electronic state S_1 to the electronic state S_4 at 40230 cm^{-1}. The submaxima at 23250, 22800 and 22620 cm^{-1} can be attributed respectively to the transitions from the vibrational levels at 18110, 18605 and 18810 cm^{-1} of the electronic state S_1 to a common vibrational level at 41400 ± 40 cm^{-1} of the electronic state S_4. Similarly, the submaxima at 23010 and 22515 cm^{-1} and the shoulder at 22280 cm^{-1} could be due to the transitions respectively from the same three vibrational levels of S_1 state to another common vibrational level at 41110 ± 20 cm^{-1} of the S_4 state while the two shoulders at 22080 and 21840 cm^{-1} probably represent the transitions from the vibrational levels at 18605 and 18810 cm^{-1} of S_1 respectively to yet another common vibrational level at 40670 ± 20 cm^{-1}. These transitions are given in table 2 and are shown in figure 5. Finally, assuming that the submaximum at 23580 cm^{-1} also results from a transition involving the lowest vibrational level of S_1, one finds the upper level to be at 41690 cm^{-1} which lies within the bandwidth of the S_4 state.

The other maxima in the ESSA observed by earlier workers are outside the region investigated here. However, transitions responsible for these maxima may be identified on the basis of the energy level diagram obtained from the present work (see table 2). The maximum at 4000 Å (24993 cm^{-1}) probably represents a transition from the S_1

CC-0. In Public Domain. Gurukul Kangri Collection, Haridwar

Digitized by Arya Samaj Foundation Chennai and eGangotri

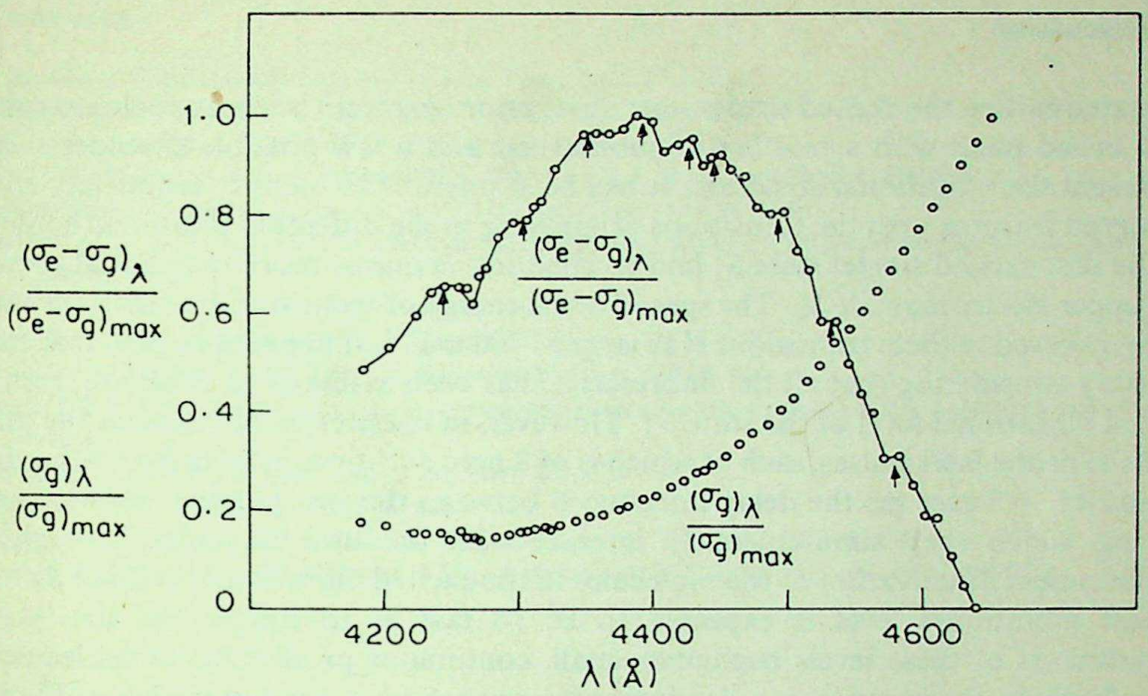

Figure 5. Excited singlet state absorption spectrum of Rhodamine 6G($6{\cdot}7 \times 10^{-4}$ M/l in ethanol) in the region, 4175–4640 Å.

Table 2. Transition assignments to the observed features in the ESSA spectrum of Rhodamine 6G.

ESSA Maximum submaximum or shoulder			Transition assignment			
Earlier work		Present work	Vibrational levels T_e, v (in cm^{-1})		Upper electronic state	Absorption maximum
λ(in Å)	ν(in cm^{-1})	ν(in cm^{-1})	Lower	Upper	(Sn)	ν (in cm^{-1})
4000*†	24990		18110	43100	*S*5	44730
		23580	18110	41690	*S*4	40420
		23250	18110	41400 ± 40	*S*4	,,
		23010	18110	41400 ± 20	*S*4	,,
4400*†	22720	22800	18605	41400 ± 40	*S*4	,,
		22620	18810	41400 ± 40	*S*4	,,
		22515	18605	41110 ± 20	*S*4	,,
		22280	18810	41110 ± 20	*S*4	,,
		22080	18605	40670 ± 20	*S*4	,,
		21840	18810	40670 ± 20	*S*4	,,
5300†xx	18860		18110	36970	*S*3	36220
5650xx	17695		18110	35805	*S*3	36220

* Dolan and Goldschmidt (1976); † Magde *et al* (1981); xx Sahar and Treves (1977).

state to the electronic state S_5 at 44950 cm^{-1}. The absorption maxima at 5300 Å (18863 cm^{-1}) and 5660 Å (17663 cm^{-1}) are probably due to transitions from the electronic state S_1 to S_3 at 36220 cm^{-1} as suggested by Sahar and Treves (1977). The separation of 1200 cm^{-1} between the two absorption maxima may correspond to one of the vibrational frequencies associated with the S_3 state.

CC-0. In Public Domain. Gurukul Kangri Collection, Haridwar

Digitized by Arya Samaj Foundation Chennai and eGangotri

4. Discussion

As stated earlier, the excited singlet state absorption spectrum has been found to consist of a broad band with a number of submaxima and a few possible shoulders which represent the vibrational structure. It has been possible to identify tentatively all the observed features with the transitions originating in the different vibrational sublevels of the first excited singlet state S_1 and terminating in one or more vibrational levels of the upper electronic state S_4. The spread in the energy of the vibrational levels of the S_1 state involved in these transitions is as large as 700 cm^{-1}. It appears, at first, that this is unlikely considering that all the fluorescence has been assumed to originate from the lowest vibrational level of the state S_1^*. However, in the present experiment the pump and the probe laser pulses, each of which is of 8 nsec duration, overlap each other for a period of ~ 5 nsec (as the delay introduced between the two pulses is about 3 nsec), during which they simultaneously interact with the dye molecule. Though the radiationless deactivation of the molecules in the excited vibrational levels of S_1 to its lowest vibrational level is expected to be so fast as to render the steady-state populations of these levels negligibly small, continuous production of molecules in these levels by the pump laser pulse during its entire width can maintain detectable non-equilibrium populations in them. It should therefore be possible for absorptive transitions to occur from these excited vibrational levels** in addition to those occurring from the lowest vibrational level of the S_1 state during the period of overlap of the two pulses.

But the expectation that the steady-state population of the higher vibrational levels of the S_1 state is negligible is valid only when the temperature is so low that these vibrational levels are not already thermally populated by the Boltzmann distribution of the molecules in that state. However, at the temperature at which the present experiments were conducted the S_1 state has been found to be populated up to a height of 645 cm^{-1} as demonstrated by the short-wavelength edge of the fluorescence spectrum. Since the first excited vibrational level of the S_1 state lies within the energy bandwidth of that state it is possible for that level to have a "non-negligible" steady-state population. Therefore, the submaxima or shoulders in ESSA due to transitions from the first excited vibrational level of S_1 should be somewhat stronger than the other submaxima or shoulders but weaker than those corresponding to the transitions from the lowest vibrational level. Contrary to this expectation, however, in the present studies it has been observed that the submaxima and shoulders due to transitions from the first vibrational level are almost of equal strength as those due to transitions from the lowest and the second vibrational levels of S_1. However, since the Franck-Condon factors depend on the relative positions of the classical turning points of motion in the initial and final levels of the different transitions, it is quite possible for the transitions from the higher excited vibrational levels of S_1 to have appreciably larger values for the FCF's and hence for the corresponding submaxima and shoulders to have almost the same strength as the others.

---

* As shown in the following paragraph this assumption is not entirely valid.

** It may be recalled that in self-absorption, a process that affects the optimum wavelength at which the dye laser operates, thermal populations of the different vibrational levels of the ground state undergo similar transitions to the first excited state S_1 (Peterson 1979).

CC-0. In Public Domain. Gurukul Kangri Collection, Haridwar

Digitized by Arya Samaj Foundation Chennai and eGangotri

References

Dolan G and Goldschmidt C R 1976 *Chem. Phys. Lett.* **39** 320
Falkenstein W, Penzkofer A and Kaiser W 1978 *Opt. Commun.* **27** 151
Leheny R F and Shah J 1975 *IEEE J. Quantum Electron.* **QE11** 70
Magde D, Gaffney S T and Campbell B F 1981 *IEEE J. Quantum Electron.* **QE17** 489
Pavlopoulos T G and Hammond P R 1974 *J. Am. Chem. Soc.* **96** 6568
Peterson O G 1979 Dye lasers in *Methods of experimental physics*: 15*A Quantum Electronics* (New York: Academic Press)
Sahar E and Wieder I 1973 *Chem. Phys. Lett.* **23** 518
Sahar E and Wieder I 1974 *IEEE J. Quantum Electron.* **QE10** 612
Sahar E and Treves D 1977 *IEEE J. Quantum Electron.* **QE13** 962
Schafer F P 1983 Principles of dye laser operation in *Topics in applied physics: I Dye Lasers* (Berlin: Springer-Verlag)
Shah J and Leheny R F 1974 *Appl. Phys. Lett.* **24** 562
Shank C V 1975 *Rev. Mod. Phys.* **47** 649
Sorokin P P, Lankard J R, Hammond E C and Moruzzi V L 1967 *IBM J.* 130
Sorokin P P, Lankard J R, Moruzzi V L and Hammond E C 1968 *J. Chem. Phys.* **48** 4726

CC-0. In Public Domain. Gurukul Kangri Collection, Haridwar

Digitized by Arya Samaj Foundation Chennai and eGangotri

CC-0. In Public Domain. Gurukul Kangri Collection, Haridwar

Digitized by Arya Samaj Foundation Chennai and eGangotri

Pramāṇa – J. Phys., Vol. 28, No. 1, January 1987, pp. 73–79. © Printed in India.

Precise lattice parameter measurements in CsCl-Br solid solutions between room temperature and 90°K by powder x-ray diffraction*

V GANESAN and K S GIRIRAJAN

Department of Biophysics and Crystallography, University of Madras, Guindy Campus, Madras 600 025, India

MS received 3 July 1986; revised 24 October 1986

Abstract. Solid solutions of CsCl-Br in five different concentrations were prepared in sealed quartz tubes by heating the mixture to 1123°K for 6–8 hr and quenching to room temperature. X-ray diffractograms were taken at eight different temperatures between room temperature and 90°K for these solid solutions using the YPC50NM powder diffractometer and a continuous flow cryostat. The observed lattice parameters for each sample at each temperature obtained from the powder diffractograms were then extrapolated to give the true lattice parameters using the least square method with Nelson-Riley extrapolation scheme. The values of the true lattice parameters at each concentration and at each temperature were tabulated and the results discussed. It is shown that the lattice parameters vs temperature for some concentrations exhibit an anomalous behaviour.

Keywords. Solid solutions; continuous flow cryostat; true lattice parameters; Nelson-Riley extrapolation scheme.

PACS No. 65·70

1. Introduction

Study of mechanical, electrical and thermal properties of solid solutions is very important in solid state physics and in the recent past a number of people have started work in this area (Shukla *et al* 1976; Natarajan *et al* 1970; and Beg and Kobbelt 1982). In some of these solid solutions of alkali halides it has even become possible to grow single crystals for inelastic neutron scattering work to measure phonon dispersion relations (Beg and Kobbelt 1982). Shukla *et al* (1976) and Natarajan *et al* (1970) have claimed good success in forming solid solutions other than KCl-KBr systems. They were able to prove that CsCl forms good solid solutions with other alkali halides and crystallize in Pm3m structure and retain the structure throughout the concentration range in which the salts were mixed. They substantiated their results in the case of CsCl based solid solutions by heat of solution and heat of mixing measurements and by testing the homogeneity of the samples by x-ray lattice parameter measurements. Hence it was considered worthwhile to take CsCl-Br system as a case study in order to (i) obtain the lattice parameter shifts as a function of concentration and as a function of temperature and (ii) look how the lattice parameter behaves for each concentration at low temperatures down to 90°K as there is no experimental data available for these salts in this temperature range.

Contribution No. 691

CC-0. In Public Domain. Gurukul Kangri Collection, Haridwar

Digitized by Arya Samaj Foundation Chennai and eGangotri

2. Preparation of samples and experiment

Analar pure CsCl and CsBr compounds supplied by BDH and Fluka were first ground to a very fine powder and passed through a 325 mesh. They were dried at 420°K for several hours before forming the solid solutions. Each compound was then weighed in proper molal ratios in a microbalance to form solid solutions of concentrations CsCl-Br[0·8-0·2, 0·6-0·4, 0·5-0·5, 0·4-0·6 and 0·2-0·8]. The two accurately weighed samples of CsCl and CsBr for each concentration were mixed homogeneously and were filled in five different quartz tubes which were later evacuated and sealed. These sealed quartz tubes were heated in a furnace upto 1123°K for 6–8 hr and quenched to room temperature (RT). These quartz tubes containing the samples were then broken to retrieve the resulting mixture. Each of them were then ground to fine powder which will pass through a 325 mesh and labelled properly for x-ray work. For each sample x-ray diffractograms were taken at eight different temperatures between RT and 90°K using the YPC50NM powder diffractometer available in the department and the continuous flow cryostat designed for this unit (Srinivasan and Girirajan 1982). Copper radiation was used in all these measurements with nickel filter. The scanning speed of the sample for all these measurements was 1/4° per minute. The diffractograms were taken in each sample at least two times to ensure reproducibility.

3. Analysis of experimental data

The diffractograms for each concentration taken at eight different temperatures between RT and 90°K were analyzed in the following way. Bragg peak positions in 2θ scale were obtained from the diffractograms for each Bragg reflection for each concentration and each temperature after properly indexing the Bragg peaks. These Bragg angles along with the h, k, l and the x-ray wavelengths where α_1 and α_2 resolutions showed up were used to obtain the observed lattice parameters from the Bragg formula. These observed lattice parameters were subjected to a least square analysis using the extrapolation function of Nelson-Riley (1945) $[\cos^2\theta/\sin\theta + \cos^2\theta/\theta]$ described in Ganesan and Girirajan (1986) and the true lattice parameters were obtained. The prominent higher angle reflections from $2\theta = 70°$ to $2\theta = 130°$ were used for extrapolation. Figure 1 gives a sample plot of the observed lattice parameter a_T(obs) vs Nelson-Riley extrapolation function for the room temperature measurement of CsCl-Br(0·8-0·2). Table 1 presents the true lattice parameters obtained by the least square method along with the error estimate in obtaining them for each concentration and each temperature of measurement. Figure 2 gives a plot of the true lattice parameter vs concentration at RT along with the values of Natarajan *et al* (1970). Figure 3 gives a plot of the true lattice parameters vs temperature for each of the samples. A look at the behaviour of the true lattice parameters with temperature from figure 3 indicates that (i) not in all concentrations the lattice parameters could be fitted into a single polynomial of T and (ii) the samples other than CsCl-Br(0·8-0·2) molal concentration indicates a tendency to behave anomalously with temperature. The sample with CsCl-Br(0·8-0·2) molal concentration only behaves in a systematic fashion with respect to temperature like either CsCl or CsBr and in this case the true lattice parameters were fitted to a cubic polynomial as given below. (a_T (true) $= a_0 + C_1T + C_2T^2 + C_3T^3$ where a_0, C_1, C_2 and C_3 are constant coefficients.) The values of the constant coefficients for this

CC-0. In Public Domain. Gurukul Kangri Collection, Haridwar

Digitized by Arya Samaj Foundation Chennai and eGangotri

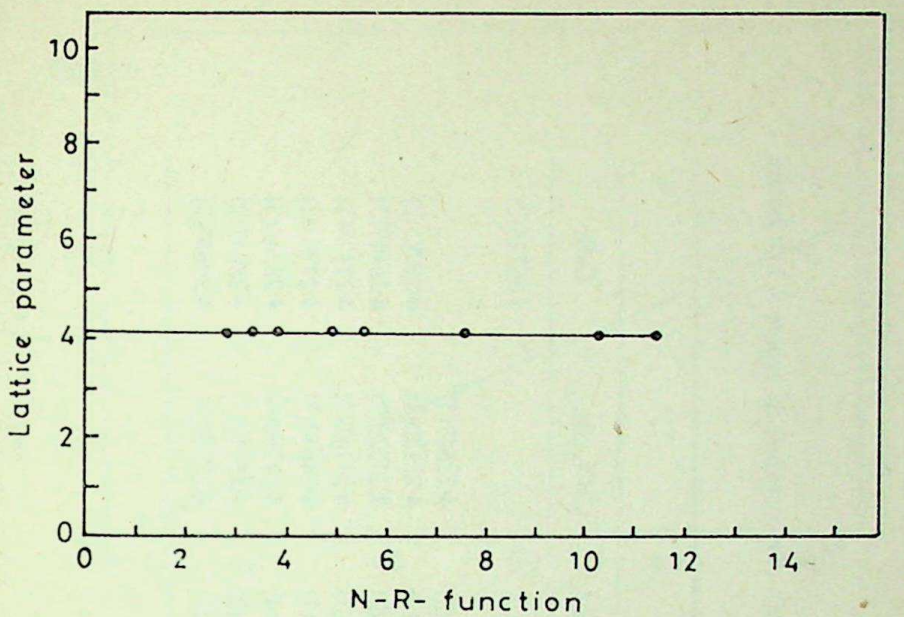

Figure 1. Plot of lattice parameter vs N-R function at room temperature for CsCl-Br(0·8-0·2) solid solution.

concentration were $a_0 = 4{\cdot}10767$, $C_1 = -5{\cdot}156 \times 10^{-5}$, $C_2 = 1{\cdot}091 \times 10^{-6}$ and $C_3 = -1{\cdot}546 \times 10^{-9}$. The thermal expansion coefficient α_T for this concentration was obtained by differentiating a_T(true) with respect to temperature and dividing by a_0. Table 2 presents the thermal expansion coefficients of CsCl-Br(0·8-0·2) solid solution at eight different temperatures of measurement along with the values obtained for CsCl and CsBr for comparison.

4. Discussion

In CsCl-Br solid solutions system Shukla *et al* (1976) and Natarajan *et al* (1970) have done an exhaustive study of the lattice parameters at RT and higher temperatures and their aim was to look for the effects of concentrations near the phase transformation which the CsCl or CsBr individually undergoes from Pm3m to Fm3m. They have done for six different molal concentrations from CsCl-Br(0·95-0·05) to CsCl-Br(0·5-0·5) at two different temperatures RT and 560°K. However, they have not gone below (0·5, 0·5) molal concentrations. Besides there are no low temperature measurements available for these samples on the lattice parameters. Hence it was considered worthwhile to pursue this study to (i) provide values of the true lattice parameters in these solid solutions system below RT down to 90°K and (ii) to report any anomalous behaviour of these lattice parameters in this temperature range. It is found from our measurements that the solid solution composition CsCl-Br(0·8-0·2) has a behaviour which resembles qualitatively either CsCl or CsBr with the difference that in this case the thermal expansion coefficient increases as temperature is lowered from RT to 230°K and then falls off as the temperature is further lowered down to 90°K. The situation is not as simple in the remaining four concentrations where the lattice parameters themselves do not report a steady decreasing behaviour as the temperature is lowered. This is a clear indication of the fact that in the remaining four concentrations there are evidently

CC-0. In Public Domain. Gurukul Kangri Collection, Haridwar

Digitized by Arya Samaj Foundation Chennai and eGangotri

Table 1. Temperature vs lattice parameter for CsCl, CsBr, CsCl:CsBr solid solutions (Temperature in degree K and lattice parameter in angstroms).

		Lattice parameter						
No.	Temp.	CsCl	$CsCl_{0.8}Br_{0.2}$	$CsCl_{0.6}Br_{0.4}$	$CsCl_{0.5}Br_{0.5}$	$CsCl_{0.4}Br_{0.6}$	$CsCl_{0.2}Br_{0.8}$	CsBr
1.	78·2		4·10947(3)					4·25726(3)
	90·0	4·09048(2)						
	92·0			4·20359(3)	4·13283(3)	4·19342(3)	4·22649(5)	
2.	101·0	4·09202(2)	4·11236(3)	4·20564(2)	4·16307(3)	4·19796(3)	4·23180(3)	4·26085(2)
3.	125·8	4·09574(2)	4·11518(4)	4·20208(3)	4·16183(3)	4·18838(3)	4·23520(3)	4·26449(3)
4.	166·1	4·10210(2)	4·12148(3)	4·15438(3)	4·18223(3)	4·20735(3)	4·24242(3)	4·27178(3)
5.	200·2	4·10783(2)	4·12952(3)	4·16282(2)	4·16688(2)	4·19947(3)	4·24452(3)	4·27775(3)
6.	230·8	4·11329(2)	4·13504(3)	4·17437(2)	4·17918(3)	4·21884(4)	4·25360(4)	4·28348(3)
7.	258·7	4·11841(4)	4·13994(3)	4·18639(3)	4·18667(2)	4·20111(2)	4·25918(3)	4·28843(2)
8.	298·0	4·12599(2)	4·14846(3)	4·18803(3)	4·20899(2)	4·23342(2)	4·27141(3)	4·29645(2)

(E.S.D's are given in parantheses)

CC-0. In Public Domain. Gurukul Kangri Collection, Haridwar

Digitized by Arya Samaj Foundation Chennai and eGangotri

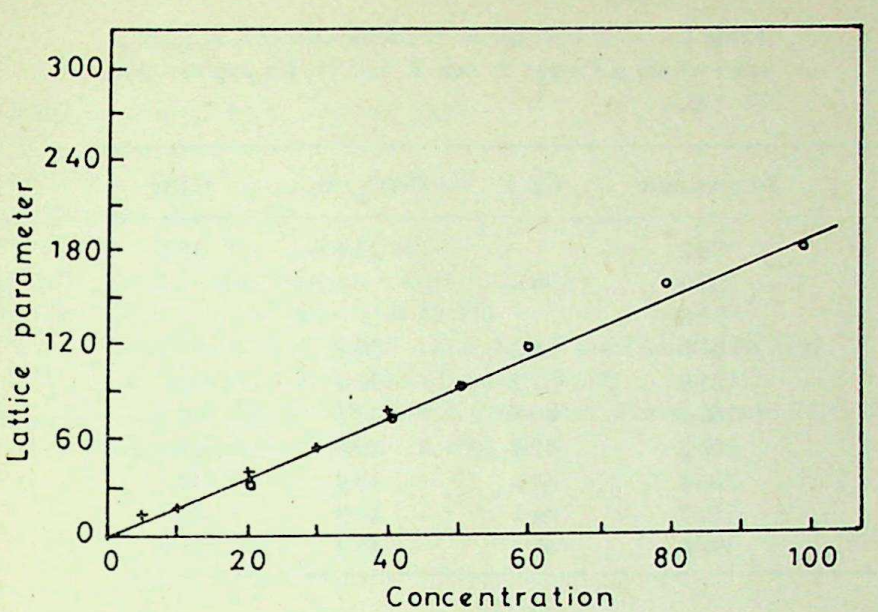

Figure 2. Plot of $[a_T(\text{true}) - 4{\cdot}12] \times 1000$ vs concentration at room temperature for CsCl-Br solid solutions. Dots represent values and "+" marks represent Natarajan *et al* (1970) values.

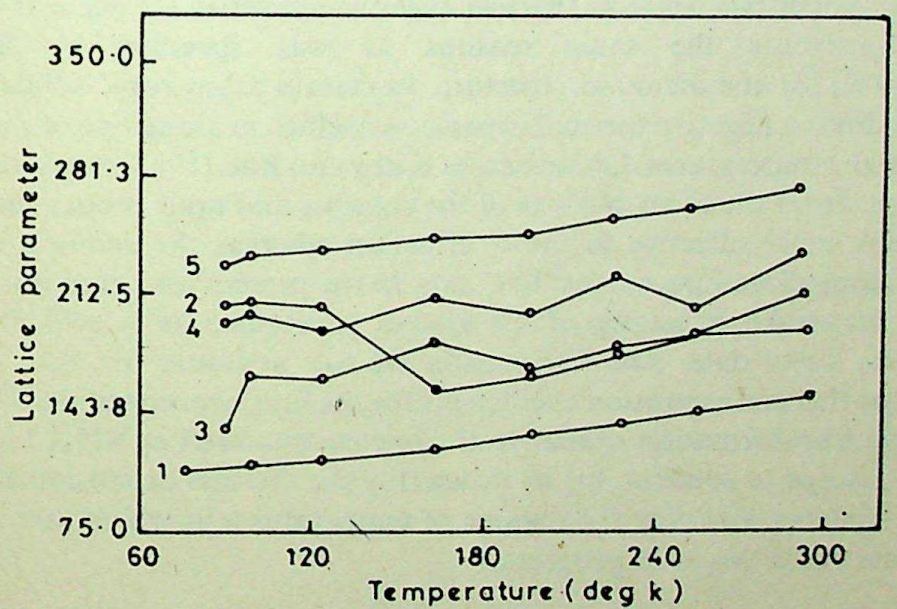

Figure 3. Plot of $[a_T(\text{true}) - 4{\cdot}0] \times 1000$ vs temperature for CsCl-Br solid solutions. (1) CsCl-Br(0·8-0·2) (2) CsCl-Br(0·6-0·4) (3) CsCl-Br(0·5-0·5) (4) CsCl-Br(0·4-0·6) and (5) CsCl-Br(0·2-0·8) compositions.

regions of temperatures in which the thermal expansion coefficients become negative. This was found to be true from an estimate of the average thermal expansion coefficients for these concentrations and not by fitting the true lattice parameters into a cubic polynomial. There are a number of cases in literature in which certain solids exhibit this negative thermal expansion. This is generally said to be arising from the vibrational free energy of the lattice at low temperatures. Glass and crystals having

CC-0. In Public Domain. Gurukul Kangri Collection, Haridwar

Digitized by Arya Samaj Foundation Chennai and eGangotri

Table 2. Thermal expansion coefficients of $CsCl_{0.8}Br_{0.2}$ solid solution (Temp. in deg. K and (α_T) is expressed in 10^{-6}/K).

No.	Temperature	CsCl	$CsCl_{0.8}Br_{0.2}$	CsBr
1.	78·2		22·1	35·8
	90·0	34·4		
	92·0			
2.	101·0	35·2	29·6	37·2
3.	125·8	37·2	36·4	38·7
4.	166·1	40·1	44·5	41·0
5.	200·2	42·4	48·5	42·8
6.	230·8	44·4	49·9	44·2
7.	258·7	46·1	49·3	45·4
8.	298·0	48·4	45·3	46·9

diamond structures are examples of this type. Blackmann (1957, 1958, 1959) discussed this in a series of papers adopting Barron's (1955) theoretical treatment and attributed this anomalous behaviour due to the low-lying transverse acoustic branch at low temperatures is predominant in absorbing energy. However, in the present case as the temperature at which this negative thermal expansion coefficients occur is fairly high one cannot attribute the same reasons as was specified by Blackmann (1957, 1958, 1959) for the diamond structure. In certain anisotropic solids like FeF_2 and RuO_2 one finds a negative thermal expansion coefficient along one of the principal directions at high temperatures. In these cases Kirby and Rao (1967) suggested that this behaviour arises from the contributions of the acoustic and optic modes such that the optic modes are more effective in the *C* direction whereas the acoustic modes are predominant along directions normal to *C* axis. In the present case even this argument fails because the isotropic nature of the system is retained as is evident from the indexing of the x-ray data. The one reason we can attribute for this anomalous behaviour of the thermal expansion coefficients for the four concentrations is that there may be a phase transformation similar to the one encountered in NH_4Cl at 242·6°K. More work is needed to confirm this by measuring the thermal expansion and specific heats in these systems well near the regions of temperatures at which this anomalous behaviour occurs and this is in progress.

Acknowledgements

The authors thank Professor R Srinivasan, Department of Biophysics and Crystallography, University of Madras for the useful suggestions he gave during this work and Professor R Srinivasan, Head, Low Temperature Laboratory, IIT, Madras for his encouragement and help in carrying out this work. The authors also thank the technical staff of the LTL and the staff in glass blowing section at both IIT, Madras and the University of Madras, Biophysics Department for their technical assistance. One of the authors (VG) acknowledges the research fellowship offered to him by the UGC during the period of this work.

CC-0. In Public Domain. Gurukul Kangri Collection, Haridwar

Digitized by Arya Samaj Foundation Chennai and eGangotri

References

Beg M M and Kobbelt M 1982 *Phys. Rev.* **B26** 1893
Barron T H K 1955 *Philos. Mag.* **46** 720
Blackmann M 1957 *Proc. Phys. Soc.* (*London*) **70** 827
Blackmann M 1958 *Philos. Mag.* **3** 831
Blackmann M 1959 *Proc. Phys. Soc.* (*London*) **47** 17
Ganesan V and Girirajan K S 1986 *Pramana – J. Phys.* **27** 469
Kirby R and Rao K J 1967 *Nat. Bur. Standards* **71** 363
Natarajan M, Rao K J and Rao C N R 1970 *J. Chem. Soc.* (*Farad. Trans.*) **66** 2497
Nelson J B and Riley D P 1945 *Proc. Phys. Soc.* (*London*) **37** 160
Shukla K K, Ahluwalia J C and Rao C N R 1976 *J. Chem. Soc.* (*Farad. Trans.*) **72** 1288
Srinivasan R and Girirajan K S 1982 *Pramana – J. Phys.* **19** 1

CC-0. In Public Domain. Gurukul Kangri Collection, Haridwar

Digitized by Arya Samaj Foundation Chennai and eGangotri

CC-0. In Public Domain. Gurukul Kangri Collection, Haridwar

Digitized by Arya Samaj Foundation Chennai and eGangotri

Pramāṇa – J. Phys., Vol. 28, No. 1, January 1987, pp. 81–86. © Printed in India.

X-ray diffraction and colour centre studies on RbCl-RbBr mixed crystals

K SRINIVAS, MOHD. ATEEQUDDIN and D B SIRDESHMUKH
Physics Department, Kakatiya University, Warangal 506 009, India

MS received 11 August 1986; revised 13 October 1986

Abstract. X-ray diffraction and colour centre studies have been carried out on RbCl-RbBr mixed crystals. The lattice constant closely follows the linear form of Vegard's law. The mean Debye-Waller factor shows a highly nonlinear composition dependence. The composition dependence of the F-band peak position is slightly nonlinear but that of the F-band half-width is highly nonlinear. The Ivey-Mollow relation holds for this system with an index of 2·5. The 'size effect' is found to have a dominant effect on the F-band width.

Keywords. Alkali halide mixed crystals; rubidium halides; lattice constants; Debye-Waller factor; colour centres.

PACS Nos 61·10; 61·14; 63·20; 65·90; 61·70

1. Introduction

The physical properties of alkali halide mixed crystals have been recently reviewed by Hari Babu and Subba Rao (1984) and Sirdeshmukh and Srinivas (1986). From these reviews it appears that no information is available regarding the RbCl-RbBr mixed crystal system. As a part of a continuing programme in this laboratory on studies of mixed crystals, x-ray diffraction and colour centre experiments have been carried out on this system which have yielded information on the composition dependence of the lattice constant (a), the Debye-Waller factor (B), the Debye temperature (θ), the F-band peak position (λ_{max}) and the F-band halfwidth (W). The results are presented in this paper.

2. Experimental

2.1 *Material preparation and characterization*

Analar grade chemicals supplied by E Merck were used to obtain crystals of RbCl, RbBr and their mixed crystals. The powdered material was taken in a crucible and allowed to melt in an electric 'Bunsen' furnace. The melt was cooled very slowly by a regulated reduction of the energy input to the furnace. From the solidified mass, single crystals of dimensions $5 \times 5 \times 2$ mm^3 could be cleaved out. As these dimensions were sufficient for the present studies, no effort was made to obtain larger crystals. Although the composition of the mixed crystals grown by the melt method will be generally close to the composition of the starting mixture, there can be some variation in the

CC-0. In Public Domain. Gurukul Kangri Collection, Haridwar

Digitized by Arya Samaj Foundation Chennai and eGangotri

composition of the different parts of the solidified melt and hence it is necessary to determine the exact composition of the actual sample employed in an experiment. In the present work, the composition of the mixed crystals was determined by the potentiometric titration method with an accuracy of 1–2%.

The x-ray studies as well as the colour centre studies were carried out at room temperature.

2.2 *X-ray diffraction experiments*

To determine the lattice constants, x-ray powder photographs were obtained with a Debye-Scherrer camera (11·46 cm) employing CuKα radiation. Back reflection lines were measured and lattice constants determined accurately by a least squares treatment using the Nelson-Riley error function. For all the compositions, solid solution formation was complete as evidenced from the fact that the x-ray diffraction photographs revealed no reflections except those pertaining to the mixed crystal.

The Debye-Waller factor was determined by measuring the intensities of Bragg reflections using a Philips powder diffractometer fitted with a proportional counter; copper radiation was used. The details of the corrections applied to the measured intensities and the procedure for obtaining the mean Debye-Waller factor and the Debye temperature have been discussed in earlier papers (Subhadra and Sirdeshmukh 1977; Srinivas and Sirdeshmukh 1985).

2.3 *Colour centre experiments*

For colour centre studies, clear crystals $4 \times 4 \times 1$ mm^3 in size were used. Irradiation was done with x-rays from a copper target tube operated at 30 kV and 10 mA. To obtain sufficient coloration, an irradiation time of 1 hr was considered sufficient for pure crystals whereas for mixed crystals, irradiation for 15–20 hr was necessary. This is consistent with the observation of Arends *et al* (1965) that the colorability of mixed crystals is smaller than that of pure crystals. The absorption spectrum was recorded with a Shimadzu double beam UV-visible spectrophotometer. The F-band peak position and the halfwidth were read from the absorption spectrum obtained with a strip-chart recorder.

3. Results and discussion

3.1 *Composition dependence of the parameters*

The values of the lattice constants of $RbCl_xBr_{(1-x)}$ mixed crystals with various compositions are given in table 1 and illustrated in figure 1. The composition dependence of the lattice constant is slightly nonlinear with negative deviations from linearity. The lattice constants of mixed crystals follow the equation

$$a^n = x a_1^n + (1-x)\, a_2^n, \tag{1}$$

where a, a_1 and a_2 are the lattice constants of the mixed crystal and the two end members. x and $(1-x)$ are the molar fractions of the two members in the mixed crystal. Sirdeshmukh and Srinivas (1986) pointed out that for most alkali halide mixed crystal systems the index n takes the value 1 while for a few it takes the value 3. Values of a for

CC-0. In Public Domain. Gurukul Kangri Collection, Haridwar

Digitized by Arya Samaj Foundation Chennai and eGangotri

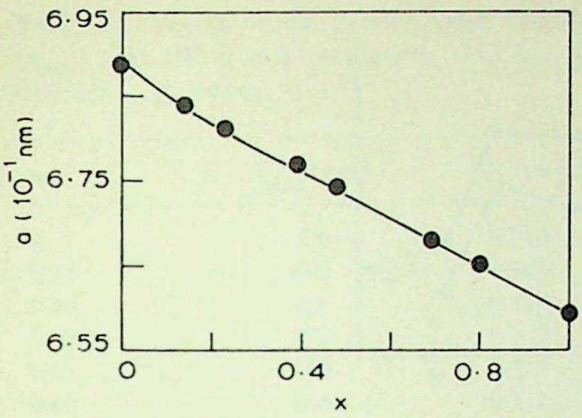

Figure 1. Plot of lattice constant a vs composition x for the $RbCl_xBr_{(1-x)}$ system.

Table 1. Values of the lattice constant (a) Debye-Waller factor (B) and Debye temperature (θ) for the $RbCl_xBr_{(1-x)}$ system.

		a_C (nm)		B (nm^2)		θ (K)	
x	a_E (nm)	$n=1$	$n=3$	exp.	static	X-rays	Equation (2)
0	0·68892	—	—	0·0218	0	138·6	—
0·14	0·68394	0·68479	0·68494	0·0225	0·00071	140·1	141·3
0·23	0·68128	0·68213	0·68235	0·0238	0·00105	143·4	143·2
0·39	0·67712	0·67741	0·67771	0·0237	0·00141	144·9	146·8
0·48	0·67448	0·67475	0·67507	0·0250	0·00148	147·9	149·0
0·69	0·66818	0·66856	0·66883	0·0231	0·00126	157·5	154·7
0·80	0·66540	0·66531	0·66552	0·0225	0·00095	161·1	158·0
1·0	0·65941	—	—	0·0211	0	165·0	—

Errors: $\Delta a = \pm 0{\cdot}00007$ nm; $\Delta B = \pm 0{\cdot}0008$ nm^2; $\Delta\theta = \pm 3$ K

the RbCl-RbBr system calculated from (1) with $n = 1$ and 3 are given in table 1. Following the method of Slagle and McKinstry (1966), the values of $(a_C - a_E)$ are shown in figure 2 as a function of x. Here a_E is the experimental value of the lattice constant and a_C the value calculated from (1). It can be seen that the values with $n = 1$ are closer to experimental values than those with $n = 3$ although even for $n = 1$ the values of $(a_C - a_E)$ are slightly larger than the estimated errors in a_E.

The values of the mean Debye-Waller factor (B_{exp}) are given in table 1 and plotted in figure 3 as a function of the composition (x). The composition dependence is highly nonlinear; the values of mixed crystals of some compositions are found to exceed the values of the end members. This composition dependence of the Debye-Waller factor for the RbCl-RbBr system is similar to that observed for the KBr-RbBr system (Srinivas and Sirdeshmukh 1985). As discussed earlier by Srinivas and Sirdeshmukh (1985), the presence of two ions of different sizes in a mixed crystal creates a local strain in the lattice. Because of this 'size effect', the atomic displacements in mixed crystals have a static component resulting in a static contribution to the Debye-Waller factor. This static contribution (B_{stat}) can be calculated theoretically. The values of B_{stat} calculated from the model proposed by Dernier *et al* (1976) are included in table 1. The

CC-0. In Public Domain. Gurukul Kangri Collection, Haridwar

Digitized by Arya Samaj Foundation Chennai and eGangotri

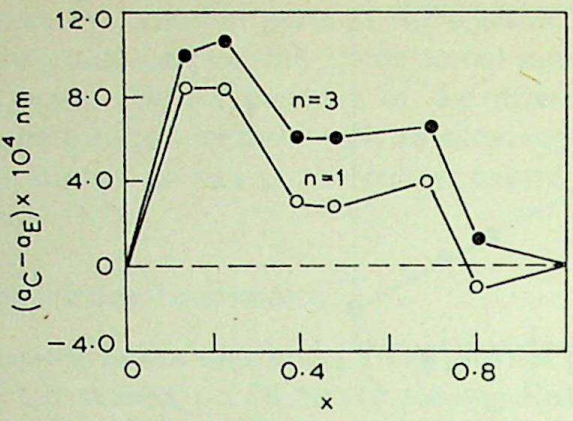

Figure 2. Plot of $(a_C - a_E)$ against the composition x for the $RbCl_xBr_{(1-x)}$ system.

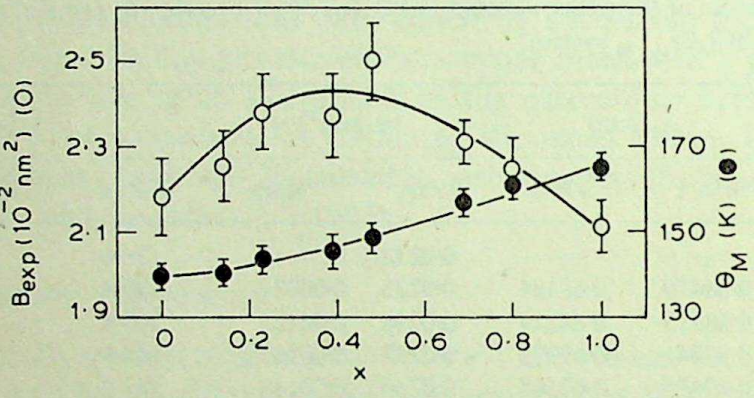

Figure 3. Plot of B_{exp} and θ_M against the composition x for the $RbCl_xBr_{(1-x)}$ system.

values of the Debye temperature (θ) calculated from the Debye-Waller factor (corrected for the static contribution) are also given in table 1 and shown in figure 3. The variation of the Debye temperature with composition is slightly nonlinear with negative deviations from linearity. The Debye temperatures of several mixed crystal systems follow the Kopp-Neumann relation

$$\theta^{-3} = x\,\theta_1^{-3} + (1-x)\,\theta_2^{-3}, \tag{2}$$

where θ, θ_1 and θ_2 are the Debye temperatures of the mixed crystal and the two end members. The values calculated from (2) are included in table 1. There is fair agreement between these values and those obtained from x-ray intensities.

The values of the F-band peak position (λ_{max}) and the halfwidth (W) are given in table 2 and shown in figure 4. λ_{max} varies with composition in a slightly nonlinear manner with positive deviations from linearity in the chlorine-rich region. The F-bandwidth shows a clearly nonlinear composition dependence.

3.2 *Interrelation between the parameters*

The F-band peak wavelength (λ_{max}) and the interionic distance (d) of alkali halide crystals are related through the expression

$$\lambda_{max} = \text{constant} \times d^n. \tag{3}$$

CC-0. In Public Domain. Gurukul Kangri Collection, Haridwar

Digitized by Arya Samaj Foundation Chennai and eGangotri

Table 2. Values of the F-band peak position (λ_{max}) and the F-band halfwidth (W) for the $RbCl_xBr_{(1-x)}$ system

x	λ_{max} (nm)	W (eV)
0	706	0·344
0·25	690	0·369
0·39	680	0·374
0·505	672	0·377
0·61	670	0·377
0·80	654	0·372
1·0	634	0·361

Errors: $\Delta\lambda_{max} = \pm 5$ mm; $\Delta W = \pm 0{\cdot}01$ eV

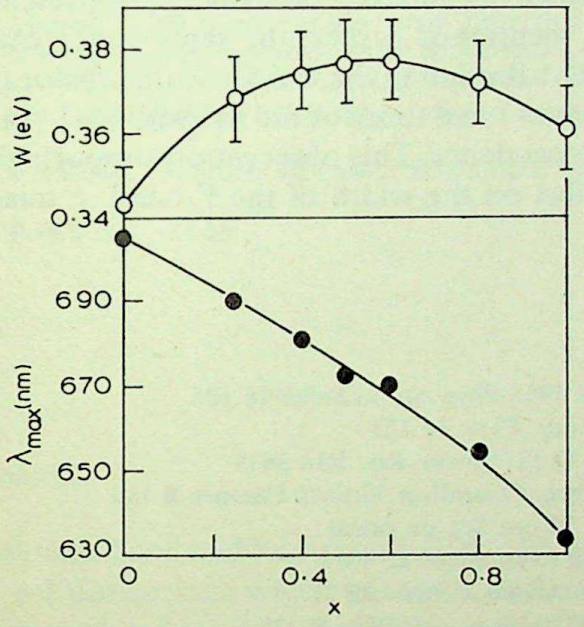

Figure 4. Plot of λ_{max} and W against the composition x for the $RbCl_xBr_{(1-x)}$ system.

For alkali halides with NaCl structure, d is half the lattice constant. This is known as the Ivey-Mollow relation; values ranging from 1·8 to 2·5 have been suggested for the index n (Compton and Rabin 1964). A log-log plot of λ_{max} and d is given in figure 5 for the RbCl-RbBr system. It is a straight line with a slope of 2·5. Thus the Ivey-Mollow relation holds for this system with an index of 2·5.

The halfwidth of the F-band has been found to vary nonlinearly with composition in this system, increasing with composition x, reaching a maximum in the equimolar region and then decreasing with x. Arends *et al* (1965) suggested a correlation between the F-bandwidth and the dislocation densities for the mixed crystals studied by them (KCl-RbCl, KCl-KBr, KBr-RbBr). Subramaniam and Bansigir (1981) reinvestigated the KCl-KBr system and showed that there was no correspondence between the dislocation densities and the F-band halfwidth in this system. Subramaniam and Bansigir suggested that the 'size effect' in mixed crystals has a significant effect

CC-0. In Public Domain. Gurukul Kangri Collection, Haridwar

Digitized by Arya Samaj Foundation Chennai and eGangotri

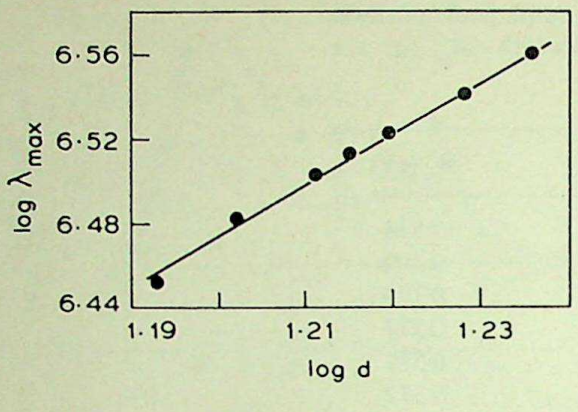

Figure 5. Plot of $\log\lambda_{max}$ vs $\log d$ for the $RbCl_xBr_{(1-x)}$ system.

on the concentration variation of the F-band halfwidth. The 'size effect' is the production of local strains in the lattice of a mixed crystal due to the presence of ions of different sizes at a lattice site. As mentioned earlier, the same factor causes a static atomic displacement and a static contribution to the Debye-Waller factor (B_{stat}). It can be seen from the values of B_{stat} in table 1 and those of the halfwidth (W) in table 2 that both have a similar composition dependence. This observation supports the view that the 'size effect' has a dominant effect on the width of the F-band in mixed crystals.

References

Arends J, Hartog H W D and Dekker A J 1965 *Phys. Status Solidi* **10** 105
Compton W D and Rabin H 1964 *Solid State Phys.* **16** 121
Dernier P D, Weber W and Longinotti L D 1976 *Phys. Rev.* **B14** 3635
Hari Babu V and Subba Rao U V 1984 *Prog. Crystallogr. Growth Charact.* **8** 189
Sirdeshmukh D B and Srinivas K 1986 *J. Mater. Sci.* (in press)
Slagle O D and McKinstry H A 1966 *Acta Crystallogr.* **21** 1013
Srinivas K and Sirdeshmukh D B 1985 *Pramana–J. Phys.* **25** 71
Subhadra K G and Sirdeshmukh D B 1977 *Pramana–J. Phys.* **9** 223
Subramaniam B and Bansigir K G 1981 *Pramana–J. Phys.* **17** 445

CC-0. In Public Domain. Gurukul Kangri Collection, Haridwar

Digitized by Arya Samaj Foundation Chennai and eGangotri

Pramāṇa – J. Phys., Vol. 28, No. 1, January 1987, pp.87–93. © Printed in India.

Existence of quantum soliton for ϕ^6-like field theories in $1+1$ dimensions

C N KUMAR and B K PARIDA*

Institute of Physics, Sachivalaya Marg, Bhubaneswar 751 005, India
* Faculty of Physics, Regional College of Education, Ajmer 305 004, India

MS received 31 July 1986

Abstract. We reexamine the recent claim that the soliton of the $1+1$ dimensional field theories does not survive quantum corrections if the adjacent minima of the potential do not have same curvature and show that it is in fact possible to choose counter terms such that the quantum correction to the soliton mass is finite.

Keywords. Solitons; 2-D scalar field model; triple-well potential.

PACS No. 11·15

1. Introduction

In a recent article, Kaul and Rajaraman (1985) (KR) have considered the ϕ^6 field theory model in $1+1$ dimensions which has three degenerate minima and have claimed that the quantum soliton does not exist in this model. These authors have claimed that the quantum soliton will not exist in all those $1+1$ dimensional field theory models in which the curvatures at the adjacent degenerate absolute minima are unequal. In particular they showed that in all these cases the quantum correction to the soliton mass has a L-dependent piece which diverges as the length L of the box in which the system is quantized goes to infinity.

We find this claim rather surprising since all such neutral scalar field theories are in fact renormalizable in $1+1$ dimensions. We have therefore taken a fresh look at this problem and find that in *all* these cases, contrary to the claim of KR it is in fact possible to choose the counterterms in such a way that the quantum correction to the soliton mass is finite.

The paper is organized as follows. In §2 we sketch the essential steps of KR so as to make the paper self-contained. In §3 we demonstrate as to how counterterms can be appropriately chosen to make the quantum correction to the soliton mass finite. Finally, in §4 we compute one-loop effective potential for the case of ϕ^6-field theory with the same counterterms and show the phenomenon of spontaneous symmetry breaking.

CC-0. In Public Domain. Gurukul Kangri Collection, Haridwar

Digitized by Arya Samaj Foundation Chennai and eGangotri

2. Kaul-Rajaraman argument

Kaul and Rajaraman (1985) have considered in detail the following field theory model in $1+1$ dimensions

$$L = \tfrac{1}{2}(\partial_\mu \phi)(\partial^\mu \phi) - \tfrac{1}{2}S^2(\phi), \tag{1}$$

where

$$\tfrac{1}{2}S^2(\phi) \equiv V(\phi) = \frac{\lambda^2}{2m^2}\phi^2\left(\phi^2 - \frac{m^2}{\lambda}\right)^2. \tag{2}$$

At the classical level, this model has three degenerate minima at $\phi = 0$, and $\phi = \pm m/\sqrt{\lambda}$. The soliton solution of this model (Khare 1979) is

$$\phi_s(x) = \frac{m}{\sqrt{2\lambda}}(1 + \tanh mx)^{1/2}, \tag{3}$$

and the corresponding soliton mass is

$$M_s^{\mathrm{cl}} = m^3/3\lambda. \tag{4}$$

The other three soliton solutions can be trivially obtained by exchanging $\phi \leftrightarrow -\phi$ and $x \leftrightarrow -x$ and all of them have same soliton mass as given by (4).

KR have calculated the quantum correction to the soliton mass M_s^{cl} as given by equation (4) and have claimed that it is L divergent, L being the length of the box in which the system is quantized. They have argued that the origin of this L-divergence can be quite easily anticipated by considering the vacuum of the theory. In particular, they have argued that since the curvature of the potential at $\phi = 0$ is less than that of $\phi = \pm m/\sqrt{\lambda}$ i.e.,

$$\left.\frac{\mathrm{d}^2V}{\mathrm{d}\phi^2}\right|_{\phi=0} = m^2, \qquad \left.\frac{\mathrm{d}^2V}{\mathrm{d}\phi^2}\right|_{\phi=\pm m/\sqrt{\lambda}} = 4m^2. \tag{5}$$

Hence the zero-point energy of the vacuum at $\phi = 0$ will be lower than that of the vacuum at $\phi = \pm m/\sqrt{\lambda}$. To order $\hbar$, the difference of these vacuum energies is

$$(E_{\mathrm{vac}})_{\phi=\pm m/\sqrt{\lambda}} - (E_{\mathrm{vac}})_{\phi=0} = \frac{\hbar L}{2}\int\frac{\mathrm{d}k}{2\pi}\left[(k^2+4m^2)^{1/2} - (k^2+m^2)^{1/2}\right] \tag{6}$$

from which they have concluded that the states built around $\phi = \pm m/\sqrt{\lambda}$ have higher energy density per unit length. As a result the quantum soliton will also have higher energy (compared to the vacuum) that would tend to infinity as $L \to \infty$. KR have further argued that this reasoning will apply for any model in $1+1$ dimensions for which the potential has unequal curvatures at the neighbouring degenerate minima. Thus according to them, quantum soliton will not exist in all these cases. KR have also done a detailed analysis of the one-loop correction to the soliton mass which is given by

$$M_s^{1\text{-loop}} = \frac{\hbar}{2}\left[\sum_{\mathrm{sol}}\omega - \sum_{\mathrm{vac}}\tilde{\omega}\right] + \left[\Delta E_{\mathrm{c.t.}}(\mathrm{sol}) - \Delta E_{\mathrm{c.t.}}(\mathrm{vac})\right] \tag{7}$$

where ω are fluctuation frequencies. By anticipating the true vacuum to be at $\phi = 0$ they

CC-0. In Public Domain. Gurukul Kangri Collection, Haridwar

Digitized by Arya Samaj Foundation Chennai and eGangotri

obtain

$$\frac{\hbar}{2}\sum_{\text{vac}}\tilde{\omega} = \hbar L\int\frac{dk}{2\pi}(k^2+m^2)^{1/2}. \tag{8}$$

They further show that

$$\frac{\hbar}{2}\sum_{\text{sol}}\omega = \frac{\hbar L}{2}\int_0^\infty (k^2+m^2)^{1/2} + \frac{\hbar L}{2}\int_0^\infty \frac{dk'}{2\pi}(k'^2+4m^2)^{1/2} + L \text{ independent terms.} \tag{9}$$

The one-loop renormalization counter term for the Lagrangian (1) is of the form

$$L_{\text{c.t.}} = \frac{\hbar C}{2}((S')^2 + SS''), \tag{10}$$

where C is the loop integral which has been chosen by KR as

$$C = \frac{1}{2\pi}\int_0^\infty \frac{dk}{(k^2+m^2)^{1/2}}. \tag{11}$$

With this they show that one-loop radiative correction to the soliton mass is

$$M_s^{\text{1-loop}} = \frac{\hbar L}{2}\int_0^\infty \frac{dk}{2\pi}\left[(k^2+4m^2)^{1/2} - (k^2+m^2)^{1/2} - \frac{3}{2}\frac{m^2}{(k^2+m^2)^{1/2}}\right] + L \text{ independent terms.} \tag{12}$$

Since the first term is L- divergent (even though ultraviolet finite) they conclude that the finite energy classical soliton does not survive quantum correction and hence quantum soliton does not exist.

3. Existence of quantum soliton

We do not agree with the argument of KR for the following reasons. There is no compulsion to choose the mass parameter in the loop integral C as m^2 (equation (11)). In fact, the correct procedure would be to keep it arbitrary (say μ^2) and then adjust μ^2 so that even to the order $\hbar$ the difference of the vacuum energies of the neighbouring minima is zero. One should then calculate the quantum correction to the soliton mass with such choice of $L_{\text{c.t.}}$ (equation (10)). We shall show below that with this procedure the quantum correction to the soliton mass is indeed L-independent and finite. We shall also see that this procedure applies to any potential with different curvatures at the neighbouring degenerate minima. Similar analysis was done by Lohe and O'Brien (1981). Even though the final aim in both is to achieve L-independent finite correction to soliton mass the procedures in the two are slightly different and in the light of KR's paper we thought it worth reporting the same.

The difference of vacuum energies (to order $\hbar$) as given by (6) is divergent. Let us try to make it finite by choosing $L_{\text{c.t.}}$ as given by (10) but with the mass parameter in the

CC-0. In Public Domain. Gurukul Kangri Collection, Haridwar

Digitized by Arya Samaj Foundation Chennai and eGangotri

loop integral C being arbitrary i.e.

$$C = \frac{1}{2\pi}\int \frac{dk}{(k^2+\mu^2)^{1/2}}. \tag{13}$$

Hence

$$(\Delta E_{c.t.})_{\phi=\pm m/\sqrt{\lambda}} - (\Delta E_{c.t.})_{\phi=0} = -\frac{3}{4\pi}\hbar L m^2 \int \frac{dk}{(k^2+\mu^2)^{1/2}}. \tag{14}$$

Thus the 'true' difference of vacuum energies will be

$$\hbar L \int_0^\infty \frac{dk}{2\pi}\left[(k^2+4m^2)^{1/2} - (k^2+m^2)^{1/2} - \frac{3}{2}\frac{m^2}{(k^2+\mu^2)^{1/2}}\right] \tag{15}$$

which is zero provided.*

$$\ln\left(\frac{\mu^2}{m^2}\right) = \tfrac{4}{3}\ln 4 - 1. \tag{16}$$

i.e. μ^2 lies between m^2 and $4m^2$. In other words, with this choice of μ^2 in the loop integral C, the vacuum energies are degenerate even to the order $\hbar$.

Let us now compute the quantum correction to the soliton mass by using the *same* $L_{c.t.}$ as given by (10), (13) and (16). On using the soliton solution (3) it is easy to compute the contribution from the counterterms to the soliton mass. Taking (10) and (13) one finds that

$$\Delta E_{c.t.}(\text{sol}) - \Delta E_{c.t.}(\text{vac}) = \tfrac{3}{4}m^2\hbar L \int \frac{dk}{2\pi}\frac{1}{(k^2+\mu^2)^{1/2}}. \tag{17}$$

From (7) to (9) it then follows that

$$M_s^{1\text{-loop}} = \frac{\hbar L}{2}\int_0^\infty \frac{dk}{2\pi}\left[(k^2+4m^2)^{1/2} - (k^2+m^2)^{1/2} - \frac{3}{2}\frac{m^2}{(k^2+\mu^2)^{1/2}}\right] + L \text{ independent terms.} \tag{18}$$

Note that here the vacuum is chosen at $\phi^2 = 1$. This choice is unimportant. Even if one chooses $\phi = 0$ as the true vacuum and does calculations one will be able to obtain the same L-independent part with L dependent part (which any way cancels out) differing by an overall sign.

In view of (15) and (16) it is then clear that $M_s^{1\text{-loop}}$ is L-independent and finite. In a sense this result is understandable since, with our choice of $L_{c.t.}$ the two vacuum energies are degenerate to order $\hbar$. Hence it follows that the soliton exists to order $\hbar$. Needless to say that with this prescription, the supersymmetric soliton will also have finite quantum correction to order $\hbar$.

This prescription is not special to this particular problem but can in fact be generalized to any model in $1+1$ dimensions when the potential has unequal

* This result is obtained by following the approach of Kaul and Rajaraman (1985) for calculating soliton fluctuations contribution which is different from that of Lohe and O'Brien (1981).

CC-0. In Public Domain. Gurukul Kangri Collection, Haridwar

Digitized by Arya Samaj Foundation Chennai and eGangotri

curvatures at the neighbouring degenerate minima (Lohe and O'Brien 1981). In particular, if the potential has curvatures u_+ and u_- at the two neighbouring degenerate minima (so that classical soliton exists) then it can be shown that the difference of the vacuum energies is zero provided the $L_{\text{c.t.}}$ is given by (10) and (13) with μ^2 given by

$$\left(\frac{u_+}{u_+ - u_-}\right)\ln\left(\frac{u_+}{\mu^2}\right) - \left(\frac{u_-}{u_+ - u_-}\right)\ln\left(\frac{u_-}{\mu^2}\right) = 1. \tag{19}$$

By following the above arguments it is then clear that in these cases the one-loop quantum correction to the soliton mass is L-independent and finite.

4. One-loop effective potential with the new counterterm

In the last section we have shown that if the $L_{\text{c.t.}}$ is as given by (10), (13) and (16) then the one-loop quantum correction to the soliton mass is L-independent and finite. KR may criticize this choice of $L_{\text{c.t.}}$ by pointing out that the mass parameter in the loop integral has to be m^2 (and not μ^2) since at one-loop level $\phi = 0$ is the true vacuum of the theory. However, this is not necessarily so and the true vacuum of the theory crucially depends on the renormalization prescription. To demonstrate it, in this section we compute one-loop effective potential with $L_{\text{c.t.}}$ as given by (10), (13) and (16) and show that $\phi = 0$ is in fact not the true vacuum of the theory.

We shall follow the elegant procedure of Coleman and Weinberg (1973) while calculating the effective potential. Consider the Lagrangian density

$$\tilde{L}(\tilde{x}, \tilde{t}) = \tfrac{1}{2}(\tilde{\partial}_\mu \tilde{\phi})^2 - \tfrac{1}{2}S^2(\tilde{\phi}), \tag{20}$$

where

$$\tfrac{1}{2}S^2(\tilde{\phi}) \equiv V_0(\tilde{\phi}) = \frac{\lambda'^2}{2m^2}\tilde{\phi}^2\left(\tilde{\phi}^2 - \frac{m^2}{\lambda'}\right)^2. \tag{21}$$

On changing variables

$$\phi = \frac{\sqrt{\lambda'}}{m}\tilde{\phi}, \qquad x_\mu = \frac{m^2}{\lambda'}\tilde{x}_\mu, \tag{22}$$

equation (20) takes the form

$$L(x, t) = \frac{1}{\lambda}[\tfrac{1}{2}(\partial_\mu \phi)^2 - V_0(\phi)], \tag{23}$$

where

$$V_0(\phi) = \tfrac{1}{2}\phi^2(\phi^2 - 1)^2, \qquad \lambda = \frac{\lambda'^3}{m^6}. \tag{24}$$

To one-loop order the effective potential is given by

$$V_{\text{eff}}(\phi) = \frac{1}{\lambda}V_0(\phi) + \lambda^0 V_1(\phi), \tag{25}$$

where $V_0(\phi)$ is given by (24), the one-loop term $V_1(\phi)$ can be obtained by summing up

CC-0. In Public Domain. Gurukul Kangri Collection, Haridwar

Digitized by Arya Samaj Foundation Chennai and eGangotri

of infinitely many one-loop graphs. As in the work of Coleman and Weinberg (1973) it is not difficult to show that $V_1(\phi)$ is given by

$$V_1(\phi) = \frac{1}{8\pi} V_0''(\phi)\left[\ln\left(\frac{\Lambda^2}{V_0''(\phi)}\right)+1\right], \tag{26}$$

where Λ is cut off and terms that vanish as $\Lambda^2 \to \infty$ have been dropped. The divergence in $V_1(\phi)$ can be taken care of by adding $L_{\text{c.t.}}$ as given by (10), (13) and (16) which in this case has the form

$$L_{\text{c.t.}} = \frac{1}{8\pi}(1 + \ln\Lambda^2 - \tfrac{1}{3}\ln 4)\, V_0''(\phi). \tag{27}$$

Hence V_{eff} upto one-loop level is given by

$$V_{\text{eff}}(\phi) = \frac{1}{\lambda} V_0(\phi) + \frac{V_0''(\phi)}{8\pi}[\tfrac{1}{3}\ln 4 - \ln V_0''(\phi)], \tag{28}$$

where $V_0(\phi)$ is given by (23). From here we notice that

$$V_{\text{eff}}(\phi = 0) = \frac{1}{24\pi}\ln 4, \quad V_{\text{eff}}(\phi = \pm 1) = -\frac{1}{3\pi}\ln 4, \tag{29}$$

so that $\phi = 0$ is *not* the true vacuum of the theory.

Before concluding the paper, we would like to make a few remarks regarding the general question of spontaneous symmetry breaking by radiative corrections.

(i) For our problem, at the classical level the potential $V_0(\phi)$ has three degenerate minima at $\phi = 0, \pm 1$ which is the typical case of first-order transition point. However the 1-loop effective potential as given by (28) show that $\phi = 0$ is no more the true vacuum of the theory i.e. the symmetry is spontaneously broken. The true vacuum of the theory is at $\phi = 1$ provided $\lambda < \lambda_c$. While for $\lambda > \lambda_c$ the true vacuum is around $\phi = \pm 1$.

(ii) In an interesting article Rajaraman and Raj Lakshmi (1981) had started with the classical potential

$$V_0(\phi) = (\phi^2 + a^2)(\phi^2 - 1)^2 - a^2, \quad 0 < a^2 < \tfrac{1}{2} \tag{30}$$

which has local minima at $\phi = 0$ and degenerate absolute minima at $\phi = \pm 1$. By using the renormalization conditions at $\phi = 0$ they calculated the corresponding one-loop effective potential and showed that the true vacuum of the theory is now at $\phi = 0$ provided $\lambda > \lambda_1$ i.e. the symmetry is restored by radiative corrections if $\lambda > \lambda_1$ (λ_1 being some constant). However, if instead one calculated V_{eff} by using the renormalization conditions at $\phi = \pm 1$ rather than at $\phi = 0$ then one finds that symmetry is not restored no matter what the value of λ is. This again demonstrates that the true vacuum of the theory at one-loop level depends quite crucially on the renormalization prescription.

Acknowledgements

One of us (CNK) would like to thank Dr A Khare for his encouragement and help in

CC-0. In Public Domain. Gurukul Kangri Collection, Haridwar

Digitized by Arya Samaj Foundation Chennai and eGangotri

preparing the manuscript, and Dr P Majumdar for discussion. BKP is indebted to Professor T Pradhan for a summer visitorship at the Institute of Physics and the members of Institute for helpful discussions.

References

Coleman S and Weinberg E J 1973 *Phys. Rev.* **D7** 1888
Kaul R K and Rajaraman R 1985 *Pramana – J. Phys.* **24** 837
Khare A 1979 *Lett. Math. Phys.* **3** 475
Lohe M A and O'Brien D M 1981 *Phys. Rev.* **D23** 1771
Rajaraman R and Raj Lakshmi M 1981 *Phys. Rev.* **D23** 2399

CC-0. In Public Domain. Gurukul Kangri Collection, Haridwar

Digitized by Arya Samaj Foundation Chennai and eGangotri

CC-0. In Public Domain. Gurukul Kangri Collection, Haridwar

Digitized by Arya Samaj Foundation Chennai and eGangotri

Pramāṇa – J. Phys., Vol. 28, No. 1, January 1987, pp. L95–L96. © Printed in India.

Some remarks on the finiteness of soliton mass

R K KAUL and R RAJARAMAN
Centre for Theoretical Studies, Indian Institute of Science, Bangalore 560012, India

MS received 29 September 1986

Abstract. Some subtleties regarding regularizations in computing the soliton energy of degenerate systems are discussed.

Keywords. Solitons; 2-D scalar field theories; regularizations

PACS Nos 11·15; 11·30

Some time back we had demonstrated for a class of scalar field theories with classically degenerate vacua that the energy of the quantum soliton is infinite as volume tends to infinity even though its classical energy is finite (Kaul and Rajaraman 1985). This demonstration employed a specific regularization. However, Kumar and Parida (KP) have made the interesting point that there exists a regularization for which the soliton energy is finite (Kumar and Parida 1986). This happens because their specific regularization leaves the vacua degenerate even at the quantum level.

We agree with the calculations of KP and their point is well taken. Strictly speaking within the confines of their model their regularization is as permissible as any other. However, in the larger context, the specific regularization used by them violates a guiding principle in field theory. This is the principle of naturalness. In the Kumar-Parida regularization, the parameter m^2/μ^2 has to be finely tuned and that too afresh at each order in perturbation theory. This is undesirable. For example, the well-known gauge hierarchy problem in grand unified theories arises for the same reason and fine tuning there is not considered desirable.

In fact the fine tuning required by Kumar and Parida is infinitely more stringent than that which arises in the gauge hierarchy problem in grand unified theories. For instance in their one-loop result (equation (16)), the quantity $\ln(\mu^2/m^2) - \frac{4}{3}\ln 4 + 1$ must be tuned to be exactly zero as distinct from that in the case of the gauge hierarchy problem, where the corresponding parameter has to be only small. By contrast the regularization we employed was generic. Our result that the soliton energy diverges as $L \to \infty$ is valid for all regularizations except for the special infinitely fine-tuned one that Kumar and Parida have used.

Furthermore, if one were to apply such models to quasi one-dimensional condensed matter systems, which provide a definite characteristic cut-off Λ, the corresponding parameter m^2/Λ^2 is fixed and not free to be tuned. Therefore, a result from continuum theory will hold only if it is obtained using a generic regularization.

CC-0. In Public Domain. Gurukul Kangri Collection, Haridwar

Digitized by Arya Samaj Foundation Chennai and eGangotri

Kumar and Parida have also compared their work with that of Rajaraman and Raj Lakshmi (1981), where too the relative ordering of the quantum energies of classical vacua can be reversed by a suitable regularization. But that result holds for a whole class of regularizations and not just for an infinitely tuned one.

Lastly KP give as a motivation for the large L finiteness of the soliton energy the fact that the theory is renormalizable. We do not agree with this. The renormalizability they are referring to is in the ultraviolet. That does not preclude divergences in the infrared ($L \to \infty$). Otherwise, for example, no renormalizable theory could ever have a false vacuum.

References

Kaul R K and Rajaraman R 1985 *Pramana – J. Phys.* **24** 837
Kumar C N and Parida B K 1986 *Pramana – J. Phys.* **28** 87
Rajaraman R and Raj Lakshmi M 1981 *Phys. Rev.* **D23** 2399

CC-0. In Public Domain. Gurukul Kangri Collection, Haridwar

Digitized by Arya Samaj Foundation Chennai and eGangotri

Pramāṇa – J. Phys., Vol. 28, No. 2, February 1987, pp. 97–107. © Printed in India.

पुस्तकालय
गुरुकुल कांगड़ी विश्वविद्यालय
हरिद्वार
27/3/87

Implementation and comparative study of random sequences for nonlinear least square data fitting

TAPAS BANDYOPADHYAY and P K SARKAR
Health Physics Unit, Variable Energy Cyclotron Centre, I/AF Bidhan Nagar, Calcutta 700 064, India

MS received 19 November 1986

Abstract. A numerical study of nonlinear least square data fitting using random numbers from the congruential generator and several quasi-random generators is presented. The results indicate that at least up to five dimensions some of the quasi-random sequences yield better accuracy than the congruential pseudo-random sequence. Some recommendations for selecting the generators of quasi-random sequences are also given.

Keywords. Least square data fitting; random search; quasi-random sequences; pseudo-random sequences; global optimization; Gaussian detector response.

PACS No. 02·60

1. Introduction

In an earlier work (Bandyopadhyay and Sarkar 1985) the authors have shown that the quasi-random search (QRS) technique can be used effectively to fit experimentally observed data (detector responses) with empirical expressions. It has also been shown that the QRS out-performs classical optimization techniques especially when the experimentally observed data are associated with poor statistics. This is because, with the introduction of statistical uncertainty the function to be optimized has a high probability of becoming multi-extremal defined over some multi-variate parameter space, and as such the traditional techniques can suffer severely from trapping in local minima for such problems. This limitation of the traditional techniques is crucial in experimental physics and astrophysics where observed data is often required to be fitted with empirical relations. The quasi-random search technique with importance sampling (Bandyopadhyay and Sarkar 1985) can avoid such trapping with proper choice of the importance function so that the localization of search is achieved rather slowly.

In the present work, we carry out numerical studies to investigate the effective implementation of the method using several quasi-random sequences (QRS) and one congruential pseudo-random sequence in dimensions three, four and five. Further, we compare these sequences to determine their relative merits for nonlinear least square fitting problems. Theoretical estimates of the error bounds of optimization can be obtained by using the extremal discrepancy of the sequence and the modulus of continuity of the function (Niederreiter 1983), but such estimates are not very precise. Furthermore, estimation of the extremal discrepancy of the sequences and the modulus

CC-0. In Public Domain. Gurukul Kangri Collection, Haridwar

Digitized by Arya Samaj Foundation Chennai and eGangotri

of continuity of the functions is extremely difficult and time consuming especially at high dimensions. It is therefore practical to side step this problem heuristically by carrying out numerical experimentations with test functions of the type involved. For practical applications in solving nonlinear least square fitting problems, several sequences can be tried on test problems—giving perhaps relevant experience to choose with some confidence. It may be noted that quasi-random sequences have been used for optimization and random search in hypercubes by Neiderreiter and Mc Curley (1979), Neiderreiter and Peart (1982), Aird and Rice (1977), Sobol (1979) and Fox (1986). The present study though carried out with Gaussian-like functions, the results obtained and conclusions drawn therefrom can generally be believed to hold true for other nonlinear least square fitting problems also. It may be noted that in this study of Monte Carlo optimization we will only consider the case where we are interested in the global optimum of a function.

2. Computational aspects

2.1 *Description of the sequences*

Before describing the sequences used for the present study let us first define the radical inverse function $\phi_r(n)$.

Let n be a non-negative integer and r an integer with $r \geqslant 2$.

Let $$n = \sum_{i=0}^{k} b_i r^i \quad \text{with} \quad b_1 \in [0, 1, \ldots, g-1],$$

for $0 \leqslant i \leqslant k$ be the r-adic expansion of n. The radical inverse function $\phi_r(n)$ is then given by

$$\phi_r(n) = \sum_{i=0}^{k} b_i r^{-i-1}. \tag{1}$$

We now describe the individual sequences.

Hammersley sequence (*HAM*): The Hammersley sequence (Zaremba 1968) of order N in $I^s (I^s = 0, 1)^s$, the s-dimensional unit cube, $s \geqslant 2$ consists of

$$a_n = \left[\frac{n}{N}, \phi_r(n), \ \ldots \ \phi_{r_{s-1}}(n) \right], \quad n = 0, 1, \ldots N-1$$

where the bases $r_1, \ldots r_{s-1}$ are the pairwise relative prime. Usually, one takes $r_1, \ldots r_{s-1}$ as the first $s-1$ primes.

Halton sequence (*HAL*): The Halton sequence (Halton 1960) in s dimensions is defined by

$$a_n = [\phi_2(n), \phi_3(n), \ldots \phi_{p(s)}(n)]$$

where $p(s)$ are the first s primes.

Zaremba sequence (*ZAR*): The Zaremba sequence (Halton and Zaremba 1969) in s

CC-0. In Public Domain. Gurukul Kangri Collection, Haridwar

Digitized by Arya Samaj Foundation Chennai and eGangotri

dimensions is defined by

$$a_n[\psi_2(n), \ldots \psi_{p(s)}(n)]$$

where $\psi_r(n)$ is the folded radical inverse function and is given by:

$$\psi_r(n) = (b_0 + 0)_{\mathrm{mod}\, r} r^{-1} + (b_1 + 1)_{\mathrm{mod}\, r} r^{-2} + \ldots + (b_i + i)_{\mathrm{mod}\, r} r^{-i-1} + \ldots .$$

Haber sequence (*HAB*): The sequence suggested by Haber (1970) can be described as follows:

$$a_n = \left[\left\{ \frac{n(n+1)}{2} \sqrt{2} \right\}, \ldots \left\{ \frac{n(n+1)}{2} \sqrt{p_s} \right\} \right],$$

where $\{y\}$ denotes the fractional part of y.

Sequence 5 (*SEQ* 5): This is a sequence (Warnock 1972) defined by

$$a_n = [n/N, \psi_2(n), \ldots \psi_{p(s-1)}].$$

Sequence 6 (*SEQ* 6): This sequence (Warnock 1972) is defined by

$$a_n = [\{m\sqrt{2}\}, \ldots, \{m\sqrt{p(k)}\}].$$

Scrambled Halton sequence (*SCR-HAL*): This is closely related to the Halton sequence and is defined as follows:

$$x_n = \sum_{i=0}^{\infty} \sigma_i(b_i) r^{-i-1},$$

where $\Sigma = (\sigma_i)_{i \geqslant 0}$ are a set of permutations on the ensemble $(0, 1, 2, \ldots, r_3 - 1)$. The permutations Σ are obtained in such a manner as to reduce the one-dimensional r.m.s. discrepancy obtained with the integer r_s. In this work, we used the set of permutations suggested by Braaten and Weller (1979).

Pseudo-random sequence (*PRS*): A set of random numbers which pass some specified statistical test for randomness are known as pseudo-random numbers (Neiderreiter 1978). The commonly used sequence of pseudo-random numbers, called the congruential pseudo-random numbers in the unit interval [0, 1], may be generated as follows: let $m \geqslant 2$ be an integer. Generate a sequence (Y_n), $n = 0, 1, \ldots$ integers in the least residue system modulo m using the recursion $Y_{n+1} = \lambda Y_n + r \pmod m$, with Y_0 as integer satisfying $0 \leqslant Y_0 \leqslant m$ and λ is a positive integer relatively prime to m. Then the sequence (x_n), $n = 0, 1, \ldots$, where $x_n = Y_n/m$ is a sequence of congruential pseudo-random numbers provided the parameters m, λ, Y_0 and r are chosen so that the sequence will pass the test for randomness. In the present work we have chosen $m = 2^{31}$, $r = 0$, $\lambda = 65539$ and $Y_0 = 3115$.

In order to evaluate the performance of the sequences described, numerical results were obtained with the QRS technique as proposed by Bandyopadhyay and Sarkar (1985) which can be described briefly as follows.

CC-0. In Public Domain. Gurukul Kangri Collection, Haridwar

Digitized by Arya Samaj Foundation Chennai and eGangotri

2.2 *Description of the method*

Let $\chi^2 = F(x) = F(x_1, x_2, \ldots x_n)$ be the function to be minimized, where x_1, $x_2, \ldots$ etc denote the unknown parameters of χ^2. Let $F(x)$ be a bounded real valued function where the value of $M = \min F(x)$ is required. We select the points ${}^1x$, ${}^2x, \ldots {}^Nx$ on the hyperdimensional space on which F is defined and then estimate M and the optimized parameters x^* by the following algorithm:

$$
\begin{aligned}
{}^1x^* &= x \quad \text{and} \quad m_1 = F({}^1x),\\
{}^2x^* &= \begin{cases} {}^1x^* \text{ and } m_2 = m_1 & \text{if } F({}^2x) \geqslant m,\\ {}^2x \text{ and } m_2 = F({}^2x) & \text{if } F({}^2x) < m_1, \end{cases}\\
{}^{i+1}x^* &= \begin{cases} {}^ix^* \text{ and } m_{i+1} = m_i & \text{if } F({}^{i+1}x) \geqslant m_i,\\ {}^{i+1}x \text{ and } m_{i+1} = F({}^{i+1}x) & \text{if } F({}^{i+1}x) < m_i, \end{cases}
\end{aligned}
$$

with ${}^ix = f'({}^ia)$, a random n-tuple

$$
{}^ia = {}^ia_1, {}^ia_2, \ldots, {}^ia_n
$$

and
$$
{}^ix_j = f'_j({}^ia_j), \quad 0 \leqslant {}^ia_j \leqslant 1, \quad j = 1, 2, \ldots n. \tag{2}
$$

$f' = (f'_j)$, $j = 1, 2, \ldots n$ is a mapping of an n-dimensional unit cube into another n-dimensional space of given shape (Gaussian in our case). The convergence of m_N to M as $N \to \infty$ is guaranteed whenever f is continuous and the sequence ${}^ix$, $i = 1, 2, \ldots$ is dense in the hyperspace.

The sampling scheme is incorporated into the above technique in the following manner.

Let $C = C(x^g, \sigma)$ denote a totally bounded space bounded by a n-dimensional Gaussian of standard deviation

$$
\sigma = [\sigma_1, \sigma_2, \ldots \sigma_n] \quad \text{and} \quad \text{mean } x^g = [x_1^g, x_2^g, \ldots x_n^g].
$$

Let $f_g^1(a, x^g, \sigma)$ be a function taking values in C such that for every

$$
t_i^2 = \frac{[f'_g(a_i, x_i, \sigma_i) - x_i^g]^2}{\sigma_i^2}, \quad i = 1, 2, \ldots n
$$

$$
(2\pi)^{1/2} \int_0^\infty \exp(-t_i^2/2)\, dt_i = Q_i
$$

where
$$
\begin{aligned}
Q_i &= a_i \text{ for } a_i \leqslant 0{\cdot}5,\\
&= 1 - a_i \text{ for } a_i > 0{\cdot}5.
\end{aligned} \tag{3}
$$

It is clear that if a_i is sampled from an uniform distribution between 0 and 1, $f'_g(a_i, x_i^g, \sigma_i)$ will be a member of a Gaussian population having a standard deviation σ_i and mean x_i^g. In other words f_g maps the n-dimensional unit hyper cube in C. Now for given N random n-tuples ${}^1a, {}^2a, \ldots {}^Na$ and a function F to be minimized, we set

$$
\begin{aligned}
m_N(C) &= \min[F(x^g)], \min_{1 \leqslant l \leqslant N} F(f_g({}^la, x^g, \sigma) \qquad f'_g({}^la, x^g, \sigma) \in C\\
&= F[x^*(C)],
\end{aligned} \tag{4}
$$

CC-0. In Public Domain. Gurukul Kangri Collection, Haridwar

Digitized by Arya Samaj Foundation Chennai and eGangotri

where $x^*(C) \in C$ is one of the points at which F has been evaluated in this formula.

Further, we chose a sequence of n-tuples ${}^0\sigma, {}^1\sigma, {}^2\sigma, \ldots$ of positive numbers converging montonically to zero and define a sequence $C_0, C_1, \ldots$ of n-dimensional Gaussian bounded spaces as follows:

$$C_0 = C({}^0x^g, {}^0\sigma),\ C_1 = C(x^*(C_0), {}^1\sigma)$$

$$C_{i+1} \begin{cases} = C(x^*(C_i), {}^{i+1}\sigma); & \text{if} \quad m_N(C_1) < m_N(C_{i-1}) \\ = C(x^*(C_{i-1}), {}^{i+1}\sigma); & \text{otherwise.} \end{cases} \tag{5}$$

Thus the sequence $m_N(C_0), m_N(C_1), \ldots m_N(C_i)$ is non-increasing and for suitably large i the value of $x^*(C_i)$ is taken an estimate of the optimized parameters. Here ${}^0x^g$ and ${}^0\sigma$ are the initial guesses of the respective parameters x^g and σ.

In selecting the sequence ${}^0\sigma, {}^1\sigma, {}^2\sigma$ it should be noted that if the sequence converges too quickly to zero, it may happen that the sequence of $m_N(C_i)$ does not converge to M. For the present study we have, by trial and error, found the following algorithm to be effective

$${}^1\sigma = {}^0\sigma \times {}^1t,$$

$${}^i\sigma = {}^{i-1}\sigma \times {}^it$$

where $${}^it = {}^{i-1}t \times 0{\cdot}95 \quad \text{and} \quad {}^1t = 0{\cdot}9 \tag{6}$$

The algorithm described above, when used with a random sequence, is a Monte Carlo method for minimizing F. The performance of such a sequence will be measured and compared with performance of other sequences in the following manner. We will use a number of carefully selected test functions. Let χ^2 be one of these functions and ${}^1x, {}^2x, \ldots {}^Nx$ a sequence generated by a low discrepancy random sequence in I^s, with N a fixed integer. Let

$$m_N = \min_{1 \leqslant i \leqslant N} [\chi^2({}^ix)] = \chi^2({}^lx), \quad 1 \leqslant l \leqslant N,$$

where $$\chi^2({}^ix) = \frac{1}{L-S} \sum_{i=1}^{L} [y_i(x^*) - y_i({}^ix)]^2. \tag{7}$$

The function χ^2 attains its minimum at x^* and $\chi^2(x^*) = 0$. The quantity m_N is used as a measure of performance of the sequence with respect to the minimization of χ^2. Also, the quantity $\delta_i = [(x_i^* - {}^1x_i)/x_i^*] \times 100$ is used to show in certain selected cases the convergence of the variables in the minimization problem. The forms of the function $y_i(x)$ used in the present study depend on the dimensionality of the problem. We now describe these functions in dimensions 3, 4 and 5 and the numerical results obtained.

3. Results and discussion

We now present numerical results as values of χ^2 in the fourth and eighth iterations (i.e. $i = 4$ and $i = 8$ in equation (5)). Each iteration consists of a set of 500 random searches i.e. $N = 500$.

In three dimensions the test function chosen is of the following type:

$$Y_i(x) = {}^1x \exp(c_i - {}^2x)^2/{}^3x,$$

CC-0. In Public Domain. Gurukul Kangri Collection, Haridwar

Digitized by Arya Samaj Foundation Chennai and eGangotri

where c_i's represent the x-axis values of the distribution Y_i. Four different test sets y_i (**x***) are generated and the random search is initiated with initial values of x different from x^*. Table 1 gives the results in three dimensions for following sets of x^* and the corresponding initial guesses:

(a) $x^* = [35600, 34{\cdot}263, 4{\cdot}964]$; initial guess = [35197, 34·0, 5·2]

(b) $x^* = [50291, 40{\cdot}016, 6{\cdot}066]$; initial guess = [49963, 40·0, 6·98]

(c) $x^* = [29128, 109{\cdot}65, 20{\cdot}137]$; initial guess = [28901, 110·0, 21·173]

(d) $x^* = [57187, 126{\cdot}16, 23{\cdot}775]$; initial guess = [57034, 126·0, 25·44]

From table 1, though it is difficult to judge precisely the relative merits of different sequences, it is evident that the pseudo-random sequence performs poorly compared to the quasi-random sequences. Among the quasi-random sequences, no sequence gives the best performance consistently for all the four cases; for example the Zaremba sequence gives the best performance for spectra number 4 whereas it is worst for spectra number 1. However judging from the overall performance it appears that the Haber sequence is best, the next is the scrambled Halton sequence and then the Zaremba sequence.

As for the performance of the method itself, the method works very well for this case. This is evident from table 2 which gives the values of δ_i for each variable at iteration steps 4 and 8 for spectra number 1. The table indicates good convergence even in the fourth iteration step and at the eight iteration step the convergence is almost absolute. The zeros in the table indicate the values less than 0·0005.

In four dimensions the test function is of the type

$$y_i(x) = {}^1x \exp[(c_i - {}^2x)^2/{}^3x] + {}^4x|c_i - {}^2x|^4.$$

The values of x^* and initial guess values are as follows:

1. $x^* = [35600, 34{\cdot}263, 4{\cdot}964, 2{\cdot}517\ (-9)]$
   initial guess = [35197, 34·0, 5·2, 1·125 (−8)]
2. $x^* = [50291, 40{\cdot}016, 6{\cdot}066, 2{\cdot}611\ (-9)]$
   initial guess = [49963, 40·0, 6·98, 2·213 (−10)]
3. $x^* = [29128, 109{\cdot}65, 20{\cdot}137, 1{\cdot}351\ (-9)]$
   initial guess = [28901, 110·0, 21·173, 7·4563 (−8)]
4. $x^* = [57187, 126{\cdot}16, 23{\cdot}775, 1{\cdot}119\ (-9)]$
   initial guess = [57034, 126·0, 25·44, 9·873 (−8)].

Table 3 gives the values of χ^2 for the four-dimensional study of the sequences. Here again the pseudo-random sequence performs poorly compared to the quasi-random sequences. However, for spectra number 1, it gives the best performance. Among the QRS, sequence 6 gives the best performance followed by the Haber and the Zaremba sequences. In this case, the performance of the scrambled Halton sequence has deteriorated. In fact, the Halton sequence is a shade better than the scrambled Halton sequence.

Table 4 gives the values of δ_i for spectra number 1 of this case. In this case also the convergence of the parameters is very good except for the parameter ${}^4x$. This is

CC-0. In Public Domain. Gurukul Kangri Collection, Haridwar

Digitized by Arya Samaj Foundation Chennai and eGangotri

Table 1. Values of χ^2 in three dimensional test cases with different random sequences.

Spectra number	Iteration number	HAM	HAL	ZAR	HAB	SEQ-5	SEQ-6	SCR-HAL	PRS
1	4	2·87(+4)*	8·95(+4)	1·17(+5)	2·86(+4)	5·02(+4)	1·73(+4)	3·37(+4)	7·39(+4)
	8	6·98(−1)	2·00(−2)	1·70(+0)	3·31(−1)	1·51(+0)	1·21(+0)	2·29(−1)	8·45(−1)
2	4	1·31(+5)	2·41(+5)	2·83(+5)	1·10(+5)	3·16(+5)	2·15(+5)	1·50(+5)	6·51(+5)
	8	4·81(+0)	2·04(+0)	7·41(−1)	1·41(+0)	1·90(+0)	3·99(+0)	2·64(+0)	5·86(+0)
3	4	3·11(+8)	2·72(+8)	1·19(+8)	2·33(+8)	2·09(+8)	3·07(+8)	2·85(+8)	9·53(+8)
	8	4·95(+3)	6·04(+3)	1·55(+3)	8·20(+3)	5·92(+3)	1·38(+5)	5·24(+3)	1·03(+7)
4	4	4·08(+9)	2·24(+9)	5·77(+8)	2·28(+8)	1·06(+9)	9·45(+8)	6·11(+8)	1·38(+9)
	8	3·73(+8)	5·38(+7)	8·23(+6)	2·47(+5)	1·05(+6)	5·20(+4)	9·72(+3)	6·53(+7)

*To be read as $2{\cdot}87 \times 10^{+4}$.

Table 2. Values of δ in three-dimensional test cases with different random sequences for spectra number 1.

Iteration number	HAM	HAL	ZAR	HAB	SEQ-5	SEQ-6	SCR-HAL	PRS
4	2·92(−3)*	2·92(−3)	2·92(−3)	8·76(−3)	2·92(−3)	0·00(+0)	2·92(−3)	2·92(−3)
	5·06(−2)	1·15(−1)	8·12(−2)	1·40(−2)	3·37(−2)	1·69(−2)	5·34(−2)	1·78(−2)
	1·17(−1)	1·11(−1)	1·71(−1)	2·03(−1)	1·41(−2)	3·83(−2)	6·85(−2)	5·64(−2)
8	0·00(+0)	0·00(+0)	0·00(+0)	0·00(+0)	0·00(+0)	0·00(+0)	0·00(+0)	0·00(+0)
	0·00(+0)	0·00(+0)	0·00(+0)	0·00(+0)	0·00(+0)	0·00(+0)	0·00(+0)	0·00(+0)
	2·01(−3)	0·00(+0)	0·00(+0)	0·00(+0)	0·00(+0)	0·00(+0)	0·00(+0)	0·00(+0)

*To be read as $2{\cdot}92 \times 10^{-3}$.

CC-0. In Public Domain. Gurukul Kangri Collection, Haridwar

Table 3. Values of χ^2 in four-dimensional test cases with different random sequences.

Spectra number	Iteration number	HAM	HAL	ZAR	HAB	SEQ-5	SEQ-6	SCR-HAL	PRS
1	4	3·26(+4)*	8·77(+4)	1·13(+5)	2·97(+4)	6·10(+4)	1·77(+4)	3·79(+4)	7·99(+4)
	8	2·03(+2)	2·51(+3)	2·27(+3)	2·25(+2)	1·51(+3)	1·77(+2)	1·23(+3)	1·79(+1)
2	4	1·47(+5)	2·59(+5)	2·95(+5)	1·30(+5)	3·17(+5)	2·38(+5)	1·62(+5)	7·28(+5)
	8	1·27(+4)	1·19(+3)	1·00(+3)	1·07(+3)	1·26(+3)	1·34(+3)	1·20(+3)	1·29(+3)
3	4	1·30(+11)	6·72(+9)	5·41(+9)	1·11(+10)	3·64(+9)	1·75(+9)	2·33(+10)	6·89(+10)
	8	1·07(+11)	2·58(+9)	1·06(+9)	1·41(+9)	2·02(+9)	6·50(+8)	1·44(+10)	3·55(+10)
4	4	3·94(+11)	9·59(+10)	1·21(+11)	1·63(+11)	3·48(+11)	5·43(+10)	2·84(+11)	2·54(+11)
	8	3·32(+11)	5·46(+10)	9·44(+10)	9·80(+10)	3·06(+11)	5·05(+10)	2·63(+11)	2·07(+11)

* To be read as $3{\cdot}26 \times 10^{+4}$.

Table 4. Values of δ in four-dimensional test cases with different random sequences for spectra number 1.

Iteration number	HAM	HAL	ZAR	HAB	SEQ-5	SEQ-6	SCR-HAL	PRS
4	2·92(−3)*	2·92(−3)	2·92(−3)	8·76(−3)	0·00(+0)	0·00(+0)	2·92(−3)	2·92(−3)
	5·06(−2)	1·15(−1)	8·15(−2)	1·40(−2)	3·37(−2)	1·69(−2)	5·34(−2)	1·18(−2)
	1·17(−1)	1·11(−1)	1·71(−1)	2·03(−1)	1·41(−2)	3·83(−2)	6·85(−2)	5·64(−2)
	3·67(+3)	7·42(+2)	7·48(+2)	5·84(+2)	3·11(+3)	2·20(+1)	5·35(+2)	1·03(+2)
8	0·00(+0)	0·00(+0)	0·00(+0)	0·00(+0)	0·00(+0)	0·00(+0)	0·00(+0)	0·00(+0)
	2·81(−3)	2·81(−3)	2·81(−3)	2·81(−3)	0·00(+0)	0·00(+0)	2·81(−3)	0·00(+0)
	8·06(−3)	2·42(−2)	2·22(−2)	2·01(−2)	6·04(−3)	6·04(−3)	1·61(−2)	2·01(−3)
	2·66(+2)	7·67(+2)	7·30(+2)	5·96(+2)	2·29(+2)	3·42(+0)	5·36(+2)	6·23(+1)

* To be read as $2{\cdot}92 \times 10^{-3}$.

Digitized by Arya Samaj Foundation Chennai and eGangotri

CC-0. In Public Domain. Gurukul Kangri Collection, Haridwar

Digitized by Arya Samaj Foundation Chennai and eGangotri

expected to be so because of the relatively low importance of this parameter in the function to be minimized.

In five dimensions we have the test function as

$$Y_i(\mathbf{x}) = {}^1x\exp[(c_i - {}^2x)^2/{}^3x] + {}^4x|c_i - {}^2x|^4 + {}^5x|c_i - {}^2x|^{12}.$$

The values of x^* and the initial guess values are as follows:

1. x^* = [35600, 34·263, 4·964, 2·517 (−4), 3·911 (−10)]
   initial guess = [35197, 34·0, 5·2, 1·125 (−3), 1·526 (−11)]
2. x^* = [50291, 40·016, 6·066, 2·611 (−4), 1·595 (−10)]
   initial guess = [49963, 40·0, 6·98, 2·213 (−3), 1·111 (−11)]
3. x^* = [29128, 109·65, 20·137, 1·351 (−4), 7·129 (−13)]
   initial guess = [28901, 110·0, 7·4563 (−5), 8·9235 (−12)]
4. x^* = [57187, 126·16, 23·775, 1·119 (−4), 3·205 (−13)]
   initial guess = [57034, 126·0, 25·44, 9·873 (−3), 1·2345 (−11)].

Table 5 gives the values of χ^2 for five-dimensional cases. It is seen that the overall performance of the PRS is better than some of the QRS. Among the QRS, SEQ-6 gives the best performance followed by the Zaremba sequence and the Hammersley sequence. Here also the scrambled Halton sequence does not show any improvement over the Halton sequence, and both perform poorly compared to the PRS.

Table 6 gives the values of δ_i for the five-dimensional case for spectra number 1. Here again the overall convergence is good except for the parameters ${}^4x$ and ${}^5x$ which is expected.

From the numerical study carried out it is evident that the quasi-random search technique with the Gaussian importance sampling scheme works well for the type of least square data fitting described in the text, even with 500 random searches per iterative step at least up to 5-dimensions. The PRS performs poorly, in general, compared to the QRS, at least to some of them. However, there is an indication that with the increase in the dimensionality, the relative performance of the PRS is improving and at 5-dimensions it has outperformed some of the QRS on an overall basis. Among the QRS, the Zaremba sequence has shown consistently good performance over the range of dimensions considered here. At dimensions 3 and 4 the Haber sequence gives good performance whereas at dimensions 4 and 5 sequence 6 gives good performance. There is no advantage gained by scrambling the Halton sequence—a result which contradicts those obtained for multidimensional integrals (Braaten and Weller 1979), but supports what is obtained for integral equations (Sarkar and Prasad 1987).

In the present study no attempt was made to compare the efficiencies of the different sequences which would also have involved the estimation of the generation time for each sequence. This was because the relative importance of the generation time for any sequence will greatly depend on the type of problem studied. Secondly, and more importantly, in the present scheme a set of 500 random numbers can be generated and stored once for all at the beginning of the computation or they may be given as an input data. However, as one would except, the QRS takes much more computing time than the PRS.

CC-0. In Public Domain. Gurukul Kangri Collection, Haridwar

Digitized by Arya Samaj Foundation Chennai and eGangotri

Table 5. Values of χ^2 in five-dimensional test cases with different random sequences.

Spectra number	Iteration number	HAM	HAL	ZAR	HAB	SEQ-5	SEQ-6	SCR-HAL	PRS
1	4	8·68(+5)*	1·24(+6)	8·38(+5)	8·20(+5)	8·24(+5)	9·06(+6)	1·09(+6)	8·24(+5)
	8	8·14(+5)	7·77(+5)	6·76(+5)	7·29(+5)	7·17(+5)	7·67(+5)	7·95(+5)	7·11(+5)
2	4	9·23(+6)	3·15(+7)	1·05(+7)	9·45(+6)	9·91(+6)	8·82(+6)	1·32(+7)	9·60(+6)
	8	8·47(+6)	1·90(+7)	9·36(+6)	8·82(+6)	9·38(+6)	8·36(+6)	1·01(+7)	8·75(+6)
3	4	8·61(+10)	5·83(+10)	1·05(+11)	2·23(+11)	2·18(+11)	1·84(+10)	7·18(+10)	1·90(+11)
	8	5·62(+10)	4·97(+10)	9·41(+10)	1·72(+11)	1·23(+11)	5·91(+9)	2·39(+10)	1·58(+11)
4	4	1·01(+13)	3·93(+13)	2·53(+12)	3·40(+13)	4·38(+12)	3·46(+12)	3·66(+13)	3·46(+13)
	8	5·79(+11)	3·21(+13)	8·47(+11)	3·33(+13)	3·47(+11)	7·75(+11)	3·56(+13)	3·38(+13)

* To be read as $8{\cdot}68 \times 10^{+5}$.

Table 6. Values of δ in five-dimensional test cases with different random sequences for spectra number 1.

Iteration number	HAM	HAL	ZAR	HAB	SEQ-5	SEQ-6	SCR-HAL	PRS
	2·92(−3)*	1·75(−2)	8·76(−3)	5·84(−3)	2·92(−3)	2·92(−3)	8·76(−3)	5·84(−3)
	9·55(−2)	1·25(−1)	6·74(−2)	3·65(−2)	1·85(−1)	4·49(−2)	8·99(−2)	0·00(+0)
4	4·25(−1)	4·37(−1)	4·43(−1)	2·84(−1)	5·90(−1)	7·29(−1)	3·44(−1)	3·32(−1)
	5·80(+1)	1·63(+0)	4·53(+1)	4·08(+1)	5·08(+1)	7·20(+1)	2·15(+1)	3·97(+1)
	9·90(+1)	9·82(+1)	9·20(+1)	9·46(+1)	9·60(+1)	9·79(+1)	9·79(+1)	9·43(+1)
	0·00(+0)	0·00(+0)	0·00(+0)	0·00(+0)	0·00(+0)	2·92(−3)	0·00(+0)	0·00(+0)
	6·46(−2)	4·21(−2)	5·62(−2)	6·18(−2)	6·46(−2)	6·46(−2)	1·40(−2)	5·62(−2)
8	5·10(−1)	3·53(−1)	4·43(−1)	4·63(−1)	4·92(−1)	5·14(−1)	1·99(−1)	4·41(−1)
	5·03(+1)	3·93(+1)	4·43(+1)	4·63(+1)	4·82(+1)	4·99(+1)	3·08(+1)	4·44(+1)
	9·89(+1)	9·82(+1)	9·19(+1)	9·47(+1)	9·55(+1)	9·81(+1)	9·79(+1)	9·43(+1)

* To be read as $2{\cdot}92 \times 10^{-3}$.

CC-0. In Public Domain. Gurukul Kangri Collection, Haridwar

Digitized by Arya Samaj Foundation Chennai and eGangotri

4. Conclusions

(i) The quasi-random search technique with importance sampling can be effectively used for nonlinear least square data fitting.

(ii) The pseudo-random sequence from the congruential generator does not perform well as compared to the quasi-random sequences at least up to five dimensions.

(iii) The Zaremba sequence shows consistently good performance. The Haber sequence and sequence 6 also performs well. No advantage was obtained by scrambling the Halton sequence.

Acknowledgement

We thank Dr Harald Niederreiter for useful suggestions and correspondence.

References

Aird T J and Rice J R 1977 *SIAM J. Numer. Anal.* **14** 296
Bandyopadhyay T and Sarkar P K 1985 *Pramana–J. Phys.* **24** 643
Braaten E and Weller G 1979 *J. Comp. Phys.* **33** 249
Fox B L 1986 Implementation and relative efficiency of quasi random sequence generators (to be published)
Haber S 1970 *SIAM Rev.* **12** 481
Halton J H 1960 *Numer. Math.* **2** 84
Halton J H and Zaremba S K 1969 *Montash. Math.* **73** 316
Niederreiter H 1978 *Bull. Amer. Math. Soc.* **84** 957
Niederreiter H 1983 in *Studies in pure mathematics* (Budapest: Akademiaikiado) p. 523
Niederreiter H and McCurley K 1979 *Computing* **22** 119
Niederreiter H and Peart P 1982 *Caribbean J. Math.* **1** 27
Sarkar P K and Prasad M A 1987 *J. Comp. Phys.* **67** 257
Sobol I M 1979 *SIAM J. Numer. Anal.* **16** 790
Warnock T T 1972 *Application of number theory to numerical analysis* (ed.) S K Zaremba (New York: Academic Press) p. 319
Zaremba S K 1968 *Ann. Polon. Math.* **21** 85

CC-0. In Public Domain. Gurukul Kangri Collection, Haridwar

Digitized by Arya Samaj Foundation Chennai and eGangotri

CC-0. In Public Domain. Gurukul Kangri Collection, Haridwar

Digitized by Arya Samaj Foundation Chennai and eGangotri

Pramāṇa – J. Phys., Vol. 28, No. 2, February 1987, pp. 109–115. © Printed in India.

Kerr-Newman metric in deSitter background

L K PATEL, SHARDA S KOPPAR and P V BHATT*
Department of Mathematics, Gujarat University, Ahmedabad 380 009, India
*Department of Mathematics, Saurashtra University, Rajkot 360 005, India

MS received 5 July 1986; revised 13 October 1986

Abstract. In addition to the Kerr-Newman metric with cosmological constant several other metrics are presented giving Kerr-Newman type solutions of Einstein-Maxwell field equations in the background of deSitter universe. The electromagnetic field in all the solutions is assumed to be source-free. A new metric of what may be termed as an electrovac rotating de-Sitter space-time—a space-time devoid of matter but containing source-free electromagnetic field and a null fluid with twisting rays—has been presented. In the absence of the electromagnetic field, our solutions reduce to those discussed by Vaidya.

Keywords. Kerr-Newman metric; deSitter universe; electromagnetic fields.

PACS No. 04·20

1. Introduction

The Kerr-Newman (Newman *et al* 1965) solution is believed to represent the ultimate state of collapsing body with rotation, mass and electric charge. Therefore considerable significance is attached to the Kerr-Newman solution. When the charge is absent, the Kerr-Newman solution reduces to the well-known Kerr solution (Kerr 1963). Patel and Trivedi (1982) considered the Kerr-Newman metric in cosmological background, the background metric being the Robertson-Walker metric. In the absence of the electromagnetic field, their solution reduces to the Vaidya solution (Vaidya 1977) which describes the Kerr metric in the background of the Robertson-Walker universe.

We know that the deSitter metric can be expressed as a particular case of the general Robertson-Walker metric. But the deSitter model has features which are geometrically distinct from those of Robertson-Walker model. Again the simple deSitter metric represents an empty and expanding universe. The deSitter space-time is an immediate generalization of Minkowski flat space-time. These facts inspired Vaidya (1984) to discuss the Kerr metric in the background of deSitter universe. The main purpose of the present article is to obtain the electromagnetic generalizations of the solutions discussed by Vaidya (1984). Our earlier paper (Patel and Trivedi 1982) will be referred to hereafter as I. In this paper we merely report the main results by avoiding the computational details and the lengthy expression for some of the quantities.

In §§ 2 and 3 we use the following Einstein-Maxwell field equations

$$R_{ik} - \tfrac{1}{2} g_{ik} R + \Lambda g_{ik} = -8\pi E_{ik}, \tag{1}$$

$$E_{ik} = -g^{lm} F_{il} F_{km} + \tfrac{1}{4} g_{ik} F_{lm} F^{lm}, \tag{2}$$

CC-0. In Public Domain. Gurukul Kangri Collection, Haridwar

Digitized by Arya Samaj Foundation Chennai and eGangotri

$$F_{ik} = A_{i,k} - A_{k,i}, \tag{3}$$

$$F^{ik}_{;k} = 0. \tag{4}$$

The various symbols occurring in the above field equations have their usual meanings. We permit the electromagnetic field tensor F_{ik} to vanish.

2. Kerr-Newman metric with Λ

Vaidya (1984) has shown that the deSitter metric can be put in the form conformal to the Einstein universe metric with negative curvature. Thus the geometry of the deSitter universe is described by the line-element

$$ds^2 = \frac{R^2}{R^2 + (x^2+y^2+z^2)}\left[dt^2 - dx^2 - dy^2 - dz^2 - \frac{(x\,dx + y\,dy + z\,dz)^2}{R^2 + (x^2+y^2+z^2)}\right], \tag{5}$$

where R is a constant. Vaidya (1984) has given a transformation from the co-ordinates (x, y, z) to the spheroidal polar co-ordinates which transforms the metric (5) into the form

$$ds^2 = \left[\cosh^2(r/R)\left(1 + \frac{a^2}{R^2}\sin^2\alpha\right)\right]^{-1} ds_0^2, \tag{6}$$

where R is a constant and ds_0^2 is given by

$$ds_0^2 = 2\,(du + a\sin^2\alpha\, d\beta)\, dt - (du + a\sin^2\alpha\, d\beta)^2 - M^2\left[\left\{1 + \frac{a^2}{R^2}\sin^2\alpha\right\}^{-1} d\alpha^2 + \sin^2\alpha\, d\beta^2\right]. \tag{7}$$

Here $u = t - r$ and

$$M^2 = (R^2 + a^2)\sinh^2(r/R) + a^2\cos^2\alpha. \tag{8}$$

Following the scheme of I, we can write down the Kerr-Newman metric in deSitter background as

$$ds^2 = \left[\cosh^2(r/R)\left\{1 + \frac{a^2}{R^2}\sin^2\alpha\right\}\right]^{-1} ds_1^2, \tag{9}$$

$$ds_1^2 = ds_0^2 - (2m\mu - 4\pi e^2\gamma)\,(du + a\sin^2\alpha\, d\beta)^2, \tag{10}$$

where m, e and a are constants, ds_0^2 is given by (7), M^2 is given by (8) and μ and γ are given by the following equations:

$$\mu M^2 = R\sinh(r/R)\cosh^3(r/R), \tag{11}$$

$$\gamma M^2 = \cosh^4(r/R). \tag{12}$$

We have verified that the metric (9) along with (10), (11) and (12) satisfies the Einstein-

CC-0. In Public Domain. Gurukul Kangri Collection, Haridwar

Digitized by Arya Samaj Foundation Chennai and eGangotri

Maxwell field equations (1), (2), (3) and (4) with

$$\Lambda = 3/R^2, \qquad A_i = (A, 0, Aa\sin^2\alpha, 0), \tag{13}$$

where

$$A = [eR \sinh (r/R) \cosh (r/R)]/M^2, \tag{14}$$

M^2 being given by (8). Here e is a constant of integration and the co-ordinates are named as $x^1 = u$, $x^2 = \alpha$, $x^3 = \beta$ and $x^4 = t$.

When $e = 0$, the electromagnetic field vanishes and the metric given by (9) along with (10), (11) and (12) reduces to the Kerr metric with a Λ-term in the form discussed by Vaidya (1984). The metric given by (9), (10), (11) and (12) can be transformed in the conventional Boyer-Lindquist type co-ordinates. The required transformation equations can be obtained from those given by Vaidya (1984) for the uncharged case by minor modifications. We shall not give these transformation equations here. We have verified that when $e = 0$, the Kerr-Newman metric with cosmological constant in these co-ordinates reduces to the Kerr metric with Λ term in Boyer Lindquist co-ordinates given by Demianski (1973).

When $R \to \infty$, Λ becomes zero and we recover the Kerr-Newman metric in the form

$$ds^2 = 2(du + a\sin^2\alpha\, d\beta)\, dt - (r^2 + a^2\cos^2\alpha)\,(d\alpha^2 + \sin^2\alpha\, d\beta^2) - \left[1 + \frac{2mr - 4\pi e^2}{r^2 + a^2\cos^2\alpha}\right](du + a\sin^2\alpha\, d\beta)^2. \tag{15}$$

Here it should be noted that the Kerr-Newman metric with a Λ-term discussed by us is contained in the family of solutions of electrovac field equations with cosmological constant given by Debever *et al* (1984) (§ 2). Their co-ordinates are different from our co-ordinates. There must be a co-ordinate transformation which transform our solution into the solution given by Debever *et al* (1984). But we have not been able to find out the explicit form of this transformation. One of the advantages of our co-ordinate system is that Vaidya's results for the uncharged case become transparent on switching off the electromagnetic field in our solution. We also feel that our special form can be handled more easily than the form given by Debever *et al* (1984).

3. Anti-deSitter background

When the cosmological constant Λ is negative, say $\Lambda = -3/R^2$, R = constant, the space-time described by the deSitter metric is known in the literature as the anti-deSitter space-time. A surprising result is that the following axially symmetric line-element, conformal to the usual deSitter line-element, represents the anti-deSitter space time.

$$ds^2 = \frac{R^2}{r^2\cos^2\alpha}\left[\left(1 - \frac{r^2}{b^2}\right)dt^2 - \left(1 - \frac{r^2}{b^2}\right)^{-1} dr^2 - r^2(d\alpha^2 + \sin^2\alpha\, d\beta^2)\right]. \tag{16}$$

CC-0. In Public Domain. Gurukul Kangri Collection, Haridwar

Digitized by Arya Samaj Foundation Chennai and eGangotri

The above metric satisfies the field equations

$$R_{ik} = \Lambda g_{ik}, \quad \Lambda = -3/R^2,$$

b^2 being undetermined constant. Vaidya (1984) discussed the Kerr metric in the background of (16). It would be interesting to obtain the Kerr-Newman metric in the anti-deSitter background (16). However we shall not derive this metric here. Instead we note a simple particular case of (16) obtained by choosing the constant $b \to \infty$. The background anti-deSitter metric then reduces to the following simple plane symmetric metric

$$ds^2 = \frac{R^2}{z^2}(dt^2 - dx^2 - dy^2 - dz^2). \tag{17}$$

The relations between the spherical polar co-ordinates and the Cartesian co-ordinates (x, y, z) are well known and hence not given here. We now give in a nutshell the Kerr-Newman metric in the anti-deSitter background (17). The explicit form of the Kerr-Newman metric in the background of (17) is given by

$$ds^2 = \frac{R^2}{r^2\cos^2\alpha}\Bigg[2(du + a\sin^2\alpha\, d\beta)\,dt - (r^2 + a^2\cos^2\alpha)(d\alpha^2 + \sin^2\alpha\, d\beta^2) - \left(1 + \frac{2mr^3 - 4\pi e^2 r^4 R^{-2}}{r^2 + a^2\cos^2\alpha}\right)(du + a\sin^2\alpha\, d\beta)^2\Bigg]. \tag{18}$$

where m and e are constants. Equation (18) gives a very simple metric for the Kerr-Newman-like gravitational field satisfying the field equations (1), (2), (3) and (4) with

$$\Lambda = -\frac{3}{R^2}, \qquad A_i = \left(\frac{er}{r^2 + a^2\cos^2\alpha}, 0, \frac{ear\sin^2\alpha}{r^2 + a^2\cos^2\alpha}, 0\right). \tag{19}$$

That Λ has to be non-zero is a condition for the existence of the background metric of anti-deSitter space-time given by (16) or (17).

The solution (18) cannot be a member of the family of solutions given by Debever *et al* (1984). In their solutions, the cosmological constant Λ is allowed to vanish. But $\Lambda \neq 0$ is a condition for the existence of our solution (18).

When $e = 0$ (i.e. in the absence of electromagnetic field), the metric (18) reduces to the Kerr-like metric in the anti-deSitter background discussed by Vaidya (1984).

4. The electrovac deSitter space-time with twisting null rays

We know that the geometry of the Reissner-Nordstrom solution is described by the line element

$$ds^2 = 2du\,dt - \left(1 + \frac{2m}{r} - \frac{4\pi e^2}{r^2} + \frac{r^2}{R^2}\right)du^2 - r^2(d\alpha^2 + \sin^2\alpha\, d\beta^2). \tag{20}$$

Here we have assumed that the cosmological constant $\Lambda = 3/R^2$ is non-zero. We also know that the Kerr-Newman solution is described under the Minkowskian space-time. Thus in the absence of the source the Kerr-Newman solution reduces to the flat space-

CC-0. In Public Domain. Gurukul Kangri Collection, Haridwar

Digitized by Arya Samaj Foundation Chennai and eGangotri

time. This fact suggests an immediate generalization of (20) to the following metric

$$ds^2 = 2(du + g\sin\alpha\, d\beta)\, dt - H(r^2 + y^2)d\Omega^2$$

$$-\left(1 + \frac{2mr - 4\pi e^2}{r^2 + y^2} + \frac{r^2 + y^2}{R^2}\right)(du + g\sin\alpha\, d\beta)^2, \tag{21}$$

with

$$g = g(\alpha), \quad y = y(\alpha), \quad H = H(\alpha), \quad \Lambda = 3/R^2 \quad \text{and}$$

$$d\Omega^2 = d\alpha^2 + \sin^2\alpha\, d\beta^2.$$

It may be noted that if $\Lambda = 0$, with $g\sin\alpha = a\sin^2\alpha$, $y = -a\cos\alpha$ and $H = 1$, (21) gives us the usual Kerr-Newman metric. Here a is a constant. It is easy to see that the metric (21) is a particular case of the Kerr-NUT metric (Vaidya *et al* 1976)

$$ds^2 = 2(du + g\sin\alpha\, d\beta)\, dt - M^2\, d\Omega^2 - 2L(du + g\sin\alpha\, d\beta)^2, \tag{22}$$

and so we can freely use the tetrad formalism developed in that paper to work out the physics of the metric (21). Using the tetrad

$$\theta^1 = du + g\sin\alpha\, d\beta, \quad \theta^2 = M d\alpha, \quad \theta^3 = M\sin\alpha\, d\beta,$$

$$\theta^4 = dt - L\theta^1, \tag{23}$$

the tetrad components $R_{(ab)}$ of the Ricci tensor for the metric (22) are also recorded there. It should be noted that the metric (22) takes the form

$$ds^2 = 2\theta^1\theta^4 - (\theta^2)^2 - (\theta^3)^2,$$

in terms of the Cartan's frame (23). It can be easily checked that if one chooses

$$g\, d\alpha = dy, \quad H = -f/y, \quad 2f = (\partial g/\partial\alpha) + g\cot\alpha, \tag{24}$$

one finds that for the metric (21)

$$R_{(24)} = R_{(34)} = R_{(12)} = R_{(13)} = R_{(44)} = R_{(23)} = 0,$$

$$R_{(14)} = \Lambda - [4\pi e^2/(r^2 + y^2)^2],$$

$$R_{(22)} = R_{(33)} = -\Lambda - \frac{4\pi e^2}{(r^2 + y^2)^2} + [2 + \tfrac{4}{3}\Lambda y^2 - yG]\,(r^2 + y^2)^{-1},$$

$$R_{(11)} = -\frac{2y}{3}\Lambda\left[\frac{g^2}{f} + 2y\right](r^2 + y^2)^{-1} + 8\pi\frac{y}{f}e^2g^2\,(r^2 + y^2)^{-3}. \tag{25}$$

We have verified that for the metric (21) the Maxwell equations (4) give us the electromagnetic 4 potential A_i as

$$A_i = \left(\frac{er}{r^2 + y^2}, 0, \frac{erg\sin\alpha}{r^2 + y^2}, 0\right). \tag{26}$$

CC-0. In Public Domain. Gurukul Kangri Collection, Haridwar

Digitized by Arya Samaj Foundation Chennai and eGangotri

In (24) the quantity G is defined by

$$2fG = g^2\left[\frac{1}{y^2}+\frac{\partial}{\partial y}\left(\frac{1}{f}\frac{\partial f}{\partial y}\right)\right]+2\frac{\partial f}{\partial y}-2.$$

It is clear that if we choose

$$8\pi\sigma = \frac{2y\Lambda}{3}\left[\frac{g^2}{f}+2y\right](r^2+y^2)^{-1}$$

and $$Gy-2-\tfrac{4}{3}\Lambda y^2 = 0, \tag{27}$$

we shall have $R_{ik} = \Lambda g_{ik} - 8\pi E_{ik} - 8\pi\sigma\,\xi_i\xi_k$, where ξ_i is a null vector defined by $\xi_i dx^i = du + g\sin\alpha d\beta$. We have verified that the null congruence ξ_i is geodetic and expanding. It should also be noted that the twist of the null congruence ξ_i is non-zero. Equations (24) and (27) are the three equations which determine the unknown functions of α in the metric (21).

If $R\to\infty$, $\Lambda = 0$ and (24) and (27) are satisfied by $f = -y = a\cos\alpha$, $g = a\sin\alpha$, a being a constant. The metric (21) then becomes the usual Kerr-Newman metric. Vaidya (1984) showed that the metric (21) with (24) and (27) gives a rotating deSitter space-time provided the mass parameter m and the charge parameter e are zero. Thus the metric

$$\begin{aligned} ds^2 = {} & 2(du+g\sin\alpha\,d\beta)\,dt-\left(\frac{f}{-y}\right)(r^2+y^2)\,(d\alpha^2+\sin^2\alpha\,d\beta^2) \\ & -\left[1+\frac{2mr-4\pi e^2}{r^2+y^2}+\frac{r^2+y^2}{R^2}\right](du+g\sin\alpha\,d\beta)^2, \end{aligned} \tag{28}$$

with

$$dy = g\,d\alpha, \quad f = f(y) \quad \text{and} \quad Gy-2-\tfrac{4}{3}\Lambda y^2 = 0$$

becomes the Kerr-Newman metric in the cosmological background of the rotating deSitter universe. The particular case $m = 0$ of (28) gives us the electrovac deSitter space-time with twisting null rays.

In the solutions discussed by Debever *et al* (1984) the radiation density σ is zero. But for the solution discussed in this section σ is non zero. Therefore we can say that the solution of this section is not contained in the family of solutions given by Debever *et al* (1984).

Acknowledgements

It is a pleasure to thank Professor P C Vaidya for enlightening discussions regarding the problem. Two of us (PVB and SSK) wish to thank the University Grants Commission for financial assistance. Thanks are also offered to the referees for helpful suggestions.

References

Debever R, Kamran N and McLenaghan R G 1984 *J. Math. Phys.* **25** 1955
Demianski M 1973 *Acta Astron.* **23** 221

CC-0. In Public Domain. Gurukul Kangri Collection, Haridwar

Digitized by Arya Samaj Foundation Chennai and eGangotri

Kerr R P 1962 *Phys. Rev. Lett.* **11** 237
Newman E, Couch E, Chinnapared R, Exton A, Prakash A and Torrence R 1965 *J. Math. Phys.* **6** 918
Patel L K and Trivedi H B 1982 *J. Astrophys. Astr.* **3** 63
Vaidya P C, Patel L K and Bhatt P V 1976 *Gen. Rel. Grav.* **7** 701
Vaidya P C 1977 *Pramana – J. Phys.* **8** 512
Vaidya P C 1984 *Pramana – J. Phys.* **22** 151

CC-0. In Public Domain. Gurukul Kangri Collection, Haridwar

Digitized by Arya Samaj Foundation Chennai and eGangotri

CC-0. In Public Domain. Gurukul Kangri Collection, Haridwar

Digitized by Arya Samaj Foundation Chennai and eGangotri

Pramāṇa – J. Phys., Vol. 28, No. 2, February 1987, pp. 117–130. © Printed in India.

Analytic representation for ^{3}He form factors

K N AGRAWALLA and M K PARIDA*

Kendrapara College, Kendrapara, Cuttack 754 211, India
*Physics Department, North Eastern Hill University, Shillong 793 003, India

MS received 14 March 1986; revised 5 November 1986

Abstract. A modified N/D method is applied for the cases of ^{3}He charge and magnetic form factors. Anomalous cut positions are computed using possible exchanges at the photon-^{3}He electromagnetic vertex, and one of them is found at $t_a = 0{\cdot}0618$ GeV^2. The D-function is used to parametrize the two-pion cut while the N-function is taken to represent the effect of an anomalous or the three-pion cut. Excellent fits to the available experimental data on charge and magnetic form factors are obtained and several useful information on the form factors computed.

Keywords. Analytic representation; modified N/D method; ^{3}He form factors.

PACS Nos 13·40; 11·50; 25·30

1. Introduction

A modified N/D method of analytic representation of electromagnetic form factors was found to be very successful in parametrizing the experimental data on pion and nucleon form factors and obtaining useful information about them (Deo and Parida 1973, 1974; Deo 1974). In this method, the nearest normal cut contribution in the t-plane was represented by the D function and an effective range type of formula, obtainable from dispersion relation, but the next nearest normal-cut contribution was assumed to be represented by the N-function approximated by optimized polynomial expansion in a suitably chosen conformally mapped variable, Z, which maps the cut in the t plane onto the boundary of a parabola in the Z plane (Cutkosky and Deo 1968; Ciulli 1969; Deo and Parida 1971). Further modifications have been suggested in order that this approach be applicable for the form factors of light nuclei (Parida 1979; Parida *et al* 1983; Agrawalla and Parida 1985). The applicability of the modified N/D method has been successfully tested for isoscalar light nuclei like deuteron and ^{4}He. In the case of the deuteron, the anomalous cut is nearer to the origin than any other cut, but computations in the case of ^{4}He revealed that all anomalous cut positions are farther away than the normal three-pion cut in t-plane (Agrawalla and Parida 1985). Parametrizing the anomalous cut contribution by the N function, and including the exponential weight function in the Laguerre polynomial expansion, have resulted in obtaining excellent fits to the data on charge and magnetic form factors of deuteron and the charge form factor of ^{4}He (Agrawalla and Parida 1985). In this paper the modified

* To whom correspondence should be addressed.

CC-0. In Public Domain. Gurukul Kangri Collection, Haridwar

Digitized by Arya Samaj Foundation Chennai and eGangotri

formula is applied to the cases of charge and magnetic form factors of a nonisoscalar target like ^{3}He.

In § 2 we present the working formula and compute the anomalous cut positions. In §§ 3 and 4 we present our results on the data analysis of ^{3}He magnetic and charge form factors, respectively. Our results are summarized and conclusions stated in § 5.

2. The modified N/D method and analytic structure

In this section we mention the modified N/D representation and also compute the positions of the anomalous cut using several possible exchanges at the photon-^{3}He vertex.

2.1 *The modified N/D representation*

The formula proposed for the form factor of a light nucleus is (Parida 1979; Parida *et al* 1983; Agrawalla and Parida 1985)

$$F(t) = N(t)/D(t), \tag{1}$$

where the D-function is assumed to represent the effect of the nearest normal cut, but the N-function is taken to represent the effect of an anomalous cut or the next-nearest-normal cut. The D-function is parametrized using an effective range type of formula obtainable from dispersion relation, but the N-function is approximated by optimized polynomial expansion. For ^{3}He form factors the nearest normal cut starts at $t = 4m_\pi^2$, which contributes to the D-function as (Deo and Parida 1973, 1974)

$$D(t) = \sum_n a_n t^n + h(t) + \frac{m_\pi^2}{\pi}, \tag{2}$$

where

$$h(t) = \frac{2}{\pi}\frac{k^3}{\sqrt{t}} \ln\left[\left(\frac{t}{4m_\pi^2}\right)^{1/2} + \left(\frac{t}{4m_\pi^2} - 1\right)^{1/2}\right] - i\frac{k^3}{\sqrt{t}}, \tag{3}$$

with

$$k = \left(\frac{t}{4} - m_\pi^2\right)^{1/2}. \tag{4}$$

The next nearest normal physical cut occurs at $t = 9m_\pi^2 \simeq 0{\cdot}18\ \mathrm{GeV}^2$. This or an anomalous cut starting at $t = t_a$ can be mapped onto the boundary of a parabola in the Z plane with the physical region of the t plane being mapped onto the physical region, $0 \leqslant \mathrm{Re}\, Z \leqslant \infty$, of Laguerre polynomial expansion whose domain of convergence is the interior of the parabola. Then (Parida 1979)

$$N(t) = \exp(-\alpha Z) \sum_l g_l L_l(2\alpha Z), \tag{5}$$

with

$$Z(t) = \left\{\ln\left[\left(\frac{-t}{t_a}\right)^{1/2} + \left(\frac{-t}{t_a} + 1\right)^{1/2}\right]\right\}^2. \tag{6}$$

Assuming that the series (5) converges sufficiently rapidly, we can rewrite the

CC-0. In Public Domain. Gurukul Kangri Collection, Haridwar

Digitized by Arya Samaj Foundation Chennai and eGangotri

N-function for the first M significant terms as

$$N(t) = \exp(-\alpha Z) \sum_{l=0}^{M} e_l Z^l. \tag{7}$$

Comparing (5) and (7), the relations between the unknown parameters g_l's and e_l's can be written down easily. The t dependence for the charge form factor, $F_c(t)$, or the magnetic form factor, $F_m(t)$, are given by (1)–(7) but with different sets of parameters, α, e_l, g_l, a_n and t_a for each. These sets of parameters are to be determined from data fitting to know the functions $F_c(t)$ and $F_m(t)$. Besides the N/D representation, we also use two other formulas to compute the root mean square radii

$$r_i = [6\, F_i'(0)]^{1/2}, \tag{8}$$

and the charge or magnetic moment density distribution

$$\rho_i(r) = \frac{1}{4\pi^2 r} \int_0^\infty F_i(|t|) \sin(r\sqrt{|t|})\, \mathrm{d}|t|, \tag{9}$$

where $i = c$ or m, corresponding to the charge or magnetic form factor, in (8) and (9).

2.2 *Computation of the anomalous cut positions*

We have computed the anomalous cut positions using the photon-^{3}He vertex of figure 1, where each of a, b and c stand for an exchanged particle, multiparticle, a light nucleus state like deuteron, or their combination. The most familiar exchanges correspond to these objects being deuteron, proton or neutron. The formula representing the cut position can be written as (Eden *et al* 1966; Hamilton 1968; Agrawalla and Parida 1985)

$$\begin{aligned} -t = \frac{1}{2m_c^2} [&(m_b^2 + m_c^2 - M^2)(m_c^2 + m_a^2 - M^2) \\ &\pm \{16 m_a^2 m_b^2 m_c^4 + (m_b^2 + m_c^2 - M^2)^2 (m_c^2 + m_a^2 - M^2)^2 \\ &- 4 m_b^2 m_c^2 (m_c^2 + m_a^2 - M^2)^2 - 4 m_c^2 m_a^2 (m_b^2 + m_c^2 - M^2)^2 \}^{1/2}] \\ &- (m_a^2 + m_b^2), \end{aligned} \tag{10}$$

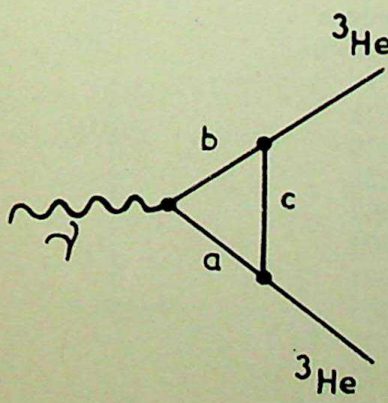

Figure 1. Vertex graph for computation of the anomalous cuts of ^{3}He form factors as described in the text.

CC-0. In Public Domain. Gurukul Kangri Collection, Haridwar

Digitized by Arya Samaj Foundation Chennai and eGangotri

where m_a, m_b, m_c and M represent masses of a, b, c and ^{3}He, respectively. In (10), only the plus route yields the correct anomalous-cut position as can be verified using exchanges with $a = b$. We denote the values corresponding to the plus route of (10) as t_a. In table 1 we have calculated t_a values for familiar transitions like $^3\text{He} \to p + d$, and others like $^3\text{He} \to pp + n$, $^3\text{He} \to n\pi^+ + d$, $^3\text{He} \to d + N^*$, and $^3\text{He} \to p + d\pi^0$. The nearest anomalous cut at $t_a = 0{\cdot}0618$ GeV^2 is found to occur for the simplest vertex corresponding to the transition $^3\text{He} \to p + d$ and the (a, b, c) combination (p, p, d). This cut position occurs sufficiently below the two-pion cut. The next nearest anomalous cut at $t_a = 0{\cdot}075$ GeV^2 occurs for the less familiar and plausible transition, $^3\text{He} \to pp + n$ and the (a, b, c) combination (n, n, pp) and almost coincides with the two-pion cut. A third and the next nearest anomalous cut, which exists between the three-pion and the four-pion cuts, is due to the simple (a, b, c) combination (d, d, p) and also seems plausible. Other anomalous cuts existing at more distant points in the t plane and their (a, b, c) combinations are presented in table 1. As found out by us (Agrawalla and Parida 1985) all the anomalous cuts for ^{4}He charge form factor occur above the three-pion cut, but for ^{3}He, this computation shows that there exists one anomalous cut sufficiently below the two-pion cut. Thus, whereas the nearest threshold in the t plane for ^{4}He form factor is a normal threshold, for the ^{3}He form factors it is an anomalous threshold.

3. Analysis of the magnetic form factor data and extrapolation

We have taken all the available 32 data points with their errors reported by several experimental groups (McCarthy *et al* 1977; Frosch *et al* 1967; McAllister *et al* 1956). As explained in §2, the D-function defined through formulas (2)–(4) is used to parametrize the two-pion cut. For the sake of convenience in data fitting, the N-function is chosen in the form (7), and assumed to represent the contribution due to an anomalous cut, or a normal cut other than the two-pion cut. Setting the normalization condition on two unknown parameters as $e_0 = a_0$ and using $\alpha = 0$, which corresponds to the absence of

Table 1. Computation of anomalous-cut positions with various exchanges, a, b and c in the vertex graph of figure 1.

a	b	c	Anomalous-cut positions t_a (GeV^2)
p	p	d	0·0618
d	d	p	0·2470
n	n	pp	0·0750
pp	pp	n	0·2993
$d\pi^0$	$d\pi^0$	p	0·2573
p	p	$d\pi^0$	1·3381
$n\pi^+$	$n\pi^+$	d	1·7385
d	d	$n\pi^+$	5·2530
$p\pi^0$	$p\pi^0$	d	1·6535
d	d	$p\pi^0$	5·2015
$N^*(1470)$	$N^*(1470)$	d	3·8173
d	d	$N^*(1470)$	8·6569

CC-0. In Public Domain. Gurukul Kangri Collection, Haridwar

Digitized by Arya Samaj Foundation Chennai and eGangotri

the exponential weight function in the N function, yielded a very large value of total χ^2 ($\simeq 300$), for all values of t_a given in table 1, and also the normal cut positions like $t_a = 9m_\pi^2$, $16m_\pi^2$ or $25\ m_\pi^2$. Treating t_a as a free parameter also did not improve the fit significantly. But the introduction of the parameter, $\alpha \neq 0$ and the exponential weight function in the N function drastically reduced the total χ^2 value. The necessity of the exponential weight function for the deuteron magnetic form factor has been emphasized by one of us (Parida 1979). For the lowest anomalous cut position at $t_a = 0{\cdot}0618$ GeV^2, the best fit curve yielded total $\chi^2 = 50{\cdot}4$ with 6 free parameters, corresponding to $\chi^2/DF = 1{\cdot}8$. This fit has been shown by the curve I in figure 2 and the parameters are given in table 2 (case I). Increasing the parameters in the formula did not significantly improve the fit.

To see if the fit can be improved further, we tried different t_a values given in table 2 and also $t_a = 9m_\pi^2$ or $16\,m_\pi^2$. The fit did not improve much with the next nearest anomalous

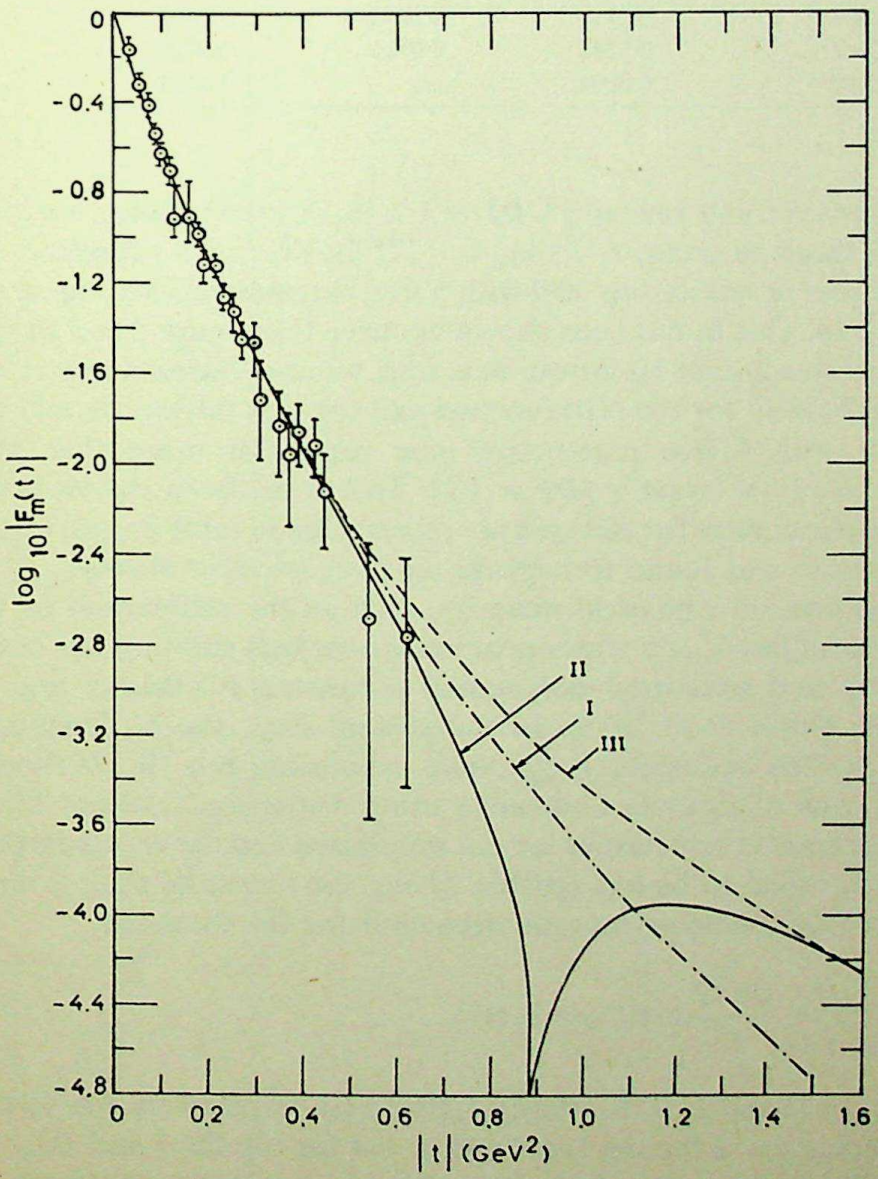

Figure 2. Fits to the ^{3}He magnetic form factor data as a function of various cut positions. Curves I, II and III represent best fits with $t_a = 0{\cdot}0618$, $0{\cdot}175$ and $0{\cdot}247$ GeV^2, respectively, in the N-function, but with the two-pion cut in the D-function.

CC-0. In Public Domain. Gurukul Kangri Collection, Haridwar

Digitized by Arya Samaj Foundation Chennai and eGangotri

Table 2. Unknown parameters in the N/D representation obtained form analysis of the magnetic form factor data corresponding to curves I, II and III of figure 2. Here g_i's are the coefficients of the optimized polynomial expansion of the N function used for the magnetic form factor.

	I	II	III
t_a (GeV^2)	0·0618	0·1750	0·2470
χ^2/DF	1·80	1·14	1·21
α	2·3730	2·1360	2·7020
a_0 (GeV^2)	0·5696	0·6177	0·6161
a_1	0·5869	0·5840	0·5778
a_2 (GeV^{-2})	0·6609	0·6624	0·6602
e_0 (GeV^2)	0·5696	0·6177	0·6161
e_1 (GeV^2)	−2·6510	−0·2500	−0·4949
e_2 (GeV^2)	0·0086	0·0	0·1381
g_0 (GeV^2)	0·0116	0·5592	0·5341
g_1 (GeV^2)	0·5573	0·0585	0·0726
g_2 (GeV^2)	0·0006	0·0	0·0094

cut at $t_a = 0{\cdot}075$ GeV^2 and yielded $\chi^2/DF = 1{\cdot}7$. As our next choice, we used the next nearest normal three-pion cut, $t_a = 9m_\pi^2 = 0{\cdot}175$ GeV^2, for the function N, and the total χ^2 for the best fit reduced to 30·9 with 5 free parameters, yielding an excellent fit with $\chi^2/DF = 1{\cdot}14$. This fit has been shown as curve II in figure 2 and the parameters are presented in table 2 (case II). As our next step, we used the next nearest anomalous cut at $t_a = 0{\cdot}2475$ GeV^2 for the $N(t)$ function and the best fiit was found to yield total $\chi^2 = 31{\cdot}58$, but with 6 free parameters (one parameter more than the case II) corresponding to a little larger $\chi^2/DF = 1{\cdot}21$. This fit has been shown as curve III in figure 2 and the parameters for this case are represented in table 2 (case III). Increasing the t_a values further was found to increase the total χ^2 value slowly.

The extrapolation of a physical quantity, such as the differential or total cross-section, or the form factor, is a tricky problem whose best solution has been obtained using analyticity and optimized polynomial expansion (Cutkosky and Deo 1968; Cutkosky 1969; Ciulli *et al* 1975). In the present case, the N function has been approximated by the optimized polynomial expansion, but the D function by an effective range type of formula obtainable using dispersion relation. Therefore, the errors in the extrapolated quantities are not minimized and the extrapolation for large $|t|$ values are supposed to be less reliable. Using the results of table 2 and formulas (1)–(7) yields the following asymptotic behaviour for the three fits

$$F_m(t) \underset{t\to\infty}{\to} \frac{(\ln t)^p}{t^n} \exp[-\alpha(\ln t)^2] \tag{11}$$

with $\alpha = 2{\cdot}373$, 2·136 and 2·702 for the fits I, II and III, respectively. For all the three fits $n = 2$, but whereas $p = 2$ for the best fit II, $p = 4$ for the fits I and III.

The extrapolated values of the form factor for smaller $|t|$ regions, where data are not available, are shown in figures 3, 4 and also in figure 2. The presence of a dip at $|t| \simeq 0{\cdot}88$ GeV^2 and a second maximum at $|t| \simeq 1{\cdot}1$–$1{\cdot}3$ GeV^2 is predicted by the best

CC-0. In Public Domain. Gurukul Kangri Collection, Haridwar

Digitized by Arya Samaj Foundation Chennai and eGangotri

fit II as shown in figure 2. For the fits I and III, the zeros of the N-function did not exist in the physical region and the dip or the second maximum does not occur for those fits. But since curve III represents an almost equally good fit as curve II, the occurrence of a dip or a second maximum is not a necessary prediction of this analysis.

Extrapolation onto the smaller and larger t values in the time-like regions are shown in figures 3 and 4. Figure 3 exhibits a large slope value of the form factor at $t = 0$ for the lowest value of t_a. Using the parameters of table 2 and the formula (8), we compute the root mean square radius of magnetic moment distribution for ^3He

$$\gamma_m = \begin{cases} 3{\cdot}230 \text{ fm}, & \text{FIT I} \\ 1{\cdot}384 \text{ fm}, & \text{FIT II} \\ 1{\cdot}747 \text{ fm}, & \text{FIT III.} \end{cases} \tag{12}$$

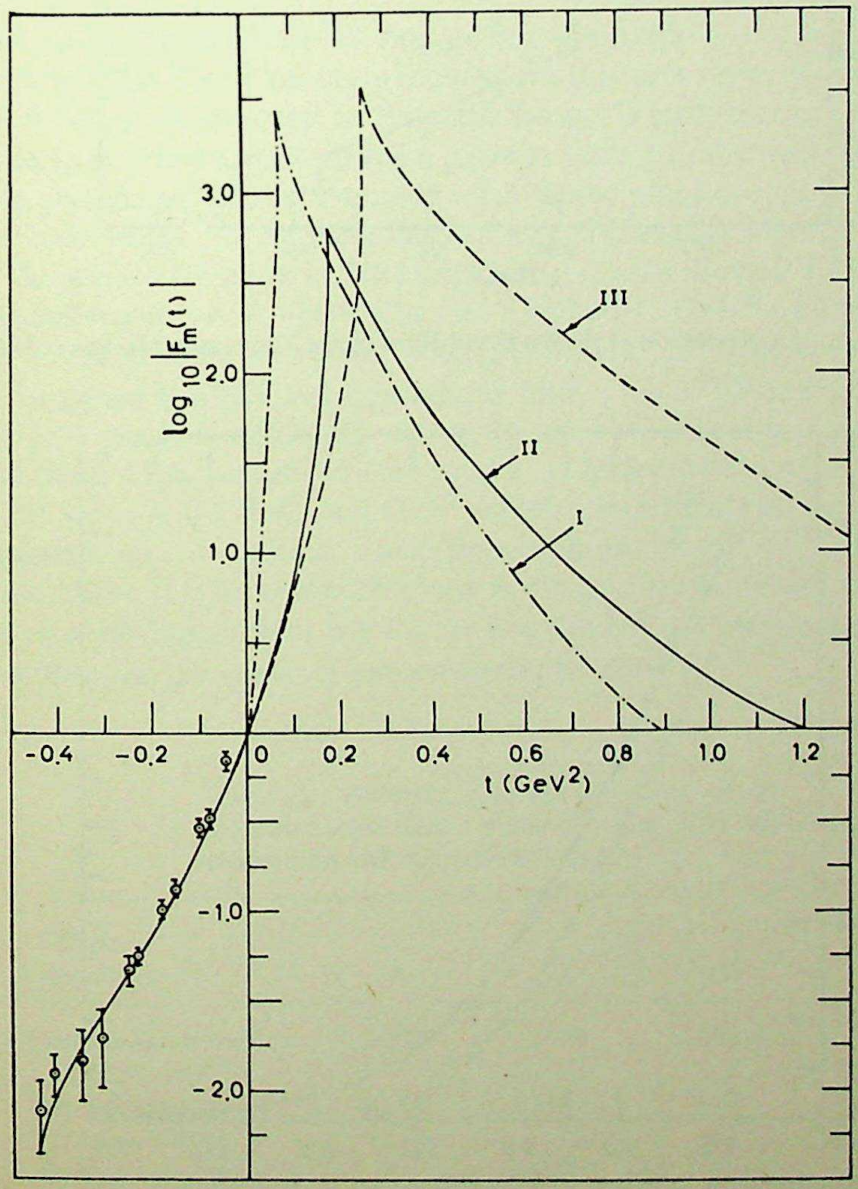

Figure 3. Extrapolation of the ^3He magnetic form factor onto the time-like region with various fits described as curves I, II and III corresponding to figure 2.

CC-0. In Public Domain. Gurukul Kangri Collection, Haridwar

Digitized by Arya Samaj Foundation Chennai and eGangotri

In the case of the lowest anomalous cut position, the radius appears to be more than twice the value obtained for the three-pion cut which is closer to the accepted value. Because of this reason, the fit I with the nearest anomalous cut seems to be ruled out as an analytic representation for the magnetic form factor. Using the parameters of table 2 and the formula (8), we also compute the density of magnetic moment distribution $\rho_m(r)$, as a function of r, as shown in figure 5. As compared to the cases with the normal

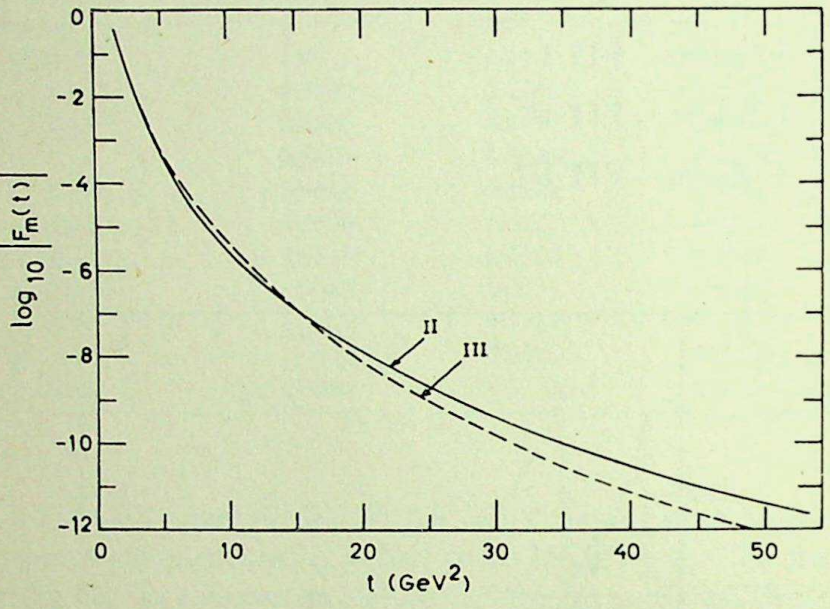

Figure 4. Extrapolation of the fits II and III of figure 2 onto larger $|t|$ values in the spacelike region.

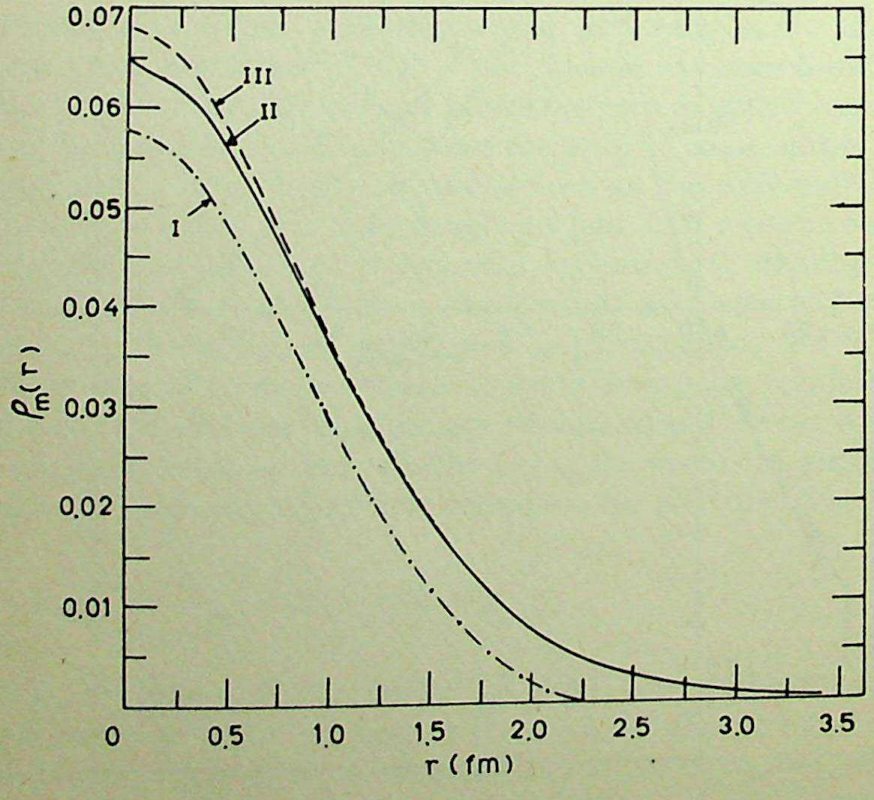

Figure 5. Computation of density of magnetic moment distribution, $\rho_m(r)$ as a function of distance r from the origin corresponding to the fits I, II and III of figure 2.

CC-0. In Public Domain. Gurukul Kangri Collection, Haridwar

Digitized by Arya Samaj Foundation Chennai and eGangotri

three-pion cut or the distant anomalous cut (cases II or III), the nearest anamalous cut (case I) yields the density distribution nearly 25% less for all values of $r < 2{\cdot}5$ fm. For each curve plotted in figure 5, we compute the half density distribution of magnetic moments as

$$\gamma_m h = \begin{cases} 1{\cdot}100 \text{ fm}, & \text{FIT I} \\ 1{\cdot}075 \text{ fm}, & \text{FIT II} \\ 1{\cdot}125 \text{ fm}, & \text{FIT III.} \end{cases} \tag{13}$$

Computed values of physical parameters for the magnetic form factor are shown in table 3 for the three different fits.

4. Analysis of the charge form factor data and extrapolation

We have taken all the available 65 data points with their errors reported by different experimental groups. The D function is chosen in the form (2) with formulas (3) and (4), and the N function is assumed to have the form (7) with formula (6), where t_a was chosen to be an anomalous cut position given in table 1 or the next nearest normal-cut position. As in the case of the magnetic form factor, the exponential weight function with $\alpha > 0$ was found to be essential for any reasonable description of the data. Including the weight function in $N(t)$ we tried to obtain the best possible fits with the nearest anomalous cuts at $t_a = 0{\cdot}01618$ GeV^2 and $0{\cdot}075$ GeV^2. In both cases the fits to the data were found to be very poor. With $t_a = 0{\cdot}0618$ GeV^2 the fit has been presented as curve I in figure 6 which corresponds to total $\chi^2 = 371{\cdot}5$ and $\chi^2/DF = 6{\cdot}2$. With $t_a = 0{\cdot}075$ GeV^2 the fit is similar. However, the total χ^2 reduces drastically by increasing the t_a value. With 6 free parameters the total $\chi^2 = 68{\cdot}8$ ($104{\cdot}5$) and $\chi^2/DF = 1{\cdot}16$ ($1{\cdot}77$) are obtained for $t_a = 0{\cdot}175$ ($0{\cdot}247$) GeV^2 which corresponds to the three-pion (third nearest-anomalous)-cut position. These fits are shown by curves II and III in figure 6. Out of these, curve II is an acceptable best fit which does not predict the presence of a second dip or a third maximum, but fits the first dip and the second maximum very well. The parameters for the curve II are presented in table 4.

Table 3. Different physical quantities of the magnetic form factor obtained using N/D representation and experimental data.

Physical quantities	I	II	III
Root-mean-square radius (fm)	3·230	1·384	1·747
Half-density radius (fm)	1·100	1·075	1·125
Position of first zero (GeV^2)	—	−0·880	—
Position of second maximum (GeV^2)	—	−1·10 to −1·30	—

CC-0. In Public Domain. Gurukul Kangri Collection, Haridwar

Digitized by Arya Samaj Foundation Chennai and eGangotri

Table 4. Unknown parameters of the N/D representation of the charge form factor obtained by fitting the experimental data as described in the text for two different cut positions, $t_a = 0{\cdot}175$ GeV^2 and $0{\cdot}19$ GeV^2 of the N-function. Here g_i's are the coefficients of the optimized polynomial expansion used for the N-function.

	II	IV
t_a (GeV^2)	0·175	0·190
χ^2/DF	1·16	1·06
α	2·110	1·9093
a_0 (GeV^2)	0·645	0·6460
a_1	0·0133	0·0837
a_2 (GeV^{-2})	0·605	0·0431
e_0	0·645	0·6460
e_1 (GeV^2)	−0·3266	−0·6102
e_2 (GeV^2)	−0·0587	0·1136
g_0 (GeV^2)	0·5612	0·5017
g_1 (GeV^2)	0·0903	0·1288
g_2 (GeV^2)	−0·0065	0·0155

To know if the fit can be improved further, we treated t_a as a free parameter along with α; e_i and a_m, and found a minimum of total $\chi^2 = 61{\cdot}8$ ($\chi^2/DF = 1{\cdot}06$) with $t_a = 0{\cdot}19$ GeV^2 and 6 free parameters presented in table 4. This fit has been shown by the solid-line curve IV in figure 6. Besides fitting the first dip (second maximum) at $|t| = 0{\cdot}44$ ($0{\cdot}60$) GeV^2, this fit is consistent with the presence of a second dip (third maximum) at $-t = 2{\cdot}4$ ($3{\cdot}0$–$3{\cdot}2$) GeV^2. Thus, although the two fits corresponding to curves II and IV are almost equally acceptable, the latter needs the presence of the second dip and the third maximum. Our analysis on the behaviour of the total χ^2 value as a function of t_a can be summarized in the following manner: as the cut position in the N function starts increasing from $t_a = 0{\cdot}0618$ GeV^2, the total χ^2 decreases, reaches a minimum for $t_a = 0{\cdot}19$ GeV^2 and increases again as t_a is increased beyond this value.

As we have found, there are two almost equally acceptable good fits for the ^{3}He charge form factor with $t_a = 0{\cdot}175$ and $0{\cdot}19$ GeV^2, subject to the limitations that error in the extrapolated quantity increases as we move farther away from the region in the t-plane at which experimental data exist (Cutkosky and Deo 1968; Cutkosky 1969; Ciulli *et al* 1975), the two fits satisfy the asymptotic behaviour of the type

$$F_c(t) \underset{t\to\infty}{\to} \exp\left[-\alpha(\ln t)^2\right]\frac{\ln t^4}{t^2}, \tag{13}$$

where $\alpha = 2{\cdot}110$ ($1{\cdot}909$) for the fit II (IV) of figure 6. Using the parameters of the two fits from table 4, we find that both the fits have the first zero of their $N(t)$ function at the experimentally observed dip position, $-t = 0{\cdot}44$ GeV^2. The second zero of the $N(t)$ function for the fit II does not occur in the physical region, but for fit IV, it occurs at $-t = 2{\cdot}40$ GeV^2. Similarly the third maximum for the fit IV appears to exist at $-t = 3{\cdot}0$–$3{\cdot}2$ GeV^2. Since the fits II and IV are almost equally acceptable, the present analysis does not definitely predict the second dip structure. Experimentally, however,

CC-0. In Public Domain. Gurukul Kangri Collection, Haridwar

Digitized by Arya Samaj Foundation Chennai and eGangotri

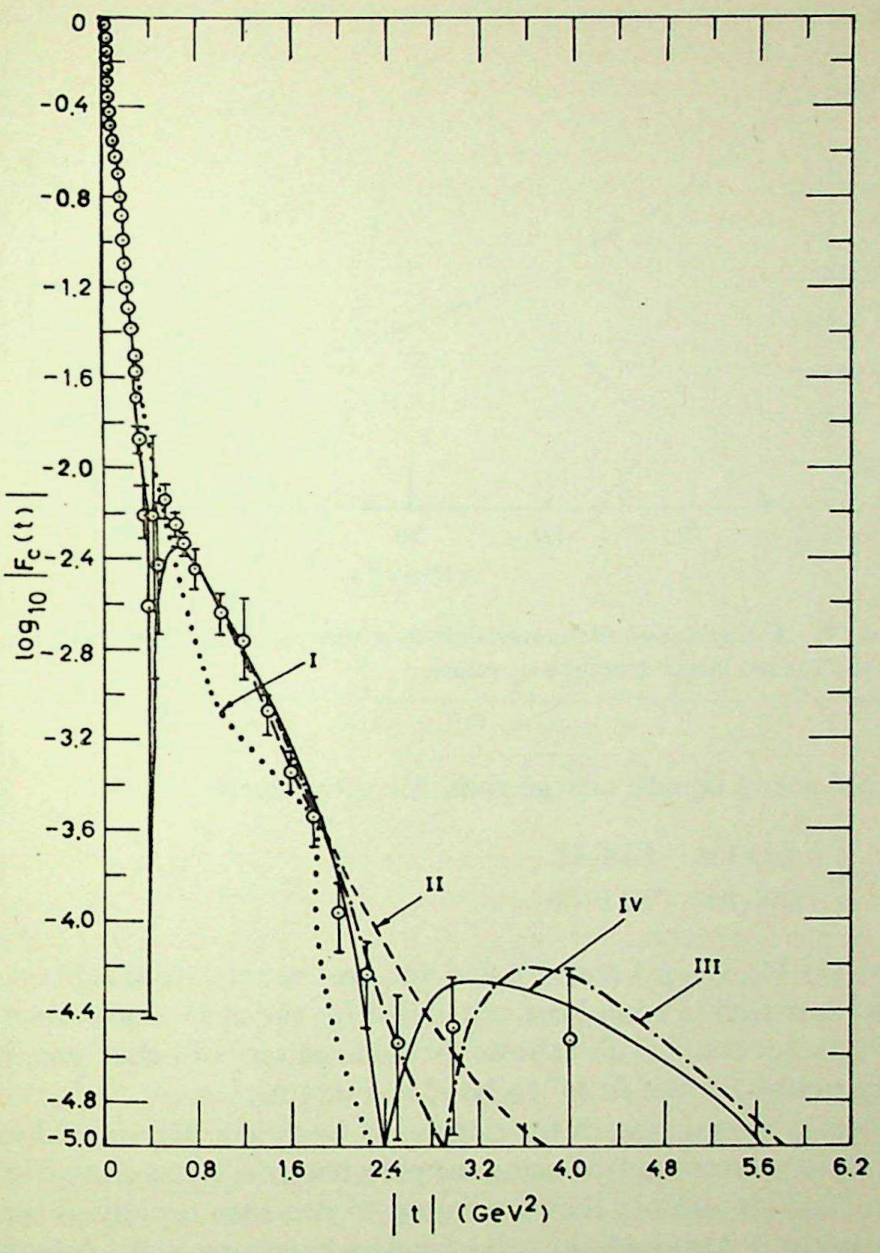

Figure 6. Fits to the available data on ^{3}He charge form factor with the two-pion cut for the D-function. Curves I, II, III and IV represent fits with $t_a = 0{\cdot}0618, 0{\cdot}175, 0{\cdot}247$ and $0{\cdot}19$ GeV^2, respectively, for the N-function as described in the text.

the data clearly exhibit the existence of a shoulder with rather large errors around $-t = 2$–3 GeV^2, which has been interpreted as the region of the second dip and third maximum in the fit IV. We suggest that accurate measurements of the charge form factor be carried out for $2{\cdot}0 \leqslant |t| \leqslant 4{\cdot}0$ GeV^2 in order to confirm the presence of the second dip.

Extrapolation of the fit IV onto the larger space-like and time-like t values are shown in figures 7 and 8 respectively. From figure 8 it is clear that the form factor extrapolates smoothly onto the time-like region, producing threshold enhancement at $t_a = 0{\cdot}19$ GeV^2, but having no resonance peaks. The behaviour of fit II, on extrapolation, is similar except that the threshold enhancement in the time-like region occurs at $t_a = (3m_\pi)^2 = 0{\cdot}175$ GeV^2. Using formula (8) and the parameters of table 4 we

CC-0. In Public Domain. Gurukul Kangri Collection, Haridwar

Digitized by Arya Samaj Foundation Chennai and eGangotri

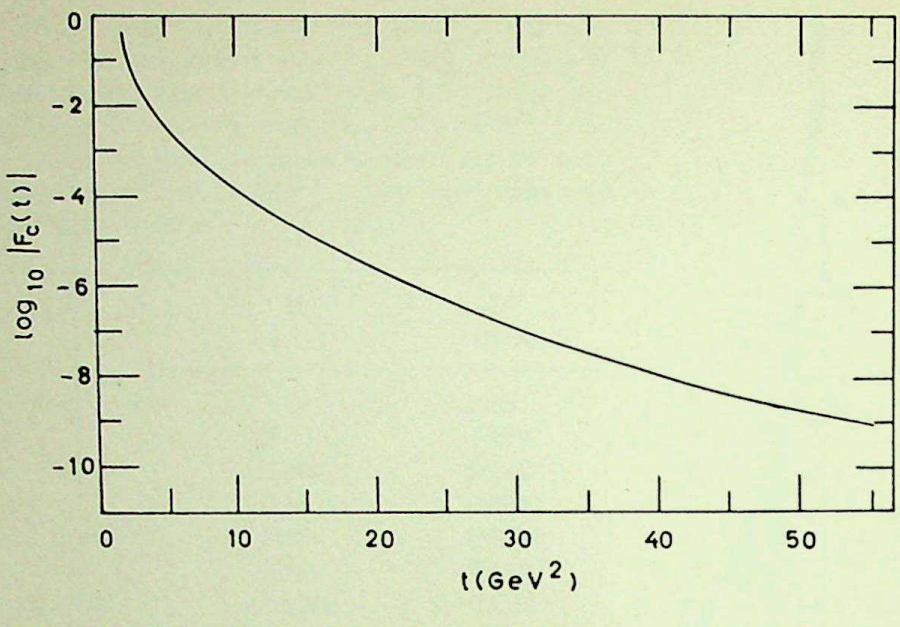

Figure 7. Extrapolation of the solid-line-fit of the ^{3}He charge form factor shown in figure 6 (curve IV) onto larger spacelike $|t|$ values.

calculate the root mean square charge radii for the two fits

$$r_c = \begin{cases} 1{\cdot}875 \text{ fm}, & \text{FIT II} \\ 1{\cdot}966 \text{ fm}, & \text{FIT IV.} \end{cases} \tag{14}$$

Using formulas (1)–(4), (6), (7) and (9), and the parameters from table 4, the charge density $\rho_c(r)$ as a function of r has been calculated for the fit IV and shown in figure 9. The plot of $\rho_c(r)$ vs r for the fit II also shows the same pattern of behaviour. We compute the half density radius for the fit IV to be $r_c^h = 1{\cdot}05$ fm.

The parameters g_i's occurring in the optimized Laguerre polynomial expansion in the N function have been computed using the parameters e_i's and shown in table 4 and comparing formulas (5) and (7); they are found to decrease rapidly as we go over to higher order terms in Z. Although the a_n parameters occurring in the D function for the fit IV are found to decrease with increasing order in t, such a behaviour is not evident in the case of fit II.

5. Summary, discussion and conclusion

This analysis reveals that the proposed N/D method of analytic representation for form factors, which has been successfully tested for isoscalar light nuclei like deuteron and ^{4}He (Parida 1979; Parida *et al* 1983; Agrawalla and Parida 1985), is capable of describing the charge, and magnetic-form-factor data of a nonisoscalar light nucleus like the ^{3}He. Acceptable excellent fits are obtained when the N-function is used to parametrize the three-pion cut, or the anomalous cut at $t_a = 0{\cdot}247$ GeV^2; and, in the former case only, the presence of a dip (secondary maximum) is predicted at $-t = 0{\cdot}88$ $(1{\cdot}1–1{\cdot}3)$ GeV^2.

In the case of the charge form factor, two almost equally acceptable fits are found to exist when the N-function is used to parametrize the three-pion cut, or an effective cut

CC-0. In Public Domain. Gurukul Kangri Collection, Haridwar

Digitized by Arya Samaj Foundation Chennai and eGangotri

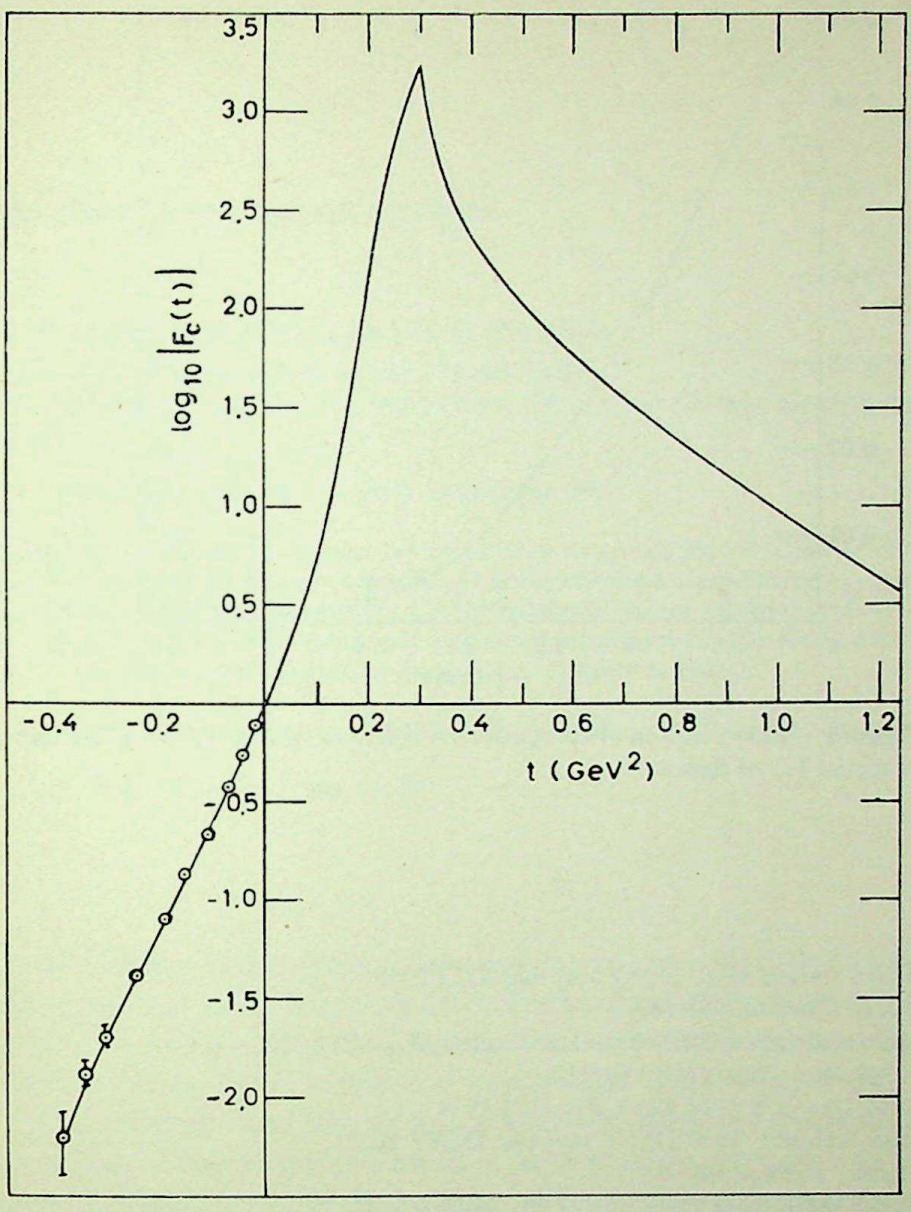

Figure 8. Extrapolation of the ^{3}He charge form factor onto the time-like region using the solid-line fit (curve IV) of figure 6.

very close to it. In the latter case only, the presence of a second dip and a third maximum is predicted to occur. We suggest that accurate charge-form factor measurements in the region $2{\cdot}0 \leqslant -t \leqslant 4{\cdot}0$ GeV^2 be carried out to confirm whether such structures exist.

As we have observed in this and earlier analyses, the presence of the exponential weight function is essential for the nuclear form factors, which contributes a factor $\exp[-\alpha(\ln t)^2]$, to their asymptotic behaviour. It is natural to suppose that since, according to QCD, the hadrons constituting the nucleus are themselves composed of coloured quarks, the quark form factor should occur as a factor in the actual nuclear form factor at least for large $|t|$ values. In fact such a type of asymptotic behaviour of the quark form factor in the leading logarithmic order has been calculated using QCD and asymptotic dynamics (Dahman *et al* 1980; Kulish *et al* 1970, 1971).

CC-0. In Public Domain. Gurukul Kangri Collection, Haridwar

Digitized by Arya Samaj Foundation Chennai and eGangotri

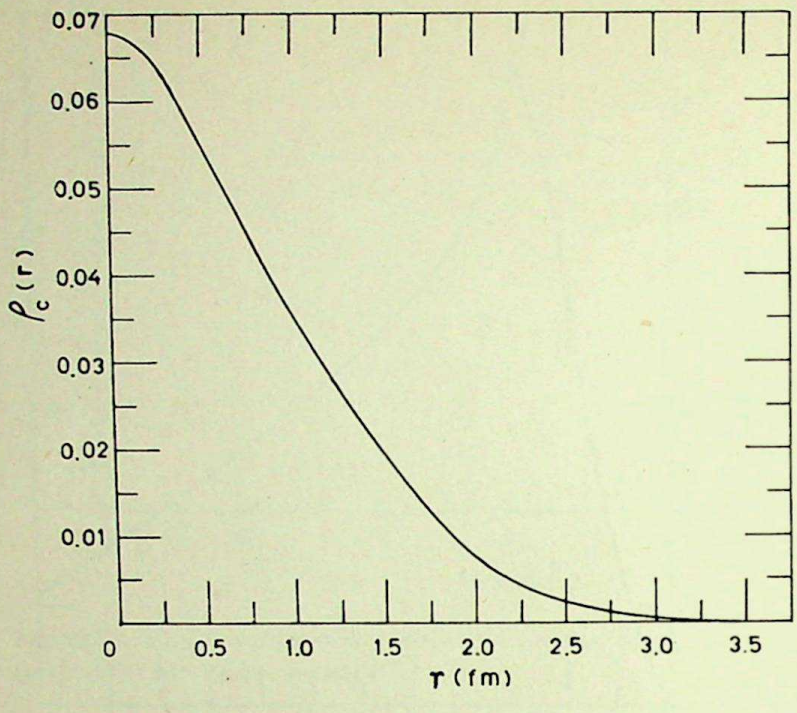

Figure 9. Computation of charge density $\rho_c(r)$ as a function of r for ^{3}He using the solid-line fit (curve IV) of figure 6.

References

Agrawalla K N and Parida M K 1985 *Phys. Rev.* **D32** 2359
Ciulli S 1969 *Nuovo Cimento* **A61** 787
Ciulli S, Pomponiu and Sabba Stefanescu I 1975 *Phys. Rep.* **C17** 133
Cutkosky R E 1969 *Ann. Phys.* (*N.Y.*) **54** 110
Cutkosky R E and Deo B B 1968 *Phys. Rev.* **174** 1859
Dahman H D and Steiner F 1980 DESY preprint DESY 80/37
Deo B B 1974 *Indian J. Phys.* **48** 705
Deo B B and Parida M K 1971 *Phys. Rev. Lett.* **26** 1609
Deo B B and Parida M K 1973 *Phys. Rev.* **D8** 2939
Deo B B and Parida M K 1974 *Phys. Rev.* **D9** 2068
Eden R J, Landshoff P V, Olive D I and Polkinghorne J C 1966 *The analytic S-matrix* (Cambridge: University Press)
Frosch R F, McCarthy J S, Rand R E and Yearian M R 1967 *Phys. Rev.* **160** 874
Hamilton J 1968 Lecture given at the Neils Bohr Institute, NORDITA (Nordita Publications)
Kulish P P and Faddeev L D 1970 *Theor. Maten Fiz.* **4** 153
McAllister R W and Hofstadter R 1956 *Phys. Rev.* **102** 851
McCarthy J S, Sick I and Whitney R R 1977 *Phys. Rev.* **C15** 1396
Parida M K 1979 *Phys. Rev.* **D19** 3320
Parida M K, Patel S and Agrawalla K N 1983 *Phys. Rev.* **D27** 1187

CC-0. In Public Domain. Gurukul Kangri Collection, Haridwar

Digitized by Arya Samaj Foundation Chennai and eGangotri

Pramāṇa – J. Phys., Vol. 28, No. 2, February 1987, pp. 131–158. © Printed in India.

Relativistic effects on meson spectra

S P MISRA, S NAIK and A R PANDA*

Institute of Physics, Bhubaneswar 751 005, India

* Permanent address: Physics Department, Kendrapara College, Kendrapara 754 211, India

MS received 23 July 1986; revised 29 October 1986

Abstract. The meson masses are considered to retain total relativistic effects for spinors instead of Fermi-Breit approximation. This necessitates a diagonalization approach instead of solutions of differential equations. Correction over Fermi-Breit form appears to be significant. For heavy quark systems agreement with experiment is found. The method will be quite useful if the quark-antiquark dynamics becomes sufficiently known.

Keywords. Relativistic meson spectra; Fermi-Breit approximation; decay widths.

PACS Nos 12·40; 12·90; 13·20

1. Introduction

Spectroscopy of hadrons in the quark model has been dealt with by many authors in the recent past (Eichten *et al* 1978; Schnitzer 1978; Richardson 1979; Buchmuller *et al* 1980; Martin 1980; Stanley and Robson 1980; Barik and Jena 1981; Gupta and Radford 1982; Gupta *et al* 1982; Mitra 1981; Mitra and Santhanam 1981; Mittal and Mitra 1984; Gupta 1977). The hyperfine and fine structure splittings of heavy quarkonia are usually considered by Fermi-Breit Hamiltonian as a perturbation over spin-averaged levels, where terms are retained only upto the leading orders. On the other hand we aim here to derive the same retaining the total relativistic effects for different phenomenological potentials.

In §2, we describe the framework of the approach to evaluate the effective Hamiltonian in field theory. Here the full contribution from the Dirac spinors is retained, instead of the lowest order approximation. Unlike solving the Schrödinger's differential equation for spin-averaged state and doing perturbation calculation for spin structure, we adopt here the diagonalization approach for obtaining the relevant spectra. This permits a fully relativistic treatment of the spinor components. Section 3 is devoted to the discussion of some approximation schemes. In §4, we apply the scheme to illustrate with different potentials. With Cornell type of potential (Eichten *et al* 1978) and with a vector exchange even for a heavy quark system, a significant correction to Fermi-Breit form is observed. As usual, we also include a scalar confining potential (Bardeen *et al* 1975). We further observe a variation of the potential parameters according to the mass of the fermion constituents and the size of the mesons (Gupta and Radford 1982), as expected. parallel to the renormalization scheme.

Our objective here has been to develop a fully relativistic approximation scheme and apply it for a few simple cases. Although we have succeeded in some of the applications,

CC-0. In Public Domain. Gurukul Kangri Collection, Haridwar

Digitized by Arya Samaj Foundation Chennai and eGangotri

it appears that the problem should be really tackled when we can be in a position to *derive* the potential. The method indicated here will enable us to obtain full relativistic corrections in such an eventuality. It is quite possible that the calculations of lattice QCD may help us in this direction.*

2. General theory

As mentioned earlier, we consider here the matrix elements of the Hamiltonian operator for an enumerable quark-antiquark basis and then diagonalize this operator as approximated by a finite number of elements of this basis. We retain the four-component Dirac spinors instead of making Fermi-Breit approximation.

2.1 *Effective Hamiltonian*

We first consider the potential in the context of quantum chromodynamics (QCD) as an illustration, and later, introduce phenomenological potentials. Thus, in the second order in quantum chromodynamics (QCD) the S-matrix element corresponding to one-gluon exchange will simply be related to the *effective* potential $v(x)$ by the equation,

$$S_2 = \frac{(-i)^2}{2!}\int :\bar{Q}(x)\gamma^\mu \frac{\lambda_a}{2} Q(x)\,\bar{\tilde{Q}}(y)\gamma^\nu \frac{\lambda_0}{2}\tilde{Q}(y): \mathrm{d}^4x\,\mathrm{d}^4y$$
$$\times \frac{ig^2}{(2\pi)^4} D_{\mu\nu}(q)\exp\left[-iq\cdot(x-y)\right]\mathrm{d}^4q$$
$$\equiv (-i)\int v(x)\,\mathrm{d}^4x. \tag{1}$$

In the above, we choose the Coulomb gauge (Berestetskii *et al* 1971) such that $D_{00}(q) = 1/q^2$, $D_{0i} = D_{i0} = 0$ and $D_{ij}(q) = (-\delta_{ij} + q_iq_j/|\mathbf{q}|^2)/q^2$. This yields

$$v(x) = -\frac{1}{(2\pi)^4}\int :\bar{Q}(x)\gamma^\mu \frac{\lambda_a}{2} Q(x)\bar{\tilde{Q}}(y)\gamma^\nu \frac{\lambda_a}{2}\tilde{Q}(y):$$
$$\times g^2 D_{\mu\nu}(q)\exp\left(-iq(x-y)\right)\mathrm{d}^4y\,\mathrm{d}^4q. \tag{2}$$

In general, $v(x)$ will be a function of space and time. $Q(x)$ and $\tilde{Q}(y)$ in (2) represent the *four-component* quark annihilation and anti-quark creation operators (Misra 1978). For such quark field operators *for hadrons at rest* a specific *time dependence* had been suggested (Misra 1978). It was considered, *as an approximation scheme*, that $Q(x) = Q(\mathbf{x})\exp(-ik_1^0 t)$ where k_1^0 is the energy value of the quark Q in the hadron *at rest*, and is a constant. We shall presently see that *with this assumption* $v(x)$ in (2) will become independent** of $x^0 = t$. We thus have in equation (2), when we consider hadrons at rest, $\bar{\tilde{Q}}(\mathbf{y}) = \bar{\tilde{Q}}(\mathbf{y})\exp(-ik_2^0 y^0)$ and $\tilde{Q}(y) = \tilde{Q}(\mathbf{y})\exp(ik_2^0 y^0)$, with the same value k_2^0 since both $\tilde{Q}$ and $\bar{\tilde{Q}}$ corresponding to the same constituent antiquark of the

---

* One example of this type is by one of the authors (Naik 1986) with a mean field approximation.

** The assumption considered implies that the *constituent* quark field operators (Misra 1978) yield quarks with variable momentum but fixed energy. The theoretical situation however is unclear (Caswell and Lepage 1978).

CC-0. In Public Domain. Gurukul Kangri Collection, Haridwar

Digitized by Arya Samaj Foundation Chennai and eGangotri

hadron under consideration §. Hence, when $v(x)$ is applied to hadrons at rest, as will be case for hadron spectroscopy §§, y^0 and q^0 integrations in (2) can be trivially performed, and we obtain that

$$v(\mathbf{x}) = -\frac{1}{(2\pi)^3}\int : \bar{Q}(\mathbf{x})\gamma^\mu \frac{\lambda_a}{2} Q(\mathbf{x})\,\bar{\bar{Q}}(\mathbf{y})\gamma^\nu \frac{\lambda_a}{2}\tilde{Q}(\mathbf{y}):$$
$$\mathrm{d}\mathbf{q}\,\mathrm{d}\mathbf{y}\cdot g^2\cdot D_{\mu\nu}(q)\exp(i\mathbf{q}\cdot(\mathbf{x}-\mathbf{y})). \tag{3}$$

The time independence of the potential "density" in (3) as advertised may be noted. This fact is only true when we consider the operator $v(x)$ applied to the hadrons in their rest frame (Misra 1978) as for hadron spectroscopy, and, is true to the extent quarks in hadrons at rest occupy *fixed* energy levels.

We can rewrite (3) as

$$v(\mathbf{x}) = \frac{1}{(2\pi)^3}\int\Bigg[:\bar{Q}(\mathbf{x})\gamma^\mu \frac{\lambda_a}{2} Q(\mathbf{x})\,\bar{\bar{Q}}(\mathbf{y})\gamma_\mu \frac{\lambda_a}{2}\tilde{Q}(\mathbf{y}):$$
$$+:\bar{Q}(\mathbf{x})(\gamma\cdot\mathbf{q})\frac{\lambda_a}{2}Q(\mathbf{x})\bar{\bar{Q}}(\mathbf{y})(\gamma\cdot\mathbf{q})\frac{\lambda_a}{2}\tilde{Q}(\mathbf{y}):/|\mathbf{q}|^2\Bigg]$$
$$\times\,\tilde{V}(\mathbf{q})\exp(i\mathbf{q}\cdot(\mathbf{x}-\mathbf{y}))\,\mathrm{d}\mathbf{q}\,\mathrm{d}\mathbf{y}, \tag{4}$$

where we have substituted

$$\tilde{V}(\mathbf{q}) = g^2(|\mathbf{q}|)/|\mathbf{q}|^2 = 4\pi\alpha_s(Q)/Q^2. \tag{5}$$

In (5), we have in mind, the renormalization group improved perturbation theory (Marciano and Pagels 1978) and, we may have, e.g. a *phenomenological* extrapolation of $\alpha_s(Q)$ to the infrared regime given as

$$\alpha_s(Q) = \frac{12\pi}{(33-2n_f)}\Big/\log\left(1+\frac{Q^2}{\Lambda^2}\right), \tag{6}$$

as considered by Richardson and others. The potential in coordinate space is given as

$$V(\mathbf{r}) = (2\pi)^{-3}\int \tilde{V}(\mathbf{q})\exp(i\mathbf{q}\cdot\mathbf{r})\mathrm{d}\mathbf{q}. \tag{7}$$

Whenever we take a *phenomenological* central potential (Rosner 1981) the identification will be made by (7), where while doing this it is to be recognised that the colour degree of freedom is still present in (4).

We now proceed to evaluate the *operator* part of (4), which, with the four-component structure of the operators will give rise to orbital, hyperfine, spin-orbit and tensor operators in the nonrelativistic limit (Berestetskii *et al* 1971; Rosner 1981), and in the general case will include momentum (velocity) dependence in the potential arising as

---

§ The fact that having energy dependence as suggested may be a reasonable approximation finds further support (Biswal and Misra 1982; Misra 1983).

§§ The idea may be good only for hadrons at rest. Otherwise one may take relativistic Bethe Salpeter equations (e.g. Mittal and Mitra 1984).

CC-0. In Public Domain. Gurukul Kangri Collection, Haridwar

Digitized by Arya Samaj Foundation Chennai and eGangotri

relativistic corrections. For this purpose we write (Rosner 1981)

$$Q(\mathbf{x}) = (2\pi)^{-3/2} \int u(\mathbf{k}) Q_I(\mathbf{k}) \exp(i\mathbf{k}\cdot\mathbf{x})\, d\mathbf{k}, \tag{8a}$$

and

$$\tilde{Q}(\mathbf{y}) = (2\pi)^{-3/2} \int v(\mathbf{k}) \tilde{Q}_I(\mathbf{k}) \exp(-i\mathbf{k}\cdot\mathbf{y})\, d\mathbf{k}, \tag{8b}$$

where

$$u(\mathbf{k}) = \begin{bmatrix} f(\mathbf{k}) \\ g\sigma\cdot\mathbf{k} \end{bmatrix}, \tag{9a}$$

and

$$v(\mathbf{k}) = \begin{bmatrix} g(\mathbf{k})\sigma\cdot\mathbf{k} \\ f(\mathbf{k}) \end{bmatrix}. \tag{9b}$$

We here note that $f(\mathbf{k}) = [(p^0 + m_Q)/2p^0]^{1/2}$ and $g(\mathbf{k}) = [2p^0(p^0+m_Q)]^{-1/2}$ with $p^0 = \sqrt{\mathbf{k}^2 + m_Q^2}$. Further, the two *component* annihilation and creation for the quark antiquark and in (8) are given as $(Q_I(\mathbf{k}) = \sum_r Q_{Ir}(\mathbf{k}) u_{Ir}$ and $\tilde{Q}_I(\mathbf{k}) = \sum_r \tilde{Q}_{Ir}(\mathbf{k})\, v_{Ir}$.

Now we have

$$\begin{aligned} P &\equiv \int v(\mathbf{x})\, d\mathbf{x} \\ &= (2\pi)^{-3} \iint \Big[Q_I^\dagger(\mathbf{k}_1')\bar{u}(\mathbf{k}_1')\gamma^\mu \frac{\lambda_a}{2} u(\mathbf{k}_1) Q_I(\mathbf{k}_1) \\ &\quad \times :\tilde{Q}_I(\mathbf{k}_2)^\dagger \bar{v}(\mathbf{k}_2)\gamma_\mu \frac{\lambda_a}{2} v(\mathbf{k}_2')\tilde{Q}_I(\mathbf{k}_2'): \\ &\quad + Q_I(\mathbf{k}_1')^\dagger \bar{u}(\mathbf{k}_1')(\gamma\cdot\mathbf{q}) \frac{\lambda_a}{2} u(\mathbf{k}_1) Q_I(\mathbf{k}_1) \\ &\quad \times :\tilde{Q}_I(\mathbf{k}_2)^\dagger \bar{v}(\mathbf{k}_2)(\gamma\cdot\mathbf{q}) \frac{\lambda_a}{2} v(\mathbf{k}_2')\tilde{Q}_I(\mathbf{k}_2'): /|\mathbf{q}|^2 \Big] \\ &\quad \times \tilde{V}(\mathbf{q})\, d\mathbf{k}_1\, d\mathbf{k}_2\, d\mathbf{q}. \end{aligned} \tag{10}$$

In equation (10), $\mathbf{k}_1' = \mathbf{k}_1 + \mathbf{q}$ and $\mathbf{k}_2' = \mathbf{k}_2 - \mathbf{q}$.

In order to evaluate (10) we now note that

$$\begin{aligned} &\bar{u}(\mathbf{k}_1')\gamma^\mu u(\mathbf{k}_1) \otimes \bar{v}(\mathbf{k}_2)\gamma_\mu v(\mathbf{k}_2') \\ &+ \bar{u}(\mathbf{k}_1')(\gamma\cdot\mathbf{q}) u(\mathbf{k}_1) \otimes \bar{v}(\mathbf{k}_2)(\gamma\cdot\mathbf{q}) v(\mathbf{k}_2')/|\mathbf{q}^2|^2 \\ &= U_1 + U_2 + U_3 + U_4, \end{aligned} \tag{11}$$

where

$$\begin{aligned} U_1 &= (f_1' f_1 + g_1' g_1 (\mathbf{k}_1'\cdot\mathbf{k}_1))(f_2' f_2 + g_2' g_2 (\mathbf{k}_2'\cdot\mathbf{k}_2)) \\ &\quad + \left\{ \frac{(\mathbf{k}_1\cdot\mathbf{q})(\mathbf{k}_2\cdot\mathbf{q})}{|\mathbf{q}|^2} - \mathbf{k}_1\cdot\mathbf{k}_2 \right\} \\ &\quad \times \{ f_2 f_1 g_1' g_2' + f_1' f_2' g_1 g_2 + f_1 f_2' g_1' g_2 + f_1' f_2 g_1 g_2' \}, \end{aligned} \tag{12}$$

CC-0. In Public Domain. Gurukul Kangri Collection, Haridwar

Digitized by Arya Samaj Foundation Chennai and eGangotri

$$U_2 = i(f'_2 f_2 + g'_2 g_2 (\mathbf{k}_2 \cdot \mathbf{k}'_2)) g'_1 g_1 \sigma \cdot (\mathbf{q} \times \mathbf{k}_1)$$
$$- i(f_2 g'_2 + f'_2 g_2) \sigma_1 \cdot \Big\{ f_1 g'_1 (\mathbf{q} \times \mathbf{k}_2)$$
$$- (f'_1 g_1 - f_1 g'_1) \Big(\mathbf{k}_1 \times \Big(\mathbf{k}_2 - \frac{\mathbf{k}_2 \cdot \mathbf{q}}{|\mathbf{q}|^2} \mathbf{q} \Big) \Big) \Big\}$$
$$+ i(f'_1 f_1 + g'_1 g_1 \mathbf{k}'_1 \cdot \mathbf{k}_1) g'_2 g_2 \sigma_2 \cdot (\mathbf{q} \times \mathbf{k}_2)$$
$$- i(f_1 g'_1 + f'_1 g_1) \sigma_2 \cdot \Big\{ f_2 g'_2 (\mathbf{q} \times \mathbf{k}_1)$$
$$+ (f_2 g'_2 - f'_2 g_2) \Big(\mathbf{k}_1 - \frac{\mathbf{k}_1 \cdot \mathbf{q}}{|\mathbf{q}|^2} \mathbf{q} \Big) \times \mathbf{k}_2 \Big\}. \tag{13}$$

$$U_3 = (\sigma_1 . \sigma_2) [f'_1 f_2 g_1 g'_2 \, \mathbf{k}_1 \cdot \mathbf{k}'_2 + f_1 f'_2 g'_1 g_2 \, \mathbf{k}'_1 \cdot \mathbf{k}_2$$
$$- f_1 f_2 g'_1 g'_2 \, \mathbf{k}'_1 \cdot \mathbf{k}'_2 - f'_1 f'_2 g_1 g_2 \, \mathbf{k}_1 . \mathbf{k}_2], \tag{14}$$

$$U_4 = [f_1 f_2 g'_1 g'_2 (\sigma_1 \cdot \mathbf{k}'_2)(\sigma_2 \cdot \mathbf{k}'_1) + f'_1 f'_2 g_1 g_2 (\sigma_1 . \mathbf{k}_2)(\sigma_2 \cdot \mathbf{k}_1)$$
$$- f'_1 f_2 g_1 g'_2 (\sigma_1 \cdot \mathbf{k}'_2)(\sigma_2 \cdot \mathbf{k}_1) - f_1 f'_2 g'_1 g_2 (\sigma_1 \cdot \mathbf{k}_2)(\sigma_2 \cdot \mathbf{k}'_1)$$
$$- g_1 g_2 g'_1 g'_2 (\sigma_1 \cdot (\mathbf{q} \times \mathbf{k}_1))(\sigma_2 . (\mathbf{q} \times \mathbf{k}_2))$$
$$- (f'_1 g_1 - f_1 g'_1)(f_2 g'_2 - f'_2 g_2) \sigma_1 . (\mathbf{q} \times \mathbf{k}_1) \sigma_2 \cdot (\mathbf{q} \times \mathbf{k}_2)]. \tag{15}$$

In the above, we have substituted $\sigma_1 = \sigma \otimes I$ and $\sigma_2 = I \otimes \sigma$. For an identification of the above terms, and otherwise, we may verify the nonrelativistic limit as

$$U_1 \simeq 1 - \Big(\frac{1}{8m_1^2} + \frac{1}{8m_2^2} \Big) \mathbf{q}^2 + \frac{1}{m_1 m_2} \Big(- \mathbf{k}_1 \cdot \mathbf{k}_2 + \frac{(\mathbf{k}_1 \cdot \mathbf{q})(\mathbf{k}_2 \cdot \mathbf{q})}{|\mathbf{q}|^2} \Big), \tag{16}$$

$$U_2 \simeq \frac{i}{4m_1^2} \sigma_1 \cdot (\mathbf{q} \times \mathbf{k}_1) - \frac{i}{2m_1 m_2} \sigma_1 \cdot (\mathbf{q} \times \mathbf{k}_2)$$
$$+ \frac{i}{4m_2^2} \sigma_2 \cdot (\mathbf{q} \times \mathbf{k}_2) - \frac{i}{2m_1 m_2} \sigma_2 \cdot (\mathbf{q} \times \mathbf{k}_1), \tag{17}$$

$$U_3 \simeq (\sigma_1 \cdot \sigma_2) \mathbf{q}^2 / (4m_1 m_2), \tag{18}$$

and

$$U_4 \simeq - \frac{1}{4 m_1 m_2} (\sigma_1 \cdot \mathbf{q})(\sigma_2 \cdot \mathbf{q}). \tag{19}$$

The terms in this limit are, as expected, identical (Berestetskii *et al* 1971) except for an apparent change in sign for the terms involving σ_2. This arises due to the difference in the convention regarding the writing of the state. The masses of Q and $\tilde{Q}$ may be different. We note that in the above, U_2 yields the spin orbit term, (2/3) U_3 yields the hyperfine term and (1/3) $U_3 + U_4$ yields the tensor term (Rosner 1981). The completely nonrelativistic version corresponds to $U_1 = 1$ and $U_2 = U_3 = U_4 = 0$. In the present analysis however, we shall use the fully relativistic expressions (12) to (15).

To obtain the total Hamiltonian operator, we now note that the free field

CC-0. In Public Domain. Gurukul Kangri Collection, Haridwar

Digitized by Arya Samaj Foundation Chennai and eGangotri

Hamiltonian density is given as

$$\mathscr{H}_0(x) = \sum :\psi_Q^\dagger(x)\,(-i\alpha\cdot\nabla + \beta m_Q)\psi_Q(x): \tag{20}$$

$$T = \int \mathscr{H}_0\,(\mathbf{x})\,\mathrm{d}\mathbf{x}$$

$$= \int [Q_I\,(\mathbf{k}_1)^\dagger Q_I(\mathbf{k}) p_1^0 - :\tilde{Q}_I(\mathbf{k}_1)^\dagger \tilde{Q}_I(\mathbf{k}_1): p_2^0]\,\mathrm{d}\mathbf{k}_1\,, \tag{21}$$

where, obviously, $p_1^0 = (m_1^2 + \mathbf{k}^2)^{1/2}$ and $p_2^0 = (m_2^2 + \mathbf{k}^2)^{1/2}$.

Thus the effective Hamiltonian operator for the quark Q of mass m_1 and antiquark $\tilde{Q}$ of mass m_2 is given by, with (10) and (21),

$$H = T + P. \tag{22}$$

We generate the nonrelativistic limit of the Hamiltonian by substituting e.g. $p_1^0 = m_1 + \mathbf{k}_1^2/(2m_1)$ and using equations (16) to (19), which will yield Schrödinger equation with appropriate spin orbit, hyperfine and tensor interactions. We shall here however retain the relativistic expressions everywhere. We *shall not* however, use differential equations (which will be obviously impossible to solve), but utilize instead the alternative scheme of approximations through choosing a basis and diagonalizing the Hamiltonian operator.

2.2 *The basis for mesons*

We shall now consider the *basis* for the quark-antiquark states. For this purpose, let the radial quantum number be n, and the orbital quantum numbers l and m, we write the $S = 0$ states as (Misra 1978)

$$|n, J, J_z, \mathbf{0}\rangle = \frac{1}{\sqrt{6}} \int \tilde{u}_{nJ}(K_1)\, \mathscr{Y}_{JJ_z}(\hat{k}_1)\,\mathrm{d}\mathbf{k}_1\,\mathrm{d}\mathbf{k}_2$$

$$\times \delta(\mathbf{k}_1 + \mathbf{k}_2)\, Q_I^i(\mathbf{k}_1)^\dagger \tilde{Q}_I^i(\mathbf{k}_2)|\mathrm{vac}\rangle. \tag{23}$$

As earlier, (23) defines a "meson" state of zero momentum. Also $(l, m) = (J, J_z)$, i is the colour index which is summed. $K_1 = |\mathbf{k}_1|$, and $\hat{k}_1 = \mathbf{k}_1/K_1$. Also, the relationship with the basis in coordinate space is given by

$$\tilde{u}_{nl}(K) = (2/\pi)^{1/2} \int u_{nl}(r) j_l(Kr)\, r^2\,\mathrm{d}r \tag{24}$$

and

$$\mathscr{Y}_{lm}(\Omega) = (-i)^l Y_{lm}(\Omega).$$

Obviously, we have put

$$\tilde{u}_{nl}(K)\, \mathscr{Y}_{lm}(\hat{k}) = (2\pi)^{-3/2} \int u_{nl}(r) Y_{lm}(\hat{r}) \exp(-i\mathbf{k}\cdot\mathbf{r})\,\mathrm{d}\mathbf{r}. \tag{25}$$

We shall substitute $\tilde{u}_{nl}(K)\mathscr{Y}_{lm}(\hat{k}) \equiv \tilde{u}_{nlm}(\mathbf{k})$ and $u_{nl}(r)Y_{lm}(\hat{r}) \equiv u_{nlm}(\mathbf{r})$. These states satisfy the usual ortho-normalization condition. We note that here $\tilde{u}_{nlm}(\mathbf{k})$ or $u_{nlm}(\mathbf{r})$ form a *complete* set of orthonormal basis, such that (23) includes all possible spin singlet states which can be constructed with the given angular momenta. Construction of such states with a field theoretic *notation* in (23) is here merely a matter of convenience, which was used earlier*.

---

* Incoherent phenomena with the same type of states as above have also been considered (Misra 1980; Misra and Panda 1980).

CC-0. In Public Domain. Gurukul Kangri Collection, Haridwar

Digitized by Arya Samaj Foundation Chennai and eGangotri

We next construct $S = 1$ states. This will involve addition of angular momenta. We however choose a Cartesian basis for spin and write

$$|n, l, J J_z; \mathbf{0}\rangle = \frac{1}{\sqrt{6}} \int \tilde{u}_{nl}(K_1) g_m(l, J, J_z, \hat{k}_1) \delta(\mathbf{k}_1 + \mathbf{k}_2)\, \mathrm{d}\mathbf{k}_1\, \mathrm{d}\mathbf{k}_2$$
$$\times Q_I^i((\mathbf{k}_1)^\dagger \sigma_m \tilde{Q}_I^i(\mathbf{k}_2))|\mathrm{vac}\rangle. \tag{26}$$

Here, there is summation over the dummy index m, and, as mentioned, σ_m are the Cartesian (usual) components of the Pauli spin vector. Further, $g_m(l, J; J_z; \hat{k}_1)$ is determined from the equation

$$g_m(l, J, J_z; \hat{k}_1)\sigma_m = \langle lm'1m'_1 \mid J J_z\rangle \mathscr{Y}_{lm'}(\hat{k}_1)\sigma^P_{m'_1}. \tag{27}$$

In (27), $\sigma^P_{m'_1}$ are the Pauli spin matrices in polar co-ordinates given as

$$\sigma^P_1 = -\frac{1}{\sqrt{2}}(\sigma_1 + i\sigma_2); \quad \sigma^P_0 = \sigma_3; \quad \sigma^P_{-1} = \frac{1}{\sqrt{2}}(\sigma_1 - i\sigma_2). \tag{28}$$

Equation (26) yields all possible "meson" states having $S = 1$ and with zero momentum. Clearly $l = J + 1$, J or $J - 1$ and in contrast to (23), (26) implies that it is a state with $S = 1$. The quantities $g_m(l, J, J_z, \hat{k}_1)$ are explicitly given in Appendix A for $l = J - 1$, J and $J + 1$ for ready reference. Equations (23) and (26) yield a complete basis of states, and, we shall use this basis to obtain the matrix elements of the Hamiltonian operator in (22) which will be diagonalized. We next proceed to consider the matrix elements of H.

2.3 *Matrix elements of the Hamiltonian for vector exchange*

We note that the states as in (26) involve the normalization

$$\langle \mathbf{p}|\mathbf{p}'\rangle = \delta(\mathbf{p} - \mathbf{p}'), \tag{29}$$

and thus when $\mathbf{p} = \mathbf{p}' = 0$, there will be a spurious infinity. In order to get rid of the above and obtain the matrix elements of H or of T and P, we shall use the translational invariance. In fact, we then have, e.g.,

$$\langle n' J' J'_z|T|nJJ_z\rangle = (2\pi)^3 \langle n' J' J'_z; \mathbf{0}|\mathscr{H}_0(0)|nJJ_z; \mathbf{0}\rangle. \tag{30}$$

Similarly,

$$\langle n' J' J'_z|P|nJJ_z\rangle = (2\pi)^3 \langle n' J' J'_z; \mathbf{0}|v(0)|nJJ_z; \mathbf{0}\rangle. \tag{31}$$

These define the conventional matrix elements of $H = T + P$. Obviously from Wigner Eckart theorem the above matrix elements, and those with $|nlJJ_z; \mathbf{0}\rangle$ for $S = 1$ states, will automatically maintain the rotational invariance.

We may notice one aspect of (31) which will soon arise in applications. The confining potentials, strictly speaking, *do not* have Fourier transforms, and this gets reflected in there being *spurious* infrared divergences when we consider the integral in momentum space, as for example will be the case with $1/|\mathbf{q}|^4$ coming from the "Fourier transform" of the linear potential. This aspect will be tackled later. We shall conveniently adopt the

CC-0. In Public Domain. Gurukul Kangri Collection, Haridwar

Digitized by Arya Samaj Foundation Chennai and eGangotri

harmonic oscillator basis. Thus we take (Davydov 1968)

$$\tilde{u}_{nl}(K) \equiv f_{nl}(K)(RK)^l \exp(-\tfrac{1}{2}R^2K^2), \tag{32}$$

where

$$f_{nl}(K) = (-1)^n N_{nl} R^{3/2} F(-n, l+\tfrac{3}{2}, R^2K^2). \tag{33}$$

In (33),

$$N_{nl} = [2\Gamma(n+l+\tfrac{3}{2})/\Gamma(n+1)]^{1/2}/\Gamma(l+\tfrac{3}{2}) \tag{34}$$

and the hypergeometric function is given as

$$F(-n, l+\tfrac{3}{2}, R^2K^2) = \sum_{k=0}^{n} A(n, l, k)(R^2K^2)^k, \tag{35}$$

where

$$A(n, l, k) = \frac{(-1)^k}{\Gamma(k+1)} \cdot \frac{\Gamma(n+1)}{\Gamma(n-k+1)} \cdot \frac{\Gamma(l+3/2)}{\Gamma(l+k+3/2)}. \tag{36}$$

(i) *Matrix elements for $S = 0$ states*

We shall now utilize equations (30) and (31). The states are given by (23). The matrix elements of T are trivially obtained. In fact, we have, for a given J,

$$\langle n'|T^{(J)}|n\rangle = \int f_{n'J}(K) f_{nJ}(K)(R^2K^2)^J (p_1^0 + p_2^0) \exp(-R^2K^2) K^2 \, dK, \tag{37}$$

where, $p_1^0 = (m_1^2 + K^2)^{1/2}$ and $p_2^0 = (m_2^2 + K^2)^{1/2}$. The matrix elements for the potential P in (10) will need the evaluation of (11) corresponding to the state (23). In fact, we obtain that

$$\langle n' J J_Z | P_V | n J J_Z \rangle \equiv \langle n' | P_V^J | n \rangle \tag{38}$$

$$= (2\pi)^{-3} \int \tilde{u}_{n'J}(K_1') \mathcal{Y}_{JJ_z}(\hat{k}_1')^* F_{PS}^V(\mathbf{k}_1', \mathbf{k}_1) \times \tilde{u}_{nJ}(K_1) \mathcal{Y}_{JJ_z}(\hat{k}_1) \tilde{V}_c^V(\mathbf{q}) \, d\mathbf{k}_1' \, d\mathbf{k}_1. \tag{39}$$

In (39) $\tilde{V}_c(\mathbf{q}) = (-4/3)\tilde{V}(\mathbf{q})$, and we have substituted

$$F_{PS}^V(\mathbf{k}_1', \mathbf{k}_1) = \tfrac{1}{2} \mathrm{Tr}[\bar{u}(\mathbf{k}_1')\gamma^\mu u(\mathbf{k}_1) v(-\mathbf{k}_1)\gamma_\mu v(-\mathbf{k}_1')]$$

$$+ \frac{1}{2|\mathbf{q}|^2} \mathrm{Tr}[\bar{u}(\mathbf{k}_1')(\gamma \cdot \mathbf{q}) u(\mathbf{k}_1) \bar{v}(-\mathbf{k}_1)(\gamma . \mathbf{q}) v(-\mathbf{k}_1')]. \tag{40}$$

In (39) and (40) as before, $\mathbf{k}_1' = \mathbf{k}_1 + \mathbf{q}$. In the context of the potential operator in (10) and (11) we have in fact

$$F_{PS}^V = \tfrac{1}{2} \mathrm{Tr}[U_1 + U_2 + U_3 + U_4]. \tag{40a}$$

Here, with A and B as 2×2 matrices of U_i, $i = 1, 2, 3, 4$ in (12) to (15), and in the context of our definition of the states in (23), we have here used the notation that $\mathrm{Tr}[A \otimes B] = \mathrm{Tr}[AB]$. We have also substituted $\mathbf{k}_2 = -\mathbf{k}_1, \mathbf{k}_2' = -\mathbf{k}_1'$ in the matrices U_i for evaluation of F_{PS}. These can be explicitly verified while evaluating (31). We also substitute $\mathbf{k}_1 = \mathbf{K} - \frac{1}{2}\mathbf{q}$, $\mathbf{k}_1' = \mathbf{K} + \frac{1}{2}\mathbf{q}$ such that $\mathbf{k}_1' \cdot \mathbf{k}_1 = K^2 - \frac{1}{4}Q^2$, where

CC-0. In Public Domain. Gurukul Kangri Collection, Haridwar

Digitized by Arya Samaj Foundation Chennai and eGangotri

$Q = |\mathbf{q}|$. Also we take $\mathbf{k}.\mathbf{q} = KQ\cos\theta$. We then put, from rotational invariance, $F_{PS}(\mathbf{k}_1', \mathbf{k}_1) = F_{PS}(K, Q, \cos\theta)$. In the nonrelativistic limits with equations (16) to (19) we explicitly have

$$F^{V}_{PS} \simeq \left(1 + \frac{K^2 \sin^2\theta}{m_1 m_2}\right) + \frac{Q^2}{8}\left(\frac{4}{m_1 m_2} - \frac{1}{m_1^2} - \frac{1}{m_2^2}\right). \tag{40b}$$

The relativistic expression is given in Appendix B. We also obtain, *summing* (39) *for different* J_z *values and dividing by* $(2J+1)$, that

$$\begin{aligned}\langle n'|P^J_V|n\rangle &= (2\pi)^{-3}\int f_{n'J}(K_1')\, f_{nJ}(K_1)\,(R^2 K_1' K_1)^J \cdot \frac{1}{4\pi}\cdot P_J(\cos\theta_1) \\ &\quad \times F^{V}_{PS}(K, Q, \cos\theta)\,\tilde{V}_c(Q)\exp(-R^2K^2 - \tfrac{1}{4}R^2Q^2)\,\mathrm{d}\mathbf{q}\,\mathrm{d}\mathbf{K} \\ &= \frac{1}{4\pi^2}\int f_{n'J}(K_1')\, f_{nJ}(K_1)\,(R^2K_1'K_1)^J P_J(\cos\theta_1) \\ &\quad \times F^{V}_{PS}(K, Q, \cos\theta)\,\tilde{V}^{V}_c(Q)\exp(-R^2K^2 - \tfrac{1}{4}R^2Q^2) \\ &\quad \times K^2\mathrm{d}K Q^2\mathrm{d}Q\,\mathrm{d}(\cos\theta).\end{aligned} \tag{41}$$

We note that $|\mathbf{k}_1| = \left(K^2 + \frac{Q^2}{4} - KQ\cos\theta\right)^{1/2}$ and $|\mathbf{k}_1'| = \left(K^2 + \frac{Q^2}{4} + KQ\cos\theta\right)^{1/2}$.

As earlier stated for a confining potential like ar, $\tilde{V}(Q)$ varies as $1/Q^4$, and thus (41) will have an apparent infrared divergence. This however is spurious, since in coordinate space the corresponding matrix elements converge. This is associated with the fact that ar has *no* Fourier transform. We may replace r by $r\exp(-\lambda r)$, in which case the Fourier transform is $-8\pi(Q^2 - 3\lambda^2)/(Q^2+\lambda^2)^3$, which has *no* infrared divergence. We can next take the limit $\lambda \to 0$.

We also now discuss an alternative procedure for dealing with the situation. Let us substitute

$$\begin{aligned}F_V(K, Q, \cos\theta) &= f_{n'J}(K_1')\, f_{nJ}(K_1)\,(R^2K_1'K_1)^J\, P_J(\cos\theta_1) \\ &\quad \times F^{V}_{PS}(K, Q, \cos\theta).\end{aligned} \tag{42}$$

When $Q = 0$, we obtain,

$$F_V(K, 0, \cos\theta) = f_{n'J}(K)\, f_{nJ}(K)\,(R^2K^2)^J\, F^{V}_{PS}(K, 0, \cos\theta). \tag{43}$$

We note that terms $(\mathbf{q}\cdot\mathbf{k}_1')(\mathbf{q}\cdot\mathbf{k}_1)/|\mathbf{q}|^2$ introduces $\cos\theta$ dependence for the other terms in (43). Clearly

$$F_V(K, Q, \cos\theta) - F_V(K, 0, \cos\theta) \tag{44}$$

will have a zero in Q, which, we shall see, will in general be adequate to cancel the divergence introduced in $\tilde{V}_c(Q)$ for small Q. We shall thus write

$$\langle n'|P^J_V|n\rangle = \langle n'|P^J_{V0}|n\rangle + \langle n'|\Delta P^J_V|n\rangle, \tag{45}$$

CC-0. In Public Domain. Gurukul Kangri Collection, Haridwar

Digitized by Arya Samaj Foundation Chennai and eGangotri

where

$$\langle n'|\Delta P^J_V|n\rangle = \frac{1}{4\pi^2}\int (F_V(K,Q,\cos\theta) - F_V(K,0,\cos\theta)) \times \exp(-R^2K^2 - \tfrac{1}{4}R^2Q^2)\,\tilde{V}^V_c(Q)K^2\,dK\,Q^2\,dQ\,d(\cos\theta) \quad (46)$$

and

$$\langle n'|P^J_{V0}|n\rangle = \langle n'|I^J_{V0}|n\rangle V^V_0, \quad (47)$$

where

$$\langle n'|I^J_{V0}|n\rangle = \tfrac{1}{2}\int F_V(K,0,\cos\theta)\exp(-R^2K^2)K^2\,dK\,d(\cos\theta), \quad (48)$$

and

$$V^V_0(R) \equiv P_0 \equiv \frac{1}{2\pi^2}\int \tilde{V}^V_c(Q)\exp(-\tfrac{1}{4}R^2Q^2)\,Q^2\,dQ \quad (49)$$

$$= \frac{4}{\pi^{1/2}R^3}\int V^V_c(r)\exp(-r^2/R^2)r^2\,dr. \quad (50)$$

We note that separability of the integrals in the matrix elements of P^J enabled us to evaluate the *formal* integral (49) in coordinate space by equation (50), where the Fourier transform (7) has been utilized. For the QCD potential, usually well defined in the momentum space, a further variation of the technique will be needed, which will be described later at the appropriate place. For the phenomenological potentials defined in coordinate space, (50) will be adequate in dealing with the above spurious divergence. We may also note that P_0 is *independent* of the states under consideration, and, *depends only* on the basis through the variable R^2.

(ii) *Matrix elements for $S = 1$ states*

Here, for the matrix elements of H, or of T and P, we have to choose states as given by (26) instead of (23). We first note that corresponding to (21), the l dependence will be absent in T, such that, explicitly from an equation similar to (30), we get

$$\langle n'l'|T^l|nl\rangle = \delta_{ll'}\int f_{n'l}(K)f_{nl}(K)(R^2K^2)^l(p_1^0 + p_2^0)\exp(-R^2K^2)K^2\,dK. \quad (51)$$

Equation (51) is parallel to (37) written down earlier.

We next consider the matrix elements of P in equation (10), which as before, will need the evaluation of $\langle n', l', J', J'_z; \mathbf{0}|v(0)|n, l, J, J_z; \mathbf{0}\rangle$ parallel to (31). Looking at the states as in (26), we note that for this purpose we shall need the expression

$$F^V_{m'm}(\mathbf{k}'_1, \mathbf{k}_1) = \tfrac{1}{2}\mathrm{Tr}[\bar{u}(\mathbf{k}'_1)\gamma^\mu u(\mathbf{k}_1)\sigma_m\bar{v}(-\mathbf{k}_1)\gamma_\mu v(-\mathbf{k}'_1)\sigma_{m'}] + \frac{1}{2|\mathbf{q}|^2}\mathrm{Tr}[\bar{u}(\mathbf{k}'_1)(\gamma\cdot\mathbf{q})u(\mathbf{k}_1)\sigma_m\bar{v}(-\mathbf{k}_1)(\gamma\cdot\mathbf{q}) v(-\mathbf{k}'_1)\sigma_{m'}] \quad (52)$$

which is the parallel of (40). In fact, we really have, in the context of potential operator (10) and (11), the relationship

$$F^V_{m'm}(\mathbf{k}'_1, \mathbf{k}_1) = \tfrac{1}{2}\mathrm{Tr}[(U_1 + U_2 + U_3 + U_4)\sigma_m \otimes \sigma_{m'}] \quad (52a)$$

where, as in (40), $\mathbf{k}_2 = -\mathbf{k}_1$ and $\mathbf{k}'_2 = -\mathbf{k}'_1$ in equations (12) to (15). Further, as earlier

CC-0. In Public Domain. Gurukul Kangri Collection, Haridwar

Digitized by Arya Samaj Foundation Chennai and eGangotri

we have used the notation that

$$\mathrm{Tr}\,[(A\otimes B)\,\sigma_m\otimes\sigma_{m'}] = \mathrm{Tr}\,[A\sigma_m B\sigma_{m'}]$$

as is obvious in the context of definitions of the states in (26). The relativistic expression for $F^{V}_{m'm}$ is explicitly given in Appendix B. In the nonrelativistic limits with equations (16) to (19), we explicitly have,

$$F^{V}_{m'm} = \delta_{m'm}\left[1-\left(\frac{1}{m_1^2}+\frac{1}{m_2^2}\right)\mathbf{q}^2+\frac{K^2\sin^2\theta}{m_1m_2}\right]$$
$$+\left(\frac{1}{4m_1^2}+\frac{1}{4m_2^2}+\frac{1}{m_1m_2}\right)(q_{m'}K_m-K_{m'}q_m)-\frac{1}{2m_1m_2}q_{m'}q_m. \quad (52b)$$

We then obtain, parallel to equation (39)

$$\langle n'l'|P^J|nl\rangle \equiv (2\pi)^3\int \tilde{u}_{n'l'}(K_1')\,g^*_{m'}(l',J,J_z,\hat{k}_1')\,F^{V}_{m'm}(\mathbf{k}_1',\mathbf{k}_1)$$
$$\times g_m(l,J,J_z,\hat{k}_1)\,\tilde{u}_{nl}(K_1)\,\tilde{V}_c(\mathbf{q})\mathrm{d}\mathbf{k}_1\,\mathrm{d}\mathbf{k}_1'. \quad (53)$$

In (53), summation over m and m' is understood; however, J_z remains fixed, although, as earlier, from rotational invariance the expressions are *independent* of J_z.

We next substitute, for convenience,

$$F^{V}_{V}(\mathbf{k}_1',\mathbf{k}_1) = \frac{4\pi}{2J+1}\sum_{J_z}\sum_{m',m} g^*_{m'}(l',J,J_z,\hat{k}_1')\,F^{V}_{m'm}(\mathbf{k}_1',\mathbf{k}_1)g_m(l,J,J_z,\hat{k}_1)$$

$$\equiv \sum A^{V}_{m'm}\,F^{V}_{m'm}(\mathbf{k}_1',\mathbf{k}_1). \quad (54)$$

The expression for $A^{V}_{m'm}$ for different l and J values are given in Appendix A. We then have, for triplet matrix elements,

$$\langle n'l'|P^J_V|nl\rangle = \frac{1}{4\pi^2}\int f_{n'l'}(K_1')f_{nl}(K_1)(RK_1')^{l'}(RK_1)^l\,F^{V}_{V}(K,Q,\cos\theta)$$
$$\times\,\tilde{V}^{V}_c(Q)\exp(-R^2K^2-\tfrac{1}{4}R^2Q^2)K^2\,\mathrm{d}K\,Q^2\,\mathrm{d}Q\,\mathrm{d}(\cos\theta). \quad (55)$$

This equation is the parallel of equation (41). In $F^{V}_{V}(\mathbf{k}_1',\mathbf{k}_1)$ the superscript V represents the interaction is due to vector exchange and subscript V represents the state is spin 1 state. The complete expression for $F^{V}_{V}(\mathbf{k}_1',\mathbf{k}_1)$ is given in Appendix B. As before, it will have a *spurious* infrared divergence, which can be tackled in the same way. Here, instead of (42), we shall have to make the substitution.

$$F_V(K,Q,\cos\theta) = f_{n'l'}(K_1')f_{nl}(K_1)(RK_1')^{l'}(RK_1)^l\,F^{V}_{V}(K,Q,\cos\theta) \quad (56)$$

and proceed in the same manner parallel to equations (42) to (50). In particular we may note that P_0 of equation (50) remains unaltered; however the other expressions need to be appropriately modified.

2.4 *Matrix element for the Hamiltonian for scalar exchange*

For the sake of completeness, we supplement an interaction potential due to exchange of a scalar particle to the earlier described interaction potential due to vector exchange

CC-0. In Public Domain. Gurukul Kangri Collection, Haridwar

Digitized by Arya Samaj Foundation Chennai and eGangotri

(Gupta *et al* 1982). We then have parallel to (38), the contribution of P_s^J from scalar interaction obtained with $F_{PS}^{V}(\mathbf{k}_1', \mathbf{k}_1)\tilde{V}_c^{V}(Q)$ being replaced by $F_{PS}^{S}(\mathbf{k}_1', \mathbf{k}_1)\tilde{V}_c^{S}(Q)$. Here,

$$F_{PS}^{S}(\mathbf{k}_1', \mathbf{k}_1) = -\tfrac{1}{2}\,\mathrm{Tr}\,[\bar{u}(\mathbf{k}_1')u(\mathbf{k}_1)\bar{v}(-\mathbf{k}_1)v(-\mathbf{k}_1')], \tag{57}$$

which is more explicitly given in Appendix B. We may note that the negative sign arises due to the normalization of spinors. Now parallel to (19) we have the nonrelativistic limit of (57) as

$$F_{PS}^{S}(\mathbf{k}_1', \mathbf{k}_1) = 1 - \left(\frac{1}{2m_1^2} + \frac{1}{2m_2^2}\right)K^2. \tag{58}$$

Also $F_V(K, Q, \cos\theta)$ and $F_{PS}^{V}(K, Q, \cos\theta)$ in equation (42) are replaced by $F_S(K, Q, \cos\theta)$ and $F_{PS}^{S}(K, Q, \cos\theta)$ respectively. Further, in (45) and (46), P_V^J and ΔP_V^J will be replaced by P_S^J and ΔP_S^J respectively. The potential $\tilde{V}_c^{V}(Q)$ for vector exchange interaction will be replaced by $\tilde{V}_C^{S}(Q)$ in this case. For spin 1 states, parallel to (52) there will be $F_{m'm}^{S}(\mathbf{k}_1', \mathbf{k}_1)$ written as

$$F_{m'm}^{S}(\mathbf{k}_1', \mathbf{k}_1) = -\tfrac{1}{2}\,\mathrm{Tr}\,[\bar{u}(\mathbf{k}_1')u(\mathbf{k}_1)\sigma_m\bar{v}(-\mathbf{k}_1)v(-\mathbf{k}_1')\sigma_{m'}] \tag{59}$$

which is more explicitly given in Appendix B. However, we give the expression for the nonrelativistic limit of (59) as,

$$F_{m'm}^{S}(\mathbf{k}_1', \mathbf{k}_1) = \delta_{m'm}\left(1 - \left(\frac{1}{2m_1^2} + \frac{1}{2m_2^2}\right)K^2\right) - \left(\frac{1}{4m_1^2} + \frac{1}{4m_2^2}\right)\varepsilon_{imm'}(\mathbf{q}\times\mathbf{k})_i. \tag{60}$$

Parallel to (53) we have now,

$$\langle n'l'|P_S^J|nl\rangle = (2\pi)^3 \int \tilde{u}_{n'l'}(K_1')\, g_{m'}(l', J, J_z, \hat{k}_1')\, F_{m'm}^{s}(\mathbf{k}_1', \mathbf{k}_1) \times g_m(l, J, J_z, \hat{k}_1)\,\tilde{u}_{nl}(K_1)\,\tilde{V}_c^{s}(\mathbf{q})\,\mathrm{d}\mathbf{k}_1'\,\mathrm{d}\mathbf{k}_1. \tag{61}$$

In equation (54) $F_{m'm}^{V}(\mathbf{k}_1', \mathbf{k}_1)$ will be replaced by $F_{m'm}^{s}(\mathbf{k}_1', \mathbf{k}_1)$. There will be another expression $F^{s}(K, Q, \cos\theta)$ parallel to (56) due to scalar exchange.

For spin zero states now the matrix element for total potential is written as

$$\begin{aligned}\langle n'|P|n\rangle &= \langle n'|P_V^J|n\rangle + \langle n'|P_S^J|n\rangle \\ &= \frac{1}{4\pi^2}\int f_{n'J}(K_1')\, f_{nJ}(K)\,(R^2KK')^l\, P_J(\cos\theta_1) \\ &\quad\times [F_{PS}^{V}(K, Q, \cos\theta)\,\tilde{V}_c^{V}(Q) + F_{PS}^{S}(K, Q, \cos\theta)\,\tilde{V}_c^{S}(Q)] \\ &\quad\times \exp(-R^2K^2 - \tfrac{1}{4}R^2Q^2)\,K^2\mathrm{d}K\,Q^2\mathrm{d}Q\,\mathrm{d}(\cos\theta).\end{aligned} \tag{62}$$

Similarly for spin 1 case, the matrix elements for the total potential is given by,

$$\langle n'|P^J|n\rangle = \langle n'l'|P_V^J|nl\rangle + \langle n'l'|P_S^J|nl\rangle$$

CC-0. In Public Domain. Gurukul Kangri Collection, Haridwar

Digitized by Arya Samaj Foundation Chennai and eGangotri

$$= \frac{1}{4\pi^2} \int f_{n'l'}(K'_1) f_{nl}(K_1) (RK'_1)^{l'} (RK_1)^{l} [F^{V}_{V}(K, Q, \cos\theta) \times \tilde{V}^{V}_{c}(Q) + F^{S}_{V}(K, Q, \cos\theta) V^{S}_{c}(Q)] \exp(-R^2K^2 - \tfrac{1}{4}R^2Q^2) \times K^2 dK\, Q^2 dQ\, d(\cos\theta). \quad (63)$$

3. Approximation schemes

We have given here the general framework for the sake of completeness. $S = 0$ and $S = 1$ states do not mix due to CP invariance. Then, with specific values of J^P, we can construct the matrix elements of H corresponding to a *finite* subset of the basis, and diagonalize the Hamiltonian. For a large enough basis, we expect progressive convergence for the masses of the low-lying levels. However, we may note that R^2 is an arbitrary parameter of the basis, and the dynamics, including the mass levels, has to be independent of this. Further, a small subset of the basis may yield more *rapid* convergence to the actual wave functions for a suitable value of R^2 as compared to other values. Hence, we shall obviously adopt the variational procedure to optimize the basis in the context of the eigenvalues; in fact, for each finite choice of elements of the basis, we shall first do so. The rate of convergence of the results when we change the number of elements of the basis will broadly indicate the degree of reliability of the corresponding values quoted. We shall now develop an approximation which is relativistic, but depends on the dominance of the values of the matrix elements on small values of the variable Q. Such an approximation may be sometimes reasonable since $\tilde{V}(Q)$ has terms like $1/Q^2$ or $1/Q^4$.

(a) *Small Q dominance*

To make this approximation, we first note that $F(K, Q, \cos\theta)$ in (46) is effective always even in $\cos\theta$. Hence we can use the expansion in Q^2 yielding

$$F(K, Q, \cos\theta) - F(K, 0, \cos\theta) = -Q^2 F_1(K, \cos\theta). \quad (64)$$

One *then* has from (46)

$$\langle n' | \Delta P^J | n \rangle = \langle n' | I_1 | n \rangle V_1, \quad (65)$$

where

$$V_1 = V_1(R) = \frac{R^2}{2\pi^2} \int (-Q^2 \tilde{V}(Q)) \exp(-R^2Q^2/4) Q^2 dQ, \quad (66)$$

and

$$\langle n' | I_1^J | n \rangle = \frac{1}{2R^2} \int F_1(K, \cos\theta) \exp(-R^2K^2) K^2 dK\, d(\cos\theta). \quad (67)$$

In (66) for the Cornell potential, or Martin potential, the momentum space integration has no spurious divergence. In case we find this to be there, we can use equation (7) and write the parallel of equation (50). As mentioned, the method here includes relativistic corrections, but depends crucially on the dominance of the matrix elements for small Q. One can still make a nonrelativistic approximation for

CC-0. In Public Domain. Gurukul Kangri Collection, Haridwar

Digitized by Arya Samaj Foundation Chennai and eGangotri

$F_1(K, \cos\theta)$ in (64) and derive the conventional results of Schrödinger equation, including the corrections mentioned in equation (16) to (19).

We may now consider e.g. the Cornell potential (Eichten *et al* 1978) given as

$$V_c(r) = -\frac{K_0}{r} + ar. \tag{68}$$

From (7) we have

$$\tilde{V}_c(Q) = -\left[\frac{4\pi K_0}{Q^2} + \frac{8\pi a}{Q^4}\right]. \tag{69}$$

Also, we get

$$V_0|_{\text{Cornell}} = \frac{2}{\sqrt{\pi}\,R}[-K_0 + aR^2], \tag{70}$$

and

$$V_1|_{\text{Cornell}} = \frac{4}{\sqrt{\pi}\,R^3}[K_0 + aR^2]. \tag{71}$$

For the Martin potential (Martin 1980) given as

$$V_c(r) = A + Br^{\alpha}, \tag{72}$$

we similarly get

$$V_0|_{\text{Martin}} = A + B\cdot\frac{2R^{\alpha}}{\sqrt{\pi}}\,\Gamma\left(\frac{3+\alpha}{2}\right), \tag{73}$$

and

$$V_1|_{\text{Martin}} = B\cdot\frac{2}{\sqrt{\pi}}\,\alpha(\alpha+1)R^{\alpha}\,\Gamma\left(\frac{\alpha+1}{3}\right). \tag{74}$$

We next note that for the Richardson potential (Richardson 1979) from (5) and (6) we get

$$\tilde{V}_c(Q) = -\frac{4}{3}\cdot\frac{48\pi^2}{(33-2n_f)}\cdot\frac{1}{Q^2\ln(1+Q^2/\Lambda^2)}. \tag{75}$$

For small Q, we clearly have

$$\tilde{V}_c(Q) = -\frac{4}{3}\cdot\frac{48\pi^2}{(33-2n_f)}\cdot\frac{\Lambda^2}{Q^4}, \tag{76}$$

such that from (69) this part behaves in coordinate space like ar with

$$a = \frac{4}{3}\cdot\frac{6\pi\Lambda^2}{(33-2n_f)}.$$

Separating this, we thus obtain from (49) the value of V_0 as

$$V_0|_{\text{Richardson}} = \frac{2R}{\sqrt{\pi}}\cdot\frac{4}{3}\cdot\frac{6\pi\Lambda^2}{(33-2n_f)} + I_{\text{Richardson}}, \tag{77}$$

CC-0. In Public Domain. Gurukul Kangri Collection, Haridwar

Digitized by Arya Samaj Foundation Chennai and eGangotri

where from (49) and (70)

$$I_{\text{Richardson}} = \frac{1}{2\pi^2}\cdot\left(-\frac{4}{3}\right)\cdot\frac{48\pi^2}{(33-2n_f)}\cdot\int\left\{\frac{1}{\ln(1+Q^2/\Lambda^2)}-\frac{\Lambda^2}{Q^2}\right\} \times \exp(-R^2Q^2/4)Q\,\mathrm{d}Q. \tag{78}$$

(b) *Nonrelativistic limit*

The nonrelativistic expressions for $F_V^V(K, Q, \cos\theta)$, $F_{PS}^V(K, Q, \cos\theta)$, $F_V^S(K, Q, \cos\theta)$ and $F_{PS}^S(K, Q, \cos\theta)$ are explicitly given in Appendix B. We can easily compare our expressions due to hyperfine, spin-orbit and tensor interactions with the earlier standard calculations (Rosner 1981). From equation (40b) and (74), the splitting due to the hyperfine interaction is

$$\Delta H|_{\text{hyperfine}} = -\frac{2}{3}\frac{Q^2}{m^2}\tilde{V}_c(Q). \tag{79}$$

In our usual Fourier transform technique

$$\Delta H|_{\text{hyperfine}} = \frac{2}{3m^2}\nabla^2 V(r). \tag{80}$$

From equation (B.13), (B.17) and (B.19) in Appendix B we can compare the expressions due to dyadic, hyperfine, spin-orbit and tensor interactions for different ^3P_J states.

The expressions due to the dyadic term which arises due to the four-component Dirac spinor is the same for all the ^3P_J states. It does not give rise to any splitting and is given by

$$\Delta F_J^V(K, Q, \cos\theta)|_{\text{Dyadic}} = 1 + \frac{K^2\sin^2\theta}{m^2} - \frac{Q^2}{4m^2}. \tag{81}$$

The expressions due to spin-orbit interaction for all the ^3P_J states are given by,

$$R^2K_1K_1'\Delta F_J^V(K, Q, \cos\theta)\Big|_{^3P_0}^{\text{s.o.}} = \frac{3}{2m^2}R^2K^2Q^2\sin^2\theta, \tag{82}$$

$$R^2K_1K_1'\Delta F_J^V(K, Q, \cos\theta)\Big|_{P_1}^{\text{s.o.}} = \frac{3}{4m^2}R^2K^2Q^2\sin^2\theta, \tag{83}$$

and

$$R^2K_1K_1'\Delta F_J^V(K, Q, \cos\theta)\Big|_{^3P_2}^{\text{s.o.}} = -\frac{3}{4m^2}R^2K^2Q^2\sin^2\theta. \tag{84}$$

(c) *Extreme relativistic limit*

In extreme relativistic limit we make a very crude approximation (Bardeen *et al* 1975) by taking quark mass to be zero. In this approximation, the expression for p^0, $f(\mathbf{K})$ and $g(\mathbf{K})$ in equations (9a) and (9b) get simplified as $p^0 = |(\mathbf{K})|$, $f(\mathbf{K}) = 1/\sqrt{2}$ and $g(K) = |\mathbf{K}|/\sqrt{2}$.

To get the matrix elements for kinetic energy, we take $p_1^0 = p_2^0 = p^0 = K$ in equation (51) and easily evaluate the integral. The simplified expressions in this approximation scheme for $F_{PS}^V(\mathbf{k}_1, \mathbf{k}_1')$, $F_{PS}^S(\mathbf{k}_1, \mathbf{k}_1')$, $F_V^V(\mathbf{k}_1, \mathbf{k}_1')$ and $F_V^S(\mathbf{k}_1, \mathbf{k}_1')$, can be

CC-0. In Public Domain. Gurukul Kangri Collection, Haridwar

Digitized by Arya Samaj Foundation Chennai and eGangotri

found out using (B.2a), (B.5a), (B.10a), (B.12a), (B.16a), (B.23a), (B.25a) and (B.29a) of Appendix B.

4. Applications

We now apply our model and the approximation scheme to calculate different mass levels and compare them with the experiments wherever available. To do this, as mentioned earlier, we test the convergence of the minimum energy of a particular state with respect to the number of matrix elements. To test the reliability of our calculations we have applied our scheme to some known calculations, that of Martin (1980) and Bhaduri and Brack (1982). Next, we optimize our potential parameters with respect to the exact relativistic calculations and use the same parameters for nonrelativistic calculations of heavy quark systems.

4.1 *Illustrations for different potentials*

(i) *Martin potential*

As described our scheme can be applicable to any potential. To test the reliability of our scheme we do some known calculations. Here, we take that of Martin (1980) with the potential given in equation (72), and using our scheme calculate the corresponding spin average mass levels and find that they are similar to that of Martin's as given in table 1.

(ii) *Bhaduri's model*

Next, we compare calculations in our scheme with Bhaduri's model (Bhaduri and Brack 1982) and find that they also agree, which may be seen from table 2. We may remark that

Table 1. Comparison of our calculation with Martin's potential with that of Martin's parameters are: $A = -8{\cdot}064$, $B = 6{\cdot}681$, $\alpha = 0{\cdot}1$, $m_c = 1{\cdot}8$ GeV, $m_b = 5{\cdot}174$ GeV and $m_s = 0{\cdot}518$ GeV (Martin 1980).

States	Our calculation (in GeV)	Martin's calculation (in GeV)
J/ψ	3·086	3·095
ψ'	3·691	3·687
ψ''	4·050	4·032
ψ'''	4·307	4·307
Average P-state	3·510	3·502
Average D-state	3·793	3·787
Υ	9·46	9·46
Υ'	10·040	10·025
Υ''	10·38	10·36
Υ'''	10·62	10·60
Υ^{IV}	10·85	10·76
$1P$	9·871	9·851
$2P$	10·250	10·242
ϕ	0·99	1·02
ϕ'	1·626	1·634
$E(1^{++})$	1·43	1·42

CC-0. In Public Domain. Gurukul Kangri Collection, Haridwar

Digitized by Arya Samaj Foundation Chennai and eGangotri

Table 2. Comparison of Bhaduri's results with our calculation, with same parameters (Bhaduri and Brack 1982). $m_q = 0{\cdot}5$, $a_0 = 0{\cdot}054$ in GeV units.

States	Our calculation	Bhaduri's calculation
$1S$	0·334	0·331
$2S$	0·584	0·579
$3S$	0·788	0·772
$4S$	0·975	0·961
$1P$	0·480	0·476
$1d$	0·606	0·602
$1f$	0·721	0·715
$1g$	0·827	0·821

Bhaduri showed that non-relativistic Schrödinger's equation with some effective mass and effective potential can simulate the solutions of relativistic Dirac equation of a massless particle with a known scalar potential, taken as $V = a_0 r$. We have here shown the same by variational method.

These two calculations give quite a good amount of reliability and confidence in our calculations.

4.2 *Heavy quark: Relativistic effects (present model)*

With the test of reliability of our scheme as mentioned in § 4.1 we do the calculations for relativistic heavy quark systems. For this, we choose a Cornell (Eichten *et al* 1978) type of potential (68) for the interaction due to the exchange of a vector particle. We recognize that in all applications, a scalar potential is needed. Thus we supplement the above potential with a purely linear confining potential and a constant to scalar exchange potential as has been taken by (Gupta *et al* 1982), written as

$$V_c^S(r) = a_{0s} r - A_c, \tag{85}$$

which in momentum space becomes

$$\tilde{V}_c^S(Q) = -\frac{8\pi a_{0s}}{Q^4} - (2\pi)^3 \cdot A_c \delta(\mathbf{q}). \tag{86}$$

The calculated results correspond to this sum of the two potentials, and, thus we optimize the four-potential parameters along with the quark mass to get the lowest lying levels of charmonium. Also, we calculate the masses of the excited states and $^1P_1$ state, as given in table 3 along with the experimental data (Particle Data Group 1984). We may note here that our prediction for the mass of $^1P_1$ state agrees with the limit given by the Crystal Ball Data (Porter 1982). Further, we calculate the wave function at the origin and use them along with the Van Royen and Weiskopf (1967) formula, to calculate the leptonic widths as well as the photonic widths of $^1S_0$ and $^3S_1$ states. We also compare our calculations against the experimental data (Particle Data Group 1984) whenever available as in table 4. We may note here that the agreement appears to be reasonably good. We would like to note here that our estimation of $\Gamma(\eta_c \to \gamma\gamma)$ agrees with that of Rosner (1981). Also, our calculations for $\Gamma(J/\psi \to 3\gamma)$ agrees well with the

CC-0. In Public Domain. Gurukul Kangri Collection, Haridwar

Digitized by Arya Samaj Foundation Chennai and eGangotri

Table 3. $c\bar{c}$ spectrum with $m_c = 1{\cdot}648$, $a_0 = a_{0s} = 0{\cdot}11$, $K = 0{\cdot}46$, $A_c = 0{\cdot}69$.

State	Calculated mass in GeV	R^2 in GeV^{-2}	Experimental values in GeV
$1\,^1S_0\,(\eta_c)$	2·993	1·5	$2{\cdot}981 \pm 0{\cdot}006$
$1\,^3S_1\,(\psi)$	3·109	2·0	$3{\cdot}097 \pm 0{\cdot}0001$
$1\,^3P_0\,(\chi_0)$	3·410	2·0	$3{\cdot}415 \pm 0{\cdot}0001$
$1\,^3P_1\,(\chi_1)$	3·500	3·0	$3{\cdot}510 \pm 0{\cdot}00006$
$1\,^3P_2\,(\chi_2)$	3·544	4·0	$3{\cdot}5558 \pm 0{\cdot}00006$
$1\,^1P_1\,(\ \ )$	3·546	5·0	
$2\,^1S_0\,(\eta_c')$	3·636	3·0	3·590
$2\,^3S_1\,(\psi')$	3·710	3·5	$3{\cdot}686 \pm 0{\cdot}0001$

Table 4. Electromagnetic width.

Decay mode	Calculated width (in keV)	Experimental width (in keV)
$\Gamma(\psi \to e^+e^-)$	4·992	$4{\cdot}662 \pm 0{\cdot}756$
$\Gamma(\Upsilon \to e^+e^-)$	1·208	$1{\cdot}176 \pm 0{\cdot}462$
$\Gamma(\psi' \to e^+e^-)$	2·855	$1{\cdot}36 - 2{\cdot}55$
$\Gamma(\Upsilon' \to e^+e^-)$	0·4040	$0{\cdot}51 \pm 0{\cdot}18$
$\Gamma(\eta_c \to \gamma\gamma)$	6·656	
$\Gamma(\eta_b \to \gamma\gamma)$	1·610	
$\Gamma(\psi \to \gamma\gamma\gamma)$	$3{\cdot}709 \times 10^{-3}$	$\leqslant 3{\cdot}5 \times 10^{-3}$

experiment (Rosner 1981; Partridge *et al* 1980). The leptonic width formula (Van Royen and Weiskopf 1967) we use is written as

$$\Gamma(V \to e^+e^-) = \frac{16\pi\alpha^2 e_q^2}{M^2(q\bar{q})} \cdot |\psi(\mathbf{0})|^2. \tag{88}$$

$\psi(\mathbf{0})$ is the wave function at the origin given by $\psi(0) = \Sigma C_n U_{n00}(\mathbf{0})$. $U_{n00}(\mathbf{0})$ is calculated from (24) and C_{ns}' are eigenvectors of $\langle n'|H^J|n\rangle$. The photonic width formula (Rosner 1981) for $^1S_0$ and $^3S_1$ states are respectively written as

$$\Gamma(^1S_0 \to 2\gamma) = \tfrac{4}{3}\Gamma(^3S_1 \to e^+e^-), \tag{89}$$

and

$$\Gamma(^3S_1 \to 3\gamma) = \frac{2^8(\pi^2-9)}{3^7} \cdot \alpha\Gamma(^3S_1 \to e^+e^-). \tag{90}$$

Observing a reasonable agreement of our calculations with the experimental data (Particle Data Group 1984) for charmonium family, we now proceed in a similar manner to do our calculations and the optimization for upsilon family. We note here that we need here a different set of potential parameters (Gupta and Radford 1982) and the quark mass for the optimization of lowest lying states. Then as in the case of charmonium family we make our calculations for excited states and compare them with experiments wherever available as in table 5. Further we also calculate the electromagnetic widths for Υ-family using (87)–(89) and compare them with the experiment

CC-0. In Public Domain. Gurukul Kangri Collection, Haridwar

Digitized by Arya Samaj Foundation Chennai and eGangotri

Table 5. bb^- spectrum with $m_b = 5{\cdot}005$, $a_0 = 0{\cdot}16$, $K = 0{\cdot}288$, $a_{0s} = 0{\cdot}187$, $A_c = 0{\cdot}954$.

State	Calculated mass (in GeV)	R^2 (in GeV^{-2})	Experimental mass (in GeV)
$1\,^1S_0$	9·410	0·6	
$1\,^3S_1$	9·460	0·6	$9{\cdot}460 \pm 0{\cdot}0003$
$1\,^3P_0$	9·869	1·1	$9{\cdot}8729 \pm 0{\cdot}0058$
$1\,^3P_1$	9·896	0·6	$9{\cdot}8945 \pm 0{\cdot}0035$
$1\,^3P_2$	9·912	0·6	$9{\cdot}9146 \pm 0{\cdot}0024$
$2\,^1S_0$	10·04	1·1	
$2\,^3S_1$	10·07	1·1	$10{\cdot}0234 \pm 0{\cdot}0003$
$2\,^3P_0$	10·35	1·5	
$2\,^3P_1$	10·37	1·5	$10{\cdot}2537 \pm 0{\cdot}0034$
$2\,^3P_2$	10·38	1·5	$10{\cdot}271 \pm 0{\cdot}0024$

wherever available as in table 4. We may note here that our calculation agrees reasonably with the experimental data.

Next, with the parameters as above, we do the nonrelativistic calculations for heavy quark systems i.e. for charmonium and upsilon systems, to estimate the magnitude of the fully relativistic corrections. We find that these corrections over nonrelativistic calculations are of the order of 50 MeV for charmonium family and 20 MeV for the upsilon family, which is similar to the magnitude of the splittings, and are *not* the same for all sublevels. Thus, with this we do feel that the relativistic corrections for the light quark systems will be quite relevant.

5. Discussion

We have derived the effective Hamiltonian in field theory. Next, we have used it retaining all relativistic effects. Further, we have done the diagonalization of the expectation values of the Hamiltonian instead of solving differential equations, for obtaining mass levels of mesons. For this, we have taken different phenomenological potentials as the quark-antiquark potential is not yet known. In our calculations, we notice a significant effect due to the totally relativistic calculations, over the Fermi-Breit approximation.

We may also find out a major difference of our model in contrast to most of the models. The potential parameters are taken to be fixed except for a variation dependent when we go from charmonium to upsilon system, as expected on the basis of renormalization group equation (e.g. Gupta and Radford 1982). However the radial wave function has been optimized separately for each radial or angular quantum number.

Although good agreement was obtained for heavy quark systems, this was not possible for light quark systems. This is surprising, since our calculations include relativistic effects. We attribute this to our inadequate knowledge of the structure of dynamics at low energies for quantum chromodynamics (QCD). In case we derive a potential from QCD, our relativistic format for bound state will be useful. For this

CC-0. In Public Domain. Gurukul Kangri Collection, Haridwar

Digitized by Arya Samaj Foundation Chennai and eGangotri

purpose, in Appendix B, we have included the expressions for the relevant contributions when quarks are massless.

An alternative way of looking at the bound state is also possible in terms of Lagrangian density (Misra 1985) which is a covariant formalism and an equivalent approach through Hamiltonian density (Misra and Panda 1986). Further attempts in this direction are in progress. Also the present technique can be applied to the positronium system. However, since this method is numerical, and exact analytical methods exist, such an exercise will be merely a verification in addition to those quoted in §4.

Acknowledgement

The authors would like to thank S Panda for discussions.

Appendix A. Angular momentum coefficients

From equation (7) we have,

$$g_m(l, J, J_z, \hat{k}_1)\sigma_m = \langle lm'1m'_1 | J J_z \rangle \mathcal{Y}_{lm'} \sigma^P_{m'_1}. \tag{A.1}$$

For $J = l-1$,

$$g_1(l, J, J_z, \hat{k}_1) = (-i)^l \cdot \frac{1}{\sqrt{2}} \cdot \left\{ Y_{l,J_z+1}(\hat{k}_1) \left(\frac{(l+J_z+1)(l+J_z)}{2l(2l+1)} \right)^{1/2} - Y_{l,J_z-1}(\hat{k}_1) \left(\frac{(l-J_z)(l-J_z+1)}{2l(2l+1)} \right)^{1/2} \right\}. \tag{A.2}$$

$$g_2(l, J, J_z, \hat{k}_1) = (-i)^l \cdot \frac{-i}{\sqrt{2}} \left\{ Y_{l,J_z+1}(\hat{k}_1) \left(\frac{(l+J_z+1)(l+J_z)}{2l(2l+1)} \right)^{1/2} + Y_{l,J_z-1}(\hat{k}_1) \left(\frac{(l-J_z)(l-J_z+1)}{2l(2l+1)} \right)^{1/2} \right\}, \tag{A.3}$$

$$g_3(l, J, J_z, \hat{k}_1) = (-i)^l Y_{l,J_z-1}(\hat{k}_1) \left(\frac{(l^2-J_z^2)}{l(2l+1)} \right)^{1/2}. \tag{A.4}$$

For $J = 1$

$$g_1(l, J, J_z, \hat{k}_1) = (-i)^l \cdot \frac{1}{\sqrt{2}} \cdot \left\{ Y_{l,J_z+1}(\hat{k}_1) \left(\frac{(l-J_z)(l+J_z+1)}{2l(l+1)} \right)^{1/2} - Y_{l,J_z-1}(\hat{k}_1) \left(\frac{(l+J_z)(l+J_z+1)}{2l(l+1)} \right)^{1/2} \right\}, \tag{A.5}$$

$$g_2(l, J, J_z, \hat{k}_1) = (-i)^l \cdot \frac{-i}{\sqrt{2}} \left\{ Y_{l,J_z+1}(\hat{k}_1) \left(\frac{(l-J_z)(l+J_z+1)}{2l(l+1)} \right)^{1/2} - Y_{l,J_z-1}(\hat{k}_1) \left(\frac{(l+J_z)(l-J_z+1)}{2l(l+1)} \right)^{1/2} \right\}, \tag{A.6}$$

CC-0. In Public Domain. Gurukul Kangri Collection, Haridwar

Digitized by Arya Samaj Foundation Chennai and eGangotri

$$g_3(l, J, J_z, \hat{k}_1) = (-i)^l Y_{l,J_z}(\hat{k}_1) \frac{J_z}{\sqrt{l(l+1)}}. \tag{A.7}$$

For $J = l+1$,

$$g_1(l, J, J_z, \hat{k}_1) = (-i)^l \cdot \frac{1}{\sqrt{2}} \cdot \left\{ Y_{l,J_z+1}(\hat{k}_1) \left(\frac{(l-J_z)(l-J_z+1)}{(2l+1)(2l+2)} \right)^{1/2} - Y_{l,J_z-1}(\hat{k}_1) \left(\frac{(l+J_z)(l+J_z+1)}{(2l+1)(2l+2)} \right)^{1/2} \right\}. \tag{A.8}$$

$$g_2(l, J, J_z, \hat{k}_1) = (-i)^l \cdot \frac{-i}{\sqrt{2}} \left\{ Y_{l,J_z+1}(\hat{k}_1) \left(\frac{(l-J_z)(l-J_z+1)}{(2l+1)(2l+2)} \right)^{1/2} + Y_{l,J_z-1}(\hat{k}_1) \left(\frac{(l+J_z)(l+J_z+1)}{(2l+1)(2l+2)} \right)^{1/2} \right\}, \tag{A.9}$$

$$g_3(l, J, J_z, \hat{k}_1) = (-i)^l Y_{l,J_z}(\hat{k}_1) \left(\frac{(l-J_z+1)(l+J_z+1)}{(2l+1)(l+1)} \right)^{1/2}. \tag{A.10}$$

From equation (54), we have

$$A^V_{m'm}(\hat{k}'_1, \hat{k}_1) = \frac{4\pi}{2J+1} \sum_{J_z} g^*_{m'}(l', J, J_z, \hat{k}') g_m(l, J, J_z, \hat{k}_1). \tag{A.11}$$

For $l = 0$ and $J = 1$, i.e. for $^3S_1$ state, we have

$$A^V_{m'm}(\hat{k}'_1, \hat{k}_1) = \frac{1}{3} \delta_{m'm}. \tag{A.12}$$

For $l = 1$ and $J = 0$, i.e. for $^3P_0$ state we have,

$$A^V_{m'm}(\hat{k}'_1, \hat{k}_1) = \hat{k}'_{1m'} \hat{k}_{1m}. \tag{A.13}$$

For $l = 1$ and $J = 1$, i.e. for $^3P_1$ state we have,

$$A^V_{m'm}(\hat{k}'_1 \cdot \hat{k}_1) = \tfrac{1}{2}(\hat{k}'_1, \hat{k}_1) \delta_{m'm} - \tfrac{1}{2} \hat{k}_{1m'} \hat{k}'_{1m}. \tag{A.14}$$

For $l = 1$ and $J = 2$, i.e. for $^3P_2$ state we have

$$A^V_{m'm}(\hat{k}'_1, \hat{k}_1) = [\tfrac{3}{10}(\hat{k}'_1 \cdot \hat{k}_1)\delta_{m'm} - \tfrac{1}{5} \hat{k}'_{1m'} \hat{k}_{1m} + \tfrac{3}{10} \hat{k}'_{1m} \hat{k}_{1m'}]. \tag{A.15}$$

Appendix B. Relativistic corrections

From equation (40) we have

$$F^V_{PS}(\mathbf{k}'_1, \mathbf{k}_1) = \tfrac{1}{2} \mathrm{Tr}[\bar{u}(\mathbf{k}'_1)\gamma^\mu u(\mathbf{k}_1)\bar{v}(-\mathbf{k}_1)\gamma_\mu v(-\mathbf{k}'_1)] + \frac{1}{2|\mathbf{q}|^2} \mathrm{Tr}[\bar{u}(\mathbf{k}'_1)\gamma \cdot \bar{\mathbf{q}} u(\mathbf{k}_1)\bar{v}(-\mathbf{k}_1)\gamma \cdot \mathbf{q} v(-\mathbf{k}'_1)] \tag{B.1}$$

$$= f'_1 f_1 f'_2 f_2 + (\mathbf{k}'_1 \cdot \mathbf{k}_1)(f'_1 f_1 g'_2 g_2 + f'_2 f_2 g'_1 g_1)$$

CC-0. In Public Domain. Gurukul Kangri Collection, Haridwar

Digitized by Arya Samaj Foundation Chennai and eGangotri

$$+2(f_1 f_2 g_1' g_2' K_1'^2 + f_1' f_2' g_1 g_2 K_1^2) + g_1' g_2' g_1 g_2 K_1'^2 K_1^2$$
$$-\frac{2}{|\mathbf{q}|^2}(f_1' f_2 g_1 g_2' + f_1 f_2' g_1' g_2)(\mathbf{k}_1' \cdot \mathbf{q})(\mathbf{k}_1 \cdot \mathbf{q}), \tag{B.2}$$

which for quark mass being zero becomes,

$$F_{PS}^{V}(\mathbf{k}_1', \mathbf{k}_1) = \tfrac{3}{2} + \tfrac{1}{4}\cos\theta_1 - \frac{1}{K_1' K_1}\left(K^2\cos^2\theta - \frac{Q^2}{4}\right), \tag{B.2a}$$

where $\cos\theta_1 = (\mathbf{k}_1' \cdot \mathbf{k}_1)/K_1' K_1$.

From equation (52) we have,

$$F_{m'm}^{V}(\mathbf{k}_1', \mathbf{k}_1) = \tfrac{1}{2}\,\mathrm{Tr}\,[\bar{u}(\mathbf{k}_1')\gamma^\mu u(\mathbf{k}_1)\sigma_m \bar{v}(-\mathbf{k}_1)\gamma_\mu v(-\mathbf{k}_1')\sigma_{m'}]$$
$$+\frac{1}{2|\mathbf{q}|^2}\,\mathrm{Tr}\,[\bar{u}(\mathbf{k}_1')\gamma\cdot\mathbf{q}\, u(\mathbf{k}_1)\sigma_m \bar{v}(-\mathbf{k}_1)\gamma\cdot\mathbf{q}\, v(-\mathbf{k}_1')\sigma_{m'}] \tag{B.3}$$

$$= \Bigg[(f_1' f_1 + g_1' g_1(\mathbf{k}_1' \cdot \mathbf{k}_1))(f_2' f_2 + g_2' g_2(\mathbf{k}_1' \cdot \mathbf{k}_1))$$
$$+\left(K_1^2 - \frac{(\mathbf{k}_1 \cdot \mathbf{q})^2}{|\mathbf{q}|^2}\right)(f_1 f_2 g_1' g_2' + f_1' f_2' g_1 g_2 + f_1 f_2' g_1' g_2$$
$$- f_1' f_2 g_1 g_2')\Bigg]\delta_{m'm} + \Bigg[-2f_1 f_2 g_1' g_2' - 2(f_1' f_2' g_1 g_2$$
$$- f_1 f_2 g_1' g_2')\frac{\mathbf{k}_1 \cdot \mathbf{q}}{|\mathbf{q}|^2} - (f_1' f_2 g_1 g_2' + f_1 f_2' g_1' g_2)$$
$$- (f_1 f_1' g_2 g_2' + f_2 f_2' g_1 g_1') - 2g_1 g_2 g_1' g_2'(\mathbf{k}_1' \cdot \mathbf{k}_1)\Bigg]\varepsilon_{imm'}(\mathbf{q} \times \mathbf{k}_1')_i$$
$$+[(f_1' f_2 g_1 g_2' + f_1 f_2' g_1' g_2)(\mathbf{k}_1' \cdot \mathbf{k}_1) - f_1 f_2 g_1' g_2' K_1'^2$$
$$- f_1' f_2' g_1 g_2 K_1^2]\delta_{m'm} - [(f_1' f_2 g_1 g_2' + f_1 f_2' g_1' g_2)((\mathbf{k}_1' \cdot \mathbf{k}_1)\delta_{m'm}$$
$$- K_{1m'}' K_{1m} - K_{1m'} K_{1m}') + f_1 f_2 g_1' g_2'(2K_{1m}' K_{1m'}' - K_1'^2 \delta_{m'm})$$
$$+ f_1' f_2' g_1 g_2(2K_{1m'} K_{1m} - K_1^2 \delta_{m'm})]$$
$$+\Bigg[g_1 g_2 g_1' g_2'\{2(\mathbf{q} \times \mathbf{K}_1)_m (\mathbf{q} \times \mathbf{K}_1)_{m'} - (\mathbf{q} \times \mathbf{K}_1)^2 \delta_{m'm}\Bigg]$$
$$+(f_1' g_1 - f_1 g_1')(f_2 g_2' - f_2' g_2)\frac{1}{|\mathbf{q}|^2}(2(\mathbf{q} \times \mathbf{K}_1)_m (\mathbf{q} \times \mathbf{K}_1)_{m'}$$
$$- (\mathbf{q} \times \mathbf{K}_1)^2 \delta_{mm'})]. \tag{B.4}$$

From equation (57) we get,

$$F_{PS}^{S}(\mathbf{k}_1', \mathbf{k}_1) = -\tfrac{1}{2}\,\mathrm{Tr}\,[\bar{u}(\mathbf{k}_1')u(\mathbf{k}_1)\bar{v}(-\mathbf{k}_1)v(-\mathbf{k}_1')]$$
$$= f_1' f_1 f_2' f_2 - (f_1' f_1 g_2 g_2' + f_2' f_2 g_1' g_1)(\mathbf{k}_1' \cdot \mathbf{k}_1)$$
$$+ g_1' g_1 g_2' g_2 K_1'^2 K_1^2, \tag{B.5}$$

CC-0. In Public Domain. Gurukul Kangri Collection, Haridwar

Digitized by Arya Samaj Foundation Chennai and eGangotri

which for quarks being massless becomes

$$F^{S}_{PS}(\mathbf{k}'_1, \mathbf{k}_1) = \tfrac{1}{2}(1 - \cos\theta_1). \tag{B.5a}$$

From equation (59),

$$\begin{aligned} F^{S}_{m'm}(\mathbf{k}'_1, \mathbf{k}_1) &= -\tfrac{1}{2}\,\mathrm{Tr}\,[\bar{u}(\mathbf{k}'_1)u(\mathbf{k}_1)\sigma_m \bar{v}(-\mathbf{k}_1)v(-\mathbf{k}'_1)\sigma_{m'}] \\ &= -[(f'_1 f_1 - g'_1 g_1(\mathbf{k}'_1\cdot\mathbf{k}_1)(g'_2 g_2(\mathbf{k}'_1\cdot\mathbf{k}_1) - f'_2 f_2)\delta_{m'm} \\ &\quad + \{(f'_1 f_1 - g'_1 g_1(\mathbf{k}'_1\cdot\mathbf{k}_1))g'_2 g_2 + (f'_2 f_2 - g'_2 g_2(\mathbf{k}'_1\cdot\mathbf{k}_1))g'_1 g_1\} \\ &\quad - \varepsilon_{imm'}(\mathbf{k}'_1\times\mathbf{k}_1)_i - g'_1 g_1 g'_2 g_2\{2(\mathbf{k}'_1\times\mathbf{k}_1)_m(\mathbf{k}'_1\times\mathbf{k}_1)_{m'} \\ &\quad - (\mathbf{k}'_1\times\mathbf{k}_1)^2\delta_{m'm}\}]. \end{aligned} \tag{B.6}$$

We have

$$F^{V}(^1S_0) = F^{V}_{PS}(\mathbf{k}'_1, \mathbf{k}_1) \tag{B.7}$$

and

$$F^{V}(^1P_1) = (\mathbf{k}'_1\cdot\mathbf{k}_1)\,F^{V}_{PS}(\mathbf{k}'_1, \mathbf{k}_1). \tag{B.8}$$

From equation (54),

$$F^{V}_{V}(\mathbf{k}'_1, \mathbf{k}_1) = \sum F^{V}_{m'm}(\mathbf{k}'_1, \mathbf{k}_1)\,A^{V}_{m'm}(\hat{k}'_1, \hat{k}_1). \tag{B.9}$$

For $l = 0$ and $J = 1$, we have $^3S_1$ state.

From (B.4) and (A.12) we get

$$\begin{aligned} F^{V}(^3S_1) &= f'_1 f_1 f'_2 f_2 + (f'_1 f_1 g'_2 g_2 + f'_2 f_2 g'_1 g_1)(\mathbf{k}'_1\cdot\mathbf{k}_1) \\ &\quad + g'_1 g_1 g'_2 g_2((\mathbf{k}'_1\cdot\mathbf{k}_1)^2 - \tfrac{1}{3}(\mathbf{k}'_1\times\mathbf{k}_1)^2) \\ &\quad + \tfrac{2}{3}f'_1 f'_2 g_1 g_2\left(K^2 - 2K^2\cos^2\theta - \frac{Q^2}{4} + KQ\cos\theta\right) \\ &\quad + \tfrac{2}{3}f_1 f_2 g'_1 g'_2\left(K^2 - 2K^2\cos^2\theta - \frac{Q^2}{4} - KQ\cos\theta\right) \\ &\quad + \tfrac{2}{3}(f'_1 f_2 g_1 g'_2 + f_1 f'_2 g'_1 g_2)\left(K^2 + K^2\sin^2\theta - \frac{Q^2}{4}\right), \end{aligned} \tag{B.10}$$

which for quarks being massless becomes

$$\begin{aligned} F^{V}(^3S_1) &= \tfrac{1}{4} + \tfrac{1}{2}\cos\theta_1 + \tfrac{1}{4}(\cos^2\theta_1 - \tfrac{1}{3}\sin^2\theta_1) \\ &\quad + \frac{1}{6K'^2_1}\left(K^2 - 2K^2\cos^2\theta - \frac{Q^2}{4} - KQ\cos\theta\right) \\ &\quad + \frac{1}{6K^2_1}\left(K^2 - 2K^2\cos^2\theta - \frac{Q^2}{4} + KQ\cos\theta\right) \\ &\quad + \frac{1}{3K'_1 K_1}\left(K^2 + K^2\sin^2\theta - \frac{Q^2}{4}\right). \end{aligned} \tag{B.10a}$$

CC-0. In Public Domain. Gurukul Kangri Collection, Haridwar

Digitized by Arya Samaj Foundation Chennai and eGangotri

In the non-relativistic limit and equal mass case,

$$F^V({}^3S_1) = 1 + \frac{K^2}{m^2} - \frac{K^2\cos^2\theta}{m^2} - \frac{5}{12m^2}Q^2. \tag{B.11}$$

For $l = 1$ and $J = 0$, we have ${}^3P_0$ state. From (B.4) and (A.13) we have

$$\begin{aligned} F^V = ({}^3P_0) = {} & f_1' f_1 f_2' f_2 (\mathbf{k}_1' \cdot \mathbf{k}_1) + (f_1' f_1 g_2' g_2 + f_2' f_2 g_1' g_1 + 2 f_1' f_2 g_1 g_2' \\ & + 2 f_1 f_2' g_1' g_2)(K_1' K_1)^2 + g_1' g_1 g_2' g_2 (K_1' K_1)^2 (\mathbf{k}_1' \cdot \mathbf{k}_1) \\ & - 2(f_1' f_2' g_1 g_2 K_1^2 + f_1 f_2 g_1' g_2' K_1'^2)(\hat{q} \cdot \mathbf{k}_1)(\hat{q} \cdot \mathbf{k}_1'). \end{aligned} \tag{B.12}$$

For quarks being massless, this becomes,

$$\begin{aligned} F^V({}^3P_0) = {} & \left\{\frac{1}{4}(1+\cos\theta_1)^2 + \frac{2K^2\sin^2\theta}{4}\left(\frac{1}{K_1^2} + \frac{1}{K_1'^2}\right)\right\}\left(K^2 - \frac{Q^2}{4}\right) \\ & + \left(\frac{1}{2K_1'^2} + \frac{1}{K_1' K_1}\right) K^2 Q^2 \sin^2\theta + \frac{1}{2}\left(\frac{1}{K_1'^2} - \frac{1}{K_1^2}\right) \\ & \times \left(K^3 Q \sin^2\theta\cos\theta - \frac{K^2 Q^2 \sin^2\theta}{2}\right) \\ & + \frac{1}{4K_1'^2 K_1^2}\left(K^2 - \frac{Q^2}{4}\right) K^2 Q^2 \sin^2\theta \\ & - \left(K^2 - \frac{Q^2}{4}\right) + \frac{1}{2K_1' K_1}\{(\mathbf{k}_1' \cdot \mathbf{k}_1)^2 + K_1'^2 K_1^2\}. \end{aligned} \tag{B.12a}$$

In the non-relativistic limit and equal mass case

$$\begin{aligned} F^V({}^3P_0) = {} & K^2 + \frac{K^4}{m^2} - \frac{K^4\cos^2\theta}{m^2} - \frac{Q^2}{4} + \frac{K^2 Q^2}{m^2} \\ & - \frac{7K^2Q^2\cos^2\theta}{4m^2} + \frac{3Q^4}{16m^2}. \end{aligned} \tag{B.13}$$

For $l = 1$, $S = 1$ and $J = 1$, we have for ${}^3P_1$ state,

$$F^V({}^3P_1) = K_1' K_1 F_V^V(\mathbf{k}_1', \mathbf{k}_1).$$

From (B.4) and (A.14) we then have,

$$F^V({}^3P_1) = \tfrac{3}{2}(\mathbf{k}_1' \cdot \mathbf{k}_1) F^V({}^3S_1) - \tfrac{1}{2} F_V^e({}^3P_0), \tag{B.14}$$

where we have taken,

$$F_V^e({}^3P_0) = \sum_{m',m} k_{1m}' k_{1m'} F_{m'm}^V(\mathbf{k}_1', \mathbf{k}_1). \tag{B.15}$$

Hence,

$$\begin{aligned} F_V^e({}^3P_0) = {} & [(f_1' f_1 + g_1' g_1 (\mathbf{k}_1' \cdot \mathbf{k}_1))(f_2' f_2 + g_2' g_2 (\mathbf{k}_1' \cdot \mathbf{k}_1)) \\ & + 2K^2 \sin^2\theta (f_1 f_2 g_1' g_2' + f_1' f_2' g_1 g_2)](\mathbf{k}_1' \cdot \mathbf{k}_1) \end{aligned}$$

CC-0. In Public Domain. Gurukul Kangri Collection, Haridwar

Digitized by Arya Samaj Foundation Chennai and eGangotri

$$-\Big[(2f_1f_2g_1'g_2' + f_1'f_2g_1g_2' + f_1f_2'g_1'g_2 + f_2f_2'g_1g_1' + f_1f_1'g_2g_2')Q^2K^2\sin^2\theta + 2(f_1'f_2'g_1g_2 - f_1f_2g_1'g_2')\Big(K^3Q\sin^2\theta\cos\theta - \frac{K^2Q^2\sin^2\theta}{2}\Big) + 2g_1g_2g_1'g_2'\Big(K^2 - \frac{Q^2}{4}\Big)K^2Q^2\sin^2\theta\Big]$$
$$-2\Big(K^2 - \frac{Q^2}{4}\Big)\{f_1f_2g_1'g_2'K_1'^2 + f_1'f_2'g_1g_2K_1^2\} + (f_1'f_2g_1g_2' + f_1f_2'g_1'g_2)((\mathbf{k}_1'\cdot\mathbf{k}_1)^2 + K_1K_1'^2) - g_1g_2g_1'g_2'\Big(K^2 - \frac{Q^2}{4}\Big)K^2Q^2\sin^2\theta, \tag{B.16}$$

which for quarks being massless becomes,

$$F_V^e({}^3P_0) = \Big\{\frac{1}{4}(1+\cos\theta_1)^2 + \frac{K^2\sin^2\theta}{2}\Big(\frac{1}{K_1^2} + \frac{1}{K_1'^2}\Big)\Big\}\Big(K^2 - \frac{Q^2}{4}\Big) - \Big\{\Big(\frac{1}{2K_1'^2} + \frac{1}{K_1'K_1}\Big)K^2Q^2\sin^2\theta + \frac{1}{2}\Big(\frac{1}{K_1'^2} - \frac{1}{K_1^2}\Big) \times \Big(K^3Q\sin^2\theta\cos\theta - \frac{K^2Q^2\sin^2\theta}{2}\Big) + \frac{3}{4K_1^2K_1'^2}\Big(K^2 - \frac{Q^2}{4}\Big)K^2Q^2\sin^2\theta\Big\} - \Big(K^2 - \frac{Q^2}{4}\Big) + \frac{1}{2K_1'K_1}\{(\mathbf{k}_1'\cdot\mathbf{k}_1)^2 + K_1'^2K_1^2\}. \tag{B.16a}$$

In the non-relativistic limit and equal mass case,

$$F^V({}^3P_1) = K^2 + \frac{K^4}{m^2} - \frac{K^4\cos^2\theta}{m^2} - \frac{Q^2}{4} + \frac{K^2Q^2}{6m^2} - \frac{3K^2Q^2\cos^2\theta}{4m^2} + \frac{Q^4}{16m^2}. \tag{B.17}$$

For $l = 1$, $S = 1$ and $J = 2$, we have ${}^3P_2$ state.

From (B.4) and (A.15) we get

$$F^V({}^3P_2) = \tfrac{9}{10}(\mathbf{k}_1'\cdot\mathbf{k}_1)F^V({}^3S_1) - \tfrac{1}{15}F^V({}^3P_0) + \tfrac{3}{10}F_V^e({}^3P_0). \tag{B.18}$$

In the non-relativistic limit and equal mass case

$$F^V({}^3P_2) = K^2 + \frac{K^4}{m^2} - \frac{K^4\cos^2\theta}{m^2} - \frac{Q^2}{4} - \frac{7K^2Q^2}{5m^2} + \frac{19K^2Q^2\cos^2\theta}{20m^2} + \frac{9Q^4}{80m^2}. \tag{B.19}$$

CC-0. In Public Domain. Gurukul Kangri Collection, Haridwar

Digitized by Arya Samaj Foundation Chennai and eGangotri

Similarly for scalar exchange,

$$F^S(^1S_0) = F^S_{PS}(\mathbf{k}'_1, \mathbf{k}_1) \tag{B.20}$$

and

$$F^S(^1P_1) = (\mathbf{k}'_1 \cdot \mathbf{k}_1)\, F^S(^1S_0). \tag{B.21}$$

Also, we have

$$F^S_V(\mathbf{k}'_1, \mathbf{k}_1) = \sum_{m'm} A^V_{m'm}(\mathbf{k}'_1, \mathbf{k}_1)\, F^S_{m',m}(\mathbf{k}'_1, \mathbf{k}_1) \tag{B.22}$$

Combining (B.6) and (A.12) we get,

$$\begin{aligned} F^S(^3S_1) = {} & f'_1 f_1 f'_2 f_2 - (f'_2 f_2 g'_1 g_1 + f'_1 f_1 g'_2 g_2)(\mathbf{k}'_1 \cdot \mathbf{k}_1) \\ & + g'_1 g_1 g'_2 g_2 (\mathbf{k}'_1 \cdot \mathbf{k}_1)^2 - \tfrac{1}{3} g'_1 g_1 g'_2 g_2 K^2 Q^2 \sin^2\theta, \end{aligned} \tag{B.23}$$

which for quarks being massless becomes,

$$F^S(^3S_1) = \tfrac{1}{4} - \tfrac{1}{2}\cos\theta_1 + \tfrac{1}{4}\left(\cos^2\theta_1 - \tfrac{1}{3}\sin^2\theta_1\right). \tag{B.23a}$$

In the non-relativistic limit

$$F^S(^3S_1) = 1 - \frac{K^2}{m^2}. \tag{B.24}$$

From (B.6) and (A.13),

$$\begin{aligned} F^S(^3P_0) = {} & [\{(f'_1 f_1 - g'_1 g_1 (\mathbf{k}'_1 \cdot \mathbf{k}_1))(g'_2 g_2 (\mathbf{k}'_1 \cdot \mathbf{k}_1) - f'_2 f_2)\}(\mathbf{k}'_1 \cdot \mathbf{k}_1) \\ & + \{(f'_1 f_1 - g'_1 g_1 (\mathbf{k}'_1 \cdot \mathbf{k}_1))g'_2 g_2 \\ & + (f'_2 f_2 - g'_2 g_2 (\mathbf{k}'_1 \cdot \mathbf{k}_1))\} K^2 Q^2 \sin^2\theta \\ & + g'_1 g_1 g'_2 g_2 (\mathbf{k}'_1 \cdot \mathbf{k}_1) K^2 Q^2 \sin^2\theta], \end{aligned} \tag{B.25}$$

which for quark mass being zero becomes,

$$\begin{aligned} F^S(^3P_0) = {} & -\left[-\tfrac{1}{4}(1 - \cos\theta_1)^2 \left(K^2 - \frac{Q^2}{4}\right) \right. \\ & \left. + \tfrac{1}{2} K'_1 K_1 \sin^2\theta \left(1 - \frac{\cos\theta_1}{2}\right)\right]. \end{aligned} \tag{B.25a}$$

In the non-relativistic limit

$$F^S(^3P_0) = K^2 - \frac{K^4}{m^2} - \frac{Q^2}{4} - \frac{K^2 Q^2}{4m^2} + \frac{K^2 Q^2 \cos^2\theta}{2m^2}. \tag{B.26}$$

From (B.6) and (A.14) we get

$$F^S(^3P_1) = \tfrac{3}{2}(\mathbf{k}'_1 \cdot \mathbf{k}_1)\, F^S(^3S_1) - \tfrac{1}{2} F^e_s(^3P_0), \tag{B.27}$$

CC-0. In Public Domain. Gurukul Kangri Collection, Haridwar

Digitized by Arya Samaj Foundation Chennai and eGangotri

where

$$F_S^e(^3P_0) = \sum_{m',m} k'_{1m} k_{1m'} F^S_{m'm}(\mathbf{k}'_1, \mathbf{k}_1). \tag{B.28}$$

$$\begin{aligned} &= -[\{(f'_1 f_1 - g'_1 g_1 (\mathbf{k}'_1 \cdot \mathbf{k}_1))(g'_2 g_2 (\mathbf{k}'_1 \cdot \mathbf{k}_1) - f'_2 f_2)\}(\mathbf{k}'_1 \cdot \mathbf{k}_1) \\ &\quad - \{(f'_1 f_1 - g'_1 g_1 (\mathbf{k}'_1 \cdot \mathbf{k}_1))g'_2 g_2 + (f'_2 f_2 - g'_2 g_2 (\mathbf{k}'_1 \cdot \mathbf{k}_1))g'_1 g_1\} \\ &\quad \times K^2 Q^2 \sin^2\theta + g'_1 g_1 g'_2 g_2 (\mathbf{k}'_1 \cdot \mathbf{k}_1) K^2 Q^2 \sin^2\theta], \end{aligned} \tag{B.29}$$

which for quark mass being zero becomes

$$\begin{aligned} F_S^e(^3P_0) = -\Bigg[&-\tfrac{1}{4}(1-\cos\theta_1)^2 \left(K^2 - \frac{Q^2}{4}\right) \\ &-\tfrac{1}{2} K'_1 K_1 \sin^2\theta_1 \left(1 - \tfrac{3}{2}\cos\theta_1\right) \Bigg]. \end{aligned} \tag{B.29′}$$

In the non-relativistic limit

$$F^S(^3P_1) = K^2 - \frac{K^4}{m^2} - \frac{Q^2}{4} + \frac{K^2 Q^2 \cos^2\theta}{4m^2}. \tag{B.30}$$

From (B.6) and (A.15) we get

$$F^S(^3P_2) = \tfrac{9}{10}(\mathbf{k}'_1 \cdot \mathbf{k}_1) F^S(^3S_1) - \tfrac{1}{5} F^S(^3P_0) + \tfrac{3}{10} F_s^e(^3P_0). \tag{B.31}$$

In the non-relativistic limit,

$$F^S(^3P_2) = K^2 - \frac{K^4}{m^2} - \frac{Q^2}{4} + \frac{K^2 Q^2}{2m^2} - \frac{K^2 Q^2 \cos^2\theta}{4m^2}. \tag{B.32}$$

References

Bardeen W A, Charnowicz M S, Drell S D, Weinstein M and Yan T M 1975 *Phys. Rev.* **D11** 1904
Barik N and Jena S N 1981 *Phys. Rev.* **D22** 1704
Bereteskii V B, Lifshitz E M and Pitaevski V 1971 *Relativistic quantum theory* (Oxford: Pergamon) p. 280
Biswal K and Misra S P 1982 *Phys. Rev.* **D26** 1175
Bhaduri R and Brack M 1982 *Phys. Rev.* **D25** 1443
Buchmuller V, Grunberg G and Tye S H H 1980 *Phys. Rev. Lett.* **45** 103
Caswell W E and Lepage G P 1978 *Phys. Rev.* **A18** 810
Davydov A S 1968 *Quantum mechanics* (Oxford: Pergamon)
Eichten E, Gottfried K, Kinoshita T, Lane K D and Yan T M 1978 *Phys. Rev.* **D17** 3090
Gupta S N and Radford S F 1982 *Phys. Rev.* **D25** 2690, 3430
Gupta S N, Radford S F and Repko W 1982 *Phys. Rev.* **D26** 3305
Gupta V 1977 *Advances in high energy physics* (Bombay: TIFR) p. 73
Marciano W and Pagels H 1978 *Phys. Rep.* **C36** 137
Martin A 1980 *Phys. Lett.* **B93** 338
Misra S P 1978 *Phys. Rev.* **D18** 1661, 1673
Misra S P 1980 *Phys. Rev.* **D21** 1231
Misra S P 1985 ICTP Preprint No. IC/85/89 (to appear in SAPP Proceedings, Bangalore)
Misra S P and Panda A R 1980 *Phys. Rev.* **D21** 3094

CC-0. In Public Domain. Gurukul Kangri Collection, Haridwar

Digitized by Arya Samaj Foundation Chennai and eGangotri

Misra S P and Panda S 1986 *Pramana–J. Phys.* **27** 523
Mitra A N 1981 *Z. Phys.* **C8** 25
Mitra A N and Santhanam I 1981 *Z. Phys.* **C8** 33
Mitra A N and Santhanam I 1981 *Phys. Lett.* **B104** 62
Mittal A and Mitra A N 1984 *Phys. Rev.* **D29** 1408
Naik S 1986 *Nucl. Phys.* **B271** 442
Particle Data Group 1984 *Rev. Mod. Phys.* 56, Part II, p.S1
Partridge *et al* 1980 *Phys. Rev. Lett.* **44** 712
Porter F C 1982 SLAC-PUB-2881
Richardson J L 1979 *Phys. Lett.* **B82** 272
Rosner J L 1981 Lectures at Advanced Studies Institute on techniques and concepts of high energy physics, St. Croix (Unpublished)
Schnitzer H J 1978 *Phys. Rev.* **D18** 3482
Stanley D P and Robson D 1980 *Phys. Rev.* **D21** 3180
Van Royen R and Weiskopf V F 1967 *Nuovo Cimento* **50** 617

CC-0. In Public Domain. Gurukul Kangri Collection, Haridwar

Digitized by Arya Samaj Foundation Chennai and eGangotri

Pramāṇa – J. Phys., Vol. 28, No. 2, February 1987, pp. 159–165. © Printed in India.

Isotope shift studies in the spectrum of boron monosulphide

SHEILA GOPAL and G LAKSHMINARAYANA
Spectroscopy Division, Bhabha Atomic Research Centre, Bombay 400 085, India

MS received 7 August 1986; revised 29 November 1986

Abstract. The spectrum of boron monosulphide has been excited in microwave discharge and photographed at moderate dispersion. The $C^2\Pi_r$–$X^2\Sigma^+$, $B^2\Sigma^+$–$A^2\Pi_i$ and $A^2\Pi_i$–$X^2\Sigma^+$ band systems extending from 2100–9000 Å have been obtained for $B^{32}S$ and $B^{34}S$ species. Isotope shifts for all these band systems have been measured. Comparison of the observed isotope shifts with the theoretically calculated isotope shifts confirms the emitter as well as the vibrational assignments of all these band systems.

Keywords. Emission band spectrum; boron monosulphide; isotope shifts.

PACS No. 33·20 Je

1. Introduction

Boron monosulphide molecule has an extensive electronic band spectrum in the 2200–9000 Å region in which several band systems have been identified:

$A^2\Pi_i$–$X^2\Sigma^+$ (4300–9000 Å), $B^2\Sigma^+$–$A^2\Pi_i$ (4900–5050 Å),

$C^2\Pi_r$–$X^2\Sigma^+$ (2400–2900 Å), $D^2\Delta_i$–$A^2\Pi_i$ (3100 Å),

$F^2\Delta_r$–$A^2\Pi_i$ (4100 Å) and $E^2\Sigma^+$–$X^2\Sigma^+$ (2100–2300 Å).

Although vibrational and rotational structure analyses of several of these band systems have been carried out, (Zeeman 1951; McDonald and Innes 1969; Singh *et al* 1971; Bell and McClean Megan 1976; Jenouvrier and Pascat 1981), extensive isotope shift studies of this spectrum have not so far been carried out. The isotope shift studies help identify the emitter of the spectrum as well as provide a check on the correctness of the vibrational assignments in various electronic band systems. We have taken up the isotope shift studies of this molecule by exciting the spectra of $B^{32}S$ and $B^{34}S$ in microwave discharge and by recording the spectrum under moderate dispersion (5·6 Å/mm). We have obtained experimental isotope shifts and compared them with the corresponding theoretical shifts for various band systems. The details of these studies are presented in this paper.

2. Experimental details

The spectra of $B^{32}S$ and $B^{34}S$ molecules have been excited by microwave discharge (200 Watt, 2450 MHz) through a sealed quartz discharge tube containing small

CC-0. In Public Domain. Gurukul Kangri Collection, Haridwar

Digitized by Arya Samaj Foundation Chennai and eGangotri

quantities of pure elemental sulphur (^{32}S and ^{34}S), boron and neon gas at a pressure of 2 torr. As soon as the discharge is initiated a strong spectrum of S_2 is produced. As the discharge tube warms up, the sulphur vapour reacts with boron metal to form the BS molecule. When sulphur is completely reacted the spectrum of S_2 disappears and only the spectrum of BS persists. The spectra were photographed on a 3 m Jarrell Ash grating spectrograph at a dispersion of 5·60 Å/mm. The band heads were measured against iron standard lines. The accuracy of head measurement is expected to be about 0·5 cm^{-1}.

3. Results and discussion

The spectrum of BS molecule, which extends from 2200–9000 Å, consists mainly of three strong band systems, namely, $C^2\Pi_r$–$X^2\Sigma^+$, $B^2\Sigma^+$–$A^2\Pi_i$ and $A^2\Pi_i$–$X^2\Sigma^+$. These band systems are very intense and extend over wide spectral regions. There are two more short groups of bands at around 3100 Å and 4100 Å which have been assigned to $D^2\Delta_i$–$A^2\Pi_i$ and $F^2\Delta_r$–$A^2\Pi_i$ transitions respectively. Recently, yet another band system was observed in the 2100–2300 Å region and assigned to $E^2\Sigma^+$–$X^2\Sigma^+$ transition (Bell and McClean Megan 1976). In the present studies all band systems except the E–X have been photographed both for $B^{32}S$ and $B^{34}S$ molecules. The experimental isotope shifts have been evaluated for all these band systems and compared with the corresponding theoretical isotope shifts. We discuss below the results for each one of the systems.

3.1 $A^2\Pi_i$–$X^2\Sigma^+$ *system* (4300–9000 Å)

Zeeman (1951) was the first to photograph the A–X bands in the region (5100–9000 Å) and to carry out rotational analysis of a few of them. He found good agreement between the calculated and the experimentally determined isotope shift for 4–0 band of $^{10}B^{32}S$ and $^{11}B^{32}S$ molecules. This system was further extended on the lower wavelength side to 4300 Å by Singh *et al* (1971) who excited these bands thermally in a King furnace. A few of the typical bands of the A–X system of $B^{32}S$ and $B^{34}S$ photographed in the present studies are shown in figure 1b. The experimental isotope shifts for $B^{32}S$ and $B^{34}S$ have been evaluated and presented in table 1. The theoretical isotope shifts ($\Delta\nu$) have been calculated from the well-known formula, viz

$$\begin{aligned}\Delta\nu = \nu - \nu^i = {} & (1-\rho)[\omega_e(v'+1/2) - \omega_e''(v''+1/2)] \\ & -(1-\rho^2)[\omega_e' x_e'(v'+1/2)^2 - \omega_e'' x_e''(v''+1/2)^2] \\ & +(1-\rho^3)[\omega_e' y_e'(v'+1/2)^3 - \omega_e'' y_e''(v''+1/2)^3], \end{aligned} \quad (1)$$

where $\rho = \mu/\mu^i$ and i refers to $B^{34}S$.

The following vibrational constants are used: for the A state, $\omega_e = 754{\cdot}23\ cm^{-1}$, $\omega_e x_e = 4{\cdot}85\ cm^{-1}$ and $\omega_e y_e = 0{\cdot}019\ cm^{-1}$; for the X state, $\omega_e = 1179{\cdot}91\ cm^{-1}$, $\omega_e x_e = 9{\cdot}1\ cm^{-1}$ and $\omega_e y_e = -0{\cdot}0083\ cm^{-1}$ (Jenouvrier and Pascat 1981). The computed isotope shift values are also presented in table 1. The agreement between the experimental and theoretical isotope shifts is found to be satisfactory thereby confirming the present vibrational assignments.

CC-0. In Public Domain. Gurukul Kangri Collection, Haridwar

Digitized by Arya Samaj Foundation Chennai and eGangotri

Table 1. Isotope shifts (in cm^{-1}) of the $A^2\Pi_r$–$X^2\Sigma^+$ bands of $B^{32}S$ and $B^{34}S$.

	$^2\Pi_{1/2}$		$^2\Pi_{3/2}$		Isotope shifts		
					$\Delta\nu_{obs}$	$\Delta\nu_{obs}$	$\Delta\nu_{cal}$
Band	$\nu(N)$	$\nu(I)$	$\nu(N)$	$\nu(I)$	$(^2\Pi_{1/2})$	$(^2\Pi_{3/2})$	
1–1	—	—	15244·67	15249·50	—	−4·83	−4·78
2–1	16305·75	16305·05	15974·85	15975·10	+0·70	−0·23	+0·64
3–1	17039·51	17033·78	16701·22	16696·13	+5·73	+5·09	+5·92
2–0	17480·56	17472·85	17160·30	17149·52	+7·71	+10·78	+9·38
3–0	18200·74	18184·45	17872·47	17858·31	+16·29	+14·16	+14·66
4–0	18913·22	18893·41	18583·81	18563·82	+19·81	+19·99	+19·81
5–0	19628·16	19605·38	19292·34	19266·06	+22·78	+26·28	+24·81
6–0	20333·73	20307·63	19993·72	19967·48	+26·10	+26·24	+29·69
7–0	21025·94	20993·75	20678·16	20642·59	+32·19	+35·57	+34·44
8–0	21670·33	21630·62	21365·04	21331·89	+39·71	+33·15	+39·06
9–0	22531·94	22487·68	22351·76	22309·38	+44·26	+42·38	+43·55
10–0	23020·12	22978·67	22690·52	22640·11	+41·45	+50·41	+47·92

Table 2. Isotope shifts (in cm^{-1}) of the $C^2\Pi_r$–$X^2\Sigma^+$ bands of $B^{32}S$ and $B^{34}S$.

	$^2\Pi_{1/2}$		$^2\Pi_{3/2}$		Isotope shifts		
					$\Delta\nu_{obs}$	$\Delta\nu_{obs}$	$\Delta\nu_{cal}$
Band	$\nu(N)$	$\nu(I)$	$\nu(N)$	$\nu(I)$	$(^2\Pi_{1/2})$	$(^2\Pi_{3/2})$	
0–1	37613·63	37623·13	37730·55	37738·92	− 9·50	−8·37	−9·78
0–2	36478·40	36460·12	36575·67	36592·59	−18·28	−16·92	−18·27
1–3	36195·19	36125·33	—	—	−20·14	—	−20·07
2–4	35927·71	35950·10	—	—	−22·39	—	−21·88
0–3	35317·45	35344·27	35433·48	35458·30	−26·82	−24·82	−26·58
1–4	35065·90	35094·08	—	—	−28·18	—	−28·18
2–5	34837·58	34864·19	34937·06	34963·50	−26·61	−26·44	−29·80

3.2 $C^2\Pi_r$–$X^2\Sigma^+$ *system* (2500–3400 Å)

The C–X bands which are red degraded exhibit a double-headed structure. Each electronic band consists of two such double-headed bands separated by about 115 cm^{-1}, being the spin splitting in the $C^2\Pi_r$ state. Rotational structure analyses of some of the C–X bands were carried out by Zeeman (1951) and recently by Jenouvrier and Pascat (1981). We have photographed the C–X bands of $B^{32}S$ and $B^{34}S$ molecules which are shown in figure 1a. From these spectra the isotope shifts have been determined. Theoretical shifts have been calculated from equation (1) by using the following vibrational constants: for the C state, $\omega_e = 887{\cdot}6\ cm^{-1}$, $\omega_e x_e = 9{\cdot}1\ cm^{-1}$ and for X state, $\omega_e = 1179{\cdot}91\ cm^{-1}$, $\omega_e x_e = 6{\cdot}25\ cm^{-1}$, $\omega_e y_e = -0{\cdot}0083\ cm^{-1}$ (Jenouvrier and Pascat 1981). These shifts together with the experimental shifts have been given in table 2. They agree satisfactorily, confirming the vibrational assignment.

CC-0. In Public Domain. Gurukul Kangri Collection, Haridwar

Digitized by Arya Samaj Foundation Chennai and eGangotri

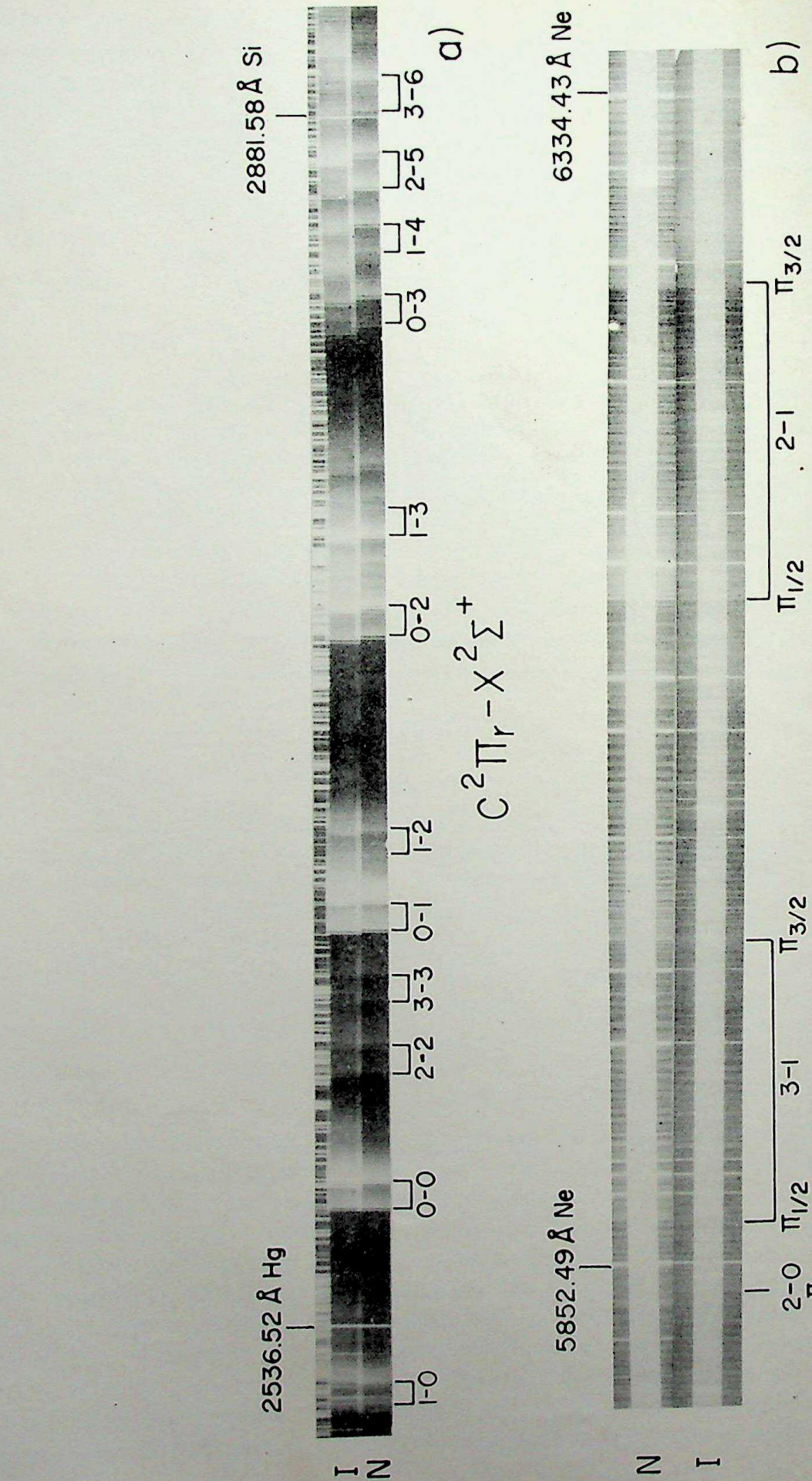

CC-0. In Public Domain. Gurukul Kangri Collection, Haridwar

Digitized by Arya Samaj Foundation Chennai and eGangotri

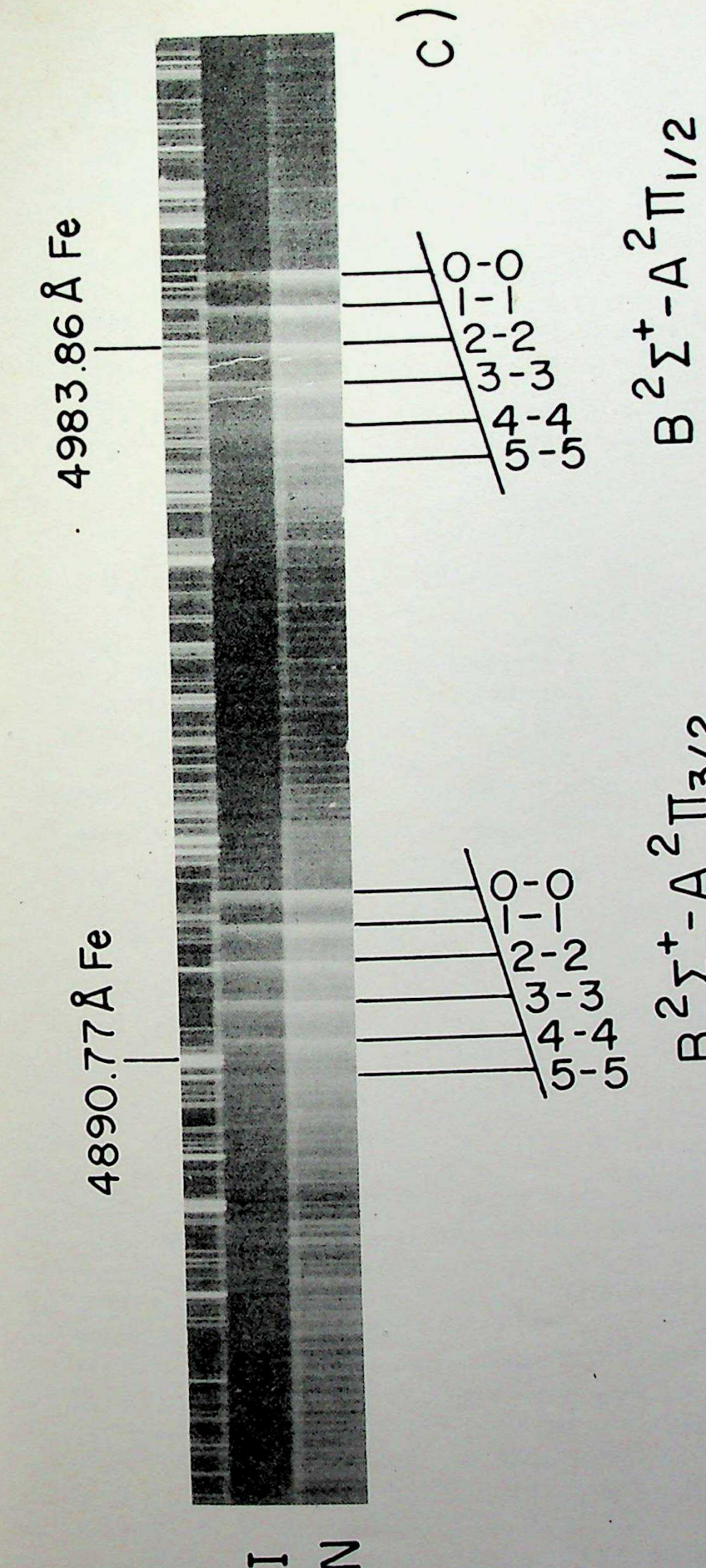

Figure 1. Electronic band spectrum of $B^{32}S$ and $B^{34}S$ molecules. (**a**) $C^2\Pi_r - X^2\Sigma^+$ system, (**b**) a few bands of the $A^2\Pi_i - X^2\Sigma^+$ system, (**c**) $B^2\Sigma^+ - A^2\Pi_i$ system (N: $B^{32}S$ and I: $B^{34}S$).

CC-0. In Public Domain. Gurukul Kangri Collection, Haridwar

Digitized by Arya Samaj Foundation Chennai and eGangotri

Table 3. Isotope shifts (in cm^{-1}) of the $B^2\Sigma^+ - A^2\Pi_i$ bands of $B^{32}S$ and $B^{34}S$.

	$^2\Pi_{1/2}$		$^2\Pi_{3/2}$		Isotope shifts		
					$\Delta\nu_{obs}$	$\Delta\nu_{obs}$	$\Delta\nu_{cal}$
Band	$\nu(N)$	$\nu(I)$	$\nu(N)$	$\nu(I)$	$(^2\Pi_{1/2})$	$(^2\Pi_{3/2})$	
0–0	20011·70	20011·55	20348·44	20348·20	+0·15	+0·24	+0·06
0–1	20030·26	20029·89	20366·26	20365·83	+0·37	+0·43	+0·22
2–2	20050·41	20049·95	20387·62	20387·27	+0·46	+0·35	+0·40
3–3	20062·25	20061·69	20407·68	20407·20	+0·56	+0·48	+0·59
4–4	20095·10	20094·53	20431·43	20430·70	+0·57	+0·78	+0·73
2–3	—	—	19661·27	19664·85	—	−3·58	−4·88
3–4	—	—	19692·44	19696·48	—	−4·04	−4·55
4–5	—	—	19724·36	19728·69	—	−4·33	−4·23

3.3 $B^2\Sigma^+ - A^2\Pi_i$ *system* (4900–5050 Å)

The B–A system consists of strong $\Delta V = 0$ sequence bands and very weak $\Delta V = -1$ sequence bands. McDonald and Innes (1969) confirmed by isotope substitution of ^{10}B and ^{34}S the emitter of these bands as BS molecule. We have obtained experimental isotope shifts of these bands for $B^{32}S$ and $B^{34}S$ molecules and presented them in table 3. The bands belonging to the $\Delta V = 0$ sequence are shown in figure 1c. The theoretical isotope shifts have been calculated from equation (1) using the following constants (in cm^{-1});

for the B state, $\omega_e = 768{\cdot}71$, $\omega_e x_e = 3{\cdot}05$, $\omega_e y_e = -0{\cdot}109$;

for the A state, $\omega_e = 754{\cdot}23$, $\omega_e x_e = 4{\cdot}85$, $\omega_e y_e = 0{\cdot}019$.

The agreement between the values of the experimental and theoretical isotope shifts (table 3) is found to be satisfactory. The existing vibrational assignments have thus been confirmed.

3.4 *Other band systems*

There are two groups of rather closely-spaced bands at 4100 Å and 3100 Å which are assigned to two band systems. In each of these systems only $\Delta V = 0$ sequence bands appear with significant intensity. The 3100 Å group was studied by McDonald and Innes (1969) and assigned to $D^2\Delta_i - A^2\Pi_i$ transition. The 4100 Å group was reported by Jenouvrier and Pascat (1981). In view of the fact that these band systems primarily consist of $\Delta V = 0$ sequences extensive vibrational and rotational analyses have not been done. We have photographed both these band systems for $B^{32}S$ and $B^{34}S$. Although we have determined experimental isotope shifts for both the groups of bands we have not considered it worthwhile to calculate the theoretical shifts because the vibrational constants are not well determined for the electronic states involved. It must also be mentioned that the $E^2\Sigma^+ - X^2\Sigma^+$ bands (2100–2300 Å) reported by Bell and McClean Megan (1976) could not be excited by the present method of excitation.

CC-0. In Public Domain. Gurukul Kangri Collection, Haridwar

Digitized by Arya Samaj Foundation Chennai and eGangotri

Acknowledgements

The authors thank Dr S L N G Krishnamachari for his interest in this work.

References

Bell S and McClean Megan M L 1976 *J. Mol. Spectrosc.* **63** 521
Jenouvrier A and Pascat B 1981 *Can. J. Phys.* **59** 1851, 1862
McDonald J K and Innes K K 1969 *J. Mol. Spectrosc.* **29** 251
Singh J, Tewari D P and Mohan H 1971 *Indian J. Pure Appl. Phys.* **9** 269
Zeeman P B 1951 *Can. J. Phys.* **29** 336

CC-0. In Public Domain. Gurukul Kangri Collection, Haridwar

Digitized by Arya Samaj Foundation Chennai and eGangotri

CC-0. In Public Domain. Gurukul Kangri Collection, Haridwar

Digitized by Arya Samaj Foundation Chennai and eGangotri

Pramāṇa – J. Phys., Vol. 28, No. 2, February 1987, pp. 167–179. © Printed in India.

Electron impact excitation of hydrogen and helium in Coulomb-projected Born methods

C S SINGH and D K RAI
Department of Physics, Banaras Hindu University, Varanasi 221 005, India

MS received 21 July 1986; revised 4 December 1986

Abstract. Coulomb-projected Born methods for the theoretical study of electron impact excitation of hydrogen and helium are reviewed. The results obtained by using different forms of Coulomb-projected Born methods are compared with other theoretical and experimental results and analyzed. The inadequacy of the variable charge Coulomb-projected Born approximation (VCCPB)—the most recent form of the Coulomb-projected Born methods—in giving good results in processes where exchange is dominant is discussed in detail. The 'modified' VCCPB approximation obtained by modifying the VCCPB method to remove its shortcomings is also discussed and its application to electron impact excitation of 2^3s state of helium is studied.

Keywords. Electron impact excitation; hydrogen; helium; Coulomb projection; screening; distorted wave; exchange potential; antisymmetrized.

PACS No. 34·80

1. Introduction

The Coulomb-projected Born approximation consists basically of modifying the usual Born approximation by taking an explicit account of the Coulomb interaction between the projectile and the target nucleus. Different ways of taking this Coulomb interaction into account have led to different CPB methods—Geltman's Coulomb-projected Born approximation (CPB) (Geltman 1971, 1976), generalized Coulomb-projected Born approximation (GCPB) (Stauffer and Morgan 1975) and variable-charge Coulomb-projected Born approximation (VCCPB) (Schaub-Shaver and Stauffer 1980a). Geltman's CPB method has been applied by Geltman and Hidalgo (1971) and Hidalgo and Geltman (1972) to evaluate the direct scattering amplitude for electron impact with hydrogen and helium. No account of exchange was taken. A better CPB study of e^--H scattering was carried out by Stauffer and Morgan (1975) who also included exchange contributions. These authors extended the CPB approximation by introducing a screening parameter which takes partial account of the screening of the nuclear charge by the bound electrons. Calculations were carried out for several values of the screening parameter and results in (reasonable) agreement with experiment were obtained. More recently Schaub-Shaver and Stauffer (1980a) generalized this model by making the screening parameter a function of the distance between the incident particle and the target atom. This VCCPB approximation has been applied to electron impact excitation of hydrogen (Schaub-Shaver and Stauffer 1980a) and hydrogen-like ions (Schaub-Shaver and Stauffer 1980b) and it was found that the calculated total cross-

CC-0. In Public Domain. Gurukul Kangri Collection, Haridwar

Digitized by Arya Samaj Foundation Chennai and eGangotri

sections are in better (as compared to the results for a fixed screening parameter) agreement with experimental and other theoretical results. When applied to electron impact excitation of 1^1S-2^1S excitation in helium (Singh *et al* 1983a) and helium-like ions (Singh *et al* 1983b) it was seen that for low impact energy the VCCPB approximation gave results which were not as good as was expected. Comparing the VCCPB method with Bhatia and Temkin's (1977) distorted wave (DW) method it was concluded that the VCCPB approximation is inadequate for processes where exchange contribution is significant. This inadequacy of the VCCPB method was discussed by Singh *et al* (1984) who also modified the VCCPB approximation to remove this shortcoming. This 'modified' VCCPB method together with the original VCCPB method has been applied to electron impact excitation of 1^1S-2^3S transition in helium. The results obtained by the 'modified' VCCPB method are in much better agreement with the experimental and other accurate theoretical results.

2. General theory of the CPB approximation

It has long been accepted that the first Born approximation (FBA) gives a reasonably accurate account of total cross-sections for a large class of inelastic processes at some sufficiently high energy. It remains unclear how high this energy (of course, this limiting energy depends on the process under consideration) must be for FBA results to be reliable within some preassigned error. Comparison of experimental and theoretical results also shows that FBA does not describe well the inelastic differential cross-sections at large angles, but again, there is no way of specifying in advance the angular range over which one can expect FBA results to be accurate within a preassigned error at a specified energy. To improve upon the Born approximation modifications of this basic approximation e.g. distorted wave Born method, Vainshtein-Presnyakov and Sobelman (VPS) method, Eikonal Born series method, Coulomb-projected Born method etc have been suggested. These modified approximations take account of the incident particle-target nucleus and incident particle-bound electron interactions to different extents. We shall mainly discuss the CPB approximation in some details.

The Coulomb-projected Born (CPB) approximation was formulated by Geltman (1976) making use of the fact that one may split the total Hamiltonian H of a system in an arbitrary way between an unperturbed part H and a perturbation V. The most common choice is to assume that the unperturbed part consists of the (N-electron) target and a non-interacting incident particle (electron in our case). We thus write

$$H = H_A - \tfrac{1}{2}\nabla^2_{r_{N+1}} \tag{1}$$

and consequently

$$V = -\frac{Z}{r_{N+1}} + \sum_{i=1}^{N} \frac{1}{|\mathbf{r}_{N+1} - \mathbf{r}_i|}, \tag{2}$$

H_A is the Hamiltonian of the target atom with N electrons. $\mathbf{r}_{N+1}$ represents the co-ordinate of the projectile and $\mathbf{r}_i$'s, for $i = 1, \ldots N$ represent the co-ordinates of the N bound electrons. The target nucleus is assumed to be infinitely heavy and at rest and is also taken as the origin of the co-ordinate system.

The transition matrix element T_{if} for a transition in which the target atom goes from

CC-0. In Public Domain. Gurukul Kangri Collection, Haridwar

Digitized by Arya Samaj Foundation Chennai and eGangotri

an initial state i to a final state f can be written as

$$T_{if} = \langle \exp(i\mathbf{k}_f \cdot \mathbf{r}_{N+1})\, \varphi_f(\mathbf{r}_1, \mathbf{r}_2, \ldots \mathbf{r}_N) | V | \Psi_i(\mathbf{r}_1, \mathbf{r}_2, \ldots \mathbf{r}_{N+1}) \rangle. \tag{3}$$

Geltman included the $-Z/r_{N+1}$ term in the unperturbed part of the full Hamiltonian and wrote

$$H_0 = H_A - \tfrac{1}{2}\nabla^2_{r_{N+1}} - \frac{Z}{r_{N+1}}, \tag{4}$$

and

$$V = \sum_{i=1}^{N} \frac{1}{|\mathbf{r}_{N+1} - \mathbf{r}_i|}. \tag{5}$$

With this choice of the interaction potential the T-matrix element takes the form

$$T_{if} = \left\langle \psi_f \left| \sum_{i=1}^{N} \frac{1}{|\mathbf{r}_{N+1} - \mathbf{r}_i|} \right| \Psi_i^{(+)} \right\rangle. \tag{6}$$

For this choice of H_0 the total wavefunction ψ_f for the final state can be written in the form

$$\psi_f = \chi_f(\mathbf{k}_f, \mathbf{r}_{N+1})\, \varphi_f(\mathbf{r}_1, \mathbf{r}_2, \ldots \mathbf{r}_N), \tag{7}$$

where χ_f is the Coulomb wavefunction of the projectile electron (with wave vector $\mathbf{k}_f$) in the Coulomb field of the nuclear charge Z of the target atom. In the earlier way of separating H (equations (1) and (2)) the corresponding ψ_f is similar to (7) but χ_f has to be replaced by a free wave $\exp(i\mathbf{k}_f \cdot \mathbf{r}_{N+1})$ (as in this case no net positive charge is acting). It is this replacement of a Coulomb wave in place of a plane wave in the expression for T_{if} due to which Geltman's procedure is referred to as the Coulomb-projected form of the transition matrix element.

The Coulomb-projected Born approximation is obtained in the usual manner by replacing the exact scattering solution $\Psi_i^{(+)}$ by an approximate solution of the form $\exp(i\mathbf{k}_i \cdot \mathbf{r}_{N+1})\, \varphi_i(\mathbf{r}_1, \mathbf{r}_2, \ldots \mathbf{r}_N)$ in equation (6). $\mathbf{k}_i$ is the initial wave vector of the projectile electron and φ_i is the wavefunction of the target atom in its initial state. If we make the same replacement for $\Psi_i^{(+)}$ in expression (3) we get the Born approximation. In the Born approximation the incident electron-nucleus interaction term $-Z/r_{N+1}$ makes no contribution to the direct excitation amplitude as it vanishes due to the orthogonality of the atomic wavefunction. However, in the Coulomb-projected Born approximation i.e. equation (6), the $-Z/r_{N+1}$ term does contribute significantly even in the direct amplitude and this approximation is a better representation of the electron-atom collision process.

When applied to electron impact excitation of hydrogen (Geltman and Hidalgo 1971) (1*s*-2*s*, 1*s*-2*p*, 1*s*-3*s* transitions) the evaluated CPB total cross-sections converge to Born results at high energies, but the differential cross-sections at large angles show marked disagreement with the Born approximation though the CPB values are in reasonable agreement with experimental results.

The reason for the qualitative success of the CPB is its inclusion of the interaction between the incident electron and the target nucleus, an effect which is neglected entirely in the first Born approximation but is included in higher Born approximations. The CPB is thus analogous to a complete summation of that part of the Born series which involves the interaction between the incident electron and the target nucleus.

CC-0. In Public Domain. Gurukul Kangri Collection, Haridwar

Digitized by Arya Samaj Foundation Chennai and eGangotri

However, the incident electron-atomic electron interaction is included only upto the first order.

3. Generalization of the CPB method

Later Stauffer and Morgan (1975) argued that a more accurate description of electron-atom collisions must note that the incident (also the scattered) electron never 'sees' the bare nucleus, and hence does not experience its full charge but only 'sees' a partially screened charge. This screening is provided by the bound electrons in the target atom. Normally the most important contribution to the *e-A* inelastic processes involving the excitation or ionization of any particular electron from the atom A comes from impact parameters which are comparable to the appropriate shell radius. Since we are interested usually in excitation of outer valence electrons the incident electron spends most of its time outside the inner shells which effectively screen the nucleus, at least partially. At very low incident energies this argument may not hold and the incident particle may have to penetrate inside the shell in which case the screening gets changed drastically. Even the effective binding energy of the bound electrons may get changed. Such effects are well studied in the inner shell ionization of atoms by heavy charge particles (Brandt *et al* 1966a, 1966b). In this case the appropriate choices for the unperturbed Hamiltonian and the interaction are

$$H_0 = H_A - \tfrac{1}{2}\nabla^2_{r_{N+1}} - \frac{\xi}{r_{N+1}} \tag{8}$$

and

$$V = \frac{Z-\xi}{r_{N+1}} + \sum_{i=1}^{N} \frac{1}{|\mathbf{r}_{N+1} - \mathbf{r}_i|} \tag{9}$$

where $0 \leqslant \xi \leqslant Z$. The corresponding transition matrix element then becomes

$$T_{if} = \langle \varphi_f(\mathbf{r}_1, \mathbf{r}_2, \ldots, \mathbf{r}_N)\, \chi_f(\xi, \mathbf{r}_{N+1}) | V | \varphi_i(\mathbf{r}_1, \mathbf{r}_2, \ldots \mathbf{r}_N) \times \exp(i\mathbf{k}_i \cdot \mathbf{r}_{N+1}) \rangle. \tag{10}$$

In (10) χ_f is a Coulomb wavefunction describing the scattered free electron in the field of a charge situated at the position of the nucleus. This approximation (equation (10)) is referred to as the generalized Coulomb-projected Born (GCPB) approximation and reduces to the first Born approximation for $\xi = 0$ and to the Geltman's CPB approximation for $\xi = Z$. A further modification of the method was later suggested by Schaub-Shaver and Stauffer (1980a) in which one assumes that ξ, the screened nuclear charge, is a function of the position of the incident electron. This approximation is referred to as the variable-charge Coulomb-projected Born approximation (VCCPB) and is described in the following.

In the VCCPB approximation the perturbation potential V is taken as

$$V = -\frac{Z - \xi(\mathbf{r}_{N+1})}{\mathbf{r}_{N+1}} + \sum_{i=1}^{N} \frac{1}{\mathbf{r}_{N+1} - \mathbf{r}_i}. \tag{11}$$

Here $\xi(\mathbf{r}_{N+1})$ is the screened charge seen by the free scattered electron which depends on

CC-0. In Public Domain. Gurukul Kangri Collection, Haridwar

Digitized by Arya Samaj Foundation Chennai and eGangotri

the position of the scattered electron. The VCCPB choice for $\xi(r_{N+1})$ is based on the following arguments.

The charge density (in units of e) due to a single electron, say electron 1, in the N-electron system described by a wavefunction $\varphi(\mathbf{r}_1, \mathbf{r}_2, \ldots \mathbf{r}_N)$ can be written as

$$\rho_1(r_1) = \int d\mathbf{r}_2\, d\mathbf{r}_3 \ldots . d\mathbf{r}_N |\varphi(\mathbf{r}_1, \mathbf{r}_2, \ldots, \mathbf{r}_N)|^2. \tag{12}$$

The charge density $\rho(r)$ at position $\mathbf{r}$ due to all the atomic electrons is therefore given by

$$\rho(r) = N\rho_1(r). \tag{13}$$

The potential experienced by the incident electron at position $\mathbf{r}_{N+1}$ due to this total electronic charge density $\rho(r)$ at the point $\mathbf{r}$ is given by

$$U(r_{N+1}) = \int \frac{\rho(r)}{|\mathbf{r} - \mathbf{r}_{N+1}|} d\mathbf{r}. \tag{14}$$

Hence from (12) and (13), we have

$$U(r_{N+1}) = N \int \frac{|\varphi(\mathbf{r}_1; \mathbf{r}_2, \ldots, \mathbf{r}_N)|^2}{|\mathbf{r}_1 - \mathbf{r}_{N+1}|} d\mathbf{r}_1\, d\mathbf{r}_2 \ldots d\mathbf{r}_N. \tag{15}$$

The total potential of the incident electron is thus given by

$$-\frac{Z}{r_{N+1}} + U(r_{N+1}). \tag{16}$$

If we write $Q(r_{N+1})/r_{N+1} = U(r_{N+1})$, then the effective potential felt by the incident electron can be written as

$$-\frac{Z}{r_{N+1}} + \frac{Q(r_{N+1})}{r_{N+1}}$$

or by
$$-[Z - Q(r_{N+1})]/r_{N+1}. \tag{17}$$

(This expression is just the static potential of the atom when it is in the state described by the wavefunction $\varphi(\mathbf{r}_1, \mathbf{r}_2, \ldots, \mathbf{r}_N)$). Based on this description the screened charge seen by the scattered particle can be taken as

$$\xi(r_{N+1}) = Z - Q(r_{N+1}). \tag{18}$$

It is clear that as long as the unperturbed part of the Hamiltonian i.e. H_0 can be written as the sum of two terms—one representing the target atom and another which is a function of the projectile electron co-ordinate $\mathbf{r}_{N+1}$, we can always write for ψ_f

$$\psi_f = \varphi_f(\mathbf{r}_1, \mathbf{r}_2, \ldots, \mathbf{r}_N) \cdot F(\mathbf{r}_{N+1}). \tag{19}$$

$F(\mathbf{r}_{N+1})$ represents the wavefunction of the scattered particle. Since in the VCCPB approximation the above decomposition of H_0 holds, in this VCCPB method ψ_f is represented as in (19).

Transition matrix element for the VCCPB approximation for electron-helium

CC-0. In Public Domain. Gurukul Kangri Collection, Haridwar

Digitized by Arya Samaj Foundation Chennai and eGangotri

scattering is obtained by putting $N = 2$ in (10), replacing $\chi_{\mathbf{k}_f}(\xi, \mathbf{r}_{N+1})$ by $F(\mathbf{r}_3)$ and antisymmetrizing the initial state wavefunction

$$T_{if}^{\text{VCCPB}} = \langle \varphi_f(1,2)\, F(\mathbf{r}_3) | V | \mathscr{A} \varphi_i(1,2) \exp(i\mathbf{k}_i \cdot \mathbf{r}_3) \rangle. \tag{20}$$

V is given by equation (11). $\mathscr{A}$ is the antisymmetrization operator.

Direct T^d and exchange T^{ex} transition matrices were obtained (Schaub-Shaver and Stauffer 1980b) separately by expanding $F(\mathbf{k}_f, \mathbf{r})$ as a sum over partial waves

$$F(\mathbf{k}_f, \mathbf{r}) = \frac{1}{\sqrt{k_f}} \sum_l \frac{(2l+1)\, i^l \exp(i\delta l)\, U_l(k_f, r)\, P_l(\cos\theta)}{r}, \tag{21}$$

where θ represents the angle between the final momentum vector $\mathbf{k}_f$ of the scattered electron and its radius vector $\mathbf{r}$ and $P_l(\cos\theta)$ is the Legendre polynomial of degree l. $U_l(k_f, r)$ satisfies the differential equation

$$\left(\frac{\mathrm{d}^2}{\mathrm{d}r^2} + k_f^2 - \frac{l(l+1)}{r^2} + \frac{2\xi(r)}{r}\right) U_l(k_f, r) = 0. \tag{22}$$

The boundary conditions to be satisfied by U_l are

$$U_l(k_f, r) = 0 \qquad r \to 0 \tag{23}$$

and

$$U_l(k_f, r) = k_f^{-1/2} \sin\left(k_f r - \frac{l\pi}{2} - \delta_l\right). \qquad r \to \infty$$

Equation (22) was solved by a non-iterative procedure due to Marriot (1958), the normalization being obtained by comparison with the JWKB solution (Burgess 1963).

The differential cross-section was obtained by using the expression

$$\frac{\mathrm{d}\sigma}{\mathrm{d}\Omega} = \frac{1}{4\pi^2} |T^d - T^{\text{ex}}|^2. \tag{24}$$

The total cross-section σ is obtained after integrating this expression over the angular co-ordinates.

When applied to helium-like atoms (Singh *et al* 1983a, b) for 2^1S excitation by electron impact it is seen that the results obtained using VCCPB method at higher energies are in agreement with other theoretical and experimental results. Differential cross-section obtained by this method at 100 eV and 200 eV in the case of helium atom is in better agreement with the experimental results than CPB results (Singh *et al* 1983a). At low energies the results obtained by this method (VCCPB) diverge from other (similar) theoretical and experimental results (Singh *et al* 1983a, b).

This method (VCCPB) was further applied (Singh *et al* 1984) to electron impact excitation of 2^3S state in helium atom. The results obtained are in very poor agreement with other theoretical and experimental results (for all values of the impact energy) (figure 1). Looking at these results it was conjectured that the VCCPB approximation gives poor result in processes where exchange phenomenon is dominant. (The 2^3S excitation of helium atom by electron impact can occur only through exchange because

CC-0. In Public Domain. Gurukul Kangri Collection, Haridwar

Digitized by Arya Samaj Foundation Chennai and eGangotri

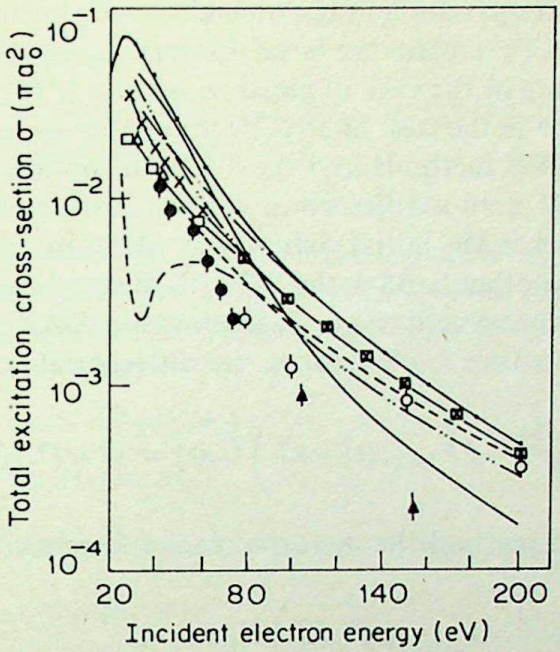

Figure 1. Total cross-section for 1^1S-2^3S transition in helium by electron impact. **Theory**: –□–□– 'modified' VCCPB results; —— VCCPB results; –..– R-matrix (Fon *et al* 1979); –.– Many body theory (Thomas *et al* 1974); — — DWPO results (Scott and McDowell 1975); – × – × – DW results (Baluja and McDowell 1979); ----- Second-order potential method (Winters 1974 cited in Scott and McDowell 1975); —·—·— Born calculation (Felden and Felden 1977). **Experiment**: ○ Yagishita (1978a); △ Trajmar (1973); ● Crooks *et al* (1972); ▲ Vriens *et al* (1968).

relativistic effects are being neglected and in electron impact excitation of 2^1S state of helium-like atoms exchange is considerable at low energies). To verify this conclusion we shall analyze the VCCPB method and compare it with Bhatia and Temkin's (1977) (BT) distorted wave approach as there is an apparent similarity between the two methods even though the results obtained by the VCCPB method in the case of electron impact excitation of helium-like ions (Singh *et al* 1983b) are not in reasonable agreement with those obtained by the BT method.

4. Excitation of 2^3S state of helium

It is easy to show that the VCCPB model, in which the effective nuclear charge as seen by the projectile varies with the latter's position, is essentially a distorted wave Born (DWB) approximation wherein the distortion is included in the final channel only. The screening parameter determines the static potential of the target system in its initial state and the distortion of the scattered particle wavefunction by this potential is considered.

The VCCPB method when applied to electron impact excitation of 1^1S-2^1S transition in helium-like ions yields cross-section results, at low incident energies (where exchange contributions are significant), which are in very poor agreement with results obtained by Bhatia and Temkin (1977). This particular form (BT model) of the DW model is very similar to the VCCPB model differing only in the choice of channel in which distortion is included. The BT model includes distortion in the initial channel

CC-0. In Public Domain. Gurukul Kangri Collection, Haridwar

Digitized by Arya Samaj Foundation Chennai and eGangotri

while the VCCPB model includes it in the final channel. Both models do not take any account of polarization. To explain the large discrepancy between the VCCPB results and the other DW results in the case of electron impact 1^1S-2^1S excitation in helium and helium-like ions and in the case of 1^1S-2^3S transition in helium atom we examine (Singh *et al* 1984) the DW methods and the VCCPB method.

We see that in the DW methods distortion is taken into account in both the channels or, if in only one channel, in the initial channel for which the wavefunction is properly antisymmetrized. On the other hand in the VCCPB method, distortion is considered in the final channel where the wavefunction ψ_f is unsymmetrized. In the DW methods the distorted radial wavefunction $U_l(r)$ satisfies the differential equation

$$\left(\frac{d^2}{dr^2}-\frac{l(l+1)}{r^2}-2V_{1s,1s}(r)+k_f^2\right)U_l(r)=W(r)\,U_l(r), \tag{25}$$

whereas in the VCCPB method the distorted radial function satisfies the equation

$$\left(\frac{d^2}{dr^2}-\frac{l(l+1)}{r^2}-V_{1s,1s}(r)+k_f^2\right)U_l(r)=0. \tag{26}$$

These two equations differ from one another in an important manner, namely the presence of an additional antisymmetrization (also sometimes referred to as exchange potential, Baluja *et al* 1978) potential $W(r)$ in the former equation. $V_{1s,1s}(r)$ and $V_{1s,2s}(r)$ are the static potentials of helium in the ground and excited configurations respectively. Thus in the DW methods the additional Hartree-Fock exchange potential $W(r)$ is included while solving the radial part of the distorted wavefunction whereas in the VCCPB method this is not so. The distortion introduced in the VCCPB method is, therefore, inadequate.

Recently we used a VCCPB type DW model utilizing the prior form of T-matrix to remove this discrepancy and obtained very good results for 1^1S-2^3S excitation of helium by electron impact. The mathematical details are as follows:

In the case of electron helium scattering

$$H=-\sum_{i=1}^{3}\frac{1}{2}\nabla_i^2-\sum_{i=1}^{3}\frac{Z}{r_i}+\sum_{\substack{i=1\\ j>i}}^{3}\frac{1}{r_{ij}}. \tag{27}$$

Z is the nuclear charge and is equal to 2 in the case of helium, but can take other values for other helium-like systems. In the decomposition

$$H=H_i+V_i \tag{28}$$

we take

$$H_i=\sum_{i=1}^{3}\frac{1}{2}\nabla_i^2-\sum_{i=1}^{2}\frac{Z}{r_i}+\frac{1}{r_{12}} \tag{29}$$

and

$$V_i=-\frac{Z}{r_3}+\sum_{i=1}^{2}\frac{1}{r_{13}}. \tag{30}$$

Let us write V_i as a sum of two terms

$$V_i=U_i+W_i \tag{31}$$

CC-0. In Public Domain. Gurukul Kangri Collection, Haridwar

Digitized by Arya Samaj Foundation Chennai and eGangotri

and take

$$U_i = \langle \varphi_f(1,2)|V_i|\varphi_f(1,2)\rangle. \tag{32}$$

In other words U_i is the static potential of the target in the final state. The prior form of the T-matrix element then takes the form

$$\langle \mathscr{A}\varphi_f(1,2)\,F_f(3)|V_i - U_i|\varphi_i(1,2)\,F_i(3)\rangle. \tag{33}$$

In the above equation we have replaced the exact total wavefunction of the final channel i.e. $\Psi_f^{(-)}$ by an approximate but properly antisymmetrized function $\mathscr{A}\varphi_f(1,2)\,F_f(3)$.

For the ground state 1^1S of helium atom we have used a wavefunction due to Byron and Joachain (1966) of the form

$$\varphi_i(\mathbf{r}_1, \mathbf{r}_2) = (4\pi)^{-1}\, R_i(r_1, r_2) \tag{34}$$

with
$$R_i(r_1, r_2) = R_{1s}(r_1)\,R_{1s}(r_2) \tag{35}$$

The one-electron radial functions were represented by a sum of two exponentials:

$$R_{1s}(r) = (Ae^{-pr} + Be^{-qr}). \tag{36}$$

The parameters have the values

$$A = 2{\cdot}60505, \quad B = 2{\cdot}081144, \quad p = 1{\cdot}41, \quad q = 2{\cdot}61$$

The excited state wavefunction $\varphi_f(\mathbf{r}_1, \mathbf{r}_2)$ for the 2^3S state is represented in the form (Van den Bos 1969)

$$\varphi_f(\mathbf{r}_1, \mathbf{r}_2) = (4\pi)^{-1}\, R_f(r_1, r_2) \tag{37}$$

with
$$R_f(r_1, r_2) = \phi_1(r_1)\,\phi_2(r_2) - \phi_1(r_2)\,\phi_2(r_1). \tag{38}$$

The one-electron functions ϕ_1 and ϕ_2 are again represented in terms of exponentials:

$$\phi_1(r) = \exp(-a_n r) \quad \text{and} \quad \phi_2(r) = N[\exp(-c_n r) - br\exp(-b_n r)]. \tag{39}$$

The parameters have the values

$$a_n = 2{\cdot}0, \quad c_n = 1{\cdot}57, \quad b_n = 0{\cdot}61, \quad N = 4{\cdot}1956, \quad b = 0{\cdot}340.$$

If we expand $F_n(\mathbf{r}_3)$ $[n = i, f]$ in terms of partial waves in the form

$$F_n(\mathbf{r}_3) = k_n^{-1/2}\, r_3^{-1} \sum_{l=0}^{\infty} (2l+1)\, i^l \exp[\pm i\{\delta_l + \eta_l(k_n)\}] \times U_l^n(k_n, r_3)\, P_l(\cos \hat{k}_n \cdot \hat{r}_3) \tag{40}$$

($\pm$ sign is used in the exponential according to whether it is an outgoing or an incoming distorted wave), we see that U_l^n satisfies the differential equation

$$\left(\frac{d^2}{dr^2} - \frac{l(l+1)}{r^2} - 2U_i(r) + k_n^2\right) U_l^n(r) = \delta_{nf}\left[\frac{4}{2l+1}\,(F_1 Y_l^{\{1\}}(r) + F_2 Y_l^{\{2\}}(r)) + 2\delta_{l0}\, r\, S(r)\right]. \tag{41}$$

CC-0. In Public Domain. Gurukul Kangri Collection, Haridwar

Digitized by Arya Samaj Foundation Chennai and eGangotri

We have used the following definitions of $Y_l^{(1)}$ and $Y_l^{(2)}$

$$Y_l^{(1)}(r_3) = r_3 \int_0^\infty \phi_1(r_1)\, U_l^n(r_1) r_1 \frac{(r_{13})_<^l}{(r_{13})_>^{l+1}}\, dr_1 \tag{42}$$

and

$$Y_l^{(2)}(r_3) = r_3 \int_0^\infty \phi_2(r_1)\, U_l^n(r_1) r_1 \frac{(r_{13})_<^l}{(r_{13})_>^{l+1}}\, dr_1. \tag{43}$$

These quantities $Y_l^{(1)}$ and $Y_l^{(2)}$ satisfy the following Hartree type exchange equations:

$$\frac{d^2}{dr^2} Y_l^{(j)}(r) = \frac{l(l+1)}{r^2} Y_l^{(j)}(r) - (2l+1)\, \phi_j(r)\, U_l^n(r) \tag{44}$$

$$j = 1, 2.$$

F_1, F_2 and S are functions of r and depend on the final state atomic wavefunction parameters.

From equation (41) the following points emerge:

(i) The radial part $U_l^i(r)$ of the wavefunction $F_i(\mathbf{r})$ satisfies a homogeneous differential equation as in this case the right hand side vanishes as $\delta_{nf} = \delta_{if} = 0$. The resulting homogeneous differential equation is

$$\left(\frac{d^2}{dr^2} - \frac{l(l+1)}{r^2} + k_i^2 - U_i(r)\right) U_l^i(r) = 0$$

and differs from a free partial wave of momentum $\mathbf{k}_i$ only in the presence of the potential $U_i(r)$. This potential as already mentioned above is the static potential of the helium atom in the final state. So the radial wave $U_l^i(r)$ contains distortion effects only due to this potential.

(ii) (a) The radial function U_l^f for the $l = 0$ partial wave in the final channel satisfies an inhomogeneous equation. The inhomogeneous term in this case consists of two parts namely

$$\frac{4}{2l+1}(F_1(r) Y_l^{(1)}(r) + F_2(r) Y_l^{(2)}(r)) \quad \text{and} \quad 2rS(r).$$

Both these terms contain contributions from both initial and final atomic states. In addition, the first term, i.e. the term involving $Y_l^{(1)}(r)$ and $Y_l^{(2)}(r)$, incorporates exchange terms of the type one sees in atomic calculations using the Hartree-Fock method.

Thus we find that $U_0^f(r)$ satisfies an equation which differs from a free wave equation and includes distortion effects not only due to the static potential U_i but also due to the Hartree exchange potential.

(b) For waves with $l \neq 0$ the term $2\delta_{l0} rS(r)$ on the right-hand side of equation (41) vanishes and hence the inhomogeneity consists of one term i.e.

$$\frac{4}{2l+1}(F_1(r) Y_l^{(1)}(r) + F_2(r) Y_l^{(2)}(r)).$$

However, in view of the remarks in (iia) even this partial wave includes distortion due to Hartree exchange potential in addition to that due to the static potential U_i.

CC-0. In Public Domain. Gurukul Kangri Collection, Haridwar

Digitized by Arya Samaj Foundation Chennai and eGangotri

We compared the present results (total cross-section) (figure 1) obtained for the 1^1S-2^3S excitation of helium atom by electron impact using the VCCPB method as well as the 'modified' VCCPB method with other calculations. The results obtained in the VCCPB model are in very poor agreement with the results of other distorted wave models (Scott and McDowell 1975; Baluja and McDowell 1979, Winters 1974) and also with other calculations (Thomas *et al* 1974; Fon *et al* 1979; Felden and Felden 1977). The results obtained by using the 'modified' VCCPB method on the other hand are in close agreement with the experimental results (Yagishita 1978; Trajmar 1973; Crooks 1972; Vriens *et al* 1968) even for low incident energies. For incident energies $\geqslant 80$ eV the 'modified' VCCPB results nearly coincide with the results obtained in the very sophisticated DW calculation due to Baluja and McDowell (1979). Differential cross-sections obtained at 40·1 eV and 100 eV also show a qualitative agreement with the experimental results (figures 2–3).

We take the prior form of the T matrix in the modified VCCPB method and write

$$T = \langle \Psi_f^{(-)} | V_i - U_i | \psi_i \rangle$$

and include the effect of distortion in $\Psi_f^{(-)}$. Since $\Psi_f^{(-)}$ is now a properly symmetrized wavefunction the distorted wavefunction is forced to satisfy the symmetry constraint (see equation (41) and comments on it) referred to above. This results in a proper inclusion of the Hartree-Fock exchange (symmetrization) potential in the radial part of the distorted wave equation thereby removing the shortcoming of the original VCCPB method. The wave-function ψ_i in the initial channel also includes distortion but only due to the potential U_i which we took as the static potential in the final state of the target helium atom. Since we retain the concept of the variable screening in our calculations with this scheme and retain distortion in the final channel as in the VCCPB

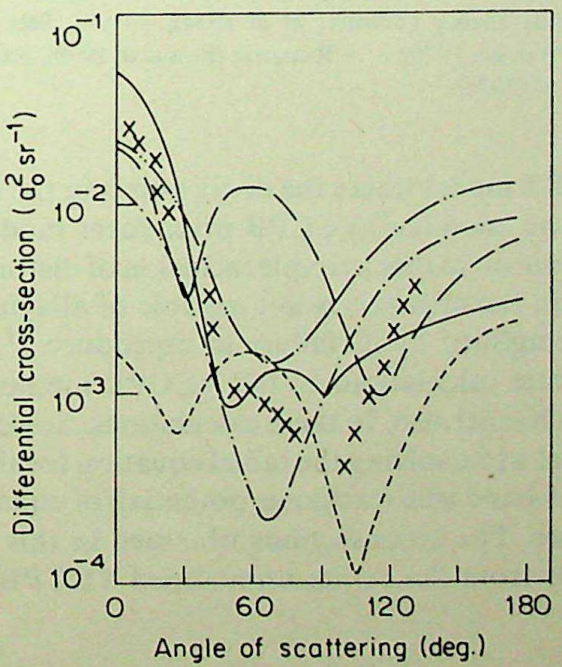

Figure 2. 1^1S-2^3S differential cross-section at 40·1 eV electron impact energy. —— 'modified' VCCPB results; —— VCCPB results; – – – – DWPO results (Scott and McDowell 1975); –.– DW results (Shelton *et al* 1973); –..– Many-body theory (Thomas *et al* 1974); × Experimental results of Trajmar (1973).

CC-0. In Public Domain. Gurukul Kangri Collection, Haridwar

Digitized by Arya Samaj Foundation Chennai and eGangotri

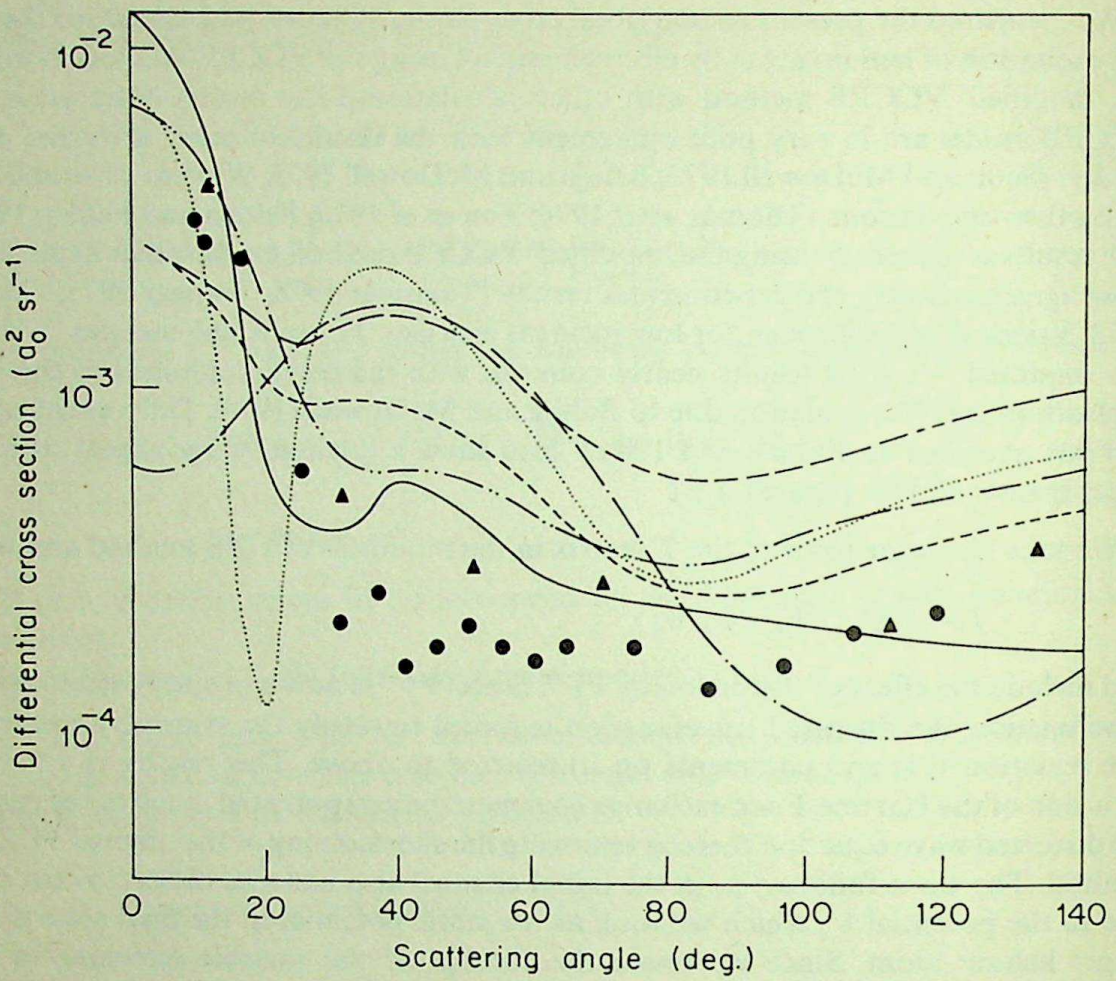

Figure 3. Same as figure 2 but for 100 eV electron impact energy. **Theory**: . . . . . 'modified' VCCPB results; —— VCCPB results; –.– DWPO results (Scott and McDowell 1975); —— Many body theory (Thomas *et al* 1974); – – – – – Second order potential method (Bransden and Winters 1975); –..– R-matrix (Fon *et al* 1979). **Experiment**: ▲ Crooks (1972); ● Yagishita *et al* (1976).

method (in contrast to BT model where the distortion is in the initial channel only) we refer to this model as the 'modified' VCCPB prior form model.

In order to convince ourselves that a simple inclusion of distortion (in the sense of the VCCPB method) in both the channels is not capable of allaying the deficiency of the VCCPB method as exemplified by its failure to reproduce 1^1S-2^3S excitation cross-sections we made separate calculations in the VCCPB method itself after including distortion in the initial channel also. In these calculations, however, we did not include symmetrization potential while solving the radial equation for the distorted wave in the initial channel. The right-hand side (exchange potential) of equation (41) was put equal to zero in both the cases. The cross-sections obtained in this set of calculations are almost indistinguishable from the earlier unmodified VCCPB results.

References

Baluja K L and McDowell M R C 1979 *J. Phys.* **B12** 835
Baluja K L, McDowell M R C, Morgan L A and Myerscough V P 1978 *J. Phys.* **B11** 715

CC-0. In Public Domain. Gurukul Kangri Collection, Haridwar

Digitized by Arya Samaj Foundation Chennai and eGangotri

Bhatia A K and Temkin A 1977 *J. Phys.* **B10** 981
Brandt W, Laubert R and Sellin I 1966a *Phys. Lett.* **21** 518
Brandt W, Laubert R and Sellin I 1966b *Phys. Rev.* **151** 51
Bransden B H and Winters K H 1975 *J. Phys.* **B8** 1459
Burgess A 1963 *Proc. Phys. Soc.* **81** 442
Byron F W and Joachain C J 1966 *Phys. Rev.* **146** 1
Crooks G B 1972 Ph.D. Thesis, University of Nebraska (unpublished)
Crooks G B, Dubois R D, Golden D E and Rudd M E 1972 *Phys. Rev. Lett.* **29** 329
Felden M M and Felden M A 1977 *Can. J. Phys.* **55** 396
Fon W C, Berrington K A, Burke P G and Kingston A E 1979 *J. Phys.* **B12** 1861
Geltman S 1971 *J. Phys.* **B4** 1288
Geltman S 1976 *Electron and photon interactions with atoms* (ed.) H Kleinpoppen and M R C McDowell (New York: Plenum Press) p. 387
Geltman S and Hidalgo M B 1971 *J. Phys.* **B4** 299
Hidalgo M B and Geltman S 1972 *J. Phys.* **B5** 617
Marriot R 1958 *Proc. Phys. Soc.* **72** 121
Schaub-Shaver J A and Stauffer A D 1980a *J. Phys.* **B13** 1457
Schaub-Shaver J A and Stauffer A D 1980b (Private communication)
Scott T and McDowell M R C 1975 *J. Phys.* **B8** 1851
Shelton W N, Baluja K L and Madison D H 1973 *Proc. Eighth Int. Conf. on Physics of Electronic and Atomic Collisions* (Belgrade Institute of Physics) Abstract p. 296
Singh C S, Rai S N, Srivastava R and Rai D K 1984 *Z. Phys.* **A319** 9
Singh C S, Srivastava R and Rai D K 1983a *Phys. Rev.* **A27** 302
Singh C S, Srivastava R and Rai D K 1983b *Can. J. Phys.* **61** 981
Stauffer A D and Morgan L A 1975 *J. Phys.* **B8** 2172
Thomas L D, Csanak G, Taylor H S and Yarlagadda B S 1974 *J. Phys.* **B7** 1779
Trajmar S 1973 *Phys. Rev.* **A8** 191
Vanden Bos J 1969 *Phys. Rev.* **181** 191
Vriens L, Simpson J A and Mielczarck S R 1968 *Phys. Rev.* **165** 7
Winters K H 1974 Ph.D. Thesis, University of Durham
Yagishita A 1978 (quoted in Fon *et al* 1979)
Yagishita A, Takayanagi T and Suzuki H 1976 *J. Phys.* **B9** L53

CC-0. In Public Domain. Gurukul Kangri Collection, Haridwar

Digitized by Arya Samaj Foundation Chennai and eGangotri

CC-0. In Public Domain. Gurukul Kangri Collection, Haridwar

Digitized by Arya Samaj Foundation Chennai and eGangotri

Pramāṇa – J. Phys., Vol. 28, No. 2, February 1987, pp. 181–193. © Printed in India.

Near perpendicular propagation of ion cyclotron modes in a deuterium-hydrogen-oxygen fusion plasma

CHANDU VENUGOPAL
Department of Physics, University of Kerala, Kariavattom 695 581, Kerala, India

MS received 25 July 1986

Abstract. A dispersion relation for the near perpendicular propagation of the electromagnetic ion cyclotron wave has been derived in a fusion plasma that has deuterium as a majority species, hydrogen as a minority species and fully ionized oxygen as an impurity constituent; all being modelled by loss cone distribution functions. The wave has a frequency ω around the deuterium ion gyrofrequency-Ω_D and a wavelength much longer than its Larmor radius γ_{LD} ($k_\perp \gamma_{LD} < 1$); the plasma itself being characterized by large ion plasma frequencies ($\omega_{PD}^2 \gg \Omega_D^2$). Two modes, a low frequency (LF) and a high frequency (HF) mode of opposite electrical energy can propagate in the plasma; the instabilities that arise are thus due to an interaction of modes of opposite energies. We find that while hydrogen tends to destabilize the plasma, the impurity oxygen ions have the reverse effect. Also the plasma is most stable when the ratios of the perpendicular components of oxygen-to-deuterium and hydrogen-to-deuterium temperatures are kept low. Detailed studies of the wave propagation characteristics and energy reveal the close resemblance of a loss cone plasma containing oxygen to a stable Maxwellian plasma in regard to wave stability, propagation and energy.

Keywords. Ion cyclotron wave; fusion plasma; dielectric tensor; approximation scheme; tensor elements; dispersion relation; wave group velocity.

PACS No. 52·40

1. Introduction

In early research in fusion plasma it was realized that the resonances between the natural motion of an ion and an electromagnetic (EM) wave at the same frequency provided an excellent, alternative approach to plasma heating (Stix and Palladino 1958). This method of plasma heating is of great relevance today as fusion physicists find it difficult to achieve the high temperatures necessary by the conventional method of ohmic heating of plasmas. Of the many options available, EM wave in the ion cyclotron range of frequencies (ICRF) has distinguished itself as one of the most successful methods available for the bulk heating of plasmas (Equipe 1981; Perkins 1984).

Fusion plasmas often contain mixtures of deuterium and hydrogen (in a relatively low concentration). Such plasmas, which are in the keV range, also contain metallic impurities such as iron, nickel and chromium. Multiply-ionized oxygen impurity ions can be found in the peripheral low temperature regions (Janzen 1981).

EM wave propagation in multi-ion species plasmas is of great interest since heavy ions, even in small concentrations and low temperatures, greatly modify the propagation and amplification of these waves. In particular, it has been shown that new

CC-0. In Public Domain. Gurukul Kangri Collection, Haridwar

Digitized by Arya Samaj Foundation Chennai and eGangotri

resonances and cut-offs occur, the wave group velocity is greatly altered and that strong coupling may occur in the vicinity of the cross-over frequency (Smith and Brice 1964; Leer *et al* 1978). Such studies, for waves around the ICRF, have been carried out for 2, 3 and n-ion component plasmas by Jessup and McCarthy (1978) and Janzen (1980, 1981); the investigations on the hybrid resonances between the two ion components have been used to successfully explain wave heating results.

On the experimental side, as mentioned above, heating of plasmas by waves around the ICRF has been very successful. Thus in a plasma containing deuterium as the majority species and hydrogen as the minority species considerable increases in both ion and electron temperatures have been achieved (Equipe 1982; Owens *et al* 1983). Similar increases in ion and electron temperatures have also been achieved in the PDX and PLT machines, these plasmas containing either hydrogen or helium as the minority species (Davies *et al* 1983).

Our representative fusion plasma therefore has deuterium (denoted by D^+) as the majority species, hydrogen (H^+) as the minority species and fully ionized oxygen (O^{8+}) as the impurity constituent. The electrons provide only a neutralizing background; all the four constituents of the plasma have been modelled by loss cone distributions to simplify the algebra.

This paper purports to examine whether this successful method of plasma heating by waves around the ICRF could give rise to the reverse process in the form of instabilities. We have therefore derived a dispersion relation for the near perpendicular propagation of the EM ion cyclotron wave in the above representative plasma. The ion cyclotron wave has a frequency around the fundamental harmonic of the D^+ ion gyrofrequency Ω_D and a wavelength much larger than its ion Larmor radius $\gamma_{LD}(k_\perp \gamma_{LD} < 1)$; the plasma itself being characterized by large ion plasma frequencies ($\omega_{PD}^2 \gg \Omega_D^2$). A study of the dispersion relation, which can be used for both the anisotropic Maxwellian and the loss cone plasma, shows that the plasma can support two modes: a higher frequency mode (HF mode) which starts at $Z_D \approx 1 (Z_D = \omega/\Omega_D$; ω being the wave angular frequency) and a lower frequency mode (LF mode) which starts with a small frequency and finally attains a value of $Z_D \approx 1$. We find the LF and HF modes to be of positive and negative electrical energies respectively; the instabilities that arise in the plasma due to a coalescing of the modes can thus be interpreted physically as being due to an interaction between modes of opposite electrical energy (Hasegawa 1975). The stability of these modes has also been studied as a function of three temperature ratios namely, $T_{\perp,eD} = (T_{\perp,e}/T_{\perp,D})$, $T_{\perp,HD} = (T_{\perp,H}/T_{\perp,D})$ and $T_{\perp,OD} = (T_{\perp,O}/T_{\perp,D})$ where $T_{\perp,D}$, $T_{\perp,H}$, $T_{\perp,O}$ and $T_{\perp,e}$ are the temperatures of D^+, H^+, O^{8+} and electrons perpendicular to the ambient magnetic field. We find the plasma to be most stable when $T_{\perp,eD}$ is large and $T_{\perp,HD}$ and $T_{\perp,OD}$ are low. Also while fully ionized oxygen has a stabilizing influence on the plasma, the lighter hydrogen ions tend to enhance the instability of the modes. Detailed studies of the wave propagation velocity, polarization and energy have also been made.

2. The dielectric tensor

We start with the wave equation

$$\frac{c^2}{\omega^2}[\mathbf{k} \times (\mathbf{k} \times \mathbf{E})] + \boldsymbol{K} \cdot \mathbf{E} = 0, \tag{1}$$

CC-0. In Public Domain. Gurukul Kangri Collection, Haridwar

Digitized by Arya Samaj Foundation Chennai and eGangotri

where c is the velocity of light and $\mathbf{k}$ the wave vector. $\mathbf{k}$ has components

$$\mathbf{k} \equiv (k_x = k_\perp; \quad k_y = 0 \quad \text{and} \quad k_z = k_\parallel).$$

$\boldsymbol{K}$, the hot plasma dielectric tensor, can be derived from the coupled kinetic Vlasov-Maxwell equations (Montgomery and Tidman 1964) and the expressions for the individual components $K_{ij}\,(i,j = x,y,z)$ are well known.

As mentioned earlier, we are interested in ion cyclotron wave propagation in a plasma in which all the four components namely deuterium (D), hydrogen (H), oxygen (O) and electrons (e) are modelled by loss cone distribution functions. The equilibrium particle distribution function f_0 is therefore, in general, given by

$$f_0 = [j!\,\pi^{3/2} W^{2j+2} U]^{-1} \left(\frac{v_\perp^2}{W^2}\right)^j \exp\left[-\frac{v_\parallel^2}{U^2} - \frac{v_\perp^2}{W^2}\right] \tag{2}$$

where

$$U^2 = 2T_\parallel/M \quad \text{and} \quad W^2 = 2T_\perp/M(j+1).$$

In (2) j is the loss cone index while T and M denote the temperature and mass respectively.

Substituting (2) into the expressions for the elements K_{ij} (Landau and Cuperman 1971) and carrying out the $dv_\parallel$ and $dv_\perp$ integrations we get the following expressions for the elements of the dielectric tensor $\boldsymbol{K}$:

$$\begin{matrix} K_{xx}-1 \\ K_{xy} \\ K_{yy}-1 \end{matrix} = \sum_s \frac{\omega_p^{2'}}{z} C' \sum_{n=-\infty}^{\infty} \frac{j'n}{\alpha} \frac{n^2}{\alpha^2} \begin{Bmatrix} I_p^j & & I_p^{j-1} \\ I_{\alpha p}^j\left[\frac{1-E}{n-z} - \frac{AE}{z}\right] - j\left[\frac{1-E}{n-z} - \frac{E}{z}\right] & & I_{\alpha p}^{j-1} \\ I_{\alpha\beta p}^j & & I_{\alpha\beta p}^{j-1} \end{Bmatrix}$$

$$\begin{matrix} K_{zx} \\ K_{zy} \end{matrix} = \sum_s \frac{\omega_p^{2'}}{z} C' \sum_{n=-\infty}^{\infty} \begin{matrix} \frac{n}{\theta\alpha^2} \\ \frac{j'}{\theta\alpha} \end{matrix} \begin{Bmatrix} I_p^j & & I_p^{j-1} \\ \left[E + \frac{A}{z}(n-z)E\right] - j\left[E + \frac{1}{z}(n-z)E\right] & & \\ I_{\alpha p}^j & & I_{\alpha p}^{j-1} \end{Bmatrix}$$

and

$$K_{zz} - 1 = \sum_s \frac{\omega_p^{2'}}{z} C' \sum_{n=-\infty}^{\infty} \frac{1}{\theta^2\alpha^2} \left\{ I_p^j \left[\frac{nA}{z} + \frac{W^2}{U^2}\right](z-n)E - j\left[\frac{n}{z}(z-n)E\right] I_p^{j-1} \right\}. \tag{3}$$

CC-0. In Public Domain. Gurukul Kangri Collection, Haridwar

Digitized by Arya Samaj Foundation Chennai and eGangotri

In (3) the summation over s indicates a summation over the species and the definitions of the other parameters, with the subscripts suppressed are:

$$\Omega = \pm\frac{eB_0}{MC}, \quad \omega_p^2 = \frac{4\pi ne^2}{M}, \quad \omega_p^{2'} = \omega_p^2/\Omega^2, \quad j' = \sqrt{-1},$$

$$z = \frac{\omega}{\Omega}, \quad \alpha = \frac{k_\perp}{\Omega}, \quad \theta = \frac{k_\parallel}{k_\perp}, \quad A = 1 - \frac{W^2}{U^2} \quad \text{and}$$

$$C' = 4[j!W^{2j+2}]^{-1}, \tag{4a}$$

$$I_p^j = pL^j I(\alpha, \alpha), \quad I_p^{j-1} = L^{j-1} I(\alpha, \alpha), \tag{4b}$$

$$I_{\alpha p}^j = pL^j\left(\frac{\mathrm{d}}{\mathrm{d}\alpha}\frac{I(\alpha,\alpha)}{2}\right), \quad I_{\alpha p}^{j-1} = L^{j-1}\left(\frac{\mathrm{d}}{\mathrm{d}\alpha}\frac{I(\alpha,\alpha)}{2}\right), \tag{4c}$$

$$I_{\alpha\beta p}^j = pL^j\left(\frac{\mathrm{d}^2 I(\alpha,\beta)}{\mathrm{d}\alpha\,\mathrm{d}\beta}\right), \quad I_{\alpha\beta p}^{j-1} = L^{j-1}\left(\frac{\mathrm{d}^2 I(\alpha,\beta)}{\mathrm{d}\alpha\,\mathrm{d}\beta}\right), \tag{4d}$$

where

$$p \equiv \frac{1}{W^2}, \quad L^j = (-1)^j\frac{\mathrm{d}^j}{\mathrm{d}p^j} \quad \text{and} \quad L^{j-1} = (-1)^{j-1}\frac{\mathrm{d}^{j-1}}{\mathrm{d}p^{j-1}}. \tag{4e}$$

$I = I(\alpha, \beta)$ arises from the $\mathrm{d}v_\perp$ integrations and in its most general form is given by

$$I(\alpha,\beta) = \frac{W^2}{2}\exp\left(-\frac{(\alpha^2+\beta^2)W^2}{4}\right)I_n(\alpha\beta W^2/2). \tag{5}$$

In (4b) we have $\alpha = \beta$ in $I(\alpha, \beta)$, in (4c) we differentiate $I(\alpha, \alpha)$ with respect to α and in (4d) we differentiate $I(\alpha,\beta)$ with respect to α and β and finally set $\alpha = \beta$. These are then differentiated j or $(j-1)$ times with respect to p. The arguments of the Bessel function $I_n = I_n(l'_\perp)$, where

$$l'_\perp = \alpha^2 W^2 = \frac{2}{(j+1)}l_\perp, \tag{6}$$

with

$$l_\perp = k_\perp^2 T_\perp/\Omega^2 M. \tag{7}$$

The E-function, which arises from the $\mathrm{d}v_\parallel$ integration, is defined as (Landau and Cuperman 1971)

$$E(s) = -\tfrac{1}{2}Z'(s/\sqrt{2}), \quad s = (z-n)/\theta\sqrt{l_\parallel}$$

with

$$l_\parallel = k_\perp^2 T_\parallel/\Omega^2 M. \tag{8}$$

Z' is the derivative of the plasma dispersion function of Fried and Conte.

In addition to the above and the definitions of $T_{\perp,eD}$, etc we also define

$$N_{HD} = N_H/N_D, \quad N_{OD} = N_O/N_D \text{ and } \quad N_{eD} = N_e/N_D, \tag{9}$$

where N_D, N_H, N_O and N_e are the densities of D^+, H^+, O^{8+} and electrons respectively.

CC-0. In Public Domain. Gurukul Kangri Collection, Haridwar

Digitized by Arya Samaj Foundation Chennai and eGangotri

We also use the following simplifying relations

$$M_D = 2M_H \quad \text{and} \quad M_O = 8M_D,$$

where M_D, M_H and M_O are the masses of deuterium, hydrogen and oxygen ions respectively. Thus

$$Z_H = \omega/\Omega_H = \tfrac{1}{2}Z_D, \tag{10a}$$

$$Z_O = \omega/\Omega_O = Z_D, \tag{10b}$$

$$Z_e = \omega/\Omega_e = -(M_e/M_D)Z_D, \tag{10c}$$

and

$$\omega_{pH}^{2'} = \frac{N_{HD}}{2}\omega_{pD}^{2'}, \tag{10d}$$

$$\omega_{pO}^{2'} = 8N_{OD}\omega_{pD}^{2'}, \tag{10e}$$

$$\omega_{pe}^{2'} = N_{eD}\frac{M_e}{M_D}\omega_{pD}^{2'}. \tag{10f}$$

3. The approximation scheme

We are interested in the near perpendicular propagation ($k_\parallel \ll k_\perp$) of the *EM* ion cyclotron wave around the fundamental harmonic of the ion gyrofrequency Ω_D of the majority species deuterium. The wave, with a wavelength larger than the D^+ Larmor radius γ_{LD} ($k_\perp \gamma_{LD} < 1$), can have a small range of frequencies both above and below Ω_D; we denote this deviation from the exact first harmonic by means of a small parameter ε. Again, it is assumed that this plasma, which is characterized by large ion plasma frequencies, is approximately temperature isotropic not only with respect to the temperatures parallel and perpendicular to the magnetic field ($T_\parallel$ and $T_\perp$ respectively) but also with respect to the different species themselves. These assumptions regarding the ion cyclotron wave and the plasma in which it propagates permit us the following ordering scheme in terms of a small parameter ε:

$$\nu_D = 1 - Z_D^2 \sim \varepsilon; \quad l'_{\perp,D}, l_{\parallel,D}, \theta \quad \text{and} \quad 1/\omega_{pD}^{2'} \sim \varepsilon;$$

$$T_{eD}, T_{HD}, T_{OD} \quad \text{and} \quad T_\perp/T_\parallel \sim 1 \quad \text{and} \quad M_e/M_D \sim \varepsilon^2. \tag{11a}$$

where

$$T_{eD} = T_e/T_D, \text{ etc.}$$

From the definition of ν_D and using (10a), we get

$$\nu_H = 1 - Z_H^2 = 1 - \frac{Z_D^2}{4} = \tfrac{1}{4}(3 + \nu_D).$$

Thus whenever ν_H occurs in the denominator it can be expanded binomially as

$$\frac{1}{\nu_H} \simeq \tfrac{4}{3} - \tfrac{4}{9}\nu_D \ldots \sim (1 - \varepsilon) \tag{11b}$$

CC-0. In Public Domain. Gurukul Kangri Collection, Haridwar

Digitized by Arya Samaj Foundation Chennai and eGangotri

and from the definition of $l'_{\perp}$, namely (6), we have

$$l'_{\perp,\mathrm{H}} = \tfrac{1}{2} T_{\perp,\mathrm{HD}} l'_{\perp,\mathrm{D}} \sim \varepsilon. \tag{11c}$$

These quantities in the case of O^{8+}, become

$$\nu_{\mathrm{O}} = 1 - Z_{\mathrm{O}}^2 = \nu_{\mathrm{D}} \sim \varepsilon \tag{11d}$$

and

$$l'_{\perp,\mathrm{O}} = \tfrac{1}{8} T_{\perp,\mathrm{OD}} l'_{\perp,\mathrm{D}}. \tag{11e}$$

Though from (11e) we find $l'_{\perp,\mathrm{O}}$ to be only $\frac{1}{8}$ of $l'_{\perp,\mathrm{D}}$ (for $T_{\perp,\mathrm{OD}} = 1{\cdot}0$) the term was retained as such in the expressions for the tensor elements for the following reasons: firstly, since $l'_{\perp,\mathrm{O}}$ always occurred in the numerator and secondly (but more importantly) because it allows us to consider temperature ratios $T_{\perp,\mathrm{OD}} > 1$. In fact a value as high as 8 can be considered when $l'_{\perp,\mathrm{O}} = l'_{\perp,\mathrm{D}}$.

4. The tensor elements and dispersion relation

The expressions for the various tensor elements in (3) retaining terms of order $1/\varepsilon$, 1 and ε and using the ordering scheme of (11a) were derived earlier (Chandu Venugopal, 1983 hereinafter referred to as I). This was for a two-component plasma consisting of protons and electrons; for a compact description of these and the present tensor elements we introduce the following notation. The tensor elements will be written down as a sum of simple brackets containing numerals and carrying subscripts—the numerals indicate the number of terms in the above descending order (that is, the number of terms of order $1/\varepsilon$, 1 and ε) while the subscripts denote the contribution from the particular constituent of the plasma. With this notation, the tensor elements in I can be written as:

$$K_{xx}/\omega_{pi}^{2'} = (1, 2, 6)_i; \quad K_{yy}(Z_i/\omega_{pi}^{2'}) = (1, 3, 6)_i + (0, 0, 1)_e$$

$$\frac{K_{xy}}{j'}\frac{Z_i}{\omega_{pi}^{2'}} = (1, 2, 5)_i + (0, 1, 0)_e; \quad K_{xz}/\omega_{pi}^{2'} = (0, 1, 3)_i,$$

and

$$\frac{K_{zy}}{j'}\frac{Z_i}{\omega_{pi}^{2'}} = (0, 1, 3)_i + (0, 1, 2)_e,$$

where the subscript i refers to ions and $j' = \sqrt{-1}$. Only one term, of order $1/\varepsilon^2$, was retained in K_{zz}. The following equality relations were also found to hold among these tensor elements, namely

$$K_{xy} = j' K_{yy} = j' K_{xx}$$

and

$$K_{yz} \approx -j' K_{xz}. \tag{12}$$

We have assumed a loss cone distribution for all the four constituents of the present plasma and hence their initial contributions to the tensor elements are all similar; however, a number of terms drop out on conversion to the deuterium parameters (using

CC-0. In Public Domain. Gurukul Kangri Collection, Haridwar

Digitized by Arya Samaj Foundation Chennai and eGangotri

(10a) to (10f) and (11b) to (11e)). We shall now briefly describe the tensor elements. The deuterium ion contributions to the tensor elements are similar to the ionic contributions in I (noting, however, the change of ionic species). As mentioned earlier the electrons form only a neutralizing background and hence their contributions to the tensor elements can be got by multiplying the electron contributions in I by N_{eD} (we have normalized all quantities with respect to the deuterium parameters and $N_{eD} = 1$ only for a two-component plasma). Since $v_O = v_D$ and $l'_{\perp,O} \sim l'_{\perp,D}$ the contributions of O^{8+} to the tensor elements are very similar to the contributions of the D^+ ions. And finally, the H^+ ions contribute only to K_{xx}, K_{xy} and K_{yy} and that too only terms of order 1 and ε due to the binomial expansion of terms involving $1/v_H$. Thus the tensor elements in a four-component plasma have the form

$$
\begin{aligned}
&K_{xx}/\omega_{pD}^{2'} = (1, 2, 6)_D + (0, 1, 2)_H + (1, 2, 5)_O,\\
&K_{yy}(Z_D^2/\omega_{pD}^{2'}) = (1, 3, 6)_D + (0, 1, 2)_H + (1, 3, 5)_O + (0, 0, 1)_e,\\
&\frac{K_{xy}}{j'}\frac{Z_D}{\omega_{pD}^{2'}} = (1, 2, 5)_D + (0, 1, 2)_H + (1, 2, 5)_O + (0, 1, 0)_e,\\
&K_{xz}/\omega_{pD}^{2'} = (0, 1, 3)_D + (0, 1, 3)_O,\\
&\frac{K_{zy}}{j'}\frac{Z_D}{\omega_{pD}^{2'}} = (0, 1, 3)_D + (0, 1, 3)_O + (0, 1, 2)_e.
\end{aligned}
\tag{13}
$$

Again only one term of order $1/\varepsilon^2$, was retained for K_{zz}; the equality relations of (12) also hold good. Once more the numerals indicate the number of terms of order $1/\varepsilon$, 1 and ε.

It was shown in I that the dispersion formula for the near perpendicular propagation of ion cyclotron waves is given by

$$
\frac{K_{xx}}{\omega_{pD}^{2'}}\left[-\frac{l_{\perp,D}}{\beta_{\perp,D}} + K_{yy}\frac{Z_D^2}{\omega_{pD}^{2'}}\right] + \left[K_{xy}\frac{Z_D}{\omega_{pD}^{2'}}\right]^2 = 0, \tag{14}
$$

when the dielectric tensor elements are of the above order and the equality relations of (12) hold good. $l_{\perp,D}/\beta_{\perp,D}$, in (14), is ~ 1 and $\beta_{\perp,D}$ is defined as

$$
\beta_{\perp,D} = (4\pi N_D T_{\perp,D})/B_0^2.
$$

Thus substituting the explicit expressions for the tensor elements K_{xx}, K_{xy} and K_{yy} (whose general form is given in (13)) in (14), simplifying and retaining terms ~ 1 we get the dispersion relation as

$$
Av^2 + Bv - C - D = 0, \tag{15}
$$

where

$$
A = \frac{2}{3}N_{HD}\left[\frac{4}{3}(1 + 8N_{OD}) + 2N_{HD} - 4N_{eD} + \frac{l_\perp}{\beta_\perp}\right] + N_{eD}^2
$$

$$
B = -(1 + 8N_{OD})\left(1 + \frac{2}{3}N_{HD} + 8N_{OD} - \frac{l_\perp}{\beta_\perp}\right) - \sigma
$$

CC-0. In Public Domain. Gurukul Kangri Collection, Haridwar

Digitized by Arya Samaj Foundation Chennai and eGangotri

with

$$\sigma = \Big[(1+8N_{OD})\,(\tfrac{1}{3} - 2N_{eD}T_{\perp,eD} - \tfrac{16}{15}N_{HD}T_{\perp,HD} + \tfrac{1}{3}N_{OD}T_{\perp,OD})$$
$$+ (1+N_{OD}T_{\perp,OD})\,(1+\tfrac{8}{3}N_{HD}+8N_{OD}-4N_{eD})$$
$$+ (1+N_{OD}T_{\perp,OD})\frac{l_\perp}{\beta_\perp}\Big] + \frac{2}{\omega_{pD}^{2'}}(1+8N_{OD})$$

$$C = l_\perp^2\Big[\frac{3}{4}(1+8N_{OD})\frac{(j+2)}{(j+1)}\Big(1+\frac{N_{OD}T_{\perp,OD}^2}{8}\Big)$$
$$- (1+N_{OD}T_{\perp,OD})^2\Big] \quad \text{and}$$

$$D = 4\frac{\theta^2 l_\parallel}{\nu}\Big(1+N_{OD}\frac{T_{\parallel,O}}{T_{\parallel,D}}\Big)\Big(1+\frac{2}{3}N_{HD}+8N_{OD}-\frac{l_\perp}{\beta_\perp}\Big).$$

In (15) all un-subscripted parameters refer to the majority species deuterium. And as a check on our results we note that for $N_{HD} = N_{OD} = 0$ ($N_{eD} = 1{\cdot}0$), (15) reduces to the dispersion relation in I.

Inspecting (15) we find that in the assumed ordering more terms may be dropped: for the first three terms to be of order ε^2 we need to set

$$\Big(1+\frac{2}{3}N_{HD}+8N_{OD}-\frac{l_\perp}{\beta_\perp}\Big) \quad \text{to be } \sim \varepsilon.$$

Unfortunately now the D term is of order ε^3 and thus does not contribute to the dispersion relation as the other terms are all of order ε^2. Thus the dispersion relation for the near perpendicular propagation of ion cyclotron waves is of the form $Av^2 + Bv - C = 0$.

5. Wave group velocity, polarization and energy

Differentiating (15) with respect to $k_\perp \gamma_{LD}$ we get a dimensionless quantity $\partial Z_D/\partial k_\perp \gamma_{LD}$ which is, however, proportional to the group velocity V_{gr} of the ion cyclotron waves. We find this expression for V_{gr} to be sensitively dependent on the loss cone index j and on the number densities and temperatures of the constituents of the plasma.

The wave equation (1) can be expanded as a system of homogeneous, simultaneous equations in the perturbed electric fields E_x, E_y and E_z. These can then be solved and expressions obtained for E_z/E_x and E_y/E_x in terms of the dielectric tensor elements K_{ij}. Substituting for the expressions for the tensor elements K_{ij} from (13), one can obtain, after a long and tedious simplification, expressions for E_z/E_x and $j' E_y/E_x$.

It was found that the expression for $j' E_y/E_x \to \infty$ as $Z_D \to 0$ (linear polarization); it is equal to 1 when $Z_D = 1$ (circular polarization) and is greater than 1 when $Z_D > 1$ (elliptic polarization).

The expressions for E_z/E_x and E_y/E_x can also be used to study the wave electrical energy, which we define to be

$$E^2/E_x^2 = [1 + (E_y^2/E_x^2) + (E_z^2/E_x^2)]. \tag{16}$$

CC-0. In Public Domain. Gurukul Kangri Collection, Haridwar

Digitized by Arya Samaj Foundation Chennai and eGangotri

6. Results

We consider typical fusion conditions. $n_D = 10^{14}$ particles cm^{-3}, $T_{\perp,D} = T_{\parallel,D} = 20$ keV and $B_0 = 10$ kG. With these parameters $\beta_{\perp,D} = 0{\cdot}4023$.

Figure 1 depicts the dispersion relation (15) as plots of Z_D versus $k_\perp \gamma_{LD}$ for $\beta'_\perp = 2\beta_{\perp,D}$, $j = 10$ and all temperature ratios = 1·0. The individual plots 1(a) to 1(d) correspond to plasmas of the following compositions: D^+, $D^+ + 10\%H^+$, $D^+ + 5\%O^{8+}$ and $D^+ + 10\%H^+ + 5\%O^{8+}$ respectively. Plot 1(a) also depicts (15) for a purely Maxwellian plasma ($j = 0$ and indicated by dotted lines). We find that in all the cases two modes can propagate in the plasma: a LF mode which starts with a frequency $\omega < \Omega_D$ and finally reaches $\omega \approx \Omega_D$ and an HF mode which starts at $\omega \approx \Omega_D$ and reaches $\omega > \Omega_D$. A common characteristic of all the plots is the mode conversion that exists between these waves. The existence of mode conversion between two waves propagating in an ICRF-heated plasma was anticipated very early (Jacquinot *et al* 1977); mode conversion has since then been experimentally observed in ICRF-heated D^+ and H^+ plasmas on a number of occasions (Ida *et al* 1984). Such mode conversion mechanisms are of interest in RF-heated thermonuclear plasmas as they are expected to play a key role in the understanding of wave damping mechanisms (Colestock and Kashuba 1983).

We now consider the individual plots of figure 1. Plot 1(a) depicts the variation of Z_D versus $k_\perp \gamma_{LD}$ for two values of j (= 0 and 10 and depicted as dotted and solid lines respectively). We find the two modes to be well-separated for $j = 0$. They, however,

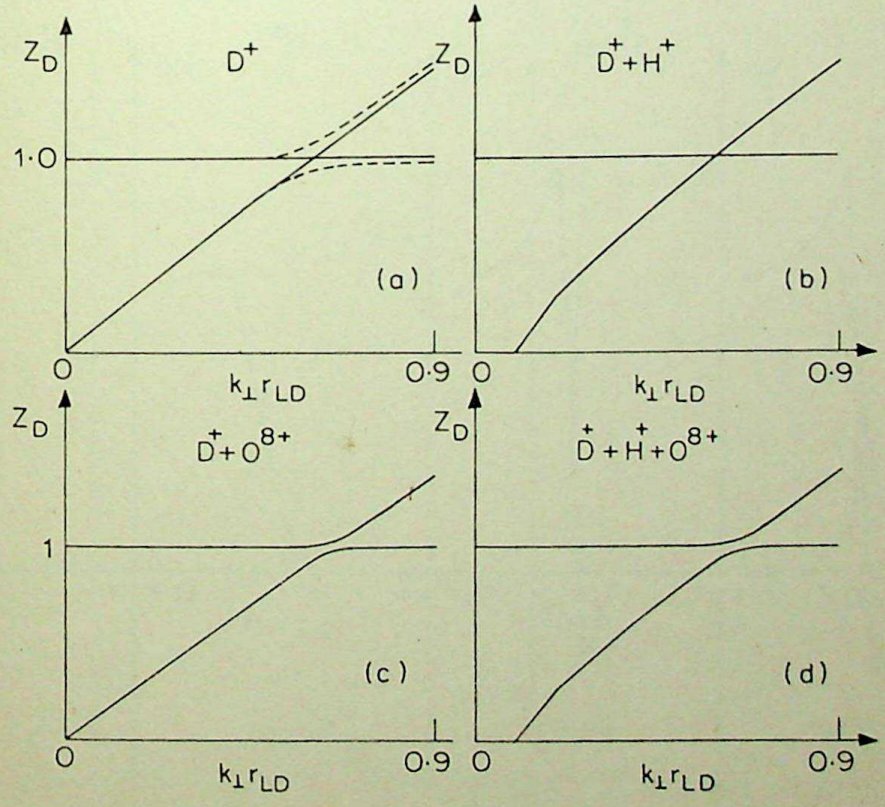

Figure 1. Plots of Z_D vs $k_\perp \gamma_{LD}$ for $\beta'_\perp = 2\beta_{\perp,D}$ and all temperature ratios equal to 1. The solid lines correspond to $j = 10$, the dotted lines of plot 1(a) correspond to $j = 0$. The plasma is stable when the dispersion curves do not intersect.

CC-0. In Public Domain. Gurukul Kangri Collection, Haridwar

Digitized by Arya Samaj Foundation Chennai and eGangotri

come closer for $j = 10$ suggesting that they may coalesce for some higher value of j. (A coalescing of the two modes indicates an instability as it results in a pair of complex conjugate roots for the dispersion relation). In plot 1(b), which is for a plasma containing D^+ and 10% H^+, the two modes coalesce at $k_\perp \gamma_{LD} = 0{\cdot}6$ thus indicating an instability. Thus, with all other parameters being the same, the introduction of a small amount of H^+ makes the plasma unstable. Plot 1(c) is for a plasma containing D^+ and 5% O^{8+}. We find the two modes to be well separated; this dispersion diagram closely resembles the dotted line plot in 1(a) which was for a stable Maxwellian plasma ($j = 0$). The plot of 1(d) is for a plasma of $D^+ + 10\%H^+ + 5\%O^{8+}$. Once again the two modes are well separated; the instability in plot 1(b) is thus removed by the addition of a small amount of O^{8+}. We can thus conclude that the impurity O^{8+} has a stabilizing influence on the plasma. Based on our discussions in § 5 we find that the polarizations of the modes change: the LF mode changes its polarization from linear to circular and the HF mode from circular to elliptic.

Figure 2 reveals the plots of V_{gr} versus $k_\perp \gamma_{LD}$ for $\beta'_\perp = \beta_{\perp,D}$, $j = 10$ and all temperature ratios equal to 1; the compositions of plots 2(a) to 2(d) being identical to that in plots 1(a) to 1(d). Plot 2(a) thus reveals the variation of V_{gr} vs $k_\perp \gamma_{LD}$ for two values of j, namely 0 and 10 in a plasma containing D^+ alone. When $j = 0$ (Maxwellian plasma) the group velocities of both the modes are essentially positive over the entire wavelength range studied. When $j = 10$, however, both modes have wavelength ranges over which the group velocities are negative; the LF and HF modes have peak values of negative V_{gr} at $k_\perp \gamma_{LD} = 0{\cdot}6$ and $0{\cdot}5$ respectively. Thus in a plasma prone to an instability the group velocities of the modes can have negative values. Plot 2(b) is for a

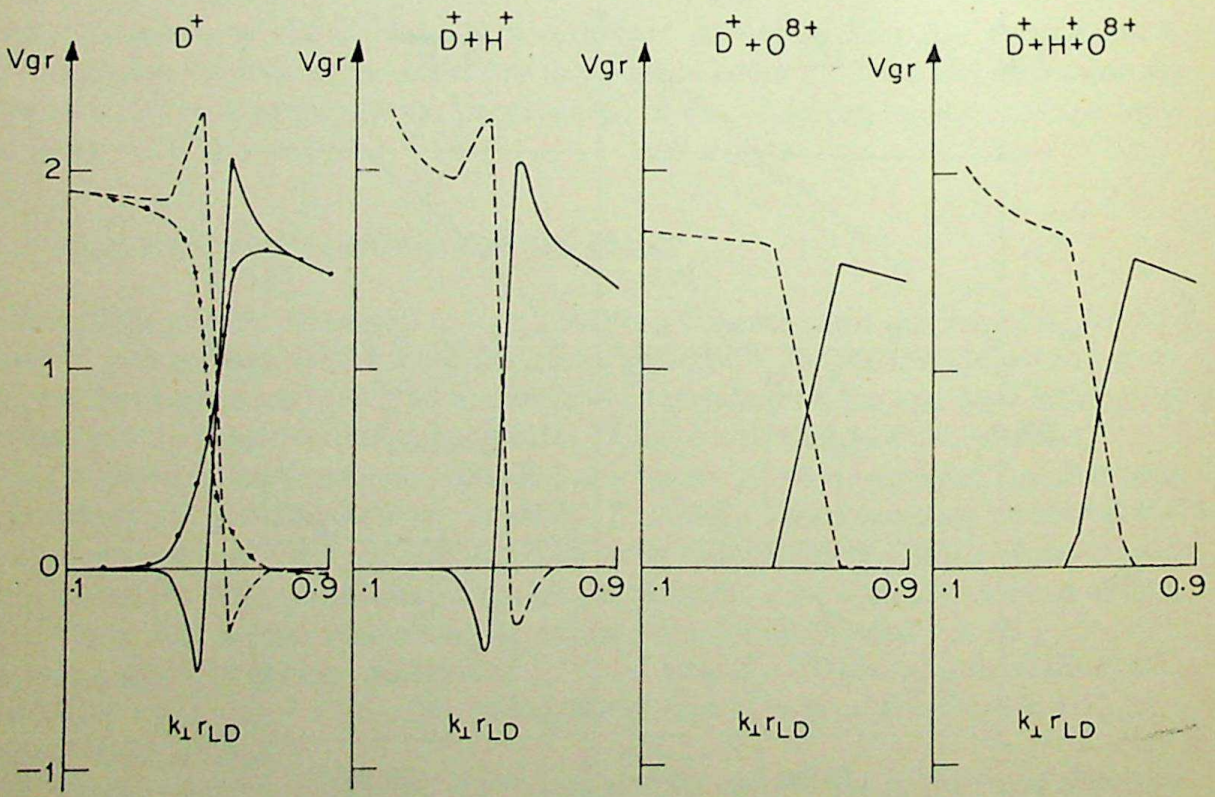

Figure 2. Plots of V_{gr} vs $k_\perp \gamma_{LD}$ for $\beta'_\perp = \beta_{\perp,D}$ and all temperature ratios equal to 1. The solid and dotted lines correspond to the group velocities of the HF and LF modes respectively for $j = 10$; the same for $j = 0$ is indicated by dots in the figures of plot 2(a).

CC-0. In Public Domain. Gurukul Kangri Collection, Haridwar

Digitized by Arya Samaj Foundation Chennai and eGangotri

plasma containing D^+ and 10%H^+ with $j = 10$. As already mentioned the addition of H^+ tends to make the plasma unstable and thus the negative group velocities of the modes persists for this case also. Plots 2(c) and 2(d) are for plasmas containing O^{8+}. In both cases the group velocities of the modes are positive. From plots 1(a), 1(c) and 1(d) we know that the plasma is stable when $j = 0$ or when it contains O^{8+} ions. Thus we may conclude from plots 2(a), 2(c) and 2(d) that the group velocities of the modes are positive in a stable plasma.

Figure 3 depicts the variation of V_{gr} with $k_\perp \gamma_{LD}$ for two values of $T_{\perp,OD}$, namely 1·0 and 8·0 for a plasma containing D^+ and 5%O^{8+} with $j = 10$ and $\beta'_\perp = \beta_{\perp,D}$. Plot 3(a) is the same as 2(c); the group velocities of both the modes are positive as the plasma is stable. A solution of the dispersion relation (15) shows that the plasma is unstable for $T_{\perp,OD} \geq 4{\cdot}0$. In concurrence with our earlier conclusion we find that the group velocities of the modes are negative in this unstable plasma containing O^{8+}. Also the group velocities of the modes are a maximum at the coalescing point $k_\perp \gamma_{LD} = 0{\cdot}6$.

A plot similar to figure 3 was made for a plasma containing D^+ and 10%H^+ for two values of $T_{\perp,HD}$(= 0·1 and 2·0), the other parameters of the plasma being $\beta'_\perp = \beta_{\perp,D}$, $j = 10$ and $T_{\perp,eD} = 1{\cdot}0$. The plots were similar to 2(b) which was for $T_{\perp,HD} = 1{\cdot}0$. However, we find that with increasing $T_{\perp,HD}$ the maximum positive value of V_{gr} increases for the LF mode and decreases for the HF mode. The reverse, however, holds true on the negative side: V_{gr} increases for the HF mode and decreases for the LF mode.

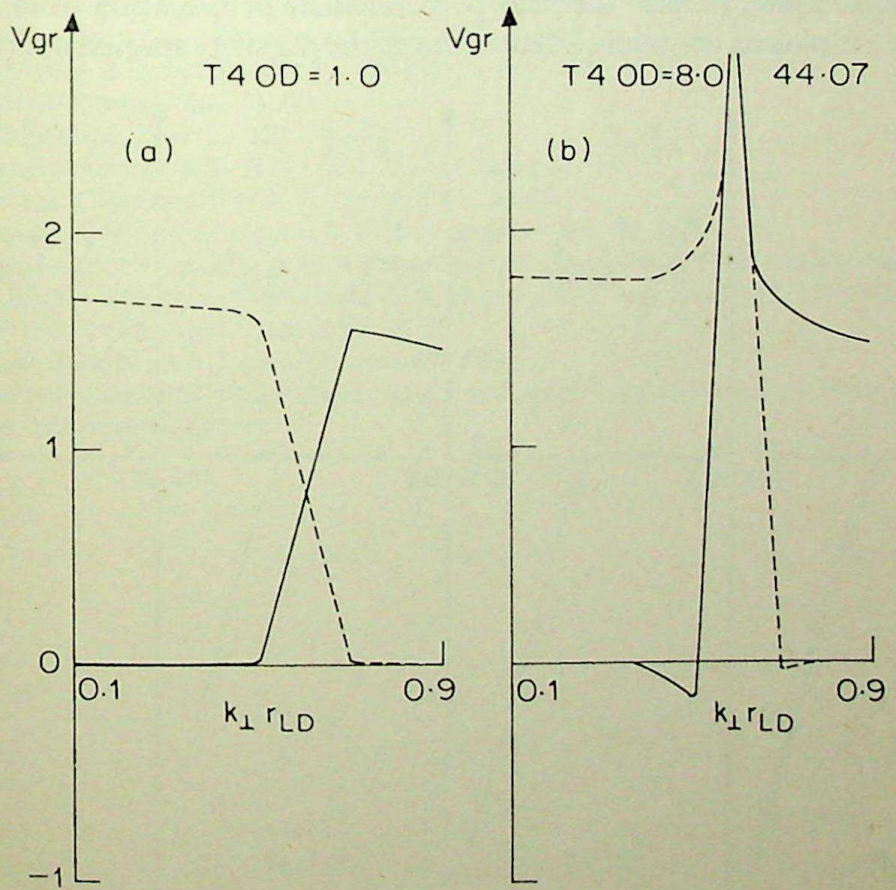

Figure 3. Plots of V_{gr} vs $k_\perp \gamma_{LD}$ in a plasma of $D^+ + 5\%O^{8+}$ for two values of $T_{\perp,OD}$(= 1·0 and 8·0) with $j = 10$, $T_{\perp,eD} = 1{\cdot}0$ and $\beta'_\perp = \beta_{\perp,D}$. The solid and dotted lines correspond to the HF and LF modes respectively.

CC-0. In Public Domain. Gurukul Kangri Collection, Haridwar

Digitized by Arya Samaj Foundation Chennai and eGangotri

We plot, in figure 4, the wave electrical energy E^2/E_x^2 versus $k_\perp \gamma_{LD}$ for a plasma characterized by $\beta'_\perp = \beta_{\perp,D}$, $j = 10$ and all temperature ratios equal to 1: the plasmas of the individual plots having the same compositions as the plasmas in plots of figures 1 and 2. We find that, in general, the LF mode to be a positive energy wave while the HF mode has a negative energy over a major portion of the wavelength region studied. Thus when an instability occurs due to a coalescing of the modes, it may be interpreted as being due to an interaction between waves of opposite electrical energy (Hasegawa 1975). We now consider the individual plots. Plot 4(a) compares the wave electrical energy for two values of j namely 0 and 10. For $j = 0$ the two modes are well separated in energy; in particular, the LF wave has a positive energy throughout the wavelength region studied. However, in a plasma prone to an instability (plot 4(a) when $j = 10$ and 4(b)), the LF mode has a wavelength region of very small negative electrical energy. In cases where the two modes coalesce (for example when $\beta'_\perp > 2\beta_{\perp,D}$ or when $T_{\perp,OD} \geqslant 4{\cdot}0$), the two modes have the same energy at the coalescing point. In stable plasmas containing O^{8+} (plots 4(c) and 4(d)) the LF mode, as for the case of a Maxwellian plasma, is a positive energy wave over the wavelength region studied. Also as can be seen from these plots the two modes are well separated in energy thus precluding any instability.

7. Conclusions

We have, in this paper, studied the near perpendicular propagation of ion cyclotron waves in a fusion plasma containing deuterium as the majority species, hydrogen as the

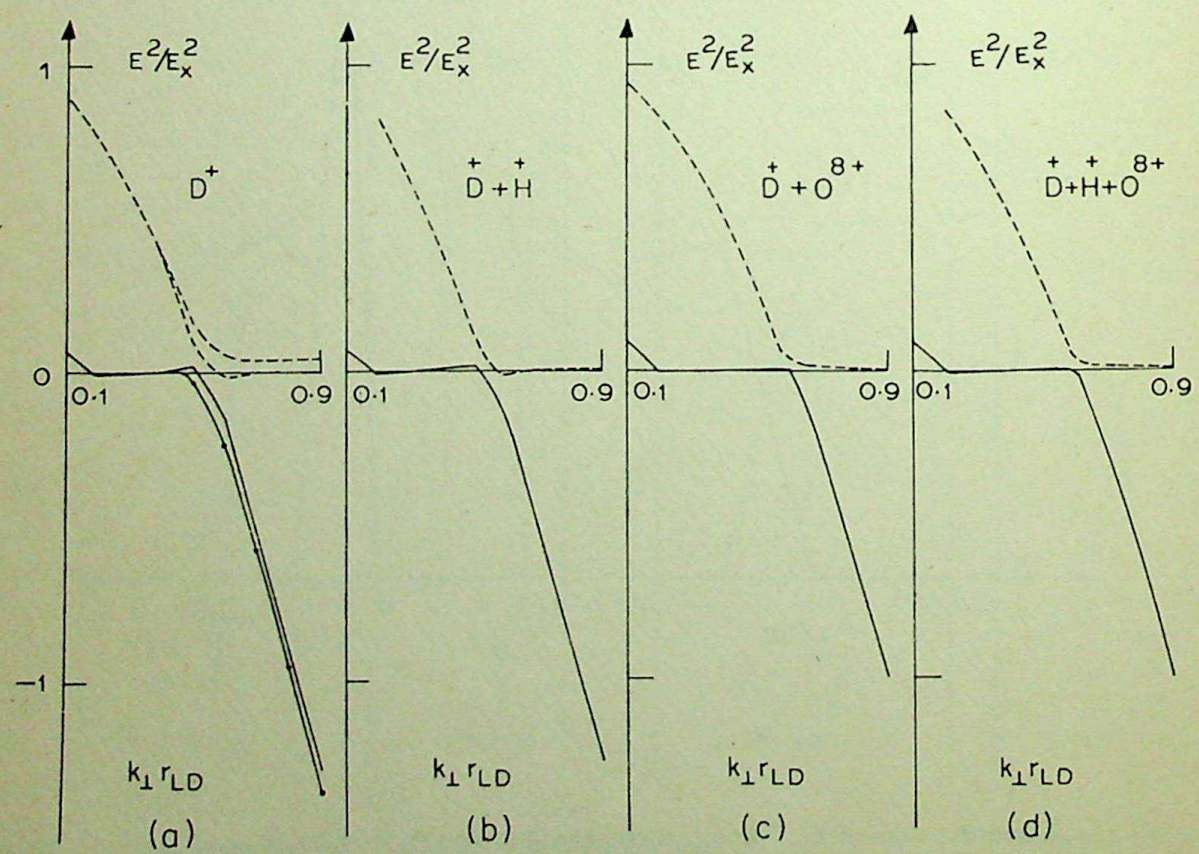

Figure 4. Plots of E^2/E_x^2 vs $k_\perp \gamma_{LD}$ for $\beta'_\perp = \beta_{\perp,D}$ and all temperature ratios equal to 1. The solid and dotted lines correspond to the HF and LF modes respectively for $j = 10$; the same for $j = 0$ in plot 4(a) is indicated by dots on the curves.

CC-0. In Public Domain. Gurukul Kangri Collection, Haridwar

Digitized by Arya Samaj Foundation Chennai and eGangotri

minority species and fully ionized oxygen as the impurity constituent. We find the plasma to be stable when $\beta_{\perp,D}$ is low and when the perpendicular component of oxygen-to-deuterium and hydrogen-to-deuterium temperature ratios are also kept low. The resemblance of a loss cone plasma containing a small amount of impurity O^{8+} ions with a Maxwellian plasma as regards wave stability, propagation and energy has also been brought out.

Acknowledgement

The author thanks Prof. K S Viswanathan for his constant help and encouragement throughout the course of this work.

References

Chandu Venugopal 1983 *Pramana–J. Phys.* **21** 1
Colestock P L and Kashuba R J 1983 *Nucl. Fusion* **23** 763
Davies S L, PDX and PLT groups 1983 *Plasma Phys.* **25** 189
Equipe T F R 1981 *Plasma Physics and controlled fusion research Proc. 8th Int. Conf. Brussels* 1980 **2** 75 (Vienna: IAEA)
Equipe T F R 1982 *Plasma Phys.* **24** 615
Hasegawa A 1975 *Plasma instabilities and nonlinear effects* (New York: Springer Verlag)
Ida K, Naito O, Ochiai I and Shinohara S 1984 *Nucl. Fusion* **24** 375
Jacquinot J, McVey B D and Scharer J E 1977 *Phys. Rev. Lett.* **39** 88
Janzen G 1980 *J. Plasma Phys.* **23** 321
Janzen G 1981 *Plasma Phys.* **23** 629
Jessup B L and McCarthy A L 1978 *IEEE Trans. Plasma Sci.* **6** 220
Landau R W and Cuperman S 1971 *J. Plasma Phys.* **6** 495
Leer E, Johansen K M and Albrigtsen R 1978 *J. Geophys. Res.* **83** 3125
Montgomery D C and Tidman D A 1964 *Plasma kinetic theory* (New York: McGraw Hill)
Owens T L, Mullen J H, Baity F W, Davis W A, Eldridge O C and Hillis D L 1983 *Nucl. Fusion* **23** 49
Perkins F W 1984 *IEEE Trans. Plasma Sci.* **12** 53
Smith R L and Brice N 1964 *J. Geophys. Res.* **69** 5029
Stix T H and Palladino R W 1958 *Plasma Physics and controlled fusion research Proc. Second Int. Conf. Geneva* **31** 282 (Vienna: IAEA)

CC-0. In Public Domain. Gurukul Kangri Collection, Haridwar

Digitized by Arya Samaj Foundation Chennai and eGangotri

CC-0. In Public Domain. Gurukul Kangri Collection, Haridwar

Digitized by Arya Samaj Foundation Chennai and eGangotri

Pramāṇa – J. Phys., Vol. 28, No. 2, February 1987, pp. 195–203. © Printed in India.

Temperature invariance of S_0-parameter of polymers

B K SHARMA* and R R REDDY†

Department of Physics, Regional College of Education, Bhubaneswar 751 007, India
†Department of Physics, S K University, Anantpur 515 003, India
*Present address: Physics Group, DMES & DP, National Council of Educational Research and Training, New Delhi 110 016, India

MS received 3 December 1985; revised 29 September 1986

Abstract. The parameter S_0 which is characteristic of molten alkali halides and liquids has also been shown to be characteristic of a wide variety of polymers. Calculated data using the volume expansivity of the polymer establish the temperature invariance and constancy of the S_0-parameter which retains, on an average, a constant value of 1·11 for polymers. Further understanding of the significance of fractional free volume and S_0-parameter in describing various thermoacoustic properties and the anharmonic behaviour in polymers, has been developed.

Keywords. Polymer; S_0-parameter; volume expansivity; heat capacity; Grüneisen parameter; fractional free volume.

PACS Nos 61·40; 62·90; 65·70

1. Introduction

The Grüneisen parameter has been shown to be an important quantity of current interest and useful as a measure of anharmonicity of molecular vibrations in studying the internal structure, molecular order and other thermoacoustic properties of polymers (Gibbons 1974; Sharma 1982a, b, 1983a, b). Recently Sharma (1983a) has shown that three dimensionless anharmonic parameters, the isobaric Γ, isochoric Γ'' and isothermal Γ' microscopic (lattice) Grüneisen parameters for polymers are related to each other. Following a model-dependent approximation by Dugdale and MacDonald (1953), which is valid at all pressures, Γ and Γ'' can be determined by using the isobaric and isochoric temperature dependence of bulk modulus respectively and Γ' from the isothermal pressure dependence of the bulk modulus for polymers (Sharma 1982a, b, 1983a, b). In this paper, an attempt has been made to relate Γ' (as a measure of anharmonicity of molecular vibration) with fractional free volume f (as a measure of disorder due to increased mobility of the molecules) and also the S_0-parameter and evaluate them for a wide variety of polymers from the volume expansivity data at various temperatures. The S_0-parameter which is characteristic of molten alkali halides, polyatomic ionic liquids, quasi-spherical molecular liquids and fluid hydrogen isotopes, has, on the average, a constant value of $1{\cdot}11 \pm 0{\cdot}01$ in a wide variety of substances (Sharma 1983d, 1985, 1986a, b). It is shown that the S_0-parameter retains its constant

*To whom all correspondence should be addressed.

CC-0. In Public Domain. Gurukul Kangri Collection, Haridwar

Digitized by Arya Samaj Foundation Chennai and eGangotri

value even in polymers at various temperatures and describes the temperature and volume or pressure dependence of several thermoacoustic and anharmonic parameters of polymers.

2. S_0-parameter and Grüneisen parameter

The parameter S_0 may be expressed as (Sharma 1985, 1986a; Sharma and Reddy 1985)

$$S_0 = -(x/2)(3+4\alpha T) = \tilde{B}(1+2\alpha T)(3+4\alpha T) \tag{1}$$

where $x = (\mathrm{d}\ln p_i/\mathrm{d}\ln T)v$ is the isochoric temperature coefficient of internal pressure, $\tilde{B} = (B/B^*) = (\tilde{V})^{C_1}$ the reduced isothermal bulk modulus, $\tilde{V} = (V/V^*)$ is the reduced specific volume, V^*, B^* are respectively the hard core specific volume and bulk modulus at absolute zero temperature, $C_1 = (\mathrm{d}B/\mathrm{d}p)_T$ the Moelwyn-Hughes parameter, $p_i = (\alpha TB)$ the internal pressure which is identical to kinetic pressure in the zero pressure limit (at normal atmospheric pressure), α, B are respectively the volume expansivity and bulk modulus of the polymer at absolute temperature T and pressure p.

Using equation (1) the Huggins parameter, F for a polymer (Sharma 1983a) can be shown to be related to S_0 as

$$\begin{aligned} F &= 1+(2/3)\alpha T-(\mathrm{d}\ln B/\mathrm{d}\ln T)_v \\ &= 2[1+S_0/(3+4\alpha T)]-(3+4\alpha T)/3. \end{aligned} \tag{2}$$

The isochoric and isothermal lattice Grüneisen parameters for a polymer (Sharma 1982a, 1983a) and S_0, using (1) and (2), as

$$\Gamma'' = (\mathrm{d}\ln \mathrm{B}/\mathrm{d}\ln \mathrm{T})_v/2\alpha T = 1-S_0[\alpha T(3+4\alpha T)]^{-1}, \tag{3}$$

$$\begin{aligned} \Gamma'' &= (1/2)[(\mathrm{d}B/\mathrm{d}p)_T-1] = \Gamma+\Gamma'' \\ &= (2/3)(4+\alpha T)+(2\alpha T)^{-1}-S_0[\alpha T(3+4\alpha T)]^{-1} \\ &= (2/3)\alpha T+(2-F+4\alpha T)(2\alpha T)^{-1}. \end{aligned} \tag{4}$$

Equation (3) shows that Γ'' is a negative quantity for a polymer, unlike quasi-spherical molecular liquids and fluorocarbon fluids (Sharma 1983c, d). Theoretical justification of this proposal has also been reported by Sharma (1983a) using the experimental data available on the temperature and pressure derivatives of the bulk modulus for the polymer. Equations (2)–(4) show that the parameters, F, Γ' and Γ'' are related to S_0 and can be expressed in terms of only the volume expansivity of the polymer. The present proposal of relating Γ' to α agree closely with the suggestion of Hartmann (1979) and Curro (1973) that the anharmonicity of intermolecular energy or potential is also governed by thermal expansion and a number of internal degrees of freedom. During the volume expansion of the polymer, more and more disorder is introduced which results in the changes in molecular vibration frequency, molecular order and structure, making the polymer less anharmonic at higher temperature than at lower temperature (Gibbons 1974; Warfield 1974; Gilmour *et al* 1978).

The fractional free volume as a measure of disorder due to increased mobility of

CC-0. In Public Domain. Gurukul Kangri Collection, Haridwar

Digitized by Arya Samaj Foundation Chennai and eGangotri

molecules in a polymer can be expressed in terms of Γ' as (Sharma 1983d)

$$f = (V_a/V) = (\Gamma' + 1)^{-1}, \tag{5}$$

where $V_a = (V - V^*)$ is the free (available) volume of the molecules of the polymer. Equation (5) may be rearranged to give the dimensionless parameter A^* in terms of f and Γ' as

$$A^* = 1 + (f/\Gamma') = 1 + f^2/(1-f). \tag{6}$$

Equation (6) shows that at low temperatures, close to absolute zero, the polymeric system would tend to be ordered, exhibiting little thermal expansion and fractional free volume, thereby making the parameter A^* a constant equal to unity.

Equations (1)–(6) demonstrate the significance of f and S_0 in describing thermoacoustic properties and the anharmonic behaviour in polymers. Using these equations the parameters X, Γ'', Γ', f, F, A^* and S_0 have been evaluated for 27 polymers. The necessary experimental data on α are taken from literature (Allen *et al* 1960; Sharma 1982a, b, 1983a, b; Orwoll and Flory 1967; Eichinger and Flory 1968; Barker and Chen 1967). The results are presented in table 1. The parameter S_0 for polystyrene, nylon 6 and teflon at various temperatures from 173 K to 383 K has been calculated using experimental data on α from literature (Urzendowski and Guenther 1970). A plot of S_0 as a function of temperature for these polymers is shown in figure 1.

3. Isochoric temperature coefficient of heat capacity and bulk modulus

Treating the fluctuation of intermolecular energy as the perturbation due to localized ordering of molecules, arising out of the effect of order in the random or disordered state in a polymer (Sharma 1980), the internal energy E may be expressed as

$$E = p_i V + TC_v = \Phi[1 + (\bar{\Gamma})^{-1}] \tag{7}$$

in which the thermodynamic Grüneisen parameter, $\bar{\Gamma}$ treated as a measure of thermal stress for a polymer may be expressed as (Gilmour *et al* 1978; Sharma 1983d)

$$\bar{\Gamma} = V(\mathrm{d}p/\mathrm{d}E)_v = p_i V/TC_v, \tag{8}$$

where $C_v = (\mathrm{d}E/\mathrm{d}T)_v$ is the isochoric heat capacity and $\Phi = p_i V$ the intermolecular energy of the polymer. From thermodynamic considerations, using (1), (3), (7) and (9),

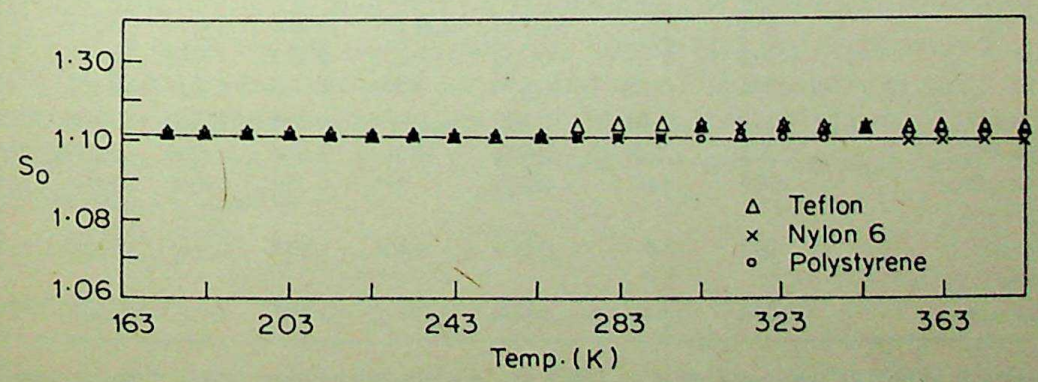

Figure 1. A plot of S_0 vs temperature of polystyrene, nylon 6 and teflon.

CC-0. In Public Domain. Gurukul Kangri Collection, Haridwar

Digitized by Arya Samaj Foundation Chennai and eGangotri

Table 1. Calculated values of the S_0 constant and other related anharmonic and thermoacoustic parameters of polymers.

Polymer	T (K)	$\alpha \times 10^{4}$ [a–c] (K^{-1})	X	Γ''	Γ'	F	f	A^*	S_0
1	2	3	4	5	6	7	8	9	10
n-Tetradecane	293	9·0	−0·552	−0·048	3·691	1·201	0·213	1·057	1·120
Squalane	293	8·1	−0·568	−0·196	3·736	1·251	0·211	1·054	1·121
Polystyrene	293	6·8	−0·590	−0·482	3·827	1·325	0·207	1·048	1·121
Poly(ethyl acrylate)	293	6·8	−0·590	−0·482	3·827	1·325	0·207	1·048	1·121
Squalene	293	7·6	−0·576	−0·294	3·767	1·279	0·210	1·052	1·121
Natural rubber	293	6·7	−0·592	−0·509	3·836	1·331	0·207	1·048	1·121
Poly(ethylene oxide dimethyl ether)	293	7·8	−0·573	−0·253	3·754	1·268	0·210	1·052	1·121
Poly(propylene oxide dimethyl ether)	293	7·8	−0·573	−0·253	3·754	1·268	0·210	1·052	1·121
Poly (dimethyl siloxane)	293	9·0	−0·552	−0·048	3·691	1·201	0·213	1·057	1·120
Poly(methyl phenyl siloxane)	293	7·6	−0·576	−0·294	3·767	1·279	0·210	1·052	1·121
Poly(trifluoro-chloroethylene)	293	8·1	−0·568	−0·196	3·736	1·251	0·211	1·054	1·121
Phenolic polymer	303	3·1	−0·661	−2·520	4·532	1·536	0·181	1·026	1·116
Polyphenyl quinoxaline	303	2·6	−0·673	−3·269	4·797	1·568	0·172	1·021	1·115
Polymethyl	298	2·1	−0·685	−4·472	5·226	1·601	0·161	1·017	1·113
Methacrylate	303	2·70	−0·670	−3·097	4·736	1·561	0·174	1·022	1·115
Polyethylene oxide	298	3·30	−0·658	−2·346	4·470	1·527	0·183	1·027	1·117
	358	14·0	−0·437	−0·564	3·562	0·769	0·219	1·073	1·094
Poly(acrylonitrile butadiene styrene)	293	3·0	−0·666	−2·787	4·626	1·549	0·178	1·024	1·116
Polyethylene terephthalate	298	1·6	−0·696	−6·304	5·881	1·633	0·145	1·012	1·111
SBR rubber	298	6·6	−0·592	−0·505	3·835	1·330	0·207	1·048	1·121
Buty IIR	298	5·7	−0·609	−0·793	3·930	1·383	0·203	1·043	1·121
Polyisobutylene	273	5·51	−0·622	−1·067	4·024	1·421	0·199	1·039	1·120
	298	5·55	−0·612	−0·850	3·950	1·392	0·202	1·042	1·120
	323	5·60	−0·602	−0·664	3·887	1·361	0·205	1·045	1·121
	373	5·68	−0·583	−0·375	3·792	1·300	0·209	1·050	1·121
	423	5·77	−0·564	−0·155	3·723	1·238	0·212	1·055	1·121
Polymethylene	298	6·92	−0·586	−0·421	3·807	1·311	0·208	1·049	1·121
	373	7·12	−0·551	−0·038	3·688	1·197	0·213	1·057	1·120
	413	7·20	−0·534	+0·102	3·649	1·137	0·215	1·061	1·118
	453	7·37	−0·515	+0·229	3·616	1·070	0·217	1·064	1·116
Teflon	295	1·35	−0·703	−7·823	6·425	1·650	0·135	1·010	1·110
	303	2·70	−0·670	−3·097	4·736	1·561	0·174	1·022	1·115
Nylon 6	303	2·40	−0·677	−3·656	4·935	1·580	0·168	1·020	1·114
Lexan PC	303	2·00	−0·686	−4·663	5·294	1·606	0·159	1·016	1·113
Polyethylene	303	4·60	−0·629	−1·258	4·089	1·444	0·196	1·037	1·120
Hexamethyl disiloxane	293	13·8	−0·480	−0·406	3·579	0·941	0·218	1·069	1·108
Octamethyl trisiloxane	293	12·4	−0·500	−0·312	3·597	1·015	0·218	1·066	1·113

[a] Allen *et al* (1960); [b] Sharma (1982a, b, 1983a, b); [c] Eichinger and Flory (1968); [d] Barker and Chen (1967); [e] Orwoll and Flory (1967).

CC-0. In Public Domain. Gurukul Kangri Collection, Haridwar

Digitized by Arya Samaj Foundation Chennai and eGangotri

together with the expressions of isothermal volume derivatives of C_v and $\bar{\Gamma}$ obtained earlier (Sharma 1986a), the first order isochoric and isobaric temperature coefficients of C_v and $\bar{\Gamma}$ for a polymer can be shown to be related to S_0 as

$$Y = (\mathrm{d}\ln C_v/\mathrm{d}\ln T)_v = 2S_0\bar{\Gamma}(3+4\alpha T)^{-1}, \tag{9}$$

$$Y' = (\mathrm{d}\ln C_v/\mathrm{d}\ln T)_p = S_0\bar{\Gamma}(3+4\alpha T)^{-1}(2-\alpha T), \tag{10}$$

$$Z = (\mathrm{d}\ln\bar{\Gamma}/\mathrm{d}\ln T)_v = -[1+2S_0(\bar{\Gamma}+1)(3+4\alpha T)^{-1}], \tag{11}$$

$$Z' = (\mathrm{d}\ln\bar{\Gamma}/\mathrm{d}\ln T)_p = Z+\lambda\alpha T = -[1+\alpha T(2\Gamma''-1) + 2S_0(3+4\alpha T)^{-1} + S_0\bar{\Gamma}(3+4\alpha T)^{-1}(2-\alpha T)]. \tag{12}$$

in which $\lambda = (\mathrm{d}\ln\bar{\Gamma}/\mathrm{d}\ln V)_T$ expresses the isothermal volume derivative of $\bar{\Gamma}$ for the polymer. Equations (11) and (12) show that $\bar{\Gamma}$ decreases with rise of temperature at constant volume and at constant pressure for the polymer. This proposal agrees closely with the suggestion of Gibbons (1974) that the thermal stress developed within the polymer chains due to large number of internal degrees of freedom is reduced, resulting in the drop of $\bar{\Gamma}$ in polymers at high temperatures.

The relationship between the adiabatic bulk modulus, B_s and isothermal bulk modulus, B can be expressed as (Swenson 1968; Roberts and Smith 1970)

$$B_s - B = TC_v(\bar{\Gamma})^2/V. \tag{13}$$

Equations (8)–(13) lead to the general relations between the isochoric temperature and isothermal pressure coefficients of B_s and B as

$$(B_s/B)(\mathrm{d}\ln B_s/\mathrm{d}\ln T)_v - (\mathrm{d}\ln B/\mathrm{d}\ln T)_v = \bar{\Gamma}\alpha T[1+2S_0\bar{\Gamma}(3+4\alpha T)^{-1}+(2Z/\bar{\Gamma})], \tag{14}$$

$$(\mathrm{d}B/\mathrm{d}p)_T - (\mathrm{d}B_s/\mathrm{d}p)_T = \bar{\Gamma}\alpha T[1-4\Gamma''+S_0\bar{\Gamma}(3+4\alpha T)^{-1}]. \tag{15}$$

By assuming that $\bar{\Gamma}$ has no intrinsic (constant volume) temperature dependence, equations (14) and (15) reduce to the approximate relations obtained by Swenson (1968) and Roberts and Smith (1970). The present result presents an improvement over the work of these workers and expresses the correct isothermal volume and isochoric temperature dependence of C_v and $\bar{\Gamma}$ for the polymer. Equations (9)–(12), (14) and (15) demonstrate further the significance of S_0 in describing temperature, volume or pressure dependence of C_v, $\bar{\Gamma}$, B_s and B for a polymer and evaluating them from the knowledge of $\bar{\Gamma}$ and α for the polymer. Using (1), (8), (9)–(12) the parameters $\bar{\Gamma}$, S_0, Y, Y', λ and $(Z'-Z)$ have been evaluated for 23 polymers. The necessary experimental data on thermoacoustic parameters are taken from literature (Warfield 1974; Eichinger and Flory 1968; Sharma 1982a, b, 1983a, b; Urzendowski and Guenther 1970). The results are presented in table 2.

4. Results and discussion

The calculated values of the isochoric temperature coefficient of both the internal pressure and bulk modulus in table 1 are negative. The absolute values of X range from

CC-0. In Public Domain. Gurukul Kangri Collection, Haridwar

Digitized by Arya Samaj Foundation Chennai and eGangotri

Table 2. Calculated values of temperature and volume derivatives of the isochoric heat capacity and thermodynamic Grüneisen parameter of polymers.

Polymer	T (K)	$\alpha \times 10^{4}$ [a–d] (K^{-1})	$\bar{\Gamma}$ [a, b]	S_0	Y	Y'	λ	$(Z'-Z)$
Phenolic polymer	303	3·1	1·3	1·116	0·859	0·819	6·470	0·608
Polyphenyl quinoxaline	303	2·6	1·0	1·115	0·673	0·646	7·874	0·622
Polystyrene	293	2·11	0·79	1·113	0·541	0·524	11·170	0·690
Polymethyl methacrylate	298	2·1	0·82	1·113	0·562	0·544	10·225	0.640
Polyethylene	298	5·0	0·52	1·120	0·322	0·297	3·155	0·489
Polypropylene	298	4·8	0·96	1·119	0·602	0·559	3·687	0·527
Polymethylene oxide	298	2·43	0·51	1·114	0·345	0·333	8·525	0·617
Poly(4-methyl pentene-1)	298	3·80	1·07	1·118	0·692	0·653	5·060	0·573
Polyethylene oxide (Solid)	298	3·3	1·02	1·117	0·671	0·638	6·020	0·593
Polyethylene oxide (melt)	358	14·0	1·02	1·094	0·446	0·334	2·351	1·178
Polybutene-1	298	4·5	0·66	1·119	0·418	0·390	3·929	0·527
Polychlorotri-fluoroethylene	293	8·1	0·36	1·121	0·204	0·180	1·494	0·354
Polytetrafluoroethylene	295	1·35	0·40	1·110	0·281	0·275	16·787	0·668
Polyisobutylene	298	5·55	1·09	1·120	0·667	0·612	3·034	0·502
Polychloroprene	298	6·0	0·60	1·121	0·362	0·330	2·553	0·456
Polyepoxide + D	298	2·7	0·54	1·114	0·362	0·347	7·521	0·605
Polyvinyl chloride	298	2·5	0·61	1·114	0·412	0·397	8·280	0·617
Polyvinyl acetate	298	2·07	1·12	1·113	0·768	0·744	10·502	0·648
Polycarbonate	298	1·5	0·27	1·111	0·189	0·185	14·734	0·659
Transpolybutadiene	298	7·8	0·16	1·121	0·091	0·080	1·500	0·348
Polyethylene terephthalate	298	1·6	0·42	1·111	0·292	0·285	13·754	0·656
Polyisoprene	298	5·1	0·68	1·120	0·422	0·390	3·297	0·501
SBR rubber	298	6·6	0·74	1·121	0·438	0·395	2·229	0·438
Butyl IIR	298	5·7	0·68	1·121	0·414	0·379	2·793	0·474

[a] Warfield (1974); [b] Sharma (1982a, b, 1983a b); [c] Eichinger and Flory (1968); [d] Urzendowski and Guenther (1970).

about 0·44 to 0·77 and those of F from about 1·0 to 1·7 which are of the same order as observed for crystalline and molten alkali halides, liquid alkali metals, ionic and quasi-spherical molecular liquids (Sharma 1983d, 1986a, b). Large volume expansivity for a polymer at the same temperature corresponds to a small absolute value of X, Γ' and F which decreases with rise of temperature for the polymer. The decrease in Γ' with temperature, arising due to large number of internal degrees of freedom and the nature of anharmonic interactions in a polymer may be indicative of some kind of molecular ordering effect. This suggests that the structural ordering process continues in the polymer due to the increasing storage of energy in high frequency vibrations as the temperature is raised in the glassy region, and Γ' and f become constant at the glass temperature of the polymer (Curro 1973; Warfield 1974; Gilmour *et al* 1978; Simha and Boyer 1962).

CC-0. In Public Domain. Gurukul Kangri Collection, Haridwar

Digitized by Arya Samaj Foundation Chennai and eGangotri

The values of f increase with temperature thereby introducing greater additional disorder in a polymer. For most of the polymers, the values of f are around 0·20, which are of the same order as observed for saturated hydrocarbons (Soczkiewicz 1977) and polycrystalline alkali halides, rare earth metals, liquid alkali metals, alkali halides and polyatomic ionic liquids (Sharma and Reddy 1985). The quasi-constancy of the quantity f at 293 K for a wide variety of polymers and liquids has echoes in the universal value of the fractional free volume at the glass temperature in the WLF theory (Williams *et al* 1955). The parameters S_0 and A^* have, on the average, constant values of $1{\cdot}11 \pm 0{\cdot}01$ and $1{\cdot}05 \pm 0{\cdot}01$ respectively, for all the polymers examined presently. This implies that, on the average, the approximate relationships $S_0 = 5{\cdot}55f$ and $A^* = 5{\cdot}25f$ hold true for the polymers.

The plot of S_0 as a function of temperature shown in figure 1 confirms the constancy and the temperature invariance of S_0 for the polymers over the whole temperature range of 173 K to 383 K.

Equation (1) shows that S_0 is proportional to the product of X and $(3 + 4\alpha T)$. It is interesting to note that a large α corresponds to a small absolute value of X for a polymer. However, the value of the term $(3 + 4\alpha T)$ increases with rise of temperature in such a way that S_0 tends to be independent of the value of α for the polymer. The temperature dependence of the sound speed of polymers in the glassy state is linear and is governed by the bulk modulus and not the density (Hartmann 1980). The logarithmic temperature derivative of the bulk modulus in a polymer is twice that of the sound speed in the polymer (Hartmann 1975, 1980). This shows that S_0 in equation (3) is useful for imparting a negative isochoric temperature coefficient of sound speed indicating a decrease in the sound speed with temperature, in accordance with the earlier work (Sharma 1983a) for a polymer. This implies that volume changes caused by temperature have a greater effect on the bulk modulus or sound speed than equal volume changes caused by pressure for the polymer.

It has also been established (Sharma 1985, 1986b) that S_0 may be termed as a molecular constant which retains its constancy for a wide variety of substances in polycrystalline, molten and liquid state. Due to the additive property implied in S_0, the possibility of computing the isochoric temperature coefficient of sound speed and bulk modulus for liquid mixtures and polymer solutions from equations (1) and (3) is extremely useful.

At the melting point T_m, the relationship $0{\cdot}31 \leqslant \alpha T_m \leqslant 0{\cdot}33$ has been obtained for polymer melts (Simha and Jain 1978). Taking the average value of $\alpha T_m = 0{\cdot}32$, $S_0 = 1{\cdot}11$ for polymer melts, using equation (1) and the earlier expression (Sharma 1985) for C_1, the calculated values so obtained for C_1, $\tilde{B}$ and $\tilde{V}$ are 7·885, 0·158 and 1·264 respectively. This value of $\tilde{V}$ is of the same order as observed for polymer melts (Simha and Jain 1978). Since B^* and V^* are constant for a polymer, these values render a relationship $VB^{(1/7\cdot885)} =$ constant for polymers. An analogous relationship $VB_s^{(1/7)} =$ constant has been obtained by Wada for liquids (Jain and Pandey 1975) which is widely used for investigating the physico-chemical behaviour of fluids and fluid mixtures. This shows that S_0 is useful in interpreting the bulk modulus in molecular terms for a polymer, leading to the relation $B \propto V^{-7\cdot885}$, analogous to that of Wada for a liquid.

At the glass transition temperature T_g, the average value of $\alpha T_g = 0{\cdot}17$ has been obtained for polymer glasses (Simha and Boyer 1962). Using equation (1) and taking $S_0 = 1{\cdot}11$ for polymer glasses, the calculated values for C_1, $\tilde{B}$ and $\tilde{V}$ are 10·442, 0·225

CC-0. In Public Domain. Gurukul Kangri Collection, Haridwar

Digitized by Arya Samaj Foundation Chennai and eGangotri

and 1·153 respectively. This value of the reduced specific volume at T_g, based on the constancy and temperature invariance of S_0, renders the value of (V^*/V) as 0·87 which is identical to that obtained for polymers in the glassy state (Breuer *et al* 1966). This shows that equation (1) for S_0 can be employed for estimating the molecular bulk modulus, B^* from the experimental data on α and B at T_g for polymer glasses. The anharmonicity of molecular vibrations and the bulk modulus of a polymeric material are determined primarily by the inter-chain forces and are not dependent on the bonding along the macromolecule (Sharma 1983b). Thus S_0 is useful for a wide variety of polymers and is significant for investigating various physicochemical, thermoacoustic and anharmonic properties.

The calculated values of the quantity Y and Y' as given in table 2 are positive and range from 0·09 to 0·86 and about 0·08 to 0·82 respectively for the polymers presently examined, indicating an increase in the isochoric heat capacity with temperature. This shows that the values of the isochoric and isobaric temperature coefficients of C_v are of the same order and differ by a factor less than 0·1, within 10% of Y, similar to that observed for cubic solids (Swenson 1968). The calculated values of λ are positive and range from about 2 to 17 for polymers as compared to 3 to 5 for fluorocarbon fluids and liquefied gases, and around 1 to 2 for alkali halides (Sharma 1983d). However, the values of the quantity $(Z'-Z)$ expressing the difference between the isobaric and isochoric temperature coefficients of $\bar{\Gamma}$ are low ($< 0{\cdot}7$) which is within 20% of λ for these polymers. This shows that $\bar{\Gamma}$ increases with volume at constant temperature for polymer. A similar pattern has also been observed for cubic solids and alkali halides (Swenson 1968; Sharma 1983d).

The present treatment offers a convenient means for establishing the constancy and temperature invariance of S_0 and for investigating several thermoacoustic properties by relating it to the isothermal lattice Grüneisen parameter, fractional free volume, and isobaric and isochoric temperature coefficients of thermodynamic Grüneisen parameter and isochoric heat capacity of polymers. This allows further understanding of the significance of S_0 in describing anharmonic behaviour with regard to molecular order and interchain forces in glassy polymers and polymer melts.

Acknowledgements

The authors wish to thank Dr B Hartmann, Polymer Physics Group, Naval Surface Weapon Centre, Silver Spring, Maryland, USA and Prof. R N Haward, Centre of Materials Sciences, University of Birmingham, England for helpful correspondence.

References

Allen G, Gee G, Managaraj D, Sims D and Wilson G J 1960 *Polymer* **1** 467
Barker R E and Chen R Y S 1967 *J. Appl. Phys.* **38** 4234
Breuer J, Haward R N and Rehage G 1966 *Polymer Lett.* **4** 375
Curro J G 1973 *J. Chem. Phys.* **58** 374
Dugdale J S and MacDonald D K C 1953 *Phys. Rev.* **89** 832
Eichinger B E and Flory P J 1968 *Macromolecules* **1** 285
Gibbons T G 1974 *J. Chem. Phys.* **60** 1094
Gilmour I, Trainor I and Haward R N 1978 *J. Polym. Sci. Polym. Phys.* Ed. **16** 1277, 1291
Hartmann B 1975 *J. Appl. Polym. Sci.* **19** 3241

CC-0. In Public Domain. Gurukul Kangri Collection, Haridwar

Digitized by Arya Samaj Foundation Chennai and eGangotri

Hartmann B 1979 *J. Acoust. Soc. Am.* **65** 1392
Hartmann B 1980 *J. Appl. Phys.* **51** 310
Jain R P and Pandey J D 1975 *Acustica* **32** 336
Orwoll R A and Flory P J 1967 *J. Am. Chem. Soc.* **69** 6814
Roberts R W and Smith C S 1970 *J. Phys. Chem. Solids* **31** 619
Sharma B K 1980 *Acoust. Lett.* **4** 11
Sharma B K 1982a *Acoust. Lett.* **6** 25
Sharma B K 1982b *J. Phys.* **D15** 1273, 1735
Sharma B K 1983a *J. Phys.* **D16** 1959
Sharma B K 1983b *Polymer* **24** 314
Sharma B K 1983c *J. Acoust. Soc. Am.* **73** 106
Sharma B K 1983d *Phys. Lett.* **A96** 133
Sharma B K 1983d *Phys. Lett.* **A99** 227
Sharma B K 1985 *Proc. Second Int. Symp. Hydrogen produced from renewable energy* (Florida, Solar Energy Centre) p. 337
Sharma B K 1986a *Pramana – J. Phys.* **26** 223
Sharma B K 1986b *Acoust. Lett.* **9** 101
Sharma B K and Reddy R R 1985 *Indian J. Pure Appl. Phys.* **23** 396
Simha R and Boyer R F 1962 *J. Chem. Phys.* **37** 1003
Simha R and Jain R K 1978 *J. Polym. Sci. Polym. Phys.* Ed. **16** 1471
Soczkiewicz E 1977 *Archiv. Acoust.* **2** 325
Swenson C A 1968 *J. Phys. Chem. Solids* **29** 1337
Urzendowski S R and Guenther A H 1970 *Analytical calorimetry* (New York: Plenum) p. 77–94
Warfield R W 1974 *Macromol. Chem.* **175** 3285
Williams M L, Landel R F and Ferry J D 1955 *J. Am. Chem. Soc.* **77** 3701

CC-0. In Public Domain. Gurukul Kangri Collection, Haridwar

Digitized by Arya Samaj Foundation Chennai and eGangotri

CC-0. In Public Domain. Gurukul Kangri Collection, Haridwar

Digitized by Arya Samaj Foundation Chennai and eGangotri

Pramāṇa – J. Phys., Vol. 28, No. 2, February 1987, pp. 205–215. © Printed in India.

Collective excitation modes in the intermediate and superconducting states of doped and undoped indium and lead

V V JOSHI and K D CHAUDHURI
Department of Physics and Astrophysics, University of Delhi, Delhi 110007, India

MS received 30 March 1985; revised 25 September 1986

Abstract. Ultrasonic attenuation was studied in pure In, In + 0·003 at. % Pb, pure Pb and Pb + 0·003 at. % In in the intermediate states (for the magnetic fields 0·7 H_c and 0·9 H_c) and superconducting states, for frequencies varying from 9·9 to 29·7 MHz, in the temperature range 4·2 to 1·4 K. Collective excitation modes were observed in both the states for all the samples. There exist two distinct phases in the intermediate state but only one phase in the superconducting state in all the samples. The first phase was dependent on the magnetic field and independent of the concentration and nature of the dopant. The second phase was independent of the magnetic field and dependent essentially on the concentration of vacancies and marginally on the concentration of the dopant. The origin of the two phases has been discussed.

Keywords. Collective excitation mode; superconductivity; indium; lead; ultrasonic attenuation.

PACS No. 74·00

1. Introduction

The BCS theory (Bardeen and Schriffer 1957) explain superconductivity on the basis of single-electron phonon interaction. The rapid drop in ultrasonic attenuation of superconductors below the transition temperature follows from the BCS theory by postulating single-electron phonon interaction. Besides the concept of single-electron phonon interaction, the possibility of collective excitation modes in the excitation spectrum of superconductors was postulated by Bogoliubov (1957) and Anderson (1958). Anderson and Bogoliubov showed that there are low frequency collective excitation modes for the electrons in the superconducting state which correspond to pressure waves in a neutral Fermi gas. The concept of a pressure associated with the superconducting state was first considered in regard to the electromagnetic stresses at the boundary of a superconducting region. A change in volume δV of the superconducting phase, which involves no change in free energy density f changes the total free energy F by an amount

$$\delta F = -(f_n - f_s)\,\delta V.$$

The normal material is converted into superconducting material in δV. There is an effective pressure $P = -\delta F/\delta V$. Collective type excitation modes for the electrons in the superconducting state can be produced under the influence of the effective pressure P. Ultrasonic attenuation studies by Claiborne and Einspruch (1960) in Nb-Zr alloys,

CC-0. In Public Domain. Gurukul Kangri Collection, Haridwar

Digitized by Arya Samaj Foundation Chennai and eGangotri

by Olsen *et al* (1966) on high purity single crystals of tin by Chaudhuri and Jain (1969) on impure and strained single crystals of tin have revealed oscillatory behaviour in the superconducting state which cannot be explained in terms of single electron phonon scattering process.

Similar behaviour has been reported by Mahajan and Chaudhuri (1972, 1974), Agarwal and Chaudhuri (1976) and Chaudhuri and Agarwal (1979) in the intermediate state of superconductors. The temperature-dependent oscillatory attenuation peaks have been observed by Chaudhuri and Singh (1979, 1980, 1982), both in the intermediate and superconducting states. This oscillatory attenuation observed by different workers in the superconducting and intermediate states, gives direct evidence for the existence of collective excitation modes with energies lying within the energy gap. They also give evidence for the interaction of collective excitation modes of the electron gas with the lattice phonons. Claiborne and Einspruch (1963) proposed a phenomenological model to explain the temperature-dependent oscillatory attenuation observed in the superconducting state. They assumed formation of some superconducting microstructures near localized strain sites or around impurity centers. These microstructures are separated from the bulk superconductor with distinct phase boundaries. Under the influence of a hydrodynamic pressure wave, these boundaries undergo isothermal displacements. At equilibrium condition, the displacement of the boundary would lead to a linear restoring force and, hence, to a set of temperature-dependent modes of vibration. The model interprets the presence of absorption peaks due to the exchange of energy from a compressional ultrasonic wave to the lattice phonons via the excitation modes. The maximum exchange of energy occurs from the ultrasonic wave to the electron gas when the sound frequency ν_s is equal to the frequency of one of the harmonic standing wave modes i.e. absorption peaks would occur at temperatures for which $\nu_s = \nu_n$. The condition for resonance is given by,

$$\nu_s = \nu_n = n\nu_0(1 - aT^2 + bT^4)^{1/2} \quad \text{for fixed boundaries,}$$

$$\nu_s = \nu_n = (2_{n+1})\nu_0(1 - aT^2 + bT^4)^{1/2} \quad \text{for free boundaries,}$$

where T is the temperature, a, b and ν_0 are constants, n is a positive integer, ν_s is the sound frequency and ν_0 is the fundamental frequency for a particular excitation mode in the superconducting phase at absolute zero. Its value is given by,

$$\nu_0 = C_0(2\,Z_s)^{-1}, \tag{1}$$

Z_s being the thickness of the superconducting region and C_0 is a constant. In the intermediate state, as the bulk is divided into alternate superconducting (S) and normal (N) layers, with distinct phase boundaries, boundary effects, besides S and N layers, are also likely to contribute to the total attenuation. Several workers (1964, 1966, 1968, 1972) have essentially discussed the effect of magnetic field on the ultrasound absorption in the intermediate state with electron mean free path l larger than the thickness of normal layers and $T < T_c$. It has been shown that positions of absorption peaks remain unaffected when attenuation due to N layers and boundary effects is subtracted from the total attenuation in the intermediate state. One can, therefore, utilize the total attenuation absorption peaks to calculate a, b and ν_0 in the intermediate state using Claiborne and Einspruch theory.

CC-0. In Public Domain. Gurukul Kangri Collection, Haridwar

Digitized by Arya Samaj Foundation Chennai and eGangotri

The structure of the intermediate state is greatly influenced by the magnetic field and the surface energy. According to Kuper's relation (1951),

$$Z_s/d = 1/(2h)^{1/2}\,(\Delta/d_1)^{1/2} \tag{2}$$

where Z_s is the superconducting laminar thickness, $h = H/H_c$, H being the applied magnetic field and H_c the critical field, Δ is the surface energy parameter and $\Delta \approx \xi - \lambda_D$, ξ being the coherence length and λ_D the penetration depth. Any change in Δ will change Z_s; then according to equation (1) will effect ν_0, the fundamental frequency. According to Chaudhuri and Singh (1979, 1982) two distinct phases do exist in the intermediate state of the superconductor, irrespective of the presence or nature of the dopant. The first phase, identified with a small set of absorption peaks, is due to the formation of laminar structure created by the application of the magnetic field. The second phase, giving rise to large sets of absorption peaks, is due to the formation of microstructure within the superconducting laminar thickness. From the comprehensive study of the ultrasonic attenuation in the intermediate and superconducting state of In (99·9999 %), In doped with 0·003 at. % Pb, Pb doped with 0·003 at. % In and pure Pb (99·9999 %), it is possible to identify the collective excitation modes in both the states. The purpose of the present study is to correlate the role of imperfections in producing appropriate microstructures responsible for producing oscillatory attenuation in both the states.

2. Experimental

Ultrasonic attenuation measurements were taken on the single crystals of In (99·9999 %), In + 0·003 at. % Pb, Pb + 0·003 at. %, In and pure Pb (99·9999 %), using standard double ended pulse echo technique for temperatures 4·2 K to 1·4 K, in the frequency range, 9·9 to 29·7 MHz. Two X-cut quartz transducers were bonded to the single crystal using high viscosity vacuum grease. One quartz transducer was excited by 1–2 μsec radio frequency pulse to generate ultrasonic longitudinal wave. This wave, after passing through the sample, suffers partial reflection at the surface of the sample. Part of the energy is given to the receiver transducer while the remaining returns to the sample. This process goes on till the wave is completely absorbed. The receiver transducer, converts the ultrasonic energy to electrical energy. These electrical signals were amplified, detected and then displayed on the oscilloscope. The echo height was monitored with a calibrated pulse comparator. Attenuation was calculated using successive peak heights. The accuracy of measurement of attenuation was 0·02 db cm^{-1}. Single crystals of 1 cm diameter and 4 cm length were grown using Bridgman method with carbon-coated glass moulds. The ingots were cut to the length of about 1 cm using a machine described by Maddin and Asher (1950). The faces of the sample were made parallel to each other to within half a degree by a slow lapping process using 3200 mesh abrasive powder. Finally, the crystals were electropolished in $CH_3OH + HNO_3$ solution, (3:1). All the samples were then annealed for 80 hours. Samples were brought to the intermediate state by applying a transverse magnetic field of 0·7 H_c and 0·9 H_c, and readings were taken over the entire range of temperature i.e. 4·2 K to 1·4 K for 0·7 H_c, 0·9 H_c and 0 H_c. The values of the critical field H_c for different temperatures below T_c were calculated using the relation given by Lock *et al* (1951) for

CC-0. In Public Domain. Gurukul Kangri Collection, Haridwar

Digitized by Arya Samaj Foundation Chennai and eGangotri

In and In doped with Pb and from the graph of H_c vs T for Pb and Pb doped with In. These values are correct to within 0·5 % the experimental values. Vapour pressure on the helium bath was reduced by pumping over it and the corresponding temperature was obtained from standard tables. Magnetic field was measured at the site of the specimen by means of a calibrated Hall probe, which gave the field with 2 % accuracy.

3. Results and discussion

Ultrasonic attenuation measurements on single crystals of In, In doped with Pb, Pb doped with In and pure Pb were studied; 9·9–29·7 MHz in the intermediate state (with fields 0·7 H_c and 0·9 H_c) and superconducting states from 4·2 to 1·4 K. Temperature-dependent oscillatory behaviour of attenuation was observed for all the samples in both the states. The results of measurements are indicated in figures 1–4 for In, In doped with Pb, Pb doped with In and pure Pb respectively. This is explained by the Claiborne and Einspruch model, where in each set, successive resonance peak represents the consecutive harmonic of the fundamental mode of excitation. Temperatures of successive absorption peak values were used to calculate the values of a, b and ν_0 for respective samples. The values of constants are shown in tables 1 and 2.

3.1 *Intermediate states*

In the intermediate state of all the samples, for a particular magnetic field, 2 sets of absorption peaks have been found—small and large. For the first phase, characterized by a small set of absorption peaks, ν_0 values increase with increase in the magnetic field i.e. from 0·7 H_c to 0·9 H_c, H_c being the critical field. According to equation (1), this

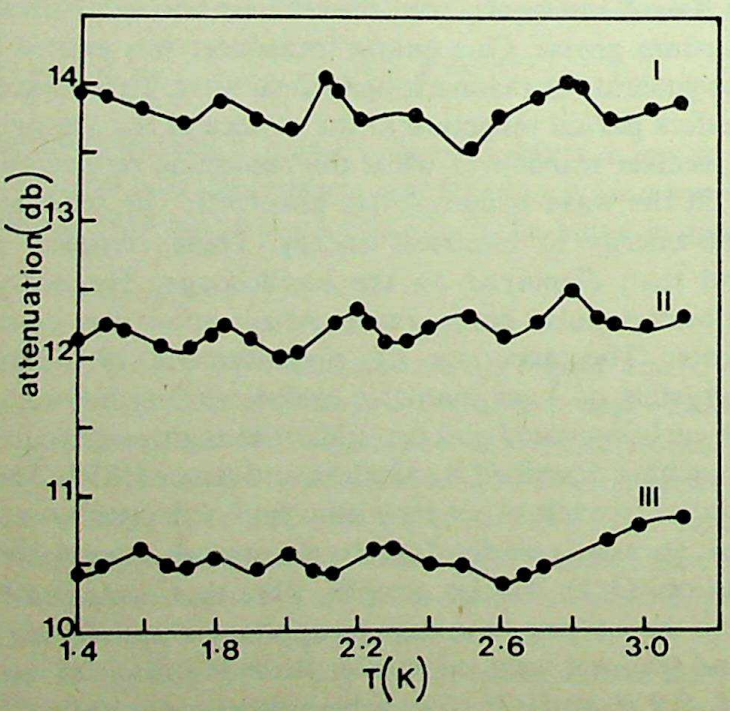

Figure 1. Plot of attenuation (db) as a function of temperature for pure In at 16·5 MHz. I. 0·7 H_c, II. 0·9 H_c, III. Superconducting state.

CC-0. In Public Domain. Gurukul Kangri Collection, Haridwar

Digitized by Arya Samaj Foundation Chennai and eGangotri

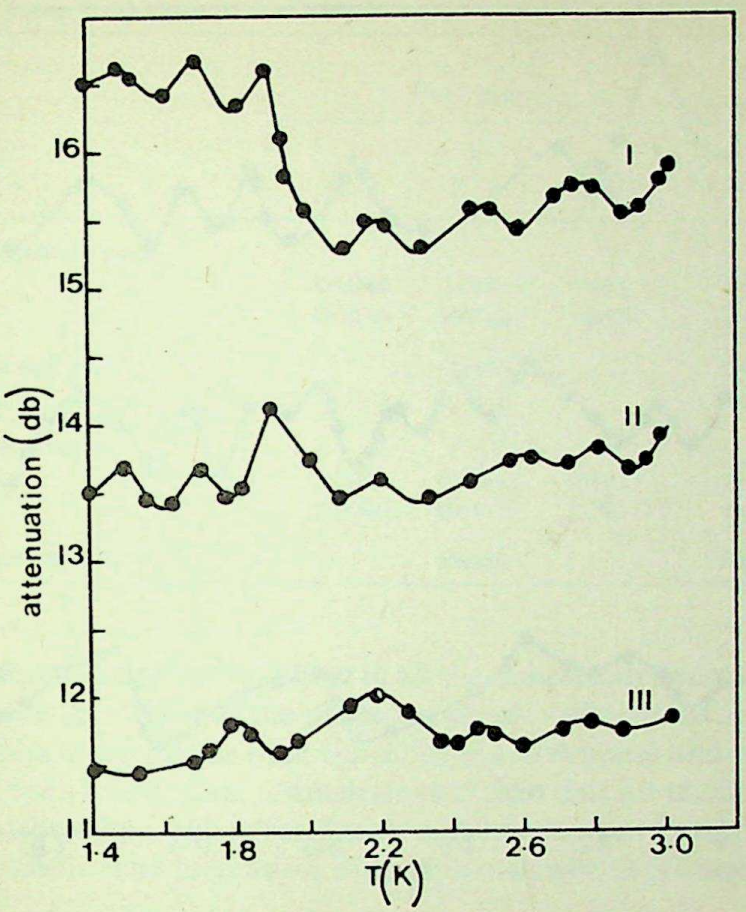

Figure 2. Plot of attenuation (db) as a function of temperature for In + 0·003 at.% Pb at 16·5 MHz. I. 0·7 H_c II. 0·9 H_c III. Superconducting state.

Table 1. Values of constants a, b and ν_0 at 16·5 MHz.

Fields	First phase			Second phase		
	a K^{-2}	b K^{-4}	ν_0 MHz	a K^{-2}	b K^{-4}	ν_0 MHz
Pure In:						
Intermediate state						
(i) 0·7 H_c	0·0042	0·0977	0·633	0·0091	0·1597	4·98
(ii) 0·9 H_c	0·0029	0·0813	0·941	0·0091	0·1597	4·98
Superconducting state	... absent ...			0·0091	1·1597	4·98
In doped with 0·003 at.% Pb:						
Intermediate state						
(i) 0·7 H_c	0·0042	0·0977	0·633	0·0095	0·1875	7·5
(ii) 0·9 H_c	0·0029	0·0813	0·941	0·0095	0·1875	7·5
Superconducting state	... absent ...			0·0095	0·1875	7·5

indicates a decrease in the laminar thickness Z_s. This decrease in Z_s with increase in the magnetic field is in accordance with the relation given by equation (2). The origin of this phase is, therefore, due to the formation of laminar structure on account of the application of the magnetic field.

CC-0. In Public Domain. Gurukul Kangri Collection, Haridwar

Digitized by Arya Samaj Foundation Chennai and eGangotri

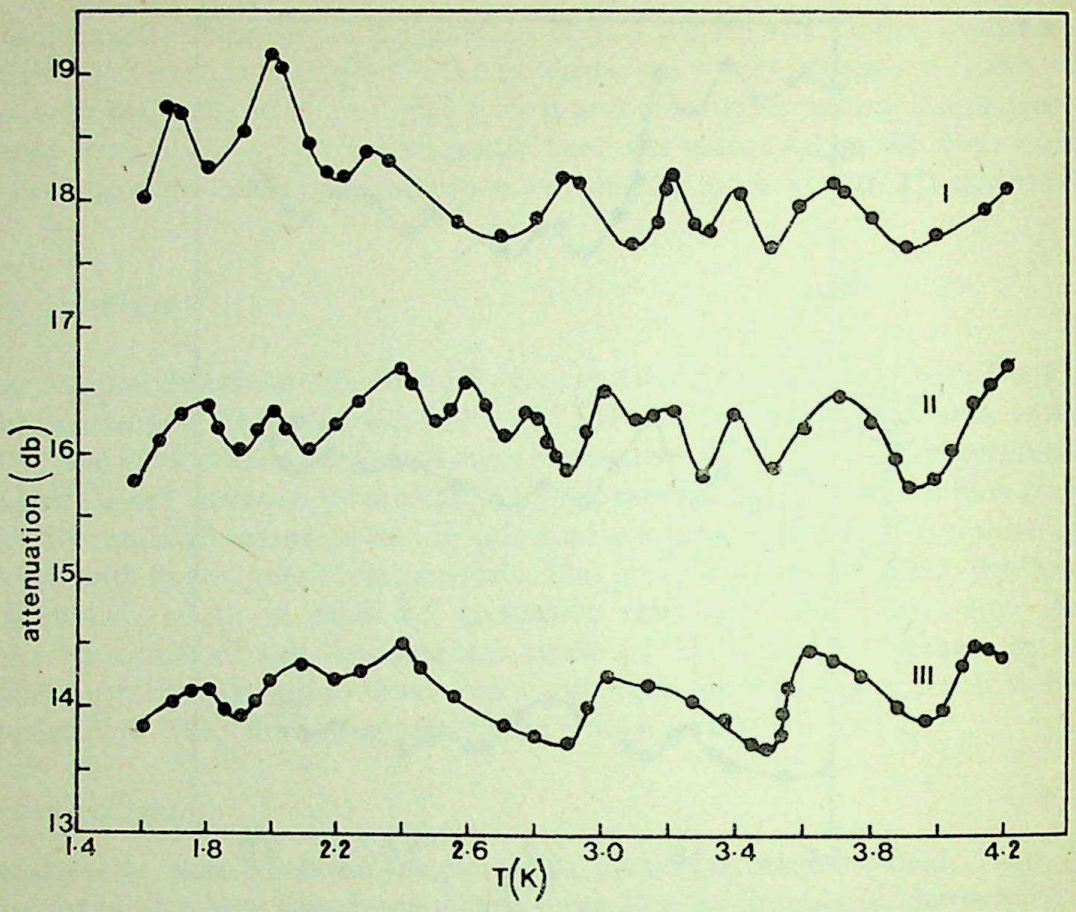

Figure 3. Plot of attenuation (db) as a function of temperature for Pb + 0·003 at.% In at 16·5 MHz. I. 0·7 H_c, II. 0·9 H_c, III. Superconducting state.

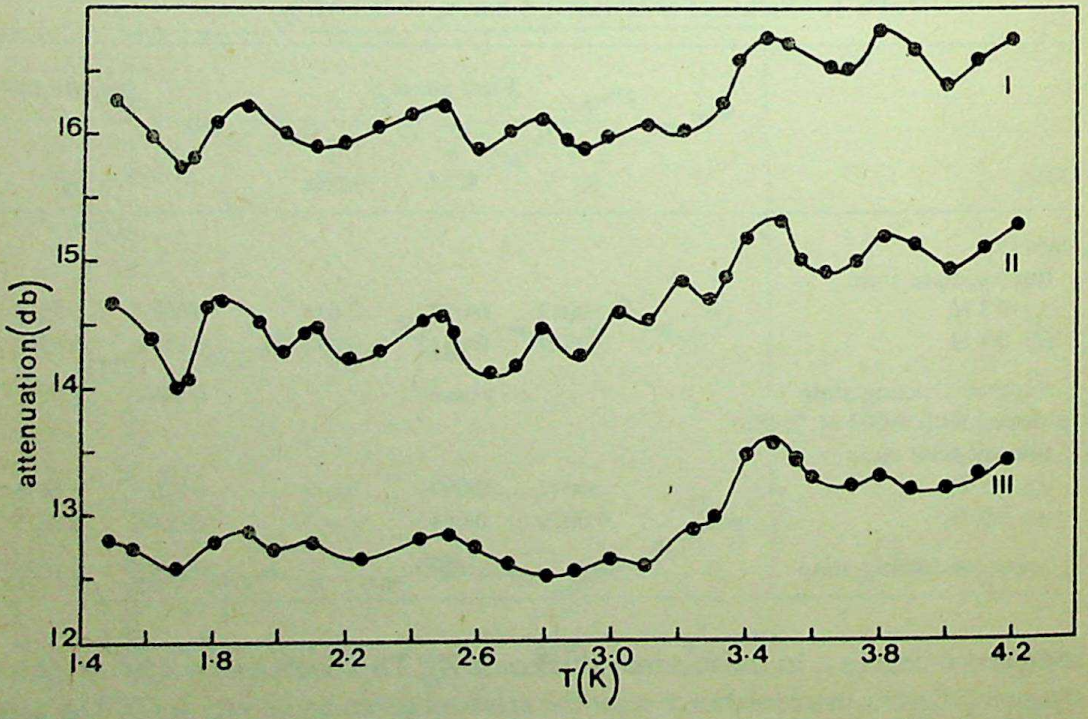

Figure 4. Plot of attenuation (db) as a function of temperature for pure Pb at 16·5 MHz. I. 0·7 H_c, II. 0·9 H_c, III. Superconducting state.

CC-0. In Public Domain. Gurukul Kangri Collection, Haridwar

Digitized by Arya Samaj Foundation Chennai and eGangotri

Table 2. Values of constants a, b and ν_0 at 16·5 MHz.

Fields	First phase			Second phase		
	a K^{-2}	b K^{-4}	ν_0 MHz	a K^{-2}	b K^{-4}	ν_0 MHz
Pure Pb Intermediate state						
(i) 0·7 H_c	0·0044	0·0943	0·693	0·0067	0·1498	4·8
(ii) 0·9 H_c	0·0036	0·0863	1·087	0·0067	0·1498	4·8
Superconducting state	... absent ...			0·0067	0·1498	4·8
Pb doped with 0·003 at.% of In						
Intermediate state						
(i) 0·7 H_c	0·0051	0·0962	0·693	0·0041	0·1140	6·0
(ii) 0·9 H_c	0·0040	0·0870	1·086	0·0041	0·1140	6·0
Superconducting state	... absent ...			0·0041	0·1140	6·0

The ν_0 values for the second phase in all the samples are independent of the magnetic field and hence the origin of the phase is entirely different. Moreover, the ν_0 values of the second phase are higher than those for the first phase and hence indicate that the thickness of the second phase is much smaller than that for the first phase. The origin of this phase is, therefore, due to formation of microstructure within the superconducting laminar thickness. The formation of the microstructure is discussed in detail in § 3.4.

3.2 *Superconducting state*

Attenuation peaks show the presence of only one phase. Absence of the first phase is expected as the laminar structure is absent in the superconducting state. According to table 1 the values of a, b and ν_0 for pure In agree exactly with the corresponding values for the second phase in the intermediate state, showing that the same microstructure is also present in the superconducting state. A similar result has been obtained by Chaudhuri and Singh (1982). This shows that the microstructure is related to the basic physical state of the sample.

3.3 *First phase*

From table 1, it can be seen that ν_0 values for the first phase at 0·7 H_c for pure In and In doped with Pb are the same i.e. 0·633 MHz. Similarly ν_0 values for In and In doped with Pb at 0·9 H_c for the first phase are the same i.e. 0·941 MHz. From table 2, it is seen that the same result is repeated for Pb and Pb doped In samples. Using equation (2), this means that superconducting laminar thickness at a particular magnetic field (either at 0·7 H_c or at 0·9 H_c) for pure and doped samples is the same. This shows that superconducting laminar thickness, and hence the origin of the first phase is independent of the nature or presence of the dopant and is entirely dependent upon the magnetic field.

From tables 1 and 2, it can be seen that ν_0 values for the first phase in In and In doped with Pb at 0·7 H_c are different from those in Pb and Pb doped with In for the respective magnetic fields. This shows that the superconducting laminar thickness Z_s is different in both the cases. In and Pb, being two different materials, have different values of

CC-0. In Public Domain. Gurukul Kangri Collection, Haridwar

Digitized by Arya Samaj Foundation Chennai and eGangotri

coherence length ξ and penetration depth λ_D. As the surface energy parameter is $\Delta \approx \xi - \lambda_D$, Δ also is different in both the cases. This according to equation (2), means that the values of Z_s will be different. Now, using the relation $\nu_0 = C_0/2Z_s$, we obtain

$$\frac{\nu_{0\,0{\cdot}7\,H_c}}{\nu_{0\,0{\cdot}9\,H_c}} = \frac{Z_{s\,0{\cdot}9\,H_c}}{Z_{s\,0{\cdot}7\,H_c}}$$

From table 1, for pure In, we get

$$\frac{Z_{s\,0{\cdot}9\,H_c}}{Z_{s\,0{\cdot}7\,H_c}} = \frac{0{\cdot}633}{0{\cdot}941} = 0{\cdot}67. \qquad \text{(a)}$$

From relation (2), we get:

$$\frac{Z_{s\,0{\cdot}7\,H_c}}{d_1} = \frac{1}{(2\times 0{\cdot}7)^{1/2}}\,(\Delta/d_1)^{1/2}, \quad \frac{Z_{s\,0{\cdot}9\,H_c}}{d_1} = \frac{1}{(2\times 0{\cdot}9)^{1/2}}\,(\Delta/d_1)^{1/2},$$

$$\frac{Z_{s\,0{\cdot}9\,H_c}}{Z_{s\,0{\cdot}7\,H_c}} = (0{\cdot}7/0{\cdot}9)^{1/2} = 0{\cdot}88 \qquad \text{(b)}$$

This value is higher than the value given by the relation (a). Similarly, for pure lead, we get,

$$\frac{Z_{s\,0{\cdot}9\,H_c}}{Z_{s\,0{\cdot}7\,H_c}} = \frac{0{\cdot}693}{1{\cdot}086} = 0{\cdot}63.$$

We see that this is in good agreement with that obtained for pure In according to relation (a). Thus, the ratio of the laminar thickness at $0{\cdot}9\,H_c$ to that at $0{\cdot}7\,H_c$, as obtained from the concept of collective excitation mode, is in good agreement for pure In and pure Pb but is lower than the ratio obtained from the consideration of the role of surface energy parameter and the breaking up of type I superconductors into normal and superconducting layers on the application of suitable magnetic field. This difference may be attributed to the approximations involved in computing Z_s according to Kuper's relation. We also observe from table 1 that for pure In and In doped with Pb samples ν_0 value is 0·633 MHz for $0{\cdot}7\,H_c$ and is 0·941 MHz for $0{\cdot}9\,H_c$. Thus ν_0 value for particular magnetic field is the same for doped and undoped samples. Similar results are obtained for pure lead and lead doped with indium samples. This means that superconducting laminar thickness Z_s for a particular magnetic field is same for the doped and undoped samples. This according to equation (2), implies that the surface energy parameter is the same for doped and undoped samples. This also means that surface energy parameter is unaffected by doping. As $\Delta \approx \xi - \lambda_D$, ξ and λ_D being coherence length and penetration depth respectively, either the difference of the two or ξ and λ_D independently should remain unchanged. Now,

$$\xi = \frac{0{\cdot}6\,(l\xi_0)^{1/2}}{(1-l)^{1/2}} \quad \text{where} \quad \xi_0 = \frac{2\hbar V_F}{\pi E_g} \text{ and } l = \text{mean free path}$$

$$\lambda_D = \lambda_L(\xi_0/l)^{1/2} \quad \text{where} \quad \lambda_L = (mc^2/4\pi ne^2)^{1/2}.$$

From these equations, it is seen that the nature of dependence of ξ and λ_D on l is different and hence Δ cannot be maintained constant if l changes. Hence values of ξ and λ_D

CC-0. In Public Domain. Gurukul Kangri Collection, Haridwar

Digitized by Arya Samaj Foundation Chennai and eGangotri

involved here, cannot be related to the mean free path l. It appears, therefore, that one has to consider the intrinsic values of coherence length and penetration depth i.e. ξ_0 and λ_L.

3.4 *Second phase*

It can be seen from tables 1 and 2 that the ν_0 value of 4·97 MHz for pure In is very nearly equal to 4·8 MHz for pure Pb. Since $\nu_0 = C_0(2Z_s)^{-1}$, ν_0 is a measure of Z_s i.e. the extent of the second phase. It is evident from the results that the extent of microstructure in both the samples is the same. This indicates that the nature and type of pinning responsible for the formation of microstructure is the same.

The value of ν_0 for In doped with Pb is 7·5 MHz whereas that for Pb doped with In is 6·0 MHz. These results show that ν_0 values have been slightly affected on account of doping.

The ultrasonic attenuation measurements by Chaudhuri and Verma (1978) in single crystals of pure tin at 300 K for frequencies varying from 3–50 MHz exhibit resonance type of behaviour in the attenuation which arises due to dislocations only, excluding the contribution due to electrons which is negligible at room temperature. Granato and Lücke (1956) have drawn the analogy between the vibration under an alternating stress of a dislocation line segment pinned through Cottrell (1948) mechanism by point defects i.e. vacancies or interstitial atoms, substitutional or interstitial impurity atoms and the problems of forced vibration of a damped vibration string. The resonance frequency is given by

$$\omega_R = 2\pi\nu_R = \frac{1}{L_c}(2G/\rho(1-\sigma)^{1/2}, \tag{3}$$

where G is the shear modulus of the material, ρ the density of the material and σ the Poisson's ratio. The length L_c is determined by minor pins due to point defects. In our experimental crystal of high purity In (99·9999 %) and high purity Pb (99·9999 %), the point defects are mainly vacancies and act as minor pins. It is assumed that for zero applied stress, the dislocations are straight and pinned down by the vacancies already present in the crystal. The interaction between the vacancy and the dislocation causes the vacancy to segregate round dislocations in equilibrium distribution. Each dislocation gathers round itself an atmosphere of vacancies. The concentration C of vacancies according to Granato and Lücke (1966) is given by a/L_c where a is the atomic distance along the dislocation line and consequently it increases with dislocation density, since it has been found (Chaudhuri and Verma 1979; Verma and Chaudhuri 1981) that L_c decreases with increase in dislocation density. It is, therefore, clear that localized inhomogeneity which acts as a microstructure, can be created between two pinning points of the dislocation.

Ultrasonic attenuation measurements by Chaudhuri and Das (1976) at 1·3 K, in the superconducting state of tin and by Chaudhuri and Verma (1978) at helium temperatures, 77 K and 300 K, in tin, show that ultrasonic attenuation versus frequency has a resonance type of behaviour and the resonance frequency goes on decreasing as the dislocation density is reduced. According to equation (3), the dislocation resonance frequency is inversely proportional to the average loop length. This means that the average loop length increases with decrease in dislocation density. If the microstructure is formed between the pinning points, then its thickness is likely to increase with

CC-0. In Public Domain. Gurukul Kangri Collection, Haridwar

Digitized by Arya Samaj Foundation Chennai and eGangotri

decrease in dislocation density. A study of ultrasonic attenuation in the intermediate state of In doped with 0·002 at.% of Bi for various physical states by Chaudhuri and Singh (1982) shows that the extent of the second phase is very much dependent on the physical state of sample. Table 3 giving the results of their measurement, show that the direct correspondence between ν_R and ν_0 value of the second phase and the size of the microstructure in the second phase can be correlated with the average distance between the pinning points. The table also shows that ν_R and ν_0 change appreciably with change in the physical state of the sample.

If we observe the ν_0 value of the second phase for the doped and undoped highly annealed specimens, it will be noticed that the ν_0 value does not change appreciably with doping.

The value of ν_0 for annealed 99·9999 % In sample studied by us is 4·8 MHz, and that for annealed In doped with 0·002 at. % Bi, as stated before, is 6·5 MHz, while that for In doped with 0·003 at. % Pb studied by us is 7·5 MHz. These results clearly shows that the ν_0 value for the second phase is governed more by the physical state of the specimen than by the concentration of the dopant. It should be noted here that one can compute n, the number of point defects per cc, and the concentration C of the point defects along the dislocation string, if the dislocation density Λ is known. Table 3 also incorporates the result of computation for In doped with 0·002 at. % Bi.

Table 4 gives the values of ν_0, ν_R, Z_s, L_c, Λ, n and C for pure In and pure Pb samples studied by us which were annealed for 80 hours. It is observed from table 3 that as ν_R value i.e. ν_0 value increases with increase in dislocation density Λ, the concentration of the point defects C along the dislocation line also goes on increasing and the number of point defects available for pinning also increases. Comparison of the number of point

Table 3. Values of ν_0, ν_R, Z_s, L_c, Λ, n and C for In doped with 0·002 at.% of Bi.

Annealing time Hours	Λ cm^{-2} ($\times 10^5$)	ν_0 MHz	ν_R MHz	Extent of micro-structure Z_s(cm)($\times 10^{-3}$)	Average loop length L_c cm($\times 10^{-3}$)	$n = \Lambda/L_c$ cm^{-3}	$C = a/L_c$ ($\times 10^{-8}$)
24	8	21·5	18	2·33	1·6	50×10^7	625
29	2·5	15·8	12	3·17	2·39	$10{\cdot}5 \times 10^7$	417
80	0·01	6·5	5	7·69	5·73	$17{\cdot}5 \times 10^4$	175

Table 4. Values of ν_0, ν_R, Z_s, L_c, Λ, n and C for pure In and pure Pb.

Samples	ν_0 (MHz)	ν_R (MHz)	Z_s (cm) ($\times 10^{-3}$)	L_c (cm) ($\times 10^{-3}$)	Λ (cm^{-2}) ($\times 10^5$)	n (cm^{-3}) ($\times 10^4$)	$C = a/L_c$ ($\times 10^{-8}$)
Pure In 99·9999 % annealed for 80 hr	5	3·85	10	7·44	0·006	8	134
Pure Pb 99·9999 % annealed for 80 hr	4·8	3·7	10·4	7·74	0·006	7·75	129

CC-0. In Public Domain. Gurukul Kangri Collection, Haridwar

Digitized by Arya Samaj Foundation Chennai and eGangotri

defects in the highly annealed doped In sample with that of vacancies in the highly annealed undoped In sample shows that the number of point defects in the doped sample is of the same order of magnitude as that of vacancies for the undoped one. Thus, the point defects are mainly vacancies. Hence vacancies, which characterize the physical state of the specimen, are the main source of pinning the dislocation string and hence are primarily responsible for the formation of microstructure.

The marginal increase in ν_0 value of the doped samples can be attributed to the addition of impurity atoms which offer more pinning points.

4. Conclusions

Ultrasonic attenuation measurements in the intermediate and superconducting states show the importance of the results in identifying the mechanism of absorption which is different from the one postulated by the BCS theory. Further, the microstructures or laminar structures which can be produced either by inhomogeneity in the system due mainly to the localized strain sites or by suitable application of a magnetic field which give rise to a temperature-dependent oscillatory attenuation. These results have been utilized to identify the origin of the structures and throw considerable light on the role of vacancies for the creation of microstructures.

References

Agarwal S K and Chaudhuri K D 1976 *Solid State Commun.* **19** 447
Anderson P W 1958 *Phys. Rev.* **112** 1900
Andreev A F 1964 *Zh. Eksp. Teor. Fiz.* **46** 1823; (*Sov. Phys. JETP* **19** 1228)
Andreev A F 1968 *Sov. Phys. JETP* **26** 426
Andreev A F and Bruk Yu-M 1966 *Sov. Phys. JETP* **23** 942
Bardeen Cooper L N and Schriffer J R 1957 *Phys. Rev.* **108** 1175
Bogoliubov N N 1957 *Zh. Eksp. Teor-Fiz.* **34** 58; (*Sov. Phys. JETP* 7 41)
Chaudhuri K D and Agarwal S K 1979 *J. Phys.* **F9** 529
Chaudhuri K D and Jain M C 1969 *Cryogenics* **9** 235
Chaudhuri K D and Mahajan S K 1974 *Cryogenics* **14** 321
Chaudhuri K D and Mahajan S K 1976 *J. Low Temp. Phys.* **24** 131
Chaudhuri K D and Das H L 1976 *Cryogenics* **16** 346
Chaudhuri K D and Singh R 1979 *J. Low Temp. Phys.* **36** 689
Chaudhuri K D and Singh R 1982 *J. Low Temp. Phys.* **47** 329
Chaudhuri K D and Verma B M 1978 *J. Low Temp. Phys.* **31** 93
Chaudhuri K D and Verma B M 1979 *Cryogenics* **19** 293
Claiborne L T and Einspruch N G 1963 *Phys. Rev.* **132** 621
Cottrell A H 1948 *Rept. Conf. Strength Solids* (*Phys. Soc. London*) 30
Granato A V and Lucke K 1956 *J. Appl. Phys.* **27** 583
Granato A V and Lucke K 1966 *Physical acoustics* (New York: Academic Press) Vol. 4, p. 238
Kuper C G 1951 *Philos. Mag.* **42** 961
Lock J M, Pippard A B and Shoenherg D 1952 *Proc. Camb. Philos. Soc.* **47** 881
Maddin R and Asher W R 1950 *Rev. Sci. Instrum.* **21** 881
Mahajan S K and Chaudhuri K D 1972 *Phys. Lett.* **39A** 31
Mahajan S K and Chaudhuri K D 1974 *Solid State Commun.* **14** 1083
Olsen T, Claiborne L T and Einspruch N G 1966 *J. Appl. Phys.* **37** 760
Singh O and Jericho M H 1972 *Phys. Rev.* **B5** 3542
Verma B M and Chaudhuri K D 1981 *Pramana–J. Phys.* **17** 415

CC-0. In Public Domain. Gurukul Kangri Collection, Haridwar

Digitized by Arya Samaj Foundation Chennai and eGangotri

CC-0. In Public Domain. Gurukul Kangri Collection, Haridwar

Digitized by Arya Samaj Foundation Chennai and eGangotri

Pramāṇa – J. Phys., Vol. 28, No. 2, February 1987, pp. 217–228. © Printed in India.

A three-body force shell model calculation of Schottky defect formation energies of ionic crystals with CsCl structure

V MISHRA, S P SANYAL* and R K SINGH†

Department of Physics, Bhopal University, Bhopal 462 026, India
*Present address: Max-Planck-Institut fur Festkörperforschung, Heisenbergstraße 1, D-7000, Stuttgart-80, Federal Republic of Germany.
†Centre for Science and Technology Development Studies, MAPCOST, Bhopal 462 016, India

MS received 19 May 1986; revised 4 November 1986

Abstract. A three-body force shell model (TSM) for the calculation of Schottky defect formation energies in solids with cesium chloride structure has been developed by incorporating the effects of long-range three-body interactions (TBI) in the shell model. These TBI in the defect lattice arise from the deformation of electron shells when the nearest neighbour ions get relaxed from their equilibrium position. This model has been used to calculate the cation and anion extraction and Schottky defect formation energies of CsCl, CsBr, CsI, TlCl, TlBr and NH_4Cl crystals. The calculated values of these defect properties agree reasonably well with their measured values.

Keywords. Schottky defect energy; rigid shell model; polarizable point ion model; three-body force shell model.

PACS No. 61·70

1. Introduction

In an earlier paper (Mishra *et al* 1986) (referred to as I), we have reported a modified polarizable point ion (PPI) model which includes the effects of long-range three-body interactions (TBI) for the calculation of point defect formation energies of solids with CsCl structure. As pointed out in I, the PPI model neglects the dependence of the short-range forces on the electronic polarization of ions and predicts substantially higher values of static and dielectric constants. In the presence of an electric field, the electrons get displaced and consequently, the short-range forces between the ions also change. Since the PPI model considers the ions to be point charges, it fails to account for the electronic polarization and hence fails to predict the Cauchy violation in the elastic constants, phonon dispersion curves, dielectric and optical properties of ionic solids.

A satisfactory prediction of the polarization effects in ionic solids has been achieved from the rigid shell model (RSM) developed by Woods *et al* (1960). The ionic charges (Ze) in RSM consists of core (Xe) and shell (Ye) charges such that $Ze = Xe + Ye$. Its shell can move bodily with respect to its core and this mechanism gives rise to electronic polarization. The corresponding cation (α_+) and anion (α_-) polarizabilities have been defined in terms of the core-shell force constant ($K_\pm$) as (Woods *et al* 1960):

$$\alpha_\pm = (Y_\pm e)^2/(K_\pm + R_0), \tag{1}$$

†To whom all correspondence should be addressed.

CC-0. In Public Domain. Gurukul Kangri Collection, Haridwar

Digitized by Arya Samaj Foundation Chennai and eGangotri

with R_0 as the short-range force constant. In RSM, the short-range forces are regarded as acting between the shells only and arise from overlap and exchange interactions between the shell-electrons. The basic principles of this model for diatomic crystals are schematically illustrated in figure 1.

In recent years, the Schottky defect formation energies of ionic crystals have been extensively studied by several workers (Faux and Lidiard 1971; Boswarva and Simpson 1973; Catlow *et al* 1976; Murty and Usha 1978) following the semi-discrete approximation of Mott and Littleton (1938). Similar calculations for alkaline earth fluorides (Franklin 1968; Chakravorty 1971; Norgett 1971; Keeton and Wilson 1973; Catlow and Norgett 1973; Catlow *et al* 1977) and oxides (Catlow *et al* 1976; Mackrodt and Stewart 1979; Sangster and Rowell 1981; Vempati and Jacobs 1983) have also been made in the framework of RSM using HADES programme developed by Norgett (1974). The RSM calculations of Schottky defect formation energies in cesium halides have been reported by Uppal *et al* (1978). No such calculation has yet been reported for other crystals with CsCl structure.

It is also obvious that studies have been made only on two-body potentials which generally consist of long-range Coulomb and short-range repulsive and/or, van der Waals interactions. The major limitation of these potentials is that they fail to reproduce the elastic and dielectric constants of ionic crystals (Singh 1982). This is true because the electronic polarizability introduced in RSM has no effect on the elastic constant and hence RSM does not go beyond the PPI model in this regard. In order to overcome these common weaknesses, a three-body force shell model (TSM) was developed by Singh and Verma (1969) for successful description of lattice dynamical, dielectric and elastic properties of ionic solids (Singh 1982).

Recently, it has been emphasized by several workers (Catlow and Mackrodt 1982; Lidiard and Norgett 1972) that the effects of long-range three-body forces in the defect structure and properties of ionic solids should be explored. Motivated from this remark, we have employed the TSM formalism for calculating the Schottky defect formation energies in cesium, thallium and ammonium halide crystals. The essential theory for these calculations will be described in § 2 indicating the modifications introduced by three-body interactions (TBI) in the ionic charges in the defect formation energy when they are incorporated through the TSM framework. The Schottky defect formation energy has been calculated by us using the method of minimization of defect energy (Norgett 1974; Silvarajan 1978; Catlow and Mackrodt 1982). A brief account of this is presented in § 3. Section 4 collects the computed results, and the results discussed in § 5.

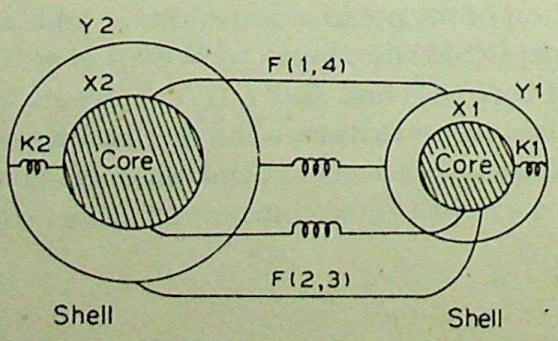

Figure 1. Schematic diagram representing the shell model for ionic crystals.

CC-0. In Public Domain. Gurukul Kangri Collection, Haridwar

Digitized by Arya Samaj Foundation Chennai and eGangotri

2. Theory

2.1 *Three-body interaction potential*

The development of the three-body force shell model (Singh and Verma 1969) basically rests on the fact that the ions during lattice vibrations suffer an appreciable overlap and consequently their electron shells undergo deformation. This mechanism causes a transfer of charge between the overlapping ions. In turn, these transferred charges interact with all other charges of the lattice via Coulomb field and give rise to the long-range many body interactions (Singh 1982). The TSM formalism can be derived from the three-body potential written as

$$E_L(r) = \sum_{ij}{}' \frac{Z_i Z_j e^2}{r_{ij}} + \sum_{ijk}{}' \frac{Z_i Z_j e^2}{r_{ij}} f(r_{ik}) + \sum_{ij} c_{ij} r_{ij}^{-6} + \sum_{ij} d_{ij} r_{ij}^{-8}$$

$$+ \sum_{ij} \beta_{ij} b \exp((r_i + r_j - r_{ij})/p), \tag{2}$$

where the first and second terms are the long-range Coulomb and three-body interactions respectively. The third and fourth terms correspond to van der Waals interactions. The last term is the overlap repulsion operative upto the second neighbour ions. Here, the short-range potential has only two parameters (b and p) and the TBI potential has one parameter $f(r)$, which is the measure of overlap between adjacent ions. The physical concept underlying the mechanism of charge transfer is reviewed by Singh (1982). Accordingly, the transferred charge between the adjacent ions i and k can be written as

$$\Delta q_i = Z_i e f(r_{ik}), \tag{3}$$

which consequently modifies the ionic charge ($Z_i e$) of the ith ion as

$$Z_{mi} e = \pm Z_i e[1 + n f(r_{ik})]^{\frac{1}{2}}, \tag{4}$$

with $f(r_{ik})$ as a TBI function (Singh 1982) and n as the number of nearest neighbour ions. This modification in ionic charge corresponds to a change in core and shell charges from ($X_i e$, $Y_i e$) such that

$$Z_{mi} e = (X_{mi} + Y_{mi}) e = (x_i Z_{mi} + y_i Z_{mi}) e, \tag{5}$$

with $x_i + y_i = 1$. The corresponding modification in the core-shell spring constants (K_m) is given by (Singh 1982)

$$K_{mi} = ((Y_{mi} e)^2 / \alpha_{mi}) - R_0, \tag{6}$$

where α_{mi} is the modified polarizability and R_0 is the short-range force constant between cation and anion as defined by Singh (1982).

2.2 *Effective charge in defect region*

In TSM formalism, we define Q_{mv}, Q_{mc}, Q_{ms} and Q_{md} as the modified virtual, core, shell and defect charges of the ions, respectively, in region I which consists of vacancy and its surrounding neighbours. Also, X_c, X_s and X_T are the core, relative core-shell and total

CC-0. In Public Domain. Gurukul Kangri Collection, Haridwar

Digitized by Arya Samaj Foundation Chennai and eGangotri

fractional displacements of the ions in this region. In defect lattice, due to creation of a point defect, the overlap effect between the ions increases significantly with the displacements of nearest neighbours of the vacancy from their original position. A schematic representation of this effect has been shown in figure 2. The creation of a point defect at (0, 0, 0) will lead to the displacements of shells of the nearest neighbour ions (2 to 9) from their original positions. Let these displacements (away from the vacancy) be $\mathbf{X}_T$ which will change the amount of overlap between the vacancy and the nearest neighbour ions. Accordingly, this change can be defined as

$$f_d(r) = f_0 \exp(-r_0(1 + X_T)/p). \tag{7}$$

This modifies the defect charge as

$$Q_{md(d)}e = Ze(1 + 8 f_d(r)). \tag{8}$$

Also, the second neighbour ions get displaced due to the creation of the vacancy. Let $\mathbf{X}_1$ be the displacement of an ion at a distance $\pm a$ from the vacancy. Similarly, $\mathbf{X}_2$ and $\mathbf{X}_3$ be the displacements of the ions at distances $\pm\sqrt{2}a$ and $\pm\sqrt{3}a$ from the vacancy. These displacements change the ionic charges of the first neighbours of the vacancy such that (Singh *et al* 1984)

$$\begin{aligned} Z_{m(dd)}e = Ze\Big\{1 + f_0\Big[& 3\exp\Big(-(2(\tfrac{1}{2} + \tfrac{1}{2}X_T)^2 + (\tfrac{1}{2} + X_1 - \tfrac{1}{2}X_T)^2)^{1/2}\frac{2r_0}{\sqrt{3}p}\Big) \\ & + 3\exp\Big(-((\tfrac{1}{2} + \tfrac{1}{2}X_T)^2 + 2(1 + X_2 - \tfrac{1}{2}X_T)^2)^{1/2}\frac{2r_0}{\sqrt{3}p}\Big) \\ & + \exp\Big(-(3(\tfrac{1}{2} + X_3 - \tfrac{1}{2}X_T)^2)^{1/2}\frac{2r_0}{\sqrt{3}p}\Big) \\ & + \exp(-r_0(1 + X_T)/p)\Big]\Big\}. \end{aligned} \tag{9}$$

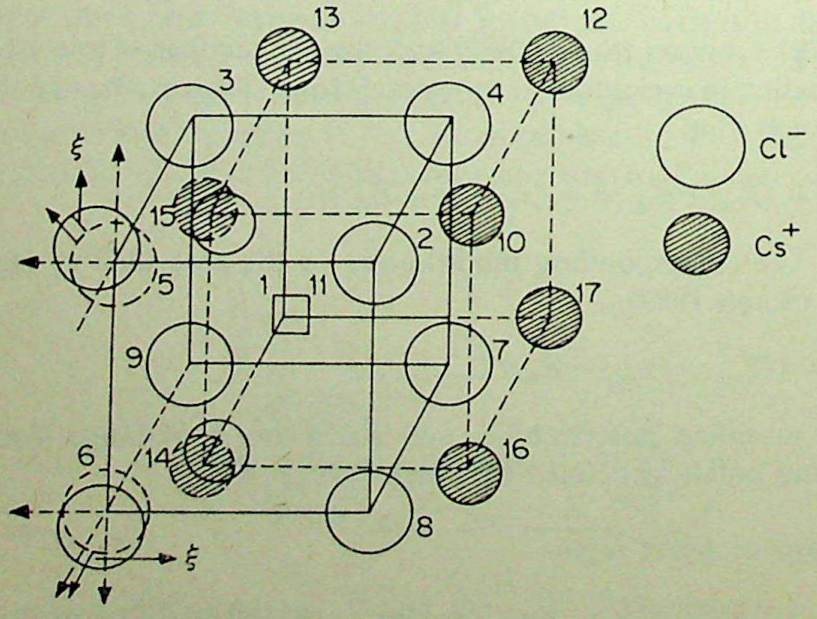

Figure 2. Description of a defect lattice with CsCl structure. The ions shown with circles of full and dotted lines are the virtual and real charges respectively.

CC-0. In Public Domain. Gurukul Kangri Collection, Haridwar

Digitized by Arya Samaj Foundation Chennai and eGangotri

This modified ionic charge due to the creation of a defect will change the original shell charges from Y_m to $Y_{m(dd)}$ such that

$$Z_{m(dd)}e = (X_m + Y_{m(dd)})e = (Q_{mc} + Q_{ms(dd)})e, \tag{10}$$

of each ion at their displaced positions. However, the virtual charge $Q_{mv}e(=Z_{mv}e)$ remains the same. These modified ionic and shell charges can be used to minimize the energy of the defect lattice. Besides these modifications, the TBI introduces modifications in the polarization mechanism in the defect lattice. These modifications have been discussed in detail in I.

3. Method of calculation

For the calculation of formation energy of Schottky defect, we have followed the semi-discrete approximation (Mott and Littleton 1938) and the general formulation for treating the defect lattice developed by Lidiard and Norgett (1972) and Norgett (1974). Accordingly, the defect crystal is divided into two regions; region I consists of the defect and its nearest neighbours, while rest of the lattice is considered as region II. Each ion in the defect lattice can be described by its displacement from its original position in a perfect lattice and by its electronic dipole moment. Since these displacements and moments of the ions in region II are small, they are treated in the harmonic approximation (Catlow and Mackrodt 1982). The displacements and dipole moments of the ions in region II are derived using Mott and Littleton (ML) method, while those for ions in region I are obtained by minimizing the energy of the defect lattice with respect to these parameters. The details of the method of defect energy minimization have been reviewed by Norgett (1974), Lidiard and Norgett (1972) and Catlow and Mackrodt (1982).

In the framework of TSM, the total energy of the defect configuration can be minimized with respect to the relaxations of the cores and shells of each ion surrounding the defect. Thus, the total energy of the defect configuration can be written as (Silvarajan 1978)

$$E_f = E_1(x) + E_2(x, X) + E_3(X). \tag{11}$$

Here, $E_1(x)$ is the energy of the defect region, $E_3(X)$ is the energy of the outer region and $E_2(x, X)$ is the interaction energy between the two regions with x and X as the displacements of defect and outer region ions, respectively. $E_3(X)$ is a quadratic function of X and can be expressed as (Catlow and Mackrodt 1982)

$$E_3(X) = -\frac{1}{2}\left(\frac{\mathrm{d}E_2(x, X)}{\mathrm{d}X}\right)_{X=\bar{X}} \cdot \bar{X}, \tag{12}$$

and hence the total energy of the defect configuration, E_f, will be

$$E_f = E_1(x) + E_2(x, X) - \frac{1}{2}\left(\frac{\mathrm{d}E_2(x, X)}{\mathrm{d}X}\right)_{X=\bar{X}} \cdot \bar{X}, \tag{13}$$

where $\bar{X}$ is the equilibrium value of X. If we make an assumption on the equilibrium displacements of region II ions (Mott and Littleton 1938), then the revised expression

CC-0. In Public Domain. Gurukul Kangri Collection, Haridwar

Digitized by Arya Samaj Foundation Chennai and eGangotri

for E_f is a function of only region I variables with respect to which E_f can be minimized to get the final equilibrium configuration of region I and also the energy of formation of the defect. The details of the formulation developed for these calculations are given in Appendix A.

4. Results and discussion

The Schottky defect formation energy (h_s) has been computed for the solids with CsCl structure (CsCl, CsBr, CsI, TlCl, TlBr and NH_4Cl) by employing the TSM for defect lattice (Mishra 1985). The values of r_0 and the calculated values of potential and shell model parameters have been listed in table 1. The calculated values of equilibrium relaxations of core and relative core-shell of first neighbour ions surrounding a cation and an anion vacancy with their corresponding extraction energies (E_+ and E_-) are given in table 2. The calculated values of Schottky defect energies (h_s) are also presented in the same table.

In the present study, the calculations of defect energies have been performed by restricting the defect region to contain the first neighbour ions (first shell) only. The calculations carried out for CsCl, by enhancing the defect region to contain next nearest neighbours of the vacancy (second shell) have, however, shown insignificant difference

Table 1. Values of constant used for calculation of defect energies.

Parameters	CsCl	CsBr	CsI	TlCl	TlBr	NH_4Cl
r_0 (Å)†	3·591	3·750	3·990	3·310	3·440	3·348
b (10^{12} ergs)	0·244	0·268	0·378	0·502	0·430	0·259
ρ (Å)	0·307	0·350	0·430	0·385	0·387	0·313
$f(r)$ ($\times 10^{-3}$)	−3·15	−1·73	2·37	−11·45	−12·14	−3·88
Y_{m+}	−10·87	−10·47	−6.48	−3·30	−3·01	−4·29
Y_{m-}	−5·05	−1·80	−1·17	−1·85	−1·60	−1·89
Km_+ (10^4 dyn/cm^2)	969·00	1007·31	280·95	60·03	45·66	236·93
Km_- (10^4 dyn/cm^2)	217·20	22·06	2·47	28·90	11·81	27·47

† Values correspond to 300 K.

Table 2. Equilibrium values of relaxations of nearest neighbour cores (X_c) and shells (X_s) (in units of r_0), extraction energies of cation (E_+) and anions (E_-) (in units of eV) and Schottky defect formation energies (h_s) (in eV) of solids with CsCl structure.

	Cation vacancy			Anion vacancy			
Solids	X_c	X_s	E_+	X_c	X_s	E_-	h_s
CsCl	0·062	0·006	4·359	0·065	−0·004	4·284	1·952
CsBr	0·055	0·012	4·346	0·071	−0·004	4·196	2·079
CsI	0·052	0·018	4·330	0·082	−0·006	3·725	1·941
TlCl	0·045	0·014	5·468	0·095	−0·016	3·271	1·227
TlBr	0·032	0·021	5·294	0·095	−0·018	3·154	1·109
NH_4Cl	0·055	0·012	4·614	0·085	−0·008	3·954	1·528

CC-0. In Public Domain. Gurukul Kangri Collection, Haridwar

Digitized by Arya Samaj Foundation Chennai and eGangotri

between the values of Schottky defect energies (h_s = 1·952 and 1·953 eV for region I consisting of 8 ions (first shell) and 20 ions (second shell), respectively). This fact is in agreement with previous calculations carried out by Boswarva and Simpson (1973) and Murty and Usha (1978) who have shown that the relaxations and defect energies converge rapidly as the region I is expanded.

The experimental values of h_s in cesium halides have been derived by Harvey and Hoodless (1967) and Lynch (1960) from the results of conductivity and diffusion studies. Lynch (1960) has, however, concluded from the self-diffusion measurements in CsBr and CsI that both cations and anions take part significantly in the mass transport processes. For TlCl, experimental values of Schottky energy have been derived from thermoelectric power measurements (Christy and Dobbs 1967) and conductivity studies (Friauf 1961). More recently, the Schottky energy in thallous halides has been predicted by Samara (1979) from conductivity measurements. All these investigations have provided evidences suggesting the predominance of Schottky defects in cesium and thallous halides. On the other hand, experimental studies on defect properties in the case of ammonium halides are less numerous. Harrington and Staveley (1964) reported the values of h_s to be 0·81 eV in the case of NH_4Cl, corresponding to low activation energy of the order of 0·75 eV.

The earlier defect properties of solids with CsCl structure have been studied by Boswarva (1967), Murthy and Murty (1971) and Shukla *et al* (1972) using polarizable point ion (PPI) model and by Uppal *et al* (1978) using the shell model. Boswarva (1967) made extensive calculations of defect energies of cesium halides by varying the description of the polarization and displacement fields and also by describing the short-range potential in different forms. However, he has obtained negative values of equilibrium relaxations which obviously indicate the hardness of the short-range potential. Moreover, the reported values of h_s are substantially lower than their measured values. This might be due to the incorrect prediction of dielectric properties by PPI model. The increased hardness inherent in the potentials of Boswarva (1967) results in higher values of the energy required to create cation and anion vacancies, leading to smaller values of h_s. This situation has been considerably improved by Murthy and Murty (1971) who used a softer potential to represent the short-range interactions and obtained fairly reasonable values of h_s in the case of CsCl. Their results in the case of other members of this family of solids have, however, shown poor agreement with experimental results. Subsequently, shell model calculations of h_s in alkali halides with NaCl and CsCl structures have been carried out by Uppal *et al* (1978) using the potential devised by Sangster and Atwood (1978). In particular, the defect formation energies reported by Uppal *et al* (1978) for cesium halides, referred to in table 3, are at the lower side of the experimental values.

Table 2 shows that the extraction energies of cation (E_+) and anion (E_-) in cesium and thallous halides obtained from the present calculations show a systematic variation and the cation extraction energy is higher in comparison to that of anion. However, as the polarizability of anion increases from Cl^- to I^-, the anion extraction energy reduces considerably. This fact is consistent with other theoretical results, like oxides (Mackrodt and Stewart 1979; Sangster and Rowell 1981) in which a similar trend is observed.

A comparison between the results obtained from the two models (modified PPI and TSM), as presented in table 3, reveals that no substantial change in the Schottky defect formation energy is observed in the case of cesium halides. One, however, notes a

CC-0. In Public Domain. Gurukul Kangri Collection, Haridwar

Digitized by Arya Samaj Foundation Chennai and eGangotri

Table 3. Comparison of Schottky defect energies (in eV) in solids with CsCl structure.

Solids	Present			Other theoretical results		
	PPI	TSM	Expt.	(Boswarva 1967)	(Murthy and Murty 1971)	
CsCl	2·024	1·952	1·86[a]	1·648	1·986	1·79[g]
CsBr	2·019	2·079	2·0[b]	1·521	1·878	1·86[g]
CsI	2·094	1·941	1·9[b]	1·490	1·517	1·82[g]
TlCl	0·851	1·227	0·84–1·3[c,d] 1·03[e]	—	1·349	0·79[h]
TlBr	0·810	1·109	—	—	1·322	0·69[h]
NH_4Cl	1·890	1·528	0·81	—	1·387	

[a] Harvey and Hoodless (1967); [b] Lynch (1960); [c] Christy and Doobs (1967); [d] Friauf (1961); [e] Samara (1979); [f] Harrington and Staveley (1964); [g] Uppal *et al* (1978); [h] Shukla *et al* (1972).

marked enhancement in the value of h_s in thallous halides obtained from TSM. This fact, thus, clearly emphasizes that the modified PPI model fails to predict the dielectric behaviour of some solids where the static dielectric constant is too large. A more consistent value of h_s has been obtained from TSM in the case of NH_4Cl. Moreover, it has recently been pointed out by Catlow *et al* (1981) that to avoid misleading situations of comparing static lattice defect energies calculated at constant volume with an experimental enthalpy at constant pressure, one must carry out such defect energy calculations over a range of lattice parameters. In view of this, we have calculated the values of Schottky defect energies of all the solids under consideration, over a range of $\pm$ 0·15 Å of the respective lattice parameters corresponding to 300 K. The calculated values of h_s from this procedure do not, however, go beyond the experimental uncertainties in the present system of solids. Referring to the uncertainties involved in the measurements of these defect properties, the agreement achieved from TSM seems to be good. Moreover, the theoretical estimates of defect energies emphasize the need for further detailed experimental efforts to reveal the defect structure and properties in this family of solids.

Acknowledgements

The authors are grateful to Professors S Lundqvist, P W M Jacobs, C R A Catlow, Y V G S Murty and Dr P C Dash for valuable suggestions and discussions. They are also thankful to the Department of Science and Technology and CSIR, New Delhi for financial support.

Appendix A. TSM formulation for defect energy

The energy of region I consists of various combinations of contributions from core, shell, virtual and defect charges. The Schottky defect formation energy (h_s) is given by

$$h_s = E_+ + E_- - E_L \tag{A1}$$

CC-0. In Public Domain. Gurukul Kangri Collection, Haridwar

Digitized by Arya Samaj Foundation Chennai and eGangotri

in terms of the energy (E_+ and E_-) required to extract an ion (cation and anion) from the lattice and the lattice energy (E_i) given by (1). The energy E_+ (or E_-) consists of several contributions such that

$$E_\pm = \sum_{j=1}^{8} E_{j\pm}. \tag{A2}$$

The evaluation of these contributions from E_1 to E_8 is made from the following expressions.

(i) *Rigid unpolarizable lattice energy*

The energy required to extract an ion from the rigid unpolarized lattice E_1 is given by

$$\begin{aligned} E_1 = {} & \alpha_m e^2 Z m^2 r_0^{-1} - 8B_{+-}\exp(-r_0/p) - 6B_{++}\exp(-2r_0/\sqrt{3}p) \\ & + 8c_{+-}r_0^{-6} + 8d_{+-}r_0^{-8} + 6c_{++}(2/\sqrt{3})^{-6}r_0^{-6} \\ & + 6d_{++}(2/\sqrt{3})^{-8}r_0^{-8} \end{aligned} \tag{A3}$$

with $B_{+-} = b\beta_{+-}\exp((r_+ + r_-)/p)$

and $B_{++} = b\beta_{++}\exp(2r_+/p)$.

(ii) *Long range attractive energy*

The long-range (LR) attractive energy, E_2 of region I is contributed by various combinations of the charges as expressed below:

(a) W_1 is the energy due to interactions between core-core, shell-shell and virtual-virtual expressed as

$$W_1 = 2(1+3\sqrt{3}+3\sqrt{3}/2)[Q_{mc}(1+X_c)^{-1} + (Q_{ms(dd)}^2 + Q_{mv}^2)(1+X_T)^{-1}]. \tag{A4}$$

(b) W_2 is the energy due to the interaction between core and shell charges given by

$$\begin{aligned} W_2 = {} & Q_{mc}Q_{ms(dd)}\{12\sqrt{3}[2(\tfrac{1}{2}X_c - \tfrac{1}{2}X_T)^2 + (1+\tfrac{1}{2}X_c + \tfrac{1}{2}X_T)^2]^{-1/2} \\ & + 12\sqrt{3}[(\tfrac{1}{2}X_c - \tfrac{1}{2}X_T)^2 + 2(1+\tfrac{1}{2}X_c + \tfrac{1}{2}X_T)^2]^{-1/2} \\ & + 4(1+\tfrac{1}{2}X_c + X_T)^{-1}\} \end{aligned} \tag{A5}$$

(c) W_3 is the LR interaction energy between core and virtual charges given by

$$\begin{aligned} W_3 = {} & Q_{mc}Q_{mv}\{12\sqrt{3}[\tfrac{1}{2}X_c^2 + (1+\tfrac{1}{2}X_c)^2]^{-1/2} \\ & + 12\sqrt{3}[\tfrac{1}{4}X_c^2 + 2(1+\tfrac{1}{2}X_c)^2]^{-1/2} + 4(1+\tfrac{1}{2}X_c)^{-1}\}. \end{aligned} \tag{A6}$$

(d) W_4 is the LR interaction energy between shell and virtual charges expressed as

$$\begin{aligned} W_4 = {} & Q_{ms(dd)}Q_{mv}\{12\sqrt{3}[\tfrac{1}{2}X_T^2 + (1+\tfrac{1}{2}X_T)^2]^{-1/2} \\ & + 12\sqrt{3}[\tfrac{1}{4}X_T^2 + 2(1+\tfrac{1}{2}X_T)^2]^{-1/2} + 4(1+\tfrac{1}{2}X_T)^{-1}\}. \end{aligned} \tag{A7}$$

CC-0. In Public Domain. Gurukul Kangri Collection, Haridwar

Digitized by Arya Samaj Foundation Chennai and eGangotri

(e) W_5 is the energy due to interaction of defect with core, shell and virtual charges, expressed as

$$W_5 = 8Q_{md(d)}[Q_{mv} + Q_{mc}(1+X_c)^{-1} + Q_{ms(dd)}(1+X_T)^{-1}]. \tag{A8}$$

Thus, the modified LR energy of region I due to the Coulomb and TBI is given by

$$E_2 = \frac{e^2}{r_0}(W_1 + W_2 + W_3 + W_4 + W_5). \tag{A9}$$

(iii) *Polarization energy*

In the framework of TSM, polarization of ions is accounted through K_m. In region I, the core and shell interaction of the same ion represents the linear spring energy (Silvarajan 1978)

$$E_3 = 8(\tfrac{1}{2}K_m X_s^2 r_0^2) \tag{A10}$$

given in terms of the modified core-shell spring constant K_m. The polarization energy in region II arises from the interaction of region II dipoles with the effective charge of the vacancy, which is of $1/|\mathbf{R}|^4$ type, and is expressed as

$$E_4 = \frac{Q_{md(d)}^2 e^2}{2r_0}(5{\cdot}3392\,M_- + 9{\cdot}2295\,M_+). \tag{A11}$$

An additional contribution to the polarization energy obtained from the dipole-dipole interaction between the two regions is given by

$$E_5 = \frac{4Q_{mv}e^2}{r_0}(Q_{mc}X_c + Q_{ms(dd)}X_T)[0{\cdot}352\,M_- + 5{\cdot}333\,M_+] \tag{A12}$$

with M_- and M_+ as Mott and Littleton parameters.

(iv) *Short range interaction energy*

In region I (defect region), the short-range interaction energy is written as

$$E_6 = 12\Bigg\{[B_{--}\exp(-2r_0(1+X_T)/\sqrt{3}p) + B_{--}\exp(-2r_0/\sqrt{3}p)]$$
$$-\frac{c_{--}}{(2/\sqrt{3})^6 r_0{}^6}\left(\frac{1}{(1+X_T)^6}-1\right) - \frac{d_{--}}{(2/\sqrt{3})^8 r_0^8}\left(\frac{1}{(1+X_T)^8}-1\right)\Bigg\}, \tag{A13}$$

and for region II, this contribution is

$$E_7 = 8[\phi_{+-}(R_1) - \phi_{+-}(G_1)] + 24[\phi_{+-}(R_2) - \phi_{+-}(G_2)]$$
$$+ 24[\phi_{+-}(R_3) - \phi_{+-}(G_3)] + 24[\phi_{--}(R_4) - \phi_{--}(G_4)], \tag{A14}$$

CC-0. In Public Domain. Gurukul Kangri Collection, Haridwar

Digitized by Arya Samaj Foundation Chennai and eGangotri

where

$$\phi_{+-}(r) = B_{+-}\exp(-r_0/p) - c_{+-}r_0^{-6} - d_{+-}r_0^{-8}, \tag{A15}$$

$$\phi_{--}(r) = B_{--}\exp(-2r_0/\sqrt{3}p) - c_{--}(2r_0/\sqrt{3})^{-6} - d_{--}(2r_0/\sqrt{3})^{-8}, \tag{A16}$$

with

$$\begin{aligned} R_1 &= 3(\tfrac{1}{2} + X_3 - \tfrac{1}{2}X_T)\,(2/\sqrt{3}r_0), \\ R_2 &= [2(\tfrac{1}{2} + X_T)^2 + (\tfrac{1}{2} + X_1 - \tfrac{1}{2}X_T)^2]^{1/2}\,(2/\sqrt{3}r_0), \\ R_3 &= [(\tfrac{1}{2} + \tfrac{1}{2}X_T)^2 + (\tfrac{1}{2} + X_2 - \tfrac{1}{2}X_T)^2]^{1/2}\,(2/\sqrt{3}r_0), \\ R_4 &= [(1 + 3X_4 - \tfrac{1}{2}X_T)^2 + 2(X_4 - \tfrac{1}{2}X_T)^2]^{1/2}\,(2/\sqrt{3}r_0), \end{aligned} \tag{A17}$$

Gi (i = 1–4), can be obtained by putting $X_T = 0$ in R_i (i = 1–4) in (A17).

The interaction energy between regions I and II (given by E_3 in (14)) also contributes to the short-range energy and it is expressed as

$$E_8 = -\sum_{i=1}^{4} \left.\frac{\mathrm{d}E_7}{\mathrm{d}X}\right|_{X = X_i} \cdot \bar{X} \tag{A18}$$

which can be evaluated from the knowledge of E_7 as defined earlier.

References

Boswarva I M 1967 *Philos. Mag.* **16** 827

Boswarva I M and Simpson J H 1973 *Can. J. Phys.* **51** 1923

Catlow C R A and Norgett M J 1973 *J. Phys.* **C9** 1325

Catlow C R A, Faux I D and Norgett M J 1976 *J. Phys.* **C9** 419

Catlow C R A, Norgett M J and Ross T A 1977 *J. Phys.* **C10** 1627

Catlow C R A, Corish J, Jacobs P W M and Lidiard A B 1981 *J. Phys.* **C14** L121

Catlow C R A and Mackrodt W C 1982 *Computer simulation of solids* (Berlin: Springer Verlag)

Chakravorty D 1971 *J. Phys. Chem. Solids* **32** 1092

Christy R F and Dobbs H S 1967 *J. Chem. Phys.* **46** 722

Faux I D and Lidiard A B 1971 *Z. Naturforsch.* **269** 62

Franklin A D 1968 *J. Phys. Chem. Solids* **32** 1092

Friauf R F 1961 *J. Phys. Chem. Solids* **18** 203

Harrington T M and Staveley L A K 1964 *J. Phys. Chem. Solids* **25** 927

Harvey P J and Hoodless I M 1967 *Philos. Mag.* **16** 543

Keeton S C and Wilson W D 1973 *Phys. Rev.* **B7** 834

Lidiard A B and Norgett M J 1972 in *Computational solid state physics* (eds) F Harman, N W Daltan and T R Koehler (New York: Plenum Press)

Lynch D W 1960 *Phys. Rev.* **118** 468

Mackrodt W C and Stewart R F 1979 *J. Phys.* **C12** 431

Mishra V 1985 *Investigation of defect properties of binary solids*, Ph.D. thesis, Rani Durgawati University, Jabalpur

Mishra V, Sanyal S P and Singh R K 1987 *Philos. Mag.* (in press)

Mott N F and Littleton M J 1938 *Trans. Faraday Soc.* **34** 485

Murthy C S N and Murty Y V G S 1971 *J. Phys.* **C4** 1108

Murty Y V G S and Usha V 1978 *Physica* **B93** 219

Norgett M J 1974 AERE Harwell Report 7650

Norgett M J 1971 *J. Phys.* **C4** 298

CC-0. In Public Domain. Gurukul Kangri Collection, Haridwar

Digitized by Arya Samaj Foundation Chennai and eGangotri

Sangster M J L and Rowell D K 1981 *Philos. Mag.* **A44** 613
Sangster M J L and Atwood R M 1978 *J. Phys.* **C11** 1541
Samara G A 1979 *J. Phys. Chem. Solids* **40** 509
Silvarajan T V 1978 Ph.D. thesis, IIT Madras
Singh R K and Verma M P 1969 *Phys. Status. Solidi* **B33** 769
Singh R K 1982 *Phys. Rep.* (Netherlands) **85** 259
Singh R K, Mishra V and Sanyal S P 1984 *Proc. Int. Conf. on Defects in Insulating Crystals, Utah* (USA)
Shukla A K, Ramdas S and Rao C N R 1972 *J. Phys. Chem. Solids* **34** 761
Uppal M K, Rao C N R and Sangster M J L 1978 *Philos. Mag.* **38** 341
Vempati C S and Jacobs P W M 1983 *Cryst. Latt. Def. and Amorph. Mater.* **10** 3
Woods A D B, Cochran W and Brockhouse B N 1960 *Phys. Rev.* **119** 980

CC-0. In Public Domain. Gurukul Kangri Collection, Haridwar

Digitized by Arya Samaj Foundation Chennai and eGangotri

Pramana – J. Phys., Vol. 27, No. 2, February 1987, pp. L229–L231. © Printed in India.

High-temperature superconductivity in the 100 K region in perovskite-related oxides of the Ln-Ba-Cu-O (Ln = Y or La) system†

P GANGULY, A K RAYCHAUDHURI*, K SREEDHAR and C N R RAO**

Solid State and Structural Chemistry Unit, *Department of Physics, Indian Institute of Science, Bangalore 560 012, India

Abstract. Oxides of the Y-Ba-Cu-O system are found to show onset of superconductivity in the 100–120 K region.

Keywords. High-temperature superconductivity; yttrium-barium copper oxides.

PACS No. 74.70

In the wake of the sensational high T_c oxide superconductors discovered recently (Uchida *et al*; Cava *et al* 1987; Chu *et al* 1987; Rao and Ganguly 1987), we have been investigating several oxides in the Ln-Sr-(Ba)-Cu-O system where Ln is Pr, Nd or Y (Ganguly and Rao 1986; Ganguly *et al* 1987). This system has yielded many oxides where the onset of superconductivity, T_c°, is in the vicinity of 40 K. As part of this programme, we studied the oxide $La_4BaCu_5O_{13+\delta}$ (Michel *et al* 1985). A sample of this oxide showed a current-dependent resistivity behaviour around 160 K shown in figure 1(a), suggesting the possible presence of an oxide phase with a fairly high T_c. We have also studied several other related La-Ba-Cu oxides. Thus, $La_{3.75}Ba_{1.25}Cu_5O_{13+\delta}$ showed the onset of superconductivity, T_c°, at 20 K and current dependence of resistivity around 50 K as can be seen in figure 1(b). $La_3Ba_3Cu_6O_{14}$ however did not show any indication of superconductivity and remained semiconducting throughout.

We have been carrying out experiments on several lanthanide copper oxides analogous to the La-Ba-Cu oxides discussed above as indicated in an earlier communication (Rao and Ganguly 1987). Thus, we find that the oxide of nominal composition $Y_3Ba_3Cu_6O_{14}$ shows a T_c° at ~ 100 K (figure 2). An x-ray study of this oxide indicates the presence of two phases, the predominant one being a perovskite; the minor phase seems to be Y_2BaCuO_5 which is a green insulator. The Y-Ba-Cu oxide in which the high T_c superconductivity has just been reported by Wu *et al* (1987) is likely to contain these phases. However, no oxide phase of K_2NiF_4 structure seems to be present in any of these preparations.

What is specially significant in our study is that the oxide system $Y_{2.4}Ba_{3.6}Cu_6O_{14}$ shows a T_c° of around 115 K as shown in figure 2(a). Magnetic susceptibility measurements also show a similar T_c° (figure 2b). Zero resistivity is attained at ~ 85 K. This oxide composition mainly contains the perovskite phase, but no oxide of K_2NiF_4 structure; the Y_2BaCuO_5 phase is present only to a small extent.

† Contribution No. 429 from the Solid State and Structural Chemistry Unit.
** To whom all correspondence should be addressed.

CC-0. In Public Domain. Gurukul Kangri Collection, Haridwar

Digitized by Arya Samaj Foundation Chennai and eGangotri

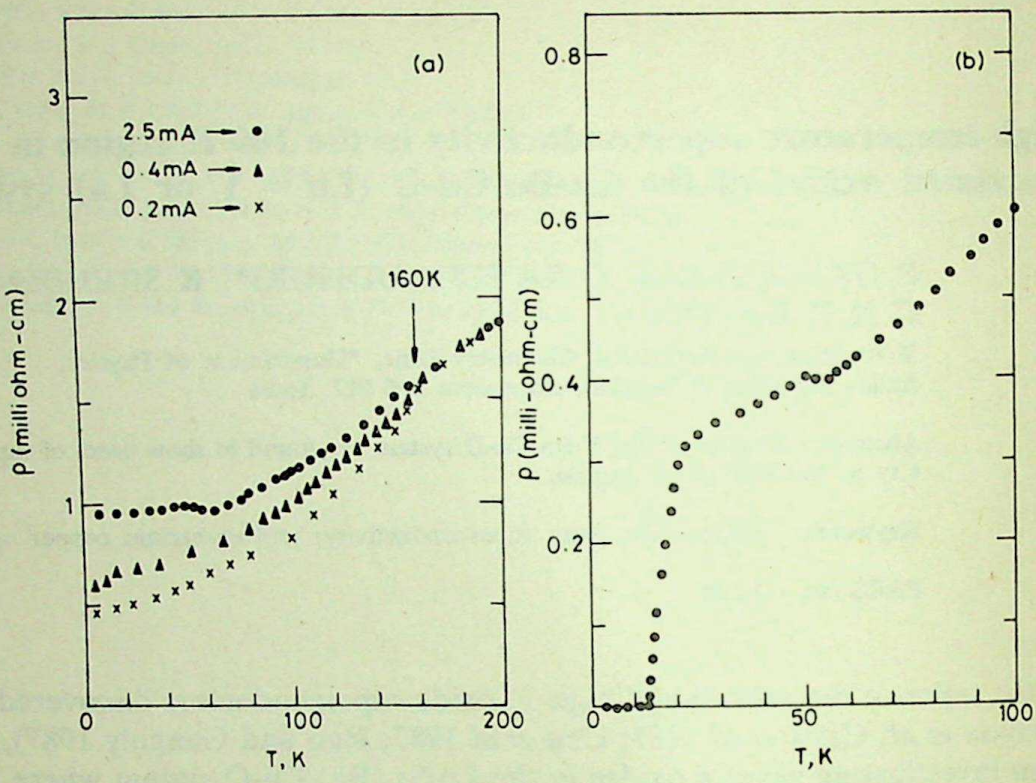

Figure 1. (a). Resistivity data on $La_4BaCu_5O_{13+\delta}$ as a function of measuring current. Note that current-dependence starts at $\sim$ 160 K. **(b)** Resistivity data on $La_{3.75}Ba_{1.25}Cu_5O_{13+\delta}$ showing superconducting transition at $\sim$ 20 K. Note an interesting anomaly around $\sim$ 50 K.

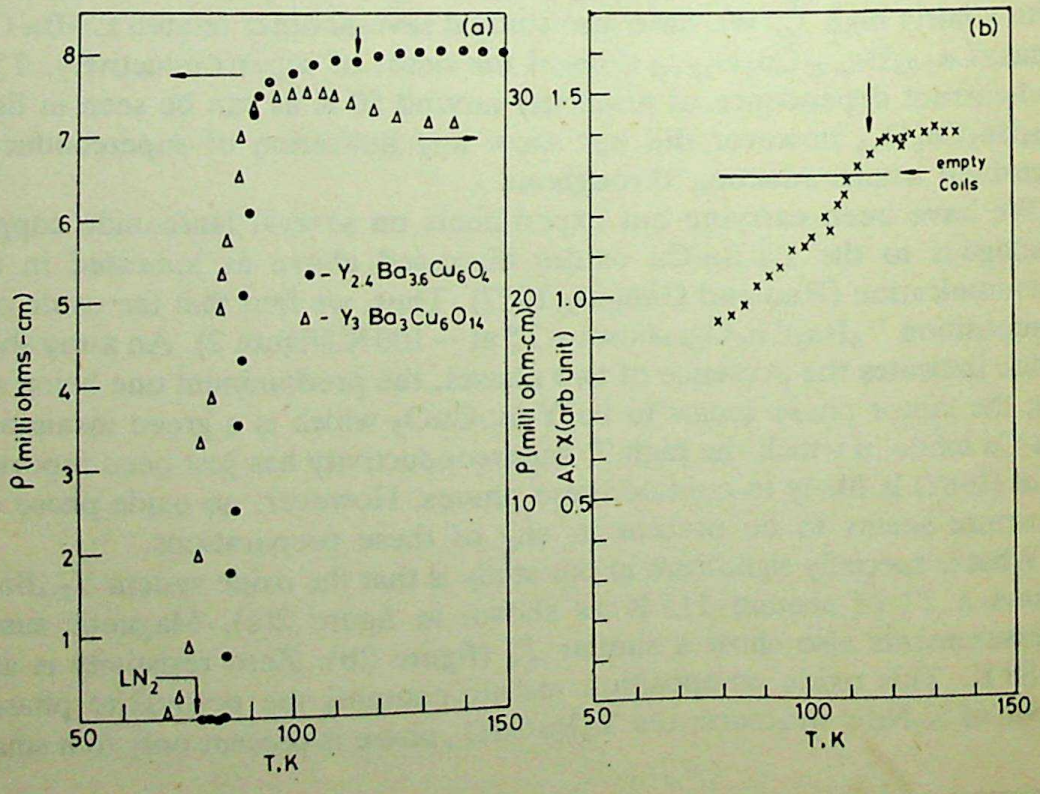

Figure 2. (a). Resistivity data on $Y_3Ba_3Cu_6O_{14}$ and $Y_{2.4}Ba_{3.6}Cu_6O_{14}$. Note that T_c^* in the latter is $\sim$ 115 K. **(b)** Magnetic susceptibility data on $Y_{2.4}Ba_{3.6}Cu_6O_{14}$.

CC-0. In Public Domain. Gurukul Kangri Collection, Haridwar

Digitized by Arya Samaj Foundation Chennai and eGangotri

We are at present measuring properties of a variety of oxides of the Y-Ba-Cu-O system wherein Y is substituted by Lu, Sc and other cations and Ba is partly substituted by Sr. In addition, measurements on certain oxide composites are also in progress.

The authors thank the University Grants Commission and the Department of Science and Technology, Government of India, for support of this research.

References

Cava R J, van Dover R B, Batlogg B and Reitman E A 1987 *Phys. Rev. Lett.* **58** 408
Chu C W, Hor P H, Meng R L, Gao L, Huang Z J and Wang Y Q 1987 *Phys. Rev. Lett.* **58** 405
Ganguly P and Rao C N R 1986 *Proc. Indian Acad. Sci. (Chem. Sci.)* **97** 631
Ganguly P, Mohan Ram R A, Sreedhar K and Rao C N R 1987 *Solid State Commun.* (in print)
Michel C, Er-Rakho L and Raveau B 1985 *Mater. Res. Bull.* **20** 667
Rao C N R and Ganguly P 1987 *Curr. Sci.* **56** 47
Uchida S, Takagi H, Kitazawa K and Tanaka S 1987 *Jpn. J. Appl. Phys.* **26** L1
Wu, M K, Ashburn J R, Torng C J, Hor P H, Meng R L, Gao L, Huang Z J, Wang Y Q and Chu C W 1987 *Phys. Rev. Lett.* **58** 908

CC-0. In Public Domain. Gurukul Kangri Collection, Haridwar

Digitized by Arya Samaj Foundation Chennai and eGangotri

CC-0. In Public Domain. Gurukul Kangri Collection, Haridwar

Digitized by Arya Samaj Foundation Chennai and eGangotri

Pramāṇa – J. Phys., Vol. 28, No. 3, March 1987, pp. 233–239. © Printed in India.

पुस्तकालय
गुरुकुल कांगड़ी विश्वविद्यालय
हरिद्वार

The generalized Pauli-Lubanski vector for massless spinning particles in arbitrary space-time dimensions

M V ATRE
Theoretical Physics Group, Tata Institute of Fundamental Research, Homi Bhabha Road, Colaba, Bombay 400005, India

MS received 25 November 1986

Abstract. The concept of the Pauli-Lubanski vector is generalized for classical relativistic massless spinning particles to arbitrary space-time dimensions. The properties of this generalized Pauli-Lubanski "vector" are studied and used to set up a Hamiltonian description of such particles in a compact way.

Keywords. Pauli-Lubanski vector; classical spinning particles.

PACS Nos 03·20; 03·30

1. Introduction

Any free relativistic physical theory has Poincaré invariance and gives rise to the ten well-known conservation laws. The ten generators of the Poincaré group ($\mathscr{P}$) are denoted, in the canonical formalism, by

$$P_\mu = p_\mu, \quad M_{\mu\nu} = x_\mu p_\nu - x_\nu p_\mu + S_{\mu\nu}. \tag{1}$$

Here, the greek indices take values $0, 1, \ldots, d-1$, where d is the dimension of the underlying Minkowski space-time M_d with metric $(-, +, \ldots, +)$. It is well known (Sudarshan and Mukunda, 1974) that in M_4, the information regarding spin is contained in the Pauli-Lubanski vector (PLV)

$$W_\mu = \tfrac{1}{2}\varepsilon_{\mu\nu\rho\lambda} M^{\nu\rho} P^\lambda. \tag{2}$$

The Casimirs invariants of $\mathscr{P}$ are

$$P^\mu P_\mu = P^2 = -m^2,$$

$$W^\mu W_\mu = W^2 = s(s+1). \tag{3}$$

It is easy to see that

$$S_{\mu\nu} = 0 \Leftrightarrow W_\mu = 0. \tag{4}$$

In the quantum theory, the irreducible representations of $\mathscr{P}$ describe a particle with mass m and spin s. Thus the PLV plays a very important role in the analysis of spinning particles.

CC-0. In Public Domain. Gurukul Kangri Collection, Haridwar

Digitized by Arya Samaj Foundation Chennai and eGangotri

Though PLV has been studied in detail for a massive particle, the same cannot be said for a massless particle. We introduce the notion of a generalized Pauli-Lubanski "vector" (GPLV) for a classical relativistic massless spinning particle (CRMSP) which leads to a unified description of such particles in space-times M_d of any dimension d. It also helps in defining the spin tensor and the $\mathscr{P}$ generators in a compact way. Though the algebra is simple, it suggests a new easy method to study a CRMSP. The entire analysis is not manifestly covariant and hence it is necessary to display the $\mathscr{P}$ generators at each stage.

That the description a CRMSP in M_4 can be obtained from a nonrelativistic charge-monopole system by a canonical transformation and a suitable choice of the Hamiltonian, is well known (Balachandran *et al* 1983). This is recast in different form in §2 which suggests a straightforward generalization to M_d. The GPLV is introduced in §3 and its properties studied. These are carried out in M_6, as an illustrative example. In §4, the results of §3 are used to set up a Hamiltonian description of a CRMSP in M_d. Discussions and conclusions are presented in §5.

All greek indices take values $0, 1, \ldots, d-1$; latin indices in the middle of the alphabet $1, 2, \ldots, d-1$; and latin indices in the beginning of the alphabet $1, 2, \ldots, d-2$.

2. CRMSP in M_4

We first describe a nonrelativistic charge-monopole system in three dimensions and then obtain a description of a CRMSP in M_4 via suitable canonical transformations. We shall be very brief here. The details may be found in Balachandran *et al* (1983).

Consider a massive charge moving in $\mathscr{R}^3$ in the field of a monopole which is at the origin $\mathbf{x} = 0$. The configuration space is $\mathscr{R}^3 - \{0\}$, i.e. the charge and the monopole are prevented from occupying the same point. The equation of motion (EOM) of the charge is

$$m\dot{x}_j = -\frac{\lambda}{|\mathbf{x}|^3}\varepsilon_{jkl}x_k\dot{x}_l. \tag{5}$$

This is produced by the Hamiltonian

$$H = |\mathbf{p}|^2/2m \tag{6}$$

provided the basic Poisson brackets (PB's) are chosen to be

$$\{x_j, x_k\} = 0, \tag{7a}$$

$$\{x_j, p_k\} = \delta_{jk}, \tag{7b}$$

$$\{p_j, p_k\} = \lambda\varepsilon_{jkl}x_l/|\mathbf{x}|^3. \tag{7c}$$

It is easy to verify that

$$M_{jk} = x_j p_k - x_k p_j - (\lambda\varepsilon_{jkl}x_l)/|\mathbf{x}| \tag{8}$$

is a constant of motion. That this is indeed the generator of rotation can be verified by

CC-0. In Public Domain. Gurukul Kangri Collection, Haridwar

Digitized by Arya Samaj Foundation Chennai and eGangotri

proving that

$$\{M_{jk}, p_l\} = p_k\delta_{jl} - p_j\delta_{kl}. \tag{9}$$

The last term in (8) is the additional contribution to the total angular momentum besides the usual orbital term. It can be thought of as contributing a helicity

$$\mathbf{J}\cdot\hat{x} = -\lambda, \tag{10}$$

where

$$\hat{x}_j = x_j/|\mathbf{x}|, \tag{11}$$

is the unit vector along the line joining the charge and the monopole, and

$$J_j = \varepsilon_{jkl}x_k p_l - \lambda\hat{x}_j. \tag{12}$$

Now a photon, which is a massless spinning particle, has a helicity contribution in the direction of its momentum. This can be obtained by taking the charge-monopole system and making the transformations

$$x_i \to -p_i, \quad p_i \to x_i. \tag{13}$$

The system is then described by the Hamiltonian

$$H = |\mathbf{p}|, \tag{14}$$

and the PB's

$$\{p_j, p_k\} = 0, \tag{15a}$$

$$\{x_j, p_k\} = \delta_{jk}, \tag{15b}$$

$$\{x_j, x_k\} = -(\lambda\varepsilon_{jkl}p_l)/|\mathbf{p}|^3. \tag{15c}$$

The total angular momentum is

$$J_j = \varepsilon_{jkl}x_k p_l + \lambda\hat{p}_j \tag{16}$$

with helicity

$$\mathbf{J}\cdot\hat{p} = \lambda. \tag{17}$$

All that has been described so far is well known (see Balachandran *et al* 1983 for further details). We now express the above equations for the massless particle in a manner which helps us understand the system of equations better.

The P-L vector is defined as

$$W_\mu = \tfrac{1}{2}\varepsilon_{\mu\nu\rho\sigma}M^{\nu\rho}P^\sigma.$$

Define an antisymmetric quantity A_{jk} as

$$A_{jk} = \varepsilon_{ojkl}\frac{W^o p^l}{|\mathbf{p}|}. \tag{18}$$

Choosing

$$W^o = \lambda|\mathbf{p}|, \tag{19}$$

CC-0. In Public Domain. Gurukul Kangri Collection, Haridwar

Digitized by Arya Samaj Foundation Chennai and eGangotri

we get

$$A_{jk} = -\lambda(\varepsilon_{jkl}\, p_l) \tag{20}$$

to yield

$$M_{jk} = x_j\, p_k - x_k\, p_j - A_{jk}/|\,\mathbf{p}\,|. \tag{21}$$

This suggests that we define an antisymmetric object called spin as

$$S_{jk} = -A_{jk}/|\,\mathbf{p}\,|. \tag{22}$$

The Poincaré generators are then realized by

$$P^o = H = |\,\mathbf{p}\,|, \tag{23a}$$

$$P_i = p_i, \tag{23b}$$

$$M_{jk} = x_j\, p_k - x_k\, p_j + S_{jk}, \tag{23c}$$

$$M_{oj} = x_j\, |\,\mathbf{p}\,|. \tag{23d}$$

The $\mathscr{P}$ algebra can be explicitly verified by using PB's (equation (15)). The derivation of the above expressions by starting from a manifestly covariant theory together with constraints is given elsewhere (Atre *et al* 1986).

The PB's may be rewritten as

$$\{p_j,\, p_k\} = 0, \tag{24a}$$

$$\{x_j,\, p_k\} = \delta_{jk}, \tag{24b}$$

$$\{x_j,\, x_k\} = -S_{jk}/|\mathbf{p}|^2, \tag{24c}$$

and these, along with the $\mathscr{P}$ generators (equation (23)) fully describe the massless spinning particle of helicity λ.

In the next section, we generalize the study of particles in M_6. It will be seen that by introducing the notion of a GPLV, the formal structure of (23) and (24) is left unchanged. Also the GPLV yields a nice method to understand the helicity.

3. GPLV in M_6

Let M_6 be the six-dimensional space-time manifold with metric $(-+++++)$ and $M_{\mu\nu}$ the generators of SO(5, 1) (the six-dimensional homogeneous Lorentz group) in the canonical formalism. Define

$$W_{\alpha\beta\gamma} = \tfrac{1}{2}\varepsilon_{\alpha\beta\gamma\mu\nu\lambda}\, M^{\mu\nu} P^{\lambda}, \tag{25}$$

P^{μ} are the space-time translation generators, $\varepsilon_{\alpha\beta\gamma\mu\nu\lambda}$ is the completely antisymmetric constant tensor

$$\varepsilon_{012345} = 1. \tag{26}$$

We call $W_{\alpha\beta\gamma}$ the GPLV (though, in principle, it is a third-rank tensor under SO(5, 1))

CC-0. In Public Domain. Gurukul Kangri Collection, Haridwar

Digitized by Arya Samaj Foundation Chennai and eGangotri

and now study its properties. To this end, we first split up the GPLV into terms which contain the zero component and those which do not. Thus

$$W_{ojk} = \tfrac{1}{2}\varepsilon_{ojklmn}\, M^{lm} P^n, \tag{27}$$

$$W_{jkl} = \tfrac{1}{2}\varepsilon_{jklmnq}\, M^{mn} P^q. \tag{28}$$

Making use of the identity

$$W_{\mu\nu\lambda}\, P^\lambda = 0 \tag{29}$$

results in

$$W_{ojk} = W_{jkl}\, P^l / |\mathbf{P}|. \tag{30}$$

Hence W_{ojk} is defined in terms of W_{jkl} parallel to $\mathbf{P}$. It is also easy to see that

$$\varepsilon_{ojklmn}\, W^{klm} P^n = 0 \tag{31}$$

which says there are no components of W_{jkl} perpendicular to $\mathbf{P}$. Next, we have (from equation (27))

$$W_{ojk}\, P^k = 0, \tag{32}$$

i.e. W_{ojk} has no component parallel to $\mathbf{P}$.

To make things clearer, if we choose a special frame of reference defined by

$$p^\mu = (|\mathbf{p}|, 0, 0, 0, 0, |\mathbf{p}|), \tag{33}$$

then (27) reduces to

$$W_{oab} = W_{ab5} \quad (a, b = 1, 2, 3, 4). \tag{34}$$

Thus we see that in the special frame of reference there are only six independent components of the GPLV, and these we choose as W_{oab} (which are perpendicular to $\mathbf{P}$). The others (W_{ab5}, parallel to $\mathbf{P}$) are defined in terms of these. Thus, in any generic Lorentz frame, we choose the independent quantities of the GPLV to be W_{ojk}. $(j, k = 1, \ldots, 5)$ and all other quantities are to be defined in terms of these. Analogous to what was done in § 2, we define

$$A_{jk} = (\tfrac{1}{2}\varepsilon_{ojklmn}\, W^{olm} P^n)/|\mathbf{P}|, \tag{35}$$

and

$$S_{jk} = -A_{jk}/|\mathbf{P}|. \tag{36}$$

Having introduced the GPLV and using it to define a quantity called S_{jk}, we now set up a Hamiltonian description for the dynamics of a CRMSP in M_6.

4. CRMSP in M_6

From the definition of the GPLV (equation (25)), and using the properties of the ε tensor, it can be shown that

$$M_{jk} = x_j\, p_k - x_k\, p_j + S_{jk}, \tag{37}$$

CC-0. In Public Domain. Gurukul Kangri Collection, Haridwar

Digitized by Arya Samaj Foundation Chennai and eGangotri

where S_{jk} is defined in (36). A straightforward algebra enables us to check that

$$P^o = |\mathbf{P}| = |\mathbf{p}| = H, \tag{38a}$$

$$P_i = p_i, \tag{38b}$$

$$M_{jk} = x_j p_k - x_k p_j + S_{jk}, \tag{38c}$$

$$M_{oj} = x_j |\mathbf{p}|, \tag{38d}$$

satisfy the $\mathscr{P}$ algebra provided we choose the fundamental PB's to be

$$\{p_j, p_k\} = 0, \tag{39a}$$

$$\{x_j, p_k\} = \delta_{jk}, \tag{39b}$$

$$\{x_j, x_k\} = -S_{jk}/|\mathbf{p}|^2. \tag{39c}$$

Equations (38) and (39) thus describe a CRMSP and also justify our calling S_{jk} as the spin generator. It is easy to check that

$$\{A_{jk}, P_l\} = 0, \tag{40}$$

$$\{A_{jk}, x_l\} = -\frac{1}{|\mathbf{p}|^2}(A_{jk} p_l - A_{jl} p_k + A_{kl} p_j). \tag{41}$$

In the special frame of reference,

$$S_{ab} = -A_{ab}/|\mathbf{p}|, \tag{42}$$

and it is not difficult to show that

$$\{S_{ab}, S_{cd}\} = g_{ac} S_{bd} - g_{bc} S_{ad} - g_{ad} S_{bc} + g_{bd} S_{ac}. \tag{43}$$

Thus the six quantities, S_{ab}, which form the spin contribution, also generate the group SO(4). This is in fact the stability group of the momentum (equation (33)) and is the non-abelian generalization of the photon in M_4 with U(1) or (or SO(2)) as the helicity group.

Generalization to M_d, for any d, is now trivial.

5. Discussion and conclusions

Starting from a charge-monopole system we have been able to set up a Hamiltonian description of CRMSP in M_d. The notion of GPLV helped us in setting up the fundamental PB's and the P generators in a compact way. The spin generators defined in terms of the GPLV were shown to generate the stability group of the momentum.

The entire description of the above system can be set up in a manifestly covariant Lagrangian formulation, with constraints. The constraint analysis then helps in setting up the PB's and the $\mathscr{P}$ algebra in terms of the first class variables, which are identical to (38) and (39). The quantization of the above system can be carried out. Also, reversing

CC-0. In Public Domain. Gurukul Kangri Collection, Haridwar

Digitized by Arya Samaj Foundation Chennai and eGangotri

our arguments, it is possible to define new charge-monopole systems in higher dimensions. All this has been done and will be published elsewhere (Atre *et al* 1986).

Acknowledgements

The author thanks Prof. A P Balachandran for suggesting the problem and for fruitful discussions. He also thanks Prof. K C Wali for his hospitality at Syracuse University where this work was begun.

References

Atre M V, Balachandran A P and Govindarajan T R 1986 (Syracuse University, preprint, to be published)

Balachandran A P, Marmo G, Skagerstam B S and Stern A 1983 *Lecture notes in physics* (Berlin: Springer Verlag) Vol. 188, p. 48

Sudarshan E C G and Mukunda N 1974 *Classical dynamics: A modern perspective* (New York: John Wiley) p. 447

CC-0. In Public Domain. Gurukul Kangri Collection, Haridwar

Digitized by Arya Samaj Foundation Chennai and eGangotri

CC-0. In Public Domain. Gurukul Kangri Collection, Haridwar

Digitized by Arya Samaj Foundation Chennai and eGangotri

Pramāṇa – J. Phys., Vol. 28, No. 3, March 1987, pp. 241–245. © Printed in India.

Nonsingular cosmological models with torsion determined by vacuum polarization of quantum fields

I L BUCHBINDER and S D ODINTSOV
High-current Electronics Institute, SBAC. SCI. USSR, Tomsk 634055, USSR

MS received 21 October 1986

Abstract. Nonsingular cosmological models with reducing torsion induced by vacuum quantum effects are constructed. The metric of the models described corresponds to the inflationary universe. Moreover, anisotropic nonsingular cosmological model with constant torsion is constructed.

Keywords. Cosmological models; torsion; anisotropic model; curved space-time with torsion; effective action.

PACS No. 98·80

1. Introduction

In a recent paper (Buchbinder *et al* 1985) we calculated the effective action of gravity with torsion* induced by vacuum quantum effects. Nonsingular spatially flat Friedmann universe has been built on the basis of calculated effective action. In the present paper we construct some new cosmological models with torsion based on effective action (Buchbinder *et al* 1985). The metrics of our models correspond to the closed and open Friedmann and anisotropic universes.

Let us consider asymptotically free and asymptotically conformally invariant quantum field theory (Buchbinder and Shapiro 1985; Buchbinder and Odintsov 1983, 1984, 1985) in curved space-time with torsion. In the framework of such theories for the description of quantum effects in early universe the approximation of free conformally invariant fields, which include non-minimal interaction with the curvature and torsion, is good enough. In accordance with the above remarks the classical action should be chosen in the form (Buchbinder *et al* 1985)

$$S = \int \mathrm{d}^4x \sqrt{-g} \left\{ \sum_i^{N_0} (\tfrac{1}{2} g^{\alpha\beta} \nabla_\alpha \varphi_i \nabla_\beta \varphi_i + \tfrac{1}{12} R \varphi_i^2 + \tfrac{1}{2} \xi_i S_\mu S^\mu \varphi_i^2) + \sum_j^{N_{1/2}} (i\psi_j \gamma^\mu(x) \nabla_\mu \psi_j - \zeta_j \bar{\psi}_j \gamma_5 \gamma^\mu \psi_j S_\mu) - \tfrac{1}{4} \sum_k^{N_1} F^{k\mu\nu} F^k_{\mu\nu} \right\}, \quad (1)$$

* The survey for classical gravity with torsion is given by Hehl *et al* (1976). Some quantum aspects of gravity with torsion are given by Rumpf (1979), Ponomarev and Pronin (1979), Kimura (1981), Nieh and Yan (1982), Obukhov (1983), Buchbinder and Shapiro (1985), Orzalesi and Ventura (1984), Tseytlin (1982 a, b) and Barth and Christensen (1983)

CC-0. In Public Domain. Gurukul Kangri Collection, Haridwar

Digitized by Arya Samaj Foundation Chennai and eGangotri

where φ, ψ, A_μ are scalars, spinors and gauge fields, ξ, ζ are nonminimal coupling constants of scalars and spinors with torsion; R, ∇_μ are scalar (without torsion) curvature, covariant (without torsion) derivative, $S_\nu = \varepsilon_{\alpha\beta\mu\nu} T^{\alpha\beta\mu}$, $T^{\beta}_{\alpha\mu}$ is the torsion tensor, which for simplicity is supposed to be antisymmetric.

2. Nonsingular cosmological models with torsion

The anomalous trace of stress-energy tensor in curved space-time with torsion for theory (1) is calculated by Buchbinder *et al* (1985) and has the form

$$\langle T^{\mu}_{\mu} \rangle = -[a_1 C^2_{\mu\nu\alpha\beta} + a_2 E + a_3 \Box R + a_4 F^2_{\mu\nu} + a_5 (S_\mu S^\mu)^2 + a_6 \Box (S_\mu S^\mu) + a_7 \nabla_\mu (S_\nu \nabla^\nu S^\mu - S^\mu \nabla_\nu S^\nu)], \tag{2}$$

where $C_{\mu\nu\alpha\beta}$ is the Weyl tensor, E the Gauss-Bonnet invariant, $F_{\mu\nu} = \partial_\mu S_\nu - \partial_\nu S_\mu$, factors a_1, a_2, a_3 are well known for fields with spin 0, 1/2, 1 (see Birrell and Davies 1982 for instance),

$$a_4 = -\frac{2}{3(4\pi)^2} \sum_i^{N_{1/2}} \zeta_i^2, \qquad a_5 = \frac{1}{2(4\pi)^2} \sum_i^{N_0} \xi_i^2$$

$$a_6 = \frac{1}{3(4\pi)^2} \left(-\frac{1}{2} \sum_i^{N_0} \xi + 2 \sum_i^{N_{1/2}} \zeta_i^2 \right), \qquad a_7 = -\frac{2}{3(4\pi)^2} \sum_i^{N_{1/2}} \zeta_i^2.$$

Buchbinder *et al* (1985) derived the effective action from the anomalous trace of the stress-energy tensor. Consider metric $g_{\mu\nu}(x) = a^2(\eta)\bar{g}_{\mu\nu}(x)$, where $\bar{g}_{\mu\nu}$ is the static metric, corresponding to spatially flat ($k = 0$), closed ($k = +1$) or open ($k = -1$). The Friedmann universe, η is the conformal time connected with cosmological time t by means of relation $dt = a(\eta)d\eta$. In accordance with the conditions of homogeneity and isotropy we shall consider that $S_\mu = (T(\eta), 0, 0, 0)$ (Ponomarev 1971). In this notation the effective action could be written in the form

$$\Gamma = V_3 \int d\eta \{k_1 (\ln a)''^2 + k_2 (\ln a)'^4 + k_3 T^2 (\ln a)'' + k_4 T^2 (\ln a)'^2 + k_5 T^4 \ln a - 6k k_6 (\ln a)'^2\}, \tag{3}$$

where $a' = da/d\eta$, V_3 is the three-dimensional volume, $k_1 = -3a_3$, $k_2 = -(3a_3 + 2a_2)$, $k_3 = a_6$, $k_4 = a_6 + \frac{3}{2}a_7$, $k_5 = a_5$, $k_6 = a_3 + 2a_2$; For $k = 0$ the effective action is given by Buchbinder *et al* (1985). The effective action (3) may be regarded as quantum correction caused by vacuum effects to the classical action. Classical gravitational action depending on the metric and torsion is written in the form

$$S = -\frac{1}{\kappa^2} \int d^4x \sqrt{-g}\, (R + hS^2 - 2\Lambda), \tag{4}$$

where h is the parameter of nonminimal connection of metric with torsion (when $h = -1/24$, equation (4) is the action of Einstein-Cartan theory), the curvature is calculated with metric $g_{\mu\nu}$.

Let us consider now the equations of motion

$$\delta(S + \Gamma)/\delta a = 0, \qquad \delta(S + \Gamma)/\delta S_\mu = 0. \tag{5}$$

CC-0. In Public Domain. Gurukul Kangri Collection, Haridwar

Digitized by Arya Samaj Foundation Chennai and eGangotri

It is easy to understand that the second part of equation (5) is the same as in Buchbinder *et al* (1985). Therefore when $h(k_3+k_5)>0_j$, $k_5=0$, the solution of this equation could be rewritten as (Buchbinder *et al* 1985):

$$a^2(\eta)=\frac{1}{H^2\eta^2}, \qquad H^2=\frac{h}{\kappa^2(k_3+k_4)}. \tag{6}$$

The solution of the first part of equation (5) could be written as

$$T^2(t)=d_1\exp(-2Ht)+d_2\exp\{[(2k_4+k_3)/k_3]Ht\}+C\exp(2Ht)+A, \tag{7}$$

where

$$A=\frac{6k(k_6\kappa^2H^2+1)}{(k_4\kappa^2H^2+h)},$$

d_1, d_2 are arbitrary constants,

$$C=\frac{3(k_1-k_2+2\kappa^{-2}H^{-2}+2\Lambda/3\kappa^2H^4)}{2k_4-k_3},$$

if $2k_4-k_3\neq 0$, and C is arbitrary if $2k_4-k_3=0$ (in this case we should assume that $k_1-k_2+(2/\kappa^2H^2)+(2\Lambda/3\kappa^2H^4)=0$). Expression (7) when $k=0$ ($A=0$) was obtained by Buchbinder *et al* (1985). Thus, we get non-singular Friedmann universes with torsion for $k=\pm 1, 0$. It is interesting to note that when compared with the nonsingular cosmological models without torsion (Starobinsky 1980; Mamayev and Mostepanenko 1980) in the theory with torsion, the scale factor is the same for open, closed and spatially flat Friedmann universes. In all these cases the scale factor is given by equation (6), $a^2(\eta)$ does not depend upon cosmological constant.

It is natural to assume that torsion decreases as time grows. Otherwise because of exponential inflation the torsion can become great that contradicts the astronomical data. That is why the following conditions are necessary to be true: $C=0$; when $d_2\neq 0$ $[(2k_4+k_3)/k_3]<0$, and $|A|\ll 1$. In this case $T^2(t)\sim A+\exp(-2Ht)$ and as the time flows the torsion decreases to a small value. If we substitute $H^2=h/[\kappa^2(k_3+k_4)]$ into expression $C=0$ it could be reduced to

$$h^2(k_1-k_2)+2h(k_3+k_4)+\tfrac{2}{3}\Lambda\kappa^2(k_3+k_4)^2=0. \tag{8}$$

Since $k_i=k_i(\xi,\zeta)$ then (8) is the condition imposed on parameters of nonminimal connection h, ξ, ζ. Note that as in Buchbinder *et al* (1985) we can show that the solutions $a(t)=\exp(Ht)$, $T^2(t)\sim\exp(-2Ht)+A$, which were obtained when $k_5=0$ are also approximate solutions as when $k_5\neq 0$.

Consider now an anisotropic metric of two spheres (Kofman *et al* 1983)

$$\mathrm{d}s^2=a^2(\mathrm{d}t^2-\cosh^2t\,\mathrm{d}x^2-\mathrm{d}\theta^2-\sin^2\theta\,\mathrm{d}\varphi^2)=a^2\bar{g}_{\mu\nu}\mathrm{d}x^\mu\mathrm{d}x^\nu, \tag{9}$$

where $a^2=\text{const}$, $-\infty<t<\infty$, $0\leqslant\theta\leqslant\pi$, $0\leqslant\varphi<2\pi$, $-\pi\leqslant x<\pi$.

We shall consider the torsion S_μ to be a constant vector. In metric (9) with constant torsion, the classical action with quantum corrections has the form:

$$S+\Gamma=V_4\left[-\frac{a^2}{\kappa^2}(-4-2\Lambda a^2+hS^2)+\ln a(\tfrac{16}{3}a_1+8a_2+a_5S^4)\right], \tag{10}$$

CC-0. In Public Domain. Gurukul Kangri Collection, Haridwar

Digitized by Arya Samaj Foundation Chennai and eGangotri

where $S^2 = \bar{g}_{\mu\nu}S^\mu S^\nu$ and V_4–4-volume. Equations (5) for action (10) have the following solutions:

(i) $S_\mu = 0$: When $\Lambda = 0$, $a^2 = -\kappa^2[\frac{2}{3}a_1 + a_2]$: This solution was obtained by Kofman *et al* (1983). When $\Lambda \neq 0$,

$$a^2 = \frac{-1 \pm \sqrt{1 - 4\Lambda\kappa^2(\frac{2}{3}a_1 + a_2)}}{2\Lambda}.$$

(ii) $S^2 = ha^2/(a_5\kappa^2 \ln a^2)$. When $\Lambda = 0$,

$$a^2 = \kappa^2/2(-4 + hS^2)\,[\tfrac{16}{3}a_1 + 8a_2 + a_5 S^4].$$

In early universe $a_5 \gg 1$, because of $a_5 \sim \xi^2$ and effective charge $\xi(t)$, corresponding to parameter ξ increases unlimitedly in strong gravitational field (Buchbinder and Shapiro 1985). In this case when the number of fields of different spines is not too much the iterational procedure could be applied for the solution of equation for a^2. Specifically, the first step gives

$$a_1^2 = \frac{\kappa^2}{2(-4 + ha_0(a_5 \ln a_0\kappa^2)^{-1})}\left[-8a_0 + \frac{h^2a_0^2}{a_5(\ln a_0\kappa^2)^2}\right],$$
$$S_1^2 = ha_0(a_5 \ln a_0\kappa^2)^{-1}, \tag{11}$$

where $a_0 = -(\frac{2}{3}a_1 + a_2)$ and condition $a_0 > 0$ is necessary. When $\Lambda \neq 0$ equation for a^2 is

$$-\frac{2a^2}{\kappa^2}(-4 + hS^2) + 8\Lambda a^4\kappa^{-2} + (\tfrac{16}{3}a_1 + 8a_2 + a_5S^4) = 0,$$

for which iterational procedure can also be applied. Thus, we have a anisotropic cosmological model with constant torsion induced by vacuum quantum effects. Note that solutions like $a^2 < 0$ can also be physically acceptable (Kofman *et al* 1983).

3. Conclusion

In the present paper nonsingular cosmological models with decreasing torsion, induced by vacuum quantum effects, are built. The metric of this model corresponds to spatially flat, open and closed Friedmann universes. The most interesting is the fact that for closed and open Friedmann universes the presence of torsion leads to the fact that the scale factor (equation (6)) becomes different from the scale factor in models without torsion, induced by vacuum quantum effects (Starobinsky 1980; Mamayev and Mostepanenko 1980). An anisotropic cosmological model with constant torsion is also constructed.

References

Barth N H and Christensen S M 1983 *J. Phys.* **A16** 543
Birrell N D and Davies P C W 1982 *Quantum fields in curved space* (Cambridge: University Press)

CC-0. In Public Domain. Gurukul Kangri Collection, Haridwar

Digitized by Arya Samaj Foundation Chennai and eGangotri

Buchbinder I L and Odintsov S D 1983 *Izw. Vyz. Fiz.* **N12** 108
Buchbinder I L and Odintsov S D 1984 *Sov. Nucl. Phys.* **40** 1338
Buchbinder I L and Odintsov S D 1985 *Lett. Nuovo Cimento* **42** 379
Buchbinder I L, Odintsov S D and Shapiro I L 1985 *Phys. Lett.* **B162** 92
Buchbinder I L and Shapiro I L 1985 *Phys. Lett.* **B151** 263
Hehl F W, Heyde P, Kerlick G D and Nester J M 1976 *Rev. Mod. Phys.* **48** 393
Kimura T 1981 *Prog. Theor. Phys.* **66** 2011
Kofman L A, Sakhni V and Starobinsky A A 1983 *Sov. Phys. JETP* **85** 1876
Mamayev S G and Mostepanenko V M 1980 *Sov. Phys. JETP* **78** 20
Nieh A T and Yan M L 1982 *Ann. Phys.* **138** 237
Obukhov Yu N 1983 *Nucl. Phys.* **B203** 237
Orzalesi C A and Ventura G 1984 *Phys. Lett.* **B139** 357
Ponomarev V N 1971 *Bull. Pol. Acad. Sci.* **19** 545
Ponomarev V N and Pronin P I 1979 *Theor. Math. Phys.* **39** 425
Rumpf H 1979 *Gen. Relat. Gravit.* **10** 509, 525, 647
Starobinsky A A 1980 *Phys. Lett.* **B91** 99
Tseytlin A A 1982 *J. Phys.* **A15** 105
Tseytlin A A 1982 *Phys. Rev.* **D26** 3327

CC-0. In Public Domain. Gurukul Kangri Collection, Haridwar

Digitized by Arya Samaj Foundation Chennai and eGangotri

CC-0. In Public Domain. Gurukul Kangri Collection, Haridwar

Digitized by Arya Samaj Foundation Chennai and eGangotri

Pramāṇa – J. Phys., Vol. 28, No. 3, March 1987, pp. 247–256. © Printed in India.

Off-shell variation in the binding energy of triton

MD. YASIN
P. G. Centre of Physics, Gaya College, Gaya 823 001, India

MS received 25 June 1986; revised 3 December 1986

Abstract. Phase-shift-equivalent potentials are used to study the sensitivity of triton binding energy (E_T) to the off-shell behaviour of two-nucleon T matrix in a translationally-invariant basis of harmonic oscillator wavefunction. For a smaller value of inverse range parameter λ (1·95 fm^{-1}), which is close to the attractive range of our model potential, a 21 % variation in the triton binding energy is obtained. For the other value of λ an off-shell variation of about 28 % in E_T is obtained.

Keywords. Off-shell effect; off-shell variation; triton binding energy.

PACS No. 21·10

1. Introduction

One of the basic unresolved problems in nuclear physics is the detailed nature of the two-nucleon (N-N) interaction. The two-body nuclear interaction, which acts as the input for many-body calculations, must itself be deduced either from accepted theories of strong interactions or from two-body scattering and reaction data. However, the N-N data determine only the asymptotic form of the N-N wavefunction, or alternatively, the on-energy shell properties of the N-N transition (T) matrix. Elastic N-N scattering experiments do not say anything about the off-energy shell T matrix. To predict the properties of the few or many-nucleon system, one must have a knowledge of the off-shell T matrix (Faddeev, 1961).

In this study, we propose to investigate how changes in the off-shell T matrix influence the binding energy of a three-nucleon system. We construct phase-shift equivalent potentials by employing a unitary transformation technique suggested by Ekstein (1960). Since the uncertainty in the two-nucleon interaction is at short distances, the distorting effects on the transformations considered will be restricted to coordinate space ranges smaller than those of the long-range attractive terms of the two-nucleon interactions used in the study.

To construct potentials that lead to identical on-shell but different off-shell two-body T-matrices, we generate a set of exactly phase-shift equivalent potentials, by applying unitary transformation to our model potential. All potentials, studied are unitarily equivalent, in the two-body sense, to a two-term Yukawa potential acting in the relative S-waves. The Yukawa potential is spin-independent and corresponds very closely to the V-potential of Malflait and Tjon (1969a, b, 1971). We, thus, employ a simplified model of the N-N interaction to isolate the role of off-shell properties, without considering spin dependence, tensor forces or higher partial waves in the triton problem. Since the

CC-0. In Public Domain. Gurukul Kangri Collection, Haridwar

Digitized by Arya Samaj Foundation Chennai and eGangotri

triton is believed to be in a predominantly spatially symmetric state, the averaging of the spin dependence of the N-N interaction is not an unreasonable approximation (Delves and Phillips, 1969).

2. Formalism

Details of the unitary-transformation method of generating phase-shift-equivalent potentials appear elsewhere (Coaster *et al* 1970; Haftel and Tabakin 1971). We start with a two-body untransformed Hamiltonian $H = H_0 + V$, where H_0 is the relative kinetic energy and V is the two-body potential. We introduce a two-body operator U that is short-ranged

$$\langle \mathbf{r}|u|\mathbf{r}'\rangle \to \delta(\mathbf{r}-\mathbf{r}') \qquad r \text{ or } r' \to \infty$$

and unitary ($u^+u = uu^+ = 1$). Then every continuum solution of the Schrödinger equation

$$H\psi^{(\pm)}(\mathbf{r}) = E\psi^{(\pm)}(\mathbf{r}). \tag{1}$$

The outgoing/incoming boundary conditions give rise to an analogous solution of the Schrödinger equation

$$\bar{H}\psi^{(\pm)}(\mathbf{r}) = E\bar{\psi}^{(\pm)}(\mathbf{r}), \tag{2}$$

corresponding to the same boundary condition, where

$$\bar{H} = u(T+V)u^+, \tag{3}$$

and

$$\bar{\psi}^{(\pm)}(r) = \psi^{(\pm)}(\mathbf{r}). \tag{4}$$

If the unitary operator u is regarded as a purely mathematical device for generating solutions of Schrödinger equations (i.e. the physical interpretation of the dynamical observable is not changed), then $\bar{\psi}^{(\pm)}(\mathbf{r})$ may also be regarded as the solution of a two-body Schrödinger equation in the presence of a (in general non-local) potential energy

$$\bar{V} = \bar{H} - T = u(T+V)u^+ - T, \tag{5}$$

and the potential $\bar{V}$ is phase-equivalent to V. We employ the rank-one unitary transformation

$$u = 1 - 2\Lambda; \quad \Lambda^2 = \Lambda, \tag{6}$$

with $\langle \mathbf{r}|\Lambda|\mathbf{r}'\rangle$ of rank N separable form

$$\sum_{i=1}^{N} g_i(\mathbf{r})g_i(\mathbf{r}')$$

for a real ortho-normal set $\{g_i\}$. With this form we get

$$\bar{V} = V - 2\Lambda V - 2V\Lambda - 2\Lambda H_0 - 2H_0\Lambda + 4\Lambda(H_0+V)\Lambda, \tag{8}$$

CC-0. In Public Domain. Gurukul Kangri Collection, Haridwar

Digitized by Arya Samaj Foundation Chennai and eGangotri

and such a transformed potential is, in general, non-local and velocity-dependent, even if the original one (potential) is local.

In this study, the untransformed potential is a two-term Yukawian

$$V(\mathbf{r}) = -\alpha \frac{\exp(-\mu_1(\mathbf{r}))}{\mathbf{r}} + \beta \frac{\exp(-\mu_2(\mathbf{r}))}{\mathbf{r}}, \tag{9}$$

where α and β characterize the strength of the potential, μ_1 and μ_2, the inverse range parameter for the long-range attractive and short-range repulsive interaction, with the following vlaues:

$$\begin{aligned} &\alpha = 574{\cdot}32 \text{ MeV fm}, \\ &\beta = 1448{\cdot}44 \text{ MeV fm}, \\ &\mu_1 = 1{\cdot}55 \text{ fm}^{-1} \quad \text{and} \quad \mu_2 = 3{\cdot}11 \text{ fm}^{-1}. \end{aligned} \tag{10}$$

V is given in MeV and r in fm. This potential is taken from a similar study by Haftel (1973) and is very close to the V-potential of Malflait and Tjon (1971). It represents the average of singlet and triplet S-wave potentials that individually give good fits to the $^1S_0$ and $^3S_1$ (N-N) scattering data upto 300 MeV (Lab.). This potential yields a two-body bound state at $-0{\cdot}416$ MeV. This potential, while clearly a simplification of the true N-N force, is a suitable starting point for studying the off-shell effects in triton.

For the projection operator Λ, we choose a rank one separable form

$$\langle \mathbf{r}|\Lambda|\mathbf{r}'\rangle = g(\mathbf{r})g(\mathbf{r}'), \tag{11}$$

where
$$g(\mathbf{r}) = [2/(4\pi)^{\frac{1}{2}}]\lambda^{3/2}, \exp(-\lambda \mathbf{r}), \tag{12}$$

and λ is the inverse range parameter.

We do not justify the transformation introduced by equations (6) to (11) on any specific physical ground, except for computational convenience. With the proper choice of λ, we can limit the range of transformation, so as not to affect the two-nucleon wavefunction (or potential) in the one-pion exchange (OPE) tail region ($r > 2$ fm).

The construction of translationally-invariant three-particle states of definite permutation symmetry follows the standard treatment due chiefly to Moshinsky (1969). The Hamiltonian so constructed from a truncated basis of harmonic oscillator is diagonalized and the lowest eigenvalue in the model space is sought as an upper bound to the actual ground state energy of the system. The main advantage of the method is its great flexibility in that the model space can be chosen to be as large as possible and the convergence of a number of physical observables may be tested.

3. Construction of translationally-invariant harmonic oscillator states

Starting with the relative and centre-of-mass coordinates (Jacobi coordinates) for the three-particle system defined in terms of the coordinates of the nucleons $\mathbf{r}_i$

$$\begin{aligned} \dot{r}_1 &= [1/(2)^{\frac{1}{2}}](r_1 - r_2), \\ \dot{r}_2 &= [1/(6)^{\frac{1}{2}}](r_1 + r_2 - 2r_3), \\ \text{and} \quad \dot{r}_3 &= [1/(3)^{\frac{1}{2}}](r_1 + r_2 + r_3), \end{aligned} \tag{13}$$

CC-0. In Public Domain. Gurukul Kangri Collection, Haridwar

Digitized by Arya Samaj Foundation Chennai and eGangotri

where $\dot{r}_3$ stands for the coordinates of the centre of mass and can be filtered out for translationally-invariant system, and the corresponding harmonic oscillator creation operators

$$\dot{\eta}_i = [1/(2)^{\frac{1}{2}}\,(\dot{\mathbf{r}}_i - i\,\mathbf{p}_i). \tag{14}$$

We define a transformation of the creation operators

$$\eta_1 = [1/(2)^{\frac{1}{2}}]\,(-i\dot{\eta}_1 + \dot{\eta}_2); \qquad \eta_2 = [1/(2)^{\frac{1}{2}}]\,(i\dot{\eta}_1 + \dot{\eta}_2). \tag{15}$$

The new operators $\dot{\eta}_i$ can be seen to have particularly simple behaviour under the particle interchange operators. The harmonic oscillator states

$$|n_1 l_1, n_2 l_2, [\lambda] r\rangle = A(v, [\lambda] r)[\langle |\phi_{n_1 l_1}\phi_{n_2 l_2}; \Lambda\rangle + (-1)^{l_1 + l_2 - \Lambda}\,| \phi_{n_2 l_2}\phi_{n_1 l_1}, \Lambda\rangle]. \tag{16}$$

constructed with these transformed operators are found to be translationally-invariant states of good orbital angular momentum and good particle permutation symmetry. The symmetry depends on the quantity

$$2n_1 + l_1 - 2n_2 - l_2 = v \,(\text{mod } 3). \tag{17}$$

4. Construction of matrix elements

In actual practice, we are interested only in calculating the matrix element (ME) of the intrinsic part of the Hamiltonian (i.e. Hamiltonian considered in the centre-of-mass frame) with respect to translationally-invariant harmonic oscillator states. Thus considering only two-body forces, the Hamiltonian can be written as

$$H = \frac{1}{2m}\sum_{s=1}^{3}(\mathbf{p}_s)^2 + \sum_{s<t=2}^{3} V(s, t), \tag{18}$$

the intrinsic part H_1 of the Hamiltonian H is obtained by substracting from H the centre-of-mass kinetic energy

$$\frac{1}{2}\hbar w(\dot{\mathbf{p}}_n)^2 = \frac{1}{2mn}\left(\sum_{s=1}^{n}\mathbf{p}_s\right)^2; \quad \text{for } n \text{ particles}$$

i.e.
$$H_1 = H - \frac{1}{6m}\left(\sum_{s=1}^{3}\mathbf{p}_s\right)^2, \quad \text{for} \quad n = 3 \text{ particles}$$

$$= \frac{1}{2}\hbar w \sum_{s=1}^{2}[(\dot{p}_s)^2 + (\dot{X}_s)^2] + \sum_{s<t=2}^{3} U(s, t), \tag{19}$$

with

$$U(s, t) = V(s, t) - \frac{mw^2}{6}(X_s - X_t)^2. \tag{20}$$

CC-0. In Public Domain. Gurukul Kangri Collection, Haridwar

Digitized by Arya Samaj Foundation Chennai and eGangotri

The ME of this Hamiltonian evaluated in a translationally-invariant states of good particle permutation symmetry can now be written as

$$\langle n_1' l_1', n_2' l_2'; \Lambda M; \{3\} | H_1 | n_1 l_1, n_2 l_2; \Lambda M; \{3\} \rangle, \tag{21}$$

$$= \hbar\omega[(\mathbf{n}+3)\delta_{N'N}] + 3\langle N'|U(1,2)|N\rangle, \tag{22}$$

where the state $|n_1 l_1, n_2 l_2, \Lambda M; \{3\}\rangle \equiv |N\rangle$ has been constructed as prescribed by Kramer and Moshinsky (1966) and $\mathbf{n}$ stands for $2n_1 + l_1 + 2n_2 + l_2$ i.e. the total number of oscillator quanta and

$$U(1,2) = V(\dot{X}_1) - \tfrac{1}{3}\hbar w(\dot{X}_1)^2, \tag{23}$$

where $$\dot{X}_1 = [1/(2)^{\frac{1}{2}}](X_1 - X_2). \tag{24}$$

In order to study the off-shell variation of the binding energy (BE) of triton, we need to calculate the ME of the transformed, as well as untransformed potential, between three-particle translationally-invariant states in a harmonic oscillator basis. It implies calculating the matrix elements of $U(1,2)$ i.e.

$$\langle N'|U(1,2)|N\rangle = \langle n_1' l_1', n_2' l_2'; \Lambda M; \{3\} | U(1,2) | n_1 l_1, n_2 l_2, \Lambda M \rangle, \tag{25}$$

$$= \langle N'|V(\dot{X}_1)|N\rangle - \tfrac{1}{3}\hbar w\langle N'|(\dot{X}_1)^2|N\rangle. \tag{26}$$

Now

$$\langle N'|V(\dot{X}_1)|N\rangle = \sum_{\dot{n}_1'\dot{n}_1 l_1 \dot{n}_2 \dot{l}_2} \sum_p \langle \dot{n}_1' \dot{l}_1', \dot{n}_2' \dot{l}_2'; \Lambda | n_1' l_1', n_2' l_2'; \Lambda \rangle \times \langle \dot{n}_1 \dot{l}_1, \dot{n}_2 \dot{l}_2; \Lambda | n_1 l_1, n_2 l_2, \Lambda \rangle \times B(\dot{n}_1' \dot{l}_1', \dot{n}_1 \dot{l}_1, p) I_p(V) \delta \dot{n}_2' \dot{n}_2 \delta \dot{l}_2 \dot{l}_2 \delta \dot{l}_1' \dot{l}_1, \tag{27}$$

where $I_p(V)$ is the Talmi integral for the potential $V(\dot{X}_1)$ and is given by

$$I_p(V) = \frac{2}{\Gamma(p+1{\cdot}5)} \int_0^\infty r^{2p+2} V(\mathbf{r}) \exp(-r^2)\, d\mathbf{r}, \tag{28}$$

and the B coefficient is defined as

$$B(n'l', nl, p) \equiv \tfrac{1}{2}\Gamma(p+1{\cdot}5) \sum_k a_{nlk} a'_{n'l'p-k-\frac{1}{2}(l+l')},$$

as tabulated by Broody and Moshinsky (1967). Similarly

$$\langle N'|(\dot{X}_1)^2|N\rangle = \sum \langle n_1' l_1', n_2' l_2'; \Lambda M | (\dot{X}_1)^2 | n_1 l_1, n_2 l_2, \Lambda M \rangle, \tag{29}$$

$$= \delta \dot{l}_2' \dot{l}_2 \delta \dot{l}_1' \dot{l}_1 \, \delta \dot{n}_2' \dot{n}_2 \sum_{\dot{n}_1'\dot{n}_1 l_1 \dot{n}_2 \dot{l}_2} \sum_p \langle \dot{n}_1' \dot{l}_1', \dot{n}_2' \dot{l}_2', \Lambda | n_1' l_1' n_2' l_2', \Lambda \rangle \times B(\dot{n}_1' \dot{l}_1', \dot{n}_1 \dot{l}_1, \mathbf{p})(\mathbf{p}+1{\cdot}5) \langle \dot{n}_1 \dot{l}_1, \dot{n}_2 \dot{l}_2, \Lambda | n_1 l_1, n_2 l_2; \Lambda \rangle. \tag{30}$$

CC-0. In Public Domain. Gurukul Kangri Collection, Haridwar

Digitized by Arya Samaj Foundation Chennai and eGangotri

Combining these results, we obtain the ME of the intrinsic Hamiltonian in a translationally-invariant harmonic oscillator basis as

$$\begin{aligned}\langle N'|H_1|N\rangle &= \hbar w(\mathbf{n}+3)\delta N'N + 3\delta \dot{l}'_2 \dot{l}_2 \delta \dot{n}'_2 \dot{n}_2 \delta \dot{l}'_1 \dot{l}_1 \\ &\times \sum_{\dot{n}'_1 \dot{n}_1 \dot{l}_1 \dot{n}_2 \dot{l}_2} \sum_p \langle \dot{n}'_1 \dot{l}_1, \dot{n}_2 \dot{l}_2; \Lambda | n'_1 l'_1; n'_2 l'_2; \Lambda \rangle \\ &\times \langle \dot{n}_1 \dot{l}_1, \dot{n}_2 \dot{l}_2; \Lambda | n_1 l_1, n_2 l_2; \Lambda \rangle \\ &\times B(\dot{n}'_1 \dot{l}_1, \dot{n}_1 \dot{l}_1, p)\left(I_p(V) - \frac{\hbar w}{3}(\mathbf{p}+1{\cdot}5)\right). \end{aligned} \tag{31}$$

The Talmi integral for the model potential equation (9) is given as

$$I_p(V) = -\alpha I_p(\mu_1) + \beta I_p(\mu_2),$$

where $$I_p(\mu) = \frac{2}{\Gamma(p+1{\cdot}5)} \int_0^\infty r^{2p+1} \exp(-\mu r) \exp(-r^2)\, \mathrm{d}\mathbf{r}. \tag{32}$$

For symmetric states

$$\dot{n}'_1 = \dot{n}_1, \quad \dot{l}'_1 = \dot{l}_1 \quad \text{and} \quad \Lambda = 0. \tag{33}$$

Therefore the matrix elements of the intrinsic Hamiltonian with *untransformed potential* turns out to be

$$\begin{aligned}\langle N'|H_1|N\rangle &= \hbar w(\mathbf{n}+3)\delta N'N + 3\delta \dot{l}'_2 \dot{l}_2 \delta \dot{n}'_2 \dot{n}'_2 \delta \dot{l}'_1 \dot{l}_1 \\ &\times \sum_{\dot{n}'_1 \dot{n}_1 \dot{l}_1 \dot{n}_2 \dot{l}_2} \sum_p \langle \dot{n}'_1 \dot{l}_1, \dot{n}_2 \dot{l}_2; 0 | n'_1 l'_1, n'_2 l'_2; 0 \rangle \\ &\times \langle \dot{n}_1 \dot{l}_1, \dot{n}_2 \dot{l}_2; 0 | n_1 l_1, n_2 l_2; 0 \rangle \\ &\times B(\dot{n}'_1 \dot{l}_1, \dot{n}_1 \dot{l}_1, p)\left\{ -\alpha I_p(\mu_1) + \beta I_p(\mu_2) - \frac{\hbar w}{3}(\mathbf{p}+1{\cdot}5)\right\}. \end{aligned} \tag{34}$$

Likewise the matrix elements of the Hamiltonian with *transformed potential* can be obtained as follows:

The transformed potential eq. (8) is

$$\bar{V}_{12} = V_{12} - 2\Lambda H - 2H\Lambda + 4\Lambda H \Lambda, \tag{35}$$

for which we have the following transformations:

$$\langle \mathbf{r}|\Lambda H|\mathbf{r}'\rangle = g(\mathbf{r})\left(-\frac{1}{M}\nabla^2 + V(\mathbf{r}')\right) g(\mathbf{r}'). \tag{36}$$

Similarly

$$\langle \mathbf{r}|H\Lambda|\mathbf{r}'\rangle = g(\mathbf{r}')\left(-\frac{1}{M}\nabla^2 + V(\mathbf{r})\right) g(\mathbf{r}), \tag{37}$$

and

$$\langle \mathbf{r}|\Lambda H \Lambda|\mathbf{r}'\rangle = g(\mathbf{r})g(\mathbf{r}') \int \mathrm{d}\mathbf{r}''\, g(\mathbf{r}'')\left(-\frac{1}{M}\nabla''^2 + V(\mathbf{r}'')\right) g(\mathbf{r}''). \tag{38}$$

CC-0. In Public Domain. Gurukul Kangri Collection, Haridwar

Digitized by Arya Samaj Foundation Chennai and eGangotri

Therefore

$$\left\langle N' \left| \sum_{i<J} \bar{V}_{ij} \right| N \right\rangle = 3 \langle n_1' l_1', n_2' l_1'; 00\ \{3\} | \bar{V}_{12} | n_1 l_1, n_2 l_1; 00\ \{3\} \rangle$$
$$= 3 \sum \langle n_1' l_1', n_2' l_1'; 00\ \{3\} | \dot{n}_1' \dot{l}_1', \dot{n}_2' \dot{l}_1'; 00 \rangle$$
$$\times \langle \dot{n}_1 \dot{l}_1, \dot{n}_2 \dot{l}_1; 00 | n_1 l_1, n_2 l_1; 00\ \{3\} \rangle$$
$$\times \langle \dot{n}_1' \dot{l}_1', \dot{n}_2' \dot{l}_1'; 00 | \bar{V}_{12} | \dot{n}_1 \dot{l}_1, \dot{n}_2 \dot{l}_1; 00 \rangle. \tag{39}$$

Now

$$\langle \dot{n}_1' \dot{l}_1', \dot{n}_2' \dot{l}_2'; 00 | \bar{V}_{12} | \dot{n}_1 \dot{l}_1, \dot{n}_2 \dot{l}_1; 00 \rangle$$
$$= \sum_{\dot{m}_1' \dot{m}_1} \frac{(-1)^{\dot{m}_1' + \dot{m}_1}}{\sqrt{(2\dot{l}_1 + 1)(2\dot{l}' + 1)}} \langle \dot{n}_1' \dot{l}_1' \dot{m}_1' | \bar{V}_{12} | \dot{n}_1 \dot{l}_1 \dot{m}_1 \rangle \delta \dot{n}_2' \dot{n}_2' \delta \dot{l}_1' \dot{l}_1 \delta \dot{m}_1' \dot{m}_1$$
$$= \langle \dot{n}_1' \dot{l}_1' 0 | \bar{V}_{12} | \dot{n}_1 \dot{l}_1 0 \rangle \delta \dot{n}_2' \dot{n}_2 \delta \dot{l}_1' \dot{l}_1, \tag{40}$$

as the matrix elements do not depend on m. And

$$\langle \dot{n}_1' \dot{l}_1' 0 | \bar{V}_{12} | \dot{n}_1 \dot{l}_1 0 \rangle = \int \langle \dot{n}_1' \dot{l}_1 0 | \mathbf{r}' \rangle \langle \mathbf{r}' | \bar{V}_{12} | \mathbf{r}'' \rangle \langle \mathbf{r}'' | \dot{n}_1 \dot{l}_1 0 \rangle \mathrm{d}\mathbf{r}' \mathrm{d}\mathbf{r}''$$
$$= \delta \dot{l}_1' \dot{l}_1\ \delta \dot{m}_1' \dot{m}_1 \int \psi^*_{\dot{n}_1' \dot{l}_1}(\mathbf{r}') V(\mathbf{r}') \psi_{\dot{n}_1 \dot{l}_1}(\mathbf{r}') \mathrm{d}\mathbf{r}'$$
$$- 2 \int \psi^*_{\dot{n}_1' \dot{l}_1 \dot{m}_1}(\mathbf{r}') g(\mathbf{r}') \mathrm{d}\mathbf{r}' \int H(\mathbf{r}'') g(\mathbf{r}'') \psi_{\dot{n}_1 \dot{l}_1 \dot{m}_1}(\mathbf{r}'') \mathrm{d}\mathbf{r}''$$
$$- 2 \int \psi^*_{\dot{n}_1' \dot{l}_1 \dot{m}_1}(\mathbf{r}') H(\mathbf{r}') g(\mathbf{r}') \mathrm{d}\mathbf{r}' \int \psi_{\dot{n}_1 \dot{l}_1 \dot{m}_1}(\mathbf{r}'') g(\mathbf{r}'') \mathrm{d}\mathbf{r}''$$
$$+ 4 \int \psi^*_{\dot{n}_1' \dot{l}_1 \dot{m}_1}(\mathbf{r}') g(\mathbf{r}') \mathrm{d}\mathbf{r}' \int \psi_{\dot{n}_1 \dot{l}_1 \dot{m}_1}(\mathbf{r}'') g(\mathbf{r}'') \mathrm{d}\mathbf{r}''$$
$$\times \int \mathrm{d}\mathbf{r}'' g(\mathbf{r}'') H(\mathbf{r}'''') g(\mathbf{r}''''), \tag{41}$$

where

$$H(\mathbf{r}) = \left[-\frac{1}{M} \nabla^2 + V(\mathbf{r}) \right]. \tag{42}$$

Evaluating each term of (41) one by one, one gets the ME of the transformed potential as

$$\langle N' | \bar{V}_{12} | N \rangle = 3 \sum_{\dot{n}_1' \dot{l}_1' \dot{n}_1 \dot{l}_1 \dot{n}_2 \dot{l}_2} \langle \dot{n}_1' \dot{l}_1' \dot{n}_2' \dot{l}_2' 00 | n_1' \dot{l}_1' n_2' l_1' 00; \{3\} \rangle$$
$$\times \langle \dot{n}_1 \dot{l}_1 \dot{n}_2 \dot{l}_1 00 | n_1 l_1 n_2 l_1 00; \{3\} \rangle$$
$$\times \left[\sum_p B(\dot{n}_1' \dot{l}_1, \dot{n}_1 \dot{l}_1; p) \{ -\alpha I_p(\mu_1) + \beta I_p(\mu_2) \} \right.$$
$$- 2 \frac{k^2}{c^2} \delta l_1 0 \left\{ \sum_{p,q} B(\dot{n}_1' 0, 00, p)\, 2^{(p+1.5)} \frac{\Gamma(p+2)}{\Gamma(p+1.5)} I_{(p+0.5)}(\lambda\sqrt{2}) \right.$$
$$\times B(\dot{n}_1 0, 00, q) 2^{(q+1.5)} \Big\} \Big\{ -\frac{\lambda^2}{M} \frac{\Gamma(q+2)}{\Gamma(q+1.5)} I_{(q+0.5)}(\lambda\sqrt{2})$$
$$\left. + \frac{\lambda\sqrt{2}}{M} I_q(\lambda\sqrt{2}) - \frac{\alpha}{\sqrt{2}} I_q(\lambda + \mu_1)\sqrt{2} + \frac{\beta}{\sqrt{2}} I_q(\lambda + \mu_2)\sqrt{2} \right\}$$

CC-0. In Public Domain. Gurukul Kangri Collection, Haridwar

Digitized by Arya Samaj Foundation Chennai and eGangotri

$$+\sum_{p,q} B(n'_1 0, 00, p)\, 2^{(p+1\cdot5)} \left\{ -\frac{\lambda^2}{M} \frac{\Gamma(p+2)}{\Gamma(p+1\cdot5)} I_{(p+0\cdot5)}(\lambda\sqrt{2}) \right.$$

$$\left. +\frac{\lambda\sqrt{2}}{M} I_p(\lambda\sqrt{2}) - \frac{\alpha}{\sqrt{2}} I_p(\lambda+\mu_1)\sqrt{2} + \frac{\beta}{\sqrt{2}} I_p(\lambda+\mu_2)\sqrt{2} \right\}$$

$$\times B(\dot{n}_1 0, 00, q)\, 2^{(q+1\cdot5)} \frac{\Gamma(q+2)}{\Gamma(q+1\cdot5)} I_{(q+0\cdot5)}(\lambda\sqrt{2}) \Bigg\}$$

$$+4\frac{k^4}{c^2}\delta l_1 0 \left\{ \frac{1}{4M\lambda} - \frac{\alpha}{(2\lambda+\mu_1)^2} + \frac{\beta}{(2\lambda+\mu_2)^2} \right\}$$

$$\times \sum_{p,q} B(\dot{n}'_1 0, 00; p)\, 2^{(p+1\cdot5)} \frac{\Gamma(p+2)}{\Gamma(p+1\cdot5)} I_{(p+0\cdot5)}(\lambda\sqrt{2})$$

$$\times B(\dot{n}_1 0, 00, q)\, 2^{(q+1\cdot5)} \frac{\Gamma(q+2)}{\Gamma(q+1\cdot5)} I_{(q+0\cdot5)}(\lambda\sqrt{2}) \Bigg]. \qquad (43)$$

5. Construction of Hamiltonian matrices and their diagonalization

Matrix elements of the Hamiltonian with untransformed potential (equation (34)) were then calculated and the Hamiltonian matrix diagonalized. The lowest eigenvalue gave an upper bound to the binding energy of triton for the model potential. The energy eigenvalues appear in table 1.

Similarly, the matrix elements of the "off-shell' part of the Hamiltonian, with "phase equivalent potentials" (equation (43)) for inverse range parameter $\lambda = 1{\cdot}95$ fm^{-1}, were then calculated. The Hamiltonian matrix was then constructed and diagonalized. The lowest eigenvalue gave an upper bound to the shift in the binding energy of triton due to

Table 1. Eigenvalues of the model potential.

13·04947,	6·756620,	5·90179,	4·22966,	3·32642,
2·87869,	1·74288,	0·45308,	−0·28621,	−0·53931.

Smallest eigenvalue: −0·53931 (oscillator unit)* = −6·98 MeV
Result: BE of triton nucleus = 6·98 MeV
* 1 oscillator unit = 12·95 MeV calculated theoretically.

Table 2. Eigenvalues of the phase-shift equivalent potential for $\lambda = 1{\cdot}95$ fm^{-1}.

119·81600,	95·13740,	84·32240,	66·83170,
39·71960,	29·16731,	10·61730,	4·18263,
−0·29340,	−0·67954.		

Smallest eigenvalue: −0·67594 (oscillator unit); −8·4592 MeV; −8·46 MeV. Therefore shift in the BE of triton = 1·48 MeV, i.e. about 21%.

CC-0. In Public Domain. Gurukul Kangri Collection, Haridwar

Digitized by Arya Samaj Foundation Chennai and eGangotri

Table 3. Eigenvalues of the phase-shift equivalent potential for $\lambda = 2{\cdot}51$ fm^{-1}.

151·89577,	115·29595,	107·38687,	73·37154,
33·51981,	27·11575,	10·61688,	6·41766,
−0·29700,	−0·69430.		

Smallest eigenvalue: −0·6943 (oscillator unit); −8·9873 MeV; −8·99 MeV. Therefore, shift in the BE of triton due to the off-shell variation of the $N-N$ potential is 2·01 MeV i.e. about 28 %.

the 'off-shell" distortions in the two-body N-N potential brought about by the unitary transformations employed. These results appear in table 2.

Similar calculations were performed for the phase-shift equivalent potential for the other value of $\lambda = 2{\cdot}5$ fm^{-1}. They appear in table 3.

6. Results and discussion

Tables 1 to 3 reveal significant "off-shell" contribution to the binding energy of triton. We have obtained binding energy of triton as −6·98 MeV (table 1) and a shift of 1·48 MeV i.e. about 21 % in the BE of triton, for one value of inverse range parameter ($\lambda = 1{\cdot}95$ fm^{-1}). Similarly a value of 2·01 MeV (i.e. about 28 % contribution to the BE of triton) is obtained for another value of inverse range parameter ($\lambda = 2{\cdot}5$ fm^{-1}). We have chosen these values for the inverse range parameter, as they lie between $\mu_1 = 1{\cdot}55$ fm^{-1} and $\mu_2 = 3{\cdot}11$ fm^{-1} of our model potential. This has been done so as not to affect the long range attractive part of the N-N potential, because the nature of the long range attractive N-N potential is well known.

In this context, it would be interesting to recall the observations of Haftel (Haftel 1973) who used the same two-body N-N potential and did elaborate calculations by solving the Faddeev equations, following the technique of Malfleit and Tjon (1971), in a much more comprehensive way. He found variation of upto 6 MeV in the triton BE prediction for the phase-shift equivalent potential, all but 1 MeV of this being attributable to change in the deuteron wavefunction induced by the unitary transformation employed. If the deuteron wavefunction is kept fixed, the ability of the unitary transformation to change the triton BE is considerably reduced.

We do not impose this condition in our calculation for two reasons:

(i) Relativistically speaking the deuteron wavefunction at distances below (say 1 fm) cannot be taken as precisely known, for the electromagnetic method of probing the wavefunctions is full of uncertainties. In fact, even the D-state probability is not yet conclusively fixed, as has been demonstrated by the recent photonuclear data (Hadjimacheal and Saylo 1982).

(ii) The singlet ($^1S_0$) part of the two-nucleon wavefunction is, of course, not measurable at all.

For our model potential, therefore, we need not restrict the unitary transformation to sectors orthogonal to the deuteron.

CC-0. In Public Domain. Gurukul Kangri Collection, Haridwar

Digitized by Arya Samaj Foundation Chennai and eGangotri

Acknowledgements

All the calculations reported in this paper were done on the DEC-10 computer at the Indian Institute of Technology, Kanpur. The author would like to record his gratitude to Dr J Thakur of Patna University, Patna for his stimulating guidance and useful suggestions in the preparation of this paper.

References

Baranger M 1968 in Proceedings of the International School of Physics 'Enrico Fermi' Course (New York: Academic Press) 40
Brody T A and Moshinsky M 1960 *Nucl. Phys.* **17** 16
Brody T A and Moshinsky M 1967 *Tables of transformation on brackets* (New York: Gordon and Breach)
Coaster F, Cohen S, Day B and Vincent C M 1970 *Phys. Rev.* **C1** 769
Delves L M and Phillips A C 1969 *Rev. Mod. Phys.* **41** 497
Ekstein H 1960 *Phys. Rev.* **117** 1590
Faddeev L D 1961 *Sov. Phys. JETP* **12** 1014
Friedman K A 1968 *Phys. Rev.* **165** 1579
Hadjimicheal E and Saylo D P 1982 CTP 693
Haftel M I 1973 *Phys. Rev.* **C7** 80
Haftel M I and Tabakin F 1971 *Phys. Rev.* **C3** 921
Kramer P and Moshinsky M 1966 *Nucl. Phys.* **82** 241
MacGregor M H 1969 *Phys. Rev.* **182** 1714
Malflait R A and Tjon J A 1969a *Nucl. Phys.* **127** 161
Malflait R A and Tjon J A 1969b *Phys. Lett.* **B29** 391
Malflait R A and Tjon J A 1971 *Ann. Phys. (NY)* **61** 425
Miller M D and Signell P 1969 *Phys. Lett.* **B30** 157
Moshinsky M 1969 *The harmonic oscillator in modern physics from atoms to quarks* (New York: Gordon and Breach)

CC-0. In Public Domain. Gurukul Kangri Collection, Haridwar

Digitized by Arya Samaj Foundation Chennai and eGangotri

Pramāṇa – J. Phys., Vol. 28, No. 3, March 1987, pp. 257–267. © Printed in India.

Design studies of a 100 MeV proton linear accelerator

P SINGH, R MYTHILI and M G BETIGERI
Nuclear Physics Division, Bhabha Atomic Research Centre, Bombay 400 085, India

MS received 19 July 1986; revised 5 November 1986

Abstract. Design details of a 100 MeV proton linear accelerator (Alvarez system) operating at a resonating frequency of 400 MHz have been studied. Increase in the linac operating frequency has become feasible with the possibility of injecting protons from a radio frequency quadrupole accelerator with energies higher than the conventional pre-injectors. Various electrical parameters of such a system have been calculated and compared with the existing linac injectors operating at 200 MHz.

Keywords. Linac design calculation; radio frequency quadrupole-Alvarez combination; proton linear accelerator.

PACS No. 41·70

1. Introduction

In most of the proton linear accelerators operating in the world (Cole 1971; Wheeler *et al* 1979; Michaelis 1975) the configuration follows a familiar pattern in which protons from a d.c. source, usually a Cockcroft-Walton generator of 750 kV, are bunched and injected into an Alvarez type linear accelerator (linac) operating around 200 MHz. The choice of the exciting frequency of the Alvarez linear accelerator depends on the velocity of the proton beam (β) being injected into the linear accelerator. It has been shown (Smith 1959) that as long as the quantity $2\pi a/\beta\lambda \ll 1$, the longitudinal transit time factor is insensitive to the choice of the wavelength. For $2\pi a/\beta\lambda \gg 1$, the transit time factor falls exponentially and hence the effective shunt impedance of the structure drops rapidly. However, for $2\pi a/\beta\lambda = 1$, the transit time factor is 0·79 which is still a reasonable value for design purposes. Therefore, for a drift tube bore radius a of 1 cm and $\beta = 0{\cdot}04$ (corresponding to the 750 keV protons), the wavelength works out to 157 cm or a frequency of 191 MHz and hence the choice of 200 MHz for the exciting frequency in the existing linacs is not far from the calculated value.

However, on increasing the energy of the proton beam to be injected into the linac structure, two distinct advantages may be visualized. (i) Higher incident energy would allow injection of the proton beams into an Alvarez structure being operated at higher frequency. For $\beta = 0{\cdot}08$, which corresponds to a 3 MeV proton beam, the frequency for the Alvarez system would be 400 MHz. Higher operating frequency is expected to lead to lower rf losses. (ii) The injected protons are subjected to strong radial rf defocussing forces in the first stages of the linac cavity. The effect of these forces would be stronger for small velocities of the injected protons. Hence at a higher incident energy the requirements on the quadrupole magnets enclosed within the drift tubes are expected to be less stringent.

CC-0. In Public Domain. Gurukul Kangri Collection, Haridwar

Digitized by Arya Samaj Foundation Chennai and eGangotri

The prospect of providing intense, focussed and bunched beams at MeV energies is now being realized through the radio frequency quadrupole (RFQ) accelerator (Crandall *et al* 1979; Purser *et al* 1983). If the energy of the proton beam to be injected from such an accelerator is assumed to be 3 MeV, the practical transit time considerations suggest a minimum wavelength of 75 cm for the appropriate Alvarez system.

In order to study the details of such a system, a computer program LINAC was developed (§ 2) and was used to optimize the parameters for a 400 MHz Alvarez system (§3). The calculations have resulted in a physical design for a 100 MeV proton accelerator to be realized in four linac cavities of the Alvarez type. A comparison with existing linacs is attempted in § 4 to highlight the possible advantages of the present design.

2. Formalism

The calculation of the electromagnetic eigenvectors and eigenvalues in a linac cavity of the Alvarez type containing stemless drift tubes can be accomplished by solving finite difference approximations to the wave equation derived from Maxwell's equations. Assuming a cylindrical symmetry for the unit cell, the solutions of Maxwell's equations for the TM mode lead to the well-known Helmholtz equation for the magnetic field component (Katz 1970)

$$\frac{1}{r}\frac{\partial}{\partial r}\left[\frac{r\,\partial H_\varphi}{\partial r}\right]+\frac{\partial^2 H_\varphi}{\partial z^2}+\left[k^2-\frac{1}{r^2}\right]H_\varphi=0, \tag{1}$$

where k is related to the resonant frequency by

$$k=\omega(\varepsilon\mu)^{1/2}=2\pi f(\varepsilon\mu)^{1/2}=2\pi/\lambda. \tag{2}$$

Taking the quantity $F=rH_\varphi$ as a potential function the above equation simplifies to

$$\frac{\partial^2 F}{\partial r^2}+\frac{\partial^2 F}{\partial z^2}-\frac{1}{r}\frac{\partial F}{\partial r}+k^2F=0, \tag{3}$$

subject to the boundary condition $\partial F/\partial n=0$ on the conducting walls and symmetry planes and $F=0$ along the axis.

In view of the cylindrical symmetry and the periodic structure of the linac cavity along the z axis, the region of the meridian plane (z, r) in which this equation must be solved reduces to a quarter of a cell (figure 1).

Following standard methods (Austin *et al* 1965), the finite difference approach for a rectangularly bounded region (figure 1) is accomplished by superposing a finitely spaced square mesh upon the region such that the boundary of the region everywhere coincides with the mesh lines. For a typical mesh point (i, j) in the interior of the region, Taylor series expansions of the function F in terms of the potential function $F_{i,j}$ are

$$F_{i,j+1}=F_{i,j}+\frac{h\partial F_{i,j}}{\partial r}+\frac{h^2}{2}\frac{\partial^2 F_{i,j}}{\partial r^2}+O(h^3), \tag{4a}$$

CC-0. In Public Domain. Gurukul Kangri Collection, Haridwar

Digitized by Arya Samaj Foundation Chennai and eGangotri

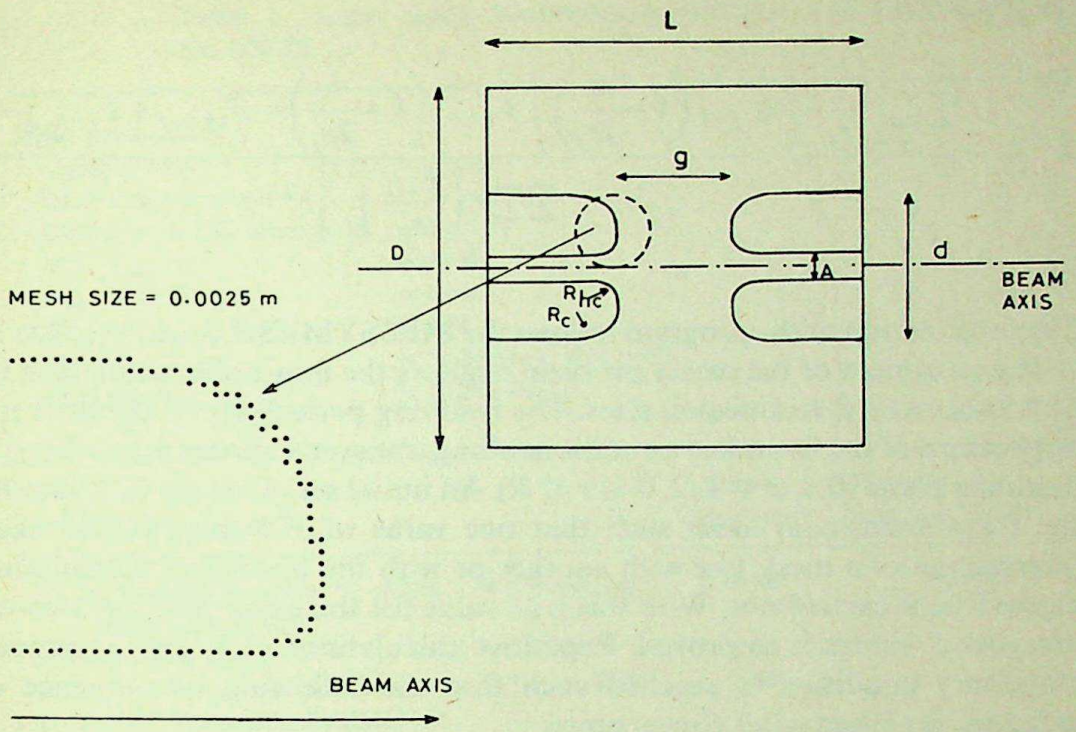

Figure 1. Unit cell geometry with cylindrical drift tube. Zigzag boundary used in the calculations is also shown.

$$F_{i,j-1} = F_{i,j} - \frac{h\partial F_{i,j}}{\partial r} + \frac{h^2}{2}\frac{\partial^2 F_{i,j}}{\partial r^2} - O(h^3), \tag{4b}$$

$$F_{i+1,j} = F_{i,j} + \frac{h\partial F_{i,j}}{\partial z} + \frac{h^2}{2}\frac{\partial^2 F_{i,j}}{\partial z^2} + O(h^3), \tag{4c}$$

$$F_{i-1,j} = F_{i,j} - \frac{h\partial F_{i,j}}{\partial z} + \frac{h^2}{2}\frac{\partial^2 F_{i,j}}{\partial z^2} - O(h^3), \tag{4d}$$

where h is the mesh spacing and $O(h^3)$ is the order of maximum error occurring due to the neglect of further terms in the expansion. Substitution of these equations into the scalar equation (3) yields

$$F_{i,j+1}\left(1 - \frac{h}{2r_j}\right) + F_{i,j-1}\left(1 + \frac{h}{2r_j}\right) + F_{i+1,j} + F_{i-1,j} + (k^2h^2 - 4)F_{i,j} + O(h^4) = 0. \tag{5}$$

The resultant error is of maximum order h^4. Therefore the smaller the mesh size, the smaller is the error. In the immediate vicinity of the boundary specifying the drift tube, the calculation of F values proceeds along a zigzag boundary made of mesh lines to approximate the smooth curvature (figure 1). The lowest eigenvalue for such a cavity is

CC-0. In Public Domain. Gurukul Kangri Collection, Haridwar

Digitized by Arya Samaj Foundation Chennai and eGangotri

given by

$$k^2 = -\frac{\sum_i \sum_j \left[\frac{F_{i,j}}{r_j}\left\{F_{i,j+1}\left(1-\frac{h}{2r_j}\right)+F_{i,j-1}\left(1+\frac{h}{2r_j}\right)+F_{i+1,j}+F_{i-1,j}-4F_{i,j}\right\}\right]}{\sum_i \sum_j \left[\left(\frac{F_{i,j}}{r_j}\right)^2\right] h^2}. \tag{6}$$

The formulation of the program follows the MESSYMESH code (MURA-713) closely.

The treatment of the cavity problem neglects the non-uniform spacing between the drift tubes and their unequal sizes. The resulting periodicity of the drift tube permits application of the boundary conditions along transverse planes at $z = 0, \pm L/2$ and the meridian plane ($0 \leqslant z \leqslant L/2, 0 \leqslant r \leqslant R$). An initial set of values for F are loaded onto the two-dimensional mesh such that one value of F is assigned to each point of intersection of a mesh line with another or with the boundary. Calculation of a trial eigenvalue is carried out. With this trial value for the eigenvalue the two-dimensional array of F values is improved. Repetitive calculations of F and k^2 proceeds until a stationary condition is reached such that the following convergence criteria are satisfied. (a) Eigenvalue convergence:

$$\left|\left[(k^{n+1}-k^n)/(k^{n+1})\right]\right| \leqslant 10^{-5}. \tag{7}$$

(b) Eigenvector convergence:

$$\left|\left[(F^{n+1}-F^n)/(F^{n+1})\right]\right| \leqslant 10^{-3}. \tag{8}$$

Once these criteria are satisfied, the potential values are used to calculate the auxiliary electromagnetic quantities (Katz 1970) namely the energy stored per unit volume, the power lost to the cavity walls per unit area, the quality factor, the average axial accelerating field, the shunt impedance, the transit time factor, the coupling coefficient and the peak surface electric field and its location.

3. Calculations

The calculations are done for a unit cell (figure 1). The geometry of the unit cell is specified by the parameters: D, the cavity diameter; L, the length of the unit cell ($\beta\lambda$); d, the drift tube diameter; R_c, the radius of curvature of the outer profile of the drift tube; R_{hc}, the radius of curvature of the drift tube bore hole corner and A, the diameter of the bore hole.

The code was checked by reproducing the MESSYMESH calculations reported in MURA-713. For the input parameters of MURA-713 (table 1) the auxiliary electromagnetic quantities were calculated. The calculations have been done for two unit cells namely linac cavity and laboratory cavity. The linac cavity consists of an outer wall of length L and two half-drift tubes (figure 2) while the laboratory cavity is of length $L/2$ with an end plate and a drift tube plate supporting a half-drift tube (figure 2). The lab cavity calculations are useful to optimize, in the initial stages, the performance of an actual cell to be adopted for fabrication. The results of the present calculations are compared with MURA-713 in table 1. Following the standard practice in all

CC-0. In Public Domain. Gurukul Kangri Collection, Haridwar

Digitized by Arya Samaj Foundation Chennai and eGangotri

Table 1. Linac cavity calculations (comparison with MURA-713 Run No. 30470).

Input parameters:

Cavity diameter	= 88 cm
Drift tube diameter	= 16 cm
Diameter of the beam hole	= 3 cm
R_c	= 4 cm
R_{hc}	= 1 cm
g/L	= 0·34
Energy	= 51·36 MeV, β = 0·318
Frequency	= 202·82 MHz

Output parameters		Present calculation	Mura-713 Run No. 30470
1) Normalization factor to obtain 1 MV/m average axial electric field		598·70	562·01
2) Mesh size (mm)		2·50	5·00
3) Stored energy per unit volume (J/m^3)	W/V	1·689	1·600
4) Power dissipation (Watts)			
To cavity walls	PW1	4431·309	3829·46
To the end plate	PW2	2482·003	2283·04
To the drift tube plate	PW3	3497·109	3396·60
To the drift tube	PW4	3194·653	3353·98
5) Q-factor			
Linac cavity	Q_1	77684·70	79291·50
Lab cavity	Q_2	30250·00	30717·00
6) Shunt impedance MΩ/m			
Linac cavity	Z_1	61·630	65·340
Lab cavity	Z_2	23·990	25·310
7) Transit time factor		0·7951	0·7786
8) Coupling coefficient		0·0608	0·0652
9) Z_1T^2 (MΩ/m)		38·967	39·609
10) Z_1T^2/Q_1 (Ω/m)		501·61	499·54
11) Peak surface electric field E_p (MV/m)		5·436	4·901
12) Peak field location (cm)			
From the axis of drift tube		5·50	5·53
From end of drift tube		0·30	0·30
13) S (= E_2/E_1)		1·04	1·05

calculations, the average axial electric field is normalized to 1 MV/m and the resulting scaling factors for the different cavities utilized to obtain the stored energy per unit volume and the power losses. The quantities Q_1, Z_1 correspond to the linac cavity while the quantities Q_2, Z_2 correspond to the lab cavity.

One of the criteria to test the consistency of the potential values is to compare the average electric field along the axis computed in two ways

$$E_1 = \frac{1}{\omega\varepsilon L}\int_0^L \frac{1}{r}\left|\frac{\partial F}{\partial r}\right|_{r=0} \mathrm{d}z \tag{9a}$$

and

$$E_2 = \frac{\omega\mu}{L}\int_0^R\int_0^L \frac{F}{r}\,\mathrm{d}r\,\mathrm{d}z. \tag{9b}$$

CC-0. In Public Domain. Gurukul Kangri Collection, Haridwar

Digitized by Arya Samaj Foundation Chennai and eGangotri

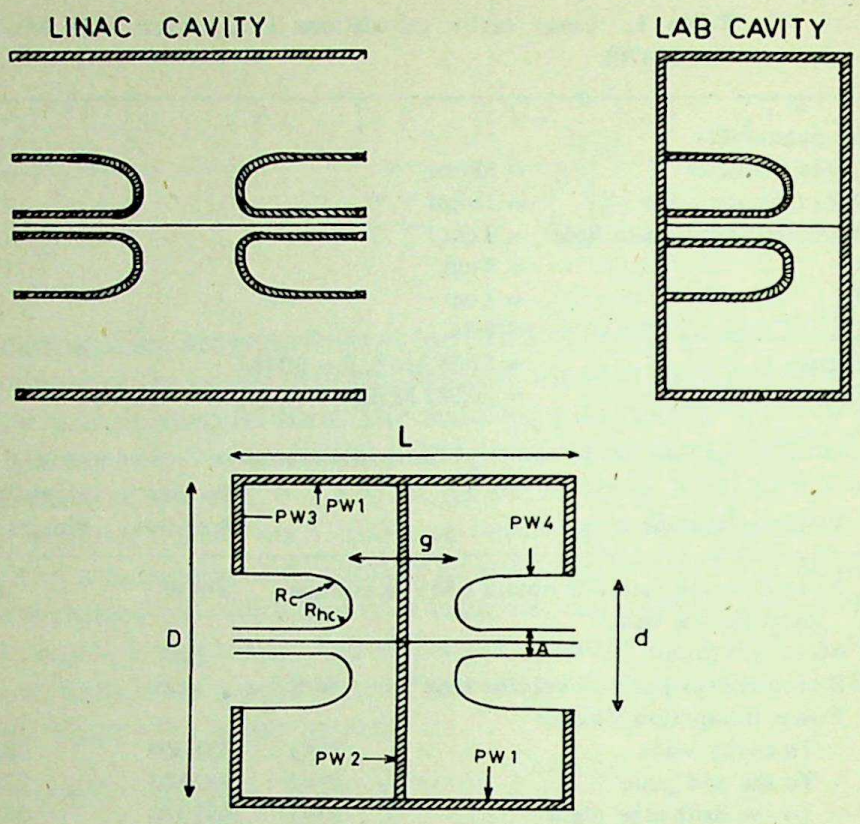

Figure 2. Linac and lab cavity-unit cell.

Their ratio $S = E_2/E_1$ is a good measurement of the consistency of the solution. Typically in the present calculations, S is of the order of 1·04 as compared with 1·05 for the MESSYMESH code, 1·02 in IDDA (Katz 1968) and 1·005 in CLAS (Martini and Warner 1968).

A further check on the program "LINAC" consisted in satisfactory reproduction of the auxiliary electromagnetic quantities for the input parameters at various energies as reported for the BNL 200 MeV linac (Wheeler *et al* 1979). After being satisfied with the program, the calculations for the unit cells at various energies for an Alvarez type cavity operating at 400 MHz were done. The diameter for a hollow cylindrical cavity excited in the lowest TM_{010} mode is given by

$$D = (2 * 2{\cdot}405)/k, \tag{10}$$

which works out to 57·42 cm for an operating frequency of 400 MHz.

However, we found that the inclusion of the drift tubes decreases the resonating frequency. Therefore to resonate the cavity at the same frequency the diameter of the cavity was reduced. In our calculations we have chosen D = 46–42 cm. The bore radius a was fixed at 1 cm for tanks at the low β end of the linac from the transit time considerations and was kept the same for all the other tanks. In view of the need to provide quadrupoles inside the drift tubes, the drift tube diameter was fixed to 12 cm. A value of 1 cm for R_{hc} was fixed for all the tanks. Choice of the other geometrical parameters g/L and R_c was made consistent with the desired resonant frequency. Variation of the frequency as a function of g/L for different values of D and d is shown in figure 3 for a proton energy of 55 MeV. Once the geometrical parameters were

CC-0. In Public Domain. Gurukul Kangri Collection, Haridwar

Digitized by Arya Samaj Foundation Chennai and eGangotri

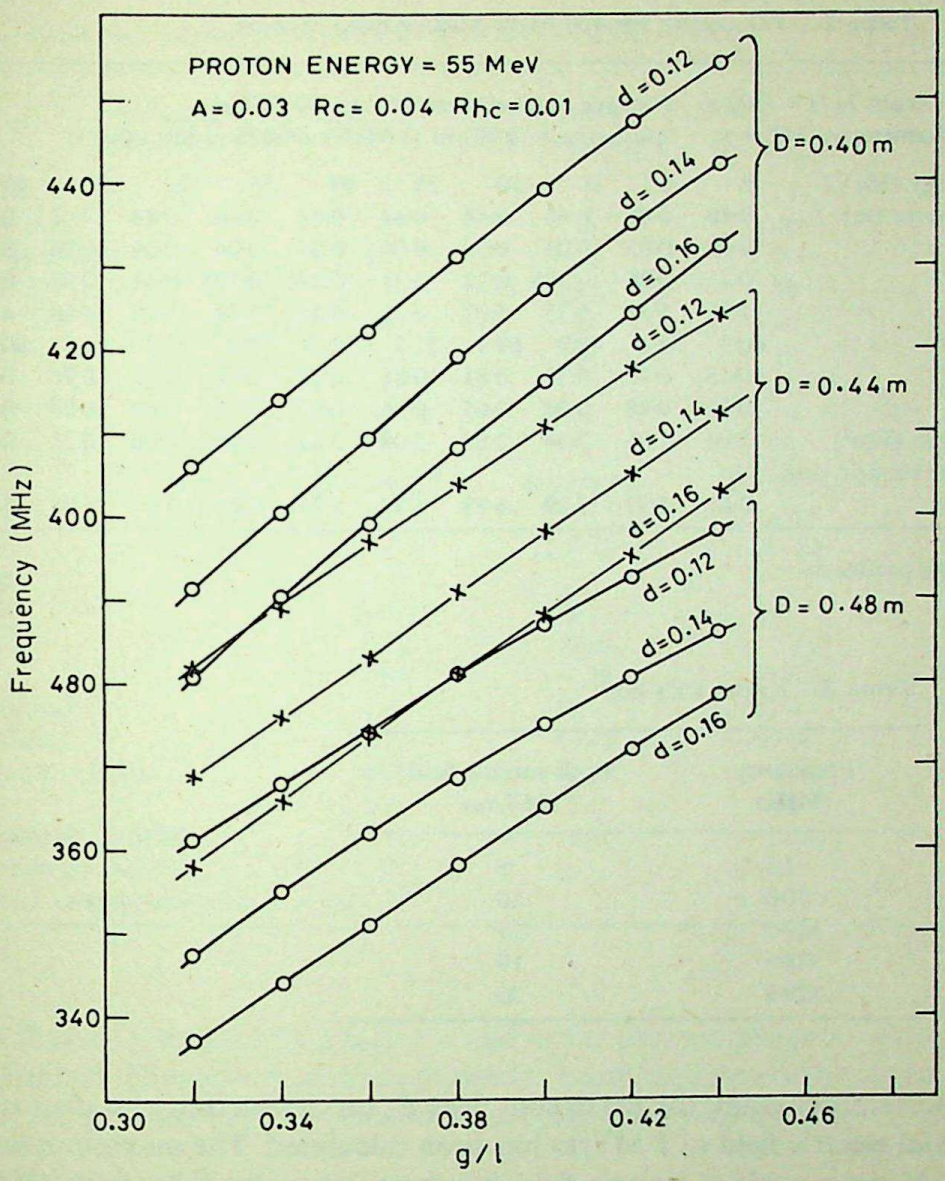

Figure 3. Variation of resonating frequency with g/L for different values of cavity and drift tube diameters.

decided, a mesh spacing was introduced in the meridian plane (z, r) and the eigenvector $F(z, r)$ was defined at the nodal points as

$$F(z, r) = F(ih, jh) = F_{i,j} \tag{11}$$

for integer values of i and j. An initial trial eigenvector was assigned. Eigenvector $F_{i,j}$ distribution was calculated in the desired region using an over relaxation successive displacement iterative procedure (Klemperer and Barnett 1971). Iterations were continued till the convergence criteria mentioned earlier were satisfied and the final set of potential values used to calculate various electrical parameters (table 2).

For the purpose of the present calculations, it was assumed that the protons gain a total energy of 100 MeV in four stages: 7 MeV in the first tank and 30 MeV each in the subsequent three tanks.

CC-0. In Public Domain. Gurukul Kangri Collection, Haridwar

Digitized by Arya Samaj Foundation Chennai and eGangotri

Table 2. Parameters for 400 MHz Alvarez linac cavities.

Diameter of beam hole = 0·02 m		Average axial electric field = 1·0 MV/m									
Drift tube diameter = 0·12 m		Mesh size = 0·001 m (3 MeV); 0·0025 m (all others)									
Proton energy (MeV)	3	6·5	10	10	25	40	55	70	70	85	100
Cavity diameter (m)	0·46	0·46	0·46	0·44	0·44	0·44	0·44	0·44	0·42	0·42	0·42
R_c (m)	0·02	0·03	0·03	0·04	0·04	0·04	0·04	0·04	0·04	0·04	0·04
g/L	0·2	0·26	0·305	0·22	0·31	0·345	0·375	0·41	0·37	0·39	0·405
Q_1 (10^4)	4·96	5·36	5·35	5·02	5·21	5·25	5·21	5·15	4·68	4·62	4·56
Z_1 (MΩ/m)	60·3	73·1	70·8	69·9	71·7	72·5	71·3	70·2	61·9	60·6	59·1
T	0·65	0·73	0·78	0·81	0·81	0·77	0·74	0·71	0·76	0·73	0·71
C*	0·09	0·08	0·06	0·05	0·06	0·07	0·08	0·09	0·07	0·08	0·08
Energy stored (J/m^3)	2·08	1·95	2·04	2·08	2·08	2·04	2·05	2·06	2·33	2·34	2·4
Peak surface electric field (MV/m)	3·87	5·37	5·29	6·98	5·73	5·31	5·2	5·2	5·58	5·5	5·58

* Coupling coefficient

Table 3. Kilpatrick's limit.

Frequency (MHz)	Peak surface field (MV/m)
7·5	5
70·0	10
209·4	15
378·5	19
428·8	20

In the present program, the maximum field E_p on the surface of a drift tube for an average axial electric field of 1 MV/m has been calculated. The maximum safe limit to the value of peak surface electric field has been given by Kilpatrick (1953) in the relationship

$$f = 1{\cdot}64\, E_{SL}^2 \exp\left[-8{\cdot}5/E_{SL}\right] \tag{12}$$

where f is the frequency in MHz and E_{SL} is the value of surface electric field in MV/m above which sparking is possible. For different values of E_{SL}, f has been calculated and are listed in table 3. For Alvarez structures operating at 400 MHz, the sparking limit allows the peak surface field value E_{SL} to be 19·5 MV/m. One may therefore scale up the average axial electric field E_0 by a ratio E_{max}/E_p where E_{max} is the maximum permitted electric field ($E_{max} < E_{SL}$) used in the calculations. The parameters for the 100 MeV linac have been worked out and are listed in table 4. The rf power P per energy gain ΔW, is given by

$$P/\Delta W = E_0 T/ZT^2 \cos\phi \tag{13}$$

The power has to be increased over a value computed from the theoretical value of Z, the shunt impedance, to allow for losses on drift tube stems, tuners, end plates, rf contacts, spring rings, pump out ports, surface roughness and contamination. The

CC-0. In Public Domain. Gurukul Kangri Collection, Haridwar

Digitized by Arya Samaj Foundation Chennai and eGangotri

Table 4. Typical parameters for a 100 mA-100 MeV linac.

Frequency = 400 MHz $\cos\varphi = 0{\cdot}90$	Total power = 19·01 MW Total cavity length = 42·5 m			
Cavity number	1	2	3	4
Input energy (MeV)	3	10	40	70
Output energy (MeV)	10	40	70	100
Energy gain (ΔW)	7	30	30	30
D (cm)	46	44	44	42
d (cm)	12	12	12	12
A^1 (cm)	2	2	2	2
R_c (cm)	2	4	4	4
R_{hc} (cm)	1	1	1	1
g/L (range)	0·20–0·305	0·22–0·345	0·345–0·41	0·37–0·405
E_0 (MV/m)	3·0	3·17	3·63	3·42
E_g (MV/m)	18·7–9·0	12·3–10·4	10·4–8·9	9·2–8·4
E_{max} (MV/m) (surface)	14·5	19	19	19
$\langle T \rangle$	0·72	0·80	0·74	0·73
$\Delta W/\Sigma L$	1·94	2·28	2·42	2·25
Cavity length (m)	3·6	13·1	12·4	13·4
$\langle ZT^2 \rangle$ (MΩ/m)	35·77	45·43	39·01	32·63
Power (practical) (MW)	0·61	2·42	2·98	3·31
κ	1·3	1·3	1·3	1·3
RF power (practical) (MW) (including beam power)	1·31	5·42	5·98	6·31

[1] A is the beam hole diameter i.e. $A = 2a$

power will thus be increased by a factor κ and in the present design a value of $\kappa = 1{\cdot}3$ has been assumed. The radio frequency power for beam loading also has to be provided. The total rf power listed in table 4 includes the beam power for a 100 mA proton beam.

4. Discussion

A large number of parameter variations, with the cavity resonating at 400 MHz were tried out and the values in table 2 are the culmination of these calculations. An increase in D produces large Z; however, it results in smaller T. Similarly a decrease in the value of d improves the value of ZT^2 slightly. The present calculations assume $d = 12$ cm and $a = 1$ cm. Further reduction in these parameters may improve ZT^2 but would lead to an impractical design. The use of higher frequency for the linac system results in a high value of E_{SL} and hence a high value for E_0 which in turn leads to a smaller length for the accelerator. However the radio frequency power lost on the cavity walls scales as α^2 where $\alpha = E_{max}/E_p$. A comparison of the present parameters with the BNL linac (Wheeler *et al* 1979) is listed in table 5. It may be noted that the reduction in the transit time factor in the present calculations amounts to less than 5 % as compared to the BNL accelerator. The parameters of linac injector to the spallation neutron source (Boardman 1982) are compared with our calculations in table 6. In spite of the higher frequency, the values of ZT^2 achieved in the present calculations are comparable with the ones obtained in the BNL machine. The usual statement that the higher the

CC-0. In Public Domain. Gurukul Kangri Collection, Haridwar

Table 5. Comparison of the present calculations with BNL data.

	Present calculations				BNL data			
	1	2	3	4	1	2	3	4
Proton energy (MeV)	3–10	10–40	40–70	70–100	0·75–10·42	10·42–37·54	37·54–66·18	66·18–92·55
Energy gain (MeV)	7	30	30	30	9·67	27·12	28·64	26·37
Cavity length (m)	3·61	13·16	12·4	13·33	7·44	19·02	16·53	16·68
Cavity diameter (m)	0·46	0·44	0·44	0·42	0·94	0·9	0·88	0·88
Drift tube diameter (m)	0·12	0·12	0·12	0·12	0·18	0·16	0·16	0·16
Bore hole diameter (m)	0·02	0·02	0·02	0·02	0·02–0·025	0·03	0·03	0·03
R_c (m)	0·02–0·03	0·04	0·04	0·04	0·02	0·04	0·04	0·04
R_{hc} (m)	0·01	0·01	0·01	0·01	0·005	0·01	0·01	0·01
g/L	0·2–0·305	0·22–0·34	0·345–0·41	0·37–0·405	0·21–0·31	0·2–0·31	0·3–0·36	0·37–0·41
T	0·65–0·78	0·81–0·77	0·77–0·71	0·76–0·71	0·64–0·81	0·86–0·81	0·82–0·75	0·75–0·69
ZT^2 (MΩ/m)	25·5–42·9	46–42·8	42·8–35·5	35·5–29·8	27–47·9	53·5–44·8	44·6–35·2	35–28·5
Average axial field (MV/m)	3·0	3·17	3·63	3·42	1·6–2·31	2·0	2·6	2·6
Cavity excitation power (practical) (MW)	0·61	2·42	2·98	3·31	0·51	1·4	2·36	2·57
κ factor	1·3	1·3	1·3	1·3	1·3	1·35	1·35	1·4
Total power (practical) (MW) for 100 mA	1·31	5·42	5·98	6·31	1·48	4·12	5·22	5·21

Digitized by Arya Samaj Foundation Chennai and eGangotri

CC-0. In Public Domain. Gurukul Kangri Collection, Haridwar

Digitized by Arya Samaj Foundation Chennai and eGangotri

Table 6. Comparison of the present calculations with the SNS injector data.

Parameters	Present calculations			SNS data			
cavity #	1	2	3	1	2	3	4
Output energy (MeV)	10	40	70	9·92	30·47	49·76	70·5
Length (m)	3·6	13·1	12·4	7·15	11·96	11·24	12·11
Accelerating rate (MV/m)	3·0	3·17	3·63	0·8–1·5	1·72	1·71	1·7–1·6
Power-theory (MW)	0·47	1·86	2·29	0·44	1·31	1·4	1·5
κ-factor	1·30	1·30	1·30	1·24	1·20	1·43	1·20
Total power (practical) for 20 mA (MW)	0·75	3·02	3·58	0·73	1·99	2·39	2·22

frequency at which the Alvarez is operated, the lower are the power losses (Wheeler *et al* 1979) must therefore be treated with caution. However, the resulting reduction in the sizes (both the diameter and the length) as compared to the 200 MHz structure is expected to lead to a substantial reduction in costs.

References

Austin B, Edwards T W, O'Meara J E, Palmer M L, Swenson D A and Young D E 1965 Report MURA-713

Boardman B (Ed.) 1982 Rutherford Appelton Laboratory Report RL-82-006

Cole F T 1971 *Particle Accelerators* **2** 1

Crandall K R, Stokes R H and Wangler T P 1979 *Proc. 10th Linear Accelerator Conf. Montauk*, New York Sept. 9–14, Brookhaven National Laboratory 1980 Report BNL-51134 p. 205

Katz A 1968 Saclay thesis (Unpublished)

Katz A 1970 *Linear accelerator* (eds) P M Lapostolle and A L Septier (Amsterdam: N. H. Publishing Company)

Kilpatrick W D 1953 A criterion for vacuum sparking design to include both R. F and D. C, Radiation Lab Report UCRL-2321

Klemperer O and Barnett M E 1971 *Electron optics* (Cambridge: University Press) III ed.

Martini M and Warner D J 1968 CERN- Report 68-11

Michaelis E 1975 *Proc. Particle Accelerator Conf., Washington, USA* 1975 *IEEE NS Trans.* **22** 1385

Purser F O, Wadlinger E A, Sander O R, Potter J M and Crandall K R 1983 *IEEE NS* **30** 3582

Smith Lloyd 1959 *Encyclopedia of physics* (ed.) S Flugge **44** 341

Wheeler G W, Batchelor K, Chasman R, Grand P and Sheeman J 1979 *Particle Accelerators* **9** 1

CC-0. In Public Domain. Gurukul Kangri Collection, Haridwar

Digitized by Arya Samaj Foundation Chennai and eGangotri

CC-0. In Public Domain. Gurukul Kangri Collection, Haridwar

Digitized by Arya Samaj Foundation Chennai and eGangotri

Pramāṇa – J. Phys., Vol. 28, No. 3, March 1987, pp. 269–275. © Printed in India.

The dielectric constant of the binary liquid system *n*. heptane + methanol near its critical temperature

Y JAYALAXMI, S GUHA, V C VANI and E S R GOPAL
Department of Physics, Indian Institute of Science, Bangalore 560012, India

MS received 11 June 1986; revised 8 January 1987

Abstract. The electrical capacitance of the binary liquid mixture *n*. heptane + methanol at its critical composition is studied in both one-phase and two-phase regions. The two-phase capacitance data are used with the known functional forms for the order parameter and the diameter to obtain T_c and c_c with greater precision. This helps in reducing the number of unknown parameters in the functional form for the one-phase capacitance. The data show consistency with an alpha (α) exponent for dc/dt in the one phase region.

Keywords. Critical phenomena; binary liquids; critical exponents; critical temperature; critical capacitance.

PACS No. 64·70

1. Introduction

The dielectric constant of binary liquid mixtures is expected to show a singular behaviour near the critical solution temperature of phase separation (Mistura 1973; Stell and Hoye 1974; Goulan *et al* 1979; Sengers *et al* 1980). The dielectric constant behaviour at the critical point is expected to behave as

$$\rho^{-1}\varepsilon = \rho_c^{-1}\varepsilon_c(1 + \varepsilon_1 t^{(1-\alpha)} + \varepsilon_2 t + \varepsilon_3 t^{(1-\alpha+\Delta)} + \ldots), \tag{1}$$

where ε = the dielectric constant of the mixture, ε_c = dielectric constant at the critical temperature T_c, $t = (T - T_c)/T_c$, ρ = density of the system, ρ_c = density of the system at the critical temperature, α = specific heat exponent = 0·11 and Δ = Wegner correction term = 0·5. This implies a density anomaly always hidden along with the intrinsic ε anomaly. However the study of the density of a few systems has shown that the density anomaly contribution is small compared to the intrinsic dielectric constant anomaly (Greer and Jacobs 1980; Theon *et al* 1981). In the absence of a density anomaly the functional form is

$$\varepsilon = \varepsilon_c + A(1)t^{(1-\alpha)} + A(2)t + A(3)t^{(1-\alpha+\Delta)}, \tag{2}$$

where $A(1) = \varepsilon_c\varepsilon_1$ and so on.

Experimental studies on the dielectric constant in binary liquids have indeed shown an anomalous behaviour above the background at the critical temperature. The early literature is reviewed by Arkhangelskii and Semencheko (1967). Jacobs and Greer (1981) report a decrease in ε as $t \to 0$ in the system polystyrene + cyclohexane. Theon

CC-0. In Public Domain. Gurukul Kangri Collection, Haridwar

Digitized by Arya Samaj Foundation Chennai and eGangotri

et al (1981) report a similar behaviour in nitroethane + cyclohexane. They found their data to be consistent with a $(1-\alpha)$ exponent as per the theoretical model. The study of ε on cyclohexane + methanol (Shetty *et al* 1983), carbon disulphide + acetonitrile (Gunasekaran *et al* 1985) and *n*. heptane + methanol (Jyothi *et al* 1984) shows an increase in ε as $t \to 0$. Similar increase in ε is seen by Cohn and Greer (1986) in the system perfluromethyl cyclohexane + carbon tetrachloride. They report a $(1-\alpha)$ exponent for ε.

The increase or decrease of ε as $t \to 0$ depends on the sign of the coefficient of the singular term in the functional form for ε. This coefficient is proportional to $-\mathrm{d}T_c/\mathrm{d}E^2$ where E is the electric field (Sengers *et al* 1980). As $t \to 0$, since $t^{(1-\alpha)} \to 0$, a negative (positive) coefficient implies an increase (decrease) in ε as $t \to 0$. So systems with positive (negative) $\mathrm{d}T_c/\mathrm{d}E^2$ will show increasing (decreasing) ε as $t \to 0$. This is consistent with the ε behaviour seen in the systems so far studied (Cohn and Greer 1986).

We have measured the capacitance c of the system *n*. heptane + methanol at its critical composition X_c. In our earlier study of c on the same system, c was studied only in the one-phase region and the data were fitted into a functional form of the type

$$(c-c_c)/c_c = At + B_1 t^{\theta} + B_2 t^{(\theta+\Delta)} + B_3 t^{(\theta+2\Delta)},$$

(c_c is the critical capacitance) where except for T_c all other parameters were unknown and were expected to come out from the numerical analysis. A large number of unknowns in the numerical analysis cause correlations among the parameters and thus give a large uncertainty in θ. So the θ value obtained showed a range dependence.

In the present study, we attempted to fix as many parameters as possible in the functional form for c. For this we measured capacitance in the two-phase region. T_c and c_c are obtained in two independent ways (Ranjan *et al* 1986): (i) As the system studied are the mixtures of polar and nonpolar liquids, if capacitance is measured in two pairs of electrodes placed on either sides of the centre of the cell, the behaviour seen in the two pairs of plates will be of opposite trend when the liquid mixture phase separates. The temperature and the corresponding value of capacitance at which two pairs of electrodes show opposite trend gives the experimental values of T_c and c_c respectively. (ii) The known functional form for the order parameter and the diameter within a small $(T_c - T)$ in the two-phase region are used to locate T_c and c_c respectively. This is discussed again later. The analysis of the resistance data in one phase shows a $(1-\alpha)$ exponent. From Kumar and Jayannavar (1981) we expect a similar behaviour in capacitance c too.

2. Experiments and observations

The capacitance of *n*. heptane + methanol is studied at 20 kHz. The cell used for the study has two pairs of electrodes to facilitate the two-phase study (Gopal *et al* 1976). The capacitance is measured using a double ratio transformer bridge with a lock-in amplifier as the detector. The bridge is able to detect changes in capacitance $\simeq 0{\cdot}005$ pF in 20 pF. The details of the bridge and its importance are discussed by Gunasekaran *et al* (1981). The temperature stability is $\pm 0{\cdot}001$ K. The temperature controller and experimental set-up are discussed in an earlier work (Gunasekaran 1983).

Though the capacitance is measured in both the electrode pairs, when the data were plotted, the data from the lower electrode pair show large scatter compared

CC-0. In Public Domain. Gurukul Kangri Collection, Haridwar

Digitized by Arya Samaj Foundation Chennai and eGangotri

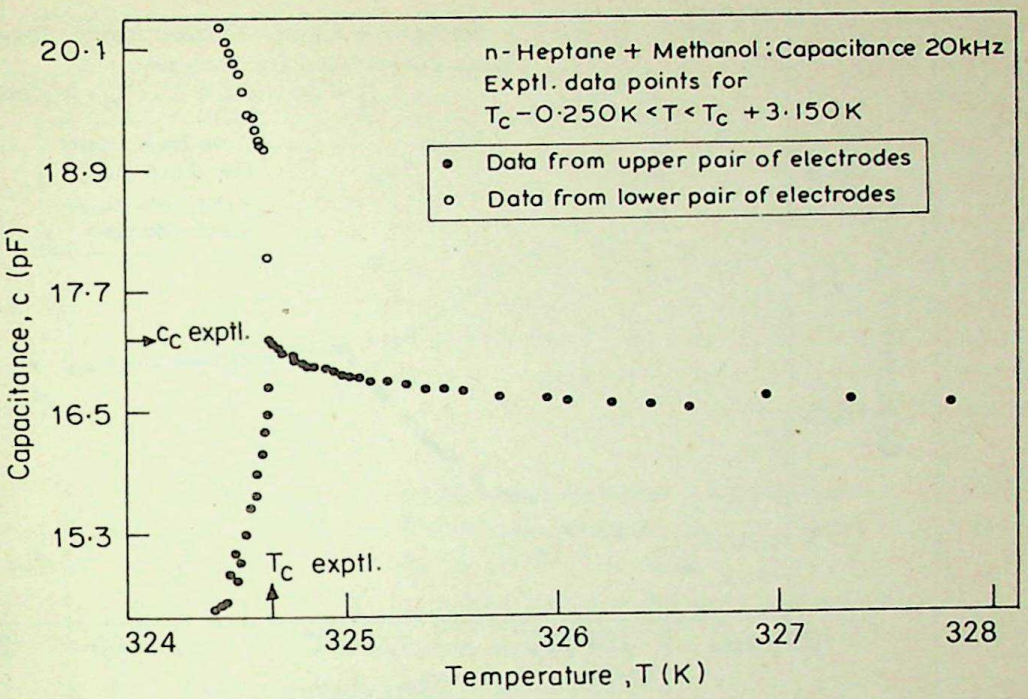

Figure 1. Experimental data points in the temperature range $(T_c - 0{\cdot}250)\ \mathrm{K} < T < (T_c + 3{\cdot}150)\ \mathrm{K}$ for the system *n*. heptane + methanol.

to that from the upper electrode pair. This is suspected to be due to some error in cell connections and is discussed later. In this system the lower electrode pair is dipped in the heavier methanol-rich phase and hence shows higher capacitance than the upper electrode pair values. Our analysis is restricted to the temperature range $(T_c - 0{\cdot}200)\ \mathrm{K} < T < (T_c - 0{\cdot}009)\ \mathrm{K}$ in the two-phase region and $(T_c + 0{\cdot}009)\ \mathrm{K} < T < (T_c + 0{\cdot}200)\ \mathrm{K}$ in the one-phase region. Within this close to T_c region the functional forms are well known (Ranjan *et al* 1986). The region within ± 9 mk around T_c is excluded, since the perturbations due to gravity are serious in this region.

The reported values of T_c and X_c for this sample are $T_c = 324{\cdot}9 \pm 0{\cdot}1$ K, $X_c = 61{\cdot}9$ mole% $\pm 0{\cdot}1$% of methanol by Chernova (1965) and $T_c = 324{\cdot}871$ K. $X_c = 61{\cdot}35$ mole% of methanol by Viswanathan *et al* (1973). Figure 1 is the values of capacitances as a function of temperature and figure 2 is the experimental data set used for analysis in the one-phase and the two-phase regions.

3. Data analysis

3.1 *Analysis of the two-phase data*

In the two-phase region, the capacitance difference as measured by the two pairs of electrodes $|c_u - c_L|$ (where $c_u = c$ from the upper pair, $c_L = c$ from the lower electrode pair) is approximated to be proportional to the concentration difference of any one of the components $|X_u - X_L|$ for $|T - T_c|$ small. Since the critical exponent for $|X_u - X_L|$ is β ($\beta = 0{\cdot}325$) in the two-phase region, $|c_u - c_L|$ can be written as

$$|c_u - c_L| = B(1)\,(T_c - T)^{0{\cdot}325}, \quad T < T_c, \tag{3}$$

CC-0. In Public Domain. Gurukul Kangri Collection, Haridwar

Digitized by Arya Samaj Foundation Chennai and eGangotri

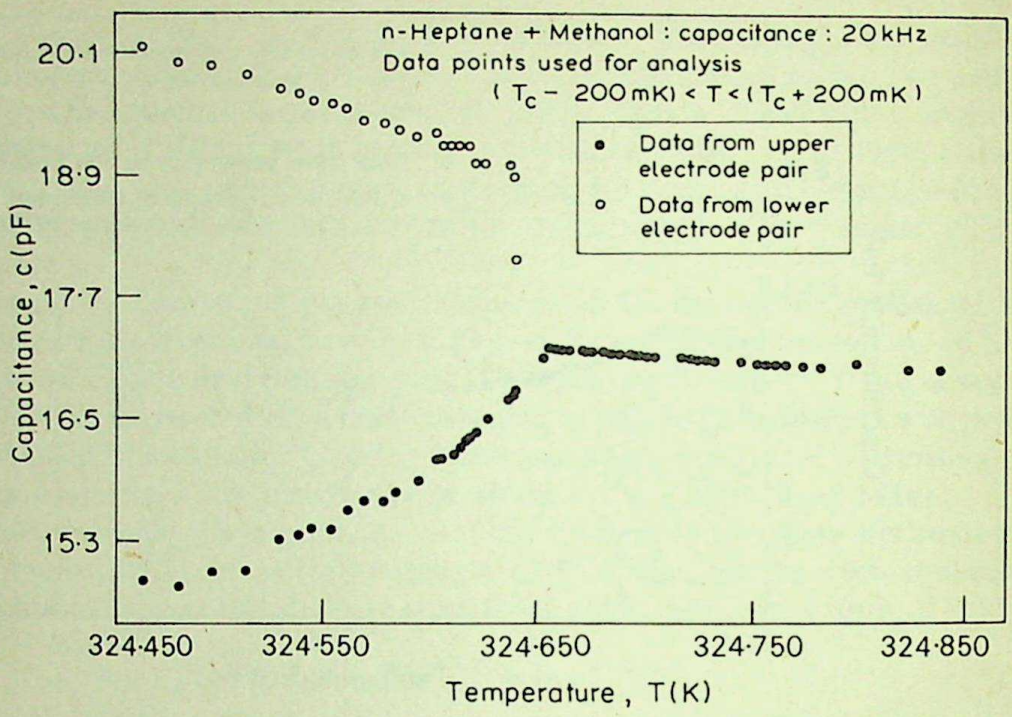

Figure 2. Experimental data points used in analysis in the temperature range ($T_c - 0{\cdot}200$) K $< T <$ ($T_c + 0{\cdot}200$) K close to T_c.

where $B(1)$ and T_c are unknowns. We have varied T_c around the experimental value of T_c ($T_{c\,\mathrm{exp}} = 324{\cdot}648$ K) in steps of 0·0002 K each time fixing it in equation (3). We have used Bevington's (1969) nonlinear least square CURFIT program for data analysis. χ_ν^2 is calculated and that value of T_c for which χ_ν^2 is the minimum is taken as the critical temperature T_c. This gives for (3),

$$B(1) = 8{\cdot}902 \pm 0{\cdot}022, \quad T_c = 324{\cdot}6472 \pm 0{\cdot}0007 \quad \text{and} \quad \chi_\nu^2 = 1{\cdot}72.$$

When all the parameters are floated, the convergence is hard and so we had to fix one of the parameters. Also χ_ν^2 is obtained by allowing 0·002 K uncertainty in temperature and 0·02 pF uncertainty in $|c_u - c_L|$. Figure 3 gives the fitted curve according to equation (3) and the experimental points. The computed best fit $T_c = 324{\cdot}647$ K agrees with the directly measured value within the experimental error.

We have used the value of T_c obtained from the order parameter analysis in the diameter analysis in the two-phase region:

$$|c_u + c_L|/2 = D(1) + D(2)\,|T_c - T| + D(3)\,|T_c - T|^{1-\alpha} + D(4)\,|T_c - T|^{2\beta} \qquad T < T_c. \tag{4}$$

When (4) is analyzed without the linear term, the value of $D(1)$ which is c_c, the critical capacitance, is found to be lower than the capacitance values even at 100 mk above T_c which is meaningless. We have traced the problem to the scatter and errors in the c_L values as mentioned earlier. So we eliminated c_L using equations (3) and (4) so that

$$c_u = D(1) + D(2)\,(T_c - T) + D(3)\,(T_c - T)^{1-\alpha} + D(4)\,(T_c - T)^{2\beta} + D(5)\,(T_c - T)^{\beta}. \tag{5}$$

CC-0. In Public Domain. Gurukul Kangri Collection, Haridwar

Digitized by Arya Samaj Foundation Chennai and eGangotri

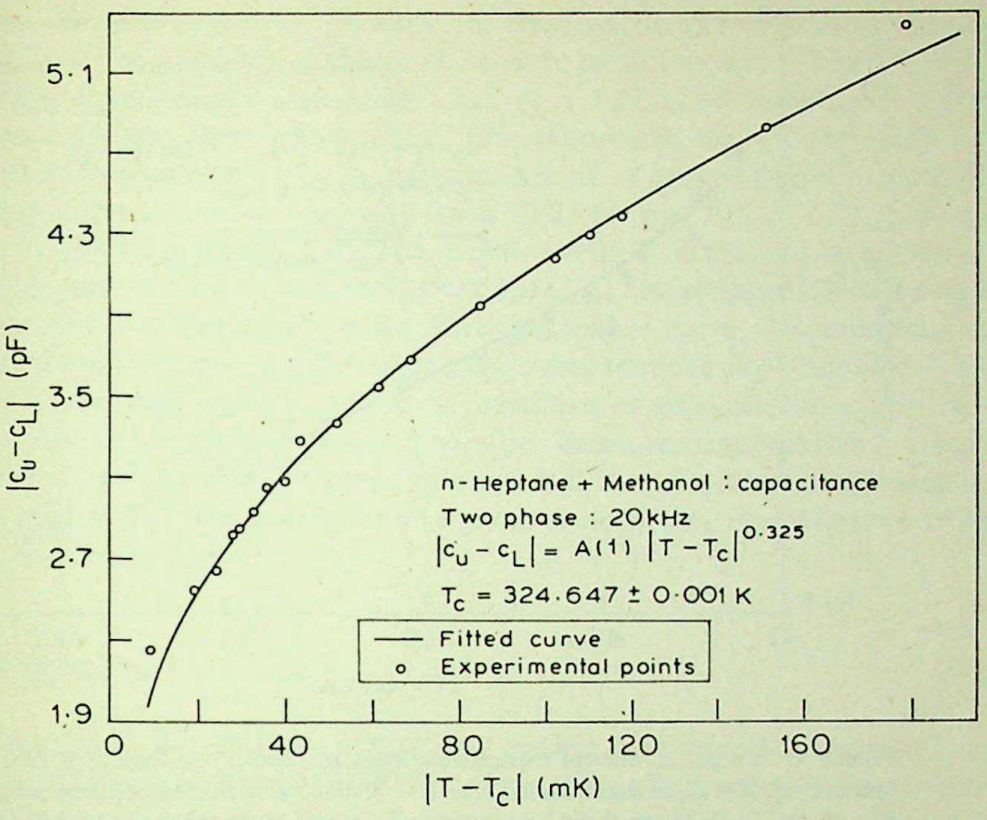

Figure 3. Order parameter $|c_u - c_L|$ as a function of $|T - T_c|$ in the two-phase region with $T_c = 324{\cdot}647$ K for $(T_c - 0{\cdot}200)$ K $< T < (T_c - 0{\cdot}008)$ K. c_u: capacitance from the upper electrode pair. For this system this is the *n*. heptane rich phase in the two-phase region. c_L: capacitance from the lower electrode pair, here methanol-rich phase. Solid line gives the fitted curve calculated from equation (3) and circles are the experimental points.

The number of unknowns is still too many in (5) to give reasonable parameter values and standard deviations. We first set $D(2) = 0$ being the background term valid far away from T_c. Next we studied the effect of dropping one term at a time on the values of χ_ν^2 and the standard deviations. The $t^{2\beta}$ term is found to give standard deviations $\simeq 50\%$ of the parameters. So this term is not justifiable. Thus we are left with

$$c_u = D(1) + D(3)\,|T - T_c|^{(1-\alpha)} + D(5)\,|T - T_c|^{\beta}. \tag{6}$$

$D(1)$ is varied in steps of 0·01 pF around the experimentally observed value 17·2398 pF (= 17·24 pF). Goodness of fit is closest to 1 when $D(1) = c_c = 17{\cdot}24$; the fitted parameters are $D(3) = -5{\cdot}23 + 0{\cdot}27$, $D(5) = -2{\cdot}40 \pm 0{\cdot}07$ and $\chi_\nu^2 = 0{\cdot}98$. The χ_ν^2 is not significantly different for $D(1) = c_c = 17{\cdot}23$ pF and 17·25 pF and so we take $c_c = 17{\cdot}24 \pm 0{\cdot}01$. Figure 4 gives the fitted curve and experimental points.

3.2 *Analysis of the one-phase data*

In the one-phase region we have used the data set in the temperature range 9 mK to 200 mK above T_c. Here an uncertainty of 0·007 pF in c and 0·001 K in temperature is allowed. The exponent $(1 - \alpha)$ in equation (2) is floated in our analysis. That is, the capacitance is fitted to the functional form

$$c_u = c_c + C(1)\,(T - T_c)^{C(2)} + C(3)\,(T - T_c)^{(C(2)+0{\cdot}5)}, \quad T > T_c. \tag{7}$$

CC-0. In Public Domain. Gurukul Kangri Collection, Haridwar

Digitized by Arya Samaj Foundation Chennai and eGangotri

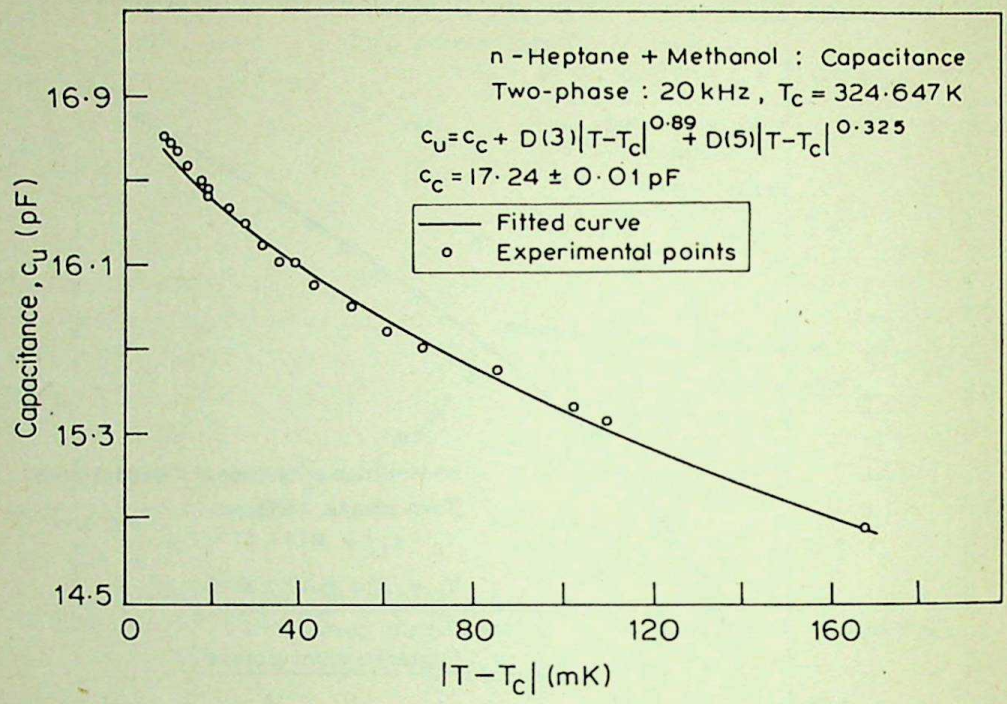

Figure 4. To get c_c, critical capacitance from the two-phase diameter. (See text). c_u as a function of $|T-T_c|$ in the two-phase for $T_c = 324{\cdot}647$ K in the temperature range $(T_c - 0{\cdot}200)$ K $< T < (T_c - 0{\cdot}008)$ K. Solid line is the fitted curve calculated from equation (6) and circles are the experimental points. c_c obtained is $17{\cdot}24 \pm 0{\cdot}01$ pF.

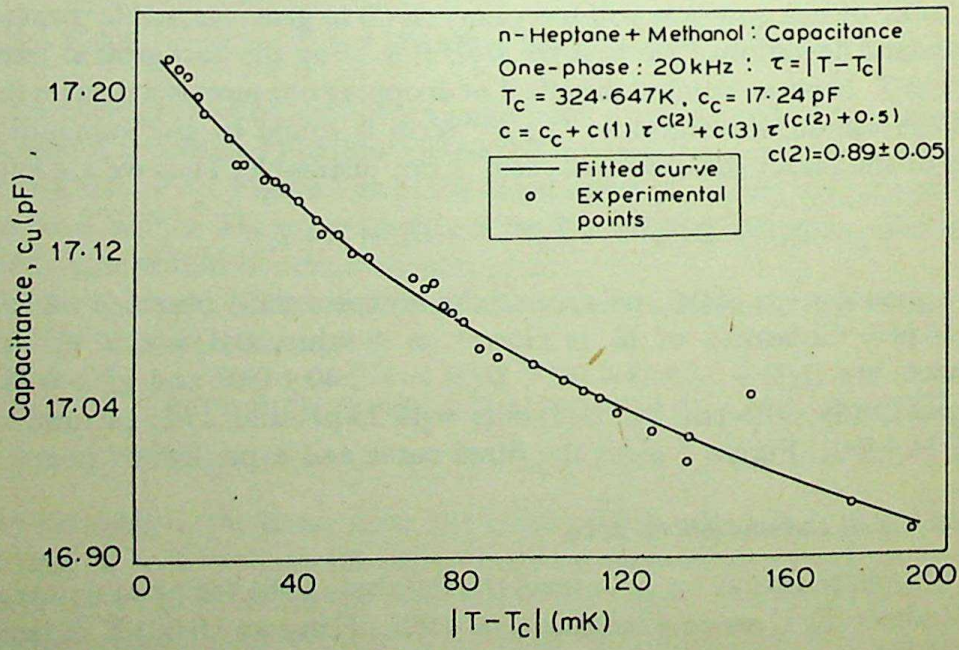

Figure 5. c_u as a function of $|T-T_c|$ in the one-phase region for $T_c = 324{\cdot}647$ K and $c_c = 17{\cdot}24$ pF (obtained from two-phase analysis) in the temperature range $(T_c + 0{\cdot}008)$ K $< T < (T_c + 0{\cdot}200)$ K. Solid line is the theoretical curve calculated from equation (5) and circles are experimental points. Exponent value obtained is $C(2) = 0{\cdot}89 \pm 0{\cdot}05$.

CC-0. In Public Domain. Gurukul Kangri Collection, Haridwar

Digitized by Arya Samaj Foundation Chennai and eGangotri

Since the data cover only 200 mK above T_c the linear term in equation (2) is not used. For $T_c = 324{\cdot}647$ K and $c_c = 17{\cdot}24$ pF the best fit parameters are $C(1) = -2{\cdot}18 \pm 0{\cdot}41$, $C(2) = 0{\cdot}89 \pm 0{\cdot}05$, $C(3) = 2{\cdot}36 \pm 0{\cdot}76$ and $\chi_\nu^2 = 1{\cdot}17$. The value $C(2) = 0{\cdot}89 \pm 0{\cdot}05$ corresponds to the exponent value. This supports the theoretically predicted $(1-\alpha) = 0{\cdot}89$ exponent for the dielectric constant of binary liquid system. The two-phase analysis gives c_c values ranging from 17·23 pF to 17·25 pF. The corresponding exponent values range from $1{\cdot}01 \pm 0{\cdot}05$ to $0{\cdot}80 \pm 0{\cdot}05$. One thus finds that the exponent value is fairly sensitive to the precise knowledge of c_c. The elimination of the data within ± 9 mk around T_c as the gravity affected region makes the c_c determination uncertain from mere data analysis—it is however interesting that the experimental T_c and c_c are recovered in the data analysis which is indicative of self-consistency of the various equations used in the critical region. Therefore measurements of higher accuracy in a system with a small gravity-affected region would be quite interesting. Such measurements are planned in the binary liquid system acetonitrile + cyclohexane which has a low gravity affected region.

Acknowledgements

The authors thank the DST and IISc-ISRO project for financial assistance in carrying out the work. They are grateful to CSIR for providing a fellowship to one of the authors (YJ). Finally the suggestions from the referees are gratefully acknowledged.

References

Arkhangelskii K V and Semencheko V K 1962 *Russ. J. Phys. Chem.* **36** 1358
Bevington P R 1969 *Data reduction and error analysis for the physical sciences* (New York: McGraw-Hill)
Chernova N I 1965 *Russ. J. Phys. Chem.* **39** 1275
Cohn R H and Greer S C 1986 *J. Phys. Chem.* **90** 4163
Gopal E S R, Lele M V, Ramakrishna J, Chandrasekhar P and Subramanyam S V 1976 *Pramana–J. Phys.* **7** 266
Goulon J, Greffe J L and Oxtoby D W 1979 *J. Chem. Phys.* **70** 4742
Greer S C and Jacobs D T 1980 *J. Phys. Chem. (USA)* **84** 2888
Gunasekaran M K, Gopal E S R, Shetty C and Jyothi S 1981 *J. Phys.* **E14** 381
Gunasekaran M K 1983 *Techniques and studies of electrical properties of critical binary liquid systems*, Ph.D. thesis, Indian Institute of Science, Bangalore
Gunasekaran M K, Guha S, Vani V and Gopal E S R 1985 *Ber. Bunsenges Phys. Chem.* **89** 1278
Jacobs D T and Greer S C 1981 *Phys. Rev.* **A24** 2075
Jyothi Balakrishnan, Gunasekaran M K and Gopal E S R 1984 *Indian J. Pure Appl. Phys.* **22** 286
Kumar N and Jayannavar A M 1981 *J. Phys.* **C14** L785
Mistura L 1973 *J. Chem. Phys.* **59** 4563
Ranjan M, Jayalaxmi Y, Vani V, Guha S and Gopal E S R 1986 *Indian J. Phys.* **A60** 98
Sengers J V, Bedeaux D, Mazur P and Greer S C 1980 *Physica* **A104** 573
Shetty C, Gunasekaran M K, Vani V and Gopal E S R 1983 *Pramana–J. Phys.* **21** 71
Stell G and Hoye J S 1974 *Phys. Rev. Lett.* **33** 1268
Theon J, Kindt R and Van Dael W 1981 *Phys. Lett.* **A87** 73
Viswanathan B, Govindarajan K and Gopal E S R 1973 *Indian J. Pure Appl. Phys.* **11** 157

CC-0. In Public Domain. Gurukul Kangri Collection, Haridwar

Digitized by Arya Samaj Foundation Chennai and eGangotri

CC-0. In Public Domain. Gurukul Kangri Collection, Haridwar

Digitized by Arya Samaj Foundation Chennai and eGangotri

Pramāṇa – J. Phys., Vol. 28, No. 3, March 1987, pp. 277–285. © Printed in India.

Effects of various ambient-aging processes in chopped and non-chopped optical films

K VIJAYA, R K PURI and R N KAREKAR
Department of Physics, University of Poona, Pune 411 007, India

MS received 4 April 1985; revised 29 December 1986

Abstract. The effects of various ambients on the non-chopped and chopped films of cryolite, MgF_2 and mixed cryolite-MgF_2, as measured by ellipsometer, are reported. The moisture decreases the refractive index whereas an increase is observed in air and other ambients. In all the ambient-aging the chopped films show smaller changes (nearly half) in refractive index than non-chopped films. Aging seems to be due to three main processes, a long-term adsorption-like surface reaction and two short-term reactions.

Keywords. Optical films; aging; chopped films.

PACS Nos 78·65; 78·20; 68·55; 42·78

1. Introduction

Many workers (Holm and Christensen 1980; Kinoshita and Nishibori 1969; Koch 1965; Koppelmann *et al* 1961; Macleod 1976; Ogura *et al* 1975, 1976; Pulkar 1971) who studied the problem of aging of optical films have found it difficult to provide a solution to the problem on a generalized level. We had earlier reported a new technique of chopping the vapour stream during deposition which reduces the aging of the films in air (Vijaya *et al* 1980). In this paper we report further studies on chopped films.

2. Experimental

The films, both non-chopped and chopped (5–6 rot/sec) of cryolite, MgF_2 and mixed cryolite-MgF_2 obtained (Vijaya *et al* 1980) by vacuum evaporation (vacuum 2×10^{-5} torr, deposition rate 15 Å/sec) were subjected, for few hours (short term aging), to different ambients: (a) air at room temperature, (b) gaseous environment (O_2 and CO_2 separately) for 21 hr, (c) heat to 120°C in air for 3 hr (heat), (d) steam for 3 hr at a flow rate of 0·23 ml/sec along with heating of substrate to 120°C to avoid condensation, (e) saturated humid atmosphere at three temperatures: (1) 12°C low temperature (LTM), (2) 27°C room temperature (RTM), (3) 55°C high temperature (HTM), each for 3 hr.

The effect of repeated (i) RTM exposures (for few hours, but totalling upto about 150 hr) and (ii) RTM heat cycling few hours each, was further studied in greater detail (Vijaya 1982).

CC-0. In Public Domain. Gurukul Kangri Collection, Haridwar

Digitized by Arya Samaj Foundation Chennai and eGangotri

About 10 films were deposited per cycle of evaporation for the different ambient aging measurements. The chopped and non-chopped films were deposited in different cycles but under similar conditions. The films were studied over a thickness range 300 Å to 1400 Å. The initial thicknesses, d_f, were found by Fizeau fringe method and also by ellipsometer. For the sake of convenience the thickness was divided into two different ranges: (i) 300–600 Å or thin films (ii) 600–1400 Å or thick films. All these films were kept in normal atmosphere for a few days to see the effect of further "long term" aging.

3. Results

The typical changes (averaged over 30 readings) in refractive index, δn_f, under different conditions for all cryolite films are given in figure 1. The trends of the changes in MgF_2 and mixed cryolite-MgF_2 are similar (see Vijaya 1982 for details). The figure shows that, in general, for all films, the refractive index increases on exposure to air, gases, heat and steam. Next, though the refractive index decreases on exposure to humidity conditions it again increases, on further aging in air after the moisture exposure. One very

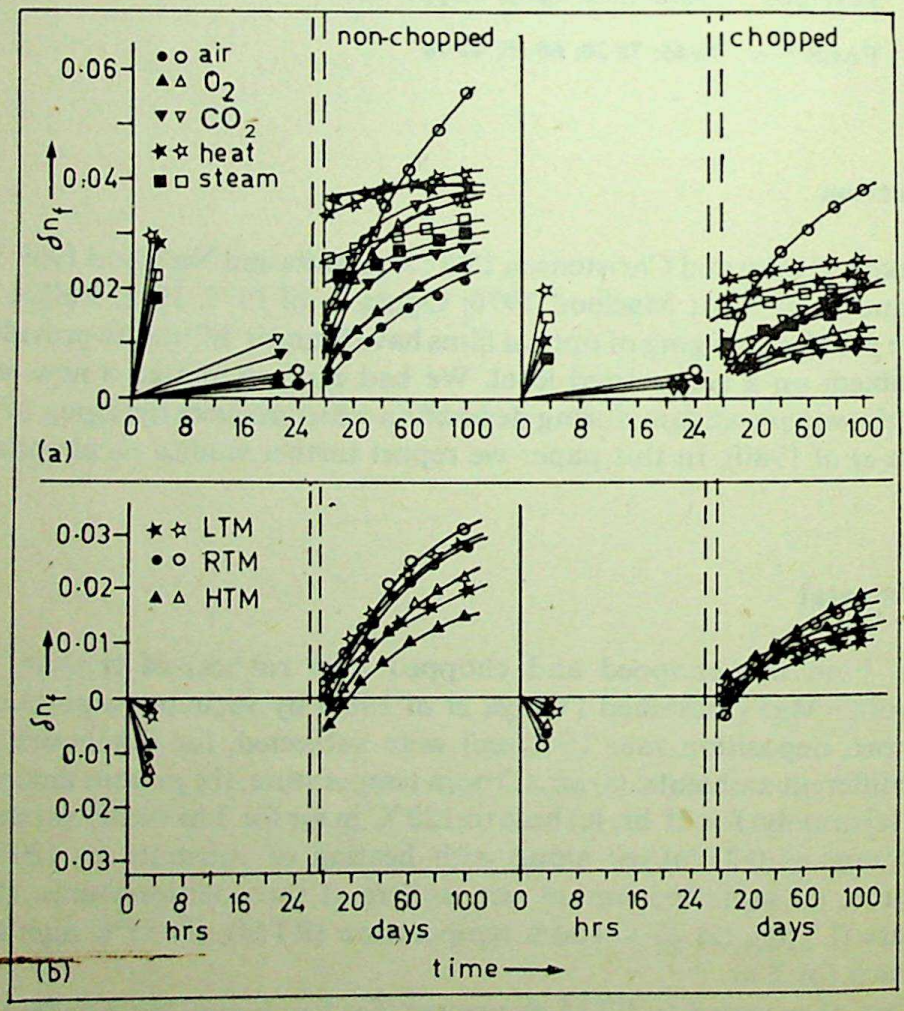

Figure 1. Average aging of cryolite films in different ambients. Open symbols—thin films; closed symbols—thick films.

CC-0. In Public Domain. Gurukul Kangri Collection, Haridwar

Digitized by Arya Samaj Foundation Chennai and eGangotri

significant result obtained is that, for all the ambients, the chopped films show lesser changes (almost 50 %) as compared to non-chopped films. Also, chopping reduces the thickness dependence of changes in refractive index. This is prominently seen in the scatter of the full data of the films (instead of averages (Vijaya 1982)).

Next, in almost all ambients there is an increase in film thickness by 50 to 100 Å (Table 1). The increase is greater ($\sim$ 100 Å) in MgF_2 and mixed cryolite-MgF_2 exposed to R.T. moisture.

Figure 1 shows that thin films (300–600 Å) show greater aging than thick films (600–1400 Å). Also the change in refractive index, δn_f, due to further air exposure (after pre-exposure to the various ambients), is comparatively smaller than that due to air exposure only.

Amongst the moisture ambients, films exposed to low temperature moisture (LTM), age the least. Exposure to moisture (especially RTM & HTM) tends to produce patches spoiling the films (table 2). About 10 % of films were thus spoiled. But the films exposed to hot moisture produce the highest percentage of spoilt films, probably due to condensation of water on the film. Table 2 also shows that chopping helps to reduce the spoiling in RTM, but in HTM it increases spoiling. HTM is apparently the only ambient where chopping deteriorates the optical films. The mixed films in RTM are not much helped by chopping.

The results with repeated RTM exposures have shown (Vijaya 1982) that after initial decrease of refractive index in about 24 hr, a saturation process is observed to occur on additional exposure. No further decrease occurs even upto 150 hr exposure. But for RTM-heat cycling exposures, it is seen (Vijaya 1982) that on each heating there is an increase in refractive index and on each moisture exposure the refractive index

Table 1. Average values of δd_f (Å) averaged over all thicknesses (error $\pm$ 25 Å).

	Average δd_f (Å)					
	Cryolite		MgF_2		Mixed cryolite-MgF_2	
Ambients	NC	C	NC	C	NC	C
Air	50	50	33	16	66	25
Gases	0	0	0	0	0	0
Further air	50	50	50	50	75	50
Heat	33	16	66	33	16	16
Further air	83	33	83	50	33	33
Steam	16	0	1[illegible]	16	16	16
Further air	16	42	50	33	33	33
LTM	0	0	0	50	75	50
Further air	25	25	75	125	88	125
RTM	0	0	83	83	117	50
Further air	25	50	142	125	158	100
HTM	0	0	50	0	—	—
Further air	50	50	150	50	—	—

NC: Non-chopped, C: Chopped.

CC-0. In Public Domain. Gurukul Kangri Collection, Haridwar

Digitized by Arya Samaj Foundation Chennai and eGangotri

Table 2. Spoil data of films under various ambients.

Ambient	Material		Total number of films	Number spoilt and %
RTM	Cryolite	NC	38	10 (33 %)
		C	28	0 (0 %)
	MgF_2	NC	35	5 (14 %)
		C	30	1 (3 %)
	Mixed	NC	35	12 (34 %)
	Cryolite-MgF_2	C	30	8 (26 %)
HTM	Cryolite	NC	8	3 (37 %)
		C	9	6 (66 %)
	MgF_2	NC	11	4 (36 %)
		C	11	6 (54 %)
	Mixed	NC	8	8 (100 %)
	Cryolite	C	6	6 (100 %)
	MgF_2			
All other ambients	All films		About 400	0 (0 %)

NC: Non-chopped, C: Chopped.

decreases. This trend is maintained even for 3–4 cycle (though slightly reduced) indicating that moisture absorption is partly a reversible phenomenon.

4. Discussion

Our results show that reducing the aging of optical films by chopping the vapour stream is advantageous since in most of the ambients the chopped films show lesser δn_f (about 50 %) than non-chopped films. Initially this was thought to be due to quenching of columnar crystal growth (Vijaya *et al* 1980). Our results however indicate that some other more dominant processes may also be operative. The aging phenomenon seems to be made up of two processes: (1) changes in refractive indices and (2) changes in geometrical thickness of the film, the former being normally more dominant.

There seems to be a difference in short-term and long-term aging (i.e. aging in few hours and few days respectively). From δn_f curves (figure 1) it appears that the aging process follows an exponential pattern expected of activation processes. Hence graphs of $\log(n_f)$ versus time were plotted which indicated that different types of processes are involved, given by straight lines with different slopes at different stages of aging. These slope values, under all ambients, have been plotted as scatter diagrams (figure 2), separately for (I) < 24 hr (II) 1 to 5 days and (III) > 5 days.

4.1 *Short-term ambient aging*

For short-term aging (< 24 hr see figure 2(I)) there are three dominant reaction groups for cryolite (figure 2a) and four reaction groups for MgF_2 (figure 2b) and mixed

CC-0. In Public Domain. Gurukul Kangri Collection, Haridwar

Digitized by Arya Samaj Foundation Chennai and eGangotri

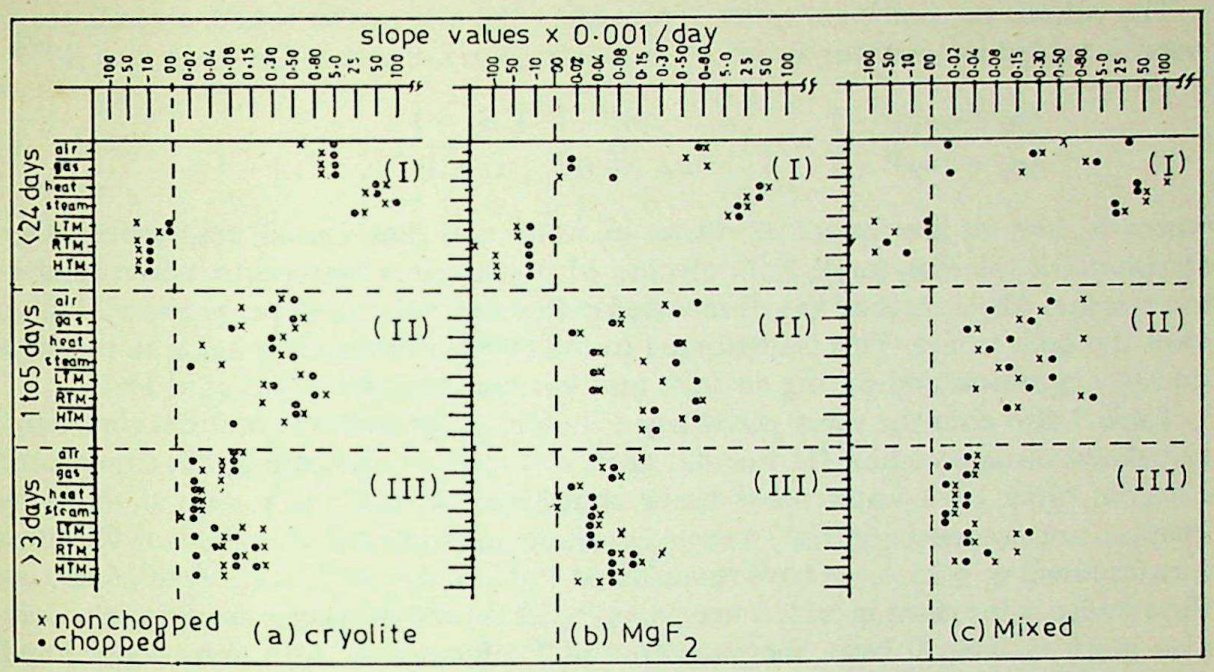

Figure 2. Scatter diagram of slope value for log (n_f) vs time curves, under different ambients (points in upper half are for thin films and those in lower half are for thick films, for each ambient).

cryolite-MgF_2 (figure 2c) films. One can distinguish 3 types of reactions: (1) air-dominant (low positive reaction rate $< 4 \times 10^{-3}$ /day); (2) temperature-dominant (high positive reaction rates in range 5×10^{-3}/day to 112×10^{-3}/day; (3) moisture-dominant (negative reaction rates in the range -3×10^{-3}/day to -112×10^{-3}/day).

In the air-dominant process, the adsorption of air/gas seems to be more important than oxidation. It is possible that, in the short time (few hours) allowed for this aging, the surface layer is easily affected (adsorption) which may not be much dependent on type of gas (air, O_2, CO_2), as in the case of chemical reactions. It can also be seen that for air-dominant process MgF_2 chopped films show different reaction rates ($0{\cdot}02 \times 10^{-3}$/day) than non-chopped films ($0{\cdot}7 \times 10^{-3}$/day to 4×10^{-3}/day). The mixed films, as expected, show the processes of both cryolite and MgF_2, though chopped mixed films behave more like MgF_2.

The process occurring due to heat and steam (large positive δn_f with slopes $> 4 \times 10^{-3}$/day) seem to be purely due to temperature effect. This may result in oxidation of films (or hydroxyl complex formation). There is a possibility of water desorption due to heating but not so for steam ambient.

For purely moisture-dominated process the slopes are negative. It can either be the moisture (a) filling up the pores (absorption) or (b) forming a layer (adsorption), which decreases the effective refractive index or (c) forming some hydroxyl complexes.

In room and high temperature moisture, the reaction seems to be the same, as indicated by slopes (average 37×10^{-3}/day and 38×10^{-3}/day) but in low temperature moisture the slope is lower (12×10^{-3}/day). At lower temperature, complex formation/absorption may be inhibited. But our special recycling experiments with moisture ambients have shown that this short-term moisture-dominant effect is reversible.

CC-0. In Public Domain. Gurukul Kangri Collection, Haridwar

Digitized by Arya Samaj Foundation Chennai and eGangotri

The volume percentage of water V present in the film can be found, assuming only water as added material for simplicity, and using the formula of De Rooji *et al* (1977).

$$\frac{(n_f+\delta n_f)^2-1}{(n_f+\delta n_f)^2+2}=\frac{d_f}{d_f+\delta d_f}\cdot\frac{n_f^2-1}{n_f^2+2}\cdot\frac{V n_\omega-1}{n_\omega+2}, \tag{1}$$

where n_ω and n_f are refractive indices of water and film (initial) respectively. Our ellipsometric values n_f (table 3) for cryolite, MgF_2 as well as the reported spectrophotometeric and Abele-method values reported earlier are in the same range and are higher than the bulk values. This is attributed to the effect of immediate aging in the films during deposition and during air inlet into vacuum chamber (Puri *et al* 1983).

Table 3 also gives the water percentage V in film under moisture ambient conditions, calculated using equation (1). For δd_f zero, it is negative indicating that either some material other than water needs to be considered or that the measured thickness changes are not very accurate. As our experimental accuracy of individual thickness measurement is ± 25 Å, we have recalculated V % for $\delta d_f = 25$ Å (instead of zero, as the average value given in table 1 may go up by 25 Å) and the corresponding values are also given in table 3. Next, the maximum of V obtained in both non-chopped and chopped films (13·8 % and 11·5 % respectively) is in RTM for MgF_2. In all cases, it is less in chopped than non-chopped films, indicating that water sorption is not just a top surface phenomenon. Probably crystal quenching reduces the porosity of chopped films, giving lesser sorption of water.

The large sorption capacity of water by MgF_2 film need not only be due to the loose-packed structure (higher porosity) of the film as assumed above but can also be due to the high polarity of MgF_2 valence bonds, whereby the high electronegative fluorine is replaced (Koch 1965). We have indicated the possibility of such complexes being formed in our fresh films from refractive index and electron diffraction data (Puri *et al* 1983).

4.2 *Long-term further aging in air*

For δn_f vs time curves, the observations that (i) films exposed to moisture for a short period, on further exposure to air (figure 1b) change from negative slopes back to positive (as for air only aging figure 1a) and (ii) the cycling experiment gives negative and positive slopes during alternate moisture and heat exposures, indicate that the moisture reaction is reversible and different from air, with a fast reaction rate (-50×10^{-3}/day) compared to air ($0{\cdot}10\times10^{-3}$/day). Naturally this reaction will not be observed in long-term aging (figure 2, II & III) and, even if exposed to moisture for longer time, it will give saturation.

The same is also true about the other fast ($+50\times10^{-3}$/day), temperature-dominant reaction (oxidation) observed during the first 24 hr. Here the reaction rate R may even be slowed down due to the reduced temperature according to equation

$$R = \mathrm{d}C/\mathrm{d}t = C_0 \exp(-E/kT), \tag{2}$$

where C_0 is the concentration of a reactant. The order of magnitude calculations indicate that R of $\sim 72\times10^{-3}$/day at 120°C will reduce to $0{\cdot}08\times10^{-3}$/day at 25°C. The latter is just the reaction rate for air-dominant processes ($0{\cdot}10\times10^{-3}$/day). This gas adsorption reaction can surely continue to be present in long-term aging. But

CC-0. In Public Domain. Gurukul Kangri Collection, Haridwar

Table 3. Volume percentage (V) of water under different moisture conditions for 3 hr exposure (for thin films). Values of V%, in brackets, are calculated assuming thickness to be 25 Å instead of zero.

Material		Initial thickness d_f Å	Initial n_f	LTM			RTM			HTM		
				δd_f	δn_f	V	δd_f	δn_f	V	δd_f	δn_f	V
Cryolite	NC	550	1·391	0	−0·003	−0·8 (4·4)	50	−0·015	5·7	50	−0·014	5·9
	C	500	1·401	0	−0·003	−0·8 (4·3)	0	−0·009	−2·3 (3·2)	0	−0·003	−0·8 (4·3)
MgF_2	NC	400	1·430	0	−0·015	−3·9 (3·5)	100	−0·042	13·8	50	−0·035	4·6
	C	450	1·463	100	−0·006	2·3	50	−0·008	11·5	0	−0·014	−3·9 (3·5)
Mixed cryolite MgF_2	NC	500	1·409	100	−0·022	5·2	100	−0·042	9·1	—	—	—
	C	400	1·433	50	−0·004	1·3	50	−0·029	6·7	—	—	—

NC: Non-chopped, C: Chopped.

Digitized by Arya Samaj Foundation Chennai and eGangotri

CC-0. In Public Domain. Gurukul Kangri Collection, Haridwar

Digitized by Arya Samaj Foundation Chennai and eGangotri

figure 2 also shows that this rate decreases progressively with time from (I) 24 hr to (III) > 5 days. This may be due to decrease in effective concentration, because of surface coverage on longer exposure. Apparently the reaction is one and the same, as shown by the smooth variation of the rate.

4.3 *Role of chopping in aging reduction*

It is generally observed in our experiments that the chopping of the vapour flow during deposition, increases the initial refractive index of the films as compared to non-chopped films (Puri *et al* 1983), indicating that chopping may enhance the immediate aging that is taking place within a few minutes of deposition. Our results show that this immediate enhanced aging also helps in reducing the further short-term (in hours) and long-term (in days) aging.

If the columnar growth and corresponding structure with voids (to be filled just by water on exposure, without any other reactions) were the only reasons for the aging of the films, then the chopping would have reduced the aging permanently by quenching the columnar growth, obtained, as shown by electron diffraction pattern (Puri *et al* 1983). But as even the chopped films show changes on short-term ambient aging and further long-term air aging, the additional and dominant reactions, indicated above, seem to be the main reason for aging the optical films. The observed reduction in aging, on chopping, seems to be due to the initially enhanced immediate aging (i) in vacuum system itself due to trapping of air between the chopped layers and (ii) just on opening the vacuum system, which may be due to larger grain boundaries available in chopped films. Such an enhanced aging will reduce the later short- and long-term aging due to slowed reaction rates (equation (2)) because of reduction in concentration (by nonavailability of reactants due to reduced available surface area).

4.4 *Thickness effects on aging*

Figure 2 shows that, in general, the thick films show a slower reaction rate than thin films, prominently so for 0–5 days air-aging. The thin films having more voids compared to thick films, might offer a greater surface area (effective concentration) for reactions to occur.

All the films show an increase in thickness (table 1) on aging. This increase is mainly seen for temperature-ambient and long-term air exposure but the short-term moisture exposure gives very little change in thickness. It may be noted that this process is expected to be reversible as well.

In the case of MgF_2 films, for example, there is a possibility of $Mg(OH)_2$ complex being formed slowly in air or on heating. The molar volume of $Mg(OH)_2$ is higher (24·6) than that of MgF_2 (19·6) and for MgO it is still lesser (11·2). The possibility of formation of hydroxyl compounds, like $Mg(OH)_2$, might be responsible for the increase in thickness. This supports an assumption of slow complex formation rather than oxidation phenomenon.

References

De Rooji N F, Sieverdink R J S and Tromp R M 1977 *Thin Solid Films* **47** 211
Holm N F and Christensen O 1980 *Thin Solid Films* **67** 239

CC-0. In Public Domain. Gurukul Kangri Collection, Haridwar

Digitized by Arya Samaj Foundation Chennai and eGangotri

Kinosita K and Nishibori M 1969 *J. Vac. Sci. Technol.* **6** 730
Koch H 1965 *Phys. Status Solidi* **12** 533
Koppelmann G, Kerbs K and Leyendecker H 1961 *Z. Phys.* **163** 557
Macleod H A 1976 *Thin Solid Films* **34** 335
Ogura S, Sugawara N and Higara R 1975 *Thin Solid Films* **30** 3
Pulkar H K 1971 *Thin Solid Films* **9** 57
Puri R K, Vijaya K and Karekar R N 1983 *Pramana–J. Phys.* **21** 311
Vijaya K, Puri R K and Karekar R N 1980 *Thin Solid Films* **70** 105
Vijaya K 1982 *Ellipsometric study of the changes in optical properties (aging) of non-chopped and chopped films of cryolite, MgF, ZnS and their co-deposited mixtures in various ambients*, Ph.D. thesis, Poona University

CC-0. In Public Domain. Gurukul Kangri Collection, Haridwar

Digitized by Arya Samaj Foundation Chennai and eGangotri

CC-0. In Public Domain. Gurukul Kangri Collection, Haridwar

Digitized by Arya Samaj Foundation Chennai and eGangotri

Pramāṇa – J. Phys., Vol. 28, No. 3, March 1987, pp. 287–292. © Printed in India.

Phonon dispersion curves of transition metals using modified general tensor force model

SATISH KUMAR MAHNA
Department of Applied Physics, Regional Engineering College, Kurukshetra 132 119, India

MS received 24 November 1986; revised 19 January 1987

Abstract. The general tensor force model has been modified by incorporating separately the electron-ion interactions. The model satisfies the translational symmetry requirements of the lattice and is used to obtain the phonon dispersion curves of chromium, molybdenum and tungsten. The agreement between the theoretical and experimental frequencies is very good.

Keywords. Umklapp processes; dispersion curves; transition metals; interference factor; tensor force.

PACS No. 63·20

1. Introduction

The general tensor force model (Begbie and Born 1947) which assumes the atomic interactions to be two-body interactions but imposes no restriction on the nature of such interactions has so far been used, with large number of force constants, mainly to analyze the experimental dispersion curves of solids. However, recently Ramamurthy and Satish Kumar (1985) used this model by incorporating volume forces separately to study the lattice dynamics of alkali metals and obtained excellent results for all alkali metals including the cross-over of lithium branches along [ζ00] direction, without violating the translational symmetry requirements of the lattice. Inspired by the success of the model we have attempted to extend it to the study of transition metals with bcc structure. Our motivation for such studies is from the fact that these metals are more complicated as their conduction electrons are relatively less free and their number per unit volume is not fixed as they lie in the (Spd) hybrid states. Large values of their elastic constants indicate strong electron-ion interactions having considerable influence over the computed phonons and therefore these metals will provide a rigorous test for this model. This paper, therefore, deals with the study of chromium, molybdenum and tungsten belonging to VIB group. Such studies for the VB group will be reported later.

2. Theory

To obtain the phonon frequencies, the ion-ion interactions are expressed in terms of tensor forces (Begbie and Born 1947) and the electron-ion interactions in terms of the volume forces which satisfy the translational symmetry requirements of the lattice. Restricting the range of ion-ion interactions upto the third nearest neighbour

CC-0. In Public Domain. Gurukul Kangri Collection, Haridwar

Digitized by Arya Samaj Foundation Chennai and eGangotri

interaction, the diagonal and off-diagonal elements of the matrix D^i could be written as

$$M D^i_{xx} = 4\{2\sigma_1(1 - C_x C_y C_z) + \sigma_2 S_x^2 + \lambda_2 (S_y^2 + S_z^2) + \sigma_3[2 - C_{2x}(C_{2y} + C_{2z})] + \lambda_3(1 - C_{2y} C_{2z})\}$$

and

$$M D^i_{xy} = 4[2\tau_1 S_x S_y C_z + \tau_3 S_{2x} S_{2y}], \tag{1}$$

where $S_x = \sin(\pi\zeta_x)$, $S_{2x} = \sin(2\pi\zeta_x)$, $C_x = \cos(\pi\zeta_x)$ and $C_{2x} = \cos(2\pi\zeta_x)$, M is the mass of the ion, $\zeta_x = q_x/q_{\max} = (a/2\pi)\, q_{\max}$, a is the lattice parameter and σ_n, λ_n, τ_n are the nth neighbour tensor force constants.

The elements of the matrix D^e which include contributions from umklapp processes are given by (Ramamurthy and Satish Kumar 1984)

$$M D^e_{xy} = \frac{C'}{2}\left[\sum_g \frac{(\mathbf{g}-\mathbf{q})_x (\mathbf{g}-\mathbf{q})_y S(\mathbf{g}-\mathbf{q})\, F(g-q)}{g - q^2 + F(g-q)/a^2}\right], \tag{2}$$

where C' is the constant related to the bulk modulus of the electron gas, $\mathbf{g}$ is a reciprocal lattice vector, $S(\eta)$ is the interference factor and its values for the exact shape of atomic polyhedron for bcc structure have been taken from the work of Ramamurthy (1978). $F(\eta)$ is the screening function and the Taylor (1978) function has been used in the present work.

3. Numerical computation

The evaluation of seven GTF constants and C' that appear in the dynamical matrix elements is carried out using the experimental values of the elastic constants and the

Table 1. Relevant input data used for evaluation of force constants.

(a) Atomic mass, lattice parameter and elastic constants

Metal	M (10^{-27} kg)	Lattice constant (Å)	Elastic constants (10^{10} Nm^{-2}) C_{11}	C_{12}	C_{44}	Ref.
Chromium	86·31	2·89	35·00	6·78	10·10	Boley and Clark (1963)
Molybdenum	159·30	3·147	44·08	17·24	12·17	Featherman and Neighbours (1963)
Tungsten	305·21	3·161	52·30	20·45	16·07	Featherman and Neighbours (1963)

(b) Experimental zone boundary frequencies (THz)

Metal	$\nu_{LT(100)}$	$\nu_{LT(\frac{1}{2}\frac{1}{2}\frac{1}{2})}$	$\nu_{L(\frac{1}{2}\frac{1}{2}0)}$	$\nu_{T_1(\frac{1}{2}\frac{1}{2}0)}$	$\nu_{T_2(\frac{1}{2}\frac{1}{2}0)}$	Ref.
Chromium	7·90	8·50	9·20	7·90	5·90	Shaw and Muhlestein (1971)
Molybdenum	5·50	6·55	8·16	5·75	4·65	Powell *et al* (1968)
Tungsten	5·60	5·51	6·75	4·63	4·15	Chen and Brockhouse (1964)

CC-0. In Public Domain. Gurukul Kangri Collection, Haridwar

Digitized by Arya Samaj Foundation Chennai and eGangotri

zone boundary frequencies along the principal symmetry directions limiting the summation to $g \leqslant \sqrt{60}$ since the summation showed convergence at this limit. The necessary data used and the numerical values of the force constants so obtained for chromium, molybdenum and tungsten are given in tables 1 and 2 respectively. Using

Table 2. Numerical values of force constants in (10^{-1} Nm^{-1}).

Force constant	Chromium	Molybdenum	Tungsten
σ_1	10184	5465	10322
σ_2	30119	34866	26879
σ_3	1443	4579	6715
λ_2	1124	683	1028
λ_3	194	1921	309
τ_1	3583	6139	3611
τ_3	1937	3163	1569
C'	18920	42688	88445

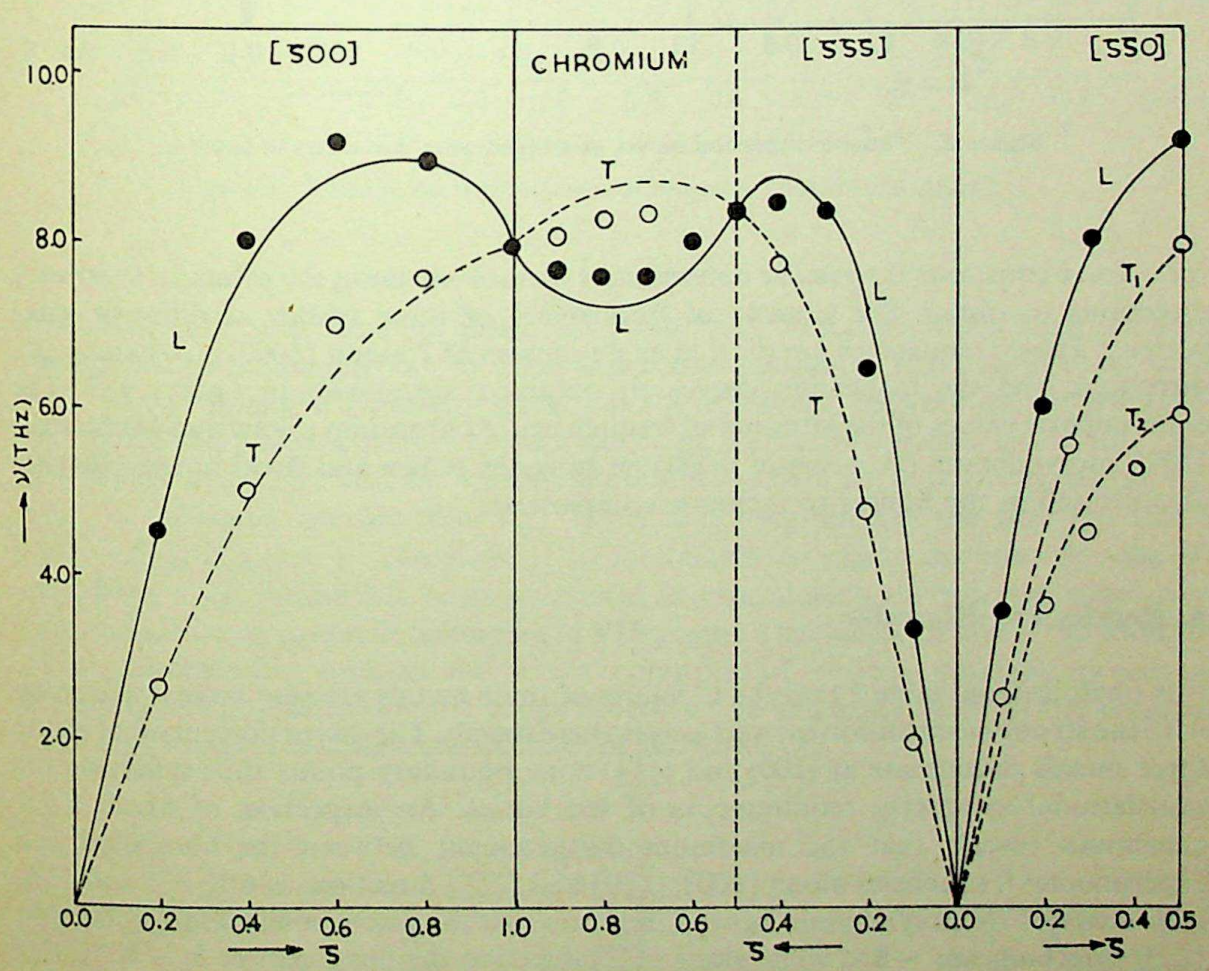

Figure 1. Phonon dispersion curves of chromium along [ζζζ], [ζζζ] and [ζζ0] direction. Longitudinal (——); Transverse (– – – – – –). Experimental values: Longitudinal (●); Transverse (○).

CC-0. In Public Domain. Gurukul Kangri Collection, Haridwar

Digitized by Arya Samaj Foundation Chennai and eGangotri

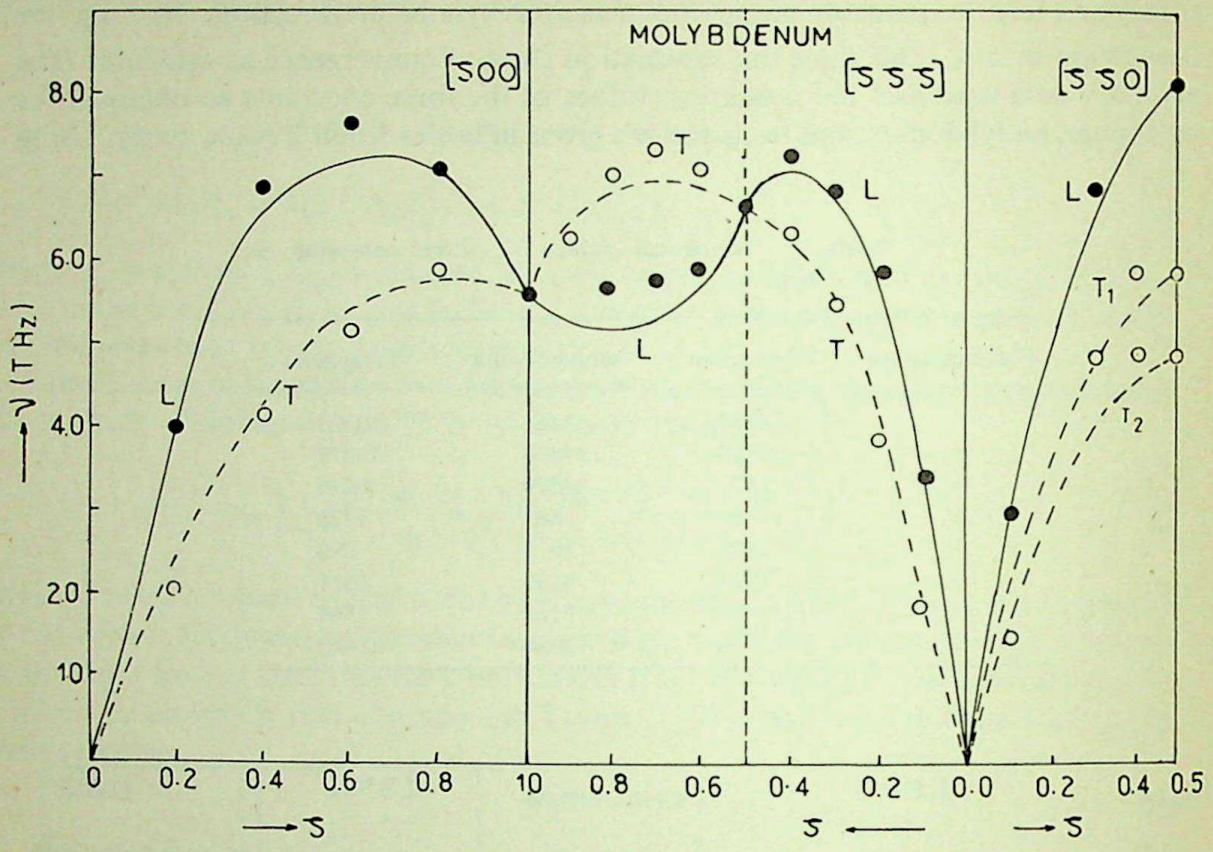

Figure 2. Phonon dispersion curves of molybdenum. Details as in figure 1.

these force constants the secular determinant was solved along the principal symmetry directions to obtain the vibrational frequencies of these metals at different wave vectors. These frequencies are plotted as a function of ζ along [ζ00], [$\zeta\zeta$0] and [$\zeta\zeta\zeta$] directions and the dispersion curves so obtained are shown in figures 1–3. The experimental values of the vibrational frequencies of chromium (Shaw and Muhlestein 1971), molybdenum (Powel *et al* 1968) and tungsten (Chen and Brockhouse 1964) are also plotted in the figures to facilitate comparison.

4. Results and discussion

It is obvious from table 2 that the C' values of these metals are very large conforming with the strong electron-ion interactions in these metals. The dispersion curves of all the three metals degenerate at (100) and $(\frac{1}{2}\frac{1}{2}\frac{1}{2})$ zone boundary points thus satisfying the translational symmetry requirements of the lattice. An inspection of figure 1 for chromium reveals that the maximum disagreement between the computed and experimental frequencies along [ζ00], [$\zeta\zeta$0] and [$\zeta\zeta\zeta$] directions is 6%, 8% and 12% respectively. For molybdenum figure 2 indicates that the discrepancies along [ζ00] and [$\zeta\zeta$0] directions are $\sim$8% while along [$\zeta\zeta\zeta$] direction the disagreement is $\sim$10%. For tungsten the maximum discrepancy along [$\zeta\zeta\zeta$] L is $\sim$8% and 5% along all other directions. In the experimental dispersion curves of chromium and molybdenum, Kohn

CC-0. In Public Domain. Gurukul Kangri Collection, Haridwar

Digitized by Arya Samaj Foundation Chennai and eGangotri

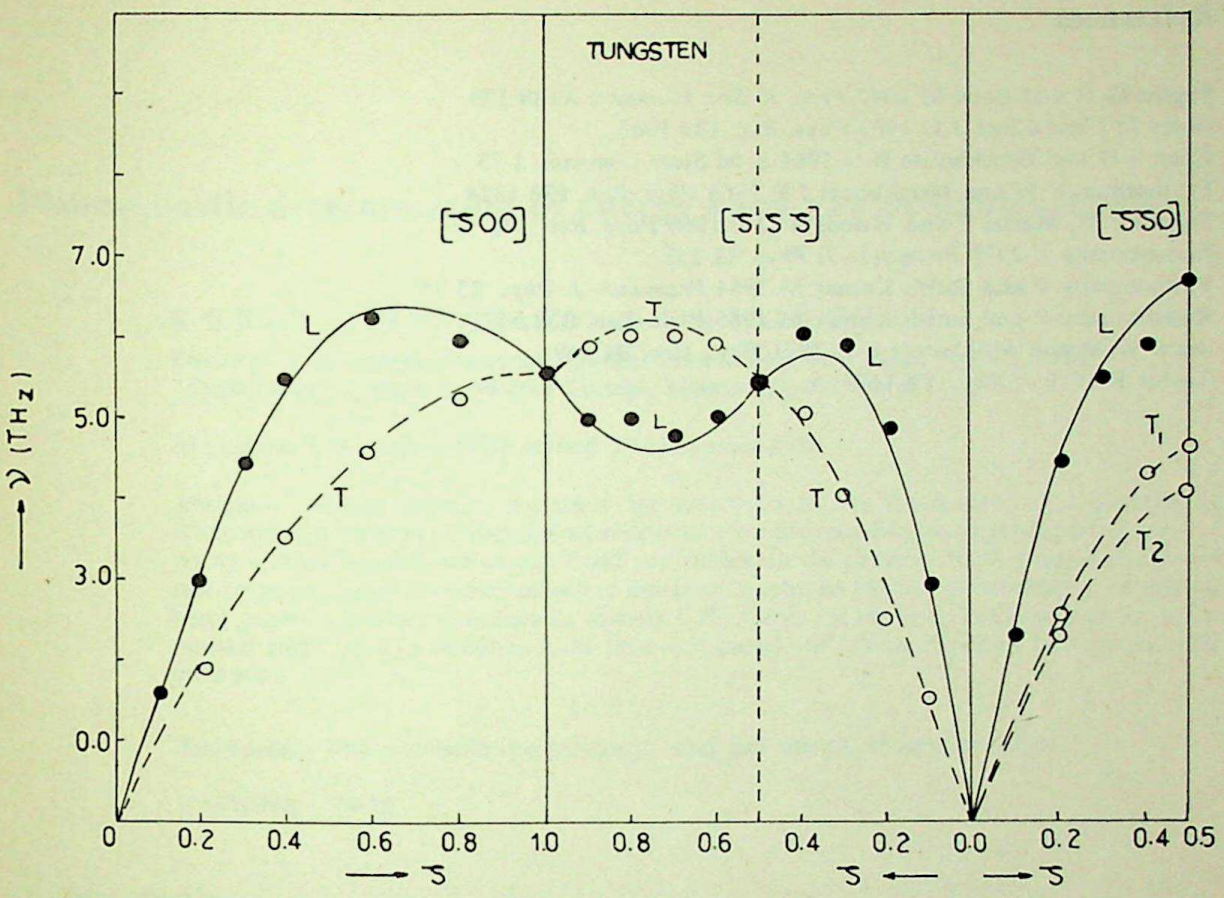

Figure 3. Phonon dispersion curves of tungsten. Details as in figure 1.

anomalies have been observed along [ζ00] and [ζζζ] directions which have not been reproduced by the present or any other force constant model. However at other wave vectors in all principal symmetry directions the agreement between the experimental and theoretical phonon frequencies is quite good. Further the metals under study are very typical ones. For instance, chromium is a metal with cubic structure but its C_{12} value is unusually smaller than C_{44} value, and tungsten has the isotropy factor $[(C_{11}-C_{12})/2C_{44}] \approx 1$. Therefore it is reasonable to claim that the present III neighbour GTF model has been successful in reproducing the phonon dispersion curves of all the three metals belonging to VIB group. This success is due to the addition of the electron-ion interactions which comprise of besides umklapp processes, screening function satisfying the compressibility rule and exact shape of the Wegner-Seitz cell, which is tetrakaideca hadron for bcc structure.

Acknowledgements

The author is grateful to Dr V Ramamurthy of IIT, Delhi and Dr S B Rajendra Prasad for many valuable and stimulating discussions.

CC-0. In Public Domain. Gurukul Kangri Collection, Haridwar

Digitized by Arya Samaj Foundation Chennai and eGangotri

References

Begbie G H and Born M 1947 *Proc. R. Soc.* (*London*) **A188** 179
Boley D I and Clark J D 1963 *Phys. Rev.* **129** 1063
Chen S H and Brockhouse B N 1964 *Solid State Commun.* **2** 73
Featherman F W and Neighbours J R 1963 *Phys. Rev.* **130** 1324
Powell B N, Martel P and Woods A D B 1968 *Phys. Rev.* **171** 73
Ramamurthy V 1978 *Pramana–J. Phys.* **11** 233
Ramamurthy V and Satish Kumar M 1984 *Pramana–J. Phys.* **23** 751
Ramamurthy V and Satish Kumar M 1985 *Phys. Rev.* **B32** 5471
Shaw W M and Muhlestein L D 1971 *Phys. Rev.* **B4** 969
Taylor R 1978 *J. Phys.* **F8** 1699

CC-0. In Public Domain. Gurukul Kangri Collection, Haridwar

Digitized by Arya Samaj Foundation Chennai and eGangotri

Pramāṇa – J. Phys., Vol. 28, No. 3, March 1987, pp. 293–297. © Printed in India.

Photoacoustic determination of energy band gap of semiconductors

R S RAM, OM PRAKASH and A N PANDEY*
Division of Standards, National Physical Laboratory, New Delhi 110012, India
*Department of Physics, Meerut College, Meerut 250001, India

MS received 21 August 1986; revised 24 December 1986

Abstract. Semiconducting materials are employed in the fabrication of a number of semiconductor devices and opto-electronic detectors etc depending on their properties, state of purity and perfection and energy band gap values. In the present study, a latest and novel photoacoustic spectroscopic technique has been employed for the determination of energy band gap of some semiconductors namely CdS, CdSe, CdTe, ZnS, ZnO, Se and Si in the powder form. Values obtained have been compared with those reported by conventional methods.

Keywords. Photoacoustic spectroscopy; band gap energy; absorption edge.

PACS No. 78·20

1. Introduction

A gap present (Dance 1969) between valence and conduction bands of a semiconductor greatly influences the latter's properties. The determination of energy band gap of semiconductors (Dance 1969; Ray 1969; Smith 1968; Gibson 1958; Nudelman and Mitra 1969) is an important parameter for their applications in research and industry. As most of the semiconductors (Pao 1977) are found in the form of powder and tiny particles of opaque nature, they pose difficulties in their conventional transmission or reflection measurements. In the reflection measurement, the sample should be ground and polished to increase its reflectivity and effective area. In the transmission measurement the sample should be grown into a large and transparent crystal. With the advent of modern technology of forming films of materials, the above difficulties are overcome easily. A method was devised for the determination of absorption band edge by measurement of reflection coefficients of material's film evaporated in the vacuum (O'Bryan 1936). In the case of some semiconductors, the edge of the fundamental optical absorption band can also be estimated by measuring the absorption coefficients at different wavelengths. A criterion for determining the width of the forbidden band in insulators and semiconductors is given by the variation with wavelength of the photoelectromagnetic (PEM) effect (Gibson 1958). The band gap energy of semiconductor used in a p.n. junction can be estimated (Despande 1975) by measuring the saturation current (I_s) at different temperatures T (lower than the room temperature) and the energy band gap is estimated from the shape of the graph $\log I_s$ vs $1/T$, with an accuracy of $\pm 0{\cdot}1$ eV. The other methods for locating the absorption band edge are based on the principles of (i) pressure dependence (Ray 1969) of the absorption edge, (ii) magneto-optical effects and cyclotron resonance measurement (Moss 1961),

CC-0. In Public Domain. Gurukul Kangri Collection, Haridwar

Digitized by Arya Samaj Foundation Chennai and eGangotri

(iii) optical reflectance modulation technique and (iv) electro-reflectance and thermo-reflectance (Gutsche and Lange 1967; Lange and Henrion 1967).

In the present study the latest and novel photoacoustic spectroscopic technique (Pao 1977) has been employed to determine the band gap energy of semiconductors like CdS, CdSe, CdTe, ZnO, ZnS, Se and Si. The values thus obtained have been compared with those reported in the literature.

2. Experimental procedure

In the present investigation, a double beam photoacoustic spectrophotometer (Bhide *et al* 1983) designed and developed in this laboratory was used to record the photoacoustic absorption spectra of CdS, CdSe, CdTe, ZnS, ZnO, Se and Si samples in powder form. CdS (99·999), CdSe (99·99), CdTe (99·999) and ZnS (99·900) were compounds taken from M/s Balzer's coating materials, Se metal (spec. pure, purity not mentioned) was from M/s Thomas Baker, London, ZnO (A.R. grade) was obtained from M/s BDH and Si (99·999) was developed at the Materials Division of this laboratory. In this method no sample preparation is needed and the sample as such is put in the photoacoustic cell and the required spectra is recorded nondestructively. About 500 mg of each sample was found to be sufficient for recording the spectra. Once all the parameters are set, it took hardly ten minutes to record the spectra, and these are shown in figures 1–3.

3. Results and discussion

Photoacoustic absorption spectra of direct band gap semiconductors (CdS, CdSe, CdTe, ZnS, ZnO and Se) and indirect band gap semiconductor (Si) (figures 1–3) show that on the shorter wavelength side of the absorption edge, the value of the absorption coefficient increases rapidly upto a certain value for CdS, CdSe, CdTe, ZnS, ZnO and

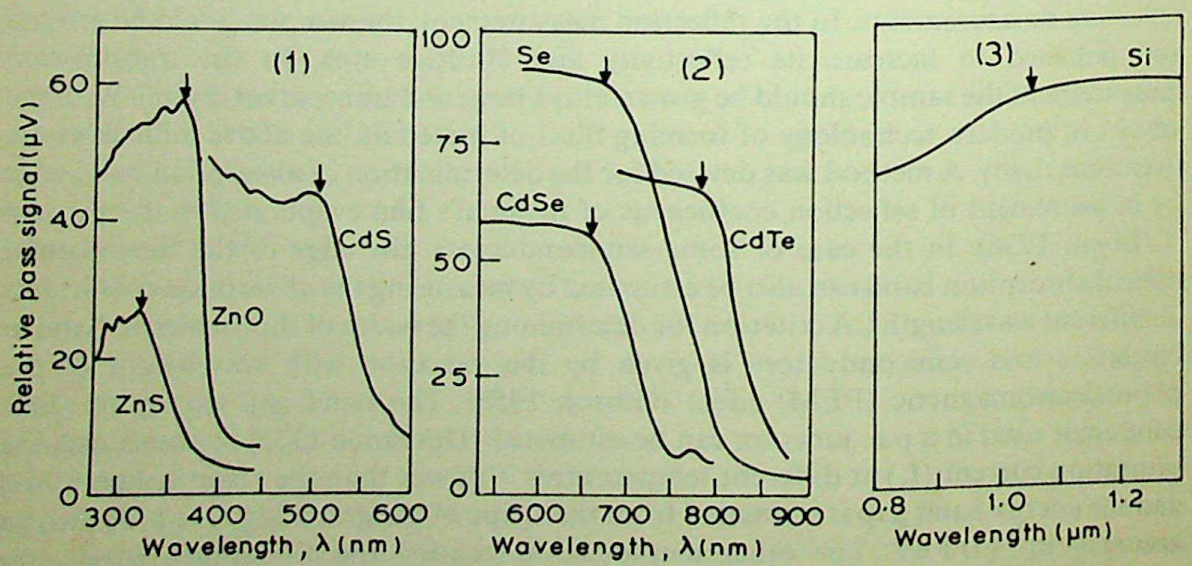

Figure 1, 2, 3. Photoacoustic spectra of CdS, ZnS, ZnO, CdSe, CdTe, Se and Si semiconductor powders.

CC-0. In Public Domain. Gurukul Kangri Collection, Haridwar

Digitized by Arya Samaj Foundation Chennai and eGangotri

Se, and then remains fairly constant over a considerable range of wavelength for CdSe, CdTe and Se. In the case of CdS and ZnO it increased further upto a certain extent. Similar results have been reported in the literature (Smith 1968). The absorption spectra of ZnS show a few absorption peaks on the shorter wavelength side of the absorption edge and these may be due to absorption by impurities (Nudelman and Mitra 1969) present in the sample. The absorption spectra of Si do not show a sharp absorption edge. The formation of an absorption edge in a semiconductor can be explained as follows.

In a semiconductor, the absorption of photons induces transitions of electrons from valence to conduction bands. These transitions are of two types namely direct and indirect transitions. In direct transitions no change in the K-value of electron takes place i.e. the valence and conduction bands extrema are located in the same point in the Brillouin zone, for example in CdS, CdSe, etc whereas indirect transitions (Miller 1983) take place between the maxima of a valence band and the minima of the conduction band of K-space. In other words, the band extrema differ in their position in K-space, e.g. in Si. For indirect transitions, the annihilation or creation of phonons (Ray 1969) to balance the crystal momentum is needed, whereas for direct transitions no phonon effect is required. Therefore, the absorption edges in direct type semiconductors are formed in the direction opposite to that of the indirect type semiconductors. Hence by recording the PAS absorption spectra one can easily distinguish between direct and indirect band gap semiconductors.

It has been found that absorption edges produced by direct band semiconductors are sharper than those produced by indirect band semiconductors. This also agrees with the results of Pao (1977). This is because the increase observed in the absorption (10^4 to 10^5 cm^{-1}) of photons of energies $h\nu > E_g$ allows one to estimate the value of the forbidden band width in direct band gap semiconductors. However, in indirect band gap semiconductors, transitions are due to low absorption at longer wavelengths. Further if there is an appreciable concentration of free carriers in the conduction or valence band the general level of absorption (Ray 1969) increases creating difficulties in the location of edge which generally depends on the absorption coefficient of 10 cm^{-1}.

The PAS spectra of CdTe, Si and ZnO have been recorded for the first time. However for other semiconductors (CdS, CdSe and ZnS) the values were reported by earlier workers (Rosencwaig 1980; Lyamov *et al* 1979). The latter workers had recorded the PAS spectra of CdS in powder and single crystal forms and found that the absorption edges in both cases correspond to the same energy band gap value, the only difference being that in the powder sample, the signal-to-noise ratio is improved.

It is evident from each spectrum that absorption is enhanced suddenly near a particular wavelength which forms the band edge. To estimate nearly the correct value of the band edge, tangents have been drawn at a point on either side of the edges in the spectral curve where the curve starts bending from its straight portion to form the edge. The cross-sectional points of these tangents give the approximate value of wavelength corresponding to the band edge. The energy band gap has been calculated by using the relation (Weast 1977), E_g (eV) = $1239{\cdot}5/\lambda$ (nm). The present values have been compared with those reported in literature and are given in table 1.

There is slight difference between the estimated and reported values of energy band gaps. This is because the earlier values are generally from crystallographic studies (Weast 1977) whereas in the present study the samples used are powders with some impurity centres. Further there may be many problems regarding the electronic

CC-0. In Public Domain. Gurukul Kangri Collection, Haridwar

Digitized by Arya Samaj Foundation Chennai and eGangotri

Table 1. Comparison of estimated and reported values of energy band gap (E_g) for powders of ZnS, ZnO, CdS, CdSe, CdTe, Se and Si semiconductors.

Semiconductor	Position of absorption edge (band edge) at room temp. (nm)	Estimated E_g at room temperature (eV)	Reported E_g at room temp. (eV)	Reference
ZnS	325·0	3·81	3·67	(Weast 1977)
			3·70	(Rosencwaig 1980)
ZnO	358·0	3·46	3·20	(Weast 1977)
			4·80 (at 0°K)	(Ray 1969)
CdS	506·0	2·45	2·42	(Weast 1977)
			2·48	(Gibson 1958)
			2·40	(Rosencwaig 1980)
CdSe	659·0	1·88	1·74	(Weast 1977)
			1·75	(Rosencwaig 1980)
CdTe	784·0	1·58	1·44	(Weast 1977)
			1·50	(Weast 1977)
Se	670·0	1·85	1·80	(Smith 1968)
			1·7	(Dance 1969)
Si	1050	1·18	1·10	(Weast 1977)
			1·09	(Vavilov 1965)
			1·12	(Dance 1969)

structure in samples. One of them may be the presence of localized states inside the gap. Another interesting problem is the change (Nudelman and Mitra 1969) of the gap during the transition from crystalline to the amorphous state. The accuracy of the method is $\pm 0{\cdot}01$ eV which corresponds to 8 nm in the visible region of the spectrum. This accuracy may not be the same for the energy band gap determination of indirect type semiconductors like Si where the absorption band edge is not sharp as explained above.

4. Conclusions

The method of photoacoustic spectroscopy for determining the absorption edge in semiconductors of both direct and indirect band gap types is accurate, quicker and non-destructive. As the sharpness of the band edge depends very much on the quality of the material, the monitoring of sophistication of semiconductors in their manufacture is of utmost importance to study their resonant properties near this edge. Also, the method of photoacoustic spectroscopy can be effectively employed for quick characterization of these materials.

CC-0. In Public Domain. Gurukul Kangri Collection, Haridwar

Digitized by Arya Samaj Foundation Chennai and eGangotri

Acknowledgements

The authors wish to express their gratitude to Dr S P Varma for useful discussions.

References

Bhide V G, Ram R S, Varma S P and Om Prakash 1983 *Res. Ind.* **28** 25
Dance J B 1969 *Photoelectronic devices* (London: Illiffe)
Despande S V 1975 *J. Phys. Edn* **3** 24
Gibson A F 1958 *Progress in semiconductors* (London: Heywood & Company) Vol. 3.
Gutsche E and Lange H 1967 *Phys. Status Solidi* **22** 229
Lange H and Henrion W 1967 *Phys. Status Solidi* **K23** 67
Lyamov V E, Madvaliev U and Shikhlinskya 1979 *Sov. Phys. Acoust.* **26** 242
Miller D A B 1983 *Laser focus* **19** 61
Moss T S 1961 *Optical properties of semiconductors* (London: Butterworths)
Nudelman S and Mitra S S 1969 *Optical properties of solids* (New York: Plenum Press)
O'Bryan H M 1936 *J. Opt. Soc. Am.* **26** 122
Pao Y H 1977 *Optoacoustic spectroscopy and detection* (New York: Academic Press)
Ray B 1969 *International series of monographs in the science of the solid state, II-VI compounds* (Oxford: Pergamon) Vol. 2
Resencwaig A 1980 *Photoacoustics and photoacoustic spectroscopy* (New York: John Wiley)
Smith R A 1968 *Semiconductors* (London: Cambridge University Press)
Vavilov V K 1965 *Effects of radiation on semiconductors*, Russian translation by Ty Dubelewiez A (New York: Consultants Bureau)
Weast R C 1977 *CAC Handbook of Chemistry and Physics* (Ohio: CRC Press)

CC-0. In Public Domain. Gurukul Kangri Collection, Haridwar

Digitized by Arya Samaj Foundation Chennai and eGangotri

CC-0. In Public Domain. Gurukul Kangri Collection, Haridwar

Digitized by Arya Samaj Foundation Chennai and eGangotri

Pramāṇa – J. Phys., Vol. 28, No. 3, March 1987, pp. 299–310. © Printed in India.

Stabilization of valence fluctuations in the cerium solid by the time-dependent collision approach

RATAN LAL
Physics Department, Regional Engineering College, Silchar 788 010, India

MS received 10 December 1985; revised 27 January 1987

Abstract. The collision-generated hybridization which has been found responsible for the on-site mixing of the atomic-like *f*-state and the band-like *d* states in mixed valence solids has been studied for the cerium solid. A practical expression which depends on the lattice constant and temperature has been obtained for the collision-generated hybridization. Numerical calculations show that the valence varies continuously with lattice constant and that temperature makes the transition smoother. The collision-generated hybridization is found to be of significant strength in the intermediate valence regime; but over a wide range of the valence near 3·5 it varies rather slowly without preferring a particular valence. Factors which can assist the collision-generated hybridization in stabilizing the mixed valence phase at a particular lattice constant are discussed.

Keywords. Mixed valence; intermediate valence; valence fluctuations; cerium solid; time-dependent collision.

PACS No. 71·70

1. Introduction

A class of rare earth solids show anomalous physical properties (Khomskii 1979; Robinson 1979; Lawrence *et al* 1981; Lee *et al* 1986). Experimental findings suggest that the state of such solid systems belongs to the non-integer valence. The origin of non-integer valence lies in the coexistence of two configurations, f^n and f^{n-1}, with similar energies. Except at very low temperatures, the fluctuations of the *f* electron between these two configurations are mainly local in character (Schlottmann 1980; Gunnarsson and Schonhammer 1983; Barnes 1985). To understand the behaviour of mixed valence solids many theoretical efforts have been made in recent years (Kasuya and Saso 1985; Lee *et al* 1986). However, almost all the existing theories work in terms of pre-assumed mixed valence conditions by taking parametric forms of relevant interactions. Development of a microscopic theory which can provide a method for the estimation of the various interaction parameters is at its initial stage only (Lal 1983, 1986). In our previous papers (Lal 1983, 1984, 1986) we have seen that the use of the time-dependent collision theory provides us a way for the estimation of the strength of the on-site hybridization interaction, the so-called "collision-generated hybridization (CGH)". The CGH does not suffer from the objections caused by the symmetry as in the case of Anderson hybridization (Lal 1984). Moreover, the fact that the two-site hybridization of Kaplan and Mahanti (1975) is neither based on the interactions which exist in the system, nor does it find any experimental support (Robinson 1979) makes the CGH

CC-0. In Public Domain. Gurukul Kangri Collection, Haridwar

Digitized by Arya Samaj Foundation Chennai and eGangotri

relatively more important than other existing types of the hybridization interactions (Lal 1984). We therefore feel that our method of the time-dependent collision theory will provide us an understanding of the stabilization of the electronic phase transition at the non-integer valence. We can further support this point by noting that the qualitative ideas of Varma and Schluter (1981), Schluter and Varma (1983) and Khomskii (1984) which focus attention on the mechanism of valence change transitions have not yet been related with the basic interactions which exist in a mixed valence system.

The aim of the present paper is to further develop the time-dependent collision theory by using suitable approximations at various stages of the theory. Our main object is to render all the quantities which appear in the theory in practical forms. Such an effort has already been made for spinless fermions at zero temperature (Lal 1984). But for real systems we must consider both the spin and the temperature. In fact we must also consider the roles of phonons (Lal 1986). But the consideration of phonons will make the theory too complicated. So, in this paper we shall not consider the roles of phonons. In this sense we shall consider only the approach presented in Lal (1983, 1984) and shall generalize it for real systems by considering spin and temperature. The model which we use for the present study is described in § 2. In § 3 we describe the process of stabilization and obtain a practical expression for the collision-generated hybridization. The method of calculation with proper approximations is described in § 4. In § 5 we present numerical values of the collision-generated hybridization and examine its role from the viewpoint of stabilization of the mixed valence phase.

2. Model

We consider electronic mechanism of valence change transitions and limit ourselves to the case of homogeneous mixed valence systems only. Under such circumstances the mixed valence system is described by the Hamiltonian

$$H_{\text{total}} = H_f + H_d + H_{ff} + H_{fd} + H_r. \tag{1}$$

Here H_f is the Hamiltonian of the non-interacting f state impurity ions, H_d is the Hamiltonian of the d-band electrons, H_{ff} is the interatomic f-f interaction, H_{fd} is the f-d interaction and H_r is the vector potential which causes decay of the excited state via photon emission (Lal 1983). The form of H_r corresponding to the ith site is of the type $U_{ri} = -e\mathbf{j}_i \cdot \mathbf{A}_i$ where e is electronic charge, $\mathbf{j}_i$ is the current density of the f electron at the ith site, and $\mathbf{A}_i$ is the electromagnetic vector potential seen by the f electron at the ith site. As mentioned earlier (Lal 1983) the purpose of H_r is to govern the decay of the excited state of the f electron at a site. The joint effect of the decay (due to H_r) and excitation (due to H_{fd}) leads to on-site mixing of the atomic-like f state and the extended d band states (Lal 1983, 1986). The repulsive Coulomb interaction between d electrons has been neglected in (1).

There is no explicit f-d hybridization term in (1). This is because most of the homogeneous mixed valence systems are inversion-symmetric, thereby forbidding the on-site mixing of the atomic-like f state with the band-like d states via the lattice potential (Anderson hybridization). Although the Anderson hybridization may cause mixing between the atomic-like state of one site with the d-Wannier function centred on another site, we emphasize that such type of mixing will be irrelevant to the mixed

CC-0. In Public Domain. Gurukul Kangri Collection, Haridwar

Digitized by Arya Samaj Foundation Chennai and eGangotri

valence problem. This is because in the mixed valence systems the mixing of the atomic-like f state and the extended d state is basically local in nature (Schlottmann 1980; Gunnarsson and Schonhammer 1983; Barnes 1985). However, we must remember that at (very) low temperatures intersite effects may make the off-site mixing of the atomic and extended states important (Lee *et al* 1986). However, in this paper we do not consider intersite effects.

We now describe the various terms of (1). We start from the consideration of the f electrons. To avoid the complexity of atomic structure which arises due to two or more f electrons per ion, we limit our study for the case of cerium solid only. However, the following treatment will be applicable, with proper generalization, to all (homogeneous) mixed valence systems. We further assume that the interaction H_{ff} is infinitely stronger so that only two configurations, f^1 and f^0, are favourable. Under such circumstances the Hamiltonian of the f electrons may be written as

$$H_f + H_{ff} \simeq \sum_i K_i, \tag{2a}$$

with

$$K_i = \sum_M E_f B_{iM}^\dagger B_{iM}. \tag{2b}$$

Here M is the quantum number of the z-component of the total angular momentum. The ground state of the cerium f state impurity will correspond to $J = 5/2$ so that M takes in all six values. E_f is the energy of the f state $|iM)$.

The creation and annihilation operators $B_{iM}^\dagger$, B_{iM} are the modified fermion operators (Foglio 1978) such that $B_{iM}^\dagger B_{iM'}^\dagger = \theta$ for all M and M'. Here θ is the null vector.

The d band Hamiltonian H_d and the Coulomb interaction between the f and d electrons are given by

$$H_d = \sum_{\mathbf{k},m} \varepsilon_{\mathbf{k}} d_{\mathbf{k}m}^\dagger d_{\mathbf{k}m}, \tag{3}$$

and

$$H_{fd} = \sum_i U_{fd,i}, \tag{4a}$$

with

$$U_{fd,i} = \sum_{\alpha,\mathbf{k},m,\mathbf{k}',m',M} (i\alpha;\, \mathbf{k}'m' \,|\, U_i \,|\, iM;\, \mathbf{k}m) \times d_{\mathbf{k}'m'}^\dagger g_\alpha^\dagger B_{iM} d_{\mathbf{k}m}. \tag{4b}$$

Here $d_{\mathbf{k}m}^\dagger$ and $d_{\mathbf{k}m}$ are creation and annihilation operators of the d electron in the state of energy $\varepsilon_{\mathbf{k}}$, and spin quantum number m. The Coulomb interaction U_i is (in atomic units) given by

$$U_i = |\mathbf{r}_{1i} - \mathbf{r}_2|^{-1}, \tag{5}$$

with $\mathbf{r}_{1i}$ and $\mathbf{r}_2$ as coordinates of the f electron (of ith site) and the d electron respectively. In (4b) α denotes collectively the ionic state quantum number (M) and those band state quantum numbers ($\mathbf{k}''$, m'') for which the energy $\varepsilon_{\mathbf{k}''}$ is greater than the Fermi energy ε_F ($\varepsilon_{\mathbf{k}''} > \varepsilon_F$). That is to say $\alpha \equiv \{\{M\}; \{\mathbf{k}''; m''\}\}$. The creation operator $g_\alpha^\dagger$ corresponds to the state $|\alpha)$.

CC-0. In Public Domain. Gurukul Kangri Collection, Haridwar

Digitized by Arya Samaj Foundation Chennai and eGangotri

The ith f state impurity is described by the following Hamiltonian

$$H_i = K_i + H_d + U_{fd,\,i} + U_{r,\,i}. \tag{6}$$

Since (for a homogeneous system) all the impurities are equivalent, we shall drop below the impurity label i from all the quantities.

3. Collision-generated hybridization

3.1 *Physical description*

We treat the interaction U_{fd} and U_r by the time-dependent collision approach developed previously for spinless systems (Lal 1983). According to this approach the density operator of the f electron is described in terms of a multiple-single-site scattering matrix. Such a density operator is a time-dependent quantity. Here we work in terms of time-independent density operator. For this purpose we use the approximation of Lal (1984) and obtain the following expression for the density operator.

$$\rho^{\text{ion}} = \sum_{\alpha,\,\alpha'} \rho^{\text{ion}}_{\alpha,\,\alpha'} g^{\dagger}_{\alpha} g_{\alpha'}, \tag{7}$$

where

$$\rho^{\text{ion}}_{\alpha,\,\alpha'} = \sum_{\mathbf{k},m,M} (\alpha;\, \mathbf{k}_{\alpha} m_{\alpha} \,|\, S \,|\, M;\, \mathbf{k}m)(M;\, \mathbf{k}m \,|\, S \,|\, \alpha';\, \mathbf{k}_{\alpha'} m_{\alpha'}). \tag{8}$$

Here $\mathbf{k}_{\alpha}$ and m_{α} are the wave vector and the spin quantum number of the d-band electron corresponding to the state $|\alpha)$ of the f electron. S is the S-operator for that single scattering before which the ion is purely in the $4f$ state (Lal 1984). Practical expression of the matrix elements of S has been obtained in § 4.

The density operator ρ^{ion} corresponds to zero temperature. In order to generalize it to finite temperature T we proceed in a way similar to that used by Ziman (1969) for generalizing his equations (5.40) to (5.49). We get

$$\rho^{\text{ion}}(\beta) = Z^{-1} \exp(-\beta \mathscr{H}) \rho^{\text{ion}}, \tag{9}$$

where

$$\mathscr{H} = H - \mu \left[\sum_{M} B^{\dagger}_{M} B_{M} + \sum_{\mathbf{k},m} d^{\dagger}_{\mathbf{k},m} d_{\mathbf{k},m} \right], \tag{10}$$

is the Hamiltonian of the grand canonical ensemble, and

$$Z = \text{Tr}\{\exp(-\beta \mathscr{H}) \rho^{\text{ion}}\}, \tag{11}$$

is the partition function. μ is the chemical potential and $\beta = (k_B T)^{-1}$ with k_B as the Boltzmann constant. Notice that μ and ε_F are different in that μ corresponds to the joint system of f and d electrons while ε_F corresponds to the (isolated) d band only.

The density operator $\rho^{\text{ion}}(\beta)$ is subject to the following normalization conditions (Lal 1984).

$$\text{Tr}\{\rho^{\text{ion}}(\beta)\} = 1, \tag{12a}$$

CC-0. In Public Domain. Gurukul Kangri Collection, Haridwar

Digitized by Arya Samaj Foundation Chennai and eGangotri

and

$$\sum_M \rho^{\text{ion}}_{M,M}(\beta) = \tfrac{1}{2} \quad \text{when } E_f = \varepsilon_F . \tag{12b}$$

The density operator $\rho^{\text{ion}}(\beta)$ corresponds to a coherent mixture of the atomic like f states $|M\rangle$ and the extended band states $|\mathbf{k}''m''\rangle$. In other words off-diagonal elements of $\rho^{\text{ion}}(\beta)$ will, in general, be non-zero. This happens due to the coherent nature of the multiple scatterings of the band electron with the impurity ion (Lal 1983). In fact due to such a coherence the energy of the excited state will be uncertain by an amount $\Delta_{\mathbf{k}''} \sim 1/\Delta t(\mathbf{k}'')$, where the time uncertainty Δt is of the order of the time which corresponds to a distance of one lattice constant, d. Thus $\Delta t \sim d/k''$ so that $\Delta_{\mathbf{k}''} \sim k''/d$. Due to this energy uncertainty, transitions to band states (energy $\varepsilon_{\mathbf{k}''}$) become possible even when $E_f < \varepsilon_F$. The stabilization of the coherent mixture of the excited state is expressed in terms of the collision-generated hybridization which is given by (Lal 1983)

$$V_{h,\text{coll}} = \sum_{\mathbf{k},m,\mathbf{k}',m',\mathbf{k}'',m'',M} (\mathbf{k}''m''; \mathbf{k}'m' \mid U \mid M; \mathbf{k}m) \langle\langle B^\dagger_M d_{\mathbf{k}'',m''} \rangle\rangle . \tag{13}$$

Here $\langle\langle PQ \rangle\rangle$ denotes the thermodynamical average of the (modified) fermion operators P and Q. That is to say,

$$\langle\langle PQ \rangle\rangle = Z^{-1} \operatorname{Tr}\{\exp(-\beta\mathscr{H})\rho^{\text{ion}} PQ\}. \tag{14}$$

Equation (13) makes it clear that the origin of $V_{h,\text{coll}}$ lies in the f-d interaction U. Thus U not only drives the valence change transition but also helps in the stabilization.

3.2 *Working formula*

We first obtain the thermodynamical average $\langle\langle PQ \rangle\rangle$ in a practical form. For this purpose we notice that the fermion operators P, Q represent both the modified Fermi operators $B^\dagger_M$, B_M and the usual Fermi operators $d^\dagger_{\mathbf{k},m}$, $d_{\mathbf{k},m}$. Thus we have to take care of this fact in obtaining the value of $\langle\langle PQ \rangle\rangle$. From (7) and (14) we get

$$\langle\langle PQ \rangle\rangle = Z^{-1} \sum_{\alpha,\alpha'} \rho^{\text{ion}}_{\alpha,\alpha'} \operatorname{Tr}\{\exp(-\beta\mathscr{H})\, g^\dagger_\alpha g_{\alpha'} PQ\}. \tag{15}$$

Employing the anticommutation properties of the fermion operators we write the product of four-fermion operators which occur in (15) as follows.

$$\begin{aligned} g^\dagger_\alpha g_{\alpha'} PQ = {} & [g^\dagger_\alpha, g_{\alpha'}]_+ PQ - g_{\alpha'}[g^\dagger_\alpha, P]_+ Q \\ & + g_{\alpha'} P[g^\dagger_\alpha, Q]_+ - g_{\alpha'} PQ g^\dagger_\alpha, \end{aligned} \tag{16}$$

where $[\ldots,\ldots]_+$ denotes an anticommutator. The contribution of the last term of (16) to the trace of (15) is given by

$$-\operatorname{Tr}\{\exp(-\beta\mathscr{H}) g_{\alpha'} PQ g^\dagger_\alpha\} = -\operatorname{Tr}\{\exp(-\beta\mathscr{H})\, g^\dagger_\alpha(\beta) g_{\alpha'} PQ\}, \tag{17}$$

where $g^\dagger_\alpha(\beta)$ is defined by

$$\frac{\mathrm{d}}{\mathrm{d}\beta} g^\dagger_\alpha(\beta) = [\mathscr{H}, g^\dagger_\alpha(\beta)]_- . \tag{18}$$

CC-0. In Public Domain. Gurukul Kangri Collection, Haridwar

Digitized by Arya Samaj Foundation Chennai and eGangotri

Here $[\ldots,\ldots]_-$ denotes a commutator. Evaluation of this commutator with the aid of (10) leads us to the following value.

$$[\mathscr{H}, g_\alpha^\dagger(\beta)]_- = \eta(g_\alpha^\dagger) g_\alpha^\dagger(\beta) + A_{0d}(\beta) + B_r. \tag{19}$$

Here $\eta(g_\alpha^\dagger)$ is a c-number which is given by

$$\eta(g_\alpha^\dagger) = \eta_1 \sum_M (\alpha \,|\, M) + \eta_2 \sum_{\mathbf{k},m} (\alpha \,|\, \mathbf{k}, m), \tag{20}$$

with

$$\eta_1 = E_f - \mu + \sum_{\mathbf{k},m} (\alpha; \mathbf{k}m \,|\, U \,|\, \alpha; \mathbf{k}, m) f_0^-(\varepsilon_\mathbf{k}), \tag{21a}$$

and

$$\eta_2 = \varepsilon_\mathbf{k} - \mu + \sum_M (M; \mathbf{k}, m \,|\, U \,|\, M; \mathbf{k}m) f_0^-(E_f). \tag{21b}$$

In (21a) and (21b) f_0^- is the usual Fermi factor, i.e.

$$f_0^-(\varepsilon) = [1 + \exp\{\beta(\varepsilon - \mu)\}]^{-1}. \tag{22}$$

The c-number η satisfies the following symmetry relation

$$\eta(g_\alpha) = -\eta(g_\alpha^\dagger). \tag{23}$$

In (19) $A_{0d}(\beta)$ is a complicated operator. It arises due to off-diagonal matrix elements of the Coulomb interaction U. From (13) we see that the off-diagonal matrix elements of U play an important role in the stabilization of the mixed valence phase. However, in (19) these matrix elements appear in a different context. In fact in (19) contributions of diagonal matrix elements of U also appear. We expect that these diagonal matrix elements are significantly stronger than the off-diagonal matrix elements so that in (19) we can neglect the latter matrix elements.

The last term of (19), B_r, arises due to the vector potential U_r (cf. equation (6)). We do not consider this term because it corresponds to the decay of the excited state. We can therefore approximate the value of the commutator of (19) by its first term only. When it is so (18) leads to the following solution for $g_\alpha^\dagger(\beta)$

$$g_\alpha^\dagger(\beta) \simeq \exp\{\beta\eta(g_\alpha^\dagger)\} g_\alpha^\dagger. \tag{24}$$

From (17) and (20) the trace of (15) may be written as follows

$$\begin{aligned} \mathrm{Tr}\{\exp(-\beta\mathscr{H}) g_\alpha^\dagger g_{\alpha'} PQ\} = f^-(\eta(g_\alpha^\dagger))\,[[g_\alpha^\dagger, g_{\alpha'}]_+ \mathrm{Tr}\{\exp(-\beta\mathscr{H}) PQ\} \\ - [g_\alpha^\dagger, P]_+ \mathrm{Tr}\{\exp(-\beta\mathscr{H}) g_{\alpha'} Q\} \\ + [g_\alpha^\dagger, Q]_+ \mathrm{Tr}\{\exp(-\beta\mathscr{H}) g_{\alpha'} P\}], \end{aligned} \tag{25}$$

where

$$f^-(\eta) = f_0^-(\eta + \mu). \tag{26}$$

In a way similar to that used for getting (25) we find that

$$\mathrm{Tr}\{\exp(-\beta\mathscr{H}) PQ\} = f^-(\eta(P))\,[P, Q]_+ \mathrm{Tr}\{\exp(-\beta\mathscr{H})\}. \tag{27}$$

CC-0. In Public Domain. Gurukul Kangri Collection, Haridwar

Digitized by Arya Samaj Foundation Chennai and eGangotri

Employing (25) and (27) the form of the thermodynamical average $\langle\langle PQ\rangle\rangle$, (15) becomes

$$\langle\langle PQ\rangle\rangle = Z^{-1}\sum_{\alpha,\alpha'}\rho^{\text{ion}}_{\alpha,\alpha'}\,\langle\langle PQ\rangle\rangle_{\alpha,\alpha'}, \tag{28}$$

with

$$\begin{aligned}\langle\langle PQ\rangle\rangle_{\alpha,\alpha'} &= f^{-}(\eta(g_\alpha))\,\mathrm{Tr}\{\exp(-\beta\mathscr{H})\\ &\quad\times[[g^{\dagger}_{\alpha}, g_{\alpha'}]_{+}[P, Q]_{+}f^{-}(\eta(P))-[g^{\dagger}_{\alpha}, P]_{+}[g_{\alpha'}, Q]_{+}\\ &\quad\times f^{+}(\eta(g^{\dagger}_{\alpha'}))+[g_{\alpha'}, P]_{+}f^{+}(\eta(g^{\dagger}_{\alpha'}))[g^{\dagger}_{\alpha}, Q]_{+}].\end{aligned} \tag{29}$$

Here $f^{+}=1-f^{-}$.

Taking $P=B^{\dagger}_{M}$ and $Q=d_{\mathbf{k}''m''}$ in (29) we get the following expression for $V_{h,\text{coll}}$.

$$\begin{aligned}V_{h,\text{coll}} &= Z_0^{-1}V^{3}(2\pi)^{-9}\sum_{\substack{\mathbf{k},m,\mathbf{k}',m',\\ \mathbf{k}'',m'',M}}(\mathbf{k}''m'';\mathbf{k}'m'\,|\,U\,|\,M;\mathbf{k}m)\\ &\quad\times\rho^{\text{ion}}_{\mathbf{k}''m'';M}f^{-}(\eta_2)f^{+}(\eta_1),\end{aligned} \tag{30}$$

where

$$Z_0=\sum_{\alpha}\rho^{\text{ion}}_{\alpha,\alpha}f^{-}(\eta(g^{\dagger}_{\alpha})), \tag{31}$$

and V is the volume of the unit cell.

4. Calculational procedure

Calculation of the collision-generated hybridization $V_{h,\text{coll}}$ requires knowledge of the atomic structure and the band structure. These two structures must be calculated in a consistent way so that $\varepsilon_F - E_f$ varies correctly with the lattice constant. Although there exists a microscopic method for solving this problem (Lal 1986), we shall consider the variation of $\varepsilon_F - E_f$ with d in a parametric way by employing the experimental information. In fact we use experimental information to find out the lattice constant which corresponds to $\varepsilon_F = E_f$. Since the valence of cerium (denoted by V) (for $\varepsilon_F = E_f$) is $V = 3{\cdot}5$ (cf. equations (12a) and (12b)), on the basis of first electronic phase transition of cerium (figure 4 of Khomskii 1979) we take $d = 5{\cdot}00$ Å (for $\varepsilon_F = E_f$). We employ this information in specifying the band structure which we assume to be of the parabolic form, i.e., $\varepsilon_{\mathbf{k}} = -(g/d)+k^2/2$ with g as independent of the lattice constant d. The parameter g is determined by requiring $\varepsilon_F = E_f$ at $d = 5{\cdot}00$ Å. As regards the atomic structure we use the hydrogen-like structure where the $4f$ electron moves in a Coulomb field of the ionic core of four units of (proton) charge.

We now turn to the matrix elements of the S-operator (cf. equation (8)). We consider only the first-order contribution of S, say $S^{(1)}$, and include distortion effects in a way suggested in Lal (1984). The partial-wave-analyzed forms of the matrix elements of $S^{(1)}$ for the $f\to f$ and $f\to d$ transitions can be expressed in the usual way in terms of time-and-radial integrals J_λ and K_λ, respectively. The radial integrals for the partial waves

CC-0. In Public Domain. Gurukul Kangri Collection, Haridwar

Digitized by Arya Samaj Foundation Chennai and eGangotri

corresponding to the angular momenta λ, l, l', l'' are given by the following expressions

$$J_\lambda(l', k, l, k) = k^{-2} \int R_{43}(r_1, t) G_{kl'}(r_2, t) w^{(1)}(r_1, r_2, t) \times R_{43}(r_1, t) G_{kl}(r_2, t)\, dr_1\, dr_2\, dt, \tag{32}$$

$$K_\lambda(l'', k'', l', k', l, k) = (kk')^{-1} \int F_{k''l''}(r_1, t) G_{k'l'} \times (r_2, t) w^{(2)}(r_1, r_2, t) R_{43}(r_1, t) G_{kl}(r_2, t)\, dr_1\, dr_2\, dt. \tag{33}$$

Here $R_{43}(r_1, t)$ and $F_{k''l''}(r_1, t)$ are the (partial) radial wave packets corresponding to the impurity; $G_{k'l'}(r_2, t)$ and $G_{kl}(r_2, t)$ are the partial radial wave packets corresponding to the d-band electron. Practical forms of these wave packets are presented in Appendix 1. The boundary conditions satisfied by the wave packets are as follows

$$R_{43}(r, t) \sim \begin{cases} r^4 \exp(-iE_f t) & (\text{for } r \to 0) \\ 0 & (\text{for } r \to \infty), \end{cases} \tag{34a}$$

and

$$I_{kl}(r, t) \sim \begin{cases} r^{l+1} \exp(-i\varepsilon_k t) & (\text{for } r \to 0) \\ \sin(kr - \tfrac{1}{2} l\pi + \delta_l) \exp(-i\varepsilon_k t) & (\text{for } r \to \infty) \end{cases}. \tag{34b}$$

Here δ_l is the phase shift produced by the potential field to which $I_{kl} = F_{kl}$ or G_{kl} corresponds.

The interactions $w^{(i)}$ which appear in (32) and (33) are given by

$$w^{(i)}(r_1, r_2, t) = v^{(i)}(r_1, r_2) - D_T(t, r_1) - D_C(t, r_2), \tag{35}$$

where

$$v^{(i)}(r_1, r_2) = r_<^\lambda r_>^{-\lambda-1} - (4\pi r_2)^{-1} \delta_{\lambda 0} \delta_{i1} \tag{36}$$

with $r_< = \min\{r_1, r_2\}$ and $r_> = \max\{r_1, r_2\}$.

Specification and the method of calculation for the time-dependent distortion potentials D_C and D_T which are involved in the above equations have been described in Lal (1984).

5. Results and discussion

In order to understand the nature of the collision-generated hybridization we have calculated values of $V_{h,\text{coll}}$ for various values of the temperature, $T = 0$ K, 5 K and 10 K. Apart from the collision-generated hybridization we have calculated values of the valence $V = 4 - n_{ff}$ also, where the f state occupation n_{ff} is given by

$$n_{ff} = \sum_M \langle\langle B_M^\dagger B_M \rangle\rangle. \tag{37}$$

The values of the valence, shown in figure 1, reveal that the electronic phase transition is continuous for all the temperatures such that as the temperature increases the transition becomes smoother. Figure 2 shows the values of $V_{h,\text{coll}}$ corresponding to the valence change from 3 to 4. It is obvious from this figure that the strength of the collision-generated hybridization is significant only in the intermediate valence regime where the valence V is sufficiently different from 3 and 4. As the valence becomes integer

CC-0. In Public Domain. Gurukul Kangri Collection, Haridwar

Digitized by Arya Samaj Foundation Chennai and eGangotri

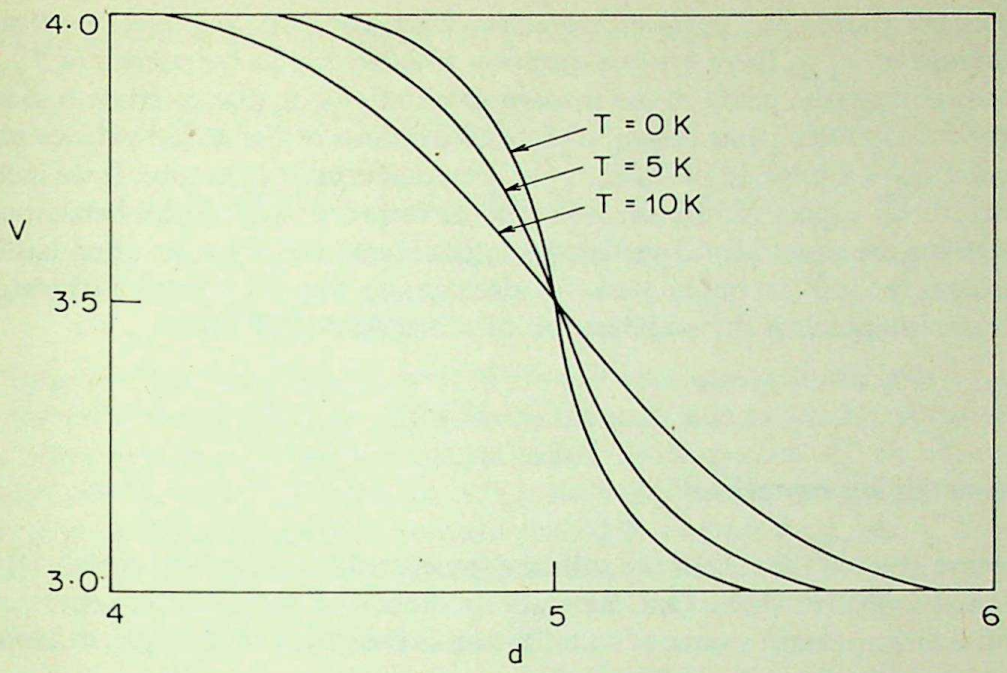

Figure 1. Values of the valence $V = 4 - n_{ff}$ for various lattice constants at $T = 0$ K, 5 K and 10 K.

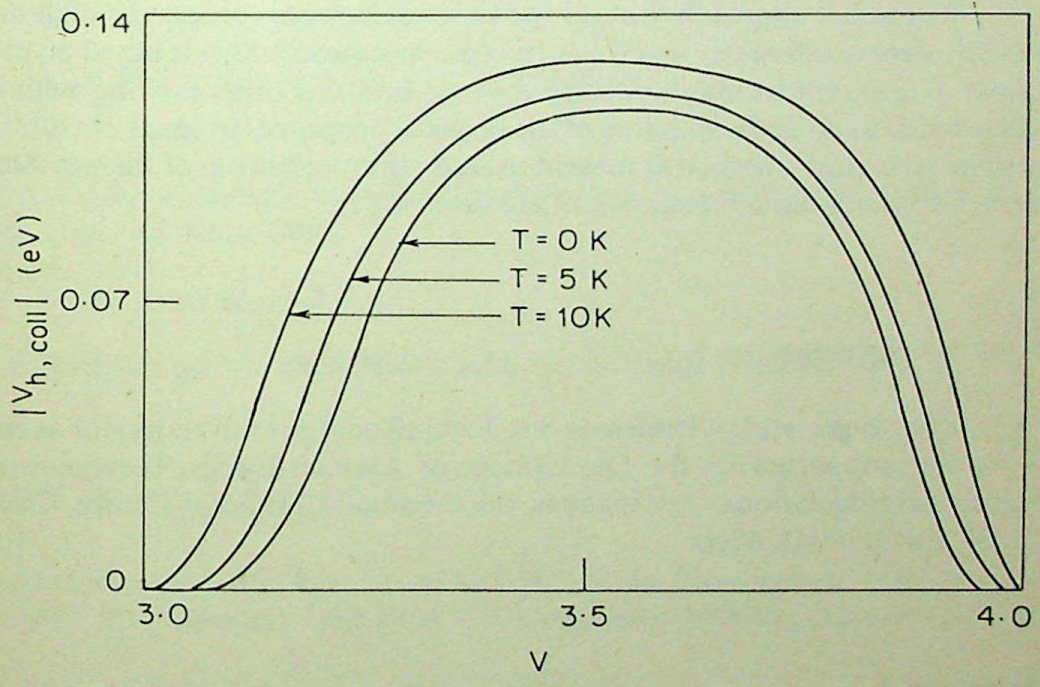

Figure 2. Values of the collision-generated hybridization $V_{h,\,coll}$ for various values of valence ($V = 3$ to $V = 4$) at $T = 0$ K, 5 K and 10 K.

(3 or 4) the value of the collision-generated hybridization approaches zero rapidly. But in the intermediate valence regime the collision-generated hybridization varies rather slowly over a wide range of V values for the temperatures considered here. In particular, the collision-generated hybridization does not show any preference for a particular valence. This is against the experimental findings according to which the mixed valence

CC-0. In Public Domain. Gurukul Kangri Collection, Haridwar

Digitized by Arya Samaj Foundation Chennai and eGangotri

phase is stabilized at a particular valence. Since our calculations do not lead to such a behaviour of $V_{h,\mathrm{coll}}$ there arises a question whether such a behaviour of $V_{h,\mathrm{coll}}$ is due to the simplifications made in the present calculations or due to contributions of other factors of non-electronic origin to the stabilizations of the mixed valence phase. In our calculations we have, in particular, not included crystal structure. If we include crystal structure we expect (Khomskii 1984) some improvement in the behaviour of $V_{h,\mathrm{coll}}$. Moreover, we must also consider the lattice dynamics because when lattice constant decreases the ion-ion interaction will also change, thereby affecting (through electron-phonon interaction) the stabilization of the crystal (Lal 1986).

6. Concluding remarks

We have studied the role of the collision-generated hybridization in the stabilization of the mixed valence phase. Our calculations show that the collision-generated hybridization is an important source of stabilization of the mixed valence phase. However, as we have seen, the time-dependent collision approach employed here is not a complete theory in that for the value of the equilibrium lattice constant d_0, the method depends upon experimental information (cf. § 4). In fact for a complete study the lattice problem must also be solved along with the electronic problem (Lal 1986). However, we can apply the present approach to study the various electronic properties of (homogeneous) mixed valence systems by working at a lattice constant which is based on experimental values. The main advantage of the present method over other existing methods is that it will provide us an understanding of the physical properties in terms of true interactions, as there is no other method at present to study the mechanism of valence fluctuations in terms of microscopic interactions (Lee *et al* 1986).

Acknowledgements

The author is grateful to Professor S K Joshi (Roorkee University) for assistance. This work was supported by the Department of Atomic Energy, Government of India. Numerical calculations were made at the Regional Computer Centre, Calcutta, India on BURROUGHS 6700.

Appendix 1.

In this appendix we present an analytic expression for the loop-analyzed version used in constructing radial wave packets (Lal and Joshi 1980) required for the calculation of the integrals J_λ and K_λ (eqs (32) and (33)). We also present an analytic (but approximate) expression for the time t. The loop-analyzed version is a single-valued, continuous and finite function of N loops which, to within a phase factor $\exp(-i\varepsilon_k t)$, is used to describe the partial radial wave packets $F_{kl}(r, t)$ and $G_{kl}(r, t)$. We denote this function by $W_{kl}^{N,a}(r)$ where a is a parameter which provides continuous variation of $W_{kl}^{N,a}$ with time (Lal and

CC-0. In Public Domain. Gurukul Kangri Collection, Haridwar

Digitized by Arya Samaj Foundation Chennai and eGangotri

Joshi 1980). We use the following form for $W_{kl}^{N,a}$ which lends itself easily to calculations

$$W_{kl}^{N,a}(r) = \delta_{N,1} r^{l+1} \exp(-\lambda r) + (1-\delta_{N,1}) \sum_{i=1}^{N} (-1)^{i+1} \times \{q_i [\tfrac{1}{4}(z_i - z_{i-1})^2 - \tfrac{1}{4}(2r - z_i - z_{i-1})^2] \theta(r - z_{i-1}) \theta(z_i - r) \times [\theta(r - z_1) + r^l \theta(z_1 - r)] (1 - \delta_{i,N}) + (r - z_{N-1}) \exp(-\lambda r) \times \theta(r - z_{N-1}) \delta_{i,N}\}. \quad \text{(A1)}$$

It should be noted that this form of $W_{kl}^{N,a}(r)$ is not continuous at the points $r = z_i$. However, this does not produce any difficulty in the calculations. Let $f_{kl}(r)$ denote that stationary state component of the partial radial wave packet F_{kl} or G_{kl} which corresponds to the energy $k^2/2$. Then, in (A1), z_i's are the first N zeros of $f_{kl}(r)$; and the parameters q_i are given in terms of the relative probabilities given by f_{kl}, say p_i, between its two consecutive zeros z_{i-1} and z_i. That is to say,

$$q_i = p_i^{1/2} [A_0 (1 - \delta_{i,1}) + A_l \delta_{i,1}]^{-1/2}. \quad \text{(A2)}$$

Here,

$$A_l = \sum_{i=0}^{4} (-1)^i x_i (2l + 5 - i)^{-1} [z_i^{2l+5-i} - z_{i-1}^{2l+5-i}],$$

with

$$x_0 = 1, \quad x_1 = 2(z_{i-1} + z_i),$$
$$x_2 = z_{i-1}^2 + 4 z_{i-1} z_i + z_i^2, \quad x_3 = x_1 z_{i-1} z_i,$$
$$x_4 = z_{i-1}^2 z_i^2.$$

The value of the parameter λ, in (A1), depends upon a, z_{N-1} and p_N in accordance with the relation (Lal and Joshi 1980)

$$4\lambda^3 a p_N = \exp(-2\lambda z_{N-1}). \quad \text{(A3)}$$

Using (A1) we can get the expectation value of the radial distance r and the kinetic energy

$$\tfrac{1}{2}k^2 \equiv -\frac{d^2}{2dr^2} + \frac{l(l+1)}{2r^2},$$

which we denote respectively by $\bar{r}(N, a)$ and $\frac{1}{2}\bar{k}^2(N, a)$. These expectation values are involved in the specification of the time t in accordance with the relation (Lal 1984)

$$t(N, a) = C_N + \int [\bar{k}^2(N, a)]^{-1/2} \, d\bar{r}(N, a). \quad \text{(A4)}$$

In order to perform this integral analytically we make the following polynomial approximation for $[\bar{k}^2(N, a)]^{-1/2}$.

$$[\bar{k}^2(N,a)]^{-1/2} = \sum_{m=1}^{3} \alpha_{N,m} [\bar{r}(N, a)]^{m-1}. \quad \text{(A5)}$$

Here, the coefficients $\alpha_{N,m}$ are easily found out by using three sets of values of $\bar{r}$ and $\bar{k}^2$ (for different values of a with a given N).

CC-0. In Public Domain. Gurukul Kangri Collection, Haridwar

Digitized by Arya Samaj Foundation Chennai and eGangotri

To find out the value of the integration constant C_N in (A4) we use the fact that the kinetic energy must vary with time monotonically. That is to say,

$$\bar{k}^2(N, a_1) > \bar{k}^2(N-1, a_2), \tag{A6}$$

for all possible values of a_1 and a_2. This condition leads to the following value of C_N.

$$C_N = \sum_{m=1}^{3} \sum_{p=1}^{N-1} (\alpha_{p,m} - \alpha_{p+1,m}) R_p^m / m. \tag{A7}$$

Here R_p is the maximum value of $\bar{r}(p-1, a_{p-1,\min})$ and at the same time it (R_p) is the minimum value of $\bar{r}(p, a_{p,\max})$ such that the condition (A6) is satisfied. In this way the minimum and maximum values of a, $a_{p,\min}$ and $a_{p,\max}$, are found out. The value of R_p is obtained from the equation

$$\sum_{m=1}^{3} (\alpha_{p,m} - \alpha_{p-1,m}) R_p^{m-1} = 0. \tag{A8}$$

Equations (A1) – (A8) completely clarify the method of employing the functions $W_{kl}^{N,a}(r)$ in calculations. In particular, (A4) is not only useful for finding out the value of time t, but is also useful in determining the form of the wave packet at a given time. This is because if t is known we can find the value of $\bar{r}$ from (A4). From the value of $\bar{r}$ we can find the value of λ by using the expression of $\bar{r}$, thereby knowing the form of the wave packet at t. This will help in evaluating the integrals J_λ and K_λ. First we take any one of the wave packets involved in J_λ or K_λ, say $G_{kl}(r_2, t)$, and then work out a set of proper values of t (from A.4) corresponding to this wave packet. Then at these values of t we work out forms of other wave packets (G_{kl}, for J_λ, $G_{k'l'}$ and $F_{k''l''}$ for K_λ). In this way, forms of all the wave packets which appear in J_λ or K_λ are obtained at the same values of t. The t-integral can then be performed easily.

References

Barnes S E 1985 *Phys. Rev. Lett.* **55** 2192

Foglio M E 1978 *J. Phys.* **C11** 4171

Gunnarsson O and Schonhammer K 1983 *Phys. Rev.* **B28** 4315

Kaplan T A and Mahanti S D 1975 *Phys. Lett.* **A51** 265

Kasuya T and Saso T (eds) 1985 *Theory of heavy fermions and valence fluctuations* (Berlin: Springer-Verlag)

Khomskii D I 1979 *Sov. Phys. Usp.* **22** 879

Khomskii D I 1984 *Solid State Commun.* **50** 197

Lal R 1983 *Phys. Rev.* **B27** 2535

Lal R 1984 *Phys. Rev.* **B30** 4422

Lal R 1986 *Phys. Rev.* **B34** 1333

Lal R and Joshi S K 1980 *Pramana – J. Phys.* **14** 191

Lawrence J M, Riseborough P S and Parks R D 1981 *Rep. Prog. Phys.* **44** 1

Lee P A, Rice T M, Serene J W, Sham L J and Wilkins J W 1986 *Comments Cond. Matter. Phys.* **12** 99

Robinson J M 1979 *Phys. Rep.* **51** 1

Schlottmann P 1980 *Phys. Rev.* **B22** 622

Schluter M and Varma C M 1983 *Helv. Phys. Acta* **56** 147

Varma C M and Schluter M 1981 in *Valence fluctuations in solids* (eds) L M Falikov, W Hanke and M B Maple (Amsterdam: North Holland) p. 37

Ziman J M 1969 *Elements of advanced quantum theory* (London: Cambridge Univ. Press) p. 154

CC-0. In Public Domain. Gurukul Kangri Collection, Haridwar

Digitized by Arya Samaj Foundation Chennai and eGangotri

Pramāṇa – J. Phys., Vol. 28, No. 3, March 1987, pp. L311–L316. © Printed in India.

Flexoelectric origin of oblique-roll electrohydrodynamic instability in nematics

N V MADHUSUDANA, V A RAGHUNATHAN and
K R SUMATHY
Raman Research Institute, Bangalore 560 080, India

MS received 4 February 1987

Abstract. We develop the theory of electrohydrodynamic instability in nematic liquid crystals by incorporating the flexoelectric terms. Using a one-dimensional linear analysis of the problem for an applied DC field, we demonstrate that for the usual materials the rolls have an oblique orientation as has been found experimentally. We also provide an experimental evidence for the strong flexoelectric influence on the director profile in the rolls.

Keywords. Nematic liquid crystals; flexoelectricity; oblique roll instability; electrohydrodynamics.

PACS Nos 61·30; 47·20; 47·65

An electrohydrodynamic (EHD) roll instability is exhibited by nematic liquid crystals with either negative or weakly positive dielectric anisotropy ($\Delta\varepsilon$) above a DC or low frequency AC threshold voltage (Blinov 1983; Chandrasekhar 1977). The first theoretical analysis of the problem was given by Helfrich (1969) for an applied DC field. It was later extended by the Orsay group (Dubois-Violette *et al* 1971; Smith *et al* 1975) to AC fields. The conductivity anisotropy ($\Delta\sigma$) of the medium gives rise to space charge densities under the action of the external field if there are bend fluctuations in a planar aligned sample. The electric force on the space charge density gives rise to EHD instabilities. The one-dimensional theories mentioned above considered only the possibility of rolls whose wavevector is along the initial undistorted orientation of the director $\mathbf{n}_0$. Recently, however, there have been a few experimental observations (Ribotta *et al* 1986; Hirata and Tako 1982) of *oblique* rolls, in which the wavevector makes an angle (α say) with $\mathbf{n}_0$, in both DC and very low frequency AC fields. Zimmermann and Kramer (1985) made a three-dimensional, linear analysis of the EHD problem. However, unrealistically, they assumed 'stress-free' boundary conditions for simplifying the analysis. They found that oblique rolls result for a certain range of material parameters, and also noted that an one-dimensional analysis would *not* lead to oblique rolls.

We must however point out that the deformation in the director field in the EHD structures gives rise to a flexoelectric polarization **P** of the medium which was not considered in the above model. The action of the external field on **P** could be expected to influence the roll structure. Some early Russian work (Ioffe 1975; Matyushichev and Kovnatskii 1975) incorporating the effect of **P** in the theory of EHD predicts the possibility of an oscillatory instability, the wavevector of the rolls remaining parallel to $\mathbf{n}_0$. In the present communication, we demonstrate that the flexoelectric terms lead to oblique rolls in an one-dimensional model itself.

CC-0. In Public Domain. Gurukul Kangri Collection, Haridwar

Digitized by Arya Samaj Foundation Chennai and eGangotri

In his original paper on flexoelectric properties of nematics, Meyer (1969) envisaged that only pear-shaped molecules with longitudinal dipoles or banana-shaped molecules with lateral dipoles could give rise to **P**. Prost and Marcerou (1977) have subsequently shown that the quadrupole density of the medium makes a very important contribution to **P** and hence flexoelectricity is a universal property of all nematics.

We consider a nematic taken in a sandwich cell, with $\mathbf{n}_0$ lying parallel to the conducting plates, along the x axis, say (Figure 1). With an applied DC field E_z, we assume that the EHD instability gives rise to oblique rolls whose wavevector **q** lies along ξ making an angle α with $\mathbf{n}_0$. In the deformed state, **n** makes polar angles θ and ϕ with the xyz system, so that the components of **n** in the $\xi\eta z$ system are $[\cos\theta\cos(\alpha-\phi), -\cos\theta\sin(\alpha-\phi), \sin\theta]$. It is well known that the one-dimensional model does not predict a nonzero value of q, but following Helfrich (1969) we can assume on physical grounds that the sample thickness d determines the width of the rolls. As in the earlier work of Smith *et al* (1975), the one-dimensional model not only brings out all the essential features of the problem, but also leads to a simple physical interpretation of the results. We assume that only the vertical component of the velocity (v_z) is nonzero, and that v_z, θ and ϕ are functions of ξ only. In the present communication we confine our attention to DC fields. We have then a stationary director profile which satisfies the torque balance equations

$$\Gamma^i_{\text{elastic}} + \Gamma^i_{\text{flexo}} + \Gamma^i_{\text{dielectric}} = \Gamma^i_{\text{hydrodyn}}, \qquad i = y, z, \tag{1}$$

where $\Gamma = \mathbf{n}\times\mathbf{h}$, **h** being the relevant molecular field (de Gennes 1975). The anisotropy of conductivity $\Delta\sigma$ gives rise to a transverse field which by symmetry has only the ξ component E_ξ. The electric displacement is given by

$$\mathbf{D} = \varepsilon_\perp \mathbf{E} + \Delta\varepsilon(\mathbf{n}\cdot\mathbf{E})\mathbf{n} + 4\pi(e_1\mathbf{n}\,\text{div}\,\mathbf{n} + e_3\,\text{curl}\,\mathbf{n}\times\mathbf{n}), \tag{2}$$

$$\Delta\varepsilon = \varepsilon_\parallel - \varepsilon_\perp,$$

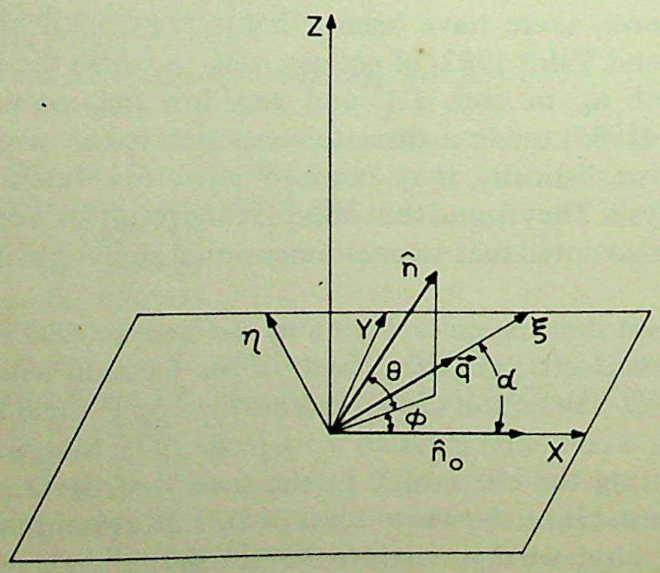

Figure 1. Illustration of the coordinate system and the definitions of angles used in the text.

CC-0. In Public Domain. Gurukul Kangri Collection, Haridwar

Digitized by Arya Samaj Foundation Chennai and eGangotri

where $\varepsilon_\parallel, \varepsilon_\perp$ are the principal dielectric constants, and e_1, e_3 the flexoelectric coefficients. The action of E_z on the total space charge density (div $\mathbf{D}/4\pi$) is used to calculate the shear stress which in turn is used to eliminate the shear rate $dv_z/d\xi$ from $\mathbf{h}_{\text{hydrodyn}}$.

Retaining only the linear terms, equations (1) yield

$$(k_2 \sin^2\alpha + k_3 \cos^2\alpha)\frac{d^2\theta}{d\xi^2} + HE_z^2\theta + \{(e_1 - e_3) - (e_1 + e_3)(F+G)\cos^2\alpha\}\sin\alpha\, E_z\frac{d\phi}{d\xi} = 0, \tag{3}$$

$$\{(e_1 + e_3)F\cos^2\alpha - (e_1 - e_3)\}\sin\alpha\, E_z\frac{d\theta}{d\xi} + (k_1 \sin^2\alpha + k_3\cos^2\alpha)\frac{d^2\phi}{d\xi^2} = 0, \tag{4}$$

along y and z respectively, where

$$F = \Delta\sigma/(\sigma_\perp + \Delta\sigma\cos^2\alpha), \quad G = -2\alpha_2/[\alpha_4 + (\alpha_5 - \alpha_2)\cos^2\alpha],$$
$$H = [\Delta\varepsilon(F\sigma_\perp/\Delta\sigma)^2 - \{\Delta\varepsilon - F(\varepsilon_\perp + \Delta\varepsilon\cos^2\alpha)\}\, G\cos^2\alpha]/4\pi, \tag{5}$$

$\alpha_2, \alpha_4, \alpha_5$ are the viscosity coefficients and k_1, k_2, k_3 the curvature elastic constants (de Gennes 1975). The coupled equations (3) and (4) admit solutions of the form

$$\theta = \theta_0 \sin q\xi, \qquad \phi = \phi_0 \cos q\xi, \tag{6}$$

in which the relative signs of θ_0 and ϕ_0 depend on those of E_z and α. The threshold for deformation is given by

$$E_{\text{th}} = q(k_2\sin^2\alpha + k_3\cos^2\alpha)^{1/2}[H + \sin^2\alpha\{(e_1 - e_3)^2 + (e_1 + e_3)^2 F(F+G)\cos^4\alpha - (e_1^2 - e_3^2)(2F+G)\cos^2\alpha\}/(k_1\sin^2\alpha + k_3\cos^2\alpha)]^{-1/2}. \tag{7}$$

Using the Helfrich condition $q = \pi/d$ we get a voltage threshold. The angle α is selected to minimise V_{th}. If $\alpha = 0$, the flexoelectric contribution vanishes completely. Note that our expression for V_{th} (for $\alpha = 0$) is slightly different from that given by Helfrich (1969) since, in his model, the dependence of E_ξ on θ is ignored in calculating $\mathbf{h}_{\text{dielec}}$. If $\alpha = \pi/2$, all the hydrodynamic contributions are absent, and the flexoelectric effect can cause a periodic static distortion of $\mathbf{n}$ if $\Delta\varepsilon$ is sufficiently small. Such flexoelectric distortions have been studied earlier both experimentally (Barnik *et al* 1978) and theoretically (Bobylev and Pikin 1977).

e_1 and e_3 have been measured only for a couple of compounds. In MBBA (4-methoxybenzylidene-4′-butylaniline) $e_1 - e_3 \simeq 1{\cdot}2 \times 10^{-4}$ e.s.u. (Dozov *et al* 1982) and $e_1 + e_3 \simeq -7 \times 10^{-4}$ e.s.u (Madhusudana and Durand 1985). Using $\varepsilon_\parallel = 4{\cdot}5$, $\varepsilon_\perp = 5$, $k_1 = 6{\cdot}1 \times 10^{-7}$ dyne, $k_2 = 4 \times 10^{-7}$ dyne, $k_3 = 7{\cdot}3 \times 10^{-7}$ dyne, $\alpha_2 = -77{\cdot}5$ cP,

CC-0. In Public Domain. Gurukul Kangri Collection, Haridwar

Digitized by Arya Samaj Foundation Chennai and eGangotri

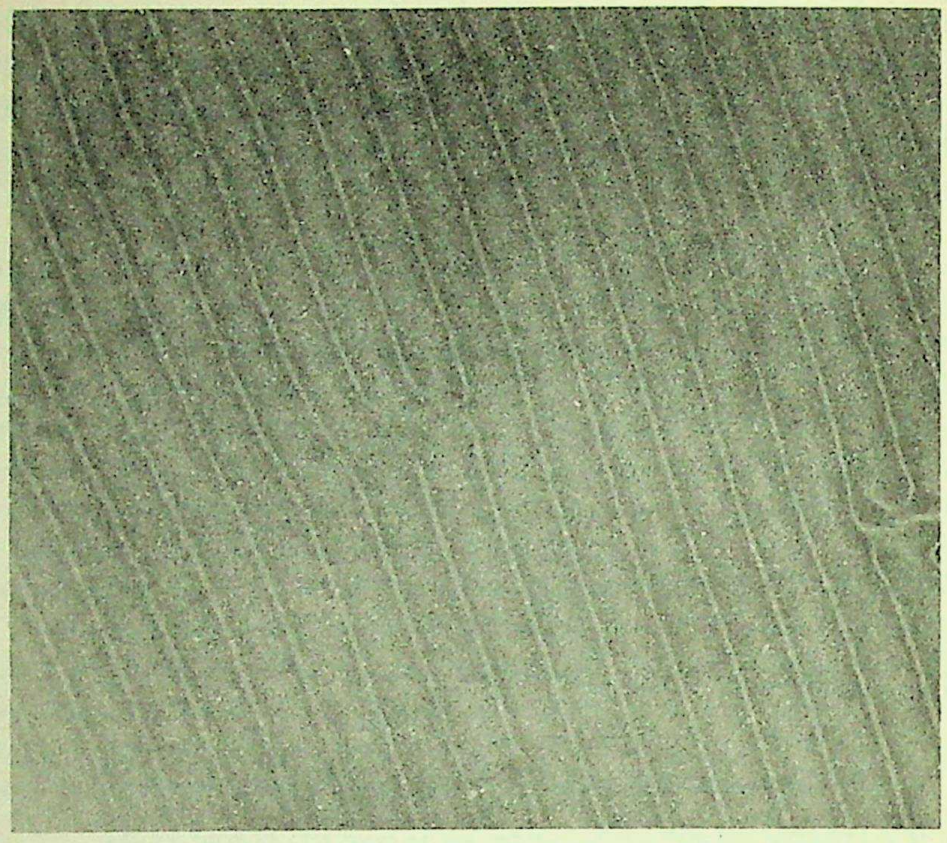

Figure 2. Photograph of the EHD pattern in a room temperature nematic. $\mathbf{n}_0$ is horizontal. Note that the edge dislocation corresponds to the addition of one optical domain, which has two hydrodynamic cells of opposite vorticity as explained in the text. Sample thickness $d \simeq 15\ \mu$m. Magnification $\times 250$.

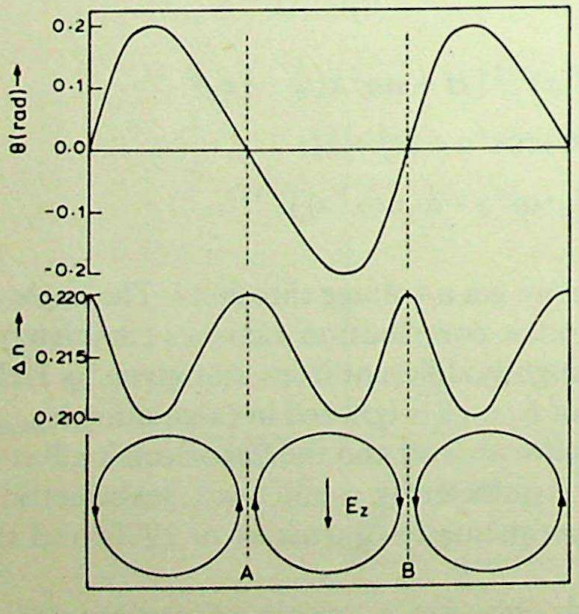

Figure 3. The non-sinusoidal θ profile obtained as a solution of equation (8) (top). The resulting variation of the effective Δn with ξ ($n_e = 1{\cdot}769$, $n_0 = 1{\cdot}549$) (middle). The disposition of the hydrodynamic rolls (bottom) agree with the observed dust particle motion, regions B corresponding to the bright lines of figure 2. A reversal of the field shifts the bright line to A.

CC-0. In Public Domain. Gurukul Kangri Collection, Haridwar

Digitized by Arya Samaj Foundation Chennai and eGangotri

$\alpha_4 = 83{\cdot}2$ cP, $\alpha_5 = 46{\cdot}3$ cP and $\Delta\sigma/\sigma_\perp = 0{\cdot}3$, which are typical values for MBBA at room temperature, we get $\alpha \simeq 47°$ and $V_{th} \simeq 1{\cdot}9$ V. Experimentally, Hirata and Tako (1982) find $\alpha \simeq 30°$ for MBBA. Ribotta *et al* (1986) also find oblique rolls in MBBA. (However the model of Zimmermann and Kramer (1985) does not lead to oblique rolls for the standard values of the material parameters of MBBA.)

We have studied the EHD patterns in a three-component mixture (containing CE-1700, CM-5115 and PCH 302 of Roche Chemicals) which is a stable room temperature nematic with $\Delta\varepsilon \simeq -0{\cdot}1$, and the values of $(e_1 + e_3)$ and $(e_1 - e_3)$ comparable to those of MBBA. We have verified by various tests that under a DC field, there is no influence of charge injection on the EHD rolls. Figure 2 shows a photograph of the EHD domains at a voltage slightly above V_{th} ($\simeq 3{\cdot}6$ V). We see oblique rolls with $\alpha \simeq 20°$, and more interestingly, the *optical* domain width, i.e., separation between two bright lines $\simeq 2d$. Indeed dust particle motion indicates that two rolls of opposite vorticity are contained in one optical domain, which corresponds to a full spatial period. Obviously, the director profile is not sinusoidal but the curvature in the region of the bright lines is much stronger than in the region midway between two bright lines (see figure 3). Further, when the voltage is reversed, the bright lines are shifted by half an optical domain width, showing that the distortion of the profile is polarity-dependent. Nonlinear terms are needed to account for the distortion of the director profile, and when $\alpha = 0$, up to second order terms equation (1) gives along y

$$K_3 \frac{d^2\theta}{d\xi^2} + H_0 E_z^2 \theta + G_0(e_1 + e_3) E_z \theta \frac{d\theta}{d\xi} = 0, \tag{8}$$

where the subscript 0 signifies that $\alpha = 0$. The lone quadratic term in (8) arises from the action of E_z on ρ_e, the flexoelectric contribution to the space charge density. Equation (8) can be solved graphically by the phase plane technique. The resulting nonsinusoidal θ profile and the effective birefringence Δn are shown in figure 3.

From (3) and (4), it is clear that a reversal of the sign of E_z can either change the sign of θ or ϕ but not both if the sign of α is fixed. Experimentally, in the material used by us, it is seen that θ does not reverse its sign with E_z and hence we conclude that ϕ changes sign with E_z. (Note that in the absence of flexoelectric terms, signs of θ and ϕ do not depend on that of E_z). Consequently, in an AC field, the flexoelectric contribution to the nonzero value of α should be ineffective beyond a frequency corresponding to a typical director relaxation rate under the given E_z. On the other hand, in the *dielectric* regime ($q \gg \pi/d$), θ oscillates with E_z (Dubois-Violette *et al* 1971; Smith *et al* 1975), and the flexoelectric contribution can again dominate. The large values of α seen in the 'chevron patterns' (Blinov 1983; de Gennes 1975) of the dielectric regime are then a natural consequence of our model. A detailed analysis of the AC regimes is underway.

When flexoelectric terms are included, the solutions (1) of Zimmermann and Kramer (1985) are not applicable in a simple three-dimensional analysis. Thus, a direct comparison of the present model with their theory is not possible. A full numerical analysis of the 3-dimensional problem is also underway.

Our thanks are due to Professor S Chandrasekhar and Dr G S Ranganath for helpful comments.

CC-0. In Public Domain. Gurukul Kangri Collection, Haridwar

Digitized by Arya Samaj Foundation Chennai and eGangotri

References

Barnik M I, Blinov L M, Trufanov A N and Umansky B A 1978 *J. Phys.* (*Paris*) **39** 417
Blinov L M 1983 *Electro-optical and magneto-optical properties of liquid crystals* (New York: Wiley)
Bobylev Yu P and Pikin S A 1977 *Sov. Phys. JETP* **45** 195
Chandrasekhar S 1977 *Liquid crystals* (Cambridge: University Press)
de Gennes P G 1975 *The physics of liquid crystals* (Oxford: Clarendon)
Dubois-Violette E, de Gennes P G and Parodi O 1971 *J. Phys.* (*Paris*) **32** 305
Dozov I, Martinot-Lagarde Ph and Durand G 1982 *J. Phys.* (*Paris*) **43** L-365
Helfrich W 1969 *J. Chem. Phys.* **51** 4092
Hirata S and Tako T 1982 *Jpn J. Appl. Phys.* **21** L607
Ioffe I V 1975 *Sov. Phys. Tech. Phys.* **19** 1012
Madhusudana N V and Durand G 1985 *J. Phys.* (*Paris*) **46** L-195
Matyushichev Yu F and Kovnatskii A M 1975 *Sov. Phys. Tech. Phys.* **20** 409
Meyer R B 1969 *Phys. Rev. Lett.* **22** 918
Prost J and Marcerou J P 1977 *J. Phys.* (*Paris*) **38** 315
Ribotta R, Joets A and Lei L 1986 *Phys. Rev. Lett.* **56** 1595
Smith I W, Galerne Y, Lagerwall S T, Dubois-Violette E and Durand G 1975 *J. Phys.* (*Paris*) **36** C1-237
Zimmermann W and Kramer L 1985 *Phys. Rev. Lett.* **55** 403

CC-0. In Public Domain. Gurukul Kangri Collection, Haridwar

Digitized by Arya Samaj Foundation Chennai and eGangotri

Pramāṇa – J. Phys., Vol. 28, No. 3, March 1987, pp. L317–L319. © Printed in India.

Electron-fluctuating distortion interaction in the new high T_c superconductors

R JAGADISH and K P SINHA

Division of Physics and Mathematical Sciences, Indian Institute of Science, Bangalore 560012, India

MS received 21 February 1987

Abstract. A mechanism involving interaction of conduction electrons with the distortion field and the phonon modes is considered for the newly discovered high T_c superconducting materials. This is capable of explaining the observed range of T_c.

Keywords. Structural distortion; superconductivity; Jahn-Teller polarons.

PACS No. 74·10

Intense research activities have started at many centres in the world after the discovery of high T_c (36 K or more) superconductivity in doped lanthanum copper oxide systems, e.g. $La_{2-x}M_x CuO_4$, M = Ba, Sr, etc (Bednorz and Müller 1986; Uchida *et al* 1987; Chu *et al* 1987; Cava *et al* 1987). Regarding possible mechanisms, it is felt that the usual acoustic phonon-mediated processes may not give high enough transition temperatures. Accordingly, one should look for new mechanisms which may involve exchange of electronic excitations (Jagadish and Sinha 1987), bipolaronic mechanisms (Chakraverty 1979; Alexandrov and Ranninger 1981), interfacial excitonic mechanisms (Allender *et al* 1973; Ginzburg and Kirzhnits 1982), antiferromagnetic correlation as in the Hubbard model (Nozieres 1984; Anderson 1987) and mechanisms emanating from local distortions and structural instabilities in the system (Phillips 1976; Ngai and Reinecke 1977; Vujicie *et al* 1981).

At this stage it is desirable to note some special features of the $La_{2-x}M_xCuO_4$ systems. They have K_2NiF_4-type structure having planes of CuO_6 octahedra which share corners. These planes are separated by (La, M) layers. The structure of pure La_2CuO_4 (with copper in Cu^{2+} state, a Jahn-Teller ion) has a slight orthorhombic distortion. It is a semiconductor with low magnetic susceptibility (Rao *et al* 1985). $LaSrCuO_4$ is an insulator with Cu^{3+} ions in the diamagnetic state (Rao and Ganguly 1987). This low spin state appears to us to be stabilized by on-site bipolaron formation owing to strong electron-phonon interaction. It also leads to the splitting of e_g electronic states (at Cu^{2+}) leading to J-T polaron formation. The metallic behaviour of $La_{2-x}M_xCuO_4$ arises from the presence of Cu^{2+} and Cu^{3+} ions in the system wherein the J-T polarons become mobile and form a very narrow conduction band. It is confined to the two-dimensional planes of CuO_6 octahedra. Further, these oxide superconductors lie near the metal insulator transitions arising from the J-T polaron formation.

CC-0. In Public Domain. Gurukul Kangri Collection, Haridwar

Digitized by Arya Samaj Foundation Chennai and eGangotri

The crucial point, in the context of the model that we shall develop here, is that the system in question exhibits structural instabilities due to tetragonal to orthorhombic distortion when it is very rich in Cu^{2+} ions. Our stipulation is that even in the M^{2+} ion stabilized tetragonal phase local structural instabilities towards orthorhombic distortions exist. This is akin to a pseudo Jahn-Teller-induced local lattice distortion. This mechanism was first suggested by Sinha and Sinha (1964) for displacive ferroelectrics (e.g. $BaTiO_3$) and the full dynamical aspect leading to phonon softening worked out by Shukla and Sinha (1966). The model involves a two-level system of configurational local distortions. This was transcribed to a pseudo-spin ($S = 1/2$) formalism for protonic ferroelectrics (see Blinc and Zeks 1974).

Thus the Hamiltonian of a system of conduction electrons (in a narrow band) interacting with phonons and a distortion field described by the two-level system can be written as

$$H = H_e + H_c + H_{\mathrm{Ph}} + H_{e-\mathrm{Ph}} + H_{df} + H_{e-df}, \tag{1}$$

where

$$H_e = \sum \varepsilon_{\mathbf{k}} C^{\dagger}_{\mathbf{k}\sigma} C_{\mathbf{k}\sigma} \tag{2}$$

($C^{\dagger}_{\mathbf{k}\sigma}\, C_{\mathbf{k}\sigma}$) are (creation, annihilation) operators for conduction electrons in the Bloch state $|\mathbf{k}\sigma\rangle$, having single particle energy $\varepsilon_{\mathbf{k}}$ wave vector $\mathbf{k}$ and spin σ; H_c is the screened coulomb interaction between conduction electrons, H_{ph} is the standard phonon Hamiltonian and $H_{e-\mathrm{ph}}$ represents the electro-phonon interaction. In the pseudo-spin representation, we can write

$$H_{df} = -E_{as} \sum S^z_m - \frac{1}{2} \sum_{l,m} J_{lm} S^x_l S^x_m, \tag{3}$$

where $E_{as} = E_a - E_s > 0$ is the energy difference between the two levels at site m; and J_{lm} represents the interaction energy between distortions at site l and m. Further,

$$H_{e-df} = \sum_{\mathbf{k}-\mathbf{k}=\mathbf{q}} V_d(\mathbf{k}, \mathbf{k}')\, C^{\dagger}_{\mathbf{k}'\sigma}\, C_{\mathbf{k}\sigma}\, S^x_{\mathbf{q}}, \tag{4}$$

which involves the scattering of a conduction electron along with a change in state of the distortion field. The effective electron-electron interaction λ_d analogous to the phonon-mediated process, can be calculated by the Eliashberg procedure. We get

$$\lambda_d = N(0) \langle I_d^2 \rangle E_{as} \langle S^z \rangle / \omega_d^2, \tag{5}$$

where ω_d is the average frequency of the distortion field mode; the average $\langle I_d^2 \rangle$ being defined in the standard way. This expression should be compared with the phonon-mediated coupling constant

$$\lambda_{\mathrm{ph}} = N(0)\, \langle I^2_{\mathrm{ph}} \rangle \langle 1/M\omega^2_{\mathrm{ph}} \rangle, \tag{6}$$

ω_{ph} being the usual phonon frequency and M the mass in question. Following Vujicic *et al* (1981) the expression for T_c can be written as

$$T_c = 1{\cdot}14\, \omega_d \exp(-1/\lambda) \tag{7}$$

CC-0. In Public Domain. Gurukul Kangri Collection, Haridwar

Digitized by Arya Samaj Foundation Chennai and eGangotri

where

$$\lambda = \lambda_d + \frac{\lambda_{ph}}{1 - \lambda_{ph} \ln(\omega_{ph}/\omega_d)}.$$

Note that the Coulomb repulsion has been neglected inasmuch as it will be negligible owing to onsite and intersite bipolaron effects.

At this stage it is difficult to give a quantitative estimate of T_c. For a rough idea the following should be noted. We expect $\langle I_d^2 \rangle$ and $\langle I_{ph}^2 \rangle$ to be comparable. But the distortion modes are low-frequency modes and hence λ_d will be much larger than λ_{ph} (cf equations (5) and (6)). Thus this interaction via the distortion field mode will strengthen the pairing of electrons further and enhance T_c. We give below a few values calculated for a choice of parameters.

$$T_c = 36\ \text{K for } \lambda_d = 1{\cdot}5, \quad \lambda_{ph} = 0{\cdot}3, \quad \omega_d = 50\ \text{K}, \quad \omega_{ph} = 300\ \text{K},$$
$$T_c = 44\ \text{K for } \lambda_d = 1{\cdot}7, \quad \lambda_{ph} = 0{\cdot}3, \quad \omega_d = 60\ \text{K}, \quad \omega_{ph} = 300\ \text{K},$$
$$T_c = 94\ \text{K for } \lambda_d = 1{\cdot}7, \quad \lambda_{ph} = 0{\cdot}6, \quad \omega_d = 100\ \text{K}, \quad \omega_{ph} = 400\ \text{K}.$$

The last entry is appropriate for the system Y–Ba–Cu–O (Wu *et al* 1987). Thus the mechanism used in the present paper is capable of explaining the observed T_c. It should, however, be noted that the system may involve electronic and bipolaronic mechanisms also.

References

Alexandrov A and Ranninger J 1981 *Phys. Rev.* **B24** 1164
Allender D, Bray J and Bardeen J 1973 *Phys. Rev.* **B3** 1020
Anderson P W 1987 *Science* (to be published)
Bednorz J G and Müller K A 1986 *Z. Phys.* **B64** 189
Blinc R and Zeks B 1974 *Soft modes in ferroelectrics and antiferroelectrics* (Amsterdam: North Holland)
Cava R J, Van Dover R B, Batlogg B and Rietman E A 1987 *Phys. Rev. Lett.* **58** 408
Chakraverty B K 1979 *J. Phys.* (*Paris*) *Lett.* **40** L-99
Chu C W, Hor P H, Meng R L, Gao L, Huang Z J and Wang Y Q 1987 *Phys. Rev. Lett.* **58** 405
Ginzburg V L and Kirzhnits D A 1982 *High temperature superconductivity* (New York: Consultants Bureau)
Jagadish R and Sinha K P 1987 *Curr. Sci.* (in press)
Ngai K L and Reinecke T L 1977 *Phys. Rev.* **B16** 1077
Nozieres P 1984 Lecture notes (unpublished)
Phillips J C 1976 *Solid State Commun.* **18** 831
Rao C N R and Ganguly P 1987 *Curr. Sci.* **56**
Rao C N R, Rao K J and Gopalakrishnan J 1985 Annual Reports C, The Royal Society of Chemistry, London
Shukla G C and Sinha K P 1966 *J. Phys. Chem. Solids* **27** 1837
Sinha K P and Sinha A P B 1964 *Indian J. Pure Appl. Phys.* **2** 273
Uchida S, Takagi H, Kitazawa K and Tanaka S 1987 *Jpn. J. Appl. Phys.* **26** L1
Vujicic G M, Aksenov V L, Plakida N M and Stamenkovic S 1981 *J. Phys.* **C14** 2377
Wu M K *et al* 1987 *Phys. Rev. Lett.* **58** 908

CC-0. In Public Domain. Gurukul Kangri Collection, Haridwar

Digitized by Arya Samaj Foundation Chennai and eGangotri

CC-0. In Public Domain. Gurukul Kangri Collection, Haridwar

Digitized by Arya Samaj Foundation Chennai and eGangotri

Pramana–J. Phys., Vol. 28, No. 3, March 1987, pp. L321–L323. © Printed in India.

Identification of the high-temperature superconducting phase in the Y-Ba-Cu-O system as the perovskite $YBa_2Cu_3O_{7\pm\delta}$

P GANGULY, R A MOHAN RAM, K SREEDHAR and C N R RAO*

Solid State and Structural Chemistry Unit, Indian Institute of Science, Bangalore 560 012, India

Abstract. The oxide responsible for high-temperature superconductivity (onset ~ 100 K, zero resistance above liquid N_2 temperature) is found to be $YBa_2Cu_3O_{7\pm\delta}$.

Keywords. High-temperature superconductivity; $YBa_2Cu_3O_7$

PACS No. 74·70

The discovery of superconducting oxides of the Y-Ba-Cu-O system, exhibiting zero resistance above the liquid nitrogen temperature (Wu *et al* 1987; Ganguly *et al* 1987), has received worldwide attention. The oxide compositions which have shown this behaviour seem to be complex and biphasic. The $Y_{1.2}Ba_{0.8}CuO_4$ composition of Wu *et al* (1987), based on the analogy with $La_{2-x}Ba_xCuO_4$ possessing the K_2NiF_4 structure (Chu *et al* 1987; Rao and Ganguly 1987), consisted of a green and a black oxide. We suspect that the green oxide was Y_2BaCuO_5 which is an insulator. We did not prepare Y-Ba-Cu oxides with compositions related to those of K_2NiF_4 structure since Y_2CuO_4 itself is not formed in this structure. Instead, we made Y-Ba-Cu oxides analogous to $La_3Ba_3Cu_6O_{14}$ (Er-Rakho *et al* 1981) which is an oxygen-deficient perovskite possessing a

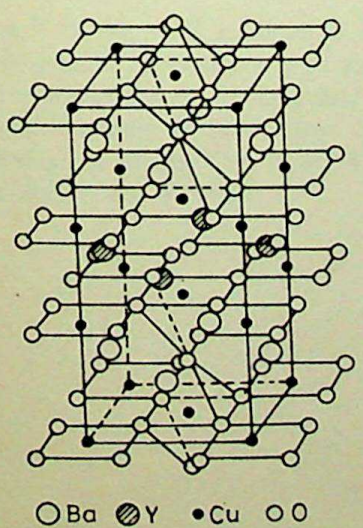

Figure 1. Proposed structure of $Y_2Ba_4Cu_6O_{14\pm\delta}$ analogous to $La_3Ba_3Cu_6O_{14}$ (following Er-Rakho *et al* 1981). A_1 and A_2 sites are shown. Y occupies A_2 sites preferentially.

Contribution No. 432 from the Solid State and Structural Chemistry Unit

* To whom all correspondence should be addressed

CC-0. In Public Domain. Gurukul Kangri Collection, Haridwar

Digitized by Arya Samaj Foundation Chennai and eGangotri

tetragonal structure with $a = a_p 2^{1/2}$ and $c = 3a_p$; the oxygen vacancies are ordered with three different copper sites. This as well as the analogous yttrium oxides are black and the a_p parameter decreases with the introduction of the smaller Y ion. Along the c-axis, the sequence is $|Cu_2O_4 - A_2O\,\square - Cu_2O_4 - A_2\,\square_2 - Cu_2O_4 - A_2O\,\square|_\infty$. The A cations with 8-coordination (A_1) and with 10-coordination (A_2) are occupied by Y (or La) and Ba ions respectively. This structure retains some features of the K_2NiF_4 structure in the sense that copper ions with essentially square-planar coordination do not

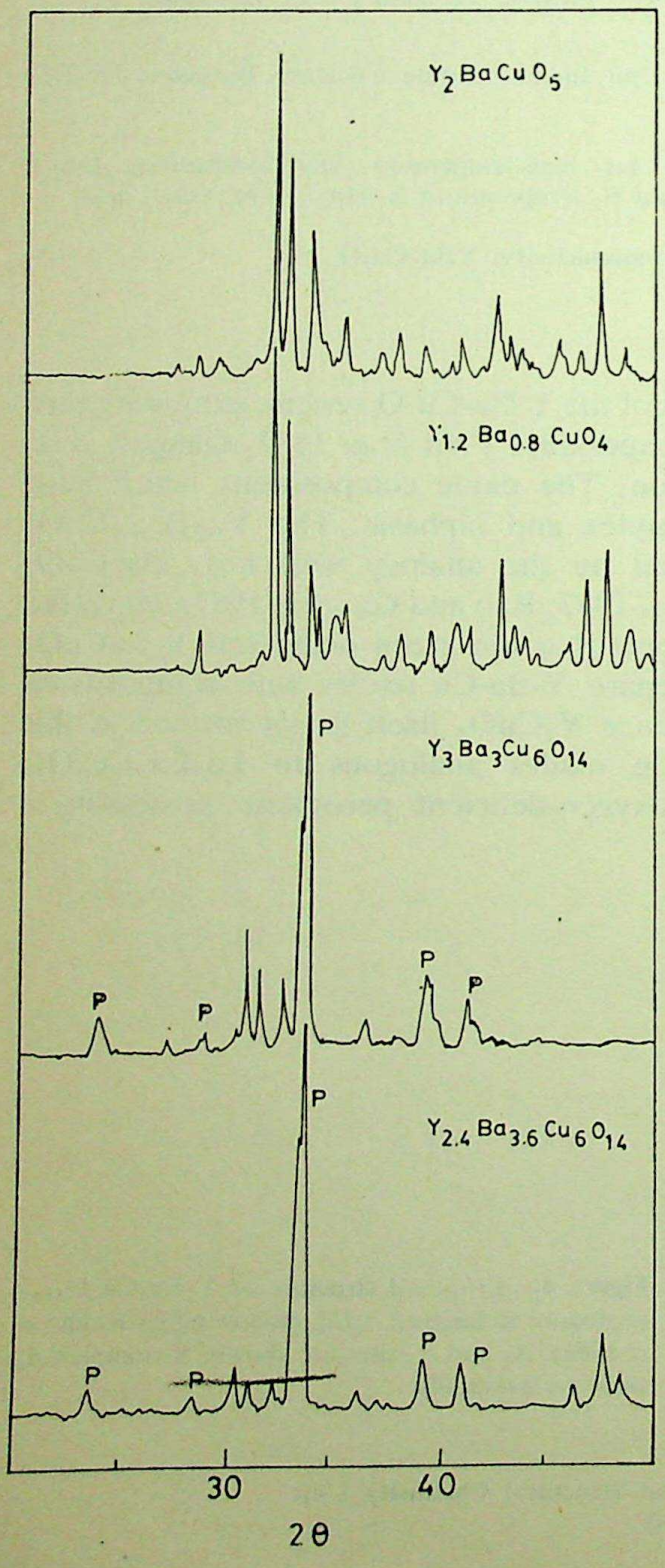

Figure 2. X-ray powder patterns of $Y_{3-x}Ba_{3+x}Cu_6O_{14}$, Y_2BaCuO_5 and $Y_{1.2}Ba_{0.8}CuO_4$.

CC-0. In Public Domain. Gurukul Kangri Collection, Haridwar

Digitized by Arya Samaj Foundation Chennai and eGangotri

interact along the *c*-axis over long distances. If Y occupies only A_2 sites, the composition will be $Y_2Ba_4Cu_6O_{14}$ (figure 1).

We have examined superconductivity of several oxides of the general formula $Y_{3-x}Ba_{3+x}Cu_6O_{14}$ and find some of them to be superconducting well above the liquid nitrogen temperature (Ganguly *et al* 1987; also unpublished results from this laboratory). Almost all the compositions are however biphasic. We have carried out an x-ray study of these oxides to establish the identity of the oxide phase responsible for high-temperature superconductivity. In figure 2, we show typical x-ray powder patterns of these oxides along with those of Y_2BaCuO_5 (green insulator) and $Y_{1.2}Ba_{0.8}CuO_5$ (composition of Wu *et al* 1987). We readily see that the last oxide has predominant features of Y_2BaCuO_5 and some weaker features of the perovskite; $Y_{3-x}Ba_{3+x}Cu_6O_{14}$ compositions, however, show the perovskite features (see intense peak marked P in figure 2). Prominently, features of Y_2BaCuO_5 are much weaker here. Based on this x-ray study, we find that the composition of the "pure" perovskite phase is likely to be close to $Y_2Ba_4Cu_6O_{14}$ or $YBa_2Cu_3O_7$. We have prepared this oxide composition by heating the component oxides in air at 1170 K and find it to be a monophasic perovskite. The perovskite phase in $Y_{3-x}Ba_{3+x}Cu_6O_{14}$ seems to be slightly less distorted compared to the pure $YBa_2Cu_3O_7$ phase; this probably arises from changes in oxygen stoichiometry. The exact composition of the high T_c oxide phase may therefore be written as $YBa_2Cu_3O_{7\pm\delta}$. This oxide heated in oxygen does indeed exhibit high-temperature superconductivity with zero resistance above liquid N_2 temperature.

The authors thank the University Grants Commission and the Department of Science and Technology for support of this research.

References

Chu C W, Hor P H, Meng R L, Gao L, Huang Z J and Wang Y Q 1987 *Phys. Rev. Lett.* **58** 405

Er-Rakho L, Michel C, Provost J and Raveau B 1981 *J. Solid State Chem.* **37** 151

Ganguly P, Raychaudhuri A K, Sreedhar K and Rao C N R 1987 *Pramana–J. Phys.* **28** 229

Rao C N R and Ganguly P 1987 *Curr. Sci.* **56** 47

Wu M K, Ashburn J R, Torng C J, Hor P H, Meng R L, Gao L, Huang Z J, Wang Y Q and Chu C W 1987 *Phys. Rev. Lett.* **58** 908

CC-0. In Public Domain. Gurukul Kangri Collection, Haridwar

Digitized by Arya Samaj Foundation Chennai and eGangotri

CC-0. In Public Domain. Gurukul Kangri Collection, Haridwar

Digitized by Arya Samaj Foundation Chennai and eGangotri
Pramāṇa – J. Phys., Vol. 28, No. 4, April 1987, pp. 325–334. © Printed in India.

पुस्तकालय
गुरुकुल कांगड़ी विश्वविद्यालय
हरिद्वार
15/87

Equivalent potentials for a nonsymmetric non-local interaction

G C SETT, U LAHA and B TALUKDAR
Department of Physics, Visva-Bharati, Santiniketan 731 235, India

MS received 4 November 1986

Abstract. Scattering formalisms which incorporate antisymmetrization of the projectile with respect to identical particles in the target result in a nonsymmetric non-local interaction. Such an interaction constraints the relative wavefunctions to be orthogonal to redundant states forbidden by the Pauli principle. Concentrating on the nonsymmetric non-local kernel of Saito we try to visualize the mechanisms by which a potential can ensure the required orthogonality. We achieve this by replacing the Saito kernel by an effective symmetric non-local potential. The constructed symmetric potential is found to be phase-equivalent only but not off-shell equivalent to the original kernel. This difference in the off-shell behaviour is attributed to the dynamical origin simulating the redundant states. In close analogy with one of our recent works we also derive an energy-momentum dependent equivalent to the local potential. Our solution of the pseudo inverse problem is exact and provides a basis for writing the phase—and quasiphase—equations. We present numerical results in support of this.

Keywords. Equivalent potentials; radial wavefunction; non-local interaction; Saito potential; phase method.

PACS Nos 25·10; 25·60; 25·70

1. Introduction

The resonating group method (RGM) (Wildermuth *et al* 1966) represents a microscopic theory for the description of the interaction between nucleon clusters or composite nuclei. As an approximation to RGM, Saito (1969) introduced the orthogonality condition model (OCM). In OCM, non-symmetric non-local potentials occur which constraint the relative wave functions to be orthogonal to redundant states forbidden by the Pauli principle. The essential feature for maintaining orthogonality provides for extra nodes in the scattering wave functions (Krasnopol'skii and Kukulin 1975). An important aspect of Saito's theory is that the redundant states appear in the model potentials. For example, the s-wave Saito potential in the presence of one redundant state $v_1(r)$ is given by

$$V(r, r') = v_1(r)\, v_1(r') \frac{d^2}{dr'^2}. \tag{1}$$

Here $v_1(r)$ is represented by a normalized function (Okai *et al* 1972)

$$v_1(r) = (4a^3)^{1/2}\, r \exp(-ar), \tag{2}$$

with $a = 2\ \mathrm{fm}^{-1}$. It has been observed (Englefield *et al* 1974) that the potential in

CC-0. In Public Domain. Gurukul Kangri Collection, Haridwar

Digitized by Arya Samaj Foundation Chennai and eGangotri

equation (1) can simulate the effect of the repulsive core of the α-α interaction as well as that of the n-p interaction in the $^1S_0$ channel.

In the present paper we consider the problem of symmetrization as well as of localization of the non-symmetric non-local potential in equation (1). The symmetrization procedure helps us visualize the mechanisms by which a potential can ensure the required orthogonality in terms of extra nodes in the scattering wave functions. The local potential constructed by us is momentum-dependent. This dependence may be expected to assume some significance when considering electromagnetic interactions (Yamaguchi 1954).

The Schrödinger equation for the Saito potential and its adjoint admits of simple analytical solution (Ghosh *et al* 1983). In § 2 we present some of these results and see that the Saito model freezes the redundant states or continuum bound states (CBS) at zero energy. We also note that although the Saito potential and its adjoint are phase-equivalent, they exhibit altogether different off-shell properties. We symmetrize the Saito potential in § 3. The symmetrization procedure converts the zero energy CBS to another redundant state called the spurious state (Coz *et al* 1970). The spurious state, however, occurs at a very high energy. Interestingly, both symmetric and non-symmetric potentials exhibit the same on-shell behaviour but they differ very much in their off-shell properties. This verifies that off-shell properties of a potential are sensitive to the nature of the redundant state it can support. We localize the Saito potential and its adjoint in § 4. In the case of a local potential the only circumstance which can cause an extra node is the presence of a bound state. In the course of our study we shall see that the constructed local potentials do not involve the effect of any extra node whatsoever. Thus the localization procedure carried out here does not spoil the repulsive nature of the Saito interaction. In § 5 we examine the quality of our local potentials by using a combined variable phase off-shell scattering theory.

2. Radial wave functions

At a positive energy $k^2 > 0$ the s-wave solutions of the radial Schrödinger equation for the potential in equation (1) belonging to the regular, irregular and outgoing wave boundary conditions are (Ghosh *et al* 1983).

$$\phi_s(k,r) = \frac{\sin kr}{k} - \frac{8a^4k^2}{D_s(k)(a^2+k^2)^4}\Bigg[(a^2+k^2)r\exp(-ar) + 2a\left\{\exp(-ar) - \cos kr + \frac{a^2-k^2}{2ak}\sin kr\right\}\Bigg], \tag{3}$$

$$f_s(k,r) = \exp(ikr) - \frac{4a^3k^2(a+ik)^2}{\Delta_s(k)(a^2+k^2)^4}[(a^2+k^2)r+2a]\exp(-ar), \tag{4}$$

and

$$\psi_s^+(k,r) = \sin kr + \frac{8a^4k^3}{D_s^+(k)(a^2+k^2)^4}[2a(\exp(ikr) - \exp(-ar)) - (a^2+k^2)r\exp(-ar)]. \tag{5}$$

In the above we have used the subscripts to specify quantities directly related to

CC-0. In Public Domain. Gurukul Kangri Collection, Haridwar

Digitized by Arya Samaj Foundation Chennai and eGangotri

scattering by the Saito potential. The same convention is also followed for the corresponding adjoint potential. We shall, however, use no subscript for quantities related to equivalent potentials to be constructed in subsequent section. Here

$$D_s(k) = 1 - a^2(a^2 - k^2)/(a^2 + k^2)^2, \tag{6}$$

represents the Fredholm determinant associated with $\phi_s(k, r)$. Also $D_s(k) = \Delta_s(k)$, the Fredholm determinant (Bagchi *et al* 1978). The Fredholm determinant associated with $\psi_s^{(+)}(k, r)$ is given by

$$D_s^{(+)}(k) = 1 - (a^2 + k^2)^{-4}(a^8 + 9a^6k^2 - 9a^4k^4 - a^2k^6 + 16\,i\,a^5k^3). \tag{7}$$

The Jost function is determined by the behaviour of the irregular solution near the origin and in this case we have

$$f_s(k) = f_s(k, 0) = 1 - \frac{8a^4k^2}{\Delta_s(k)\,(a^2 + k^2)^4}(a + ik)^2. \tag{8}$$

The phase of the Jost function is the negative of the scattering phase shift (Newton 1966). Thus the expression in (8) provides a basis for calculating the scattering phase shifts induced by the Saito potential.

In general the simultaneous zeros of $D^{(+)}(k)$ and $D(k)$ for $k \neq 0$ are called continuum bound states (Gourdin and Martin 1957). The quantities $D_s(k)$ and $D_s^{(+)}(k)$ given in (6) and (7) can be simultaneously zero only for $k = 0$. Heurestically, this is often expressed by saying that the Saito model freezes all redundant states at zero energy (Bagchi *et al* 1980). The term spurious state is reserved for a zero of $D(k)$ for $D^{(+)}(k) \neq 0$ (Coz *et al* 1970; Arnold and Mac Keller 1971). Clearly this cannot occur in our case and the Saito potential does not support a spurious state.

For the adjoint potential to that in equation (1) we denote the regular, irregular and outgoing wave solutions by $\tilde{\phi}_s(k, r)$, $\tilde{f}_s(k, r)$ and $\tilde{\psi}_s^{(+)}(k, r)$ respectively. The results for these solutions are given by

$$\tilde{\phi}_s(k, r) = \frac{\sin kr}{k} - \frac{8a^5}{(a^2 + k^2)^3\,\tilde{D}(k)}\left[\frac{a(a^2 + 3k^2)}{k(a^2 + k^2)}\sin kr - \frac{2k^2}{(a^2 + k^2)}\cos kr + \left\{\frac{2k^2}{(a^2 + k^2)} - ar\right\}\exp(-ar)\right], \tag{9}$$

$$\tilde{f}_s(k, r) = \exp(ikr) + \frac{4a^4(a + ik)^2}{(a^2 + k^2)^3\,\tilde{\Delta}_s(k)}\left[ar\exp(-ar) - \frac{2k^2}{(a^2 + k^2)}\exp(-ar)\right], \tag{10}$$

and

$$\tilde{\psi}_s^{(+)}(k, r) = \sin kr + \frac{8a^5k}{(a^2 + k^2)^4\,\tilde{D}_s^{(+)}(k)}[a(a^2 + k^2)\,r\exp(-ar) - 2k^2(\exp(-ar) - \exp(ikr))], \tag{11}$$

with

$$\tilde{D}_s(k) = (8a^4 + 3a^2k^2 + k^4)/(a^2 + k^2)^2, \tag{12}$$

$$\tilde{\Delta}_s(k) = D_s(k) = \Delta_s(k), \tag{13}$$

CC-0. In Public Domain. Gurukul Kangri Collection, Haridwar

Digitized by Arya Samaj Foundation Chennai and eGangotri

and

$$\tilde{D}_s^{(+)}(k) = D_s^{(+)}(k). \tag{14}$$

From (10) we get the Jost function for the adjoint potential in the form

$$\tilde{f}_s(k) = 1 - \frac{8a^4k^2}{(a^2+k^2)^4\,\tilde{\Delta}_s(k)}\,(a+ik)^2. \tag{15}$$

Equations (8), (13) and (15) show that the Saito potential and its adjoint are phase-equivalent (Bagchi *et al* 1978). These two, however, exhibit entirely different off-shell properties. For example, the half-shell t-matrix for the Saito potential is given by (Fuda and Whiting 1973; Ghosh *et al* 1983)

$$t_s(k, q; k^2) = \frac{32a^5q^2}{\pi f_s(k)\,\Delta_s(k)\,(a^2+k^2)^2\,(a^2+q^2)^2}, \tag{16}$$

while that for the corresponding adjoint potential is

$$\tilde{t}_s(k, q; k^2) = -\frac{32\,a^5k^2}{\pi f_s(k)\,\Delta_s(k)\,(a^2+k^2)^2\,(a^2+q^2)^2}, \tag{17}$$

where q is an off-shell momentum. Clearly $t_s(k, q; k^2) \neq \tilde{t}_s(k, q; k^2)$.

3. Symmetrization of the Saito potential

The radial Schrödinger equation for the potential in equation (1) is given by

$$\left(\frac{d^2}{dr^2} + k^2\right)\psi_s(k, r) = 4a^3\,r\exp(-ar)\int_0^\infty r'\exp(-ar')\,\frac{d^2}{dr'^2}\,\psi_s(k, r')\,dr'. \tag{18}$$

From (18) one has $\langle v_1 | \psi_s \rangle = 0$. To summarize the Saito kernel we proceed as follows.

Consider the Yamaguchi potential written as (Yamaguchi 1954)

$$V(r, r') = \lambda \exp[-\beta(r+r')]. \tag{19}$$

Here λ and β are energy-independent strength and range parameters. The regular solution for this potential is given by (Ghosh *et al* 1983)

$$\phi(k, r) = \frac{\sin kr}{k} + \frac{\lambda}{D(k)\,(\beta^2+k^2)^2}\left[\exp(-\beta r) + \frac{\beta}{k}\sin kr - \cos kr\right], \tag{20}$$

with the Fredholm determinant

$$D(k) = 1 - \lambda/2\beta\,(\beta^2+k^2). \tag{21}$$

The Fredholm determinant associated with the physical solution of Yamaguchi potential is

$$D^{(+)}(k) = D(k) + \frac{\lambda(\beta+ik)}{(\beta^2+k^2)^2}. \tag{22}$$

CC-0. In Public Domain. Gurukul Kangri Collection, Haridwar

Digitized by Arya Samaj Foundation Chennai and eGangotri

From (21) and (22) it is clear that no values of λ and β will make $D^{(+)}(k)$ zero, and therefore, a continuum bound state cannot be associated with the Yamaguchi form factor. On the other hand, $D(k)$ can be zero for a wide range of values of λ and β. Mulligan *et al* (1976) illustrated that the Yamaguchi form factor supports a spurious state at $E_{lab} = 400$ MeV for $\lambda = 21{\cdot}219$ fm^{-3} and $\beta = 1{\cdot}5$ fm^{-1}. Thus if we demand that $\langle v_1 | \phi \rangle = 0$, it will amount to simulating the effect (which is essentially an extra node or an inner oscillation) of continuum bound state of the Saito potential through a spurious state associated with the Yamaguchi form factor and both symmetric and non-symmetric potentials will be expected to be phase-equivalent. From $\langle v_1 | \phi \rangle = 0$ we immediately get

$$\lambda(k^2) = -2a\beta(\beta^2 + k^2)(a+\beta)^2/[\beta(a^2+k^2) - a(a^2-\beta^2)]. \tag{23}$$

Thus for a given β the Yamaguchi potential can have the same inner oscillation as that of the Saito potential provided the coupling constant becomes energy-dependent. The result in (23) was obtained by Bagchi *et al* (1980) by using the Fredholm's third theorem for a scattering solution to exist when $D(k)$ or $D^{(+)}(k)$ is zero.

We have numerically found that for $\beta = 1$ fm^{-1} the Yamaguchi potential with the energy-dependent coupling constant given in (23) is phase-equivalent to the Saito potential. Although the potential strength changes sign at $k^2 = 2$ fm^{-2}, this does not affect the continuity of the phase shift. Bagchi *et al* (1980) claim this as a necessary requirement for the scattering wave function to exhibit proper continuity and nodal behaviour.

The half off-shell t-matrix for the symmetric potential under consideration is given by

$$t_{sym}(k, q; k^2) = \frac{2\lambda(k^2)q}{\pi q f(k)(\beta^2+k^2)(\beta^2+q^2)D_{sym}(k)}, \tag{24}$$

with

$$f(k) = 1 + \frac{\lambda(\beta + ik)}{(\beta^2+k^2)D_{sym}(k)}. \tag{25}$$

The expression for $D_{sym}(k)$ is obtained from (21) by replacing λ by $\lambda(k^2)$. It can be seen that numerical results for $t_{sym}(k, q; k^2)$ do not agree with those for $t_s(k, q; k^2)$ or $\tilde{t}_s(k, q; k^2)$. This implies that the off-shell behaviour of the constructed symmetric potential is different from that of the Saito potentials.

4. Equivalent local potentials

We have introduced the radal Schrödinger equation for the Saito potential in (18). For adjoint scattering (Bagchi *et al* 1978) the Schrödinger equation corresponding to (18) is

$$\left(\frac{d^2}{dr^2} + k^2\right)\tilde{\psi}_s(k, r) = 4a^3 \frac{d^2}{dr^2}[r \exp(-ar)] \times \int_0^\infty r' \exp(-ar')\,\tilde{\psi}_s(k, r')\,dr'. \tag{26}$$

CC-0. In Public Domain. Gurukul Kangri Collection, Haridwar

Digitized by Arya Samaj Foundation Chennai and eGangotri

For the non-local potentials in (18) and (26) we have obtained the equivalent local potentials in the form

$$V_{\text{eq}}^{(i)}(k,r) = g_1^{(i)}(k,r) + g_2^{(i)}(k,r)\frac{\mathrm{d}}{\mathrm{d}r}, \qquad i = 1, 2, \tag{27}$$

by following a prescription given by us earlier (Talukdar *et al* 1985). The subscript $i = 1$ corresponds to (18) while $i = 2$ corresponds to (26). The expressions for $g_1^{(i)}(k,r)$ and $g_2^{(i)}(k,r)$ are given as

$$g_1^{(i)}(k,r) = \{\beta_1^{(i)}(k,r)\gamma_1^{(i)}(k,r)\, k \sin kr - \beta_2^{(i)}(k,r)\gamma_2^{(i)}(k,r) k \cos kr\} \times \frac{1}{(\beta_1^{(i)2} + \beta_2^{(i)2})}, \tag{28a}$$

and

$$g_2^{(i)}(k,r) = \{\beta_1^{(i)}(k,r)\gamma_1^{(i)}(k,r) \cos kr + \beta_2^{(i)}(k,r)\gamma_2^{(i)}(k,r) \sin kr\} \times \frac{1}{(\beta_1^{(i)2} + \beta_2^{(i)2})}, \tag{28b}$$

with

$$\beta_1^{(1)}(k,r) = \frac{(3a^2+k^2)}{8a^4}\left[1 - \frac{8a^4}{(3a^2+k^2)}\left\{\frac{r\exp(-ar)(-a\cos kr + k\sin kr)}{(a^2+k^2)} - \exp(-ar)\frac{\{(a^2-k^2)\cos kr - 2ak\sin kr\}}{(a^2+k^2)^2} - \frac{a^2-k^2}{(a^2+k^2)^2}\right\}\right], \tag{29a}$$

$$\beta_2^{(1)}(k,r) = \frac{r\exp(-ar)(-a\sin kr - k\cos kr)}{(a^2+k^2)} - \frac{\exp(-ar)\{(a^2-k^2)\sin kr + 2ak\cos kr\}}{(a^2+k^2)^2} + \frac{2ak}{(a^2+k^2)^2}, \tag{29b}$$

$$\beta_1^{(2)}(k,r) = (8a^4+3a^2k^2+k^4)\left[1 + \frac{8a^4}{(8a^4+3a^2k^2+k^4)}\left\{a^2\left(\frac{r\exp(-ar)(-a\cos kr + k\sin kr)}{(a^2+k^2)} - \frac{\exp(-ar)\{(a^2-k^2)\cos kr - 2ak\sin kr\}}{(a^2+k^2)^2} + \frac{a^2-k^2}{(a^2+k^2)^2}\right) - 2a\left(\frac{\exp(-ar)(-a\cos kr + k\sin kr)}{(a^2+k^2)} + \frac{a}{(a^2+k^2)}\right)\right\}\right], \tag{29c}$$

$$\beta_2^{(2)}(k,r) = (8a^4+3a^2k^2+k^4)\left[\frac{8a^4}{(8a^4+3a^2k^2+k^4)}\{a^2(r\exp(-ar)\right.$$

CC-0. In Public Domain. Gurukul Kangri Collection, Haridwar

Digitized by Arya Samaj Foundation Chennai and eGangotri

$$\times \frac{(-a\sin kr - k\cos kr)}{(a^2+k^2)} - \frac{\exp(-ar)\{a^2-k^2)\sin kr + 2ak\cos kr\}}{(a^2+k^2)^2} + \frac{2ak}{(a^2+k^2)^2}\Bigg) - 2a\left(\frac{\exp(-ar)(-a\sin kr - k\cos kr)}{(a^2+k^2)} + \frac{k}{(a^2+k^2)}\right)\Bigg\}\Bigg], \tag{29d}$$

$$\gamma_1^{(1)}(k,r) = -r\exp(-ar), \tag{30a}$$

$$\gamma_2^{(1)}(k,r) = r\exp(-ar), \tag{30b}$$

$$\gamma_1^{(2)}(k,r) = 8a^4[a^2 r\exp(-ar) - 2a\exp(-ar)], \tag{30c}$$

and

$$\gamma_2^{(2)}(k,r) = 8a^4[a^2 r\exp(-ar) - 2a\exp(-ar)]. \tag{30d}$$

In writing the expressions for $g_1^{(i)}(k,r)$ and $g_2^{(i)}(k,r)$ we have followed the prescription of Kermode and Melhem (1983) to ensure that the equivalent potentials are not singular for any value of k and r.

5. Phase method

To study the on- and off-shell properties of our local potentials we now make use of a generalized phase method (Talukdar *et al* 1985). In this method the equations for the phase function $\delta(k,r)$ and quasiphase function $\Delta(k,q,r)$ for the potential in (27) are given by (McKeller *et al* 1965; Talukdar *et al* 1985)

$$\delta^{(i)\prime}(k,r) = -k^{-1}[g_1^{(i)}(k,r)\sin(kr+\delta(k,r)) + kg_2^{(i)}(k,r)\cos(kr+\delta(k,r))] \times \sin(kr+\delta(k,r)), \tag{31}$$

and

$$\Delta^{(i)\prime}(k,q,r) = -[q^{-1}\sin qr + k^{-1}\Delta(k,q,r)\cos(kr+\delta(k,r))] \times \{g_1^{(i)}(k,r)\sin(kr+\delta(k,r)) + kg_2^{(i)}(k,r)\cos(kr+\delta(k,r))]. \tag{32}$$

Here prime denotes differentiation with respect to r. Initial conditions on (31) and (32) are $\delta^{(i)}(k,0) = \Delta^{(i)}(k,q,0) = 0$. The scattering phase shift $\delta^{(i)}(k) = \lim_{r\to\infty} \delta^{(i)}(k,r)$ and quasiphase (Talukdar *et al* 1983) $\Delta^{i}(kq) = \lim_{r\to\infty} \Delta^{(i)}(k,q,r)$. The quasiphase $\Delta^{(i)}(k,q)$ is related to the off-shell extension function (Noyes 1965) $F^{(i)}(k,q)$ by

$$\Delta^{(i)}(k,q) = F^{(i)}(k,q)\sin\delta^{(i)}(k). \tag{33}$$

Interestingly, $\lim_{q\to k} \Delta^{(i)}(k,q) = \sin\delta^{(i)}(k)$ and thus $F^{(i)}(k,k) = 1$.

CC-0. In Public Domain. Gurukul Kangri Collection, Haridwar

Digitized by Arya Samaj Foundation Chennai and eGangotri

The potentials in (18) and (26) which simulate the repulsive core of the α-α and n-p interactions has only one free parameter. Equivalent local potentials $V_{eq}^{(i)}(k, r)$ corresponding to these in (18) and (26) are given in (27) with $i = 1$ and 2. In figure 1 we plot $V_{eq}^{(i)}(k, r)$ as a function of r at $E_{lab} = 10$ MeV with the energy momentum conversion factor 1/41·468 $MeV^{-1}\,fm^{-2}$. The functions $g_1^{(i)}(k, r)$ are highly attractive while the corresponding $g_2^{(i)}(k, r)$ are attractive at short distances and repulsive elsewhere.

The phase-shifts induced by the Saito potentials are negative. Also on a very general ground Saito (1968) and Bagchi and Mulligan (1979) have shown that phase-shifts for the potential in equation (1) and its adjoint are equal. It is, therefore, interesting to examine if the potentials in (27) predict similar results. To that end we have calculated the phase-shifts at $E_{lab} = 10$ MeV from (18) and (26) by using a formalism developed earlier (Talukdar *et al* 1979) and found that $\delta(k) = -0{\cdot}5490$ rad. For the equivalent local potentials we have solved (31) by the Runge-Kutta method with an appropriate stability check and obtained $\delta^{(i)}(k) = 2{\cdot}5926$ rad for both $V_{eq}^{(i)}(k, r)$ in agreement with the conjecture of Saito. Clearly,

$$\delta(k) = \delta^{(i)}(k) - \pi. \tag{34}$$

The result in (34) tells us that by localizing the Saito potential we have removed the effect of CBS.

To consider the action of the different regions of the potentials in (27) in producing the scattering phase shift $\delta^{(i)}(k)$ we plot in figure 2 the phase function $\delta^{(i)}(k, r)$ as a

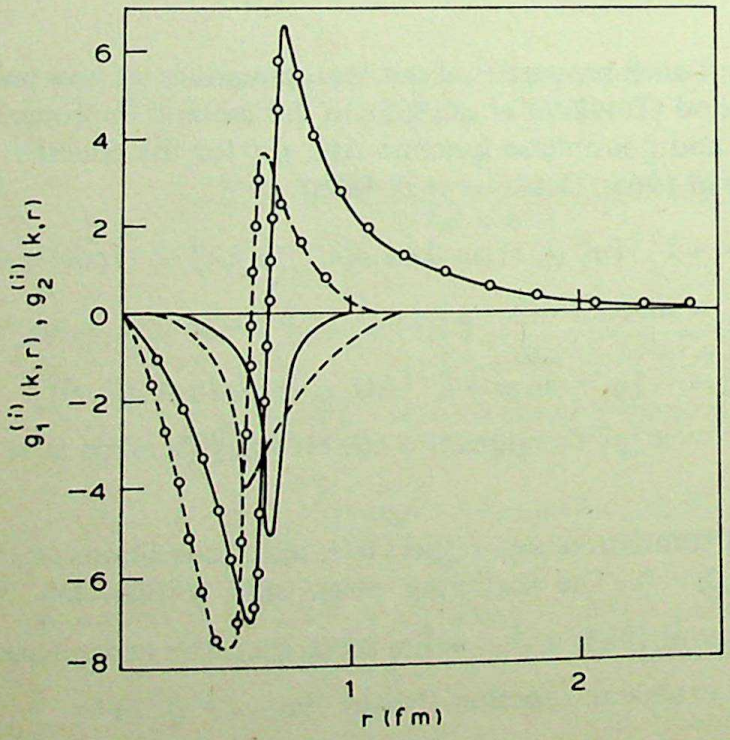

Figure 1. $g_1^{(i)}(k, r)$ and $g_2^{(i)}(k, r)$ as a function of r for the equivalent local potentials in (6). The solid curve and solid curve with circle represent the variation of $g_1^{(1)}(k, r)$ and $g_2^{(1)}(k, r)$ with r while the dashed curve and dashed curve with circle represent similar variation of $g_1^{(2)}(k, r)$ and $g_2^{(2)}(k, r)$.

CC-0. In Public Domain. Gurukul Kangri Collection, Haridwar

Digitized by Arya Samaj Foundation Chennai and eGangotri

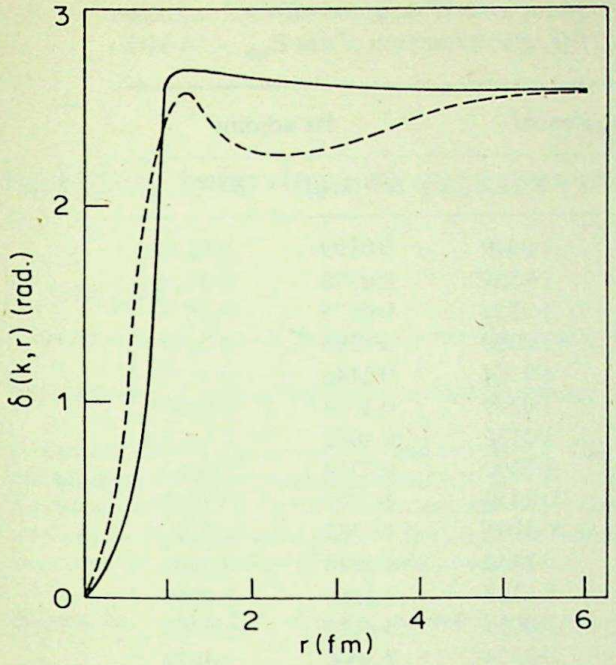

Figure 2. Phase function $\delta^{(i)}(k, r)$ for equivalent local potentials in (6) as a function of r. The solid curve represents the variation of $\delta^{(1)}(k, r)$ with r while the dashed curve represents similar variation for $\delta^{(2)}(k, r)$.

function of r. For both potentials $\delta^{(i)}(k, r)$'s increase very rapidly for small r. This is a peculiarity of non-local potentials. The asymptotic value is, however, reached through different paths. Thus, Saito and its adjoint kernel act differently in producing the phase shift.

From the above it is clear that the potentials in (27) are phase-equivalent to those in (18) and (26). This is no guarantee that these are also off-shell equivalent. To compare the off-shell behaviour of the original Saito potentials with that of $V^{(i)}_{eq}(k, r)$ we have proceeded as follows.

(i) We calculated the extersion functions $F^{(i)}(k, q)$ for the non-local kernels by a prescription given by one of us (Talukdar *et al* 1979).

(ii) For the equivalent local potentials we have solved the coupled differential equations (31) and (32) and made use of (33).

In table 1 we display our numbers for $\Delta^{(i)}(k, q)$ and $F^{(i)}(k, q)$ for $V^{(i)}_{eq}(k, r)$ as a function of q. These numbers are in exact agreement with those calculated by the method in (i). Thus $V^{(i)}_{eq}(k, r)$ are not only phase-equivalent to the Saito potentials but also off-shell equivalent. Looking closely into our numbers we see that the results for $\Delta^{(1)}(k, q)$ [or $F^{(1)}(k, q)$] and $\Delta^{(2)}(k, q)$ [or $F^{(2)}(k, q)$] do not exhibit similar behaviour as a function of q. For example, $\Delta^{(1)}(k, q)$ [or $F^{(1)}(k, q)$] first increases with q and takes up a maximum value at $q = 6k$ and then decreases. As expected, at the on-shell point $q = k$, $\Delta^{(i)}(k, k) = |\sin \delta(k)|$ for both i's and $F^{(i)}(k, k) = 1$. From our numbers it is clear that the off-shell properties of the Saito potential and its adjoint are different. This is in agreement with our observation with regard to equations (16) and (17).

CC-0. In Public Domain. Gurukul Kangri Collection, Haridwar

Digitized by Arya Samaj Foundation Chennai and eGangotri

Table 1. Quasiphase $\Delta^{(i)}(k, q)$ and off-shell extension function $F^{(i)}(k, q)$ as a function of q at $E_{lab} = 10$ MeV.

	Saito potential		Its adjoint	
q	$\Delta^{(1)}(k, q)$	$F^{(1)}(k, q)$	$\Delta^{(2)}(k, q)$	$F^{(2)}(k, q)$
$k/8$	0·5531	1·0599	0·0199	0·0228
$2k/8$	0·5515	1·0569	0·0378	0·0724
$3k/8$	0·5490	1·0521	0·0875	0·1677
$4k/8$	0·5454	1·0452	0·1396	0·2675
$5k/8$	0·5408	1·0364	0·2146	0·4113
$6k/8$	0·5353	1·0259	0·3044	0·5834
$7k/8$	0·5289	1·0136	0·4083	0·7825
k	0·5218	1·0000	0·5218	1·0000
$2k$	0·4409	0·8450	1·7682	3·3886
$4k$	0·2502	0·4795	4·0387	7·7399
$6k$	0·1274	0·2442	4·5918	8·7999
$8k$	0·0646	0·1238	4·1368	7·9279
$10k$	0·0344	0·0659	3·4419	6·5962
$12k$	0·0195	0·0374	2·8006	5·3672
$14k$	0·0116	0·0222	2·2723	4·3547

Acknowledgement

This work was supported by the Department of Atomic Energy, Government of India.

References

Arnold L G and Mac Kellar A D 1971 *Phys. Rev.* **C3** 1095
Bagchi B, Mulligan B and Quadri S B 1978 *Prog. Theor. Phys.* **60** 765
Bagchi B and Mulligan B 1979 *Phys. Rev.* **C20** 1973
Bagchi B, Mulligan B and Krause T O 1980 *Phys. Rev.* **C21** 1
Coz M, Arnold L G and Mac Kellar A D 1970 *Ann. Phys. (NY)* **59** 219
Englefield M J and Shoukry H S M 1974 *Prog. Theor. Phys.* **52** 1554
Fuda M G and Whiting J S 1973 *Phys. Rev.* **C8** 1255
Ghosh D K, Saha S, Niyogi K and Talukdar B 1983 *Czech. J. Phys.* **B33** 528
Gourdin M and Martin A 1957 *Nuovo Cimento* **6** 757
Kermode M W and Melhem Z 1983 *J. Phys.* **G9** 1497
Krasnopol'skii V M and Kukulin V I 1975 *Sov. J. Nucl. Phys.* **20** 470
Mac Kellar B H J and May R M 1965 *Nucl. Phys.* **65** 289
Mulligan B, Arnold L G, Bagchi B and Krause T O 1976 *Phys. Rev.* **C13** 2131
Newton R G 1966 *Scattering theory of waves and particles* (New York: McGraw Hill)
Noyes H P 1965 *Phys. Rev. Lett.* **15** 798
Okai S, Saito S and Tamagaki R 1972 *Prog. Theor. Phys.* **47** 484
Saito S 1968 *Prog. Theor. Phys.* **40** 893
Saito S 1969 *Prog. Theor. Phys.* **41** 705
Talukdar B, Das U and Mukhopadhyaya S 1979 *J. Math. Phys.* **20** 372
Talukdar B, Saha S, Bhattaru S R and Ghosh D K 1983 *Z. Phys.* **A312** 121
Talukdar B, Sett G C and Bhattaru S R 1985 *J. Phys.* **G11** 591
Wildermuth K and McClure W 1966 *Cluster representation of Nuclei; Springer tracts in modern physics* (Heidelberg: Springer) Vol. 41
Yamaguchi Y 1954 *Phys. Rev.* **95** 1628

CC-0. In Public Domain. Gurukul Kangri Collection, Haridwar

Digitized by Arya Samaj Foundation Chennai and eGangotri

Pramāṇa – J. Phys., Vol. 28, No. 4, April 1987, pp. 335–341. © Printed in India.

On the short-time behaviour of quantum unstable systems

V J MENON
Department of Physics, Banaras Hindu University, Varanasi 221 005, India

MS received 17 November 1986; revised 29 January 1987

Abstract. We consider the survival amplitude $A(t)$ for a normalized decaying state whose energy spectral density vanishes asymptotically as an inverse power. By using simple calculus a Taylor expansion of $A(t)$ is derived around $t = 0$, the form of the remainder term identified, and a physical significance given to the other coefficients. It is shown that the Taylor remainder may contain logarithms of t besides powers.

Keywords. Unstable particles; survival amplitude; Taylor expansion.

PACS Nos 02·90; 11·10; 11·90

1. Introduction

The problem of describing the time evolution and decay of quasi-stationary systems has drawn the attention of physicists ever since the advent of quantum mechanics. The enormous amount of work done on this delicate subject has been reviewed by Goldberger and Watson (1964), Newton (1966), Fonda *et al* (1978), Parravicini *et al* (1980), Exner (1985) and in a large number of research papers (Khalfin 1958; Fleming 1973; Degasperis *et al* 1974; Chiu *et al* 1977; Sudarshan *et al* 1978; Haake 1978; Peres 1980, 1984; Affleck 1981; Horwitz and Katznelson 1983; Menon and Lagu 1983; Grotz and Klapdor 1984; Alvarez-Estrada *et al* 1985). In the case of a *closed* system (i.e., one which develops in isolation) it has been demonstrated that the survival probablility ($\hbar = 1$ units)

$$P(t) = |A(t)|^2, \tag{1}$$

must deviate from the classical radioactive law at times much smaller (Fleming 1973; Chiu *et al* 1977; Sudarshan *et al* 1978; Peres 1980) or much bigger (Khalfin 1958; Fonda *et al* 1978) than the lifetime $\tau = 1/\Gamma$ where $A(t)$ is the amplitude of finding the system to be undecayed at the instant t. If the system is *open* (i.e., if the decaying particle interacts with the surroundings) the exponential law gets effectively restored with a changed lifetime τ', say (Degasperis *et al* 1974; Fonda *et al* 1978). Recently there has been a spurt of activity in examining the implications of these theories for resonances (Menon and Lagu 1983), conceptual as well as practical aspects of processes such as proton decay (Peres 1984; Horwitz and Katznelson 1983), double β decay (Grotz and Klapdor 1984), $n\bar{n}$ oscillations in nuclei (Alvarez-Estrada *et al* 1985) and quantum-statistical fluctuations (Haake 1978; Affleck 1981).

Several pioneering workers such as Fleming (1973), Chiu *et al* (1977) and Peres (1980) have particularly emphasized the need to study the form of the survival amplitude $A(t)$

CC-0. In Public Domain. Gurukul Kangri Collection, Haridwar

Digitized by Arya Samaj Foundation Chennai and eGangotri

as $t \to 0$ because of its direct link with the asymptotic behaviour of the underlying spectral energy distribution $U(E)$ defined in equation (4) below, and also with the occurrence of the so-called Zeno's paradox. Among the several beautiful results obtained by these workers we just mention three:

(a) Assuming the unstable state $|\xi(t)\rangle$ to have a finite norm $\|\xi\|$ together with a finite average energy $\langle H \rangle$ and employing only standard theorems of mathematical analysis it is found that the decay rate

$$-\dot{P}(t) = -\mathrm{d}P(t)/\mathrm{d}t = 0 \quad \text{at} \quad t = 0, \tag{2a}$$

in contrast to the classical value Γ of this rate at $t = 0$.

(b) If the state also possesses a finite canonical energy spread Δ then the amplitude is bounded by the Fleming (1973) limit

$$|A(t)| \geqslant \cos(t\Delta), \qquad t\Delta \leqslant \pi/2. \tag{2b}$$

Furthermore, Peres (1980) showed that the leading structure of the nondecay probability as $t \to 0$ is governed by the canonical spread Δ rather than the Gamow-Breit-Wigner width Γ:

$$P(t) \to 1 - \Delta^2 t^2 + \ldots, \quad 0 \leqslant t \leqslant T_1, \tag{2c}$$

where T_1 is of the order of the natural time period of the quasi-stationary state.

(c) Chiu *et al* (1977) demonstrated that with the help of the resolvent operator the amplitude $A(t)$ can be expressed as a contour integral in the energy plane which can be evaluated explicitly in various soluble models for the distribution $U(E)$; e.g. one could consider $U(E)$ vanishing asymptotically like $1/E^{3\cdot5}$ which leads to finite norm, energy and spread for the state. Alternatively, Peres (1980) used the powerful methods of formal scattering theory to set up an integro-differential equation for $A(t) = \exp[-b(t)]$ and solved for $b(t)$. The outcome is

$$A(t) \to 1 - iC_1 t + C_2 t^2 + B_2(t), \tag{3a}$$

where C_1, C_2 are real constants and $B_2(t)$ vanishes faster than t^2 at $t = 0$ typically like

$$B_2(t) \sim t^{2\cdot5} \quad \text{or} \quad t^3, \tag{3b}$$

in the analysis of Chiu *et al* and Peres, respectively. It is now relevant to make some comments on these results in the next section.

2. Aim of the present work

The significance of equations (2a) to (2c) is too well known to be re-emphasized here. Chiu *et al* (1977) connected these to the Zeno's paradox; Peres (1984) discussed their conceptual role in proton decay, and the time scale T_1 for double β decay has been evaluated thoroughly by Grotz and Klapdor (1984). We shall not make any attempt to extend (2a)–(2c) except that the remainder (shown dotted) on the right side of (2c) will be investigated in greater detail.

CC-0. In Public Domain. Gurukul Kangri Collection, Haridwar

Digitized by Arya Samaj Foundation Chennai and eGangotri

The present paper is aimed at giving further insight into the results of (3a) and (3b) by assuming the state to have a finite norm $\| \xi \| = 1$ and $U(E)$ to decrease like $1/E^{1+p}$ $(p > 0)$ at infinity. We shall especially investigate the following questions:

(i) Can a Taylor series like (3) be derived through simple calculus without doing contour deformations or explicit model evaluation of integrals or setting up of an integro-differential equation for $A(t)$ as was done by earlier authors?

(ii) If so, what is the physical significance of the coefficients C_1, C_2, etc on the right side of (3a), and upto what largest integral power of t can we expand for any given p? This question is not answered in a general/transparent manner by the examples taken by Chiu *et al* or by the series for $b(t) = -\log A(t)$ considered by Peres.

(iii) What is the leading form of the remainder $B_2(t)$ in (3) for general values of the index p and what role does it play in the structure of $P(t)$ (cf. (2c))? More precisely, is $B_2(t)$ of the form of a power of t as in (3b) or can it contain more complicated transcendental functions not reported by earlier authors?

It is hoped that the theory developed in § 3 below and the subsequent discussion of the above questions in § 4 will be of interest to physicists studying the area of metastable particles/resonances.

3. Theory

If the quasi-stationary system is prepared in a normalized state $| \xi \rangle$ at $t = 0$ then the survival amplitude $A(t)$ (cf. (1)) at any later time has the following standard representation

$$A(t) = \langle \xi | \exp(-iHt) | \xi \rangle, \quad t \geqslant 0,$$
$$= \int_0^\infty \mathrm{d}E\, U(E) \exp(-iEt), \tag{4}$$

where H is the Hamiltonian, the lower limit of the energy spectrum has been taken as zero without any loss of generality, and the non-negative distribution $U(E)$ is consistent with the normalization $A(0) = 1$. In the present paper we shall further assume that $U(E)$ exhibits a power law fall at infinity, i.e., there exists a number $p > 0$ and a sufficiently large energy parameter E_1 such that

$$U(E) \sim E_1^p / E^{1+p}, \quad E \geqslant E_1, \tag{5}$$

where in writing the leading behaviour symbol "$\sim$" we often omit further multiplicative constants which may occur on the right side. Our objective is now to obtain the algebraic structure of $A(t)$ in the neighbourhood of $t = 0$.

For this purpose we begin by introducing a convenient notation

$$q = p - 1 \text{ if } p \text{ is a natural number,}$$
$$= \text{integer part of } p \text{ if } p \text{ is fraction.} \tag{6}$$

CC-0. In Public Domain. Gurukul Kangri Collection, Haridwar

Digitized by Arya Samaj Foundation Chennai and eGangotri

Remembering the condition (5) and $A(0) = 1$ we see that all the moments upto order q of the distribution U are necessarily bounded, i.e.,

$$\langle H^s \rangle = \langle \xi | H^s | \xi \rangle = \int_0^\infty \mathrm{d}E\, U(E)\, E^s$$
$$< \infty \quad \text{for} \quad 0 \leqslant s \leqslant q. \tag{7}$$

If $t \to 0$ one may like to expand $\exp(-iEt)$ of (4) in an infinite Maclaurin series and integrate over E term by term but, unfortunately, the termwise integrals would certainly start diverging after some stage. Hence let us insert in (4) the finite expansion

$$\exp(-iEt) = \sum_{s=0}^{q} (-iEt)^s/s! + f(Et), \tag{8}$$

where the correction term $f(Et)$ is of order $(Et)^{q+1}$ for $t \to 0$. Indeed, the magnitude of $f(Et)$ does not exceed a small quantity $\varepsilon = O(\delta^{q+1})$ as long as Et is less than another small number δ:

$$|f(Et)| < \varepsilon = O(\delta^{q+1}) \quad \text{if} \quad Et < \delta \ll 1. \tag{9}$$

With the help of (8) we can rewrite (4) for any t as

$$A(t) = \sum_{s=0}^{q} \langle H^s \rangle (-it)^s/s! + B_q(t), \tag{10}$$

$$B_q(t) = \left\{ \int_0^{E_1} + \int_{E_1}^{\infty} \right\} \mathrm{d}E\, U(E) f(Et), \tag{11}$$

where the moments $\langle H^s \rangle$ and parameter E_1 are defined in (7) and (5), respectively. Let us now make $E_1 t < \delta$ so that the absolute magnitude of the first integral in (11) becomes less than the small quantity ε encountered in (9). The second integral on the right side of (11) can be estimated by substituting the asymptotic form (5) of U whereby

$$B_q(t) \sim (E_1 t)^p \int_{E_1 t}^{\infty} \mathrm{d}x\, f(x)/x^{1+p}, \tag{12}$$

for $t < \delta/E_1$ and $x = Et$. Remembering the definition (8) of f we see that $f(x)/x^{1+p}$ behaves as $1/x^{p-q}$ for $x \to 0$ but drops like $1/x^{1+p-q}$ for $x \to \infty$ where the integer q is read off from (6). But the *indefinite* integral $\int \mathrm{d}x/x^{p-q}$ goes like $\log x$ if $p = q+1$ and like x^{1+q-p} otherwise. It follows that for small values of $E_1 t$ the integral appearing in (12) goes as

$$\log E_1 t + \text{constant or as a constant}, \tag{13}$$

according as p is a positive integer or fraction. Therefore, putting $\hat{t} = E_1 t$ and suppressing all multiplicative complex constants we conclude from (12) that

$$B_q(t) \sim \hat{t}^p \log \hat{t}, \quad p = \text{natural number}$$
$$\sim \hat{t}^p, \qquad p = \text{fractional} > 0. \tag{14}$$

CC-0. In Public Domain. Gurukul Kangri Collection, Haridwar

Digitized by Arya Samaj Foundation Chennai and eGangotri

The derivative $dB_q(t)/dt$ behaves as $\hat{t}^{p-1}\log\hat{t}$ or as $\hat{t}^{p-1}$ accordingly. Equations (10) and (14) may be regarded as the main findings of our work.

3.1 *Special cases*

By assigning to p special values we get various predictions for the amplitude $A(t)$ (cf. (10)) and the decay rate $-\dot{P}(t)$ (cf. (2)). For example, if $\hat{t} = E_1 t$, $0 < p < 1$, $q = 0$, $\langle H \rangle = \infty$ we notice $-\dot{P}(t)$ to blow up at $t = 0$ like $\hat{t}^{p-1}$, but if $p > 1$, $\langle H \rangle < \infty$ then $-\dot{P}(t)$ vanishes there in conformity with (2). An interesting possibility (which we feel to be a new result) is to take

$$p = 1, \quad \langle H \rangle = \infty, \quad -\dot{P}(t) \sim \log\hat{t}. \tag{15}$$

Finally, if $p > 2$ the norm $\langle H^0 \rangle^{1/2}$, the mean energy $\langle H \rangle$ and the canonical energy spread Δ given by

$$\Delta^2 = \langle H^2 \rangle - \langle H \rangle^2, \tag{16}$$

become all bounded. Then from (14)

$$\begin{aligned} B_2(t) &\sim \hat{t}^p, \qquad 2 < p < 3, \\ &\sim \hat{t}^3 \log\hat{t}, \quad p = 3, \end{aligned} \tag{17}$$

which is a new finding in contrast to the old assertion (3b). It may be remarked that if we wish to convert the "$\sim$" sign into an equality the right side of (17) will have to be multiplied by a constant of order $(\Gamma/E_1)^3$ for $p = 3$.

3.2 *Numerical estimates*

Table 1 gives a sample display of the $\hat{t}^3$ and $\hat{t}^3\log\hat{t}$ estimates of the right sides of (3b) and (17), respectively, when $p = 3$. The difference between the two estimates is significant for $\hat{t} < 10^{-1}$. One may ask in what region of time is the above theory applicable? Consider an unstable particle of mass $M \sim 1$ GeV and take the energy scale $E_1 \sim 10$ GeV. Then the times of interest satisfy $t \ll 1/E_1 \sim 10^{-28}$ sec. Though extremely short on the laboratory scale such times are of great interest in the physics of the very early universe.

Table 1. Numerical estimates of the right side of (3b) and (17) with $p = 3$ and $\hat{t} = E_1 t$. The absolute value of $B_2(t)$ is obtained upon multiplying the entries by a constant of order $(\Gamma/E_1)^3$.

$\hat{t}$	$\hat{t}^3$	$\lvert\hat{t}^3\log\hat{t}\rvert$
10^{-3}	10^{-9}	$6{\cdot}9 \times 10^{-9}$
10^{-2}	10^{-6}	$4{\cdot}6 \times 10^{-6}$
10^{-1}	10^{-3}	$2{\cdot}3 \times 10^{-3}$

CC-0. In Public Domain. Gurukul Kangri Collection, Haridwar

Digitized by Arya Samaj Foundation Chennai and eGangotri

4. Discussion

The deviations from an exponential decay law of metastable systems have already been studied rigorously by several workers and the present paper attempts at supplementing the known results (equations (3a) and (3b)), derived by Chiu *et al* (1977) and Peres (1980) at times t very small compared to the lifetime. The salient features of this work can be summarized as follows:

(i) We take a normalized state and a power-like asymptotic fall (cf. (5)) of the spectral distribution $U(E)$ which lends itself readily to the analysis of § 3. Both fractional and integral values of p can be realized in practice. [Indeed, for a resonance in three dimensions decaying into two nonrelativistic fragments of relative momentum k the phase space factor $k^2 \mathrm{d}k$ goes as $E^{1/2}\mathrm{d}E$ implying that p be half-integral. On the other hand, if the decay occurs in a two-dimensional layer the phase space element $k\mathrm{d}k$ behaves as $\mathrm{d}E$ which implies an integral p]. Thereupon we show that a Taylor series (equations (10), (14)) can indeed be derived for the survival amplitude $A(t)$ with the aid of simple calculus. Resort to contour deformations and integro-differential equations is not necessary.

(ii) Comparison of the earlier form (3) with our Taylor expression (10) leads to a direct physical significance of the coefficients $C_1, C_2, \ldots$ in terms of the moments $\langle H \rangle, \langle H^2 \rangle, \ldots$ of the distribution. Also, the highest integer power of t occurring in the expansion (10) is q defined by (6). This information cannot be guessed in a general/transparent manner from the examples of Chiu *et al* or the series for $\log A(t)$ developed by Peres if $U(E)$ falls like (5).

(iii) The remainder $B_q(t)$ has a leading behaviour given by (14) for any positive p. We note that $B_q(t)$ may contain not only powers of $E_1 t$ but also logarithms—a *new* result to our knowledge. This fact has an immediate consequence with regard to the short-time structure (2c) derived by Peres. If $2 < p \leqslant 3$ then (17) tells that the remainder of $A(t)$, and hence of $P(t)$, must be of order $\hat{t}^p$ or $\hat{t}^3 \log \hat{t}$ which *rules out* the possibility $O(t^3)$ naively expected from the older estimate (3b). A numerical comparison of the old and new estimates done in table 1 shows that their difference is significant if $t < 10^{-1}$. The concerned times are extremely small ($< 10^{-28}$ sec, for example) which could be relevant to metastables formed just after the big bang. Of course, if $p > 3$ then $B_2(t)$ becomes of $O(t^3)$ on the right side of (3a).

We have thus answered all the questions raised in § 2. Since the interest in the field of unstable systems/resonances has recently been revived their time evolution needs to be investigated as thoroughly as possible.

Acknowledgements

The author is thankful to Prof. S N Mukherjee, Prof. R S Srivastava and to the UGC for the award of a research associateship. He also acknowledges stimulating discussions with Prof. E C G Sudarshan at Madras.

References

Affleck I 1981 *Phys. Rev. Lett.* **46** 388

Alvarez-Estrada R F, Fernandez L A and Sanchez Gomez J L 1985 *Z. Phys.* **C26** 615

CC-0. In Public Domain. Gurukul Kangri Collection, Haridwar

Digitized by Arya Samaj Foundation Chennai and eGangotri

Chiu C B, Sudarshan E C G and Misra B 1977 *Phys. Rev.* **D16** 520
Degasperis A, Fonda L and Ghirardi G C 1974 *Nuovo Cimento* **A21** 471
Exner P 1985 *Open quantum systems and Feynman integrals* (Dordrecht: D. Reidel) Ch. 1, 2
Fleming G N 1973 *Nuovo Cimento* **A16** 232
Fonda L, Ghirardi G C and Rimini A 1978 *Rep. Prog. Phys.* **41** 587
Goldberger M L and Watson K M 1964 *Collision theory* (New York: John Wiley) Ch. 8
Grotz K and Klapdor H V 1984 *Phys. Rev.* **C30** 2098
Haake F 1978 *Phys. Rev. Lett.* **41** 1685
Horwitz P and Katznelson E 1983 *Phys. Rev. Lett.* **50** 1184
Khalfin L A 1958 *Sov. Phys.* (*JETP*) **6** 1053
Menon V J and Lagu A V 1983 *Phys. Rev. Lett.* **51** 1407
Newton R G 1966 *Scattering theory of waves and particles* (New York: McGraw Hill) Ch. 19
Parravicini G, Gorini V and Sudarshan E C G 1980 *J. Math. Phys.* **21** 2208
Peres A 1980 *Ann. Phys.* (*N.Y.*) **129** 33
Peres A 1984 *Found. Phys.* **14** 1131
Sudarshan E C G, Chiu C B and Gorini V 1978 *Phys. Rev.* **D18** 2914

CC-0. In Public Domain. Gurukul Kangri Collection, Haridwar

Digitized by Arya Samaj Foundation Chennai and eGangotri

CC-0. In Public Domain. Gurukul Kangri Collection, Haridwar

Digitized by Arya Samaj Foundation Chennai and eGangotri

Pramāṇa – J. Phys., Vol. 28, No. 4, April 1987, pp. 343–353. © Printed in India.

Thermodynamic properties of molecular fluid mixtures of hard ellipsoids

A K SINGH,* U N SINGH and S K SINHA†

Department of Physics, L S College, Bihar University, Muzaffarpur 842001, India
*Permanent address: Department of Physics, S R K Goenka College, Sitamarhi 843301, India

MS received 29 September 1986; revised 3 February 1987

Abstract. Thermodynamic properties of molecular fluid mixtures of hard ellipsoids are calculated. Numerical results are given for equation of state and excess-free energy of the binary mixture of both additive and non-additive hard ellipsoids. It is found that the equation of state and free energy of mixtures increase with increase of anisotropy parameter χ_0.

Keywords. Hard ellipsoid; equation of state; excess free energy; anisotropy; binary mixture.

PACS No. 61·25

1. Introduction

This paper is concerned with the evaluation of thermodynamic properties of a molecular fluid mixture, whose molecules interact via hard ellipsoid potential. We consider the case where the constituent molecules have the same length to width ratio χ_0.

Many theoretical attempts such as van der Waals one- and two-fluid theories (Leland *et al* 1968; Henderson and Leonard 1971a, b) and perturbation theory (Henderson and Barker 1968; Smith 1971; Smith and Henderson 1972) have been made to understand the structural and thermodynamic properties of simple atomic fluid mixture of hard spheres, where the length-to-width ratio χ_0 is unity. The basis of the perturbation theory is to expand the properties of a hard sphere mixture about that of a one-component fluid of hard spheres of diameter d_0 in power of $(d_{\alpha\gamma}^n - d_0^n)$. It is found that the first order perturbation theory becomes identical to the van der Waals one-fluid (vdW 1) theory, when $n = 3$ (Smith and Henderson 1972; Adams and McDonald 1975) and gives good results for the thermodynamic properties (Smith 1971; Henderson and Leonard 1971b). This method can be extended to the molecular fluid mixture of hard ellipsoids.

In this paper, we examine the theory for a molecular binary mixture of hard ellipsoids and calculate the thermodynamic properties of the system. In § 2, we discuss the theory for calculating the thermodynamic properties of a binary mixture of hard ellipsoids.

---

†To whom correspondence should be addressed.

CC-0. In Public Domain. Gurukul Kangri Collection, Haridwar

Digitized by Arya Samaj Foundation Chennai and eGangotri

The results for additive and non-additive mixtures are discussed in §§3 and 4 respectively.

2. Basic theory

We consider a binary mixture of N_1 hard ellipsoid molecules of species 1 and N_2 hard ellipsoid molecules of species 2, such that the total number of molecules is $N = N_1 + N_2$. Further we assume that the constituent molecules have the same shape but differ in size, so that the parameter χ_0 is the same for all constituent molecules, where χ_0 is the length $(2a_i)$ to width $(2b_i)$ ratio of molecule of species i (i.e. $\chi_0 = a_i/b_i$ for $i = 1, 2$). The potential energy is assumed to be pair-wise additive. Thus

$$U(\bar{X}_1, \bar{X}_2, \ldots, \bar{X}_N) = \sum_{\alpha,\gamma=1}^{2} \sum_{i<j} u_{\alpha\gamma}(\bar{X}_i, \bar{X}_j), \tag{1}$$

where $u_{\alpha\gamma}(\bar{X}_i, \bar{X}_j)$ is the pair potential between molecules i of species α and molecules j of species γ and is given by

$$\begin{aligned} u_{\alpha\gamma}(\bar{X}_i, \bar{X}_j) &\equiv u_{\alpha\gamma}(r_{ij}, \Omega_i^\alpha, \Omega_j^\gamma) \\ &= \infty \qquad r_{ij} < d_{\alpha\gamma}(\hat{r}_{ij}^{\alpha\gamma}, \Omega_{ij}^{\alpha\gamma}) \\ &= 0 \qquad r_{ij} > d_{\alpha\gamma}(\hat{r}_{ij}^{\alpha\gamma}, \Omega_{ij}^{\alpha\gamma}), \end{aligned} \tag{2}$$

where Ω_i^α and Ω_j^γ denote the orientation of molecule i of species α and molecule j of species γ respectively,

$$r_{ij}^{\alpha\gamma} = |\bar{r}_i^\alpha - \bar{r}_j^\gamma| \quad \text{and} \quad d_{\alpha\gamma}(\hat{r}_{ij}^{\alpha\gamma}, \Omega_{ij}^{\alpha\gamma})$$

is the distance of closest approach between two hard ellipsoids of species α and γ. There is no simple expression for the distance of closest approach between two hard ellipsoids of revolution with arbitrary orientation. We take the Berne and Pechukas (1972) expression for $d_{\alpha\gamma}$

$$\begin{aligned} d_{\alpha\gamma}(\hat{r}_{ij}^{\alpha\gamma}, \Omega_{ij}^{\alpha\gamma}) = d_{\alpha\gamma}^0 [1 - \chi\{(\hat{r}_{ij}^{\alpha\gamma} \cdot \hat{e}_i^\alpha)^2 + (\hat{r}_{ij}^{\alpha\gamma} \cdot \hat{e}_j^\gamma)^2 \\ - 2\chi(\hat{r}_{ij}^{\alpha\gamma} \cdot \hat{e}_j^\alpha)(\hat{r}_{ij}^{\alpha\gamma} \cdot \hat{e}_j^\gamma)(\hat{e}_i^\alpha \cdot \hat{e}_j^\gamma)\}\{1 - \chi^2(\hat{e}_i^\alpha \cdot \hat{e}_j^\gamma)^2\}^{-1}]^{-1/2}, \end{aligned} \tag{3}$$

where $\hat{e}_i^\alpha$ and $\hat{e}_j^\gamma$ are unit vectors along the symmetry axes of two interacting molecules and $\hat{r}_{ij}^{\alpha\gamma}$ is the unit vector along the intermolecular axis $\hat{r}_{ij}^{\alpha\gamma}$. Here $d_{\alpha\gamma}^0 = 2b_{\alpha\gamma}$ is constant with the unit of length and

$$\chi = (\chi_0^2 - 1)/(\chi_0^2 + 1), \tag{4}$$

is an anisotropy parameter. This is a legitimate model for non-spherical molecules, oblate as well as prolate shapes of arbitrary anisotropy. The Berne-Pechukas model represents the hard-ellipsoid model correctly when the difference of length and width $(a_i - b_i)$ is small, but it cannot be exact in general when the difference is large. However, this model is used to calculate the compressibility factor for hard spherocylinders (Singh and Singh 1982) which are in very good agreement with machine simulation

CC-0. In Public Domain. Gurukul Kangri Collection, Haridwar

Digitized by Arya Samaj Foundation Chennai and eGangotri

results (Mason and Rigby 1978). It has also been used for hard ellipsoids of revolution (Singh and Singh 1986, Singh and Sinha 1986). In general the effective value of $d^0_{\alpha\gamma}$ between hard ellipsoids of unlike species may be given by

$$d^0_{12} = (1/2)(d^0_{11} + d^0_{22})(1 + \Delta), \tag{5}$$

where $d^0_{\alpha\alpha} = 2b_{\alpha\alpha}$ is the width of species α and Δ is the non-additive parameter, $\Delta = 0$ for additive mixture and $|\Delta| > 0$ for non-additive mixture.

In order to calculate the thermodynamic properties of hard ellipsoid mixture, we begin with the pressure equation

$$\frac{\beta P}{\rho} = 1 - \frac{\beta\rho}{6}\sum_{\alpha,\gamma} C_\alpha C_\gamma \int d\bar{r}_{12} r_{12} \Big\langle g_{\alpha\gamma}(r_{12}, \Omega^\alpha_1, \Omega^\gamma_2) \times \frac{\partial u_{\alpha\gamma}(r_{12}, \Omega^\alpha_1, \Omega^\gamma_2)}{\partial r_{12}} \Big\rangle_{\Omega^\alpha_1 \Omega^\gamma_2}, \tag{6}$$

where $g_{\alpha\gamma}(r_{12}, \Omega^\alpha_1, \Omega^\gamma_2)$ is the pair correlation function (PCF) of the hard ellipsoid mixture, $\rho = N/V$ is the number density and $C_\alpha \equiv N_\alpha/N$ is the concentration of species α. Here $\langle \ldots \rangle_{\Omega^\alpha_1 \Omega^\gamma_2}$ represents an unweighted average over the molecular orientations Ω^α_1 and Ω^γ_2 for the quantity within the angular bracket i.e.

$$\langle (\ldots) \rangle_{\Omega^\alpha_1 \Omega^\gamma_2} = \frac{1}{\Omega^\alpha \Omega^\gamma} \int d\Omega^\alpha_1 \int d\Omega^\gamma_2 (\ldots). \tag{7}$$

Ω^α is the normalization constant. For the linear molecule, $\Omega^\alpha = 4\pi$ and

$$d\Omega^\alpha_i = \sin\theta^\alpha_i \, d\theta^\alpha_i \, d\phi^\alpha_i .$$

The hard ellipsoid potential $u_{\alpha\gamma}(r_{12}, \Omega^{\alpha\gamma}_{12})$ satisfies the relation

$$\begin{aligned} u_{\alpha\gamma}(r_{12}, \Omega^\alpha_1, \Omega^\gamma_2) &= u_{\alpha\gamma}(r_{12}/d_{\alpha\gamma}(\hat{r}^{\alpha\gamma}_{12}, \Omega^{\alpha\gamma}_{12})) \\ &= u^{HS}_{\alpha\gamma}(r^*_{12}) = \infty \qquad r^*_{12} < 1 \\ &= 0 \qquad r^*_{12} > 1, \end{aligned} \tag{8}$$

where

$$r^*_{12} = r_{12}/d_{\alpha\gamma}(\hat{r}^{\alpha\gamma}_{12}, \Omega^{\alpha\gamma}_{12}).$$

Then

$$-\beta \frac{\partial u_{\alpha\gamma}(r_{12}, \Omega^\alpha_1, \Omega^\gamma_2)}{\partial r^*_{12}} = \delta(r^*_{12} - 1). \tag{9}$$

Using the decoupling approximation (Parson 1979), we can write

$$\begin{aligned} g_{\alpha\gamma}(r_{12}, \Omega^\alpha_1, \Omega^\gamma_2) &= g_{\alpha\gamma}[r_{12}/d_{\alpha\gamma}(\hat{r}^{\alpha\gamma}_{12}, \Omega^{\alpha\gamma}_{12})] \\ &= g^{HS}_{\alpha\gamma}(r^*_{12}), \end{aligned} \tag{10}$$

where $g^{HS}_{\alpha\gamma}(r^*_{12})$ is the PCF for the hard sphere mixture. Thus the values of $g_{\alpha\gamma}(r_{12}, \Omega^\alpha_1, \Omega^\gamma_2)$ of the hard ellipsoid under this approximation will be obtained from the values of $g^{HS}_{\alpha\gamma}(r^*_{12})$ of hard sphere mixture at packing fraction

$$\eta_{\alpha\gamma} = \rho V^{HF}_{\alpha\gamma} = \frac{\pi}{6}\rho d^{0^3}_{\alpha\gamma}\chi_0, \tag{11}$$

CC-0. In Public Domain. Gurukul Kangri Collection, Haridwar

Digitized by Arya Samaj Foundation Chennai and eGangotri

where

$$V_{\alpha\gamma}^{HF} = \frac{\pi}{6} d_{\alpha\gamma}^{03} \chi_0 .$$

The decoupling approximation has been found to give compressibility factor in good agreement (Singh and Singh 1986; Singh and Sinha 1986) with computer simulation results (Frenkel and Mulder 1985; Mulder and Frenkel 1985) for a one-component system. It is expected to provide good results even for a mixture. In the decoupling approximation, the orientational and positional degrees of freedom are completely decoupled.

Substituting (9) and (10) in (6) we obtain

$$\frac{\beta P}{\rho} = 1 + \frac{2\pi\rho}{3} \chi_0 F_1(\chi) \sum_{\alpha,\gamma} C_\alpha C_\gamma d_{\alpha\gamma}^{03} g_{\alpha\gamma}^{HS}(1), \tag{12}$$

where $g_{\alpha\gamma}^{HS}(1)$ is the value of the radial distribution function (RDF) of the hard sphere mixture at the core; and,

$$F_1(\chi) = (1-\chi^2)^{-1/2}(1 - \tfrac{1}{6}\chi^2 - \tfrac{1}{40}\chi^4 - \tfrac{1}{112}\chi^6 - \ldots). \tag{13}$$

The vdW 1 fluid theory of mixture (Leland *et al* 1968) originally developed for the hard-sphere system, can be extended in the case of hard ellipsoid mixture. This theory approximates the properties of a mixture by those of fictitious pure hard ellipsoid fluid with the parameter

$$d_0^3 = \sum_{\alpha,\gamma} C_\alpha C_\gamma d_{\alpha\gamma}^{03}. \tag{14}$$

In the vdW 1 theory of mixture, it is assumed that

$$g_{\alpha\gamma}^{HS}(1) = g^{HS}(d_0) \tag{15}$$

for all α and γ. With the help of (14) and (15), (12) can be written as

$$\beta P/\rho = 1 + 4\eta_0 g^{HS}(d_0) F_1(\chi), \tag{16}$$

where

$$\eta_0 = \frac{\pi}{6} \rho d_0^3 \chi_0 \tag{17}$$

and $g^{HS}(d_0)$ is the RDF of the hard-sphere system at the core and is given by

$$g^{HS}(d_0) = (1 - \eta_0/2)/(1-\eta_0)^3. \tag{18}$$

From (16), we get

$$\beta P/\rho = 1 + \{2\eta_0(2-\eta_0)/(1-\eta_0)^3\} F_1(\chi). \tag{19}$$

The Helmholtz free energy per particle for the mixture is given by

$$\beta A/N = [\ln \rho - 1] + \sum_\alpha C_\alpha \ln C_\alpha + H[\rho, U], \tag{20}$$

CC-0. In Public Domain. Gurukul Kangri Collection, Haridwar

Digitized by Arya Samaj Foundation Chennai and eGangotri

where the first two terms represent the free energy of an ideal gas mixture and H is the excess free energy arising from the interparticle interaction. Thus

$$H[\rho, U] = \int_0^\rho \{(\beta P/\rho) - 1\}\, \mathrm{d}\rho/\rho. \tag{21}$$

This can be solved using (19). Finally, we obtain an expression for the free energy as

$$\beta A/N = (\ln \rho - 1) + \sum_\alpha C_\alpha \ln C_\alpha + \{\eta_0(4-3\eta_0)/(1-\eta_0)^2\}\, F_1(\chi). \tag{22}$$

Other thermodynamic properties can be calculated by using (19) and (22).

These equations can be used to calculate the thermodynamic properties of a binary mixture of both additive and non-additive hard ellipsoids.

3. Binary mixture of additive hard ellipsoids

We derive expressions for the thermodynamic properties of binary mixture of additive hard ellipsoids. Using the relation

$$d^3 = C_1 d_{11}^{0^3} + C_2 d_{22}^{0^3}, \tag{23}$$

we get the following relation for the binary mixture of additive hard ellipsoids

$$\eta_0 = \eta[1 - \tfrac{3}{4} C_1 C_2 (1+R)(1-R)^2/(C_1 + C_2 R^3)], \tag{24}$$

where

$$\eta = \frac{\pi}{6}\rho\, d^3 \chi_0 = \frac{\pi}{6}\rho\chi_0 (C_1 d_{11}^{0^3} + C_2 d_{22}^{0^3}), \tag{25}$$

and $R = d_{22}^0/d_{11}^0$. Using (24) in (19) and (22) we obtain expressions for the pressure and free energy for the additive hard ellipsoid mixture

$$\begin{aligned}\beta P/\rho = 1 &+ \{2\eta(2-\eta)/(1-\eta)^3\}\, F_1(\chi) \\ &- 6C_1C_2\{\eta_a(4+4\eta-2\eta^2)/(1-\eta)^4\} \\ &\times \{(d_{11}^0 - d_{22}^0)/(d_{11}^0 + d_{22}^0)\}\, F_1(\chi) + O(C_1^2 C_2^2),\end{aligned} \tag{26}$$

and

$$\begin{aligned}\beta A/N = (\ln\rho - 1) &+ \sum_\alpha C_\alpha \ln C_\alpha + \{\eta(4-3\eta)/(1-\eta)^2\} F_1(\chi) \\ &- 6C_1C_2\{\eta_a(2-\eta)/(1-\eta)^3\} \\ &\times \{(d_{11}^0 - d_{22}^0)/(d_{11}^0 + d_{22}^0)\}\, F_1(\chi) + O(C_1^2 C_2^2),\end{aligned} \tag{27}$$

where

$$\eta_a = \frac{\pi}{6}\rho\chi_0 d_{12}^{a^3}, \tag{28}$$

$$d_{12}^a = (d_{11}^0 + d_{22}^0)/2. \tag{29}$$

However, we prefer to use (19) and (22) for calculating the pressure and free energy of the binary mixture.

CC-0. In Public Domain. Gurukul Kangri Collection, Haridwar

Digitized by Arya Samaj Foundation Chennai and eGangotri

We have calculated the equation of state $\beta P/\rho$ and excess free energy per particle $\beta f (\equiv \beta A_E/N)$ for the binary mixture of additive hard ellipsoids with different values of anisotropy parameter χ_0 and different values of R, using (19) and (22). $\chi_0 = 1{\cdot}0$ corresponds to the simple atomic fluid mixture. Here βf is the excess free energy with respect to the ideal gas at the same temperature and density.

We examine the effect of anisotropy on the thermodynamic properties of binary mixture. The value of the equation of state $\beta P/\rho$ and excess free energy per particle βf as a function of χ_0 are reported in figures 1 and 2 respectively for $C_1 = C_2 = 0{\cdot}5$ and $\rho^* = 0{\cdot}3$ and $0{\cdot}5$ at $R = 1{\cdot}1$ and $3{\cdot}0$. The quantity

$$\rho^* = \rho(C_1 d_{11}^{03} + C_2 d_{22}^{03}).$$

The results for $R = 3{\cdot}0$ are less than those for $R = 1{\cdot}1$ throughout the range of χ_0. From the figures, we find that the equation of state and free energy increase with increase of density ρ^* and with increase of χ_0. Figures 3 and 4 demonstrate the equation of state $\beta P/\rho$ and free energy βf respectively for $C_1 = C_2 = 0{\cdot}5$ and $R = 1{\cdot}1$ and $5/3$ at $\eta = 0{\cdot}3$ (with different values of ρ^*). From these figures we see that the thermodynamic properties such as pressure and free energy at given η are minimum at $\chi_0 = 1{\cdot}0$ and increase when χ_0 either increases or decreases.

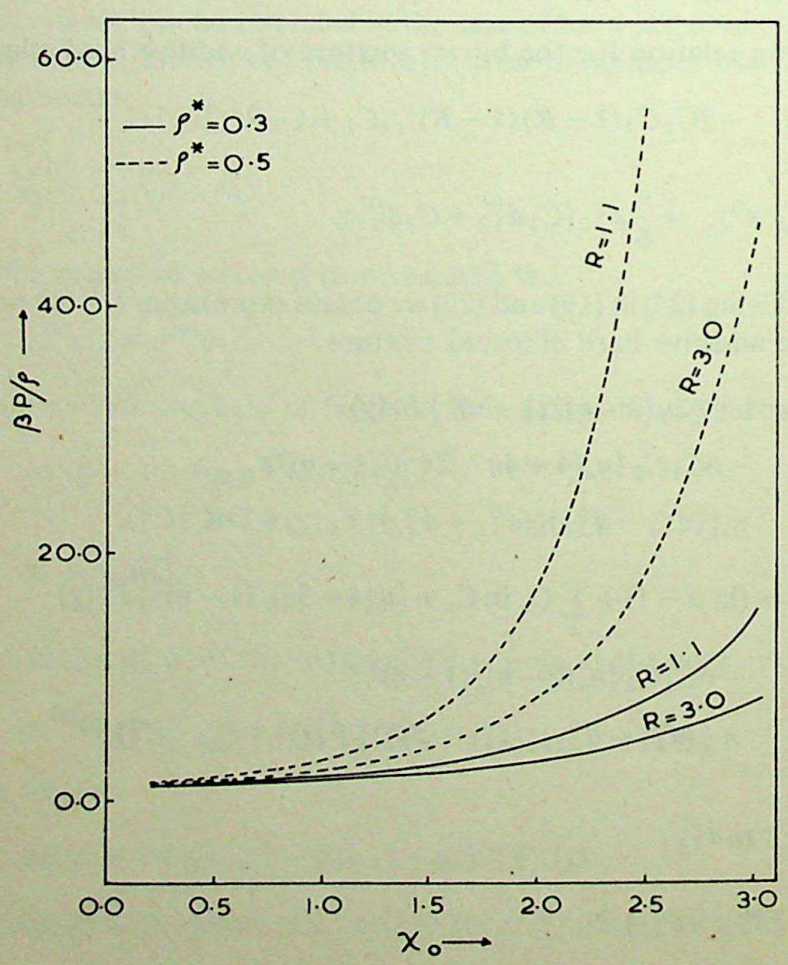

Figure 1. Equation of state $\beta P/\rho$ for binary mixture of additive hard ellipsoids as a function of χ_0 for $C_1 = C_2 = 0{\cdot}5$ and $\rho^* = 0{\cdot}3$ and $0{\cdot}5$ and for $R = 1{\cdot}1$ and $3{\cdot}0$.

CC-0. In Public Domain. Gurukul Kangri Collection, Haridwar

Digitized by Arya Samaj Foundation Chennai and eGangotri

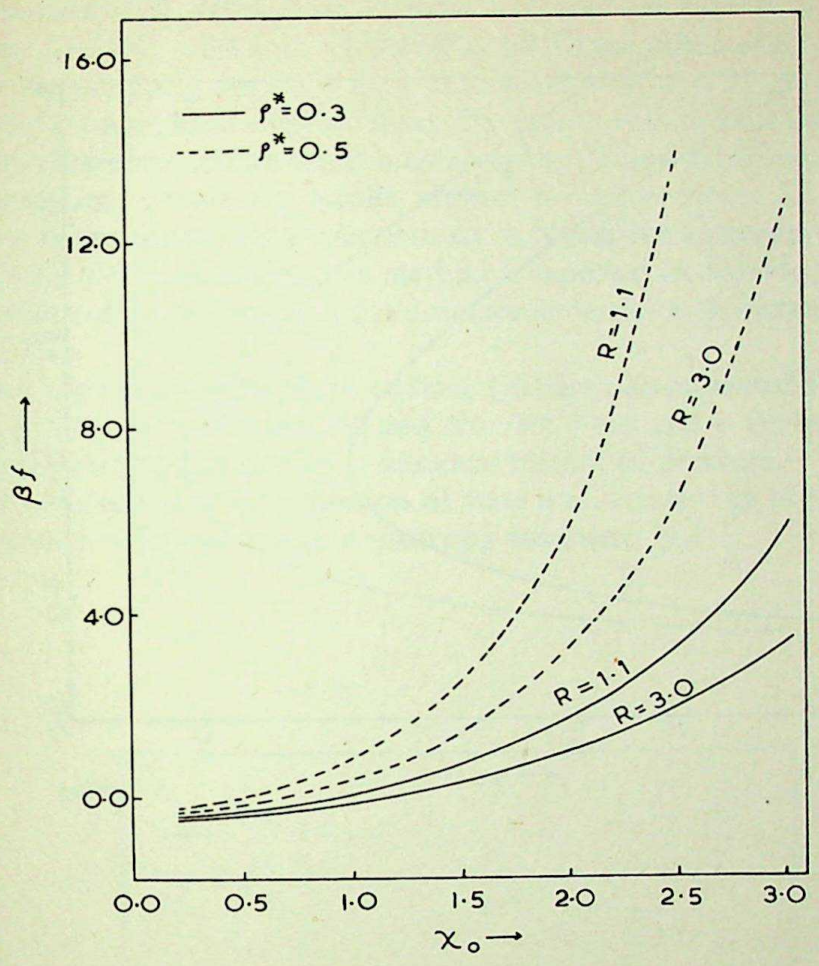

Figure 2. Excess free energy βf for binary mixture of additive hard ellipsoids as a function of χ_0 for $C_1 = C_2 = 0{\cdot}5$ and $\rho^* = 0{\cdot}3$ and $0{\cdot}5$ and for $R = 1{\cdot}1$ and $3{\cdot}0$.

4. Binary mixture of non-additive hard ellipsoids

For non-additive hard ellipsoids, (5) can be written as

$$d^0_{12} = d^a_{12}(1+\Delta), \tag{30}$$

where

$$d^a_{12} = (d^0_{11}/d^0_{22})/2.$$

Equations (19) and (22) can be written as

$$\frac{\beta(P-P^a)}{\rho} = 6C_1C_2\eta_a\{(4+4\eta-2\eta^2)/(1-\eta)^4\} \times F_1(\chi)\Delta(1+\Delta)+O(C_1^2C_2^2), \tag{31}$$

$$\frac{\beta(A-A^a)}{N} = 12C_1C_2\eta_a\{(2-\eta)/(1-\eta)^3\} \times F_1(\chi)\Delta(1+\Delta)+O(C_1^2C_2^2). \tag{32}$$

CC-0. In Public Domain. Gurukul Kangri Collection, Haridwar

Digitized by Arya Samaj Foundation Chennai and eGangotri

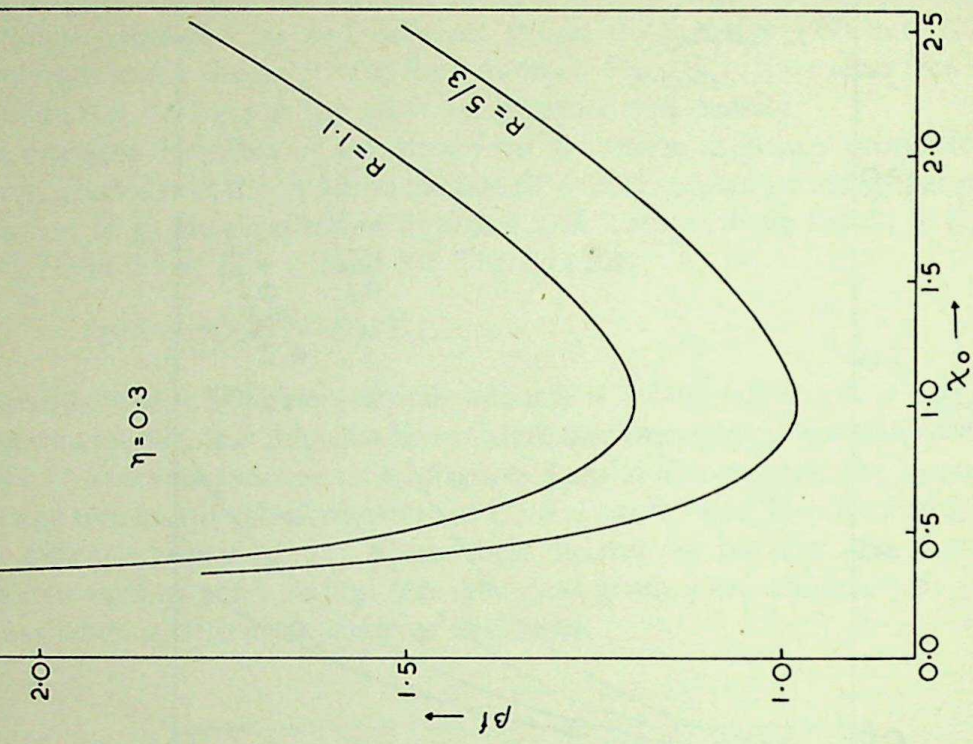

Figure 4. Excess free energy βf for binary mixture of additive hard ellipsoids as a function of χ_0 for $C_1 = C_2 = 0{\cdot}5$ and $R = 1{\cdot}1$ and 5/3 at $\eta = 0{\cdot}3$.

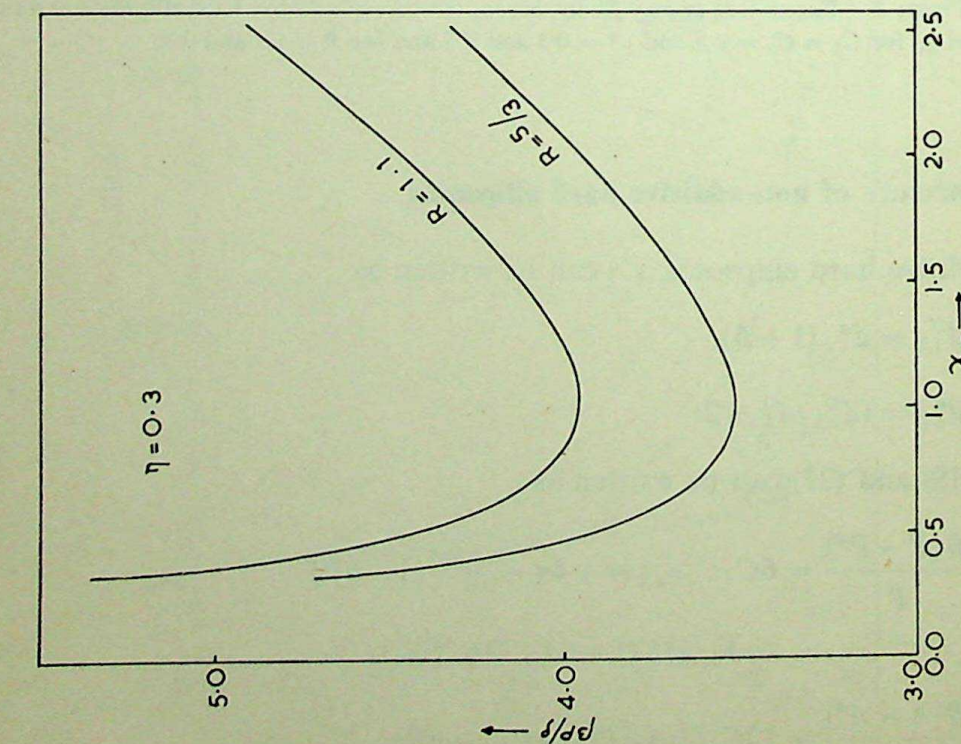

Figure 3. Equation of state $\beta P/\rho$ for binary mixture of additive hard ellipsoids as a function of χ_0 for $C_1 = C_2 = 0{\cdot}5$ and $R = 1{\cdot}1$ and 5/3 at $\eta = 0{\cdot}3$.

CC-0. In Public Domain. Gurukul Kangri Collection, Haridwar

Digitized by Arya Samaj Foundation Chennai and eGangotri

We have calculated $\beta P/\rho$ from (19) for a binary mixture of non-additive hard ellipsoids for $\Delta = 0{\cdot}0$, $-0{\cdot}1$ and $-0{\cdot}5$ at $R = 1{\cdot}0$. These values of $\beta P/\rho$ are reported in figure 5 as a function of χ_0 for $C_1 = C_2 = 0{\cdot}5$ and $\rho^* = 0{\cdot}3$ and $0{\cdot}5$. $\Delta = 0{\cdot}0$ corresponds to the one-component hard ellipsoid fluid. The results obtained for the one-component fluid is in good agreement with experimental results (Singh and Singh 1986). For binary mixture, computer simulation results are not available except for $\chi_0 = 1{\cdot}0$, which corresponds to the simple hard sphere mixture, where the agreement is good (Adams and McDonald 1975). However, this method is expected to provide good results even for other values of χ_0. We see that the pressure increases with increase of χ_0 and with increase of Δ.

In figure 6, the values of βf, obtained from (22), are demonstrated as a function of χ_0 for $C_1 = C_2 = 0{\cdot}5$; $\rho^* = 0{\cdot}3$ and $0{\cdot}5$ and $\Delta = 0{\cdot}0$, $-0{\cdot}1$ and $-0{\cdot}5$ at $R = 1{\cdot}0$. We see that the behaviour of free energy is identical to that of pressure.

Thus we conclude that the equation of state and free energy of the hard ellipsoid mixture increase with increase of anisotropy parameter χ_0.

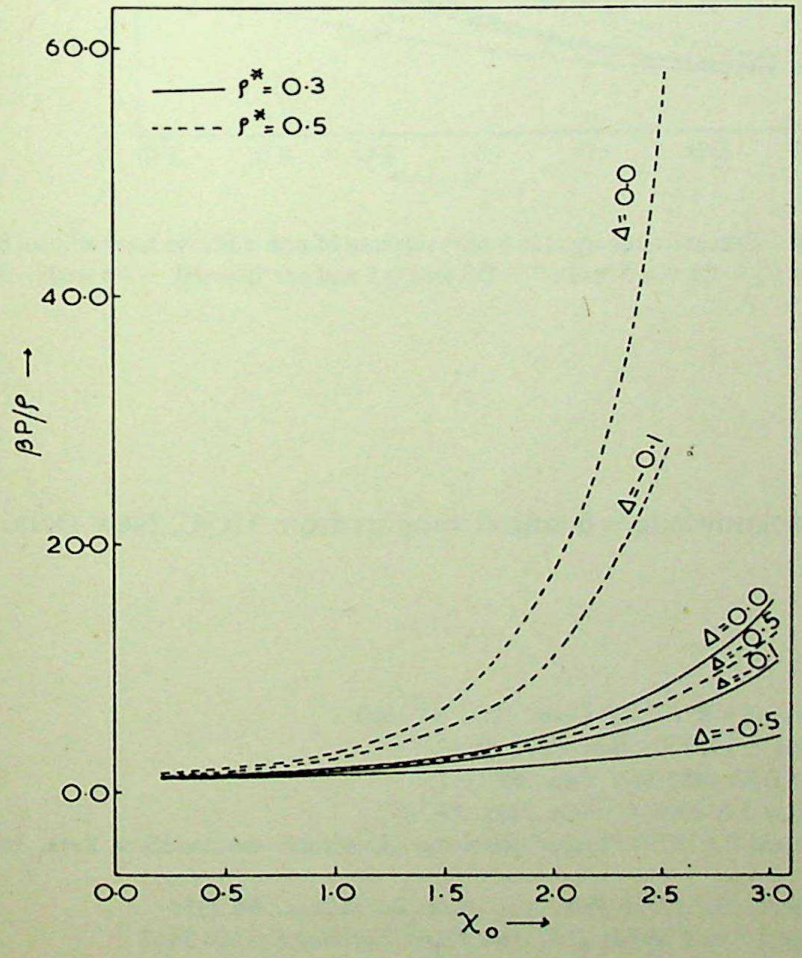

Figure 5. Equation of state $\beta P/\rho$ for binary mixture of non-additive hard ellipsoids as a function of χ_0 for $C_1 = C_2 = 0{\cdot}5$ and $\rho^* = 0{\cdot}3$ and $0{\cdot}5$ and for $\Delta = 0{\cdot}0$, $-0{\cdot}1$ and $-0{\cdot}5$ at $R = 1{\cdot}0$.

CC-0. In Public Domain. Gurukul Kangri Collection, Haridwar

Digitized by Arya Samaj Foundation Chennai and eGangotri

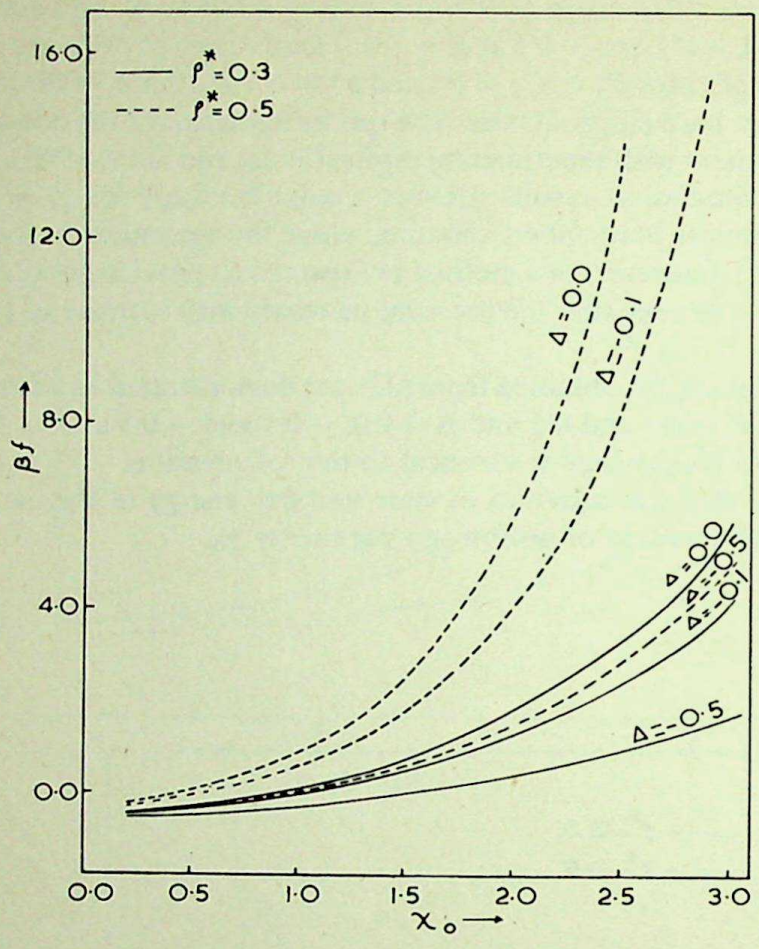

Figure 6. Excess free energy for binary mixture of non-additive hard ellipsoids as a function of χ_0 for $C_1 = C_2 = 0{\cdot}5$ and $\rho^* = 0{\cdot}3$ and $0{\cdot}5$ and for $\Delta = 0{\cdot}0$, $-0{\cdot}1$ and $-0{\cdot}5$ at $R = 1{\cdot}0$.

Acknowledgement

One of us (AKS) acknowledges financial support from UGC, New Delhi.

References

Adams D J and McDonald I R 1975 *J. Chem. Phys.* **63** 1900
Berne B J and Pechukas P 1972 *J. Chem. Phys.* **56** 4213
Frenkel D and Mulder B M 1985 *Mol. Phys.* **55** 1171
Henderson D and Barker J A 1968 *J. Chem. Phys.* **49** 3377
Henderson D and Leonard P J 1971a *Physical chemistry – An advance treatise* (New York: Academic press) Vol. **B8**
Henderson D and Leonard P J 1971b *Proc. Natl Acad. Sci. (U.S.A.)* **68** 2354
Leland T W, Rowlinson J S and Sather G A 1968 *Trans. Faraday Soc.* **64** 1447
Mason P A and Rigby M 1978 *Mol. Phys.* **35** 1337
Mulder B M and Frenkel D 1985 *Mol. Phys.* **55** 1193
Parson J D 1979 *Phys. Rev.* **A19** 1225

CC-0. In Public Domain. Gurukul Kangri Collection, Haridwar

Digitized by Arya Samaj Foundation Chennai and eGangotri

Singh U P and Sinha S K 1986 *Physica* (in press)
Singh S and Singh Y 1982 *Mol. Cryst. Liq. Cryst.* **87** 211
Singh U P and Singh Y 1986 *Phys. Rev.* **33** 2725
Smith W R 1971 *Mol. Phys.* **21** 105
Smith W R and Henderson D 1972 *Mol. Phys.* **24** 773

CC-0. In Public Domain. Gurukul Kangri Collection, Haridwar

Digitized by Arya Samaj Foundation Chennai and eGangotri

CC-0. In Public Domain. Gurukul Kangri Collection, Haridwar

Digitized by Arya Samaj Foundation Chennai and eGangotri

Pramāṇa – J. Phys., Vol. 28, No. 4, April 1987, pp. 355–359. © Printed in India.

Local quantum statistics in arbitrary curved space-time

P PRONIN and I KULIKOV
Moscow State University, 119899 GSP, Moscow, USSR

MS received 11 July 1986

Abstract. A local quantum statistics based on a finite temperature field theory in an arbitrary Riemann space-time is considered. The expressions have been derived for the partition functions, the grand thermodynamic potential and the particle distributions $\langle n_k \rangle$ of massive scalar gas and fermion gas in arbitrary space-time. It is shown that the chemical potential depends on the geometry of manifold.

Keywords. Local quantum statistics; arbitrary curved space-time.

PACS No. 5·30

The necessity to include characteristics of the Riemann manifolds in the thermodynamic description of the conditions of matter is connected with the studies on the thermodynamic processes at an early stage of the universe, inside stars or processes when one cannot neglect an influence of the gravitation field on the system which is being investigated. Evidently in this case it is necessary to construct a local quantum statistics and a local thermodynamics. In any case the laws of equilibrium theory are to be rewritten in the form of local equations and thermodynamical quantities are to have a local character and depend on a point of the space-time manifold. Therefore a dependence of the thermodynamical characteristics of the macroscopic system is defined by geometry and topology (boundary conditions on wave functions) of the Riemann space-time. The possibility of the construction of the local quantum statistics is based on two important aspects:

(i) An application of a finite temperature field theory for the description of quantum statistics based on path integral (Martin and Schwinger 1959; Dolan and Jackiw 1974).
(ii) Use of a momentum-space representation of the Green's functions for scalar and spinor fields in arbitrary curved space-times (Bunch and Parker 1979; Panangaden 1981).

Our ultimate goal is to construct a quantum statistics in terms of a finite temperature quantum field theory in curved space-time and to obtain thermal characteristics of the thermodynamic system in the local thermal equilibrium state being localized in the smallest volume of the space-time manifold.

Thus all the manifolds would have a "honeycomb" structure, that is it would consist of a large number of simplexes. The formalism of momentum-space representation based on the use of Riemann normal coordinates (Petrov 1969) gives us an opportunity to create a local quantum statistics in every simplex and then the equilibrium conditions would be given by the solution of the Einstein equations. Generally, the thermodyna-

CC-0. In Public Domain. Gurukul Kangri Collection, Haridwar

Digitized by Arya Samaj Foundation Chennai and eGangotri

mical characteristics of the macroscopic matter would be a function of the Riemann curvature. This quantity, R, appearing in the main equations of the local quantum statistics is expected to give interesting results. Strictly speaking, the chemical potential will depend on the point of the Riemann manifold through the curvature terms which will be changing from one simplex to another.

Let us formulate a method of calculation of the partition function and the thermodynamic potential in arbitrary curved space-time. To calculate the partition function Z and the thermodynamic potential we first obtain the thermal Green's function of massive scalar field and spinor field. The Schwinger-De-Witt expansion in the Riemann normal coordinates of the Green's functions is obtained from the equations:

$$(-\nabla_\mu \nabla^\mu + m^2 + \xi R)\, \hat{G}^B(x, x') = g^{-1/2}(x)\, \delta^{(4)}(x, x') \tag{1}$$

and

$$(i\gamma^\mu \nabla_\mu - m)\, \hat{S}^F(x, x') = g^{-1/2}(x)\, \delta^{(4)}(x, x') \tag{2}$$

are given by

$$\hat{G}^{B(F)}(x_0, y) = \Delta^{1/2}(x_0, y) \sum_{l=0}^{\infty} \int \frac{d^4 k}{(2\pi)^4} f_l^{B(F)}(x_0, y) \times \left(\frac{-\partial}{\partial m^2}\right)^l \frac{1}{k^2 + m^2} \cdot \exp(iky) \tag{3}$$

$$\hat{S}^F(x, x') = (i\gamma^\nu \nabla_\nu + m)\, \hat{G}^F(x, x'),$$

where ∇_μ is the covariant derivatives, $\Delta^{1/2}(x_0, y)$ is van Vleck-determinant (it is reduced in normal coordinates about x to $g^{-1/2}(x)$) R is the scalar curvature of the space-time and ξ is an arbitrary real number. The values $f_l^{B(F)}$ are the Minakshisundaram coefficients which are given by

$$\begin{aligned} f_0^B &= 1 & f_0^F &= 1 \\ f_1^B &= (\tfrac{1}{6} - \xi) R & f_1^F &= \tfrac{1}{12} R \\ &\vdots & &\vdots \\ &\text{etc} & &\text{etc.} \end{aligned} \tag{4}$$

The Riemann normal coordinates $\{y^\mu\}$ for the point x with the origin at the point x_0 are defined by

$$y^\mu = \hat{z}\, l^\mu$$

where l^μ is a unit vector at the point x_0 tangent to the geodesic between x and x_0 is the distance between them along the geodesic.

Let us introduce a finite temperature: $\beta = 1/T$. Then

$$y_0 \in [0, -i\beta] \qquad \text{and}$$

$$k^2 \to \sum_{n=-\infty}^{\infty} (-\omega_n^2 + \mathbf{k}^2); \quad \int \frac{d^4 k}{(2\pi)^4} \phi(k) \to \frac{i}{\beta} \int \frac{d^3 k}{(2\pi)^3} \sum_{n=-\infty}^{\infty} \phi(\mathbf{k}, \omega_n),$$

CC-0. In Public Domain. Gurukul Kangri Collection, Haridwar

Digitized by Arya Samaj Foundation Chennai and eGangotri

where

$$\omega_n = \begin{cases} i2\pi Tn & \text{(bosons)} \\ i2\pi T(n+1/2) & \text{(fermions)} \end{cases}$$

Using the summation formulae

$$\frac{1}{\beta}\sum_{n=-\infty}^{\infty}\frac{1}{E^2-\omega_n^2}=\frac{1}{2E}\pm\frac{1}{E[\exp(\beta E)\mp 1]} \tag{5}$$

(the upper sign for bosons and the lower sign for fermions), we can write immediately the thermal Green's functions of these fields:

$$\operatorname{tr}\hat{G}_\beta^{B(F)}(x_0,y)=s\int\frac{\mathrm{d}^3k}{(2\pi)^3}\sum_{l=0}^{\infty}f_l^{B(F)}(x_0)\left(-\frac{\partial}{\partial m^2}\right)^l\left(\frac{\pm 1}{E(\exp(\beta E)\mp 1)}\right) \tag{6}$$

s is the dimension of the γ matrix, $E^2=\mathbf{k}^2+m^2$. The bosonic and fermionic "grand thermodynamic potential" is obtained from

$$\Omega^{B(F)}=\mp\frac{1}{2}\int_{m^2}^{\infty}\mathrm{d}m^2\operatorname{tr}\hat{G}_\beta^{B(F)}(x_0,y), \tag{7}$$

thus

$$\Omega^B(x_0,y)=\sum_{l=0}^{\infty}f_l^B(x_0)\left(-\frac{\partial}{\partial m^2}\right)^l\frac{1}{\beta}\int\frac{\mathrm{d}^3k}{(2\pi)^3}\ln[1-z\exp(-\beta E)], \tag{8}$$

and

$$\Omega^F(x_0,y)=-2\sum_{l=0}^{\infty}f_l^F(x_0)\left(-\frac{\partial}{\partial m^2}\right)^l\frac{1}{\beta}\int\frac{\mathrm{d}^3k}{(2\pi)^3}\ln[1+z\exp(-\beta E)] \tag{9}$$

where we have marked $z=\exp(\beta\mu)$ the so-called chemical activity. Introducing $g_{5/2}(z)$ and $f_{5/2}(z)$ functions the explicit forms of which are given by

$$g_{5/2}(z)=-\frac{4}{\sqrt{\pi}}\int_0^{\infty}\mathrm{d}x\,x^2\ln[1-z\exp(-x^2)]=\sum_{l=1}^{\infty}\frac{z^l}{l^{5/2}}, \tag{10}$$

$$f_{5/2}(z)=\frac{4}{\sqrt{\pi}}\int_0^{\infty}\mathrm{d}x\,x^2\ln[1+z\exp(-x^2)]=\sum_{l=1}^{\infty}\frac{z^l}{l^{5/2}}(-1)^{l+1} \tag{11}$$

we have the following results for "grand thermodynamic potential"

$$\Omega^B(x_0)=\sum_{l=0}^{\infty}f_l^B(x_0)\left(-\frac{\partial}{\partial m^2}\right)^l\frac{1}{\lambda^3}g_{5/2}(z), \tag{12}$$

$$\Omega^F(x_0)=\sum_{l=0}^{\infty}f_l^F(x_0)\left(-\frac{\partial}{\partial m^2}\right)^l\frac{1}{\lambda^3}f_{5/2}(z), \tag{13}$$

$\lambda=(2\pi/mT)^{1/2}$ is the thermal wavelength of the particle. The Bose and Fermi distributions of occupation numbers in the Riemann space-time are written as

$$\langle n_{\mathbf{k}}\rangle=\sum_{l=0}^{\infty}f_l(x_0)\left(-\frac{\partial}{\partial m^2}\right)^l\frac{1}{\exp[(E-\mu)/T]\pm 1}. \tag{14}$$

CC-0. In Public Domain. Gurukul Kangri Collection, Haridwar

Digitized by Arya Samaj Foundation Chennai and eGangotri

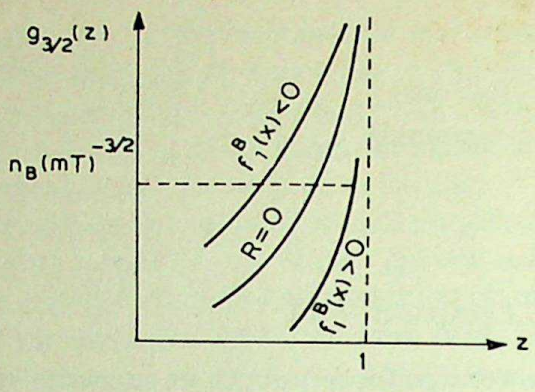

Figure 1. The graphical solutions of (15).

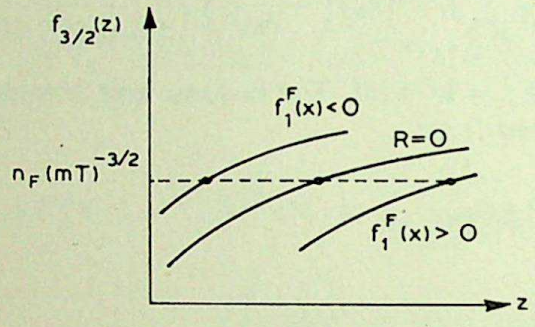

Figure 2. The graphical solutions of (16).

The dependence of the chemical activity z on the curvature, temperature and the particle density n is obtained from two main equations (Huang 1967)

$$n_B\left(\frac{2\pi}{mT}\right)^{3/2} = \left[1 - f_1^B(x_0)\frac{3}{4m^2} - \ldots\right] g_{3/2}(z) + \frac{z}{1-z}, \tag{15}$$

$$n_F\left(\frac{2\pi}{mT}\right)^{3/2} = \left[1 - f_1^F(x_0)\frac{3}{4m^2} - \ldots\right] f_{3/2}(z), \tag{16}$$

where $g_{3/2}(z) = z\dfrac{\partial}{\partial z} g_{5/2}(z)$ and $f_{3/2}(z) = z\dfrac{\partial}{\partial z} f_{5/2}(z)$.

This dependence of z on temperature and curvature is shown in figures 1 and 2.

Moreover we can obtain interesting results for the chemical potential μ in the case of high temperature and statistics like the Boltzmann distribution:

$$\mu_B \simeq \mu_0^{(B)}(T) - \frac{3T}{4m^2} f_1^B(x_0) + \ldots, \tag{17}$$

$$\mu_F \simeq \mu_0^{(F)}(T) - \frac{3T}{4m^2} f_1^F(x_0) + \ldots, \tag{18}$$

here $\mu_0^{B(F)}$ is the chemical potential in flat space-time. These formulae reveal the direct connection between $\mu^{B(F)}$ and curvature of the space-time manifold.

Our results show that quantum statistics behaviour depends on the characteristics of the space-time geometry to which this statistics is applied. One can consider equations

CC-0. In Public Domain. Gurukul Kangri Collection, Haridwar

Digitized by Arya Samaj Foundation Chennai and eGangotri

(17) and (18) as the relativistic generalization of the effect of the influence of gravitational external field on the chemical potential at high temperature. Our future research is aimed at developing a self-consistent theory in which the background geometry is defined by some material system.

References

Martin P and Schwinger J 1959 *Phys. Rev.* **115** 1342
Dolan L and Jackiw R 1974 *Phys. Rev.* **D9** 3320
Bunch T and Parker L 1979 *Phys. Rev.* **D20** 2499
Panangaden P 1981 *Phys. Rev.* **D23** 1735
Petrov A Z 1969 *Einstein spaces* (Oxford Pergamon)
Huang K 1967 *Statistical mechanics* (New York)

CC-0. In Public Domain. Gurukul Kangri Collection, Haridwar

Digitized by Arya Samaj Foundation Chennai and eGangotri

CC-0. In Public Domain. Gurukul Kangri Collection, Haridwar

Digitized by Arya Samaj Foundation Chennai and eGangotri

Pramāṇa – J. Phys., Vol. 28, No. 4, April 1987, pp. 361–366. © Printed in India.

Microscopic theory of soliton propagation in a mixture of two boson fluid films

A C BISWAS
Tata Institute of Fundamental Research, Homi Bhabha Road, Bombay 400 005, India

MS received 1 September 1986; revised 7 February 1987

Abstract. A microscopic theory of soliton propagation in a mixture of two boson fluids at $T = 0°K$ has been provided.

Keywords. Boson fluid; films; solitons.

PACS No. 67·70

Introduction

In a recent paper Warke and the author gave a microscopic theory of soliton propagation in a film of liquid ^{4}He. In this paper we give a microscopic theory of soliton propagation in a film of a mixture of two boson fluids. Such a mixture can be visualized as a mixture of superfluid ^{3}He and liquid ^{4}He. We can also think of a mixture of liquid ^{6}He and liquid ^{4}He.

The Hamiltonian is

$$H=\sum\frac{P_i^2}{2M}+\sum\frac{P_i^2}{2m}+\sum u(r_i-r_j)+\sum V(r_i-r_j)+\sum_{i,j} W(r_i-r_j)$$
$$+\sum u_1(r_i)+\sum u_2(r_j), \tag{1}$$

where $u(r_i-r_j)$ is the interaction between the particles of system (1) and $V(r_i-r_j)$ is the interaction between particles of system (2), $W(r_i-r_j)$ is the interaction between particles of system (1) and system (2), $u_1(r_i)$ and $u_2(r_j)$ are the Van der Waal's interaction for the system (1) and system (2) particles respectively.

The action is

$$L=\int\left\langle\psi\left|i\hbar\frac{\partial}{\partial t}-H\right|\psi\right\rangle dt. \tag{2}$$

We use the Hartree-Fock decomposition of the wave function and write

$$\psi=\prod_{i=1}^{N_1}\phi_1(r_i,t)\prod_{j=1}^{N_2}\phi_2(r'_j,t). \tag{3}$$

We put

$$\phi_1(r_j,t)=[\rho_{01}①(z_j-\eta)]^{1/2}\exp[i\theta(\eta_j,t)], \tag{4}$$

$$\phi_2(r'_j,t)=[\rho_{02}①(z_j-\eta)]^{1/2}\exp[i\theta(\eta_j,t)], \tag{5}$$

CC-0. In Public Domain. Gurukul Kangri Collection, Haridwar

Digitized by Arya Samaj Foundation Chennai and eGangotri

where ① (x) is the Heaviside theta function (since $z_j \leqslant \eta$ the surface height).
The action is composed of

$$I_1 = \int dt\, dx\, dz [\rho_{01} ① (z_i - \eta)]^{1/2} \exp(-i\theta_i) [\rho_{02} ① (z_j' - \eta)]^{1/2} \exp(-i\theta_j)$$

$$i\hbar \frac{\partial}{\partial t} [\rho_{01} ① (z_i - \eta)]^{1/2} [\rho_{02} ① (z_j' - \eta)]^{1/2} \exp(i\theta_i) \exp(-i\theta_j)$$

$$= \int dt\, dx\, dz\, \rho_{01} \tfrac{1}{2} i\hbar\, \delta(z_i - \eta)(-\partial/\partial t)$$

$$+ \int dt\, dx\, dz\, \rho_{02} i\hbar \tfrac{1}{2} \delta(z_j - \eta)(-\partial/\partial t)$$

$$- \int dt\, dx\, dz\, \hbar\, \rho_{01} ① (z_i - \eta)(\partial\theta_i/\partial t) - \int dt\, dx\, dz\, \rho_{02} ①$$

$$(z_j - \eta)(\partial\theta_j/\partial t)$$

$$= \int dt\, dx\, \rho_{01}\, i\hbar (-\partial\eta/\partial t) + \int dt\, dx\, \rho_{02} \tfrac{1}{2} i\hbar (-\partial\eta/\partial t) - \int dt\, dx\, \hbar\, \rho_{01}$$

$$\times \int_0^\eta \frac{\partial\theta_1}{\partial t}\, dz - \int dt\, dx\, \hbar\, \rho_{02} \int_0^\eta \frac{\partial\theta_2}{\partial t}\, dz. \tag{6}$$

Using the fact that the total number of particles in the system is conserved we derive,

$$\int \frac{\partial\eta}{\partial t}\, dx = 0,$$

$$I_2 = \int dt\, dx \frac{\hbar^2}{2m} \rho_{01} \left[\frac{1}{4} \frac{1}{h_0} \left(-\frac{\partial\eta}{\partial x} \right)^2 + \frac{1}{2} \left(-\frac{\partial^2\eta}{\partial x^2} \right) + \frac{1}{2} i \left(-\frac{\partial\eta}{\partial x} \right) \frac{\partial\theta_1}{\partial x} \bigg|_{z=\eta} \right.$$

$$\left. - \int_0^\eta \left(\frac{\partial\theta_1}{\partial x} \right)^2 dz + i \int_0^\eta \frac{\partial^2\theta_1}{\partial x^2}\, dz \right] + \int dt\, dx \frac{\hbar^2}{2M} \rho_{02} \left[\frac{1}{4} \left(-\frac{\partial\eta}{\partial x} \right)^2 \right.$$

$$\left. + \frac{1}{2} \left(-\frac{\partial^2\eta}{\partial x^2} \right) + \frac{1}{2} i \left(-\frac{\partial\eta}{\partial x} \right) \frac{\partial\theta_2}{\partial x} \bigg|_{z=\eta} - \int_0^\eta \left(\frac{\partial\theta_2}{\partial x} \right)^2 dz + i \int_0^\eta \frac{\partial^2\theta_2}{\partial x^2}\, dz \right]$$

$$- \frac{\hbar^2}{2m} \int_\eta dt\, dx\, \rho_{01} \left[\frac{1}{4} \frac{1}{h_0} + i \frac{\partial\theta_1}{\partial z} \bigg|_{z=\eta} - \int_0^\eta \left(\frac{\partial\theta_1}{\partial z} \right)^2 dz \right.$$

$$\left. + i \int_0^\eta \frac{\partial^2\theta_1}{\partial z^2}\, dz \right] - \frac{\hbar^2}{2M} \int dt\, dx\, \rho_{02} \left[\frac{1}{4} \frac{1}{h_0} + i \frac{\partial\theta_2}{\partial z} \bigg|_{z=\eta} - \int_0^\eta \left(\frac{\partial\theta_2}{\partial z} \right)^2 dz \right.$$

$$\left. + i \int_0^\eta \frac{\partial^2\theta_2}{\partial z^2}\, dz \right] - \int dt\, dx'\, dy\, dy'\, dx \int_0^\eta \int_0^{\eta'} u(|r - r'|)\, dz\, dz'$$

$$+ \int dt\, dx\, dy \int_0^\eta W_1(r)\, dz - \int dt\, dx\, dy \int_0^\eta W_2(r)\, dz. \tag{7}$$

We scale all lengths with respect to the length l which is the extent in the x-direction $(\eta \ll l)$. The action L then comes out to be

CC-0. In Public Domain. Gurukul Kangri Collection, Haridwar

Digitized by Arya Samaj Foundation Chennai and eGangotri

$$L=-\int \mathrm{d}t\,\mathrm{d}\bar{x}\,\hbar\,\rho_{01}\,l\int_0^{\bar{\eta}}\frac{\partial\theta_1}{\partial t}\,\mathrm{d}\bar{z}-\int \mathrm{d}t\,\mathrm{d}\bar{x}\,\hbar\,\rho_{02}\,l\int_0^{\bar{\eta}}\frac{\partial\theta_2}{\partial t}\,\mathrm{d}\bar{z}$$

$$-\frac{\hbar^2}{2m}\int \mathrm{d}t\,\mathrm{d}\bar{x}\,\rho_{01}\left[\frac{1}{4}\frac{1}{h_0}\left(-\frac{\partial\bar{\eta}}{\partial\bar{x}}\right)^2+\frac{1}{2}\left(-l\frac{\partial^2\bar{\eta}}{\partial\bar{x}^2}\right)+\frac{1}{2}i\left(-\frac{\partial\bar{\eta}}{\partial\bar{x}}\frac{1}{l}\frac{\partial\theta_1}{\partial\bar{x}}\bigg|_{\bar{z}=\eta}\right)\right.$$

$$\left.-\int_0^{\bar{\eta}}\left(\frac{\partial\theta_1}{\partial\bar{x}}\right)^2\frac{1}{l}\,\mathrm{d}\bar{z}+i\int_0^{\bar{\eta}}\frac{\partial^2\theta_1}{\partial\bar{x}^2}\frac{1}{l}\,\mathrm{d}\bar{z}\right]-\frac{\hbar^2}{2M}\int \mathrm{d}t\,\mathrm{d}\bar{x}\,\rho_{01}\left[\frac{1}{4}\frac{1}{h_0}\left(-\frac{\partial\bar{\eta}}{\partial\bar{x}}\right)^2\right.$$

$$+\frac{1}{2}\left(-l\frac{\partial^2\bar{\eta}}{\partial\bar{x}^2}\right)+\frac{1}{2}i\left(-\frac{\partial\bar{\eta}}{\partial\bar{x}}l\frac{\partial\theta_2}{\partial\bar{x}}\bigg|_{\bar{z}=\bar{\eta}}\right)-\int_0^{\bar{\eta}}\left(\frac{\partial\theta_2}{\partial\bar{x}}\right)^2\frac{1}{l}\,\mathrm{d}\bar{z}$$

$$\left.+i\int_0^{\bar{\eta}}\frac{\partial^2\theta_2}{\partial\bar{x}^2}\frac{1}{l}\,\mathrm{d}\bar{z}\right]-\frac{\hbar^2}{2m}\int \mathrm{d}t\,\mathrm{d}x\,\rho_{01}\left[\frac{1}{4}\frac{1}{h_0}+i\frac{1}{l}\frac{\partial\theta_1}{\partial\bar{z}}-\frac{1}{l}\int_0^{\bar{\eta}}\left(\frac{\partial\theta_1}{\partial\bar{z}}\right)^2\mathrm{d}\bar{z}\right.$$

$$\left.+i\int_0^{\bar{\eta}}\frac{1}{l}\frac{\partial^2\theta_2}{\partial\bar{z}^2}\,\mathrm{d}\bar{z}\right]-\int \mathrm{d}t\,\mathrm{d}\bar{x}'\,\mathrm{d}\bar{y}\,\mathrm{d}\bar{y}'\,\mathrm{d}\bar{x}\int_0^{\bar{\eta}}\int_0^{\bar{\eta}}u(|r-r'|)\,\mathrm{d}\bar{z}\,\mathrm{d}\bar{z}'$$

$$-\int \mathrm{d}t\,\mathrm{d}\bar{x}'\,\mathrm{d}\bar{y}\,\mathrm{d}\bar{y}'\,\mathrm{d}\bar{x}\int_0^{\bar{\eta}}\int_0^{\bar{\eta}}V(|r-R|)\,\mathrm{d}\bar{z}\,\mathrm{d}\bar{z}'$$

$$-\int \mathrm{d}t\,\mathrm{d}\bar{x}\,\mathrm{d}\bar{y}\int_0^{\bar{\eta}}W_1(r)\,\mathrm{d}\bar{z}-\int \mathrm{d}t\,\mathrm{d}\bar{x}\,\mathrm{d}\bar{y}\int_0^{\bar{\eta}}W_2(r)\,\mathrm{d}\bar{z}. \tag{8}$$

In the above h_0 is the minimum thickness of the film for which our treatment is valid.

By varying w.r.t. $\bar{\eta}$, θ_1, θ_2 we get the following equations

$$-\frac{\partial\bar{\eta}}{\partial\bar{x}}\frac{\partial\theta_1}{\partial\bar{x}}+\frac{\partial^2\theta_1}{\partial\bar{x}^2}+\frac{\partial^2\theta_1}{\partial\bar{z}^2}-\frac{\partial\theta_1}{\partial\bar{z}}=0, \tag{9}$$

$$-\frac{\partial\bar{\eta}}{\partial\bar{x}}\frac{\partial\theta_2}{\partial\bar{x}}+\frac{\partial^2\theta_2}{\partial\bar{x}^2}+\frac{\partial^2\theta_2}{\partial\bar{z}^2}-\frac{\partial\theta_2}{\partial\bar{z}}=0, \tag{10}$$

$$-\hbar C_1\frac{\partial\theta_1}{\partial t}-hC_2\frac{\partial\theta_2}{\partial t}-\left(\frac{\hbar^2C_1}{2m}+\frac{\hbar^2C_2}{2M}\right)\frac{1}{4lh_0}\frac{\partial^2\bar{\eta}}{\partial\bar{x}^2}-\frac{\hbar^2C_1}{2m}\left(\frac{\partial\theta_1}{\partial\bar{z}}\right)^2\bigg|_{\bar{z}=\bar{\eta}}$$

$$-\frac{\hbar^2C_2}{2M}\left(\frac{\partial\theta_2}{\partial\bar{x}}\right)^2\bigg|_{\bar{z}=\bar{\eta}}-C_1^2\int u(|r-r'|)\bigg|_{\substack{\bar{z}=\bar{\eta}\\ \bar{z}'=\bar{\eta}'}}\mathrm{d}x\,\mathrm{d}x'\,\mathrm{d}y\,\mathrm{d}y'-C_1C_2$$

$$\int W(|r-r'|)\bigg|_{\substack{\bar{z}=\bar{\eta}\\ \bar{z}'=\bar{\eta}'}}\mathrm{d}x\,\mathrm{d}x'\,\mathrm{d}y\,\mathrm{d}y'-C_2^2\int V(|r-r'|)\bigg|_{\substack{\bar{z}=\bar{\eta}\\ \bar{z}'=\bar{\eta}'}}\mathrm{d}x\,\mathrm{d}x'\,\mathrm{d}y\,\mathrm{d}y'$$

$$-C_1\int W_1(r)\bigg|_{\bar{z}=\bar{\eta}}\mathrm{d}x\,\mathrm{d}y-C_2\int W_2(r)\bigg|_{\bar{z}=\bar{\eta}}\mathrm{d}x\,\mathrm{d}y=0. \tag{11}$$

CC-0. In Public Domain. Gurukul Kangri Collection, Haridwar

Digitized by Arya Samaj Foundation Chennai and eGangotri

Let us consider the equation

$$-\frac{\partial\bar{\eta}}{\partial\bar{x}}\frac{\partial\theta_1}{\partial\bar{x}}+\frac{\partial^2\theta_1}{\partial\bar{x}^2}+\frac{\partial^2\theta_1}{\partial\bar{z}^2}-\frac{\partial\theta_1}{\partial\bar{z}}=0. \tag{12}$$

We put

$$\theta_1(\bar{x},\bar{z},t)=\sum_{n=0}^{\infty}\theta_1^{(n)}(x,t)\bar{z}^n,$$

$$\theta_{1\bar{z}}=0 \quad \text{at} \quad \bar{z}=0 \quad \text{gives} \quad \theta_1^{(1)}=0. \tag{13}$$

We have

$$-\eta_x\sum_{n=0}^{\infty}\theta_{1x}^{(n)}(x,t)z^n+\sum_{n=0}^{\infty}\theta_{1xx}^{(n)}z^n+\sum_{n=0}^{\infty}\theta_1^{(n)}n(n-1)z^{n-1}$$

$$-\sum_{n=0}^{\infty}\theta_1^{(n)}nz^{n-1}=0. \tag{14}$$

From (14) we have

$$(n+2)(n+1)\,\theta_1^{(n+2)}-(n+1)\,\theta_1^{(n+1)}+\theta_{1xx}^{(n)}-\bar{\eta}_x\theta_{1x}^{(n)}=0 \tag{15}$$

$$2\cdot1\;\theta_1^{(2)}=-\theta_{1\bar{x}\bar{x}}^{(0)}+\bar{\eta}_{\bar{x}}\theta_{1\bar{x}}^{(0)}.$$

Similarly

$$2\cdot1\;\theta_2^{(2)}=-\theta_{2\bar{x}\bar{x}}^{(0)}+\bar{\eta}_{\bar{x}}\theta_{2\bar{x}}^{(0)}. \tag{16}$$

Assuming both θ_1 and θ_2 slowly varying functions of $\bar{z}$ we have

$$\theta_{1\bar{x}\bar{x}}^{0}=\bar{\eta}_{\bar{x}}\theta_{1\bar{x}}^{(0)}, \tag{17}$$

$$\theta_{2\bar{x}\bar{x}}^{0}=\bar{\eta}_{\bar{x}}\theta_{2\bar{x}}^{(0)}. \tag{18}$$

Integrating (17) and (18) we have

$$\theta_{1\bar{x}}^{(0)}=C_1\,e^{\bar{\eta}}, \tag{19}$$

$$\theta_{2\bar{x}}^{(0)}=C_2\,e^{\bar{\eta}}. \tag{20}$$

C_1 and C_2 are constants to be determined. Let V be the velocity of the fluid at an infinitesimal thickness. Then

$$C_1=\frac{mVl}{\hbar}, \qquad C_2=\frac{MVl}{\hbar}. \tag{21}$$

We have then

$$\theta_{1\bar{x}}^{(0)}=\frac{mVl}{\hbar}e^{\bar{\eta}}, \qquad \theta_{2\bar{x}}^{(0)}=\frac{MVl}{\hbar}e^{\bar{\eta}}. \tag{22}$$

Expanding w.r.t. $\bar{\eta}$ and retaining upto quadratic terms

$$\theta_{1\bar{x}}^{(0)}=\frac{mVl}{\hbar}\left(1+\bar{\eta}+\frac{\bar{\eta}^2}{2}\right), \tag{23}$$

CC-0. In Public Domain. Gurukul Kangri Collection, Haridwar

Digitized by Arya Samaj Foundation Chennai and eGangotri

$$\theta_{2\bar{x}}^{(0)}=\frac{MVl}{\hbar}\left(1+\bar{\eta}+\frac{\bar{\eta}^2}{2}\right). \tag{24}$$

Equation (11) can be written as (using expansion of θ_1 and θ_2 and retaining the first terms only).

$$\begin{aligned}&-\hbar C_1\frac{\partial\theta_1^{(0)}}{\partial t}-\hbar C_2\frac{\partial\theta_2^{(0)}}{\partial t}-\left(\frac{\hbar^2C_1}{2m}+\frac{\hbar^2C_2}{2M}\right)\frac{1}{4lh_0}\frac{\partial^2\bar{\eta}}{\partial\bar{x}^2}\\&\quad-C_1^2(\alpha_1\bar{\eta}^2-2\alpha_1\bar{\eta}d+d^2)-C_1C_2(\beta_1\bar{\eta}^2-2\beta_1\bar{\eta}d+d^2)\\&\quad-C_2^2(\gamma_1\bar{\eta}^2-2\gamma_1\bar{\eta}d+d^2)-C_1(\delta_0+\delta_1\bar{\eta}^2)-C_2(\delta_2+\delta_3\bar{\eta}^2)=0,\end{aligned} \tag{25}$$

where $\alpha_1,\beta_1,\gamma_1,\delta_0,\delta_1,\delta_2,\delta_3$ are interaction constants. d is the equilibrium thickness of the film. C_1, C_2 are concentrations of the two types of boson fluids in the film.

Differentiating (25) w.r.t. $\bar{x}$ we have

$$\begin{aligned}&-\hbar C_1\frac{\partial\theta_{1\bar{x}}^{(0)}}{\partial t}-\hbar C_2\frac{\partial\theta_{2\bar{x}}^{(0)}}{\partial t}-\left(\frac{\hbar^2C_1}{2m}+\frac{\hbar^2C_2}{2M}\right)\frac{1}{4lh_0}\frac{\partial^3\bar{\eta}}{\partial\bar{x}^3}\\&\quad-C_1^2\left(2\alpha_1\bar{\eta}\frac{\partial\bar{\eta}}{\partial\bar{x}}-2\alpha_1d\frac{\partial\bar{\eta}}{\partial\bar{x}}\right)-C_1C_2\left(2\beta_1\bar{\eta}\frac{\partial\bar{\eta}}{\partial\bar{x}}-2\beta_1d\frac{\partial\bar{\eta}}{\partial\bar{x}}\right)\\&-C_2^2\left(2\gamma_1\bar{\eta}\frac{\partial\bar{\eta}}{\partial\bar{x}}-2\gamma_1d\frac{\partial\bar{\eta}}{\partial\bar{x}}\right)-C_1\left(2\delta_1\bar{\eta}\frac{\partial\bar{\eta}}{\partial\bar{x}}\right)-C_2\left(2\delta_3\bar{\eta}\frac{\partial\bar{\eta}}{\partial\bar{x}}\right)=0,\end{aligned} \tag{26}$$

$$\begin{aligned}&-\hbar C_1\frac{\partial}{\partial t}\frac{mVl}{\hbar}\left(1+\bar{\eta}+\frac{\bar{\eta}^2}{2}\right)-\hbar C_2\frac{\partial}{\partial t}\frac{MVl}{\hbar}\left(1+\bar{\eta}+\frac{\bar{\eta}^2}{2}\right)\\&\quad-\left(\frac{\hbar^2C_1}{2m}+\frac{\hbar^2C_2}{2M}\right)\frac{1}{4lh_0}\frac{\partial^3\bar{\eta}}{\partial\bar{x}^3}-C_1^2\left(\alpha_1 2\bar{\eta}\frac{\partial\bar{\eta}}{\partial\bar{x}}-2\alpha_1d\frac{\partial\bar{\eta}}{\partial\bar{x}}\right)\\&\quad-C_1C_2\left(2\beta_1\bar{\eta}\frac{\partial\bar{\eta}}{\partial\bar{x}}-2\beta_1d\frac{\partial\bar{\eta}}{\partial\bar{x}}\right)-C_2\left(2\gamma_1\bar{\eta}\frac{\partial\bar{\eta}}{\partial\bar{x}}-2\gamma_1d\frac{\partial\bar{\eta}}{\partial\bar{x}}\right)\\&\quad-C_1\left(2\delta_1\bar{\eta}\frac{\partial\bar{\eta}}{\partial\bar{x}}\right)-C_2\left(2\delta_3\bar{\eta}\frac{\partial\bar{\eta}}{\partial\bar{x}}\right)=0,\end{aligned} \tag{27}$$

$$\begin{aligned}&-\hbar C_1\frac{mVl}{\hbar}\left(\frac{\partial\bar{\eta}}{\partial t}+\bar{\eta}\frac{\partial\bar{\eta}}{\partial t}\right)-\hbar C_2\frac{MVl}{\hbar}\left(\frac{\partial\bar{\eta}}{\partial t}+\bar{\eta}\frac{\partial\bar{\eta}}{\partial t}\right)\\&\quad-\left(\frac{\hbar^2C_1}{2m}+\frac{\hbar^2C_2}{2M}\right)\frac{1}{4lh_0}\frac{\partial^3\bar{\eta}}{\partial\bar{x}^3}-C_1^2\left(2\alpha_1\bar{\eta}\frac{\partial\bar{\eta}}{\partial x}-2\alpha_1d\frac{\partial\bar{\eta}}{\partial x}\right)\\&\quad-C_1C_2\left(2\beta_1\bar{\eta}\frac{\partial\bar{\eta}}{\partial x}-2\beta_1d\frac{\partial\bar{\eta}}{\partial x}\right)-C_2^2\left(2\gamma_1\bar{\eta}\frac{\partial\bar{\eta}}{\partial\bar{x}}-2\gamma_1d\frac{\partial\bar{\eta}}{\partial x}\right)\\&\quad-C_1\left(2\delta_1\bar{\eta}\frac{\partial\bar{\eta}}{\partial x}\right)-C_2\left(2\delta_3\bar{\eta}\frac{\partial\bar{\eta}}{\partial x}\right)=0,\end{aligned} \tag{28}$$

CC-0. In Public Domain. Gurukul Kangri Collection, Haridwar

Digitized by Arya Samaj Foundation Chennai and eGangotri

$$-Vl(mC_1+MC_2)\left(\frac{\partial\bar{\eta}}{\partial t}+\bar{\eta}\frac{\partial\bar{\eta}}{\partial t}\right)-\left(\frac{\hbar^2C_1}{2m}+\frac{\hbar^2C_2}{2M}\right)\frac{1}{4lh_0}\frac{\partial^3\bar{\eta}}{\partial\bar{x}^3}$$

$$-(2\alpha_1C_1^2+2\beta_1C_1C_2+2\gamma_1C_2^2+2\delta_1C_1+2\delta_3C_2)\bar{\eta}\frac{\partial\bar{\eta}}{\partial\bar{x}}$$

$$+(2\alpha_1C_1^2+2\beta_1C_1C_2+2\gamma_1C_2^2)d\frac{\partial\bar{\eta}}{\partial\bar{x}}=0. \tag{29}$$

Put

$$Vl(mC_1+MC_2)=A, \tag{30}$$

$$(2\alpha_1C_1^2+2\beta_1C_1C_2+2\gamma_1C_2^2)d=B, \tag{31}$$

$$2\alpha_1C_1^2+2\beta_1C_1C_2+2\gamma_1C_2^2+2\delta_1C_1+2\delta_3C_2=C, \tag{32}$$

$$\left(\frac{\hbar^2C_1}{2m}+\frac{\hbar^2C_2}{2M}\right)\frac{1}{4lh_0}=D. \tag{33}$$

From (29) we have

$$A\left(\frac{\partial\bar{\eta}}{\partial t}+\bar{\eta}\frac{\partial\bar{\eta}}{\partial t}\right)+D\frac{\partial^3\bar{\eta}}{\partial\bar{x}^3}+C\bar{\eta}\frac{\partial\bar{\eta}}{\partial\bar{x}}-B\frac{\partial\bar{\eta}}{\partial\bar{x}}=0. \tag{34}$$

It is clear from equation (34) that the two fluids act as a single mixture producing a common third sound. Let us put

$$\bar{\eta}=f(\bar{x}-ct)=f(\xi). \tag{35}$$

From (34) we have

$$Df'''-(Ac+B)f'+(C-Ac)ff'=0. \tag{36}$$

Integrating (36) we have

$$f=\frac{3(Ac+B)}{C-Ac}\operatorname{sech}^2\frac{1}{6}\frac{[3(Ac+B)]^{1/2}}{D}(\bar{x}-ct). \tag{37}$$

This defines a soliton moving with velocity c, amplitude $3(Ac+B)/(C-Ac)$ and width $6\{D/[3(Ac+B)]\}^{1/2}$. Note that the amplitude is a function of velocity c and the soliton is a crest if $c>C/A$ and a trough if $c<C/A$. A soliton with $c=C/A$ is unstable.

References

Biswas A C and Warke C S 1986 *Pramana–J. Phys.* **26** 373

CC-0. In Public Domain. Gurukul Kangri Collection, Haridwar

Digitized by Arya Samaj Foundation Chennai and eGangotri

Pramāṇa – J. Phys. Vol. 28, No. 4, April 1987, pp. 367–378. © Printed in India.

Interpolation model for molecular reorientation in gases and liquids

S K DEB and A K SOOD†

Nuclear Physics Division, Bhabha Atomic Research Centre, Bombay 400 085, India
†Materials Science Laboratory, Indira Gandhi Centre for Atomic Research, Kalpakkam 603 102, India

MS received 29 November 1986

Abstract. The interpolation model for molecular reorientation in gases and liquids has been extended to the case for symmetric top molecules. It has been compared with experimental correlation functions for linear as well as prolate and oblate symmetric top molecules. The agreement is excellent for systems where the intermolecular torque is small. With increasing torque, there is discrepancy at short times whereas at intermediate and long times the decay is described quite well. However for liquids at low temperatures, the description of molecular reorientation within the framework of this model is unsatisfactory.

Keywords. Molecular rotations; infrared line shapes; Raman line shapes; generalized extended diffusion models; interpolation model.

PACS No. 61·20

1. Introduction

Reorientation dynamics of molecules in gases and liquids is being studied by a number of experimental techniques—the infrared and Raman spectroscopic techniques being the most widely used. The time-correlation function for molecular orientation vector as well as the angular velocity vector can be obtained from Fourier transform of vibration-rotation band profile in infrared and Raman spectra. The different experimental techniques and the different types of information obtained from these along with their advantages and disadvantages are reviewed in several articles (Gordon 1968; Steele 1976; Berne and Pecora 1976; McClung 1977; Vincent-Geisse 1980; Yarwood 1983 etc.). A complete understanding of the reorientation dynamics, however requires comparison of the experimental data with theoretical models. Of the several theoretical models for molecular reorientation in gases and liquids, the rotational diffusion model proposed by Debye (1928) has been the earliest and by far the simplest. This was subsequently generalized by Gordon (1966). Unlike Debye's model where the molecule reorients by infinitesimal angle, Gordon had introduced free rotation by finite angle between successive collisions. The Gordon's model, also known as the extended diffusion model (EDM) has two versions—the M and J diffusion models. The two models are indistinguishable at short times but the J diffusion model decays much faster than the M diffusion at long times. The EDM was extended to include molecules of different shapes and compared with various experimental data to obtain a clear understanding of the reorientation dynamics (McClung 1977). However, in spite of comparing a large number of experimental data, no broad consensus could be arrived

CC-0. In Public Domain. Gurukul Kangri Collection, Haridwar

Digitized by Arya Samaj Foundation Chennai and eGangotri

at regarding the applicability of either of these two versions of EDM. For example, the NMR data relating the reorientational and angular momentum correlation times for spherical molecules (Maryott *et al* 1971; Gillen *et al* 1972; Marsault *et al* 1973) and symmetric top molecules (McClung 1973; Bull 1973, 1975; DeZwaan *et al* 1974) seems to be in accord with the *J* diffusion model. However, the situation is not so encouraging for linear molecules (Krynicki and Powels 1972; Krynicki *et al* 1975)—in a few cases (Boden and Folland 1975; Schwartz and Wang 1974) the experimental data lie between the *J* and *M* diffusion limits. The experimental correlation function for a few spherical molecules seems to be well described by the *J* diffusion model (Sunder *et al* 1974; Marsault-Herail *et al* 1975; Campbell *et al* 1973) but in other cases the situation is quite ambiguous (Eagles and McClung 1973; Sunder and McClung 1973). For example, although the correlation function for neopentane has been claimed to lie between the *J* and *M* diffusion limits (Livingstone *et al* 1973) the experimental data is ambiguous. The situation is also similar for linear (Marsault *et al* 1975; Levi *et al* 1972; Perrot *et al* 1975) and symmetric top molecules (Marsault *et al* 1973; Arndt and McClung 1978; Bansal and Roy 1979; Perry *et al* 1981). In some cases the experimental correlation function seems to lie between the *J* and *M* diffusion models (Marsault *et al* 1975; Dreyfus *et al* 1982; Rothschild *et al* 1975).

An attempt to improve the situation was undertaken by Dattagupta and Sood (1979) who proposed an 'interpolation' scheme where one could calculate the correlation function intermediate between the *J* and *M* diffusion limits by varying an interpolation parameter. Thus the *M* and *J* diffusion models could be treated as limiting cases of this model. This was achieved by incorporating partial randomization of the magnitude of angular momentum in a collision as opposed to no or complete randomization in *M* and *J* diffusion limits respectively. They had dealt with linear molecules and compared with infrared and NMR data. However, a careful survey of the experimental data in the literature reveals that a large number of accurate data exist for symmetric top molecules of both prolate and oblate shape (Griffiths 1977; Vincent-Geisse 1980; Perry *et al* 1981; Bansal *et al* 1981; Deb *et al* 1986). This is particularly true for reorientation of molecules in liquids. Thus it is of considerable interest to extend this scheme to the case of symmetric top molecules and compare with a wide variety of available experimental data. We would like to emphasize here that the NMR data, which deals only with correlation time, do not constitute a critical test for a theoretical model. Also, NMR data is not always unambiguous because of uncertainty in several experimental parameters. Thus it is essential to compare with correlation function to determine the applicability of a particular model. Further, it is preferable to compare with Raman correlation function rather than with infrared data because the latter also contain a contribution from vibrational relaxation. The effect of vibrational relaxation on molecular reorientation, although can be neglected in gases, becomes quite important in liquids. However, it has been shown that (Gordon 1968) for linear and symmetric top molecules, the reorientational correlation function for tumbling motion of the molecular axis obtained from Raman band profile analysis does not contain the effect of vibrational relaxation. It is also necessary to ensure that the experimental data is free from 'collision-induced-scattering'. Keeping these in mind, we generalize the interpolation model for symmetric top molecules and examine its applicability by comparing with infrared and Raman correlation function of linear as well as symmetric top prolate and oblate molecules.

The plan of the paper is as follows. In § 2, we present the calculation of correlation

CC-0. In Public Domain. Gurukul Kangri Collection, Haridwar

Digitized by Arya Samaj Foundation Chennai and eGangotri

function for symmetric top molecule. We follow an approach similar to Dattagupta and Sood (1979), but the details are similar to that of EDM for symmetric top molecules by McClung (1977). The times (t), frequencies (ω) and angular momenta (J) are expressed in reduced units (r.u.) i.e. in units of $(I/k_BT)^{1/2}$, $(k_BT/I)^{1/2}$ and $(Ik_BT)^{1/2}$ respectively, where I is the moment of inertia perpendicular to the molecular axis, k_B the Boltzmann constant and T the absolute temperature. In § 3, we present comparison with experimental correlation function for OCS, CD_3H, propyne and CH_3I. The applicability and limitations of the model are discussed in § 4.

2. Mathematical approach

The fundamental mechanism for reorientation is the same as that of EDM where the molecule is assumed to rotate freely between successive collisions. The rotational motion of a freely rotating symmetric top molecule is described by McClung (1972). The set of Eulerian angles specifying the orientation of the symmetric top molecule with respect to a space fixed frame is denoted, for brevity, by Ω. The essential features of EDM have been retained by Dattagupta and Sood (1979) except that the change in angular momentum in a collision is represented by a collision operator which allows an interpolation between the M and J diffusion limits. The angular momentum is represented by an operator in an infinite-dimensional vector space spanned by the angular momentum. Thus the angular momentum operator ($\tilde{J}$) is a diagonal matrix whose elements are the possible values of the angular momenta.

Thus

$$\langle J|\tilde{J}|J_0\rangle = J_0\,\delta(J-J_0), \tag{1}$$

where $\delta(J-J_0)$ is the Dirac delta function.

The feature common to M and J diffusion, i.e. the complete randomization of the angular momentum direction is also retained in this scheme. Unlike in linear molecules where the angular momentum vector is normal to the molecular axis, the angular momentum has both polar and azimuthal angles for a symmetric top molecule. Therefore, both these angles are randomized in a collision. The azimuthal angle (α) is randomized to an isotropic distribution, whereas the polar angle (β) is randomized to the distribution (McClung 1977)

$$W(J,\beta) = \frac{J(\xi/2\pi)^{1/2}}{\mathrm{erf}[J(\xi/2)^{1/2}]}\exp(-\xi J^2x^2/2), \tag{2}$$

where $x=\cos\beta$ and $\mathrm{erf}(y)$ denote the error function. The change in the magnitude of angular momentum in a collision is represented by a collision operator $\tilde{T}$, whose elements $\langle J|\tilde{T}|J_0\rangle$ denote the probability that the angular momentum changes from J_0 to J in a collision.

Suppose at $t=0$, the orientation of the molecular frame with respect to the space fixed frame is denoted by Ω_0. The rotational motion of the molecule can be described by defining a diffusion trajectory of the angular momentum vectors $\mathbf{J}_0, \mathbf{J}_1, \mathbf{J}_2, \ldots, \mathbf{J}_{n-1}, \ldots$ of the molecule during successive diffusion steps and times $t_1, t_2, t_3, \ldots t_n, \ldots$ at which the first, second, third, ... nth diffusive steps terminate. Then following

CC-0. In Public Domain. Gurukul Kangri Collection, Haridwar

Digitized by Arya Samaj Foundation Chennai and eGangotri

McClung (1977), after n collisions, the transformation from the laboratory to the molecular frame is given by

$$D^{(l)}[\Omega(t)]_n = D^{(l)}[\Omega_0]\, D^{(l)}[\Delta\Omega(\mathbf{J}_0; t_1)]\, D^{(l)}[\Delta\Omega(\mathbf{J}_1; t_2 - t_1)] \ldots D^{(l)}[\Delta\Omega(\mathbf{J}_n; t - t_n)], \tag{3}$$

where $\Delta\Omega(\mathbf{J}_i; t_{i+1} - t_i)$ is the orientation by which the molecular frame rotates between the i-th and $(i+1)$th collision and $D^{(l)}$ represents the corresponding transformation matrix, which are nothing but rotation matrices representing transformation of a spherical tensor of rank l (Rose 1957). Here $l=1$ and $l=2$ correspond to infrared and Raman correlation functions respectively.

The correlation functions are calculated by evaluating the expression

$$\langle D^{(l)}[\Omega_0]\, D^{(l)*}[\Omega(t)] \rangle, \tag{4}$$

where $\langle\ \rangle$ represents ensemble average over all possible trajectories and involves averages over: (i) the number of collisions experienced by the molecule upto time t, (ii) the times at which the collisions occurred, (iii) the angular momentum in each diffusive step, and (iv) the initial molecular orientation.

As in EDM, the 'collisions' are idealized events, where the rotational motion of the molecule is instantaneously interrupted by torques which change the angular momentum state of the molecule. The collisions are completely uncorrelated and collision times follow a Poisson distribution with average time τ_J between the collisions. Then following Dattagupta and Sood (1979) and McClung (1977), the correlation function can be shown to be given by

$$C^{(l,k)}(t) = \int \mathrm{d}J \int \mathrm{d}J_0\, W(J_0) \sum_{n=1}^{\infty} \tau_J^{-n} \exp(-t/\tau_J) \int_0^t \mathrm{d}t_n \int_0^{t_n} \mathrm{d}t_{n-1} \ldots \int_0^{t_2} \mathrm{d}t_1 \int \mathrm{d}J_{n-1} \ldots \int \mathrm{d}J_1\, g(J; t - t_n) \langle J|\tilde{T}|J_{n-1}\rangle\, g(J_{n-1}; t_n - t_{n-1}) \ldots \ldots \langle J_2|\tilde{T}|J_1\rangle\, g(J_1; t_2 - t_1) \langle J_1|\tilde{T}|J_0\rangle\, g(J_0; t_1). \tag{5}$$

In the above J_0 and J are the magnitudes of angular momentum at the beginning and end of a particular collision sequence and $g(J_i; t_{i+1} - t_i)$ is given by (McClung 1977)

$$g(J_i; t_{i+1} - t_i) = \sum_{m=-l}^{l} \int W(J_i, \beta_i) \sin\beta_i |\mathrm{d}^{(l)}_{km}(\beta_i)|^2 \exp[-i(t_{i+1} - t_i) J_i (m + k\xi\cos\beta_i)]. \tag{6}$$

The probability distribution function for angular momentum magnitude is given by

$$W(J) = [(1+\xi)/\xi]^{1/2}\, J \exp(-J^2/2)\, \mathrm{erf}[J(\xi/2)^{1/2}]. \tag{7}$$

In (6), the integration over β_i represents averaging corresponding to the randomization of polar angle of angular momentum. The averaging with respect to azimuthal angle

CC-0. In Public Domain. Gurukul Kangri Collection, Haridwar

Digitized by Arya.Samaj Foundation Chennai and eGangotri

has already been performed. ξ is the asymmetry parameter defined by

$$\xi=(I/I_z-1), \tag{8}$$

where I_z is the moment of inertia around the molecular symmetry axis. $\xi>0$ for 'prolate' molecules and $\xi<0$ for 'oblate' molecules. The averaging with respect to β_i does not arise for linear molecules.

Then by taking Laplace transform it can be shown that

$$\tilde{\tilde{C}}^{(l,k)}(p)\equiv\int_0^\infty C^{(l,k)}(t)\exp(-pt)\mathrm{d}t$$

$$=\int\mathrm{d}J\int\mathrm{d}J_0\,W(J_0)\left\langle J\left|\frac{G_{\mathrm{FR}}^{(l)}(p+\lambda;\tilde{J})}{1-\lambda\tilde{T}G_{\mathrm{FR}}^{(l)}(p+\lambda;\tilde{J})}\right|J_0\right\rangle, \tag{9}$$

where

$$G_{\mathrm{FR}}^{(l)}(S;\tilde{J})=\sum_{m=-l}^{l}\int\mathrm{d}\beta\sin\beta|\mathrm{d}_{km}^{(l)}(\beta)|^2\,W(\tilde{J},\beta)\cdot$$

$$\frac{1}{S+i\tilde{J}(m+k\xi\cos\beta)}. \tag{10}$$

Here $\lambda=\tau_J^{-1}$ is a measure of the average collision frequency. The expression for Laplace transform of the correlation function is essentially similar to that given by Dattagupta and Sood (1979) except that the form of $G_{\mathrm{FR}}^{(l)}$ is much more complicated. The spectral density $I^{(l,k)}(\omega)$ is obtained from $\tilde{\tilde{C}}^{(l,k)}(p)$ by using the relation

$$I^{(l,k)}(\omega)=(1/\pi)\,\mathrm{Re}[\tilde{\tilde{C}}^{(l,k)}(i\omega)], \tag{11}$$

and the corresponding correlation function $C^{(l,k)}(t)$ is calculated from the Fourier transform of $I^{(l,k)}(\omega)$. Equation (9) is a general expression with $\tilde{T}$ as the transition operator and a particular model is obtained with a specific form of its matrix element. In the interpolation model it is given by

$$\langle J|\tilde{T}|J_0\rangle=\gamma W(J)+(1-\gamma)\,\delta(J-J_0), \tag{12}$$

where γ is the interpolation parameter. $\gamma=0$ and $\gamma=1$ correspond to the M and J diffusion limits respectively. We are interested in the correlation functions representing reorientation of the symmetry axis and the corresponding spectral densities can be obtained with $k=0$ from (9), (11) and (12) as

$$I_l(\omega)\equiv I^{(l,0)}(\omega)=\frac{1}{\pi}\mathrm{Re}\left[\frac{A}{1-\lambda\gamma A}\right], \tag{13}$$

where
$$A=\int\mathrm{d}J_0\,W(J_0)G_{\mathrm{FR}}^1(\lambda+i\omega;J_0), \tag{14}$$

and
$$G_{\mathrm{FR}}^1(S;J)=G_{\mathrm{FR}}^{(l)}(S;J)/[1-\lambda(1-\gamma)G_{\mathrm{FR}}^{(l)}(S;J)]. \tag{15}$$

CC-0. In Public Domain. Gurukul Kangri Collection, Haridwar

Digitized by Arya Samaj Foundation Chennai and eGangotri

The infrared and Raman correlation functions $C_1(t)$ and $C_2(t)$ are calculated by using the relation

$$C_l(t) = \int_0^\infty I_l(\omega) \cos \omega t \, d\omega. \tag{16}$$

The different expressions required to calculate $I_1(\omega)$, $I_2(\omega)$ and hence $C_1(t)$, $C_2(t)$ are given in the Appendix. The $C_1(t)$ and $C_2(t)$ as functions of λ and γ show similar behaviour as that for linear molecules (Dattagupta and Sood 1979). The principal difference is that the correlation time, defined as the first moment of the line shape, for a symmetric top molecule in the limit of M diffusion is finite.

3. Numerical results and comparison with experiments

The correlation functions have been obtained by first calculating the spectral densities and then taking their Fourier transform. The numerical calculations were verified by reproducing the M and J diffusion correlation functions of McClung (1977) for various values of ξ. They were also checked by reproducing correlation functions given by Dattagupta and Sood (1979) for linear molecules in the limit of large values of ξ. In the following we compare this model with a few experimental data to examine its applicability. We do not intend to compare with NMR data for the reasons stated earlier and confine to infrared and Raman correlation function for reorientation of symmetry axis of linear and symmetric top molecules only. We consider only those experimental data which are accurate and unambiguous.

3.1 *Linear molecule: Carbonyl sulphide (OCS)*

Dreyfus *et al* (1982) determined the infrared correlation function for OCS, N_2O and CO_2 mixed with rare gases in the density range 15–300 amagat. They compared their data with EDM and other models. At low densities, the M diffusion model agrees with the experimental data quite well, but it worsens at higher densities. In particular, the correlation function obtained from ν_1 mode of OCS mixed in Kr at 300 amagat lies between the J and M diffusion limits for $\lambda = 1$. Thus this is an ideal situation for examining the usefulness of the interpolation model and the fit to experimental data is shown in figure 1. The calculated correlation function for $\lambda = 1{\cdot}0$ and $\gamma = 0{\cdot}28$ fit the experimental points quite well. The agreement is excellent except at long times ($t > 3{\cdot}5$ r.u.) where the experimental $C_1(t)$ seems to decay faster. We have also shown the calculated curves for M and J diffusion and Fokker-Planck-Langevin (FPL) model and it shows that the agreement with the interpolation model is far better than with any of the models. Dreyfus *et al* do not show comparison with Steele memory function model (1981) at 300 amagat, but the curve for 272 amagat shows discrepancy after $t \approx 2$ r.u. and decays to zero beyond $t \approx 3$ r.u. However the agreement with interpolation model is better than that obtained by Dreyfus *et al* with either Fokker-Planck-Langevin or Steel memory function model. We should also mention that the contribution of vibrational relaxation in this case could be neglected because the

CC-0. In Public Domain. Gurukul Kangri Collection, Haridwar

Digitized by Arya Samaj Foundation Chennai and eGangotri

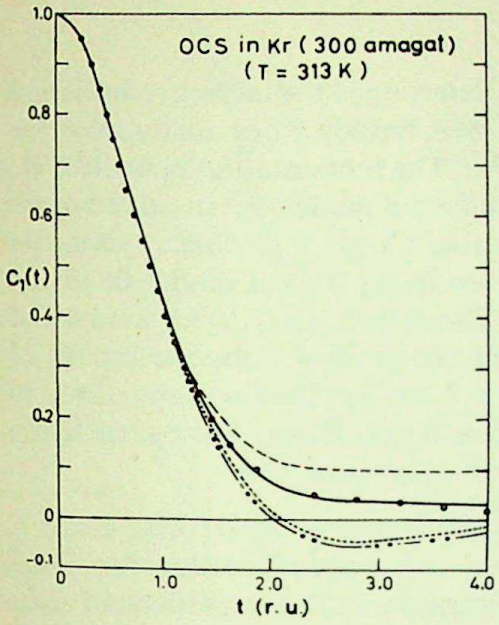

Figure 1. Experimental $C_1(t)$ for OCS in Kr (· · ·) (Dreyfus *et al* 1982) and comparison with interpolation model (——) for $\lambda = 1$ and $\gamma = 0{\cdot}28$. The M diffusion (– – –), J diffusion (–··–) and FPL (– – – – –) curves are shown for comparison.

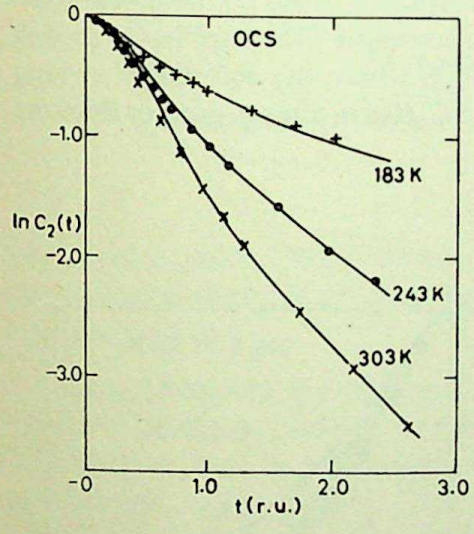

Figure 2. Raman correlation function for OCS at 183 K (+ + +), 243 K (· · ·) and 303 K (× × ×) (Hegemann and Jonas 1983) and interpolation model fit (———) for (i) $\lambda = 6{\cdot}7$, $\gamma = 0{\cdot}01$ at 183 K; (ii) $\lambda = 3{\cdot}2$, $\gamma = 0{\cdot}25$ at 243 K; (iii) $\lambda = 2{\cdot}0$, $\gamma = 0{\cdot}65$ at 303 K respectively.

isotropic Raman width has been found to be much smaller than the rotational width (Dreyfus *et al* 1982).

Hegemann and Jonas (1983) had obtained Raman correlation function for liquid OCS over a temperature range 183 K to 303 K. The contribution from the collision-induced scattering had been subtracted assuming the second moment criterion. Figure 2 shows comparison of the experimental $C_2(t)$ at 303 K, 243 K and 183 K with interpolation model. At short times ($t < 0{\cdot}8$ r.u.) the agreement is poor—the calculated $C_2(t)$ being always larger than the experiment. At long times, the experimental $C_2(t)$ at 303 K and 243 K are well reproduced for $\lambda = 2{\cdot}0$, $\gamma = 0{\cdot}65$ and $\lambda = 3{\cdot}2$, $\gamma = 0{\cdot}25$ respectively. But at 183 K, the agreement is poor even at long times. We note that, with decreasing temperature, λ increases and γ decreases such that the product $\lambda\gamma$ decreases. This agrees with the interpretation of γ by Dattagupta and Sood (1979) and Balakrishnan (1979) where $\lambda\gamma$ is an effective rate of randomization of angular momentum. The long time decay of the correlation function is governed by the angular momentum randomization and thus a larger value of $\lambda\gamma$ corresponds to faster decay.

CC-0. In Public Domain. Gurukul Kangri Collection, Haridwar

Digitized by Arya Samaj Foundation Chennai and eGangotri

3.2 *Symmetric top molecules*

3.2a *CD_3H in liquid Ar*: Marsault *et al* (1973) have determined the infrared correlation function for CH_3D and CD_3H molecules in some inert liquids. They assume that the contribution from vibrational relaxation is negligible. The reorientation in liquid CH_4 and CF_4 were reasonably well described by the J diffusion model, but in other liquids neither of the versions of EDM seemed to be applicable. CD_3H is an oblate symmetric top molecule with $\xi = -0{\cdot}2$ and figure 3 shows an interpolation model fit to the experimental $C_1(t)$ for CD_3H in liquid Ar at 84 K. The calculated $C_1(t)$ for $\lambda = 1{\cdot}4$ and $\gamma = 0{\cdot}15$ is in excellent agreement with the experiment. Marsault *et al* observe that the M diffusion curve for $\lambda = 1{\cdot}25$ agrees well only up to $t \approx 2$. r.u. but decays much slower at long times. This is evident from the M and J diffusion curves shown in the same figure for $\lambda = 1{\cdot}25$. Similar agreement can be obtained for other cases also.

3.2b *CH_3I in cyclohexane*: CH_3I is a prolate symmetric top molecule with $\xi = 19{\cdot}3$. Recently Deb *et al* (1986) have obtained Raman correlation function for CH_3I dissolved in cyclohexane at several molar concentrations. The experimental data satisfy the second moment criterion and has no contribution from collision-induced-scattering. Figure 4 shows comparison with interpolation model for pure liquid as well as in mixtures. The situation is similar to that for OCS where the agreement at long times is excellent whereas at short times the calculated $C_2(t)$ are always greater than the

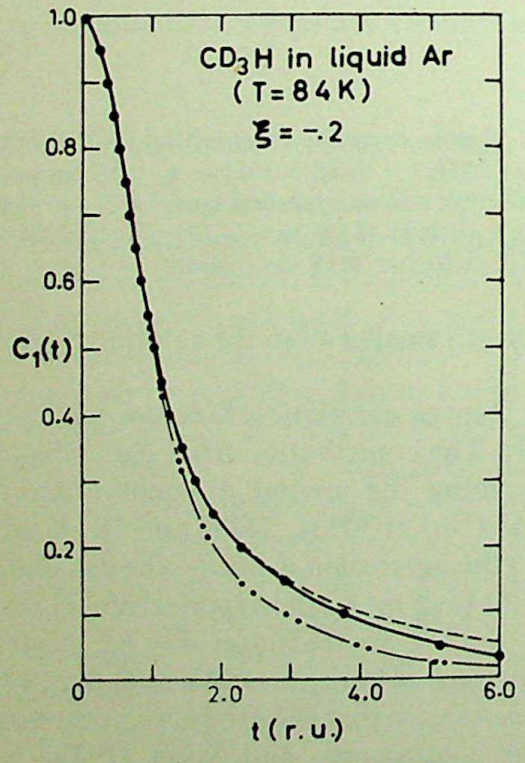

Figure 3. Comparison of calculated $C_1(t)$ (———) for $\lambda = 1{\cdot}4$ and $\gamma = 0{\cdot}15$ with the experimental data (· · ·) for CD_3H (Marsault *et al* 1973). The M diffusion (– – –) and J diffusion (–·–·–) curves are also shown.

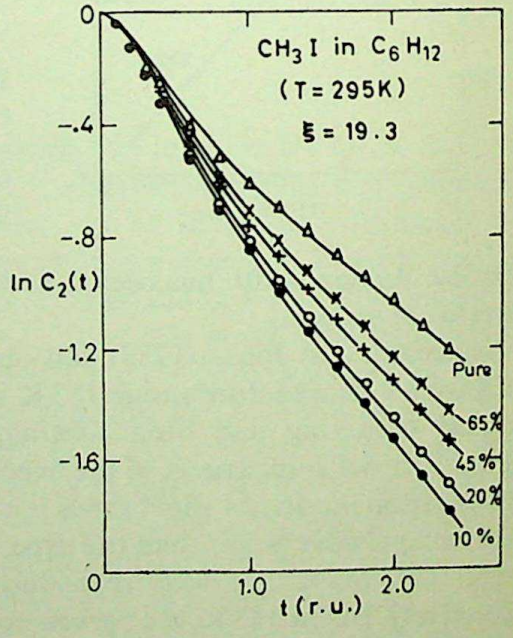

Figure 4. Comparison of experimental $C_2(t)$ (Deb *et al* 1986) and interpolation model fit (———) for CH_3I in C_6H_{12}. (i) Pure CH_3I, ($\Delta\Delta\Delta$) $\lambda = 7{\cdot}0$, $\gamma = 0{\cdot}03$; (ii) 65% mole fraction ($\times\times\times$) $\lambda = 5{\cdot}8$, $\gamma = 0{\cdot}07$ (iii) 45% mole fraction ($+++$) $\lambda = 5{\cdot}3$, $\gamma = 0{\cdot}09$ (iv) 20% mole fraction (o o o) $\lambda = 4{\cdot}7$, $\gamma = 0{\cdot}12$ (v) 10% mole fraction (· · ·) $\lambda = 4{\cdot}5$, $\gamma = 0{\cdot}15$.

CC-0. In Public Domain. Gurukul Kangri Collection, Haridwar

Digitized by Arya Samaj Foundation Chennai and eGangotri

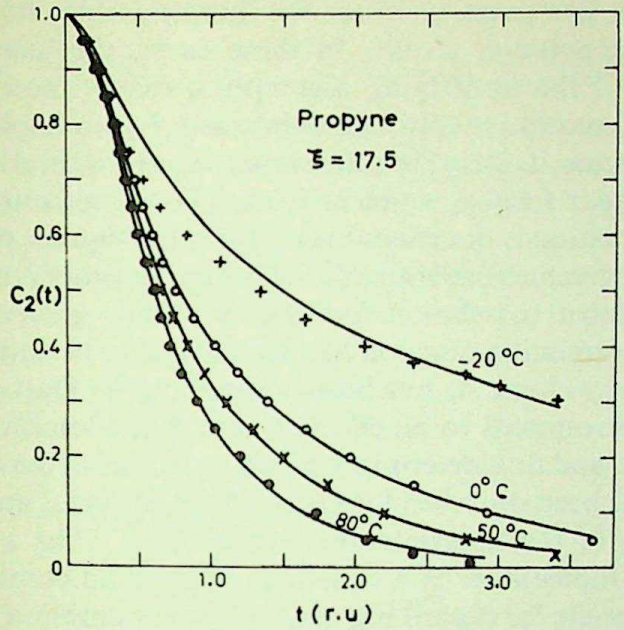

Figure 5. Experimental $C_2(t)$ for Propyne at 80°C (· · ·), 50°C (× × ×), 0°C (o o o) and −20°C (+ + +) (Perry *et al* 1981) and interpolation model fit (———) for (i) $\lambda = 2{\cdot}5$, $\gamma = 0{\cdot}8$ at 80°C; (ii) $\lambda = 3{\cdot}2$, $\gamma = 0{\cdot}4$ at 50°C (iii) $\lambda = 4{\cdot}2$, $\gamma = 0{\cdot}2$ at 0°C and (iv) $\lambda = 8{\cdot}5$, $\gamma = 0{\cdot}0$ (M-diffusion) at −20°C.

experimental value. With decreasing concentration of CH_3I, λ decreases and γ increases such that the product $\lambda\gamma$ increases. This fact is also in agreement with the interpretation of γ.

3.2c *Liquid propyne*: Propyne is also a prolate symmetric top molecule with $\xi = 17{\cdot}5$. Perry *et al* (1981) studied its reorientation dynamics in pure liquid as well as in mixture. They observe that in pure liquid, the J diffusion model agrees quite well with the experimental $C_2(t)$ at 80°C, but with decreasing temperature there is increasing discrepancy between J diffusion and experiment. Figure 5 shows comparison with interpolation model with data at 80°C, 50°C, 0°C and −20°C. At 80°C the interpolation model with $\lambda = 2{\cdot}5$ and $\gamma = 0{\cdot}8$ does not provide any agreement better than the J diffusion model of Perry *et al*. But at 50°C and 0°C the interpolation model agrees very well with the experimental $C_2(t)$. At −20°C, a satisfactory agreement with the interpolation model could not be obtained. This can be seen from the fact that the M diffusion $C_2(t)$ for $\lambda = 8{\cdot}5$ differs considerably from the experiment. An effort to obtain agreement at short times results in much faster decay at long times even at the M diffusion limit whereas a corresponding effort at long times results in slower decay at short and intermediate time. The variation of λ, γ and the product $\lambda\gamma$ at 80°C, 50°C and 0°C is similar to that for carbonyl sulphide.

4. Discussion and conclusions

We have generalized the interpolation model to the case of symmetric top molecules and compared with several experimental data. We observe that the data for systems

CC-0. In Public Domain. Gurukul Kangri Collection, Haridwar

Digitized by Arya Samaj Foundation Chennai and eGangotri

where either the density is low, like gases or where the intermolecular torque is low agrees very well with the interpolation model. In these cases, the intermolecular collisions are less frequent and the underlying assumption in the model that the molecule rotates freely between successive collisions is justified. For example, CD_3H is although a symmetric top molecule, its shape is quite close to spherical and in mixtures of inert liquid, the intermolecular torque, which is related to the anisotropy of the potential is quite small. The situation is not encouraging for other liquids, particularly at low temperature. Here, the agreement at long and intermediate times is quite good, but at short times, the calculated correlation function is always greater than the experiment. The decay of the correlation function has been found to be determined by the product $\lambda\gamma$ rather than λ or γ alone. As has been pointed out by Dattagupta and Sood (1979) the product $\lambda\gamma$ corresponds to an effective rate of randomization of the angular momentum magnitude, and thus determines the rate of decay of the correlation function at long times. This has been observed for OCS, CH_3I in C_6H_{12} and propyne and agrees with the meaning of the interpolation parameter γ. Thus a fractional randomization of the angular momentum in a collision, rather than complete or no randomization is more appropriate for describing molecular reorientation within the framework of EDM.

The discrepancy at short times can be understood from the power series expansion of correlation function ($C_l(t)$) as $t\rightarrow 0$. Lindenberg and Cukier (1975) have shown that, in a collision interrupted free rotation model the $C_l(t)$ has a positive contribution from the t^3 term which is proportional to the parameter λ. The experimental $C_l(t)$, obtained from a symmetric band profile does not have t^3 contribution. This results in theoretical $C_l(t)$ being larger than the experiment at short time. We have seen that at low temperature and for hindered systems (where the intermolecular torque is large) the value of λ is large and hence there is larger deviation at short times in such cases.

Thus in conclusion the interpolation model works very well for situations where the density is low and the intermolecular torque is small. However, in dense systems like liquids with large torque, the success of the model is limited, in the sense that the intermediate and long time behaviour of $C_l(t)$ is explained much better than either the M or J diffusion limits, whereas at short times there is considerable discrepancy. On the other hand for liquids at low temperature, the reorientation of molecules cannot be described within the framework of this model.

Appendix

Here we give the expressions used to calculate the infrared and Raman line shapes and hence the correlation functions $C_1(t)$ and $C_2(t)$. The line shapes are given by

$$I_l(\omega)=\frac{1}{\pi}\left[\frac{A_1(1-\gamma\lambda A_1)-\gamma\lambda A_2^2}{(1-\gamma\lambda A_1)^2+\gamma^2\lambda^2 A_2^2}\right],$$

where

$$A_1=\int \mathrm{d}J_0\, W(J_0)\, G^{(1)},$$

$$A_2=\int \mathrm{d}J_0\, W(J_0)\, G^{(2)}.$$

CC-0. In Public Domain. Gurukul Kangri Collection, Haridwar

Digitized by Arya Samaj Foundation Chennai and eGangotri

The $G^{(1)}$ and $G^{(2)}$ are given by

$$G^{(1)}=[\{1-\lambda(1-\gamma)G_1\}G_1-G_2^2\lambda(1-\gamma)]/Z,$$

$$G^{(2)}=[G_2\{1-\lambda(1-\gamma)G_1\}+G_1G_2\lambda(1-\gamma)]/Z,$$

where

$$Z=\{1-\lambda(1-\gamma)G_1\}^2+\lambda^2(1-\gamma)^2G_2^2.$$

The expressions for G_1 and G_2 are different for infrared and Raman cases and are given below.

(a) *Infrared*

$$G_1=\frac{J\lambda(\xi/2\pi)^{1/2}}{\mathrm{erf}[J\xi/2)^{1/2}]}\left[\frac{2I_0}{\lambda^2+\omega^2}+I_1\left\{\frac{1}{\lambda^2+(\omega-J)^2}+\frac{1}{\lambda^2+(\omega+J)^2}\right\}\right],$$

$$G_2=-\frac{J(\xi/2\pi)^{1/2}}{\mathrm{erf}[J(\xi/2)^{1/2}]}\left[\frac{2I_0\omega}{\lambda^2+\omega^2}+I_1\left\{\frac{\omega-J}{\lambda^2+(\omega-J)^2}+\frac{\omega+J}{\lambda^2+(\omega+J)^2}\right\}\right],$$

where

$$I_0=\int_0^1 x^2\exp(-\xi J^2x^2/2)\,\mathrm{d}x,$$

$$I_1=\int_0^1(1-x^2)\exp(-\xi J^2x^2/2)\mathrm{d}x,$$

(b) *Raman*

$$G_1=\frac{\lambda J(\xi/2\pi)^{1/2}}{\mathrm{erf}[J(\xi/2)^{1/2}]}\left[\frac{1}{2}\frac{I_0}{\lambda^2+\omega^2}+3I_1\left\{\frac{1}{\lambda^2+(\omega-J)^2}+\frac{1}{\lambda^2+(\omega+J)^2}\right\}\right.$$

$$\left.+\frac{3}{4}I_2\left\{\frac{1}{\lambda^2+(\omega-2J)^2}+\frac{1}{\lambda^2+(\omega+2J)^2}\right\}\right],$$

$$G_2=-\frac{J(\xi/2\pi)^{1/2}}{\mathrm{erf}[J(\xi/2)^{1/2}]}\left[\frac{1}{2}\frac{I_0\omega}{\lambda^2+\omega^2}+3I_1\left\{\frac{\omega-J}{\lambda^2+(\omega-J)^2}+\frac{\omega+J}{\lambda^2+(\omega+J)^2}\right\}\right.$$

$$\left.+\frac{3}{4}I_2\left\{\frac{\omega-2J}{\lambda^2+(\omega-2J)^2}+\frac{\omega+2J}{\lambda^2+(\omega+2J)^2}\right\}\right],$$

where

$$I_0=\int_0^1\mathrm{d}x(3x^2-1)^2\exp(-\xi J^2x^2/2),$$

$$I_1=\int_0^1\mathrm{d}x\,x^2(1-x^2)\exp(-\xi J^2x^2/2),$$

$$I_2=\int_0^1\mathrm{d}x(1-x^2)^2\exp(-\xi J^2x^2/2).$$

CC-0. In Public Domain. Gurukul Kangri Collection, Haridwar

Digitized by Arya Samaj Foundation Chennai and eGangotri

Acknowledgements

One of the authors (SKD) is grateful to Drs A P Roy, M L Bansal and B A Dasannacharya for valuable discussions during the course of this work.

References

Arndt R and McClung R E D 1978 *J. Chem. Phys.* **69** 4280
Balakrishnan V 1979 *Pramana–J. Phys* **13** 337
Bansal M L and Roy A P 1979 *Mol. Phys.* **38** 1830
Bansal M L, Deb S K and Roy A P 1981 *Chem. Phys. Lett.* **83** 83
Berne B J and Pecora R 1976 *Dynamic light scattering* (New York: John Wiley)
Boden N and Folland R 1975 *Chem. Phys. Lett.* **32** 127
Bull T E 1973 *J. Chem. Phys.* **59** 6173
Bull T E 1975 *J. Chem. Phys.* **62** 222
Campbell J H, Seymur S J and Jonas J 1973 *J. Chem. Phys.* **59** 4151
Dattagupta S and Sood A K 1979 *Pramana–J. Phys.* **13** 423
Deb S K, Bansal M L and Roy A P 1986 *Chem. Phys.* **110** 391
Debye P 1928 *Polar molecules* (New York: Dover)
DeZwaan J, Finney R J and Jonas J 1974 *J. Chem. Phys.* **60** 3223
Dreyfus C, Berreby L and Nguyen-Tan T 1982 *J. Chem. Phys.* **76** 755
Eagles T E and McClung R E D 1973 *J. Chem. Phys.* **59** 435
Gillen K T, Noggle J H and Leipert T K 1972 *Chem. Phys. Lett.* **17** 505
Gordon R G 1966 *J. Chem. Phys.* **44** 1830
Gordon R G 1968 *Adv. Mag. Reson.* **3** 1
Griffiths J E 1977 in *Vibration spectra and structure* (ed) J Durig (Amsterdam: Elsevier) Vol. 6, p. 273
Hegemann B and Jonas J 1983 *J. Chem. Phys.* **79** 4683
Krynicki K and Powels J G 1972 *J. Magn. Reson.* **6** 539
Krynicki K, Rakhamaa E J and Powels J G 1975 *Mol. Phys.* **29** 539
Levi G, Chalaye M, Marsault-Herail F and Marsault J P 1972 *Mol. Phys.* **27** 1217
Lindenberg K and Cukier R I 1975 *J. Chem. Phys.* **62** 3271
Livingstone R C, Rothschild W G and Rush J J 1973 *J. Chem. Phys.* **59** 2498
Marsault J P, Marsault-Herail F and Levi G 1973 *Mol. Phys.* **26** 997
Marsault J P, Marsault-Herail F and Levi G 1975 *J. Chem. Phys.* **62** 893
Marsault-Herail F, Marsault J P, Michoud G and Levi G 1975 *Chem. Phys. Lett.* **31** 335
Marryott A A, Farrar T C and Malmberg M S 1971 *J. Chem. Phys.* **54** 64
McClung R E D 1972 *J. Chem. Phys.* **57** 5478
McClung R E D 1973 *Chem. Phys. Lett.* **19** 304
McClung R E D 1977 *Adv. Mol. Relax. and Int. Proces.* **10** 83
Perrot M, Devaure J and Lascombe J 1975 *Mol. Phys.* **30** 97
Perry S, Zerda T W and Jonas J 1981 *J. Chem. Phys.* **75** 4214
Rose M E 1957 *Elementary theory of angular momentum* (New York: Wiley)
Rothschild W G, Rosaco G J and Livingstone R C 1975 *J. Chem. Phys.* **62** 1253
Schwartz M and Wang C H 1974 *Chem Phys. Lett.* **25** 26
Steele W A 1976 *Adv. Chem. Phys.* **34** 1
Steele W A 1981 *Mol. Phys.* **43** 141
Sunder S and McClung R E D 1973 *Chem. Phys.* **2** 472
Sunder S, Hallin K E and McClung R E D 1974 *J. Chem. Phys.* **61** 2920
Vincent-Geisse J 1980 in *Vibrational spectroscopy of molecular liquids and solids* (eds) S Bratos and R M Pick (New York: Plenum Press) p. 117
Yarwood J 1983 in *Molecular liquids—Dynamics and interactions* (eds) A J Bernes, W J Orville-Thomas and J Yarwood (Holland: D. Reidel Publishing) p. 357

CC-0. In Public Domain. Gurukul Kangri Collection, Haridwar

Digitized by Arya Samaj Foundation Chennai and eGangotri

Pramāṇa – J. Phys., Vol. 28, No. 4, April 1987, pp. 379–386. © Printed in India.

Production of tachyons and antiparticles in extended manifolds of general relativity

A P TROFIMENKO and V S GURIN

Astronomical Section, Minsk Department of Astronomical-Geodesical Society of USSR, Abonent Box No. 7, Minsk-12, 220012, USSR

MS received 20 June 1986

Abstract. The extended space-time manifold in a uniformly accelerating reference frame is considered both for positive and negative accelerations. An analogy between the light barrier and a black hole event horizon in the theory of relativity is drawn. It is shown that bradyon-tachyon-antibradyon transformations are possible in the proper reference frame by a constant acceleration, i.e. for the light barrier penetration.

Keywords. Tachyon; antiparticle; accelerating motion; black hole.

PACS Nos 04·20; 03·30

1. Introduction

In most studies on special and general relativity (GR) there exist similar peculiarities, a light barrier and an event horizon, the occurrence of which is associated with the principle of short-range interaction which is common for both the theories, i.e. the finite fundamental speed of propagation of interaction. The expressions connecting the proper with the coordinate time and distance are the following for uniform motion and the Schwarzschild gravitational field, respectively (Misner *et al* 1973):

$$t = t_0(1 - V^2/c^2)^{-1/2}, \quad l = l_0(1 - V^2/C^2)^{1/2}, \tag{1}$$

$$t = t_0(1 - 2GM/rc^2)^{1/2}, \quad l = l_0(1 - 2GM/rc^2)^{-1/2}, \tag{2}$$

where t_0 and l_0 are the proper time and the proper distance. The first pair of the equations for $V = c$ and the second pair for $r = r_g = 2GM/c^2$ (G is the gravitational constant and c is the light speed) become singular. For $V > c$ and $r < r_g$ all the left-hand values become imaginary. If we pass over to the non-relativistic limit, $c \to \infty$, then the singularities will disappear together with the division of the space-time into subluminal and superluminal regions as well as into regions over the horizon and under it. Thus, non-Euclidean topology of space-time (pseudo-singular surfaces, the higher dimensionality, etc) in relativity is conditioned by the finiteness of the fundamental speed (Trofimenko 1984).

Superluminal objects are obtained in extended (special) relativity through the generalization of the Lorentz transformations (Recami and Mignani 1974; Pavšič and Recami 1977; Recami and Rodrigues 1982) forming the generalized Lorentz group

CC-0. In Public Domain. Gurukul Kangri Collection, Haridwar

Digitized by Arya Samaj Foundation Chennai and eGangotri

(Recami and Mignani 1974)

$$G = \{+\Lambda_<\} \cup \{-\Lambda_<\} \cup \{+i\Lambda_>\} \cup \{-i\Lambda_>\}. \tag{3}$$

Here the sets $\{\pm\Lambda_<\}$ are proper orthochronous and nonorthochronous transformations and $\{\pm i\Lambda_>\}$ are superluminal ones. The above studies extend the usual Lorentz group by including the CPT-inverse and the operation of the replacement of V by the dual V^{-1} with instantaneous multiplication by $i = (-1)^{1/2}$.

The above four sets of transformations make the transitions between an original frame and a frame moving with respect to it with the arbitrary velocity ($\lesseqgtr c$). Through two consequent superluminal transformations, one can come to inverted frames corresponding to the antiobjects. Thus, extended relativity divides all the variety of objects into four separate classes: bradyons, tachyons, antibradyons and antitachyons. In the superluminal reference frame tachyons are bradyons (the duality principle) and with respect to bradyons, which are in the superluminal reference frame, antiparticles will be tachyons, i.e. double orthochronous transformations lead to inversion. Thus in order to become an antiparticle a bradyon has to become a tachyon: antiparticles are twice tachyonic objects (Trofimenko 1984).

In this paper we consider the extended manifold construction procedure in the reference frame of a uniformly accelerating observer. The possibility of transition through motion in the proper reference frame with intersection of pseudosingularities from bradyons to tachyons and to antiobjects is shown. An object passing beyond the event horizon in the proper reference frame can pass to a superluminal region, i.e. it can become a tachyonic object, with another superluminal transition, namely transition beyond the second event horizon when it becomes an antiobject. Such transitions are possible also in the Kerr extended manifold.

2. Extended manifold of a uniformly accelerating observer

Let us consider the geometry of the reference frame for an observer moving with a constant acceleration $A(>0)$ or deceleration $A(<0)$ (Kinnersley and Walker 1970; Gibbons and Perry 1980):

$$\begin{aligned} ds^2 = (1 + Ar\cos\theta)^{-2}[&(1 - A^2r^2)dt^2 - (1 - A^2r^2)^{-1}dr^2 \\ &- r^2(d\theta^2 + \sin^2\theta\, d\varphi^2)], \end{aligned} \tag{4}$$

where r is the distance from the observer, the origin of the coordinate system which is associated with the accelerating object. We use here the geometrized units where $c = G = 1$.

We consider here only the conformal structure of this spacetime, which is sufficient for the present work. This metric is very similar to the well-known de Sitter metric with constant curvature (see Tolman 1964). It takes the de Sitter form in the equatorial plane $\theta = \pi/2$ and in the renotation of the constant, $A^2 = \Lambda/3$, where Λ is the cosmological constant. In such a spacetime manifold (STM) the surfaces $r = \pm A^{-1}$ are the horizons. The de Sitter metric extension beyond the horizon was performed by Graves and Brill (1960), Geyer (1980) and Gautreau (1983). We shall apply this analysis to the metric of a uniformly accelerating observer and demonstrate the possibility of motion across the horizon surfaces $r = \pm A^{-1}$.

CC-0. In Public Domain. Gurukul Kangri Collection, Haridwar

Digitized by Arya Samaj Foundation Chennai and eGangotri

In order to remove the pseudosingularities at horizons in the metric (4) we adopt the new coordinates (Graves and Brill 1960)

$$u = 2C\exp(\gamma r^*)\cosh(\gamma t), \quad v = 2C\exp(\gamma r^*)\sinh(\gamma t) \tag{5}$$

with the ranges $-\infty < u < +\infty$, $-\infty < v < +\infty$, where C and γ are constants; then the metric gets the form

$$ds^2 = (1 + Ar\cos\theta)^{-2}[f^2(u, v)(dv^2 - du^2) - r^2(d\theta^2 + \sin^2\theta d\varphi^2)]. \tag{6}$$

Here we define

$$f^2(u, v) = \frac{1}{4}C^{-2}\gamma^{-2}(1 - A^2r^2)\exp(-2\gamma r^*), \tag{7}$$

and

$$r^* = \int(1 - A^2r^2)dr = \frac{1}{2}\log[(1 + Ar)/(1 - Ar)]. \tag{8}$$

We can easily obtain

$$f^2(u, v) = \frac{1}{4}C^{-2}\gamma^{-2}(1 + Ar)^{1-\gamma}(1 - Ar)^{1+\gamma}. \tag{9}$$

The metric of a uniformly accelerating observer (4) will not be singular at the horizons $r = \pm A^{-1}$ if the parameters are constrained within certain conditions. We choose $\gamma = \pm 1$ for $A \lessgtr 0$, respectively, and C is an arbitrary constant. Then

$$\begin{aligned} f^2 &= (1 + Ar)^2/4C^2 \quad \text{for} \quad A > 0 \ (\cos\theta > 0), \\ f^2 &= (1 - Ar)^2/4C^2 \quad \text{for} \quad A < 0 \ (\cos\theta < 0). \end{aligned} \tag{10}$$

Therefore, the new non-singular space-time coordinates are connected with (t, r)-ones by the following formulas:

$$\begin{aligned} u &= C[(1 \mp Ar)/(1 \pm Ar)]^{1/2}\cosh(\mp At) \quad \text{for} \quad A \gtrless 0, \\ v &= C[(1 \mp Ar)/(1 \pm Ar)]^{1/2}\sinh(\mp At) \quad \text{for} \quad A \gtrless 0. \end{aligned} \tag{11}$$

The inverse transformations are

$$t = \mp(1/A)\cosh^{-1}(u/v), \tag{12}$$

$$r = \pm(1/A)(C^2 - u^2 + v^2)(C^2 + u^2 - v^2)^{-1}. \tag{13}$$

With the help of the set of correlations the STM are represented as the Kruskal-like diagram in the (u, v)-coordinates. For both the $A > 0$ (acceleration) and $A < 0$ (deceleration) cases these space-times are drawn as the same diagrams (figure 1).

The compact representation of the conformal space-time structure can be done with the help of Penrose-like diagrams by transforming (u, v)-coordinates to (p, q)-ones according to the formulas

$$u = \tan p, \quad v = \tan q, \tag{14}$$

with the ranges $-\pi/2 \leqslant q \leqslant +\pi/2$ and $-\pi/2 \leqslant p \leqslant +\pi/2$ (Misner *et al* 1973). In figure 2 two cases of STM's under consideration are shown separately.

CC-0. In Public Domain. Gurukul Kangri Collection, Haridwar

Digitized by Arya Samaj Foundation Chennai and eGangotri

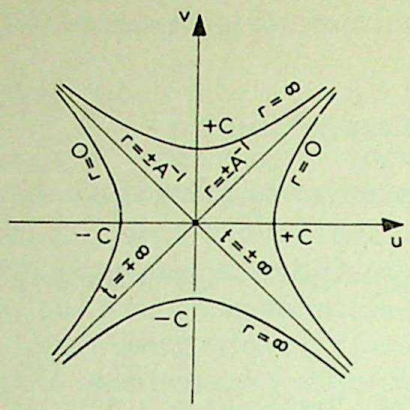

Figure 1. The Kruskal-like diagram for the extended STM of a uniformly accelerating reference frame.

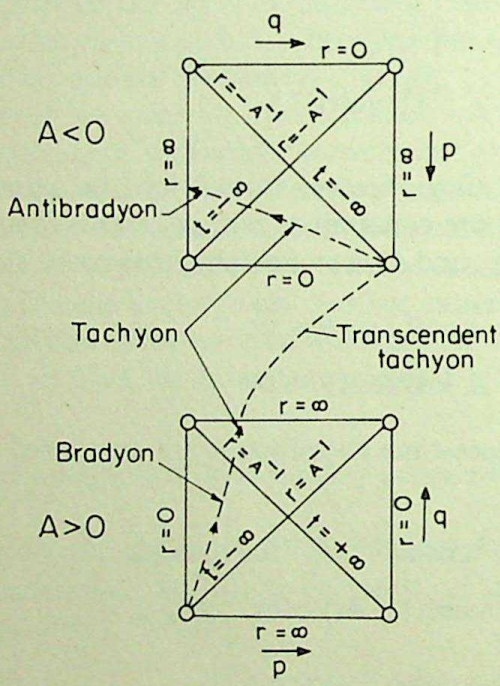

Figure 2. The representation of the extended STM's of uniformly accelerating and decelerating reference frames by means of Penrose conformal diagram. This is obtained from figure 1 through compact conformal transformations. The dashed line shows motion with transitions: bradyon → tachyon → antibradyon in the limited case via a transcendent tachyon.

One can see four regions on the diagram of the uniformly accelerating or decelerating STM which are divided by horizons. They are bounded by the origin $r = 0$ and the spatial infinity $r = \infty$, which are not singularities but emerge as physical boundaries of the space-time. Some similiarities can be seen between this representation of the uniformly accelerating STM and the analogous one for the Schwarzschild STM (see, for example, Misner *et al* 1973). The asymptotically flat Schwarzschild region corresponds to $r = 0$ here, the Schwarzschild singularity at $r = 0$ does to $r = \infty$ in our case and the Schwarzschild horizon at $r = 2M$ shows analogous properties with $r = A^{-1}$ surface.

CC-0. In Public Domain. Gurukul Kangri Collection, Haridwar

Digitized by Arya Samaj Foundation Chennai and eGangotri

3. Geodesic motion

Let us consider now the geodesic equations in the uniformly accelerating geometry (4) when $\theta = \pi/2$:

$$dr/d\tau = k(E^2 - 1 + r^2A^2 - L^2r^{-2} + L^2A^2)^{1/2}, \tag{15}$$

$$d\varphi/d\tau = Lr^{-2}, \tag{16}$$

$$dt/d\tau = E(1 - r^2A^2)^{-1}, \tag{17}$$

where τ is the proper time, E and L are the energy and the angular momentum of a moving particle per unit mass, respectively and $k = \pm 1$ depending on whether r increases or decreases in time. The geodesics behave differently depending on the value of $E^2 + L^2A^2$. In the case of $E^2 + L^2A^2 < 1$ there is the turn point at r_i defined by the equation $E^2 + L^2A^2 = r_i^2A^2 - L^2r_i^{-2}$. On achieving this point the geodesic set off to infinity of the space, and the speed of the particle increases continuously with respect to some point $r = \text{const}$. In the case of $E^2 + L^2A^2 > 1$ the particle on the geodesic is captured at $r = 0$. The case of $E^2 + L^2A^2 = 1$ is transitional where the timelike geodesic is given by the equation $r = 0$.

The geodesic equations (15) and (16) do not reveal any peculiar features on the horizons $r = \pm A^{-1}$, and the singularity in (17) is associated with the presence of the coordinate time t. We investigate the proper and coordinate time behaviour in the given STM by integrating (15) and (17) together:

$$t - t_c = kE \int_{r_c}^{r} (E^2 - 1 + x^2A^2 - L^2x^{-2} + L^2A^2)^{1/2} (1 - A^2x^2)^{-1} dx. \tag{18}$$

Here x is some radial variable of the integration, t_c and r_c are the initial coordinates of motion. It can be seen from (18) that the infinite value of the t-coordinate corresponds to the approximation to $r = \pm A^{-1}$, i.e. the flowing of the coordinate time is infinitely delayed. The proper time for the uniformly accelerating observer does not have such peculiarities; it is calculated by integrating the equation (15):

$$\tau - \tau_c = k \int_{r_c}^{r} (E^2 - 1 + x^2A^2 - L^2x^2 + L^2A^2)^{1/2} dx, \tag{19}$$

where τ_c is an initial value of the proper time. It can be seen that (19) remains finite at $r = \pm A^{-1}$, besides the coordinate and the proper time behaviour in the STM under consideration is very much analogous to that of the Schwarzschild geometry. The last fact indicates again that the passage to the region $r > A^{-1}$ from $r < A^{-1}$, i.e. from the subluminal region to the superluminal one, corresponds to the passage from the region over an event horizon to the one under it (Goldoni 1975, 1978; de Sabbata *et al* 1977; Narlikar and Dhurandhar 1978). Moreover, it can be concluded on the basis of these and other studies (Srivastava 1983; Gurin 1984, 1985; Gurin and Trofimenko 1985), that every horizon divides space-time into subluminal and superluminal regions forming an STM with non-trivial topology. In other words, taking into account a many-dimensional interpretation of superluminal phenomena and phenomena under black hole event horizon (Trofimenko 1986; Gurin 1984; Gurin and Trofimenko 1985;

CC-0. In Public Domain. Gurukul Kangri Collection, Haridwar

Digitized by Arya Samaj Foundation Chennai and eGangotri

Srivastava 1983; Chandola and Rajput 1984, 1985) the horizons and the light barrier divide ranges of real and imaginary coordinates.

Thus, in the proper reference frame the geometry covers both the regions $r < +A^{-1}$ or $r < -A^{-1}$ and $r > +A^{-1}$ or $r > -A^{-1}$.

Let us consider the qualitative picture of the accelerating motion. When an object approximates to the horizon moving with a constant acceleration, it will gradually disappear becoming asymptotic to the $r = +A^{-1}$ surface as regards the observer being at rest at some point. Such a situation is similar to some object "disappearing" when it falls on a black hole. But in the reference frame of an observer at rest the object will never pass across the surface $r = +A^{-1}$. In the proper reference frame of an accelerating body this surface is not peculiar at all, and passing across it the object goes to the superluminal region (see figure 2), i.e. it becomes a tachyon.

As can be easily seen the last will also be true for a constant deceleration crossing the $r = -A^{-1}$ surface from the superluminal region to the subluminal one. In this case a tachyon will be transformed into a bradyon with respect to the original reference frame (see figure 2).

To consider the two consequent processes of acceleration and deceleration we must take the results of extended relativity (Recami and Mignani 1974) on double superluminal transformations which lead to the complete inverse, i.e. to transition from an object to an antiobject. Hence, having accelerated across the horizon $r = +A^{-1}$ an original bradyon turns into a tachyon which can be decelerated across the horizon $r = -A^{-1}$ and turned into an antibradyon. Naturally, to go from an acceleration to a deceleration an action of force is required. Thus uniformly accelerating and decelerating STM's make it possible to produce tachyons and antiparticles in principle. It must be emphasized that such a conclusion is valid for proper reference frames of the objects and for a rest frame above the transitions are unobservable.

4. Discussion

In the extended relativity theory by Recami and Mignani (1974) superluminal speeds of inertial motion are considered on equal footing with subluminal ones, but the value of the light speed remains limited for both tachyons and bradyons. In other words, the light barrier penetration is impossible, that is bradyons will always remain as bradyons and tachyons will always be as tachyons with respect to an inertial reference frame. This thesis is unquestionably true for inertial motion and in the absence of gravitational fields.

Antiobjects also appear in extended relativity on equal footing and a transition between objects and antiobjects is the discrete operation. In general, bradyons, tachyons, and antiobjects are represented as separate classes of physical objects.

The present conclusions show that it is possible to transform continuously from one class of objects to another and this is realized due to the non-inertial motion. However, the light barrier penetration is possible only in a properly uniform accelerating or decelerating reference frame without violating the principles of relativity as compared to the relativity-violating analogous conclusions (Everett 1976; Froning 1983). Note that our results might seem a little unexpected, although the possibility of moving infinitely along with an acceleration was mentioned not once (see, for example, the

CC-0. In Public Domain. Gurukul Kangri Collection, Haridwar

Digitized by Arya Samaj Foundation Chennai and eGangotri

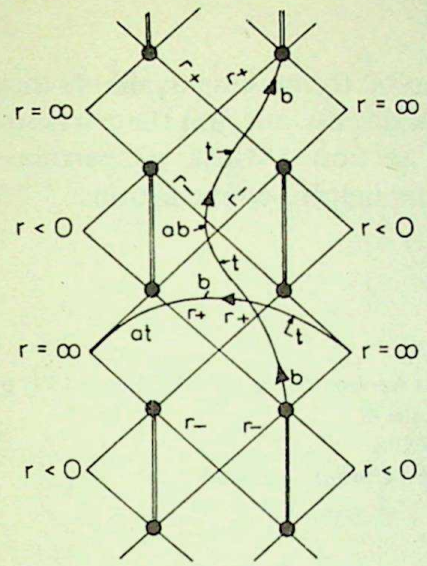

Figure 3. The Penrose diagram for the Kerr STM (Misner *et al* 1973) along the symmetry axis (the singularity is pictured conditionally). An analogous chain of transitions is shown: b—bradyon → t—tachyon → a–b—antibradyon → at—antitachyon → b—bradyon along a timelike geodesics (i.e. for an originate *b*); t—tachyon → b—bradyon → at—antitachyon along a spacelike geodesics (i.e. for an originate *t*).

book by Bondi 1964 and the paper by Morgan 1973) and they can be easily understood within the framework of GR. They are the consequence of the fundamental principle of equivalence and do not contradict the principles of special relativity because when analyzing the accelerating motion we leave its realm and pass over to GR, where, as we have shown, the light barrier penetration is quite possible.

Continuing the analogy between space-time structure with horizons for the uniformly accelerating and decelerating frames and gravitational fields we can propose the possibility of similar transformations from bradyons via tachyons to antibradyons in some black hole STM's, for example, Kerr STM (figure 3). This problem will be considered in greater detail by the authors in future. Note that the tachyon production from the simplest case of black hole, the Schwarzschild hole, was recently investigated by Srivastava (1983).

Let us perform some estimates concerning the possibility of light barrier penetration. Consider an object from the point of view of its own reference frame which travels with the constant acceleration A equalled, say, to the free fall acceleration in the earth field, g. Such an object can travel for an unlimited time without any restrictions (in its proper reference frame!). In such an accelerating frame local effects analogous to those occurring in the earth is gravitational field will be observed. In this case the distance to the accelerating horizon is $r = c^2 g^{-1} \approx 10^{18}$ cm $\approx$ a light year (Trofimenko 1984).

In conclusion, we would like to propose some astrophysical appearance of transitions between bradyons, tachyons and antiparticles considered here. Such processes can possibly develop as higher-energetic effects (gamma-bursts, quasars, superdense D-bodies by Ambartsumian, etc.). From the point of view of the STM theory they may be named by white hole explosions (the bibliography on this topic has been recently given by the present authors (Trofimenko and Gurin 1986).

CC-0. In Public Domain. Gurukul Kangri Collection, Haridwar

Digitized by Arya Samaj Foundation Chennai and eGangotri

Acknowledgements

The authors thank Profs E Recami and M Pavšič for making available their reprints, Profs G M Idlis and Y P Terletsky for useful discussions and the participants of the seminar organised by the Astronomical Section (Minsk Department) of the Astronomical-Geodesical Society of USSR for helpful conversations.

References

Bondi H 1964 *Relativity and common sense* (New York: Anchor Books Doubleday & Co.) p. 147
Chandola H C and Rajput B S 1984 *Lett. Nuovo Cimento* **40** 277
Chandola H C and Rajput B S 1985 *J. Math. Phys.* **26** 208
de Sabbata V, Pavšič M and Recami E 1977 *Lett. Nuovo Cimento* **19** 341
Everett A 1976 *Phys. Rev.* **D13** 785
Froning H D Jr 1983 *J. Br. Interplanet. Soc.* **36** 227
Gautreau R 1983 *Phys. Rev.* **D27** 764
Geyer K H 1980 *Astron. Nachricht.* **301** 135
Gibbons G W and Perry M J 1980 *Phys. Rev.* **D22** 319
Goldoni R 1975 *Acta Phys. Austr.* **41** 75, 133
Goldoni R 1978 *Lett. Nuovo Cimento* **21** 333
Graves J C and Brill D R 1960 *Phys. Rev.* **120** 1507
Gurin V S 1984 *Fizika* **16** 89
Gurin V S 1985 *Pramāna–J. Phys.* **24** 817
Gurin V S 1985 *Nuovo Cimento* **A88** 253
Gurin V S and Trofimenko A P 1985 *Fizika* **17** 101
Kinnersley W and Walker M 1970 *Phys. Rev.* **D2** 1359
Misner C W, Thorne K S and Wheeler J A 1973 *Gravitation* (San Francisco: Freeman) Ch. 30, 31
Morgan J W 1973 *Spaceflight* **32** 252
Narlikar J V and Dhurandhar S V 1978 *Lett. Nuovo Cimento* **23** 513
Pavšič M and Recami E 1977 *Lett. Nuovo Cimento* **19** 273
Recami E and Mignani R 1974 *Riv. Nuovo Cimento* **4** 209
Recami E and Rodrigues W A 1982 *Found. Phys.* **12** 709
Srivastava S K 1983 *J. Math. Phys.* **24** 1317
Tolman R S 1969 *Relativity, thermodynamics and cosmology* (Oxford: Clarendon Press) Sect. 144
Trofimenko A P 1984 Genesis and contemporary problems of oton astrophysics (in Russian) (deposited in INION of the Academy of Sciences of the USSR No. 16810).
Trofimenko A P 1986 *Fizika* (*Yugoslavia*) **18** 139
Trofimenko A P and Gurin V S 1986 *Gen. Relat. Grav.* **18** 53

CC-0. In Public Domain. Gurukul Kangri Collection, Haridwar

Digitized by Arya Samaj Foundation Chennai and eGangotri

Pramāṇa – J. Phys., Vol. 28, No. 4, April 1987, pp. 387–397. © Printed in India.

Modifications in high energy higher order Born approximation

K SUJA and H S DESAI

Physics Department, Faculty of Science, M.S. University of Baroda, Baroda 390 002, India

MS received 5 September 1986; revised 17 January 1987

Abstract. A systematic study is made to find out the differential scattering cross-section in the case of electron-atom collisions. The first and the second Born terms of $O(1/k_i)$ are calculated in the framework of Yates high energy higher order Born approximation. The second Born term of $O(1/k_i^2)$ is calculated using the second order Wallace term, the third term is calculated using the Glauber-eikonal series of Yates. The method is applied to the elastic scattering of electrons by atomic hydrogen in the energy range 100–400 eV and by helium for energies 200 eV and 400 eV. Comparison is made with other theoretical results and the experimental data.

Keywords. Elastic scattering; electron; hydrogen atom; helium atom.

PACS No. 34·80

1. Introduction

It is now an established fact that the first Born approximation holds true only in a limited class of low energy scattering problems. The second Born approximation, although a bit cumbersome, is done for atoms. However, an approximation to the second Born term on the lines of the eikonal approximation was carried out by Yates (1979). Basically this is a simple approximation and easier to compute. But it has some serious drawbacks: (i) it is easily seen that the second high energy higher order Born (HHOB) approximation term is invariant under transformation $-e \rightarrow e^+$. (ii) The results overestimate at large angles. In order to improve the HHOB method we have attempted and improved the approximation on a line similar to the Wallace treatment of the eikonal approximation. In §2 we have developed the theory and applied it to the targets of hydrogen and helium. The results of the theory are discussed in §3.

2. Theory

The T matrix can be written as

$$T = \langle \psi_f | (V + VG_0 V) | \psi_i \rangle = T^1 + T^2, \tag{1}$$

where

$$T^1 = \langle \psi_f | V | \psi_i \rangle, \tag{2}$$

$$T^2 = \langle \psi_f | VG_0 V | \psi_i \rangle, \tag{3}$$

CC-0. In Public Domain. Gurukul Kangri Collection, Haridwar

Digitized by Arya Samaj Foundation Chennai and eGangotri

where V is the interaction potential and G_0 is the particle propagator and is given by

$$G_0 = \sum \int \frac{\mathrm{d}k |\psi_n\rangle \langle \psi_n|}{\frac{k_i^2}{2} - E_0 - \frac{k^2}{2} - E_n + iE}. \tag{4}$$

The wavefunctions are given by

$$|\psi_i\rangle = (2\pi)^{-3/2} \exp(i\mathbf{k}_i \cdot \mathbf{r}_0) \Phi_i(\mathbf{r}_j) \tag{5}$$

and

$$|\psi_f\rangle = (2\pi)^{-3/2} \exp(i\mathbf{k}_f \cdot \mathbf{r}_0) \Phi_f(\mathbf{r}_j). \tag{6}$$

$\mathbf{k}_i$ and $\mathbf{k}_f$ represent the incident and the scattered wave vectors respectively. Φ_i and Φ_f are the initial and final states for the target. The approximate T matrix is obtained by using g, the particle propagator in the eikonal approximation, in place of G_0. Let us define

$$T^{(0)} = \langle \phi_f^{(-)} | V | \psi_i \rangle = \langle \psi_f | V | \phi_i^{(+)} \rangle, \tag{7}$$

where $|\phi_i^{(+)}\rangle$ and $|\phi_f^{(-)}\rangle$ used here satisfy the Lippmann-Schwinger equation, with g in place of G_0. In the co-ordinate representation of these wave vectors we have

$$\begin{aligned} |\phi_i^{(+)}(\mathbf{r}_0, \mathbf{r}_j)\rangle = (2\pi)^{-3/2} \Bigg(& 1 - \frac{i}{2k_n} \sum_n \int_{-\infty}^{z} \exp(-i\beta_{in} z_0') \\ & \times V(x_0, y_0, z_0 - z_0', \mathbf{r}_1) \mathrm{d}z_0' |\Phi_n(\mathbf{r}_i)\rangle \\ & \times \langle \phi_n(\mathbf{r}_1) \rangle \exp(i\mathbf{k}_1 \cdot \mathbf{r}_0) \Bigg) |\Phi_i(\mathbf{r}_j)|, \end{aligned} \tag{8}$$

and

$$\begin{aligned} |\phi_f^{*(-)}(\mathbf{r}_0, \mathbf{r}_1)\rangle = (2\pi)^{-3/2} \exp(-i\mathbf{k}_f \cdot \mathbf{r}_0) \Bigg(& 1 - \frac{i}{2k_n} \sum \int_{z}^{\infty} \exp(-i\beta_{in} z_0') \\ & \times |\Phi_n(\mathbf{r}_j)\rangle \langle \phi_n(\mathbf{r}_j)| V(x_0, y_0, z_0 - z_0', \mathbf{r}_j) \mathrm{d}z_0' | \Bigg) \\ & \times |\Phi_f(\mathbf{r}_j)\rangle, \end{aligned} \tag{9}$$

where $\beta_{in} = \Delta E / k_i$; ΔE is the excitation energy. Substituting (8) in (7) we have

$$\begin{aligned} T^{(0)} = (2\pi)^{-3} \langle \Phi_f | \int \exp(i\mathbf{q} \cdot \mathbf{r}) V \Bigg[& 1 - \frac{i}{2k_n} \sum \int_{-\infty}^{\infty} \exp(-i\beta_{in} z_0') \\ & \times V(x_0, y_0, z_0 - z_0', \mathbf{r}_j) \mathrm{d}z_0 |\Phi_n(\mathbf{r}_j)\rangle \\ & \times \langle \Phi_n(\mathbf{r}_j) | H_0(z_0') \Bigg] \mathrm{d}V_0 |\Phi_i(\mathbf{r}_j)\rangle |, \end{aligned} \tag{10}$$

where $H_0(z_0')$ is the Heaviside function. Using the same notations as those of Yates (1979) we can write (10) as

$$T^{(0)} = T^{(B1)} + (T^{(B2)})_{\mathrm{HEA}}. \tag{11}$$

CC-0. In Public Domain. Gurukul Kangri Collection, Haridwar

Digitized by Arya Samaj Foundation Chennai and eGangotri

We can also write the T matrix as a perturbation series. Following the methods of Wallace (1973) we can write

$$T = T^{(0)} + T^{(1)} + T^{(2)} + \cdots, \tag{12}$$

where

$$T^{(1)} = -\lambda T^{(0)} + J^{(1)}, \tag{13}$$

and $\lambda = 1 - \cos\theta/2$. θ is the scattering angle of the projectile. $J^{(1)}$ is further defined as

$$J^{(1)} = \langle \Phi_f^{(-)} | V + N_\tau | \Phi_i^{(+)} \rangle. \tag{14}$$

The meaning of N_τ is the same as that of Wallace (1973). From (8) and (9)

$$\begin{aligned} J^{(1)} = (2\pi)^{-3} \langle \Phi_f | \int \exp(i\mathbf{k}_f \cdot \mathbf{r}_0) \Big(1 - \frac{i}{2k_n} \sum |\Phi_n\rangle \\ \times \langle \Phi_n | \int_z^\infty \exp(-i\beta_{in} z_0') V(x_0, y_0, z_0') \mathrm{d}z_0' \Big) \\ \times \exp(i\mathbf{k}_i \cdot \mathbf{r}_0) \Big(1 - \frac{i}{2k_n} \sum |\Phi_n\rangle \langle \Phi_n | \int_{-\infty}^z \exp(-i\beta_{in} z_0') \\ \times V(x_0, y_0, z_0') \mathrm{d}z_0' \Big) \mathrm{d}V_0 \\ \times \exp(-i\mathbf{k}_i' \cdot \mathbf{r}_0) \Big(1 + \frac{i}{2k_n} \sum |\Phi_n\rangle \\ \times \langle \Phi_n | \int_{-\infty}^z \exp(-i\beta_{in} z_0') V(x_0, y_0, z_0') \Big) \\ \times (\lambda V + N_\tau) \exp(-i\mathbf{k}_i \cdot \mathbf{r}_0) \Big(1 - \frac{i}{2k_n} \\ \times \sum \int_{-\infty}^\infty \exp(-i\beta_{in} z_0') V(x_0, y_0, z_0') \\ \times \mathrm{d}z_0' |\Phi_n\rangle \langle \Phi_n| \Big) |\Phi_i\rangle. \end{aligned} \tag{15}$$

Further we can write

$$\begin{aligned} J^{(1)} = (2\pi)^{-3} \langle \Phi_f | \int \exp(i\mathbf{q} \cdot \mathbf{b}_0) \exp(iX_0) \\ \exp(-i\mathbf{k}_1 \cdot \mathbf{r}_0) \exp(-X_+) (V + N_\tau) \exp(i\mathbf{k}_i \cdot \mathbf{r}_0) \\ \exp(iX_+) \mathrm{d}V_0 |\Phi_i\rangle, \end{aligned} \tag{16}$$

where

$$\begin{aligned} \exp(iX_0) = 1 - \frac{i}{2k} \sum |\Phi_n\rangle \langle \Phi_n | \int_{-\infty}^\infty \exp(i\beta_{in} z_0') \\ \times V(x_0, y_0, z_0') \mathrm{d}z_0', \end{aligned} \tag{17}$$

CC-0. In Public Domain. Gurukul Kangri Collection, Haridwar

Digitized by Arya Samaj Foundation Chennai and eGangotri

and

$$\exp(iX_+) = 1 - \frac{i}{2k}\sum |\Phi_n\rangle\langle\Phi_n| \int_{-\infty}^{z} \exp(-i\beta_{in}z'_0)V(x_0, y_0, z'_0)\mathrm{d}z'_0. \quad (18)$$

Now we can show that

$$\exp(-i\mathbf{k}_i\cdot\mathbf{r}_0)\exp(-iX_+)[V(\mathbf{r}) + N_\tau]\exp(i\mathbf{k}_i\cdot\mathbf{r}_0)\exp(iX_+)$$
$$= Q\cdot[\mathbf{P}_b + \nabla X_+)(r)] - \nabla\mathbf{X}\cdot\mathbf{P} - t_i(\mathbf{r}, \mathbf{r}_j), \quad (19)$$

where the operator

$$Q = [\mathbf{P} + \mathbf{q} + X_0(b)], \quad (20)$$

and

$$t_i(\mathbf{r}, \mathbf{r}_j) = -\lambda V(\mathbf{r}, \mathbf{r}_j) + \nabla X_+ \cdot \nabla \mathbf{X}_- . \quad (21)$$

The properties of Q operator are described in detail by Wallace (1973). After eliminating the term involving Q, (16) can be expressed as

$$J^{(1)} = (2\pi)^{-3}\Bigg[\langle\Phi_f|\int\exp(i\mathbf{q}\cdot\mathbf{b}_0)\lambda V(x_0, y_0, z'_0)\mathrm{d}V_0|\Phi_i\rangle$$
$$-\frac{i}{2k_n}\langle\Phi_f|\sum\int\exp(i\mathbf{q}\cdot\mathbf{b}_0)\lambda V(x_0, y_0, z'_0)\int_{-\infty}^{\infty}\exp(i\beta_{in}z'_0)$$
$$\times V(x_0, y_0, z'_0)|\Phi_n\rangle\langle\Phi_n|\mathrm{d}z'_0|\Phi_i\rangle$$
$$-\langle\Phi_f|\int\exp(i\mathbf{q}\cdot\mathbf{b}_0)(\nabla X_+\cdot\nabla X_-)\mathrm{d}V_0|\Phi_i\rangle$$
$$+\frac{i}{2k_n}\langle\Phi_f\Bigg[|\sum\int\exp(i\mathbf{q}\cdot\mathbf{b}_0)(\nabla X_+\cdot\nabla X_-)$$
$$\times\int_{-\infty}^{\infty}\exp(-i\beta_{in}z'_0)\mathrm{d}z'_0 V(x_0, y_0, z'_0)$$
$$\times\mathrm{d}V_0|\Phi_n\rangle\langle\Phi_n|\Bigg]|\Phi_i\rangle\Bigg]. \quad (22)$$

Substituting the values of $J^{(1)}$ and $T^{(0)}$, (12) can be written as

$$T = T^1 + (T^{B(2)})_{\mathrm{HEA}} - (T^{B(2)})_{\mathrm{HEA}} - (2\pi)^{-3}$$
$$\Bigg[\langle\Phi_f|\int\exp(i\mathbf{q}\cdot\mathbf{b}_0)V\mathrm{d}V_0\sum|\Phi_n\rangle\langle\Phi_n|$$
$$\times\int_{-\infty}^{\infty}\exp(-i\beta_{in}z'_0)V(x_0, y_0, z'_0)\mathrm{d}z'_0|\Phi_i\rangle\Bigg]$$
$$-\langle\Phi_f|\int\exp(i\mathbf{q}\cdot\mathbf{b}_0)(\nabla X_+\cdot\nabla X_-)\mathrm{d}V_0|\Phi_i\rangle. \quad (23)$$

Terms of the order of k_i^{-3} are neglected in the above equation. The fifth term in the above expression is written as

$$(2\pi)^{-3}\langle\Phi_f|\int\exp(i\mathbf{q}\cdot\mathbf{b}_0)(\nabla X_+\cdot\nabla X_-)\mathrm{d}V_0|\Phi_i\rangle$$

CC-0. In Public Domain. Gurukul Kangri Collection, Haridwar

Digitized by Arya Samaj Foundation Chennai and eGangotri

$$= \frac{(2\pi)^{-3}}{4k_n^2} \langle \Phi_f | \sum_n \int \exp(i\mathbf{q}\cdot\mathbf{b}_0) \mathrm{d}\mathbf{b}_0$$
$$\times \int_{-\infty}^{\infty} \mathrm{d}z_0' \left[\int_{-\infty}^{z_0} \nabla V \, \mathrm{d}z_0' \cdot \int_{z_0}^{\infty} \nabla V \, \mathrm{d}z_0' - i\beta_{in} \int_{z_0}^{\infty} \nabla V \, \mathrm{d}z_0' \right.$$
$$\left. \times \int_{-\infty}^{z_0} \nabla(z_0' V) \mathrm{d}z_0' - i\beta_{in} \int_{-\infty}^{z_0} \nabla V \, \mathrm{d}z_0' \cdot \int_{-\infty}^{z_0} \nabla(z_0' V) \right]. \tag{24}$$

Substituting (24) in (23) and calculating the amplitude factor we get

$$f = f^{(B1)} + \mathrm{Re}\,1 (f^{(B2)})_{\mathrm{HEA}} - \lambda \mathrm{Re}\,1$$
$$\times (f^{(B2)})_{\mathrm{HEA}} + (\mathrm{Im}^{(B2)})_{\mathrm{HEA}} + \lambda \mathrm{Im}(f^{(L2)})_{\mathrm{HEA}}$$
$$+ \mathrm{Re}\, f_{w2} - 2i\beta_{in} \mathrm{Re}\, f_{w2}. \tag{25}$$

The notations have the usual meanings.

3. Calculations

The real analysis of any theoretical formulation should be its application to the practical problem. Now we apply this formulation to the elastic scattering of electron by the hydrogen and helium atoms. The ground state wave function for the hydrogen atom can be written as

$$\phi_{1S}^{H}(r_1) = (\pi)^{-1/2} \exp(-r). \tag{26}$$

The interaction potential can be written as

$$V_d = -\frac{1}{r_0} + \frac{1}{|\mathbf{r}_0 - \mathbf{r}_1|}, \tag{27}$$

where $\mathbf{r}_0$ and $\mathbf{r}_1$ are the position vectors of the incident electron and target hydrogen with respect to the target nuclei. The first Born amplitude f^{B1} can be obtained as

$$f^{B1} = -\frac{1}{2\pi} \int\int \mathrm{d}\mathbf{r}_0 \, \mathrm{d}\mathbf{r}_1 \exp(i\mathbf{q}\cdot\mathbf{r}_0) V_d \Phi_f(\mathbf{r}_1) \Phi_i(\mathbf{r}_1)$$
$$= 2\frac{(q^2+8)}{(q^2+4)^2}, \quad \text{with} \quad q = 2k \sin\theta/2. \tag{28}$$

The imaginary and the real parts of the second Born approximation are

$$\mathrm{Im}\, f_{\mathrm{HEA}}^{B2} = -\frac{4}{\pi k_i} \frac{\partial}{\partial y} \frac{1}{y^2} \left(2 I_1(\beta_i^2, y^2) - \frac{q^2}{(q^2+y^2)} I_1(\beta_i^2, 0) \right), \tag{29}$$

$$\mathrm{Re}\,1\, f_{\mathrm{HEA}}^{B2} = \frac{4}{\pi^2 k_i} \left(\frac{\partial}{\partial y} \right) \frac{1}{y^2} \left(2 I_2(\beta_i^2, y^2) - \frac{q^2}{(q^2+y^2)} I_2(\beta_i^2, 0) \right). \tag{30}$$

The integrals I_1 and I_2 are the same as those of Yates (1979). Re f_{w2} was calculated by Byron Jr *et al.* (1982). Finally for the consistent picture of DCS $O(k_i^{-2})$ we have

CC-0. In Public Domain. Gurukul Kangri Collection, Haridwar

Digitized by Arya Samaj Foundation Chennai and eGangotri

included the exchange amplitude (Byron and Joachain 1977) and the third Glauber eikonal series term (Yates 1974). The corresponding expressions are

$$g_{\text{och}} = -\frac{32}{k_i^2}(q^2+4)^{-2} \tag{31}$$

and

$$f_{\text{GES}}^{(3)} = \frac{ik_i}{2\pi}\int \mathrm{d}b_0 \exp(i\mathbf{q}\cdot\mathbf{b}_0)\frac{(iX)^3}{3!}, \tag{32}$$

where

$$X = -\frac{1}{k_i}\int_{-\infty}^{\infty} V\,\mathrm{d}z_0. \tag{33}$$

The well-known Hartree Fock wave functions are used for the ground state of the helium atom. The interaction potential for the helium atom is

$$V_d = \frac{-2}{r_0} + \frac{1}{|\mathbf{r}_0-\mathbf{r}_1|} + \frac{1}{|\mathbf{r}_0-\mathbf{r}_2|}, \tag{34}$$

where $\mathbf{r}_0, \mathbf{r}_1$ and $\mathbf{r}_2$ are the position vectors of the incident electron and target electrons with respect to the target nuclei. Following the same procedure as that for the hydrogen atom we will get the first Born amplitude as

$$f^{B1} = \sum_{k=1}^{3} C_k\left(\frac{(8y_k^2+q^2)}{(4y_k^2+q^2)}\right), \tag{35}$$

where C_k's and y_k's are constants given by

$$C_1 = 2{\cdot}420884; \quad C_2 = 0{\cdot}2336732; \quad C_3 = 1{\cdot}33543,$$

$$y_1 = 1{\cdot}41; \quad y_2 = 2{\cdot}61; \quad y_3 = 2{\cdot}01.$$

Now the imaginary and real parts of the second Born amplitude can be written as

$$\begin{aligned}\operatorname{Im} f_{\text{HEA}}^{B2} = \frac{1}{\pi k_i}\sum_{\substack{k=1,2,3,4\\ j=2,3,1,0,}}\Bigg[&-\left(A_k\frac{\partial}{\partial y_k}\frac{1}{y_k^2}\right)\Bigg|2I_1(\beta_i^2, y_k^2) \\ &-\frac{q^2}{q^2+y_k^2}I_1(\beta_i^2, 0)\Bigg| + B_{kk}\int \mathrm{d}p\Bigg|\frac{y_k^2}{A_1^2 B_1^2} \\ &+\frac{2}{A_1^2 B_1}+\frac{1}{y_k^2 A_1 B_1}\Bigg| + B_{kj}\int \mathrm{d}p\Bigg|\frac{y_k y_j}{A_2^2 B_2^2} \\ &+\frac{y_k}{y_k A_2^2 B_2^2}+\frac{y_j}{y_k A_2 B_2^2}+\frac{1}{y_k y_j A_2 B_2}\Bigg|\Bigg]\end{aligned} \tag{36}$$

$$\begin{aligned}\operatorname{Re} 1_{\text{HEA}}^{B2} = \frac{1}{\pi^2 k_i}\sum_{k=1,2,3,4}\Bigg[&A_k\left(\frac{\partial}{\partial y_k}\frac{1}{y_k^2}\right) \\ &\times\left|2I_2(\beta_i^2, y_k^2) - \frac{q^2}{q^2+y_k^2}I_2(\beta_i^2, 0)\right| \\ &-B_{kk}\left(\frac{\partial^2}{\partial y_k \partial y_k}\frac{1}{y_k^2}\frac{1}{y_k^2}\right)I_4(\beta_i^2, y_k^2, y_j^2)\Bigg].\end{aligned} \tag{37}$$

CC-0. In Public Domain. Gurukul Kangri Collection, Haridwar

Digitized by Arya Samaj Foundation Chennai and eGangotri

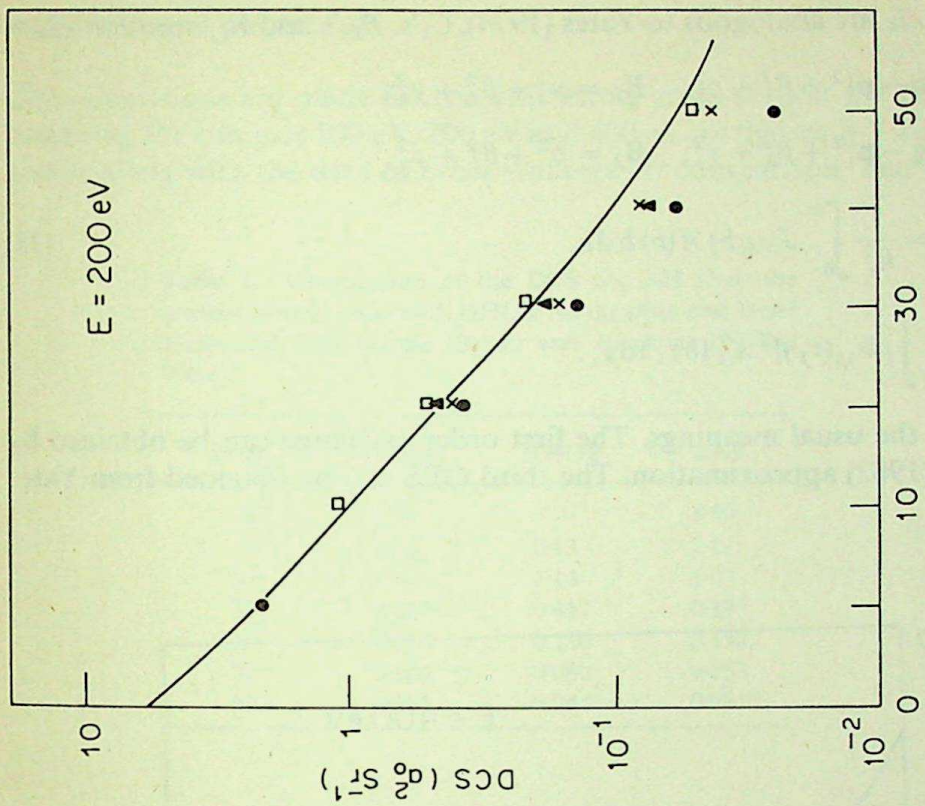

Figure 2. DCS for the elastic scattering of 200 eV electrons by atomic hydrogen. Legends are as in figure 1.

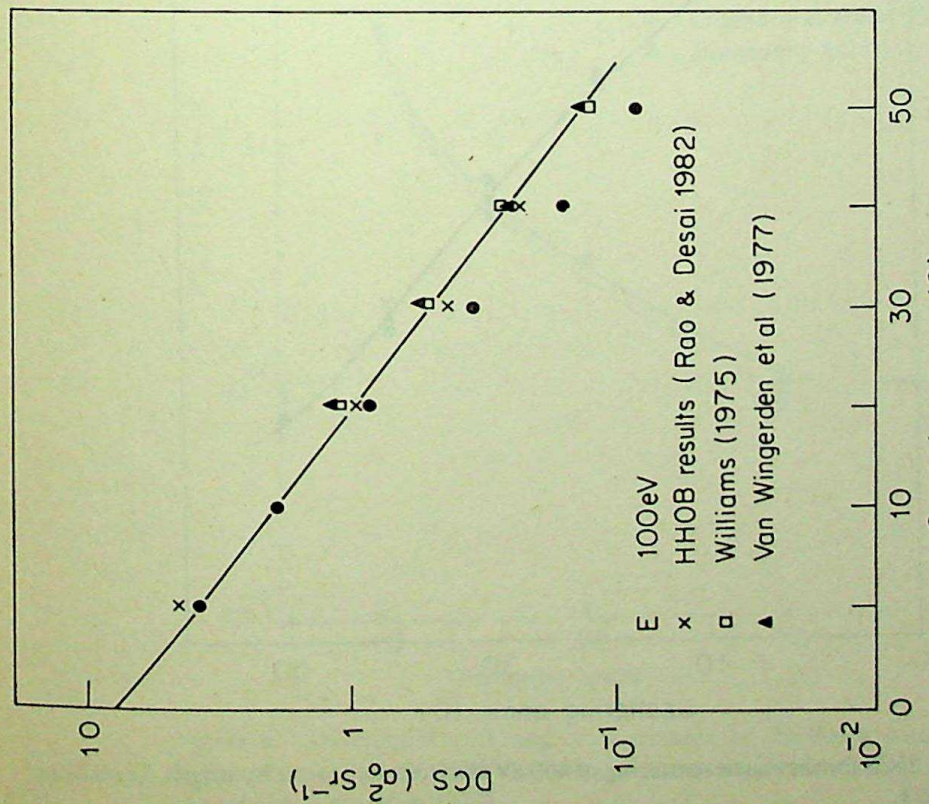

Figure 1. DCS for the elastic scattering of 100 eV electrons by atomic hydrogen. Solid curve refers to the present calculations; the solid circles are those of UEBS (Byron *et al* 1982).

CC-0. In Public Domain. Gurukul Kangri Collection, Haridwar

Digitized by Arya Samaj Foundation Chennai and eGangotri

The integrals I_1, I_2, I_4 are analogous to Yates (1974), C_k's, B_{kk}'s and B_{kj}'s are constants.

$$A_1 = |\mathbf{q}-\mathbf{p}|^2 + \beta_i^2 + y_k^2, \quad B_1 = p^2 + \beta_i^2 + y_k^2,$$

$$A_2 = |\mathbf{q}-\mathbf{p}|^2 + \beta_i^2 + y_j^2, \quad B_2 = p^2 + \beta_i^2 + y_j^2,$$

$$\text{Re}\, f_{w2} = \frac{1}{k_i^2} \int_0^\infty J_0(qb)\, A(b)\, b\, \mathrm{d}b, \tag{38}$$

where $$A(b) = \int |\Phi_{1S}(r_1)|^2 X_1(b\mathbf{r}_1)\, \mathrm{d}\mathbf{r}_1.$$

All the terms have the usual meanings. The first order exchange can be obtained by using the Ochkur (1963) approximation. The third GES can be obtained from Yates (1974).

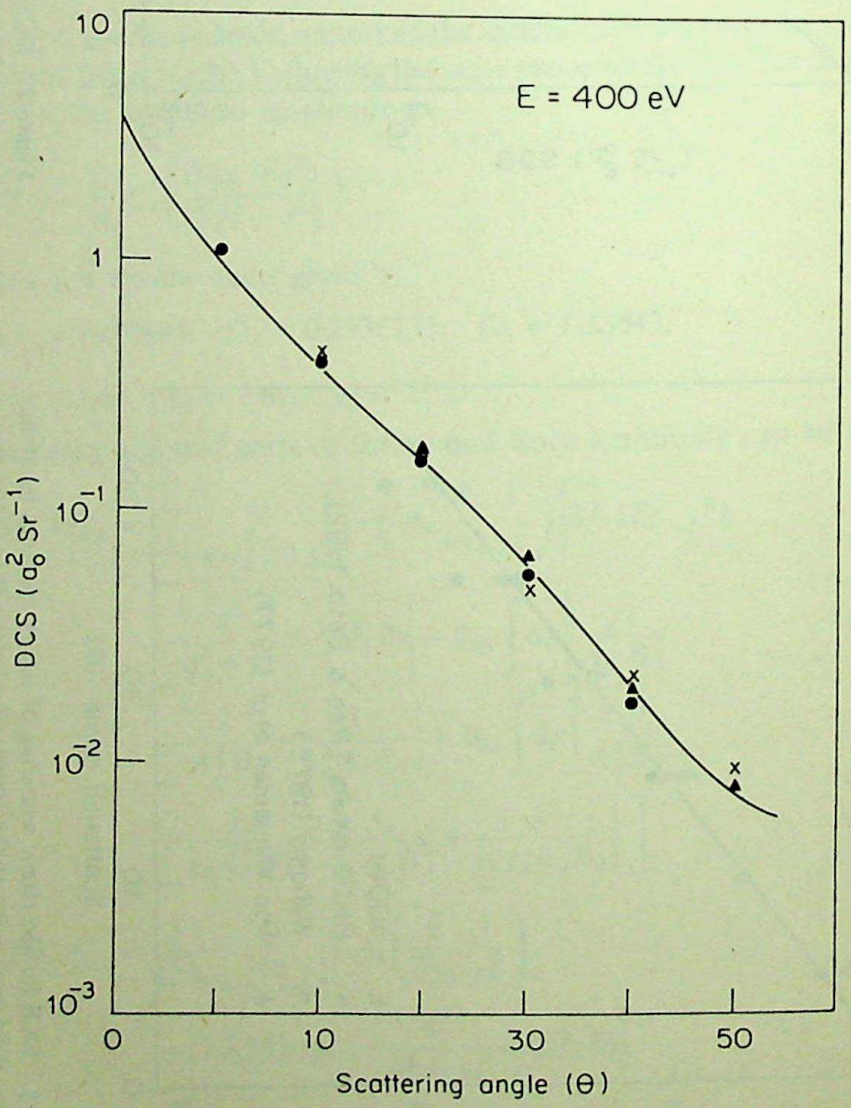

Figure 3. DCS for the elastic scattering of 400 eV electrons by atomic hydrogen. Legends are as in figure 1.

CC-0. In Public Domain. Gurukul Kangri Collection, Haridwar

Digitized by Arya Samaj Foundation Chennai and eGangotri

4. Results and discussion

The calculations are made for the differential cross-section (DCS) for the $\bar{e}$-H elastic scattering for energies 100 eV, 200 eV and 400 eV. In figures 1–3 we have displayed our results along with the data of other workers for comparison. The values are shown at

Table 1. Comparison of the DCS for $\bar{e}$-H from the present computation with HHOB results (Rao and Desai 1982) and EBS results (Byron and Joachain 1977) at 200 eV.

Angle	Present	HHOB	EBS
0	5·34	—	5·50
5	2·00	2·13	2·11
10	1·27	1·14	1·09
20	0·517	0·417	0·393
30	0·214	0·170	0·152
40	0·164	0·080	0·053
50	0·061	0·044	0·0317

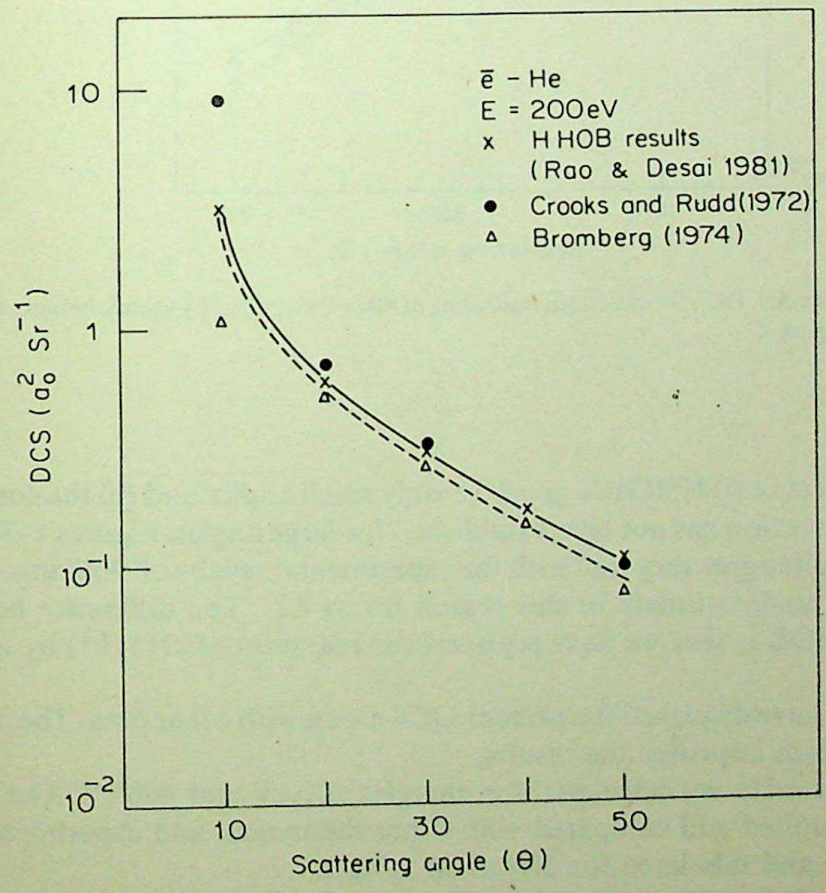

Figure 4. Differential scattering cross-sections for the elastic scattering of electrons from helium atom at 200 eV. Solid curve refers to present calculations and the broken curve to EBS results (Joachain *et al* 1977).

CC-0. In Public Domain. Gurukul Kangri Collection, Haridwar

Digitized by Arya Samaj Foundation Chennai and eGangotri

Table 2. Comparison of the DCS for $\bar{e}$-He from the present computation with HHOB results (Rao and Desai 1981) and EBS results (Byron and Joachain 1977).

Angle	Present	HHOB	EBS
10	1·35	1·31	1·34
20	0·611	0·609	0·583
30	0·316	0·313	0·288
40	0·175	0·186	0·154
50	0·104	0·108	0·088

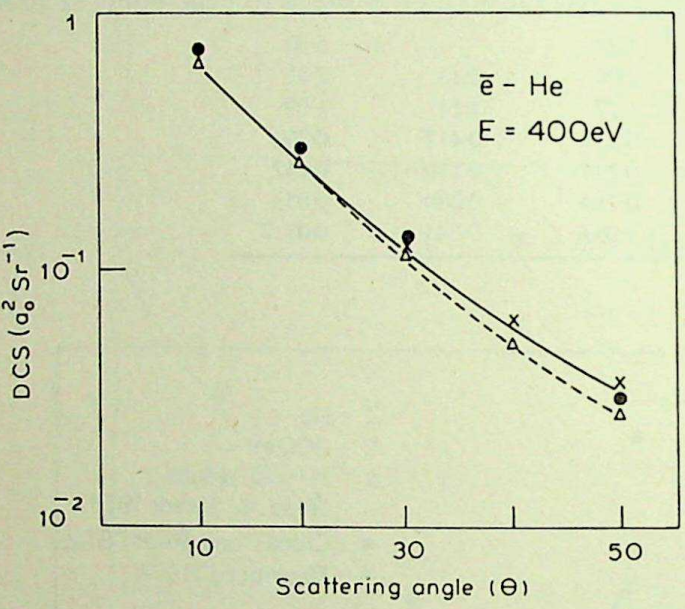

Figure 5. DCS for the elastic scattering of 400 eV electrons by atomic helium. Legends are as in figure 4.

small angles because (i) HHOB is good for only small angles and (ii) the correctness of the Wallace correction has not been established for large angles. Figures 1–3 reveal that our present results agree very well with the experimental results of Williams (1975). The HHOB results underestimate in this region up to 40°. The difference between our results and HHOB is that we have replaced the real term of $O(1/k^2)$ by the Wallace term.

In table 1 we have displayed the present DCS along with other data. The inclusion of the exchange term improves the results.

The DCS for $\bar{e}$-He are calculated for energies 200 eV and 400 eV. The results are graphically exhibited and compared with other theoretical and experimental data in figures 4 and 5 and tabulated for 200 eV in table 2.

In the light of the above discussion we conclude that the present approximation improves the basic HHOB approximation of Yates (1979) in the study of elastic scattering of electrons from hydrogen and helium atoms.

CC-0. In Public Domain. Gurukul Kangri Collection, Haridwar

Digitized by Arya Samaj Foundation Chennai and eGangotri

Acknowledgement

One of the authors (KS) is thankful to the M.S. University of Baroda for financial assistance.

References

Bromberg J P 1974 *J. Chem. Phys.* **61** 963
Byron F W Jr and Joachain C J 1977 *J. Phys.* **B10** 207
Byron F W Jr, Joachain C J and Potvliege R M 1982 *J. Phys.* **B15** 3915
Crooks G B and Rudd M E 1972 *Bull. Am. Phys. Soc.* **17** 131
Ochkur V I 1963 *Zh. Eksp. Teor. Fiz.* **45** 734
Rao N S and Desai H S 1981 *Pramana–J. Phys.* **17** 309
Rao N S and Desai H S 1982 National Workshop on Atomic and Molecular Physics. Abstract 30
Van Winger den B, Weigold E, de Heer F J and Nygaard 1977 *J. Phys.* **B10** 1345
Wallace S J 1973 *Ann. Phys. N.Y.* **78** 190
Williams J F 1975 *J. Phys.* **B8** 2191
Yates A C 1974 *Chem. Phys. Lett.* **25** 480
Yates A C 1979 *Phys. Rev.* **A19** 1550

CC-0. In Public Domain. Gurukul Kangri Collection, Haridwar

Digitized by Arya Samaj Foundation Chennai and eGangotri

CC-0. In Public Domain. Gurukul Kangri Collection, Haridwar

Digitized by Arya Samaj Foundation Chennai and eGangotri

Pramāṇa – J. Phys., Vol. 28, No. 4, April 1987, pp. 399–408. © Printed in India.

Weak electron acoustic double layers in a multicomponent plasma

K S GOSWAMI and S BUJARBARUA

Institute of Advanced Study in Science and Technology, Assam Science Society, Khanapara, Gauhati 781 022, India

MS received 24 March 1986; revised 2 December 1986

Abstract. Formation of electron acoustic double layers in a magneto-plasma with two ion species is investigated. The existence of double layers propagating almost perpendicular to the magnetic field in a plasma with two distinct ion species and cold electron is discussed.

Keywords. Electron acoustic double layer; multicomponent plasma; single-ion species, two-ion species.

PACS No. 52·35

1. Introduction

A large number of theoretical (Block 1972; Torven 1981), computer simulation (Hubbard and Joyce 1979; Kim and Crystal 1984) and experimental (Coakley and Hershkowtiz 1979; Temerin *et al* 1982) investigations have been carried out on the double layers. Recently Kim (1983) and Schamel (1983) showed that slow electron acoustic double layers (SEADL) and slow ion acoustic double layers (SIADL) can be constructed considering the effects of reflected electrons and reflected ions. However, Goswami and Bujarbarua (1985, 1986a) have shown that small amplitude ion acoustic double layers can be constructed without considering the effects of reflected particles. But in such a situation at least two types of free electrons (each described by a Maxwellian distribution) are necessary to construct such double layers. From the earlier theory of double layers (DL) it has been found that they are generally associated with the ion acoustic branch, while theoretical studies of electron acoustic solitary waves, propagating almost perpendicular to the magnetic field in a plasma with ion temperature very much larger than the electron temperature, have been performed extensively (Arefev 1970; Goedbloed *et al* 1973). Buti (1980) investigated an exact nonlinear electron acoustic waves in a multicomponent plasma and showed the effects of second ion components. With this idea in mind, the existence of small amplitude electron acoustic double layers or shocks in plasma has been investigated by Goswami *et al* (1986).

In this paper, we study the existence of small amplitude electron acoustic double layers or shocks in a multicomponent plasma. Using fluid equation for electrons and describing ion components by the Maxwell-Boltzmann relation, i.e. the free particle temperature and the reflected particle temperature of the two-ion species to be equal, we first describe the method of finding solutions with a potential ϕ that varies monotonically from a minimum value, zero to maximum value ψ (amplitude of the

CC-0. In Public Domain. Gurukul Kangri Collection, Haridwar

Digitized by Arya Samaj Foundation Chennai and eGangotri

double layer). We then describe the classical potential $V(\phi)$ which is obtained by integrating the densities with respect to ϕ. The existence of a double layer solution demands that the classical potential $V(\phi)$ and the electric field $\partial V/\partial\phi$ vanish at two extremum of ϕ i.e. $\phi = 0$ and $\phi = \psi$. The variation of classical potential $V(\phi)$ for a double layer against its potential ϕ is shown in figure 1.

In § 2, we discuss the DL solution in the presence of a single Boltzmann ion. In § 3, we obtain the DL solutions in the presence of two positive ion species (each described by a Maxwellian-Boltzmann distribution). In § 4, we obtain the DL solution in the presence of both positive and negative ions (each described by a Maxwellian-Boltzmann distribution) and § 5 contains a discussion and conclusion of our results.

2. Single ion species

We consider a homogeneous plasma with electrons and ions in the presence of external magnetic field $\vec{B} = B_0\hat{z}$ in the $\hat{Z}$ direction. We assume that $T_i > T_e$, where T_i and T_e are the ion temperature and the electron temperature respectively. Here the electron acoustic waves are assumed to propagate almost perpendicular to the magnetic field and the direction of propagation lie on the y-z plane. The electrons are governed by the following set of fluid equations

$$\partial_t n + \partial_y(nv_y) + \partial_z(nv_z) = 0, \tag{1}$$

$$\partial_t v_x + (v_y\partial_y + v_z\partial_z)v_x = -v_y, \tag{2}$$

$$\partial_t v_y + (v_y\partial_y + v_z\partial_z)v_y = v_x + \partial_y\phi, \tag{3}$$

$$\partial_t v_z + (v_y\partial_y + v_z\partial_z)v_z = \partial_z\phi. \tag{4}$$

In equations (1) to (4), we have normalized the densities by the equilibrium density n_0, the velocities by the electron acoustic speed $C_e = (T_i/m_e)^{1/2}$, the potential ϕ by T_i/e, the space variables by $\rho = C_e/\Omega_e$, and the time by the inverse of electron gyro-frequency $\Omega_e = eB_0/m_e$ and the others are the standard notations.

We consider a new frame of reference which is moving with velocity M with respect to the rest frame in the direction of the wave. In this frame the space co-ordinate is given by, $\xi = k_y y + k_z z - Mt$ where $k_y^2 + k_z^2 = 1$ and k_y, k_z are the direction cosines.

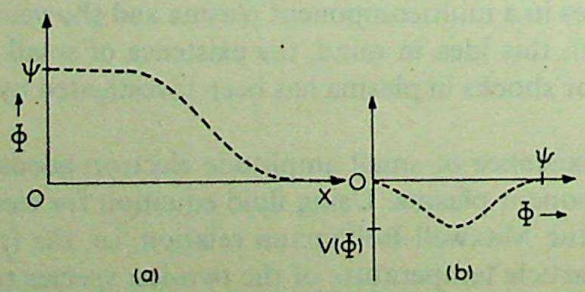

Figure 1. (**a**) A qualitative plot of the electrical potential $\phi(x)$ of a monotonic double layers as a function of x. (**b**) The corresponding classical potential $v(\phi)$ as a function of ϕ.

CC-0. In Public Domain. Gurukul Kangri Collection, Haridwar

Digitized by Arya Samaj Foundation Chennai and eGangotri

Therefore (1) to (4) can be written as

$$(k_y v_y + k_z v_z) = M\left(1 - \frac{1}{n}\right), \tag{5}$$

$$\frac{M}{n}\partial_\xi v_x = -v_y, \tag{6}$$

$$-\frac{M}{n}\partial_\xi v_y = v_x + k_y \partial_\xi \phi, \tag{7}$$

$$-\frac{M}{n}\partial_\xi v_z = k_z \partial_\xi \phi. \tag{8}$$

Integrating (8), we get

$$v_z = -\frac{k_z}{M} I(\phi), \tag{9}$$

where $$I(\phi) = \int_0^\phi n \, \mathrm{d}\phi. \tag{10}$$

Substituting v_y from (5) and using (8), we get

$$v_x = \frac{1}{k_y}\left[\left(-1 - \frac{M^2}{n^3}\frac{\partial n}{\partial \phi}\right)\frac{\partial \phi}{\partial \xi}\right]. \tag{11}$$

Substituting (11) and (5) into (6) and combining with (9), we get

$$\frac{1}{2}\partial_\phi\left(P\frac{\partial \phi}{\partial \xi}\right)^2 = P\left[\frac{k_z^2}{M^2} nI(\phi) + n - 1\right] = -\frac{\partial V}{\partial \phi}, \tag{12}$$

where $V(\phi)$ is the classical potential and

$$P = -1 - (M^2/n^3)\,\partial_\phi n. \tag{13}$$

Since for electron acoustic waves, the frequencies are much larger than the ion cyclotron frequency and the wavelengths are much smaller than the ion Larmour radius, the ions may be considered as unmagnetized and we assume that the ion density n_i obey the Boltzmann relation (Mohan and Buti 1980)

$$n_i = \exp(-\phi). \tag{14}$$

We consider small amplitude waves and assume a quasineutral condition which is valid when the electron Debye length is smaller than the electron gyro-radius. Therefore the ion density n_i may be substituted for n in equation (12).

For small ϕ, the ion density can be written as

$$n_i = 1 - \phi + \tfrac{1}{2}\phi^2 - \tfrac{1}{6}\phi^3 + \cdots. \tag{15}$$

To the lowest order, we can easily write from (13) and (15) i.e. $P \simeq -1 + M^2$. Inserting

CC-0. In Public Domain. Gurukul Kangri Collection, Haridwar

Digitized by Arya Samaj Foundation Chennai and eGangotri

the value of n from (15) into (12), we get

$$P[B_1\phi + B_2\phi^2 + B_3\phi^3] \equiv -\partial_\phi V, \tag{16}$$

where $$B_1 = \left(\frac{k_z^2}{M^2} - 1\right), \tag{17a}$$

$$B_2 = \left(\frac{1}{2} - \frac{3}{2}\frac{k_z^2}{M^2}\right), \tag{17b}$$

and $$B_3 = \left(\frac{7}{6}\frac{k_z^2}{M^2} - \frac{1}{6}\right). \tag{17c}$$

Integrating (16) and imposing the boundary condition $V(0) = 0$, we get the classical potential as

$$-V(\phi) = P[\tfrac{1}{2}B_1\phi^2 + \tfrac{1}{3}B_2\phi^3 + \tfrac{1}{4}B_3\phi^4]. \tag{18}$$

The nonlinear dispersion relation is obtained by imposing the boundary condition $V(\phi) = 0$ at $\phi = \psi$ in (18) and we get

$$B_1 = -\tfrac{2}{3}B_2\psi - \tfrac{1}{2}B_3\psi^2. \tag{19}$$

To get the DL solution we introduce another boundary condition i.e. $\partial V/\partial\phi = 0$ at $\phi = \psi$ and we get from (16),

$$B_1 = -B_2\psi - B_3\psi^2. \tag{20}$$

Equating (19) and (20), we get

$$B_1 = \tfrac{1}{2}B_3\psi^2, \tag{21a}$$

$$B_2 = -\tfrac{3}{2}B_3\psi. \tag{21b}$$

From (21a), (21b) and (18), we get

$$-V(\phi) = \frac{B_3 P}{4}\phi^2(\phi - \psi)^2. \tag{22}$$

Using (22), the potential of the double layer can be written from (12) as (Goswami and Bujarbarua 1985)

$$\phi = \frac{\psi}{2}(1 - \tanh\kappa\xi) \quad \text{with} \quad \kappa = (B_3/8P)^{1/2}\psi. \tag{23}$$

Equation (23) represents a DL provided $B_3 < 0$ (since P is negative). The velocity of this type of DL can be calculated from (17) and (21) and is given by

$$M = k_z\left(1 - \frac{1}{3}\frac{\psi}{2}\right). \tag{24}$$

CC-0. In Public Domain. Gurukul Kangri Collection, Haridwar

Digitized by Arya Samaj Foundation Chennai and eGangotri

However it is found from (17c) that $B_3 > 0$. Hence the electron acoustic double layer with single species of ions and electrons does not exist.

3. Two positive ions

We now consider the case when two isothermal positive ions are present in the system. If the gyroperiods and Larmor radii of both the ion species are much larger than the wave period and the wavelength, the ions can be taken as unmagnetized and they have a Boltzmann type distribution (Buti 1980). Therefore the total ion density can be written as

$$n = \alpha_1 \exp(-a_1\phi) + \alpha_2 \exp(-a_2\phi), \tag{25}$$

where $\alpha_1 = n_1/n_0, \alpha_2 = n_2/n_0, a_1 = T_{if}/T_1$ and $a_2 = T_{if}/T_2$ and n_1, n_2 are the densities and T_1, T_2 are the temperatures of the positive ions. T_{if} is the effective ion temperature i.e. $T_{if} = T_1T_2/(\alpha_1T_2 + \alpha_2T_1)$.

In a small amplitude limit, the total ion density can be written as,

$$n = 1 - A_1\phi + \tfrac{1}{2}A_2\phi^2 - \tfrac{1}{6}A_3\phi^3 + \cdots, \tag{26}$$

where

$$A_1 = 1, \tag{27a}$$

$$A_2 = (\alpha_1 + \alpha_2 T_1^2/T_2^2)/(\alpha_1 + \alpha_2 T_1/T_2)^2, \tag{27b}$$

and

$$A_3 = (\alpha_1 + \alpha_2 T_1^3/T_2^3)/(\alpha_1 + \alpha_2 T_1/T_2)^3. \tag{27c}$$

Substituting the value of n from (26) into (12), we get (16) where B_1, B_2 and B_3 are as follows,

$$B_1 = \left(\frac{k_z^2}{M^2} - A_1\right), \tag{28a}$$

$$B_2 = \left(\frac{1}{2} - \frac{3}{2}\frac{k_z^2}{M^2}\right), \tag{28b}$$

$$B_3 = \left[\frac{k_z^2}{M^2}\left\{\frac{2}{3}A_2 + \frac{1}{2}\right\} - \frac{A_3}{6}\right]. \tag{28c}$$

The potential of this type of DL is given by (23) when the condition $B_3 < 0$ is satisfied, and the velocity of such a type of DL is given by

$$M = k_z\left\{1 - \frac{1}{6}\left[\frac{3}{2} - \frac{1}{2}\left(\frac{\alpha_1 + \alpha_2 T_1^2/T_2^2}{(\alpha_1 + \alpha_2 T_1/T_2)^2}\right)\right]\psi\right\}. \tag{29}$$

It can be shown that in the presence of two isothermal positive ions, the value of B_3 will be negative for certain values of A_2 and A_3. For example (a) $\alpha_1 = 0{\cdot}95$, $T_1/T_2 = 10$, $A_2 = 2{\cdot}83$, $A_3 = 16{\cdot}7$, $B_2 = -0{\cdot}085$ and $B_3 = -0{\cdot}396$, (b) $\alpha_1 = 0{\cdot}95$, $T_1/T_2 = 20$, $A_2 = 5{\cdot}51$, $A_3 = 54{\cdot}11$, $B_2 = 1{\cdot}255$, $B_3 = -4{\cdot}845$. Since for case (a) both B_2 and B_3 are

CC-0. In Public Domain. Gurukul Kangri Collection, Haridwar

Digitized by Arya Samaj Foundation Chennai and eGangotri

negative and to satisfy (21b), $\psi(\phi)$ has to be negative in this case corresponding to rarefactive DL. For case (b) B_2 is positive and B_3 is negative and in this case we get the compressive DL. Hence we may conclude that for moderate values of T_1/T_2, the ratio of two positive ions, electron acoustic double layers can exist when the cold positive ion concentration i.e. α_2 is very low.

4. Presence of negative ions

Next we consider the case when both positive and negative ions are present in the system. In this case, the net positive ion density can be written as

$$n = \frac{1}{1-\alpha}\exp(-a_1\phi) - \frac{\alpha}{1-\alpha}\exp(a_2\phi), \tag{30}$$

where $\alpha = n_{j0}/n_{i0}$, $a_1 = T_{if}/T_i$ and $a_2 = T_{if}/T_j$ and the subscripts i and j denote the positive and negative ions respectively. Here T_{if}, the effective ion temperature is given by,

$$T_{if} = T_iT_j \Big/ \left(\frac{1}{1-\alpha}T_j + \frac{\alpha}{1-\alpha}T_i\right).$$

In the small amplitude limit, the expansion of (30) is the same as (26), the quantities A_1, A_2 and A_3 are given by

$$A_1 = 1, \tag{31a}$$

$$A_2 = \left(\frac{1}{1-\alpha} - \frac{\alpha}{1-\alpha}\frac{T_i^2}{T_j^2}\right)\left(\frac{1}{1-\alpha} + \frac{\alpha}{1-\alpha}\frac{T_i^2}{T_j}\right)^{-2}, \tag{31b}$$

$$A_3 = \left(\frac{1}{1-\alpha} + \frac{\alpha}{1-\alpha}\frac{T_i^3}{T_j^3}\right)\left(\frac{1}{1-\alpha} + \frac{\alpha}{1-\alpha}\frac{T_i^2}{T_j}\right)^{-3}. \tag{31c}$$

Applying the same procedure as in the case of two positive ion species, we obtain (16), where B_1, B_2 and B_3 are given by (28a) to (28c). The potential of DL is given by (23) with the condition $B_3 < 0$ and the velocity of this type of double layer is given by

$$M = k_z\left[1 - \frac{1}{6}\left\{\frac{3}{2} - \frac{1}{2}\left(\frac{\left(\frac{1}{1-\alpha} - \frac{\alpha}{1-\alpha}\frac{T_i}{T_j}\right)}{\left(\frac{1}{1-\alpha} + \frac{\alpha}{1-\alpha}\frac{T_i}{T_j}\right)^2}\right)\right\}\psi\right]. \tag{32}$$

Let us consider the following examples (a) $\alpha = 0{\cdot}1$, $T_i/T_j = 4$, $A_2 = -0{\cdot}275$, $A_3 = 2{\cdot}17$, $B_2 = -1{\cdot}6375$ and $B_3 = -0{\cdot}0467$; (b) $\alpha = 0{\cdot}1$, $T_i/T_j = 10$, $A_2 = -2{\cdot}02$, $A_3 = 10{\cdot}2$, $B_2 = -2{\cdot}51$ and $B_3 = -2{\cdot}54$. From the above examples cases (a) and (b) corresponding to the moderate values of negative ion concentration α and the ratio of positive to the negative ion temperatures, T_i/T_j. It has been found that both B_2 and B_3 are negative. Thus we conclude that the rarefactive electron acoustic double layers can exist when the densities and the temperature of positive ions are greater than the negative ions.

CC-0. In Public Domain. Gurukul Kangri Collection, Haridwar

Digitized by Arya Samaj Foundation Chennai and eGangotri

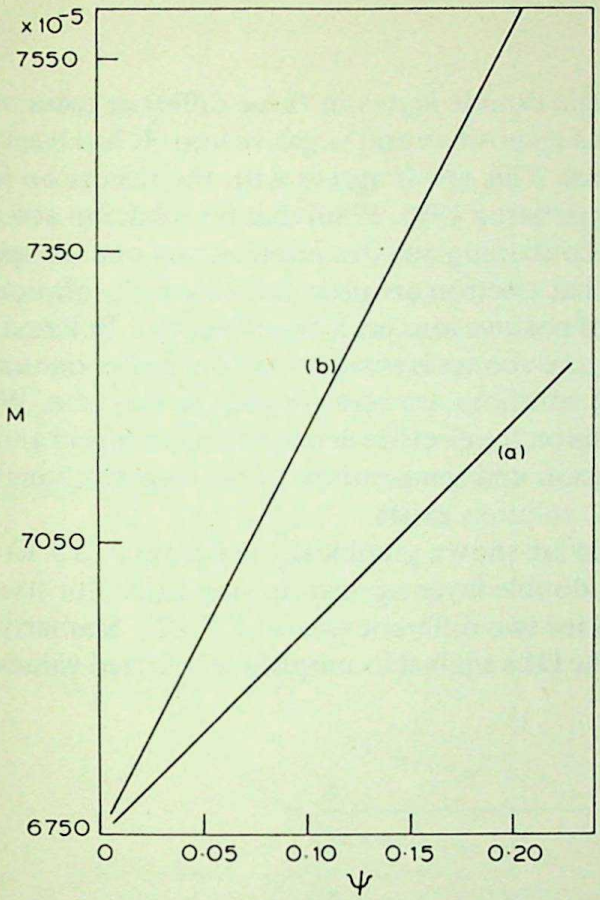

Figure 2. Variation of the double layer velocity against its amplitude. (a) $\alpha_1 = 0{\cdot}95$, $\alpha_2 = 0{\cdot}05$, $k_z = 0{\cdot}09$ and $T_1/T_2 = 10$. (b) $\alpha_1 = 0{\cdot}95$, $\alpha_2 = 0{\cdot}05$, $k_z = 0.09$ and $T_1/T_2 = 20$.

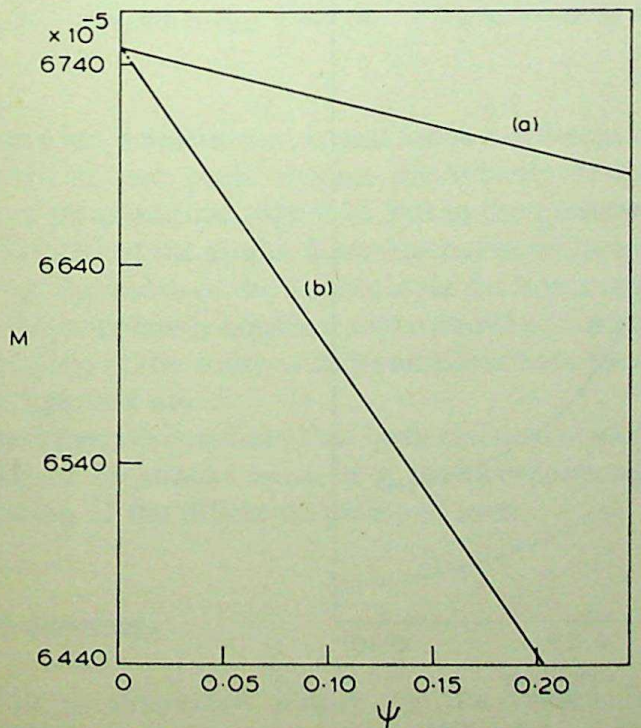

Figure 3. Variation of the double layer velocity against its amplitude. (a) $\alpha = 0{\cdot}1$, $k_z = 0{\cdot}09$ and $T_i/T_j = 4$. (b) $\alpha = 0{\cdot}1$, $k_z = 0{\cdot}09$ and $T_i/T_j = 10$.

CC-0. In Public Domain. Gurukul Kangri Collection, Haridwar

Digitized by Arya Samaj Foundation Chennai and eGangotri

5. Discussion

We have studied electron acoustic double layers in three different cases viz (a) single positive ions (b) two positive ions (c) positive and negative ions. It has been shown that for case (a) no DL solutions exist. This result agrees with the results on ion acoustic double layers (Goswami and Bujarbarua 1985, 1986) that no weak ion acoustic double layers solution exist in a plasma containing one free electron and one ion species. In the present paper, we have shown that electron acoustic DL or shock solution exists in a plasma consisting of two types of positive ions each described by a Boltzmann relation, that the concentration of colder ions species is smaller than the hotter one and that both compressive and rarefactive DL solutions are also possible in this case. We have also studied the effects of negative ions on the electron acoustic double layers and it has been shown that when the concentration and temperature of the negative ions are smaller than the positive ions, such DL solution exists.

The results of our investigation are shown graphically in figures 2 to 5. In figure 2, we have plotted the velocity of the double layer against its amplitude, for fixed values of positive ion densities and k_z and for two different values of T_1/T_2. Similarly in figure 3, we have plotted the velocity of the DLs against its amplitude for fixed values of positive

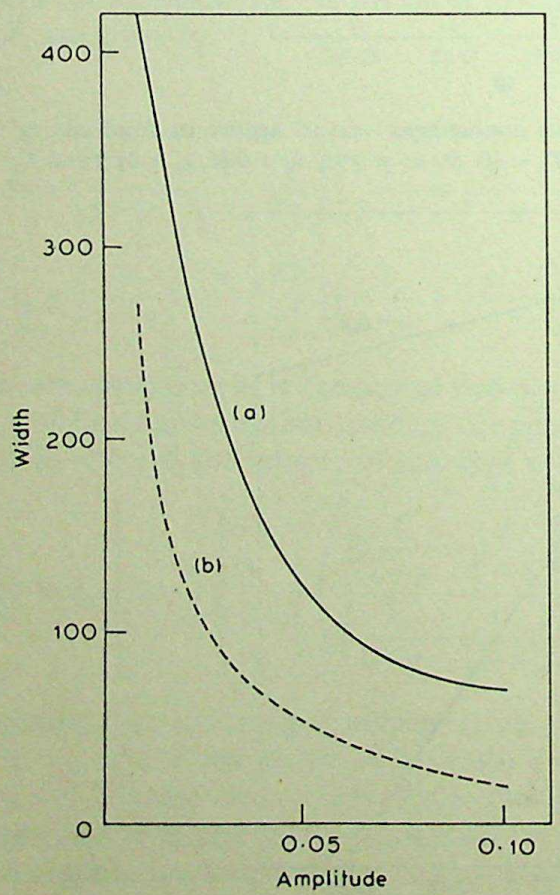

Figure 4. Width of the double layer plotted against its amplitude. (a) $\alpha_1 = 0{\cdot}95$, $\alpha_2 = 0{\cdot}05$, $k_z = 0{\cdot}09$, $M = 0{\cdot}09$ and $T_1/T_2 = 10$ and (b) $\alpha_1 = 0{\cdot}95$, $\alpha_2 = 0{\cdot}05$, $k_z = 0{\cdot}09$, $M = 0{\cdot}09$ and $T_1/T_2 = 20$.

CC-0. In Public Domain. Gurukul Kangri Collection, Haridwar

Digitized by Arya Samaj Foundation Chennai and eGangotri

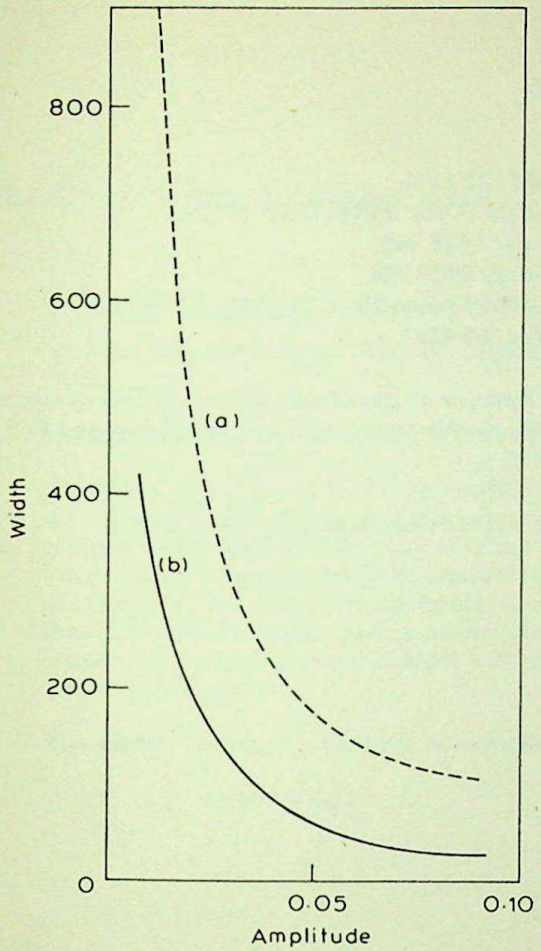

Figure 5. Width of double layer plotted against its amplitude. (a) $\alpha = 0{\cdot}1$, $k_z = 0{\cdot}09$, $M = 0{\cdot}09$ and $T_i/T_j = 4$ and (b) $\alpha = 0{\cdot}1$, $k_z = 0{\cdot}09$, $M = 0{\cdot}09$ and $T_i/T_j = 10$.

and negative ion densities and k_z and for two different values of T_i/T_j. It is seen that in the presence of two positive ions, the velocity of the double layer increases with increases of its amplitude (figure 2). But in the presence of both positive and negative ions, the velocity of the double layers decreases with increase of its amplitude (figure 3).

However, the width of the double layer decreases rapidly as the amplitude increases and then becomes nearly constant as the amplitude increases still further. The behaviour of the variation of the width with its amplitude for fixed values of temperature ratio is shown in figures 4 and 5.

Summarizing, we conclude that both rarefactive and compressive electron acoustic double layers or shocks exist in a multicomponent plasma depending upon the concentration of the different species of ions.

Acknowledgements

This work is supported jointly by the Indian Space Research Organization, Government of India and by the Department of Science, Technology and Environment, Government of Assam (India).

CC-0. In Public Domain. Gurukul Kangri Collection, Haridwar

Digitized by Arya Samaj Foundation Chennai and eGangotri

References

Arefev V I 1970 *Sov. Phys. Tech. Phys.* **14** 1487
Block L P 1972 *Cosmic Electrodynam.* **3** 349
Buti B 1980 *J. Plasma Phys.* **24** 169
Coakley P and Hershkowtiz N 1979 *Phys. Fluids* **22** 1171
Goedbloed J P, Pyatak A I and Sizonenko V L 1973 *Sov. Phys. JETP* **37** 2501
Goswami K S and Bujarbarua S 1985 *Phys. Lett.* **A108** 149
Goswami K S and Bujarbarua S 1986 *Phys. Fluids* **29**(3) 714
Goswami K S, Kalita M K and Bujarbarua S 1986 *Plasma Phys.* **28** 289
Hubbard R F and Joyce G 1979 *J. Geophys. Res.* **84** 4297
Kim K Y 1983 *Phys. Lett.* **A97** 45
Kim K Y and Crystal T L 1984 *Proc. of Second Symp. on Plasma double layers and related topics, Innsbruck, Austria; Theory and simulation of ion acoustic double layers* (eds) R Schrittwieser and G Eder
Mohan M and Buti B 1980 *Plasma Phys.* **22** 873
Schamel H 1983 *Z. Naturforsch.* **A38** 1170
Temerin M, Cerney K, Lotko W and Mozer F S 1982 *Phys. Rev. Lett.* **48** 1175
Torven S 1981 *Phys. Rev. Lett.* **A47** 1053

CC-0. In Public Domain. Gurukul Kangri Collection, Haridwar

Digitized by Arya Samaj Foundation Chennai and eGangotri
Pramāna – J. Phys., Vol. 28, No. 4, April 1987, pp. 409–413. © Printed in India.

Refinement of twinned crystal data

SANDHYA BHAKAY-TAMHANE and A SEQUEIRA

Neutron Physics Division, Bhabha Atomic Research Centre, Trombay, Bombay 400 085, India

MS received 11 September 1986; revised 30 January 1987

Abstract. The refinement of structure from diffraction intensities measured from a twinned crystal involves the evaluation of intensity contributions from the various twin domains in the crystal and the corresponding structure factor derivatives. The modifications in the standard least-squares refinement program required for analysis of data from a twinned crystal sample are discussed. The procedure can be extended to cases involving more than two types of twin domains or to samples having mixed phases. The results and limitations of structure refinement using data obtained from a twinned $LiKSO_4$ crystal in various low-temperature phases are illustrated.

Keywords. Twinned structures; pseudosymmetry; intensity addition; mixed phases.

PACS Nos 61·10; 61·70

1. Introduction

Twinning implies the symmetrical union of two crystallites at a composition plane, the two being related by reflection across a plane or rotation about an axis. According to Mallard's empirical theory (Buerger 1945), twinning is probable in a crystal species if the lattice satisfies certain symmetry requirements. Thus if the cell of the lattice or the supercell has higher symmetry than the point group symmetry of the crystal, twinning is likely. Buerger (1947) noted that twins occur with greater frequency in a derivative structure i.e. one which has been derived from a basic structure by suppressing one or more of its symmetry operations.

In diffraction experiments, especially in the study of structural phase transitions, one is frequently forced to record data from twinned samples arising especially in derivative structures. Further, quite often it is not possible to identify the existence of twins from the diffraction photographs particularly in cases involving 'merohedral' twinning (Buerger 1945) or pseudosymmetry. Twins can normally be detected optically under a polarizing microscope if the crystal is non-cubic. Twins can also be detected in diffraction experiments if they show splitting of diffraction profiles or split spots in x-ray photographs. Thus, if the two lattices are sufficiently misoriented, they can be resolved. If however there is no angular misorientation between the crystallites, i.e. if the reciprocal lattices of the twin domains coincide with each other ($\omega = 0$, twins of merohedry), the twins cannot be detected by any of the aforementioned methods. In such a case, although the magnitudes of the structure factors due to the various crystallites may be different yet the physical detection of twins is elusive. The twins

CC-0. In Public Domain. Gurukul Kangri Collection, Haridwar

Digitized by Arya Samaj Foundation Chennai and eGangotri

remain unresolved and one may misjudge point-group symmetry, space group symmetry, the $|F_{hkl}|$'s of the crystal and probably unit cell too.

Analysis of data from a twin crystal as a single crystal would mean the interpretation of a composite set of reciprocal lattices. The observed diffraction intensities would in fact be the sum of intensity contributions from the various segments or 'twin fractions' of the crystal, and the least-squares analysis would mean the refinement of this $|F_{\text{total}}|^2$. The methodology of calculating $|F_{\text{total}}|^2$ for a twin crystal and the modified derivatives required for the least-squares fitting will be discussed in the next section.

2. The procedure

If a crystal has twins with structures A and B, the intensities obtained from the crystal would be the addition of intensity contributions from the twin domains i.e.

$$|F_{\text{total}}(hkl)|^2 = |F_T|^2 = (1-f)|F_A|^2 + f|F_B|^2, \tag{1}$$

where f is the fraction of the twin crystallite B. The derivative of this $|F_T|^2$ with respect to the twin fraction will therefore be $|F_B|^2 - |F_A|^2$ and refinement has to be carried out on $|F_T|^2$.

In calculating the intensities from a twin crystal, $|F_{T,\text{calc}}|^2$, one would ideally like to calculate the intensity contributed by the various crystallites individually, weighted by their volume fractions and then summed up. This would require the introduction of the expected reflection sets due to the twin crystallites into the data set. Recalling the definition

$$|F| = \sum_i b_i a_i \exp\left[2\pi i(hx + ky + lz)\right], \tag{2}$$

we see that one can account for the different hkl contributions from the twinned sample by varying xyz instead of varying hkl. The various sets of atomic positions expected in the twin can thus be introduced in the atoms list—we will then have N_A atoms belonging to the main crystal, N_B atoms belonging to the twin crystal and $N_{\text{sum}} = N_A + N_B$ will be the total list of atoms for the whole sample. Introducing a code number depicting the number of N_A atoms, it is rather a routine calculation to compute $|F_A|^2$ for the N_A atoms and $|F_{\text{sum}}|^2$ for $(N_A + N_B)$ atoms. Then

$$|F_B|^2 = |F_{\text{sum}}|^2 - |F_A|^2, \tag{3}$$

and hence

$$|F_{T,\text{calc}}|^2 = (1-f)|F_A|^2 + f|F_B|^2, \tag{4}$$

and

$$\frac{\partial}{\partial f}|F_{T,\text{calc}}|^2 = |F_B|^2 - |F_A|^2, \tag{5}$$

can be calculated. The starting value of the twin fraction parameter f can be arbitrary and may have to be damped in the initial cycles of least-squares refinement.

In our least-squares refinement program *TRXFLS* (Rajagopal and Sequeira 1977) which is a modified version of *ORGLS* (Busing *et al* 1962), the modifications for structure factor calculations and its derivatives in twin data have been introduced in the subroutine CALC; while a code number indicating the number of atoms in the main crystal and twin crystal has been introduced via a control card. The atoms list has the

CC-0. In Public Domain. Gurukul Kangri Collection, Haridwar

Digitized by Arya Samaj Foundation Chennai and eGangotri

first N_A atoms belonging to the main crystal, the N_B atoms belonging to the twin B are introduced in the atom list after N_A and $N_{sum} = N_A + N_B$ are the total atoms contributing to the intensities.

3. Discussion and conclusions

The approach explained in the earlier section can be extended for calculating intensities from a sample having mixed phases. The contributions from the various phases along with their respective domains and twins (if any) are computed and added with due consideration to phase fraction, domain fraction and twin fraction. The mathematical details, including the associated derivatives, have been worked out in the appendix.

Such an intensity addition has been carried out for reflection data obtained on $LiKSO_4$ at room temperature i.e. in phase PI (Bhakay-Tamhane *et al* 1984). The twins in $LiKSO_4$ were not observable under a polarizing microscope, no split spots were seen in x-ray photographs nor did the diffractometer data (x-ray and neutron) show any split peaks. The room temperature neutron data were corrected for absorption, the structure refinement included anisotropic temperature factors and anisotropic (type II) extinction. Yet the structure could not be refined to a discrepancy factor [$R(F)$] better than 6·53% though the mutual agreement factor for the standard reflections (used for monitoring the stability of the experiment) was better than 3%. Disorder of the SO_4^{-2} ion was ruled out. The data refined to a minimum in the right handed co-ordinate system (xyz); the refinement with the left-handed co-ordinate system (yxz) also converged, but to a higher R-value. A refinement incorporating twinning around the [110] axis (i.e. the xyz and yxz twins) resulted in a drastic fall of $R(F)$ to 3·12%, the relative fractions of the two twin domains refined to 0·790 : 0·210(6). The average error on the fractional atomic positions is $\sim$ 0·0007 while the bond-lengths are accurate to within 0·005 Å with 300 reflections (Bhakay-Tamhane *et al* 1984). In the absence of twinning, for data obtained on the same diffractometer on $(NH_4)_2CuCl_4 \cdot 2H_2O$ (Bhakay-Tamhane *et al* 1980), the refinement gave the respective average errors as 0·0002 and 0·002 Å (on 485 reflections).

The introduction of mixed phases (PI + PII) with each phase showing twins*, further decreased the precision on atomic positions to 0·005, while on bond distances it is just 0·03 Å (Bhakay-Tamhane 1985) the refinement being carried out on 113 reflections. An introduction of mixed phases (PI + PIII) with the PIII phase having three domains mutually rotated by $\sim$ 120° and each domain in PIII having twins along with the ($A + B$) twins in PI, decreases the precisions drastically: 0·02 on atomic positions and 0·10 Å on bond lengths (135 reflections used in refinement) (Bhakay-Tamhane 1985). Some relevant results of all these refinements have been reported earlier (Bhakay-Tamhane and Sequeira 1986).

The addition of intensities and refinement on $|F|^2$ does not prove problematic for neutron data as the starting model is often known from other earlier studies; this facilitates the usage of $|F|^2$ in refinement rather than F. In x-ray studies, one may have to obtain the partial model from refining on F and then move over to the twin model refinement (i.e. use of $|F|^2$). The Fourier synthesis of a twinned crystal, however, will have to be computed with only the main crystal phases (i.e. one with the greater volume fraction) as meaningful phase factors are not possible for the composite crystal.

* Phase PI has $xyz + yxz$ twins, PII has $xyz + xy\bar{z}$ twins and phase PIII also has $xyz + xy\bar{z}$ twins.

CC-0. In Public Domain. Gurukul Kangri Collection, Haridwar

Digitized by Arya Samaj Foundation Chennai and eGangotri

Appendix A

From profile analysis and behaviour of the intensities of *hhl* reflections of $LiKSO_4$ in phase *P*III (for 189 K < T < 165 K), the following logical deductions were reached (Bhakay-Tamhane and Sequeira 1986):

(a) The sample was in a mixed phase *P*I + *P*III (*P*I is the room temperature phase $P6_3$).

(b) The phase *P*III had three distinct domains (manifested as split peaks in data collection) *A*, *B*, *C* based on [100], [010] and [110] of the hexagonal lattice as the undistorted growth directions*.

(c) The phase *P*III was pseudo-orthorhombic Cc with $\gamma \simeq 119{\cdot}2°$.

(d) In *P*I ($P6_3$), $|F(hkl)| \neq |F(khl)|$ and in *P*III (Cc), $|F(hkl)| \neq |F(hk\bar{l})|$. The $|F_{calc}|^2$ from such a sample will thus include intensity contributions from $P6_3$ phase with the *xyz* and *yxz* twins and Cc phase with its *A*, *B*, *C* domains each domain having *xyz* and $xy\bar{z}$ twins.

$$|F_{calc}|^2 = p\{|F_{P6_3}|^2\} + (1-p)\{|F_{Cc}|^2\}, \tag{A1}$$

$$= p\{|F_{P6_3}|^2\} + (1-p)\{m|F_{Cc,A}|^2 + n|F_{Cc,B}|^2 + (1-m-n)|F_{Cc,C}|^2\} \tag{A2}$$

$$= p\{(1-f_1)|F_{xyz}|^2 + f_1|F_{yxz}|^2\}_{P6_3} + (1-p)\{(1-f_2)[m|F_{A(xyz)}|^2 + n|F_{B(xyz)}|^2 + (1-m-n)|F_{C(xyz)}|^2] + f_2[m|F_{A(xy\bar{z})}|^2 + n|F_{B(xy\bar{z})}|^2 + (1-m-n)|F_{C(xy\bar{z})}|^2]\} \tag{A3}$$

where p is the fraction of $P6_3$ phase, f_1 is the fraction of *yxz* twin in $P6_3$ and f_2 is the $xy\bar{z}$ twin in Cc. m and n are the volume fractions of domains *A* and *B*; *C* naturally has the fraction $(1-m-n)$. The $(xy\bar{z})$ twin fraction has been assumed to be the same for all the domains. The derivatives with respect to these new parameters will be:

$$\frac{\partial F^2_{calc}}{\partial f_1} = \left[p\,(F^2_{yxz} - F^2_{xyz})\right]_{P6_3}, \tag{A4}$$

$$\frac{\partial F^2_{calc}}{\partial p} = \left[(1-f_1)F^2_{xyz} + f_1 F^2_{yxz}\right]_{P6_3} - \left[m(1-f_2)F^2_{A(xyz)} + f_2 m F^2_{A(xy\bar{z})} + n(1-f_2)F^2_{B(xyz)} + n f_2 F^2_{B(xy\bar{z})}\right.$$

---

*For domain *A*, based on [100]

$$\vec{a}_M = \vec{a}_H,\ \vec{b}_M = \vec{a}_H + 2\vec{b}_H,\ \vec{c}_M = \vec{c}_H;$$

for domain *B* on [010]

$$\vec{a}_M = \vec{b}_H,\ \vec{b}_M = 2\vec{a}_H + \vec{b}_H,\ \vec{c}_M = \vec{c}_H;$$

and for domain *C* on [110]

$$\vec{a}_M = \vec{a}_H + \vec{b}_H,\ \vec{b}_M = \vec{b}_H - \vec{a}_H,\ \vec{c}_M = \vec{c}_H.$$

CC-0. In Public Domain. Gurukul Kangri Collection, Haridwar

Digitized by Arya Samaj Foundation Chennai and eGangotri

$$+(1-m-n)(1-f_2)F^2_{C(xyz)}+f_2(1-m-n)F^2_{C(xy\bar{z})}\Big]_{Cc}, \quad \text{(A5)}$$

$$\frac{\partial F^2_{calc}}{\partial f_2}=(1-p)\Big[m(F^2_{A(xy\bar{z})}-F^2_{A(xyz)})+n(F^2_{B(xy\bar{z})}-F^2_{B(xyz)})$$

$$+(1-m-n)(F^2_{C(xy\bar{z})}-F^2_{C(xyz)}\Big]_{Cc}, \quad \text{(A6)}$$

$$\frac{\partial F^2_{calc}}{\partial m}=(1-p)\Big[(1-f_2)(F^2_{A(xyz)}-F^2_{C(xyz)})+f_2(F^2_{A(xy\bar{z})}-F^2_{C(xy\bar{z})})\Big]_{Cc}, \quad \text{(A7)}$$

$$\frac{\partial F^2_{calc}}{\partial n}=(1-p)\Big[f_2(F^2_{B(xy\bar{z})}-F^2_{C(xy\bar{z})})+(1-f_2)F^2_{B(xyz)}-(1-f_2)F^2_{C(xyz)}\Big]_{Cc}. \quad \text{(A8)}$$

The quantities must be damped during refinement to prevent any oscillatory behaviour. As the structures are to be represented using common symmetry elements only, suitable symmetry constraints must be introduced. The above prescription, when used for refining $LiKSO_4$ data in phase *P*III gave the following values: $p = 0{\cdot}48(3)$, $f_1 = 0{\cdot}210$ (fixed at room temperature refined value), $m = 0{\cdot}44(7)$, $n = 0{\cdot}40(9)$ and $f_2 = 0{\cdot}50(7)$. The least-squares analysis used 22 variable parameters with 135 reflections up to $(\sin\theta/\lambda) \leqslant 0{\cdot}5$ Å^{-1}.

References

Bhakay-Tamhane S 1985 *Structural investigations of low-temperature phase transitions in $LiKSO_4$ and $(NH_4)_2CuCl_4 \cdot 2H_2O$*, Ph.D. thesis, Univ. of Bombay

Bhakay-Tamhane S and Sequeira A 1986 *Ferroelectrics* **69** 241

Bhakay-Tamhane S, Sequeira A and Chidambaram R 1980 *Acta Crystallogr.* **B36** 2925

Bhakay-Tamhane S, Sequeira A and Chidambaram R 1984 *Acta Crystallogr.* **C40** 1648

Buerger M J 1945 *Am. Mineralogist* **30** 469

Buerger M J 1947 *J. Chem. Phys.* **15** 1

Busing W R, Martin K O and Levy H A 1962 ORGLS: Oak Ridge full matrix least-squares refinement program, Report ORNL-TM-305, Oak Ridge National Laboratory, Tennessee

Rajagopal H and Sequeira A 1977 TRXFLS: Trombay crystallographic full matrix least-squares program, unpublished

CC-0. In Public Domain. Gurukul Kangri Collection, Haridwar

Digitized by Arya Samaj Foundation Chennai and eGangotri

CC-0. In Public Domain. Gurukul Kangri Collection, Haridwar

Digitized by Arya Samaj Foundation Chennai and eGangotri

Pramāṇa – J. Phys., Vol. 28, No. 4, April 1987, pp. 415–424. © Printed in India.

Precession photography of fibres: Prediction of patterns

M SUNDARAMOORTHY
Molecular Biophysics Unit, Indian Institute of Science, Bangalore 560012, India

MS received 21 November 1986; revised 25 February 1987

Abstract. The Buerger precession method of recording x-ray diffraction patterns can also be used for fibres. This method has some advantages over the conventional flat plate method. Since the fibre has inherent cylindrical symmetry, the precession photograph of the fibre is equivalent to the 'rotation-precession' photograph of a single crystal. An analytical prediction of diffraction patterns of the rotation-precession photography is discussed. Also, experimental data are provided to confirm the validity of the equations derived.

Keywords. Fibre; diffraction; precession method; pattern prediction.

PACS No. 61·10

1. Introduction

X-ray diffraction patterns of fibres are generally recorded with flat plate cameras. Occasionally, necessity arises to record the meridional and near meridional reflections in the investigation of fibres. In such instances, fibres are tilted, with respect to the x-ray beam through a particular angle corresponding to the layer of interest. The major disadvantage of this method is that it requires recording of as many photographs as the number of layers and also prior knowledge of the period of repeat along the fibre axis for the calculation of tilt angles. Howsman and Walter (1960) had suggested the application of the well-known Buerger precession method which permits meridional and near-meridional reflections to be recorded on a single photograph. In addition, the precession method results in an undistorted image of the reciprocal lattice (RL). King (1966) analyzed the imaging geometry and related the resolution to the layer line screen parameters and the precession angle. He had developed a graphical method of visualizing the images using the geometrical construction of Buerger (1964). This article presents an analytical approach to constructing diffraction images produced by fibres in the precession geometry. The analysis presented here was developed from an earlier study on the "rotation-precession method" using single crystals (Sundaramoorthy *et al* 1986).

2. Diffraction geometry

The RL of a uniaxial fibre is cylindrically symmetrical about the fibre axis. In other words, the RL of a fibre is made up of rings coaxial with the fibre axis. On the other hand, for a single crystal the RL is made up of discrete points. However, single crystal x-ray diffraction might mimic fibre diffraction on rotating the crystal about a chosen axis. Similarly, precession picture recorded for a fibre is equivalent to a rotation-

CC-0. In Public Domain. Gurukul Kangri Collection, Haridwar

Digitized by Arya Samaj Foundation Chennai and eGangotri

precession photograph of the single crystal. In this paper, we derive analytical expressions describing the image of a rotation-precession or an equivalent fibre precession photograph. We also provide experimental results demonstrating the validity of the derivation and the usefulness of the method.

The normal Buerger precession camera can be used to record the rotation-precession photograph, by additionally allowing the drum to rotate at a speed unrelated to that of the precession motion. The geometry of the experimental set-up is such that: (i) the crystal tilts with respect to the x-ray beam and also it rotates about the spindle axis; (ii) the film precesses about the x-ray beam.

3. Analysis of the rotation-precession method

The precession motion of the film may be decomposed into two tilt components, (a) μ_r about the rotation axis and (b) μ_t, parallel to the rotation axis. When the crystal is exactly perpendicular to the x-ray beam, μ_r is maximum (μ_0), and μ_t is zero. On the other hand, when the crystal is maximally tilted, the film tilt μ_t is also maximum (μ_0) and μ_r is zero. The orientation of the film, during its precession, is decomposed as mentioned, with $\mu_r = \mu_0 \cos\theta$ and $\mu_t = \mu_0 \sin\theta$, where θ is the angle described by the radius vector on the base of the precession cone (The zero of this angle is defined as the position of maximum tilt of the film about the rotation axis.).

The relationships between film coordinates (x, y) and RL coordinates (ξ, ζ) are derived in four steps of increasing complexity:

(a) Crystal and film normal to the x-ray beam.
(b) Crystal perpendicular to the x-ray beam and film tilted by μ_r about the rotation axis.
(c) Crystal and film tilted by μ_t with respect to the x-ray beam.
(d) Crystal and film tilted by μ_t with respect to the x-ray beam and film tilted by μ_r about the rotation axis.

We shall assume that the crystal is continuously rotating about the mounted axis.

4. Crystal and film normal to the x-ray beam

This is the normal rotation photography used for single crystals. The expressions relating (x, y) coordinates and (ξ, ζ) coordinates can be derived with reference to figure 1. In figure 1a Δ^s SMN and SO′N′ are similar, from which

$$x = D\xi/(1-\xi\sin\phi) \tag{1}$$

and pyramids SPMN and SP′N′O′ are similar, from which

$$y = D\zeta/(1-\xi\sin\phi) \tag{2}$$

where

$$\sin\phi = (\zeta^2+\xi^2)/2\xi. \tag{3}$$

Equations (1) and (2) are not linear, which result in the distortion of the recorded

CC-0. In Public Domain. Gurukul Kangri Collection, Haridwar

Digitized by Arya Samaj Foundation Chennai and eGangotri

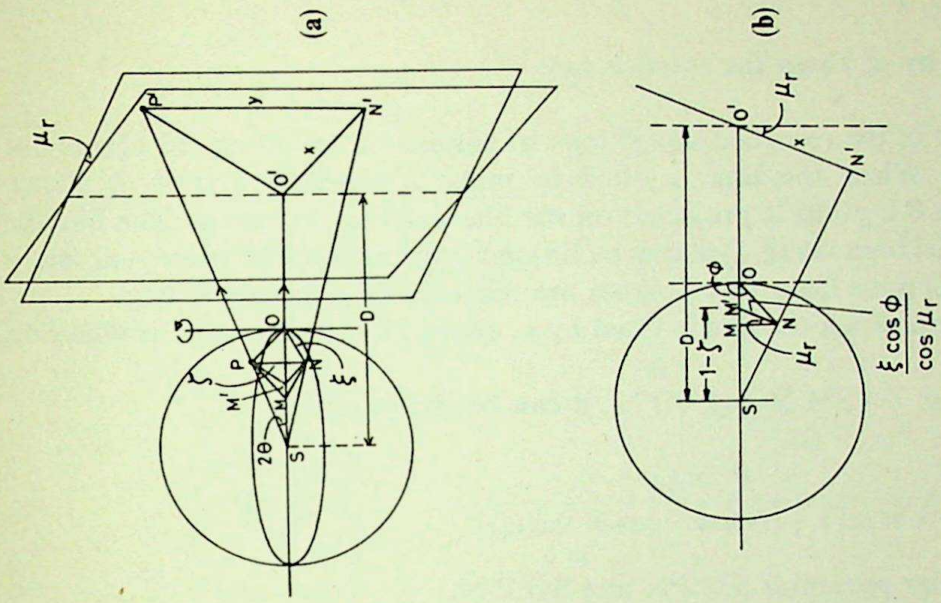

Figure 2. Rotation axis normal to the x-ray beam and film tilted about the rotation axis by μ_r. **(a)** Perspective view. **(b)** Projection perpendicular to the rotation axis.

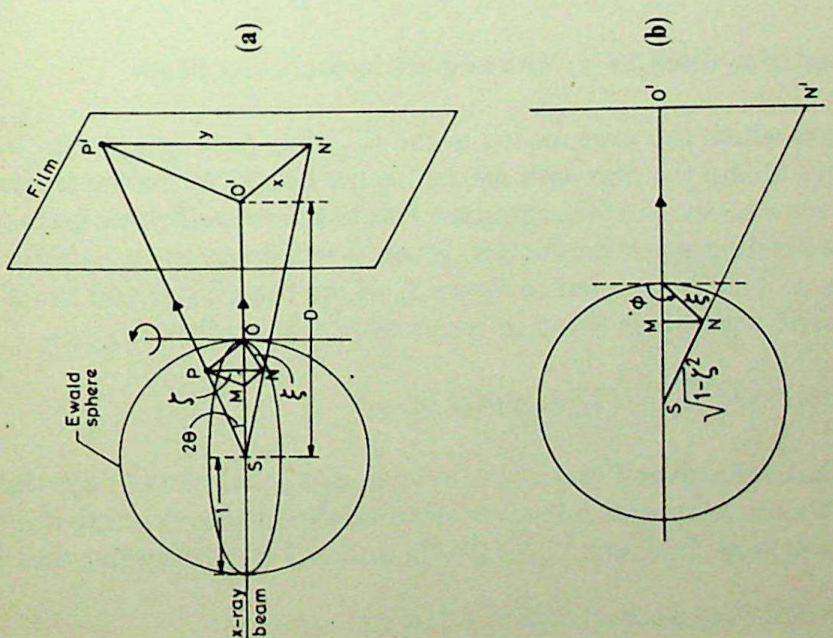

Figure 1. Rotation axis and film normal to the x-ray beam. **(a)** Perspective view. **(b)** Projection perpendicular to the rotation axis.

CC-0. In Public Domain. Gurukul Kangri Collection, Haridwar

Digitized by Arya Samaj Foundation Chennai and eGangotri

RL. Also, from equation (3) it follows that for a given ζ the RL points smaller than $\xi = 1-(1-\zeta^2)^{1/2}$ are not recorded.

5. Film tilted by μ_r about the rotation axis

The distortion of the recorded image may be eliminated by tilting the film about the rotation axis. When the film is tilted to make it parallel to a (ξ, ζ) plane, the corresponding RL point is projected on the film without distortion. The film can be brought parallel to many (ξ, ζ) planes by tilting it continuously between $-\mu_0$ and $+\mu_0$. However, reflections from other planes are recorded in a distorted way.

This situation, when the film is tilted by μ_r about the rotation axis, is illustrated in figure 2.

From similar $\triangle^s$ SM′N and SO′N′, it can be shown that

$$x = \frac{D\xi\cos\phi}{\cos\mu_r[1-\xi(\sin\phi-\cos\phi\cdot\tan\mu_r)]} \tag{4}$$

and from similar pyramids SM′PN and SO′P′N′,

$$y = \frac{D\zeta}{1-\xi(\sin\phi-\cos\phi\tan\mu_r)}. \tag{5}$$

When μ_r varies between $-\mu_0$ and $+\mu_0$ the image of an RL point is a curve described by equations (4) and (5). When $\mu_r = \phi$, ($x = D\xi$ and $y = D\zeta$) the reflection is recorded without distortion, which also lies on the curve.

6. Crystal and film tilted by μ_t with respect to the x-ray beam

The RL points which are unrecorded in the rotation photograph can be recorded by tilting the crystal and the film with respect to the beam. When the crystal is tilted, the RL point which has been just touching the Ewald sphere will either go in or come out of the sphere depending upon the tilt. However, it will come to the surface of the sphere again at new ϕ. This is depicted in figure 3, where the crystal and the film are shown tilted by μ_t. The expression for ϕ in terms of μ_t is given by,

$$\sin\phi = (\zeta^2+\xi^2-2\zeta\sin\mu_t)/(2\xi\cos\mu_t). \tag{6}$$

This shows that, for a given ζ, the minimum value of ξ that can be recorded decreases as μ_t increases. So, the RL points on the rotation axis and those closer to it can be recorded by tilting the crystal. In figure 3, $\triangle^s$ SMN and SQ′N′ are similar and hence

$$x = (D\xi\cos\phi\cos\mu_t)/(\cos\mu_t-\xi\sin\phi) \tag{7}$$

and pyramids SMNP and SQN′P′ are similar and hence,

$$y = \frac{D[\zeta\cos\mu_t-\xi\sin\mu_t\sin\phi]}{\cos\mu_t-\xi\sin\phi}. \tag{8}$$

CC-0. In Public Domain. Gurukul Kangri Collection, Haridwar

Digitized by Arya Samaj Foundation Chennai and eGangotri

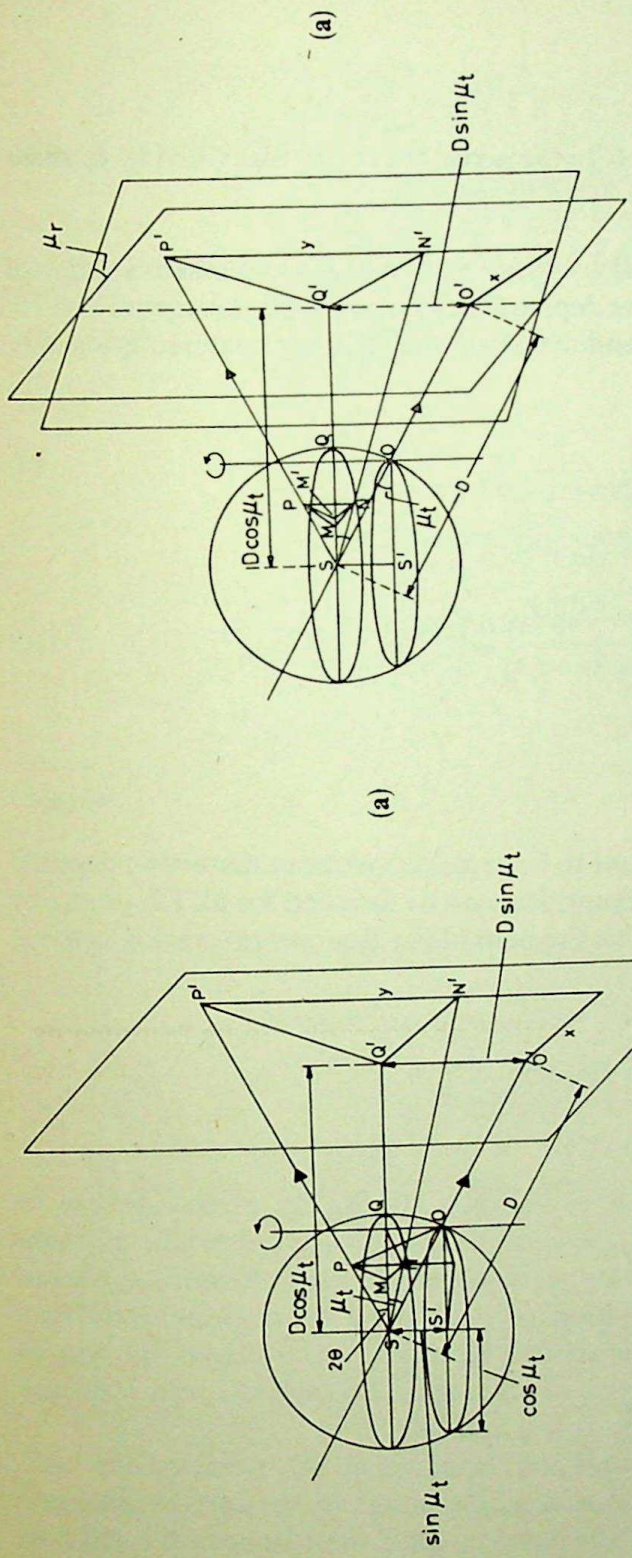

Figure 3. Rotation axis and film tilted with respect to the x-ray beam by μ_r. (**a**) Perspective view. (**b**) Projection perpendicular to the rotation axis.

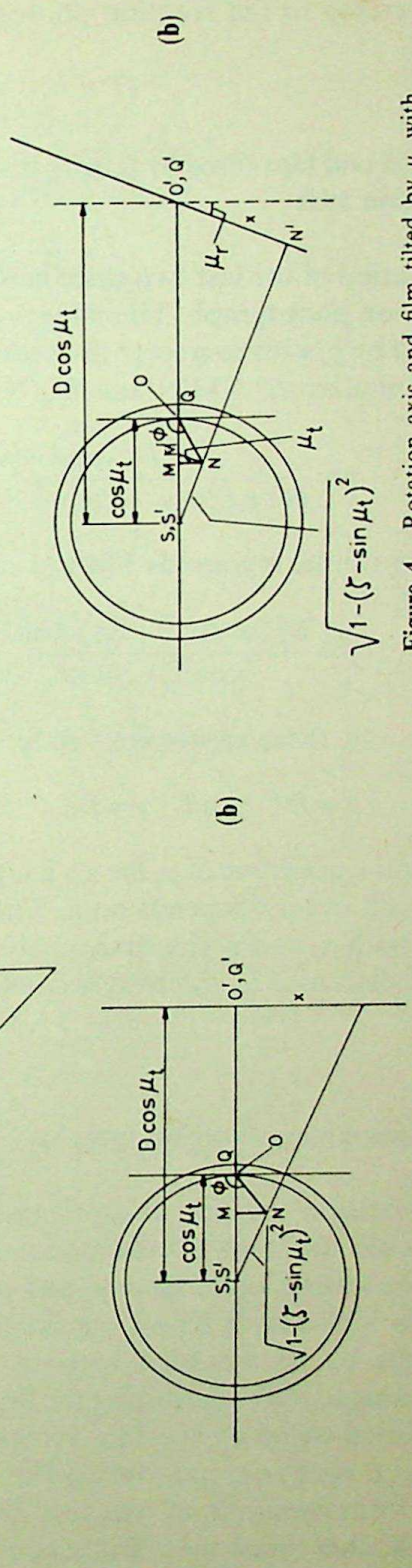

Figure 4. Rotation axis and film tilted by μ_t with respect to the x-ray beam and film tilted by μ_r about the rotation axis. (**a**) Perspective view. (**b**) Projection perpendicular to the rotation axis.

CC-0. In Public Domain. Gurukul Kangri Collection, Haridwar

Digitized by Arya Samaj Foundation Chennai and eGangotri

When μ_t varies between $-\mu_0$ and $+\mu_0$ the image of an RL is recorded in a curve according to (7) and (8), which, when $\mu_t = 0$, reduce to equations (1) and (2) respectively, corresponding to the rotation photography.

7. Crystal and film tilted by μ_t with respect to the x-ray beam and film tilted by μ_r about the rotation axis

Combination of the last two cases simultaneously eliminates the two disadvantages of the rotation photograph. This situation is depicted in figure 4, with the crystal and the film tilted by μ_t with respect to the beam and the film tilted by μ_r about the rotation axis.

From similar $\triangle^s$ SM′N and SQ′N′,

$$x = \frac{D\xi \cos\phi \cos\mu_t}{\cos\mu_r[\cos\mu_t - \xi(\sin\phi - \cos\phi \tan\mu_r)]} \tag{9}$$

and from similar pyramids SM′PN and SQ′P′N′,

$$y = \frac{D[\zeta \cos\mu_t - \xi \sin\mu_t(\sin\phi - \cos\phi \tan\mu_r)]}{[\cos\mu_t - \xi(\sin\phi - \cos\phi \tan\mu_r)]}. \tag{10}$$

When $\mu_r = \phi$, these expressions reduce to

$$x = D\xi \quad \text{and} \quad y = D\zeta. \tag{11a, b}$$

The optimum value of μ_r for an RL point to be recorded without distortion depends on ϕ, which in turn depends on μ_t. This condition can be satisfied for all RL points by varying both μ_r and μ_t simultaneously with the help of the Buerger precession camera, which is discussed in the next section.

8. Rotation-precession photography

In a precession camera, the orientation of the film during its precession can be decomposed into two tilt components, $\mu_r = \mu_0 \cos\theta$ and $\mu_t = \mu_0 \sin\theta$, where μ_0 is the precession setting angle. Both μ_r and μ_t vary, with μ_r being maximum when μ_t is 0 and vice versa. This makes it possible to bring the film to required orientations for different RL points to be recorded without distortion. However, each RL point will be contributing to its image during the full cycle of precession. So each RL point is imaged into a closed curve on the film according to (9) and (10).

Rotation of the crystal, during the precession, brings each RL point on the "zero plane" at one moment, at which it produces a single image in the correct place and during all other times, the point lies out of the plane giving double images. When it does not lie on the zero plane, it can be considered as lying on higher planes. When a zero layer screen is used these higher plane image points are cut off and only zero plane image points are recorded. The resulting photograph is an overlapped-undistorted photograph of all zero planes. These aspects are discussed by King (1966) in detail.

CC-0. In Public Domain. Gurukul Kangri Collection, Haridwar

Digitized by Arya Samaj Foundation Chennai and eGangotri

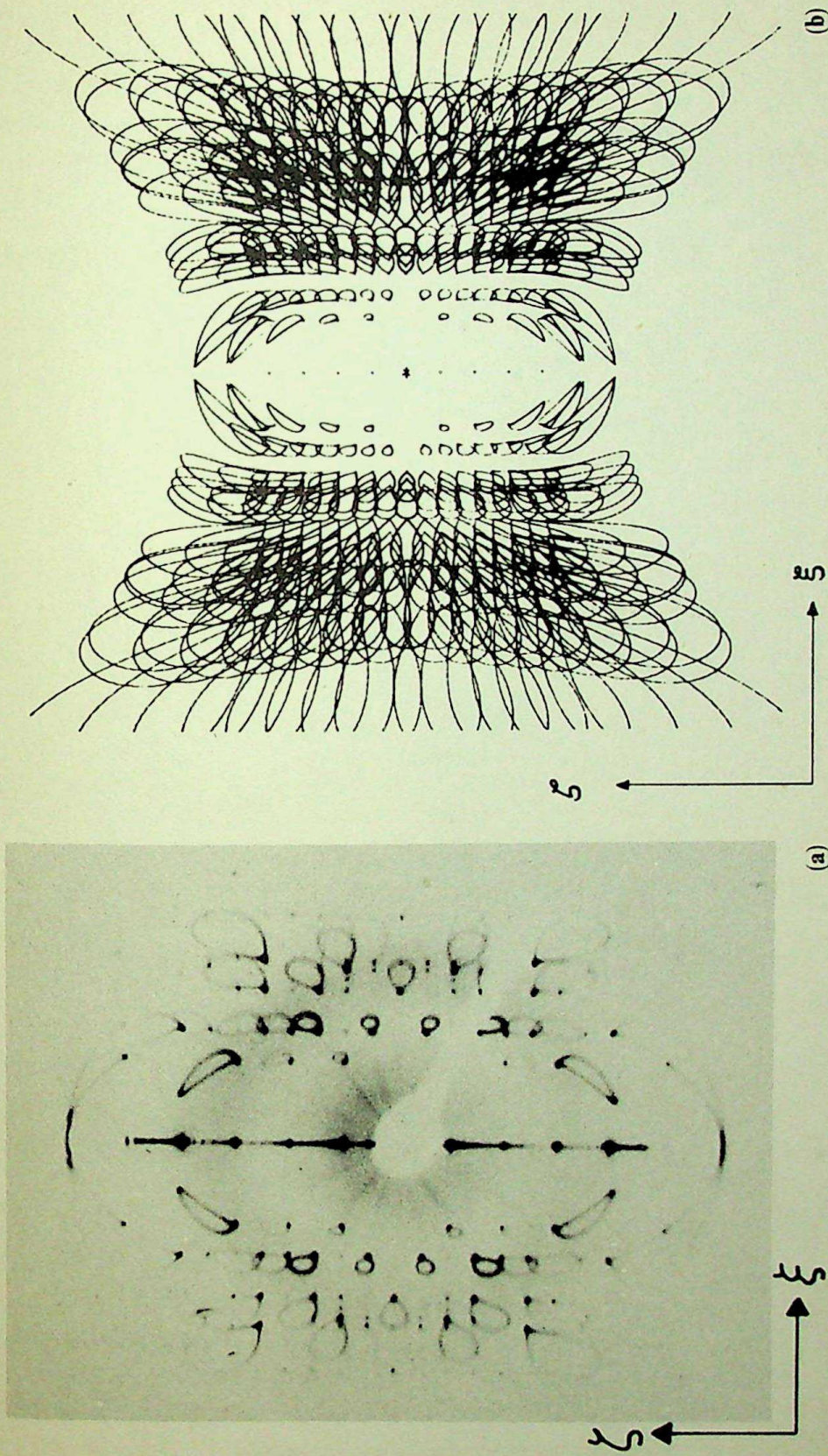

Figure 5. Screenless rotation-precession pattern of crystal of glycyl-DL-phenylalanine (CuK_α, $\lambda = 1{\cdot}5418$ Å; crystal to film distance = 60·0 mm). (a) Experimental (b) Calculated.

CC-0. In Public Domain. Gurukul Kangri Collection, Haridwar

Digitized by Arya Samaj Foundation Chennai and eGangotri

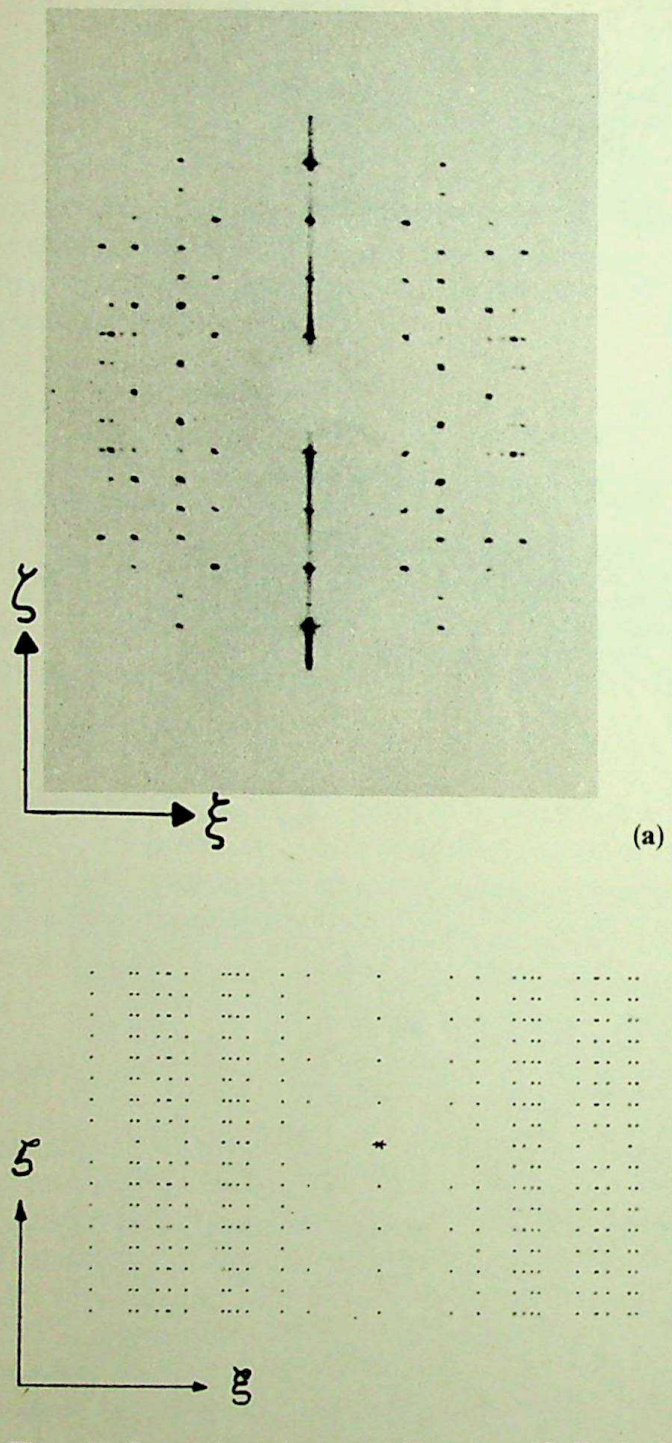

Figure 6. Screened rotation-precession pattern (CuK_α, $\lambda = 1{\cdot}5418$ Å; crystal to film distance $= 60{\cdot}0$ mm; zero level screen radius $= 10{\cdot}0$ mm). (**a**) Experimental. (**b**) Calculated.

CC-0. In Public Domain. Gurukul Kangri Collection, Haridwar

Digitized by Arya Samaj Foundation Chennai and eGangotri

9. Experimental verification

The theory presented in this paper has been tested with experiments on a crystal of glycyl-DL-phenylalanine (Space Group: P_{bca}; $a=9{\cdot}241(2)$ Å, $b=28{\cdot}91(2)$ Å and $c=8{\cdot}602(2)$ Å.) (Marsh *et al* 1976). The crystal has been mounted on the precession camera (make: Huber, D 8211 Rimsting, Germany) with the crystal to film distance of 60 mm. It has been well aligned to the accuracy of 0·1° on both the arcs to ensure that there is no splitting of reflections due to the misalignment of the crystal. The precession motion of the film has been coupled with the oscillation motion of the crystal in the plane containing the x-ray beam and the spindle axis. In addition, the crystal has been rotated continuously about the spindle axis. The crystal has been exposed with CuK_α radiation ($\lambda=1{\cdot}5418$ Å) filtered with Ni filter.

Figure 5a shows the screenless rotation-precession photograph of the crystal rotated about b-axis with 15° precession. Figure 5b shows the simulated rotation-precession pattern using (9) and (10). Figure 6a shows the screened rotation-precession photograph of the crystal and figure 6b is the calculated pattern with the condition

$$\mu_r=\sin^{-1}\left[\frac{\zeta^2+\xi^2-2\zeta\sin\mu_t}{2\xi\cos\mu_t}\right]. \tag{12}$$

The similarity of experimentally recorded photographs and analytically constructed patterns, both with and without screen, confirms the correctness of the expressions.

Systematic absences of the space group have been avoided in the simulated patterns. Although the geometry of the reflections is identical in both experimental and calculated patterns, the intensities of the reflections unavoidably differ. The intensities of the reflections in the experimental patterns depend on the nature of the atoms present in the unit cell. This variation was not incorporated in the calculations.

10. Conclusions

The reflections in the screened 'rotation-precession' photograph are distributed in equally-spaced straight layers, making the measurements and calculations easier, which, otherwise, would be distributed in unevenly spaced hyperbolic layers in a rotation photograph (Buerger 1966). Also, it contains reflections corresponding to small ξ values including those observed in the rotation photograph. These features have been observed in the photographs of DNA fibres also. For example, meridional reflections have been observed on the fourth and sixth layers of the precession photograph of B-DNA fibre, which are missing in the flat plate photograph. The application of the precession method for the DNA fibres and finer details obtained from the photographs are discussed in detail by Sundaramoorthy *et al* (1986).

Acknowledgements

The author thanks Prof. V Sasisekharan for his guidance and encouragement, Dr M R N Murthy for valuable discussions and Mr N Srinivasan for his help in

CC-0. In Public Domain. Gurukul Kangri Collection, Haridwar

Digitized by Arya Samaj Foundation Chennai and eGangotri

computer plotting. The author also thanks the Department of Science and Technology (India) for a fellowship.

References

Buerger M J 1964 *The precession method in x-ray crystallography* (New York: John Wiley)

Buerger M J 1966 *X-ray crystallography* (New York: John Wiley) p. 93

Howsman J A and Walter N M 1960 *Physical methods in chemical analysis* (ed.) W G Berl (New York: Academic Press) Vol. 1, p. 129

King M V 1966 *Acta Crystallogr.* **21** 629

Marsh R E, Ramakumar S and Venkatesan K 1976 *Acta Crystallogr.* **B32** 66

Sundaramoorthy M, Parrack P K and Sasisekharan V 1986 *Biomolecular Stereodynamics* (eds) R H Sarma and M H Sarma (New York: Adenine press) Vol. 4, p. 217

CC-0. In Public Domain. Gurukul Kangri Collection, Haridwar

Digitized by Arya Samaj Foundation Chennai and eGangotri

Pramāṇa–J. Phys., Vol. 28, No. 4, April 1987, pp. L425–L427. © Printed in India.

An "EPR" study of $YBa_2Cu_3O_7$ and related high-temperature superconductors**

S V BHAT†, P GANGULY and C N R RAO*

Solid State and Structural Chemistry Unit and †Department of Physics, Indian Institute of Science, Bangalore 560 012, India

MS received 31 March 1987

Abstract. Besides a $g \approx 2$ signal which disappears on cooling to the superconducting T_c, $YBa_2Cu_3O_7$ and related oxides show a near-zero-field signal in the superconducting state with certain unusual features attributable to a "superconducting glassy state".

Keywords. High-temperature superconductivity; $YBa_2Cu_3O_7$.

PACS No. 74·70

High-temperature superconductors of the Y-Ba-Cu-O system with T_c in the 100 K range, discovered in the last few weeks (Ganguly *et al* 1987; Mohan Ram *et al* 1987; Rao *et al* 1987; Wu *et al* 1987) have created much expectation. These materials with characteristics of type II superconductors and high upper critical fields (> 50 T), are good candidates for "EPR" investigations, especially since EPR studies of bulk superconductors have not been reported extensively in the literature. In this communication, we make a preliminary report on some novel EPR results on the monophasic perovskites $YBa_2Cu_3O_7$ and $Y_{0.75}Lu_{0.25}Ba_2Cu_3O_7$ showing the onset of superconductivity above 100 K and zero-resistance well above 77 K.

The superconducting oxides were prepared by the solid state reaction of the component oxides in air at ~ 1200 K. The resulting oxides were tested for phasic purity by x-ray diffraction. The oxides were then annealed in flowing oxygen around ~ 1100 K. EPR experiments were carried out with a Varian E-109 spectrometer (X-band) on powdered samples.

$YBa_2Cu_3O_7$ shows an asymmetric signal at $g \approx 2$ at 300 K which becomes extremely broad in the superconducting state and cannot be detected (figure 1). More interesting is the observation of a signal near zero-field in the superconducting state (figure 2). This signal is very strong and narrow (compared to the $g \approx 2$ signal at 300 K). The lineshape of the signal is nearly Lorentzian, but asymmetric. The signal disappears on warming the sample to the superconducting transition temperature, accompanied by a phase reversal (see figure 2). The temperature variation of the intensity provides an order parameter of the transition.

*To whom all correspondence should be addressed.

**Contribution No. 443 from Solid State and Structural Chemistry Unit.

CC-0. In Public Domain. Gurukul Kangri Collection, Haridwar

Digitized by Arya Samaj Foundation Chennai and eGangotri

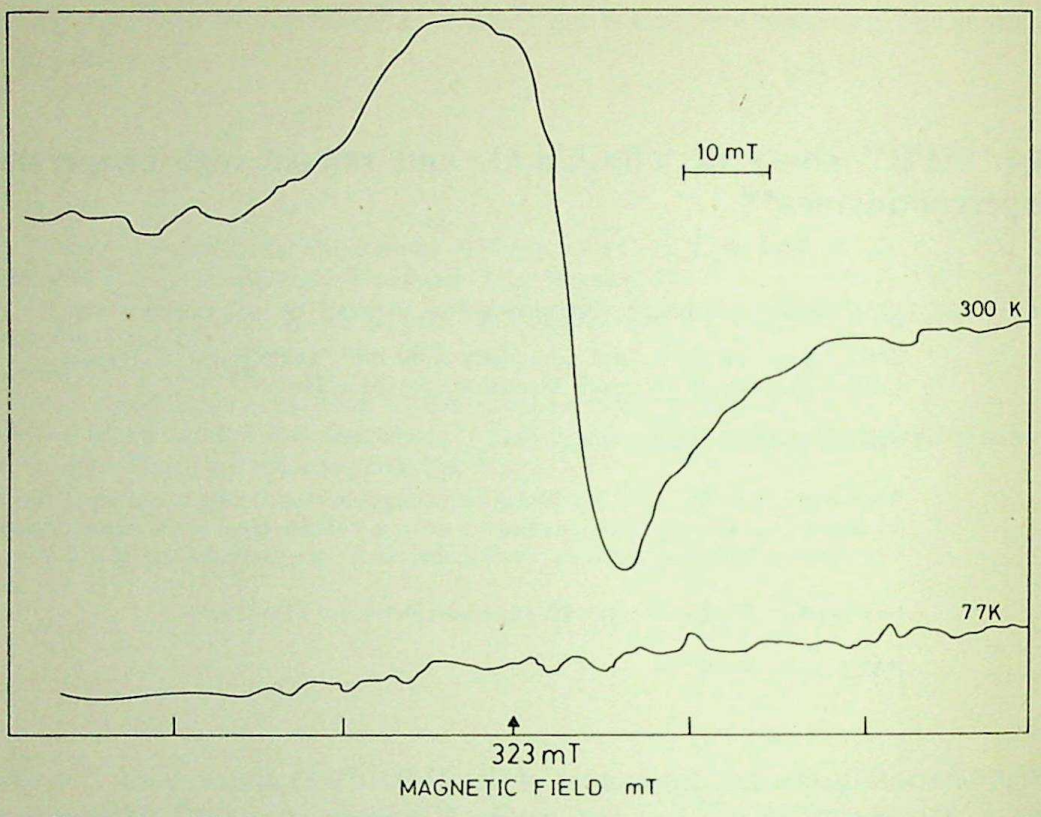

Figure 1. "EPR" of $YBa_2Cu_3O_7$ showing a $g \approx 2$ signal at room temperature; the signal is not detectable at 77 K.

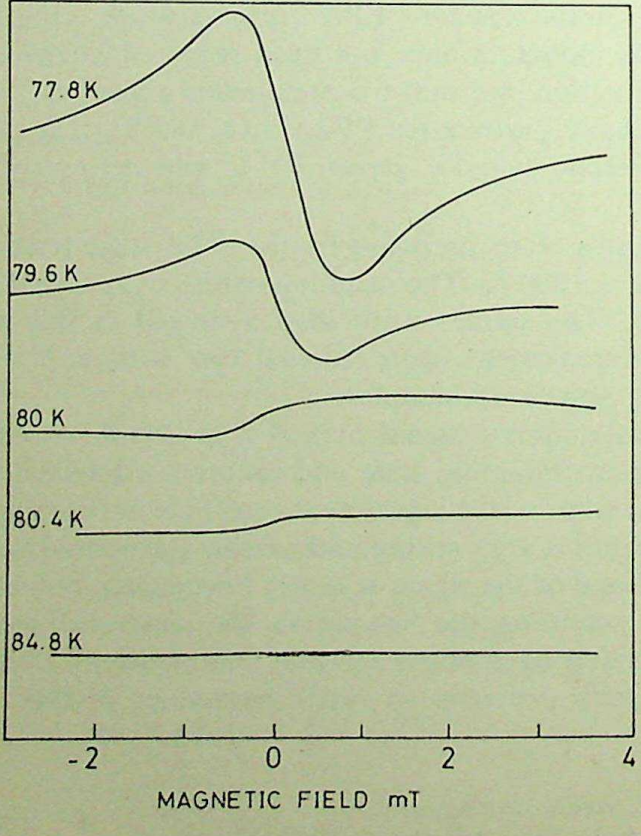

Figure 2. Near-zero-field signal of $YBa_2Cu_3O_7$ as a function of temperature.

CC-0. In Public Domain. Gurukul Kangri Collection, Haridwar

Digitized by Arya Samaj Foundation Chennai and eGangotri

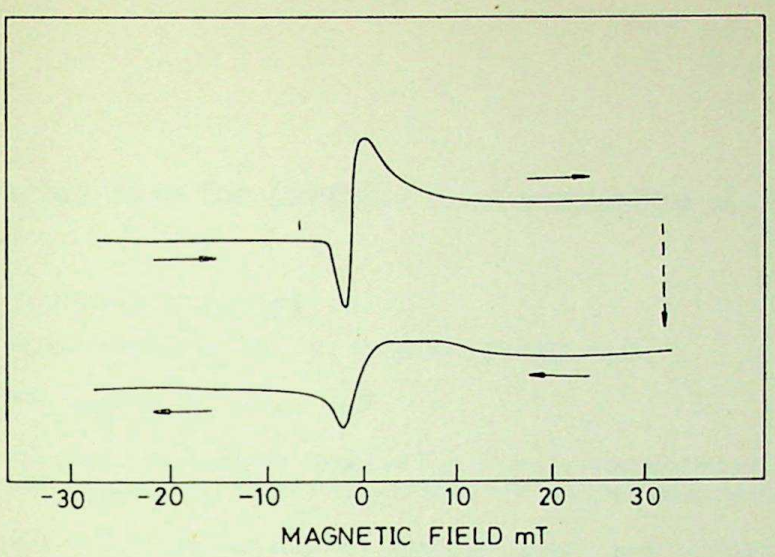

Figure 3. Lineshapes of the near-zero-field signal of $YBa_2Cu_3O_7$ in the forward and reverse field sweeps.

The lineshape of the near-zero-field signal shows pronounced differences in the forward and reverse sweep directions (figure 3). We have found a similar behaviour in the case of $Y_{0.75}Lu_{0.25}Ba_2Cu_3O_7$ which shows the signal in opposite phases in the forward and reverse sweep directions.

The observation of the near-zero-field signal as well as its unusual features can be broadly interpreted in terms of the presence of a triplet state or as due to collective excitations associated with antiferromagnetically coupled states. A more likely explanation however appears to be that based on the superconductive glass model (Ebner and Stroud 1985). This model predicts a maximum in static susceptibility close to zero field. The hysteresis effects in figure 3 are what would qualitatively be expected for a sample made up of a large number of superconducting grains of various sizes. The superconducting glassy state has been invoked by Müller *et al* (1987) to explain the magnetic properties of $La_{2-x}Ba_xCuO_4$.

Detailed "EPR" studies on these high-temperature oxide superconductors are in progress, especially to find out whether the zero-field signal is truly intrinsic to these materials.

The authors thank the University Grants Commission and the Department of Science and Technology for support of this research.

References

Ebner C and Stroud A 1985 *Phys. Rev.* **B31** 165

Ganguly P, Mohan Ram R A, Sreedhar K and Rao C N R 1987 *Pramana—J. Phys.* **28** 321

Mohan Ram R A, Sreedhar K, Raychaudhuri A K, Ganguly P and Rao C N R 1987 *Philos. Mag. Lett.* (in print)

Müller K A, Takashige M and Bednorz J G 1987 *Phys. Rev. Lett.* **58** 1143

Rao C N R, Ganguly P, Raychaudhuri A K, Mohan Ram R A and Sreedhar K 1987 *Nature (London)* (in print)

Wu M K, Ashburn J R, Torng C J, Hor P H, Meng R L, Gao L, Huang Z J, Wang Y Q and Chu C W 1987 *Phys. Rev.* **58** 908

CC-0. In Public Domain. Gurukul Kangri Collection, Haridwar

Digitized by Arya Samaj Foundation Chennai and eGangotri

CC-0. In Public Domain. Gurukul Kangri Collection, Haridwar

Digitized by Arya Samaj Foundation Chennai and eGangotri

Pramāṇa–J. Phys., Vol. 28, No. 4, April 1987, pp. L429–L432. © Printed in India.

A Lagrangian basis for Ashtekar's reformulation of canonical gravity

JOSEPH SAMUEL
Raman Research Institute, Bangalore 560 080, India

MS received 30 January 1987

Abstract. A manifestly covariant Lagrangian is presented which leads to the reformulation of canonical general relativity using new variables recently discovered by Ashtekar.

Keywords. General relativity; canonical gravity; new variables; Lagrangian formulation.

PACS No. 04·60

In the constrained Hamiltonian formulation of general relativity, as developed by Dirac and others, the basic variables are the three-metric on a spatial slice and the extrinsic curvature. Both of these have a direct geometrical interpretation, but this choice of variables leads to complicated, non-polynomial constraints, which no one has been able to consistently carry over to the quantum theory. Recently, starting from the Hamiltonian formulation of gravity in the triad formalism, Ashtekar (1986) has performed a canonical transformation to a new set of variables, which leads to a dramatic simplification of the constraints of the theory. The new variables consist of a soldering form and the Ashtekar-Sen-Witten connection. This reformulation of canonical gravity is explained in the references quoted below. It raises hopes of arriving at a consistent quantum theory of gravity and is of considerable interest in its own right.

The basic variables in Ashtekar's formulation are a canonically conjugate pair $(\tilde{\sigma}^a, A_a)$:

$$\{\tilde{\sigma}^a, \tilde{\sigma}^b\} = \{A_a, A_b\} = 0$$

$$\{A_a, \tilde{\sigma}^b\} = \delta_a^b, \tag{1}$$

$\tilde{\sigma}^a$ is a densitized soldering form and has information about the three-metric on a spatial slice. A_a is a complex SU(2) connection which has information about the extrinsic curvature of a spatial slice. With the SU(2) indices in, these objects are $\tilde{\sigma}^a_{AB}$ and A_a^{AB}. $\tilde{\sigma}^a_{AB}$ is a Hermitean, traceless 2×2 matrix. In terms of these variables, the constraints of general relativity assume a strikingly simple form. They are

(i) The "Gauss law" constraint

$$\mathcal{D}_a\tilde{\sigma}^a \approx 0, \tag{2}$$

CC-0. In Public Domain. Gurukul Kangri Collection, Haridwar

Digitized by Arya Samaj Foundation Chennai and eGangotri

where $\mathcal{D}_a$ is the covariant derivative operator corresponding to the Ashtekar-Sen-Witten connection A_a,
(ii) the vector constraint

$$\mathrm{Tr}(\tilde{\sigma}^a F_{ab}) \approx 0, \tag{3}$$

where F_{ab} is the curvature of the connection A_a and
(iii) the scalar constraint

$$\mathrm{Tr}(\tilde{\sigma}^a \tilde{\sigma}^b F_{ab}) \approx 0. \tag{4}$$

The Hamiltonian is (as in all reparametrization-invariant theories) a linear combination of the constraints. The classical evolution of the system is then determined by Hamilton's equations. Thus, equations (1)–(4) completely describe Ashtekar's theory.

As is clear from the last paragraph, the new formulation is cast in Hamiltonian language. While this is ideally suited for purposes of quantization, it lacks manifest four-dimensional covariance. It would be of some interest to derive the formulation from a covariant Lagrangian. This is the purpose of this note. A set of basic variables is postulated and a manifestly covariant Lagrangian formed out of these. A straightforward application of Dirac's procedure for singular Lagrangians leads to a constrained Hamiltonian theory identical in content to Ashtekar's. Details will appear elsewhere. For background and notation, see the references at the end of the paper.

The basic variables used are a real SL(2, C) valued connection 1-form A_μ and a Hermitean, matrix valued 1-form γ_μ. With the SL(2, C) indices in, these objects are A_μ^{AB} and $\gamma_\mu^{AA'}$. [A, B are Weyl spinor indices and take values 1, 2. Primed indices transform according to the complex conjugate representation of SL(2, C)]. A_μ^{AB} is a connection and so transforms inhomogeneously under local SL(2, C) rotations, whereas $\gamma_\mu^{AA'}$ transforms homogeneously. From these objects one can construct the curvature 2-form

$$F_{\mu\nu}^{AB} \equiv \partial_\mu A_\nu^{AB} - \partial_\nu A_\mu^{AB} + [A_\mu, A_\nu]^{AB}$$

and the antisymmetric tensor

$$\underset{\sim}{\Sigma}_{\mu\nu}^{AB} \equiv i(\gamma_\mu{}^{AA'} \gamma_{\nu A'}{}^{B} - \gamma_\nu{}^{AA'} \gamma_{\mu A'}{}^{B})$$

The trace (over internal indices) of the wedge product of Σ and F is a 4-form and can be integrated over space-time to produce a general coordinate scalar. We postulate the Action

$$I = \int \underset{\sim}{\Sigma}_A{}^B \wedge F_B{}^A \tag{5}$$

which is manifestly generally covariant and invariant under local SL(2, C) transformations.

By using the Levi-Civita tensor density $\tilde{\tilde{\eta}}^{\mu\nu\alpha\beta}$ ($\tilde{\tilde{\eta}}^{\mu\nu\alpha\beta} = \tilde{\tilde{\eta}}^{[\mu\nu\alpha\beta]}$, $\tilde{\tilde{\eta}}^{0123} = 1$), one can write the Action (5) as the integral of Lagrangian density

$$I = \int \mathrm{d}^4x \tilde{\mathcal{L}} = \tfrac{1}{2} \int \mathrm{d}^4x \tilde{\tilde{\eta}}^{\mu\nu\alpha\beta} \mathrm{Tr}(\underset{\sim}{\Sigma}_{\mu\nu} F_{\alpha\beta}). \tag{6}$$

CC-0. In Public Domain. Gurukul Kangri Collection, Haridwar

Digitized by Arya Samaj Foundation Chennai and eGangotri

(In future, we drop the internal indices and use more compact matrix notation). We now take (6) as the starting point and in a straightforward manner apply Dirac's analysis for singular Lagrangians. The Lagrangian can be written in 3 + 1 form as

$$L = \int \mathrm{d}^3x\, \tilde{\eta}^{abc}\{\mathrm{Tr}(\dot{\underline{\Sigma}}_{bc} F_{0a}) + \mathrm{Tr}(\dot{\underline{\Sigma}}_{0a} F_{bc})\}. \tag{7}$$

Defining the canonical momenta as usual

$$\pi^0 \equiv \partial L/\partial \dot{A}_0 = 0, \quad \psi^0 \equiv \partial L/\partial \dot{\gamma}_0 = 0,$$

$$\pi^a \equiv \partial L/\partial \dot{A}_a = \tilde{\eta}^{abc}\dot{\underline{\Sigma}}_{bc}, \quad \psi^a \equiv \partial L/\partial \dot{\gamma}_a = 0,$$

we find the following primary constraints

$$\pi^0 \approx 0, \tag{8}$$

$$\psi^0 \approx 0, \tag{9}$$

$$\psi^a \approx 0, \tag{10}$$

$$\pi^a - \tilde{\eta}^{abc}\dot{\underline{\Sigma}}_{bc} \approx 0. \tag{11}$$

Let us define

$$\tilde{\sigma} \equiv \tilde{\eta}^{abc}\dot{\underline{\Sigma}}_{bc}. \tag{12}$$

Since the γ's are supposed Hermitean, it follows from the definition that $\tilde{\sigma}^a$ is traceless and Hermitean. The constraint (11) now reads

$$\varphi^a \equiv \pi^a - \tilde{\sigma}^a \approx 0. \tag{13}$$

With the usual Poisson bracket structure between the canonically conjugate pairs (A_μ, π^μ), (γ_μ, ψ^μ), we find that ψ^0 and π^0 commute with all the constraints. φ^a depends on γ_b through $\tilde{\sigma}^a$ and so has a non-vanishing bracket with some of the ψ^a's. The remaining ψ^a's commute with all constraints and are so first class.

The Hamiltonian of the theory, given by $H = p\dot{q} - L$, is

$$H = \int \mathrm{d}^3x\, \mathrm{Tr}\{\tilde{\sigma}^a(\partial_a A_0 + [A_0, A_a]) - \dot{\underline{\Sigma}}_{0a} F_{bc}\tilde{\eta}^{abc}\} + \text{constraints}. \tag{14}$$

We now demand the preservation in time of the first class constraint (8). This leads to the Gauss law constraint (2). (Throughout this paper we drop surface terms; they are important, but not for this calculation.) The Hamiltonian now is

$$H = -\int \mathrm{d}^3x\, \tilde{\eta}^{abc}\,\mathrm{Tr}(\dot{\underline{\Sigma}}_{0a} F_{bc}) + \text{constraints}. \tag{15}$$

Next we demand that the first class constraint (9) is preserved in time. This leads to the constraint

$$i\tilde{\eta}^{abc}[\gamma_a, F_{bc}] \approx 0 \tag{16}$$

and modulo (16) the Hamiltonian vanishes. Since the Hamiltonian is now zero (and so certainly first class!), the constraint analysis ends. No new constraints emerge. The Hamiltonian is a linear combination of constraints. The content of (16) can be extracted by multiplying with γ's and taking the trace. Multiplying (16) by γ_b and tracing yields the vector constraint (3). Multiplying (16) by $i\tilde{\eta}^{def}\gamma_d\gamma_e\gamma_f$ and tracing yields the scalar constraint (4).

CC-0. In Public Domain. Gurukul Kangri Collection, Haridwar

Digitized by Arya Samaj Foundation Chennai and eGangotri

The constraints of the theory now are (8, 9, 10, 11) and (2, 3, 4). Let us denote by Γ_0 the initial phase space spanned by $(A_\mu, \pi^\mu, \gamma_\mu, \psi^\mu)$ endowed with the natural sympletic form:

$$\omega_0 = \mathrm{d}\pi^\mu \wedge \mathrm{d}A_\mu + \mathrm{d}\psi^\mu \wedge \mathrm{d}\gamma_\mu. \tag{17}$$

[An integral over space is understood in (17) and (18).] We now impose constraints (8, 9, 10, 11). These define a submanifold $\mathcal{M} \subset \Gamma_0$. The pull-back of the two form (17) to $\mathcal{M}$ is

$$\omega = \mathrm{d}\tilde{\sigma}^a \wedge \mathrm{d}A_a. \tag{18}$$

This form on $\mathcal{M}$ is, of course, degenerate. Vector fields in its kernel are generators of "gauge" transformations. Let us quotient $\mathcal{M}$ with respect to these "gauge" transformations. The quotient space Γ is a symplectic manifold spanned by the coordinates $(\tilde{\sigma}^a, A_a)$ and endowed with the *non-degenerate* symplectic form (18) (now regarded as a form on Γ).

From (18) we see that Γ is spanned by the variables σ^a and A_a which are canonically conjugate to each other. $\tilde{\sigma}^a$ is a Hermitean, traceless matrix and the real $SL(2, C)$ connection A_a can also be viewed as a complex $SU(2)$ connection. The theory now consists of canonically conjugate (1) variables $(\tilde{\sigma}^a, A_a)$ and the constraints (2, 3, 4). Thus the manifestly covariant Lagrangian (5) completely reproduces Ashtekar's theory. A remarkable feature of the Lagrangian (5) is that it is polynomial.

Acknowledgements

It is a pleasure to thank Abhay Ashtekar from whom I learnt about the new formulation of canonical gravity. I have also had the benefit of some unpublished notes by Paul Renteln, a collection of appendices from his Ph.D. thesis. I thank Rajaram Nityananda for reading through the manuscript and making a number of suggestions.

I understand that Ted Jacobson and Lee Smolin have also addressed and solved the problem discussed here.

References

Ashtekar A 1986 *Phys. Rev. Lett.* **57** 2244

Ashtekar A 1986 Paper presented at the Florence Conference on Constrained Systems

Ashtekar A 1986 A new Hamiltonian formulation of general relativity, Syracuse preprint

Arnowitt R, Deser S and Misner C W 1962 *Gravitation: Introduction to current research* (ed.) L Witten (New York: Wiley)

Dirac P A M 1958 *Proc. R. Soc. (London)* **A246** 326, 333

Dirac P A M 1964 *Lectures on quantum mechanics*, Belfer Graduate School of Science, Yeshiva University (New York: Academic Press)

Kuchar K 1981 *Canonical methods of quantization in quantum gravity* (eds) C J Isham, R Penrose and D W Sciama (Oxford: Clarendon) 2nd ed.

CC-0. In Public Domain. Gurukul Kangri Collection, Haridwar

Digitized by Arya Samaj Foundation Chennai and eGangotri

गुरुकुल कांगड़ा विश्वविद्यालय
हरिद्वार

FOREWORD

The second Indo-Soviet Conference on Low Temperature Physics was held at the Institute for Physical Problems of the Academy of Sciences of USSR, Moscow, from 15–25 May 1986. It coincided with the 50 years of that famous Institute started by Academician (late) P. L. Kapitza in 1936. Academician A. S. Borovik-Romanov, the present Director of the Institute, was the organizer of the conference from the Soviet side.

Ten scientists attended the conference from India and the Soviet participation was restricted to about 25. The scientific programme consisted of about a dozen reports from the Indian side and about 18 from USSR. The extensive discussions at the end or during each paper and the consequent extension of the session time were indicators of the interest and utility of the conference. The success of the first and the second Indo-Soviet conferences on low temperature physics made the participants feel the need to have another binational conference with a gap of about two years. It was felt that one could move on to a specialized theme in low temperature phenomena, instead of covering the whole canvas of low temperature studies.

In the present conference, there was inevitably a spectrum of presentations, some giving original new results and some reviewing a particular topic, while some are directed towards theoretical questions and some towards practical applications. The interplay among all these features was also clearly evident. To list the topics in superconductivity, magnetism, quantum fluids, disordered systems, metals and so on would be pointless. Low temperature physics, either as a study in its own right or as a tool to understand other phenomena, has interconnections with almost all branches of condensed matter and quantum phenomena.

The papers published in this special issue are the revised versions of the presentations in the conference. Unfortunately many soviet colleagues could not complete their task by the deadlines set; so a few abstracts and a few full papers alone were available for printing. Nevertheless the publication in a journal is not only a felicitation to the Institute of Physical Problems and the Indo-Soviet cooperation but also a record of the progress which will benefit a wider audience.

E. S. R. GOPAL and
S. RAMASESHAN

CC-0. In Public Domain. Gurukul Kangri Collection, Haridwar

Digitized by Arya Samaj Foundation Chennai and eGangotri

CC-0. In Public Domain. Gurukul Kangri Collection, Haridwar

Digitized by Arya Samaj Foundation Chennai and eGangotri

Pramāṇa – J. Phys., Vol. 28 No. 5, May 1987, pp. 435–469. © Printed in India.

High pressure techniques at low temperatures

S RAMASESHAN, G PARTHASARATHY and E S R GOPAL*

Raman Research Institute, Bangalore 560 080, India
Instrumentation and Services Unit, Indian Institute of Science, Bangalore 560 012, India
*Also Department of Physics

Abstract. The article reviews the experimental techniques used in high pressure-low temperature investigations to study a variety of physico-chemical phenomena. The general principles of producing high pressures at low temperatures, the methods of measuring P and T, the materials used for construction and the diamond anvil cell (DAC) are briefly given first. Specific pieces of apparatus to measure the mechanical properties, phase equilibria, thermal properties, electrical properties, magnetic phenomena, optical and Raman/IR spectroscopic behaviour as well as Mössbauer spectra are then discussed. While instrumentation is the main emphasis of the article, a few illustrative examples of interesting observations are also indicated. Over 250 current papers are cited.

Keywords. High pressure techniques; low temperatures; diamond anvil cell; mechanical properties; phase equilibria; thermal properties; electrical properties; magnetic phenomena; Raman spectra; Mössbauer spectra; instrumentation.

PACS No. 07·35

1. Introduction

The study of the behaviour of materials at high pressures and low temperatures has been useful not only in understanding the properties of these materials but also in the observation of new features of the physicochemical properties. It is now believed that almost all materials will become metallic at sufficiently high pressures; therefore a combination of high pressures with low temperatures is a logical step in pursuing this phenomenon. Many superconductors have been discovered at high pressures and low temperatures. Pressure as a thermodynamic parameter and as a means of perturbing the symmetry of the system has a unique role and many of the phenomena are clearly studied only at low temperatures. For instance the study of the Fermi surface of metals at high pressures has given new insights. However progress in these directions has been hampered by the experimental difficulties in performing these measurements which combine two already difficult techniques (Swenson 1960; Stewart 1962; Brandt and Ginzburg 1965, 1969; Dugdale 1969; Paureau 1977; Chu and Woolam 1978). Nevertheless the fact that a variety of new phenomena and investigations can be performed under the simultaneous application of high pressures and low temperatures makes it desirable to review the various experimental techniques used in these studies. Inevitably some indications of the physical phenomena thrown up in these investigations have to be pointed out briefly in this review. Equally inevitable are omissions

CC-0. In Public Domain. Gurukul Kangri Collection, Haridwar

Digitized by Arya Samaj Foundation Chennai and eGangotri

caused by the conference deadlines and the consequent inadequacy in the scrutiny of literature.

1.1 *General principles of high pressure generation at low temperatures*

The experiments of Simon *et al* (1930) in exploring the melting curves of the permanent gases upto 0·5 GPa could be said to be the beginning of the modern phase of high pressure-low temperature research. Bridgman (1932) studied the pressure dependence of electrical resistivity upto 0·75 GPa with helium as a pressure transmitting medium. A major interest in the 1930's was the investigations of the possible existence of a solid-fluid critical point analogous to that possessed by well-known liquid-vapour transitions. A solidified gas, in particular helium, was thought to be the most promising substance for the observation of such a phenomenon.

In 1940's Lazarev and Kan (1944) developed perhaps the simplest high pressure-low temperature apparatus (called the ice-bomb technique) using the phenomena of the ice I-III water triple point transformations (Bridgman 1937). The pressure here is produced by the solidification of water in a bomb of constant volume. A maximum pressure of about 0·17 GPa at 4·2 K is achieved. Chester and Jones (1953) introduced the important clamp technique in which by mechanical methods the pressure is locked in at room temperature and the cell is cooled down to helium temperatures. The cell can be either of the piston-cylinder design (figure 1) or of the Bridgman-anvil type (figure 11). In the original apparatus a maximum pressure of 4 GPa at 4·2 K was achieved with a Bridgman-anvil cell (Chester and Jones 1953). Subsequently techniques in which the pressure can also be changed at low temperatures were developed (Buckel and Gey 1963; Berman and Brandt 1968; Syassen *et al* 1971; Alymov *et al* 1972). In the last decade, the diamond-anvil cell has proved to be very suitable for producing high pressures at very low temperatures (Jayaraman 1983).

1.2 *Materials used for high pressure-low temperature generation*

The main requirements of a high pressure-low temperature system are: (i) A suitable material to withstand the stresses involved, especially at low temperatures. (ii) A

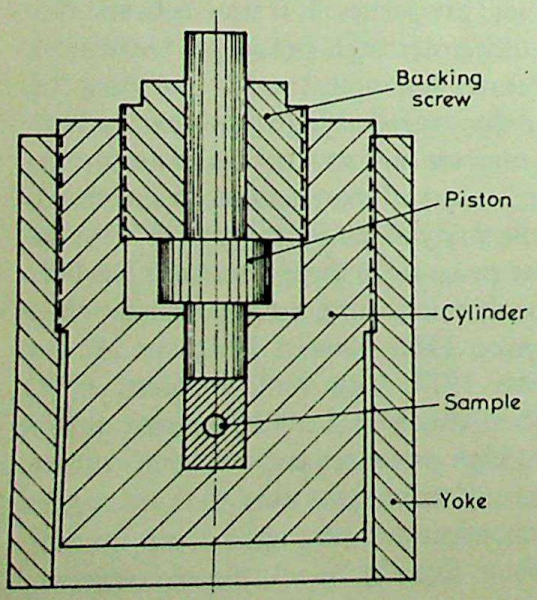

Figure 1. Clamp cell of the piston-cylinder type. The high pressure is generated by advancing the piston and locked by tightening the backing screw.

CC-0. In Public Domain. Gurukul Kangri Collection, Haridwar

Digitized by Arya Samaj Foundation Chennai and eGangotri

pressure-transmitting medium which remains soft at low temperatures, so that the pressure is hydrostatic. It must also be electrically insulating and chemically inert. (iii) A mechanism for sealing at high pressures and at low temperatures. Care must be taken to see that the materials are devoid of defects, blow holes, etc.

The most commonly used materials for the pressure vessels are Be-Cu alloys and stainless steels which have sufficient mechanical strength at low temperatures. These materials also have the added advantage of being nonmagnetic. Tungsten carbide has been successfully employed in piston-cylinder devices, upto a pressure of 2 GPa and at liquid helium temperatures. Nuclear orientation experiments upto 2 GPa pressure and temperatures down to 8 mK have been performed by using pressure cells made of Be-Cu alloy connected to dilution refrigerators (Benoit *et al* 1974; Ribault and Benoit 1978). Webb *et al* (1976) used a diamond anvil cell of 0·5 mm diameter, developing a pressure of 10 GPa down to 30 mK temperatures. The use of diamond anvil cell at very low temperature will be discussed in a later section of this review.

1.3 *Pressure-transmitting medium*

Pressure experiments which demand truly hydrostatic conditions become very difficult at temperatures below 77 K and pressures above 2 GPa. The problem arises because the plasticity of the pressure-transmitting medium decreases sharply on lowering the temperature. Various pressure transmitting media have been used. Lazarev and Kan (1944) used water which is filled in the high pressure bomb at room temperature, sealed and the bomb is cooled. The pressure is generated by the expansion of water, freezing under approximately constant volume conditions. The maximum pressure obtained in this system is limited to 0·17 GPa at liquid helium temperature, being controlled by the phase diagram of water. Unfortunately, the uniformity of pressure is not very good. In the clamp-bomb method (Itskevich 1964) a pressure of 1·5 GPa was achieved, a mixture of oil-kerosene being used as the pressure-transmitting medium. Stewart and Swenson (1954) developed a method in which liquid and solid helium is directly compressed in a piston-cylinder apparatus at 4·2 K (Schirber 1970). Poroswski *et al* (1977) improved Stewart's method with a better sealing of the piston, which permits the temperature to be changed over a wide range and also the cycling of pressure. Normally, talc and teflon are used as pressure-transmitting media instead of hydrogen or helium gas. This is because the gas medium is hazardous to work with and the pressure system with a gas medium is complex; working with hydrogen (or helium) is sometimes hazardous. Hence a solid pressure-transmitting medium is preferred and talc and teflon are found to be very satisfactory for this purpose (Bradley 1969; Giardini and Lloyd 1963; Lloyd and Giardini 1964; Bradley 1966, 1969a, 1969b; Lloyd 1971; Paureau 1977; Kelm 1978; Chu and Woolam 1978; Timmerhaus and Barber 1979; Vodar and Marteau 1980; Schilling and Shelton 1981). The use of gases like helium in a diamond anvil cell at low temperatures will be discussed later.

1.4 *Calibration*

The simplest method of estimating the pressure in an apparatus is to calculate the force over area and correct for friction. The variations of superconducting transition temperatures and critical fields as a function of pressure are available for a large

CC-0. In Public Domain. Gurukul Kangri Collection, Haridwar

Digitized by Arya Samaj Foundation Chennai and eGangotri

number of metals (For reviews see Bowen 1958; Jennings and Swenson 1958; Brandt and Ginsburg 1965; Levy and Olsen 1965). A manometer using the transition temperature of pure tin may be used to give the pressure accurate to within a few percent over the pressure range 10^5 Pa to 1 GPa. Jennings and Swenson (1958) found the equation $T_c = 3{\cdot}732 - 4{\cdot}88 \times 10^{-5} P + 3{\cdot}8 \times 10^{-10} P^2$ where P is in bars (1 bar $= 10^5$ Pa). Levy and Olsen (1965) placed two specimens in the experimental cavity using one of known dT_c/dP as a manometer, and relied on the plasticity of the specimens at the pressures used to ensure a homogeneous and equal pressure for the test specimen and the manometric specimen. Eiling *et al* (1981) demonstrated that Pb and Sn are ideally suited for use as accurate resistive manometers, enabling a reliable continuous determination of pressure (0–10 GPa) over a wide range of temperature (1–300 K). The other simple ways of calibrating pressure at low temperature are to study the pressure induced polymorphic phase transitions in Bi, Yb, Tl at different temperatures (Ilina and Itskevich 1967, 1970; Stager and Drickamer 1963; Homan 1975; Compy 1970; Lyon *et al* 1967; Parthasarathy *et al* 1984). This method is rather time-consuming in the case of clamp-type of cells. Hence for a clamp type cell the pressure dependence of superconducting temperatures of metals is much more convenient and for the continuous pressure and temperature changing system the phase transition of the elements at low temperatures is found to be most suitable for pressure calibration. For measuring the temperature between 4·2 and 300 K, chromel/alumel thermocouple is ideal because of the small shift in thermo-emf and the high reproducibility under hydrostatic pressure upto 2·2 GPa (Diatschenko and Chu 1975; Lazarus *et al* 1971). Rhodium plus 0·5 at. % iron against chromel is a new material (Guy *et al* 1986).

When cooled the pressure in a clamped cell changes slightly. For determining this pressure variation in a clamped cell at low temperature, one uses the electrical resistivity of metals as the temperature is lowered, e.g. lead (Bandyopadhyay *et al* 1980; Eiling *et al* 1981) or manganin (Fujiwara *et al* 1980; Brandt *et al* 1976; Itskevich 1964; Thompson 1984; Sinha and Srinivasan 1983). The pressure calibration of the diamond anvil cell at low temperature will be discussed in the next section.

2. Diamond anvil cell at low temperature

The diamond anvil cell (DAC) is capable of generating 2·5 megabar pressures at very low temperatures (Goettel *et al* 1985) and its development is a major step in modern high pressure research. The principles underlying the DAC, the pressure calibration, and the application of DAC in physical investigations have been reviewed by Block and Piermarini (1976), Jayaraman (1983) and Bundy (1986a). Since the DAC is small and compact the simplest method of direct immersion in a cryogenic fluid N_2, O_2 has been used. However, operation at liquid helium temperatures requires a specially designed cryostat. Webb *et al* (1976) designed an apparatus for pressures up to 10 GPa and temperature down to 30 mK, which uses a Bassett type cell (Bassett *et al* 1967; Jayaraman 1972) in a He^3-He^4 dilution refrigerator. In this, pressure can be changed from outside by applying He^4 gas pressure to a chamber with bellows, which in turn pushes the anvil. The apparatus was used to measure the effect of pressure on T_c of Al with a Squid manometer to detect the change in the magnetic moment of the sample.

CC-0. In Public Domain. Gurukul Kangri Collection, Haridwar

Digitized by Arya Samaj Foundation Chennai and eGangotri

Mao and Bell (1979) have developed low temperature techniques which are widely used with DACs down to liquid He temperatures. Here the central hole or the gasket chamber in the gasket is filled with liquid or high pressure H_2/He and then the cell is sealed. Thereafter the pressure can be increased or the temperature lowered. Shaw and Nicol (1981) described a simple DAC for optical spectroscopy to pressures of 10 GPa at temperatures down to 2 K. The cryostat is provided with optical windows and pressure is changed from outside by a helium-driven piston acting on a pivoted clamp. Diatschenko and Chu (1981) have developed a cryogenic press fabricated from Be-Cu, which enables sealing of the desired gas in central hole (the specimen chamber) of the gasket of the DAC and pressurization from outside the liquid-He and cryostat through a screw threaded mechanism. The system is used for optical observations on the melting behaviour of H_2 between 20 K and 300 K. Liebenberg (1979) devised a very simple technique for filling the central hole (the specimen chamber) of gasket with Xe. Solid xenon is found to be hydrostatic upto 30 GPa pressure. Besson and Pinceause (1979) have developed a high pressure gas loading technique for filling the specimen chamber of the gasket with He. In this, a high pressure bomb with DAC inside is pressurized to 0·2 GPa. This technique has been modified by Mills *et al* (1980) for filling He and D_2 in a Mao and Bell (1979) cell. Weinstein (1984) used a DAC for luminescence, transmission and Raman scattering measurements at low temperatures (down to 4 K). Silvera and Wijngaarden (1985) developed a DAC with a cryostat suitable for optical studies down to 1·1 K. Kobayashi (1985) described a DAC which allows optical studies at low temperatures and variable pressure to 26 GPa. In this system a bellows assembly has been designed to drive the DAC and the connected helium gas pressure source. The details of the instrumentation will be discussed in the following sections.

The pressure calibration in DAC, has been achieved by studying the shift of the R lines of ruby under pressure. The R lines of ruby are quite intense and the doublet R_1 and R_2 have the wavelengths 6927 and 6942 Å respectively at atmospheric pressure. Under pressure these shift to higher wavelengths and the shift is linear with pressure. Piermarini *et al* (1975) linked the ruby scale to NaCl through the Decker equation of state (Decker 1971) and showed that it is linear upto 19 GPa. They proposed that $P = 0{\cdot}2746\ \Delta\lambda$ where P is in GPa and $\Delta\lambda$ in Å. A recalibration was needed for this applications of the ruby manometer to low temperatures, since the value of $d\nu/dP$ changes from $-0{\cdot}757\ cm^{-1}$/kbar at 293 K to $-0{\cdot}73\ cm^{-1}$/kbar at 166·8 K. Noack and Holzapfel (1979) calibrated the ruby pressure scale at low temperatures by using the helium gas pressures upto 1·2 GPa.

In the subsequent sections the instrumental techniques specific to various physical measurements like mechanical, electrical, magnetic, optical and structural properties will be discussed.

3. Mechanical properties

A knowledge of the mechanical behaviour of materials at high pressures and low temperatures is in some sense a prerequisite for many other studies. For example the very construction of an apparatus at this combination of extremes of conditions depends upon this knowledge, as discussed in §1.2. Apart from such technical applications, one may want to study the lattice properties of materials, for which a

CC-0. In Public Domain. Gurukul Kangri Collection, Haridwar

Digitized by Arya Samaj Foundation Chennai and eGangotri

combination of high pressures and low temperatures reduces lattice vibrations and atomic diffusions to very low levels. The earlier research on the mechanical properties of materials at low temperature and high pressures has been reviewed by Swenson (1960) and Stewart (1962).

The PVT measurements have been historically a very important area of work, which continues to attract attention. Many experimental techniques have been developed for these studies (Stewart 1962; Stajdohar and Towle 1964; Van Itterbeek 1965; Fujii and Nagano 1971; Padaki *et al* 1979). In the simple PVT measurements the sample is contained in the cylinder and the load is applied by the piston directly on the material under investigation (Swenson 1960; Landau and Wurflinger 1980; Kortbeek *et al* 1986). In some cases like the measurements of gases or liquids, the material is condensed into the chamber volume. The pressure is inferred from the load on the piston after correcting for frictional losses. The volume change or compressibility is estimated from the observation of the piston displacements (Alymov *et al* 1972), a correction being required for the dimensional changes of the piston and cylinder under pressure. Phase transitions are also detected from the displacement of the piston as a function of pressure. An interesting recent study of this type is the investigation of the various forms of ice at high pressures and low temperatures, giving a complex phase diagram (Whalley 1986). In addition to the PVT measurements the temperature variation of the shear strength of solid argon has been studied with this apparatus by Stajdoher and Towle (1964) using an extrusion technique.

Volumetric measurements have also been performed in the diamond anvil cells. Wieldraaijer *et al* (1982) have measured the size of the central hole (sample chamber) of the gasket in a DAC at various pressures. The chamber contains the medium under study and the thickness of the sample is measured interferometrically. The pressure is calibrated with ruby fluorescence and so one can obtain PVT data upto 30 GPa or more down to low temperatures.

Apart from the volumetric and compressibility measurements, some experiments on ultrasonic velocity measurements at high pressures and low temperatures have also been done (Homan *et al* 1978; Padaki *et al* 1979; Hazen *et al* 1980; Cromer *et al* 1981; Schiferl *et al* 1981). Van Itterbeek and Van Dael (1958) studied the sound velocity upto 75 atmospheres in gases and in liquids in the temperature range between 1 K and 350 K. The various techniques, in particular the piston-cylinder apparatus used for the sound velocity measurements in dense fluids at high pressures and low temperatures, are reviewed by Van Dael and Van Itterbeek (1965). Homan *et al* (1978) developed a continuous pressure and temperature changing system in which the ratio of longitudinal to transverse acoustic velocity can be measured as a function pressure upto 15 GPa and temperature down to 40 K. The schematic diagram of the sample area configuration is shown in figure 2. The ultrasonic transducers on each anvil area are exposed to approximately the same temperature as the samples; however they are at ambient pressures. These transducers allow acoustic interferometric measurements to be made on the argon pressure medium using a technique described by Frankel *et al* (1977). The ratio of acoustic velocities can be used as a pressure calibration parameter itself (Homan *et al* 1978). Many other techniques are described for the measurement of ultrasonic velocities at high pressures and room temperatures, which may be applicable at low temperatures also (Litov and Anderson 1978; Fujisawa 1984; Hagelberg and Corsaro 1985).

CC-0. In Public Domain. Gurukul Kangri Collection, Haridwar

Digitized by Arya Samaj Foundation Chennai and eGangotri

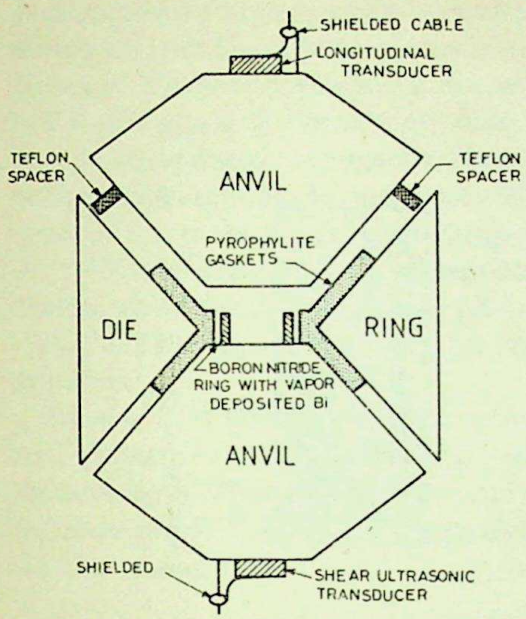

Figure 2. Schematic of the sample area in measuring ultrasonic velocities in an anvil apparatus.

Ultrasonic velocities can also be obtained from the Brillouin scattering experiments on the samples using the DAC technique, as discussed in the light scattering experiments.

The viscosity of fluids increases very rapidly at high pressures, by 6–7 orders of magnitude in some cases. An ingenious measurement of the coefficient of viscosity involves the Stokes fall of a sphere in a fluid, with the differences that the sphere is of a magnetic material and the accelerator force is not gravity but a magnetic field (Nishibata and Izuchi 1986). This method for measuring the viscosity and similar methods for measuring the friction can be easily adopted for h.p. work at low temperatures. Similarly self-diffusion data can be obtained from NMR measurements; measurements on alkanes at high pressure and low temperatures have been recently reported by Bachl and Ludemann (1986).

4. Thermal properties

The experimental methods of investigating the thermal properties of materials at atmospheric pressures can in principle be used at high pressures. There are however many difficulties and so modifications have to be made. In particular, one has a great difficulty in getting adiabatic environments for the sample at high pressures. So methods based on isothermal techniques have to be used (Lakshmikumar and Gopal 1981). For the investigation of plastic crystals in the low temperature region (100 to 300 K) and upto about 4 kbar pressure a new high pressure low temperature differential scanning calorimetry (DSC) microcalorimeter has been developed by Arntz (1980). The details of the measuring head are shown in figure 3. The heart of the device is a pair of identical cylindrical autoclaves, each of them closed by two Bridgman pistons made of Inconel 718, which are sealed by teflon. In the vessels (length 20 cm, o.d. 7 cm, i.d. 2 cm) made of a special austenitic nickel chromium steel (Amagnit 3974) for low temperature applications, the sample and reference holders are installed. The temperature is calibrated with cyclopentane and indium. Energy calibrations are based

CC-0. In Public Domain. Gurukul Kangri Collection, Haridwar

Digitized by Arya Samaj Foundation Chennai and eGangotri

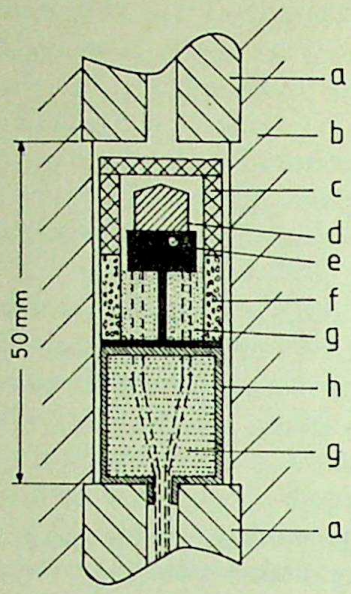

Figure 3. Head assembly of the high pressure differential scanning calorimeter.

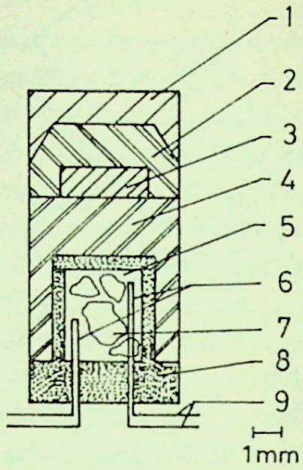

Figure 4. Cross-section of the calorimeter cell for use in a high pressure piston-cylinder apparatus.

on the transitions of cyclopentane, mercury and indium. Geijsel *et al* (1981) have developed a high pressure DSC apparatus working in the temperature range of 4 K to 1000 K and the pressure range upto 10 kbar. Solid ethane has been studied upto 12 kbar (Van der Putten *et al* 1986).

The specific heat measurements at high pressure and low temperatures, however, are rarely performed despite their valuable information on the type and distribution of excitations in the solid material as a function of the lattice parameters. The reason for this deficiency of calorimetric investigations is the technical difficulties arising from the high pressure conditions. In selecting the proper calorimetric method one has to make allowance for the fact that the sample cannot be thermally decoupled from its environment because of the pressure transmitting medium. Keeping these problems in mind, Eichler and Gey (1969) designed a high pressure-low temperature apparatus for specific heat measurements upto 35 kbar pressure and temperature down to liquid helium. The schematic diagram of the Eichler's pressure cell is shown in figure 4 (Eichler and Wittig 1968; Eichler and Gey 1969). Gallium was used as the embeddding medium for the elements and the sample, because it is easily melted and moreover, is distinguished by a comparably high thermal diffusivity and a small specific heat at low temperatures. The pressure is determined from the superconducting transition temperature of a separately mounted indium sample (figure 4). Since it was separated from the calorimetric sample by layers of teflon and diamond powder some degree of pressure difference cannot be excluded (Andersson and Backstrom 1976; Ross *et al* 1977; Berton *et al* 1979; Siddiqui and Lucas 1982; Jin *et al* 1984; Pieper *et al* 1984).

The study of phase equilibria in gas mixtures is one of the most interesting phenomena in thermal properties (Bock and Wiseneiwski 1983; Balt *et al* 1983). Berman *et al* (1980) described a cell in which the solubility of solids in high pressure gases at low temperatures can be studied. The cell contains a magnetic stirrer, since mixing by diffusion is too slow at high pressure and low temperatures. The cell is

CC-0. In Public Domain. Gurukul Kangri Collection, Haridwar

Digitized by Arya Samaj Foundation Chennai and eGangotri

pressurized through a helium chamber. This apparatus is used for studying the pressure dependence of H_2 vapour concentration in He gas at low temperatures (down to 8 K). Street *et al* (1984) developed a device to determine the compositions of coexisting gas and liquid phases for binary mixtures of hydrogen with the following substances as the second component: nitrogen, carbon monoxide, argon, methane, ethylene, ethane and carbon dioxide (Calado and Street 1978). If the conventional equipment is used for the study of mixtures, the pressure range is limited to about 1·5 GPa. Recently Schouten *et al* (1979, 1986) developed a system consisting of a DAC with a high pressure vessel to match, which can be used for the phase behaviour of gaseous mixtures at pressures upto 10 GPa. This system is utilized for studying the gas-gas equilibrium in Ne-Xe, He-H_2 systems.

Ross *et al* (1977) developed a technique for measuring the thermal conductivity at high pressures (upto 2·4 GPa) and low temperatures (down to 120 K) by using a piston-cylinder apparatus. The pressure cell is used for measuring the thermal conductivity of different phases of ice and for studying alkali halide samples (Andersson *et al* 1986; Sigalas *et al* 1986).

5. Electrical properties

The high pressure studies on the electrical properties of the materials at low temperature, led to the discovery of many pressure-induced superconductors and other phenomena (Brandt and Ginzburg 1971; Bundy 1986b). Many questions are yet to be answered, for example, are there still other pressure-induced superconductors or can superconducting properties be destroyed by very high pressures. What about heavy

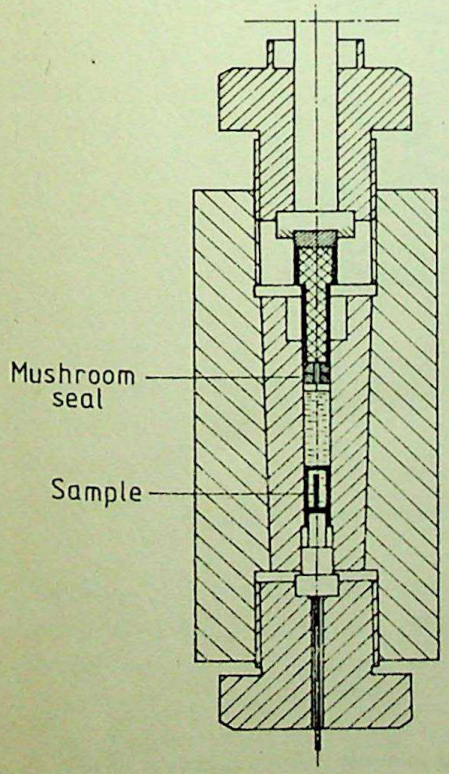

Figure 5. Beryllium-copper clamp cell for measuring electrical resistance and magneto-resistance at high pressures and low temperatures.

CC-0. In Public Domain. Gurukul Kangri Collection, Haridwar

Digitized by Arya Samaj Foundation Chennai and eGangotri

fermions, quasi one-dimensional materials, re-entrant superconductivity, organic superconductors and so on? (Smith and Chu 1967; Smith 1979; Wittig 1984; Chu *et al* 1986). In this section the techniques used in the study of the electrical resistivity, Hall effect, thermopower measurements at high pressures and low temperatures are briefly considered.

Figure 5 shows the schematic diagram of the clamp cell, developed by Itskevich (1964) to carry out low temperature experiments upto 1·8 GPa. The pressure production is closest to the method described by Vereshchagin *et al* (1958). All the parts of this cell, except the piston, the heel of the piston and the seals, are of Be-Cu. An oil-kerosene mixture is compressed in the cell by a piston equipped with a sealing device of the 'mushroom' type. The cell is cooled slowly after the pressure has been applied in the cell. The pressure calibration has been achieved by measuring the resistivity of manganin down to 20 K and with a tin manometer at 4 K (Itskevitch *et al* 1966). Electrical resistivity measurements are carried out at 20 K and 0·1 GPa. Gaidukov and Itskevich (1964) have studied the pressure dependence on the Fermi surface of zinc. Itskevitch's method has been used in various experiments, like optical experiments (Nefedova and Minin 1973; Shirokov *et al* 1973), thermal conductivities of metals (Itskevitch and Kraidenov 1975) and electron spin resonance studies (Kozhukhar *et al* 1975). Fujii and Nagano (1971) have built a high pressure apparatus operating at liquid helium temperature for studying galvanomagnetic effects of materials at high pressures and low temperatures. The schematic diagram of the apparatus and the details of the piston-cylinder cell is shown in figures 6 and 7 respectively. It is a direct piston displacement type cell where the pressure and temperature can be changed simultaneously. The apparatus consists of a piston-cylinder cell made of Be-Cu alloys, compression and tension components made of stainless steel, and a high pressure oil pump. This apparatus has been used for studying magnetoresistance and Hall coefficient of Yb and Te upto 2·0 GPa at 4·2 K. A similar type of apparatus has been

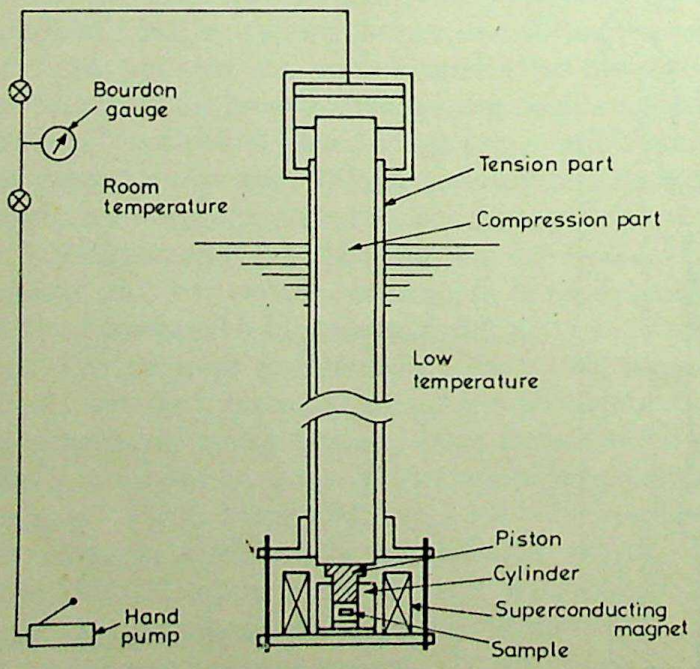

Figure 6. High pressure low temperature apparatus to study galvanomagnetic effects.

CC-0. In Public Domain. Gurukul Kangri Collection, Haridwar

Digitized by Arya Samaj Foundation Chennai and eGangotri

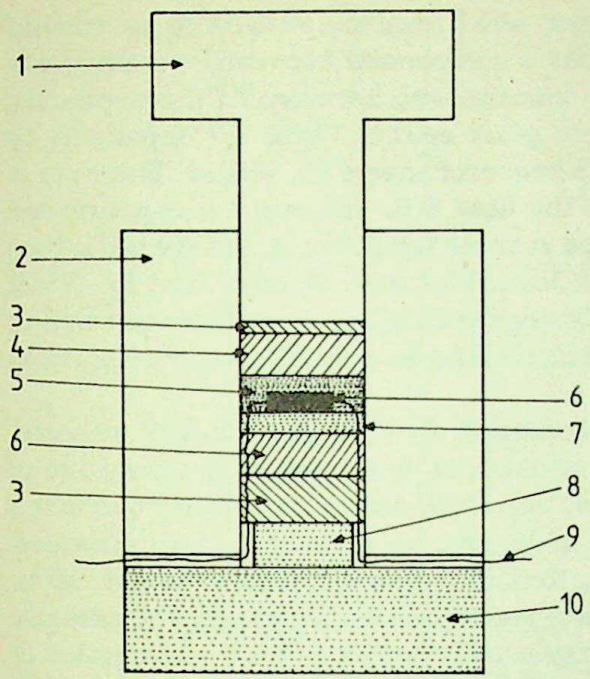

Figure 7. Details of the sample mounting for galvanomagnetic studies.

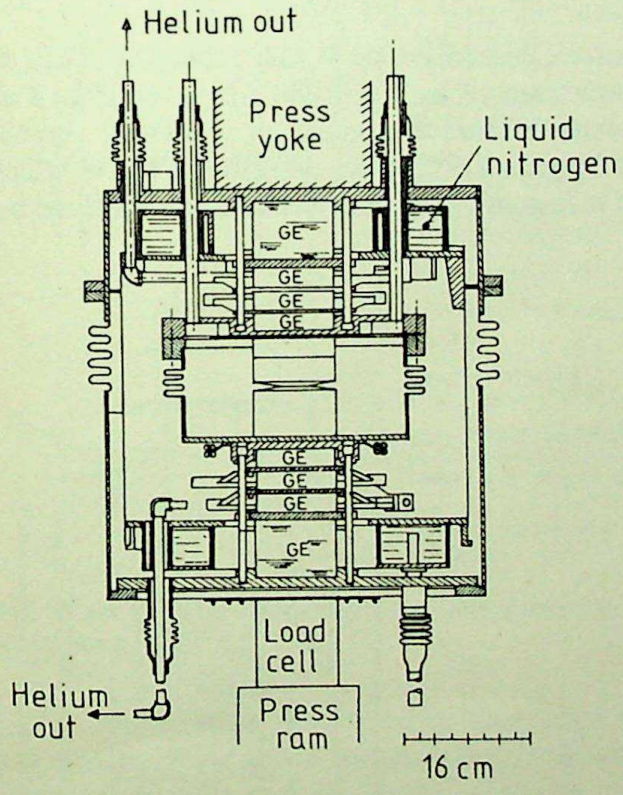

Figure 8. Low temperature high pressure cell with bellows for vacuum tight expansion joints.

developed for ultrasonic velocity measurements (Padaki *et al* 1979) and electrical resistivity measurements (Parthasarathy *et al* 1984) at high pressures and low temperatures. In the electrical resistivity measurements, the piston-cylinder cell has been replaced by the Bridgman anvil cell and the pressure range has been extended upto 8 GPa (Parthasarathy *et al* 1984).

CC-0. In Public Domain. Gurukul Kangri Collection, Haridwar

Digitized by Arya Samaj Foundation Chennai and eGangotri

Lyon *et al* (1967) fabricated an apparatus, which enables 10 GPa to be reached between 4 and 300 K (figure 8). The sample is compressed between two Bridgman anvils with the aid of a 270 ton press. The columns which transmit the compressing force to the cell consist of blocks of fibre glass epoxy. These are separated by molybdenum discs at the periphery of which heat exchangers are welded. These are in contact with helium vapour produced by the heat flow entering the experimental chamber (figure 8). The sample is compressed at room temperature and the cell is then cooled to low temperatures under constant load. This cell has been used for NMR experiments by Gossard *et al* (1970). A similar apparatus with a simplified construction has been built by Chaisse' *et al* (1970) to measure magnetic ordering temperatures upto 8 GPa between 10 and 300 K.

Vereshchagin *et al* (1969) developed an apparatus for superconductivity measurements upto 5·0 GPa (figure 9). The device consists of two pressure boosters, one of which is immersed in liquid helium. The first booster is always at room temperature, and can produce upto 1·0 GPa in oil. The oil under pressure flows along a stainless steel capillary through the sealed end of the Dewar flask into the low pressure chamber of the second booster, which consists of special steel vessels screwed together. The pressure intensification coefficient is about 40. This apparatus is exploited in the investigation of the pressure dependence of superconductivity of thallium (Vereshchagin *et al* 1969; Ilina and Itskevich 1970).

Figure 10 shows the apparatus developed by Wittig (1966) to study the pressure dependence on the superconducting of lead and tin upto 16 GPa. The sample is embedded in a steatite pressure-transmitting medium, which is surrounded by a pyrophyllite gasket. Fujii and Nagano (1972) have described a cell in which the anvils remain under compression by means of a system of two flanges and three bolts. Similar

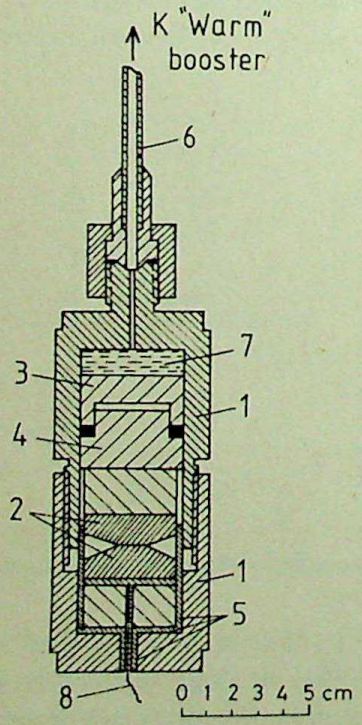

Figure 9. Low temperature pressure intensifier using anvil assemblies to study superconductivity.

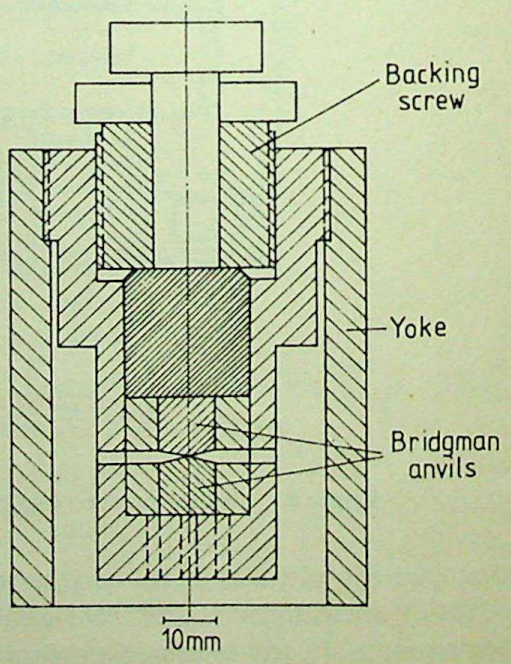

Figure 10. Clamp cell for use up to 100 kbar at low temperature, using a lock nut.

CC-0. In Public Domain. Gurukul Kangri Collection, Haridwar

Digitized by Arya Samaj Foundation Chennai and eGangotri

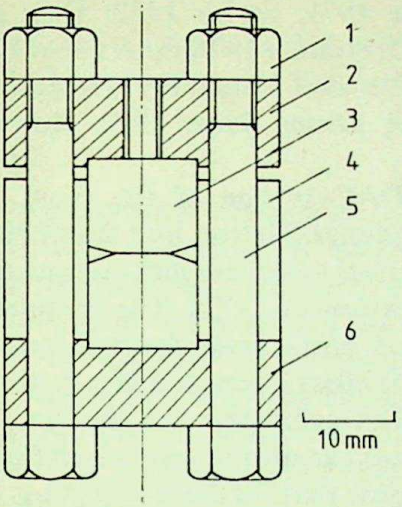

Figure 11. Clamp cell for use at low temperatures using a bolt arrangement.

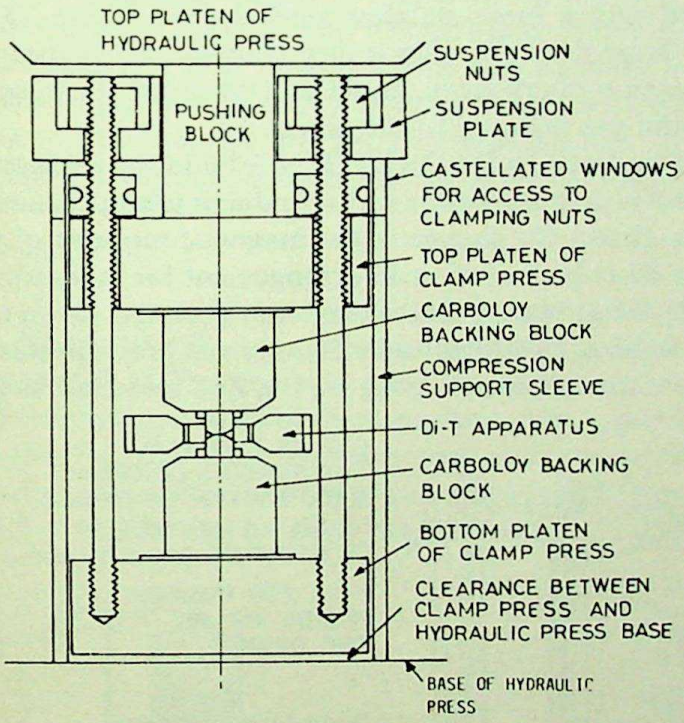

Figure 12. 50 GPa clamp-type anvil arrangement to study electrical resistivity at low temperatures.

clamp type cells have also been developed by Bandyopadhyay *et al* (1980). It is best to use this type of clamp cell for attaining temperatures lower than 100 mK, because of its small heat capacity and its small heat leakage during the experiment. A typical high pressure clamp cell for electrical resistance is shown in figure 11 (Fujii *et al* 1972; Bandyopadhyay *et al* 1980).

The above two techniques namely continuous pressure changing system and the clamp techniques are being utilized widely in the electrical resistivity measurements by many researchers with minor modifications to suit each experiment (Vereshchagin and Semechan 1961; Balchan and Drickamer 1961; Buckel and Gey 1963; Clark 1964; Itskevich 1964; Levy and Olsen 1965; Mcwane *et al* 1968; Pitt 1968; Smith *et al* 1969;

CC-0. In Public Domain. Gurukul Kangri Collection, Haridwar

Digitized by Arya Samaj Foundation Chennai and eGangotri

Pitt and Lees 1970; Wohlleben and Maple 1971; Smith 1972; Fujii *et al* 1974; Shimomura *et al* 1974, 1976; Kendall *et al* 1975; Homan 1975; Anzin *et al* 1976; Brandt *et al* 1976; Itskevich and Kraidenov 1978; Willer and Moser 1979; Kojima *et al* 1979; Itskevich *et al* 1979; Takemura *et al* 1979; Lories Susse 1980; Kawamura and Tachikawa 1980; Akahama *et al* 1986).

Electrical resistance measurement with DAC is one of the most challenging problems in the high pressure experimental science (Nelson and Ruoff 1979). Bundy and Dunn (1980a, b) have made extensive electrical resistivity measurements on several elements upto 50 GPa pressure at temperatures down to 2·7 K. The pressure apparatus is shown in figure 12. All the highly stressed parts, aside from the diamond and cemented tungsten carbide were of special stainless steels which are not subject to brittle fracture at cryogenic temperatures. The geometry and the combination of materials used were such that the thermal shrinkage during cool down from 300 K to 2·7 K was the same in the tension and compression parts of the system, thus keeping the loading of the pressure cell about constant. After the cell was loaded and clamped, the assembly was transferred into a large stainless steel dewar. Figure 13 shows the assembly hanging in the large dewar by thin-walled stainless steel tubes. One of the tubes was for the introduction of cryogenic liquid and the other for purging out the cryogenic fluid by applying gas pressure to the dewar.

Webb *et al* (1976) have developed a DAC with He^3-He^4 dilution refrigerator, which is used to measure the effect of pressure on the superconducting temperature of Al, with a Squid magnetometer to detect the change in the magnetic moment of the sample.

Sakai *et al* (1982) have described a four-lead arrangement for measuring electrical resistivity in DAC upto 25 GPa pressure and at temperature ranges down to 2 K. Thin Cu or Pb lead wires are used as electrical leads. Helium gas pressure was applied to generate the load. Pressure was calibrated using Bi, Pb, ZnS and GaP as fixed points

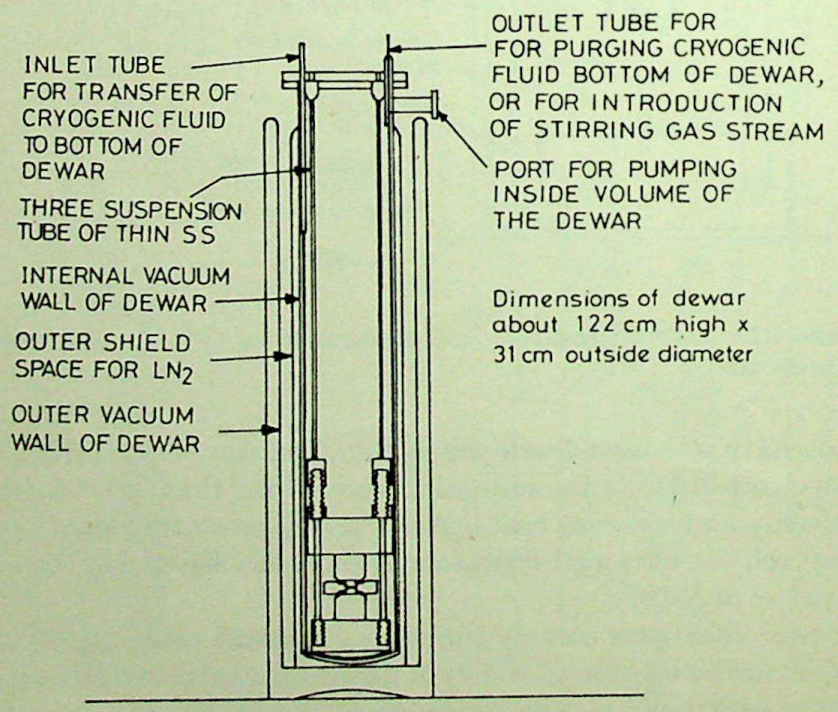

Figure 13. Pressurized clamp apparatus assembly hanging inside the large Dewar for cryogenic studies.

CC-0. In Public Domain. Gurukul Kangri Collection, Haridwar

Digitized by Arya Samaj Foundation Chennai and eGangotri

(Sakai *et al* 1982). Golopentia and Ruoff (1981) used spherically tipped diamonds with radii less than 1 μm to obtain 2 Mbars (=200 GPa) pressure at 78 K.

5.1 *Hall effect*

Hall effect measurements under high pressure have been done by a few scientists. Benedek *et al* (1954) have reported Hall measurements on Ge upto 1 GPa hydrostatic pressure using Be-Cu vessel. Fujii and Nagano (1971) have developed an apparatus for studying Hall effect at high pressures and low temperatures, which was discussed in the previous section. Vyas *et al* (1973) developed an anvil technique for Hall measurements at low temperatures by circulating liquid nitrogen through copper coils encircling the anvils. The apparatus has been used for obtaining Hall data on GaAs upto 5 GPa pressure in the temperature range 120–300 K. Lifshitz and Maines (1979) have designed a high pressure (upto 4 GPa)-low temperature (down to 150 K) Hall apparatus, by adopting the teflon cell technique (Jayaraman *et al* 1967). Porowski *et al* (1977) designed a continuous pressure and temperature changing system in which Hall measurements and resistivity measurements can be made upto 2 GPa pressure at temperatures down to 4·2 K, with purely hydrostatic pressure environment (Kadri *et al* 1986; Zitouni *et al* 1986). In this apparatus liquid and solid helium are directly compressed in the piston-cylinder apparatus at 4·2 K (Jones *et al* 1975).

5.2 *Dielectric constant*

Wurflinger (1980) developed an excellent technique to measure the dielectric constant of molecular crystals and liquids in the temperature range between 210 K and 300 K upto a pressure of 0·3 GPa. The high pressure equipment is shown in figure 14. The inner (n) and outer (o) cylinders of the capacitor are separated by plastic spacers (p, l) and held together by a screw cap (k). The pressure is transmitted through the opening (i) on to the moving piston that consists of two parts (b, e) being separated by an indium sealing (d). A hallow space (c) between two parts works like 'Bridgman's unsupported

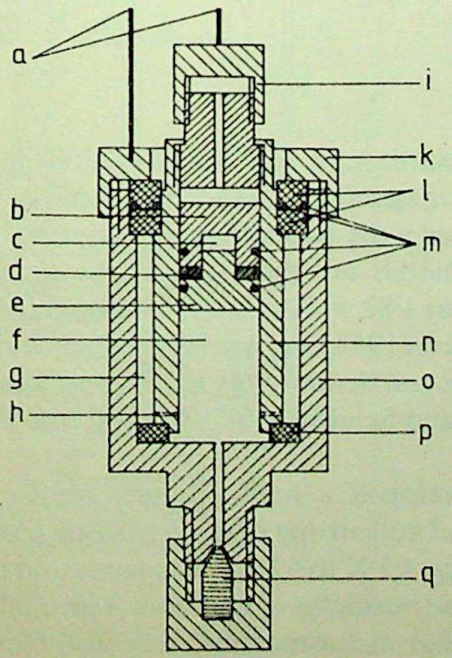

Figure 14. Dielectric cell for high pressure low temperature studies.

CC-0. In Public Domain. Gurukul Kangri Collection, Haridwar

Digitized by Arya Samaj Foundation Chennai and eGangotri

area'. By this method Wurflinger has achieved the sealing of the piston. Most of the electrode leads are guarded by the Bridgman piston that has two bores for the electrical feedthroughs. The piston and the vessel are connected with the grounded shield of the coaxial leads. With this arrangements lead capacities are avoided. Samara (1981) has made extensive studies on the pressure and temperature dependence of the dielectric constant of K_2SeO_4 by using a piston cylinder apparatus upto 1·4 GPa pressure and temperature down to 4 K. Samara (1984) found that K_2SeO_4 exhibit a λ-type anomaly in the variation of dielectric constant at the incommensurate-to-ferroelectric transition ($T_c = 93$ K). The transition temperature decreases rapidly with pressure and vanishes at a pressure above 0·72 GPa. The Peierl's transition in TaS_3 has been studied by Zhang *et al* (1981) under pressure, by thermopower measurements upto 1·9 GPa at temperatures down to 1·2 K. The Peierl's transition is first enhanced and then suppressed by pressure (Zhang *et al* 1981). Other dielectric cells for use at high pressures and low temperatures have been described by Thuillier *et al* (1986) and others.

5.3 *Fermi surface studies*

Hydrostatic pressures coupled with very low temperatures have proved to be very interesting in the study of the Fermi surface and electronic structure of metals (Brandt *et al* 1972; Schirber 1970, 1974, 1978, 1981; Gaidukov and Itskevich 1964; Itskevich 1984; Itskevich and Kashirskaya 1982). Figure 5 shows the Itskevich cell to carry out low temperature experiments upto 1·8 GPa. The main technique adopted for direct measurements of the Fermi surface is either high-field magnetoresistance or the attendant Shubnikov-de Haas oscillations. Stark and Windmuller (1968) developed a technique, which has the advantages of the field modulation deHaas-Van Alphen (DHvA) method. By this technique one could study the pressure effect on the Fermi surface of the metals without any electrical leads. DHvA effect, as well as other oscillation effects were measured in the Itskevich's cell by a modulation method in a magnetic field upto 80 kG (a superconducting solenoid with an inner diameter 6 cm). All the systems of modulation and detection coils were arranged within the cell.

6. Magnetic properties

Studies on magnetism under high pressures and low temperatures have yielded considerable information concerning the magnetic exchange interaction of electrons, magnetic ordering etc. For measuring magnetic properties of materials under high pressures, non-magnetic and hardened metals are required for the pressure vessel. Be-Cu alloy with Be concentration of about 1·82 wt% is the most popular material for construction (Patrick 1954; Adams and Davis 1958; Werner 1959; Bloch and Pauthenet 1962; Kouvel and Wilson 1961; Kondorski and Sedov 1960; Kawai and Sawaoka 1967; Fujii *et al* 1974; Alymov *et al* 1973; Fasol and Schilling 1978; Ribault and Benoit 1978; Schilling 1984).

Kawai and Sawaoka (1967) have developed a high pressure bomb capable of measuring weakly magnetic substances and anisotropy under hydrostatic pressure in a high magnetic field in the temperature range 4·2 K to 473 K. Kerosene and transformer oil in 1:1 ratio were used as the pressure-transmitting medium. The calibration has been done using a manganin gauge. Similar measurements were also carried out by

CC-0. In Public Domain. Gurukul Kangri Collection, Haridwar

Digitized by Arya Samaj Foundation Chennai and eGangotri

Svechkarev and Panfilov (1965). Apart from the magnetization experiments, techniques have been developed for measuring the Curie temperature as a function of hydrostatic pressure upto 2·5 GPa (Samara and Giardini 1965; Kaneko *et al* 1981; Kadomatsu *et al* 1982). Samara and Giardini (1965) developed a self-inductance method to find the Curie temperature and Kaneko *et al* (1981) determined the Curie temperature by the a.c. transformer method.

6.1 *Magnetic susceptibility*

Studies of the effect of pressure on the magnetic susceptibility help to understand some aspects of the structure of the energy spectrum of electrons in weakly magnetic metals and their alloys (Fujikawa *et al* 1980; Eiling *et al* 1981; Vining and Shelton 1984; Schilling 1984). Alymov *et al* (1973) have designed an apparatus, shown in figure 15. It consists of a press (1) with drive, motor (2), reduction gear (3), two dewars (4, 5) for liquid helium and nitrogen and the measuring arrangement; dynamometer (6), dilatometer (7), and coil (26) for registering the change in susceptibility. The press is connected with a vacuum packing to the top of the helium dewar by tube (8) which is firmly fixed to the casing. The sample (9) is kept in the high pressure chamber (10) and is compressed through the thrust block (11) by the advancing nut (12), which is set in motion by the electric motor (2), with a reduction gear (3) (or manually by a wheel (13)), through the

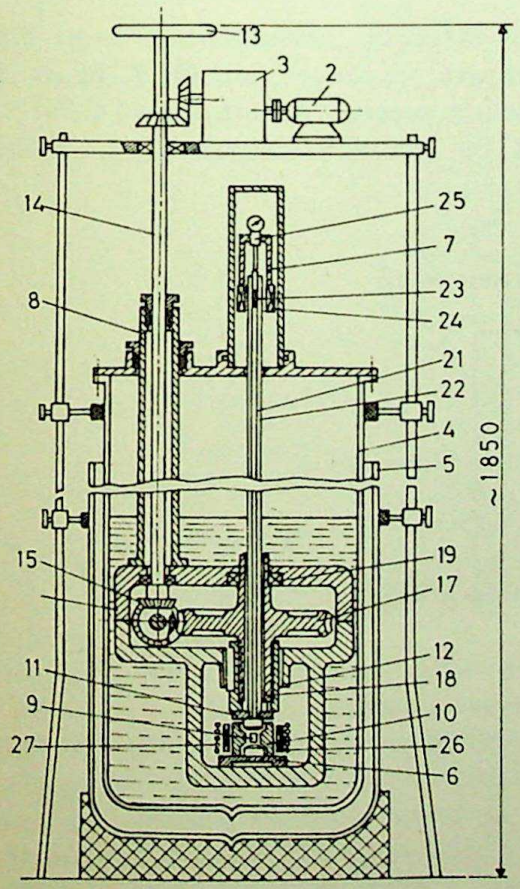

Figure 15. Measurement of magnetic susceptibility at high pressures and low temperatures.

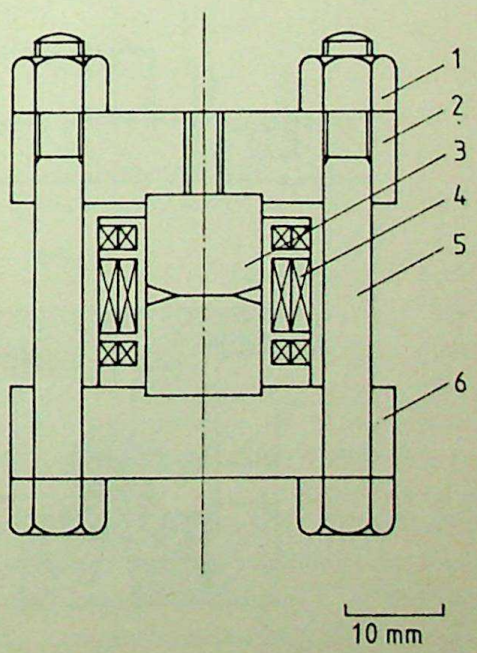

Figure 16. High pressure clamp arrangement for magnetic susceptibility measurements at very low temperatures.

CC-0. In Public Domain. Gurukul Kangri Collection, Haridwar

Digitized by Arya Samaj Foundation Chennai and eGangotri

tubular shaft (14), the pair of conical gears (15), worm (16), worm wheel (17) and screw (18). The axial load on the screw is taken up by the ball thrust bearing (19). Calibration at 4·2 K was carried out by measuring T_c of a Sn specimen in the chamber at various pressures. A superconducting or magnetic transition in the specimen is observed as a function of pressure with measuring coils (26).

Fujii *et al* (1974) have made an excellent high pressure clamp cell with dilution refrigerator for a.c. magnetic susceptibility measurements (figure 16). The primary and the secondary coils are both divided in three parts. The coils are wound with an insulated copper wire (0·08 mm diameter). The inner coil is the primary with 900 turns in the same direction. The outer coil is the secondary which is 2000 turns. The turn of the second middle part of the coil is reverse in its direction from the first (upper) and the third (lower) part and the induced voltages from each parts of the coil are compensated. The detection of the superconducting transition by the magnetic method need not require any electrical leads. The clamped high pressure cell is attached to the bottom of the mixing chamber of a 3 He/He dilution refrigerator and is cooled down to 30 mk. Webb *et al* (1976) have described an apparatus for the investigation of the magnetic properties up to 10 GPa at temperatures down to 30 mK. This apparatus incorporates a DAC, that is cooled by a 3He-4 He dilution refrigerator (figure 17). Changes in the magnetic moment of the sample (0·1 mm in diameter, 0·2 mm high) were detected with a SQUID magnetometer. Ribault and Benoit (1978) developed a high pressure Be-Cu cell for nuclear orientation experiments upto 2 GPa pressure and temperatures down to 8 mK.

Paureau (1977) discussed an apparatus for magnetic measurements under high pressure upto 2 GPa at a field of 10 T in the temperature range 2 and 300 K (figure 18). This apparatus can be equipped with either a helium pressure system (upto 1 GPa) or a piston-cylinder cell for pressures more than 1 GPa. The cell is connected to an outside

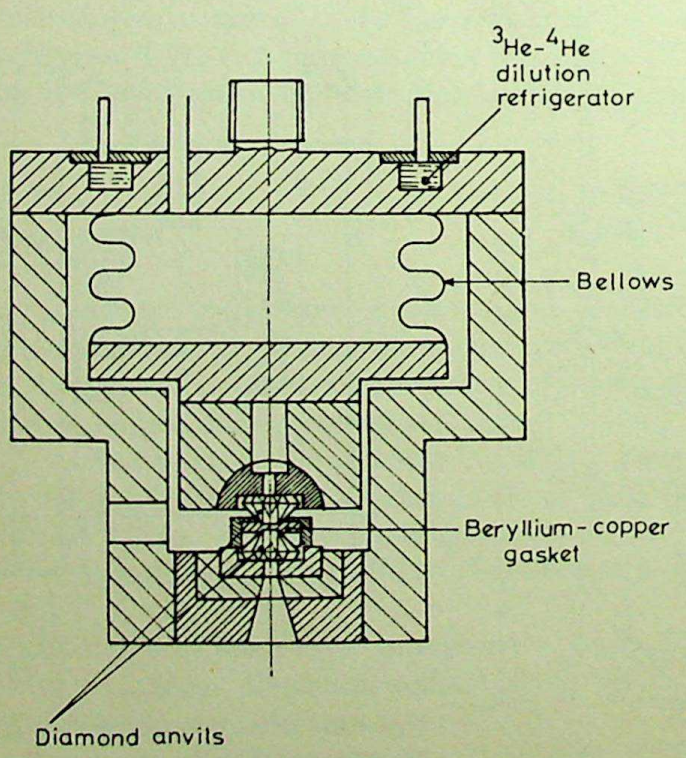

Figure 17. Diamond anvil cell for magnetic measurements in the milli-kelvin region.

CC-0. In Public Domain. Gurukul Kangri Collection, Haridwar

Digitized by Arya Samaj Foundation Chennai and eGangotri

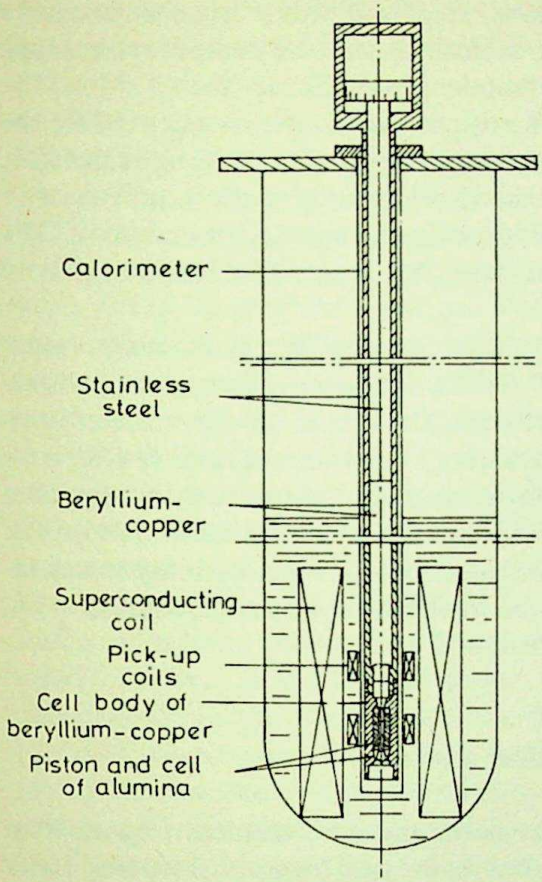

Figure 18. Magnetic balance for use at high pressures and low temperatures.

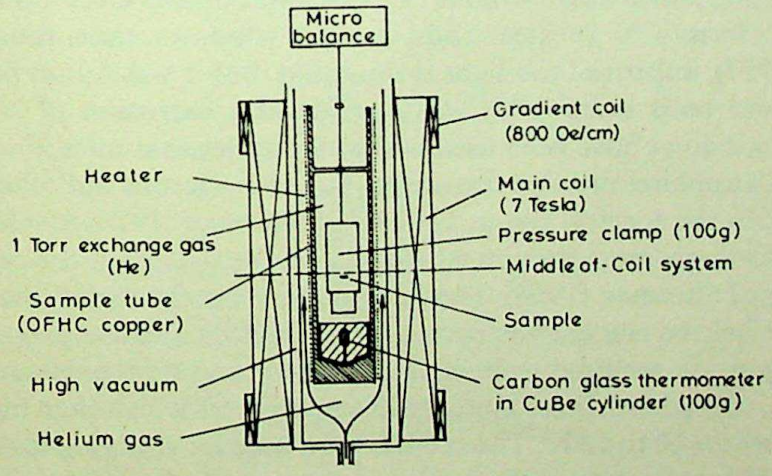

Figure 19. Faraday magnetometer for low temperature high pressure studies.

jack. The components of the high pressure cell are made from Be-Cu alloy except for the pistons and the core of the cell, which are made of high strength alumina. Lead is used as a compressing medium and manometer. Fasol and Schilling (1978) developed a hydrostatic pressure cell up to 9 GPa for precise magnetic measurements at temperatures between 1 K and 300 K. Eiling *et al* (1981) have measured the magnetic susceptibility and the upper critical field in a Faraday balance system, which is shown in figure 19. In this apparatus a small high pressure clamp (1·8 cm dia, 5 cm length,

CC-0. In Public Domain. Gurukul Kangri Collection, Haridwar

Digitized by Arya Samaj Foundation Chennai and eGangotri

100 g total weight) is in a magnetic field of constant $H(dH/dZ)$ value i.e. a constant force over the volume of the clamp. The balance system spans the temperature range 2·5–300 K with 7 T maximum field at hydrostatic pressures up to 1·5 GPa. The pressure is calibrated with a Pb manometer. The apparatus is extensively used for the investigation of the superconductivity of lanthanum chalcogenides (Eiling *et al* 1981). Some workers have used the piston-cylinder device for the susceptibility studies at high pressures and low temperatures, though the pressure range is limited to 2 GPa (Menyuk *et al* 1969; Wohlleben *et al* 1971; Guertin and Foner 1974; Hardebush *et al* 1980; Ido and Satosh 1982; Usha 1984).

Alekseevskii *et al* (1983) have studied the effect of pressure on the critical temperature of Cheverel phases with magnetic impurities at 2·0 GPa over a temperature range down to 0·1 K. They used Bridgman anvils made of yttrium-aluminum garnet single crystals ($Er_x Y_{3-x} Al_5O_{12}$; $x \approx 1{\cdot}5$). High pressures at extremely low temperatures (0·1 K) were obtained by compressing a sample in yttrium-aluminium garnet anvils and then adiabatically demagnetizing the compressed system (Alekseevskii *et al* 1985). The temperatures below 1 K were determined from the magnetic susceptibility measurements, using the Curie law. The adiabatic demagnetization from a temperature of 1·5 K and a field of 12 kOe, yielded a low temperature of 0·1 K.

7. High pressure-low temperature cells for optical studies

The high pressure optical cell with alkali halide as the pressure-transmitting medium was developed by Drickamer *et al* (1957) as the first major tool for optical studies. Later Sherman (1966) developed a variable temperature, high pressure optical cell which could be used at temperatures down to 80 K and pressures upto 5 GPa. The bulk of the cell is constructed from EN 26 steel rods. Larger windows than those used by Drickamer *et al* (1957), improved the light throughout, but it was found necessary to use sapphires as end seals since there was considerable extrusion of NaCl above 1·5 GPa. Sapphire windows have been used in the ellipsometric studies of solid helium (Franck *et al* 1986). Sapphires are also transparent up to 5 microns but other materials may be used to widen the spectral range. Lewis and Sherman (1974) developed a new liquid helium cell for high pressure optical studies. In construction, the cell design is similar to 80 K cell of Sherman (1966). The helium cell is much smaller than the 80 K cell. Moreover, the helium cell is constructed with tungsten carbide piston. About 5 litres of liquid helium are required to bring the cryostat and high pressure cell down from 77 K to 4·2 K. A further 3 litres almost fills the cryostat which then maintains its terminal temperature for 10 to 12 hr. The cell has been used for studying the absorption spectra of $CsCl/NH_4^+$ crystals at different pressures and temperatures.

Shchanov and Subbotin (1974) designed a high pressure cell with three optical windows so that absorption and emission spectra can be studied as well as reflection, luminescence and Raman spectra, up to 5 GPa pressure at temperatures ranging between 80 and 300 K. The chamber is placed for cooling in a cryostat consisting of a metal jacket covered with foam plastic and filled with liquid nitrogen. Anzin *et al* (1976) described a continuous pressure and temperature changing system for optical investigations up to 1·5 GPa in the temperature range 15–300 K. There are other high pressure-low temperature optical cells available, with essentially the same design (Medvedev *et al* 1978; Yamada and Schmidt 1978; Voloshin and Kasyanov 1980, 1982;

CC-0. In Public Domain. Gurukul Kangri Collection, Haridwar

Digitized by Arya Samaj Foundation Chennai and eGangotri

Dawson and Offen 1980; Dahan *et al* 1982; Daniels 1983; Ackermann *et al* 1985; Watson and Daniels 1986; Klug *et al* 1986).

Weinstein (1984) developed a variable pressure (0–30 GPa) and temperature (4–300 K) cryostat for luminescence studies. The cryostat is shown in figure 20. A Be-Cu DAC consisting of a piston in cylinder arrangement with diamond mounts threads into the outer tension sustaining tube. The inner tube provides compression to the DAC piston when activated by the room temperature hydraulic cylinder at the top. Optical access is through the bottom cryostat window and bottom diamond, or through the internal microscopic arrangement and the top diamond. The cryostat insert sits in a He-gas flow variable temperature optical dewar. The entire arrangement can be evacuated or purged which is necessary during loading and cooling. The pressure is calibrated by a ruby manometer.

The DAC for cryogenic temperature with optical measurement systems have been described independently by Shaw and Nicol (1981), Silvera and Wijngaarden (1985), Kobayashi (1985), Kawamura *et al* (1985) and Kourouklis *et al* (1986). The Be-Cu DAC and cryostat suitable for optical studies from 1·1 K to 300 K is shown in figures 21 and 22 respectively (Silvera and Wijngaarden 1985). Since cryostats are most easily built in a long, cylindrical shape, the cell assumed the form shown in figure 21. A cross-sectional view of the heart of the DAC is shown in figure 21(a). One diamond was mounted on a cylindrical platform 1 which has an x-y translation adjustment to allow for positioning of the diamonds opposite to each other. This platform was mounted on part 2 which screws into the main block and allows easy access to the diamond for preparation of the gasket, etc. The other diamond was mounted on a half sphere (part 3) which allows for 2° of rotation to align the diamond faces parallel to each other. This was mounted in part 4, a precision ground cylinder which is translated horizontally by a force applied to part 5. The means of applying the force is shown in figure 21(b). The screw at the top was

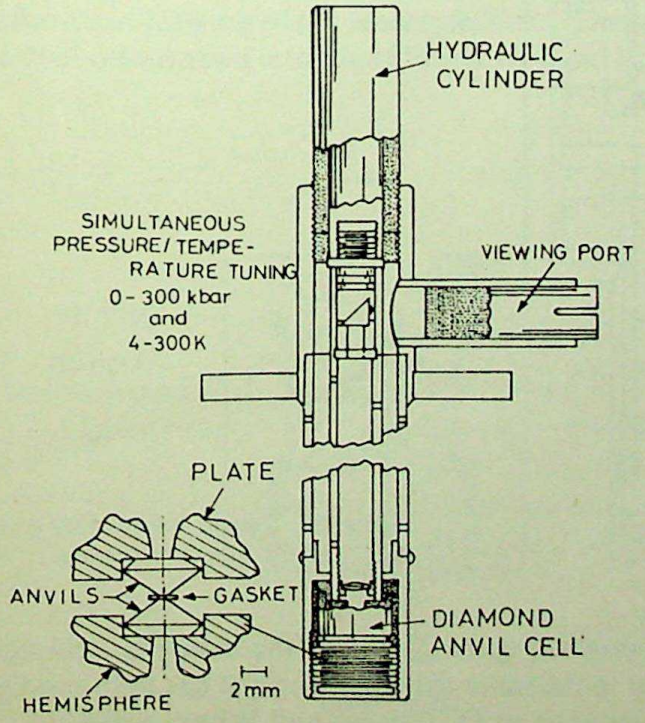

Figure 20. Cryostat for luminescence studies at high pressures using a DAC.

CC-0. In Public Domain. Gurukul Kangri Collection, Haridwar

Digitized by Arya Samaj Foundation Chennai and eGangotri

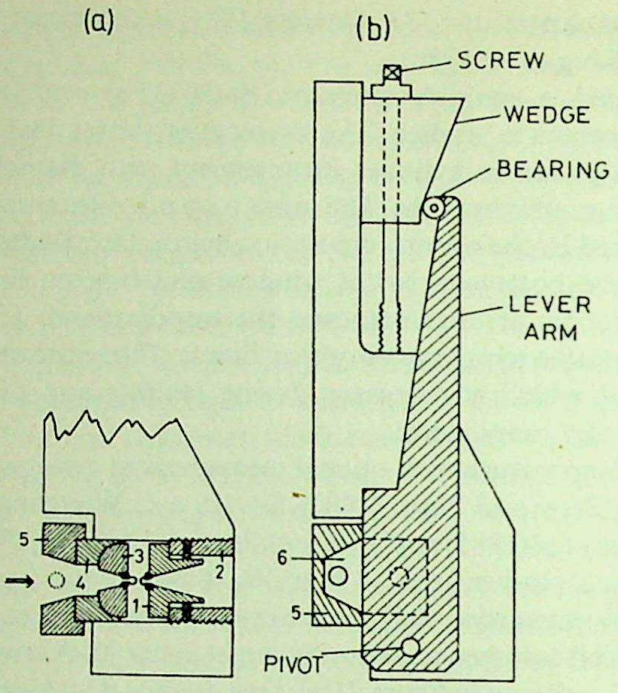

Figure 21. Details of the beryllium-copper DAC suitable for low temperature use.

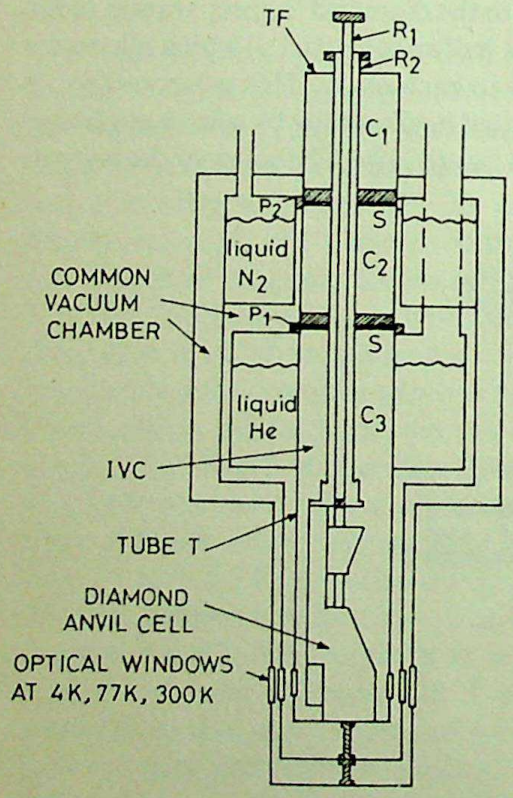

Figure 22. Liquid helium Dewar containing the DAC and the support structure.

turned to drive the wedge down. Figure 22 shows the stainless steel liquid helium cryostat with DAC mounted in the inner cylinder. The cell has been used to study the phase transitions in molecular H_2 and D_2 (Silvera and Wijngaarden 1981; Wijngaarden and Silvera 1980; Van Straaten *et al* 1982).

CC-0. In Public Domain. Gurukul Kangri Collection, Haridwar

Digitized by Arya Samaj Foundation Chennai and eGangotri

8. X-ray diffractometry at high pressure and low temperatures

The Bridgman's opposed anvil systems have been extensively used in high pressure x-ray diffraction studies over the last 20 years (Jamieson and Lawson 1962). Syassen *et al* (1971) developed a high pressure cell for x-ray diffraction, Mössbauer and nuclear gamma angular correlation studies on solids at temperatures between 4·2 and 350 K and pressures up to 18 GPa. Morosin and Schirber (1974) developed a Be-Cu cell capable of going to high pressure ~0·4 GPa, over the temperature range 80–300 K. This cell is used for single crystal x-ray studies. Skelton *et al* (1977) developed a variable pressure DAC for operation at temperatures continuously variable from 300 K down to 2 K and controllable within 10 mK. Figure 23 shows the cross-sectional view of Skelton's cell. The diamond anvils are seated on sintered tungsten carbide pellets and the pressure cavity is formed by a 0·2 mm diameter hole drilled in a metal gasket, contained between the diamond anvils. A $\pm 30°$ aperture is provided on the exit side of the cell. The pressure cell is connected to the temperature control block of a refrigerator through an indium gasket; this interfaces to a remote He storage dewar. The refrigerator system is equipped with Pt and Ge thermal sensors and temperatures between ambient and 4·2 K can be set and roughly controlled by adjusting the rate of He flow through the system via a micrometer needle valve. The rate of consumption of liquid He at 5 K is less than 1 litre/hr. Pressures were calibrated through sodium chloride. The mixture of methanol-ethanol-glycerine was used as the pressure-transmitting medium. This apparatus was used to study the low temperature phase diagram of bismuth (Skelton *et al* 1977).

Syassen and Holzapfel (1978a,b) devised an excellent high pressure low temperature x-ray powder diffractometer. The system consists of a Bridgman anvil type high pressure device with either tungsten carbide or boron carbide anvils, a liquid He cryostat and x-ray diffractometer operating in Debye-Scherrer geometry. Figure 24 shows the schematic drawing of the Holzapfel's cell. The top anvil is made of tungsten carbide and the bottom anvil is made of boron carbide. B_4C is sufficiently transparent

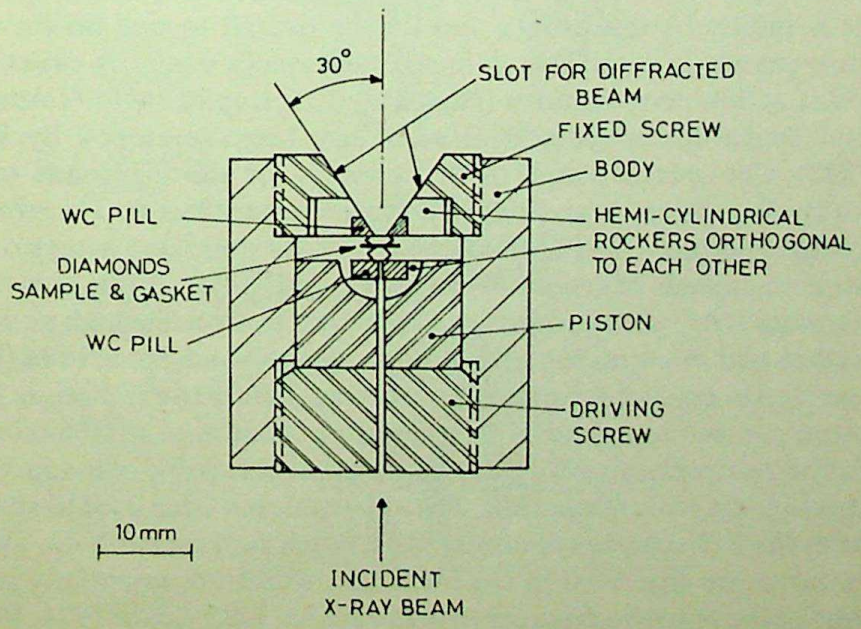

Figure 23. Diamond anvil cell with tungsten carbide sealing suitable for x-ray studies.

CC-0. In Public Domain. Gurukul Kangri Collection, Haridwar

Digitized by Arya Samaj Foundation Chennai and eGangotri

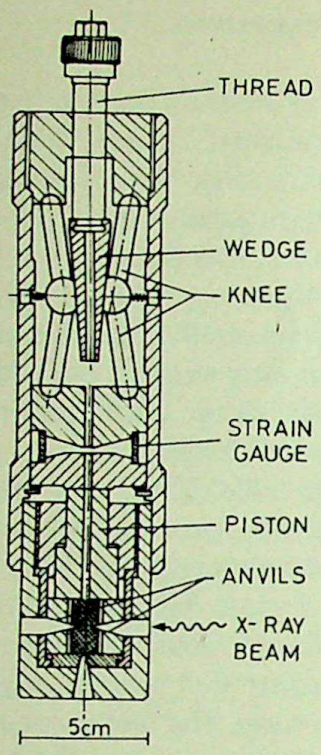

Figure 24. Anvil apparatus for x-ray studies.

to hard x-rays. For MoK_α radiation, the absorption length is about 8 mm. Both anvils are prestressed in the usual manner by supporting rings. The sample fills a small hole in a gasket on the tip of the B_4C anvil. By squeezing the two anvils together, the metal disk on the top of the hole deforms. A pressure gradient develops across the metal disk with maximum pressure in the centre just above the sample. The gasket then starts to flow into the sample region and thereby acts like a piston pressurizing the sample. X-rays pass through the B_4C anvil just below the metal disk.

A pair of coupled screws with opposite turning direction drives a wedge between two knees. The knees straighten and a maximum force of up to 15 tons can be exerted on the anvils. The advantages of this design over other designs are that (i) friction between the moving parts is reduced considerably and (ii) the overall torque on the apparatus during pressure change is zero. Therefore the Holzapfel's device is easier to handle inside a cryostat at low temperatures (Noack and Holzapfel 1978; Holzapfel 1984). Another useful device for single crystal work has been developed by Keller and Holzapfel (1977). The special shape of Be supports for the diamonds reduces the problem of x-ray absorption corrections in Be to a constant factor. The steel backings have wide conical apertures for the transmission of the diffracted x-rays over a wide angle. The device is capable of generating pressures of 10 GPa. Buras *et al* (1977) were the first to combine DAC with synchrotron radiation sources for high pressure x-ray diffraction studies and more recently Skelton *et al* (1984) and Spain *et al* (1981) have used DAC operated at cryogenic temperatures with synchrotron radiation. In order to provide pressure control at cryogenic temperatures, Skelton *et al* (1984) coupled the DAC to a dilution refrigerator with a bellows attachment capable of loading the piston of the DAC through a lever arrangement. The apparatus has been used to study the two critical points in the P-T diagram of number of Ce-rich Ce-rare earth-La alloys. A few other arrangements are described in the literature, which are essentially the same in principle as one of the above techniques (Alt and Kalus 1982; Spain 1984; Moudden *et al* 1980; Merrill and Bassett 1974).

CC-0. In Public Domain. Gurukul Kangri Collection, Haridwar

Digitized by Arya Samaj Foundation Chennai and eGangotri

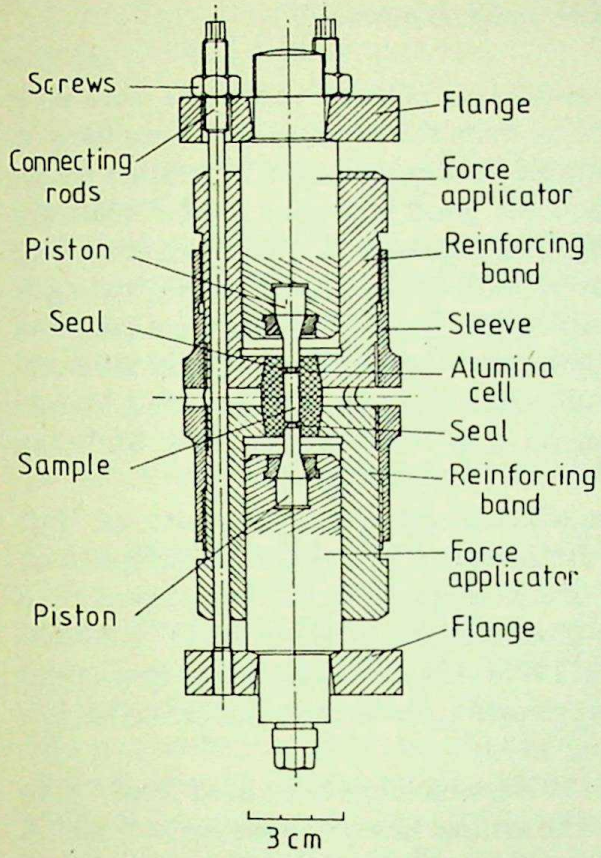

Figure 25. High pressure cell for neutron diffraction studies from 4 K to 300 K.

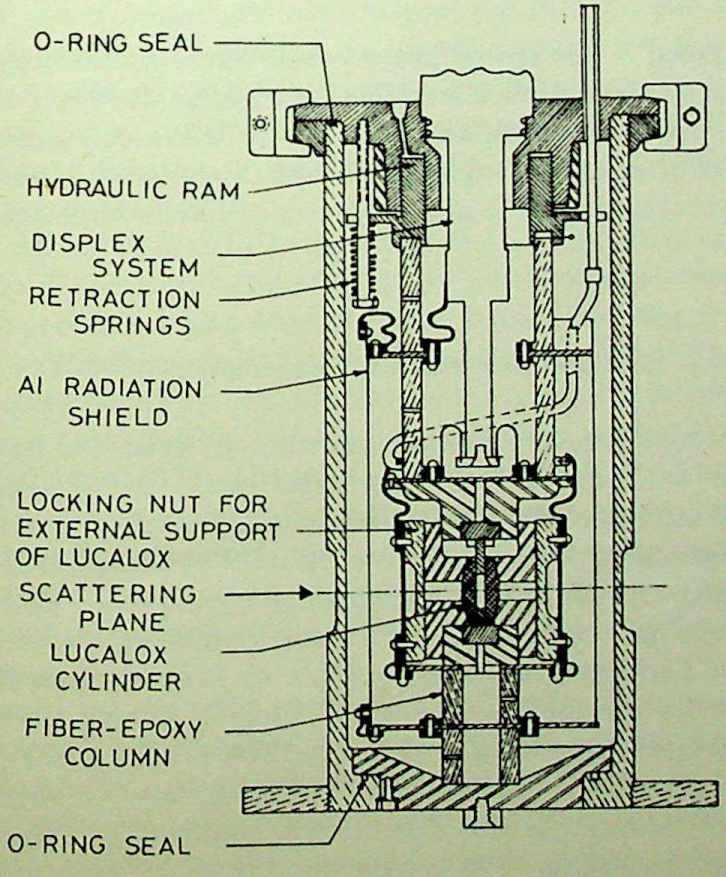

Figure 26. Neutron scattering high pressure cryostat with closed cycle refrigerators.

CC-0. In Public Domain. Gurukul Kangri Collection, Haridwar

Digitized by Arya Samaj Foundation Chennai and eGangotri

9. Neutron scattering at high pressures and low temperatures

The first inelastic neutron scattering experiments in the pressure range of 1 GPa were done in 1975. The cell design for high pressure neutron scattering depends on various parameters, such as the sample dimensions, sample absorption and temperature range. The construction materials should have sufficiently good transparency for neutrons. They are mainly aluminum alloys (Al-Zn-Mg-Cu), copper alloys (Cu-Be), maraging steels (Fe-Ni-Co-Mo) or alumina (Al_2O_3). For pressure-transmitting media, hydrogen compounds are not used due to their large incoherent scattering. The most common pressure-transmitting media are helium, C_6F_{12} fluorinert and deuterated ethanolmethanol mixture (Bloch *et al* 1976; Jansen and Will 1980; Vindryaevskii *et al* 1980; Mizuki and Endoh 1981; Kalus and Alt 1981; Kamigaki *et al* 1983; Walter 1984; McWhan 1984; Wu and Whalley 1985).

Standard cryostats are made of aluminium, which is transparent to neutrons. High pressure cells can be connected to a high pressure generator by means of a high pressure tubing. Clamped systems, with sufficiently small dimensions, allow conventional neutron cryostats to be used, as available in most reactors, without major consideration for low temperature problems (Bloch *et al* 1976). Another technique is to transmit the applied load from a hydraulic ram at room temperature to the pressure cell at low temperatures via insulating systems (McWhan 1979).

Figure 25 shows the Bloch's cell (Bloch *et al* 1976), which has been used from 4 K to 300 K and working pressures up to 0·4 GPa. The sample has a volume up to 5 cm^3. A shielding allows for safety in the reactor context. These cells have been used for 2-axes elastic scattering, 3-axes inelastic scattering as well as 4-circles elastic scattering experiments.

McWhan (1979) described a low temperature press, where a closed-cycle helium refrigerator is used to transmit the applied load from the hydraulic ram to the pressure cell via hollow fiber glass epoxy columns. The closed-cycle helium refrigerator has two cooling stations which are attached through flexible links to outer and inner radiation shields (figure 26). Temperatures of 20 K and pressures of 2 GPa have been achieved with this apparatus.

10. Raman spectroscopy at high pressure and low temperatures

The principal problem of high pressure Raman spectroscopy is to lead light into and out of a high pressure cell. In the scattering experiment, the incident light is monochromatic, and the intensity of the scattered light is measured as a function of frequency. The first Raman studies with DAC were reported by Brasch *et al* (1968) and Postmus *et al* (1968), employing forward scattering geometry. Adams *et al* (1973) found that good Raman spectra are obtainable with back scattering geometry. Many investigations have been performed on Raman effect in various materials at high pressure and room temperature (Jayaraman 1983). Only a few studies have been attempted at low temperatures (Morosin and Schirber 1974; Hawke *et al* 1974; Adams *et al* 1976; Kojima *et al* 1979; Jodl and Holzapfel 1979; Abdullah and Sherman 1980; Hirsh and Holzapfel 1981; Mazzinghi and Zoppi 1983; Hanfland and Syassen 1985; Wong 1985). Hirsch and Holzapfel (1981) have modified the Holzapfel' cell by providing a sapphire backing for the diamond to increase the angular aperture for the

CC-0. In Public Domain. Gurukul Kangri Collection, Haridwar

Digitized by Arya Samaj Foundation Chennai and eGangotri

scattered light. The sapphire block is about 10 mm in diameter, and 10 mm high and is surrounded by a slightly tapered sleeve. A simple cryostat with optical windows can be used for low temperature studies down to 77 K (Hirsch and Holzapfel 1981). Sharma *et al* (1980) have studied Raman spectra of H_2 up to 62·3 GPa using a DAC. Medina (1980) developed an optical cell for far-infrared spectroscopy up to 1·0 GPa pressure in the temperature range 10 K to 300 K. Kojima *et al* (1979) measured the Raman scattering at high pressures and low temperatures by using a DAC dipped in a liquid He cryostat combined with a double monochromater and Ar ion laser. This apparatus has been proven to be capable of measuring the polarized Raman spectra up to 5·0 GPa pressure and the unpolarized Raman spectra up to 20 GPa pressure.

11. NMR and ESR at high pressure and low temperatures

The nuclear magnetic resonance (NMR) studies at high pressures are of great use in understanding the magnetic interactions in solids at a microscopic livel. Though many articles discuss the NMR techniques at high pressures, only a few of them concentrate at low temperatures (Benedek 1963; Hauer *et al* 1980; Jonas 1980; Jonas *et al* 1981; Kiselnik 1983; Trokiner *et al* 1984). In high pressure-low temperature NMR studies the piston-cylinder apparatus made of Be-Cu alloy is commonly used (Cvec and Srinivasan 1978; Ramanathan and Srinivasan 1978; Sinha and Srinivasan 1983; Trokiner *et al* 1986). Sinha and Srinivasan (1983) have developed a clamp-type high pressure cell up to 1·0 GPa for NMR and EPR studies down to 77 K. Only a change of the bottom plug is required for a switch from a NMR to EPR experiment.

The mixture of *n*-pentane and isopentane in 1:1 ratio is used as the pressure-transmitting medium. The high pressure cell is calibrated at low temperatures by using a manganin pressure gauge. Huber *et al* (1984) developed a NMR probe head for high pressure studies up to 0·7 GPa. Helium gas is used as the pressure-transmitting medium. The apparatus is used to study the phase diagram of $RbAg_4I_5$ in the temperature range 77–300 K.

Van der Putten *et al* (1985) have devised a liquid helium cryostat containing a high pressure NMR probe, suitable for 1·5 GPa pressure in the temperature range from 2 to 100 K. The pressure cell consists of a two-part Be-Cu pressure vessel. The bottom part consists of a cylinder with an o.d. of 55 mm and length of 120 mm. The top part is fixed to it by means of a Be-Cu nut. The Be-Cu electrical feedthrough of the rf voltage to the NMR coil is mounted in the semispherical top part which is shown in figure 27 (Goedegebure *et al* 1977). The feedthrough, which meets the requirements of sealing at liquid He temperature and high pressure, has been developed by Schouten *et al* (1979). The top part of the pressure vessel contains a channel connected to the high-pressure capillary, used for filling and pressurizing the sample volume. This low temperature, high pressure probe was used in a series of NMR investigations of the properties of solid methane.

Stankowski *et al* (1976) performed EPR measurements up to 600 MPa in the temperature range 80 K to 400 K. The apparatus consisted of a cylindrical corundum resonator with TE_{112} type wave directly coupled to the wave guide by means of a matching corundum wedge. The pressure chamber, in which the resonator with two plugs was placed, was made of non-magnetic beryllium bronze. Prokhorov *et al* (1983) developed an ESR cell for pressures up to 1 GPa at temperatures 1·5 to 4·2 K. Sakai

CC-0. In Public Domain. Gurukul Kangri Collection, Haridwar

Digitized by Arya Samaj Foundation Chennai and eGangotri

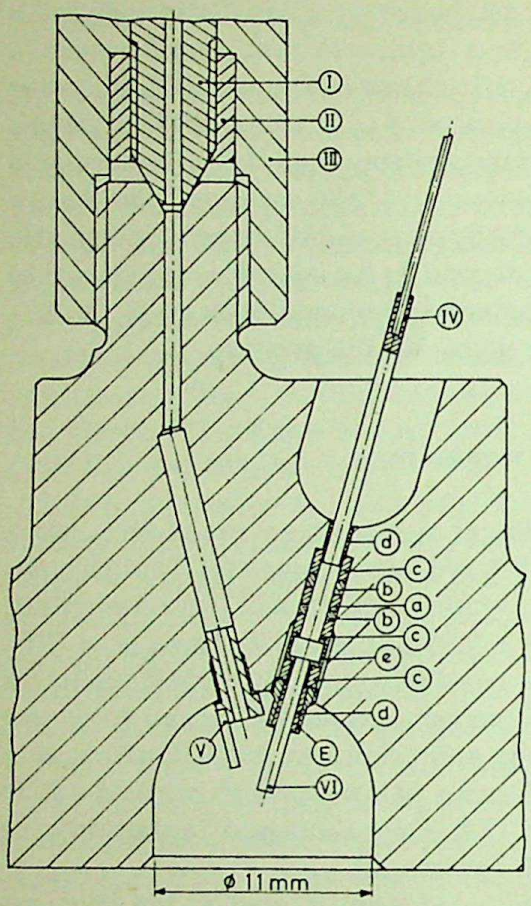

Figure 27. Electrical RF feedthroughs for high pressure NMR studies.

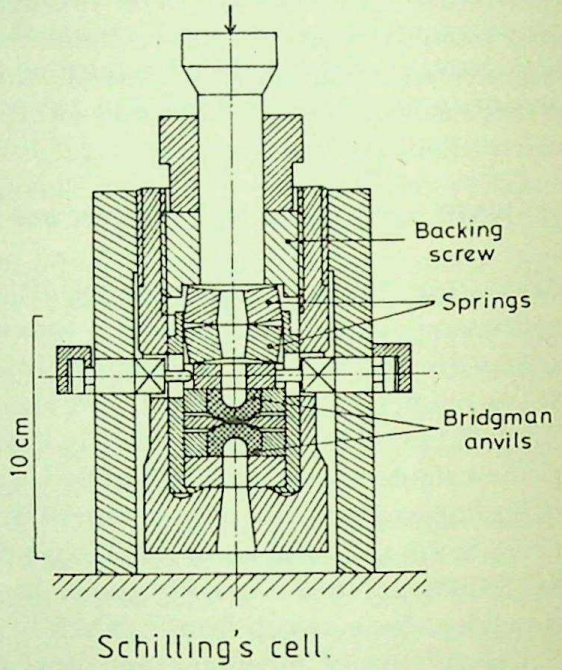

Figure 28. High pressure cell for Mössbauer studies at low temperatures.

and Pfier (1985) have developed a high pressure DAC for EPR studies. The technique for studying biomolecules at high pressure by EPR has been developed by Cannistarto (1984).

12. Mössbauer spectroscopy at high pressures and low temperatures

The effect of high pressure on Mössbauer spectroscopy of solids has been reviewed by many scientists (Holzapfel 1970, 1975, 1978; Drickamer *et al* 1965, 1969, 1970). High pressure Mössbauer studies at low temperatures are generally performed in clamp type cells (Christoe and Drickamer 1969; Syassen *et al* 1971; Schilling *et al* 1974; Liu and Ingalls 1978; Nikolaev and Potapov 1981).

Figure 28 shows the high pressure clamp cell developed by Schilling *et al* (1974) for Mössbauer studies up to 10 GPa pressures at temperatures down to 4·2 K. The major parts of the apparatus are made of Be-Cu alloy. The pressure on the sample was calibrated with a lead manometer. In the Mössbauer studies pressures in excess of 8 GPa were maintained at 4·2 K for periods of one week or longer (Bartunik *et al* 1970). Whitmore *et al* (1982) developed a ruby fluorescence system used for both Mössbauer and x-ray absorption spectroscopy with DAC at cryogenic temperatures.

CC-0. In Public Domain. Gurukul Kangri Collection, Haridwar

Digitized by Arya Samaj Foundation Chennai and eGangotri

13. Conclusions

An attempt has been made in reviewing the high pressure and low temperature techniques. Much progress has been made in this field after the introduction of the diamond anvil cell, which can produce 2 to 3 Mbar pressures at temperature down to few milli-Kelvin. A wide variety of the experimental techniques are available only for studying the transport and magnetic properties at high pressure and low temperatures. Spectroscopic measurements at high pressure and low temperature have been achieved in good measure only after the introduction of DAC in high pressure research. Though the piston-cylinder technique is the older one, limited in pressure range, this technique is still useful for NMR and ESR studies.

Acknowledgements

We express our sincere thanks to several scientists working in this area for the supply of the reprints of their publications. Over a period of time our work has been supported by research projects from the UGC, CSIR, DAE, DST, DOE and DRDO. We thank them for their sustained interest.

References

Abdullah A H and Sherman W F 1980 *J. Phys.* **E13** 1155
Ackermann H, Jones E D, Schirber J E and Overmyer D L 1985 *Cryogenics* **25** 496
Adams C Q and Davis C M 1958 *J. Appl. Phys.* **29** 372
Adams D M, Appleby R and Sharma S K 1976 *J. Phys.* **E9** 1140
Adams D M, Payne S J and Martin K M 1973 *Appl. Spectrosc.* **27** 377
Akahama Y, Endo S and Narita S 1986 *Physica* **B139/140** 397
Alekseevskii N E, Narozhnyi V N, Dodokin A P and Bagdasarvokh S 1985 *Sov. Phys. Dokl.* **30** 292
Alekseevskii N E, Narozhnyi V N and Khlybov 1983 *Sov. Phys. JETP* **57** 896
Alt H C and Kalus J 1982 *J. Phys.* **E15** 653
Alymov A V, Launkin V N, Rabinkin A G and Smirnova S A 1972 *Instrum. Exp. Tech.* **15** 214
Alymov A V, Launkin V N, Rabinkin A G and Smirnova S A 1973 *Cryogenics* **13** 112
Andersson P and Backstrom G 1976 *Rev. Sci. Instrum.* **47** 205
Andersson P, Ross R G and Slack G A 1986 *Physica* **B139/140** 163
Anzin V B, Kosichin Yu V, Kotlov Yu N and Nedezhdisnin A I 1976 *Cryogenics* **11** 376
Arntz H 1980 *Rev. Sci. Instrum.* **51** 965
Bachl F and Ludemann H D 1986 *Physica* **B139/140** 100
Balchan A S and Drickamer H G 1961 *Rev. Sci. Instrum.* **32** 308
Balt S, Musch J P, Renkena W E and Ronde H 1983 *J. Phys.* **E16** 829
Bandyopadhyay A K, Nalini A V, Gopal E S R and Subramanyam S V 1980 *Rev. Sci. Instrum.* **51** 136
Bartunik H D, Holzapfel W B and Mössbauer R L 1970 *Phys. Lett.* **A33** 469
Bassett W A, Takahashi T and Stook P W 1967 *Rev. Sci. Instrum.* **38** 37
Benedek G B 1963 *Magnetic resonance at high pressures* (New York: Wiley)
Benedek G B and Purcell E M 1954 *J. Chem. Phys.* **22** 2003
Benoit A, Delaplace R and Flouquet J 1974 *Phys. Rev. Lett.* **32** 222
Berman I V and Brandt N B 1968 *Sov. Phys. JETP Lett.* **7** 323
Berman R, Chaves F A B, Halton J and Mcilony P W A 1980 *J. Phys.* **E13** 871
Berton A, Chaussy J, Cornut B, Odin J, Paureau J and Peyard J 1979 *Cryogenics* **19** 543
Besson J M and Pinceause J P 1979 *Science* **206** 1073
Bloch D and Pauthenet R 1962 *Comp. Rend.* **254** 1222

CC-0. In Public Domain. Gurukul Kangri Collection, Haridwar

Digitized by Arya Samaj Foundation Chennai and eGangotri

Bloch D, Paureau J, Voiron J and Parisot G 1976 *Rev. Sci. Instrum.* **47** 296
Block S and Piermarini G J 1976 *Phys. Today* **29** 44, 50, 54
Bock W J and Wisneiwski R 1983 *J. Phys.* **E16** 740
Bowen D H 1958 *Proc. 5th Int. Conf. on Low Temp. Phys. and Chem.* (ed) J R Dillinger (Madison: Univ. of Wisconsin) p. 337
Bradley C C 1969 *High pressure methods in solid state research* (London: Butterworths)
Bradley R S 1966 *Advances in high pressure research* (London: Academic Press) Vol. 1
Bradley R S 1969a *Advances in high pressure research* (London: Academic) Vol. 2
Bradley R S 1969b *Advances in high pressure research* (London: Academic Press) Vol. 3
Brandt N B and Ginzburg N I 1965 *Sov. Phys. Usp.* **8** 202
Brandt N B and Ginzburg N I 1969 *Contemp. Phys.* **10** 355
Brandt N B and Ginzburg N I 1971 *Sci. Am.* **224** 83
Brandt N B, Berman I V, Kurkin Yu P and Sidorov V I 1976 *Cryogenics* **47**
Brandt N B, Itskevich E S and Minina NYa 1972 *Sov. Phys. Usp.* **14** 438
Brasch J W, Melveger A J and Lippincott E R 1968 *Chem. Phys. Lett.* **2** 99
Bridgman P W 1932 *Proc. Am. Acad. Arts. Sci.* **67** 305
Bridgman P W 1937 *Proc. Am. Acad. Arts. Sci.* **72** 45
Bridgman P W 1952 *Proc. Am. Acad. Arts and Sci.* **81** 165
Buckel W and Gey W 1963 *Z. Phys.* **176** 336
Bundy F P 1986a *Physica* **B139/140** 42, 390
Bundy F P and Dunn K J 1980 *Rev. Sci. Instrum.* **51** 26, 753
Buras B, Staun J, Olsen S, Gerward L, Will G and Hize E 1977 *J. Appl. Crystallogr.* **10** 431
Calado J C G and Street W B 1978 *Fluid Phase Equil.* **2** 275
Cannistarto S 1984 *Rev. Sci. Instrum.* **55** 996
Chaisse F, Dampne G, Humbert M and Voiron J 1970 *Proprietes Physiques des Solides sous Procession* (Paris: CNRS) p. 505
Chester P F and Jones G O 1953 *Philos. Mag.* **44** 1281
Christoe C W and Drickamer H G 1969 *Rev. Sci. Instrum.* **40** 169
Chu C W and Woolam J A 1978 *High pressure-low temperature physics* (New York: Plenum)
Chu C W, Hor P H and Zhao Z X 1986 *Physica* **B139/140** 439
Clark W G 1964 *Rev. Sci. Instrum.* **35** 316
Compy E M 1970 *J. Appl. Phys.* **41** 2014
Cromer D T, Mills R L, Schirferl D and Schwalbe L A 1981 *Acta Crystallogr.* **B37** 8
Cvec P and Srinivasan R 1978 *Rev. Sci. Instrum.* **49** 1282
Dahan N, Barrau B, Pinzutti G, Moszkowski J and Martinez G 1982 *J. Phys.* **E15** 587
Daniels W B 1983 *Rev. Sci. Instrum.* **54** 115
Dawson D R and Offen H W 1980 *Rev. Sci. Instrum.* **51** 1349
Decker D L 1971 *J. Appl. Phys.* **42** 3239
Diatschenkov V and Chu C W 1975 *Rev. Sci. Instrum.* **46** 1291
Diatschenkov V and Chu C W 1981 *Science* **212** 1393
Drickamer H G, Bastron V C, Fisher D C and Grenoble D C 1970 *J. Solid State Chem.* **2** 94
Drickamer H G, Fitch R A and Slykhouse T E 1957 *J. Opt. Soc. Am.* **47** 1015
Drickamer H G, Fung S C and Lewis Jr G K 1969 in *Advances in high pressure research* (ed.) R S Bradley (New York: Academic Press) p.1
Drickamer H G, Ingalls R L and Coston C J 1965 *Physics of solids at high pressure* (eds) I Tomizuka and R Emric (New York: Academic) p. 313
Dugdale J S 1969 *Advances in high pressure research* (ed.) R S Bradley (New York: Academic) p.101
Eichler A and Wittig J 1968 *Z. Angew Phys.* **25** 319
Eichler A and Gey W 1969 *Rev. Sci. Instrum.* **50** 1445
Eiling A, Schilling J S and Bach H 1981 *Physics of solids under high pressure* (eds) J S Schilling and R N Shelton (Amsterdam: North Holland) p. 385
Fasol G and Schilling J S 1978 *Rev. Sci. Instrum.* **49** 1722
Franck J P, Lundgren K R and McGreer K A 1986 *Physica* **B139/140** 230
Frankel J, Rich F J and Homan C G 1977 *High pressure science and technology* (eds) K D Timmerhaus and M S Barber (New York: Plenum) p. 147
Fujii G and Nagano H 1971 *Cryogenics* **11** 142
Fujii G and Nagano H 1972 *Jpn. J. Appl. Phys.* **11** 1347

CC-0. In Public Domain. Gurukul Kangri Collection, Haridwar

Digitized by Arya Samaj Foundation Chennai and eGangotri

Fujii G and Nagano H 1975 *Jpn. J. Appl. Phys.* **14** 919
Fujii G, Oda Y and Nagano H 1972 *Jpn. J. Appl. Phys.* **11** 591
Fujii G, Oda Y and Nagano H 1974 *Proc. IV Int. Conf. on High Pressure Kyoto* (ed) J. Osugi (Kyoto: The Physico-Chemical Society of Japan) p. 792
Fujikawa H, Kadomatsu H and Tohma K 1980 *Rev. Sci. Instrum.* **51** 1345
Fujisawa H 1984 *Jpn. J. Appl. Phys. Suppl.* **23-1** 51
Fujiwara H, Kadomatsu H and Tohma K 1980 *Rev. Sci. Instrum.* **51** 1345
Gaidukov Yu P and Itskevich E S 1964 *Sov. Phys. JETP* **18** 51
Geijsel J I, Shouten J A and Trappeniers N J 1982 in High pressure in Research and Industry (eds) C M Backman, T Johannison and L Tegner (Uppsala: Univ. Uppsala) p. 424
Giardini A and Lloyd E C 1963 *High pressure measurements* (New York: Butterworths)
Goedegebuure W, Schouten J A and Trappeniers N J 1977 *Rev. Sci. Instrum.* **48** 1213
Goettel K A, Mao H K and Bell P M 1985 *Rev. Sci. Instrum.* **56** 1420
Golopentia D A and Ruoff A L 1981 *Rev. Sci. Instrum.* **52** 235
Gossard A C, McWhan D B and Remeika J P 1970 *Phys. Rev.* **B2** 3762
Guertin R P and Foner S 1974 *Rev. Sci. Instrum.* **45** 863
Guy D R P, Friend R H and Levy F 1986 *Physica* **B139/140** 433
Hagelberg M P and Corsaro R D 1985 *J. Acoust. Soc. Am.* **77** 1222
Hanfland M and Syassen K 1985 *J. Appl. Phys.* **57** 2752
Hardebush U, Gerhardt W and Schilling J S 1980 *Phys. Rev. Lett.* **44** 352
Hauer H, Volkel G, Lang E and Ludemann H D 1980 in *High pressure science and technology* (eds) B Vodar and Ph. Marteau (New York: Pergamon) Vol. 2 p.794
Hawke R S, Syassen K and Holzapfel W B 1974 *Rev. Sci. Instrum.* **45** 1593
Hazen R M, Mao H O K, Finger L W and Bell P M 1980 *Appl. Phys. Lett.* **37** 288
Hirsh K R and Holzapfel W B 1981 *Rev. Sci. Instrum.* **52** 52
Holzapfel W B 1970 *High Temp-High Press.* **2** 241
Holzapfel W B 1975 *CRC Crit. Rev. Solid State Sci.* **5** 89
Holzapfel W B 1978 in *High pressure chemistry* (ed) H Kelm (New York: Reidel) p. 159
Holzapfel W B 1984 *Rev. Phys. Appl.* **19** 705
Homan C G 1975 *J. Phys. Chem. Solids* **36** 1249
Homan C G, Frankel J and Kendall P 1978 in *High pressure low temperature physics* (eds) C W Chu and J A Woollam (New York: Plenum) p. 529
Huber H, Mali M, Roes J and Brinkmann D 1984 *Rev. Sci. Instrum.* **55** 1325
Ido H and Satosh E 1982 *Solid State Phys.* **17** 157
Ilina M A and Itskevich E S 1967 *Sov. Phys. Solid State* **8** 1873
Ilina M A and Itskevich E S 1970 *Sov. Phys. Solid State* **12** 965
Itskevich E S 1964 *Cryogenics* **4** 365
Itskevich E S 1984 *Mater. Res. Soc. Symp. Proc.* **22** 331
Itskevich E S and Kashirskaya L M 1982 *Fiz. Tverd. Tela* **24** 1129
Itskevich E S and Kraidenov V F 1975 *Cryogenics* **15** 552
Itskevich E S and Kraidenov V F 1978 *Instrum. Exp. Tech.* **21** 1640
Itskevich E S, Tolmachev A W, Shirokov A M and Gridina N M 1979 *Instrum. Exp. Tech.* **22** 214
Itskevich E S, Voronovskii A N, Gowrilov A F and Sukhoparov V A 1966 *Prib. Tekh. Exsp.* **6** 161
Jamieson J C and Lawson A W 1962 *J. Appl. Phys.* **33** 776
Jansen E and Will G 1980 *High Temp. High Press.* **12** 205
Jayaraman A 1972 *Annu. Rev. Mater. Sci.* **2** 121
Jayaraman A 1983 *Rev. Mod. Phys.* **55** 65
Jayaraman A, Hudson A R, McFee J H, Coriell A S and Maines R G 1967 *Rev. Sci. Instrum.* **38** 44
Jennings L D and Swenson C A 1958 *Phys. Rev.* **112** 31
Jin X C, Hor P H, Wu M K and Chu C W 1984 *Rev. Sci. Instrum.* **55** 993
Jodl H J and Holzapfel W B 1979 *J. Raman Spectrosc.* **8** 185
Jonas J 1980 *Rev. Phys. Chem. Jpn.* **50** 19
Jonas J, Hasha D L, Lamb W J, Hoffman G A and Eguchi T 1981 *J. Magn. Res.* **42** 169
Jones Jr R E, Anderson G C and Keeler W J 1975 *Rev. Sci. Instrum.* **46** 1025
Kadomatsu H, Tohma K, Kurisu M, and Fujiwara H 1982 *Jpn. J. Appl. Phys.* **21** 140
Kadri A, Aulombard R L, Zitouni K and Konczewicz L 1986 *Physica* **B139/140** 426

CC-0. In Public Domain. Gurukul Kangri Collection, Haridwar

Digitized by Arya Samaj Foundation Chennai and eGangotri

Kalus J and Alt H 1981 *High Temp. High Press.* **13** 329
Kamigaki K, Kaneko T, Abe S and Ohashi M 1983 *Sci. Rep. RITU* **A31** 225
Kaneko T, Yoshida H, Abe S and Kamigaki K 1981 *J. Appl. Phys.* **52** 2046
Kawai N and Sawaoka A 1967 *Rev. Sci. Instrum.* **38** 1770
Kawamura H and Tachikawa K 1980 *Cryogenics* **20** 564
Kawamura H, Tachikawa K and Shimomura O 1985 *Rev. Sci. Instrum.* **56** 1903
Keller R and Holzapfel W B 1977 *Rev. Sci. Instrum.* **48** 517
Kelm H 1978 *High pressure chemistry* (Dordrecht: D. Reidel)
Kendall D P, Dembowski P and Davidson T E 1975 *Rev. Sci. Instrum.* **46** 629
Kiselnik V V 1983 *Instrum. Exp. Tech.* **26** 1459
Klug D D, Mishima O and Whalley E 1986 *Physica* **B139/140** 475
Kobayashi T 1985 *Rev. Sci. Instrum.* **56** 255
Kojima S, Nakamura T, Asaumi K, Takashige M and Minomura S 1979 *Solid State Commun.* **29** 779
Kondorski E I and Sedov V L 1960 *Sov. Phys. -JETP* **38** 773
Kortbeek P J, Biswas S N and Trappeniers N J 1986 *Physica* **B139/140** 109
Kourouklis G A, Hochheimer H D and Jayaraman A 1986 *Physica* **B139/140** 461
Kouvel J S and Wilson R H 1961 *J. Appl. Phys.* **32** 435
Kozhukhar A Yu, Lukin S N, Tsintsadze G A and Shapovalov V A 1975 *Instrum. Exp. Tech.* **18** 1252
Lakshmikumar S T and Gopal E S R 1981 *J. Indian Inst. Sci.* **A63** 277
Landau R and Wurflinger A 1980 *Rev. Sci. Instrum.* **51** 533
Lazarev B G and Kan L S 1944 *Sov. Phys. J.* **8** 361
Lazarus D, Jeffery R N and Weiss J D 1971 *Appl. Phys. Lett.* **19** 371
Levy M and Olsen J L 1965 *Rev. Sci. Instrum.* **36** 233
Lewis G J and Sherman W F 1974 *J. Phys.* **E7** 300
Libenberg D H 1979 *Phys. Lett.* **A73** 74
Lifshitz N and Maines R G 1979 *Rev. Sci. Instrum.* **50** 608
Litov E and Anderson O L 1978 *Phys. Rev.* **B18** 5705
Liu C M and Ingalls R 1979 *Rev. Sci. Instrum.* **49** 1680
Lloyd E C 1971 *Accurate characterization of high pressure environment* (NBS Special Publication)
Lloyd E C and Giardini A A 1964 *Symposium on high pressure technology* (New York: ASME Publications).
Lories Susse C 1980 *High Temp-High Press.* **12** 119
Lyon D N, McWhan D B and Stevens A L 1967 *Rev. Sci. Instrum.* **38** 1234
Mao H K and Bell P M 1979 *Science* **203** 1004
Mazzinghi R and Zoppi M 1983 *Rev. Sci. Instrum.* **54** 1585
McCumber D E and Sturge M D 1963 *J. Appl. Phys.* **34** 1682
McWane J W, Bijl D and Shiffman C A 1968 *Rev. Sci. Instrum.* **39** 1532
McWhan D B 1979 in *High pressure science and technology* (eds) K D Timmerhaus and M S Barber (New York: Plenum) p. 292
McWhan D B 1984 *Rev. Phys. Appl.* **19** 715
Medina F D 1980 *Infrared Phys.* **20** 297
Medvedev V S, Laisaar A I, Ermakov V M, Niilisk A I and Podolich V B 1978 *Instrum. Exp. Tech.* **21** 1682
Menyuk N, Kafalas J A, Dwight K and Goodenough J B 1969 *J. Appl. Phys.* **40** 1324
Merrill L and Bassett W A 1974 *Rev. Sci. Instrum.* **45** 290
Mills R L, Liebenberg D H, Bronson J C and Schmidt L C 1980 *Rev. Sci. Instrum.* **51** 891
Mizuki J and Endoh Y 1981 *J. Phys. Soc. Jpn.* **50** 914
Morosin B and Schirber J E 1974 *J. Appl. Crystallogr.* **7** 295
Moudden A H, Gatebois L, Denoyer F and Lambert M 1980 *Rev. Sci. Instrum.* **51** 836
Nefedova V V and Minin A P 1973 *Cryogenics* **13** 622
Nelson D A and Ruoff A L 1979 *Phys. Rev. Lett.* **42** 383
Nikolaev I N and Potapov V P 1981 *Instrum. Exp. Tech.* **24** 1292
Nishibata K and Izuchi M 1986 *Physica* **A13/140B** 903
Noack R A and Holzapfel W B 1979 *High pressure science and technology* (eds) K D Timmerhaus and M S Barber (New York: Plenum) p. 748
Padaki V C, Shaila M S, Sivaraman A, Sharatchandra H, Viswamitra M A and Gopal E S R 1979 *J. Acoust. Soc. India* **7** 47
Parthasarathy G, Bandyopadhyay A K, Lakshmi Kumar S T and Gopal E S R 1984 *J. Instrum. Soc. India* **14** 169

CC-0. In Public Domain. Gurukul Kangri Collection, Haridwar

Digitized by Arya Samaj Foundation Chennai and eGangotri

Patrick L 1954 *Phys. Rev.* **93** 384
Paureau J 1977 *J. Phys.* **E10** 1093
Pieper H, Schmid O and Knapp H 1984 *Cryogenics* **24** 339
Piermarini G and Block S 1975 *Rev. Sci. Instrum.* **46** 973
Pitt G D 1968 *J. Phys.* **E1** 915
Pitt G D and Lees J 1970 *Phys. Rev.* **B2** 4144
Porowski S, Konezykowski M and Bujnowski M 1977 *Proc. Int. Conf. High Pressure Low Temp. Phys.* (Ohio, Cleveland)
Postmus C, Maroni A, Ferraro J R and Mitra S S 1968 *Inorg. Nucl. Chem. Lett.* **4** 269
Prokhorov A D, Permyakov V Y, Neilo G N and Gavrish I G 1983 *Instrum. Exp. Tech.* **26** 719
Ramanathan K V and Srinivasan R 1978 *J. Phys.* **E11** 480
Ribault M and Benoit A 1978 *J. Phys. (Paris)* **C6** 1196
Ross R G, Andersson P and Backstrom G 1977 *High Temp-High Press.* **9** 87
Sakai N, Kajiwara T, Tsujik and Minomura S 1982 *Rev. Sci. Instrum.* **53** 499
Sakai N and Pfier J H 1985 *Rev. Sci. Instrum.* **56** 726
Samara G A 1981 *Physics of solids under pressure* (eds) J S Schilling and R N Shelton (Amsterdam: North Holland) p. 91
Samara G A 1984 *Solid state physics* (eds) H Ehrenreich and D Turnbull (New York: Academic Press) Vol. 38, p. 1
Samara G A and Giardini A A 1965 *Rev. Sci. Instrum.* **36** 108
Schiferl D, Cromer D T and Mills R L 1981 *Acta Crystallogr.* **B37** 1329
Schilling J S 1984 *Mater. Res. Soc. Symp. Proc.* **22** 79
Schilling J S, Kleim U F and Holzapfel W B 1974 *Rev. Sci. Instrum.* **45** 1353
Schilling J S and Shelton R N 1981 *Physics of solids under high pressure* (Amsterdam: North Holland)
Schirber J E 1970 *Cryogenics* **10** 418
Schirber J E 1974 in *Materials under high pressure* Tokyo p. 141
Schirber J E 1978 in *High pressure and low temperature physics* (eds) C W Chu and J A Woollam (New York: Plenum) p.55
Schirber J E 1981 in *Physics of solids under high pressure* (eds) J S Schilling and R N Shelton (Amsterdam: North Holland) p. 207
Schouten J A, Trappeniers N J and Goedegebuure W 1979 *Rev. Sci Instrum.* **50** 1652
Schouten J A and Van den Bergh L C 1986 *Physica* **B139/140** 57
Sharma S K, Mao H K and Bell P M 1980 *Phys. Rev. Lett.* **44** 886
Shaw R W and Nicol M 1981 *Rev. Sci. Instrum.* **52** 1103
Shchanov M F and Subbotin S I 1974 *Cryogenics* **14** 659
Sherman W F 1966 *J. Sci. Instrum.* **43** 462
Shimomura O, Asaumi K, Sakai N and Minomura S 1976 *Philos. Mag.* **B34** 839
Shimomura O, Minomura S, Sakai N, Asaumi K, Tamura K, Fukushima J and Endo H 1974 *Philos. Mag.* **B29** 547
Shirokov A M, Kosichkin Yu V, Anzin V B, Itskevich E S and Sukhoparov V A 1973 *Instrum. Exp. Tech.* **16** 902
Siddiqui M A and Lucas K 1982 *J. Chem. Thermodyn.* **14** 1183
Sigalas I, Hakansson B, Andersson P and Ross R G 1986 *Physica* **B139/140** 165
Silvera I F and Wijngaarden R J 1981 *Physica* **25** 104
Silvera I F and Wijngaarden R J 1985 *Rev. Sci. Instrum.* **56** 121
Simon F, Ruhemann M and Edwards W A M 1930 *Z. Phys. Chem.* **B6** 331
Sinha S and Srinivasan R 1983 *Rev. Sci. Instrum.* **54** 1492
Skelton E F, Spain I L, Yu S C, Liu C Y and Carpenter E R 1977 *Rev. Sci. Instrum.* **48** 879
Skelton E F, Webb A W, Qadri S B, Wolf S A, Lacoc R C, Feldman J L, Elam W T, Carpenter E R and Huang C Y 1984 *Rev. Sci. Instrum.* **55** 849
Smith T F 1972 *J. Low Temp. Phys.* **6** 171
Smith T F 1979 in *High pressure science and technology* (eds) K D Timmerhans and M S Barber (New York: Plenum) Vol. 1 p. 309
Smith T F and Chu C W 1967 *Phys. Rev.* **159** 353
Smith T F, Chu C W and Maple M B 1969 *Cryogenics* **9** 53
Spain I L 1984 *J. Phys. Colloq.* **45** 395
Spain I L, Quadri S B, Menoni C S, Webb A W and Skelton E F 1981 *Physics of solids under high pressure*

CC-0. In Public Domain. Gurukul Kangri Collection, Haridwar

Digitized by Arya Samaj Foundation Chennai and eGangotri

(eds) J S Schilling and R N Shelton (Amsterdam: North Holland) p. 73
Stager R A and Drickamer H G 1963 *Phys. Rev.* **135** 2524
Stajdohar R E and Towle L C 1965 *Symposium on high pressure technology* (eds) E C Lloyd and A A Giardini (New York: ASME)
Stankowski J, Galezewski A, Krupski M, Walplak S and Gierszal H 1976 *Rev. Sci. Instrum.* **47** 128
Stark R W and Windmiller L R 1968 *Cryogenics* **8** 272
Stewart J W 1962 *The world of high pressure* (Princeton: Van Nostrand)
Stewart J W and Swenson C A 1954 *Phys. Rev.* **94** 1069
Stewart W B and Calado J C G 1978 *J. Chem. Thermodyn.* **10** 1089
Street W B, Heintz A, Klancy P and Chokkappa D 1984 *High pressures in science and technology (Proc. Ninth ARAPT Conference, Albany)* (New York: Plenum) p. 105
Svechkarev I V and Panfilov A S 1965 *Sov. Phys. JETP Lett.* **2** 313
Swenson C A 1960 *Solid state physics* (New York: Academic Press) Vol. 11 p. 41
Syassen K, Christoe C W and Holzapfel W B 1971 *Z. Angew. Phys.* **31** 261
Syassen K and Holzapfel W B 1978a *Rev. Sci. Instrum.* **49** 1107
Syassen K and Holzapfel W B 1978b *Phys. Rev.* **B18** 5826
Takemura K, Fujii Y, Minomura S and Shimomura O 1979 *Solid State Commun.* **30** 137
Thompson J D 1984 *Rev. Sci. Instrum.* **55** 231
Thuillier J C, Konczewicz L, Aulombard R L and Kadri A 1986 *Physica* **B139/140** 417
Timmerhaus K D and Barber M S 1979 *High pressure science and technology* (New York: Plenum)
Trokiner A, Dahan N, Thaveneau H and Papon P 1984 *Rev. Sci. Instrum.* **55** 1616
Trokina A, Dahan N, Miquel J L, Theveneau H and Papon P 1986 *Physica* **B139/140** 319
Usha S 1984 *Magnetic studies at high pressures* Ph. D. Thesis, Indian Institute of Science, Bangalore, India
Van Dael W and Van Itterbeek A 1965 *Physics of high pressures and condensed phases* (ed.) A Van Itterbeek (Amsterdam: North Holland) p. 297
Van der Putten L, Prins K O, Trappeniers N J 1985 *Rev. Sci. Instrum.* **56** 603
Van der Putten L, Schouten J A and Trappeniers N J 1986 *Physica* **B139/140** 215
Van Itterbeek A 1965 *Physics of high pressures and the condensed phase* (Amsterdam: North Holland)
Van Itterbeek A and Van Dael W 1958 *Bull. Inst. Int. Froid. Ann.* **1** 295
Van Straaten J, Wijngaarden R J and Silvera I F 1982 *Phys. Rev. Lett.* **48** 97
Vereshchagin L F, Ilina M A and Itskevich E S 1969 *Instrum. Exp. Tech.* **19** 237
Vereshchagin L F, Kabaikina S S and Evdokimov V V 1958 *Prib. Tekh. Eksp.* **3** 90
Vereshchagin L F and Semechan A A 1961 *Sov. Phys. Dokl.* **136** 41
Vindryaevskii B A, Ishmaev S N, Podshibyakin V D, Sadikov I P, Chernyshov A A, Sukhoparov V A and Telepnev A S 1980 *Instrum. Exp. Tech.* **23** 1046
Vining C B and Shelton R N 1984 *Mater. Res. Soc. Symp. Proc.* **22** 29
Vodar B and Marteau Ph. 1980 *High pressure science and technology* (New York: Pergamon) Vols. 1 and 2
Voloshin V A and Kasyanov A I 1980 *Instrum. Exp. Tech.* **23** 211
Voloshin V A and Kasyanov A I 1982 *Instrum. Exp. Tech.* **25** 1243
Vyas M K P, Pitt G D and Hoult R A 1973 *J. Phys.* **C6** 285
Walter V 1984 *Rev. Phys. Appl.* **19** 833
Watson G H and Daniels W B 1986 *Physica* **B139/140** 472
Webb A W, Gubser D V and Towle L C 1976 *Rev. Sci. Instrum.* **47** 59
Weinstein B A 1984 *Philos. Mag.* **B50** 709
Werner K 1959 *Ann. Phys.* **7** 403
Whalley E 1986 *Physica* **B139/140** 314
Whitmore J E, Bruzzone C L and Ingalls R 1982 in *High pressure in research and industry* Vol. 2 (eds) C M Backman, T Johannison and L Tegner (Uppsala: Univ. of Uppsala) p. 579
Wieldraaijer H, Schouton J A and Trappeniers N J 1982 in *High pressure in research and industry* Vol. 2 (eds) C M Backman, T Johannison and L Tegner (Uppsala: Univ. of Uppsala) p. 571
Wijngaarden R J and Silvera I F 1980 *Phys. Rev. Lett.* **44** 456
Willer J and Moser J 1979 *J. Phys.* **E12** 886
Wittig J 1966 *Z. Phys.* **195** 215
Wittig J 1984 *Mater. Res. Soc. Symp. Proc.* **22** 17
Wohlleben D and Maple M B 1971 *Rev. Sci. Instrum.* **42** 1573
Wong P T T 1985 *Rev. Sci. Instrum.* **56** 1417

CC-0. In Public Domain. Gurukul Kangri Collection, Haridwar

Digitized by Arya Samaj Foundation Chennai and eGangotri

Wu A Y and Whalley E 1985 *Rev. Sci. Instrum.* **56** 1409
Wurflinger A 1980 *Bur Bunsengers Phys. Chem.* **84** 653
Yamada M and Schmidt V H 1978 *Rev. Sci. Instrum.* **49** 1226
Zhang D L, Wu M K, Lin T H, Hor P H, Chu C W and Thompson A H 1981 *Physics of solids under high pressure* (eds) J S Schilling and R N Shelton (Amsterdam: North Holland) p. 365
Zitouni K, Kadri A, Konczewicz L and Aulombard R L 1986 *Physica* **B139/140** 429

CC-0. In Public Domain. Gurukul Kangri Collection, Haridwar

Digitized by Arya Samaj Foundation Chennai and eGangotri

CC-0. In Public Domain. Gurukul Kangri Collection, Haridwar

Digitized by Arya Samaj Foundation Chennai and eGangotri

Pramāṇa – J. Phys., Vol. 28, No. 5, May 1987, pp. 471–482. © Printed in India

Low temperature elastic behaviour of As-Sb-Se and Ge-Sb-Se glasses

E S R GOPAL, T S MUKUNDAN*, J PHILIP† and S SATHISH

Department of Physics, Indian Institute of Science, Bangalore 560012, India
*Department of Physics, National College, Jayanagar, Bangalore 560011, India
†Department of Physics, University of Cochin, Cochin 682022, India

Abstract. The ternary glasses of arsenic and germanium with antimony and selenium can be prepared in large sizes for optical purposes. The elastic behaviour of eight compositions of each glass has been studied down to 4·2 K using a 10 MHz ultrasonic pulse echo interferometer. The glasses have a normal elastic behaviour, with the velocities gradually increasing as the temperature is lowered. An anharmonic solid model of Lakkad satisfactorily explains the temperature variations. The elastic moduli of $Ge_xSb_{10}Se_{90-x}$ glasses increase linearly as the Ge content is increased up to 25 at. % and beyond this the increase is nonlinear. $(AsSb)_{40}Se_{60}$ glasses show a linear increase in elastic moduli with increasing Sb content. The elastic moduli of $As_xSb_{15}Se_{85-x}$ glasses exhibit a drastic change near the stoichiometric composition $As_{25}Sb_{15}Se_{60}$. These behaviours have been qualitatively explained on the basis of the structural changes in glasses.

Keywords. Elastic behaviour; As-Sb-Se glasses; Ge-Sb-Se glasses; low temperature elasticity.

PACS Nos 61·40; 62·20

1. Introduction

Chalcogenide glasses have special electrical and optical properties (Baidkov 1966; Myuller 1966; Savage and Nielsen 1964; Webber and Savage 1976) and are becoming technologically important materials. These glasses can be prepared in large sizes. Their mechanical properties are quite important from the application point of view. In this paper we present the measurement of longitudinal and transverse ultrasonic velocities and elastic constants of two different classes of Ge-Sb-Se and As-Sb-Se glasses as a function of temperature from 300 K down to 4·2 K. In § 2 we describe the experimental methods for preparing the samples, the bonding technique and the ultrasonic velocity measurements. Section 3 discusses the results of low temperature elastic constants. These have been fitted to the Lakkad's anharmonic oscillator model. The composition dependence of the low and room temperature elastic constants has been explained using the chemically-ordered network model.

2. Experimental methods

Sample preparation

Samples for ultrasonic measurements should be fairly large in size, homogeneous and free of voids and perforations. Only a few glasses can be prepared with these properties

CC-0. In Public Domain. Gurukul Kangri Collection, Haridwar

Digitized by Arya Samaj Foundation Chennai and eGangotri

and chalcogenides are one among them. The Ge-Sb-Se and As-Sb-Se glasses in the form of cylinders (diameter 12 mm, thickness 4–8 mm) were prepared by the melt-quenching technique. As, Sb, Se and Ge (99·99% pure) obtained from Kochlight Company, UK were used. The required amount of materials were placed in a cleaned quartz tube. This is evacuated to a vacuum better than 10^{-3} mm of Hg and sealed in an argon atmosphere. The sealed ampoule is placed in a horizontal rotating furnace, the temperature raised to 1000°C and held at this temperature for 24 hr. The rotation ensures proper mixing of the constituents. The melt is then cooled to 800°C and quenched in water at 90°C. Care is taken to see that the ampoule remains vertical during quenching. The ampoule is annealed at a temperature about 5° lower than the glass transition (T_g) of the glass for an hour and then cooled slowly to room temperature. The quartz tube is broken carefully to remove the glasses without damaging the sample. Preannealing helped in removing the mechanical stress and in obtaining fairly strong samples.

For ultrasonic velocity measurements the two faces of the glasses were polished by handlapping and made parallel to each other (wedge angle better than 0·2 sec). The flatness and parallelism were checked by a dial gauge and the length of the samples was measured with a micrometer at room temperature.

3. Velocity measurements

The longitudinal and shear wave velocities have been measured in these glasses using a pulse echo interferometer which operates at a frequency of 10 MHz (Srinivasan *et al* 1975; Kartha *et al* 1980), and based on the McSkimin pulse superposition technique (McSkimin 1961; Papadakis 1976). Coaxial gold-plated X cut and Y cut quartz transducers (supplied by Bharat Electronics Ltd., Bangalore) of diameter 8 mm are used for generating longitudinal and shear waves. An adhesive from the special cellouse tape (Technical Trade Corporation, USA) has been used as a bonding material.

The bond for the ultrasonic measurements was made as follows. A thin plastic sheet with a circular aperture of about 10 mm diameter is cleaned and the cellouse tape is applied. This is placed on the cleaned surface of the sample and gently pressed uniformly so that the adhesive on the tape sticks to the sample. A drop of water is poured on the tape. After a few minutes the backing of the cellouse tape along with the plastic sheet is carefully peeled off with a sharp razor, leaving behind a thin layer of adhesive on the sample. The transducer is placed on this adhesive and gently pressed uniformly. This bond transfers both the longitudinal and transverse waves quite well and a good echo pattern could be obtained throughout the temperature range of 300 K to 4·2 K.

The ultrasonic velocities at low temperatures have been measured using the cryostat described elsewhere (Padaki *et al* 1985). Measurements were taken while the sample was cooled continuously at a slow rate of 10°C per hour.

4. Results and discussions

4.1 *Low temperature elastic constants of Ge-Sb-Se and As-Sb-Se glasses*

The ultrasonic longitudinal and transverse velocities have been measured for eight Ge-Sb-Se glasses ($Ge_{15}Sb_{10}Se_{75}$, $Ge_{20}Sb_{10}Se_{70}$, $Ge_{25}Sb_{10}Se_{65}$, $Ge_{30}Sb_{10}Se_{60}$,

CC-0. In Public Domain. Gurukul Kangri Collection, Haridwar

Digitized by Arya Samaj Foundation Chennai and eGangotri

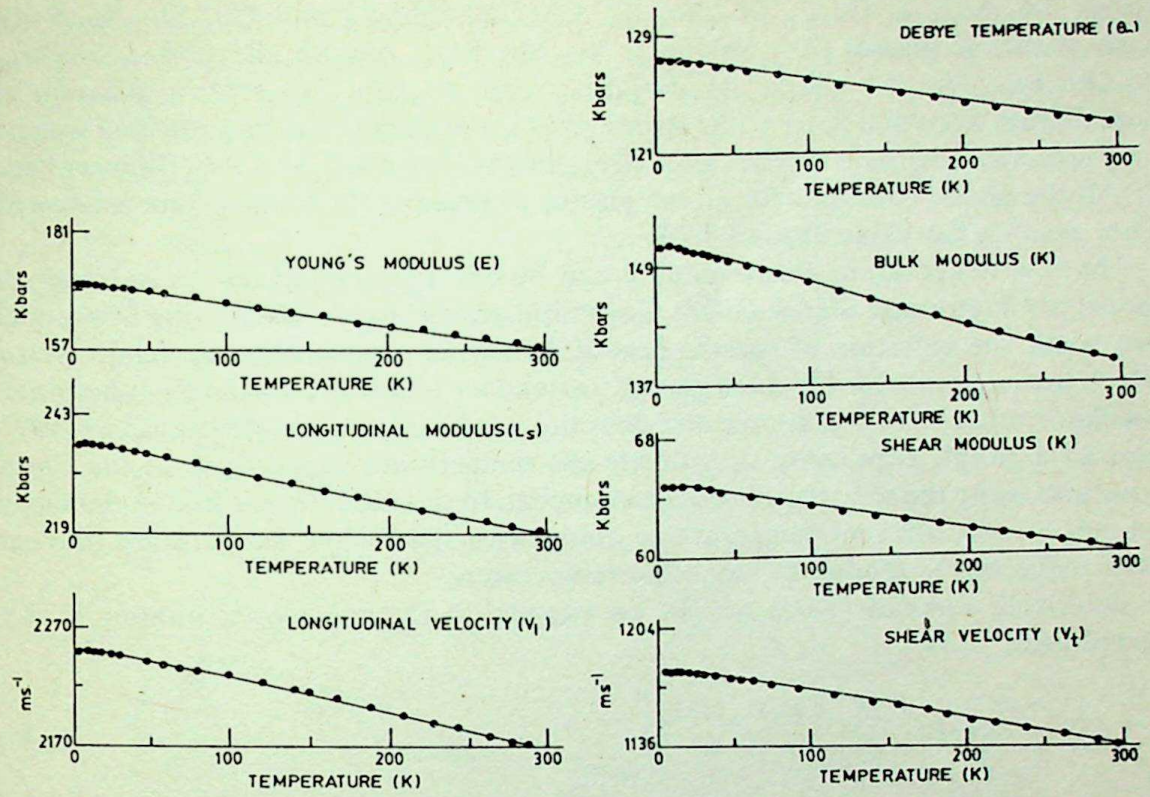

Figure 1. Temperature dependence of the elastic constants of $Ge_{15}Sb_{10}Se_{75}$ glass.

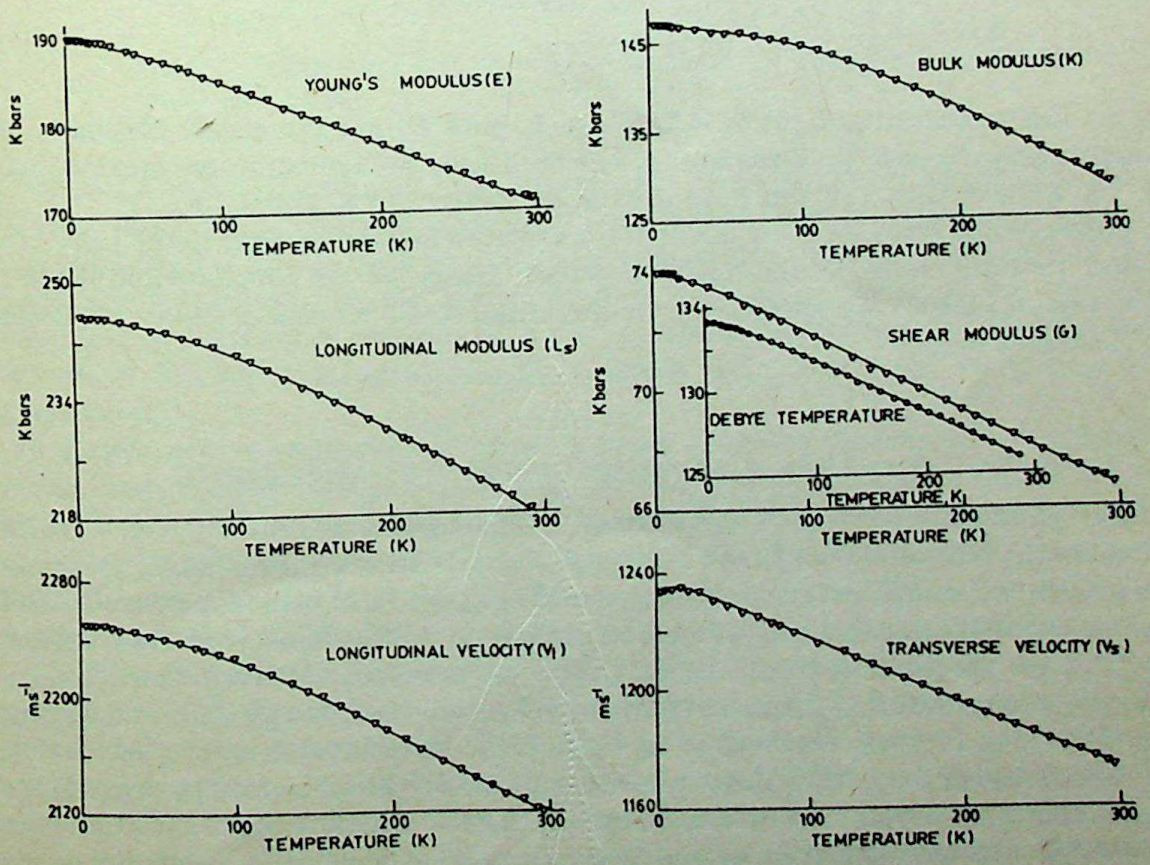

Figure 2. Temperature dependence of the elastic constants of $As_{10}Sb_{15}Se_{75}$ glass.

CC-0. In Public Domain. Gurukul Kangri Collection, Haridwar

Digitized by Arya Samaj Foundation Chennai and eGangotri

$Ge_{20\cdot84}Sb_{15}Se_{64\cdot16}$, $Ge_{16\cdot67}Sb_{20}Se_{63\cdot33}$, $Ge_{12\cdot5}Sb_{25}Se_{62\cdot5}$ and $Ge_{32}Sb_{10}Se_{58}$) and eight As-Sb-Se glasses ($As_{20}Sb_{15}Se_{65}$, $As_{25}Sb_{15}Se_{60}$, $As_{30}Sb_{15}Se_{55}$, $As_{30}Sb_{10}Se_{60}$, $As_{35}Sb_5Se_{60}$, $As_{22}Sb_{18}Se_{60}$, $As_{35}Sb_{15}Se_{60}$ and $As_{10}Sb_{15}Se_{75}$) as a function of temperature from 300 K to 4·2 K. Although a lot of data could be presented we give only representative data for each glass ($Ge_{15}Sb_{10}Se_{75}$ and $As_{10}Sb_{15}Se_{75}$) (figures 1 and 2). All the elastic constants for all the glasses increase as the temperature is lowered. They reach a flat value around 4·2 K.

The low temperature elastic moduli can be explained using the quasi-harmonic model of Claytor and Sladek (1978). To compute the elastic moduli using this model, one needs the variation of specific heat and thermal expansion at all temperatures which are not available for these glasses. Instead we follow the Lakkad's anharmonic oscillator model which is simple and does not need other parameters. Lakkad (1971) derived a simple expression to estimate the temperature dependence of the elastic constants using the anharmonic oscillator model. In this model if one knows the elastic moduli at two different temperatures along with the Debye temperature one can predict the elastic moduli at any other temperature.

Following Lakkad (1971) we get an expression for any elastic moduli E at a temperature T as

$$E = E_1 + \frac{(E_1 - E_2)}{(T_2 - T_1)}(T_1 - T), \tag{1}$$

in the high temperature limit, $\theta_D \ll T$.

$$E = E_1 + \frac{E_1 - E_2}{T_2^4 - T_1^4}(T_1^4 - T^4), \tag{2}$$

in the low temperature limit $\theta_D \gg T$, where E_1 and E_2 are the elastic constants at temperatures T_1 and T_2. Equation (1) has been used for temperatures greater than 20·5 K while equation (2) has been used in the range 20·5 K and 4·2 K.

Figures 3 and 4 clearly show the fit of the experimental data points to the Lakkad's model, for both Ge-Sb-Se and As-Sb-Se glasses. Hence we can conclude that the low temperature elastic constants for the Ge-Sb-Se and As-Sb-Se glasses can be predicted by Lakkad's model.

4.2 *Composition dependence of the elastic constants of Ge-Sb-Se glasses*

The longitudinal velocity (V_L), shear velocity (V_t), longitudinal modulus (L_s), Young's modulus (E), bulk modulus (K) and shear modulus (G) for the $Ge_xSb_{10}Se_{90-x}$ glasses as the content of germanium is increased is shown in figure 5a, at room temperature. The velocities and the elastic constants increase linearly up to 25 at.% of Ge and beyond this the changes are nonlinear, and the increase is steeper. Various properties like glass transition temperature (T_g), electrical conductivity, activation energy (ΔE), and density (d) (Savage *et al* 1978; Giridhar *et al* 1980, 1981; Narasimham *et al* 1981; Sudha Mahadevan *et al* 1983, 1984) also exhibit extrema at $Ge_{25}Sb_{10}Se_{65}$ composition. Since this nonlinear behaviour indicates a change in the basic structure of the glass Giridhar *et al* (1980, 1981) explained the properties on the basis of chemically oriented network model (CONM).

CC-0. In Public Domain. Gurukul Kangri Collection, Haridwar

Digitized by Arya Samaj Foundation Chennai and eGangotri

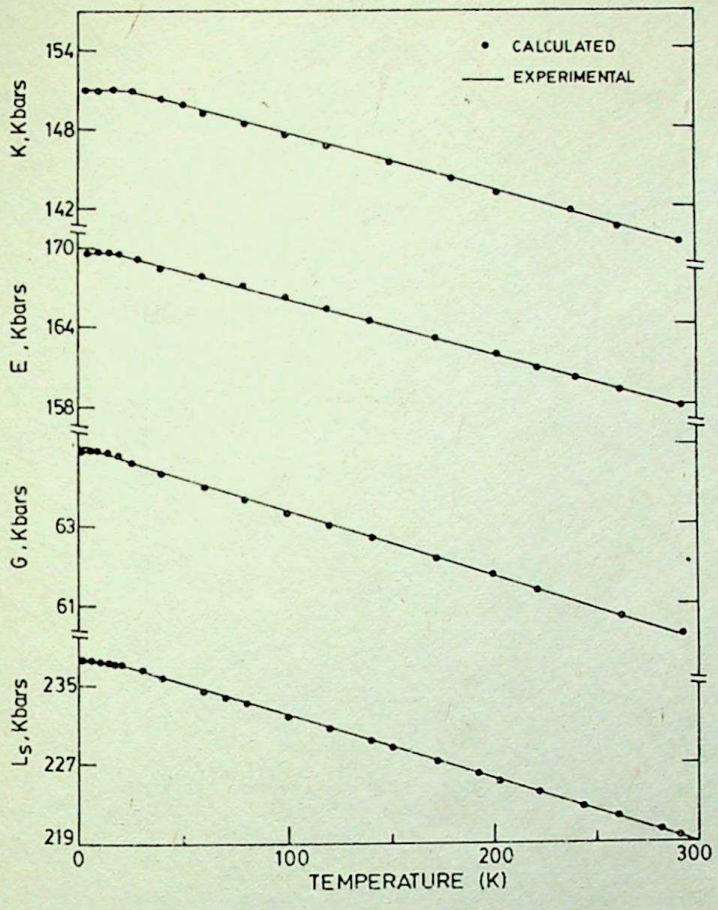

Figure 3. Temperature dependence of the calculated and experimental elastic constants of $Ge_{15}Sb_{10}Se_{75}$ glass.

The composition $Ge_{25}Sb_{10}Se_{65}$ can be written as $(GeSe_2)_{25}(Sb_2Se_3)_5$. Thus the glass structure can be pictured to be made up of cross-linked three-dimensional structural units of $GeSe_2$ and Sb_2Se_3 with Se or Ge in excess. At stoichiometric composition the bonds are heteropolar. If the Ge content is <25 at.%, some of the original $GeSe_2/Sb_2Se_3$ units are replaced by Se. Since Se is found in two-fold co-ordination, the strength of the resulting lattice would be lower than that of the stoichiometric composition.

In glasses with a small content of germanium, the three-dimensional tetrahedral $GeSe_{4/2}$ and trigonal $SbSe_{3/2}$ units are statistically distributed among the chains of extra selenium. When the germanium content in the glass increases, the excessive chains of selenium become gradually connected and the three-dimensional network of the glass develops due to increase of $GeSe_{4/2}$ units. This results in the strengthening of the glass framework and an increase of ultrasound velocity and elastic moduli as well as in the decrease of adiabatic compressibility. The selenium chains gradually degenerate into bridges of two selenium atoms -Se-Se-, while the increase of germanium over 15–20 at.% leads to their disappearance. The glass network in this part of compositions begins to build up from tetrahedrons $GeSe_{4/2}$ and pyramids $SbSe_{3/2}$ directly bonded to one another. This is completed in the glass containing 25 at.% of germanium, which lies on the pseudobinary section $GeSe_2$-Sb_2Se_3 and in which there is no excess selenium. The disappearance of bonds type -Se-Se-, that contribute to more advantageous space-

CC-0. In Public Domain. Gurukul Kangri Collection, Haridwar

Digitized by Arya Samaj Foundation Chennai and eGangotri

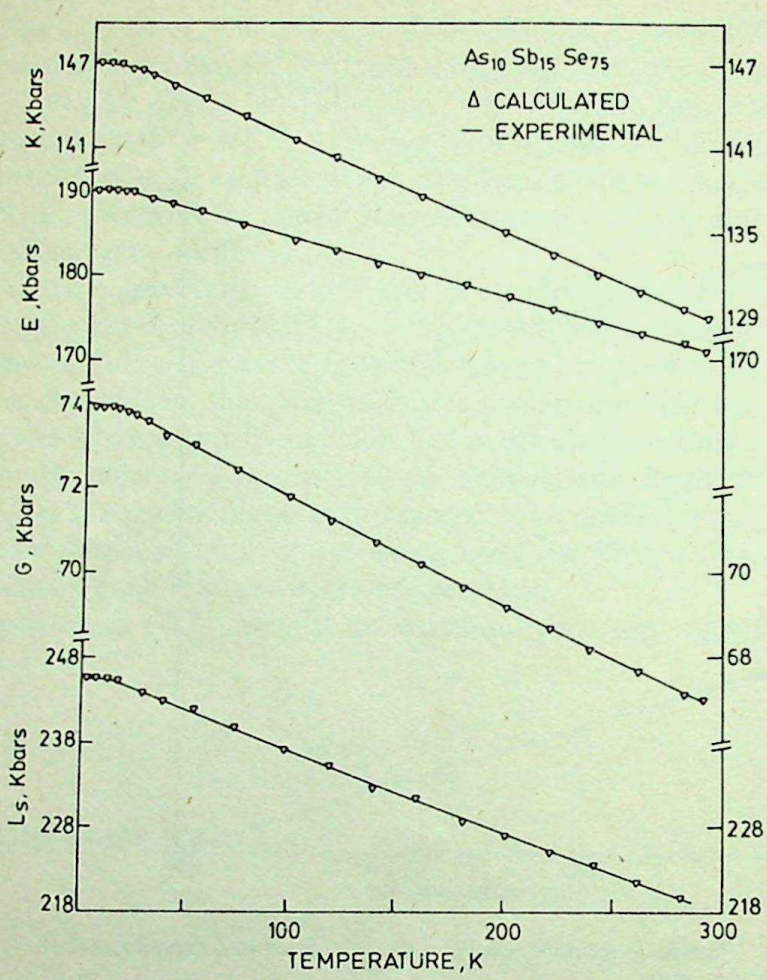

Figure 4. Temperature dependence of the calculated and experimental elastic constants of $As_{10}Sb_{15}Se_{75}$ glass.

packing of three-dimensional $GeSe_{4/2}$ and $SbSe_{3/2}$ units, result in the loosening of the structure and a decrease of density. The increase of germanium content over the stoichiometric relationship both in the binary system Ge-Se and in Ge-Sb-Se leads to an increased density; hence the moduli of elasticity rise again. Further Ge_xSe_{100-x} and $Ge_xAs_{60-x}Se_{40}$ glasses (Ota *et al* 1978; Tille *et al* 1977) exhibit a steep rise in velocities and elastic properties for Ge-rich glasses.

At room temperature the stoichiometric Ge-Sb-Se glasses with Sb = 10, 15, 20 and 25 have almost constant velocities and elastic constants as seen in figure 5b.

The bulk modulus (K) is related to mean atomic volume (V_a) by $K = \text{constant} \times V_a^{-m}$, $m = 4/3$ for a wide range of materials including alkaline earth silicate glasses and $m = 4$ for oxide and As-Se glasses. Glasses behave like crystals in showing an increase in bulk modulus with a decrease in volume. This trend is reversed in GeS_2-$GeSe_2$ (Ota *et al* 1978) and As_2S_3-As_2Se_3 glasses (Ota *et al* 1973; Thompson and Bailey 1978). Variation of ΔE, log σ, T_g with atomic percent of Ge for Ge-Se-Sb glasses and log K vs log V_a for $Ge_xSb_{10}Se_{90-x}$, $Ge_xAs_{20}Se_{80-x}$ and Ge_xSe_{100-x} containing Ge and Se as common elements are shown in figure 6. Taking the stoichiometric composition as reference in the $Ge_xSb_{10}Se_{90-x}$ system an increase in Se content reduces both mean atomic volume and bulk modulus. This may be due to weakening of structure due to an increase in chains. However the relation $K = \text{const} \times V_a^{-m}$ predicts that a decrease in

CC-0. In Public Domain. Gurukul Kangri Collection, Haridwar

Digitized by Arya Samaj Foundation Chennai and eGangotri

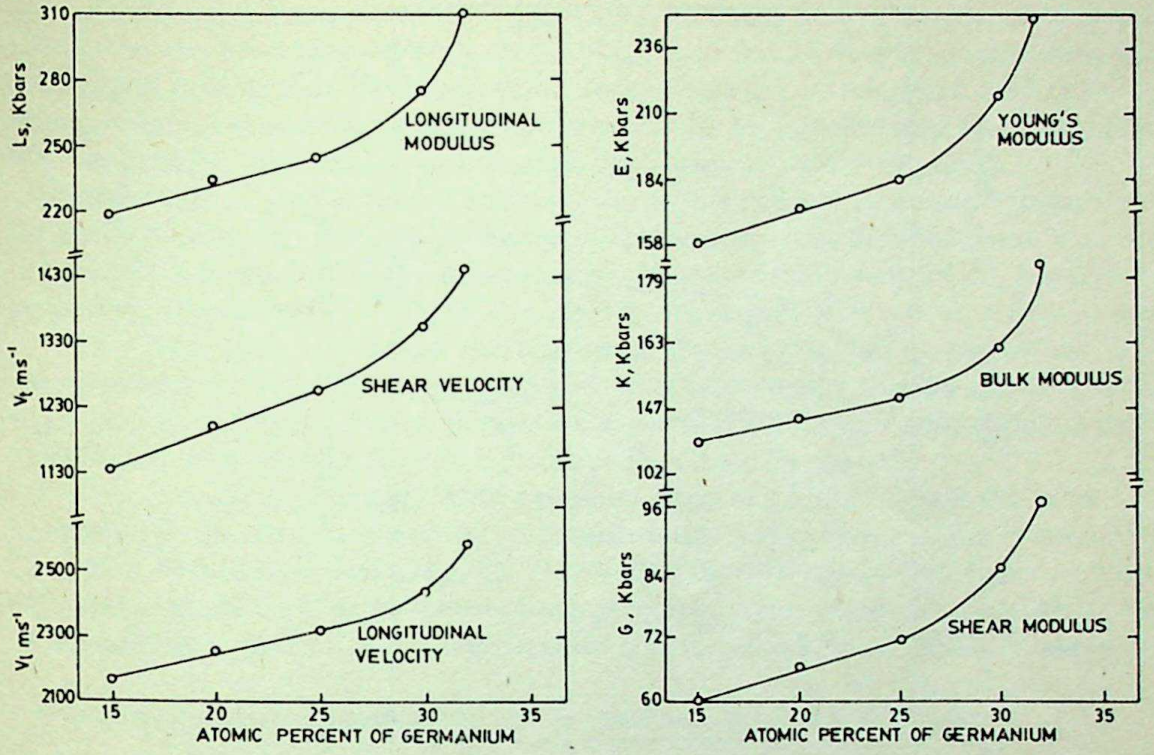

Figure 5. Variation of velocities and elastic moduli of $Ge_xSb_{10}Se_{90-x}$ glasses as Ge content is varied.

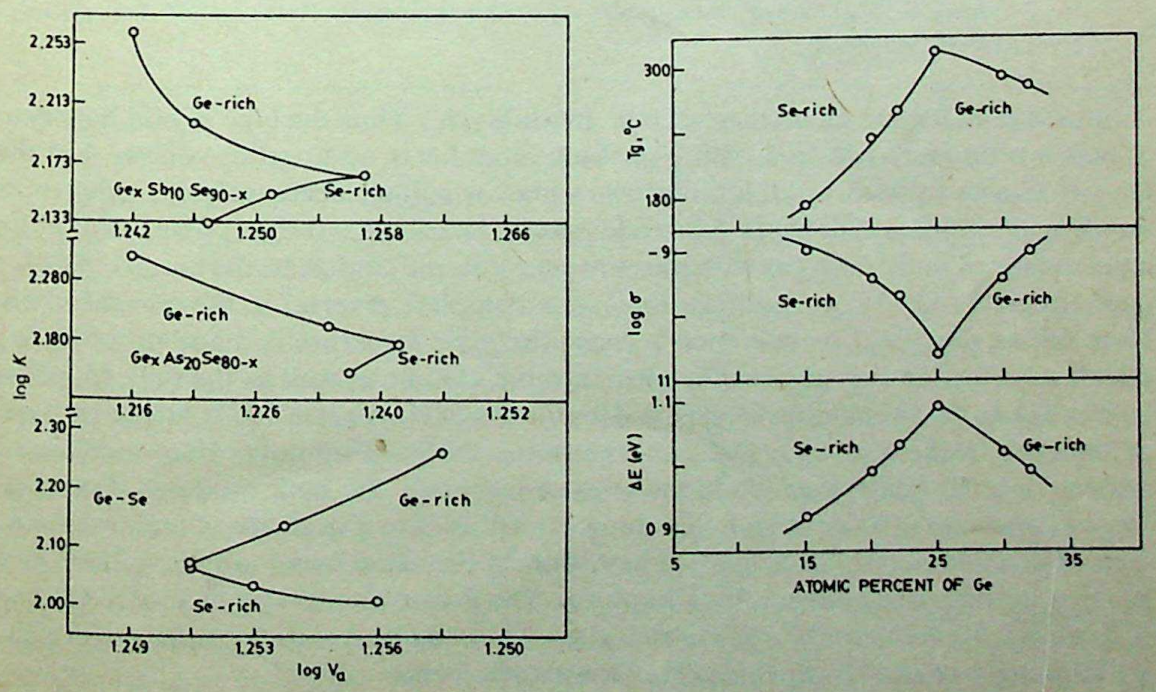

Figure 6. (a) The variation of log K with log V_a for $Ge_xSb_{10}Se_{90-x}$, $Ge_xAs_{20}Se_{80-x}$ and Ge_xSe_{100-x} glasses. (b) The variation of ΔE, log σ and T_g with Ge content for Ge-Sb-Se glasses.

CC-0. In Public Domain. Gurukul Kangri Collection, Haridwar

Digitized by Arya Samaj Foundation Chennai and eGangotri

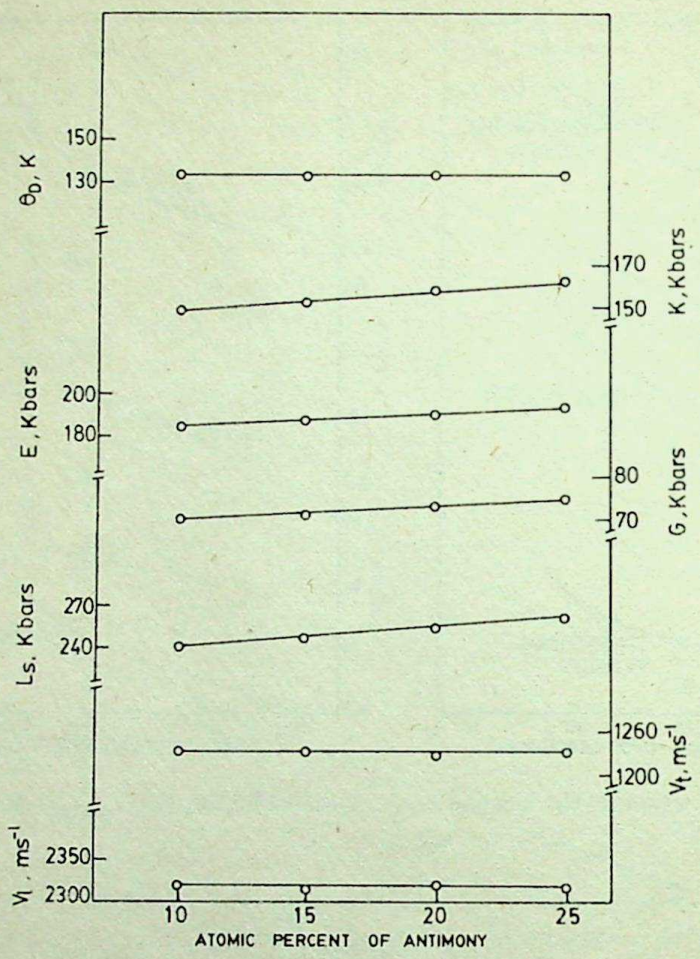

Figure 7. Variation of elastic properties for the stoichiometric $(GeSe_2)_{1-c}(Sb_2Se_3)_c$ glasses of Ge-Sb-Se system.

volume should lead to an increase of bulk modulus (K). Thus the type of bonding seem to play a prominent role in deciding the bulk modulus in addition to volume. For the Ge-rich glasses the bulk modulus increases while the volume decreased; this is due to an increase of tetrahedral network due to excess Ge. The $Ge_xAs_{20}Se_{80-x}$ glass also shows a behaviour of bulk modulus with mean atomic volume similar to the $Ge_xSb_{10}Se_{90-x}$ glass (figure 7). Ge_xSe_{100-x} glasses indicate a complete reversal in the general trend. Here taking $Ge_{20}Se_{80}$ as reference because the glass structure is made up of $GeSe_4$ tetrahedrae for Ge-rich glasses, the mean atomic volume as well as the bulk modulus increase. A similar behaviour is observed for Ge-Sb-S (Hayes *et al* 1974). Hence the type of bonding in the glasses is likely to determine the bulk modulus than increase in volume. For Se-rich region while the volume increases, the bulk modulus decreases. Thus an increase in Se content and volume contributes to a decrease of bulk modulus. The stoichiometric Ge-Sb-Se glasses have almost the same mean atomic volume and bonding leading to a constant bulk modulus. The Poisson's ratio (σ) of Se-rich Ge-Sb-Se glasses is higher than the σ of Ge-rich glass. This may be due to the structure of glass undergoing a change from chain-like to network form.

The Debye temperature (θ_D) is almost constant (133 K), because the mean atomic volume and velocities are constant.

The composition dependence of the low temperature velocities and elastic constants reveals that for $Ge_xSb_{10}Se_{90-x}$ group of glasses various properties increase smoothly

CC-0. In Public Domain. Gurukul Kangri Collection, Haridwar

Digitized by Arya Samaj Foundation Chennai and eGangotri

up to stoichiometric composition $Ge_{25}Sb_{10}Se_{65}$, whereas beyond this there is a steeper rise. In the stoichiometric glasses with Sb = 10, 15, 20 and 25 the parameters are almost constant. It is clear that the composition dependence at low temperatures follows the same pattern as that at room temperature except for an increase in magnitude. Hence the composition dependence can be explained using the CONM model.

In order to examine the role of antimony in the low temperature elastic properties of Ge-Sb-Se glasses, the percentage change of elastic properties between room temperature and 77 K is studied. In the stoichiometric glasses with Sb = 10, 15, 20, 25 at.%, the percentage change in V_L, V_t, L_s, G, E, K and θ_D are respectively $-2{\cdot}36$, $-2{\cdot}49$, $-4{\cdot}78$, $-5{\cdot}99$, $-4{\cdot}05$ and $-2{\cdot}90$ and the change is the same for all compositions. This indicates that for stoichiometric glasses of Ge-Sb-Se system, though the Sb content changes, the percentage change in elastic constants is the same. Thus antimony seems to influence very little the elastic behaviour for Ge-Sb-Se glasses.

For $Ge_xSb_{10}Se_{90-x}$ glasses with antimony kept at 10 at.%, while the content is increased (Se decreased), the elastic constants initially decrease, reach a minimum at Ge = 30 at.% and then increase again. So, we find that only Se or Ge content seems to induce changes in the elastic properties at low temperatures. Hence we conclude that Se or Ge content decides the low temperature elastic behaviour of Ge-Sb-Se glasses.

4.3 *Composition dependence of the elastic constants of As-Sb-Se glasses*

The As-Sb-Se glasses can be grouped into two categories. (a) Glasses whose composition can be represented as $(AsSb)_{40}Se_{60}$. These fall along the $(As_2Se_3)(Sb_2Se_3)$ pseudo-binary section representing the stoichiometric composition of the As-Sb-Se system. (b) Glasses whose composition can be represented as $As_xSb_{15}Se_{85-x}$. In these glasses, the $As_{25}Sb_{15}Se_{60}$ is taken as a reference stoichiometric composition and the

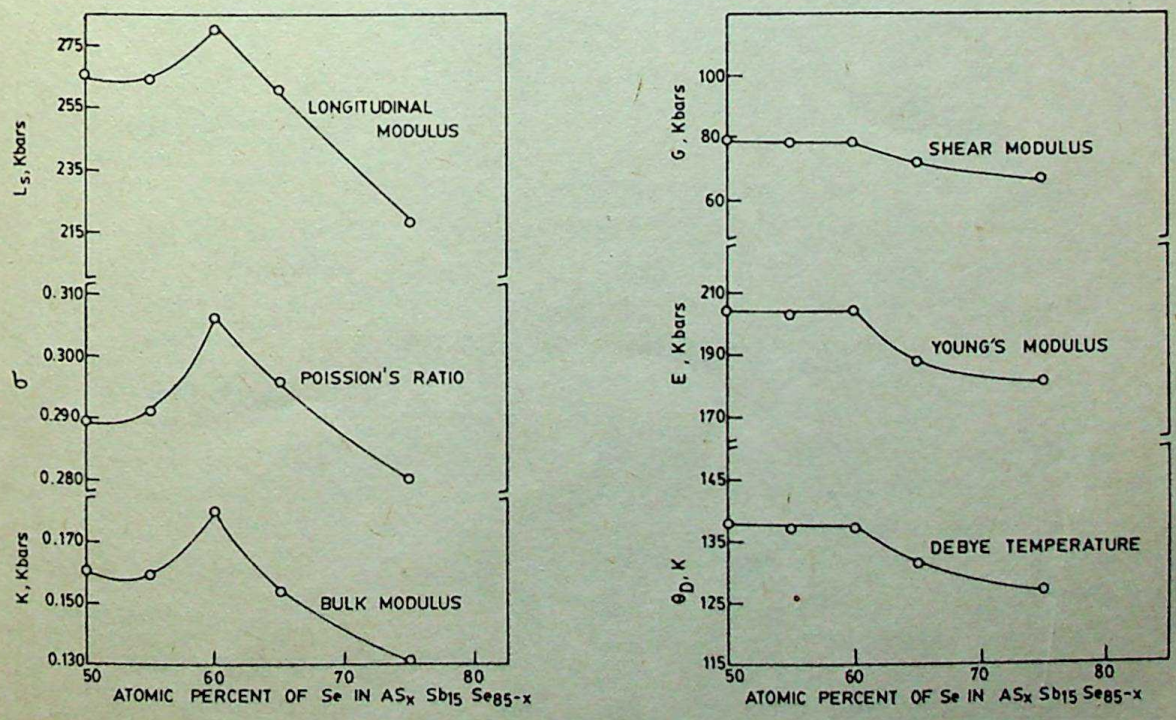

Figure 8. Variation of elastic moduli as a function of Se content for $As_xSb_{15}Se_{85-x}$ glasses.

CC-0. In Public Domain. Gurukul Kangri Collection, Haridwar

Digitized by Arya Samaj Foundation Chennai and eGangotri

glasses with >60 at.% of Se are called Se-rich glasses and glasses with <60 at.% of Se are called As-rich glasses.

The variation of longitudinal modulus (L_s), Poisson's ratio (σ), Debye temperature (θ_D), shear modulus (G), Young's modulus (E) and bulk modulus (K) for the $(As, Sb)_{40}Se_{60}$ glasses as the Sb content is increased is shown in figure 9. It is clear that the elastic moduli increase monotonically smoothly. The room temperature elastic constants are in good agreement with the measurements of Giridhar *et al* (1984). The extrapolated elastic moduli for zero at.% of Sb give the elastic constants for As_2Se_3 which are in good agreement with the measurement of Soga and Kungi (1973) for As_2Se_3.

The observation of the increase of mean atomic volume in isostructural compounds indicates an increase of bulk modulus (Anderson and Nafe 1965). For these glasses it is seen that the bulk modulus increases with increasing Sb_2Se_3 content while the corresponding volume is also increased. This shows that the type of bonding rather than the volume has a greater influence in determining the bulk modulus of these glasses. Such a dependence has been observed in many other glasses (Sudha Mahadevan *et al* 1983).

The variation of T_g, density have been observed by Giridhar *et al* and the elastic moduli do depend on these parameters. A qualitative explanation can be given for the variation of elastic moduli as follows. The T_g shows a slight increase with the increasing Sb content, indicating the strengthening of glass which is reflected in the increase of elastic moduli. The small increase is because As and Sb are isovalent and replacement of As by Sb does not drastically alter the basic structure of the glass. This is supported by the nearly equal bond energies of 52 kcal/mol and 51 kcal/mol of As-Se and Sb-Se bond (Giridhar *et al* 1982).

The elastic moduli G, E, K, L_s, σ and Debye temperature θ_D for $As_xSb_{15}Se_{85-x}$ glasses as the Se content is increased is shown in figure 8. Taking $As_{25}Sb_{15}Se_{60}$ as the

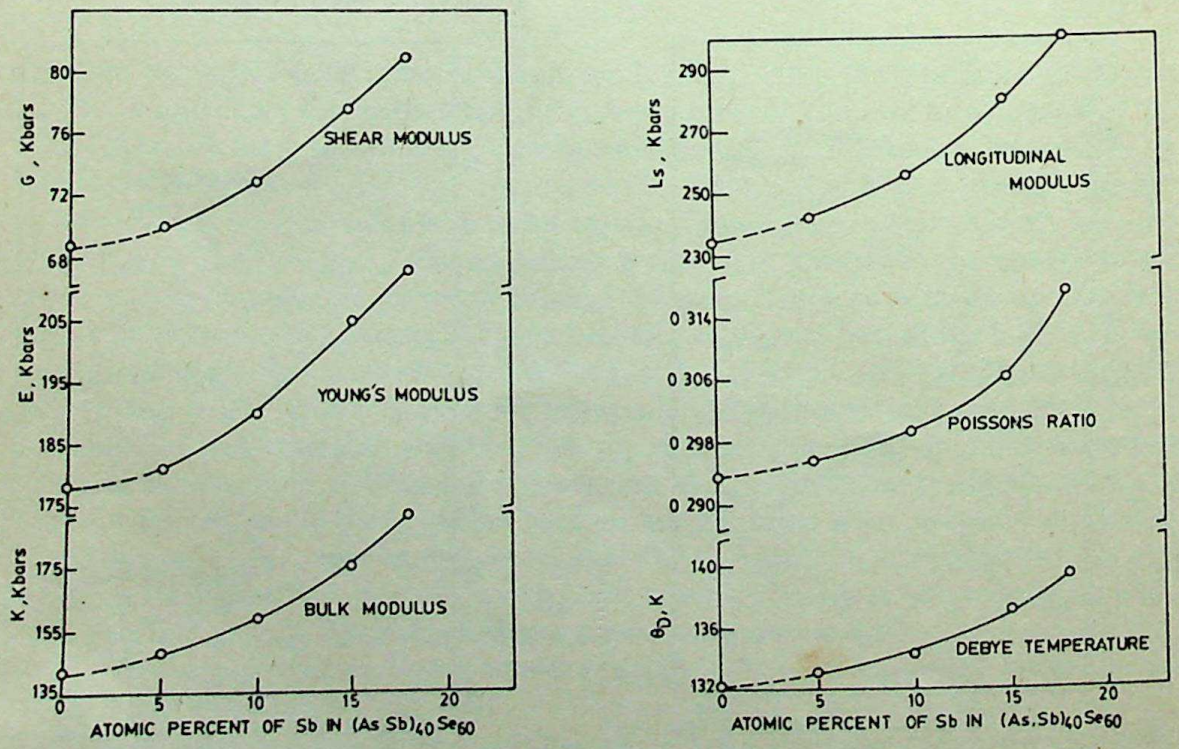

Figure 9. Variation of elastic moduli for $(As, Sb)_{40}Se_{60}$ glasses as a function of Sb content.

CC-0. In Public Domain. Gurukul Kangri Collection, Haridwar

Digitized by Arya Samaj Foundation Chennai and eGangotri

reference stoichiometric composition it is seen that the elastic moduli G, E and Debye temperature (θ_D) for As-rich glasses are constant whereas for Se-rich glasses they decrease sharply. These observations are in good agreement with the idea that higher the Se content lower the elastic moduli. The elastic moduli K, L_s and Poisson's ratio σ on the other hand show a decreasing trend on either side of the stoichiometric composition both for As as well as Se-rich glasses, with a steeper decrease on the Se-rich side compared to the As-rich side.

Using the CONM model and following the discussion for Ge-Sb-Sb glasses, we try to give a qualitative explanation for the observed behaviour of elastic moduli. The $As_{25}Sb_{15}Se_{60}$ glass can be thought of as made up of completely crosslinked three-dimensional structural units of As_2Se_3 and Sb_2Se_3 only with either As or Se in excess. For As-rich glasses some of the original AsSe units are replaced by As which does not drastically alter the resulting atomic arrangement. The As-As bond energy is 46 kcal/mol which is slightly less than the As-Se bond energy. However, with decreasing Se content in As-rich glasses the Sb_2Se_3/As_2Se_3 ratio progressively increases which slightly increases T_g. For the Se-rich glasses some of the original As_2Se_3 units are replaced by Se. Since Se is generally found in two-fold co-ordination, the T_g for these glasses can be expected to show a deep decrease. With increase in the Se content, the Sb_2Se_3 units would increase for Se-rich glasses which would increase T_g. But the lower the coordination number of Se can make T_g fall continuously for these glasses and hence the elastic moduli. The composition dependence of K and σ can be linked with the As_2Se_3 content, and As-Se bonds decide the elastic properties of these glasses. All the elastic properties show a general increase with increasing As_2Se_3 content. The Debye temperature θ_D is similar to that of selenide glasses (Sudha Mahadevan *et al* 1983). θ_D shows a variation with composition for both $(As, Sb)_{40}Se_{60}$ and $As_xSb_{15}Se_{85-x}$ series of glasses. Hence the As-Sb-Se system is relatively weakly bonded, with particularly low ultrasonic velocities and Debye temperature.

The low temperature elastic constants for various compositions of As-Sb-Se glasses at 77 K can be discussed now. It is seen that for As_x-$Sb_{15}Se_{85-x}$ glasses the elastic constants remain constant as the Se content is increased up to 60 at.%, and beyond the stoichiometric composition $As_{25}Sb_{15}Se_{60}$ they decrease drastically. This is similar to what has been observed at room temperature. So, the composition dependence can be explained using the CONM model. For the $(As, Sb)_{40}Se_{60}$ group of glasses, there is a smooth increase of elastic constants, and the percentage change in the elastic constants over the temperature range 296·4 K to 77 K is appreciable. For $As_xSb_{15}Se_{85-x}$ glasses in the As-rich range, the percentage change in elastic constants is almost constant. For selenium-rich glasses beyond stoichiometric composition, even a small addition of selenium induces a large percentage change in elastic constants. Hence, it could be concluded that selenium content plays a dominant role in deciding the low temperature elastic behaviour of As-Sb-Se glasses. In the case of $(As, Sb)_{40}Se_{60}$ glasses, the percentage changes in elastic constants are again almost constant indicating that although the As-Sb content is changing, it does not very much affect the elasticity of these glasses because the selenium content is constant. We therefore conclude that selenium plays a key role in deciding the elastic behaviour of As-Sb-Se glasses both at room and low temperatures.

A comparison of the elastic behaviour of the Ge-Sb-Se and As-Sb-Se glasses reveals that they have a negative temperature coefficient of elastic constants for all the glasses studied. A comparison can also be made of the two glasses, $Ge_{30}Sb_{10}Se_{60}$ and $As_{30}Sb_{10}Se_{60}$ in which only Ge has been replaced by As. This clearly shows that Ge-

CC-0. In Public Domain. Gurukul Kangri Collection, Haridwar

Digitized by Arya Samaj Foundation Chennai and eGangotri

based glasses are much tougher than As-based glasses, which is clearly indicated by the higher elastic moduli in Ge-based glasses. It also shows that the Ge-based glasses are less sensitive to temperature than As-based glasses.

5. Conclusions

(i) The elastic moduli of both Ge-Sb-Se and As-Sb-Se glasses smoothly increases as the temperature is decreased down to 4·2 K. (ii) The temperature dependence of low temperature elastic constants can be explained with Lakkad's anharmonic oscillator model for both the glasses. (iii) The composition dependence of elastic moduli both at low and room temperatures can be explained using the chemically ordered network model. (iv) The germanium-based glasses are much harder and less sensitive to the temperature than arsenic based glasses.

6. Acknowledgements

We specially thank Dr A K Singh and Dr (Mrs) Sudha Mahadevan for the samples used in the study.

References

Anderson O L and Nafe J E 1965 *J. Geophys.* **70** 3951
Baidakov L A 1966 *Solid state chemistry* (ed.) R L Myuller (New York: Consultants Bureau) p. 94
Claytor T N and Sladek R J 1978 *Phys. Rev.* **B18** 5842
Giridhar A, Narasimham P S L and Sudha Mahadevan 1980 *J. Non-Cryst. Solids* **37** 165
Giridhar A, Narasimham P S L and Sudha Mahadevan 1981 *J. Non-Cryst. Solids* **43** 29
Giridhar A and Sudha Mahadevan 1982 *J. Non-Cryst. Solids* **51** 1001
Giridhar A, Sudha Mahadevan and Singh A K 1984 *Bull. Mater. Sci.* **6** 1001
Hayes D J, Rechtin M D and Hilton A R 1974 *Proc. Symp. on ultrasonics* (ed.) J. de Klerk (New York: Academic Press)
Kartha P E S, Padaki V C and Gopal E S R 1980 *Proc. Int. Cong. Exhibition on Ultrasonics* (ICEV-80) New Delhi, p. 19
Lakkad S C 1971 *J. Appl. Phys.* **42** 11, 4277
McSkimin H J 1961 *J. Acoust. Soc. Am.* **33** 12
Myuller R L (ed.) 1966 *Solid state chemistry* (New York: Consultants Bureau) p. 1
Narasimham P S L, Giridhar A and Sudha Mahadevan 1981 *J. Non-Cryst. Solids* **43** 301, 365
Ota R, Soga N and Kunugi M 1973 *J. Soc. Mater. Sci. Jpn* **22** 567
Ota R, Yamata T, Soga N and Kunugi M 1978 *J. Non-Cryst. Solids* **29** 67
Padaki V C, Lakshmikumar S T, Subramanyam S V and Gopal E S R 1985 *Pramana–J. Phys.* **17** 25
Papadakis E P 1976 *Physical acoustics* (eds) W P Mason and R N Thurston (New York: Academic Press) Vol. 12
Savage J A and Nielsen S 1964 *Phys. Chem. Glasses* **5** 82
Savage J A, Webber P J and Pitt A U 1978 *J. Mater. Sci.* **13** 859
Soga N and Kunugi M 1973 *J. Phys. Chem. Solids* **34** 2143
Srinivasan K R, Sivaraman A, Nagarajan N, Ramakrishnan and Gopal E S R 1975 *Proc. Symp. Transducer Technology Cochin, India* (Cochin: NPOL Press) p. 283
Sudha Mahadevan, Giridhar A, Narasimham P S L and Singh A K *J. Non-Cryst. Solids* **65** 233
Sudha Mahadevan, Giridhar A and Singh A K 1983 *J. Non-Cryst. Solids* **57** 423
Thompson J C and Bailey K E 1978 *J. Non-Cryst. Solids* **27** 161
Tille U, Frischat G H and Leers K J 1977 *Fourth Int. Conf. on Non-Cryst. Solids, Zellerfeld* (ed.) G H Frischat (New York: Trans-Tech Publication)
Webber P J and Savage J A 1976 *J. Non-Cryst. Solids* **20** 271

CC-0. In Public Domain. Gurukul Kangri Collection, Haridwar

Digitized by Arya Samaj Foundation Chennai and eGangotri

Pramāṇa – J. Phys., Vol. 28, No. 5, May 1987, pp. 483–488. © Printed in India.

Electromagnetic generation of ultrasound in metals at low temperatures

A N VASIL'EV and Yu P GAIDUKOV
Physical Department, Lomonosov State University, Moscow 119899, USSR

Abstract. Excitation of longitudinal and transverse ultrasound by electromagnetic waves incident on the metal surface is the subject of the present work. This is a simple and convenient experimental technique. The reason for this approach is to overcome the primary difficulty during precise measurements of the frequency or temperature dependences of the velocity and attenuation of ultrasound in pure metals by the conventional methods where it is difficult to achieve reliable acoustic contact between the transducer and the sample. The reasons are (i) the creation of this contact unavoidably results in a deformation of a surface layer of the metal affecting the experimental results, (ii) as the temperature is varied over a broad range, the properties of the acoustic contact itself change resulting in non-reproducible experimental results.

Keywords. Electromagnetic generation; ultrasound in metals; low temperature.

PACS No. 62·65

1. Physical principles

Over a wide range of frequencies, magnetic fields and temperatures, different mechanisms of contactless conversion of electromagnetic and ultrasonic waves come into play at the metal boundary. Nevertheless they can be discusssd within the framework of a single approach based on a detailed analysis of the drag on the crystal lattice exerted by the conduction electrons (Kontorovich 1970; Wallace 1971; Dobbs 1973; Vasil'ev and Gaidukov 1983).

In the normal skin-effect conditions the excitation of ultrasound by an electromagnetic wave incident on the metal surface is possible only in the presence of a constant magnetic field H_0. If this field is applied parallel to the surface of the metal and perpendicular to the direction of the alternating current, a Lorentz force directed inward into the metal acts on the electrons in the skin layer δ. This force produces a space modulation of the electric charge density and the ions of the lattice in the skin layer rearrange themselves such that within the volume of the metal the condition of local electric neutrality would be satisfied. As a result, a compression wave is excited at the surface and propagates inwards into the metal.

In a magnetic field directed normal to the surface transverse sound is excited in the metal. This is due to the fact that under the action of the electric field of the wave the momenta of the electrons and the ions in the skin layer are opposite directed and the Lorentz force deflects these particles in the same direction.

In both cases when longitudinal or transverse sound is excited the equation of forced

CC-0. In Public Domain. Gurukul Kangri Collection, Haridwar

Digitized by Arya Samaj Foundation Chennai and eGangotri

acoustic oscillations for plane monochromatic waves propagating from the surface of the metal can be written in the form

$$\frac{\partial^2 u}{\partial t^2} - S^2 \frac{\partial^2 u}{\partial z^2} = \frac{1}{\rho c}[j, H_0], \tag{1}$$

where u is the displacement vector, S the sound velocity, ρ the metal density, c the velocity of light, j the current density and H_0 the magnetic field.

Assuming that the electromagnetic field at the surface varies in proportion to $\exp i(\omega t - kz)$, we can write the expression for the density of alternating current flowing in the skin layer as

$$j(z, t) = \frac{(1+i)c}{4\pi\delta} H \exp\left[-(1+i)\frac{z}{\delta}\right] \exp(i\omega t), \tag{2}$$

where H is the amplitude of the alternating magnetic field, $\delta = c/(2\pi\omega\sigma)^{1/2}$, σ is the conductivity of the metal and ω is the circular frequency. (Direction z is normal to the surface.)

In order to find the amplitude of the excited sound we substitute the last expression into the wave equation

$$\frac{\partial^2 u}{\partial z^2} + q^2 u = \frac{H_0 H(1+i)}{4\pi\rho S^2 \delta} \exp\left[-(1+i)\frac{z}{\delta}\right], \tag{3}$$

where $q = 2\pi/\lambda$ and λ is the wavelength of the sound wave. At distances greater compared to the thickness of the skin layer the solution has the form

$$|u| = \frac{H_0 H}{4\pi\rho S\omega} \frac{1}{(1+\beta^2)^{1/2}}, \tag{4}$$

where $\beta = q^2\delta^2/2$ is a parameter that takes into account through the conductivity the dependence of the amplitude of the excited ultrasound on the temperature.

As the temperature is decreased, in pure metals the mean freepath of electron (l) increases and one obtains $\delta < \lambda < l$ and one enters the regime of anomalous skin effect. In the regime of the anomalous skin-effect, excitation of transverse ultrasound in a metal is possible even in the absence of a constant magnetic field. The excitation mechanisms in weak fields and in the absence of the constant field, can be pictured in the following manner. Electrons situated in the skin layer are accelerated by the electric field of the electromagnetic excitation and by collisions transfer the excess momentum to the lattice. At the same time the ions of the lattice experience the direct action of the electric field in the skin layer. Excitation of ultrasound at the metal surface can occur if these two forces are locally unbalanced. In the absence of the constant magnetic field, this occurs when the mean free path of the carriers l exceeds the thickness of the skin layer. In this case the collision force is spatially separated from the region of the direct action of the alternating electric field, and both lead to transverse stress on the lattice.

From the point of view of the intensity of sound excited by the contactless method the most effective method is the generation of standing ultrasonic waves in plane parallel metal plates. The establishment of standing acoustic waves across the thickness of the

CC-0. In Public Domain. Gurukul Kangri Collection, Haridwar

Digitized by Arya Samaj Foundation Chennai and eGangotri

plate is accompanied by the appearance of resonance singularities in the frequency dependence of the surface impedance of the sample.

It is easy to show that the resonance increment to the surface impedance of the plate can be written in the form (Gordon and Seidel 1971)

$$\Delta Z_{res}=\frac{2i\omega}{\rho d}\frac{H_0^2}{c^2}\sum_{m=1}^{\infty}\frac{1-\cos m\pi}{\omega^2-\omega_m^2+i\gamma\omega}. \tag{5}$$

This expression was obtained on the assumption that $\delta \ll \lambda$, that is $\beta \to 0$. As the frequency, the magnetic field or the temperature varies the spatial distribution of the exciting force also varies. In the case of finite thickness of the skin layer, the expression for ΔZ_{res} can be brought to the form:

$$\Delta Z_{res}=\frac{2i\omega}{\rho d}\frac{H_0^2}{c^2}\frac{1+i\beta}{1+\beta^2}\sum_{m=1}^{\infty}\frac{1-\cos m\pi}{\omega^2-\omega_m^2+i\gamma\omega}, \tag{6}$$

where d is the thickness of the plate, and γ is the attenuation of ultrasound.

2. Experimental

A block diagram of the experimental set-up to detect singularities in the surface impedance of metal plates is shown in figure 1. The set-up include commercial (i) RF oscillator, (ii) the sample with surrounding coils, (iii) low noise amplifier, (iv) phase detector system and (v) X–Y recorder. An example of the resonance singularity of the surface impedance of white tin plate due to excitation of the transverse sound is shown in figure 2. The field dependence of the amplitude of this resonance at $T=4$ K is shown in figure 3. The decrease of the amplitude of the acoustic resonance in the high magnetic field region is connected with the strong dependence of the conductivity of tin on a magnetic field. At the maximum of the curve the parameter β is equal to unity. In metals where there is no dependence of the conductivity on a magnetic field, the amplitudes of the acoustic resonance singularities are proportional to the square of H_0 (Vasil'ev *et al* 1983).

The sharpness of the acoustic resonances in a metal plate can be used to create an oscillator in which frequency and amplitude of generation gives information about the velocity of sound and the attenuation in metal. Figure 4 shows field dependences of the velocity and attenuation of sound in white tin at $T=4$ K (Vasil'ev *et al* 1980). Change of the transverse sound polarization reveals the anisotropy of the amplitudes of quantum oscillations shown in figure 5 (Vasil'ev and Nurmagambetov 1983).

The technique of contactless excitation of ultrasound in metals can be applied to semiconductors and even insulators. It is necessary to create a thin metal layer at the

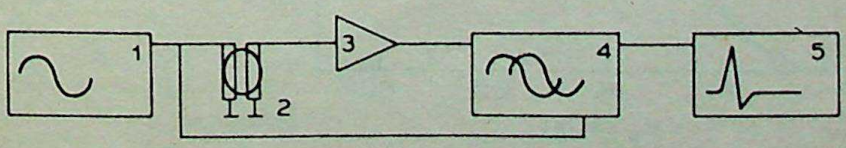

Figure 1. Experimental arrangement for observing the effect of direct generation of ultrasound in metal plates.

CC-0. In Public Domain. Gurukul Kangri Collection, Haridwar

Digitized by Arya Samaj Foundation Chennai and eGangotri

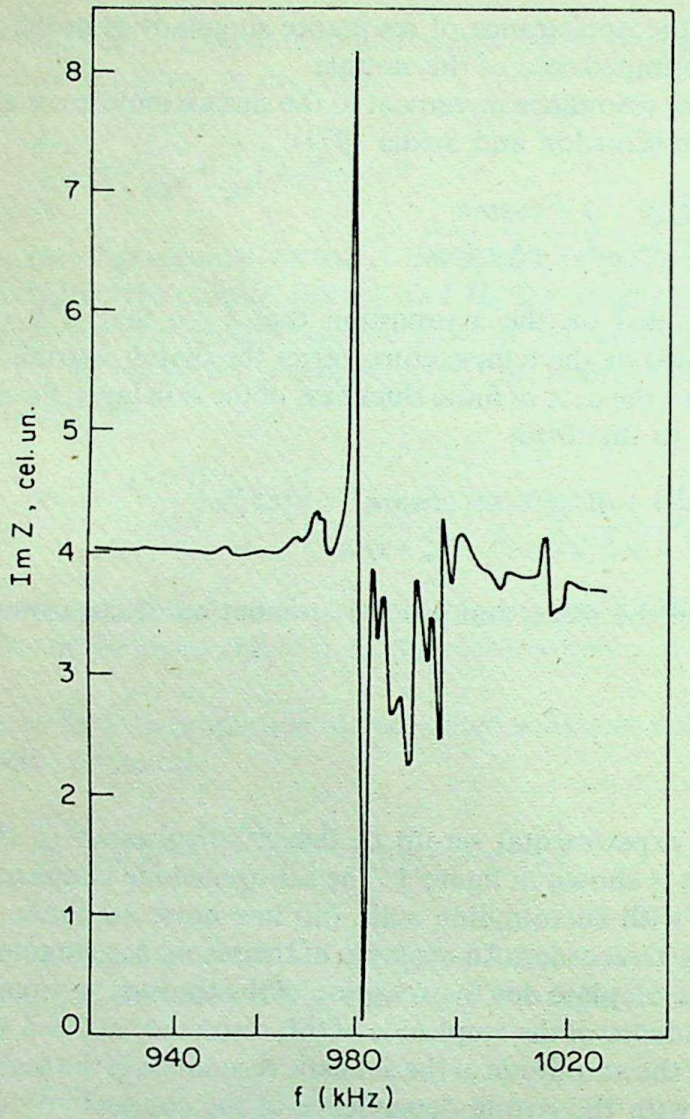

Figure 2. Resonance singularity of the surface impedance of white tin plate due to excitation of standing acoustic wave. Wave vector $q\|[100]$, polarization $p\|[010]$. $H=70$ kOe, $T=4$ K.

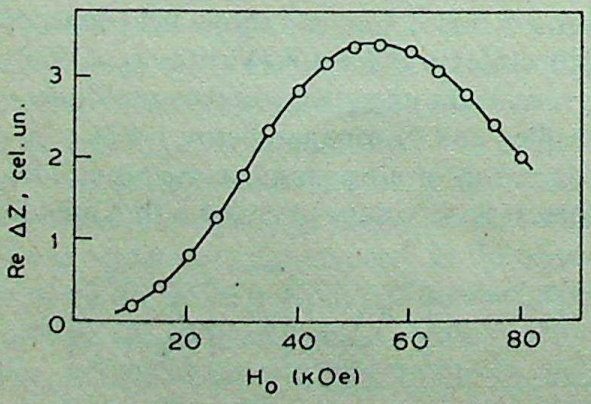

Figure 3. Field dependence of the amplitude of the acoustic resonance of the transverse ultrasound in white tin plate. $q\|[100]$, $p\|[001]$, $T=4$ K.

CC-0. In Public Domain. Gurukul Kangri Collection, Haridwar

Digitized by Arya Samaj Foundation Chennai and eGangotri

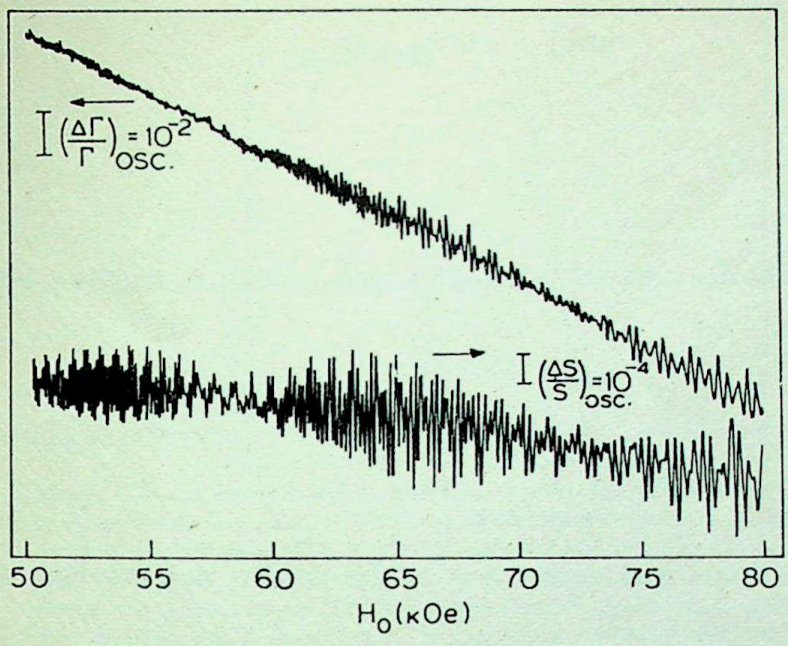

Figure 4. Field dependences of the velocity and attenuation of transverse ultrasound in white tin ($T=4$ K).

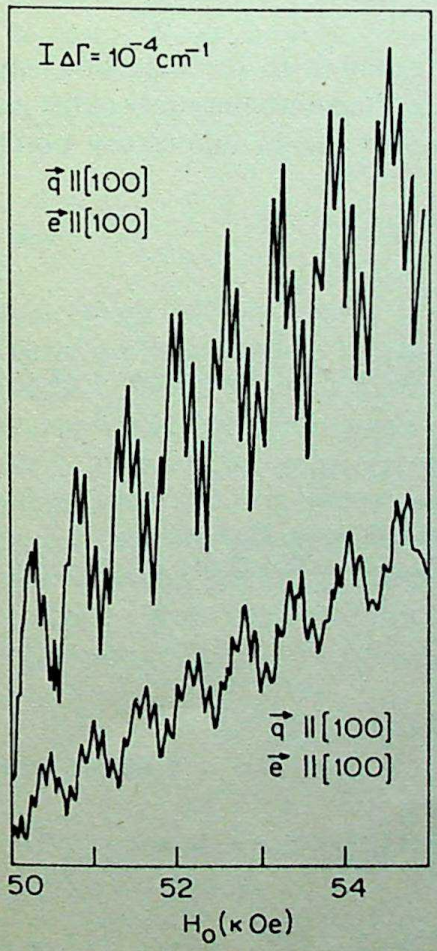

Figure 5. Quantum oscillations of the attenuation coefficient for a transverse ultrasound of different polarizations in white tin. $H\|[100]$, $T=4$ K.

CC-0. In Public Domain. Gurukul Kangri Collection, Haridwar

Digitized by Arya Samaj Foundation Chennai and eGangotri

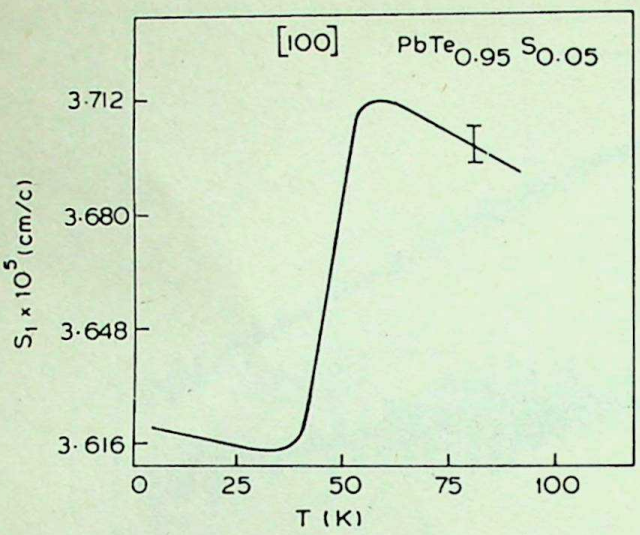

Figure 6. Temperature dependences of the velocity of longitudinal ultrasound in $PbTe_{0.95}S_{0.05}$.

surface of the sample under investigation and use one of the above mentioned methods. An example of such an investigation is shown in figure 6. By the noncontact acoustic methods anomalies were found in the velocity and attenuation of longitudinal and transverse sound due to ferroelectric transition in the semiconductor compound $PbTe_{0.95}S_{0.05}$.

We think that a further development of research in the field of electromagnetic generation of ultrasound in metals will be associated with the study of the phenomenon itself and to greater extent with its ever wider use in laboratory practice and in industrial application.

References

Dobbs E R 1973 in *Physical acoustics principles and methods* (ed.) W P Mason (New York: Academic Press)
Gordon R A and Seidel G 1971 *Phys. Lett.* **A35** 102
Kontorovich V M 1970 *J. Exp. Theor. Phys.* **59** 2116
Vasil'ev A N and Gaidukov Yu P 1983 *Usp. Fiz. Nauk.* **141** 431
Vasil'ev A N and Nurmagambetov 1983 *Fiz. Nisk. Temp.* **9** 702
Vasil'ev A N and Gaidukov Yu P and Perov A P 1980 *Prib. Tekh. Eksp.* **N6** 176
Vasil'ev A N, Gaidukov Yu P and Zolotov S I 1983 *Fiz. Tverd. Tela* **27** 831
Wallace W D 1971 *Int. J. Nondestr. Test.* **2** 309

CC-0. In Public Domain. Gurukul Kangri Collection, Haridwar

Digitized by Arya Samaj Foundation Chennai and eGangotri

Pramāna – J. Phys., Vol. 28, No, 5, May 1987, pp. 489–501. © Printed in India.

Phonon drag effect in three- and two-dimensional electron systems

N V ZAVARITSKY
Institute for Physical Problems, USSR Academy of Sciences, Moscow, USSR

Abstract. The nonequilibrium phonon flow drags the electrons, and depending upon experimental conditions manifests itself in the acoustoelectric current, acoustomagnetic field or acoustoelectric field. The results of these phenomena in Sn, Al, Ga, Ag measured with SQUID technique are discussed.

In the two-dimensional (2D) case the phonon drag is studied on the interface of bicrystals and on the cleavage (111) surface of Ge and on the inversion layer on (111) (100) planes of Si. In all these cases the phonon drag is about two orders of magnitude larger than in metals with the same charge density. This is due to the drag of surface electrons by nonequilibrium phonon of the whole specimen.

The Kohn resonance of phonons with Fermi surface and topological transitions on Fermi surface of 2D electrons produced sharp singularities of phonon drag effect in 2D cases.

Keywords. Phonon drag effect; three-dimensional electron system; two-dimensional electron system.

PACS No. 63·20

1. Introduction

Conduction electrons and the lattice vibrations in a solid influence each other. The phonon-electron interaction plays a major role in the theory of transport properties of solids. The most obvious method of measuring this interaction is to send a beam of nonequilibrium phonons or electrons and watch them being scattered and absorbed. In the experiments of this kind we study the thermal or the electrical conductivity, the ultrasonic attenuation etc. It seems reasonable to measure directly the reaction of the lattice or the electrons on the action of flow of the non-equilibrium quasiparticles. This reaction is shown on the Tcerenkov effect—sound generated by beam of electrons, and the phonon drag effect—the reaction of electrons on the action of a beam of nonequilibrium phonons.

2. Acoustoelectric field

Let W be the flow density of non-equilibrium phonons. Then the loss of their energy to interaction with electrons is

$$\Delta\varepsilon = \Gamma_{ph,\,e} W, \tag{1}$$

where $\Gamma_{ph,\,e}$, is the attenuation of phonons due to their interaction with electrons. Along

CC-0. In Public Domain. Gurukul Kangri Collection, Haridwar

Digitized by Arya Samaj Foundation Chennai and eGangotri

with the energy, the phonon transports to electrons the momentum

$$\Delta p = \frac{\Delta\varepsilon}{u} = \frac{\Gamma_{\mathrm{ph},e} W}{u}, \tag{2}$$

where u is the phonon velocity. If there is no current through the specimen, then for equilibrium, an electric field arises in the electron gas, which is given by:

$$E^a_{\mathrm{ph}} = \frac{(\Gamma_{\mathrm{ph},e} W)}{(eN_v u)}. \tag{3}$$

This is the so-called acoustoelectric field (N_v is the specific density of electrons).

Relation (3) for the acoustoelectric field was first obtained by Weinreich (1967). This equation is correct under the simple assumption concerning the dispersion law of electrons $\varepsilon(p) = p^2/2m$ (Kaganov *et al* 1980).

The acoustoelectric field was earlier studied in semiconductors (Spector 1966). In metals equation (3) gives $E^a_{\mathrm{ph}} \simeq 10^{-10}\mathrm{VW}^{-1}\,\mathrm{cm}^2$—the value that may be easily measured with SQUID device.

The apparatus used to study the acoustoelectric field is shown in figure 1. The test sample with the length $\simeq 5$ cm and the diameter $\simeq 4$ mm of known crystal orientation is in the acoustic contact with the ultrasonic transducer **T**.

To determine the acoustoelectric field E^a_{ph} the voltage (V^a) was measured along the sample between the point at which an acoustic power W passes through the cross-section of the sample and the upper end of the sample, where the sound is completely damped. The acoustic power at the lower end of the sample, W_0, was determined from the value of overheating of the sample. The potential difference is measured by a bridge arrangement with a SQUID device used as null detector.

The contacts to the sample was placed at various distances from its bottom, so that the changes in $W \sim V^a$ along the length of the sample could be measured, and the sound damping $\Gamma_{\mathrm{ph},e}$ could be determined.

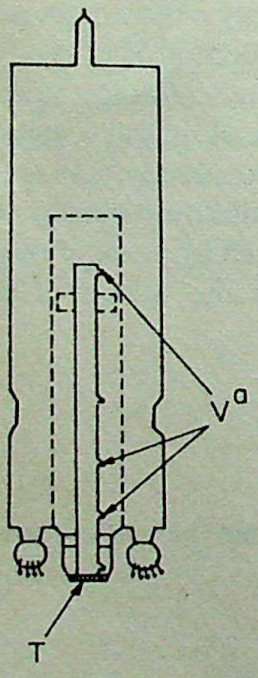

Figure 1. Apparatus for studying the acoustoelectric field. *T*-transducer.

CC-0. In Public Domain. Gurukul Kangri Collection, Haridwar

Digitized by Arya Samaj Foundation Chennai and eGangotri

To separate the voltage due to heating of the sample we measured the V^a at the temperature at which the thermoelectric power $\alpha \equiv 0$, (Zavaritsky 1978) or in the vacuum chamber with the ultrasonic power transparent germanium-wafer window (Suslov 1981). In this case the correction due to heating of the sample by the sound wave did not exceed $\sim 20\%$ of V^a and could be easily calculated. The results of acoustoelectric voltage measurement are shown in figure 2.

Under the condition of $ql_e \gg 1$ (q—wave vector of phonon, l_e—electron mean free path) the phonons interacted with electrons on the strip of the Fermi surface where $\mathbf{qv}=0$ ($\mathbf{v}$—electron velocity). In the relaxation time approximation the sound attenuation and acoustoelectric field are the sum of contribution from different strips on the Fermi surface. However with the same sign in the case of attenuation and with the sign of the reciprocal to effective-mass tensor $(\partial^2\varepsilon/\partial p_n^2)_F$ for the case of acoustoelectric field.

The average value of acoustoelectric voltage V^a was for tin $V^a \sim 0{\cdot}1 \times 10^{-10}$ VW^{-1} cm^2 and for silver $V^a \simeq 0{\cdot}7 \times 10^{-10}$ VW^{-1} cm^2.

The anisotropy of E^a in tin and silver is large. In the case of silver contributions to E^a from the "belly" and the "neck" of Fermi surface are opposite in sign. (Suslov 1981)

3. Acoustomagnetic field

If the sound beam occupies only a part of the sample a counter current of electrons outside the sound beam appears. Consequently an additional circular component on the current distribution appears (figure 3). This circular component of current produces a magnetic field H^a in the plane perpendicular to the sound propagation direction.

In the present experiment this magnetic field was measured with a movable loop of the area 1 mm^2 connected with the SQUID system. The samples used were the single crystal plate 10×20 mm and 2 mm thick. The field was measured in the direction perpendicular to the 10×20 mm plane.

It is easily seen that the acoustomagnetic field must be inhomogeneous. The maximum absolute value of the field should be expected near the boundaries of the sound beam, and the field should have opposite directions on the opposite sides of the beam. As the distance from the radiator increases the field decreases. Some field

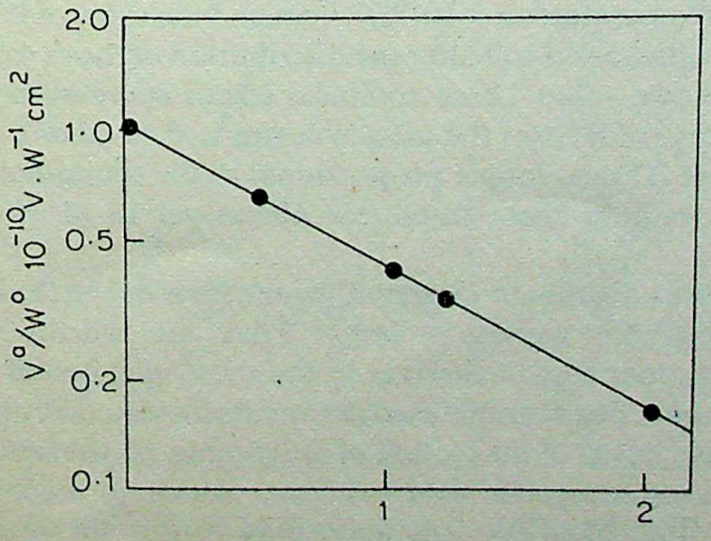

Figure 2. Measurement of the acoustoelectric voltage along the sample.

CC-0. In Public Domain. Gurukul Kangri Collection, Haridwar

Digitized by Arya Samaj Foundation Chennai and eGangotri

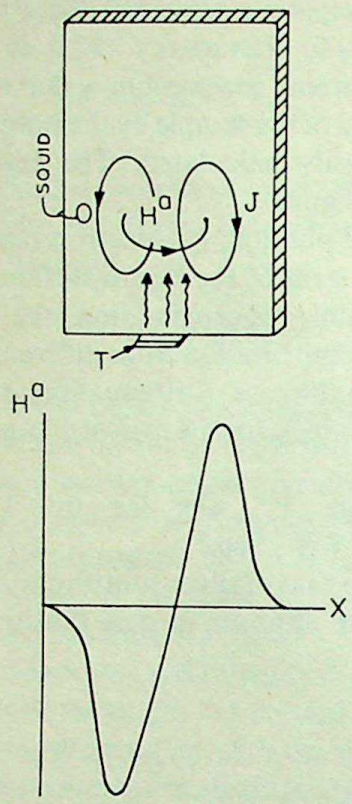

Figure 3. Distribution of acoustocurrent and acoustomagnetic field H^a in the sample.

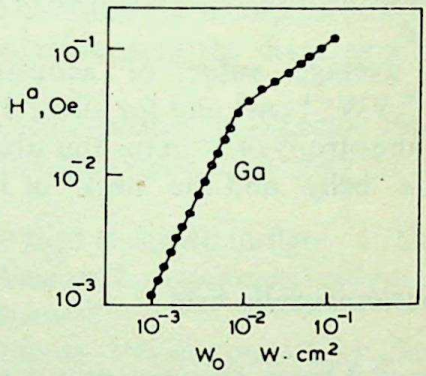

Figure 4. Dependence of H^a at the maximum of W value in gallium.

distortion due to edge effects should be observed near the boundary of the sample.

Figure 3 shows sectional views of the acoustomagnetic field. To estimate the order of magnitude we have

$$H^a \simeq \Gamma_{\text{ph, }e} \sigma W \eta, \tag{4}$$

where σ is the conductivity of the metal and η is a geometric factor that depends on the current distribution in the sample.

In pure metals at helium temperatures $\sigma \sim 10^{10} \Omega^{-1}$ cm and the value of H^a is so large that the field excited by the ultrasound will alter the distribution of the currents and by the same token influence its own value. These nonlinear effects manifest themselves in the fact that the relative change of H^a over the sample begins to depend on the intensity of the sound flux. In this case H^a is no longer proportional to the sound-flux power W (figure 4). In the case of gallium these nonlinear effects set in at $W \sim 2 \times 10^{-2}$ W-cm^{-2}.

We have demonstrated here only the simplest nonlinear effects due to the large value of H^a. Their actual conceivable variety is large. They are worthy of special consideration, since they can manifest themselves in the most unexpected fashion in various experiments with sound. For example in experiments on sound absorption, the radiator usually occupies only a part of the section of the sample. By the same token, in all these experiments an acoustomagnetic field is present which, in the case of high purity samples and high sound intensity, can noticeably distort the results of the measurement. This effect was directly observed in the ultrasonic experiments.

CC-0. In Public Domain. Gurukul Kangri Collection, Haridwar

Digitized by Arya Samaj Foundation Chennai and eGangotri

4. Thermoelectric power due to phonon drag

The flow of non-equilibrium phonons may be caused by the temperature gradient ∇T in the specimen, i.e.

$$W = \varkappa \nabla T \simeq C_L u l_{ph} \nabla T, \tag{5}$$

where l_{ph} is the phonon mean free path and $\varkappa$ is the thermal conductivity of phonons.

In metals the sound attenuation and the phonon mean free path are determined by the phonon-electron interaction, and

$$l_{ph} = \Gamma^{-1}_{ph,e}. \tag{6}$$

In this case relation (3) acquires the known form

$$E_{ph} = \frac{C_L}{eN_v} \nabla T \equiv bT^3 \nabla T, \tag{7}$$

where E_{ph} is the thermal power due to phonon drag.

It is known that the thermoelectric power of metals at low temperature can be described as

$$\alpha = aT + b_{ex} T^3, \tag{8}$$

where the term aT is connected with direct action of the temperature gradient on the electron system, $b_{ex}T^3$ is connected with the dragging of the electrons by the phonon flux, produced by the temperature gradient.

Equation (8) satisfactorily describes experimental function $\alpha(T)$ only at low temperatures, $T \lesssim 10$ K (figure 5). On raising the temperatures the phonon drag effect disappears. This is due to the Umklapp processes which appear at $T \gtrsim \theta_D/20$. In this

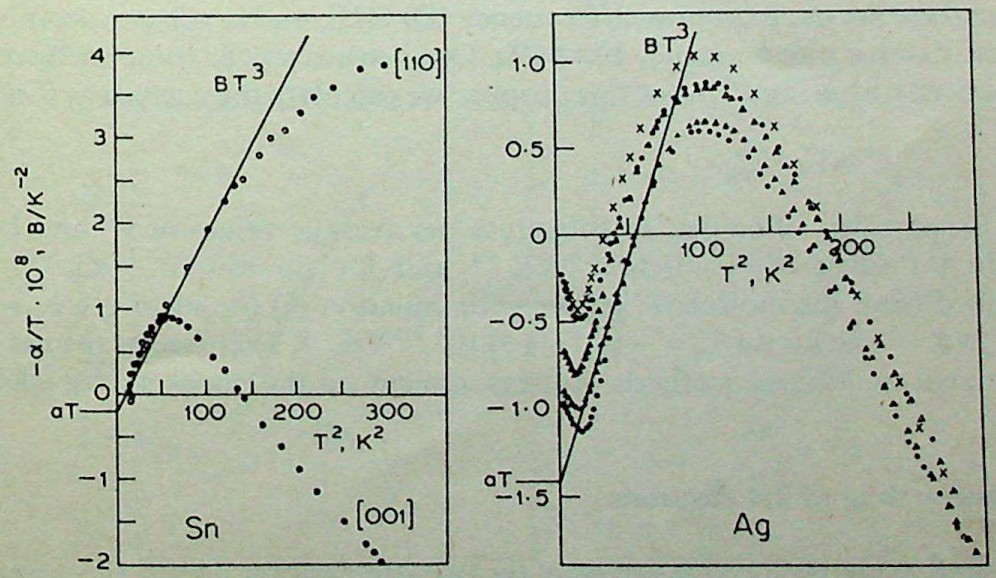

Figure 5. Dependence of d/T on T^2 in the range from 3 to 16 K for tin (Zavaritsky and Omel'yanovsky 1981) and silver (Omel'yanovsky 1985) single crystals along × [210], ● [110], ○ [111], ◇ [113].

CC-0. In Public Domain. Gurukul Kangri Collection, Haridwar

Digitized by Arya Samaj Foundation Chennai and eGangotri

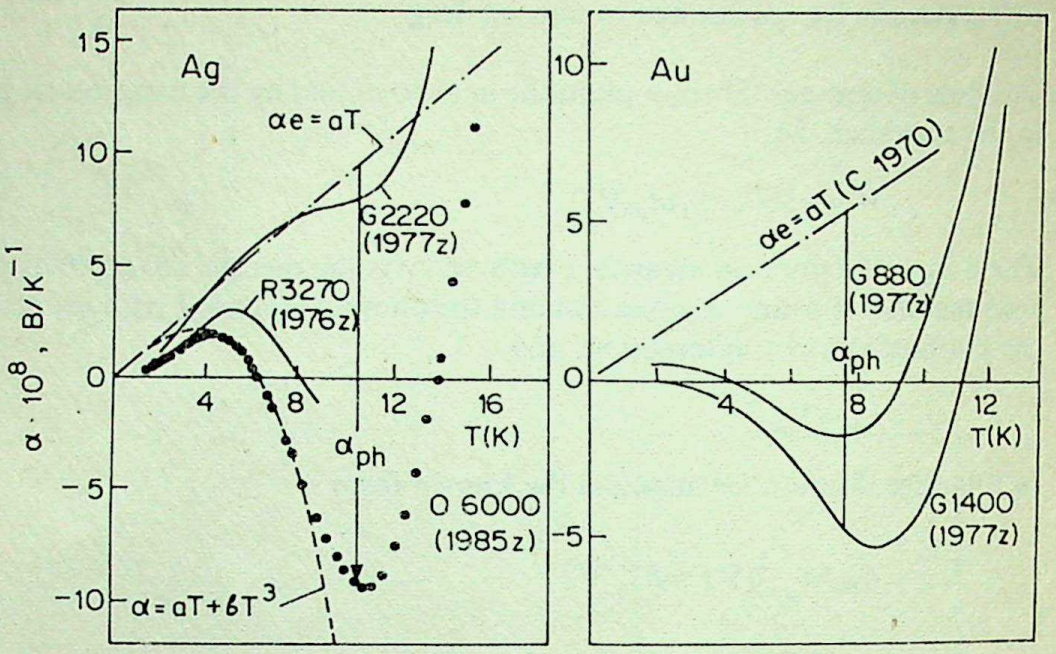

Figure 6. Thermoelectric power of pure noble metals at low temperature. Numbers indicate the resistance ratio R (300 K)/R (4·2 K) and date of publication. G, (Guenault and Hawksworth 1977); R, (Rumbo 1976); O, (Omel'yanovsky 1985); C refer to (Crips 1970).

case the nonequilibrium phonons lose their momentum in general in the phonon-phonon scattering.

Therefore, the phonon drag effect with the thermal phonon may be studied in the metals only at $T < 10$ K (figure 6).

The acoustoelectric voltage V^a_{ph} and the thermoelectric power due to the phonon wind are the results of a single physical effect, the dragging of electrons by the sound wave. The only difference is that the frequencies of the sound oscillations (phonons) responsible for these two effects differ by a factor of 10^3. In the case of the thermoelectric power these are oscillations with frequency 100 GHz, and in acoustoelectric effect these are oscillations with frequency 100 MHz. One can attempt to compare these two effects numerically by using V_{ph}. For this purpose we calculate the coefficient b in relation (7)

$$b^a \simeq C_L u V^a_{ph}. \tag{9}$$

It is necessary, of course, to substitute the average values of V^a and U. Thus, we obtain for silver $b^a = (-4)\cdot 10^{-10}\,\mathrm{VK}^{-4}$ and for tin $b^a \sim 10^{-10}\mathrm{VK}^{-4}$. The value obtained from thermoelectric power with equation (8) for silver are $b_{ex} = -(2 \div 3{\cdot}4)$ $10^{-10}\mathrm{VK}^{-4}$ and for tin $b_{ex} = -(1{\cdot}7 \div 1{\cdot}9)\,10^{-10}\,\mathrm{VK}^{-4}$. There seems to exist reasonable agreement in different methods of measurement on the phonon drag effect.

5. Phonon drag of 2D electrons

The phonon scattering by electrons of the two-dimensional conducting layers are small in comparison with other scattering mechanisms typical of dielectric crystals (boundaries, phonons, imperfection etc). This result directly follows from measuring the ballistic phonon absorption by 2D-electrons in MOSFET device (Hensel *et al* 1983) and

CC-0. In Public Domain. Gurukul Kangri Collection, Haridwar

Digitized by Arya Samaj Foundation Chennai and eGangotri

thermal conductivity of crystals with conducting layers (Zavaritsky and Zavaritsky 1981, 1982).

Here, the value of l_{ph} corresponding to phonon scattering in the specimen should be substituted for relation (5). Then one obtains

$$W = \varkappa_b \nabla T \simeq C_L l_{ph} u \nabla T, \tag{10}$$

$\varkappa_b$ is the thermal conductivity of the sample and

$$E^a_{ph} = \Gamma_{ph,e} \varkappa_b \chi \nabla T, \tag{11}$$

χ is the coefficient which describes in detail the phonon 2D electron interaction.

In the case of 2D electron gas the value of phonon drag must be larger than that calculated from (7) using $N_v = N_s \delta^{-1}$ (δ is the thickness of conductivity layer). Indeed, in 2D case (see equations (3) and (10))

$$E^a_{ph} = \frac{C_L \Gamma_{ph,e} l_{ph}}{e N_v} \nabla T \tag{12}$$

and the phonon drag value is enhanced $\Gamma_{ph,e} l_{ph}$ times. At $N_v \simeq 10^{19}$ cm^{-3} $\Gamma_{ph,e}$ is $10^{-3} - 10^{-4}$ cm and the phonon mean free path l_{ph} is close to the minimum dimension of the specimen about 0·1 to 0·01 cm. So, an increase of the phonon drag as much as by an order of magnitude could be expected. This was indeed observed in the experiment. (Zavaritsky and Zavaritsky 1981, 1982; Zavaritsky 1983, 1984).

We have studied 2D conducting layer on the inner and the outer surfaces of germanium (Zavaritsky and Zavaritsky 1981, 1982) and MOSFET structures in an *n*-type layer on silicon (100) and (111) and a *p*-type layer on surface (Zavaritsky 1983). The calculated diffusion component of the thermo-emf $\alpha_e = \pi^2 kT/\varepsilon_F$ is shown on figure 7 by the dotted line. Values of α determined in the measurement range considerably exceed α_e and have other temperature dependence. This indicates that a value of thermo-emf is mainly determined in general experimental range by the phonon drag of charges.

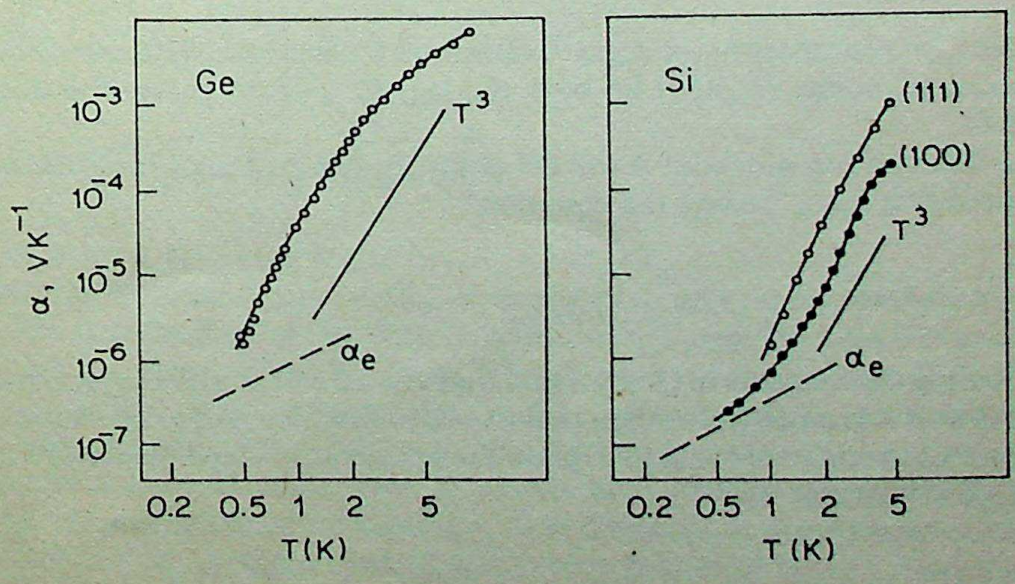

Figure 7. Thermoelectric power of conducting surfaces in germanium and silicon.

CC-0. In Public Domain. Gurukul Kangri Collection, Haridwar

Digitized by Arya Samaj Foundation Chennai and eGangotri

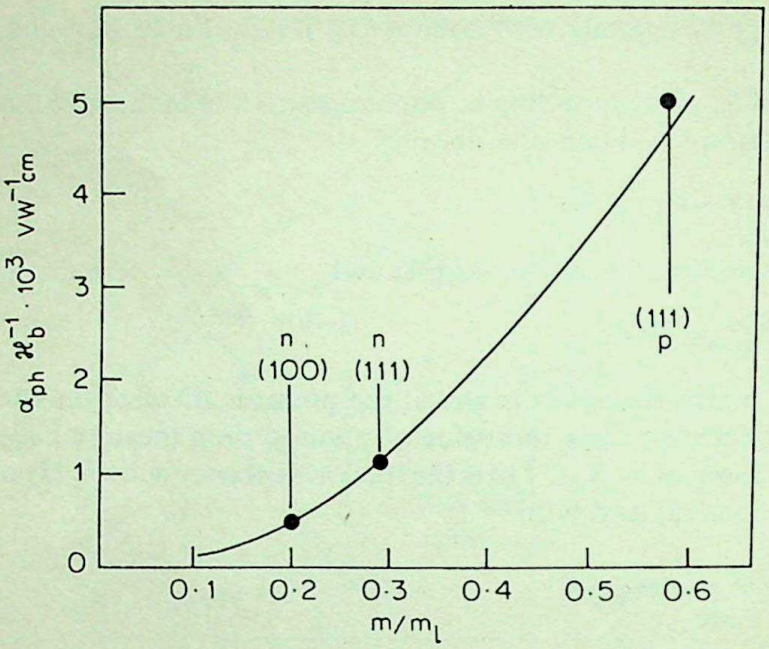

Figure 8. $\alpha_{ph}\varkappa_b^{-1}$ and effective mass m^* of carriers in Si. Dotted line: $\alpha_{ph}\varkappa_b^{-1}\sim m^{*2}$.

The phonon drag value estimation under the simplest assumption, that the conducting layer may be considered as the three-dimensional one with the charge density $N_v = N_s\delta^{-1}$ (relation (3)) is shown in figure 7 by solid lines with index T^3. The experimental data having in the first approximation the same temperature dependence are seen to be considerably (up to 10^2 times) higher than the theoretically possible value of thermopower.

The value of phonon drag in the case of Si depends on the MOSFET'S substrate orientation. It seems that it is due to the dependence of phonon drag effect on the effective mass of carriers $m^* = m/m_e$ as,

$$\Gamma_{ph,e}\sim m^{*2}\Lambda^2. \tag{13}$$

Indeed, the comparison of $\alpha_{ph}\varkappa_b^{-1}$ values with effective masses m^* shows that the experimental points $(\alpha_{ph}\varkappa_b^{-1})$ lie near the $(\alpha_{ph}\varkappa_b^{-1})\sim m^{*2}$ curve (the dotted line in figure 8).

The deformation potential Λ for 2D electrons can be found from the result of the measurements $\alpha_{ph}\varkappa_b^{-1}$ using the equation*

$$\alpha_{ph}\varkappa_b^{-1} = \frac{m^{*2}\Lambda^2}{e^3\hbar^{/3}N_S K_F u^2 \delta\rho_{3D}3\pi}. \tag{14}$$

Substituting the numbers in (14), we find that $\Lambda \simeq 10$ eV for all 2D systems are studied. This value of Λ is much lower than that ($\Lambda \sim 20$ eV) which had to be adopted in several calculations (Ando *et al* 1982) to explain the temperature dependence of the resistance of MOSFET structures.

* There are some errors in the expression of equation (14) in Zavaritsky (1984).

CC-0. In Public Domain. Gurukul Kangri Collection, Haridwar

Digitized by Arya Samaj Foundation Chennai and eGangotri

6. Singularities of the phonon drag effect in 2D systems

In the case of a two-dimensional system we can easily change the value of the electron and the phonon wave-vectors during the experiment.

Indeed, the Fermi surface wave-vector

$$K_F=(2\pi N_s g_v^{-1})^{1/2}, \tag{15}$$

where g_v is the valley degeneration, N_s the density of surface electrons which is determined by the gate voltage V_g,

$$N_s=C(V_g-V_0), \tag{16}$$

where V_g and V_0 are the gate and threshold voltages of MOSFET structure. The phonon wave-vector q corresponds to the maximum of the thermal distribution of phonons and depend on the temperature $q\simeq 5kI/\hbar u$.

Therefore, there is the possibility to study dependence of $\Gamma_{ph,e}$ value upon the properties of the phonon and the electron systems.

We shall discuss the Kohn singularity in the phonon electron interaction and phonon-drag observation of the topological transition in a 2D Fermi systems.

The so-called Kohn singularities are known to arise on dispersion phonon curves in the short-wave range due to the electron-phonon interaction. The value of these singularities on dispersion curves in the three-dimensional system is less than a few per cent. These singularities are related to the known effect of disappearance of the phonon scattering by electrons at $q>2K_F$, in the quantum limit. This effect is known to be inherent in semi-metals whose electron concentration and, hence, K_F are not very high.

In the MOSFET structure one could change the 2D-concentration N_s and, thus, $K_F\sim N_S^{1/2}$ in a controlled way. Hence, the conditions for observation of singularities at $q=2K_F$ can be easily provided in this system. Besides, the calculation shows that the singularities must be more distinct in the two-dimensional system, than in the three-dimensional one. Thus, the sound attenuation in the short-wave limit, at $q=2K_F$, appears to be equal to

$$\Gamma_{ph,e}q^{-1}=\frac{m^{*2}\Lambda^2}{2\pi\hbar^2 u\rho_{3D}}\theta(2K_F-q) \text{ for } 3D,$$

$$\Gamma_{ph,e}q^{-1}=\frac{m^{*2}\Lambda^2}{2\pi^2\hbar^2\rho_{2D}}\frac{\theta(2K_F-q)}{(|2K_F-q|)^{1/2}} \text{ for } 2D, \tag{17}$$

where $\theta(x)=1$ if $x>0$, $\theta(x)=0$ if $x<0$.

The character of the attenuation variation near $q=2K_F$ is, actually, the reflection of the obvious fact that the part of the Fermi surface, which is effective for the phonon-electron interaction, varies with q/K_F in a different manner in the 3D- and 2D-cases.

To observe this effect, it is convenient, at a given concentration N_s and, hence, at a given K_F, to select the phonon impulse value by varying the mean temperature of the specimen. The results of such experiment are shown in figure 9 for specimens of n-type on (100) plane. The distinct maximum of $\alpha_{ph}\varkappa_b^{-1}(T)$ is noticed at a given concentration of N_s which is shown in the figure over $\alpha_{ph}\varkappa_b^{-1}$ curves in units of $N_s\cdot 10^{-12}$ cm^{-2}. The temperature corresponding to the maximum T^* depends on the value of N_s and varies

CC-0. In Public Domain. Gurukul Kangri Collection, Haridwar

Digitized by Arya Samaj Foundation Chennai and eGangotri

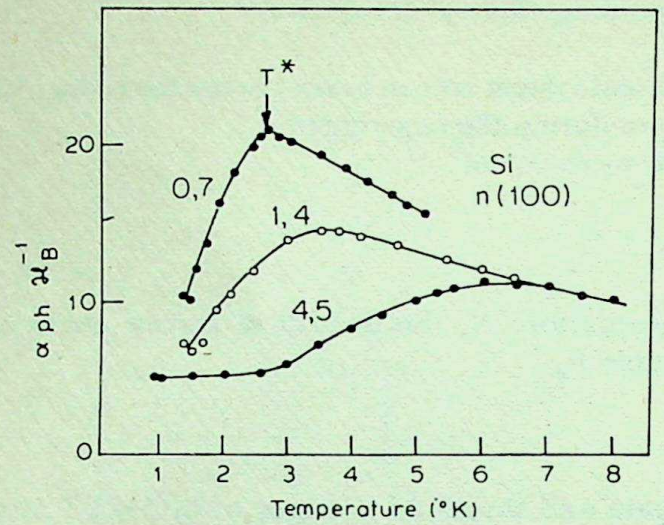

Figure 9. $\alpha_{ph}\varkappa_b^{-1}$ for the n-type MOSFET on (100) plane of Si. Number over the curves indicates concentrations N_s in units of 10^{-12} cm^{-2}.

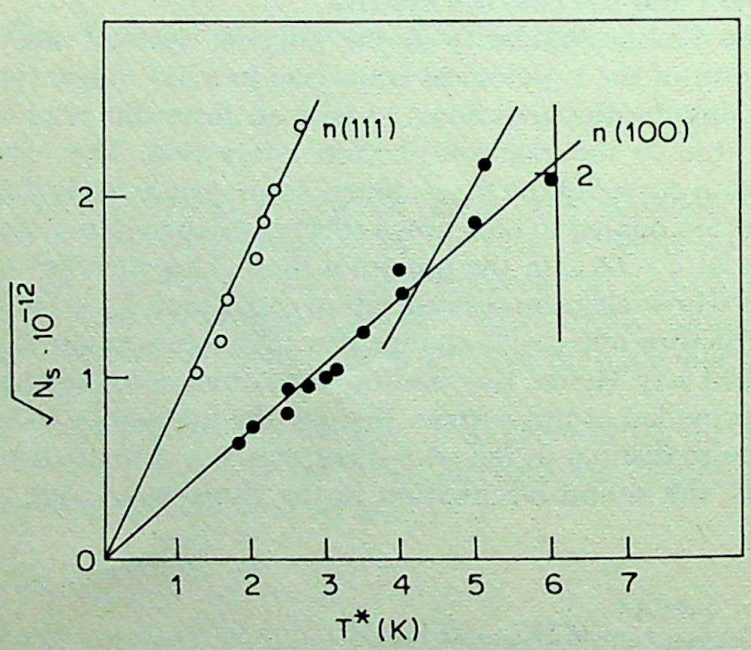

Figure 10. Concentration N_s and the temperature of maximum value of $\alpha_{ph}\varkappa_b^{-1}$.

in proportion to $N_s^{1/2}$. Since $q_T \sim T^*$, and $K_F \sim N_s^{1/2}$, it indicates that the singularity is actually related to the features of phonon-electron interaction. The straight line, drawn in figure 10, corresponds to the condition $q = 2K_F$.

It is interesting to note that the slope of $(N_s^{1/2} - T^*)$ curve is different for the MOSFET on (001) and (111) plane of Si (figure 10). This is due to different valley degeneracy of n-charge on this plane of Si. Our experimental results show that the valley degeneracy $g = 2$ is on (100) and $g = 6$ on the (111) plane of Si (Gusev *et al* 1984).

This was the first experiment in which the valley degeneracy was determined without using the magnetic field.

In the physics of inversion layers on Si, the question of valley degeneracy on (111) face is, one of the unsolved problems, as there are discrepancies between theoretical estimates (Ando *et al* 1982) and experiments in the magnetic field. The value of

CC-0. In Public Domain. Gurukul Kangri Collection, Haridwar

Digitized by Arya Samaj Foundation Chennai and eGangotri

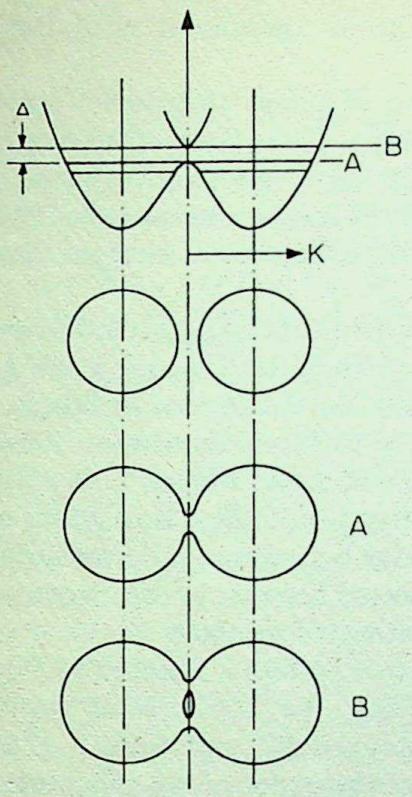

Figure 11. The electron spectrum $\varepsilon(k)$ for MOSFET structures on high-index silicon planes. The sequential change in Fermi surface as the density N_s is increased; the letters specify the topological transitions. A^M—appearance of the neck, B^M—appearance of the cavity. Dashed line—boundary of Brillouin zone.

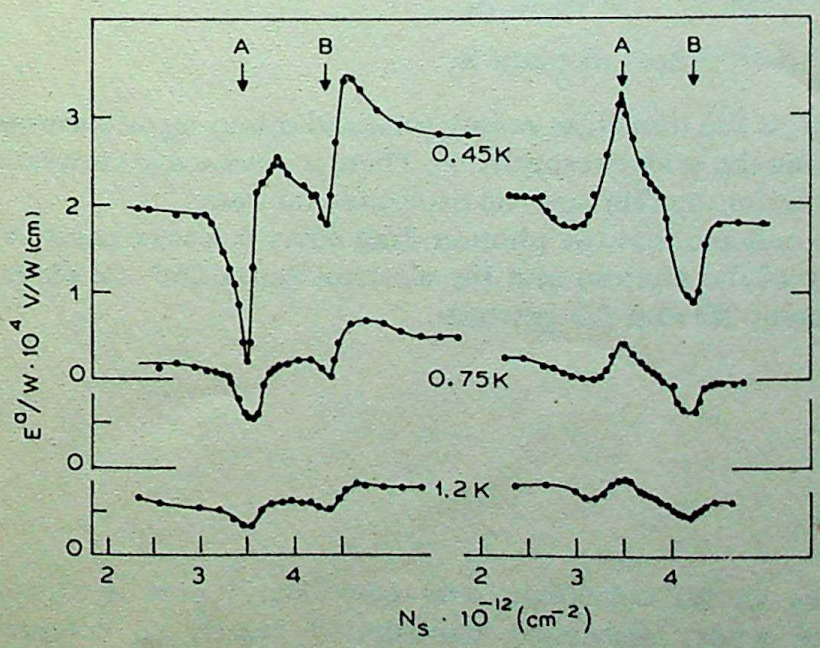

Figure 12. Topological transitions in the thermoelectric power. Specimen with the angle $\theta = 10°30'$.

CC-0. In Public Domain. Gurukul Kangri Collection, Haridwar

Digitized by Arya Samaj Foundation Chennai and eGangotri

the valley degeneracy obtained by us is in good agreement with the theoretical estimate.

Lifshitz (1960) paid attention to a new type of phase transitions consisting of a topological change of the Fermi surface of electrons. These transitions may occur either through formation (or disruption) of a bridge between two surfaces, or through formation (or disappearance) of a new cavity. These transitions must be followed by the change of both thermodynamic and kinetic characteristics of charges (Kaganov and Lifshitz 1960).

Both topological transitions occur at certain (from the experimental view point) N_s value in the inversion layers on planes close to (100) Si. In this case a new large period $(2\pi/a)\sin\theta$ (θ is the angle to (101) plane) appears in the inversion layers. The valley degeneracy in K-space is now lifted. The bottom of the electronic valleys is at 0·15 $(2\pi/a)\sin\theta$ from the boundary of 2D new Brillouin zone. Figure 11 is a sketch of the band structure in this case. It is easy to see that two topological transitions occur as the surface charge density is changed. There is a bridge between two Fermi surfaces (A) and a new band form (B). These transitions are separated because of the discontinuity of the spectrum at the zone boundary and the formation of minigap Δ.

It was found earlier (Cole *et al* 1977), that in this system a slight (3 to 5%) w-shaped change in the conductivity takes place during the topological transition. The thermopower (Zavaritsky and Kvon 1984; Zavaritsky and Suslov 1984) of these systems reveals sharp amplitude singularities, of the order of the effect measured. The value and the sharpness of the effect increase as the temperature drops. Figure 12 shows the results obtained in the structures made on the plane cut at angle $\theta = 10°30'$ to (001) plane. (The structure with angle θ from 9° to 11° were studied). E_{ph} is the electric field arising in the 2D electron gas when the heat flow W is present in a system.

The left column represents the thermal flow along the bridge (figure 12), the right one the heat flow in perpendicular direction. Letters A and B denote the position of transitions.

The calculation (Zavaritsky and Suslov 1984) has shown that

$$\begin{aligned} &\Delta\alpha_{ph} \sim \pm|\Delta\varepsilon|^{-1/2} \quad \text{at point A,} \\ &\Delta\alpha_{ph} \sim (\Delta\varepsilon)^{1/2}\theta(\Delta\varepsilon) \quad \text{at point B,} \end{aligned} \tag{18}$$

where $\Delta\varepsilon = \varepsilon_F - \varepsilon_c$ (ε_c is the transition point), plus and minus signs correspond to heat flow across and along the bridge respectively. There is reasonable correlation between the results of calculation by (18) and the experimental data.

All these results indicate that the phonon drag effect is a very effective method to study the property of the phonon and the electron states and the phonon-electron interaction in different 2D and 3D systems.

Acknowledgements

The author thanks all his colleagues who took active part in various sections of this work, and whose discussion contributed greatly to comprehension of problem discussed in this work. He would like to thank in particular Z D Kvon, O E Omel'ynovsky and I M Suslov.

CC-0. In Public Domain. Gurukul Kangri Collection, Haridwar

Digitized by Arya Samaj Foundation Chennai and eGangotri

References

Ando T, Fower A B and Stern F 1982 *Rev. Mod. Phys.* **54** 437
Cole T, Lakhani A A and Stiles P Y 1977 *Phys. Rev. Lett.* **38** 722
Crips R A 1970 *J. Rungis Phil. Mag.* **22** 217
Guenault A M and Hawksworth D G 1977 *J. Phys. F. Met. Phys.* **7** L219
Gusev C M, Zavaritsky N V, Kvon Z D and Yurgens A A 1984 *JETP Lett.* **40** 1056
Hensel J C, Dynes R C and Tsui D C 1983 *Phys. Rev.* **B28** 1129
Kaganov M I and Lifshitz I M 1979 *Usp. Fiz. Nauk* **129** 487
Kaganov M I, Mevlyut Sh. T and Suslov I M 1980 *Sov. Phys. JETP* **51** 189
Lifshitz I M 1960 *JETP* **38** 1569
Omel'yanovsky *et al* 1985 *Sov. Phys. JETP* **62** 400
Rumbo E F 1976 *J. Phys. F. Met. Phys.* **6** 85
Spector H M 1966 *Solid State Phys.* **19** 291
Suslov I M 1981 *Sov. Phys. JETP* **53** 968
Weinzeich G 1967 *Phys. Rev.* **163** 815
Zavaritsky N V 1978 *Sov. Phys. JETP* **48** 942
Zavaritsky N V 1984 *Physica* **B126** 369
Zavaritsky N V 1985 *Proc. U Conf. Phonon Physics* W.-S 211
Zavaritsky N V and Kvon Z D 1983 *JETP Lett.* **38** 85
Zavaritsky N V and Kvon Z D 1984 *JETP Lett.* **39** 61
Zavaritsky N V and Omel'yanovsky O E 1981 *Sov. Phys. JETP* **54** 1178
Zavaritsky N V and Omel'yanovsky O E 1984 *JETP Lett.* **40** 869
Zavaritsky N V and Suslov I M 1984 *Sov. Phys. JETP* **60** 1243
Zavaritsky N V and Zavaritsky V N 1981 *JETP Lett.* **34** 47
Zavaritsky N V and Zavaritsky V N 1982 *Sov. Phys. JETP* **83** 1182

CC-0. In Public Domain. Gurukul Kangri Collection, Haridwar

Digitized by Arya Samaj Foundation Chennai and eGangotri

CC-0. In Public Domain. Gurukul Kangri Collection, Haridwar

Digitized by Arya Samaj Foundation Chennai and eGangotri

Pramāṇa – J. Phys., Vol. 28, No. 5, May 1987, pp. 503–508. © Printed in India.

Low-temperature resistance fluctuation in disordered conductors

N KUMAR
Department of Physics, Indian Institute of Science, Bangalore 560 012, India

Abstract. At low temperatures the electron elastic mean free path in a disordered conductor can become much smaller than the inelastic mean free path (or more precisely the Thouless length) which in turn may be comparable with, or even larger than the sample size. In this quantum regime, the electrical resistance is dominated by the coherence effects that eventually lead to the now well-known weak or strong localization. Yet another remarkable manifestation of the quantum coherence is that it makes the resistance non-additive in series and, more importantly, non-self averaging, thus replacing the classical Ohm's law with a quantum Ohm's law describing statistical fluctuations. In this paper, we report on some of our recent work on the statistics of these "Sinai" fluctuations of residual resistance for one and higher space dimensions (d). In particular we show that the physics at the mobility edge may be dominated by these fluctuations. We also show that an external electric field tends to harness these fluctuations. Some observational consequences such as $1/f$-noise at low temperatures are discussed. Our approach is based on invariant imbedding extended by us for this purpose.

Keywords. Disordered conductors; low-temperature resistance fluctuation; residual resistance; mobility edge; Sinai fluctuations.

PACS No. 72·10

1. Introduction

Theoretical physics of disordered systems frequently involves a convenient artifice of averaging of physical quantities of interest over the probability distribution of the underlying quenched randomness which is assumed to be given. This is despite the fact that the experiment is performed on a *given* sample. The rationale for this mathematical artifice is that for a macroscopic sample, i.e., in the thermodynamic limit, different parts of the sample may be taken as different instances of the sample. Thus, if the quantity of interest is extensive i.e., expressible as an integral of a local density over the sample volume, then the observed value is reproduced by the ensemble averaging which then becomes a matter of convenience. There are, however, quantities which are not self-averaging in the above sense. Well-known examples are from the statistical mechanics of disordered systems, e.g., the archetypal spin glass. Here the partition function and several susceptibilities are in fact not self-averaging, but the free energy is. In the following we will be concerned with the (residual) resistance of a disordered conductor at low temperatures which is dominated by quantum coherence effects (Kumar 1985; Kumar and Jayannavar 1986; Kumar and Mello 1985). The latter will be shown to make the resistance non-additive and non-self averaging. This was already noted for the case of one-dimensional conductors by Mel'nikov (1980), Anderson *et al* (1980) and Abrikosov (1981). Following an invariant imbedding procedure, we derive an expression for the probability

CC-0. In Public Domain. Gurukul Kangri Collection, Haridwar

Digitized by Arya Samaj Foundation Chennai and eGangotri

distribution of these 'Sinai' fluctuations of resistance for $d = 1$. We find that variance exponentially dominates the resistance as the length tends to infinity, while the mean conductance stays infinite for all lengths due presumably to Azbel resonance (Azbel 1983). We then extend the treatment to higher dimensions in a Migdal-Kadanoff bond moving approximation (Shapiro 1986). We find that the fluctuations dominate the mean value even at the mobility edge. It appears that one must consider all the cumulants to describe the behaviour of resistance at the mobility edge (see Al'tshuler *et al* 1986 and references therein) necessitating a deeper analysis of the one-parameter scaling ansatz (Abrahams *et al* 1979). Next, we show that an external electric field tends to harness these fluctuations through its delocalizing effect. Finally, we consider the $1/f$ noise generated by these fluctuations at the surface of a disordered semi-infinite conductor. Direct experimental probing of "Sinai" fluctuations is briefly discussed at the end.

2. One-dimensional disordered conductors

Consider a one-dimensional (1-d) disordered conductor of length L, terminated at both ends in perfect leads. We can view the whole sample as a one-channel potential scatterer characterized by an amplitude reflection coefficient $R(L) = |R(L)| \exp(i\theta(L))$. The resistance ($\rho$) in units of $\pi\hbar/e^2$ can then be expressed in terms of this emergent quantity $R(L)$ as

$$\rho(L) = \frac{|R(L)|^2}{1-|R(L)|^2}. \tag{1}$$

The L-dependence of $R(L)$ can now be studied by the method of invariant imbedding (Kumar 1985) which directly addresses the emergent quantity. The imbedding equation for $R(L)$ is

$$\frac{dR(L)}{dL} = -\frac{1}{2ik}[(k^2(L)-k^2)\,(1+R^2(L))+2(k^2(L)+k^2)R(L)], \tag{2}$$

where $\hbar^2k^2/2m \equiv E$ is the incident electron energy (= the Fermi energy at $T = 0°K$) and $k(x)$ is the local wave number given by $\hbar^2k^2(x)/2m = E - V(x)$, and $V(x)$ is the random potential assumed gaussian white noise with $\langle V(x)\rangle = 0$, $\langle V(x)V(x')\rangle = V_0^2\delta(x-x')$.

Equation (2) is a stochastic differential equation. As we are interested in the probability distribution $W_\rho(\rho)$ of $\rho(L)$, and therefore, $W_r(r)$ of $r(L) = |R(L)|^2$, we have to go over to the associated Fokker-Planck equation for $W_r(r)$ which is readily obtained as

$$\frac{\partial W_r}{\partial l} = r(1-r)^2\frac{\partial^2 W_r}{\partial r^2}+(1-r)\,(1-5r)\,\frac{\partial W_r}{\partial r}+2(2r-1)\,W_r, \tag{3}$$

where we have introduced the dimensionless length $l = L/\xi$, $\xi = \hbar^2E/2mV_0^2$, the localization length. Simple change of variable gives for W_ρ

$$\frac{\partial W_\rho}{\partial l} = \rho(1+\rho)\frac{\partial^2 W_\rho}{\partial \rho^2}+(1+2\rho)\frac{\partial W_\rho}{\partial \rho}, \tag{4}$$

CC-0. In Public Domain. Gurukul Kangri Collection, Haridwar

Digitized by Arya Samaj Foundation Chennai and eGangotri

which is our central exact result. From (4), we get the moments $\rho_n \equiv \langle \rho^n \rangle$ by multiplying both sides of the equation by ρ^n and integrating by parts on the right-hand side. We have the first two moments

$$\rho_1 = \tfrac{1}{2}(\exp(2l) - 1),$$

$$\rho_2 = \tfrac{1}{12}(\exp(6l) - 6\exp(2l) + 4). \tag{5}$$

From (5) we see that for $l \ll 1$ the l-dependence is ohmic which is understandable as the cumulative effect of coherence has not built up yet. For $l \gg 1$, the mean resistance grows exponentially, and variance exponentially dominates the mean indicating non-additivity and non-self averaging. The asymptotic form of the full probability distribution is ($l \gg 1$, $\rho \gg 1$)

$$W_\rho(\rho) \sim \frac{\exp(-l/4)}{(4\pi l)^{1/2}} \rho^{-1/2} \exp\left(-\frac{1}{4l}\ln^2 \rho\right), \tag{6}$$

which gets broader as $l \to \infty$. Equation (6) shows that the $\log\rho$ (proportional to inverse of localization length) does obey the central limit theorem—the levelling property of the logarithm!

It is interesting to examine the effect of an external electric field F, which is easily included by the replacement $V(x) \to V(x) - eFx$. The modified probability distribution W_ρ^F obeys (Vijayagovindan *et al* 1986)

$$\frac{\partial W_\rho^F}{\partial L} = \frac{1}{\eta\left(1 + \dfrac{|e|FL}{E}\right)}\left[\frac{\partial}{\partial \rho}\left\{\rho(1+\rho)\left(\frac{\partial W_\rho^F}{\partial \rho} + \frac{|e|F\eta\, W_\rho^F}{E\left(1 + \dfrac{1}{1+|e|FL/E}\right)}\right)^{1/2}\right\}\right] \tag{7}$$

with

$$\eta = E^2/k^2 V_0^2.$$

The interesting point to note is that the distribution W_ρ^F saturates to a limiting Poissonian form in the limit $L \to \infty$. Also, the mean resistance given by

$$\rho_1^F \simeq \frac{1}{2}\left[\left(1 + \frac{|e|FL}{E}\right)^{\frac{2E}{|e|F\xi}} - 1\right], \tag{8}$$

interpolates between the exponential and a power-law length dependence as the field F is increased, the cross-over being at $2E/|e|F\xi \simeq 1$. This is, of course, a manifestation of the field-induced weakening of localization (Soukoulis *et al* 1983).

CC-0. In Public Domain. Gurukul Kangri Collection, Haridwar

Digitized by Arya Samaj Foundation Chennai and eGangotri

3. Fluctuations at the mobility edge (D > 1)

Our starting points is the 1-d equation (4). We assume for simplicity an anisotropic case where the disorder is only along the direction of the externally impressed current. Consider a d-dimensional hypercube b^d, and ignore the b^{d-1} bonds transverse to the chosen direction of current flow (classically these bonds connect equipotential points and hence play no role). We now combine the b units in series along the direction of current flow quantum mechanically according to (4), and then combine the b^{d-1} parallel chains in parallel classically (Kumar and Jayannavar 1986; Shapiro 1986). Thus, we get the scaling relation

$$(\rho_{(b)}^{(d)})^{-1} = \sum_{i=1}^{b^{d-1}} (\rho_i^{(1)}(b))^{-1}. \tag{9}$$

Making b a continuous variable then gives the evolution

$$\frac{\partial K_\rho^{(d)}}{\partial \ln l} = -(d-1)x\frac{\partial K}{\partial x} + \frac{1}{2}\left[x^2 \frac{\partial^2 K_\rho^{(d)}}{\partial x^2} + x^2 \left(\frac{\partial K_\rho^{(d)}}{\partial x} \right)^2 \right.$$

$$\left. + x(2-x)\frac{\partial K_\rho^{(d)}}{\partial x} - x \right] \ln(1+2\rho_1^{(d)}), \tag{10}$$

where we have introduced the characteristic function

$$K_\rho^{(d)} = \ln \int_0^\infty \exp(-x\rho)\, W_\rho^{(d)}\, \mathrm{d}\rho \tag{11}$$

and $\rho_1^{(d)}$ in the mean resistance of the d-dimensional system.

It is now readily seen that (11) has a fixed point distribution obtained by setting the left hand side to zero. The associated fixed-point probability $W_\rho^{*(d)}$ is given by a power law

$$W_\rho^{*(d)} = \frac{(1+\rho)^{-\alpha}}{(\alpha-1)}, \quad \text{with} \quad \alpha = 2(d-1)/(1+2\rho_1^{*(d)}), \tag{12}$$

where $\rho_1^{*(d)}$ is the critical resistance (mobility edge). Thus, the mean is finite but all cumulants are infinite. This extreme dominance of fluctuation may be due to assumed anisotropy that presumably over-emphasizes the one-dimensional character. This may also account for the one-parameter scaling nature of solution (12). Further analysis shows that even on the metallic side, $\rho_1^{(d)} < \rho_1^{*(d)}$, the variance remains comparable with the mean.

We have attempted the general case of isotropic disorder and our results (Kumar and Jayannavar 1985) do not support the one-parameter scaling ansatz.

CC-0. In Public Domain. Gurukul Kangri Collection, Haridwar

Digitized by Arya Samaj Foundation Chennai and eGangotri

4. Sinai fluctuations and 1/*f*-noise

Yet another manifestation of these fluctuations is the $1/f$-noise resulting from the resonant back-scattering of positive energy electrons at the interface between a semi-infinite disordered system and a perfect lead. The point is that the positive energy Anderson localized states deep inside the bulk appear as resonant states nearer the interface. Resonant reflection leads to energy dispersive phase shift θ and therefore, to a distribution of the delay time (Δt). The latter results in non-cancellation of instantaneous surface currents resulting from the incident and retarded reflected waves. The noise spectrum turns out to have the $1/f$ character. We have derived the probability distribution $W(\tau)$:

$$W(\tau)=\frac{\lambda \exp(\lambda \arctan \tau)}{(\exp(\lambda\pi/2)-1)\,(1+\tau^2)}, \tag{12}$$

with

$$\tau=\frac{2E(\Delta t)}{\sqrt{3}\hbar}, \quad \lambda=\frac{8}{\sqrt{3}}k\xi.$$

The long power law tails gives infinite delay time in-the-mean which corroborates with the fact noted earlier that the mean conductance is infinite even for infinite sample length. Noise spectrum for currents then turns out to be linear in frequency, giving a $1/f$ noise for charge or voltage fluctuations.

5. Discussion

The resistance fluctuation, its dominance over the mean and the consequent possible deviation from the one-parameter scaling ansatz are due ultimately to the coherence effects associated with the wave nature of electrons. As such we expect acoustic and optical analogues of these effects. A direct experimental observation of 'Sinai' fluctuations is, however, possible by introducing disorder coulometrically and current cycling the sample, keeping the net ampere-hours (charge-transferred) constant, (e.g. in $Ag_{2+\delta}S$). Thus, we naturally have macroscopically identical samples but differing in the microscopic complexions (i.e., depending on where the ions are lodged). Then, one would expect identical resistance at higher temperatures but a large scatter in the low-temperature resistances.

Another interesting experiment would be to observe the time-translation of 'Sinai' fluctuations at non-zero temperature possible under the condition that the sample length be small compared to the inelastic mean free path (or better still the Thouless length) but the transit-time of the electron through the sample be smaller than the period of the dominant thermal phonon. Then, the lattice-potential modulation by phonons is seen only adiabatically by the electrons (no inelastic scattering) and the successive electrons see effectively different realizations of the random potential giving an excess noise. We could call this scintillation noise somewhat after the twinkling of stars.

CC-0. In Public Domain. Gurukul Kangri Collection, Haridwar

Digitized by Arya Samaj Foundation Chennai and eGangotri

References

Abrahams E, Anderson P W, Licciardello D C and Ramakrishnan T V 1979 *Phys. Rev. Lett.* **42** 673
Abrikosov A A 1981 *Solid State Commun.* **37** 997
Al'tshuler B L, Kravstov V E and Lerner I V 1986 Academy of Sciences of the USSR (Leningrad Nuclear Physics Institute) Preprint No. 1229 (and references cited therein)
Anderson P W, Thouless B J, Abrahams E and Fisher D S 1980 *Phys. Rev.* **B22** 3519
Azbel M Ya 1983 *Solid State Commun.* **45** 527
Jayannavar A M, Vijayagovindan G V and Kumar N 1987 (to appear)
Kumar N 1985 *Phys. Rev.* **B31** 5513
Kumar N and Jayannavar A M 1986 *J. Phys.* **C19** L85
Kumar N and Mello P A 1985 *Phys. Rev.* **B31** 3109
Mel'nikov V I 1980 *Pis'ma Zh. Eksp. Teor. Fiz.* **32** 244
Pendry J B, Kirkman P D and Castano E 1986 *Phys. Rev. Lett.* **57** 2983
Shapiro B 1986 *Phys. Rev.* **B34** 4394
Soukoulis C M, Jose J V, Economon E N and Sheng P 1983 *Phys. Rev. Lett.* **59** 764
Vijayagovindan G V, Jayannavar A M and Kumar N 1987 *Phys. Rev.* **B 35** 2029

CC-0. In Public Domain. Gurukul Kangri Collection, Haridwar

Digitized by Arya Samaj Foundation Chennai and eGangotri

Pramāna – J. Phys., Vol. 28, No. 5, May 1987, pp. 509–516. © Printed in India.

Resistivity of metallic systems with a strong dynamic disorder

V F GANTMAKHER, G I KULESKO and V M TEPLINSKY
Institute of Solid State Physics, Academy of Sciences of the USSR, Chernogolovka, USSR

Abstract. If the static disorder in a system is increased the conductivity and the electron mean free path decreases to the limit where it reaches the Ioffe-Regal criterion. In this paper experimental results are presented which show that dynamic disorder (produced by electron-phonon interaction) can produce similar effects as static disorder. In certain metallic glasses it has been found that when the resistivity as a function of temperature reaches a critical value (almost equal to the maximum metallic resistivity value) the TCR changes from positive to negative values.

Keywords. Resistivity; metallic systems; dynamic disorder.

PACS No. 72·15

1. Introduction

In accordance with the known Ioffe-Regel criterion the electronic mean free path, l, cannot be shorter than the electron wavelength. When applied to the metals with the Fermi momentum K_F this means that

$$l > l_{\min} \approx \pi/K_F. \tag{1}$$

The metallic systems with l approximating $l_{\min}$ are extensively being studied in the last few years due to the progress achieved in the technique of producing amorphous alloys. Mostly the small mean free path l is the consequence of the static disorder, i.e. random arrangement of atoms at low temperatures. On the other hand, the smallest possible l can also be obtained in some cases in a perfect crystal by increasing the temperature T, i.e. by introducing the dynamic disorder.

2. Comparison between static and dynamic disorders

Let us refer to the plane $(T, \hbar/\tau)$ with the Fermi energy ε_F on both the axes as a characteristic scale (figure 1). The condition of the degeneracy of the electron gas $T < \varepsilon_F$, along with the uncertainty relation

$$\Delta\varepsilon \approx \hbar/\tau \lesssim \varepsilon_F = \hbar^2 K_F^2/2m \tag{2}$$

which isolate a square in this plane (criteria (1) and (2) actually are equivalent, differing in the numerical factor $\pi/2$ only). The formula for the resistivity

$$\rho = m/ne^2\tau = \hbar K_F/ne^2 l, \tag{3}$$

CC-0. In Public Domain. Gurukul Kangri Collection, Haridwar

Digitized by Arya Samaj Foundation Chennai and eGangotri

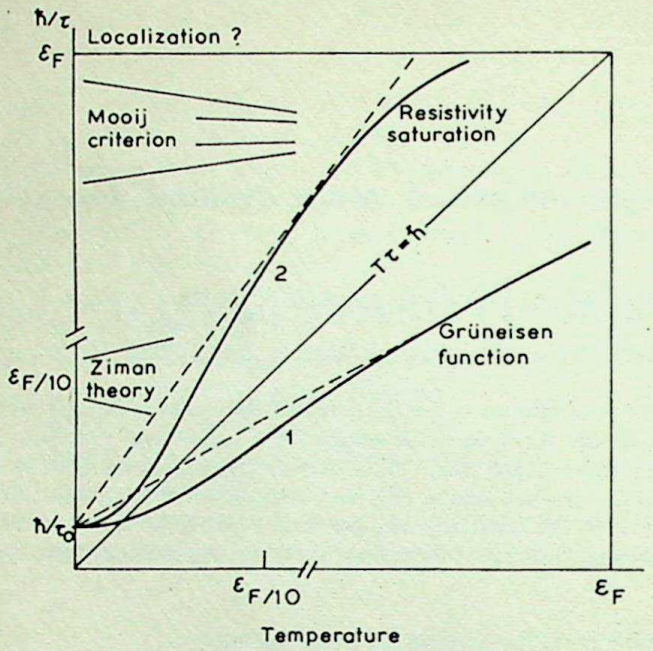

Figure 1. A diagram in $(T, \hbar/\tau)$-plane illustrating applicability of the Boltzmann equation.

enables us to plot one more scale along the ordinate. Substituting into (3) the electron density $n = va^{-3}$ (v is the number of free electrons per atom, a is the mean interatomic distance) and $K_F = (3\pi^2 n)^{1/3}$ we obtain

$$\rho = (3\pi^2)^{-1/3}(\hbar/e^2)(a^2/v^{2/3}l). \tag{4}$$

Substituting the value of $l_{\min}$ from (1) or (2) into (4), we get

$$\rho = (400 \div 600)v^{-1/3}\,\mu\Omega\cdot\text{cm}. \tag{5}$$

The dependence of ρ on v being weak, we can assume $v = 1$ for all metals. Hence we obtain the resistivity scale shown in figure 1.

Transport properties of metals with a sufficiently large electron mean free path l are accounted for by the noninteracting gas model based on the Boltzmann equation. This approach obviously is applicable inside the lower triangle in figure 1, where the electron energy uncertainty due to scattering is smaller than the temperature broadening of the Fermi distribution. However, this description is used sometimes in the upper triangle $T\tau < \hbar$. For example, shifting along the ordinate we reach a region, where the Ziman theory developed for the liquid metals is used. The wave functions in this theory are considered to be plane waves, and their scattering by a random potential is calculated in the Born approximation (Faber 1969). The success of the Ziman theory was conditioned, as a matter of fact, by a high electron density. The screening of the random potential of the ions is so strong that even in the absence of the long-range order the quantity l remains several times larger than the electron wavelength K_F^{-1}. That the quantity l can really be large in liquid follows from the values of the resistivity of pure liquid uni-, bi- and tri-valent metals (Faber 1969) that do not exceed 40 $\mu\Omega\cdot$cm.

To the alloys with the resistivity of $\rho > 100/150\,\mu\Omega\cdot$cm, Ziman's theory is not applicable. Then the empirical rule of Mooij (1973) should be used, the sign of the

CC-0. In Public Domain. Gurukul Kangri Collection, Haridwar

Digitized by Arya Samaj Foundation Chennai and eGangotri

temperature coefficient of the resistivity depends on the ρ value. It is to be emphasized that the applicability regions of the Ziman theory and the Mooij rule do not overlap. In particular, the negative sign of the temperature coefficient of resistivity of bivalent metals described by Ziman theory contravenes the Mooij rule.

If the resistivity of an alloy were $\rho \gtrsim 500\ \mu\Omega\cdot$cm at $\nu \approx 1$ ($n \approx 10^{21} - 10^{22}$ cm^{-3}) it would mean that $l < l_{\min}$. Such an alloy would be expected to undergo the Anderson transition into the dielectric state. However, the amorphous alloys consisting of "metallic" atoms with weakly bound valence electrons never have the resistivity larger than 400 $\mu\Omega\cdot$cm. On the other hand, there are no examples of the Anderson transition in metallic systems with $n \gtrsim 10^{20}$ cm^{-3}. Both facts seem to be the result of screening, that self-consistently decreases the amplitude of the random potential to a level which ensures the fulfilment of inequalities (1) and (2).

Thus, the problem of the Anderson transition near the upper side $\hbar/\tau = \varepsilon_F$ of the square in figure 1 proves to be closely connected with the screening, i.e., in the final analysis, with the electron-electron interaction. As for the latter, in the upper triangle $T\tau < \hbar$, it is affected by the elastic scattering; during the interaction time $\hbar/T$ the electrons go through many collisions with scatterers (impurities or phonons) which determine the value of τ.

In principle, the upper side of the square in figure 1 can be approached by means of the electron-phonon interaction. The Grüneisen curve $\rho_{id}(T)$, describes in terms of the kinetic equation the resistivity caused by the phonon scattering. At temperatures above the Debye temperature θ it approaches the linear dependence

$$\rho = \alpha T \quad (T \gg \theta). \tag{6}$$

According to the order-of-magnitude estimate, for a typical metal with $K_F \approx a^{-1}$ and deformation potential $D \approx \varepsilon_F \approx e^2/a$ the asymptote is just the diagonal $\hbar/\tau = T$ of the square. Because of numerical coefficients, it may lie in reality either below (curve 1 in figure 1) or above the diagonal (curve 2). Curve 1 crosses the upper triangle only at low temperatures. In this domain l and τ are controlled by the elastic impurity scattering. It is known that under these conditions the behaviour of the electron-electron (Al'tshuler and Aronov 1979) and electron-phonon (Schmid 1973; Al'tshuler 1978) scatterings changes. At $T \gg \theta$ the scattering by phonons is quasielastic and in this sense resembles the scattering by impurities. Therefore the physical ideas forming the basis of the results of Al'tshuler and Aronov (1979), Schmid (1973) and Al'tshuler (1978) are also seemingly applicable for curve 2 at high temperatures. We mean here the change in the probability of the electron-electron scattering occurring because of the diffusion of one electron in the field of another, the appearance of a density of states extremum on the Fermi level (Al'tshuler and Aronov 1979) as well as the change in the probability of scattering by long wavelength phonons with the wave vectors $q \ll l^{-1}$ (Schmid 1973; Morton *et al* 1978).

It is clear that if the curve $\rho(T)$ is situated in the upper triangle, the resistivity increase is to be limited with increasing temperature. This problem—designated as the problem of resistivity saturation—became the subject of numerous investigations after the publication of the paper by Fisk and Webb (1976) who connected for the first time the behaviour of the temperature dependence of the resistivity observed in Nb_3Sb and Nb_3Sn crystals with the Ioffe-Regel criterion. Since then a rather rich experimental

CC-0. In Public Domain. Gurukul Kangri Collection, Haridwar

Digitized by Arya Samaj Foundation Chennai and eGangotri

material has been gained (Sunandana 1979; Lawson 1985; Mori *et al* 1981; Nedellec *et al* 1985) which shows that the tendency to saturation is always present when the mean free path of carriers approaches to limit (1) (Gurvitch 1983).

Since the velocities of thermal motion of atoms are much lower than the electron velocities (static and dynamic disorders appear similar to an electron). However, when the disorder is dynamic the electron distribution function is broadened by the temperature.

3. Experimental approach to the dynamic disorder problem

The experimental study of the problem encounters some complications. Since the experiment is carried out at high temperatures and the electron structure of metals is complicated it may happen that the observed deviations of $\rho(T)$ from the linear dependence (6) are due to specific peculiarities of the electron spectrum of the material involved. One can imagine, for example, a simple semiconductor effect of the increase of the carrier density due to the excitation onto the Fermi level of electrons from a completely filled band. Along curve 2 it is the quantity $\hbar/\tau$ and not T that first becomes equal to the excitation energy. This also should affect the resistivity (Chakraborty and Allen 1979). As a matter of fact, the resistivity has to change, when T or $\hbar/\tau$ comes up to any characteristic energy describing the electron spectrum (such as the width of the peak in the density of states of A-15 superconductors (Cohen *et al* 1967); the energy of the s-d hybridization (Weger *et al* 1984 etc.).

It is difficult to consider these complications because we do not normally know the electron spectrum sufficiently well. This determines the strategy of the experimental studies of the resistivity saturation. On the one hand, this effect has to be searched for in various classes of materials and, on the other, one has to look for extra variables that could have influence on the limit value of the resistivity.

It is seen (Fisk and Webb 1976; Morton *et al* 1978; Sunandana 1979; Mori *et al* 1981; Gurvich 1983; Lawson 1985; Nedellec *et al* 1985) that resistivity saturation takes place in rather different materials. Particular attention should be drawn to the fact that the effect is observed in In_5Bi_3 (Mori *et al* 1981) containing no atoms with unfilled *d*-shells.

The present paper presents additional experimental data obtained on (i) Cu-Zr alloys in the crystalline state; for some compositions the $\rho(T)$ dependences exhibit not only saturation but even a maximum; (ii) on high quality WO_2 single crystals with a large anisotropy of ρ.

4. Alloys Cu-Zr (Gantmakher and Kulesko 1985)

The samples were produced by recrystallization of an amorphous ribbon (the accuracy in the composition determination was about 2–3%). Measurements were carried out on strips of dimensions $3{\cdot}5 \times 25$ mm^2 using d.c. method. The results of measurements are shown in figure 2 for three alloys of different compositions. Crosses stand for the values obtained before crystallization of the amorphous ribbon, circles after crystallization, the open and solid circles corresponding to different cycles of measurements.

All the known data on the electron structure of alloys of the system Cu-Zr (Ching *et al* 1984) give us no reasons to attribute the existence of a maximum in the two upper

CC-0. In Public Domain. Gurukul Kangri Collection, Haridwar

Digitized by Arya Samaj Foundation Chennai and eGangotri

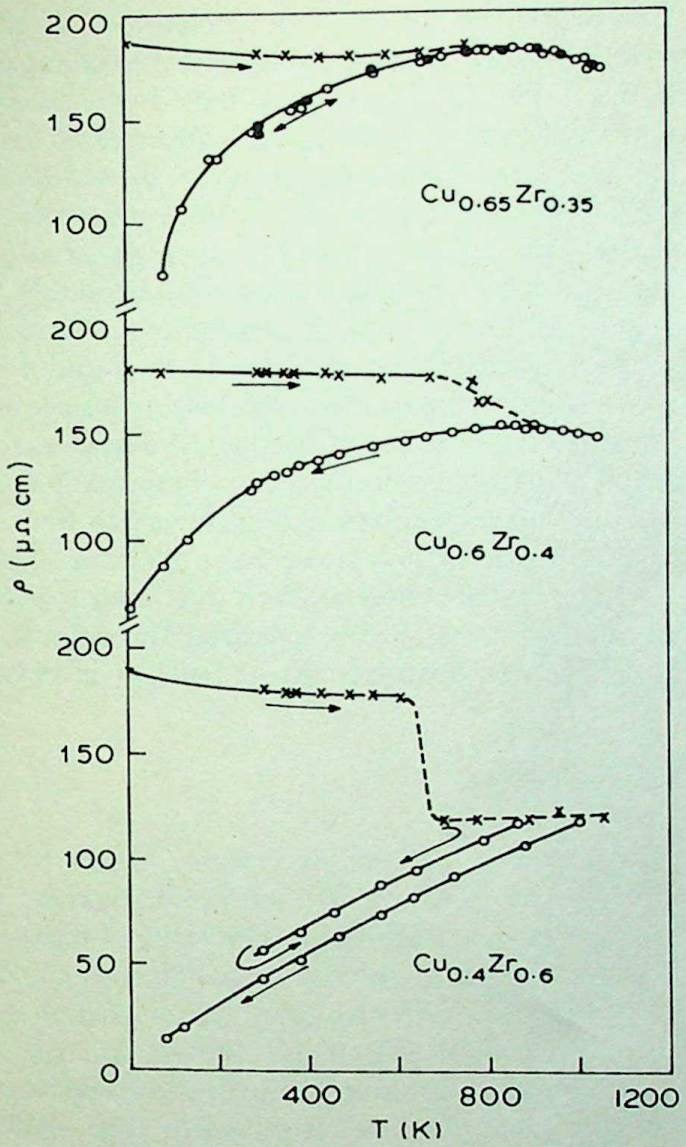

Figure 2. Resistivity of three Cu-Zr samples with different Cu content.

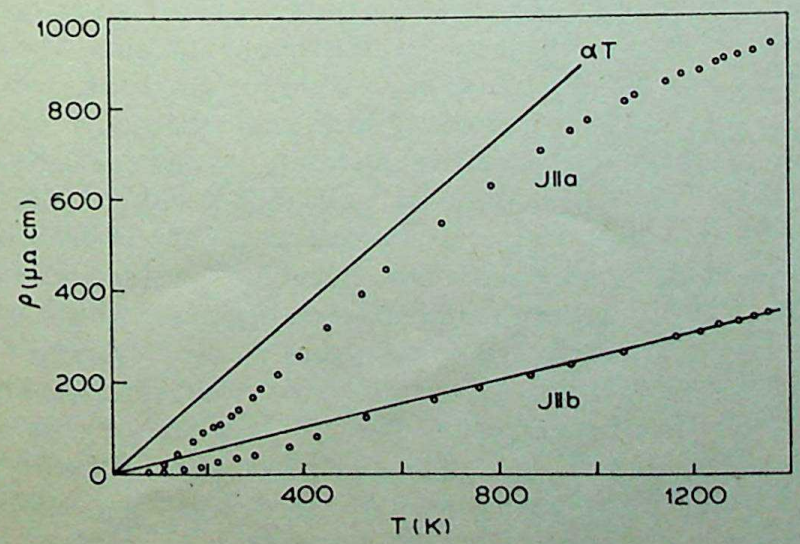

Figure 3. Temperature dependence of resistivity of WO_2 samples of different orientation.

CC-0. In Public Domain. Gurukul Kangri Collection, Haridwar

Digitized by Arya Samaj Foundation Chennai and eGangotri

curves to any peculiarity of the dispersion law in copper-rich alloys. At the same time we see correlation between the existence of a maximum and the change of ρ during crystallization. The maximum is observed only when ρ falls down during crystallization insignificantly, i.e. when the dynamic disorder is as effective as the static one.

In the above section we have affirmed that the amplitude of the scattering potential decreases self-consistently thus preventing localization. In our opinion, it is possible to pass over this affirmation using the two-band model of electron spectrum. The carriers in one of the bands may become localized whereas in the second band they may remain delocalized thus securing the conservation of metallic conductivity. Then the existence of the maximum could be explained reasonably well. Let both s- and d-electrons be present in the alloy. Starting with room temperatures the d-electrons are in a "limiting regime" $l \approx a$. If the source of scattering were static disorder, the decrease of resistivity with the temperature increase could be interpreted in terms of thermally activated hops of localized carriers. A variant of these speculations is believed to be valid also for localization induced by dynamic disorder. Then we have to admit that phonons strengthen localization at low temperatures and weaken it at high temperatures.

The proposed explanation implies coexistence of localized and delocalized state at the Fermi level. This contradicts Mott's postulate (Mott and Davis 1979).

5. Oxide WO_2 (Gantmakher *et al* 1986)

Samples in the form of sticks were cut from single crystals grown by the vapour transport. They were about 2–4 mm long and $0{\cdot}3 \times 0{\cdot}4\ \text{mm}^2$ across. The crystal orientation was determined using the x-ray technique. The residual resistance did not exceed 1–2% of the room resistance and could be neglected. The resistivity of WO_2 is anisotropic. The diagonal components of the resistivity tensor written down in the main axes at room temperatures are $\rho_1 = 50\ \mu\Omega{\cdot}\text{cm}$; $\rho_2 = 60\ \mu\Omega{\cdot}\text{cm}$; $\rho_3 = 180\ \mu\Omega{\cdot}\text{cm}$. The temperature measurements have shown that in some directions resistivity of WO_2 exhibits a tendency to saturation while in others it does not. This is illustrated in figure 3. The experimental curves $\rho(T)$ are plotted for the directions where ρ_{room} has its maximum and minimum values.

For quantitative interpretation of results we tried, as usual, to extract from the function $\rho(T)$ an "ideal" part described by the Boltzmann equation. The difficulty is that even for this ideal part the analytical expression for an arbitrary electron and phonon spectra exists only in the asymptotical form, while the analytical expressions for high-temperature corrections, which are of interest for us, are not known at all. Let us consider in detail the quantity ρ_{id}. In the isotropic model with the spherical Fermi surface and Debye phonon spectrum the dependence $\rho_{\text{id}}(T)$ is described by the Grüneisen function. Note that at $T = \theta$ the value of this function is still 6% smaller than that of the asymptote (6). So the latter can only be used beginning with $T \gtrsim (1{\cdot}5 \text{ to } 2)\theta$. For the isotropic model $\rho_{\text{id}}(T)$ is really known within the whole temperature range. However, if the Fermi surface consists of several isolated closed sheets and the phonon spectrum has optical branches the Grüneisen function becomes very complicated. In both cases a specific temperature θ_0 appears at which new processes start: transitions between sheets or scattering by optical phonons. At $T \gg \theta, \theta_0$ asymptote (6) is still valid, but at low temperatures it is impossible to calculate $\rho_{\text{id}}(T)$ without a detailed knowledge of the spectra. In WO_2 the dependence $\rho_{\text{id}}(T)$ is certainly more complicated

CC-0. In Public Domain. Gurukul Kangri Collection, Haridwar

Digitized by Arya Samaj Foundation Chennai and eGangotri

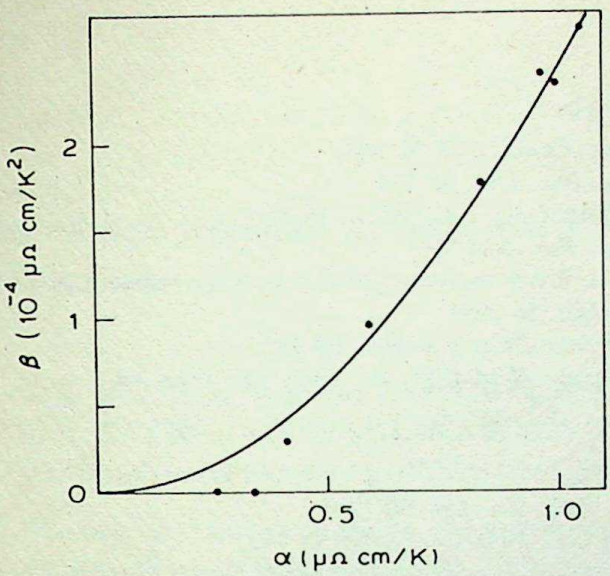

Figure 4. Correlation between coefficients α and β in the expression $\rho = \alpha T + \beta T^l$ which describes the WO_2 experimental results.

than in the isotropic model. It is difficult to say whether the complications are caused by the optical phonon scattering or by interband transitions—in all likelihood both factors are responsible. However, it became clear that the Grüneisen curve could not be used for description of $\rho_{id}(T)$ in WO_2. Therefore in the analysis of the curves we have only used the data for temperatures $T \gtrsim 700$ K assuming that in this region $\rho_{id} \sim T$. Note that the residual resistance of our samples at these temperatures was always smaller than 1% of the total and obviously could be neglected.

In all our experiments the high-temperature deviations of $\rho_{id}(T)$ from a straight line were comparatively small. Therefore it might be worthwhile assuming that the correction $\rho - \rho_{id}(T)$ is small to write it in the form

$$\rho - \rho_{id} = \beta T^l, \quad l > 1. \tag{7}$$

In principle the curves $\rho(T)$ for various directions of the current with respect to the crystal axes could be similar differing only in the scale along the ρ-axis, i.e. $\beta \sim \alpha$. This would be the case, for example, if the deviation of ρ from ρ_{id} were the result of increase of carrier density. Our measurements show, however, that in WO_2 an "enhanced anisotropy" is realized: the anisotropy of the correction (7) is larger than the anisotropy of ρ_{id} itself (see figure 4). Since the sign of the high-temperature correction is negative, the "enhanced anisotropy" of the correction means a decrease in the anisotropy of ρ with increasing T. It is known that something like this is also observed in other materials. For example, yttrium is an anisotropic metal with high absolute value of the resistivity. At high temperatures its resistivity saturates and the anisotropy of the resistivity vanishes (Zinovev *et al* 1975). This gives us reasons to believe that the phenomenon observed in WO_2 is a rather common one.

CC-0. In Public Domain. Gurukul Kangri Collection, Haridwar

Digitized by Arya Samaj Foundation Chennai and eGangotri

References

Al'tshuler B L 1978 *Sov. Phys. JETP* **48** 670
Al'tshuler B L and Aronov A G 1979 *Sov. Phys. JETP* **50** 968
Chakroborty B and Allen P B 1979 *Phys. Rev. Lett.* **42** 736
Cohen R W, Cody G D and Jalloran J J 1967 *Phys. Rev. Lett.* **19** 840
Ching S, Song A and Jaswal B 1984 *Phys. Rev.* **B30** 544
Faber T E 1969 in *The physics of metals* 1. *Electrons* (ed.) J M Ziman (Cambridge: University Press)
Fisk Z and Webb G W 1976 *Phys. Rev. Lett.* **36** 1084
Gantmakher V F and Kulesko G I 1985 *Solid State Commun.* **53** 267
Gantmakher V F, Kulesko G I and Teplinsky V M 1986 *Sov. Phys. JETP* **63** N4
Gurvitch M 1983 *Phys. Rev.* **B28** 544
Lawson A C 1985 *Phys. Lett.* **A107** 45
Mooij J H 1973 *Phys. Status Solidi* **A17** 521
Mori K, Tamura N and Saito Y 1981 *J. Phys. Soc. Jpn.* **50** 1275
Morton N, James B W and Wostenholm G H 1978 *Cryogenics* **18** 131
Mott N F and Davis E A 1979 *Electron processes in non-crystalline materials* (Oxford: Clarendon Press)
Nedellec P, Greppy F V, Dumoulin L and Burger J P 1985 *Phys. Lett.* **A111** 67
Schmid A 1973 *Z. Phys.* **259** 421
Sunandana C S 1979 *J. Phys.* **C12** L165
Weger M, de Groot R A, Muller F M and Kaveh M 1984 *J. Phys.* **F14** L207
Zinovev V E, Sokolov A L, Geld P V, Chuprikov G E and Epifanova K I 1975 *Sov. Phys. Solid State* **17** N12

CC-0. In Public Domain. Gurukul Kangri Collection, Haridwar

Digitized by Arya Samaj Foundation Chennai and eGangotri

Pramāṇa – J. Phys., Vol. 28, No. 5, May 1987, pp. 517–527. © Printed in India.

Josephson voltage standard at National Physical Laboratory, New Delhi

A K GUPTA, N S NATARAJAN, V S TOMAR, N D KATARIA, V K BATRA, A V NARLIKAR and K CHANDRA

National Physical Laboratory, Hillside Road, New Delhi 110012, India

Abstract. A C Josephson effect is now used by several countries as the reference standard for the unit of d.c. voltage. This paper describes the work done at the National Physical Laboratory (NPL), New Delhi in the realization of the unit of volt based on the a.c Josephson effect. A voltage standard at 1 mV level using a Nb-Nb point contact junction has been established and the as-maintained volt based on a bank of standard cells has been intercompared against it using a 1 : 1000 voltage divider. The experimental set-up used in this comparison and the results of recent measurements are described. The overall uncertainty in assigning the value of emf to a standard cell is about 1 ppm. The as-maintained volt has been found to agree with the Josephson voltage within overall uncertainty.

Keywords. Josephson effect; voltage standard; superconductivity; superconducting devices.

PACS No. 74·50

1. Introduction

The a.c. Josephson effect (Josephson 1962, 1964, 1965) is now used by several national laboratories (Field *et al* 1973; Harvey *et al* 1972; Melchert 1978; Hartland 1977; Witt *et al* 1983; Andreone *et al* 1983; Endo *et al* 1983; Wood and Dunn 1981) as the reference standard for the unit of d.c. voltage. The Josephson effect relates the voltage to the frequency, the most accurately known SI unit, through fundamental constants e, the charge of the electron and h, the Planck's constant. This voltage frequency relation is space- and time-invariant and forms the basis for the reference standard for the unit of volt. The earlier reference standard based on a bank of saturated Weston cadmium cells had unpredictable long-term drifts of the order of a few ppm and required periodic transportation to BIPM, France for intercomparison with their standard cells. Moreover, it was very difficult to know what portion of the difference between the values of the BIPM volt and that of the other laboratory was due to the drift in the emf of the BIPM cells. All these problems have been overcome with the development of the Josephson voltage standard. However, a bank of standard cells or a Zener-based electronic voltage standard is still maintained as the physical standard to represent the volt and is used for day-to-day calibration work. These physical standards are periodically calibrated against the Josephson voltage standard.

CC-0. In Public Domain. Gurukul Kangri Collection, Haridwar

Digitized by Arya Samaj Foundation Chennai and eGangotri

2. Josephson effect and the principle of voltage standard

In 1962, Brian D Josephson predicted an effect in superconductors which now bears his name (Josephson 1962, 1964, 1965). He predicted that a direct supercurrent could flow between two weakly coupled superconductors (known as a Josephson junction) even if the potential difference between the two is zero. The zero voltage supercurrent flows upto a characteristic value known as the critical current. This phenomenon is called the d.c. Josephson effect. Above the critical current a finite potential difference appears across the junction and an alternating supercurrent starts flowing between the two superconductors. The frequency ν of the alternating supercurrent is related to the potential difference V across the junction by the relation

$$2eV = h\nu, \tag{1}$$

where e *is* the charge of the electron and $\hbar$ is the Planck's constant. This phenomenon is called the a.c. Josephson effect. Josephson further predicted that in the presence of microwave radiations of frequency, ν_m, a direct supercurrent could flow between two weakly coupled superconductors when there was a finite potential difference V between the two superconductors, provided the following condition is satisfied

$$2eV = nh\nu_m, \tag{2}$$

where n is an integer. Thus in the presence of microwave radiations, the d.c. I-V characteristic of a Josephson junction looks like a staircase as shown in figure 1. The current steps appear at a constant voltage interval given by equation (2). The Josephson effect, thus relates the voltage to the frequency, the most accurately known SI unit, through fundamental constants. This voltage frequency relationship is exact and is space- and time-invariant. It is also independent of all physical parameters such as junction material, type of junction, frequency of microwave radiations, operating temperature, magnetic field etc. It has been experimentally shown that the relationship is accurate to within 2 parts in 10^{16}, the upper limit is set by the sensitivity of the

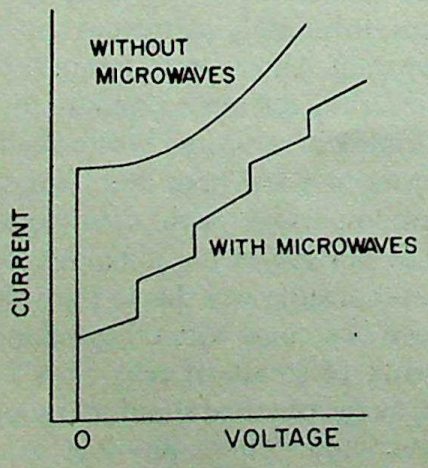

Figure 1. I-V characteristic of a Josephson junction.

CC-0. In Public Domain. Gurukul Kangri Collection, Haridwar

Digitized by Arya Samaj Foundation Chennai and eGangotri

instruments (Tsai *et al* 1983). These microwave-induced steps in the d.c. current-voltage characteristic of a Josephson junction forms the basis of a voltage standard. As the magnitude of a step voltage is very small ($\sim 20\ \mu$V for 10 GHz radiations), a large number of steps are generated to get a cumulative step voltage of the order of 1 mV or more. To achieve this the junction is suitably biased on the nth step. The cumulative step voltage is used to calibrate the standard cell at 1 volt level using an accurate resistive divider of suitable ratio as shown in figure 2 and described below:

A stable current is passed through two fixed resistors R_2 and R_1 which are connected in series. The ratio R_2/R_1 is accurately known. The current I through the resistive divider is adjusted until the emf of the standard cell, V_{sc}, is balanced across R_2. The frequency of the microwaves ν_m along with the step number n is then adjusted to get a null in the galvanometer G_1 also. When both the galvanometers are in the null position, the ratio of the standard cell emf to the cumulative Josephson step voltage, V_J, is equal to the ratio R_2/R_1

$$\frac{V_{sc}}{V_J} = \frac{R_2}{R_1}.$$

But $V_J = n(\hbar/2e)\nu_m$. Therefore $V_{sc} = n(h/2e)(R_2/R_1)\nu_m$. The internationally agreed value of $2e/h$ as recommended by CCE is 483594·0 GHz/V (CCE 1975). Thus by knowing the value of the divider ratio, microwave frequency and the step number and using the internationally agreed value of $2e/h$, the value of standard cell emf can be determined. Thus by adopting a fixed value for $2e/h$, voltage can be maintained and reproduced to a few parts in 10^9 using the Josephson effect (Kose 1976; Gupta 1980; Endo *et al* 1983). Unfortunately the absolute value of $2e/h$ is not known to a desired level of accuracy. The above mentioned value has an uncertainty of 2·6 ppm (Cohen and Taylor 1973). Any further reduction in the uncertainty in the value of $2e/h$ would raise the accuracy of the absolute volt to a level at which the volt can be reproduced by the a.c. Josephson effect.

3. Various types of Josephson junctions and their suitability for voltage standard

Figure 3 shows four broad types of Josephson junctions. These are (i) a thin film tunnel junction consisting of two superconducting films separated by a thin oxide layer, or a

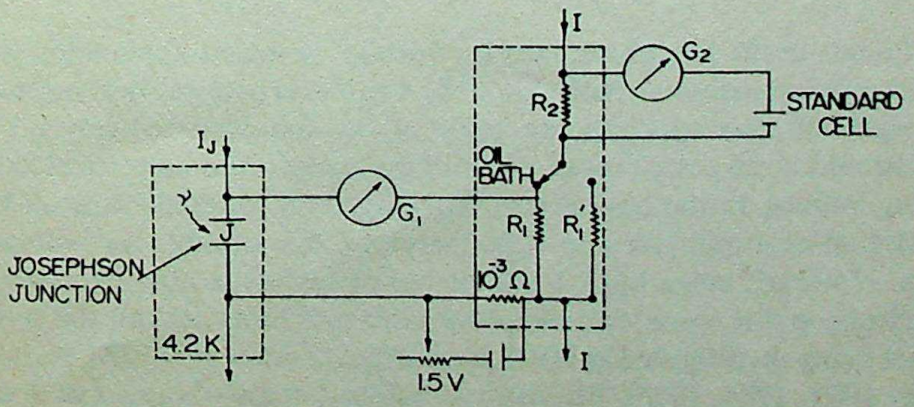

Figure 2. Block diagram of the Josephson voltage standard set-up.

CC-0. In Public Domain. Gurukul Kangri Collection, Haridwar

Digitized by Arya Samaj Foundation Chennai and eGangotri

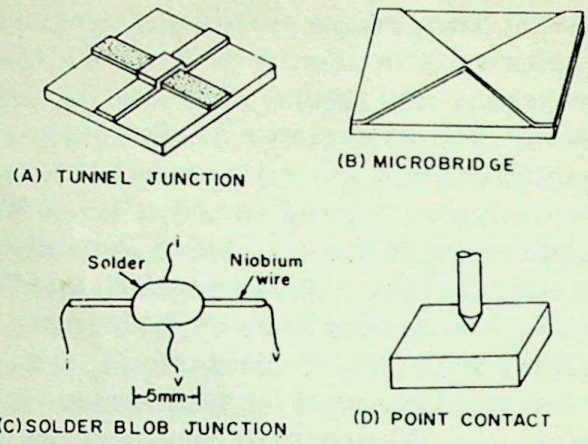

Figure 3. Various types of Josephson junctions.

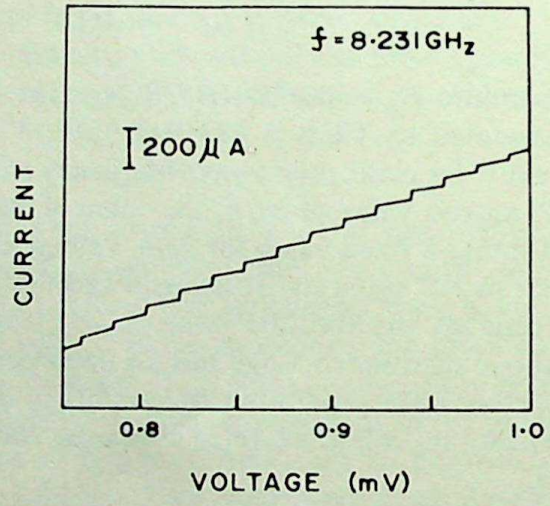

Figure 4. Microwave-induced steps at 1 mV level in I-V characteristic of a solder blob junction.

thicker layer of a normal metal, semiconductor or a photoconductor, (ii) a superconducting film with a constriction ($\sim 1\ \mu$m) called a microbridge, (iii) solder blob junction consisting of a blob of Pb-Sn solder frozen around an oxidized niobium wire and (iv) a point contact between a needle and a base, both made of superconducting material.

The usefulness of the Josephson step for voltage standard application is characterized by (i) its voltage position which should be 1 mV and preferably as large as possible, approaching 1 volt, the approximate value of the standard cell emf, (ii) its current amplitude should be 50 μA or more, and (iii) the step should be vertical having dI/dV approaching infinity. In the case of a microbridge it is generally difficult to get steps above a fraction of a millivolt and it is, therefore, not suitable for voltage standard application. However, steps upto 1 mV or above could be obtained using thin film tunnel junctions, point contacts and solder blob junctions and all the three types of junctions are being investigated at NPL, New Delhi (Tomar *et al* 1978; Natarajan 1980; Gupta *et al* 1983, 1984, 1986). Microwave-induced steps obtained in a solder blob junction during our early experiments are shown in figure 4 (Gupta *et al* 1984). Using a

CC-0. In Public Domain. Gurukul Kangri Collection, Haridwar

Digitized by Arya Samaj Foundation Chennai and eGangotri

single point contact (Harvey *et al* 1972) or a solder blob junction (Petley and Morris 1970) it is difficult to obtain a large amplitude ($\sim 50\ \mu A$) step above 1 mV and it is also difficult to connect several such junctions in series to achieve a larger cumulative step voltage. However, by using a tunnel junction usable steps upto 3 mV or more can be obtained (Finnegan *et al* 1971; Witt and Reymann 1983; Andreone *et al* 1983). Moreover, it is possible to fabricate an array of thin film tunnel junctions on the same substrate to get a larger cumulative step voltage (Finnegan *et al* 1971; Endo *et al* 1983) reaching upto 1 V (Niemeyer *et al* 1984a, b, 1985; Hamilton *et al* 1985).

The present Josephson voltage standard at NPL uses a simple Nb-Nb point contact and is operated at 1 mV level. The point contact junction has been selected because it is easy to make and does not require sophisticated experimental facilities for its fabrication. Moreover, the characteristics of the junction can be suitably altered in situ by changing the contact pressure using manual controls outside the liquid helium cryostat. However, work is in progress to develop an array of thin film tunnel junctions to get a larger cumulative step voltage (Gupta *et al* 1986).

4. Experimental details

4.1 *Josephson junction and liquid helium cryostat*

Figure 5 shows the schematic diagram of the cryostat and the point contact junction. The junction is placed inside a brass cavity and is irradiated with highly stabilized phase-locked microwave signal at about 10 GHz using a copper clad coaxial cable. The point contact is made of 3 mm dia Nb base and a 0·5 mm dia wire whose one end is used to make a fine point. The electric leads to the Nb are spot-welded. A total of six copper wires are connected to the point contact, four leads for the usual four terminal I-V measurement and the other two for accurate measurement of the step voltage. As the potential leads come out from liquid helium temperature (4·2 K) to room temperature

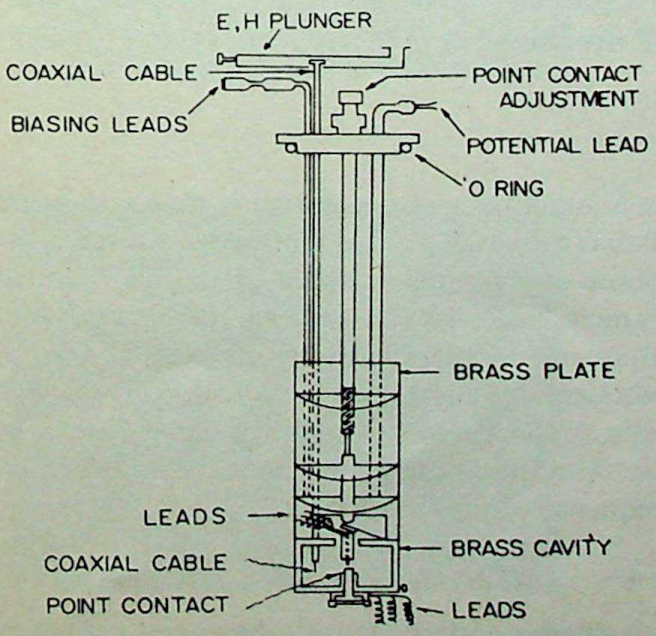

Figure 5. Schematic diagram of the liquid helium cryostat.

CC-0. In Public Domain. Gurukul Kangri Collection, Haridwar

Digitized by Arya Samaj Foundation Chennai and eGangotri

(295 K), they experience a large temperature gradient which gives rise to thermal-emf. Extreme care is taken to minimize the thermal emf and its variation in the potential leads. The thermal emf is minimized by twisting the potential leads which are made of single pieces of low thermal emf enamelled copper wire from the same spool. The variation in the thermal-emf is minimized by maintaining a fixed temperature distribution along their length. In order to achieve this the potential leads are taken out of the cryostat through a copper tube whose lower end is sealed and is always dipped in the liquid helium bath. Moreover, those parts of the potential leads which are at room temperature are covered with thermal insulating material and are directly connected to a copper block which is connected to the divider circuit. The copper block is kept inside a thermally insulated box.

The constant voltage steps in the I-V characteristic of the point contact are usually observed upto 1·5 mV by suitably adjusting (i) the microwave power using a variable attenuator and (ii) the contact pressure using a differential screw arrangement. A current amplitude of about 70 μA is achieved for steps at 1 mV level.

4.2 *Shielding and noise filtering*

Josephson junctions are very sensitive to a broad band of electromagnetic radiations. External noise produces a finite slope in the step (Kose and Sullivan 1970) which may introduce uncertainty in voltage determination. To achieve steps with near infinite slope the following precautions have been taken.

(i) Measurements are carried out inside a shielded room. The liquid helium cryostat and the d.c. voltage divider are kept inside the shielded room, while the microwave system is kept outside.

(ii) All the electrical measuring instruments inside the shielded room are operated with batteries.

(iii) The brass cavity containing the point contact is further shielded by using a superconducting lead shield.

(iv) A noise reduction filter is provided in the electrical power line before it enters the shielded room. This filter is effective for noise in the frequency range from 10^{-2} MHz to 10^{3} MHz.

4.3 *Microwave equipment*

The schematic diagram of the X-band microwave system is shown in figure 6. Water-cooled X-band klystron (150 mW) is used as the microwave source. For frequency stabilization, the tenth harmonic of a reference signal of suitable frequency from a synthesized signal generator is mixed with the klystron signal. The resultant IF signal is compared with the reference frequency of a temperature-controlled quartz oscillator to produce a phase correction voltage. This correction voltage is fed back to the reflector voltage of the klystron. In this way short term frequency stability (over a period of 15 minutes) of ± 2 Hz is achieved. The time base of the frequency counter is calibrated against the cesium atomic frequency standard at NPL.

4.4 *Voltage comparison system*

In the present case, a resistive divider of 1 : 1000 ratio has been used. Ten standard

CC-0. In Public Domain. Gurukul Kangri Collection, Haridwar

Digitized by Arya Samaj Foundation Chennai and eGangotri

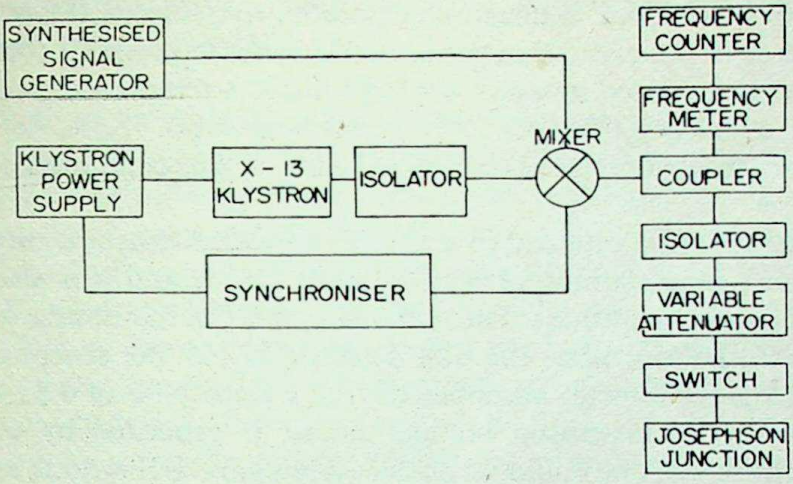

Figure 6. Block diagram of stabilized microwave source.

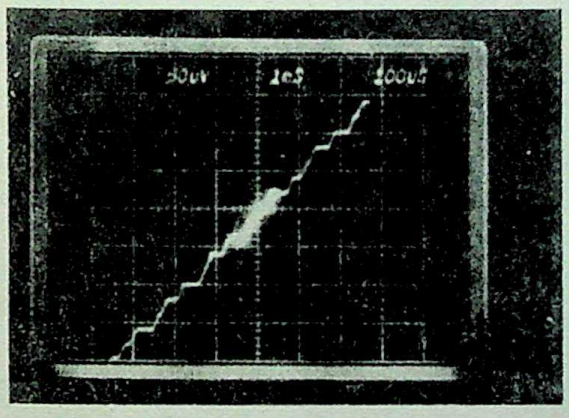

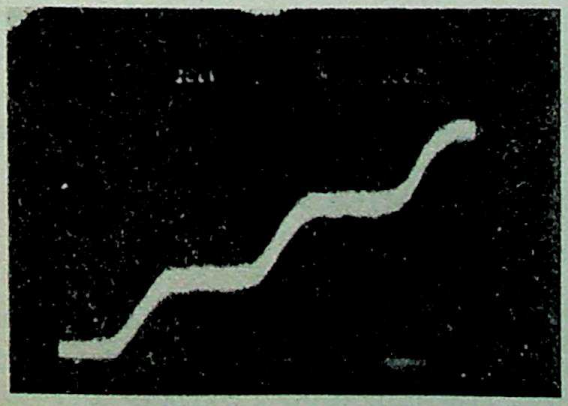

Figure 7. Oscilloscopic display of microwave induced steps at 1·02 mV level. X-axis represents current and Y-axis represents voltage.

CC-0. In Public Domain. Gurukul Kangri Collection, Haridwar

Digitized by Arya Samaj Foundation Chennai and eGangotri

resistances of one ohm each are connected in parallel to generate 0·1 ohm and ten standard resistances of 10 ohms each are connected in series to generate 100 ohms. The two sets of resistances connected in series, are kept inside a temperature-regulated oil bath (temperature stability $\pm 0{\cdot}001°C$). The resistance ratio R_2/R_1 is accurately measured just before and after the experiment using a d.c. comparator resistance bridge.

The current in the divider is supplied by a battery-powered constant current source which exhibits a short term stability of better than 0·1 ppm, and it is also manually adjusted between different operations. The null detector G_2 in the standard cell circuit has a sensitivity of 0·1 μV/div while the null detector, G_1, in the Josephson voltage circuit is a photocell galvanometer amplifier having a sensitivity of 0·2 nV/div.

The thermal-emf in the Josephson voltage circuit is cancelled by a small emf generated across a resistor of one milliohm as shown in figure 2. It is done by switching the divider current, I, from R_1 to R_1' ($\sim R_1$) so that the load on the current source remains unchanged. The microwave signal to the junction is switched off and the junction is biased at the zero voltage step. The emf across the one milliohm resistor is adjusted to bring the reading of the galvanometer G_1 to zero, thus cancelling most of the thermal emf. However, there is a small drift in the thermal emf in the Josephson circuit. This drift is linear in time during the short duration (~ 3 to 4 minutes) of measurement and is compensated by correcting the junction unbalance by linear interpolation. The value of this correction is of the order of 2 nanovolts.

4.5 *Biasing circuit for oscilloscopic display of junction's I-V characteristic*

An electronic circuit has been developed to display I-V characteristic of the junction on the screen of an ordinary oscilloscope. Display of junction's characteristic helps in quickly optimizing the contact pressure and the microwave power to obtain large amplitude steps at 1 mV level. The circuit also has the capability of displaying any small portion of the characteristic on the screen which helps in locating the desired step and in seeing its quality.

The circuit essentially consists of three parts (i) an oscillator which generates the saw tooth signal, (ii) an arrangement by which the signal can be fed to the X and Y axes of the oscilloscope via the Josephson junction and (iii) a d.c. amplifier which can amplify the voltage which is fed to the Y axis of the oscilloscope to either 1000 times or 5000 times with the help of a selector switch, thus making the sensitivity of the oscilloscope either 50 μV/cm or 10 μV/cm. Provision is also made in the circuit to apply only d.c. to the oscilloscope and reach upto the desired d.c. voltage level and then sweep at that voltage. Thus the details of a small portion of the characteristic at 1 mV level can be seen as shown in figure 7.

4.6 *As-maintained volt at NPL*

The as-maintained volt at NPL is based on a bank of standard cadmium cells maintained in a constant temperature air enclosure (temperature stability $\pm 0{\cdot}005°C$). Through a recent intercomparison with Australia using a transportable standard cells and Zener-based electronic voltage standard as travelling standards, it has been found that the as-maintained volt of Australia and India agrees to 0·5 μV.

CC-0. In Public Domain. Gurukul Kangri Collection, Haridwar

Digitized by Arya Samaj Foundation Chennai and eGangotri

5. Results of a recent intercomparison of the as-maintained volt with the Josephson voltage standard

At the NPL, the d.c. electrical standards laboratory where a bank of standard cells are maintained as a physical standard to represent the volt is about 100 m away from the low temperature laboratory where the Josephson voltage standard is set up. Hence a direct intercomparison is not feasible. Instead, a transfer standard consisting of a bank of four standard cells in a constant temperature air enclosure of temperature stability of $\pm 0{\cdot}005°C$ is used to intercompare the two. The cells of the transfer standard are assigned values by intercomparison against the as-maintained volt as well as against the Josephson voltage standard. The intercomparison is carried out using the standard potentiometric technique having a resolution of 0·1 μV, while against the Josephson voltage it is done using the voltage divider described above. A cumulative Josephson step voltage of the order of 1 mV is generated by biasing the junction on the 50th step. The results are given in table 1. Estimated uncertainties are given in table 2.

Table 1. Intercomparison of the as-maintained volt with the Josephson voltage standard.

Value assigned to the standard cells against as-maintained volt (volt)	Value assigned to the standard cells against Josephson volt (volt)	Difference between two values (μV)
1·0181908	1·0181904	0·4
1·0181908	1·0181905	0·3
1·0181905	1·0181903	0·2
1·0181712	1·0181702	1·0
	Mean difference	0·5

Table 2. Estimated uncertainties in the assignment of value to the transfer standard cells.

(a) Assignment of the value against the Josephson voltage		
(i)	Uncertainty in the balance of step voltage against the resistor R_1 which takes into account many contributions including thermal emf	0·8 ppm
(ii)	Uncertainty in the divider ratio	0·4 ppm
(iii)	Uncertainty in the microwave frequency	0·001 ppm
(iv)	Uncertainty in the galvanometer (G_1) reading	0·1 ppm
	Total R S S uncertainty	0·90 ppm
(b) Assignment of value against the as-maintained volt		
(i)	Uncertainty due to temperature variations of the cells (56 μV/K)	0·28 ppm
(ii)	Random uncertainty in calibration	0·15 ppm
	Total R S S uncertainty	0·32 ppm

CC-0. In Public Domain. Gurukul Kangri Collection, Haridwar

Digitized by Arya Samaj Foundation Chennai and eGangotri

6. Conclusions and discussion

The d.c. voltage standard based on the a.c. Josephson effect using a Nb-Nb point contact junction at 1 mV level is in operation at NPL and is periodically used to check the emf of the standard cells of the as-maintained volt. The Josephson voltage at the 50th step is used to assign value to the cells of a transfer standard consisting of four Weston standard cells in a temperature regulated air enclosure (temperature stability $\pm 0{\cdot}005°C$). The same cell is also assigned a value by intercomparison against the as-maintained volt. The two values are found to agree within an overall uncertainty of about 1 ppm.

The main source of uncertainty in the present Josephson set-up is in the null detection at 1 mV level. Even a small drift of 1 nV in thermal emf in the potential leads of the Josephson circuit introduces an uncertainty of 1 ppm. The drift in the thermal emf in the potential leads is due to (i) change in the room temperature, and (ii) change in temperature distribution along the potential leads inside the liquid helium dewar. It is, therefore, desirable to generate a larger cumulative Josephson step voltage to lower the uncertainty in null detection. If the step voltage is raised to 10 mV level, a drift of 1 nV would lower the uncertainty in null detection by an order of magnitude, from 1 ppm to 0·1 ppm. Furthermore, in this situation one would need a resistive divider ratio of 100:1 rather than 1000:1. One may, therefore, use commercially available series-parallel type of Hamon resistors to make a divider of 100:1 ratio. The ratio of commercially available Hamon resistors is known with an uncertainty of 0·01 ppm, in contrast to 0·4 ppm of uncertainty prevailing in the existing resistive divider. Thus by increasing the cumulative Josephson step voltage to 10 mV, the two major sources of uncertainties, viz, null detection and calibration of the divider ratio, would be considerably reduced. Work is in progress to develop an array of tunnel junctions to achieve it (Gupta *et al* 1986).

Shifting of the transfer standard from the Josephson voltage standard laboratory to the d.c. electrical standard laboratory, which is required in the present method of intercomparison is also a source of uncertainty. Although sufficient time (about 1 week) was given to the transfer standard cells to recover after each shifting it is estimated that an uncertainty of the order of 1 ppm is introduced. It is, therefore, desirable to keep the as-maintained volt near the Josephson voltage standard so that the shifting of transfer standard is not required. One may even have a direct intercomparison between the cells of the as-maintained volt and the Josephson voltage.

An alternative approach followed by some laboratories (Harvey 1976; Kose 1976; Hartland 1977) to enhance the accuracy is to use a cryogenic resistive divider along with a SQUID as a null detector and to use superconducting current comparator (Harvey 1972) to determine the resistance ratio. Thus the entire low voltage circuit containing the Josephson junction, the resistive divider and the SQUID null detector can be in a common liquid helium bath and the uncertainties due to thermal emf's are completely eliminated.

It has recently been shown that it is possible to obtain steps in the 1 volt region from large series arrays of Josephson tunnel junctions (Niemeyer *et al* 1984a, b, 1985; Hamilton *et al* 1985). The arrays are part of an integrated microwave circuit and are driven in the zero crossing step mode (Levinsen *et al* 1977). Thus a direct intercomparison, without using a voltage divider, is feasible and the uncertainty in the intercomparison of the order of a few parts in 10^{10} can be achieved.

CC-0. In Public Domain. Gurukul Kangri Collection, Haridwar

Digitized by Arya Samaj Foundation Chennai and eGangotri

Acknowledgements

The authors acknowledge the valuable help provided by PTB Braunschweig, West Germany in establishing the Josephson Voltage Standard. The major part of the equipment was obtained from PTB under Indo-German Technical Aid Programme.

References

Andreone D, Arri E, Lacquaniti V and Marullo G 1983 *IEEE Trans. Instrum. Meas.* **IM-32** 272
Cohen E R and Taylor B N 1973 *J. Phys. Chem. Ref. Data* **2** 663
CCE (Comité Consultatif d'Electricité) 1975 **14** E6-E7 English Translation Metrologia Vol. 11 p. 1982
Endo T, Koyanagi M and Nakamura A 1983 *IEEE Trans. Instrum. Meas.* **IM-32** 267
Field B F, Finnegan T F and Toots J 1973 *Metrologia* **9** 155
Finnegan T F, Denenstein A and Langenberg D N 1971 *Phys. Rev.* **B4** 1487
Gupta A K 1980 *Indian J. Cryogenics* **5** 59
Gupta A K, Tomar V S, Kataria N D and Chauhan M P S 1983 *Indian J. Cryogenics* **8** 81
Gupta A K, Tomar V S and Chauhan M P S 1983 *J. Low Temp. Phys. (USA)* **50** 257
Gupta A K, Tomar V S and Kataria N D 1984 *VIII National Symp. on Cryogenics*, Aurangabad
Gupta A K, Tomar V S and Kataria N D 1986 *Indian J. Phys.* **A60** 224
Hamilton C A, Kautz R L, Steiner R L and Lloyd F L 1985 *Elec. Dev. Lett.* **EDL-6** 623
Hartland A 1977 Euromeas 77, IEE Publication **152 10**
Harvey I K 1972 *Rev. Sci. Instrum.* **43** 1626
Harvey I K, Macfarlane J C and Frenkel R B 1972 *Metrologia* **8** 46, 114
Harvey I K 1976 *Metrologia* **12** 47
Josephson B D 1962 *Phys. Lett.* **1** 251
Josephson B D 1964 *Rev. Mod. Phys.* **36** 216
Josephson B D 1965 *Adv. Phys.* **14** 419
Kose V and Sullivan D B 1970 *J. Appl. Phys.* **41** 169
Kose V 1976 *IEEE Trans. Instrum. Meas.* **IM-25** 483
Levinsen M T, Chio R Y, Feldman M J and Tucker B A 1977 *Appl. Phys. Lett.* **31** 776
Melchert F 1978 *Metrologia* **14** 167
Natarajan N S 1980 *Nucl. Phys. Solid State Phys. India* **C23** 48
Niemeyer J, Hinken J H and Meier W 1984a *IEEE Trans. Instrum. Meas.* **IM-33** 311
Niemeyer J, Hinken J H and Kautz R L 1984b *Appl. Phys. Lett.* **45** 478
Niemeyer J, Grimm L and Meier W 1985 *Appl. Phys. Lett.* **47** 1222
Petley B W and Morris K 1970 *Metrologia* **6** 46
Tomar V S, Kataria N D, Prasad M and Gupta A K 1978 *Nucl. Phys. Solid State Phys.* **C21** 6
Tsai J, Jain A K and Lukens J B 1983 *Phys. Rev. Lett.* **51** 316
Witt T J and Reymann D 1983 *IEEE Trans. Instrum. Meas.* **IM-32** 260
Wood G H and Dunn A F 1981 *Can. J. Phys.* **59** 363

CC-0. In Public Domain. Gurukul Kangri Collection, Haridwar

Digitized by Arya Samaj Foundation Chennai and eGangotri

CC-0. In Public Domain. Gurukul Kangri Collection, Haridwar

Digitized by Arya Samaj Foundation Chennai and eGangotri

Pramāna – J. Phys., Vol. 28; No. 5, May 1987, pp. 529–545. © Printed in India.

Transformation kinetics of A-15 superconductors formed by solid state reactions

A V NARLIKAR
National Physical Laboratory, Hillside Road, New Delhi 110012, India

Abstract. Various fabrication processes devised for making multifilamentary A-15 superconductors are all based on solid state reactions, transforming the host metal into the binary A-15 phase. The kinetics of the growth process involved in the compound formation form the theme of this paper.

Keywords. A-15 superconductors; Nb_3Sn; diffusion; grain boundaries; ordering.

PACS No. 74·50

1. Introduction

Phase transformation of bcc Nb into Nb_3Sn of A-15 crystal structure caused by solid state diffusion of Sn into Nb has led to several processing routes for fabricating Nb_3Sn in multifilamentary form. They include the conventional bronze process, in-situ and powder metallurgy techniques, the modified jelly roll process, etc. Actually, these processes are really no more than different ways of realizing composite conductors containing a large number of fine Nb filaments in a bronze matrix. Diffusion reactions at 550 to 800°C result in Nb_3Sn layers at the bronze-Nb interfaces (figure 1). V_3Ga and V_3Si are two other important binary A-15s of A_3B type produced in this way.

In any phase transformation one is confronted with two pertinent questions: (a) why does a particular phase change occur?, and (b) how does it occur? The answer to (a) requires thermodynamic considerations while that to (b) involves the kinetics. The thermodynamics of A-15 formation, described elsewhere (Dew-Hughes and Luhman 1978; Narlikar and Dew-Hughes 1985a, b) is considered outside the scope of the present paper.

Turning to kinetics, there are four types of kinetics associated with A-15 layer formation: (i) nucleation, (ii) grain growth, (iii) layer growth and (iv) ordering. Nucleation kinetics are of prime importance for compound formation. The critical current density J_c of the A-15 layer is controlled by grain growth kinetics. The overall critical current I_c is determined by layer growth kinetics. Finally, the critical temperature T_c depends sensitively on the long range order (LRO) of the compound layers, which in turn is determined by ordering kinetics. Interestingly, all the four processes come into operation almost simultaneously with the start of diffusion annealing.

In this paper we briefly describe the four kinds of kinetics. Although the kinetics story is basically independent of various fabrication routes referred above a greater emphasis is laid on the results obtained with bronze process. This is because its

CC-0. In Public Domain. Gurukul Kangri Collection, Haridwar

Digitized by Arya Samaj Foundation Chennai and eGangotri

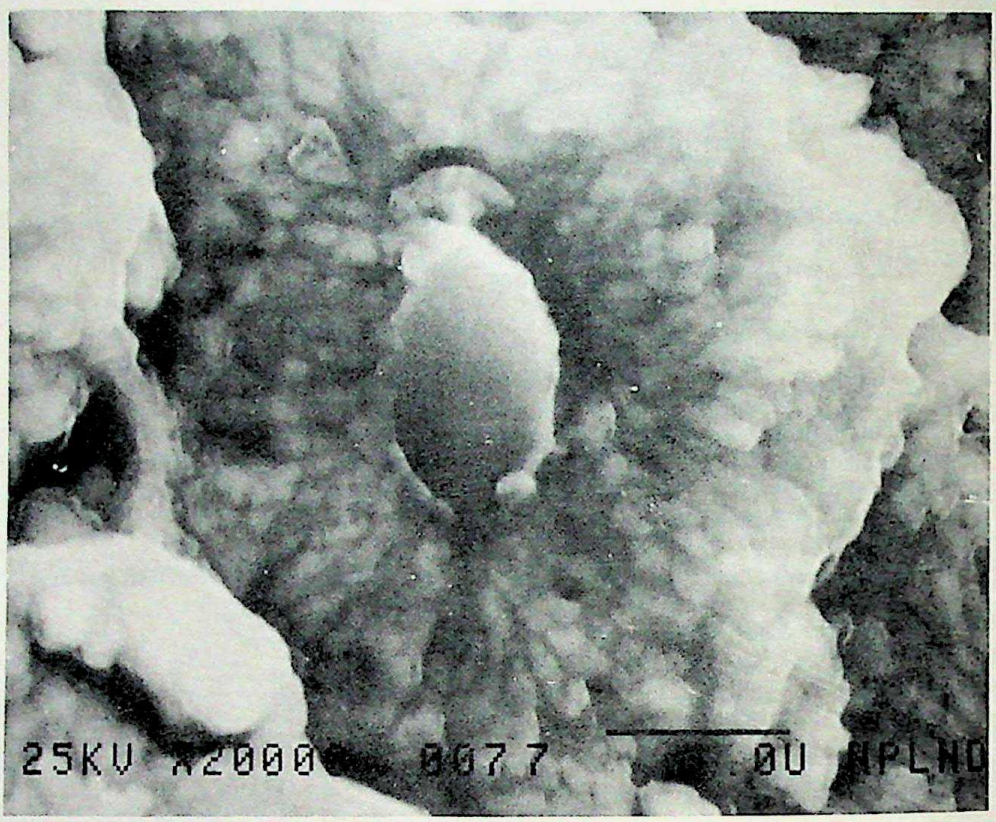

Figure 1. Scanning electron micrograph of Nb_3Sn layers formed at the bronze-Nb interfaces.

commercial viability is proven and there is an abundance of data on the bronze-processed samples.

2. Nucleation kinetics

The problem of nucleation of A-15 phase in a diffusion couple has received little attention so far. It is clear that the nuclei for the initial layer form at the bronze-Nb interface and for the subsequent layers at the Nb_3Sn-Nb interface. The driving force for nucleation must arise from two factors: (a) the free energy difference between the transformed (i.e. Nb_3Sn) and transforming phases (i.e. Nb), and (b) release of stored energy of heavily deformed Nb filaments by formation of strain free A-15 grains—a situation analogous to recrystallization. The negative contribution of volume energy ΔG_v favouring the formation of Nb_3Sn is countered by two positive contributions: (i) the surface energy ΔG_s associated with the creation of an interface between Nb and Nb_3Sn, and (ii) the volume contribution of strain energy ΔG_m caused by 37% of volume expansion when Nb is transformed to Nb_3Sn. The free energy change associated with the formation of Nb_3Sn particle of radius r is given by,

$$\Delta G = -A_1 r^3 + A_2 r^2, \tag{1}$$

where A_1 and A_2 are constants and ΔG_m is considered simply to modify ΔG_v. For a particle of small radius the positive surface energy term dominates whereas when the radius exceeds a certain critical value r_0 the overall free energy becomes negative and

CC-0. In Public Domain. Gurukul Kangri Collection, Haridwar

Digitized by Arya Samaj Foundation Chennai and eGangotri

Pramāna – J. Phys., Vol. 28, No. 5, May 1987, pp. 529–545. © Printed in India.

Transformation kinetics of A-15 superconductors formed by solid state reactions

A V NARLIKAR
National Physical Laboratory, Hillside Road, New Delhi 110012, India

Abstract. Various fabrication processes devised for making multifilamentary A-15 superconductors are all based on solid state reactions, transforming the host metal into the binary A-15 phase. The kinetics of the growth process involved in the compound formation form the theme of this paper.

Keywords. A-15 superconductors; Nb_3Sn; diffusion; grain boundaries; ordering.

PACS No. 74·50

1. Introduction

Phase transformation of bcc Nb into Nb_3Sn of A-15 crystal structure caused by solid state diffusion of Sn into Nb has led to several processing routes for fabricating Nb_3Sn in multifilamentary form. They include the conventional bronze process, in-situ and powder metallurgy techniques, the modified jelly roll process, etc. Actually, these processes are really no more than different ways of realizing composite conductors containing a large number of fine Nb filaments in a bronze matrix. Diffusion reactions at 550 to 800°C result in Nb_3Sn layers at the bronze-Nb interfaces (figure 1). V_3Ga and V_3Si are two other important binary A-15s of A_3B type produced in this way.

In any phase transformation one is confronted with two pertinent questions: (a) why does a particular phase change occur?, and (b) how does it occur? The answer to (a) requires thermodynamic considerations while that to (b) involves the kinetics. The thermodynamics of A-15 formation, described elsewhere (Dew-Hughes and Luhman 1978; Narlikar and Dew-Hughes 1985a, b) is considered outside the scope of the present paper.

Turning to kinetics, there are four types of kinetics associated with A-15 layer formation: (i) nucleation, (ii) grain growth, (iii) layer growth and (iv) ordering. Nucleation kinetics are of prime importance for compound formation. The critical current density J_c of the A-15 layer is controlled by grain growth kinetics. The overall critical current I_c is determined by layer growth kinetics. Finally, the critical temperature T_c depends sensitively on the long range order (LRO) of the compound layers, which in turn is determined by ordering kinetics. Interestingly, all the four processes come into operation almost simultaneously with the start of diffusion annealing.

In this paper we briefly describe the four kinds of kinetics. Although the kinetics story is basically independent of various fabrication routes referred above a greater emphasis is laid on the results obtained with bronze process. This is because its

CC-0. In Public Domain. Gurukul Kangri Collection, Haridwar

Digitized by Arya Samaj Foundation Chennai and eGangotri

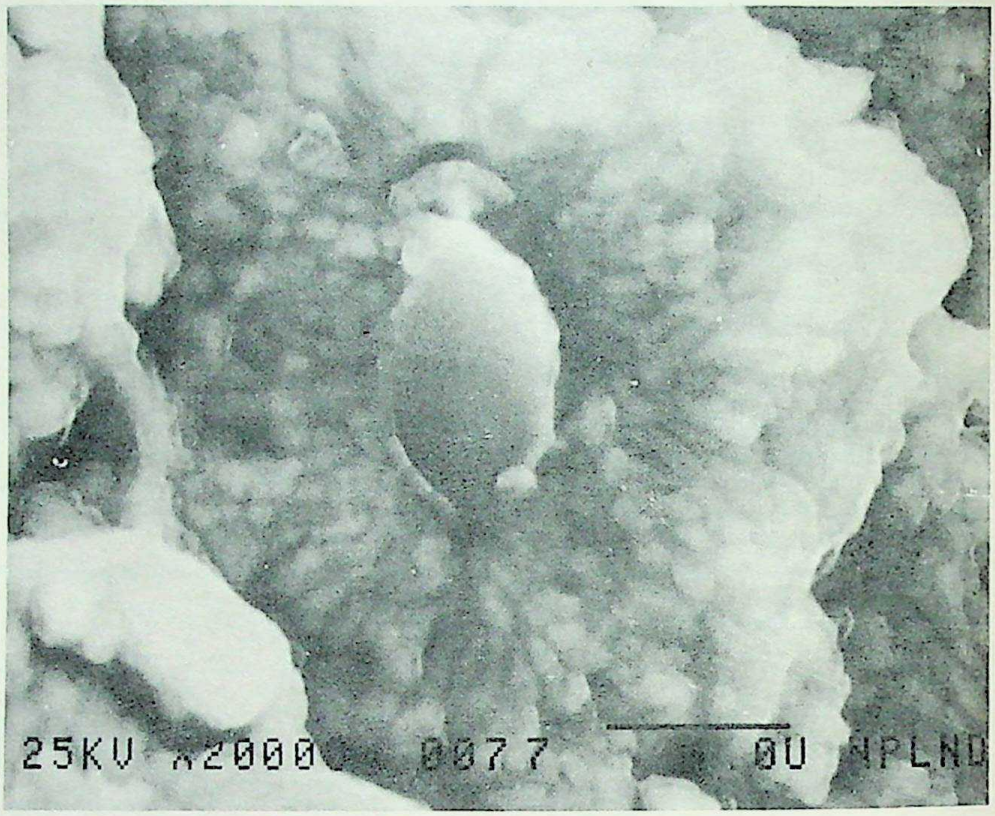

Figure 1. Scanning electron micrograph of Nb_3Sn layers formed at the bronze-Nb interfaces.

commercial viability is proven and there is an abundance of data on the bronze-processed samples.

2. Nucleation kinetics

The problem of nucleation of A-15 phase in a diffusion couple has received little attention so far. It is clear that the nuclei for the initial layer form at the bronze-Nb interface and for the subsequent layers at the Nb_3Sn-Nb interface. The driving force for nucleation must arise from two factors: (a) the free energy difference between the transformed (i.e. Nb_3Sn) and transforming phases (i.e. Nb), and (b) release of stored energy of heavily deformed Nb filaments by formation of strain free A-15 grains—a situation analogous to recrystallization. The negative contribution of volume energy ΔG_v favouring the formation of Nb_3Sn is countered by two positive contributions: (i) the surface energy ΔG_s associated with the creation of an interface between Nb and Nb_3Sn, and (ii) the volume contribution of strain energy ΔG_m caused by 37% of volume expansion when Nb is transformed to Nb_3Sn. The free energy change associated with the formation of Nb_3Sn particle of radius r is given by,

$$\Delta G = -A_1 r^3 + A_2 r^2, \tag{1}$$

where A_1 and A_2 are constants and ΔG_m is considered simply to modify ΔG_v. For a particle of small radius the positive surface energy term dominates whereas when the radius exceeds a certain critical value r_0 the overall free energy becomes negative and

CC-0. In Public Domain. Gurukul Kangri Collection, Haridwar

Digitized by Arya Samaj Foundation Chennai and eGangotri

the transformation to the new phase is favoured (figure 2). E_0 in the figure represents the nucleation barrier.

As Nb_3Sn has a crystal structure and the lattice parameter both considerably differing from Nb its nucleation will be heterogeneous. Nuclei formed at a lower reaction temperature are expected to be more Sn-deficient than those formed at a higher temperature and in regard to the lattice parameter they would be relatively closer to Nb. Thus, a lower reaction temperature would favour smaller nuclei more closely spaced, while the situation will be just opposite at higher temperatures. Thus, the initial grain size of A-15 layers formed at a lower reaction temperature would be smaller than that formed at a higher temperature. This is corroborated experimentally (Okuda *et al* 1983) and it holds relevance to the layer growth kinetics.

Junction points of grain boundaries and dislocation cell walls in Nb filaments are expected to provide the favoured sites for A-15 nucleation. Finer Nb filaments formed by heavy reductions would have large number of closely spaced nucleation sites, leading to smaller A-15 grains as reported by Okuda *et al* (1983).

Growth of Nb_3Sn nuclei would occur by migration of Nb_3Sn-Nb boundaries towards Nb. If there are N nucleation sites per unit volume along the reaction interface, for spherical nuclei growing with a velocity u, the volume fraction transformed $V(t)$ after a time t is given by Cahn and Hagel (1962),

$$V(t) = 1 - \exp(-\tfrac{4}{3}\pi N(ut)^3), \tag{2}$$

where $u = C\exp(-U_m/kT)$. The growth of the nuclei is due to thermally activated transfer of atoms from one crystal to another across a moving interface. The parameter C in the above equation includes the chemical potential difference between the final (i.e. Nb_3Sn) and the initial (i.e. Nb) phases which provide the driving force for boundary migration. This process would continue until the neighbouring grains of Nb_3Sn have a

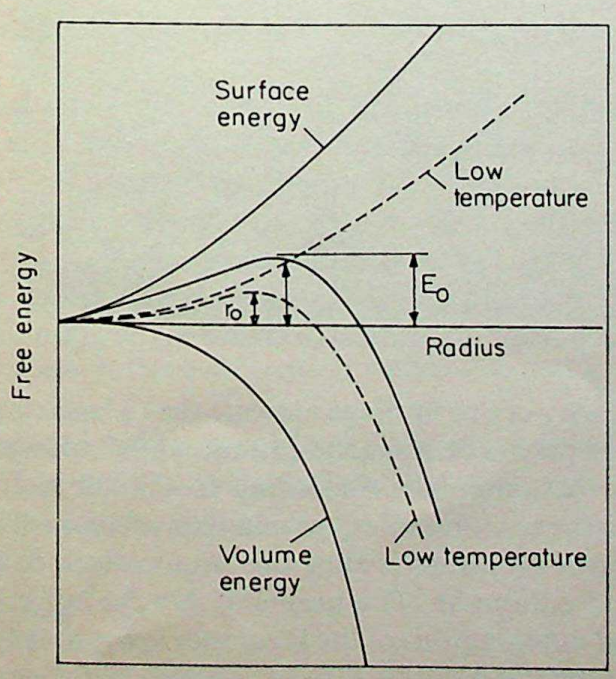

Figure 2. Energies involved in A-15 phase nucleation.

CC-0. In Public Domain. Gurukul Kangri Collection, Haridwar

Digitized by Arya Samaj Foundation Chennai and eGangotri

common grain boundary. Thereafter, grain growth in the conventional sense occurring in fully recrystallized metal will follow.

3. Grain growth kinetics

When the grain structure is free from variations in stored energy and possesses the same phase throughout, the driving force for grain growth stems from decrease in the free energy resulting from reduction in the grain boundary area. Since the grain diameters of A-15 layers tend to be rather small, reliable data of their growth kinetics are still lacking. Theory of grain growth in metallic systems applies to the ideal situation of the behaviour of cells in a soap froth which grow or shrink at the expense of each other so as to reduce the total boundary area. This gives a parabolic cell growth of the form,

$$d_t^2 - d_0^2 = K't, \tag{3}$$

where d_0 is the initial grain diameter and d_t after a time t. Boundaries advance to their centres of curvature by thermally activated process with activation energy U, and (3) becomes,

$$d_t^2 - d_0^2 = K_0 \exp[-U/kT]t. \tag{4}$$

This holds also for A-15 grains formed by solid state reactions. The available information on A-15s is summarized below.

(i) Effect of melting and reaction temperatures: Larger the melting temperature smaller is the grain growth at a fixed reaction temperature. Nb_3Sn, V_3Si and V_3Ga possess melting temperatures of 2100, 1900 and 1300°C respectively and of these V_3Ga exhibits the largest and Nb_3Sn the smallest grain growth and grain sizes (Livingston 1977).

(ii) Effect of cold-work: More heavily cold worked filaments give rise to smaller A-15 grains after diffusion reactions.

(iii) Addition of impurities: Adding impurities to diffusion couple can affect the grain size in two ways: (a) layer growth is enhanced and thus a lesser time is available for grains to grow, and (b) grain boundaries get pinned by impurities. Addition of impurities like Al, Zn, or Mg to the bronze matrix and Ti, Zr or Hf to filaments enhances the layer growth and the grain size is found to be smaller.

(iv) Grain size distribution: The grains closer to the bronze interface are formed prior to the inner grains and hence there is a radical decrease in the grain size towards the filament centre (figure 3).

(v) Grain morphology: A majority of our findings indicate that a faster layer growth occurring at higher temperatures produces equiaxed grains, while at lower temperatures the grains formed tend to be columnar. According to Okuda *et al* (1983) an enhanced delivery of Sn atoms to the reaction interface makes nucleation of new grains favourable. When transportation of Sn atoms is slow the atoms attach themselves to the existing grains making them columnar. The grains at Nb_3Sn-Nb interface are columnar while in the middle and outer regions of the layer they are generally equiaxed (figure 4). Cave and Weir (1983) attributed this to 37% of volume expansion associated with Nb_3Sn formation which pushes the reaction interface outwards. The strain

CC-0. In Public Domain. Gurukul Kangri Collection, Haridwar

Digitized by Arya Samaj Foundation Chennai and eGangotri

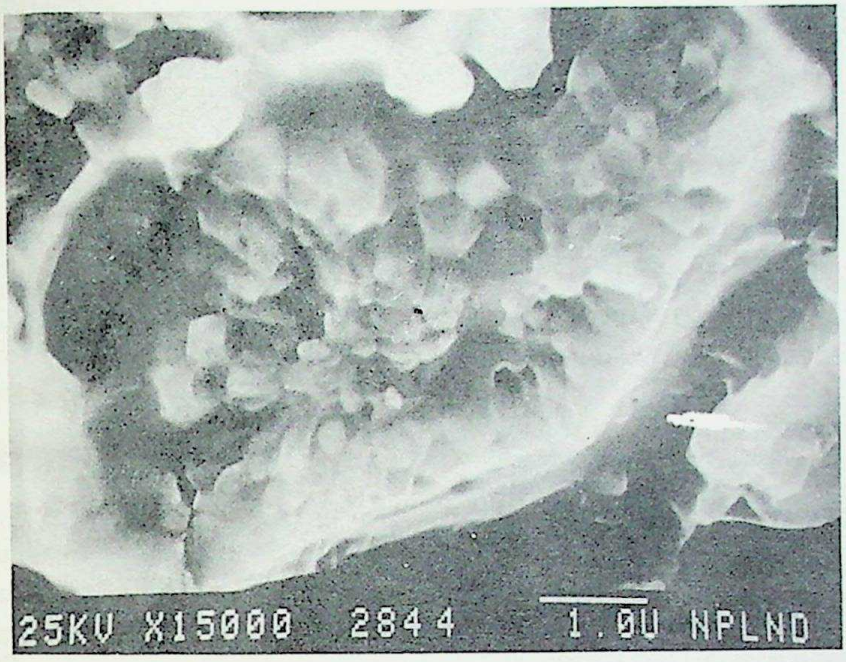

Figure 3. Grains in fully reacted Nb_3Sn layer.

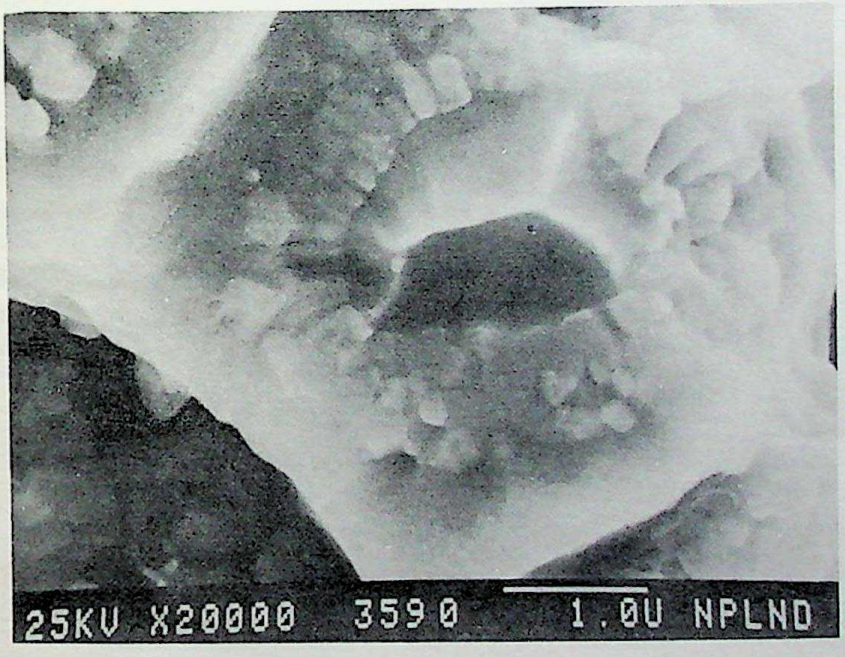

Figure 4. Columnar grains at Nb_3Sn-Nb interface.

relaxation does not take place through creation of cracks but by a different process that creates dislocations to separate off the tips of the columnar grains which subsequently relax by rotation and sliding.

4. Growth laws

Thickness of the A-15 layer of Nb_3Sn and V_3Ga formed in bronze-processed samples has been extensively studied at the National Physical Laboratory (NPL) and elsewhere

CC-0. In Public Domain. Gurukul Kangri Collection, Haridwar

Digitized by Arya Samaj Foundation Chennai and eGangotri

as a function of various process parameters such as diffusion temperature, reaction time and concentration of *B* element (i.e., Sn or Ga) in copper matrix etc., and as a rule the growth is found to be controlled by the general equation:

$$R = kt^n, \tag{5}$$

where R is the layer thickness formed at a fixed reaction temperature after a time t, n is the numerical time exponent, and k is the reaction rate constant. The parameter k, as will be seen later, is related to the diffusivity of *B* element relevant to the pertinent rate-controlling step responsible for the layer growth and also depends upon various process parameters.

Growth is parabolic, subparabolic or superparabolic respectively when n is equal to, less than or more than 0·5. Interestingly, diffusion couples composed of the same components are found to yield all the three growth laws under different situations. In fact, as may be seen from table 1, the observed time exponents vary in a wide range from 0·15 to 1·0. Further, k and n respond in an intriguing way to the process conditions; the enhanced growth rate stems sometimes from increase in k and sometimes from increase in n. For Nb_3Sn, in multifilamentary composites the growth is invariably subparabolic while in the monofilamentary situation it is either parabolic or superparabolic. V_3Ga, on the other hand, shows mostly parabolic growth.

Results reported in a recent literature survey (Narlikar and Dew-Hughes 1985b) of layer growth studies seem diverse and conflicting. Growth models, compatible with the general principles of solid state diffusion and physical metallurgy, must correctly predict reported growth rates and the whole range of n values observed under different process conditions. The relevance of such model calculations in sorting out the anomalies is obvious.

Reddi *et al* (1978) and Agarwal *et al* (1984) have developed growth kinetic models which provide a starting point to understand various features of the compound layer

Table 1. Effect of impurities on layer growth kinetics (Narlikar and Dew-Hughes 1985a).

Matrix	Core	Grain size/ grain growth	Layer growth	n
Cu-6%Sn-0·5%Mg	Nb	Reduced	Increased	0·5
Cu-7%Sn-0·9%Mg	Nb	-do-	-do-	0·5
Cu-5%Sn-4%Ga	Nb	-do-	-do-	0·5
Cu-7%Sn-1·5%Ti	Nb	-do-	-do-	0·58
Cu-6%Sn-4%Al	Nb-1%Al	-do-	-do-	0·58–0·71
Cu-(2%to10%Sn)	Nb	-do-		0·55–0·9
Cu-10%Sn	Nb-1%U	-do-		1·0
Cu-12%Sn	Nb	-do-	-do-	0·26–0·48
Cu-14%Sn	Nb	-do-	-do-	0·17
Cu-12%Sn	Nb	-do-	-do-	0·30
Cu-17·5%Ga	V-6·5%Ga	-do-	-do-	0·5
Cu-8%Ga	V-2%Ti	-do-	-do-	0·5
Cu-19%Ga-0·5%Mg	V-6%Ga	-do-	-do-	0·5
Cu-18%Ga	V	Increased	Decreased	0·35

CC-0. In Public Domain. Gurukul Kangri Collection, Haridwar

Digitized by Arya Samaj Foundation Chennai and eGangotri

formation. Some salient features of these models are consolidated in the following section.

5. Analytical models

Consider a three-component system: the pure Nb core, growing Nb_3Sn layer and Cu-Sn matrix. The growth of the compound layer occurs by diffusion of Sn from bronze through the existing layer of Nb_3Sn and the reaction takes place at the Nb_3Sn-Nb interface. The rate of layer growth will depend upon three rate-controlling steps, namely, the rate at which (i) Sn is supplied from bronze matrix to bronze-Nb_3Sn interface, (ii) Sn is transported across the Nb_3Sn layer to the Nb_3Sn-Nb interface, and (iii) Sn reacts with Nb to produce Nb_3Sn. If these processes proceed at different rates, the rate of layer growth will be controlled by whichever of them is the slowest. (iii) is the fastest, being almost instantaneous and, consequently, it is the slowness of (i) and (ii) that turns out to be the rate-controlling step. The models consider the two situations separately and predict various growth laws as summarized below.

5.1 *Growth controlled by diffusion through bronze matrix*

Various concentration profiles of the B element (Sn) in the composite are as shown in figure 5. The following parameters appear in the calculation: r_c, composite radius; r_F, initial radius of the filament; r', radius of the unreacted filament after a time t of diffusion reaction; C_i, initial concentration of the B element in the matrix, expressed as number of B atoms per unit volume; $C_{\alpha\beta}$, interface concentration of B in the matrix in equilibrium with the reacted compound β; $C_{\beta\alpha}$, interface concentration of B in the layer in equilibrium with the matrix α; $C_{\beta F}$, concentration of B in the layer at the β-F interface.

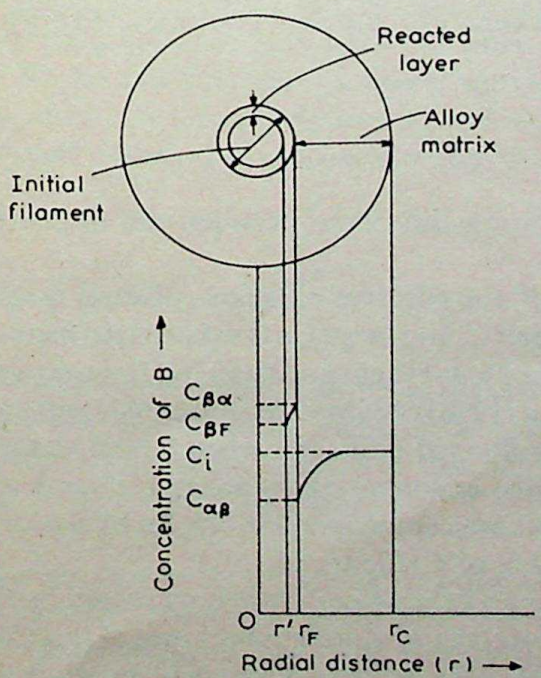

Figure 5. Various concentration profiles in the composite (after Reddi *et al* 1978).

CC-0. In Public Domain. Gurukul Kangri Collection, Haridwar

Digitized by Arya Samaj Foundation Chennai and eGangotri

Since the thickness of the reacted layer R is small compared to r_F, the concentration profile within the reacted layer can be assumed to be linear, giving the mean concentration of B in the reacted layer to be

$$\bar{C}_\beta = (C_{\beta\alpha} + C_{\beta F})/2.$$

As the layer growth is controlled by diffusion of B through the α-matrix, the flux at the α-β interface determines the overall kinetics. In this situation the models developed lead to three possibilities described below.

5.1a *Small depletion distance*: Depletion distance refers to the distance in the bronze matrix measured from α-β interface over which the Sn concentration drops from C_i to $C_{\alpha\beta}$. Small depletion distance leads to a parabolic growth,

$$R = k_1 t^{1/2}, \tag{6}$$

with rate constant,

$$k_1 = (D_\alpha^{1/2}/\bar{C}_\beta)\,(C_i - C_{\alpha\beta}), \tag{7}$$

where D_α is the diffusivity of B in α-matrix.

5.1b *Large depletion distance*: The growth law predicted is of the form

$$R = k_2 t^{2/3}, \tag{8}$$

with

$$k_2 = \frac{3D_\alpha^{2/3}}{2\bar{C}_\beta (9r_F)^{1/3}} (C_i - C_{\alpha\beta}). \tag{9}$$

5.1c *Depletion distance exceeding thickness of α-matrix*: The predicted growth is linear,

$$R = k_3 t, \tag{10}$$

with

$$k_3 = (D_\alpha/\bar{C}_\beta) k_0, \tag{11}$$

where k_0 is related to the concentration difference between the outer rim and α-β interface.

When C_i is large or when t is small, the effective diffusion distance is small and the growth predicted is parabolic. For small C_i and large t, n is expected to increase from 0·5 to 0·67. Results of Suenaga *et al* (1974), Dew-Hughes *et al* (1976), Luhman and Suenaga (1977) and Dew-Hughes and Suenaga (1978) obtained for monofilamentary Nb_3Sn all substantiate this contention. After prolonged diffusion, when the Sn-concentration at the outer rim starts depleting, the time exponent approaches 1·0. Increase in n with decrease in C_i, predicted by the model, was confirmed for Nb_3Sn by Reddi *et al* (1983) who found $n = 0{\cdot}9$ for the lowest value of C_i (figure 6).

When the growth is superparabolic and the growth rate is increased by the addition of impurities in the matrix or in the core, the obvious explanation of this from (8) is the increase in D_α. Addition of about 2% of Ti or Zr to V cores is found to significantly enhance Ga diffusion rate in the matrix, as confined by the formation of a large number

CC-0. In Public Domain. Gurukul Kangri Collection, Haridwar

Digitized by Arya Samaj Foundation Chennai and eGangotri

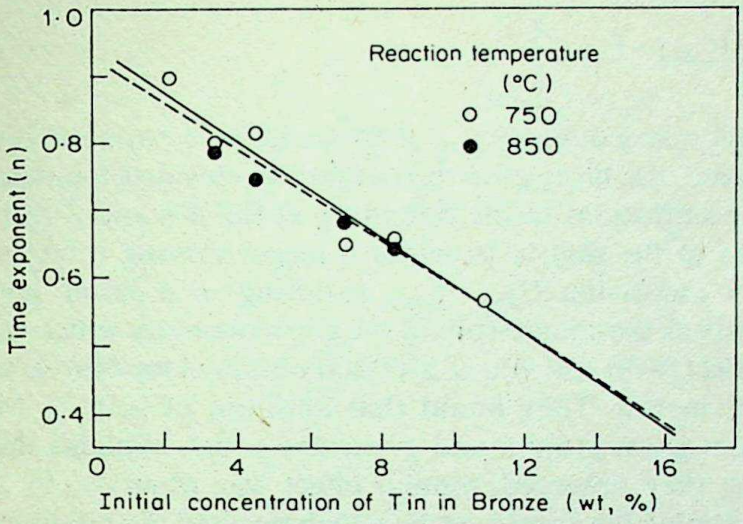

Figure 6. Increase in n with decrease in Sn-content in bronze (after Reddi *et al* 1983).

of Kirkendall voids at the α-β interface and the growth as reported by Berthel *et al* (1978) and Suenaga (1981) is superparabolic. Similarly, the addition of Al and Zn to the bronze enhances the growth rate of Nb_3Sn, as shown by Dew-Hughes *et al* (1976) and Wada *et al* (1978). Al and Zn in bronze are expected to enhance the vacancy concentration and thereby D_α is increased, giving rise to a higher reaction rate constant.

5.2 *Growth controlled by diffusion through layer*

We examine two possibilities: (a) bulk diffusion through the compound layer; (b) grain boundary diffusion through the compound layer: Here there are two situations to be considered: (i) zero grain growth; (ii) grain growth when (a) initial grain size is small and (b) initial grain size is large.

5.2a *Growth controlled by bulk diffusion through the layer*: The bulk diffusion tends to dominate over the grain boundary diffusion when the reaction temperature $T \geqslant T_m/2$. In the case of Nb_3Sn and V_3Si the reaction temperatures are too low for bulk diffusion, but for V_3Ga which has a relatively low T_m of 1300°C the possibility of bulk diffusion exists. When bulk diffusion is rate-controlling, the models yield a parabolic growth,

$$R = k_4 t^{1/2}, \tag{12}$$

with

$$k_4 = \left(\frac{2D_\beta}{\bar{C}_\beta}(C_{\beta\alpha} - C_{\beta F})\right)^{1/2}, \tag{13}$$

where D_β is the bulk diffusivity of B atoms in the compound layer. Thus, the growth rate would increase with temperature. Most of the growth kinetic studies of V_3Ga have yielded a parabolic growth in support of this mechanism. However, $n = 0{\cdot}5$ can also result from grain boundary diffusion.

5.2b *Growth controlled by grain boundary diffusion*

(i) Zero grain growth. When the grain diameter d of the compound layer remains constant throughout diffusion reaction, the models again predict a parabolic growth

$$R = k_5 t^{1/2},$$

CC-0. In Public Domain. Gurukul Kangri Collection, Haridwar

Digitized by Arya Samaj Foundation Chennai and eGangotri

with $$k_5 = 2\left(\frac{aD_{gb}}{\alpha \bar{C}_\beta}(C_{\beta\alpha g} - C_{\beta F g})\right)^{1/2}, \tag{14}$$

where D_{gb} is the grain boundary diffusivity of B atoms in the compound layer. Since it increases with temperature, the layer growth is higher at elevated temperatures. $C_{\beta\alpha g}$ and $C_{\beta F g}$ are the Sn-concentrations in the boundary at the β-α and β-F interfaces. A higher Sn-concentration in the matrix provides a larger driving force for diffusion through boundaries by increasing $C_{\beta\alpha g} - C_{\beta F g}$ resulting in a faster layer growth. Further, R varies inversely as the square root of the grain diameter which corroborates the results of Togano *et al* (1979) and Wu *et al* (1983) obtained for Nb_3Sn layer grown from Mg-doped bronze matrix. They found that addition of $<0{\cdot}5\%$ Mg led to a considerable reduction in grain growth and grain size which explains the enhanced parabolic growth which they observed. Similar effect was observed by Sekine and Tachikawa (1979) after doping Nb cores with Hf which resulted in doubling of the layer growth with simultaneous reduction in grain growth. In fact, wherever the grain growth has been negligible and there is an enhanced parabolic growth, zero grain growth model seems to be the right choice.

(ii) *Grain growth superimposed on grain boundary diffusion*: Consider an arbitrary grain growth described by

$$d_t = d_i + Gt^m, \tag{15}$$

where d_i is the initial or nucleation grain diameter, d_t the grain diameter after diffusion annealing at a fixed temperature for a time t, G is a temperature-dependent coefficient and m is a numerical time exponent.

(a) Small initial grain size: When the initial grain size is small the models predict grain growth-dependent layer growth given by

$$R = k_6 t^{(1-m)/2}, \tag{16}$$

with $$k_6 = 2\left(\frac{aD_{gb}}{\bar{C}_\beta G(1-m)}(C_{\beta\alpha g} - C_{\beta F g})\right)^{1/2}. \tag{17}$$

As discussed earlier (17) explains the observed increase in growth rate with temperature and Sn-concentration.

Whenever the layer growth is subparabolic the above model is the only choice. A parabolic grain growth, i.e., $m = 0{\cdot}5$, yields $n = 0{\cdot}25$. For grain growth slower than parabolic the n values will be intermediate between 0·25 and 0·5. When the grain growth is faster than parabolic n is expected to be $<0{\cdot}25$. Thus the model explains the observed n values in subparabolic range reported in the literature. In general, a higher grain growth is expected at higher temperatures and the resulting n values are thus expected to decrease. This is consistent with the results of Larbalestier *et al* (1975) for Nb_3Sn, and Critchlow *et al* (1974) and Tachikawa *et al* (1972) obtained for V_3Ga. By careful transmission electron microscopic studies of grain growth and scanning electron microscopic studies of layer growth the interrelation between the layer growth kinetics and the grain growth kinetics has been experimentally confirmed (figure 7) by Agarwal and Narlikar (1985a).

CC-0. In Public Domain. Gurukul Kangri Collection, Haridwar

Digitized by Arya Samaj Foundation Chennai and eGangotri

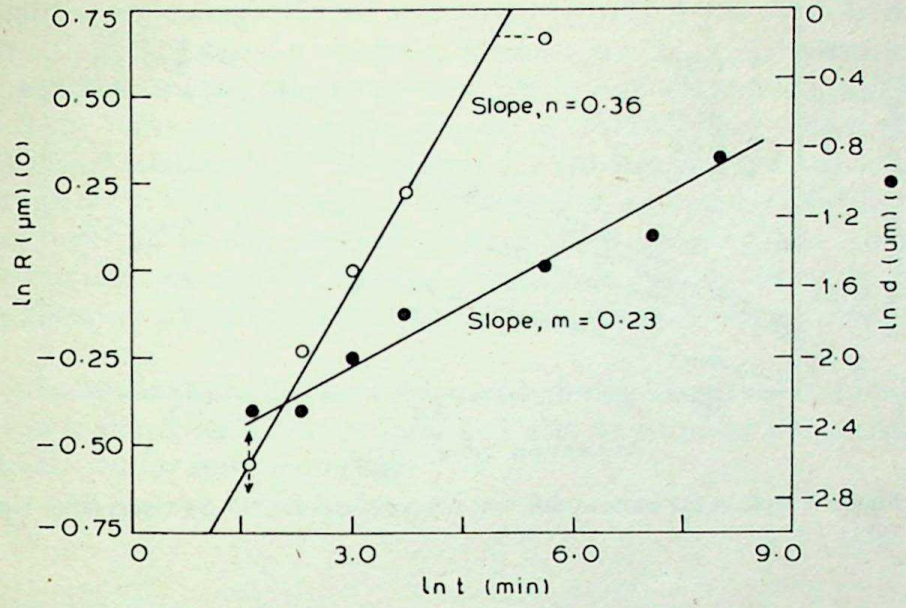

Figure 7. Interdependence of layer growth kinetics on grain growth kinetics (after Agarwal and Narlikar 1985a).

It is clear from (16) and (17) that the kinetics of layer growth can respond in a complicated way to various rate-controlling parameters. When the time exponent of layer growth $(1-m)/2$ is enhanced (due to decrease in temperature), k_6 is reduced by a factor $(1-m)$. Moreover, when the reaction temperature is lowered D_{gb} and G are expected to become smaller. Thus, the net increase or decrease of the layer growth with temperature would be determined by the overall effects of the above factors.

(b) *Large initial grain size*: When the initial grain size is large further grain growth is expected to have relatively less effect in reducing the grain boundary channels for diffusion. The situation, in effect, becomes analogous to that of zero grain growth described earlier. As expected, the growth law is parabolic

$$R = k_7 t^{1/2},$$

with
$$k_7 = 2\left(\frac{aD_{gb}}{d_i \bar{C}_\beta}(C_{\beta\alpha g} - C_{\beta F g})\right)^{1/2}, \tag{18}$$

which again shows that the growth rate would increase with temperature and the Sn-concentration in the matrix. Reaction rate constant decreases with increase in d_i. As already discussed in §3 the nucleation grain size increases with temperature, and consequently if the grain growth is small it is expected that the n values will gradually approach 0·5 as the reaction temperature is raised. Moreover, since $k_7 \propto d_i^{-1/2}$, and if the temperature dependence of d_i is more pronounced than D_{gb}, a decrease in the reaction rate constant would accompany increase in n as the reaction temperature is raised. These contentions have been substantiated by growth kinetic studies of Upadhyay *et al* (1981) (figure 8) and Agarwal *et al* (1984) on multifilamentary Nb_3Sn samples (figure 9). This mechanism can explain the parabolic growth frequently exhibited by V_3Ga. The grain size of V_3Ga layers is found to be two or three times larger than Nb_3Sn layers and consequently the time exponent for the growth of V_3Ga layer is expected to approach 0·5.

CC-0. In Public Domain. Gurukul Kangri Collection, Haridwar

Digitized by Arya Samaj Foundation Chennai and eGangotri

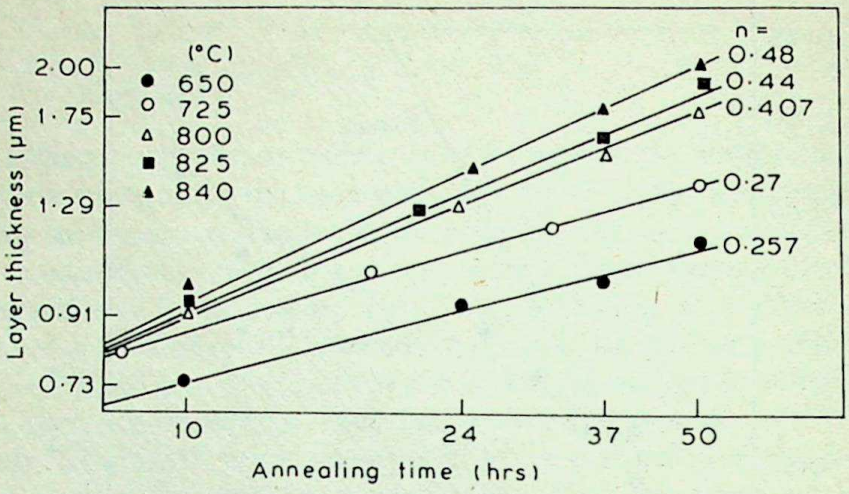

Figure 8. ln R vs ln t plots at different temperatures for Nb_3Sn layers (after Upadhyay *et al* 1981).

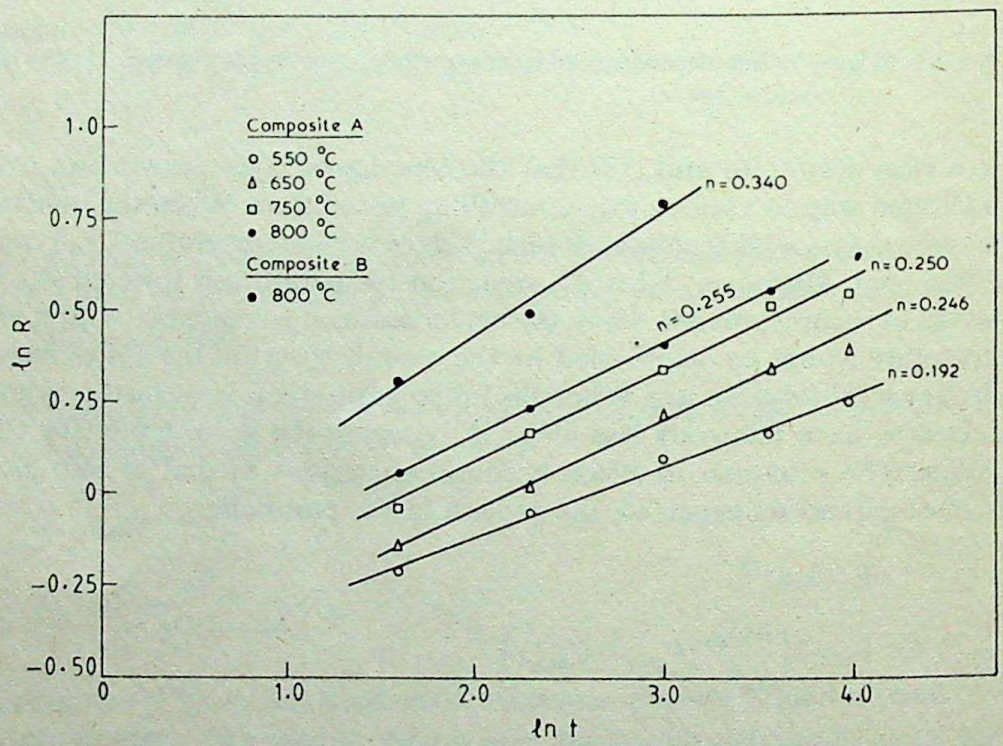

Figure 9. ln R vs ln t plots showing increase in n with reaction temperature (after Agarwal *et al* 1984).

6. Ordering kinetics

By ordering is meant the right species of atoms occupying the right crystallographic lattice sites. The LRO is measured by Bragg-Williams order parameter S, such that $S=1$ when the compound is fully ordered and $S=0$ when it is completely disordered. In the case of A-15 superconductors the critical temperature T_c depends sensitively on LRO and the ratio $T_c/T_{c(0)}$ serves as a satisfactory measure of S, where $T_{c(0)}$ is the optimum T_c value corresponding to $S=1$.

CC-0. In Public Domain. Gurukul Kangri Collection, Haridwar

Digitized by Arya Samaj Foundation Chennai and eGangotri

Although the annealing-induced reordering of bulk A-15s, initially disordered by neutron irradiation or rapid quenching, has been studied fairly extensively, there are little data available to date on the ordering effects in A-15 layers formed by solid state diffusion. X-ray diffraction studies of Okuda *et al* (1983) have shown that the layers reacted at lower temperatures have lower T_c, are less ordered and are slightly tin-deficient than those formed at higher temperatures, and contain antisite defects. The kinetics of ordering as the compound layer starts growing has remained mostly unexplored to date. In contrast to the layer growth kinetics where the bulk or grain boundary diffusion are both possible, the ordering kinetics are governed only by bulk diffusion.

It is worthwhile to examine the problem of ordering kinetics of A-15 layers from the viewpoint of a simple diffusion process and also to consider the reordering kinetic models developed for bulk materials.

6.1 *Analytical models*

(i) Simple diffusion process

The process is simply vacancy filling by the right species of atoms, i.e. Sn atoms moving into vacant Sn sites and Nb into vacant Nb sites. The grains formed initially after the start of diffusion reaction are Nb-rich with excess Sn vacancies with surplus Sn concentration in the boundary region (Suenaga and Jansen 1983). In the first instance an increase in T_c with annealing can be attributed to the gradual filling up of Sn vacancies by flux of Sn atoms coming from the grain boundary region whereby the Sn concentration C within the grains is raised to the stoichiometric level. The process leads to

$$0{\cdot}25 - C = (0{\cdot}25 - C_i)\exp(-t/\tau), \tag{19}$$

which may be related directly to T_c,

$$T_{c(0)} - T_c = [T_{c(0)} - T_{ci}]\exp(-t/\tau), \tag{20}$$

where T_{ci} is T_c at $t=0$, τ is the relaxation time for filling up of vacancies, related to the bulk diffusivity of Sn in the compound layer, and $C = C_i$ is the Sn concentration at $t=0$. C_i and T_{ci} are attributed to the compound formed during intermittent annealings while wire drawing. If the above process were solely responsible for the observed T_c increase one should obtain the same relaxation time independently from Sn concentration and T_c data. Any substantial deviation would mean the presence of antisite disorders occurring as precurser to the final ordering.

(ii) Reordering kinetic models

Following Welch (unpublished), Dew-Hughes (1980) developed reordering kinetic models to explain the observed increase in T_c of disordered bulk materials after annealing in terms of vacancy assisted hopping of atoms from wrong lattice sites to the correct ones, and the rate of ordering is determined by the slower of the two species. Accordingly, when Sn atoms are slower than Nb atoms, the rate of ordering is governed by first order kinetics, giving

$$\ln\xi = \ln\xi_0 - 16 f_{v_0} \nu_B \exp[-U_{R(B)}/kT]t, \tag{21}$$

CC-0. In Public Domain. Gurukul Kangri Collection, Haridwar

Digitized by Arya Samaj Foundation Chennai and eGangotri

for t-small, and

$$\ln\xi = \ln\xi_0 - 16 V_0 \nu_B \exp[-\{U_{R(B)} + U_f\}/kT]t, \tag{22}$$

for t-large. When Sn atoms are faster than Nb atoms the kinetics is of second order, given by

$$\frac{1}{\xi} = \frac{1}{\xi_0} + 12 f_{v_0} \nu_A \exp[-U_{R(A)}/kT]t, \tag{23}$$

for t small, and

$$\frac{1}{\xi} = \frac{1}{\xi_0} + 12 V_0 \nu_A \exp[-\{U_{R(A)} + U_f\}/kT]t, \tag{24}$$

for t-large. $\xi = 1 - T_c/T_{c(0)}$ is a measure of order. $U_{R(A)}$ and $U_{R(B)}$ are the activation energies for reordering of Nb and Sn atoms respectively with ν_A and ν_B their attempt frequencies, and

$$f_v = f_{v_0} \exp(t/\tau) + V_0 \exp(-U_f/kT), \tag{25}$$

where f_{v_0} is the vacancy concentration in excess of the equilibrium value is associated with the vacancy formation energy U_f.

Experimental results of Winkel and Bakker (1985) on bulk samples of V_3Ga and the theoretical analysis of Nb_3Sn by Welch *et al* (1984) have indicated that while the grain boundary diffusivities of Ga and Sn are dominant in these systems their bulk diffusivities are respectively smaller than of V and Nb. Consequently, they attribute the ordering to be governed by first order kinetics.

Figure 10 depicts the results of Agarwal and Narlikar (1985b) showing the time dependence of T_c of Nb_3Sn layer formed after short durations of diffusion reaction. Long annealing times are of little use to understand ordering as the outermost grains of a layer formed in the beginning have already attained a near optimum T_c and the measuring techniques are not sensitive enough to record T_c increase due to subsequent ordering of inner grains. By measuring the lattice parameter and estimating the Sn concentration in the layer, Agarwal *et al* (1986) have found that the relaxation time obtained from (19) are over 30% smaller than determined from T_c data using (20). This rules out the simple diffusion process to be responsible for the observed T_c increase. On the other hand, if one considers the first order kinetics process operating over the whole time domain under study given by (21) and (22) a comparison of the slopes of $\ln\xi$ vs t plots (figure 11) yields a negative value of U_f which is clearly inconsistent. Similarly, attributing the observed change in the slope of $1/\xi$ vs t at $t \simeq 400$ sec to t-small and t-large of (23) and (24) of second order kinetics is also unrealistic since the relaxation times involved are two or three times larger. Agarwal *et al* (1986) instead find that the observed data can be best explained by a duplex process. Initially the kinetics is of second order and subsequently changing over to first order. $U_{R(A)}$ and $U_{R(B)}$ are found to be 1·46 and 1·13 eV respectively, which are consistent with the values reported by Dew Hughes (1980).

The above findings are of course preliminary and need to be further substantiated by more data on other systems. Unfortunately, relatively little is known about the

CC-0. In Public Domain. Gurukul Kangri Collection, Haridwar

Digitized by Arya Samaj Foundation Chennai and eGangotri

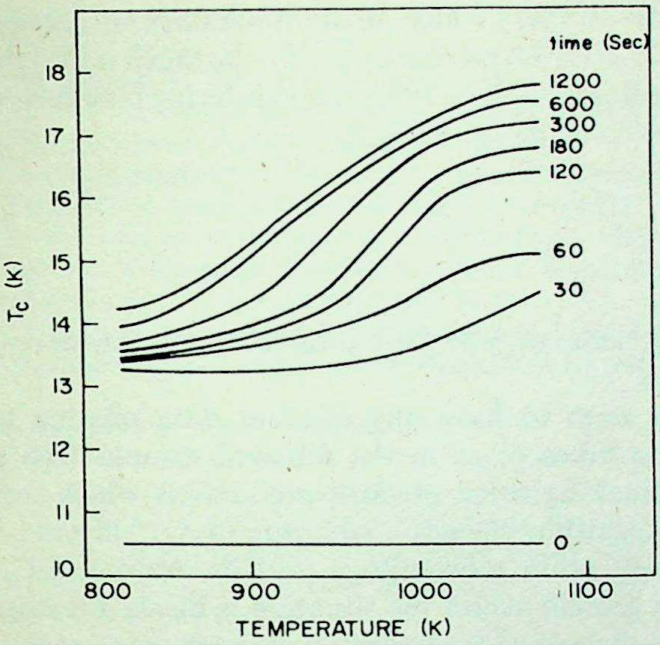

Figure 10. Time dependence of T_c of Nb_3Sn formed after short durations of reaction (after Agarwal and Narlikar 1985b).

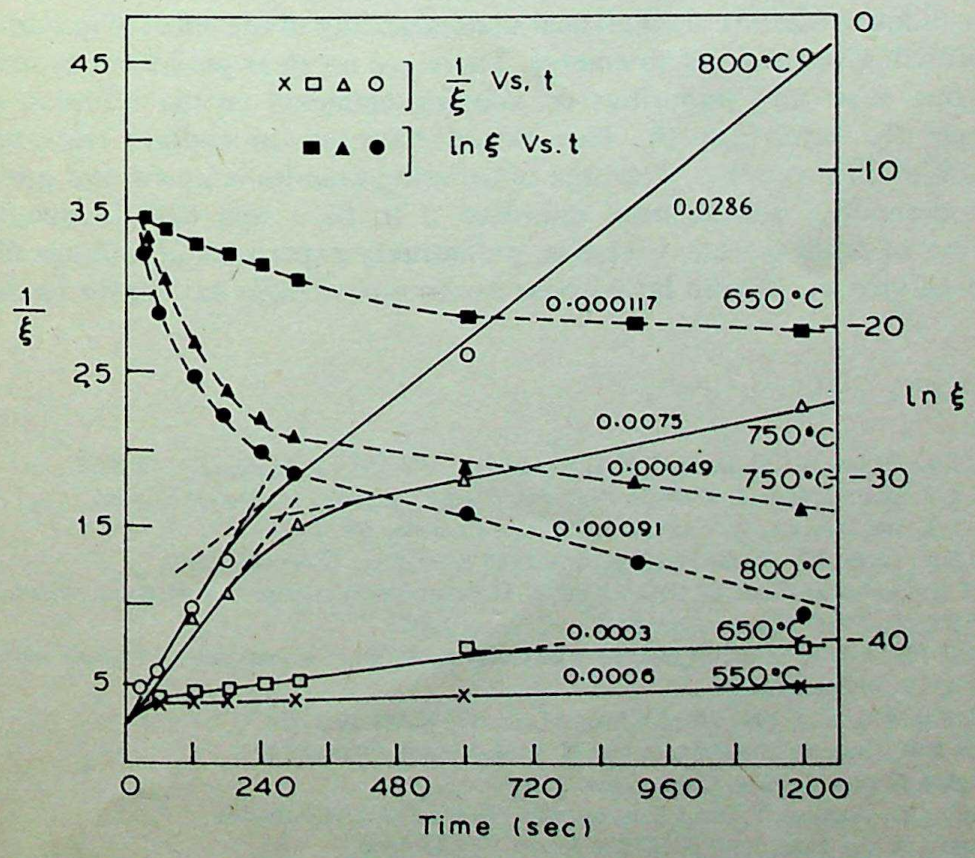

Figure 11. Plot of various ordering mechanisms (after Agarwal *et al* 1986).

CC-0. In Public Domain. Gurukul Kangri Collection, Haridwar

Digitized by Arya Samaj Foundation Chennai and eGangotri

behaviour of point defects in A-15s, in fact, in intermetallics in general, and the theoretical analysis of Welch *et al* (1984) has indicated it to be much more complex than known for pure metals. According to Welch (1985) the reordering kinetic models need a considerable refinement to become more realistic.

7. Conclusions

The story of transformation kinetics of A-15 formation may be summed up by making following broad observations.

To start with, we do not seem to have any relevant data relating to how the nucleation of the A-15 phase takes place in the diffusion couple. The problem is discussed in a general way, making some obvious predictions which seem to have experimental confirmation. Regarding the grain structure of A-15 layers considerable information is available about grain morphology and its dependence on process parameters, but on the grain growth aspect the situation is bleak. Presence of rather small grain sizes necessitates the use of transmission electron microscopy technique where the sample preparation of multifilamentary composites is an art mastered by a few. In lieu of adequate knowledge of grain growth data there is little choice left but to make some speculative assumptions pertaining to grain growth in order to explain the observed data on layer growth. The present knowledge of layer growth kinetics is however on a firm footing. The variation of growth laws seem explicable by model calculations compatible with the process conditions. A few gaps in the story still remain: one already mentioned above, i.e., the grain growth kinetics, and the second, the role of impurities. An unequivocal understanding of the effect of impurities on the layer growth kinetics is yet to emerge. There are no clear guidelines available about which one must add impurities or alloying elements to the diffusion couple to accelerate the layer growth. This would have an immediate relevance to the optimization of properties. The area of ordering kinetics is a new and growing area. Recent theoretical studies have indicated it to be a rich field involving unusual behaviour of point defects. Likewise, preliminary experimental findings of ordering kinetics of growing Nb_3Sn layers pose exciting challenges calling for further work.

References

Agarwal S K, Samanta S B, Batra V K and Narlikar A V 1984 *J. Mater. Sci.* **19** 2057

Agarwal S K and Narlikar A V 1985a *Proc. Int. Conf. Cryogenics* (*Calcutta*) in press

Agarwal S K and Narlikar A V 1985b *Solid State Commun.* **55** 563

Agarwal S K, Nagpal K C and Narlikar A V 1986 *Solid State Commun.* **58** 89

Berthel K H, Fischer K, Fuchs G, Grunberger W, Holzhauseer W, Lange F, Rohr S and Schumann H J 1978 *Proc. VI Int. Conf. Magnet-Technology ALFA*, p. 1007

Cahn J and Hagel W 1962 *Decomposition of austenite by diffusion process* (eds) V Zackay and H Aaronson (New York: Interscience) p. 134

Cave J R and Weir C A 1983 *IEEE Trans. Magnetics* **MAG-19** 1120

Critchlow P R, Gregory E and Marancik W 1974 *J. Appl. Phys.* **45** 5027

Dew-Hughes D 1980 *J. Phys. Chem. Solids* **41** 851

Dew-Hughes D, Luhman T S and Suenaga M 1976 *Nucl. Technol.* **29** 268

Dew-Hughes D and Luhman T S 1978 *J. Mater. Sci.* **13** 1868

Dew-Hughes D and Suenaga M 1978 *J. Appl. Phys.* **49** 357

CC-0. In Public Domain. Gurukul Kangri Collection, Haridwar

Digitized by Arya Samaj Foundation Chennai and eGangotri

Larblestier D C, Madsen P F, Lee J A, Wilson M N and Harlesworth J P 1975 *IEEE Trans. Mag.* **11** 247
Livingston J D 1977 *J. Mater. Sci.* **12** 1759
Luhamn T S and Suenaga M 1977 *Adv. Cryog. Engg.* **22** 356
Narlikar A V and Dew-Hughes D 1985a *Fabrication techniques for A-15 compound superconductors* (ed.) D Dew-Hughes (Amsterdam: North Holland) to be published
Narlikar A V and Dew-Hughes D 1985b *Proc. Int. Conf. Cryogenics* (*Calcutta*) in press
Okuda S, Suenaga M and Sabatini R L 1983 *J. Appl. Phys.* **54** 289
Reddi B V, Ray S, Raghavan V and Narlikar A V 1978 *Philos. Mag.* **A38** 559
Reddi B V, Raghavan V, Ray S and Narlikar A V 1983 *J. Mater. Sci.* **18** 1165
Sekine H and Tachikawa K 1979 *Appl. Phys. Lett.* **35** 472
Suenaga M, Horigami O and Luhman T S 1974 *Appl. Phys. Lett.* **25** 624
Suenaga M 1981 *Superconductor materials sciences* (eds) S Foner and B B Schawartz (New York: Plenum) p. 201
Suenaga M and Jansen 1983 *Appl. Phys. Lett.* **43** 791
Tachikawa K, Yoshida Y and Rinderer L 1972 *J. Mater. Sci.* **7** 1154
Togano K, Asan T and Tachikawa K 1979 *J. Less Common Metals* **68** 15
Upadhyay P, Samanta S B and Narlikar A V 1981 *Mater. Res. Bull.* **16** 741
Wada H, Kimura M and Tachikawa K 1978 *J. Mater. Sci.* **13** 1943
Welch D O, Diences G J, Lazareth O W Jr and Hatcher R D 1984 *J. Phys. Chem. Solids* **45** 1125
Welch D O 1985 Private Communication
Winkel A V and Bakker H 1985 *J. Phys.* **F15** 1556
Wu I W, Dietderich D R, Hottuis W V and Morris J W Jr 1983 *IEEE Trans. Magnetics* **MAG-19** 1437

CC-0. In Public Domain. Gurukul Kangri Collection, Haridwar

Digitized by Arya Samaj Foundation Chennai and eGangotri

CC-0. In Public Domain. Gurukul Kangri Collection, Haridwar

Digitized by Arya Samaj Foundation Chennai and eGangotri

Pramāṇa – J. Phys., Vol. 28, No. 5, May 1987, pp. 547–553. © Printed in India.

Disorder in superconductors—a study on $Cu_2Mo_6S_8$

P CHADDAH

Nuclear Physics Division, Bhabha Atomic Research Centre, Trombay, Bombay 400 085, India

Abstract. Some of the recent work on disorder-induced changes in T_c is reviewed. Shock-pressures induce a disorder uncomplicated by antisite disorder typical of particle irradiation, and have generated interest because of the shock-synthesis of A-15 Nb_3Si. In this paper we present our results on laser-induced shock-damage, and compare it with the results on V_3Si and the results on particle irradiation of Chevrel phase superconductors.

Keywords. Superconductors; disorder.

PACS No. 74·70

1. Introduction

The effect of disorder on superconductivity has been studied for about a decade now. In addition to affecting the normal state properties, disorder affects the three macroscopic superconducting parameters viz, transition temperature, critical field and critical current. The last two are of interest in view of the large scale applications of superconducting magnets, but in this paper we shall concentrate on the effect of disorder on the transition temperature T_c.

Disorder has been introduced in the past by irradiation with fast neutrons (Sweedler *et al* 1978; Brown *et al* 1977), with protons (Dierker *et al* 1983) and with heavy charged particles (Lehmann *et al* 1981; Adrian *et al* 1981). Some representative results in high T_c materials will be reviewed in the next section. Superconductors have also been prepared in the disordered state by going off-stoichiometry or by quenching. We shall also review in § 2 some theoretical efforts to explain the variation of T_c with disorder in terms of variations caused in relevant microscopic parameters like the electronic density of states $N(E_F)$, the electron-phonon coupling λ, and Coulomb repulsion μ^*. In § 3 we present our results on laser-induced shock damage in $Cu_2Mo_6S_8$ and compare them with other recent results on shock-damaged superconductors. We conclude by comparing our results with earlier studies on neutron irradiated and charged-particle irradiated Chevrel phase superconductors, and present a possible explanation for the apparently conflicting results.

2. Disorder in superconductors—status review

Sweedler *et al* (1978) studied the change in T_c of various A-15 compounds under irradiation with fast neutrons for fluence ($E > 1$ MeV) upto 10^{20} neutrons/cm^2. On

CC-0. In Public Domain. Gurukul Kangri Collection, Haridwar

Digitized by Arya Samaj Foundation Chennai and eGangotri

plotting T_c/T_{c0} as a function of irradiated fluence they found Nb_3Al, Nb_3Ge, Nb_3Pt, Nb_3Sn, Nb_3Ga and V_3Si to follow a universal curve. T_c dropped to about 20% of its unirradiated value at a fluence of $\approx 4 \times 10^{19}$ neutrons/cm^2 before saturation set in. Sweedler *et al* (1978) explained their data on the basis of antisite defects created by the irradiation. Brown *et al* (1977) studied V_2Hf (C-15 Laves phase), Nb_3Al and $PbMo_6S_7$ and $SnMo_5S_8$ (in Chevrel phase) under fast neutron irradiation going upto a fluence ($E > 0{\cdot}1$ MeV) of $1{\cdot}6 \times 10^{19}$ neutrons/cm^2. They found a decrease of only $\approx 5\%$ in the T_c of V_2Hf, a decrease of $\approx 23\%$ for Nb_3Al, while $PbMo_6S_7$ showed a decrease of $\approx 61\%$ and $SnMo_5S_8$ of $\approx 51\%$ in T_c. They thus found a much larger depression in the T_c of Chevrel phase compounds. Sweedler *et al* (1978) also reported a measurement on $PbMo_6S_8$ where T_c decreased from 12·8 K to below 4·2 K at a fluence ($E > 1$ MeV) of 10^{19} neutrons/cm^2, which is larger than that found by them for the A-15 compounds. They have concluded that the T_c's of the Chevrel phases are "the most sensitive to neutron irradiation of the materials studied to date". They have also reported that elemental Nb shows "little or no change" in T_c under irradiation to high fluences.

V_3Si has also been irradiated with 37 MeV protons to a fluence of $4{\cdot}6 \times 10^{18}$/cm^2, resulting in a drop of T_c from 16·33 K to 5·42 K, with the width of the transition increasing from 0·17 K to 1·31 K (Dierker *et al* 1983). α-particle irradiation on $SmRh_4B_4$ films has recently been reported by Terris *et al* (1984). Irradiation of A-15 compounds with 20 MeV ions of ^{32}S has been reported by Lehmann *et al* (1981) where fluence $> 10^{15}$/cm^2 yields saturation effects in Mo_3Si and Mo_3Ge. Adrian *et al* (1981) irradiated $PbMo_6S_8$ films with 20 MeV ^{32}S ions and found that T_c drops from 12·7 K to $< 1{\cdot}2$ K at a fluence of 10^{14}/cm^2. These results again indicate higher sensitivity of Chevrel phase T_c's to particle irradiation as compared to the A-15 T_c's.

Before proceeding to theoretical efforts we shall point out that inelastic neutron scattering measurements (Cox and Tarvin 1978) and sound velocity measurements (Guha *et al* 1978) on neutron-irradiated V_3Si have shown that the softening of the transverse acoustic mode is absent in the irradiated compound indicating that the phonon properties, and possibly the electron-phonon coupling constant, are modified by irradiation. Dierker *et al* (1983) have done Raman scattering on the proton irradiated V_3Si mentioned above. By studying the temperature variation of the linewidth of the E_g phonon in irradiated and unirradiated samples they conclude that the electron-phonon coupling is reduced in the irradiated sample. It should be mentioned that they believe this reduction to be due to the broadening of the peak at $N(E_F)$.

Based on electron-microscopic observations of the disorder caused in their samples, Pande (1977, 1978) proposed a model based on proximity effect to explain the decrease of T_c with disorder. Farrell and Chandrasekhar (1977) proposed that disorder decreases gap anisotropy and reduces T_c. These two models required an excessive volume fraction of disordered regions, and an excessive gap anisotropy respectively, and have not been pursued much (Dierker *et al* 1983). Other microscopic models discuss the variation of the microscopic parameters $N(E_F)$, λ and μ^* with disorder. Appel (1976) related T_c of the A-15's to the long-range order parameters S using McMillan's equation with both λ and $N(E_F)$ being functions of S. The drawback is that a critical component of the theory, the variation of $N(E_F)$ with S, must be independently determined. Testardi and Mattheiss (1978) treat the effect of the disorder via electron-lifetime broadened density of states. The electrical resistivity of the disordered sample is used to determine the life-time, and an effective $N(E_F)$ is obtained. Assuming λ to be

CC-0. In Public Domain. Gurukul Kangri Collection, Haridwar

Digitized by Arya Samaj Foundation Chennai and eGangotri

proportional to $N(E_F)$ averaged over an energy equal to the Debye energy, they also related T_c to the resistivity of the disordered sample. With these assumptions, they obtained a reasonable agreement with data for V_3Si except in the low resistivity region. Anderson *et al* (1983) were the first to consider the effect of disorder on T_c via its effect on μ^*. They noted that the normalized T_c of many high temperature superconductors decreases similarly with increasing resistivity and took this to be the single parameter specifying disorder. They further stated that since the electron-phonon coupling is strong in these materials, a one-electron description (which is the basis of the models discussing the variation of $N(E_F)$ with disorder) is unrealistic. They proposed that Anderson localization in extremely disordered systems provides an explanation for the degradation of T_c. They showed that μ^* increases with increasing resistivity and using McMillan's formula

$$T_c = \frac{\omega_D}{1{\cdot}45} \exp\left[-\frac{1{\cdot}04(1+\lambda')}{\lambda' - \mu^*(1+0{\cdot}62\lambda')} \right]; \quad \lambda' = N(E_F)\lambda,$$

obtained the degradation of T_c with increasing resistivity. They have obtained good agreement with the experimental data for Nb_3Ge, V_3Si and $LuRh_4B_4$. They need, however, a low value of the critical resistivity ($\rho_c \approx 0{\cdot}04\rho_c^f$, the free electron gas estimate) to obtain this agreement. There are two viewpoints contradicting this model. Leavens (1985) claims that a detailed solution of the Eliashberg-gap equations, with $\rho_c \approx 0{\cdot}04\rho_c^f$, actually results in T_c increasing with increasing disorder due to the dominant effect of the renormalization function $Z(\omega)$. He believes that though the effect considered by Anderson *et al* is correct, it is not the primary cause of the degradation of T_c and the extremely low ρ_c used by Anderson *et al* is not justified.

Following the proposal of Anderson *et al* (1983), two-electron tunneling measurements on Nb_3Sn have reported μ^* for samples with differing Sn concentration and differing T_c. Geerk *et al* (1984) have made measurements for Sn concentration 25, 23, 20 and 19 at.%, while Rudman and Beasley (1984) had Sn concentration varying from 22·4 to 26·7 at.%. While T_c vs resistivity follows the universal behaviour, μ^* shows no measurable variation with resistivity, in contrast to large variation predicted by Anderson *et al*.

To sum up the present status, there does not exist a generally accepted understanding of the degradation of T_c with disorder. The model of Pande (1977, 1978) and the work of Appel (1976) corresponds to different ideas about the effect of the disorder on microscopic structure. The concept of antisite defects proposed by Sweedler *et al* (1978) and by Appel (1976) is relevant to damage by particle bombardment but perhaps not to compositionally disordered samples. Similarly, shock-generated disorder yields defects which are dominantly dislocation lines for shock pressures above ≈ 100 kbar. In the next section we shall report our studies (Chaddah *et al* 1986) on $Cu_2Mo_6S_8$ samples disordered by laser-induced shock. Shock-induced disorder has also been studied in V_3Si (Stewart *et al* 1985) and in Nb (Nellis *et al* 1985) and these will be discussed below.

3. Details of our measurement

We have studied the effect of laser-induced shock on $Cu_2Mo_6S_8$ (Chaddah *et al* 1986) as a representative compound of the high-T_c Chevrel phase compounds. The sample

CC-0. In Public Domain. Gurukul Kangri Collection, Haridwar

Digitized by Arya Samaj Foundation Chennai and eGangotri

preparation procedure (Gopalakrishnan *et al* 1984) is outlined below. The sample was obtained in powder form, which was pelletized for our measurements. $Cu_2Mo_6S_8$ was prepared by direct reaction of molybdenum (99·9%), copper (99·99%) and sulphur (99·99%) powders in vacuum. Appropriate mixtures were pelletized and sealed under vacuum in quartz tubes after flushing with pure argon for 30 minutes. These were heated at 300°C for 3 hr, 400°C for 5 hr, 550°C for 16 hr and 850°C for 24 hr and furnace-cooled. The quartz ampules were then vigorously shaken and reheated at 900°C for 24 hr. The product was subsequently ground, pelletized, sealed again under vacuum and re-sintered at 1250°C for 4 hr. X-ray diffraction showed only single-phase $Cu_2Mo_6S_8$ with no detectable contamination of MoS_2 or any other impurity phases. The hexagonal lattice parameters of this sample are $a = 9{\cdot}60$ Å and $C = 10{\cdot}24$ Å.

The T_c was measured by the a.c.-inductive technique. The primary coil was wound of Cu-clad Nb-Zr and the secondary was wound using a copper wire. The sample, the standard (lead was used) and the thermometer and the heater were mounted on a 5N-pure Cu rod, and the sample volume used was ≈ 1 mm^3. The change in inductance was monitored using a PAR 124A lock-in amplifier, and the frequency was 31 Hz.

The shock was generated using a Nd-glass laser having a wavelength of 1·06 μm. The pulse width was 5 nsec and the laser power used was 4·5 Joules and 7·8 Joules. The laser pulse was focused to 270 μm diameter on the sample surface, the sample being maintained in vacuum. The power density on the sample surface, was thus $1{\cdot}46 \times 10^{12}$ W/cm^2 and $2{\cdot}53 \times 10^{12}$ W/cm^2 respectively. To estimate the shock pressures generated, we have modelled the shock propagation using a one-dimensional hydrodynamic code. Among the input physical parameters of $Cu_2Mo_6S_8$ required were the sound velocity, the thermal expansion coefficient and the specific heat, all above room temperature. For the specific heat we extended the fit of Lachal *et al* (1984), while the sound velocity for the polycrystalline pellet was estimated from the phonon distribution curves (Bader *et al* 1982). Thermal expansion data were not available, and we have used the triclinic cell parameters (Baillif *et al* 1979) to provide an estimate. The pressures indicated in table 1 correspond to pressures obtained by using these estimates of input physical parameters.

Figure 1 shows the results of our measurement in the neighbourhood of the $Cu_2Mo_6S_8$ transition. Table 1 gives the values of T_c and ΔT_c obtained for the unshocked and the shocked samples. We note that the broadening of the transition is slight (ΔT_c goes up from 0·42 to upto 0·66), while the depression in T_c is as large as 0·45 K. The only other reported T_c measurements on shock-disordered samples (though these do not use laser driven shocks) are on V_3Si (Stewart *et al* 1985) and on Nb (Nellis *et al* 1985). In the case of Nb the maximum depression in T_c was 0·035 K while in the case of V_3Si the depression was $\approx 1{\cdot}8$ K but the transition width broadened from ≈ 1 K to $\approx 3{\cdot}5$ K. The results for Nb are not surprising since, as mentioned earlier, it shows no change in T_c under neutron irradiation. Nb_3Si has been synthesized in the A-15 phase (Olinger and Newkirk 1981) using a shock compression, but shows a transition width of only $\approx 0{\cdot}7$ K. The electronic specific heat coefficient γ in shocked Nb_3Si is 24 ± 6 mJ/mol against 45 ± 2 mJ/mol in shocked V_3Si ($\gamma = 58 \pm 2$ mJ/mol in their unshocked V_3Si sample) and Stewart *et al* (1985) explain the increased ΔT_c for V_3Si (under shock conditions similar to that of Nb_3Si) as due to the higher $N(E_F)$ in V_3Si. The value of $N(E_F)$ for $Cu_2Mo_6S_8$ is $N_{bs}(0) = 0{\cdot}35$ states/eV-atom-spin (Fischer 1978), while $N_{bs}(0)$ for V_3Si is $> 1{\cdot}24$ states/eV-atom-spin (Junod *et al* 1983) and thus the small depression in T_c seen by us appears to be in accordance with Stewart's

CC-0. In Public Domain. Gurukul Kangri Collection, Haridwar

Digitized by Arya Samaj Foundation Chennai and eGangotri

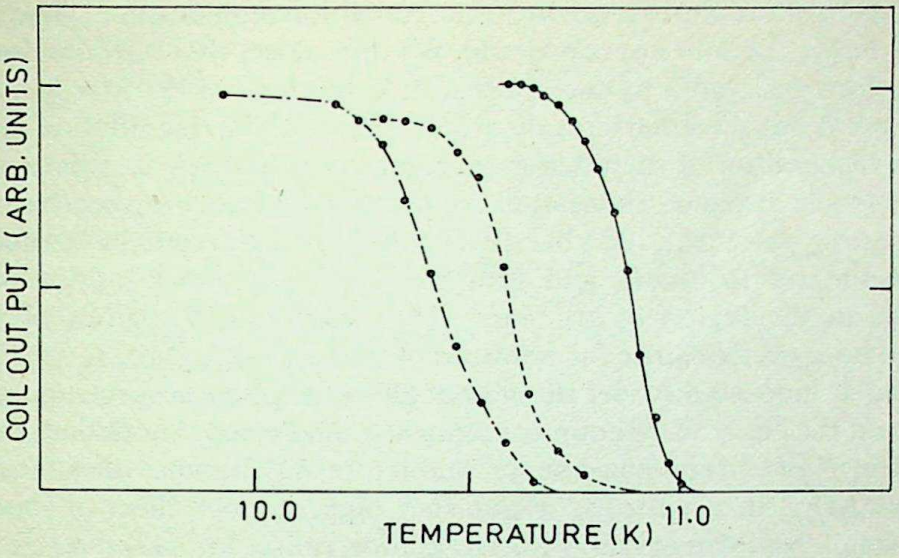

Figure 1. Results of our T_c measurements. The full line corresponds to sample I, the dashed line to sample II, and the dot-dashed line to sample III.

Table 1. Various parameters for the $Cu_2Mo_6S_8$ samples are listed. ΔT corresponds to 10% to 90% of the transition.

Sample	Laser power density (W/cm^2) ($\times 10^{12}$)	Peak pressure (kbar)	T_c (mid-pt) (K)	ΔT (K)
I	—	—	10·88	0·42
II	1·46	950	10·60	0·48
III	2·53	1200	10·43	0·66

explanation that a higher $N(E_F)$ is more depressed by disorder. This does not however explain why $PbMo_6S_8$ ($N_{bs}(0) = 0{\cdot}67$) and other Chevrel compounds show such a large depression of T_c under particle irradiation. We believe that one must also consider the effect of disorder on the electron-phonon coupling, and this is described below.

4. Discussion

The electron-phonon interaction in Chevrel phase compounds is discussed in detail by Pobell *et al* (1982). It is believed that since the peak in $N(E_F)$ is due to the Mo 4*d* electrons, the electron-phonon coupling of the conduction electrons is dominantly to internal deformations of a Mo_6S_8 cluster, while phonons involving intercluster coupling do not play a major role in superconductivity. The displacements of the copper atoms as well as those of rigid Mo_6S_8 clusters may contribute to superconductivity only to the extent that these modes are hybridized with internal modes of the Mo_6S_8 cluster. This viewpoint has received a lot of support from the isotope effect measurements (Pobell 1981) which show that the vibrations of the 6 Mo and 8 Se atoms

CC-0. In Public Domain. Gurukul Kangri Collection, Haridwar

Digitized by Arya Samaj Foundation Chennai and eGangotri

(in Mo_6Se_8) contribute almost equally to the transition temperature, while those of the Sn atom (in $SnMo_6Se_8$) do not contribute. We thus assert that $N(E_F)$ is dominated by the Mo 4*d* electrons, and λ by the internal deformations of the Mo_6S_8 cluster.

We now point out Sweedler's results which attribute the degradation in T_c to anti-site defects. Generation of such defects is common to particle-irradiation where the impinging particle displaces an atom in the lattice by a knock-on scattering while for shock pressures greater than 100 kbar dislocations are believed to be the major defects. Available estimates (Morosin and Graham 1983) on shock-induced dislocation densities are in the region of $10^{11}/cm^2$. Thus undamaged regions of dimensions ≈ 100 Å can be expected. Since the phonons of interest in $Cu_2Mo_6S_8$ are intra-cluster phonons, shock-induced disorder should not affect the phonon spectrum in the region of interest and the electron-phonon coupling λ is unaffected. Shock-induced-disorder will thus affect T_c of Chevrel phase superconductors only because of changes caused in $N(E_F)$. Since $N(E_F)$ in $Cu_2Mo_6S_8$ is not very high, the net effect of shock-induced disorder is small. Neutron or heavy ion irradiation causes knock-on reactions and the intra-cluster phonons are directly affected. Thus both $N(E_F)$ and λ are reduced and the large depression in T_c (even in comparison to A-15 compounds) can be understood. This distinction will be characteristic of compounds where dominant electron-phonon coupling is with localized phonon modes. Since such localized modes do not occur in A-15 compounds T_c depression will not be dependent on the type of disorder caused. If our understanding is correct, the type of disorder caused will be of major importance for Chevrel phase compounds and a single parameter fit for the degradation of T_c (as done by Anderson *et al* for A-15's) will not be possible.

Acknowledgement

The author is grateful to Shri P A Naik for providing the laser facility for shock-induced disorder.

References

Adrian H, Hertel G, Bieger J, Saemann-Ischenko G and Soldner L 1981 *Physica* **B107** 647
Anderson P W, Muttalib K A and Ramakrishnan T V 1983 *Phys. Rev.* **B28** 117
Appel J 1976 *Phys. Rev.* **B13** 3203
Bader S D, Sinha S K, Schweiss B P and Renker B 1982 *Superconductivity in ternary compounds* (eds) O Fischer and M B Maple (Berlin: Springer-Verlag) p. 224
Baillif R, Yvon K, Flukinger R and Muller J 1979 *J. Low. Temp. Phys.* **37** 231
Brown B S, Hafstrom J W and Klippert T E 1977 *J. Appl. Phys.* **48** 1759
Chaddah P, Gopalakrishnan I K, Yakhmi J V and Godwal B K 1986 (to be published)
Cox D E and Tarvin J A 1978 *Phys. Rev.* **B18** 22
Dierker S B, Merlin R, Klein M V, Chandrasekhar B S and Blue J W 1983 *Phys. Rev.* **B27** 3571
Farrel D E and Chandrasekhar B S 1977 *Phys. Rev. Lett.* **38** 788
Fischer O 1978 *Appl. Phys.* **16** 1
Geerk J, Rietschel H and Schneider V 1984 *Phys. Rev.* **B30** 459
Guha A, Sarachik M P, Smith F W and Testardi L R 1978 *Phys. Rev.* **B17** 9
Junod A, Jarlborg T and Muller J 1983 *Phys. Rev.* **B27** 1568
Gopalakrishnan I K, Yakhmi J V, Iyer R M, Ota S B and Chaddah P 1984 *Solid State Phys. (India)* **C27** 140
Lachal B, Junod A and Muller J 1984 *J. Low. Temp. Phys.* **55** 195
Leavens C R 1985 *Phys. Rev.* **B31** 6072

CC-0. In Public Domain. Gurukul Kangri Collection, Haridwar

Digitized by Arya Samaj Foundation Chennai and eGangotri

Morrison B and Graham R A 1983 in *Shock waves in condensed matter* (eds) J R Asay, R A Graham and G K Straub (Amsterdam: Elsevier) p. 355
Lehmann M, Saemann-Ischenko G, Adrian H and Nolscher C 1981 *Physica* **B107** 473
Nellis W J, Moss W C, Radonsky H B, Mitchell A C, Summers L T, Dalder E N, Maple M B and McElfresh M 1985 *Physica* **B135** 240
Olinger B and Newkirk L R 1981 *Solid State Commun.* **37** 613
Pande C S 1977 *Solid State Commun.* **24** 241
Pande C S 1978 *J. Nucl. Mater.* **72** 83
Pobell F 1981 in *Proc. Int. Conf. on Ternary Superconductors* (eds) G K Shenoy, B D Dunlap and F Y Fradin (Amsterdam: North Holland) p. 35
Pobell F, Rainer D and Wuhl H 1982 in *Superconductivity in ternary compounds* (eds) O Fischer and M B Maple (Berlin: Springer-Verlag) p. 251
Rudman D A and Beasley M R 1984 *Phys. Rev.* **B30** 2590
Stewart G R, Olinger B and Newkirk L R 1985 *Phys. Rev.* **B31** 2704
Sweedler A R, Cox D E and Moehlecke S 1978 *J. Nucl. Mater.* **72** 50
Terris B D, Gray K E, Kampwirth R T, Zasadzinski J and Vaglio R 1984 *Phys. Rev.* **B30** 5370
Testardi L R and Mattheiss L F 1978 *Phys. Rev. Lett.* **41** 1612

CC-0. In Public Domain. Gurukul Kangri Collection, Haridwar

Digitized by Arya Samaj Foundation Chennai and eGangotri

CC-0. In Public Domain. Gurukul Kangri Collection, Haridwar

Digitized by Arya Samaj Foundation Chennai and eGangotri

Pramāṇa – J. Phys., Vol. 28, No. 5, May 1987, pp. 555–564. © Printed in India.

Structural instability and superconductivity in niobium-titanium alloys

T S RADHAKRISHNAN
Indira Gandhi Centre for Atomic Research, Kalpakkam 603 102, India

Abstract. Niobium-titanium is the most widely used technical superconductor. Titanium-rich transition metal alloys, quenched from high temperatures, can generally be retained in the bcc β phase. This phase is metastable and the instability is relieved by a variety of low temperature structural transformations. This aspect has been investigated using x-ray, TEM, low temperature resistivity, T_c and dH_{c2}/dT studies, in a series of Nb-Ti alloys. The instability has been characterized by the normal state resistivity ρ_n and $d\rho/dT$.

The commercially used Nb-Ti alloys are Ti rich per atom-wise. This stems basically from the anomalous increase in the normal state resistivity ρ_n as the Ti concentration is increased. This is a consequence of a dynamical process through which the β phase instability tends to be relieved leading to athermal ω precipitation. The resulting anomalous resistivity behaviour can be understood in terms of a 'two-level system' model generally invoked for amorphous materials. It has also been possible to induce instability towards athermal ω precipitation in a system spontaneously undergoing a martensitic transformation to become stable. Thus in an alloy of Nb-83 at % Ti, addition of 1% nitrogen has suppressed the martensitic transformation, giving a three-fold increase in ρ_n (about 150 $\mu\Omega$ cm), the highest known in Nb-Ti so far.

The increase in the normal state resistivity has beneficial effects on the upper critical field. From studies on several Nb-Ti alloys, it is inferred that a peak in $H_{c2}(0)$ occurs at 17–18 tesla at a ρ_n value of 100 $\mu\Omega$ cm. It is pointed out that in the present commercial alloys, the sequence of thermo-mechanical treatments given to optimize J_c, restricts ρ_n, perhaps owing to the partial relieving of the metastability of the β phase. They are therefore non-optimized with respect to H_{c2}.

Keywords. Ti-Nb system; resistivity; structural instability; superconductivity; ω transformation; proximity effect; upper critical field.

PACS No. 74·70

1. Introduction

The relationship between structural and lattice instabilities and superconductivity has been a subject of many inconclusive discussions (Allen 1980; Smith and Finlayson 1980; Geballe 1983). The basis for this discussion is the McMillan equation

$$T_c = \frac{\theta_D}{1{\cdot}45} \exp\left(\frac{1{\cdot}04(1+\lambda)}{\lambda - \mu^*(1+0{\cdot}62\lambda)}\right), \tag{1}$$

linking T_c with the attractive electron-phonon coupling parameter λ. This is defined in terms of normal state properties

$$\lambda = [N(0)\langle I^2\rangle]/M\langle\omega^2\rangle. \tag{2}$$

There is thus the suggestion that a phonon softening viz a decrease of average phonon

CC-0. In Public Domain. Gurukul Kangri Collection, Haridwar

Digitized by Arya Samaj Foundation Chennai and eGangotri

frequency leads to an increase in T_c and vice-versa. This lattice instability is to be distinguished from a structural instability leading to permanent displacement of ions in the crystal.

Experimentally, many high T_c systems like the A15 (e.g. V_3Si and Nb_3Sn) and the transition metal carbides and nitrides (e.g. NbC and TaC) show phonon anomalies. Some of the A15 compounds also undergo structural transformation (cubic to tetragonal). However relative changes in $M\langle\omega^2\rangle$ calculated from the phonon spectra (from neutron and tunnelling experiments) do not account for the change in λ calculated from measured T_c.

In this paper we report our investigations on the instability of the β phase in niobium-titanium alloys and its consequence to the normal state and superconducting properties. Structural investigations carried out using x-ray and TEM on a series of Nb-Ti alloys and the measurements of resistivity, the superconducting transition temperature and the variation of the upper critical field with temperature will be presented. We point out a mechanism for the observed enhancement of the normal state resistivity (ρ_n) of these alloys which can be controlled at will. Enhancement of $H_{c2}(0)$ also occurs which is inferred to be about 17–18 tesla at a ρ_n value of 100 $\mu\Omega$ cm. Some remarks will be made concerning the present route for commercial fabrication of these alloy wires.

2. Niobium-titanium

Niobium-titanium alloys are the most widely used superconductors. When quenched from high temperatures (900°C), these alloys can generally be retained in the β (bcc) phase. The retained β phase is metastable and the instability is relieved by a variety of low temperature structural transformations. Commercial alloys are Ti-rich per atom-wise despite the fact that T_c has a peak on the Nb-rich side (Larbalestier 1981). The reason for this comes basically from the anomalous increase in ρ_n as Ti concentration is increased. This increase in ρ_n more than compensates for the slight decrease in γ, the electronic specific heat coefficient and T_c, resulting in an enhancement of H_{c2}. Thus this instability can have a bearing on the training and degradation behaviour observed in superconducting magnets. Evidence now exists for stress-induced low temperature structural transformation (Obst *et al* 1980) which results in the reduction of ρ_n (Hariharan *et al* 1984, 1986a).

2.1 *Phase diagram*

The equilibrium phase (Collings 1983) consists of hcp α at the Ti end and goes over to a mixture of α (formation is sluggish; obtained by prolonged heating above 400°C) and bcc β as the Nb concentration is increased. A spontaneous martensitic transformation stabilizes the alloy in the Ti-rich side forming α'' orthorhombic phase. The metastable β can also decompose into other metastable hexagonal ω phases. These are the athermal ω which forms diffusionless and reversibly on cooling and the thermal ω which forms as a result of moderate annealing (200–400°C). Thermal and athermal ω phases have the same hexagonal crystal structure and may vary slightly in composition. The unit cell is hexagonal with atoms at the positions (000), $\pm$(1/3, 2/3, u), u being 0·48 to 0·50.

CC-0. In Public Domain. Gurukul Kangri Collection, Haridwar

Digitized by Arya Samaj Foundation Chennai and eGangotri

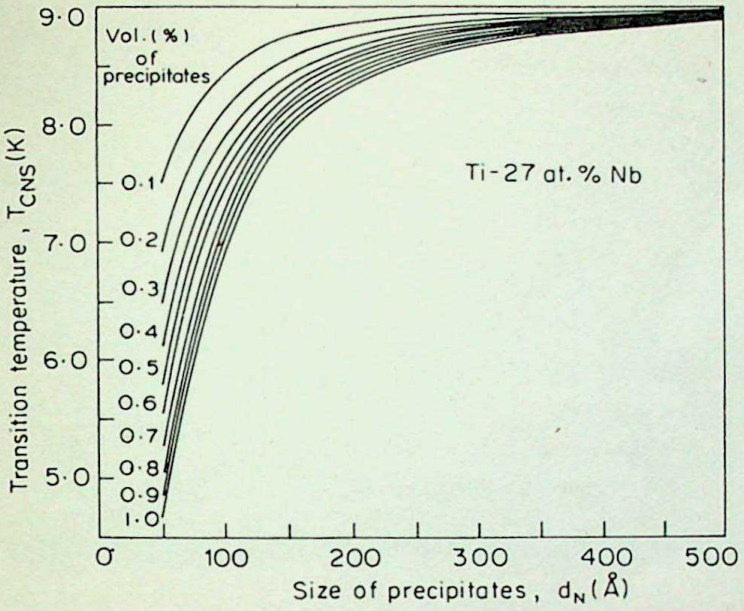

Figure 1. Calculation of the proximity effect controlled T_{cNS} between the superconducting β matrix and the second phase normal precipitates.

Athermal ω precipitates are submicroscopic with a size of about 50 Å and a large number density, whereas thermal ω forms by nucleation and growth, the average size depending on the temperature of annealing. ω precipitates form predominantly till the lower limit of retention of β phase. This phase boundary is however not sharp and ω instabilities may persist with decreasing magnitude all the way till pure Nb.

3. Transition temperature

For an alloy of any particular composition, T_c is known to increase generally with aging at relatively low temperatures (e.g. 400°C) (Savitskii *et al* 1973). This effect had been erroneously attributed to Nb enrichment of the alloy matrix as a result of formation of the second phase precipitates α and ω. This in fact is due to the varying extent of the superconducting proximity effect between the good superconducting β matrix and the poorly superconducting second phase precipitates (Hariharan *et al* 1981). Figure 1 shows a calculation of the proximity effect controlled T_c as a function of the size and the volume fraction of the normal precipitates that evolve on thermal aging with time. This is in agreement with the experimental situation and is generally applicable to all titanium-transition metal alloy systems.

4. Structural transformations and anomalous resistivity

Figure 2 shows the resistivity behaviour of a series of Nb-Ti alloys (Hariharan *et al* 1984). Figure 3 shows ρ_n (before the onset of T_c) and $d\rho/dT$ for the same alloys. As the Ti concentration is increased $d\rho/dT$ decreases. For the Nb-83 at% Ti alloy (designated as Ti-83) an α'' transformation stabilizes the β phase and $d\rho/dT$ is positive. When 1 at% nitrogen is added to this alloy (Ti 83 N), the resistivity behaviour completely changes,

CC-0. In Public Domain. Gurukul Kangri Collection, Haridwar

Digitized by Arya Samaj Foundation Chennai and eGangotri

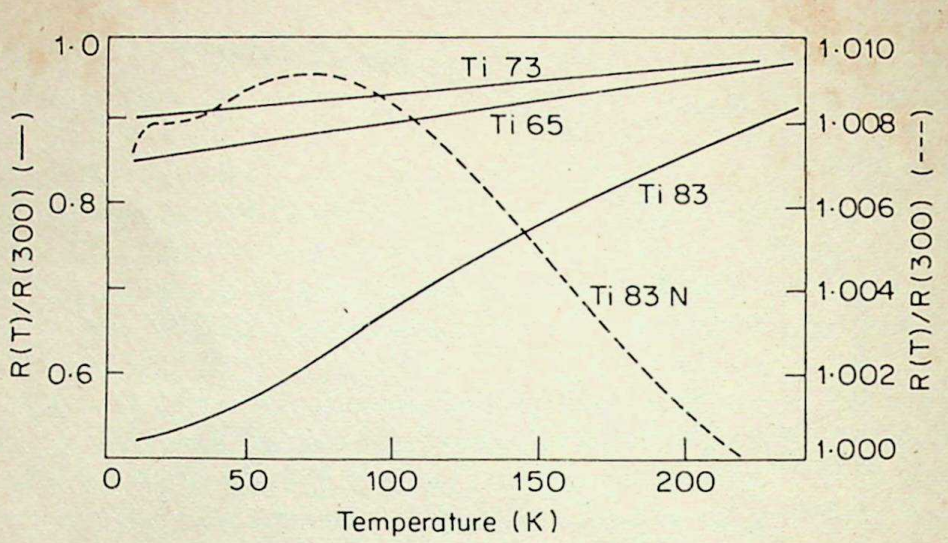

Figure 2. Resistivity vs temperature of several Nb-Ti alloys: (1) Ti83, (2) Ti83N, (3) Ti65, (4) Ti73.

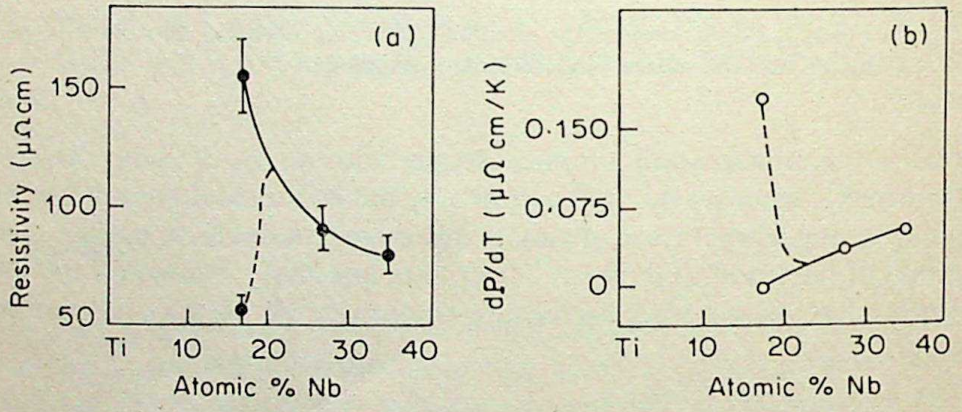

Figure 3. Normal state resistivity ρ_n and $d\rho/dT$ of Nb-Ti alloys as a function of concentration. Point at the end of the dashed line represents the value in the martensitic phase. Full line represents β phase alloys.

ρ_n increases three times and $d\rho/dT$ becomes negative to trend with the other Nb richer alloys.

X-ray and TEM investigations reveal that Ti83 is mostly orthorhombic α'' (figure 4a) whereas Ti83N is bcc β. The other alloys Ti73 and Ti65 are also in the β phase. The TEM pattern in figure 4b for Ti83N is completely unlike figure 4a and shows microstructural features on a fine scale. The selected area diffraction shown in figure 4c also corresponds to Ti83N and indicates pronounced streaking indicative of ω reflections.

Results of a very similar nature have been reported by Hochstuhl and Obst (1982) for the alloy Ti78. Here a stress-induced martensitic transformation to α'' makes $d\rho/dT$ turn positive from an initial negative value in the β quenched state. Thus the decreasing $d\rho/dT$ as Ti concentration increases (while the alloy is still in the β phase), manifesting in the extreme as negative, indicates the increasing amount of instability of the β phase to ω formation. Viewed in detail a slope change in the ρ vs T observed for Ti73 (Hariharan *et al* 1981) around 35 K can be interpreted as being due to athermal ω formation. For the case Ti83N, this happens at a much higher temperature, viz., around 100 K.

CC-0. In Public Domain. Gurukul Kangri Collection, Haridwar

Digitized by Arya Samaj Foundation Chennai and eGangotri

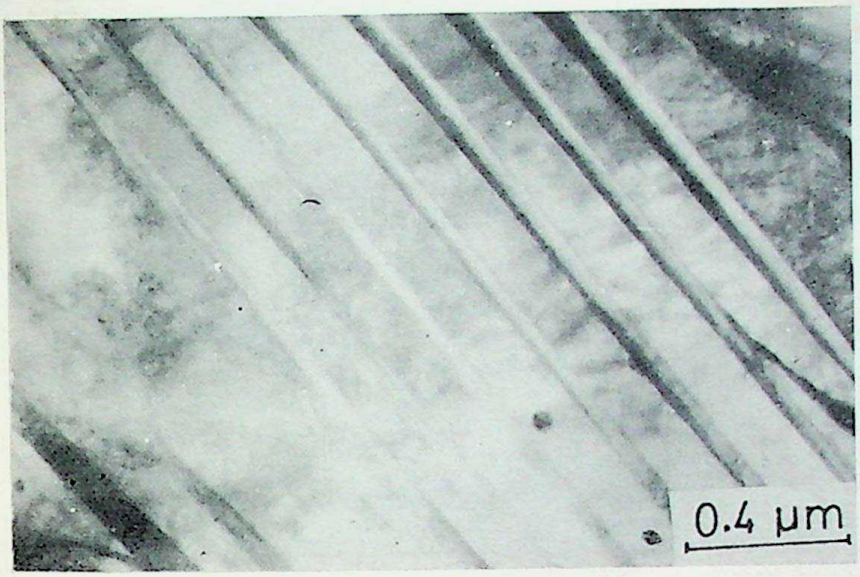

Figure 4a. TEM micrograph for Ti83. Plate-like structure corresponds to α'' martensite.

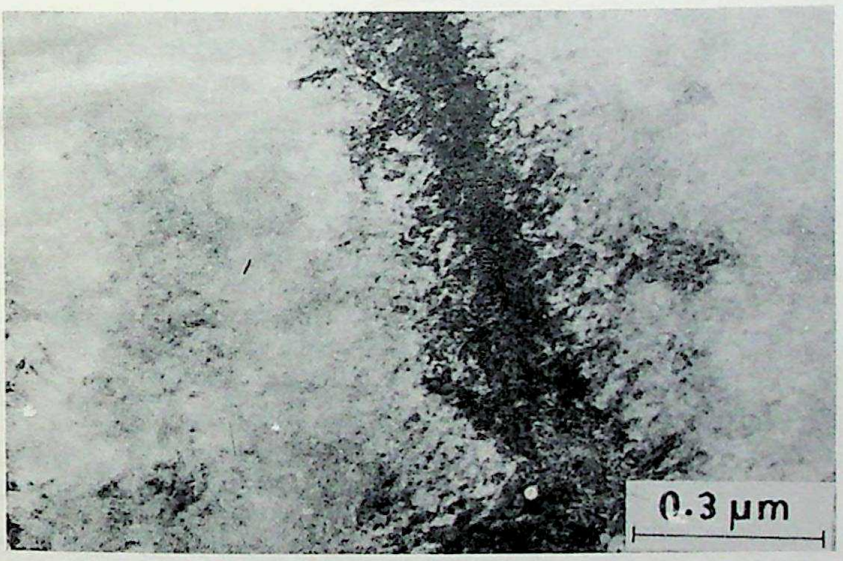

Figure 4b. Bright field micrograph for Ti83N. Microstructural features on a very fine scale are seen.

5. Origin of the anomalous resistivity

Many Ti-transition metal alloys such as Ti-Cr (Chandrasekaran *et al* 1974), Ti-V (Prekul *et al* 1974) and Ti-Mo (Ho and Collings 1972) have shown small or negative $d\rho/dT$ and hence high ρ_n in the concentration range that is prone maximum to athermal ω transformation. Many mechanisms have been proposed for the origin of this anomalously high resistivity (Collings 1974). β to ω transformation can be effected by a sequential displacement of (111) planes (Sikka *et al* 1981). The 'dynamical ω fluctuations' can then be represented by a double well potential representing the β and ω positions. The height of the barriers and their energy difference Δ will depend upon the local Nb concentration, local strain and the number of planes taking part in the

CC-0. In Public Domain. Gurukul Kangri Collection, Haridwar

Digitized by Arya Samaj Foundation Chennai and eGangotri

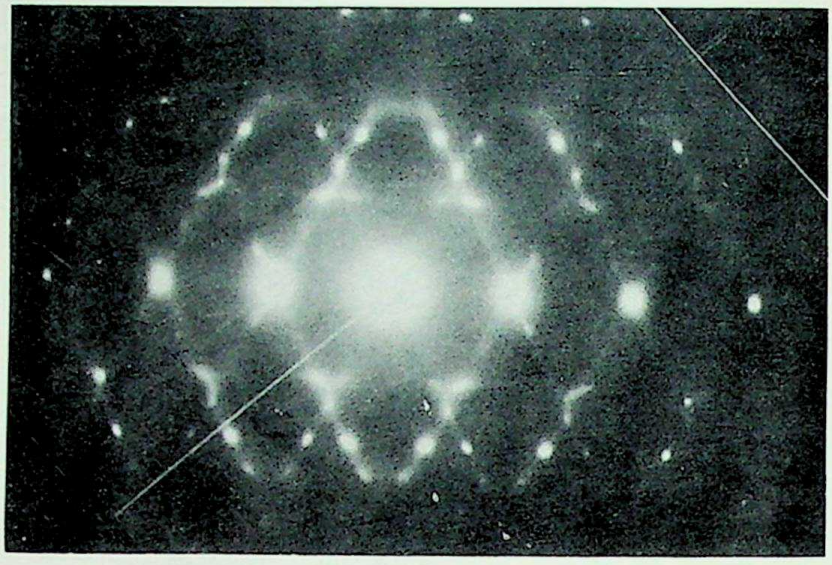

Figure 4c. Selected area diffraction pattern of a region in 4b. Intense streaking ⟨111⟩ indicates ω instability. Parent structure is bcc.

transformation. Cochrane *et al* (1975) derived a relation for the electrical resistivity of a system exhibiting such a 'two-level' (TLS) behaviour (Anderson *et al* 1972)

$$\rho(T) = A + \rho_n(T) + B \ln(T^2 + \Delta^2), \tag{3}$$

where A, B and Δ are constants. $\rho_n(T)$ is the usual phonon term and can be determined from a reference system not exhibiting such a resistance anomaly. This is generally difficult in Nb-Ti alloys as the ω instability which is responsible for the anomalous behaviour persists all the way upto pure Nb. However this contribution has been taken from the Ti83 alloy which has undergone the α'' martensitic transformation and is therefore devoid of the ω instability.

The fitting of the resistivity behaviour (Hariharan *et al* 1986b) of the Nb-Ti alloys to the above expression is satisfactory. Such a fit is shown in figure 5 for the alloy Ti83N. The departure of the fit from the experimental points at a high temperature is due to the decreasing importance of the ω instability and shows the inadequacy of the Ti83 alloy to represent the phonon term due to its different crystal structure. At the low temperature end departure from experimental points comes about because of the β to ω transformation having actually taken place. In this case an additional resistance will come into picture because of the β to ω interfaces.

The fluctuations associated with the ω instability are the most dominant scatterers of electrons and they persist even after the β to ω transformation has taken place. Physically this comes about because of the lifetimes of 10^{-7} sec associated with the dynamical ω fluctuations (Lin *et al* 1976). This is very large compared to the electronic life-times. The electrons can thus distinguish between the two low-lying degrees of freedom and get scattered. The ρ_n value of $154 \pm 15\,\mu\Omega\,\text{cm}$ for the alloy Ti83N is probably the largest reported for the Nb-Ti system so far.

CC-0. In Public Domain. Gurukul Kangri Collection, Haridwar

Digitized by Arya Samaj Foundation Chennai and eGangotri

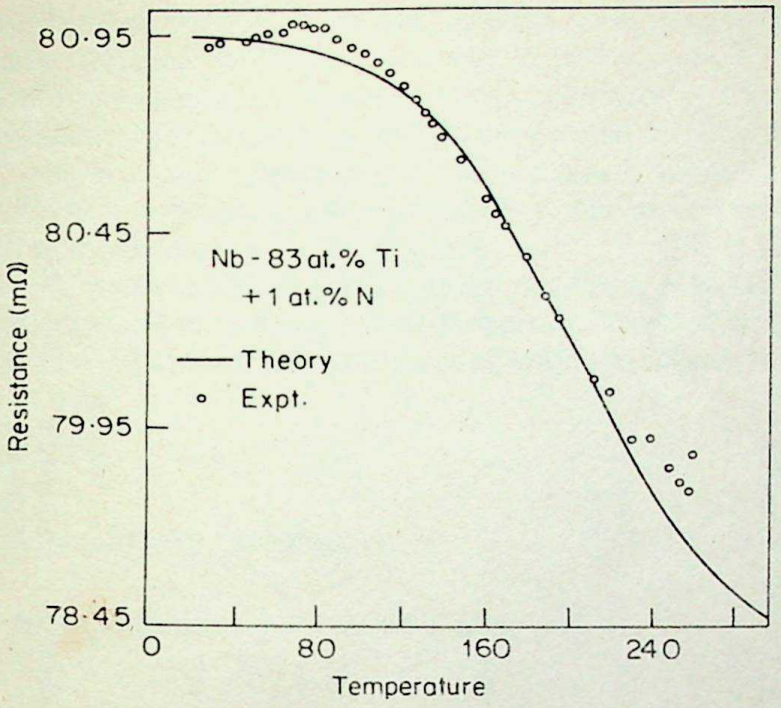

Figure 5. Experimentally measured resistivity and theoretical fit to eqn (3) for Ti83N.

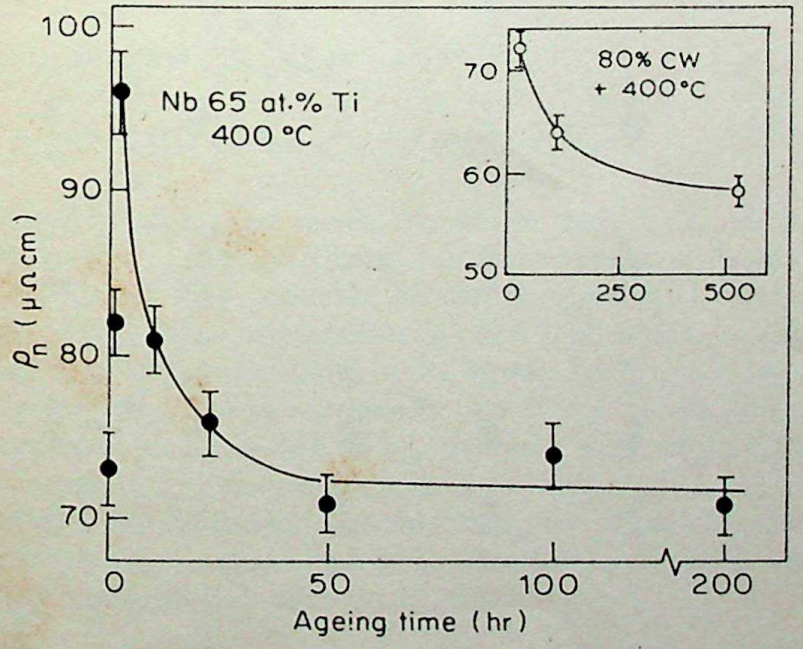

Figure 6. Variation of resitivity as a function of aging at 400°C for Ti65 which was originally β quenched. The alloy in the inset was 80% cold-worked after β quenching.

6. Upper critical field

The enhanced resistivity in the Nb-Ti alloys which is directly related to the inherent instability of the β phase to ω transformation leads to enhancement in $H_{c2}(0)$ in the alloys used for commercial production of superconducting wire. Figure 6 shows the evolution of ρ_n as a function of aging time at 400°C for the β quenched Ti 65, an alloy

CC-0. In Public Domain. Gurukul Kangri Collection, Haridwar

Table 1. Upper critical fields and associated parameters in Nb-Ti alloys ($\gamma = 9{\cdot}9$ mJ mol^{-1} K^{-2}, assumed the same for all alloys)

Alloy	T_c(K)	ρ_n $\mu\Omega$cm	$-dH_{c2}/dT$ T/K	$\mu_0 H^*_{c2}(0)$ T	$H_{c2}(0)$ (Maki) T	$H_{c2}(0)$ calculated T	H_{c2} measured T	$H_{c2}(0)$ WHH T
Ti65 β quencehd	8·97	73 ± 1·8	2·49	18·9	9·9	15·5	11 at 4·2 K	13·04 for $\lambda_{s0} = 0{\cdot}5$ 15·75 for $\lambda_{s0} = 3{\cdot}0$
Ti65 β quenched 1 hr at 400°C	8·82	82 ± 2·1	2·58	20·9	10·1	15·8	11·5 at 4·2 K	
Ti65 β quenched 2 hr at 400°C	8·79	96 ± 2·4	2·72	24·4	10·4	16·6		14·5 for $\lambda_{s0} = 0{\cdot}5$ 19·1 for $\lambda_{s0} = 3{\cdot}0$
Ti65 β quenched 80% CW 400°C 110 hr	9·23	64 ± 1·6	2·37	17·0	9·8	15·2		
Ti65 β quenched 80% CW 400°C 525 hr	9·35	58 ± 1·5	2·27	15·7	9·6	14·7		
Ti64·2 Hawksworth and Larbalestier (1980)	9·0	65	2·64	16·9		16·46	11·5 at 4·2 K 14·25 at 2 K	
Ti65 + 10% Ta Hawksworth and Larbalestier (1980)	8·6	67	2·76	16·6		16·44	11·6 at 4·2 K 15·4 at 2 K	

Digitized by Arya Samaj Foundation Chennai and eGangotri

CC-0. In Public Domain. Gurukul Kangri Collection, Haridwar

Digitized by Arya Samaj Foundation Chennai and eGangotri

used widely. After a sharp initial increase, ρ_n starts falling and saturates for long time aging. This is a consequence of the growth of the ω precipitates. TEM results (Terrance *et al* 1986) confirm the sluggishness of the growth of ω particles after about 100 hours of aging. The initial sharp increase in ρ_n is attributed to the formation of very small sized (< 50 Å) ω particles (or ω fluctuations) by the mechanism discussed earlier. The inset in figure 6 shows the resistivity of cold-worked alloy. The more rapid fall of ρ_n is due to precipitation of α (Terrance *et al* 1986).

Table 1 shows the measured H_{c2} at 4·2 K (De *et al* 1986), $\mathrm{d}H_{c2}/\mathrm{d}T|_{T_c}$ (Hariharan *et al* 1986c) along with other normal state properties. The following well-established relationships have been used (Hariharan *et al* 1986c) to calculate the various critical fields listed in table 1.

Orbital critical field

$$\mu_0 H^*_{c2}(0) = 3{\cdot}11 \times 10^3 \gamma \rho_n T_c, \tag{4}$$

$$H_{c2}(0)\ \text{(calculated)} = -0{\cdot}693\, T_c (\mathrm{d}H_{c2}/\mathrm{d}T)|_{T_c}. \tag{5}$$

Maki parameter

$$\alpha = 2{\cdot}35 \times 10^3 \gamma \rho_n, \tag{6}$$

$$H_{c2}(0)\ \text{Maki} = H^*_{c2}(0)\ (1+\alpha^2)^{-1/2}, \tag{7}$$

$$H_{c2}(0)\ \text{WHH} = h^*(\alpha, \lambda_{so})\ H^*_{c2}(0)/0{\cdot}693. \tag{8}$$

We can draw some important conclusions from table 1. $H_{c2}(0)$ calculated from the measured values of $\mathrm{d}H_{c2}/\mathrm{d}T$ and T_c (superconducting state measurements) are closer to the actual $H_{c2}(0)$ and may probably be used to predict $H_{c2}(0)$. Alloying additions (Hawksworth *et al* 1980) do not increase H_{c2} at 4 K although a significant increase has been seen at 2 K. On the other hand in the binary Ti65, enhancing ρ_n by β instability mechanism enhances H_{c2}(4 K) marginally and $H_{c2}(0)$ calculated significantly. $H_{c2}(0)$ calculated increases as a function of ρ_n, reaches a peak around 100 $\mu\Omega$ cm but falls further due to paramagnetic limiting factors. A limit of about 17 T may probably be reached in Nb-Ti. During the commercial fabrication of the alloys into wires, the series of thermomechanical treatments have the effect of greatly reducing ρ_n (see figure 6). This will have a detrimental effect on $H_{c2}(0)$.

7. Conclusion

It is seen that in Nb-Ti, the instability of the β phase controls the resistivity and thereby influences the upper critical field. The decomposition of the β phase resulting in the structural transformation to $\beta+\omega$ or $\beta+\alpha$ greatly reduces the resistivity. T_c is marginally influenced through the superconducting proximity effect.

We have not explicitly considered here the phonon anomalies that may be associated with the β phase instability. This is an area not much reported upon. It may be possible

CC-0. In Public Domain. Gurukul Kangri Collection, Haridwar

Digitized by Arya Samaj Foundation Chennai and eGangotri

to retain the incipient instability of the β phase without forming ω precipitates. This may open up newer avenues for raising T_c and the other superconducting properties. Mention may be made of the observation of 'extra-ordinarily high T_c' of 16·5 K in $Nb_{40}Zr_{60}$ under pressure by Kawamura *et al* (1984) although the reasons are not known.

Acknowledgements

This paper is a summary of about 5 years of work on Nb-Ti in the author's laboratory. Much of the work mentioned here has formed a part of Mr Y Hariharan's Ph.D. thesis. Many colleagues contributed to the present author's understanding of the field in these years. The author would like to acknowledge many discussions he had with Mr Y Hariharan, Mr V S Sastry, Dr U De, Dr V S Raghunathan and Mr A L E Terrance. He also acknowledges the support received for the superconductivity programme from Mr C V Sundaram, Director of our Centre, Dr G Venkataraman and Dr P Rodriguez.

References

Allen P B 1980 in *Dynamical properties of solids.* (Ed) G K Horton and A A Maradudin (Amsterdam: North Holland) Vol. 3, p. 95

Anderson P W, Halperin B I and Varma C M 1972 *Philos. Mag.* **25** 1

Chandrasekaran V, Taggart R and Polonis D H 1974 *J. Mater. Sci.* **9** 961

Cochrane R W, Harris R, Strom-Olson J O and Zuckermann M J 1975 *Phys. Rev. Lett.* **35** 676

Collings E W 1974 *Phys. Rev.* **B9** 3989

Collings E W 1983 *Sourcebook on titanium alloy superconductivity* (New York: Plenum) p. 215

De U, Hariharan Y and Radhakrishnan T S 1986 (to be published)

Geballe T H 1983 in *Advances in superconductivity*, Nato ASI series 100 (eds) B Deaver and J Ruvalds (New York: Plenum) p. 387

Hawksworth D G and Larbalestier D C 1980 in *Advances in cryogenic engineering materials* (eds) A F Clark and R P Reed (New York: Plenum) **26** 479

Hariharan Y, Valsakumar M C and Radhakrishnan T S 1981 *J. Low Temp. Phys.* **43** 341

Hariharan Y, Terrance A L E and Radhakrishnan T S 1984 *17th Int. Conf. on Low Temp. Phys. Karlsruhe* (eds) V Eckern, A Schmid, W Weber and H Wuhl (Amsterdam: Elsevier) p. 1371

Hariharan Y, Janawadkar M P, Radhakrishnan T S, Terrance A L E, Dixit G A and Raghunathan V S 1986a *Pramana – J. Phys.* (to appear)

Hariharan Y, Janawadkar M P and Radhakrishnan T S 1986b *Solid State Commun.* (to appear)

Hariharan Y, Sastry V S, Janawadkar M P and Radhakrishnan T S 1986c Presented at the Int. Conf. on Cryogenic Engg. (ICEC 11) Berlin

Ho J C and Collings E W 1972 *Phys. Rev.* **B6** 3727

Hochstuhl P and Obst B 1982 *J. Phys.* (*Paris*) **43** 133

Kawamura H, Wittig J, Bireckoven B and Buckel W 1984 *Physica* **B126** 485

Larbalestier D C 1980 in *Advances in cryogenic engineering materials* (eds) A F Clark and R P Reed (New York: Plenum) **26** 10

Lin W, Splat H and Batterman B W 1976 *Phys. Rev.* **B13** 5158

Obst B, Pattanayak D and Hochstuhl P 1980 *J. Low Temp. Phys.* **41** 595

Prekul A F, Rassokhin V A and Volkenshtein N V 1974 *Sov. Phys. JETP* **40** 1134

Savitskii E M, Baron V V, Efimov Yu V, Bychkova M J and Myzenkova L F 1973 *Superconducting materials* (New York: Plenum)

Sikka S K, Vohra Y K and Chidambaram R 1981 *Progr. Mater. Sci.* **27** 245

Smith T F and Finlayson 1980 *Contemp. Phys.* **21** 265

Terrance A L E, Raghunathan V S and Radhakrishnan T S 1986 (to be published)

CC-0. In Public Domain. Gurukul Kangri Collection, Haridwar

Digitized by Arya Samaj Foundation Chennai and eGangotri

Pramāṇa – J. Phys., Vol. 28, No. 5, May 1987, pp. 565–571. © Printed in India.

Theoretical studies on magnetic superconductors

R JAGADISH and K P SINHA

Division of Physical and Mathematical Sciences, Indian Institute of Science, Bangalore 560 012, India

Abstract. The discovery of magnetic superconductors has posed the problem of the coexistence of two kinds of orders (magnetic and superconducting) in some temperature intervals in these systems. New microscopic mechanisms developed by us to explain the coexistence and reentrant behaviour are reported. The mechanism for antiferromagnetic superconductors which shows enhancement of superconductivity below the magnetic transition is found relevant for rare-earth systems having less than half-filled f-atomic shells. The theory will be compared with the experimental results of $SmRh_4B_4$ system. A phenomenological treatment based on a generalized Ginzburg-Landau approach will also be presented to explain the anomalous behaviour of the second critical field in some antiferromagnetic superconductors.

These magnetic superconductors provide two kinds of Bose fields, namely, phonons and magnons which interact with each other and also with the conduction electrons. Theoretical studies of the effects of the excitations of these modes on superconducting pairing and magnetic ordering in these systems will be discussed.

Keywords. Magnetic superconductors; second critical field; coexistence; enhancement of superconductivity.

PACS Nos 74·70; 74·90

1. Introduction

The discovery of a large number of magnetic superconductors in the last ten years has led to considerable amount of theoretical and experimental investigations. It was believed that these two kinds of cooperative states were mutually exclusive. In the singlet superconductors we have ordering of conduction electrons in the momentum space in the time-reversed state ($\mathbf{k}\uparrow$; $-\mathbf{k}\downarrow$). In magnetic cooperative phenomena, we have ordering of magnetic moments in the ordinary space. It was thought that the generation of large internal fields in magnetic superconductors would destroy time reversal symmetry and hence suppress singlet superconductivity completely.

The appearance of both kinds of orders in some temperature intervals and even their coexistence in some rare earth compounds had posed theoretical challenges and opened avenues for new experiments. A vast amount of literature has been gathered in the last few years. We shall not review here the present status of experimental results and various theoretical models developed. These are now available in two review articles (Shrivastava and Sinha 1984; Bulaevskii *et al* 1985). We shall, therefore, address ourselves to some specific systems and specific properties. The coexistence is most pronounced in antiferromagnetic superconductors (RRh_4B_4, R = Nd, Sm, Tm; RMo_6S_8, R = Gd, Tb, Dy). The system RMo_6S_8 exhibits anomalous depression of H_{C2} (second critical field) near but below T_N. For $SmRh_4B_4$, H_{C2} increases below T_N

CC-0. In Public Domain. Gurukul Kangri Collection, Haridwar

Digitized by Arya Samaj Foundation Chennai and eGangotri

after a break in slope, suggesting an enhancement of superconductory in this system with the onset of antiferromagnetic ordering (Maple 1982). The mechanism involving suppression of magnetic scattering below T_N alone will not be adequate to explain the observed enhanced superconducting pair density. For example in $TmRh_4B_4$ one gets a depression of H_{C2} below T_N. In fact a bell-shaped curve for H_{C2} versus temperature (T) is obtained (Hamaker *et al* 1981). It would appear therefore that the state of rare-earth ions in the crystal is important in determining the mechanism of enhancement. The most obvious difference is that for all those systems where depression of H_{C2} below T_N occurs the rare earth ions have half-filled or more than half-filled f-shells. The systems showing enhancement (e.g., $SmRh_4B_4$) have rare earth ion (e.g. Sm) containing less than half-filled f-shell. This situation makes the emergence of a new mechanism possible which can be strong enough to counter the exchange scattering mechanism and, in effect, lead to the enhancement of the strength of superconducting pairing interaction below the antiferromagnetic ordering temperature. In what follows, we shall discuss the role of one such mechanism (Sinha 1979).

Furthermore, in magnetic superconductors we can produce real boson fields e.g. magnons and phonons by the application of appropriate fields. The presence of such Bose fields will be explored in the context of enhancement or suppression of superconducting pairing and magnetic order.

2. Mechanism and enhancement of superconducting order

The Hamiltonian for the system comprising conduction electron derived from Rh 4d orbitals, localized f electrons and various interactions can be written as

$$H=\sum_{\mathbf{k}\sigma}(\varepsilon_{\mathbf{k}}-\mu)\,C^{+}_{\mathbf{k}\sigma}\,C_{\mathbf{k}\sigma}+\sum_{n}E_n\,C^{+}_{n\sigma}\,C_{n\sigma}$$
$$-V\sum_{\mathbf{k}\mathbf{k}'}C^{+}_{\mathbf{k}'\uparrow}\,C^{+}_{-\mathbf{k}'\downarrow}\,C_{-\mathbf{k}\downarrow}\,C_{\mathbf{k}\uparrow}$$
$$+\left(\sum_{\mathbf{k}lm}g^{lm}_{\mathbf{k}}\,C^{+}_{l\uparrow}\,C^{+}_{m\downarrow}\,C_{-\mathbf{k}\downarrow}\,C_{\mathbf{k}\uparrow}+\text{h.c.}\right)+\sum_{lm}H_{lm}\,(\text{ex}), \tag{1}$$

where the first two terms are the conduction electron (creation, annihilation) operators $C^{+}_{\mathbf{k}\sigma}$, $C_{\mathbf{k}\sigma}$ for the Bloch state $|\mathbf{k}\sigma\rangle$, and rare-earth site localized (creation, annihilation) operators ($C^{+}_{n\sigma}$, $C_{n\sigma}$), at site $\mathbf{R}_n$ with single particle energies ($\varepsilon_{\mathbf{k}}$ = conduction electron energy, E_n = rare earth localized electron energy). The third term is the usual phonon mediated BCS pairing interaction between conduction operators, V being the interaction coefficient. The fourth term is the new interaction, involving conduction electron pairs making transition to localized states at sites l and m respectively; $g^{lm}_{\mathbf{k}}$ being the interaction constant. The last term $\sum_{lm}H_{lm}(\text{ex})$ represents the effective exchange interaction between rare-earth magnetic ions which may arise from various mechanisms (direct and indirect). Here l and m run over two magnetic sublattices respectively. The effect of the new interaction (cf fourth term of equation (1)) can be taken account either in the gap function (Sinha 1979), or in giving an additional pairing

CC-0. In Public Domain. Gurukul Kangri Collection, Haridwar

Digitized by Arya Samaj Foundation Chennai and eGangotri

interaction which depends on antiferromagnetic order. In the present paper, we shall follow the latter procedure. This term in the first order can be eliminated by a suitable canonical transformation. This leads to an interaction term which gives BCS like pairing of two conduction electrons but the coefficient depends on the antiferromagnetic order. In fact, it can be shown to depend on sub-lattice magnetization and hence the strength of this interaction will increase with sublattice magnetization as the temperature is decreased below T_N (the Ne'el temperature). The new pairing interaction can be explicitly written as (Jagadish and Sinha 1986),

$$-\sum_{\mathbf{k}\mathbf{k}'}\left(\sum_{lm}\frac{g_{\mathbf{k}}^{lm}\, g_{\mathbf{k}}^{lm*}}{\Delta E_0}(|S_l^z|+|S_m^z|)\right) C_{\mathbf{k}'\uparrow}^{+}\, C_{-\mathbf{k}'\downarrow}^{+}\, C_{-\mathbf{k}\downarrow}\, C_{\mathbf{k}\uparrow}\,. \tag{2}$$

Combining this with BCS pairing interaction, the effective pairing interaction can be recast in the form

$$\lambda_{\text{eff}}=\lambda_{\text{BCS}}[1+\alpha_m\, m(T)]$$

or

$$\bar{V}N(0)=VN(0)\,[1+\alpha\, m(T)]=V\bar{N}(0), \tag{3}$$

where $m(T)$ is the reduced sub-lattice magnetization $m(T)=M(T)/M(0)$ and α_m is the coefficient. The magnetic exchange scattering considered by Machida (1980) (who extended the treatment of Abrikosov and Gorkov 1961), namely, $(I/2N)\,(g_J-1)\,\mathbf{J}\cdot\sigma$ where $\mathbf{J}$ is the rare-earth ion angular momentum, g_J the Lande factor, I the exchange constant for scattering between conduction electrons and localized magnetic moments, also leads to a similar expression but with opposite sign.

$$-\alpha m(T), \tag{4}$$

where

$$\alpha=\frac{1}{4\pi}(g_J-1)\,[J(J+1)]^{1/2}\,\frac{|I|}{\varepsilon_F\, VN(0)}, \tag{5}$$

ε_F being the Fermi energy. Owing to the appearance of this form it is convenient to define α_m as the sum total of the new attractive interaction suggested here and the magnetic exchange scattering effect. More explicitly

$$\alpha_m=\alpha_c-\alpha, \tag{6}$$

where α_c arises from the new interaction (pair healing). For rare earth ions having more than half-filled f-shells, the energy denominator ΔE_0 is very high (owing to the existence of two electrons in the same orbital) and α_c will be much weaker than α. However, for less than half-filled shells, this is not so and α_c is likely to be larger than (or comparable with) α. In such situations, α_m is positive and one will have enhancement of superconducting pairing. In figure 1, we compare the experimental data on $SmRh_4B_4$ with the calculated curve for the second critical field H_{C2} against temperature. For this purpose we compute the gap function $\Delta(T)$ in the regions $T_C>T>T_N$ and $T_N>T>0$. In the latter portion the role of the new mechanism is taken into account. Having computed the gap function, H_{C2} is calculated via H_C, namely,

$$H_{C2}=\sqrt{2}\,\kappa\, H_C, \tag{7}$$

CC-0. In Public Domain. Gurukul Kangri Collection, Haridwar

Digitized by Arya Samaj Foundation Chennai and eGangotri

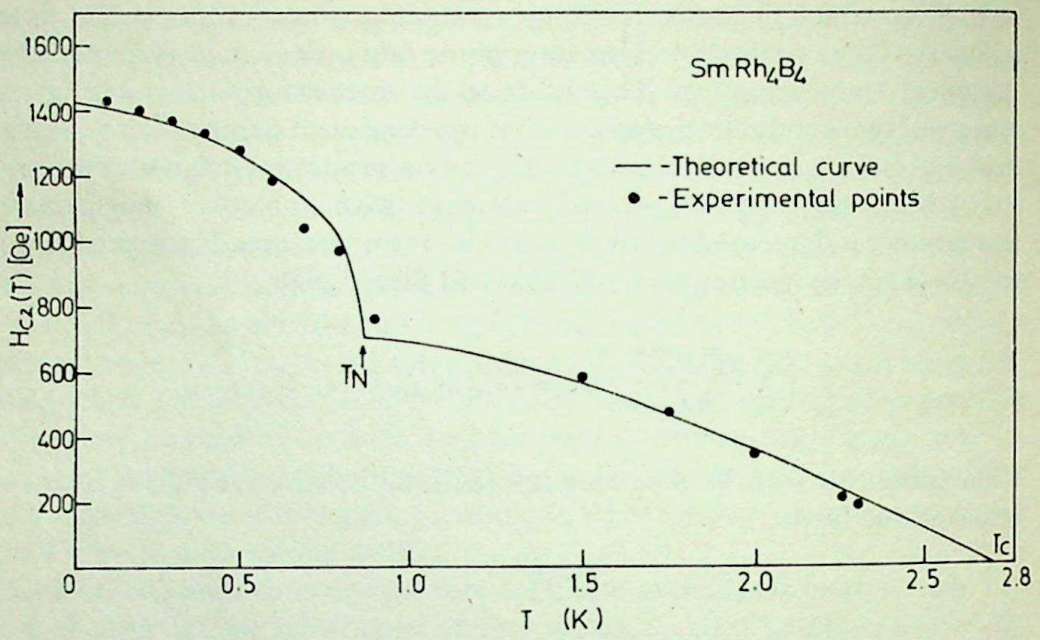

Figure 1. Temperature dependence of the critical field H_{C2} in $SmRh_4B_4$. The enhancement of H_{C2} below T_N is a direct result of the additional positive contribution to the interaction strength or equivalently to the density of states $N(0)$. Below T_N the coefficient of the BCS term in the Hamiltonian is $N(0)\,V(1+\alpha_m\,m(T))$. The value used for $N(0)$ is 0·57 states/eV-atom-spin direction, that for α_m is 0·2. The form $[1-(T/T_N)]^{0\cdot5}$ is used for $m(T)$. A constant value of $\kappa=2\cdot1$ is assumed for the region above T_N. Since κ depends on the density of states, which changes below T_N, the average value of $\kappa(=1\cdot55)$ below T_N is different.

$$\frac{-H_C^2}{8\pi} = -\frac{1}{2}N(0)\,\Delta^2 - N(0)\,\Delta^2 \ln\left|\frac{\Delta_0}{\Delta}\right| - 4\,N(0)\,k_B\,T\int_0^{\hbar\omega_D} d\varepsilon \ln\left[1+\exp(-\beta\varepsilon)\right] + \frac{1}{3}\pi^2\,N(0)\,(k_B\,T)^2. \tag{8}$$

The agreement between calculated and experimental values is satisfactory.

3. Phenomenological treatment

The phenomenological treatment for the temperature dependence of the second critical field H_{C2} for an antiferromagnetic superconductor is given in terms of a generalized Ginzburg-Landau (GGL) theory (Mahanti *et al* 1981) involving two order parameters $\psi(\mathbf{r})$ and $M(\mathbf{r})$. The Gibbs free energy of the system

$$G(T, \mathbf{H}; \psi, \mathbf{h}, \mathbf{M}) = F_S(T, \psi, \mathbf{h}) + F_m(T, \mathbf{M}) + F_{Sm}(T, \psi, \mathbf{M}) - \frac{1}{4\pi}\int (\mathbf{h}\cdot(\mathbf{H}+4\pi\,\mathbf{M}))\,dr, \tag{9}$$

CC-0. In Public Domain. Gurukul Kangri Collection, Haridwar

Digitized by Arya Samaj Foundation Chennai and eGangotri

where $F_S(T, \psi, \mathbf{h})$ is the Helmholtz free energy of a superconductor characterized by a microscopic field $\mathbf{h}(r)$. This includes the term $(1/8)\int h^2\,\mathrm{d}r$. Explicitly

$$F_S(T, \psi, \mathbf{h}) = \int \mathrm{d}\mathbf{r}\,[\tfrac{1}{2}\,a|\psi^2 + \tfrac{1}{4}\,b|\psi|^4 + p_0|(\nabla - ir_0\,\mathbf{A})\,\psi|^2 + |\mathbf{h}(r)|^2/8\pi]$$

$$p_0 = \hbar^2/2m^*, \quad r_0 = 2e/\hbar c, \tag{10}$$

$$\tilde{F}_m(T, \mathbf{M}) = F_m(T, \mathbf{M}) + \int 2\pi\, M^2\,\mathrm{d}r, \tag{11}$$

$F_m(T, \mathbf{M})$ being the Helmholtz free energy of the rare earth magnetic system, and

$$F_{Sm}(T, \psi, \mathbf{M}) = \tfrac{1}{2}\int (\eta_1\,|\mathbf{M}|^2 + \eta_2\,|\nabla\,\mathbf{M}|^2)\,|\psi|^2\,\mathrm{d}r. \tag{12}$$

A few words about the coefficients η_1 and η_2 will be appropriate here. Here η_1 takes into account the combined effect of exchange (pair-breaking) scattering and the new mechanism (pair-healing) discussed in § 2. Thus the overall sign of η_1 will depend on the fact as to which of the two mechanisms is the dominant one in a particular system. Similarly for η_2 as we can approximate $\eta_2 = \xi^2\eta_1$, ξ being the superconducting coherence length. We get generalized G-L equations by minimizing G with respect to ψ^*, $\mathbf{h}$ and $\mathbf{M}$. The equations can be solved under various degrees of approximations. We shall write down only the important results. The effect of antiferromagnetic long range order on the superconducting order parameter to leading order in M turns out to be (on going over the q-space).

$$|\psi(T, \mathbf{M})| = |\psi(T, 0)|\left[1 - \frac{1}{b}\left\{(\eta_1 + \eta_2\,Q^2)/|\psi(T, 0)|^2 + \frac{4\pi\,Q^2\,\lambda^2(T, 0)}{|\psi(T, 0)|^4\,(1 + Q^2\,\lambda^2(T, 0))^2}\right\} M^2\right]^{1/2}, \tag{13}$$

where Q is the wave-vector defining antiferromagnetic order and λ is the London length. Thus we see that the effect of M on ψ can be of two types. First there is the electrodynamic effect whose strength depends on the quantity $Q\lambda$. This will act against the coexistence of non-zero $|\psi|$ and M. The second is the direct coupling effect whose strength depends on η_1 and η_2. This direct effect can go either way depending on the sign of η_1 and η_2.

If η_1 and η_2 are negative and adequately strong, then $\psi(T, M)$ will be enhanced below the magnetic transition. Now $\eta_1 = \eta_{1s} + \eta_{1c}$ where η_{1s} arises from pair-breaking and η_{1c} from the new mechanism. If the latter dominates then η_1 might become negative. This is expected to be the situation for $SmRh_4B_4$. When pair-breaking (exchange) scattering dominates we will have lowering of $\psi(T, M)$ below the magnetic transition.

These effects are experimentally seen clearly by measuring the second criterial field H_{C2} as a function of temperature (T). Accordingly, we shall give the highlights of these calculations on the basis of the generalized GL model for antiferromagnetic superconductors.

We consider the situation first without direct interaction between ψ and M (Mahanti *et al* 1981) i.e., $F_{sm} = 0$. For $H \approx H_{C2}$, the superconducting order parameter is small and one can linearize the GGL equations by keeping terms linear in ψ. The relevant

CC-0. In Public Domain. Gurukul Kangri Collection, Haridwar

Digitized by Arya Samaj Foundation Chennai and eGangotri

equations are

$$a\psi - 2p_0 (\nabla - ir_0 \mathbf{A})^2 \psi = 0. \tag{14}$$

$$\mathbf{h} = \mathbf{H} + 4\pi \mathbf{M} \equiv \nabla \times \mathbf{A}. \tag{15}$$

In the absence of an external field the magnetization density is taken to be of the form

$$\mathbf{M}(\mathbf{r}) = \hat{m} M_Q \cos \mathbf{Q} \cdot \mathbf{r} \tag{16}$$

where $\mathbf{Q}$ is the wave vector of AF order. In the presence of a field we have

$$\mathbf{M}(\mathbf{r}) = \hat{Z} \bar{\chi}(T) \mathbf{H} + \hat{m} M_Q(H, T) \cos \mathbf{Q} \cdot \mathbf{r}, \tag{17}$$

$\bar{X}$ being the average uniform ($q = 0$) susceptibility. Also the vector potential is separated into two parts i.e., $\mathbf{A} = \mathbf{A}_0 + \mathbf{A}_1$, with

$$\mathbf{A}_0 = \hat{y}(1 + 4\pi \bar{\chi}) Hx, \tag{18}$$

$$\mathbf{A}_1 = \frac{\hat{\mathbf{n}}\, 4\pi M_Q(H, T)}{Q} \sin \mathbf{Q} \cdot \mathbf{r}. \tag{19}$$

The solution for the second critical field is found to be

$$\frac{H_{C2}(T)}{H^0_{C2}(T)} = \frac{1}{1 + 4\pi\bar{\chi}} \left[1 - \left(\frac{4\pi M_Q}{H^0_{C2}} \right)^2 \frac{1}{(Q\xi)^2} \right], \tag{20}$$

where $H^0_{C2} = \phi_0 / 2\pi\xi^2$, ($\phi_0 = eh/2c$, the flux quantum) is the critical field in the absence of screening and effects arising from magnetic order. The above expression takes into account uniforming screening effect proportional to $(1 + 4\pi\bar{\chi})^{-1}$ which tends to suppress H_{C2} and an electrodynamic effect which depends on M_Q and suppresses H_{C2} below T_N. Computation for some actual systems shows that apart from giving a dip around T_N in a few systems (e.g. $Dy(Mo)_6S_8$), the indirect effect is not adequate to explain the observed lowering or enhancements in other systems. It appears, therefore, that we must take into account the direct coupling F_{sm}. This will introduce additional terms such as $(\eta_1 M^2 + \eta_2 |\nabla M|^2)\psi$ in (14); similarly for $M(r)$. Then the expected form for H_{C2} is given by

$$\frac{H_{C2}(T)}{H^0_{C2}} = \frac{1}{1 + 4\pi\bar{X}} \left[1 - \left(\frac{4\pi M_Q}{H^0_{C2}} \right)^2 \frac{1}{(Q\xi)^2} - (\eta_1 M_Q^2 + \eta_2 Q^2 M_Q^2) \xi^2 \right]. \tag{21}$$

If η_1 and η_2 have positive signs i.e., they are dominated by exchange scattering and pair-breaking effects, the additional terms will lead to lowering of $H_{C2}(T)$ below T_N. This is actually so in systems such as $TmRh_4B_4$ and $Dy(MO)_6S_8$ etc. However, when they have negative signs owing to the domination of the new mechanism, the additional terms will enhance $H_{C2}(T)$ below T_N. This is the case for $SmRh_4B_4$ where the new mechanism not only quenches exchange scattering but leads to the enhancement of the

CC-0. In Public Domain. Gurukul Kangri Collection, Haridwar

Digitized by Arya Samaj Foundation Chennai and eGangotri

superconducting order parameter and the second critical field below T_N. Thus the new mechanism, which operates in some systems effectively only when antiferromagnetic order sets in, leads to the enhancement.

4. Concluding remarks

In the foregoing sections, we have discussed the role of a new mechanism which involves transitions of a Cooper pair to two localized states with anti-parallel spins at two rare earth ion sites. This is found to be important for the enhancement for superconducting order in some systems ($SmRh_4B_4$). It can effectively quench exchange scattering and even lead to enhancement below T_N. Both microscopic and phenomenological treatments are discussed.

The gap function (both in the microscopic and phenomenological approaches) depends on the staggered magnetization below T_N in antiferromagnetic superconductors. The question naturally arises as to what effects will be produced when magnetization is changed by the excitation of spin wave modes. As the magnetization decreases on the excitation of these modes on the application of external perturbations one can expect either of the two possibilities. For systems dominated by exchange scattering, spin wave excitation will help superconducting order. On the other hand, when the new mechanism (pair-healing) dominates spin wave excitation will go in the opposite direction. It is worthwhile conducting experiments on magnetic superconductors and see what effects spin wave excitations produce on superconducting order-parameter or the second critical field.

References

Abrikosov A A and Gorkov L P 1961 *Sov. Phys. JETP* **12** 243
Bulaevskii L N, Buzdin A I, Kulic M L and Panjukov 1985 *Adv. Phys.* **34** 175
Jagadish R and Sinha K P 1986 in preparation
Hamaker H C, Mackay H B, Torikachvili M S, Woolf L D and Maple M B 1981 *J. Low. Temp. Phys.* **44** 553
Machida K 1980 *Jap. J. Appl. Phys. Suppl.* **19** 385
Mahanti S D, Sinha K P and Atre M V 1981 *J. Low. Temp. Phys.* **44** 1
Maple M B 1982 *Proc. Int. Conf. Magnetism* **8** *Kyoto* Japan
Shrivastava K N and Sinha K P 1984 *Phys. Rept.* **115** 93
Sinha K P 1979 *Solid State Commun.* **31** 201

CC-0. In Public Domain. Gurukul Kangri Collection, Haridwar

Digitized by Arya Samaj Foundation Chennai and eGangotri

CC-0. In Public Domain. Gurukul Kangri Collection, Haridwar

Digitized by Arya Samaj Foundation Chennai and eGangotri

Pramāṇa – J. Phys., Vol. 28, No. 5, May 1987, pp. 573–581. © Printed in India.

Phase transition studies of paramagnetic crystals at low temperatures

S K DUTTA ROY and B GHOSH*

Department of Physics, Indian Institute of Technology, Kharagpur 721 302, India
*Saha Institute of Nuclear Physics, 92, Acharya Prafulla Chandra Road, Calcutta 700 009, India

Abstract. Magnetic, thermal, electrical and optical properties of a series of paramagnetic compounds of general formula $ABF_6,6H_2O/6D_2O$ and $A(ClO_4)_2,6H_2O$ where A = Co, Na, Zn, Hg and B = Si, Ti, Zr, showing structural transition from room temperature hexagonal with one molecule in the unit cell to low temperature monoclinic with two molecules in the unit cell, are reviewed.

Keywords. Phase transition; paramagnetic crystals; low temperatures.

PACS No. 75·20

1. Introduction

The beginning of the phase transition study of paramagnetic crystals was in 1956 when a number of experiments were performed at the Indian Association for the Cultivation of Science on the magnetic susceptibility of a series of double sulphate and double selenate chromic alums. The anomalous magnetic susceptibility behaviour observed in these alums in the temperature region 180 to 220 K was confirmed by Mitra *et al* (1964). However, the most important experiment in phase transition study of paramagnetic crystals was by Datta and Mazumdar (1965) who observed from magnetic anisotropy measurements in the temperature region 90–300 K, that the magnetic symmetry in $CoSiF_6,6H_2O$ single crystals undergoes a transition at $T_c \sim 246$ K from uniaxial to orthorhombic. Dutta Roy and Ghosh (1968) obtained similar results in $CoF_25HF,6H_2O$ and $CoZrF_6,6H_2O$. It was also shown that the magnetic anisotropy anomaly observed in fluosilicates, hydrofluorides, and fluozirconates were due to a structural transition from room temperature hexagonal to low temperature monoclinic structure (Dutta Roy *et al* 1971). Chowdhury and Ghosh (1974) included a number of perchlorates in the series of paramagnetic crystals showing phase transition. Further evidences were given by Ghosh *et al* (1979), in deuterated fluosilicate and fluotitarnate crystals. It is well known that a series of paramagnetic crystals of general formula $ABF_6,6H_2O/6D_2O$ and $A(ClO_4)_2,6H_2O/6D_2O$ where A = Co, Mn, Fe, Zn, Mg, and B = Si, Ti, Zr undergo phase transition in the temperature region 77–300 K. Recently thermal (Sinha *et al* 1976), optical (Choudhury *et al* 1983), and electrical properties (Ghosh *et al* 1979) of these compounds have also revealed anomalous characteristics, at their respective transition temperatures. It is, therefore, important to review at this stage all the important results observed in these compounds for a possible

CC-0. In Public Domain. Gurukul Kangri Collection, Haridwar

Digitized by Arya Samaj Foundation Chennai and eGangotri

understanding of the interaction mechanism responsible for structural transition in paramagnetic crystals.

Section 2 describes the typical magnetic anisotropy results in fluosilicates including the pressure and dilution effect on the transition temperature. Heat capacity and thermal expansion results are given in § 3. Section 4 deals with electrical properties, the optical studies are presented in § 5 and the concluding remarks in § 6.

2. Magnetic anisotropy in $ABF_6,6H_2O/6D_2O$ and $A(ClO_4)_2,6H_2O/6D_2O$ compounds

Extensive magnetic anisotropy data of the above compounds are available. Therefore, the magnetic anisotropic characteristics of a typical compound is shown in figure 1 where the magnetic anisotropy of $CoSiF_6,6H_2O$ in the symmetry plane as well as perpendicular to the symmetry plane is shown. It may be noted that the temperature variation of magnetic anisotropy in the plane containing the room temperature symmetry axis (c-axis)$\Delta\chi.T^2$ shows an inflexion point near $T_c \sim 246 \pm 1$ K. The

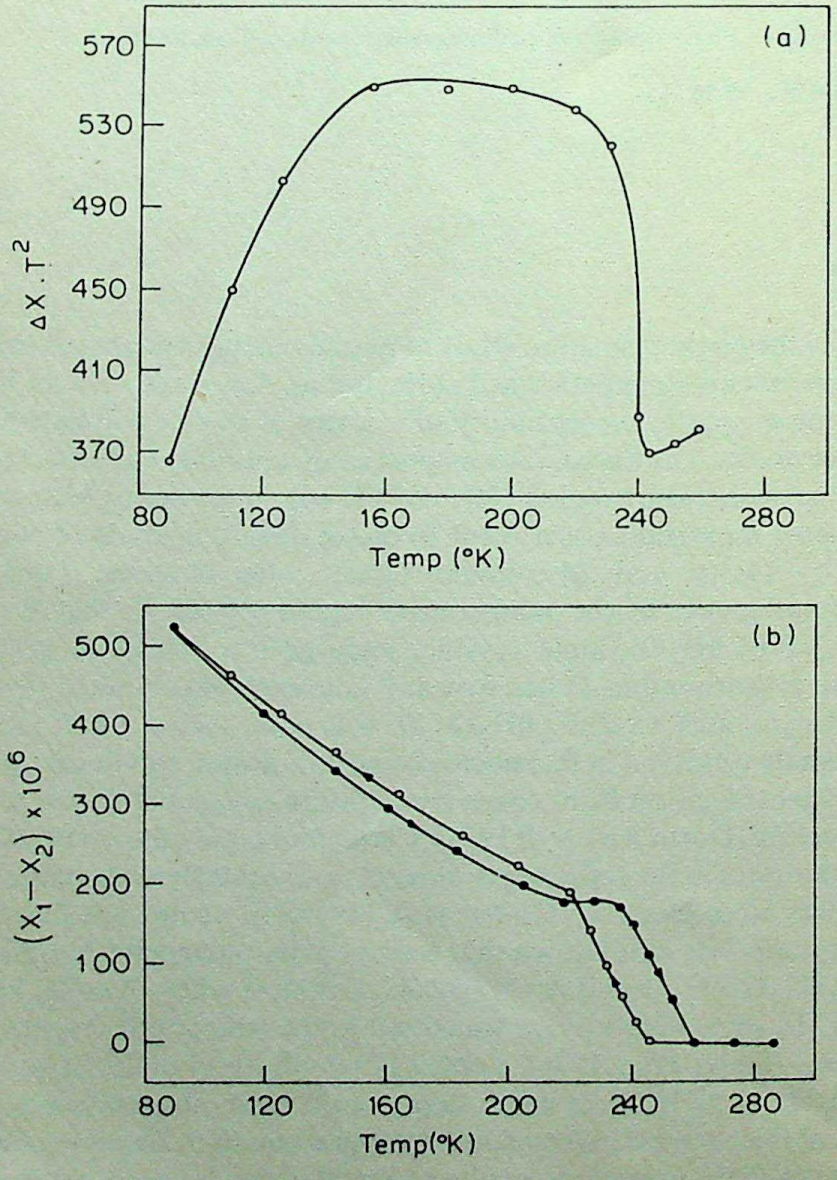

Figure 1. Magnetic anisotropy of $CoSiF_6,6H_2O$ in (**a**) the plane containing the c-axis; (**b**) the symmetry plane.

CC-0. In Public Domain. Gurukul Kangri Collection, Haridwar

Digitized by Arya Samaj Foundation Chennai and eGangotri

magnetic anisotropy in the plane perpendicular to the symmetry axis shows negligible anisotropy at room temperature. The anisotropy occurs at $T_c(c) \sim 246 \pm 1$ K and again disappears at $T_c(h) \sim 258 \pm 1$ K.

The effect of uniaxial pressure on the phase transition temperature is shown in figure 2 for $CoSiF_6,6H_2O$. The curves shown in figure 2(a) record the change occurring during the cooling process and have been plotted as $\Delta\chi.T^2$ against T. The sharp inflexion points at 246 ± 1 K, 254 ± 1 K, 259 ± 1K and 261 ± 1 K correspond to changes in transition temperature with pressure. Figure 2(b) indicates that $T_c(c)$ moves towards high temperature with increase of pressure.

The variation of transition temperature $T_c(c)$ with concentration x for $Co_{1-x}Zn_xF_2,5HF,6H_2O$ and $Co_{1-x}Zn_xSiF_6,6H_2O$ is shown in figure 3. The two

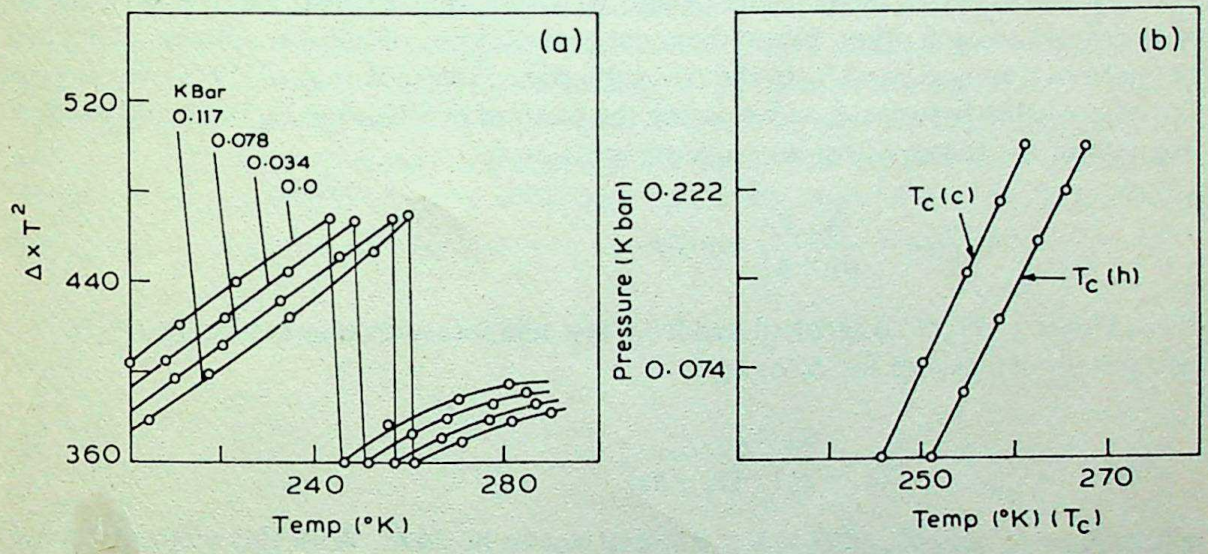

Figure 2. Effect of uniaxial pressure on the phase transition temperature, (**a**) change occurring during cooling process, (**b**) change of $T_c(c)$ as a function of uniaxial pressure.

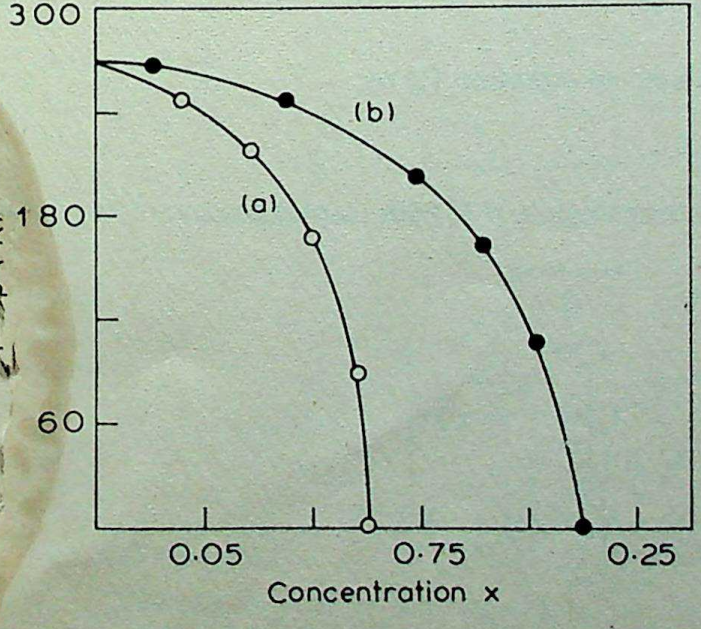

Figure 3. Variation of transition temperature $T_c(c)$ as a function of concentration x for $Co_{1-x}Zn_xF_2,5HF,6H_2O$ and $Co_{1-x}Zn_xSiF_6,6H_2O$.

CC-0. In Public Domain. Gurukul Kangri Collection, Haridwar

Digitized by Arya Samaj Foundation Chennai and eGangotri

curves indicate that $T_c(c)$ follows a nonlinear variation with concentration x. Also a critical concentration x_c exists at which the phase transition disappears. It is noteworthy that dilute crystals behave more or less in a fashion similar to those of the concentrated crystals except for the shift of the transition temperature towards the low temperature side as the zinc concentration in the crystal increases.

Low temperature structural data (Roy *et al* 1973) given in figure 4 show that in the unit cell of $CoSiF_6,6H_2O$, there are two types of Co^{2+} ions and the crystal symmetry is monoclinic with monoclinic axis (b_2) perpendicular to the room temperature hexagonal axis (C-axis). The ionic trigonal axes of the two Co^{2+} ions in the unit cell are oriented at angle ϕ with respect to room temperature hexagonal axis. The two types of Co^{2+} spins in the unit cell are at an angle ϕ_S with respect to room temperature hexagonal axis. Hence it is evident that the two sub-lattices are formed from adjacent Co^{2+} spins located in the two sites (A and B) whose ionic axes are tilted at an angle 2ϕ with respect to each other. Using the most general form of bilinear spin-spin coupling between two spins S_1 and S_2 in the two sublattices, Dutta Roy *et al* (1971) worked out the relationship between ϕ and ϕ_S using the method of Silvera *et al* (1964) and the final expression for the equilibrium angle of spins as,

$$\tan 2\phi_S = -\frac{2g_{\xi'}g_{\zeta'}}{g_{\xi'}^2+g_{\zeta'}^2}\tan 2\phi. \tag{1}$$

If for $CoSiF_6,6H_2O$ 2ϕ is calculated from low temperatures magnetic anisotropy data using the relationship for $K_{\parallel} > K_{\perp}$

$$\cos 2\phi = \frac{\chi_1-\chi_3}{2(\chi_1-\chi_2)-(\chi_1-\chi_3)}, \tag{2}$$

where $K_3 = K_{\parallel}$ and $K_1 = K_2 = K_{\perp}$, is found out to be 24·6°. With this value of 2ϕ and anisotropic g values from the ESR observation of Bleaney and Ingram (1957) which are,

$$g_{\eta'} = g_{\xi'} = 2{\cdot}796,$$
$$g_{\zeta'} = 4{\cdot}235.$$

The angle $2\phi_S$ is calculated in equation (1) as,

$$2\phi_S = -22{\cdot}8$$

which gives a spin-centering angle $\sim 0{\cdot}9°$ with respect to room temperature h

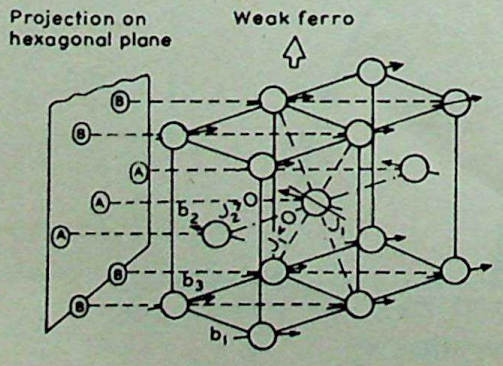

Figure 4. Low temperature crystal structure of $CoSiF_6,6H_2O$. ·xis; (b) the

CC-0. In Public Domain. Gurukul Kangri Collection, Haridwar

Digitized by Arya Samaj Foundation Chennai and eGangotri

axis. The result is in close agreement with low temperature magnetization data of Ohtsubo (1965). It is also to be noted that dilution experiment gives the information that after a critical value of dilution of $CoSiF_6,6H_2O$ crystal with Zr Si $F_6,6H_2O$, the phase transition disappears, i.e., $\phi = 0$ and weak ferromagnetism also does not exist in dilute crystals.

3. Heat capacity in $ABF_6,6H_2O$ and $A(ClO_4)_2,6H_2O$ compounds

The temperature variation of heat capacity of the three compounds in the series $ABF_6,6H_2O$ is shown in figure 5, and the heat capacity of the three compounds in the series $AB(ClO_4)_2,6H_2O$ is shown in figure 6. Heat capacity anomaly observed in these compounds coincides with the transition temperature $T_c(h)$ obtained from magnetic anisotropy data. The characteristics of the transition in $ABF_6,6H_2O$ compounds is that in region $T < T_c$ the heat capacity rises sharply with temperature whereas in the region $T > T_c$ the heat capacity decreases at a comparatively slower rate. In $A(ClO_4)_2,6H_2O$ compounds, in the region $T < T_c$ the heat capacity increases at a comparatively slower rate and in the region $T > T_c$ the heat capacity falls sharply with temperature. An analysis of the heat capacity results around the phase transition

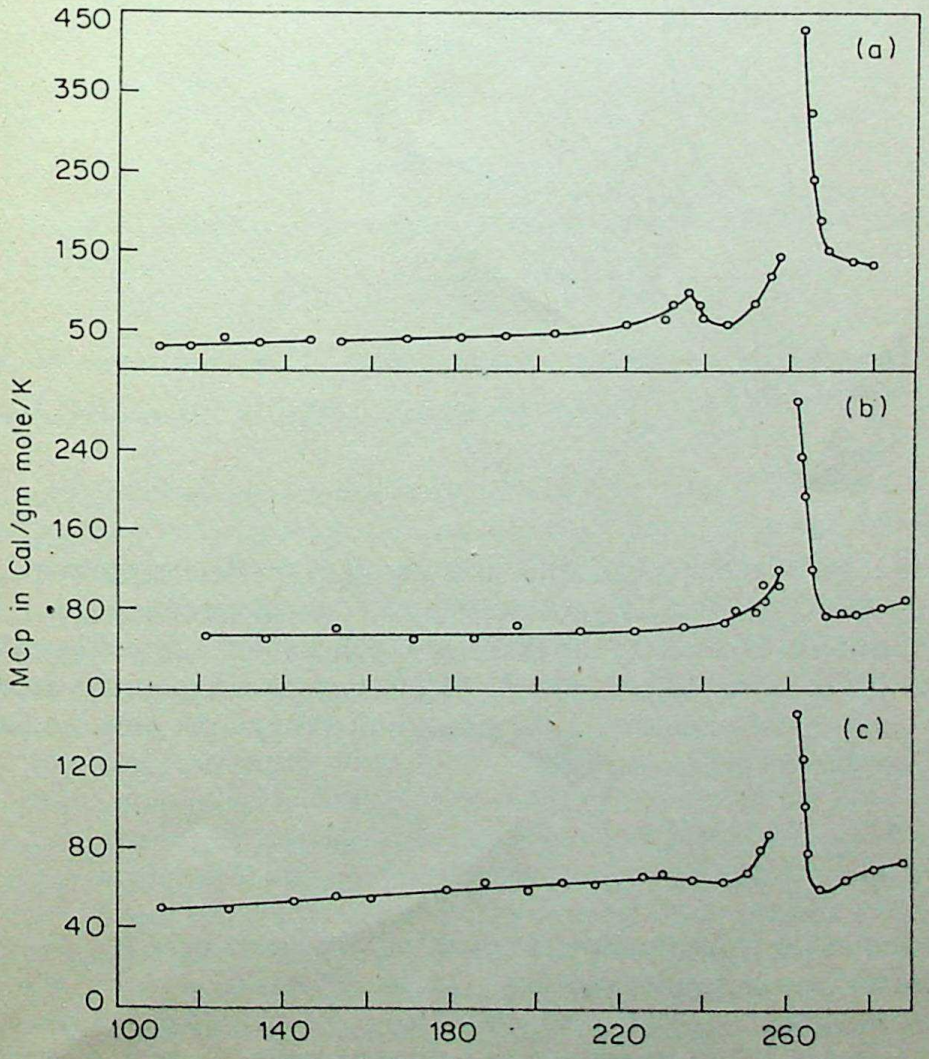

Figure 5. Thermal variation of heat capacity of the three compounds in the series $ABF_6,6H_2O$.

CC-0. In Public Domain. Gurukul Kangri Collection, Haridwar

Digitized by Arya Samaj Foundation Chennai and eGangotri

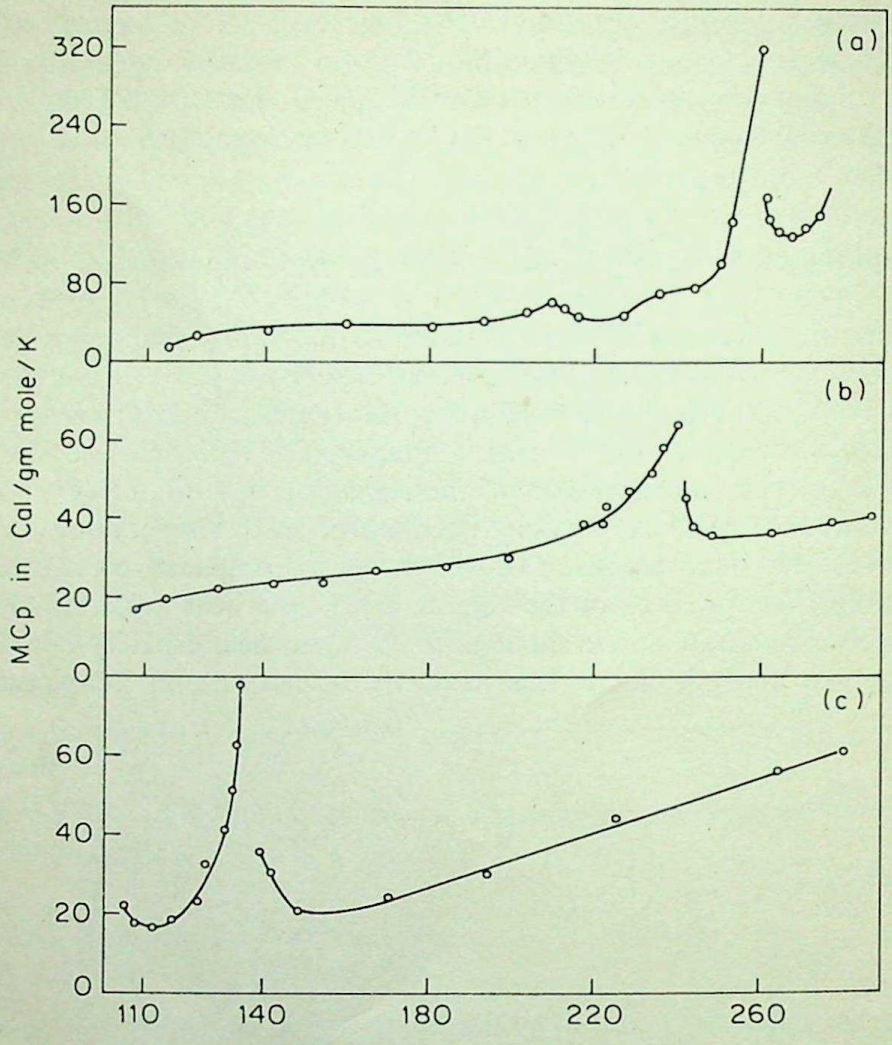

Figure 6. Thermal variation of heat capacity of the three compounds in the series $A(ClO_4)_2,6H_2O$.

temperature suggests that a logarithmic singularity in the heat capacity exists both in $ABF_6,6H_2O/6D_2O$ and $A(ClO_4)_2,6H_2O/6D_2O$ types of compounds.

The temperature dependence of thermal expansion of one of the $ABF_6,6H_2O$ compounds is shown in figure 7. From the anomalous temperature dependence of thermal expansion, information on the transition energy with pressure is calculated from the Clausius-Clapeyron equation

$$\frac{dT_c}{dp} = T_c\left(\frac{\Delta V}{L_0}\right), \tag{3}$$

where T_c denotes the transition temperature, L_0, the latent heat and ΔV the volume change from the heat capacity data; heat of transition is 600 cal mol^{-1} or 4·257 cal/cc. The value of volume change ΔV is calculated from the thermal expansion data $\Delta l/l$ at $T_c(h)$. The value of dT_c/dp turns out to be $-12{\cdot}2\ kbar^{-1}$ which suggests that the structural transition may have the first order origin.

CC-0. In Public Domain. Gurukul Kangri Collection, Haridwar

Digitized by Arya Samaj Foundation Chennai and eGangotri

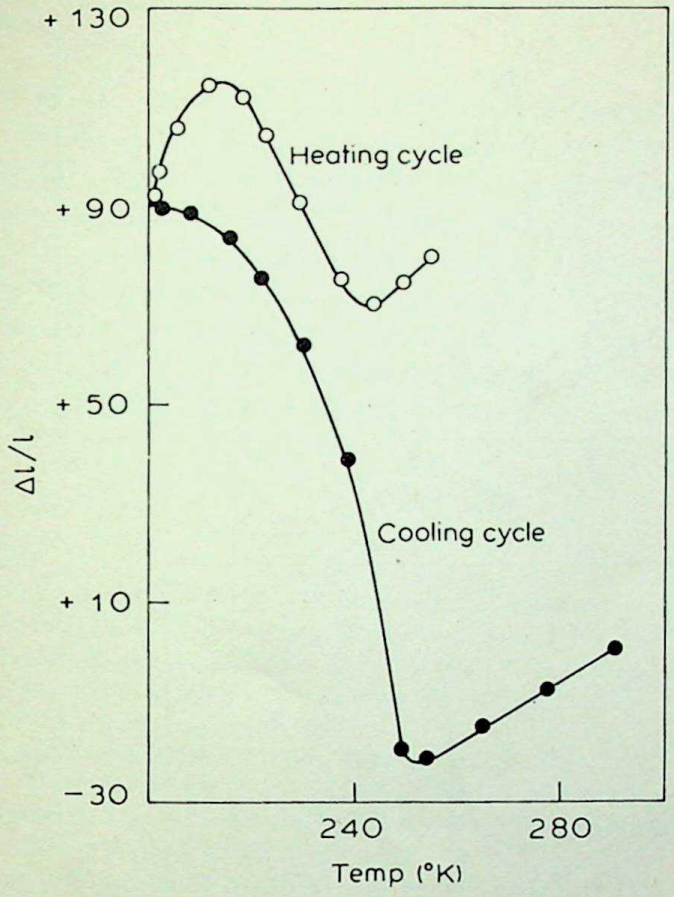

Figure 7. Temperature variation of thermal expansion of one of the compounds in the series $ABF_6,6H_2O$.

4. Electrical conductivity of $ADF_6,6H_2O$ and $A(ClO_4)_2,6H_2O$

Figure 8 is a plot of electrical conductivity $\log \sigma$ as a function of T^{-1} for $CoSiF_6,6H_2O$ and shows that conductivity decreases linearly with decrease in temperature down to 246 K maintaining a constant slope. At 246 K anomalous conductivity fluctuation of σ_{res} and σ_{true} occurs. The increase in conductivity is very sharp and $\log \sigma$ increases from π to $\bar{5}$ within a temperature spread of 2 K. During heating cycle $\log \sigma$ increases from π to $\bar{6}$. Figure 8 shows a similar conductivity plot for an ammonium chloride crystal for comparison.

The striking feature in the electrical property during transition is that in successive runs the conductivity jump in $CoSiF_6,6H_2O$ crystal occurs at the same temperature $T_c \sim 246$ K, but the magnitude of the conductivity jump decreases appreciably in the second and the third run. As the crystal passes through the transition, a large number of internal cracks appear and this number increases in the successive run, resulting in lowering the magnitude of the conductivity jump in the transition region. Also an unusual feature in fluosilicate crystals is a disorder in the position in one of the six fluorine atoms between two sites unrelated by symmetry elements with unequal occupancy number (Roy *et al* 1973). It is presumed that the high electrical conductivity of $CoSiF_6,6H_2O$ crystals at room temperature arises from the disordering of the ions in

CC-0. In Public Domain. Gurukul Kangri Collection, Haridwar

Digitized by Arya Samaj Foundation Chennai and eGangotri

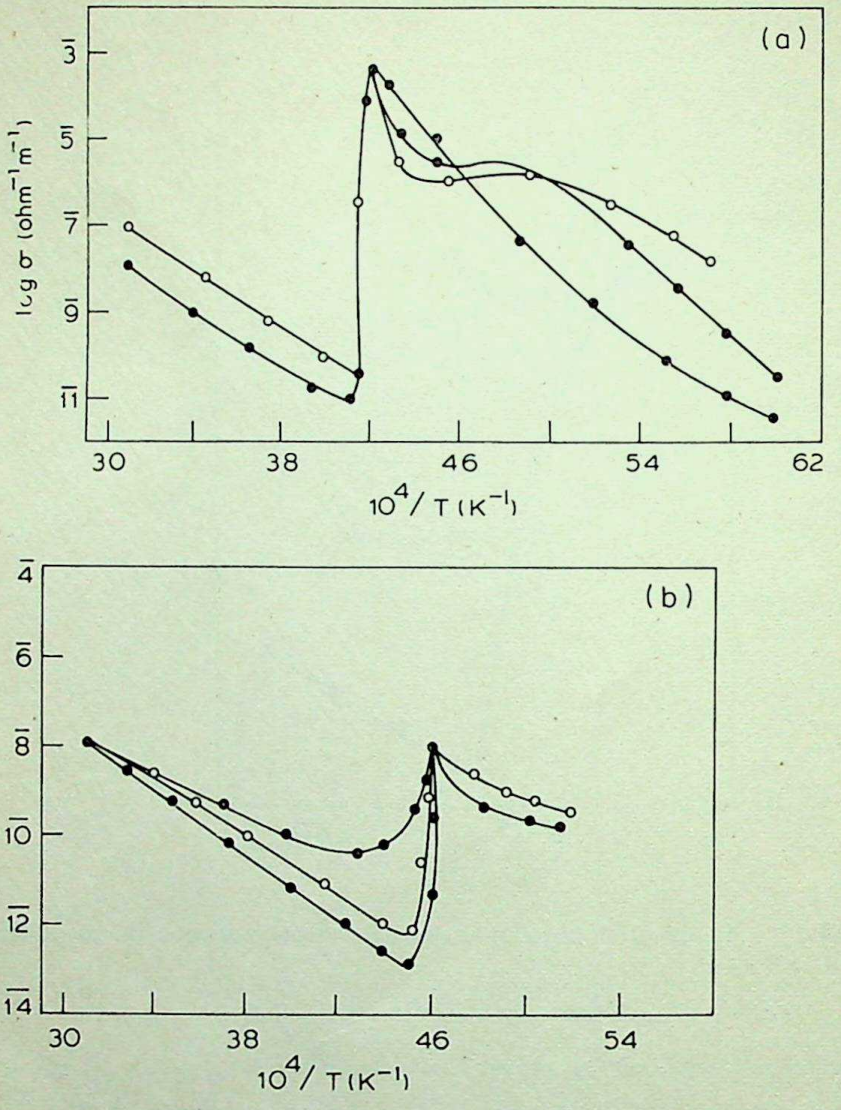

Figure 8. Electrical conductivity log σ as a function of T^{-1} for (**a**) $CoSiF_6,6H_2O$, (**b**) $(NH_4)_2SO_4$.

the lattice. In the transition zone disordering effect increases appreciably causing increase in electrical conductivity until the new crystal structure stabilizes.

5. Optical studies and mode coupling phenomena using Raman scattering

Choudhury *et al* (1983) studied the variation of Laser Raman spectra with temperature in $ABF_6,6H_2O/6D_2O$ system for various polarizations. A sharp change in the Raman intensity of the band 614 cm^{-1} has been observed in the YZ polarization at 200 ± 3 K during the cooling cycle and at 228 ± 3 K during the heating cycle. A feature common in all the observations (Chowdhury *et al* 1985) is that as one traverses from room temperature to a low temperature phase, the frequencies of vibration which are connected to $A(H_2O)_6/(D_2O)_6$ octahedra increase whereas those related to BF_6 octahedra decrease. This change in frequency depends on the strength of the coupling between the soft mode and the other modes.

CC-0. In Public Domain. Gurukul Kangri Collection, Haridwar

Digitized by Arya Samaj Foundation Chennai and eGangotri

6. Conclusion

The present results show that the study of temperature dependence of magnetic anisotropy in a series of compounds of the type $ABF_6,6H_2O/6D_2O$ and $A(ClO_4)_2,6H_2O$ is important in the understanding of structural transition phenomena in paramagnetic crystals. The crystals of the above compounds have shown a structural transition at T_c from hexagonal to monoclinic leading to anomalous changes in magnetic, thermal, electrical and optical properties. It is presumed that the interaction mechanism responsible for such a structural transition is to be obtained from a quantitative estimation of the frequency dependence of the strength of coupling between soft mode and other modes of vibration in the crystal.

References

Bleaney B and Ingram D J E 1957 *Proc. R. Soc.* (*London*) **A208** 153
Chowdhury B K and Ghosh D 1974 *Phys. Status Solidi* **23** 651
Choudhury P, Ghosh B, Lambo O P and Bist H D 1983 *J. Phys.* **C16** 1609
Datta S K and Mazumdar M 1965 *J. Chem. Phys.* **42** 418
Dutta Roy S K 1956 *Indian J. Phys.* **30** 169
Dutta Roy S K and Ghosh B 1968 *J. Phys. Chem. Solids* **29** 1511
Dutta Roy S K, Ghosh B and Kar S 1971 *J. Phys. Chem. Solids* **32** 857
Ghosh B, Chatterjee N, Das A N and Chatterjee A 1979 *J. Phys.* **C12** 3283
Mitra S and Dutta Roy S K 1964 *Physica* **30** 1557
Mitra S S, Ghorai S K and Dutta Roy S K 1979 *Bull. Mater. Sci.* **2** 79
Ohtsubo A 1965 *J. Phys. Soc. Jpn.* **20** 82
Roy S, Zakin A and Templeton D H 1973 *Acta Cryst.* **B29** 2741
Silvera I F, Thornley J H M and Tinkham M 1964 *Phys. Rev.* **A136** 695
Sinha M P, Pal A and Dutta Roy S K 1976 *J. Phys.* **C9** 2783

CC-0. In Public Domain. Gurukul Kangri Collection, Haridwar

Digitized by Arya Samaj Foundation Chennai and eGangotri

CC-0. In Public Domain. Gurukul Kangri Collection, Haridwar

Digitized by Arya Samaj Foundation Chennai and eGangotri

Pramāṇa – J. Phys., Vol. 28, No. 5, May 1987, pp. 583–587. © Printed in India.

Nuclear magnetic resonance studies in rare earth ternary phosphides

R VIJAYARAGHAVAN
Tata Institute of Fundamental Research, Bombay 400 005, India

Abstract. The results of ^{31}P Knight shift (KS) and spin-lattice relaxation time (T_1) measurements in the temperature interval 4·2–300 K are reported for the compounds $RENi_2P_2$(RE = Ce, Eu, Yb) in order to understand the nature of the ground state in these compounds. KS results conclusively establish that all these compounds exhibit non-magnetic ground states. The temperature dependence of spin-fluctuation temperature (T_{sf}) in each case is estimated from the measured data. For $EuNi_2P_2$ the values of T_{sf} above 77 K qualitatively agree with those obtained from Mössbauer and susceptibility data employing ionic interconfigurational fluctuation model, but disagree at lower temperatures.

Keywords. Nuclear magnetic resonance; rare earth ternary phosphides; Knight shift; spin-lattice relaxation.

PACS No. 76·60

Ever since the phenomenon of valence instabilities has been realized in rare earth systems, there has been growing interest in the application of several experimental methods in understanding the nature of the ground state in these compounds (Lawrence *et al* 1981). Among these methods, nuclear magnetic resonance (NMR) occupies a special place, as it gives a lot of information about the static as well as the dynamic part of the 4*f* magnetism through the measurement of Knight shift (KS) and spin-lattice relaxation time (T_1) of a suitable non-magnetic nucleus, respectively. As a part of our programme on the application of NMR to such rare earth systems, we have investigated the compounds $RENi_2P_2$ (RE = Ce, Eu, Yb), crystallizing in the $ThCr_2Si_2$-type tetragonal structure. We have chosen this relatively new series of compounds because a lattice volume anomaly (figure 1) has been observed for Ce, Eu and Yb indicating a non-trivalent state of these ions in this series (Jeitschko and Jaberg 1980). It should be mentioned here that $EuNi_2P_2$ has been earlier identified to be an interesting intermediate valent compound with a non-magnetic ground state (Nagarajan *et al* 1985). Therefore, from the systematics observed in the $ThCr_2Si_2$ type compounds, one would naively expect that $CeNi_2P_2$ and $YbNi_2P_2$ also should exhibit non-magnetic ground states. The present work is aimed at verifying this hypothesis microscopically by the measurement of ^{31}P Knight shift. Another aspect of this work is to obtain an estimate of the spin-fluctuation temperature (T_{sf}) from the measured T_1, KS and susceptibility (χ) values and to compare such results with those obtained by traditional methods. Such academic exercises are helpful in understanding the validity of the models of valence fluctuation.

The samples were prepared as described in the literature (Jeitschko and Jaberg 1980).

CC-0. In Public Domain. Gurukul Kangri Collection, Haridwar

Digitized by Arya Samaj Foundation Chennai and eGangotri

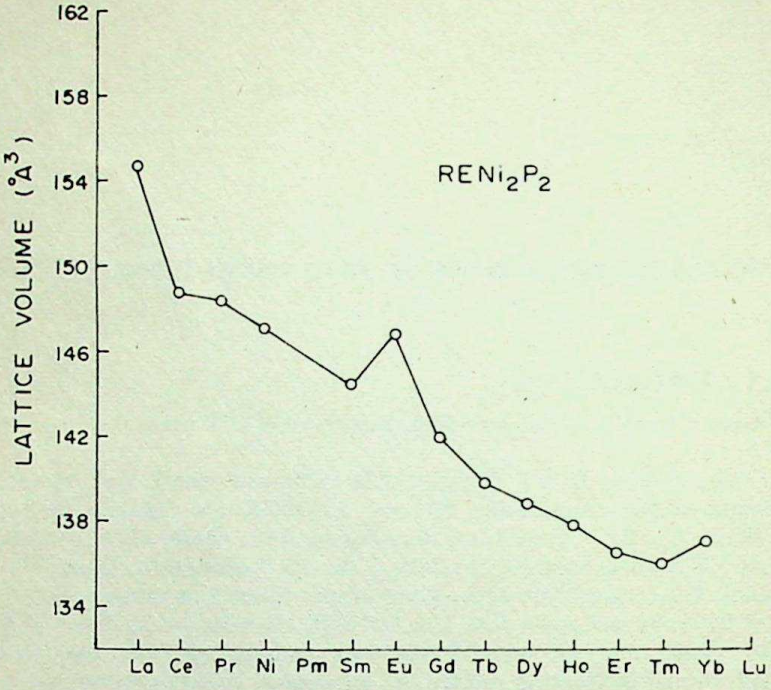

Figure 1. The lattice volume as a function of rare earth (RE) atomic number in $RENi_2P_2$ series.

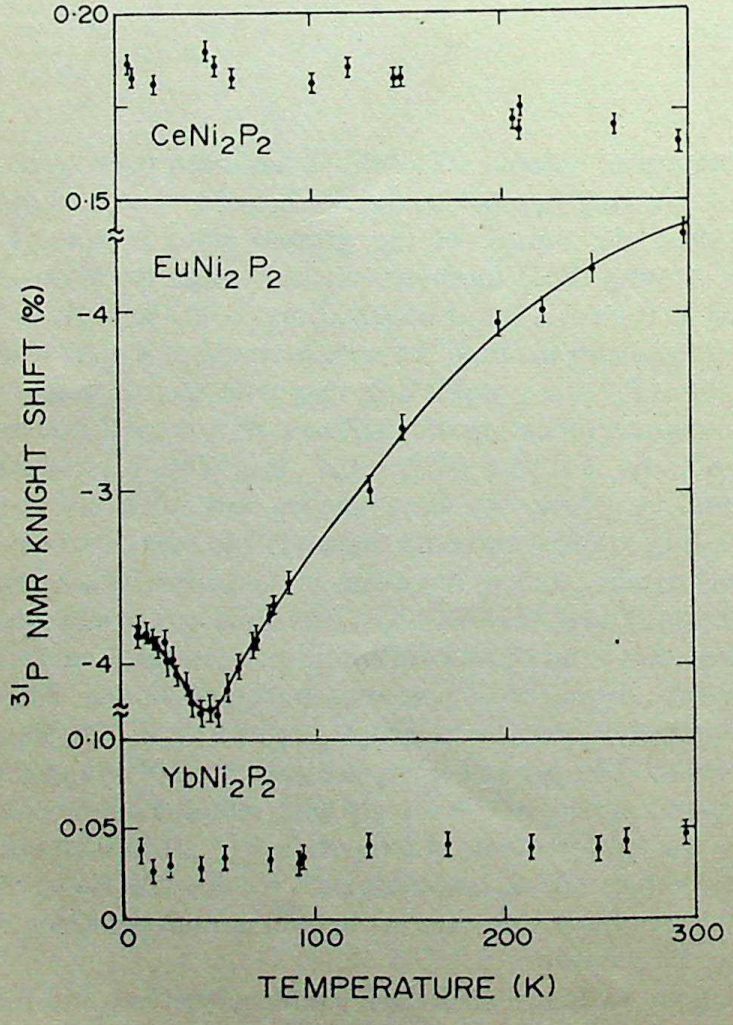

Figure 2. ^{31}P Knight shift as a function of temperature in $CeNi_2P_2$, $EuNi_2P_2$ and $YbNi_2P_2$.

CC-0. In Public Domain. Gurukul Kangri Collection, Haridwar

Digitized by Arya Samaj Foundation Chennai and eGangotri

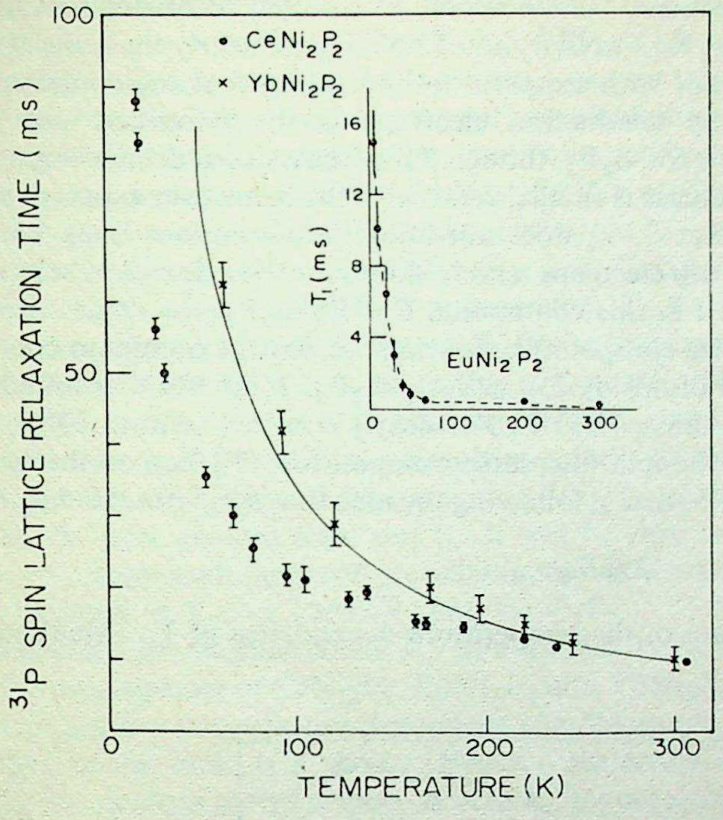

Figure 3. ^{31}P Spin-lattice relaxation time (T_1) in $CeNi_2P_2$, $EuNi_2P_2$ and $YbNi_2P_2$. The solid line represents $T_1T = 3{\cdot}6$ sec K.

NMR KS and T_1 values in the temperature interval 4·2–300 K were obtained employing pulsed spectrometers.

The results of ^{31}P KS and T_1 measurements are shown in figures 2 and 3 respectively. In the case of $CeNi_2P_2$ and $YbNi_2P_2$, KS is very small and nearly temperature-independent. This observation shows that in both the compounds, the ground state is non-magnetic. The non-magnetism of $CeNi_2P_2$ is presumably due to strong spin fluctuations and not due to zero-4*f* occupation number, as tetravalent metallic Ce compounds are ruled out. This is further supported by a large, but nearly temperature-independent susceptibility (χ) (not reported in this paper). (However, we have observed an increase in χ below 30 K, which is presumably due to magnetic impurities, in view of the absence of such a rise in the KS data). This conclusion is consistent with the observation of a double-peaked L_{III} edge x-ray absorption spectrum (Sampathkumaran 1984 (unpublished)) typical of intermediate valent, metallic Ce materials. At present, it is rather difficult to say whether the non-magnetism of $YbNi_2P_2$ is due to $4f^{14}$ configuration (Yb^{2+} state) or due to valence fluctuations as the observed magnitude of KS is too small to distinguish. Susceptibility studies are underway to clarify this point. For $EuNi_2P_2$, KS is very large and strongly temperature-dependent with a peak at about 40 K. The magnitude of KS clearly shows that 4*f* contribution to KS is the dominant one and this proves that the non-magnetic ground state is due to fractional 4*f* count. On the basis of these results, it was earlier (Sampathkumaran *et al* 1985) argued that the breakdown of the linear relationship between KS and χ (with temperature as an implicit parameter) in intermediate valent materials is due to the formation of the 4*f*-conduction band hybridized ground state.

CC-0. In Public Domain. Gurukul Kangri Collection, Haridwar

Digitized by Arya Samaj Foundation Chennai and eGangotri

The temperature-dependent behaviour of T_1 is found to be different for the three samples. The values of T_1 for $CeNi_2P_2$ and $YbNi_2P_2$ are nearly the same at 300 K. For $YbNi_2P_2$, T_1T is constant with temperature indicating that the contribution to the relaxation behaviour by conduction electrons is the dominant one (Korringa-relaxation). However, for $CeNi_2P_2$, though T_1 increases with decreasing temperature, the magnitude of the increase is smaller relative to the behaviour expected on the basis of constancy of T_1T (that is, T_1 does not follow a continuous line). We, therefore, conclude that (magnetic) 4*f* electrons tend to dominate the relaxation behaviour as the temperature is decreased in this compound. For $EuNi_2P_2$, the values of T_1 are very small relative to other two compounds, showing thereby the dominant contribution of 4*f* electrons. In support of this, in $Eu_{0.05}Y_{0.95}Ni_2P_2$, T_1 at 300 K is found to be very large (about 10 msec). Above 77 K T_1T is nearly constant (within 20%).

An NMR estimate of the spin-fluctuation temperature (T_{sf}) can be obtained from the measured values of KS, T_1 and χ, following the idea that h/τ_{eff} obtained by the relation

$$(K^2T_1T)^{-1}\chi = 2\gamma_n^2 K_B \tau_{eff},$$

is a quantitative estimate of the temperature dependence of T_{sf} (MacLaughlin *et al*

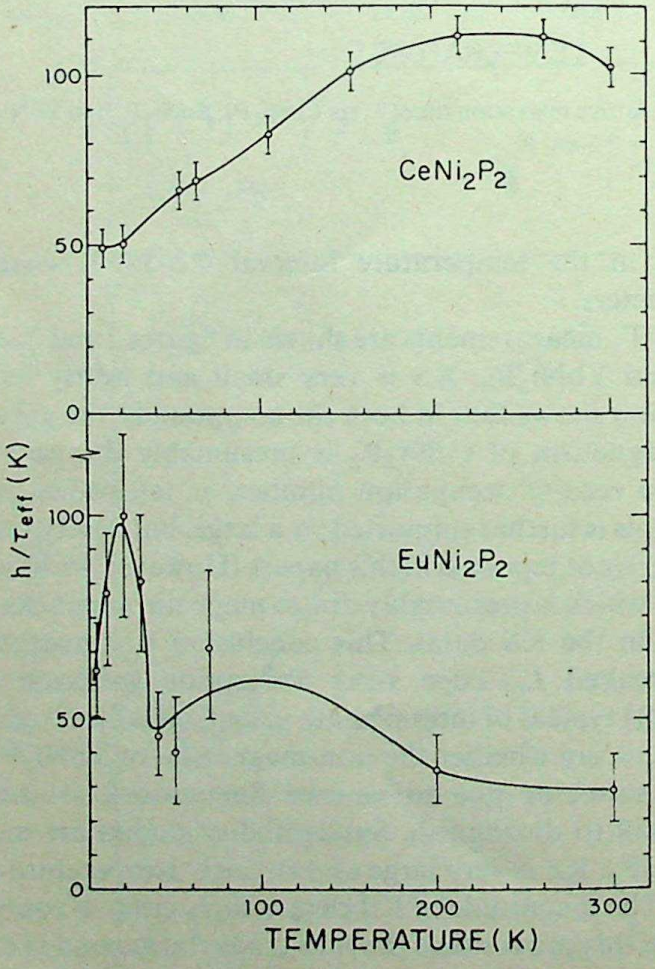

Figure 4. Effective spin correlation parameter (a measure of T_{sf}) as a function of temperature for $CeNi_2P_2$ and $EuNi_2P_2$. A smooth line drawn through the points in each case, is a guide to the eye.

CC-0. In Public Domain. Gurukul Kangri Collection, Haridwar

Digitized by Arya Samaj Foundation Chennai and eGangotri

1979). Here γ_n is the gyromagnetic ratio. The values of h/τ_{eff} thus obtained are plotted in figure 4 for $CeNi_2P_2$ and $EuNi_2P_2$. For $CeNi_2P_2$, h/τ_{eff} is found to undergo a decrease with decreasing temperature. For $EuNi_2P_2$, h/τ_{eff} passes through a maximum above 100 K and this trend is in good agreement with that obtained from Mössbauer isomer shift and susceptibility data employing ionic interconfiguration fluctuation (ICF) model, thereby rendering support to the validity of ICF model at high temperatures. It should be remarked at this point that similar support to ICF model was rendered from Raman spectroscopic studies on $EuPd_2Si_2$ and $EuCu_2Si_2$ by Zirngiebl *et al* (1985, 1986). However, below 100 K, it appears that T_{sf} as inferred from h/τ_{eff} goes through another maximum at 40 K (figure 4); this feature cannot be obtained from the ICF model (Nowik *et al* 1985). It is interesting to note that this anomaly occurs at the same temperature where the 4*f*-hybridized ground state is proposed to set in (Sampathkumaran *et al* 1985). This anomaly may indicate that (i) the assumptions of ICF model are not valid at low temperatures and (ii) the relaxation mechanism is also modified as the pure ground state sets in. It will be very interesting to verify these conclusions by the measurements of quasielastic line width in neutron scattering, which is again a measure of T_{sf}, for $CeNi_2P_2$ and $EuNi_2P_2$.

To summarize, the present NMR KS studies clearly establish the non-magnetic nature of the ground state of $CeNi_2P_2$, $EuNi_2P_2$ and $YbNi_2P_2$. Our results are helpful in understanding the temperature-dependent spin-fluctuation behaviour and to test the reliability of the ionic ICF model. Neutron scattering studies are called for to confirm our conclusions in this respect. A detailed report along with our susceptibility results will be published elsewhere.

The author wishes to thank N Nambudripad and E V Sampathkumaran of TIFR, Bombay and I Stang and K Luders of Free University, Berlin for collaboration in these studies.

References

Jeitschko W and Jaberg B 1980 *J. Solid State Chem.* **35** 312
Lawrence J M, Riseborough P S and Parks R D 1981 *Rep. Prog. Phys.* **44** 1
MacLaughlin D E, de Boer F R, Bijvoet J, de Chatel P F and Mattens W C M 1979 *J. Appl. Phys.* **50** 2094
Nagarajan R, Shenoy G K, Gupta L C and Sampathkumaran E V 1985 *Phys. Rev.* **B32** 2846
Nowik I, Sampathkumaran E V and Kaindl G 1985 *Solid State Commun.* **55** 721
Sampathkumaran E V 1984 (unpublished)
Sampathkumaran E V, Stang I, Vijayaraghavan R, Kaindl G and Luders K 1985 *Phys. Rev.* **B31** 6099
Zirngiebl E, Blumenroder S, Guntherodt G, Jayaraman A, Batlogg B and Croft M 1985 *Phys. Rev. Lett.* **54** 213
Zirngiebl E, Blumenroder S, Guntherodt G and Sampathkumaran E V 1986 *J Mag. Mag. Mater.* **54–57** 343

CC-0. In Public Domain. Gurukul Kangri Collection, Haridwar

Digitized by Arya Samaj Foundation Chennai and eGangotri

CC-0. In Public Domain. Gurukul Kangri Collection, Haridwar

Digitized by Arya Samaj Foundation Chennai and eGangotri

Pramāṇa – J. Phys., Vol. 28, No. 5, May 1987, p. 589. © Printed in India.

Layered structure of superfluid ^{4}He at supercritical motion

L P PITAEVSKII

Institute for Physical Problems, USSR Academy of Sciences, 117334, Moscow, USSR

Abstract. Landau's criterion plays an important role in the theory of superfluidity. According to this criterion, superfluid motion is possible if $\tilde{\varepsilon}(\mathbf{p}) \equiv \varepsilon(p) + \mathbf{pV} > 0$ along the curve of the spectrum $\varepsilon(p)$ of excitations. For ^{4}He it means that $v < v_c$, $v_c \approx 60$ m/sec. v_s is equal to the tangent of the slope to the roton part of the spectrum. The question of what happens to the liquid when this velocity is exceeded, as far as we know, remains unclear. We shall show that for small excesses above v_c a one-dimensional periodic structure appears in the helium. A wave vector of this structure oriented opposite to the flow and equal to $\rho_c/\hbar$ where ρ_c is the momentum at the tangent point. The quantity $\tilde{\varepsilon}(\mathbf{p})$ is the energy of excitation in the liquid moving with velocity $\mathbf{v}$. Inequality of Landau ensures that $\tilde{\varepsilon}$ is positive. If $\tilde{\varepsilon}$ becomes negative, then the boson distribution functio . $n(\tilde{\varepsilon})$ becomes negative, indicating the impossibility of thermodynamic equilibrium of the ideal gas of rotons; therefore the interaction between them must be taken into account. The final form of the energy operator is

$$\hat{H} = \int \{\hat{\psi} + \tilde{\varepsilon}(\mathbf{p})\hat{\psi} + \frac{g}{2}\hat{\psi} + \hat{\psi} + \hat{\psi}\hat{\psi}\} \mathrm{d}^3x, \quad g \sim 2 \cdot 10^{-38} \text{ erg.cm.}$$

Then we can seek the roton ψ-operator in the form $\psi = \eta \exp(i\mathbf{p}_c\mathbf{r}/\hbar)$, determining η from the condition that the energy is minimized. The result is $(\eta)^2 = (v - v_c)\rho_c/g$, for $v > v_c$. The plane wave ψ corresponds to a uniform distribution of rotons. It leads, however, to a spatial modulation of the density of the helium, since the density operator $\hat{n}$ contains a term which is linear in the operator ψ: $\hat{n} = n_0 + (n_0)^{1/2} A/\hat{\psi} \to \hat{\psi}^+$), where $|A|^2 \sim \rho_c^2/2m\varepsilon(\rho_c)$. Finally we find that the density of helium is modulated according to the law

$$\frac{n - n_0}{n_0} = \left[\frac{|A|^2(v - v_c)\rho_c}{n_0 g}\right]^{1/2} \sin \rho_c x \approx 2{,}6 \left[\frac{v - v_c}{v_c}\right]^{1/2} \sin \rho_c x.$$

This phenomenon can be observed, in principle, in the experiments on scattering of x-rays in moving helium.

Keywords. Superfluid ^{4}He; supercritical motion; layered structure.

PACS No. 67·40

CC-0. In Public Domain. Gurukul Kangri Collection, Haridwar

Digitized by Arya Samaj Foundation Chennai and eGangotri

Pramāṇa – J. Phys., Vol. 28, No. 5, May 1987, p. 590. © Printed in India.

Study of the two-domain processing structure in the superfluid ^{3}He-B

A S BOROVIK-ROMANOV, Yu M BUNKOV, V V DMITRIEV, Yu M MUKHARSKY and I A FOMIN

Institute for Physical Problems and L D Landau Institute for Theoretical Physics, USSR Academy of Sciences, 117334, Moscow, USSR

Abstract. The systematic experimental and theoretical investigation of the longlived induction signal, known to exist in the ^{3}He-B, has shown that even very small nonuniformity of a steady magnetic field H_0 changes qualitatively the precession pattern arising in the pulsed NMR experiments after tipping of the magnetization. The spin supercurrents redistribute magnetization within the experimental cell to produce the precessing structure, consisting of two domains. In one-domain, situated in the higher field region, magnetization M has its equilibrium value and is parallel to H_0. In the other domain the angle between M and H_0 is slightly larger than $\theta_0 = \arccos(-\frac{1}{4})$. The structure precesses with frequency, equal to the Larmor frequency at the site of the wall, separating the domains. The relaxation of this structure goes via the growth of the equilibrium domain at the expense of the precessing domain; therefore in the course of the relaxation the frequency of the precession has to decrease with time. The calculated rate decrease agrees with the observed value. Experiments were carried out directly demonstrating the existence of the two-domain structure.

After the formation of the two-domain structure, as well as after a perturbation of the structure by short r.f. pulses, low frequency ($\sim$200 Hz) modulation of the induction signal is observed due to vibration of the structure. These vibrations are the standing spin waves in the precessing domain, their frequency being proportional to the size of the domain. The observed dependence of the frequency on other parameters is in agreement with theoretical calculations.

The analysis of the data on the vibration and relaxation of the two-domain structure enables us to find the spin wave velocity and the spin diffusion coefficient in ^{3}He-B.

Further investigation of the two-domain structure enables the study of spin supercurrents in ^{3}He-B.

Keywords. Two-domain structure; helium.

PACS No. 67·60

CC-0. In Public Domain. Gurukul Kangri Collection, Haridwar

Digitized by Arya Samaj Foundation Chennai and eGangotri

Pramāṇa – J. Phys., Vol. 28, No. 5, May 1987, p. 591. © Printed in India.

Roughening (faceting) transitions on the helium crystal-superfluid interface

A V BABKIN, K O KESHISHEV, D B KOPELIOVICH and A YA PARSHIN

Institute for Physical Problems, USSR Academy of Sciences, 117334, Moscow, USSR

Abstract. The concept of roughening transitions (RT) was first introduced into theory by Burton and Cabrera (1949). RT, which manifests itself in disappearance of smooth facets in equilibrium shape of the crystal (faceting transition), has been under intensive theoretical study in the last few years (Andreev 1981; Rottman and Wortis 1984). Current interest in this field is connected mainly with the problems of "quantum roughening" and critical behaviour of the surface stiffness. Experimental studies of RT in usual classical crystals meet with serious difficulties due to very long crystal shape relaxation times. In this respect, helium crystals seem to be the best candidates because of their extremely fast growth kinetics which ensures sufficiently short shape relaxation times (Keshishev *et al* 1982).

We have recently investigated the equilibrium shape of large ^{4}He crystals in the vicinities of the two different RT ($T_R = 1{\cdot}2$ K and 0·9 K) by a simple optical technique which provides the temperature and angular dependences of the surface stiffness (Babkin *et al* 1958, 1984, 1985). The data obtained by this method show, in accord with theory, that both studied RT being continuous phase transitions. However, the measured critical behaviour of the surface stiffness cannot be explained satisfactorily by current theories, either by the phenomenological "mean field" theory (Andreev 1981) or by the lattice model calculation (Rottman and Wortis 1984).

Keywords. Roughening transitions; helium crystal.

PACS No. 67·80

References

Andreev A F 1981 *Sov. Phys. JETP* **53** 1063
Babkin A V, Keshishev K O, Kopeliovich D B and Parshin A Ya 1958 *Appl. Surf. Sci.* **22/23** 696
Babkin A V, Keshishev K O, Kopeliovich D B and Parshin A Ya 1984 *JETP Lett.* **39** 633
Babkin A V, Kopeliovich D B and Parshin A Ya 1985 *Zh. Eksp. Teor. Fiz.* **89** 2288
Burton W K and Cabrera N 1949 *Disc. Farad. Soc.* **5** 33
Keshishev K O, Parshin A Ya, Shal'nikov A J 1982 in *Soviet scientific reviews, Section A: Phys Rev.* (ed.) I M Khaltnikov (Harwood Academic Chur) V. 4 p. 155
Rottman C and Wortis M 1984 *Phys. Rev.* **B29** 328

CC-0. In Public Domain. Gurukul Kangri Collection, Haridwar

Digitized by Arya Samaj Foundation Chennai and eGangotri

Pramāṇa – J. Phys., Vol. 28, No. 5, May 1987, p. 592. © Printed in India.

Quantum interference of electrons in disordered metals

YU V SHARVIN

Institute for Physical Problems, USSR Academy of Sciences, 117334, USSR

Abstract. Investigation of the galvanomagnetic properties of disordered metals in weak magnetic fields [$r(H) \gg l$, where $r(H)$ is the electron trajectory radius and l, the electron free path], proved to be one of the effective experimental methods of studying disordered metals. The phase difference between the interfering electron waves is affected by the presence of magnetic flux in the sample. One of the observable effects is the oscillatory magnetoresistance $K(H)$ of multiconnected samples predicted by Altshuler *et al* (1981). The period of $K(H)$ oscillations for the hollow cylinders, networks or chains with orifices cross-sections areas S is $\Delta H = \phi_0/2\,S$ [where $\phi_0 = hc/e$]. The amplitude and the phase of the oscillations depend on the spin orbit interaction, the intensity of superconductive fluctuation etc.

It should be noted that in small "mesoscopic" single loops the oscillations with the period $\Delta H \cong \phi_0/S$ were also observed recently (see also Altshuler *et al* 1987 included in this issue).

Keywords. Electron quantum interference; disordered metals.

PACS No. 72·10

References

Altshuler B L, Aronov A G and Spivak B Z 1981 *Zh. Eksp. Teor. Fiz. Pis'ma Red.* **33** 101
Altshuler B L, Aronov A G and Spivak B Z 1981 *JETP Lett.* **33** 94
Altshuler B L, Khmel'nitskii D E and Spivak B Z 1987 *Pramana – J. Phys.* **28**

CC-0. In Public Domain. Gurukul Kangri Collection, Haridwar

Digitized by Arya Samaj Foundation Chennai and eGangotri

Pramāṇa – J. Phys., Vol. 28, No. 5, May 1987, p. 593. © Printed in India.

Residual conductance fluctuations of tiny disordered conductors

B L ALTSHULER, D E KHMEL'NITSKII and B Z SPIVAK

Leningrad Nuclear Physics Institute, Solid State Physics Institute, Institute of Analytical Instrumentation, USSR Academy of Sciences, Leningrad, USSR

Abstract. Conductances of the equivalent samples differ randomly (Stone 1985). At zero temperature these fluctuations were found to be of the order of e^2/h for samples of arbitrary size and form (Altshuler 1985; Lee and Stone 1985). Experimentally such fluctuations manifest themselves as e.g. the reproducible aperiodic oscillations of the given sample conductance in magnetic field (Webb *et al* 1985; Stone 1985). These oscillations can be understood in terms of the correlation function (Lee and Stone 1985; Altshuler and Khmel'nitskii 1985) of the conductances in different fields. The characteristic field scale of the aperiodic oscillations corresponds to the unit magnetic flux through the sample.

Conductance fluctuations decrease with the growth of temperature if the sample size is larger than the diffusion length within the time $\hbar/T$ (Stone 1985; Lee and Stone 1985; Webb *et al* 1984, 1985; Altshuler and Khmel'nitskii 1985). These fluctuations are proportional to $T^{-1/4}$, $T^{-1/2} \log T$, and $T^{-1/2}$ in the 3-d, 2-d and 1-d cases, respectively (Altshuler and Khmel'nitskii 1985) (the experiments of Webb *et al* 1984, 1985 correspond to the latter case).

Random potential in tiny samples breaks all space symmetries. All effects which are forbidden in the average by these symmetries should manifest themselves by (i) conductance anisotropy, (ii) its dependence on the electric field direction and (iii) giant generation of the second harmonic in the granular sample under light radiation (Altshuler and Khmel'nitskii 1985).

Conductance changes aperiodically with variation of the chemical potential (Lee and Stone 1985). Because of this thermopower fluctuations are much larger than its average value (Altshuler and Khmel'nitskii 1985).

Conductance fluctuations are very sensitive to the random impurity potential variations (Altshuler and Spivak 1985). For instance, the change of the film conductance due to the shift of *one* impurity is *finite* for any film size. This effect can be used for the super flow impurity diffusion investigations. Variations of the localized spins realization in spin glasses change the conductance. This can explain (Altshuler and Spivak 1985) the conductance dependence on the magnetic field direction observed by Webb *et al* (1984, 1985).

Keywords. Residual conductance fluctuations; disordered conductors.

PACS No. 72·10

References

Altshuler B L 1985 *Pis'ma JETP* **41** 530
Altshuler B L and Khmel'nitskii D E 1985 *JETP Pis'ma* **42** 291
Altshuler B L and Spivak B Z 1985 *JETP Pis'ma* **42** 363
Lee P A and Stone A D 1985 *Phys. Rev. Lett.* **55** 1622
Stone A D 1985 *Phys. Rev. Lett.* **B54** 2692
Webb R A, Washburn S, Umbach C F and Laibowitz R B 1984 *Phys. Rev.* **B30** 4048
Webb R A, Washburn S, Umbach C F and Laibowitz R B 1985 *Phys. Rev. Lett.* **51** 2696

CC-0. In Public Domain. Gurukul Kangri Collection, Haridwar

Digitized by Arya Samaj Foundation Chennai and eGangotri

Pramāṇa – J. Phys., Vol. 28, No. 5, May 1987, p. 594. © Printed in India.

Experimental study of resistivity of metallic materials with dynamic disorder

V F GANTMAKHER, G I KULESKO and V M TEPLINSKY
Institute of Solid State Physics, Academy of Sciences of the USSR, Chernogolovka, USSR

Abstract. As a result of strong electron-phonon interaction, the enhancement of scattering with increasing temperature may decrease the mean free path l in crystals down to interatomic distances: $l \approx a$. This means that with respect to the electron wave the degree of the atomic disorder in these crystals is approximately the same as in amorphous metal. Because of a high electron velocity the dynamic character of the disorder seems to be unimportant. At the same time, the degree of disorder can be easily changed by varying the temperature. This makes it possible to simulate and study the transport properties of the disordered media on high-quality crystals with strong phonon scattering. The sign that indicates the fitness of a crystalline metallic material for such studies is the saturation of its resistivity ρ that ceases to grow as the temperature is increased.

The saturation of resistivity was investigated experimentally on (i) Cu-Zr alloys in the crystalline state, (ii) single crystals of WO_2, which is a metal with well-defined Fermi surface.

The samples of Cu-Zr were produced by the recrystallization of amorphous ribbon. Some of these samples reveal resistivity saturation. With further increase of T a maximum in the $\rho(T)$ dependence was observed at those compositions which slightly decreased their ρ value under recrystallization. This unusual dependence can be explained in terms of the two-band model assuming that the d-electrons reach the minimal free path, $l \approx a$, while the s-electrons do not.

The WO_2 crystals were used to study the anisotropy of (T). In the directions, where ρ is high, there is a tendency to saturation. Where ρ is low, no tendency to saturation is observed. The quantitative analysis of the curves has shown that not only the absolute value but also the relative value of the deviation from the Boltzmann law $\rho \sim T$ decreases down as the resistivity decreases.

Keywords. Resistivity; dynamic disorder.

PACS No. 72·10

CC-0. In Public Domain. Gurukul Kangri Collection, Haridwar

Digitized by Arya Samaj Foundation Chennai and eGangotri

Pramāṇa – J. Phys., Vol. 28, No. 5, May 1987, p. 595. © Printed in India.

Nonstationary phenomena in Si MOSFETs in the quantum Hall effects regime

V M PUDALOV, S G SEMENCHINSKY and V S EDEL'MAN
Institute for Physical Problems, USSR Academy of Sciences, 117334, Moscow, USSR

Abstract. We report the observation of nonstationary hysteresis phenomena in charging of Si MOSFET at a quantizing magnetic field. In these experiments (Pudalov *et al* 1984; Pudalov and Semenchinsky 1985) the charging current J_g of the capacitance gate-2D-layer was measured while sweeping of the magnetic field H or a gate voltage V_g at a constant rate. The numerical integration of the measured values J_g with respect to time gave the dependences of change in Q_s vs V_g or vs H.

At low temperature $T<1$ K there arise deviations from the linear dependence $Q_s(V_g)$ near those integer values of Landau level filling $\nu=n_s/n_H=2, 4, 6, 8, 12$, which correspond to the most deep minima in ρ_{xx} and flat plateaux in ρ_{xy}. Here n_s is the 2D electron density, n_H being Landau level degeneracy number, ρ_{xx} and ρ_{xy} —the resistivity tensor components. The inherent feature of the curve $Q_s(V_g)$ is the hysteresis: at increasing V_g the charge Q_s is less than the equilibrium value, while at decreasing V_g the charge exceeds the equilibrium one.

The maximum difference of charges at an increase and decrease of V_g grows-rapidly at lowering T and at $T=0{\cdot}42$ K amounts to $\sim 10\%$ of the full charge confined by one Landau level ($n_H{\cdot}e{\cdot}S$). It is worth to note that such behaviour of $Q_s(V_g)$ does not influence the values of ρ_{xy} (with accuracy of $\sim 10^{-5}$) and the shape of ρ_{xy} plateaux and ρ_{xx}-minima.

Measurements at various sweep rates dV_g/dt demonstrated that if the sweep rate is lower, the hysteresis region is narrower and the deviation of charges Q_s from its equilibrium value is smaller. By extrapolating the dependence of hysteresis loop width on dV_g/dt, the ultimate sweep rate may be estimated, for which a hysteresis will completely disappear. Thus, for instance, at $T=0{\cdot}42$ K and $\nu=4$ it will occur when the time interval of one Landau level filling τ_H will be equal to 100 years.

A similar hysteresis in 2D-layer charge occurs in varying magnetic field also, when the gate voltage is disconnected with the battery and hence the charge in MOSFET is maintained constant. This hysteresis loop rapidly vanishes at temperatures >1 K.

The long relaxation time of a nonequilibrium charge in 2D-layer can be connected phenomenologically with small drift velocities of electrons along the potential gradient due to a small value of conductivity σ_{xx}. This relaxation time may be estimated as $\tau \sim C/\sigma_{xx}$ where C is the electrical capacitance of MOSFET area with a nonequilibrium charge. The value of $\tau \sim 10^9$ s gives $\sigma_{xx}<10_a^{-18}$ Ohm$^{-1}/\square$, i.e. $\rho_{xx}<10^{-11}$ Ohm/$\square$. Simultaneously with nonequilibrium charge relaxation in 2D-layer there arise circular Hall currents decaying with the same rate.

In conclusion, we observed and investigated nonequilibrium charging of 2D-layer in quantum Hall effect regime. To explain the phenomenon we supposed that circular Hall currents is comparable to the eddy currents excited in a superconducting ring.

PACS No. 72·15

References

Pudalov V M, Semenchinsky S G and Edelman V S 1984 *Solid State Commun.* **51** 713
Pudalov V M and Semenchinsky S G 1985 *Usp. Phys. Nauk* **146** 534

CC-0. In Public Domain. Gurukul Kangri Collection, Haridwar

Digitized by Arya Samaj Foundation Chennai and eGangotri

Pramāṇa – J. Phys., Vol. 28, No. 5, May 1987, p. 596. © Printed in India.

Electron fluid and quasiparticles in the quantum Hall effect

V L POKROVSKY and A L TALAPOV

Landau Institute of Theoretical Physics, USSR Academy of Sciences, 117334, Moscow, USSR

Abstract. To explain fractional quantum Hall effect, it is necessary to take into account both the interaction between electrons and their interaction with impurities. We propose a simple model, where the Coulomb repulsion is replaced by a short range potential. For this model we are able to find many-body wave functions of the electron system interacting with impurities and calculate the Hall conductivity σ_{xy}. A simple physical picture, arising in the framework of this model, provides the understanding of a general reason for both fractional and integral quantum Hall effect.

In the model, electrons forming a two-dimensional system, is supposed to occupy the first Landau level. The interaction of electrons is regarded as being small compared with the distance between the Landau levels. The radius of interaction is much less than the magnetic length. The following statements have been proved (Pokrovsky and Talapov 1985a,b; Trugman and Kivelson 1985). For the filling $\nu = 1/m$ of the first Landau level the ground state is nondegenerate and has the wave function ψ_u, proposed by Laughlin (1983). For ν, which is slightly less than $1/m$ the ground state is highly degenerate in the absence of impurities. It can be described as a system of noninteracting quasiholes as proposed by Laughlin (1983). These quasiholes float in the uniform incompressible fluid. Each quasihole has the charge $|e|/m$. The total number of quasiholes is $q = S - mN$, where S is a number of states on the Landau level, N is the number of electrons. The impurities capture quasiholes. If the number of quasiholes q is less than the number of impurities N_i, then the ground state becomes nondegenerate. This fact permits us to calculate σ_{xy} (Pokrovsky and Talapov 1985b). Let there be a small electric field E in the system. In the absence of impurities the electron fluid is at rest in the frame of reference, moving with velocity $v = cE/H$. In this frame of reference the impurities move with the velocity $-v$, carrying captured quasiholes. Therefore, the quasihole current is $j_q = (-v)(|e|/m)\,q$. Hence, in the initial frame of reference the total current is $j = Nev + j_q = Sev/m$. This means that $\sigma_{xy} = (1/m)(e^2/2\pi\hbar)$.

Keywords. Quantum Hall effect; electron fluid; quasiparticles.

PACS No. 72·15

References

Pokrovsky V L and Talapov A L 1985a *J. Phys.* **C18** L691
Pokrovsky V L and Talapov A L 1985b *Pisma V JETF* **42** 68
Trugman S A and Kivelson S 1985 *Phys. Rev.* **B31** 5280
Laughlin R B 1983 *Phys. Rev. Lett.* **50** 1395

CC-0. In Public Domain. Gurukul Kangri Collection, Haridwar

Digitized by Arya Samaj Foundation Chennai and eGangotri

Pramāṇa – J. Phys., Vol. 28, No. 5, May 1987, p. 597. © Printed in India.

Unusual superconductivity and its physical properties

L P GOR'KOV

Landau Institute of Theoretical Physics, USSR Academy of Sciences, 117334, Moscow, USSR

Abstract. Physical properties are discussed, which, in principle, would allow us to distinguish between nontrivial superconductivity and superconductivity of the ordinary type thus establishing its superconducting class. These properties are: the anisotropy of the upper and low critical fields, the magnetization curve, some peculiarities of the penetration depth, the impedance behaviour etc. It is pointed out that these superconductors could possess some magnetic properties. The role of defects is investigated and, in particular, the possibility of the magnetization in these superconductors which originates from the presence of ordinary defects.

The problem of nontrivial superconductivity is discussed in connection with available experimental data concerning new materials with the so-called "heavy fermions".

Keywords. Superconductivity.

PACS No. 74·20

CC-0. In Public Domain. Gurukul Kangri Collection, Haridwar

Digitized by Arya Samaj Foundation Chennai and eGangotri

Pramāṇa – J. Phys., Vol. 28, No. 5, May 1987, p. 598. © Printed in India.

Superconductivity of the twinning plane

I N KHLUSTIKOV

Institute for Physical Problems, USSR Academy of Sciences, 117334, Moscow, USSR

Abstract. Lately superconductivity of a new object, twinning plane (TP) of metal crystals, has been discovered and investigated (Shaikin and Khlustikov 1981; Khlustikov and Khaikin 1982; Buzdin and Khlustikov 1984; Khlustikov and Moskvin 1985). The only one monolayer of atoms of the samples is in crystallographically shaped position, which proves TP to be unique. The monolayer of atoms generating TP is a two-dimensional crystal. The two-dimensional crystal is supposed to have its own two-dimensional electrons and phonons (Khaikin and Khlustikov 1981). Superconductivity of twinning plane (STP) is the first effect discovered which demonstrates unusual properties in such two-dimensional systems.

STP is essentially different from three-dimensional superconductivity and is observed in a number of metals, such as In, Nb, Re, Sn and Tl. The fact that STP emerges at higher temperatures than three-dimensional superconductivity is a case of special interest to this problem. Superconductors of first type (Sn) and of second type (Nb) have been studied in detail. The measurements of phase (H, T) diagram STP in these metals have been carried out. STP is shown to appear in Sn by the first type phase transition (Khlustikov and Khaikin 1982; Buzdin and Khlustikov 1984), and in Nb, most likely, by the second type phase transition. Topological phase transition of Berezinsky-Kosterlitz-Thouless (Khlustikov and Moskvin 1985) transition type was discovered in twins of Nb.

Keywords. Superconductivity; twinning plane.

PACS No. 74·60

References

Khaikin M S and Khlustikov I N 1981 *JETP Pis'ma* **33** 167
Khlustikov I N and Khaikin M S 1982 *JETP Pis'ma* **36** 132
Buzdin A I and Khlustikov I N 1984 *JETP Pis'ma* **40** 140
Khlustikov I N and Moskvin S I 1985 *JETP* **89** 1846

CC-0. In Public Domain. Gurukul Kangri Collection, Haridwar

Digitized by Arya Samaj Foundation Chennai and eGangotri

Pramāṇa – J. Phys., Vol. 28, No. 5, May 1987, p. 599. © Printed in India.

Investigations of UBe_{13} of other compounds of Be and U in normal and superconductive states

N E ALEKSEEVSKII

Institute for Physical Problems, USSR Academy of Sciences, 117334, Moscow, USSR

Abstract. During the last few years superconductive systems of heavy fermions with highly large values of m^* and electronic heat capacity γT have been thoroughly investigated.

The following compounds viz $CeCu_2Si_2$ ($T_c = 0{\cdot}6$ K; $\gamma = 1100^*$), UBe_{13} ($T_c = 0{\cdot}95$ K; $\gamma = 1000$) and UPt_3 ($T_c = 0{\cdot}5$ K; $\gamma = 450$) (I) may be referred to such systems as well as the U and Ce compounds: $U_2Pt\ C_2$ ($T_c = 1{\cdot}47$ K; $\gamma = 75$), U_6Fe ($T_c = 3{\cdot}86$ K; $\gamma = 25$), U_6Co ($T_c = 2{\cdot}3$ K; $\gamma = 21$), URu_2Si_2 ($T_c = 0{\cdot}68$ K, $\gamma = 17{\cdot}6$), as well as α-U ($T_c = 2{\cdot}1$; $\gamma = 12$), $CeRu_3Si_2$ ($T_c = 1$ K; $\gamma = 39$), $CeOs_2$ ($T_c = 1,1$ K; $\gamma = 22$), $CeRu_2$ ($T_c = 6$ K; $\gamma = 23{\cdot}3$) and α-Ce ($T_c \lesssim 2$K; $\gamma = 14$) (Alekseevskii and Homskiy 1985).

It should be noted that there exists a class of U and Ce compounds with a similar structure as those given above, which undergo transition to superconductive state, but are not characterized by abnormal values of m^* (Alekseevskii 1984).

Many authors considered superconductivity of heavy fermion systems as unusually anisotropic where charge carrier coupling occurs in P-state (Stewart 1984). On the other hand such a view does not agree with many experimental results, e.g. lack of anisotropy Hc_2 for UBe_{13} (Alekseevskii *et al* 1985) as predicted by Gorkov (1984) and the results of investigation of the Josephson effect. The Hall-effect investigations for UBe_{13} in a wide range of fields and temperatures (Alekseevskii 1984) make it possible to consider systems with two types of carriers—heavy and light. The unique properties of the above systems in a number of cases are possibly caused by these two types of carriers and the peculiarity of interaction between them.

Keywords. Heavy fermions; superconductive systems.

PACS No. 74·70

References

Alekseevskii 1984 *Pis'ma JETP* **40** 66

Alekseevskii N E and Homskiy D I 1985 *Usp. Fiz. Nauk* **147** 4, 767

Alekseevskii N E, Mitin A V, Nizhankovsky V I, Firsov V I and Khlybov E P 1985 *Pis'ma JETP* **41** 335

Alekseevskii N E, Narozhniy V N, Nizhankovsky V I, Nikolaev E G and Khlybov E P 1984 *Pis'ma JETP* **40** 421

Gorkov L P 1984 *Pis'ma JETP* **40** 351

Stewart G R 1984 *Rev. Mod. Phys.* **56** 755

CC-0. In Public Domain. Gurukul Kangri Collection, Haridwar

Digitized by Arya Samaj Foundation Chennai and eGangotri

Pramāṇa – J. Phys., Vol. 28, No. 5, May 1987, p. 600. © Printed in India.

Disordered magnets

M V FEIGEL'MAN

Landau Institute for Theoretical Physics, USSR Academy of Sciences, 117334, Moscow, USSR

Abstract. The physics of strongly-disordered magnets and especially that of spin glass is an example of a scientific problem whose ideas and results are widely used in different and sometimes rather distant areas (up to biology, for example). This is the consequence of the paradoxical nature of the main question of this problem: how does ordering occur in systems which do not possess any apparent order at all? In other words, how can one find genuine (but hidden) internal variables which determine dynamics (and thermodynamics) of the system having no macroscopic order parameter.

From the theoretical point of view the "generic model" for such a system is the well-studied model of spin glass with infinite-range interaction. The next necessary step is to understand the degree of applicability of the results of infinite-range models to real systems. Further there are a number of phenomena which are completely beyond the frame of this model and are governed by fluctuation effects. The theory of fluctuation phenomena in strongly disordered magnets is at the very beginning of its development. In this report we discuss some relevant problems which have been well studied. In the case of genuine spin glasses the problems are as follows: whether there exists a thermodynamic phase transition to the spin glass phase and how does it occur? What is the physics of non-exponential relaxation far above the transition point? Further there are a number of systems belonging to the spin glass universality class (in the sense of phase-transition theory) but possessing the same sort of short-range order. We consider the following spin glasses with local helical order (for example, the diluted yttrium-based alloys YEr, YDy); amorphous magnets with strong random-axis anisotropy; disordered magnets with strong dipolar interaction. We discuss mainly the structures of low-temperature phases in these systems.

Keywords. Disordered magnets; spin glasses.

PACS No. 75·10

CC-0. In Public Domain. Gurukul Kangri Collection, Haridwar

Digitized by Arya Samaj Foundation Chennai and eGangotri

Pramāṇa – J. Phys., Vol. 28, No. 5, May 1987, p. 601. © Printed in India.

Spin waves in paramagnetic Boltzmann gases

E P BASHKIN

Institute for Physical Problems, USSR Academy of Sciences, 117334, Moscow, USSR

Abstract. As the temperature is lowered we get an interesting temperature region $\varepsilon_d \ll T \ll \hbar^2/mr_0^2$ (where ε_d is the quantum degeneracy temperature, m the mass of a gas molecule, r_0 the radius of interparticle interaction) in which the thermal de Broglie wavelength Λ of a particle is considerably greater than its size r_0 though Λ turns out to be less than the mean interparticle distance $N^{-1/3} \gg \Lambda \gg r_0$. Although the gas molecules obey the classical Boltzmann-Maxwell statistics the system as a whole begins to exhibit a large number of essentially quantum macroscopic collective features. One of the most interesting and dramatic features is the possibility of propagation of weakly damped spin oscillations in spin-polarized gases (external magnetic field, optical pumping). Such oscillations can propagate both in the low-frequency $\omega\tau \ll 1$ regime and the high frequency $\omega\tau \gg 1$. The last case is highly non-trivial for a Boltzmann gas with a short range interaction between particles. The weakness of relaxation damping of spin modes implies that the degree of polarization is high enough $1 \geqslant |\alpha| \gg |a|/\Lambda$, where $\alpha = (N_+ - N_-)N$, a is the two-particle s-wave scattering length. Under these conditions the spectrum of magnons has the form (Bashkin 1981, 1984; Lhuillier and Laloe 1982)

$$\omega = \Omega_H + (K^2 v_T^2/\Omega_{\text{int}})\,(1 - i/\Omega_{\text{int}}\tau), \quad \Omega_{\text{int}} = -4\pi a\hbar N\alpha/m, \quad v_T^2 = T/m, \tag{1}$$

where Ω_H is the Larmor precession frequency for spins in the magnetic field **H**. Collisionless Landau damping restricts the region of applicability of (1) with not too large wave vectors $Kv_T \ll |\Omega_{\text{int}}|$. The existence of collective spin waves has been experimentally confirmed in NMR-experiments with gaseous atomic hydrogen H↑ (Johnson *et al* 1984). The presence of undamped spin oscillations means automatically the existence of long range correlations for transverse magnetization. Such correlations decrease with the distance according to the power law

$$\delta_{ik}(r) = 2|a|\frac{(\beta N\alpha)^2}{\gamma}\delta_{ik}. \tag{2}$$

Here β is the molecule magnetic moment. Spin waves being even damped can nevertheless reveal themselves at $T \gtrsim \hbar^2/mr_0^2$ or when $|\alpha| \lesssim r_0/\Lambda$. The first experimental discovery or damped spin waves in gaseous ^{3}He↑ has been done in Nacher *et al* 1984. Oscillations of magnetization can also propagate in some condensed media such as liquid ^{3}He-^{4}He solutions, semimagnetic semiconductors etc.

Keywords. Spin waves; Boltzmann gas.

PACS No. 75·20

References

Bashkin E P 1981 *JETP Pis'ma* **33** 11
Bashkin E P 1984 *JETP* **87** 1948
Lhuillier C and Laloe F 1982 *J. Phys.* (*Paris*) **43** 197, 225, 833
Johnson B R *et al* 1984 *Phys. Rev. Lett.* **52** 1508
Johnson B R *et al* 1984 *Phys. Rev. Lett.* **53** 302
Nacher P J *et al* 1984 *J. Phys. Lett.* **45** 441

CC-0. In Public Domain. Gurukul Kangri Collection, Haridwar

Digitized by Arya Samaj Foundation Chennai and eGangotri

Pramāṇa – J. Phys., Vol. 28, No. 5, May 1987, p. 602. © Printed in India.

Magnetic properties and peculiarity of magnetic states in dilute antiferromagnets $Mn_{1-x}Zn_xF_2$

A N BAZHAN and S V PETROV

Institute for Physical Problems, USSR Academy of Sciences, 117334, Moscow, USSR

Abstract. The dependence of magnetic moment and susceptibility on temperature, magnetic field and frequency of some single crystals $Mn_{1-x}Zn_xF_2$ ($x \approx x_c = 0{\cdot}75$—percolation limit) were experimentally investigated. Our experiments show that (Bazhan and Petrov 1984; Cowley *et al* 1984; Villain 1984) in these crystals the nonequilibrium magnetic state of spin-glass type with finite correlation length appears as temperature decreases $T < T$ in weak magnetic fields. This state is determined by fluctuation magnetic moments $\sqrt{n}\,\mu$ (where n is the number of magnetic ions, corresponding to finite correlation length and μ the magnetic moment Mn^{+1}).

In the experiments in low magnetic fields and frequencies there are no peculiarities in the magnetic susceptibility temperature dependence at $T \neq T_f$. At temperatures $T > T_f$ and $T < T_f$ magnetic susceptibility is determined by

$$\chi(T > T_f) = \frac{N\langle\mu\rangle^2}{3k(T+\theta)} = \frac{N}{n}\frac{\langle\sqrt{n}\mu\rangle^2}{3k(T+\theta)} = \chi(T < T_f).$$

In strong magnetic fields and large frequencies there are peculiarities in the $\chi(T)$ dependence at $T = T_f$. At $T < T_f$ and strong magnetic fields $\chi(T) = \chi_0$ and $T < T_f$ and at large frequencies $\chi(T) = \chi_0 + \alpha/T$.

The dependences of magnetic susceptibility on the frequency are determined by the magnetic system relaxation. Calculations and comparison with experiments show that the relaxation of the investigated magnetic systems at $T < T_f$ follows the relaxation law $M(t) = M(0)\exp[-(t/\tau)^r]$, suggested in Palmer *et al* (1984) for spin-glasses relaxation taking into account the time relaxation distribution $\tau_0 \ldots . \tau_{max}$ in the system and its 'hierarchically' dynamics.

Keywords. Magnetic properties; antiferromagnets.

PACS No. 75·50

References

Bazhman A N and Petrov S V 1984 *J. Exp. Theor. Phys.* **86** 2179
Cowley R A, Yoshizawa H, Shirane G, Hagen M and Birgeneau B J 1984 *Phys. Rev.* **B30** 6650
Palmer R G, Stein D I, Abrams E and Anderson P W 1984 *Phys. Rev. Lett.* **53** 958
Villain J 1984 *Phys. Rev. Lett.* **52** 1543

CC-0. In Public Domain. Gurukul Kangri Collection, Haridwar

Digitized by Arya Samaj Foundation Chennai and eGangotri

Pramāṇa – J. Phys., Vol. 28, No. 5, May 1987, p. 603. © Printed in India.

Periodic density redistribution of parametrically excited spin waves in an antiferromagnet

A I SMIRNOV

Institute for Physical Problems, USSR Academy of Sciences, 117334, Moscow, USSR

Abstract. A nonuniform distribution of the density of parametrically excited magnons is observed experimentally in an antiferromagnetic $CsMnF_3$ sample. The nonuniform distribution occurs at a high pumping power when oscillations of the high frequency susceptibility occur. These oscillations were observed earlier and their nature was not clear. It is found that during the increase of the absorbed power on the occurrence of the oscillation, the spin wave condenses near the middle of the sample. The condensation occurs as a result of a nonlinear shift of the magnon spectrum and is similar to self-focusing of light in nonlinear media. The electromagnetic radiation of parametrically excited spin waves is studied. It is found that the periodic redistribution of the density exerts an additional restrictive effect on the amplitude of the parametrically excited magnons.

Keywords. Antiferromagnet; periodic density distribution.

PACS No. 75·50

CC-0. In Public Domain. Gurukul Kangri Collection, Haridwar

Digitized by Arya Samaj Foundation Chennai and eGangotri

Pramāṇa – J. Phys., Vol. 28, No. 5, May 1987, p. 604. © Printed in India.

Frozen photoconductivity in PbTe films

I P KRYLOV and YA B POJARKOV
Institute for Physical Problems, USSR Academy of Sciences, Moscow, USSR

Abstract. We have studied PbTe films of thickness $d = 200/10000$ A made with telluride vapour deposition on glass substrate at room temperature. The estimate of the donor concentration $\sim 10^{19}$ cm^{-3} of the fresh-deposited film compared with the impurity content in the bulk raw material $\sim 10^{17}$ cm^{-3} shows that the donors were mainly film defects or non-stoichiometric Pb atoms. Electrical conductivity of the freshly deposited film increased with lowering of the temperature. After deposition the donors were compensated with an oxidation in the laboratory air. Transition to the thermally activated conductivity resulted from oxidation. At temperatures below $T \approx 100$ K the resistance of the compensated films followed Mott's rule $R = R_0 \exp(T_0/T)^{1/3}$. The square film value 1 Mohm and $T_0 \approx 100$ K for $d = 1000$ A.

At low temperatures an exposure to light resulted in sharp decrease of the film resistance. At liquid helium temperatures the resistance dropped 10^3–10^6 times and stayed at the low value for an indeterminate time. The heating of the film above $T = 100$ K gave rise to an initial high resistive state. The critical temperature T_c, when the frozen photoconductivity became negligible, varied with samples in the temperature region 90–120 K. Near the critical temperature we could measure the time dependence of the film resistance after the light exposure, which followed the equation $R = A + B \cdot \ln t$ for $t > 1$ sec with the empirical constants A and B. After a time interval τ the resistance gained the initial "dark" value and remained stationary. The value $\ln \tau \approx \alpha \cdot (T_c - T)$, where the factor α approximately was $\alpha \approx 0{\cdot}5$ K^{-1}.

Some results of these experiments were published earlier (Krylov and Nadgorny 1982; Krylov and Pojarkov 1984).

Keywords. Photoconductivity; PbTe films.

PACS No. 78·60

References

Krylov I and Nadgorny B 1982 *JETP Lett.* **35** 56
Krylov I and Pojarkov Ya 1984 *JETP Lett.* **40** 5

CC-0. In Public Domain. Gurukul Kangri Collection, Haridwar

Digitized by Arya Samaj Foundation Chennai and eGangotri

ERRATUM

The dates of receipt of the following articles were not printed in the journal. We regret the omission.

(1) P GANGULY, A K RAYCHAUDHURI, K SREEDHAR and C N R RAO
Pramāṇa—J. Phys., Vol. **28,** pp. L229–L231 (February 1987)

Date of receipt: Original 21 February 1987; revised 7 March 1987

(2) P GANGULY, R A MOHAN RAM, K SREEDHAR and C N R RAO
Pramāṇa—J. Phys., Vol. **28,** pp. L321–L323 (March 1987)

Date of receipt: 19 March 1987

CC-0. In Public Domain. Gurukul Kangri Collection, Haridwar

Digitized by Arya Samaj Foundation Chennai and eGangotri

CC-0. In Public Domain. Gurukul Kangri Collection, Haridwar

Digitized by Arya Samaj Foundation Chennai and eGangotri

Pramāṇa – J. Phys., Vol. 28, No. 6, June 1987, pp. 607–616. © Printed in India.

Chou-Yang model and predictions for high-energy pion-deuteron scattering

SUNACHAND PATEL and M K PARIDA*

Physics Department, N. A. C. College, Burla, Sambalpur 76817, India
*Physics Department, North Eastern Hill University, Shillong 793003, India

MS received 6 November 1986; revised 16 March 1987

Abstract. Using fits to the available data on the pion and deuteron electromagnetic form factors and the Chou-Yang model, the computed values of differential cross-sections for high-energy pion-deuteron elastic scattering agree reasonably well with the available experimental data. Whereas only a shoulder is expected to appear up to energies of several hundreds of GeV, a dip and a secondary maximum are predicted to be conspicuous only for $P_{lab} \gg 400$ GeV/C. The position of the dip starts at a much lower value, $|t_d| \simeq 0{\cdot}5$–$0{\cdot}6$ GeV^2, as compared to the corresponding position in the pp scattering. The positions of the first dip are plotted against total cross-section which can be verified by future high-energy experiments. Limitations of the model predictions for ultrahigh energies are pointed out.

Keywords. Chou-Yang model; hadron-nucleus scattering; pion-deuteron scattering.

PACS Nos 11·80; 12·40; 13·85; 25·80

1. Introduction

Until about six years ago, the Chou-Yang model (Chou and Yang 1967, 1968, 1979; Durand and Lipes 1968; Clarke and Lo 1974; Kac 1973; Chan *et al* 1978) with the Hayot-Sukhatme modifications (Hayot and Sukhatme 1974) was considered to provide an excellent description of the elastic hadron-hadron scattering at high energies including the forward diffraction peak and the dip regions. Besides simplicity, another aesthetically appealing feature of the model is its proposed ability to provide total and differential cross-section values in terms of the interaction strength and the electromagnetic charge form factors of the colliding hadrons. However, critical analyses of the available experimental data at CERN ISR and $\bar{p}p$ collider energies have revealed several shortcomings of the model: For pp scattering with $P_{lab} \gg 400$ GeV/C, the proposed factorization hypothesis for the eikonal, as two separate functions of the impact parameter (b) and the centre of mass energy [$(s)^{1/2}$], breaks down, and the inelastic overlap function differs significantly from the model prediction (Amaldi and Schubert 1980). Also the standard Chou-Yang model fails to account for the observed slope-break at $|t| \simeq 0{\cdot}1$ GeV^2. Similar deficiencies of the model have also been noted in the case of $\bar{p}p$ scattering and new forms of the eikonal have been suggested for

* To whom correspondence should be addressed.

CC-0. In Public Domain. Gurukul Kangri Collection, Haridwar

Digitized by Arya Samaj Foundation Chennai and eGangotri

better description of the data at the ISR and collider energies (Chou and Yang 1983; Fearnley 1985).

In spite of these and other shortcomings, the model has still several impressive successes (Chou and Yang 1968, 1979; Durand and Lipes 1968; Clarke and Lo 1974; Kac 1973; Chan *et al* 1978). For $P_{\text{lab}} \lesssim 400$ GeV/C, it provides a good description of the elastic differential cross-section data for pp and $\pi^{\pm}\, p$ scattering existing in the forward peak and the dip regions. At the ISR energies, the pp differential cross-section data for values of $|t|$ somewhat below the dip region ($|t| \lesssim 1{\cdot}1$ GeV^2) are reasonably well represented by the model; besides, as noted by Chou and Yang (1979), the predicted dip position, as a function of total cross-section, agrees well with the experimental data. At the CERN collider energies also, a reasonably good description of the gross features of the differential cross-section data is possible for $\bar{p}p$ scattering within a limited $|t|$ range below the dip. For example, at $(s)^{1/2} = 546$ GeV, gross features are well reproduced for $|t| \lesssim 0{\cdot}5$ $(0{\cdot}75)$ GeV^2 when real part effects are neglected (included) (Fearnley 1985). Expecting similar successes of the model, we make predictions for high-energy hadron-nucleus scattering in this paper so that successes and failures of the model can be assessed, partially, by using the available data at limited values of P_{lab} and $|t|$ and perhaps completely, by future high-energy experiments. In this paper, we use the Chou-Yang model with Hayot-Sukhatme modifications and the well-known fits to the pion and deuteron charge form factors, to predict differential cross-section and its possible structures.

The paper is planned in the following manner: In § 2, we briefly describe the formulas relevant to the model. In § 3, the predictions of the model are reported. In § 4, we discuss our results and their range of validity.

2. Theoretical aspects of the model

Ignoring the real part and spin effects at high energies, the scattering amplitude, $A(s, t)$, for pion-deuteron scattering and its differential cross-section $\mathrm{d}\sigma/\mathrm{d}t$ can be expressed as

$$\mathrm{d}\sigma/\mathrm{d}t = \pi |A(s, t)|^2, \tag{1}$$

$$A(s, t) = \int \frac{\mathrm{d}^2 b}{2\pi} [1 - S(\mathbf{b})] \exp(\mathbf{ik}\cdot\mathbf{b}) \tag{2}$$

where
$$S(\mathbf{b}) = \exp[-\Omega(\mathbf{b})] \tag{3}$$

with $\mathbf{k}^2 = -t$, t being the square of four-momentum transfer. Here $\mathbf{b}$ is the two-dimensional impact parameter and $\Omega(\mathbf{b})$ is the opaqueness function, whose Fourier transform can be related to the pion and the deuteron form factors,

$$\langle \Omega \rangle = \mu F_{\pi}(t) F_d(t). \tag{4}$$

In the above expression μ is the $\pi^- d$ interaction strength which is generally a function of s, the square of centre of mass energy. Using equation (4) in (2), the scattering amplitude

CC-0. In Public Domain. Gurukul Kangri Collection, Haridwar

Digitized by Arya Samaj Foundation Chennai and eGangotri

can be written as a series in increasing order of the convolution products of form factors,

$$A(s,t)=\mu F_\pi(t)F_d(t)-\frac{\mu^2}{2!}F_\pi(t)F_d(t)*F_\pi(t)F_d(t)$$
$$+\frac{\mu^3}{3!}F_\pi(t)F_d(t)*F_\pi(t)F_d(t)*F_\pi(t)F_d(t). \tag{5}$$

The method of computation is simplified by assuming an exponential form of parametrization for the product of the two-form factors,

$$F_\pi(t)F_d(t)=\sum_{i=1}^{4}a_i\exp(-b_i|t|) \tag{6}$$

leading to the scattering amplitude

$$A(s,t)=\mu\sum_i a_i\exp(-b_i|t|)-\frac{\mu^2}{2!}\sum_{i,j}\frac{a_ia_j}{2Y_{ij}}\exp\left(-\frac{b_ib_j|t|}{Y_{ij}}\right)$$
$$+\frac{\mu^3}{3!}\sum_{i,j,l}\frac{a_ia_ja_l}{2^2Y_{ijl}}\exp\left(-\frac{b_ib_jb_l|t|}{Y_{ijl}}\right)$$
$$-\frac{\mu^4}{4!}\sum_{i,j,l,m}\frac{a_ia_ja_la_m}{2^3Y_{ijlm}}\exp\left(-\frac{b_ib_jb_lb_m|t|}{Y_{ijlm}}\right)+\ldots \tag{7}$$

where

$$Y_{ij}=b_i+b_j,$$
$$Y_{ijl}=Y_{ij}b_l+b_ib_j,$$
$$Y_{ijlm}=Y_{ijl}b_m+b_ib_jb_l. \tag{8}$$

Using the optical theorem and the series (7), the total cross-section can be related to the interaction strength at a given energy as

$$\sigma_T^{\pi d}=\mu-\frac{\mu^2}{2!}\sum_{i,j}\frac{a_ia_j}{2Y_{ij}}+\frac{\mu^3}{3!}\sum_{i,j,l}\frac{a_ia_ja_l}{2^2Y_{ijl}}-\frac{\mu^4}{4!}\sum_{i,j,l,m}\frac{a_ia_ja_la_m}{2^3Y_{ijlm}}+\ldots. \tag{9}$$

Assuming that the above series converges sufficiently rapidly, so that it approximately terminates after a finite number of terms, μ can be calculated numerically to match the total cross-section data at the given energy. Alternatively, we also calculate the total cross-section values for assumed values of μ at higher energies where neither total nor differential cross-section measurements are available.

3. Predictions on differential cross-sections

Available experimental data on the pion form factor are well represented by the familiar vector dominance formula

$$F_\pi(t)=1/[1+(|t|/m_\rho^2)]. \tag{10}$$

CC-0. In Public Domain. Gurukul Kangri Collection, Haridwar

Digitized by Arya Samaj Foundation Chennai and eGangotri

Throughout this paper we use all masses in GeV and t in GeV^2. The square of the deuteron charge form factor has been well approximated by the analytic representation (Parida 1979; Parida *et al* 1983),

$$F_d^2(t)=\frac{e_0\exp(-\alpha z)}{e_0+e_1t+e_2t^2+e_3t^3+h(t)+\frac{2}{3}m_\pi^2/\pi}, \tag{11}$$

where

$$z(t)=\{\ln([(-t/t_a)^{\frac{1}{2}}]+[(-t/t_a)+1]^{\frac{1}{2}})\}^2$$

$$h(t)=\frac{2}{\pi}\frac{k^3}{\sqrt{t}}\ln\left[\frac{k}{m_\pi}+\left(\frac{k^2}{m_\pi^2}+1\right)^{1/2}\right]-\frac{ik^3}{\sqrt{t}}$$

$$k=\left(\frac{t}{9}-m_\pi^2\right)^{1/2}$$

$$\alpha=0{\cdot}858, \qquad e_0=0{\cdot}947\ \text{GeV}^2,$$

$$e_1=5{\cdot}772, \qquad e_2=111{\cdot}97\ \text{GeV}^{-2},$$

$$e_3=0{\cdot}188\ \text{GeV}^{-4}, \qquad t_a=0{\cdot}033\ \text{GeV}^2. \tag{12}$$

Using formulas (10)–(12), we first obtain the curve for the function $F_\pi(t)F_d(t)$ as a function of $|t|$ in the spacelike region for $0\leqslant -t\leqslant 10$ GeV^2 and then fit this curve by formula (6). The best fit is shown in figure 1 and has the following parameters

$$a_1=0{\cdot}647, \qquad b_1=15{\cdot}98\ \text{GeV}^{-2},$$

$$a_2=0{\cdot}320, \qquad b_2=7{\cdot}984\ \text{GeV}^{-2},$$

$$a_3=0{\cdot}018, \qquad b_3=1{\cdot}985\ \text{GeV}^{-2},$$

$$a_4=2{\cdot}7\times10^{-4}, \qquad b_4=0{\cdot}492\ \text{GeV}^{-2}. \tag{13}$$

In figure 1 the circles represent the product function $F(t)=F_\pi(t)F_d(t)$ as given by formulas (10)–(12) and the solid-tune is the fit by the formula (6) with the parameters given in (13). Visually, this appears to be an excellent fit. Since the experimental data on the deuteron (pion) form factor is available up to $|t|=6$ GeV^2 (2 GeV^2) and the formula (11) ((10)) fits them very well, we propose that the four-exponential fit given by (6) is a very good approximation to the product function at least upto $t=2$ GeV^2. To make the model calculations more reliable, our predictions on the differential cross-sections at various energies are confined to the region $|t|\lesssim 2$ GeV^2.

In order to calculate the differential cross-section, we have first calculated the interaction strength μ, for a given value of total cross-section using (9) with values of parameters given by (13). The value of μ and other parameters were then used in (1) and (7) to calculate the differential cross-sections. For our calculations we have retained the first five terms in (8) and (9) as the higher order terms were not found to be significant. For example, at the available laboratory momentum $P_{\text{lab}}=9$ GeV/C (15·2 GeV/C) the

CC-0. In Public Domain. Gurukul Kangri Collection, Haridwar

Digitized by Arya Samaj Foundation Chennai and eGangotri

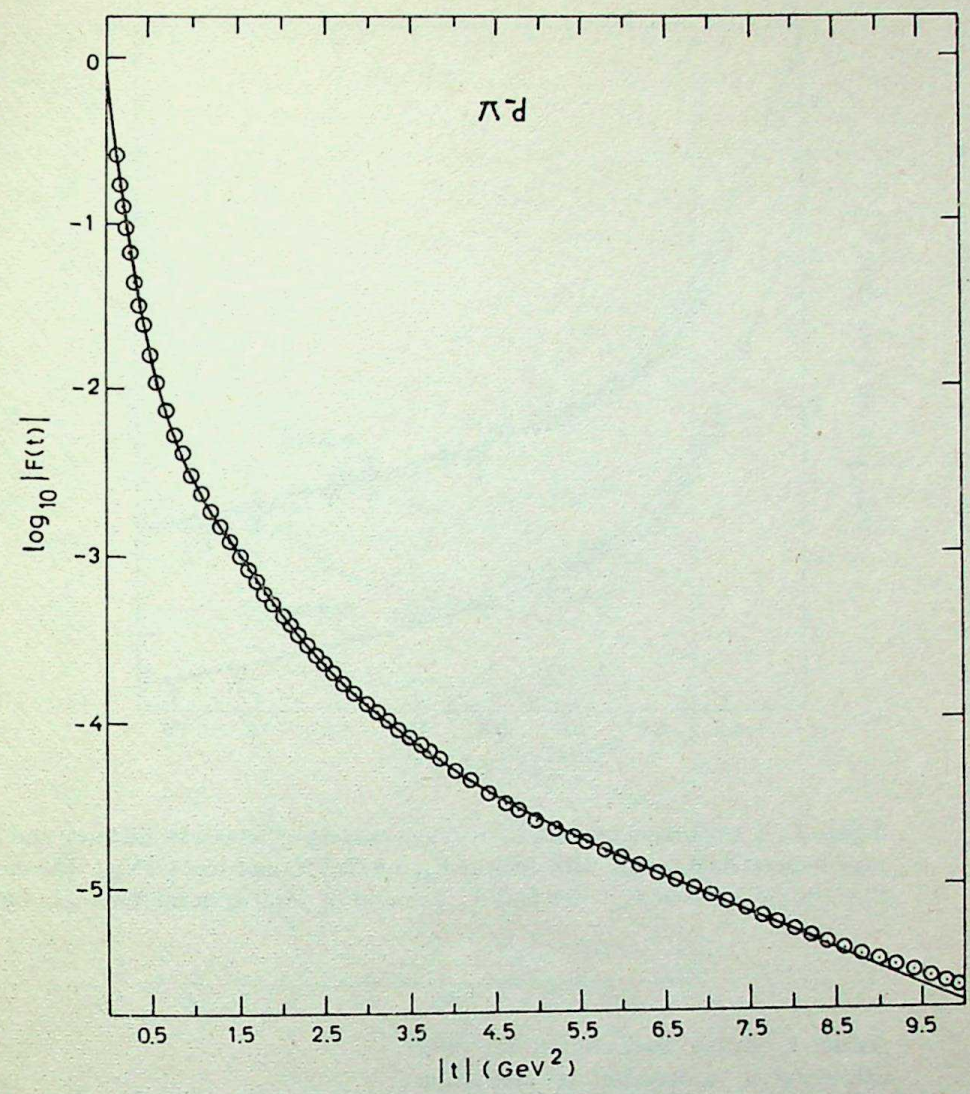

Figure 1. Demonstration of the agreement between the product function of the pion and the deuteron form factors and the four exponential approximation given by equation (6) with the parameters given in (13).

formula (9) yields $\mu = 11{\cdot}58\ \text{GeV}^{-2}$ ($10{\cdot}76\ \text{GeV}^{-2}$) corresponding to the measured value (Bradamante *et al* 1970) of total cross-section, $\sigma_T = 50{\cdot}0$ ($46{\cdot}8$) mb. The predicted values of the differential cross-section at each of these values as a function of $|t|$ are shown in figure 2 by the solid lines. Agreement with the experimental data at larger $|t|$ region with $|t| > 0{\cdot}4\ \text{GeV}^2$ seems to be good. But the predicted values of $d\sigma/dt$ appear to lie 50–100% above the data in the diffraction peak region for $|t| < 0{\cdot}4\ \text{GeV}^2$. Since the differential cross-section at $t = 0$ has been normalized to σ_{tot} via an optical theorem, the predicted values are expected to lie at or below the data points, depending upon whether or not the real part is negligible. Such seemingly contrasting behaviour between the data and the model predictions could be due to the possible presence of a slope-break around $-t \simeq 0{\cdot}1\ \text{GeV}^2$ that the model fails to account. However, since the theory is essentially a high-energy model, we expect better agreement with the future data at higher energies ($P_{lab} \simeq 50$–100 GeV/C).

Calculated values of total cross-section for higher values of interaction strengths using (9) are presented in table 1 for which the available energy and cross-sections have

CC-0. In Public Domain. Gurukul Kangri Collection, Haridwar

Digitized by Arya Samaj Foundation Chennai and eGangotri

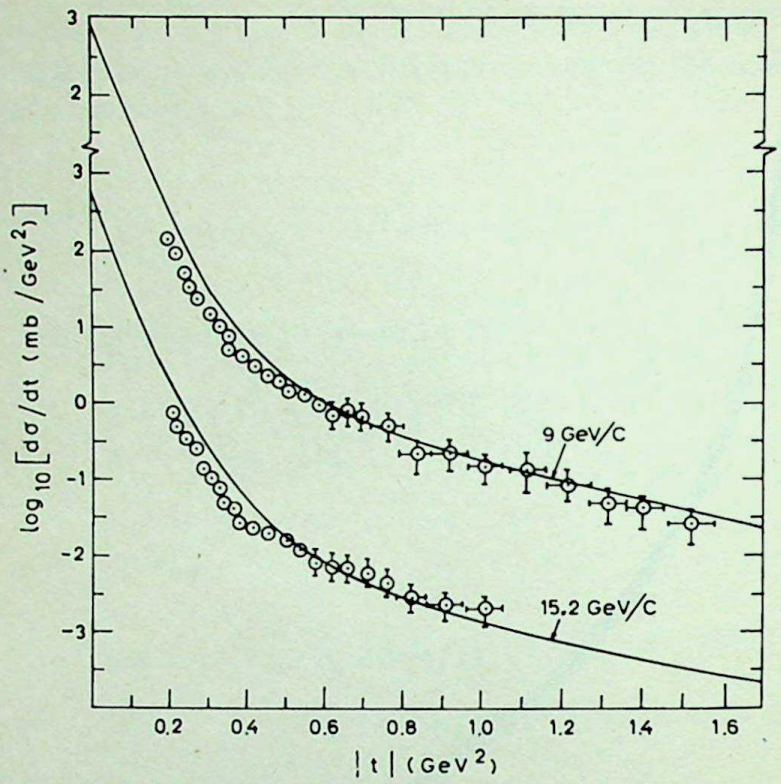

Figure 2. Comparison between Chou-Yang model predictions (solid lines) and the available experimental data (circles with dots) at $P_{lab}=9$ GeV/C and 15·2 GeV/C. The data points for $|t|\gtrsim 1{\cdot}01$ GeV^2 are at $P_{lab}=8{\cdot}9$ GeV/C. The unit of $d\sigma/dt$ is in mb/GeV^2, in figures 2–4.

Table 1. Total cross-section for $\pi^- d$ scattering as a function of interaction strength.

μ (GeV^{-2})	σ_T (mb)
10·75	46·80
11·58	50·00
15·00	62.81
17·50	73·44
20·00	80·22
25·00	96·23
30·00	111·03

not been experimentally measured. The predicted values of differential cross-section as a function of $|t|$ are shown in figure 3 for $\mu=15{\cdot}0$, 17·5, 20·0 and 25 GeV^2, and also in figure 4 for $\mu=30$ GeV^{-2}. We observe that only a shoulder appears in the differential cross-section for $\mu=17{\cdot}5$–20 GeV^{-2} in the region $|t|=0{\cdot}6$–$0{\cdot}8$ GeV^2, but a conspicuous dip structure appears for $\mu\gtrsim 25$ GeV^{-2}. As μ increases from 25 GeV^{-2} to 30 GeV^{-2},

CC-0. In Public Domain. Gurukul Kangri Collection, Haridwar

Digitized by Arya Samaj Foundation Chennai and eGangotri

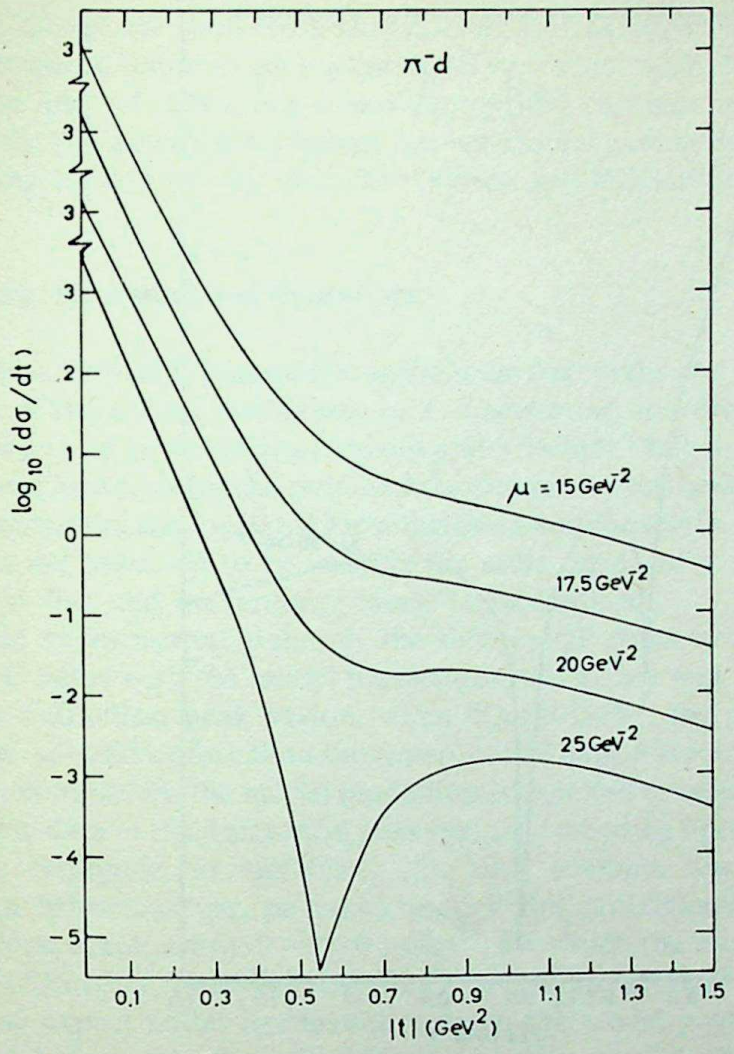

Figure 3. Predictions for the differential cross-sections and positions of shoulders, dips, and higher order maxima.

the diffraction peak shrinks and the dip moves from $|t_d| = 0{\cdot}55$ GeV^2 to $|t_d| = 0{\cdot}4$ GeV^2. With $\mu = 30$ GeV^{-2}, the differential cross-section, besides exhibiting the prominent first dip and the second maximum, also displays the presence of a prominent second dip at $t_d = 0{\cdot}7$ GeV^2 and a third maximum in the range $|t| = 0{\cdot}9$–$1{\cdot}1$ GeV^2, which is rather broad. As shown in table 1, our calculations for $\pi^- d$ scattering predict the increase of total cross-section from 62·8 mb to 111 mb with μ increasing between 15·0 and 30 GeV^{-2}. A plot of the position of the first dip position as a function of total cross-section is shown in figure 5 which can be verified from the total and differential cross-section measurements at very high energies in future. The occurrence of the first dip at the highest position $|t_d|^{\max} \simeq 0{\cdot}5$–$0{\cdot}6$ GeV^2 for $\mu \simeq 22$–25 GeV^{-2} is in sharp contrast to such positions in pp and $\bar{p}p$ scattering for which $|t_d|^{\max} \gtrsim 1{\cdot}5$ GeV^2. Note that our earlier analysis revealed the Chou-Yang model prediction for pd scattering to be $|t_d|^{\max} \simeq 0{\cdot}35$–$0{\cdot}4$ GeV^2 which is also in contrast to pp, $\bar{p}p$ and $\pi^{\pm} p$ scattering and also somewhat lower than the model prediction for $\pi^- d$ scattering. Our predictions of differential cross-sections at such energies for which a dip appears are subject to the limitations, as stated in §§ 1 and 4. Using the analogy of the model predictions for πN and NN scattering with those in πd and pd scattering, it is possible to have a rough idea

CC-0. In Public Domain. Gurukul Kangri Collection, Haridwar

Digitized by Arya Samaj Foundation Chennai and eGangotri

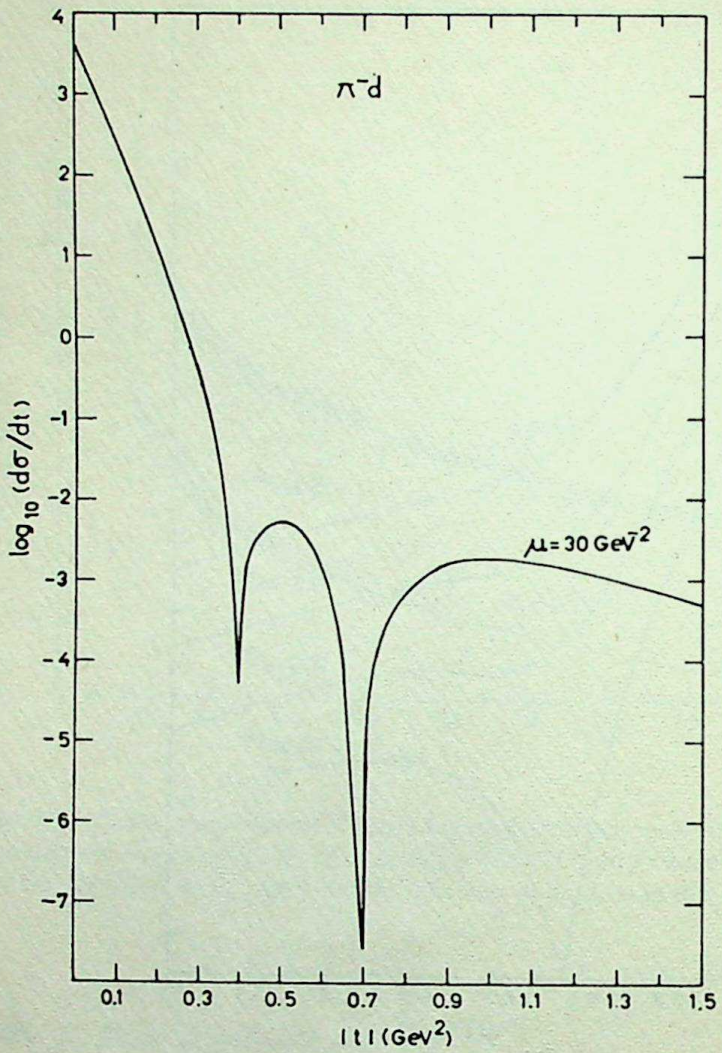

Figure 4. Same as figure 3 but for $\mu = 30\ \text{GeV}^{-2}$.

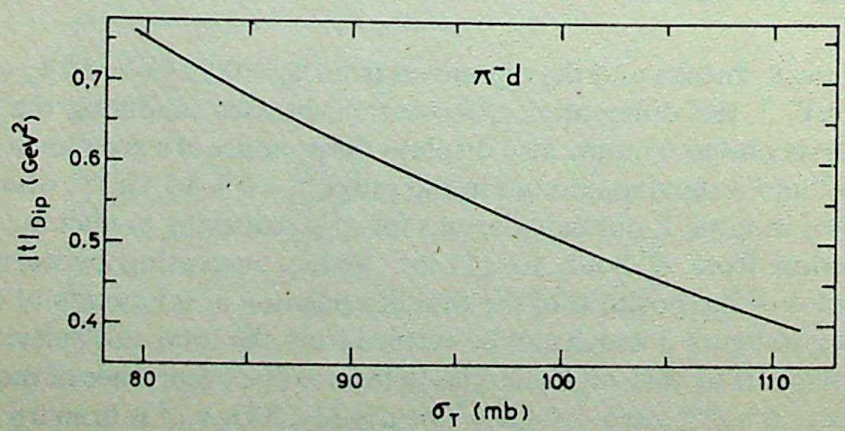

Figure 5. A plot of given values of total cross-sections and predicted first dip positions at very high energies.

about the approximate energy region for which a shoulder would continue to appear in the πd scattering. It is well known that within $|t| \lesssim 2\ \text{GeV}^2$, the dip structure in $\pi^{\pm} p$ scattering does not set in earlier in energy scale than the pp scattering. One of the possible reasons for such a phenomenon in the model may be due to the fact that at a

CC-0. In Public Domain. Gurukul Kangri Collection, Haridwar

Digitized by Arya Samaj Foundation Chennai and eGangotri

given high energy, the total cross-section in $\pi^{\pm}p$ is less (approximately two-third) than its corresponding value in pp scattering. If we expect a similar analogy to be valid between pd and πd scattering, a shoulder would continue to appear at least until $P_{\text{lab}} \simeq 400$ GeV/C since such a feature has been found among the model predictions for pd scattering carried out by us earlier (Parida and Patel 1981).

4. Summary, discussion and limitations

In this section we briefly summarize and discuss our results and point out limited range of validity of the model predictions in $\pi^- d$ scattering, in view of the existing critical analyses in pp and $\bar{p}p$ scattering (Amaldi and Schubert 1980; Fearnley 1985). Since the interpolating formulas for the pion and the deuteron electromagnetic form factors are found to reproduce the available form-factor data in the region $|t| \lesssim 2$ GeV^2, the model predictions are expected to be valid in the same region of $|t|$ in which the predicted positions of dips and maxima are found to be confined.

Available experimental data on the differential cross-sections at $P_{\text{lab}} = 9{\cdot}0$ and 15·2 GeV/C agree with the model predictions reasonably well for $0{\cdot}4 \lesssim |t| \lesssim 1{\cdot}5$ GeV^2; but in the diffraction peak region, when $|t| < 0{\cdot}4$ GeV^2, the predicted cross-section seems to be 50–100% more than the experimental data. Since we have ignored the real part effects completely, the model prediction is expected to be the same as, or less than the available data in the diffraction peak region, depending upon whether the real part effects are negligible, or significant, for such energies. Such type of apparently contrasting behaviour can be understood if the experimental cross-section has a possible slope break around $-t \simeq 0{\cdot}1$ GeV^2, for which the model furnishes no exact explanation. Further, by noting that the Chou-Yang model is meant to apply at higher energies, we expect better agreement between the model predictions and the future experimental data for $P_{\text{lab}} \simeq 50$–100 GeV/C. We predict that a shoulder in the differential cross-section would continue to appear in the region $-t \simeq 0{\cdot}6$–$0{\cdot}8$ GeV^2 until such energies for which $\mu \simeq 20$ GeV^{-2} and $\sigma_T \simeq 80$ mb; but a conspicuous dip structure would appear only for $\mu \gtrsim 25$ GeV^{-2}, or $\sigma_T \gtrsim 90$ mb. As μ increases from 25 GeV^{-2} to 30 GeV^{-2} with increasing energy, the diffraction peak is predicted to shrink and the dip is predicted to move from $|t_d| \simeq 0{\cdot}55$ GeV^2 to $|t_d| \simeq 0{\cdot}4$ GeV^2. These features of the dip in respect of the energy and the position, at which it is expected to appear, are in sharp contrast to pp scattering where the first appearance of the dip takes place at $P_{\text{lab}} \simeq 50$–100 GeV/C and $|t_d| \lesssim 1{\cdot}5$ GeV^2. But the highest dip position in $\pi^- d$ scattering is larger than the corresponding one in pd scattering, for which, using the Chou-Yang model, we predicted $|t_d|^{\max} \simeq 0{\cdot}35$–$0{\cdot}4$ GeV^2 (Parida and Patel 1981). At present, it is possible to predict the appearance and position of a dip as a function of μ or σ_{tot}, but not as a function of energy, since measurements of σ_{tot} at sufficiently high energies are not available.

As discussed in § 1, detailed analyses of the pp and $\bar{p}p$ differential cross-section data at the ISR and CERN collider energies have revealed that the Chou-Yang model fails to account for the observed variation of the differential cross-section near and away from the dip region. Also it fails to account for the observed slope break at $|t| = 0{\cdot}1$ GeV^2 in pp scattering. Despite these and other failures, the gross features of the forward peak upto $|t| \simeq 1{\cdot}1$ GeV^2 in pp at the ISR energies and $|t| \simeq 0{\cdot}75$ GeV^2 in $\bar{p}p$ at the collider energies are described by the model reasonably well. Also, as noted by Chou and Yang

CC-0. In Public Domain. Gurukul Kangri Collection, Haridwar

Digitized by Arya Samaj Foundation Chennai and eGangotri

(1979), the positions of the dip, as a function of total cross-section or energy, are predicted and found to agree reasonably well with the observed values in pp at the ISR energies. For $P_{lab} \lesssim 400$ GeV/C, however, the agreement of the model predictions with the high energy data in the forward peak and dip regions have been found to be good. In the high-energy hadron nucleus scattering, expecting similar successes and failures, we note that the future experimental data on $\pi^- d$ scattering would agree with our predictions upto at least $P_{lab} \simeq 500$ GeV/C. For $P_{lab} \gg 500$ GeV/C, disagreements may appear in the region $|t| \gtrsim 0{\cdot}5$ GeV^2 when the dip and the secondary maximum are conspicuous.

Acknowledgement

The authors are thankful to the Computer Centre, Utkal University for help in computation.

References

Amaldi U and Schubert K R 1980 *Nucl. Phys.* **B166** 301
Bradamante F *et al* 1970 *Phys. Lett.* **B31** 87
Chan S C, Lo S T, Low H B and Phua K K 1978 *Phys. Rev.* **D17** 802
Chou T T and Yang C N 1967 *High energy physics and nuclear structure* (ed.) G Alexander (Amsterdam: North Holland) 348
Chou T T and Yang C N 1968a *Phys. Rev. Lett.* **20** 1213
Chou T T and Yang C N 1968b *Phys. Rev.* **170** 1591
Chou T T and Yang C N 1979 *Phys. Rev.* **D19** 3268
Chou T T and Yang C N 1983 *Phys. Lett.* **B128** 457
Clarke D J and Lo S Y 1974 *Phys. Rev.* **D10** 1519
Durand L and Lipes R 1968 *Phys. Rev. Lett.* **20** 637
Fearnley T 1985 CERN Report EP/85-137
Hayot F and Sukhatme U P 1974 *Phys. Rev.* **D17** 802
Kac M 1973 *Nucl. Phys.* **B62** 402
Parida M K 1979 *Phys. Rev.* **D19** 3320
Parida M K and Patel S 1981 *Phys. Rev.* **D24** 1865
Parida M K, Patel S and Agrawalla K N 1983 *Phys. Rev.* **D27** 1187

CC-0. In Public Domain. Gurukul Kangri Collection, Haridwar

Digitized by Arya Samaj Foundation Chennai and eGangotri

Pramāṇa – J. Phys., Vol. 28, No. 6, June, 1987, pp. 617–619 © Printed in India.

Equivalence of stochastic quantization to field theories from supersymmetry

S CHATURVEDI, A K KAPOOR* and V SRINIVASAN*
Institute of Mathematical Sciences, Adyar, Madras 600 113, India
*School of Physics, University of Hyderabad, Hyderabad 500 134, India

MS received 17 November 1986; revised 6 March 1987

Abstract. Using the Ward-Takahashi identities from the hidden supersymmetry in Langevin equation we present a very simple proof of the equivalence of stochastic quantization to field theories.

Keywords. Stochastic quantization; supersymmetry; Ward-Takahashi identities.

PACS Nos 12·20; 11·10

The stochastic quantization of Parisi and Wu (1981) scheme has been a subject of intensive study over the past few years. Several authors have proved the equivalence of this method to the conventional quantization method (Cardy 1983; Nakazato *et al* 1983; Grimus and Huffel 1983; Gozzi 1984; Krischner 1984; Gangopadhyay *et al* 1986). It is now well known that there is a superspace of formulation of the Langevin equation which brings out the hidden supersymmetry (SUSY) associated with the Langevin equation (Chaturvedi *et al* 1984a; Gozzi 1983; Egorian and Kalitzin 1983; Feigelman and Tsevlik 1982). This SUSY implies certain Ward-Takahashi identities that were derived by the authors and were used to give a very simple proof of the fluctuation dissipation theorem (Chaturvedi *et al* 1984b). In this paper we shall use the SUSY identities alone to give a very simple and direct proof of the equivalence.

Consider the Langevin equation

$$\frac{\partial\varphi(x,t)}{\partial t}=-\frac{\delta S}{\delta\varphi(x,t)}+\eta(x,t) \tag{1}$$

where $\varphi(x, t)$ is a scalar field and $\eta(x, t)$ a gaussian white noise source. The generating functional for the Green functions $Z(j)$, has been shown to be given by (Chaturvedi *et al* 1984a; Gozzi 1983; Egorian and Kalitzin 1983; Feigelman and Tsevlik 1982).

$$Z(j)=\int\mathscr{D}\varphi\mathscr{D}\pi\mathscr{D}\psi\mathscr{D}\bar{\psi}\exp[\int dx\,dt\,d\alpha\,d\bar{\alpha}\{-\mathscr{L}_{ss}+\mathscr{J}\Phi\}]. \tag{2}$$

Here, $\alpha, \bar{\alpha}$ are anticommuting Grassman variables and

$$\mathscr{L}_{ss}=\frac{1}{2}\Phi\frac{\partial}{\partial t}\Phi-\Phi\frac{\partial^2}{\partial\bar{\alpha}\partial\alpha}\Phi-\Phi\alpha\frac{\partial^2}{\partial\alpha\partial t}\Phi+\mathscr{L}(\Phi), \tag{3}$$

CC-0. In Public Domain. Gurukul Kangri Collection, Haridwar

Digitized by Arya Samaj Foundation Chennai and eGangotri

where Φ is the superfield defined by

$$\Phi=\varphi+\bar{\alpha}\psi+\bar{\psi}\alpha+\alpha\bar{\alpha}\pi \tag{4}$$

and the source $\mathscr{J}$ is

$$\mathscr{J}(x,t)=j(x)\delta(t). \tag{5}$$

The superspace Lagrangian is invariant under the following SUSY transformations.

$$\delta\varphi=\bar{\varepsilon}\psi+\bar{\psi}\varepsilon; \qquad \delta\psi=\varepsilon(\dot{\varphi}-\pi);$$
$$\delta\bar{\psi}=-\bar{\varepsilon}\pi; \qquad \delta\pi=-\varepsilon\dot{\bar{\psi}}. \tag{6}$$

Taking the source to be $\mathscr{J}=K+\bar{\alpha}L+\bar{L}\alpha+\alpha\bar{\alpha}J$, the Ward-Takahashi relations associated with these sources are obtained in an earlier paper (Chaturvedi *et al* 1984b), and are given by

$$\int dx\,dt\left[K(x,t)\frac{\partial}{\partial t}\frac{\delta Z}{\delta L(x,t)}+J(x,t)\frac{\delta Z}{\delta L(x,t)}-\bar{L}(x,t)\left(\frac{\partial}{\partial t}\frac{\delta Z}{\delta J(x,t)}-\frac{\delta Z}{\delta K(x,t)}\right)\right]=0 \tag{7}$$

and

$$\int dt\,dx\left[J(x,t)\frac{\delta Z}{\delta\bar{L}(x,t)}-L(x,t)\frac{\delta Z}{\delta K(x,t)}\right]=0. \tag{8}$$

Differentiating (4) with respect to $\bar{L}(x,t)$ and setting $\bar{L}=L=0$ we arrive at

$$\int dy\,d\tau\left[-\frac{\partial}{\partial\tau}K(y,\tau)+J(y,\tau)\right]\frac{\delta^2 Z}{\delta\bar{L}(x,t)\,\delta L(y,\tau)}\bigg|_{L=\bar{L}=0}+\left(\frac{\partial}{\partial t}\frac{\delta Z}{\delta J(x,t)}-\frac{\delta Z}{\delta K(x,t)}\right)\bigg|_{L=\bar{L}=0}=0. \tag{9}$$

The equation of motion for the π field is

$$2\frac{\delta Z}{\delta K(x,t)}-\frac{\partial}{\partial t}\frac{\delta Z}{\delta J(x,t)}+\left\langle\frac{\delta S(\varphi)}{\delta\varphi(x,t)}\right\rangle+K(x,t)=0, \tag{10}$$

where we have used the notation

$$\langle f(\varphi)\rangle=\int\mathscr{D}\varphi\mathscr{D}\pi\mathscr{D}\psi\mathscr{D}\bar{\psi}\exp\left[\int dx\,dt\,d\alpha\,d\bar{\alpha}\left(-\mathscr{L}_{ss}+\mathscr{J}\Phi\right)\right]f(\varphi). \tag{11}$$

Equations (9) and (10) with $K=0$ imply

$$\frac{\partial}{\partial t}\frac{\delta Z_0}{\delta J(x,t)}+2\frac{\delta S}{\delta\varphi}\bigg|_{\varphi=\delta/\delta J}Z_0=2\int dy\,d\tau\,J(y,\tau)\frac{\delta^2 Z_0}{\delta\bar{L}(x,t)\,\delta L(y,\tau)}, \tag{12}$$

where Z_0 is the generating functional Z for $K=L=\bar{L}=0$. If we take J as in (5) the right

CC-0. In Public Domain. Gurukul Kangri Collection, Haridwar

Digitized by Arya Samaj Foundation Chennai and eGangotri

hand side of (12) involves the value of $\delta^2 Z_0/\delta\bar{L}\,\delta L$ at equal times $t=\tau=0$. It can be easily proved that (Nakano 1983)

$$\left.\frac{\delta^2 Z_0}{\delta\bar{L}(x,t)\,\delta L(y,\tau)}\right|_{t=\tau}=\frac{1}{2}\delta(x-y)Z_0. \tag{13}$$

Also in the steady state we must have

$$\frac{\partial}{\partial t}\frac{\delta Z_0}{\delta J(x,t)}=0. \tag{14}$$

Using (12), (13) and (14) we get

$$\left.\frac{\delta S}{\delta\varphi}\right|_{\varphi=\delta/\delta j} Z_0=j(x)Z_0. \tag{15}$$

The above equation implies that the generating functional $Z(j)$ has the form

$$Z_0(j)=\int\mathscr{D}\varphi\exp[-S(\varphi)+\int j(x)\varphi(x)\,dx]. \tag{16}$$

This completes the desired proof.

References

Cardy J 1983 *Phys. Lett.* **B125** 470
Chaturvedi S, Kapoor A K and Srinivasan V 1984a *J. Phys.* **A17** 2037
Chaturvedi S, Kapoor A K and Srinivasan V 1984b *Z. Phys.* **B57** 2037
Egorian E and Kalitzin S 1983 *Phys. Lett.* **B129** 320
Feigelman M V and Tsevlik A M 1982 *Sov. Phys. JETP.* **56** 825
Gangopadhyay D, Chatterjee A and Majumdar P 1986 *J. Phys.* **G12** L1
Gozzi E 1983 *Phys. Rev.* **D28** 1922
Gozzi E 1984 *Phys. Lett.* **B143** 183
Grimus W and Huffel H 1982 *Z. Phys.* **C18** 29
Krischner 1984 *Phys. Lett.* **B139** 180
Nakano Y 1983 *Progr. Theor. Phys.* **69** 361
Nakazato H, Namiki M, Ohaba I and Okano K 1983 *Progr. Theor. Phys.* **70** 298
Parisi G and Wu Y S 1981 *Sci. Sin.* **24** 483

CC-0. In Public Domain. Gurukul Kangri Collection, Haridwar

Digitized by Arya Samaj Foundation Chennai and eGangotri

CC-0. In Public Domain. Gurukul Kangri Collection, Haridwar

Digitized by Arya Samaj Foundation Chennai and eGangotri

Pramāṇa – J. Phys., Vol. 28, No. 6, June 1987, pp. 621–632. © Printed in India.

Supersymmetric $SU_C(4) \times SU_L(2) \times SU_R(2)$ and spontaneous breakdown of symmetries

B BHUYAN and B B DEO
Department of Physics, Utkal University, Bhubaneswar 751 004, India

MS received 15 July 1986; revised 6 December 1986

Abstract. A supersymmetric version of the left right symmetric partial unification group $SU_C(4) \times SU_L(2) \times SU_R(2)$ is presented. The spontaneous breakdown of gauge symmetry in a favourable chain of descent has been studied in detail. The mass spectra have been calculated. The method of O'Raifeartaigh has been used to break supersymmetry. The lifting of degeneracy of mass levels between physical multiplets has been shown to occur due to radiative corrections.

Keywords. Gauge symmetry; supersymmetry; radiation correction.

PACS Nos 11·30; 11·15

1. Introduction

Pati and Salam (1973) proposed to unify the strong, electromagnetic and weak interaction by gauging a symmetry group $SU_C(4)$ associated with a multiplet containing both quarks and leptons. The semi-simple group $SU_C(4) \times SU_L(2) \times SU_R(2)$ called the Pati-Salam group with fractionally charged quarks is the only rank 5 partial unification group and one of the most attractive extensions of the standard electroweak model. The model is left right symmetric and is formulated so that parity has to be a spontaneous broken symmetry.

To include both bosons and fermions in the same multiplet one has to supersymmetrize the theory which also gives a natural solution to hierarchy problem in grand unified theories. However if supersymmetric gauge theories are to explain low energy phenomenon both supersymmetry and gauge symmetries are to be broken. Even though spontaneous breakdown of gauge symmetry can be easily induced, supersymmetry is not easily broken.

The breakdown of supersymmetry in the case of standard model $SU_C(3) \times SU_L(2) \times U(1)$ has been studied by Dine and Fischler (1982). But the supersymmetric version of the Pati-Salam group and the subsequent supersymmetric breakdown to $SU_C(3) \times U_{EM}(1)$ has not yet been worked out.

Breakdown of gauge invariance in supersymmetric SO(10) has been studied by Gipson and Marshak (1984) who considered the chain of symmetry breaking

$$SO(10) \rightarrow SU_C(4) \times SU_L(2) \times SU_R(2) \rightarrow SU_C(3) \times SU_L(2) \times SU_R(2) \times U_{B-L}(1)$$
$$\rightarrow SU_C(3) \times SU_L(2) \times U_Y(1) \rightarrow SU_C(3) \times U_{EM}(1),$$

CC-0. In Public Domain. Gurukul Kangri Collection, Haridwar

Digitized by Arya Samaj Foundation Chennai and eGangotri

by the multiplet $\chi(15, 1, 1)$, $\Delta_L(10, 3, 1)$ $\bar{\Delta}_R(\overline{10}, 1, 3)$ and $\Phi(1, 2, 2)$. In this chain, the left right symmetry breaking occurs in the GUT scale. To get an intermediate scale, one has to break partiy. However it has been found (Marshak and Mohapatra 1984) that the most favourable chain breaking including two-loop correction is

$$\mathrm{SO}(10)\xrightarrow[210(54)]{M_X(M_P)}\mathrm{SU}_C(4)\times\mathrm{SU}_L(2)\times\mathrm{SU}_R(2)$$
$$(1, 1, 1)$$
$$\xrightarrow[210]{M_R}\mathrm{SU}_C(3)\times\mathrm{U}_{B-L}(1)\times\mathrm{SU}_L(2)\times\mathrm{U}(1)$$
$$(15, 1, 3)$$
$$\xrightarrow[126]{M_R^\circ}\mathrm{SU}_C(3)\times\mathrm{U}_Y(1)\times\mathrm{SU}_L(2).$$
$$(10, 1, 3)$$

What we have attempted here is supersymmetrizing at the left right symmetric stage which might have descended from any grand unified group and followed the above most favourable chain of gauge symmetry breaking. The calculation of supersymmetry breaking and gauge symmetry breaking is actually highly involved and will be given in the text. In § 2, we have studied the spontaneous breakdown of gauge symmetry $\mathrm{SU}_C(4)\times\mathrm{SU}_L(2)\times\mathrm{SU}_R(2)$ to $\mathrm{SU}_C(3)\times\mathrm{U}_{EM}(1)$ through intermediate stages, preserving supersymmetry. In § 3, we discuss supersymmetry breaking by the O'Raifeartaigh mechanism. The supersymmetry breaking is not directly coupled to the physical light world. The O'Raifeartaigh sector of superheavy supermultiplets which are responsible for supersymmetry breaking is coupled to the light world. This produces indirect couplings. Due to mass splitting of the supermultiplets their differing contribution as intermediate state breaks the supersymmetry of the physical world.

2. Spontaneous breakdown of gauge symmetry

For the left right symmetric model there will be three gauge superfields. They belong to adjoint representation of $\mathrm{SU}_C(4)$, $\mathrm{SU}_L(2)$ and $\mathrm{SU}_R(2)$. The colour gauge field is a fifteenplet and the left right gauge fields are triplet in nature.

A gauge superfield $V=V^\dagger$ in the Wess Zumino gauge (Wess and Zumino 1974)

$$V(y\theta\bar{\theta})=-\theta\sigma^m\bar{\theta}V_m(y)+i\theta\theta\bar{\theta}\bar{\lambda}(y)-i\bar{\theta}\bar{\theta}\theta\lambda(y)$$
$$+\tfrac{1}{2}\theta\theta\bar{\theta}\bar{\theta}[D(y)-i\partial^m V_m(y)]. \tag{1}$$

The associated non-abelian gauge transformation is $\exp(gv)\to[\exp(i\Lambda^\dagger)\cdot\exp(gv)\cdot\exp(i\Lambda)]$. Both Λ and v are matrices. $\Lambda=T^a\Lambda^a$, $V=T^aV_a$. The gauge and superinvariant Lagrangian L_g for the gauge multiplet is of the form

$$L_g=\mathrm{Tr}[-\tfrac{1}{4}(V_{\mu\nu}V^{\mu\nu})-i\lambda\sigma^m D_m\bar{\lambda}+\tfrac{1}{2}D^2], \tag{2}$$

where $V_{\mu\nu}=\partial_\mu V_\nu-\partial_\nu V_\mu+ig[V_\mu, V_\nu]$,

and $D_m\bar{\lambda}=\partial_m\bar{\lambda}+ig[V_m\bar{\lambda}]$.

We have made the replacement $V_\mu\to 2gV_\mu$, $\lambda\to 2g\lambda$, $D\to 2gD$. Now we study the

CC-0. In Public Domain. Gurukul Kangri Collection, Haridwar

Digitized by Arya Samaj Foundation Chennai and eGangotri

spontaneous breakdown of $SU_C(4) \times SU_L(2) \times SU_R(2)$ as mentioned in the introduction. Introducing the chiral multiplets $\varphi_c(15, 1, 3)\, \Phi_{1R}(10, 1, 3), \Phi_{2R}(\overline{10}, 1, 3), \Phi(1, 2, 2)$ as well as the three singlets X, Y, Z the correct gauge symmetry breaking can be implemented. The component fields of φ_c, Φ_R and Φ are $(A_C \Psi_C F_C)$, $(A_R \Psi_R F_R)$ and $(A \Psi F)$; respectively. For the singlets X, Y, Z $(a_x \Psi_x f_x)$, $(a_y \Psi_y f_y)$ and $(a_z \Psi_z f_z)$ respectively are the component fields.

The invariant Lagrangian is taken to be

$$\begin{aligned} L_H = [&\mathrm{Tr}\{\varphi_C^\dagger \exp(V_C + V_R)\varphi_C + \Phi_{1R}^\dagger \exp(V_C + V_R)\Phi_{1R} \\ &+ \Phi_{2R} \exp -(V_C + V_R)\Phi_{2R}^\dagger + \Phi_1^\dagger \exp(V_L + V_R)\Phi_1 \\ &+ \Phi_2^\dagger \exp[-(V_L + V_R)]\Phi_2\} + X^*X + Y^*Y + Z^*Z]_D \\ &- \mathrm{Tr}[\{a(\varphi_C^2 - M_C^2)X + b(\Phi_{2R}\Phi_{1R} - M_R^2)\, Y + c(\Phi \tau_2 \Phi^* \tau_2 \\ &- 2\, mm')Z\}F + \mathrm{c.c}] \end{aligned} \tag{3}$$

where $\Phi_1 \equiv \Phi$ and $\Phi_2 \equiv \tau_2 \Phi^* \tau_2$. M_C is the mass scale for lepton colour symmetry breaking and is usually of the order of 10^{15} to 10^{16} GeV. M_R is the left right symmetry-breaking scale and can range from 10^4 GeV upwards. m is of the electroweak scale of 10^2 GeV. The equation of motion for the auxiliay fields are

$$\begin{aligned} &F_C^\dagger = 2aA_C a_x, && f_x^* = \mathrm{Tr}\, a(A_C^2 - M_C^2) \\ &F_{1R}^\dagger = bA_{2R}a_y, && f_y^* = \mathrm{Tr}\, b(A_{1R}A_{2R} - M_R^2), \\ &F_{2R}^\dagger = bA_{1R}a_y, && f_z^* = \mathrm{Tr}\, cA\tau_2 A^* \tau_2 - c2mm', \\ &F_1^\dagger = c\tau_2 A_1^* \tau_2 a_z, && D_L = -g_L(A_1 A_1^\dagger - A_2 A_2^\dagger) \\ &F_2^\dagger = cA_1 a_z, \\ &D_c^{\gamma\alpha} = -g_c[A_c A_c^\dagger]_{ii}^{\gamma\alpha} - g_c(A_{1R_{ji}}^{\gamma\beta} A_{1R_{ij}}^{\dagger\beta\alpha} - A_{2R_{ji}}^{\dagger\gamma\beta} A_{2R_{ij}}^{\beta\alpha} \\ &\qquad + A_{1R_{ji}}^{\delta\gamma} A_{1R_{ij}}^{\dagger\alpha\delta} - A_{2R_{ji}}^{\dagger\delta\gamma} A_{2R_{ij}}^{\alpha\delta}) \\ &D_{R_{ij}} = -g_R[A_c A_c^\dagger]_{ij}^{\alpha\alpha} - g_R(A_{1R_{ik}}^{\alpha\beta} A_{1R_{kj}}^{\dagger\beta\alpha} - A_{2R_{ik}}^{\dagger\alpha\beta} A_{2R_{kj}}^{\beta\alpha} + A_{1R_{ki}}^{\alpha\beta} A_{1R_{jk}}^{\dagger\beta\alpha} \\ &\qquad - A_{2R_{ki}}^\dagger A_{2R_{jk}}) - g_R(A_1 A_1^\dagger - A_2 A_2^\dagger)_{ij}. \end{aligned} \tag{4}$$

Here the upper indices refer to colour and lower indices refer to flavour quantum numbers. The potential is

$$\begin{aligned} U = \mathrm{Tr}[&\tfrac{1}{2}D_c^2 + \tfrac{1}{2}D_L^2 + \tfrac{1}{2}D_R^2 + F_1^\dagger F_1 + F_2^\dagger F_2 + F_c^\dagger F_c + F_{1R}^\dagger F_{1R} \\ &+ F_{2R}^\dagger F_{2R} + f_x^* f_x + f_y^* f_y + f_z^* f_z]. \end{aligned} \tag{5}$$

This potential has supersymmetric minima at

$$\begin{aligned} &U = 0, \quad \langle A_c \rangle = M_c = m_c \mathrm{diag}(1, 1, 1, -3), \\ &\langle A_{R_1 + i2}^{44} \rangle = m_R, \quad \langle A \rangle = \begin{pmatrix} m & 0 \\ 0 & m' \end{pmatrix}, \\ &\langle X \rangle = \langle Y \rangle = \langle Z \rangle = 0. \end{aligned} \tag{6}$$

CC-0. In Public Domain. Gurukul Kangri Collection, Haridwar

Digitized by Arya Samaj Foundation Chennai and eGangotri

U is a sum of several positive terms. So the value at minimum is zero. The vacuum expectation values (VEVs) for these fields which lead to this minima are obtained by differentiation and by choosing the appropriate values to follow the desired symmetry-breaking pattern. The non-zero VEVs break the gauge symmetry spontaneously. $\langle A_c \rangle$ breaks $SU_C(4)$ to $SU_C(3) \times U_{B-L}(1)$ and $SU_R(2)$ to $U_R(1)$, $\langle A^{44}_{R_{1+i2}} \rangle$ combines $U_{B-L}(1) \times U_R(1)$ to $U_Y(1)$ and $\langle A \rangle$ breaks $SU_L(2) \times U_Y(1)$ to $U_{EM}(1)$. Shifting the chiral fields by their VEVs and diagonalizing the mass matrices (Sohnius 1977) we get

$$\begin{aligned} L_H^m = {} & (64g_c^2m_c^2 + 4g_c^2m_R^2)[|V^{i4}_{\mu c}|^2 + |P|^2] \\ & + (64g_c^2m_c^2 + 4g_c^2m_R^2)^{1/2}[\bar{E}_{c1}E_{c1} - \bar{E}_{c2}E_{c2} + \bar{E}_{c3}E_{c3} - \bar{E}_{c4}E_{c4}] \\ & + M_1^2(|w_1|^2 + |W_1|^2) + M_1(\bar{E}_{1L}E_{1L} + \bar{E}'_{1L}E_{1L}) + M_2^2(|w_2|^2 + |W_2|^2) \\ & + M_2(\bar{E}_{2L}E_{2L} + \bar{E}'_{2L}E_{2L}) + M_3^2(\tfrac{1}{2}Z_{\mu_1}^2 + \tfrac{1}{2}w_3^2) + M_3(\bar{E}_3E_3 + \bar{E}'_3E_3) \\ & + M_4^2[\tfrac{1}{2}Z_{\mu_2}^2 + \tfrac{1}{2}w_4^2] + M_4[\bar{E}_4E_4 + \bar{E}'_4E_4] + 96a^2m_c^2[|a_x|^2 + |w_c|^2] \\ & + (96)^{1/2}am_c(\bar{E}_{x2}E_{x2} - \bar{E}_{x1}E_{x1}) + 2b^2m^2[|a_y|^2 + |w_R|^2] \\ & + (2)^{1/2}bm_R(\bar{E}_{y2}E_{y2} - E_{y1}E_{y1}) + 2c^2(m^2 + m'^2)[|a_z|^2 + |w|^2] \\ & + 2(m^2 + m'^2)^{1/2}c(\bar{E}_{z2}E_{z2} - \bar{E}_{z1}E_{z1}). \end{aligned} \tag{7}$$

Notations with details are given in Appendix A. The mass spectrum is given in table 1. This shows that for each mass there is an equal number of fermionic as well as bosonic degrees of freedom. Thus supersymmetry is preserved even though the gauge symmetry breaks. In the process of gauge breaking the gauge particles get mass. The mass of the lepto quarks ($V^{i4}_{\mu c}$) of the fifteenplet is of the order of m_c in the limit $m_c \gg m_R$. The mass of the neutral component S^0($V^{44}_{\mu c}$ of the fifteenplet) is of the order of m_R as it gets mass from the VEVs of Φ_R (10, 1, 3). In $SU_L(2)$ and $SU_R(2)$ group the W_0 and $W^{\pm}$ mesons get mixed due to VEVs of $\Phi(122)$. However in the limit of $m_c \gg m_R \gg m$ and m', $W^{\pm}$ are decoupled. The mass of one of them comes to be very large and is of the order of m_c whereas the other one has a low mass of the order of $(m^2 + m'^2)^{1/2}$. Thus we see two sets of W mesons, W_R which is very heavy and W_L which is much lighter. By calculating the

Table 1. Mass spectrum of bosons and fermions when gauge symmetry $SU_C(4) \times SU_L(2) \times SU_R(2)$ breaks to $SU_C(3) \times U_{EM}(1)$.

Particle (bosons)	Mass	Particle (fermions)	Mass
$V^{i4}_{\mu c}$, P	$2g_c(m_R^2 + 16m_c^2)^{\frac{1}{2}}$	E_{c_1}, E_{c_2}, E_{c_3}, E_{c_4}	$2g_c(m_R^2 + 16m_c^2)^{\frac{1}{2}}$
w_1, W_1	M_1	$E_{1L}E'_{1L}$	M_1
w_2, W_2	M_2	$E_{2L}E'_{2L}$	M_2
$z_{\mu 1}$, w_3	M_3	E_3, E'_3	M_3
$z_{\mu 2}$, w_4	M_4	$E_4E'_4$	M_4
a_x, w_c	$(96)^{\frac{1}{2}}am_c$	E_{x1}, E_{x2}	$(96)^{\frac{1}{2}}am_c$
a_y, w_R	$(2)^{\frac{1}{2}}bm_R$	E_{y1}, E_{y2}	$(2)^{\frac{1}{2}}bm_R$
a_z, w	$2^{\frac{1}{2}}(m^2 + m'^2)^{\frac{1}{2}}c$	E_{z1}, E_{z2}	$2^{\frac{1}{2}}(m^2 + m'^2)^{\frac{1}{2}}c$

CC-0. In Public Domain. Gurukul Kangri Collection, Haridwar

Digitized by Arya Samaj Foundation Chennai and eGangotri

mass spectra and eigenvectors it is found that the photon field is

$$A_\mu = e\left[\frac{W_{0L}}{g_L} - \frac{W_{0R}}{g_R} + \left(\frac{2}{3}\right)^{\frac{1}{2}}\frac{S^0}{g_c}\right]$$

and the coupling constant e satisfies the relation

$$\frac{1}{e^2} = \frac{1}{g_L^2} + \frac{1}{g_R^2} + \frac{2}{3}\frac{1}{g_c^2}.$$

Furthermore the neutral components S^0, W_{0L} and W_{0R} get mixed to give the photon field A_μ with zero mass and Z^0 fields, $Z_{\mu 1}$ and $Z_{\mu 2}$ with masses M_3 and M_4 respectively. In the above limit $Z_{\mu 1}$ turns to be very much massive ($M_3 \simeq m_R$) and $Z_{\mu 2}$ very light.

To discuss quarks and leptons we have to include the matter field. We consider two chiral multiplets $\Psi_L(4, 2, 1)$ and $\Psi_R(4, 1, 2)$. The superpotential part of the Lagrangian containing Yukawa couplings is given by Mohapatra and Senjanovic (1981),

$$L_Y = \mathrm{Tr}[h_1 \bar{\Psi}_L \Phi_1 \Psi_R + h_2 \bar{\Psi}_L \Phi_2 \Psi_R + i h_3 (\Psi_R^T C \tau_2 \Phi_{1R} \Psi_R) + \mathrm{h.c.}] \tag{8}$$

C is the Dirac charge conjugation matrix. The potential has supersymmetric minima at $\langle \Psi_L \rangle = \langle \Psi_R \rangle = 0$. It is interesting to study the neutrino sector. The VEVs of Φ_R and Φ contribute to the following mass terms for ν_L and ν_R sector,

$$L_\nu^{\mathrm{mass}} = (h_1 m + h_2 m')(\bar{\nu}_L \nu_R) + \bar{\nu}_R \nu_L) + h_3 m_R (\nu_R^T C \nu_R + \nu_R C \nu_R^*). \tag{9}$$

This can be simplified into

$$L_\nu^{\mathrm{mass}} = (h_1 m + h_2 m') \nu^T C N - h_3 m_R (N^T C N) + \mathrm{h.c.}, \tag{10}$$

where ν and N are effectively two component complex spinors

$$\nu \equiv \nu_L, \quad N \equiv C(\bar{\nu}_R)^T.$$

In terms of the matrix M it can be written as

$$L^{\mathrm{mass}} = (\nu^T, N^T) M C \begin{pmatrix} \nu \\ N \end{pmatrix} + \mathrm{h.c.}, \tag{11}$$

where
$$M = \begin{pmatrix} 0 & \frac{1}{2}(h_1 m + h_2 m') \\ \frac{1}{2}(h_1 m + h_2 m') & -h_3 m_R \end{pmatrix}. \tag{12}$$

There will be two eigenstates for neutrinos with masses m_1 and m_2

where $$m_1 = \frac{1}{4}\frac{(h_1 m + h_2 m')^2}{h_3 m_R}, \quad m_2 = -h_3 m_R.$$

In the limit $m_R \gg m$ and m', m_1 is negligibly small and m_2 is very large. The states with small mass is defined as ν_e and that with larger mass as N_e. For $m_R \to \infty$, $m_{\nu_e} \to 0$ and $m_{N_e} \to \infty$. The Yukawa coupling gives rise to the mass of the electron as $m_e = (h_1 m' + h_2 m)$.

CC-0. In Public Domain. Gurukul Kangri Collection, Haridwar

Digitized by Arya Samaj Foundation Chennai and eGangotri

Since the superpotential L_y given by (8) is supersymmetric at all energy scales the supersymmetric partners of these fermions have the same mass.

Here we see that SUSY does not break for matter field. Thus in tree level SUSY remains unbroken both for Higgs field and matter field. To break SUSY for Higgs field we shall use the mechanism of O'Raifeartaigh (1975). This breaks the SUSY of Higgs scalars which are singlets. To break SUSY of Higgs multiplets we have to consider the radiative corrections. This will be done in the succeeding section.

3. Breakdown of supersymmetry

In the last section we have used three singlet fields X, Y and Z for gauge symmetry breaking. To implement both gauge symmetry and supersymmetry breaking we require two O'Raifeartaigh singlets A_{01} and A_{02}. It is to be noted that models with spontaneous broken SUSY at low energy have serious phenomenological difficulties (see e.g. Dimopoulos and Georgi 1981 and Weinberg 1982). So the singlets A_{01} and A_{02} are made to interact with the singlets X, Y and Z which in turn are coupled to the low energy sector. This will be in similar spirit to the work of Ellis *et al* (1982). We construct the superpotential part of the Lagrangian as

$$\begin{aligned} L=&[\chi+g_{1x}(X-M_x)^2+g_{1y}(Y-M_y)^2+g_{1z}(Z-M_z)^2]A_{01}+[m_x(X-M_x)\\ &+m_y(Y-M_y)+m_z(Z-M_z)]A_{02}+\mathrm{Tr}[g_{2x}(\varphi_c^2-M_c^2)(X-M_x)\\ &+g_{2y}(\Phi_{2R}\Phi_{1R}-M_R^2)(Y-M_y)+g_{2z}(\Phi\tau_2\Phi^*\tau_2-2mm')(Z-M_z)]\\ &+g_{3x}X^3+g_{3y}Y^3+g_{3z}Z^3+\mathrm{h.c.} \end{aligned} \tag{13}$$

The mass of the singlet A_{02} is the order of $m_x\simeq m_y\simeq m_z$. One can take this to be superheavy and $M_x\simeq M_y\simeq M_z$ to be of an intermediate energy scale. The treatment for symmetry breaking is, however, quite general. The equations of motion for the auxilary fields are

$$\begin{aligned} F_{01}^*&=-[\chi+g_{1x}(a_x-M_x)^2+g_{1y}(a_y-M_y)^2+g_{1z}(a_z-M_z)^2],\\ F_{02}^*&=-[m_x(a_x-M_x)+m_y(a_y-M_y)+m_z(a_z-M_z)],\\ F_x^*&=-[2g_{1x}a_{01}(a_x-M_x)+m_xa_{02}+3g_{3x}a_x^2+\mathrm{Tr}g_{2x}(A_c^2-M_c^2)],\\ F_y^*&=-[2g_{1y}a_{01}(a_y-M_y)+m_ya_{02}+3g_{3y}a_y^2+\mathrm{Tr}g_{2y}(A_{2R}A_{1R}-M_R^2)],\\ F_z^*&=-[2g_{1z}a_{01}(a_z-M_z)+m_za_{02}+3g_{3z}a_z^2+\mathrm{Tr}g_{2z}(A_1\tau_2A_1^*\tau_2-2mm')],\\ F_c^\dagger&=-2g_{2x}A_c(a_x-M_x),\quad F_{1R}^\dagger=-g_{2y}(a_y-M_y)A_{2R},\\ F_{2R}^\dagger&=-g_{2y}A_{1R}(a_y-M_y),\quad F_1^\dagger=-g_{2z}\tau_2A_1^*\tau_2(a_z-M_z),\\ F_2^\dagger&=-g_{2z}A_1(a_z-M_z). \end{aligned} \tag{14}$$

Evaluating the potential in terms of the auxilary fields and minimizing it we obtain

$$\begin{aligned} &\langle a_x\rangle=M_x,\quad \langle a_y\rangle=M_y,\quad \langle a_z\rangle=M_z,\quad \langle a_{01}\rangle=0\\ &\langle a_{02}\rangle=-3g_{3x}(M_x^2/m_x)=-3g_{3y}(M_y^2/m_y)=-3g_{3z}(M_z^2/m_z). \end{aligned} \tag{15}$$

CC-0. In Public Domain. Gurukul Kangri Collection, Haridwar

Digitized by Arya Samaj Foundation Chennai and eGangotri

The fields of the R invariance breaking terms X^3, Y^3, Z^3 are shifted by M_x, M_y, M_z respectively. Bilinear fermionic terms like $M_x\bar{\psi}_x\psi_x$, $M_y\bar{\psi}_y\psi_y$ and $M_z\bar{\psi}_z\psi_z$ arise due to such shifts. Internal fermion lines of Feynmann diagrams (see figures 1a–d) carry this information. On evaluating these diagrams we find that the gluinoes get their masses. These have been explicitly calculated in the subsequent paragraphs.

The equations of motion for F_x, F_y and F_z clearly show that A_{02} is required to make $F_x^*F_x$, $F_y^*F_y$ and $F_z^*F_z$ part of $U_{\min}$ zero by properly choosing $\langle a_{02}\rangle$ and the respective coupling constants. All the auxilary fields contributes zero to $U_{\min}$ except $F_{01}^*F_{01}$. This makes $U_{\min} > 0$ and is equal to χ^2 where χ is the O'Raifeartaigh parameter.

Shifting of the chiral fields about its VEVs gives

$$F_{01}^*F_{01} = \chi[g_{1x}(a_x^2 + a_x^{*2}) + g_{1y}(a_y^2 + a_y^{*2}) + g_{1z}(a_z^2 + a_z^{*2})].$$

This shows that χ enters the mass of a_x, a_y and a_z that is the bosonic part of X, Y and Z. The products of $F_x^*F_x$, $F_y^*F_y$, $F_z^*F_z$, $F_{02}^*F_{02}$ contain terms like a_xA_c, a_yA_R, a_zA_1, a_xa_{02}, a_ya_{02} and a_za_{02} with some $(\text{mass})^2$ as coefficients. To obtain the masses of all these participating fields, one has to diagonalize a fairly large mass matrix. What is relevant and important is that the masses of all these objects will contain the O'Raifeartaigh parameter χ. Their fermionic partners, however, will have mass values independent of χ. As a result SUSY will break down in this sector at the tree level.

To break the SUSY of the remaining components of φ_c, Φ_R and Φ, we consider radiative correction. For this we collect cubic and quadratic terms from Yukawa couplings and draw Feynmann diagrams. Figures 2a, b are the quadratic divergent one-loop diagrams which can contribute additional mass to A_c. The infinite contribution of figure 2a cancels with that from figure 2b, as there is a negative sign from

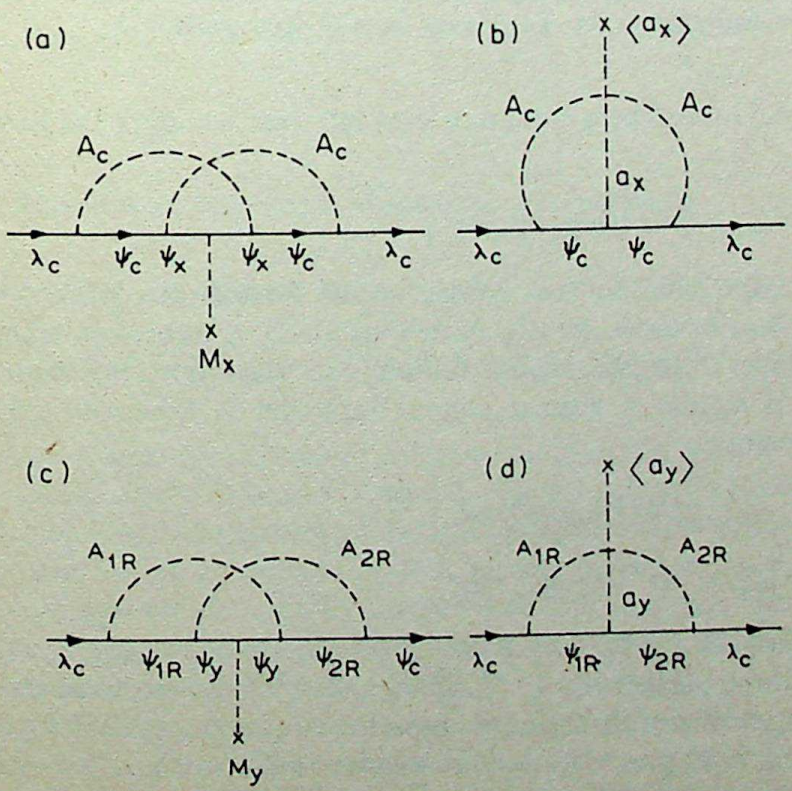

Figures 1a–d. Graphs contributing to the mass of gauginoes.

CC-0. In Public Domain. Gurukul Kangri Collection, Haridwar

Digitized by Arya Samaj Foundation Chennai and eGangotri

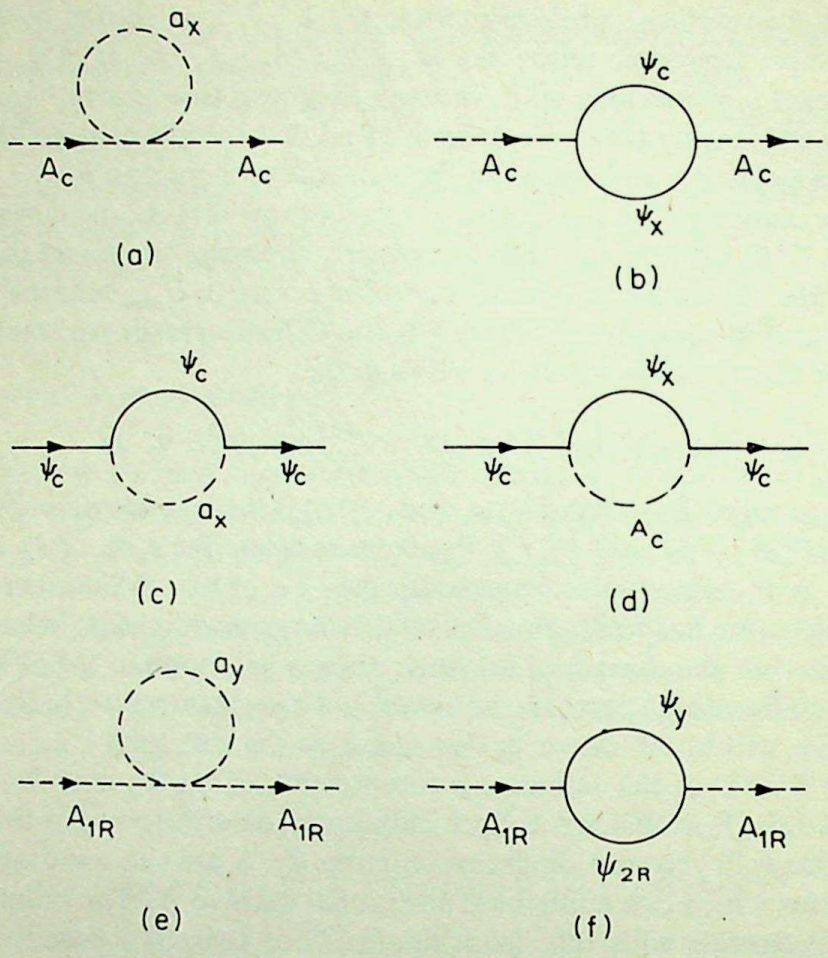

Figure 2. Graphs contributing to the masses of: a, b. Bosonic parts of Higgs scalar φ_c; c, d. Fermionic parts of φ_c; e, f. Bosonic parts of Higgs scalar Φ_R.

the fermionic closed loop. There is a finite term left over which in the lowest order is given as

$$\delta m^2_{A_c} = (g^2_{2x} m^2_x / 4\pi^2) \log (m^2_{ax} / m^2_{\Psi_x}). \tag{16}$$

Figures 2c, d contribute to the masses of the fermionic partners Ψ_c and the contribution vanishes to the order g^2_{2x}. Note that SUSY is unbroken when $m_{\Psi_x} = m_{a_x} = m_x$; similarly figures 2e, f and 3c, d contribute a finite mass to the bosonic components of Φ_R and Φ that is A_R and A, whereas figures 3a, b and 3e, f contribute zero mass to their fermionic partners.

$$\delta m^2_{A_R} = (g^2_{2y} m^2_y / 4\pi^2) \log (m^2_{a_y} / m^2_{\Psi_y}), \tag{17}$$

$$\delta m^2_A = (g^2_{2z} m^2_z / 4\pi^2) \log (m^2_{a_z} / m^2_{\Psi_z}). \tag{18}$$

These bosonic parts of φ_c, Φ_R and Φ are directly coupled to $V^{i4,4i}_{\mu c}$, $V^{j2,2j}_{\mu R}$, $V^{j2,2j}_{\mu L}$ whereas the fermionic partners to $\lambda^{i4,4i}_c$, $\lambda^{j2,2j}_R$, and $\lambda^{j2,2j}_L$. So it can be easily inferred that the six leptoquarks and their gauginoes in the colour gauge field $V_{\mu c}$, the two $w^{\pm}$ and their gauginoes in $V_{\mu R}$ and $V_{\mu L}$ acquire different masses, due to the one-loop level correction. Supersymmetry between the remaining gauge bosons and gauginoes is also broken due to radiative correction (Ellis *et al* 1982). Gauge bosons remain massless

CC-0. In Public Domain. Gurukul Kangri Collection, Haridwar

Digitized by Arya Samaj Foundation Chennai and eGangotri

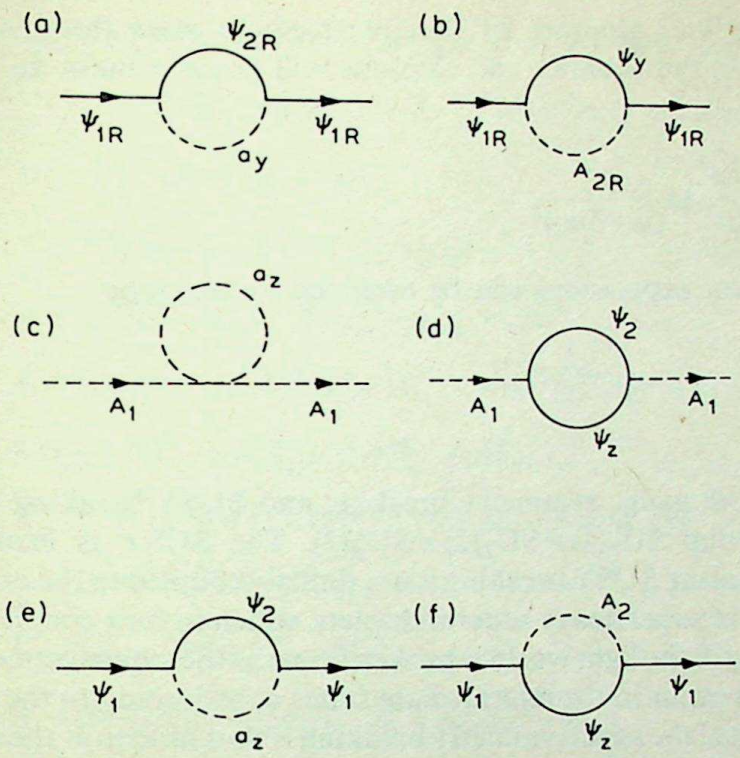

Figure 3. Graphs contributing to the masses of: a, b. Fermionic parts of Φ_R; c, d. Bosonic parts of Higgs scalar Φ; e, f. Fermionic parts of Φ.

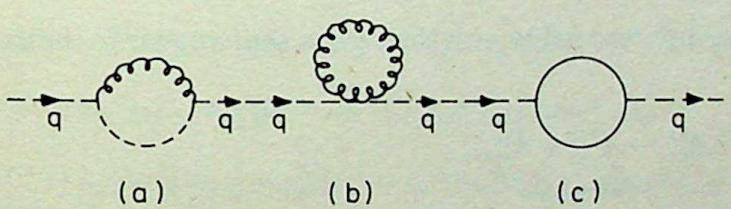

Figures 4a–c. Radiative contributions to squar masses.

whereas the gauginoes acquire mass, which is given by the expression,

$$(\delta m)_{\tilde{g}} = \frac{3g_c^2}{4(2\pi)^4}[g_{2x}^2 g_{3x} M_x \log(m_{a_x}^2/m_{\Psi_x}^2) + g_{2y}^2 g_{3y} M_y \log(m_{a_y}^2/m_{\Psi_y}^2)]. \qquad (19)$$

The diagrams which contribute to the mass of gaugino are shown in figures 5a–d. Similar diagrams can be drawn for λ_R and λ_L. There are four Feynmann diagrams for λ_c. In addition, there will be two more diagrams for λ_R because V_R couples with $\varphi_c(15, 1, 3)$, $\Phi_R(10, 1, 3)$ and $\Phi(1, 2, 2)$ whereas V_c couples with φ_c and Φ_R only. Furthermore there are only two diagrams for λ_L as V_L couples with Φ only. Contributions (δm) to mass of the corresponding gauginoes can be given by an expression similar to $(\delta m)_{\tilde{g}}$.

So far we have not considered the SUSY breaking of matter field. When one introduces the super matter field the SUSY can also be broken by radiative corrections. The fermions will still remain massless due to chiral invariance. The bosonic partners, squarks and sleptons, will have loops of gluinoes and other gauge bosons. Assume for instance $SU_L(2)$ and $SU_R(2)$ are not broken. Due to imperfect cancellation of the

CC-0. In Public Domain. Gurukul Kangri Collection, Haridwar

Digitized by Arya Samaj Foundation Chennai and eGangotri

superpartners, gluons and gluinoes in the intermediate state (loop and tadpole diagrams, figures 4a–c) the squarks and sleptons will acquire mass. In the leading logarithmic order

$$(\delta m^2)_q = \frac{g_c^2 \mu^2}{2\pi^2} \ln \frac{\mu^2}{(\mu + \delta m_{\tilde{g}})^2}$$

where $\mu = 8 g_c m_c$. Similar expressions can be obtained for sleptons.

4. Conclusion

We have discussed both gauge symmetry breaking and SUSY breaking of the Pati-Salam unification group $SU_C(4) \times SU_L(2) \times SU_R(2)$. The SUSY is broken by the O'Raifeartaigh mechanism. SUSY breaking is not directly coupled to the ordinary light world, but to a world of super heavy supermultiplets, which in turn couple to the light world. Supersymmetry in the light world is broken down as the supersymmetry-broken heavy supermultiplets occur in the intermediate states contributing to the mass shifts. Most of the machinery of the supersymmetry breaking is thus hidden at the super heavy scale.

Appendix A

In this appendix we give different fields with their mass that appear in the expression for L_H^m (equation (7))

$$p = \tfrac{1}{2}(A_{c_{11}}^{\dagger i4} - A_{c_{11}}^{i4} - A_{c_{22}}^{\dagger i4} + A_{c_{22}}^{i4}),$$

$$E_{c_1} = \frac{1}{(2)^{\frac{1}{2}}}(i\lambda_c^{i4} + \Psi_{c_1}), \quad E_{c_2} = \frac{1}{(2)^{\frac{1}{2}}}(i\lambda_c^{i4} - \Psi_{c_1}),$$

$$E_{c_3} = \frac{1}{(2)^{\frac{1}{2}}}(-i\lambda_c^{4i} + \Psi_{c_2}), \quad E_{c_4} = \frac{1}{(2)^{\frac{1}{2}}}(-i\lambda_c^{4i} - \Psi_{c_2}),$$

$$\Psi_{c_1} = \frac{[(2)^{\frac{1}{2}} g_c m_R (\Psi_{1R_{12}}^{i4} - \Psi_{2R_{12}}^{4i}) - 4(2)^{\frac{1}{2}} g_c m_c (\Psi_{c_{11}}^{i4} - \Psi_{c_{22}}^{i4})]}{(64 g_c^2 m_c^2 + 4 g_c^2 m_R^2)^{1/2}},$$

$$\Psi_{c_2} = \frac{[4(2)^{\frac{1}{2}} g_c m_c (\Psi_{c_{11}}^{4i} - \Psi_{c_{22}}^{4i}) - (2)^{\frac{1}{2}} g_c m_R (\Psi_{1R_{12}}^{4i} - \Psi_{2R_{12}}^{i4})]}{(64 g_c^2 m_c^2 + 4 g_c^2 m_R^2)^{1/2}},$$

$$M_1^2 = \tfrac{1}{2}[(x+y) + \{(x-y)^2 + 4z^2\}^{\frac{1}{2}}], \quad x = 4g_R^2 m_R^2 + 96 g_c^2 m_c^2 + 2g_R^2(m^2 + m'^2),$$

$$M_2^2 = \tfrac{1}{2}[(x+y) - \{(x-y)^2 + 4z^2\}^{\frac{1}{2}}], \quad y = 2g_L^2(m^2 + m'^2)$$

$$z = 2 g_L g_R (m^2 + m'^2),$$

$$w_1 = [Z V_{\mu R}^{12} + (M_1 - x) V_{\mu L}^{12} / [Z^2 + (M_1^2 - x)^2]^{\frac{1}{2}},$$

$$w_2 = w_1 \text{ (with } M_1 \to M_2)$$

CC-0. In Public Domain. Gurukul Kangri Collection, Haridwar

Digitized by Arya Samaj Foundation Chennai and eGangotri

$$W_1 = N[M_1^2 a' b' c'(B) + c'\{M_1^2(M_1^4 - a'^2) - (M_1^2 - a'^2)(M_1^2 - b'^2) + a'^2 b'^2\}K]$$
$$+ b'\{(M_1^2 - a'^2)(M_1^2 - b'^2) - a'^2 b'^2\}w], \quad N = \text{normalization constant}$$

$$W_2 = W_1 \text{ (with } M_1 \to M_2),$$

$$a' = (96)^{\frac{1}{4}} g_R m_c, \quad b' = [2(g_L^2 + g_R^2)(m^2 + m'^2)]^{\frac{1}{4}}, \quad c' = 2g_R m_R,$$

$$B = [(A_{c_{21}}^{\dagger ii} - A_{c_{21}}^{ii}) - 3(A_{c_{12}}^{\dagger 44} - A_{c_{12}}^{44})]/(24)^{\frac{1}{4}},$$

$$K = [(mA_1^{12} - m'A_2^{12}) + (m'A_1^{12} - mA_2^{12})]/[2(m^2 + m'^2)]^{\frac{1}{4}},$$

$$w = \tfrac{1}{2}[(A_{1R_{22}}^{\dagger 44} + A_{2R_{22}}^{\dagger 44}) - (A_{1R_{11}}^{44} + A_{2R_{11}}^{44})],$$

$$E_{1L} = N[(y)^{\frac{1}{4}}(M_1^2 - A')\lambda_{\mu L}^{12} + (B')^{\frac{1}{4}} M_n^2 \lambda_{\mu R}^{12} + M_1(M_1^2 - A')\Psi_2$$
$$= +(A'B')^{\frac{1}{4}} M_1 \Psi_1],$$

$$E_{2L} = E_{1L} \text{ (with } M_1 \to M_2),$$

$$A' = (96 g_R^2 m_c^2 + 4 g_R^2 m_R^2), \quad B' = 2g_R^2(m^2 + m'^2),$$

$$\Psi_1 = [(2)^{\frac{1}{4}} g_R m_R(\Psi_{1R_{22}}^{44} - \Psi_{2R_{22}}^{\dagger 44}$$
$$+ (8)^{\frac{1}{4}} g_c m_c(3\Psi_{c_{11}}^{44} - \Psi_{c_{21}}^{ii})]/[(4g_R^2 m_R^2 + 96 g_c^2 m_c^2)]^{\frac{1}{4}},$$

$$\Psi_2 = (m\Psi_1^{21} - m'\Psi_2^{21}/[(m^2 + m'^2)]^{\frac{1}{4}},$$

$$M_3^2 = (B'' + [B''^2 + 4c'']^{\frac{1}{4}}), \quad M_4^2 = (B'' - [B''^2 - 4c'']^{\frac{1}{4}}),$$

$$B'' = 8g_c^2 m_R^2 + 4g_L^2(m^2 + m'^2) + 4g_R^2 2m_R^2 + m^2 + m'^2),$$

$$C'' = 8g_c^2 m_R^2[4(g_L^2 + g_R^2)(m^2 + m'^2) + 32 g_L^2 g_R^2 m_R^2(m^2 + m'^2)],$$

$$Z_{\mu 1} = N(a_1 b_1 c_1 V_{\mu c}^{44} + b_1 c_1 d_1 V_{\mu R}^{11} + a_1 de V_{\mu L}^{11}),$$

$$Z_{\mu 2} = Z_{\mu 1} \text{ (with } M_3 \to M_4),$$

$$a_1 = 8g_c g_R m_R^2, \quad b_1 = 2g_c g_R m_R^2, c_1 = \left[\frac{M_1}{2} - 4g_L^2(m^2 + m'^2)\right],$$

$$d = \left(\frac{M_1}{2} - 8g_c^2 m_R^2\right), \quad e = g_c g_R(m^2 + m'^2)$$

$$w_3 = N[b_1' x + (M_3^2 - a_1')z]/[b_1'^2 + (M_3^2 - a_1')^2]^{\frac{1}{4}}, \quad w_4 = w_3 \text{ (with } M_3 \to M_4),$$

$$b_1' = 4[2(m^2 + m'^2)^{\frac{1}{4}}] g_R^2 m_R, \quad a_1' = 4(g_c^2 + g_R^2)(m^2 + m'^2),$$

$$x = [(mA_1^{11} - m'A_2^{\dagger 11}) + (mA_1^{\dagger 11} - m'A_2^{11})]/[2(m^2 + m'^2)]^{\frac{1}{4}},$$

$$Z = \tfrac{1}{2}(A_{1R_{21}}^{\dagger 44} + A_{2R_{21}}^{\dagger 44} + A_{1R_{12}}^{44} + A_{2R_{12}}^{44}),$$

$$E_3 = N[x_1 y_1(M_3^2 - W^2)\lambda_{\mu c}^{44} + (M_3^2 - x^2)(M_3^2 - W^2)\lambda_{\mu R}^{11} + wZ_1(M_3^2 - x^2)\lambda_{\mu L}^{11}$$
$$- M_3 y_1(M_3^2 - W^2) i\Psi_1^* - M_3 Z_1(M_3^2 - x^2) i\Psi_2^*],$$

CC-0. In Public Domain. Gurukul Kangri Collection, Haridwar

Digitized by Arya Samaj Foundation Chennai and eGangotri

$$x_1 = 4g_c m_R, \quad y_1 = 4g_R m_R, \quad z_1 = 2[2(m^2+m'^2)]^{\frac{1}{2}} g_R,$$

$$w = 2[2(m^2+m'^2)]^{\frac{1}{2}} g_L, \quad \Psi_1 = \frac{1}{(2)^{\frac{1}{2}}}(\Psi^{44}_{1R_{12}} - \Psi^{\dagger 44}_{2R_{21}}),$$

$$\Psi_2 = \frac{1}{(m^2+m'^2)^{\frac{1}{2}}}(m\Psi^{11}_1 - m'\Psi^{11}_2), \quad w_e = \frac{1}{(24)^{\frac{1}{2}}}(A^{ii}_{c_{11}} - A^{ii}_{c_{22}} - 3A^{44}_{c_{11}} + 3A^{44}_{c_{22}}),$$

$$W_R = \frac{1}{(2)^{\frac{1}{2}}}(A^{44}_{1R_{11}} + A^{44}_{2R_{21}}), \quad W = (mA^{22}_1 + m'A^{11}_1)/(m^2+m'^2)^{\frac{1}{2}},$$

$$E_{x1} = \frac{1}{(2)^{\frac{1}{2}}}(\Psi + \Psi_x), \quad \Psi = \frac{1}{(24)^{\frac{1}{2}}}(\Psi^{ii}_{c_{11}} - \Psi^{ii}_{c_{22}} - 3\Psi^{44}_{c_{22}}),$$

$$E_{x2} = \frac{1}{(2)^{\frac{1}{2}}}(\Psi - \Psi_x), \quad \Psi' = \frac{1}{(2)^{\frac{1}{2}}}(\Psi^{21}_{1R_{44}} + \Psi^{21}_{2R_{44}}),$$

$$E_{y1} = \frac{1}{(2)^{\frac{1}{2}}}(\Psi' + \Psi_y), \quad \Psi'' = \frac{(m'\Psi_{11} + m\Psi_{22} + m'\Psi^*_{11} + m\Psi^*_{22})}{[2(m^2+m^2)]^{\frac{1}{2}}}.$$

$$E_{y2} = \frac{1}{(2)^{\frac{1}{2}}}(\Psi' - \Psi_y),$$

$$E_{z1} = \frac{1}{(2)^{\frac{1}{2}}}(\Psi'' + \Psi_z),$$

$$E_{z2} = \frac{1}{(2)^{\frac{1}{2}}}(\Psi'' - \Psi_z),$$

References

Dimopoulos S and Georgi H 1981, *Nucl. Phys.* **B193** 150
Dine M and Fischler W 1982 *Phys. Lett.* **B110** 227
Ellis J, Ibanez L and Ross G G 1982 *Phys. Lett.* **B113** 283
Gipson J M and Marshak R E 1984 VPI-HEP-84/1
Marshak R E and Mohapatra R N 1984 VPI-HEP-84/10
Mohapatra R N and Senjanovic G 1981 *Phys. Rev.* **D23** 165
O'Raifeartaigh L 1975 *Nucl. Phys.* **B96** 33
Pati J and Salam A 1973 *Phys. Rev.* **D8** 1240
Sohnius M 1977 *Nucl. Phys.* **B291**
Weinberg S 1982 *Phys. Rev.* **D26** 287
Wess J and Zumino B 1974 *Nucl. Phys.* **B78** 1

CC-0. In Public Domain. Gurukul Kangri Collection, Haridwar

Digitized by Arya Samaj Foundation Chennai and eGangotri

Pramāṇa – J. Phys., Vol. 28, No. 6, June 1987, pp. 633–639. © Printed in India.

Relativistic extension of the Hohenberg-Kohn theorem

S N DATTA
Department of Chemistry, Indian Institute of Technology, Powai, Bombay 400076, India

MS received 5 February 1987; revised 10 April 1987

Abstract. Using the configuration-space Hamiltonian H_+ which is derivable within the framework of quantum electrodynamics, we extend the Hohenberg-Kohn theorem to the relativistic theory of electrons in atoms or molecules.

Keywords. Continuum dissolution; variational collapse; Hohenberg-Kohn; relativistic.

PACS Nos 03·65; 03·70; 11·10

1. Introduction

Many authors (Rajagopal and Callaway 1973; Rajagopal 1978; Ramana and Rajagopal 1979; MacDonald and Vosko 1979) have formulated the relativistic density functional theory (DFT) and used it to discuss simplified systems like the electron gas. They have expressed the expectation value of the (field-theoretical) Hamiltonian as a functional of the four-current (and charge) density,

$$\langle H\rangle = E_{A^\mu_{\text{ext}}}[J_\mu]. \tag{1}$$

The four-current (and charge) density is given by

$$J_\mu(\mathbf{r}) = e\langle{:}\bar{\psi}(\mathbf{r})\gamma_\mu\psi(\mathbf{r}){:}\rangle. \tag{2}$$

To our knowledge, all these formulations depend on the assumption that the correct J_μ minimizes $E_{A^\mu_{\text{ext}}}$ and yields the energy of the ground state; (of course, the minimization is subject to the conditions that $\partial^\mu J_\mu = 0$ and that the total number of electrons remains constant). In other words, it is assumed that the Hamiltonian possesses a ground state (Rajagopal 1979; see also Xing-Xu *et al* 1984). With this assumption the (non-relativistic) Hohenberg-Kohn theorem (Hohenberg and Kohn 1964) is readily extended to the relativistic case.

Now, there are two problems connected with relativistic quantum chemical calculations using the linear expansion technique (Schwarz and Wallmeier 1982): (i) one needs a relativistic Hamiltonian which has at least a partially discrete eigenvalue spectrum, (the Dirac-Coulomb Hamiltonian suffers from continuum dissolution) and (ii) calculations based on usual relativistic Hamiltonians are not always safe from variational collapse (a term that is commonly used to describe a finite basis set effect). The first difficulty is usually waived by relying on projected Hamiltonians derived from

CC-0. In Public Domain. Gurukul Kangri Collection, Haridwar

Digitized by Arya Samaj Foundation Chennai and eGangotri

QED (Brown and Ravenhall 1951; Sucher 1980; Mittleman 1981). However, the second difficulty remains. To solve the problem, various methodologies have been recently developed (Datta 1980, 1984; Datta and Devaiah 1986; Datta and Jagannathan 1984; Gazdy and Ladanyi 1984; Mark and Schwarz 1982; Lee and McLean 1982; Wood *et al* 1985).

Actually, all previous treatments of the relativistic DFT have in one way or another taken cognizance of the first difficulty, that is, certain safeguards have been built into those treatments. Regarding the second difficulty, most of the theoretical work employ a filled negative-energy sea (see Rajagopal 1979 for a detailed discussion). From a calculational point of view the second difficulty can be really serious sometimes; this is illustrated in §2. In §3 we consider a configuration-space Hamiltonian which is derivable (Sucher 1980) within the framework of quantum electrodynamics and use it to extend the Hohenberg-Kohn theorem to the relativistic case.

2. Illustration

We use the set of trial spinors

$$\Psi_n=(1+\lambda_n^2)^{-1/2}\begin{bmatrix}\begin{pmatrix}s_n\\0\end{pmatrix}\\ \dfrac{i\lambda_n}{3^{1/2}}\begin{pmatrix}p_{zn}\\p_{xn}+ip_{yn}\end{pmatrix}\end{bmatrix},\quad (n=1,2,\ldots), \tag{3}$$

where the nonrelativistic orbitals s_n, p_{xn}, p_{yn} and p_{zn} are described by the same radial function:

$$R_n(r)=(2\zeta_n)^{n+1/2}(2n!)^{-1/2}r^{n-1}\exp[-\zeta_n r],\quad (n=1,2,3,\ldots).$$

Expectation values of the external field Dirac Hamiltonian for a one-electron atom ($H_{D,\mathrm{ext}}$) are calculated. Further, $\langle H_{D,\mathrm{ext}}\rangle_n$ is optimized through a mini-max procedure (maximum with respect to λ_n, minimum with respect to ζ_n) (Datta 1984). For every n, the optimized value equals the least eigenvalue of positive energy, that is,

$$\min_{\zeta_n}\max_{\lambda_n}\langle H_{D,\mathrm{ext}}\rangle_n=c^2\eta,$$

where $\eta=(1-Z^2/c^2)^{1/2}$, $Z|e|$ being the nuclear charge. The corresponding (optimum) parameters are:

$$\lambda_{n;\mathrm{opt}}=\lambda^0=\frac{c}{Z}(1-\eta)\quad\text{and}\quad\zeta_{n,\mathrm{opt}}=2nc\lambda^0.$$

Optimal radial densities are shown in figure 1. Corresponding four-current (and charge) densities are given by

$$e\rho_n=c^{-1}J_{n,0}=es_n^2\quad\text{and}\quad J_n=\frac{2\lambda}{1+\lambda^2}J_{n,0}n_{xy}$$

where $n_{xy}=(-\mathbf{i}y+\mathbf{j}x)/r$, for $n=1,2,3,\ldots$. That for each n the four-vector J_μ produces

CC-0. In Public Domain. Gurukul Kangri Collection, Haridwar

Digitized by Arya Samaj Foundation Chennai and eGangotri

the same minimum energy $[\min_{\zeta_n} \langle H_{D;\,\mathrm{ext}} \rangle_n^{\lambda^0} = c^2\eta]$ indicates that the relativistic density functional treatment even for a one-electron atom can be ambiguous in practice.

In fact, Cortona *et al* (1985) have extended the von Barth-Hedin (1972) local-spin-density theory to the relativistic treatment of the rare-earth ions and numerically solved the resulting coupled Dirac equations. The numerical approach to solving wave equations has always been very successful (Desclaux 1973, 1975). This is so since the angular behaviour of a relativistic atomic orbital is precisely known and the corresponding rádial components can be easily estimated. On the contrary, the numerical method of solving wave equation is computationally intractable for almost all molecular systems. Besides, the Hohenberg-Kohn theorem itself is based on arguments of analytical calculations, and most of the density functional calculations are performed in the same spirit.

3. A relativistic extension of the Hohenberg-Kohn theorem

An approach to the relativistic Hohenberg-Kohn theorem can start from the configuration-space Hamiltonian H_+ suggested by Sucher (1980)

$$H_+ = \sum_{i=1}^{N} H_{D,\,\mathrm{free}}(i) + \Lambda_+ \left[e \sum_{i=1}^{N} \{A^0_{\mathrm{ext}}(\mathbf{r}_i) - \alpha_i \cdot A_{\mathrm{ext}}(\mathbf{r}_i)\} + \sum_{i<j} \frac{e^2}{r_{ij}} \right] \Lambda_+, \tag{4}$$

where

$$\Lambda_+ = \prod_{i=1}^{N} \Lambda_+(i) \quad \text{and} \quad \Lambda_+(i) = \sum_{\alpha} |u_\alpha(i)\rangle \langle u_\alpha(i)|, \; u_\alpha(i)$$

being a positive-energy eigenfunction of the free-particle Dirac Hamiltonian, $H_{D,\,\mathrm{free}}(i)$. The Hamiltonian H_+ is not bounded from below. Therefore, one must require that the many-electron wave function $\Psi(1 \ldots N)$ be constrained by

$$\Lambda_+(i)\Psi(1 \ldots N) = \Psi(1 \ldots N) \quad [i = 1, 2, \ldots N], \tag{5}$$

so that the minimum of $\langle H_+ \rangle$ can act as an upper bound. However, the task of relating $J_\mu(r)$ with a Ψ constrained by (5) is not a trivial one.

Actually, the problem of finding a good Ψ is solved in case the upper and the lower components of the spinors are decoupled. A convenient way to do so is to use a free-particle Foldy-Wouthuysen transformation (Foldy and Wouthuysen 1950) on H_+. The positive energy part of the transformed Hamiltonian is written as (Sucher 1980; Hess 1986):

$$\tilde{H}_+ = \sum_i \hat{E}_i + \sum_i \hat{V}_{\mathrm{eff}}(i) + \sum_{i<j} \hat{U}_{\mathrm{eff}}(i,j), \tag{6}$$

where

$$\hat{E}_i = (c^2 p_i^2 + m^2 c^4)^{1/2}, \tag{7}$$

$$\hat{V}_{\mathrm{eff}}(i) = -e\hat{A}_i [A^0_{\mathrm{ext}}(i) + \hat{R}_i A^0_{\mathrm{ext}}(i) \hat{R}_i - \hat{R}_i \sigma_i \cdot A_{\mathrm{ext}}(i) - \sigma_i \cdot A_{\mathrm{ext}}(i) \hat{R}_i] \hat{A}_i,$$

and

$$\hat{U}_{\mathrm{eff}}(i,j) = \hat{A}_i \hat{A}_j [e^2/r_{ij} + \hat{R}_i (e^2/r_{ij}) \hat{R}_i + \hat{R}_j (e^2/r_{ij}) \hat{R}_j + \hat{R}_i \hat{R}_j (e^2/r_{ij}) \hat{R}_i \hat{R}_j] \hat{A}_i \hat{A}_j.$$

CC-0. In Public Domain. Gurukul Kangri Collection, Haridwar

Digitized by Arya Samaj Foundation Chennai and eGangotri

In (7), $\hat{A}_i=[(mc^2+E_i)/2E_i]^{1/2}$ and $\hat{R}_i=[c/(E_i+mc^2)]\sigma_i\cdot p_i$. The four-current (and charge) density is rewritten as

$$J_0(r_1)=ecN\int d\mathbf{r}_2 \ldots d\mathbf{r}_N \Phi^+(\mathbf{r}_1 \ldots \mathbf{r}_N)\Phi(\mathbf{r}_1 \ldots \mathbf{r}_N) \tag{7a}$$

and

$$J_\mu(r_1)=ec^2N\int d\mathbf{r}_2 \ldots d\mathbf{r}_N \Phi^+(\mathbf{r}_1 \ldots \mathbf{r}_N)\frac{p_{1\mu}}{E_1}\Phi(\mathbf{r}_1 \ldots \mathbf{r}_N),\ (\mu=1, 2, 3), \tag{7b}$$

where Φ is the many-electron wavefunction in the new representation.

The operator $\tilde{H}_+$ can be used to extend the Hohenberg-Kohn theorem to the relativistic problem. We see that the expectation value of

$$\sum_i \hat{E}_i+\sum_{i<j}\hat{U}_{\text{eff}}(i,j)$$

is a universal functional of $J_\mu(\mathbf{r})$, written as $F_{\text{rel}}[J_\mu(\mathbf{r})]$. Since $\tilde{H}_+$ has a least value among its eigenvalues, it can be easily proved (by reductio ad absurdum) that to an additive constant $V_{\text{eff}}(\mathbf{r})$ is a unique functional of the ground state $J_\mu(\mathbf{r})$. Now, $V_{\text{eff}}(\mathbf{r})$ is written in terms of the four-potential and the operators $\hat{A}_i$ and $\hat{R}_i$. The latter operators ($\hat{A}_i$ and $\hat{R}_i$) appear through the free-particle Foldy-Wouthuysen transformation, and remain unchanged for various four-potentials. (These will change only if the nature of the transformation changes). Therefore, there is a one-to-one correspondence between $V_{\text{eff}}(\mathbf{r})$ and the four-potential. We conclude that the four-potential is a unique functional of the ground state (single particle) 4-current (and charge) density. We write

$$F_{\text{rel}}[J_\mu(\mathbf{r})]=\left\langle \Psi\left|\sum_i(mc^2\beta_i+c\alpha_i\cdot p_i)+\sum_{i<j}\frac{e^2}{r_{ij}}\right|\Psi\right\rangle$$

(old representation) and

$$F_{\text{rel}}[J_\mu(\mathbf{r})]=\left\langle \Phi\left|\sum_i\hat{E}_i+\sum_{i<j}\hat{U}_{\text{eff}}(i,j)\right|\Phi\right\rangle$$

(new representation). For a given (external) four-potential, the ground-state energy functional is

$$E_{A^\mu_{\text{ext}}}[J_\mu]=-\frac{1}{c}\int d^3r J_\mu(\mathbf{r})A^\mu_{\text{ext}}(\mathbf{r})+F_{\text{rel}}[J_\mu(\mathbf{r})]$$

(old representation), (8a)

or

$$E_{V_{\text{eff}}}[J_\mu]=V[J_\mu(\mathbf{r})]+F_{\text{rel}}[J_\mu(\mathbf{r})]$$

(new representation), (8b)

where $V[J_\mu(\mathbf{r})]=\langle\Phi|V_{\text{eff}}(\mathbf{r})|\Phi\rangle$. It is easily checked [from (2) or (7)] that for a normalized many-electron wave-function [Ψ or Φ] the total number of particles is a constant,

$$N[J_0]=e^{-1}c^{-1}\int d^3r J_0(\mathbf{r})=N. \tag{9}$$

CC-0. In Public Domain. Gurukul Kangri Collection, Haridwar

Digitized by Arya Samaj Foundation Chennai and eGangotri

Energy as a functional of a trial state $|\Phi'\rangle$ is written as $E_{V_{\text{eff}}}[\Phi']$. It is minimized when $|\Phi'\rangle$ is the correct ground state $|\Phi\rangle$. If $|\Phi''\rangle$ is the ground state associated with a distinctly different four-potential (one which is not obtained from the given four-potential through a gauge transformation), then

$$E_{V_{\text{eff}}}[\Phi''] = V[J''_\mu] + F_{\text{rel}}[J''_\mu] \quad \rangle$$

$$E_{V_{\text{eff}}}[\Phi] = V[J_\mu] + F_{\text{rel}}[J_\mu]. \tag{10}$$

Thus the correct $J_\mu(r)$ minimizes the ground-state energy $E_{V_{\text{eff}}}$ which is a unique functional of $J_\mu(r)$.

If one investigates the one-electron atom by using the trial two-component spinors $\tilde{\phi}_n$ where

$$\tilde{\phi}_n = \begin{pmatrix} s_n \\ 0 \end{pmatrix},$$

one would observe that the radial densities shown in figure 1 give different expectation values, $\langle \tilde{H}_+ \rangle$. These radial densities do not represent the optimal densities. In fact,

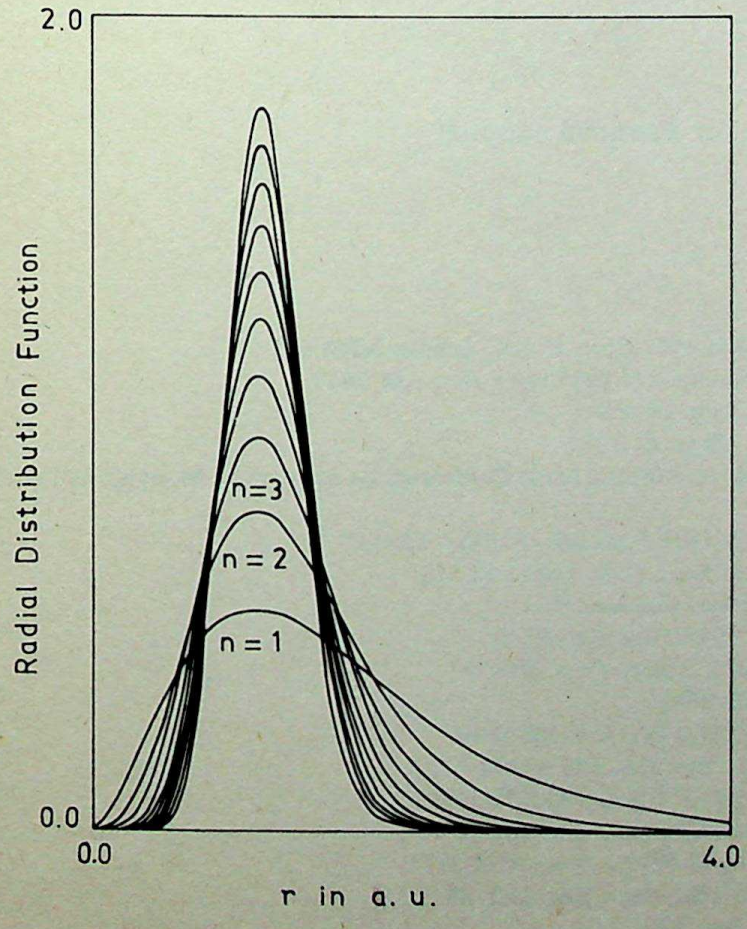

Figure 1. Radial densities which yield the same expectation value: $\langle H_{D,\text{ext}} \rangle_n = E_{1s}$ where E_{1s} is the least (positive-energy) eigenvalue of the Hamiltonian for the Dirac hydrogen atom.

CC-0. In Public Domain. Gurukul Kangri Collection, Haridwar

Digitized by Arya Samaj Foundation Chennai and eGangotri

the latter correspond to the new optimum parameters:

$$\zeta_{n,\,\mathrm{opt}} = \left(2 - \frac{1}{n}\right) Z + O(c^{-2}),$$

with the optimized values:

$$\langle \tilde{H}_+ \rangle_{n,\,\mathrm{opt}} = c^2 - \left(\frac{1}{n} - \frac{1}{2n^2}\right) Z^2 + O(c^{-2}).$$

This indicates that the minimum of $\langle \tilde{H}_+ \rangle$ will be achieved from a unique density, that is, using $\tilde{H}_+$ one can practice the relativistic density functional treatment in an unambiguous manner.

A relativistic density functional treatment can start from the relativistic extension of the Hohenberg-Kohn theorem as discussed here. Following the work of Stanton and Havriliak (1984) on finite basis calculations using kinetic balance we conclude that the newly formulated relativistic DFT will provide an upper bound which can be in error by an amount of order c^{-4} only. Therefore, the new method can give the accurate value of relativistic correction to total energy. Moreover, Sucher's construction of H_+ (or $\tilde{H}_+$) opens up the possibility of systematically studying QED effects in atoms or molecules, and the DFT based on $\tilde{H}_+$ can be used to calculate these effects.

Acknowledgement

We acknowledge CSIR for financial support.

References

Brown G E and Ravenhall D G 1951 *Proc. R. Soc. London* **A208** 552
Cortona P, Doniach S and Sommers C 1985 *Phys. Rev.* **A31** 2842
Datta S N 1980 *Chem. Phys. Lett.* **74** 568
Datta S N 1984 *Pramana–J. Phys.* **23** L275
Datta S N and Devaiah G 1986 in: Abstract of the Conference on Relativistic Many Body Problems, Trieste (Italy)
Datta S N and Jagannathan S 1984 *Pramana–J. Phys.* **23** 467
Desclaux J P 1973 *Atom. Data Nucl. Data Tables* **12** 312
Desclaux J P 1975 *Comput. Phys. Commun.* **9** 31
Foldy L and Wouthuysen A 1950 *Phys. Rev.* **78** 29
Gazdy B and Ladanyi K 1984 *J. Chem. Phys.* **80** 4333
Hess B A 1986 *Phys. Rev.* **A33** 3742
Hohenberg P and Kohn W 1964 *Phys. Rev.* **136** B864
Kohn W and Sham L J 1965 *Phys. Rev.* **140** A1133
Lee Y S and McLean A D 1982 *J. Chem. Phys.* **76** 735
MacDonald A H 1983 *J. Phys.* **C16** 3869
MacDonald A H and Vosko S H 1979 *J. Phys.* **C12** 2977
Mark F and Schwarz W H E 1982 *Phys. Rev. Lett.* **48** 673
Mittleman M H 1981 *Phys. Rev.* **A24** 1167
Rajagopal A K 1978 *J. Phys.* **C11** L943
Rajagopal A K 1979 *Adv. Chem. Phys.* **41** 59

CC-0. In Public Domain. Gurukul Kangri Collection, Haridwar

Digitized by Arya Samaj Foundation Chennai and eGangotri

Rajagopal A K and Callaway J 1973 *Phys. Rev.* **B7** 1912
Ramana M V and Rajagopal A K 1979 *J. Phys.* **C12** L845
Schwarz W H E and Wallmeier H 1982 *Mol. Phys.* **46** 1045
Stanton R E and Havriliak S 1984 *J. Chem. Phys.* **81** 1910
Sucher J 1980 *Phys. Rev.* **A22** 348
Von Barth U and Hedin L 1972 *J. Phys.* **C5** 1624
Wood J, Grant I P and Wilson S 1985 *J. Phys.* **B18** 3027
Xing-Xu B, Rajagopal A K and Ramana M V 1984 *J. Phys.* **C17** 1339

CC-0. In Public Domain. Gurukul Kangri Collection, Haridwar

Digitized by Arya Samaj Foundation Chennai and eGangotri

CC-0. In Public Domain. Gurukul Kangri Collection, Haridwar

Digitized by Arya Samaj Foundation Chennai and eGangotri

Pramāṇa – J. Phys. Vol. 28, No. 6, June 1987, pp. 641–644 © Printed in India.

Density of nucleons in heavy nuclei

NAZAKAT ULLAH
Tata Institute of Fundamental Research, Homi Bhabha Road, Bombay 400 005, India

MS received 13 February 1987

Abstract. A shell model description of heavy nuclei is used to show that the density of nucleons in heavy nuclei is of the form $\rho(r)=K(a^2-r^2)^{3/2}$, K, a being constants. Two broad features of this distribution are mentioned.

Keywords. Nucleons; heavy nuclei; shell model density.

PACS No. 21·60

One of the earliest developments in the area of nuclear physics was to study the distribution of nucleons in a nucleus. The model which was put forward in the beginning was that of uniform distribution of nucleons inside a sphere of radius R. It was later established by electron scattering (Hofstadter 1956; Brown *et al* 1979) that the density distribution does not have a sharp cut-off but has a tail. With the development of nuclear shell model it was possible to calculate the form of the shell model density $\rho(r)$ for a number of light nuclei. As the number of nucleons starts increasing one has to carry out summations over a large number of shells. The purpose of the present work is to derive an approximate analytic form of $\rho(r)$ when the number of nucleons becomes large.

To keep the formulation simple we shall treat neutrons and protons alike and consider single nucleon orbits in a harmonic oscillator potential without spin-orbit term. The density of single nucleons $\rho(\bar{r})$ can be written as

$$\rho(\bar{r})=\frac{4}{A}\sum_i |\phi_i(\bar{r})|^2, \tag{1}$$

where A is the total number of nucleons and ϕ_i are the single nucleon wave functions. The factor 4 arises from spin and isospin. Also $\rho(\bar{r})$ is normalized so that $\int\rho(\bar{r})\,d\bar{r}=1$ and the sum goes over the occupied orbits.

In a three-dimensional isotropic harmonic oscillator (Morse and Feshbach 1953) the radial wave functions $R_{nl}(r)$, $n=1, 2, \ldots; l=0, 1, 2, \ldots n-1$ are given by

$$R_{nl}=N_{nl}\exp(-\alpha r^2)\, r^l\, M(-(n-1), l+\tfrac{3}{2}, 2\alpha r^2), \tag{2}$$

where N_{nl} is the normalization constant, α the harmonic oscillator parameter and $M(a, b, x)$ is the confluent hypergeometric function (Abramowitz and Stegun 1965). The wave functions ϕ_i are products of R_{nl} and spherical harmonics. It turns out that

CC-0. In Public Domain. Gurukul Kangri Collection, Haridwar

Digitized by Arya Samaj Foundation Chennai and eGangotri

there is no simple way to carry out summation in expression (1) using the wave functions given by (2). The way out of this difficulty is to write the wave functions in Cartesian coordinates, take the Fourier transform of $\rho(\bar{r})$ and write it as

$$g(\bar{k})=\frac{4}{A}(2\pi)^{-\frac{3}{2}}\exp\left(-\frac{1}{8\alpha}\sum k_i^2\right)$$

$$\sum_{N=0}^{N_0}\sum_{n_1,n_2,n_3} L_{n_1}(k_1^2/4\alpha)\,L_{n_2}(k_2^2/4\alpha)\,L_{n_3}(k_3^2/4\alpha), \tag{3}$$

where L_n is the Laguerre polynomial, and $n_1+n_2+n_3=N$ and N_0 is the number of oscillator quanta which are fully occupied. To carry out the summations we introduce the contour integral

$$\frac{1}{2\pi i}\oint\frac{\mathrm{d}Z}{Z^{N-(n_1+n_2+n_3)+1}},$$

which allows us to sum independently over n_i. Using the generating function for Laguerre polynomial and after some simplification we get

$$g(\bar{k})=\frac{4}{A}(2\pi)^{-\frac{3}{2}}\exp\left(-\frac{1}{8\alpha}\sum k_i^2\right)L_{N_0}^{(3)}\left(\frac{1}{4\alpha}\sum k_i^2\right). \tag{4}$$

Also N_0 is related to A by the relation

$$A=\frac{4(N_0+3)!}{3!\,N_0!}. \tag{5}$$

We now consider N_0 to be large, then $L_{N_0}^{(3)}$ can be approximated by (Bateman 1953) a Bessel function and we can write g as

$$g(\bar{k})=48(2\pi)^{-3/2}\frac{J_3([(N_0/\alpha)\sum k_i^2]^{\frac{1}{2}})}{[(N_0/\alpha)\sum k_i^2]^{3/2}}. \tag{6}$$

It is now a simple matter to write the approximate form of $\rho(r)$ when the number of nucleons is large using the Fourier transform of $g(\bar{k})$. It is given by

$$\rho(r)=\frac{16\alpha^3}{3\pi^2 A}\left(\frac{(\frac{3}{2}A)^{\frac{1}{3}}}{\alpha}-r^2\right)^{\frac{3}{2}}, \tag{7}$$

$r\leqslant(\frac{3}{2}A)^{1/3}/\alpha$ and zero outside.
In expression (7) we have written N_0 in terms of A using expression (5). Therefore the density of nucleons in a heavy nucleus is of the form

$$\rho(r)=K[a^2-r^2]^{\frac{3}{2}},\quad r\leqslant a. \tag{8}$$

We now discuss the results. The first result is that expression (4) gives exact shell model form factor for closed shell nuclei ^{4}He, ^{16}O and ^{40}Ca by taking $N_0=0$, 1 and 2

CC-0. In Public Domain. Gurukul Kangri Collection, Haridwar

Digitized by Arya Samaj Foundation Chennai and eGangotri

respectively. For example for ^{16}O, the Fourier transform $g(k)$ is given by

$$g(k)=(2\pi)^{-\frac{3}{2}}[\exp(-k^2/8\alpha)]\left(1-\frac{k^2}{16\alpha}\right). \tag{9}$$

which apart from the factor $(2\pi)^{-\frac{3}{2}}$ used in the definition of the Fourier transform (Morse and Feshbach 1953) checks with the expression obtained using the usual definition

$$g(k)=\tfrac{1}{4}\langle R_{1S}|j_0(kr)|R_{1S}\rangle+\tfrac{3}{4}\langle R_{1p}|j_0(kr)|R_{1p}\rangle, \tag{10}$$

where $j_0(kr)$ is the spherical Bessel function.

The second point is that we could calculate r.m.s. radius R using the distribution given by expression (8) and write $\rho(r)$ as

$$\rho(r)=\rho(0)[1-(3r^2/8R^2)]^{\frac{3}{2}} \qquad 0\leqslant r\leqslant\frac{\sqrt{8}}{3}R. \tag{11}$$

To see the broad features of $\rho(r)$ in heavy nuclei we have plotted $\rho(r)/\rho(0)$ against r/R in figure 1. We see from this figure that the constant density region has become somewhat smaller but the tail portion is now more prominent.

We have also tried to see how the distribution given by expression (8) fits the observed $\rho(r)$ for some heavy nucleus like ^{197}Au. This fit is shown in figure 2. The unknown parameter a is fitted using the value of $\rho(r)$ at $r=6{\cdot}5$ fm the point at which $\rho(r)$ has approximately fallen to half its peak value. The observed and calculated values of $\rho(r)$ are in fair agreement.

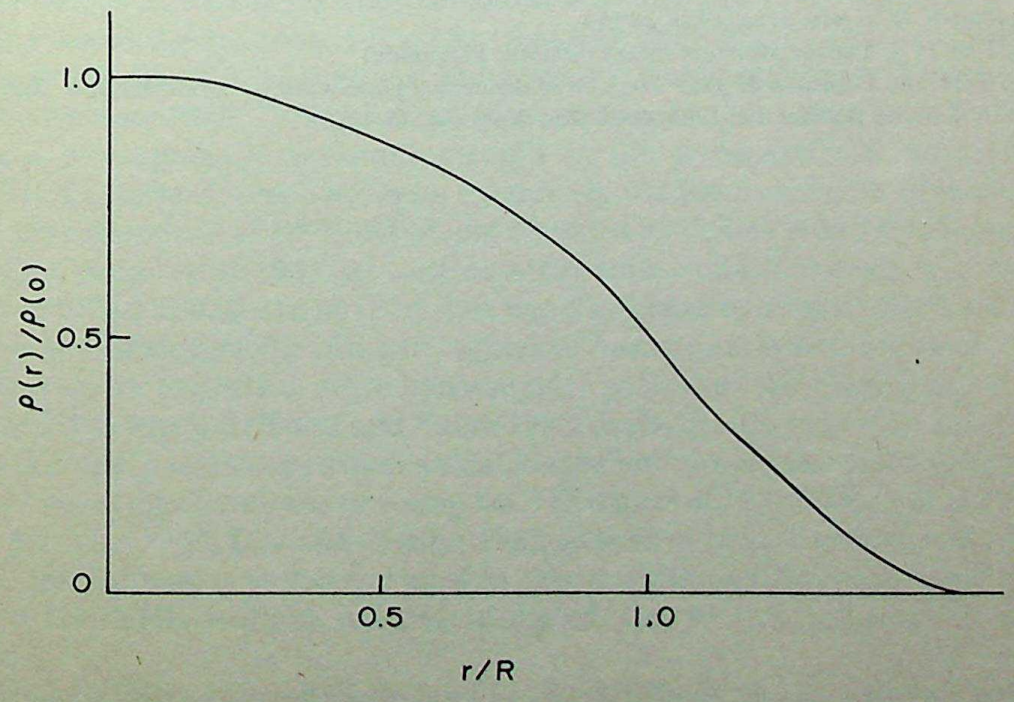

Figure 1. A plot of $\rho(r)/\rho(0)$ against r/R, R being the r.m.s. radius.

CC-0. In Public Domain. Gurukul Kangri Collection, Haridwar

Digitized by Arya Samaj Foundation Chennai and eGangotri

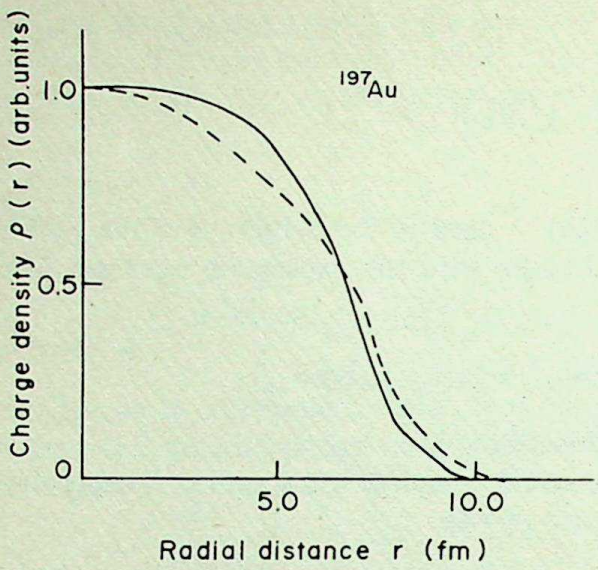

Figure 2. Comparison of $\rho(r)$ for ^{197}Au using expression (i) (– – –) with experimental curve (——).

Finally we calculate the value of r_0 using the radius of the equivalent uniform distribution and taking $\hbar\omega = 41A^{-1/3}$ MeV (Irvine 1972). It turns out to be 1·21 fm which is in good agreement with the value extracted from electron scattering data on heavy nuclei (Nolen Jr and Schiffer 1969).

References

Abramovitz M and Stegun I 1965 *Handbook of mathematical functions* (New York: Dover)
Bateman H 1953 *Higher transcendental functions* (ed.) A Erdelyi (New York: McGraw Hill)
Brown B A, Masseh S E and Hodgson P E 1979 *J. Phys.* **G5** 1655
Hofstadter R 1956 *Rev. Mod. Phys.* **28** 214
Irvine J M 1972 *Nuclear structure theory* (Oxford: Pergamon)
Morse P M and Feshbach H 1953 *Methods of theoretical physics* (New York: McGraw Hill) vol. 2
Nolen Jr J A and Schiffer J P 1969 *Annu. Rev. Nucl. Sci.* **19** 471

CC-0. In Public Domain. Gurukul Kangri Collection, Haridwar

Digitized by Arya Samaj Foundation Chennai and eGangotri

Pramāṇa – J. Phys., Vol. 28, No. 6, June 1987, pp. 645–651. © Printed in India.

Calculation of geometrical coupling coefficients for the hyperspherical harmonics approach

TAPAN K DAS and TUSHAR BARAN DE
Physics Department, University of Burdwan, Burdwan 713 104, India

MS received 4 February 1987

Abstract. An elegant and fast method for the calculation of geometrical structure coefficients needed for an expansion of a few-body wavefunction and interaction in hyperspherical harmonics has been proposed. A sum rule for the GSC has also been derived, which is useful for an independent check of the coefficients. The proposed method of computation is many orders of magnitude faster than conventional methods.

Keywords. Nuclear structure; few-body problem; hyperspherical harmonics method; geometrical structure coefficients.

PACS Nos 02·30; 21·40; 02·70

1. Introduction

An exact solution of the few-body Schrödinger equation is of great interest in many branches of physics. Apart from the inherent interest in the precise structure and physics of few-body systems, such systems are very good testing grounds for few-particle interactions as well as for approximation methods. For exact calculations of the few body systems the methods of Faddeev (Faddeev 1960; Schmid and Ziegeimann 1974) or Yakubowski (1967) equations and hyperspherical harmonics (Ballot and Fabre 1980; Simonov 1966, 1972) (also called K harmonics) have been widely used. Among these a particularly powerful method is the hyperspherical harmonics expansion (HHE) method, which has been extensively used to investigate trinucleons (Erens *et al* 1971; Demin *et al* 1973; Ballot and Navarro 1975; Das *et al* 1982; Das and Coelho 1982; Coelho *et al* 1983) as well as other three- and four-body problems (Vallieres *et al* 1976a, b; Ballot *et al* 1972). The hyperspherical harmonics (HH) are the multidimensional analog of the ordinary spherical harmonics, which are used as a complete basis set for expansion of the hyperangular part of the few-body space wave function. The HHE method (Ballot and Fabre 1980) deals directly with wave function in configuration space and this provides a clear insight into the physics of the problem. Inclusion of long-range, hard-core or many-body (Erens *et al* 1971; Demin *et al* 1973; Ballot and Navarro 1975; Das and Coelho 1982; Das *et al* 1982; Coelho *et al* 1983; Fabre 1979) interactions is straightforward in this method and the structure of the equations in the HHE method remains unaltered due to the inclusion of such interactions.

In the standard HHE approach (Ballot and Fabre 1980) both the space wavefunction and the interaction potential are expanded in terms of suitable HH basis. Substitution

CC-0. In Public Domain. Gurukul Kangri Collection, Haridwar

Digitized by Arya Samaj Foundation Chennai and eGangotri

of these into the Schrödinger equation and projection on to a particular HH results in a set of coupled differential equations in which the coupling term becomes a product of potential multipoles and interaction independent coefficients which are called geometrical structure coefficients (GSC).

The GSC is usually calculated by numerical integration which is both slow and inaccurate for large values of its arguments.

In this paper we report an elegant mathematical treatment utilizing the completeness property of the Jacobi polynomials, which makes the calculation of GSC particularly simple, economical and accurate. This method also yields a sum rule satisfied by the GSC which can be utilized as an independent check for the calculated GSC.

In §2, the HHE method is briefly reviewed and the GSCs are defined. Section 3 presents the mathematical analysis leading to a set of linear inhomogeneous equations for GSC. A sum rule for GSC is also derived. In §4 the present and other existing methods for calculating GSC have been compared.

2. HHE method and GSCs

For fermion systems, the space wavefunctions are chosen to have an appropriate symmetry to combine with the spin isospin wavefunctions giving rise to a fully antisymmetric total wavefunction. In the HHE method (Ballot and Fabre 1980; Erens *et al* 1971; Demin *et al* 1973; Ballot and Navarro 1975; Das *et al* 1982 and Coelho *et al* 1983) each symmetry component $\Psi(r, \Omega)$ of the N-fermion system is expanded in the hyperspherical harmonics $\mathscr{P}_{k\alpha}(\Omega)$,

$$\Psi(r, \Omega) = \frac{1}{r^{\frac{1}{2}(3N-4)}} \sum_{k\alpha} \Phi_{k\alpha}(r) \mathscr{P}_{k\alpha}(\Omega). \tag{1}$$

Here r is the hyperradial variable which is the invariant global length in a $(3N-3)$ dimensional space and Ω represents a set of $3N-4$ hyperangles (Faddeev 1960; Schmid and Ziegelmann 1974; Yakubowski 1967).

The HH $\mathscr{P}_{k\alpha}(\Omega)$ are the angular part of the homogeneous harmonic polynomials of degree k, which are the solutions of $(3N-3)$ dimensional Laplace equation. The HH is the $3N-3$ dimensional counterpart of ordinary three-dimensional spherical harmonics; k is called the 'grand orbital quantum number' and is the analog of ordinary orbital angular momentum. Here α represents a set of $3N-5$ quantum numbers necessary for a complete characterization. The appropriate symmetry set (Ballot and Fabre 1980) of HH is chosen for the expansion (1) to correspond with the desired symmetry of the wavefunction $\Psi(r, \Omega)$. Explicit expression for the HH can be found in Ballot and Fabre (1980).

The interaction potential is also expanded in a suitable HH basis,

$$V(r, \Omega) = \sum_{k''\alpha''} V_{k''\alpha''}(r)\, \mathscr{P}_{k''\alpha''}(\Omega), \tag{2}$$

where $\{\mathscr{P}_{k''\alpha''}\}$ is the appropriate set consistent with the nature of the interaction.

Substitution of (1) and (2) into the Schrödinger equation and projection on to a

CC-0. In Public Domain. Gurukul Kangri Collection, Haridwar

Digitized by Arya Samaj Foundation Chennai and eGangotri

particular $\mathscr{P}_{k'\alpha'}(\Omega)$ lead to a system of coupled differential equations (CDE) (Faddeev 1960; Schmid and Ziegelmann 1974; Yakubowski 1967),

$$\left(-\frac{\hbar^2}{m}\frac{\mathrm{d}^2}{\mathrm{d}r^2}+\frac{\hbar^2}{m}\frac{\Lambda_k(\Lambda_k+1)}{r^2}-\mathscr{E}\right)\Phi_{k\alpha}(r)+\sum_{k'\alpha'}V_{k\alpha,\,k'\alpha'}(r)\Phi_{k'\alpha'}(r)=0, \tag{3}$$

where
$$V_{k\alpha,\,k'\alpha'}(r)=\sum_{k''\alpha''}\langle k\alpha|k''\alpha''|k'\alpha'\rangle V_{k''\alpha''}(r) \tag{4}$$

and
$$\Lambda_k=2k+N-3/2. \tag{5}$$

The quantity $\langle k\alpha|k''\alpha''|k'\alpha'\rangle$, called the geometrical structure coefficients (GSC), is essentially an integral of the product of three $\mathscr{P}_{k\alpha}$ functions over the hyperangles. Clearly the GSC does not depend on the interaction and hence can be calculated once only and stored for eventual future use, must like the Clebsch-Gordon coefficients.

The explicit expression for the GSC needed for the space-totally-symmetric S state ($\alpha\equiv 0$) of the three-body system ($N=3$) interacting via a central two-body force (Fabre 1983) is

$$\begin{aligned}\langle k0|k''0|k'0\rangle=&\frac{\pi}{16}C^{(0)}_{2k}C^{(0),(2)}_{2k',2k''}P^{00}_{2k''}(0)\\&\times\sum_{l=0}^{\min(k,\,k')}(2l+1)\left(\sum_{(0)}{}^{(2)}P^{ll}_{2k}(\theta)\right)\left(\sum_{(0)}{}^{(2)}P^{ll}_{2k'}(\theta)\right)\\&\times\langle{}^{(2)}P^{ll}_{2k}|{}^{(2)}P^{00}_{2k''}|{}^{(2)}P^{ll}_{2k'}\rangle,\end{aligned} \tag{6}$$

where
$$[C^{(0)}_{2k}]^{-2}=\sum_{l=0}^{k}(2l+1)\left[\sum_{(0)}{}^{(2)}P^{ll}_{2k}(\theta)\right]^2,$$

$${}^{(2)}P^{l_2l_1}_{2k}=N^{l_2l_1}_{2k}(\sin\theta)^{l_1}(\cos\theta)^{l_2}P_n^{l_1+\frac{1}{2},l_2+\frac{1}{2}}(\cos 2\theta), \tag{7}$$

$P_n^{\alpha,\beta}(x)$ is a Jacobi polynomial and

$$N^{l_2l_1}_{2k}=\left(\frac{4(k+1)n!(n+l_1+l_2+1)!}{\Gamma(n+l_1+3/2)\Gamma(n+l_2+3/2)}\right)^{1/2},$$

$$n=(2k-l_1-l_2)/2$$

$$\sum_{(0)}f(\theta)=(1/3)[f(0)+f(2\pi/3)+f(-2\pi/3)]. \tag{8}$$

The $2P$ coefficients in equation (6) is defined as

$$\begin{aligned}\langle{}^{(2)}P^{ll}_{2k}|{}^{(2)}P^{00}_{2k''}|{}^{(2)}P^{ll}_{2k'}\rangle&=\int_0^{\pi/2}{}^{(2)}P^{ll}_{2k}(\theta)\,{}^{(2)}P^{00}_{2k''}(\theta)\,{}^{(2)}P^{ll}_{2k'}(\theta)(\sin\theta)^2(\cos\theta)^2\,\mathrm{d}\theta\\&=N^{ll}_{2k}N^{00}_{2k''}N^{ll}_{2k'}\frac{1}{2^{(2l+3)}}\int_{-1}^{+1}(1-x)^{l+\frac{1}{2}}(1+x)^{l+\frac{1}{2}}\\&\quad\times P^{l+\frac{1}{2},\,l+\frac{1}{2}}_{k-l}(x)\,P^{\frac{1}{2},\frac{1}{2}}_{k''}(x)\,P^{l+\frac{1}{2},\,l+\frac{1}{2}}_{k'-l}(x)\,\mathrm{d}x.\end{aligned} \tag{9}$$

CC-0. In Public Domain. Gurukul Kangri Collection, Haridwar

Digitized by Arya Samaj Foundation Chennai and eGangotri

Thus the straightforward calculation of GSC involves a sum of numerical integrations of a product of three Jacobi polynomials (equations (6) and (9)). This process is very slow for a prescribed precision.

Fabre (1983) suggested a double sum for a fast calculation of the GSC. With the help of the Rodrigues formula for Jacobi polynomials (Abramowitz and Stegun 1970) and using the following power expansion for the product of two Jacobi polynomials (Fabre 1983)

$$P_n^{\alpha,\beta}(x)P_k^{\rho,\lambda}(x)=\frac{\Gamma(\alpha+n+1)\Gamma(\rho+k+1)}{n!k!\Gamma(\alpha+\beta+n+1)\Gamma(\rho+\lambda+k+1)}$$
$$\times\sum_{q=0}^{n+k}(-1)^q A_q(1-x)^q, \tag{10}$$

where

$$A_q=2^{-q}\sum_{p=\max(0,\,q-n)}^{\min(k,\,q)}\binom{n}{q-p}\binom{k}{p}\frac{\Gamma(\alpha+\beta+n+q-p+1)\Gamma(\rho+\lambda+k+p+1)}{\Gamma(\alpha+q-p+1)\Gamma(\rho+p+1)},$$

one obtains the following expression for the $3P$ coefficient:

$$\langle {}^{(2)}P_{2k}^{ll}|{}^{(2)}P_{2k''}^{00}|{}^{(2)}P_{2k'}^{ll}\rangle=2^{(2l+2)}\frac{\Gamma(k+3/2)\Gamma(k'+3/2)\Gamma(k''+3/2)}{(k'-l)!(k'')!\Gamma(k'+l+2)\Gamma(k''+2)}$$
$$\times\sum_{q=k-l}^{k'+k''-l}(-1)^q\binom{q}{k-l}\frac{\Gamma(l+q+3/2)}{\Gamma(k+q+l+3)}\sum_{p=\max(0,\,q-k'+l)}^{\min(k'',\,q)}\binom{k'-l}{q-p}$$
$$\times\binom{k''}{p}\frac{\Gamma(k'+q-p+l+2)\Gamma(k''+p+2)}{\Gamma(q-p+l+3/2)\Gamma(p+3/2)}, \tag{11}$$

where $$\binom{a}{b}=\frac{a!}{b!(a-b)!}$$

Thus the integration is replaced by a double sum, which is faster in computation, but equation (11) involves a sum of oscillating terms which are ratios of gamma functions of large arguments for large values of k, k' and k''. This causes uncontrollably large errors to creep into the calculations.

3. Linear inhomogeneous equation for GSC and the sum rule

The Jacobi polynomials are solutions of a differential equation in Sturm-Liouville form and hence are orthogonal and satisfy completeness relation (Abramowitz and Stegun 1970)

$$\sum_n (h_n^{\alpha,\beta})^{-1}P_n^{\alpha,\beta}(x)P_n^{\alpha,\beta}(x')=\delta(x-x')/w(x), \tag{12}$$

where $w(x)=(1-x)^\alpha(1+x)^\beta$,

CC-0. In Public Domain. Gurukul Kangri Collection, Haridwar

Digitized by Arya Samaj Foundation Chennai and eGangotri

$$h_n^{\alpha,\beta}=\frac{2^{(\alpha+\beta+1)}}{2n+\alpha+\beta+1}\frac{\Gamma(n+\alpha+1)\Gamma(n+\beta+1)}{n!\Gamma(n+\alpha+\beta+1)}$$

Multiplying (6) by $\dfrac{(h_{k''}^{1/2,\,1/2})^{-1}P_{k''}^{1/2,\,1/2}(x')}{N_{2k''}^{00,(2)}P_{2k''}^{00}(0)}$, summing over k'' on both sides and utilizing equation (12) one gets

$$\sum_{k''}\frac{(k'')!}{\Gamma(k''+3/2)}P_{k''}^{1/2,\,1/2}(x')\langle k0|k''0|k'0\rangle=\frac{(\pi)^{1/2}}{8}C_{2k}^{(0)}C_{2k'}^{(0)}$$
$$\times\sum_{l=0}^{\min(k,k')}(2l+1)\left(\sum_{(0)}^{(2)}P_{2k}^{ll}(\theta)\right)\left(\sum_{(0)}^{(2)}P_{2k'}^{ll}(\theta)\right)N_{2k}^{ll}N_{2k'}^{ll}\frac{1}{2^{2l}}$$
$$\times(1-x')^l(1+x')^lP_{k-l}^{l+\frac{1}{2},\,l+\frac{1}{2}}(x')P_{k'-l}^{l+\frac{1}{2},\,l+\frac{1}{2}}(x'). \tag{13}$$

Putting $x'=1$ in (13) we get a sum rule satisfied by the GSC:

$$\sum_{k''}\langle k0|k''0|k'0\rangle=C_{2k}^{(0)}C_{2k'}^{(0)}\left(\sum_{(0)}^{(2)}P_{2k}^{00}(\theta)\right)\left(\sum_{(0)}^{(2)}P_{2k'}^{00}(\theta)\right)(k+1)(k'+1). \tag{14}$$

On the other hand (13) can be utilized to calculate GSC in a very simple manner. Since (13) is valid for any x' in the interval $[-1, 1]$, choosing an appropriate number of points (x') in this interval, one can solve the set of linear inhomogeneous equations (13) for the unknown coefficients $\langle k0|k''0|k'0\rangle$ with fixed values of k and k'. This method however cannot be utilized if the series on the left side of (13) were an infinite series. Fortunately since $\langle k0|k''0|k'0\rangle=0$ unless k, k', k'' satisfy the triangle relation (Fabre 1983) the series in (13) is finite and there is a finite number $[=2\min(k, k')+1]$ of GSC for fixed values of k, k'.

4. Comparison with other methods

The conventional methods for calculating GSC are both inaccurate and time-consuming for large values of k, k' and k''. Since $P_n^{\alpha,\beta}$ is a rapidly oscillating function for large n numerical integrations become inaccurate unless a quadrature with a large number of points is employed. This makes the calculation of GSC extremely slow.

The double sum method for the evaluation of the GSC is faster computationally but the expression involves sum of oscillating terms which are ratios of gamma functions of large arguments. This introduces so much rounding of error that computation of GSC for $k, k'>11$ becomes completely unreliable. So the existing two methods are not suitable for the calculation of GSC for large values of k, k'.

Since very fast codes for accurate numerical solution of a set of linear inhomogeneous equations exist, GSC can be calculated extremely fast and accurately by the present method.

We have calculated GSC using (13) for $-0{\cdot}9<x'<0{\cdot}9$. For a quantitative comparison, the same coefficients have been calculated also by the integration and the double sum methods. All the calculations were done in double precision on the Burroughs 6700 computer system at the Regional Computer Centre, Calcutta. A

CC-0. In Public Domain. Gurukul Kangri Collection, Haridwar

Digitized by Arya Samaj Foundation Chennai and eGangotri

Table 1. Comparison of GSC calculation by various methods.

		CPU time (sec.)			Percentage deviation from sum rule		
k	k'	Integral method	Double sum method	Present work	Integral method	Double sum method	Present work
2	2	22·756	1·144	0·711	$2{\cdot}87\times10^{-4}$	$4{\cdot}73\times10^{-18}$	$6{\cdot}33\times10^{-21}$
3	3	34·952	1·947	0·913	$7{\cdot}01\times10^{-4}$	$1{\cdot}29\times10^{-16}$	$1{\cdot}62\times10^{-20}$
5	5	104·698	6·732	1·622	$2{\cdot}41\times10^{-3}$	$1{\cdot}17\times10^{-12}$	$1{\cdot}40\times10^{-19}$
7	7	192·251	19·778	2·643	$5{\cdot}75\times10^{-2}$	$4{\cdot}39\times10^{-7}$	$7{\cdot}37\times10^{-19}$
8	8	−(a)	36·640	3·596	−(a)	$3{\cdot}72\times10^{-6}$	$1{\cdot}55\times10^{-18}$
11	11	−(a)	104·262	6·942	−(a)	7·90	$4{\cdot}86\times10^{-16}$
12	12	−(a)	149·853	8·387	−(a)	106·70	$1{\cdot}88\times10^{-15}$

(a) Not calculated.

comparison of the calculations of some typical GSC by these methods has been presented in table 1.

The third, fourth and fifth columns give the CPU time for the integration, the double sum and the present method respectively. Calculations by integration method (using a 320-point gaussian quadrature for $l\neq0$ and a 512-point gaussian quadrature for $l=0$) were done for $k, k'\leqslant7$. For larger values of k, k' a quadrature with a larger number of points is necessary for a comparable accuracy; this makes the already slow calculations even slower. Hence such calculations were not done for $k, k'>7$.

The percentage deviations of the sum of calculated GSC from the right side of (14) have been presented in the last three columns of table 1. It is seen that as k, k' increases, the CPU time increases very rapidly for the integration method and quite rapidly for the double sum method, but quite slowly for the present method. Furthermore it is seen that the accuracy of the calculation rapidly decreases with increasing k, k' for both integration or double sum methods, whereas it remains extremely high even for $k=k'=12$ by the present method. This shows that the present method (linear equation method) is both highly dependable and very economical, in striking contrast to other available and usually practised methods. This remarkable contrast in dependability (accuracy) and economy becomes even more prominent as k, k' increase or for the GSC needed in other symmetry components of the wave function, for which a larger number of terms in the intermediate l-sum [similar to right side of equation (13)] contribute. Since the confidence on a calculation by the HHE method is ultimately limited by the accuracy of the GSC coefficients, the present method is of great practical utility in such calculations.

Acknowledgement

This work was done under a grant from the University Grants Commission (UGC), India.

CC-0. In Public Domain. Gurukul Kangri Collection, Haridwar

Digitized by Arya Samaj Foundation Chennai and eGangotri

References

Abramowitz M and Stegun I A (eds) 1970 *Handbook of mathematical functions* (New York: Dover) p. 773
Ballot J L, Beiner M and Fabre de la Ripelle M 1972 *Present status and novel developments in the nuclear many-body problems*, Rome (eds) F Calogera and C Ciofidegli Atti (Editrice Compositori, Bologna 1973) p. 565
Ballot J L and Fabre de la Ripelle M 1980 *Ann. Phys.* **127** 62
Ballot J L and Navarro J 1975 *J. Phys.* **B8** 172
Coelho H T, Das T K and Robilotta M R 1983 *Phys. Rev.* **C28** 1812
Das T K and Coelho H T 1982 *Phys. Rev.* **C26** 754
Das T K, Coelho H T and Fabre de la Ripelle M 1982 *Phys. Rev.* **C26** 2288
Demin V F, Pokrovsky Y E and Efros V D 1973 *Phys. Lett.* **B44** 227
Erens G, Visschers J L and Van Wageningen R 1971 *Ann. Phys.* **67** 461
Fabre de la Ripelle M 1979 *C. R. Acad. Sci. Ser.* **B288** 325
Fabre de la Ripelle M 1983 *Ann. Phys.* **147** 281
Faddeev L D 1960 *Zurn. Eksp. Theor. Fiz.* **39** 1459 (1961 *Sov. Phys. JETP* **12** 1014)
Schmid E W and Ziegelmann H 1974 *The quantum mechanical three-body problem*, in *Vieweg tracts in pure and applied physics* (Vieweg: Braunschweig).
Simonov Y A 1966 *Yad. Fiz.* **3** 630 (1966 *Sov. J. Nucl. Phys.* **3** 461)
Simonov Y A 1972 *Present status and novel developments in the nuclear many-body problems*, Rome (eds) F Calogera and C Ciofi degli Atti (Editrice Compositori, Bologna 1973) p. 527
Vallieres M, Das T K and Coelho H T 1976a *Nucl. Phys.* **A257** 389
Vallieres M, Coelho H T and Das T K 1976b *Nucl. Phys(* **A271** 95
Yakubowski O A 1967 *Yad. Fiz.* **5** 1312 (1967 *Sov. J. Nucl. Phys.* **5** 937)

CC-0. In Public Domain. Gurukul Kangri Collection, Haridwar

Digitized by Arya Samaj Foundation Chennai and eGangotri

CC-0. In Public Domain. Gurukul Kangri Collection, Haridwar

Digitized by Arya Samaj Foundation Chennai and eGangotri

Pramāṇa – J. Phys., Vol. 28, No. 6, June 1987, pp. 653–660 © Printed in India.

Quenching of excitations in an impure molecular crystal

S PRIYADARSHY and S N DATTA
Department of Chemistry, Indian Institute of Technology, Powai, Bombay 400076, India

MS received 4 September 1986; revised 19 January 1987

Abstract. The rate of quenching of excitons in a one-dimensional molecular crystal by an impurity is quantum-mechanically calculated.

Keywords. Excitons; molecular crystal; quenching.

PACS Nos 71·25; 71·35; 71·55

1. Introduction

There are two basic mechanisms of quenching of an exciton in a molecular crystal, viz (i) the exciton-phonon coupling and (ii) the coupling of the electronic (vibronic) excitations of an impurity with the electronic excitations of the rest of the crystal. Various authors (Kenkre and Reineker 1982) have discussed the first mechanism. The second process has been described by a generalized master equation (Lakatos-Lindenberg *et al* 1972; Pearlstein 1972; Huber 1979, 1981; Ghosh and Huber 1980; Klafter and Silbey 1980, 1981; Kenkre and Wong 1981; Scher and Wu 1981). Incidentally, the Schrödinger equation for one-electron moving in an impure crystal has been solved by Koster and Slater (1954). Although the work of Koster and Slater is for a localized carrier in a semiconductor, the final working equations are algebraically similar to the equations of motion describing a site excitation in the tight binding limit. Therefore, from the algebraic point of view, excitonic solutions will mimick the electronic ones. Koster and Slater derived the electronic solutions by applying periodic boundary conditions and basing their argument on the symmetry of the chain. In the present work we point out that these solutions are obtained simply from the structure of the Hamiltonian matrix ($H_{ij}=H_{ji}$) rather than the detailed symmetry of the Hamiltonian. As any calculation (diagonalization of the Hamiltonian matrix) would reveal, the so-called 'localized' solution (found by Koster and Slater) is wrong. Instead, we find a solution which is always spread over a few sites around the impurity and which looks like a localized solution only when the chain is sufficiently large. Finally, we discuss a quantum-mechanical formulation of the simplest trapping model (which is a familiar model for the generalized master equation approach to exciton trapping).

2. Excitons in an impure molecular crystal

We consider a one-dimensional crystal with ε_e and $\varepsilon_{e\zeta}$ as excitation energies of the normal species and the impurity respectively. The impurity occupies the ζth site.

CC-0. In Public Domain. Gurukul Kangri Collection, Haridwar

Digitized by Arya Samaj Foundation Chennai and eGangotri

Excited electronic states are

$$\psi_{ek} = \sum_{j}^{\text{sites}} C_j \phi_{ej},$$

where ϕ_{ej} is the many-electron function describing the crystal when the jth molecule is excited to the eth level and the others are unexcited. The coefficients C_j's are determined from the secular equation:

$$\varepsilon_e^k C_j = \varepsilon_e C_j + \Omega(C_{j+1} + C_{j-1} \quad \text{for } j \neq \zeta, \zeta \pm 1, \tag{1a}$$

$$\varepsilon_e^k C_{\zeta \pm 1} = \varepsilon_e C_{\zeta \pm 1} + \Omega C_{\zeta \pm 2} + \Omega'_{\mp} C_{\zeta}, \tag{1b}$$

and

$$\varepsilon_e^k C_{\zeta} = \varepsilon_{e\zeta} C_{\zeta} + \Omega'_{+} C_{\zeta+1} + \Omega'_{-} C_{\zeta-1}, \tag{1c}$$

where Ω, Ω'_{+}, and Ω'_{-} are the corresponding elements of the Hamiltonian matrix H. The eigenvalues of (1) are

$$\varepsilon_e^k = \varepsilon_e + 2\Omega \cos kr, \tag{2}$$

where r is the lattice constant. These values are associated with the solutions

$$C_j = a \exp[i(j+\delta_+)kr] + b \exp[-i(j+\delta_+)kr] \quad (j > \zeta), \tag{3a}$$

and

$$C_j = A \exp[i(j+\delta_-)kr] + B \exp[-i(j+\delta_-)kr] \quad (j < \zeta). \tag{3b}$$

The phases δ_+ and δ_- and the coefficients a, b, A and B are still unknown. Since the Hamiltonian is hermitian, H may be written as a real symmetric matrix by making an appropriate choice of the functions ϕ_{ej}. [With usual Hamiltonians, this is achieved by choosing ϕ_{ej}'s as real functions]. If H is a real symmetric matrix, the coefficients can be chosen as purely real or purely imaginary functions. Thus there are three types of solutions: the 'cosine' type, the 'sine' type and a single eigenvector which is quasi-localized. The last solution will be henceforth called the 'singleton'.

We write the cosine solution as

$$\begin{aligned} C_j &= 2a \cos(j+\delta_+)kr \quad (j > \zeta), \\ C_j &= 2A \cos(j+\delta_-)kr \quad (j < \zeta), \end{aligned} \tag{3c}$$

and

$$C_{\zeta} = (\Omega/\Omega'_{+})\, 2a \cos(\zeta+\delta_+)kr = (\Omega/\Omega'_{-}) 2A \cos(\zeta+\delta_-)kr$$

the sine solutions as

$$\begin{aligned} C_j &= 2ia \sin(j+\delta_+)kr \quad (j > \zeta), \\ C_j &= 2iA \sin(j+\delta_-)kr \quad (j < \zeta), \end{aligned} \tag{3d}$$

and

$$C_{\zeta} = (\Omega/\Omega'_{+})\, 2ia \sin(\zeta+\delta_+)kr = (\Omega/\Omega'_{-}) 2iA \sin(\zeta+\delta_-)kr$$

CC-0. In Public Domain. Gurukul Kangri Collection, Haridwar

Digitized by Arya Samaj Foundation Chennai and eGangotri

and the singleton as

$$C_{\zeta+p} = a\exp(-\gamma rp) + b\exp(\gamma rp),$$
$$C_{\zeta-p} = A\exp(-\gamma rp) + B\exp(\gamma rp), \tag{3e}$$

where $\gamma = ik$ and a, b, A and B are coefficients which will be determined from the (periodic) boundary conditions. The singleton is associated with the eigenvalue

$$\varepsilon_e^{\gamma} = \varepsilon_e + 2\Omega\cosh(\gamma r).$$

Solutions of the cosine and sine type and their corresponding eigenvalues resemble those derived by Koster and Slater (1954) from a consideration of symmetry of the single-particle states where the impurity is assumed to occupy the zeroth site (that is, $\zeta = 0$). The results of the above consideration, however, follow the assumption that H is a real symmetric matrix and the location of the impurity is not the deciding factor.

The localized solution discussed by Koster and Slater (1954) (and which corresponds to the singleton) is not truly orthogonal to the 'symmetric' (cosine) solutions. The constraint of orthogonality requires that both $\exp(-\gamma rp)$ and $\exp(+\gamma rp)$ have to be linearly combined (equation (3e)). Because of the exponentially increasing part, the singleton is not really localized around the impurity, but spread over a few sites. However, as the chain length increases, it seems that the singleton is localized around the impurity.

3. Cyclic boundary conditions

We use the cyclic boundary conditions

$$C_{N/2+1} = C_{-N/2}$$

and

$$C_{N/2} = C_{-N/2-1}$$

in order to determine the phases $\delta_{\pm}$. There are $(N+1)$ unit species in the crystal.

The cosine solutions have phases $\delta_{\pm} = \delta_0 \mp (N+1)/2$ where $\delta_0 = 2m\pi/kr - \zeta$, m being a real positive integer. The boundary condition at the impurity site requires that $a\Omega'_- = A\Omega'_+$. Therefore, these solutions are quasi-symmetric on both sides of the impurity,

$$C_{\zeta\pm p} = \frac{\Omega'_{\pm}}{\Omega}\cos\left(p - \frac{N+1}{2}\right)kr \tag{4a}$$

with

$$C_{\zeta} = \cos\left(\frac{N+1}{2}\right)kr.$$

CC-0. In Public Domain. Gurukul Kangri Collection, Haridwar

Digitized by Arya Samaj Foundation Chennai and eGangotri

The wave vector (k) is found from

$$(\varepsilon_e - \varepsilon_{e\zeta}) = \left(\frac{\Omega'^2_+ + \Omega'^2_-}{\Omega} - 2\Omega\right)\cos kr + \frac{(\Omega'^2_+ + \Omega'^2_-)}{\Omega}\sin kr \tan\left(\frac{N+1}{2}\right)kr. \quad (4b)$$

The sine solutions are quasi-antisymmetric,

$$C_{\zeta \pm p} = \pm\frac{\Omega'_\mp}{\Omega}\sin\left(p - \frac{N+1}{2}\right)kr \quad (5a)$$

with

$$C_\zeta = 0.$$

The wavevector (k) is given by

$$k = 2\pi m/(N+1)r, \quad (5b)$$

where $m = 1, 2 \ldots, N/2$ if N is even or $m = 1, 2 \ldots, (N-1)/2$ if N is odd.

For the singleton the boundary condition $C_{\zeta - p} = C_{\zeta + (N+1-p)}$ yields

$$b = -\frac{\Omega'_- - \Omega'_+ \exp[-\gamma r(N+1)]}{\Omega'_- - \Omega'_+ \exp[-\gamma r(N+1)]}a \quad (6a)$$

such that the wave vector γ satisfies the relation

$$\varepsilon_e - \varepsilon_{e\zeta} = \frac{(\Omega'_+ + \Omega'_-)^2}{\Omega}\frac{\sinh \gamma r}{\sinh[\gamma r(N+1)]} + \frac{(\Omega'^2_+ + \Omega'^2_-)}{\Omega}\frac{\sinh \gamma r(N-1)/2}{\sinh \gamma r(N+1)/2} - 2\Omega \cosh \gamma r. \quad (6b)$$

We note that for $\Omega'_+ = \Omega'_- = \Omega$ these coefficients and eigenvalues are not identical with those derived by Koster and Slater (1954). Secondly, for a molecular crystal Ω'_+ need not necessarily equal Ω'_-.

4. Lifetime of excitations

The quenching process implies a redistribution of the excitation energy among different electronic levels and vibrational modes (VI) of the impurity. In other words these vibronic states (VI) are coupled with the excited levels (EX) of the host crystal. The projected amplitude of excitation will change in time according to an effective Hamiltonian, $\hat{H}_{\text{eff}}$. Similar considerations in the context of unimolecular fragmentation have led Nordholm and Rice (1975) to suggest a dissipative part $-i\hat{H}_D$ of the effective Hamiltonian,

$$\hat{H}_{\text{eff}} = \hat{H} - i\hat{H}_D.$$

The Markoffian approximation will be justified in the present case if the time spent in the transition EX→VI is very short on the time scale of the excitonic motion, and if the escape from the transition zone to the EX modes is irreversible. Similar models have been used earlier (Mies and Krauss 1966; Mies 1969) to describe radiative deactivation.

CC-0. In Public Domain. Gurukul Kangri Collection, Haridwar

Digitized by Arya Samaj Foundation Chennai and eGangotri

We assume that the dissipative part gives rise to an imaginary term in $\varepsilon_{e\zeta}$ only, $\varepsilon_{e\zeta}=\varepsilon^r_{e\zeta}+i\varepsilon^i_{e\zeta}$, such that the off-diagonal matrix elements are still arranged in a real symmetric form (although because of the ζth diagonal element the Hamiltonian matrix of (1) is no longer hermitian). In general, eigenvalues and the coefficients (C's) will be complex. However, translational symmetry of the host molecule part of the crystal remains unaltered giving a constant ratio of coefficients C_{j+1}: C_j, $(j\neq\zeta, \zeta-1)$ and indicating that if the sine type of solutions exist, these will be accompanied by the cosine type of solutions. Now, the sine solutions remain unaffected by $\varepsilon_{e\zeta}$; hence these remain valid. Therefore, the cosine type of solutions (and the singleton) still holds. Eigenvalues and coefficients corresponding to the cosine type of solutions (and the singleton) are found by a straightforward substitution of k by $k'+ik''$ (γ by $\gamma'+i\gamma''$).

Eigenvalues for the cosine solutions are given by

$$\varepsilon^k_e=\varepsilon_e+2\Omega\,(\cos k'r\cosh k''r-i\sin k'r\sinh k''r),$$

where k' and k'' are found by solving the two equations

$$\varepsilon_e-\varepsilon^r_{e\zeta}=\left(\frac{\Omega'^2_+ +\Omega'^2_-}{\Omega}-2\Omega\right)\cos k'r\cosh k''r$$
$$+\frac{(\Omega'^2_+ +\Omega'^2_-)}{\Omega}(\alpha\sin k'r\cosh k''r-\beta\cos k'r\sinh k''r)$$

and

$$\varepsilon^i_{e\zeta}=\left(\frac{\Omega'^2_+ +\Omega'^2_-}{\Omega}-2\Omega\right)\sin k'r\sinh k''r$$
$$-\frac{(\Omega'^2_+ +\Omega'^2_-)}{\Omega}(\alpha\cos k'r\sinh k''r+\beta\sin k''r\sinh k''r)$$

in a self-consistent manner. Here α and β are given by

$$\alpha=\tan\left(\frac{N+1}{2}\right)k'r\Big/\left[\cosh^2\left(\frac{N+1}{2}\right)k''r\right.$$
$$\left.+\tan^2\left(\frac{N+1}{2}\right)k'r\sinh^2\left(\frac{N+1}{2}\right)k''r\right]$$

and

$$\beta=\tanh\left(\frac{N+1}{2}\right)k''r\Big/\left[\left(\cos^2\left(\frac{N+1}{2}\right)k'r\right)\right.$$
$$\left.+\sin^2\left(\frac{N+1}{2}\right)k'r\tanh^2\left(\frac{N+1}{2}\right)k''r\right].$$

The eigenvalue corresponding to the singleton is

$$\varepsilon_{e\gamma}=\varepsilon_e+2\Omega(\cosh\gamma'r\cos\gamma''r+i\sinh\gamma'r\sin\gamma''r)$$

where γ' and γ'' are similarly determined by a self-consistent procedure.

Imaginary parts of the eigenvalue give the characteristic lifetime for the quasi-symmetric excitations, that is, they are the velocity constants for quenching of these

CC-0. In Public Domain. Gurukul Kangri Collection, Haridwar

Digitized by Arya Samaj Foundation Chennai and eGangotri

excitons. A positive value of $\mathrm{Im}(\varepsilon_e^k)$ is unacceptable on physical grounds. In practice, one may not encounter this difficulty if the impurity causes a small perturbation only, that is, effects of $\varepsilon_{e\zeta}^i$ are evaluated by the lowest orders in perturbation theory (or else one has to modify (1) so that mixing of different bands is taken into account). Using (1) in their present form, a small negative value of $\varepsilon_{e\zeta}^i$ suffices to yield physically acceptable solutions.

5. Discussion

Pearlstein (1972) discussed the quenching of fully coherent, Frenkel, excitons by an ad-hoc linear differential equation. The latter gives a time-dependent description of the

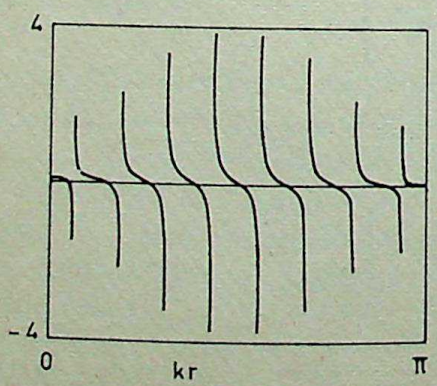

Figure 1a. Right hand side of equation (4b) vs *kr*.

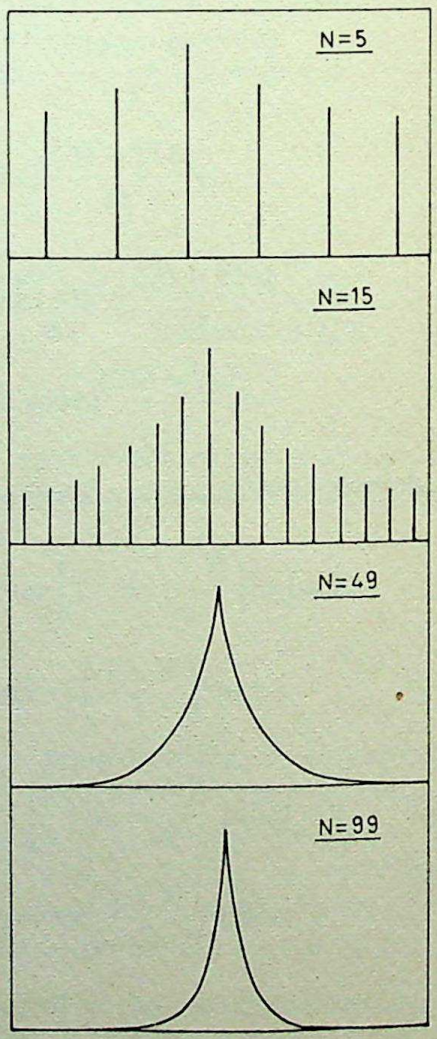

Figure 1b. Coefficients of linear combination for the singleton vs the length of the crystal. For $N=5$ and $N=15$ these coefficients are shown as line spectra spread over different sites. For larger values of N ($N=49$ and 99) a continuous line is drawn.

CC-0. In Public Domain. Gurukul Kangri Collection, Haridwar

Digitized by Arya Samaj Foundation Chennai and eGangotri

motion of a Frenkel exciton packet in a given band and has complex eigenvalues. According to Pearlstein this equation is not strictly derivable from the Schrödinger equation. Our analysis, based on single excitons and a projected Hamiltonian (Nordholm and Rice 1975), yields the difference equation for each eigenvector.

In figure 1(a), the right hand side of (4b) is plotted against kr. Points where these plots intersect the $y=\varepsilon_e-\varepsilon_{e\zeta}$ axis give eigenvalues for the cosine excitations. The least eigenvalue is found with the singleton. For a pure crystal, the singleton represents the lowest energy cosine excitation.

In figure 1(b), we show the singleton eigenvector for different values of N. This excitation is always spread over a few sites. When N is large enough, it looks like an excitation localized on a small fraction of the chain length around the impurity.

An imaginary term in $\varepsilon_{e\zeta}$ will change some of the eigenvalues. Such changes for $N=15$ (a chain of 16 unit species) are shown in table 1. In general, the singleton excitation shows the fastest decay (particularly if N is large), a consequence of its localization in the neighbourhood of the quencher. Time dependence of the probability of finding the crystal in different quasi-symmetric excited states is shown in figure 2.

Our analysis predicts that the longest wavelength excitation will spread over a few lattice sites around the impurity and will be quenched quickly. Theoretical computations and time-resolved experiments on the excited states of heteronuclear aromatic organic molecules (although not directly comparable to molecular crystals) support these results. These conclusions, with appropriate quantitative modifications, can be directly extended to the case of a three-dimensional doped molecular crystal. However, experimental results will be greatly influenced by three factors, viz (i) scattering by other excitons (Haken and Strobl 1973; Reinecker 1979), (ii) scattering by phonons (Soules and Duke 1971) and (iii) disorder in the lattice, which is a common occurrence in molecular crystals.

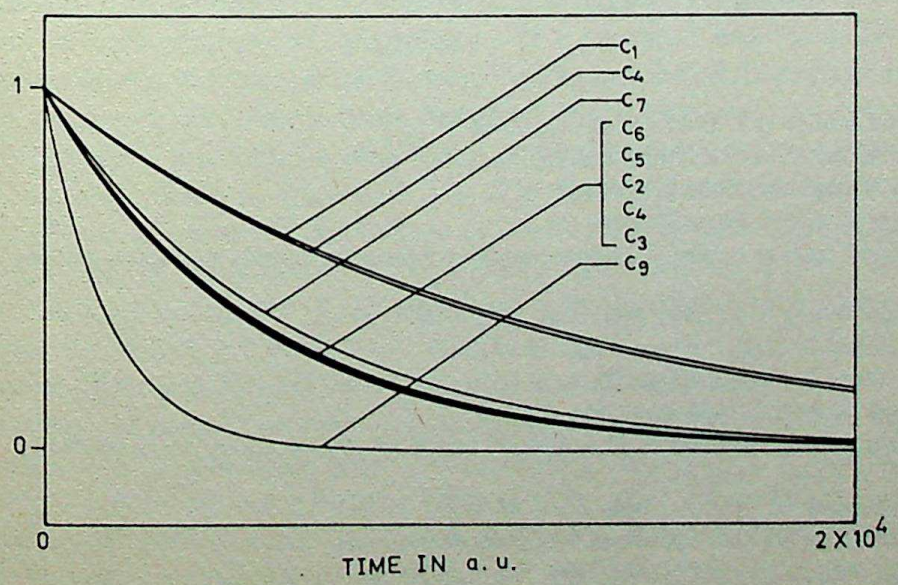

Figure 2. Time dependence of the probability of finding the crystal in different quasi-symmetric excited states. Eigenvalues are listed in table 1.

CC-0. In Public Domain. Gurukul Kangri Collection, Haridwar

Digitized by Arya Samaj Foundation Chennai and eGangotri

Table 1. Eigenvalues for $N = 15$ (Number of unit species = 16).

	Pure crystal, (a)	Crystal with impurity, (b)	Crystal with impurity, (c)	Crystal with impurity as a quencher (d)	
	ε_e^k	ε_e^k	ε_e^k	Re ε_e^k	Im $\varepsilon_e^k \times 10^{-4}$
C_1	−0·300	−0·302	−0·301	−0·300	−0·044
C_2	−0·315	−0·320	−0·316	−0·310	−0·101
C_3	−0·358	−0·364	−0·361	−0·361	−0·108
C_4	−0·423	−0·429	−0·427	−0·427	−0·102
C_5	−0·500	−0·506	−0·505	−0·505	−0·101
C_6	−0·576	−0·583	−0·583	−0·583	−0·098
C_7	−0·641	−0·647	−0·649	−0·649	−0·089
C_8	−0·685	−0·691	−0·692	−0·692	−0·046
C_9	−0·700	−0·706	−0·715	−0·715	−0·318

(a) $\varepsilon_e = \varepsilon_{e\zeta} = -0{\cdot}500$ a.u., $\Omega = \Omega'_+ = \Omega'_- = -0{\cdot}1$ a.u.
(a) $\varepsilon_e = -0{\cdot}500$ a.u., $\varepsilon_{e\zeta} = -0{\cdot}550$ a.u., $\Omega = \Omega'_+ = \Omega'_- = -0.1$ a.u.
(c) $\varepsilon_e = -0{\cdot}500$ a.u., $\varepsilon_{e\zeta} = -0{\cdot}550$ a.u., $\Omega = -0{\cdot}1$ a.u., $\Omega'_+ = \Omega'_- = -0{\cdot}11$ a.u.
(d) $\varepsilon_e = -0{\cdot}500$ a.u., $\varepsilon'_{e\zeta} = -0{\cdot}550$ a.u., $\varepsilon^i_{e\zeta} = -0{\cdot}001$ a.u., $\Omega = -0{\cdot}1$ a.u., $\Omega'_+ = \Omega'_- = -0{\cdot}11$ a.u.

Acknowledgements

This work was orally presented by one of the authors (SP) at the National Conference on Spectroscopy and Theoretical Chemistry, held at Calcutta University and the Indian Association for the Cultivation of Science, Jadavpur, Calcutta and dedicated to Prof. Sadhan Basu, on his 65th birthday. We acknowledge financial support from the Department of Atomic Energy.

References

Ghosh K K and Huber D L 1980 *J. Lumines.* **21** 2431
Haken H and Strobl G 1973 *Z. Phys.* **262** 135
Huber D L 1979 *Phys. Rev.* **B20** 2307, 5333
Huber D L 1981 *J. Chem. Phys.* **75** 4709
Kenkre V M and Reineker P 1982 *Exciton dynamics in molecular crystals and aggregates* (Berlin: Springer-Verlag)
Kenkre V M and Wong Y M 1981 *Phys. Rev.* **B23** 3748
Klafter J and Silbey R 1980 *J. Chem. Phys.* **72** 843
Klafter J and Silbey R 1981 *J. Chem. Phys.* **74** 3510
Koster G F and Slater J C 1954 *Phys. Rev.* **95** 1167
Lakatos-Lindenberg K, Hemenger R P and Pearlstein R M 1972 *J. Chem. Phys.* **56** 4852
Mies F H 1969 *J. Chem. Phys.* **51** 787
Mies F H and Krauss M 1966 *J. Chem. Phys.* **45** 4455
Nordholm S and Rice S A 1975 *J. Chem. Phys.* **62** 157
Pearlstein R M 1972 *J. Chem. Phys.* **56** 2431
Reinecker P 1979 *Phys. Rev.* **B19** 1999
Scher H and Wu C H 1981 *Proc. Natl Acad. Sci. USA* **78** 22
Soules T and Duke C B 1971 *Phys. Rev.* **B3** 262

CC-0. In Public Domain. Gurukul Kangri Collection, Haridwar

Digitized by Arya Samaj Foundation Chennai and eGangotri

Pramāṇa – J. Phys., Vol. 28, No. 6, June 1987, pp. 661–667 © Printed in India.

Kramers-Kronig type of dispersion relation in nonlinear optics

P SEN and P K SEN
Department of Physics, Bhopal University, Bhopal 462 026, India

MS received 31 October 1986; revised 31 March 1987

Abstract. The applicability of Kramers-Kronig (K-K) relation under nearly sharp resonant transition regime in narrow-gap semiconductors has been established and consequently, a generalized dispersion relation for nonlinear optical susceptibility of a dielectric is derived. This relation can be employed in the study of nonlinear optical processes in solids as well as in plasmas over a wide frequency spectrum.

Keywords. Kramers-Kronig dispersion relation; nonlinear optical susceptibility; nonlinear refraction; nonlinear absorption.

PACS No. 42·65

1. Introduction

Kramers-Kronig (K-K) dispersion relations which connect the dispersive and absorptive aspects of matter-radiation interaction processes are extremely useful in many areas of physics. In particular, the utility of K-K relations in the determination of different optical constants by reflectivity data as well as in the derivation of sum rules is well known and needs very few physically well-founded assumptions (Landau and Lifshitz 1959; Wooten 1972).

The extension of K-K relations to the nonlinear regime is regarded as a difficult and subtle problem because optical nonlinearity of a medium has been the origin of a variety of phenomena in contrast to the simple absorptive and dispersive aspects of the linear material response of the medium. Nonlinear refraction and absorption are two of the vital properties of the medium which play critical roles in the observation of optical bistability, optical phase conjugation via degenerate four-wave mixing and pulse shaping, etc. These phenomena have large technological potential in integrated optics. The investigations of such nonlinear optical effects could be much simplified if an analytical tool similar to the K-K relations is available. Unfortunately, no such relations seems to have yet been established.

The present literature reveals that there is a controversy about the applicability of K-K relations in the nonlinear regime. Flytzanis (1975) commented that these relations are applicable even in the nonlinear optical effects but are not so useful as in linear optics. On the other hand, according to Yariv (1975), these relations are invalid because of the presence of poles in both the upper and lower halves of complex ω-plane and violate the causality principle in the nonlinear regime. K-K relations were used by Miller *et al* (1981) probably for the first time in nonlinear optics under the approximation that the quantum mechanical phases of the carriers are randomized by thermalizing collisions. They developed a semi-empirical theory that fits well with

CC-0. In Public Domain. Gurukul Kangri Collection, Haridwar

Digitized by Arya Samaj Foundation Chennai and eGangotri

the experimentally observed band-gap resonant nonlinear refraction in III-V semiconductors, viz InSb.

Keeping in view the above discussion, we have dealt with a couple of fundamental questions: (i) whether the intensity-dependent optical susceptibility (χ) can be regarded as causal or not; (ii) what would have been the form of the K-K relation for the nonlinear optical susceptibility of a crystal, that could, under band-gap resonant transition, yield nonlinear refraction (via $\chi_r^{(3)}$) in terms of the measured nonlinearity in absorption (via $\chi_i^{(3)}$); (iii) derivation of a generalized form of dispersion relation which can enable one to estimate the nonlinear refractive index simply from the knowledge of nonlinear absorption coefficient and vice versa over an arbitrarily wide photon energy spectrum in a centrosymmetric crystal.

2. Theoretical formulations

To start with, we consider the generalized form of the nth order polarization in terms of the response function as (Ducuing 1977)

$$P_\sigma^{(n)}(t)=\int_0^\infty d\tau_1 \int_0^\infty d\tau_2 \ldots \int_0^\infty d\tau_n R^{(n)}_{\sigma,\lambda_1,\lambda_2,\ldots,\lambda_n}(\tau_1,\tau_2,\ldots,\tau_n)E_{\lambda_1}(t-\tau_1)$$
$$\times E_{\lambda_2}(t-\tau_2)\ldots E_{\lambda_n}(t-\tau_n). \tag{1}$$

Here, $R^{(n)}_{\sigma,\lambda_1,\lambda_2,\ldots,\lambda_n}$ is the response function of nth order and $E_{\lambda_1}, E_{\lambda_2}, \ldots, E_{\lambda_n}$ are the electric field amplitudes of the spatially uniform interacting waves. For an arbitrary decomposition of the electric field, one can also have

$$P_\sigma^{(n)}(t)=\varepsilon_0 \int_{-\infty}^\infty d\omega_1 \int_{-\infty}^\infty d\omega_2 \ldots \int_{-\infty}^\infty d\omega_n\ \chi^{(n)}_{\sigma,\lambda_1,\lambda_2,\ldots,\lambda_n}(\omega_1,\omega_2,\ldots\omega_n)$$
$$\times E_{\lambda_1}(\omega_1)E_{\lambda_2}(\omega_2)\ldots E_{\lambda_n}(\omega_n)\ \exp[i(\omega_1+\omega_2+\omega_3\ldots+\omega_n)t], \tag{2}$$

$\chi^{(n)}_{\sigma,\lambda_1,\lambda_2,\ldots,\lambda_n}$ being the nth order susceptibility tensor. This generalized expression for the nth order polarization characterizes almost all possible types of nonlinearities like nonlinear refraction and absorption (viz., $\omega;\omega;-\omega;\omega$), harmonic generation ($\omega_n=n\omega$), sum and difference frequency mixing (viz., $\omega_1=\omega_2\pm\omega_3$), etc.

A relation between the optical susceptibility and the response function can be obtained by comparing (1) and (2) whence one gets

$$\chi^{(n)}_{\sigma,\lambda_1,\lambda_2,\ldots,\lambda_n}(\omega_1,\omega_2,\ldots,\omega_n)$$
$$=\int_0^\infty d\tau_1 \int_0^\infty d\tau_2 \ldots \int_0^\infty d\tau_n R^{(n)}_{\sigma,\lambda_1,\lambda_2,\ldots,\lambda_n}(\tau_1,\tau_2,\ldots,\tau_n)$$
$$\times\exp[-i(\omega_1\tau_1+\omega_2\tau_2+\ldots+\omega_n\tau_n)]. \tag{3}$$

Equation (3) clearly indicates that the properties of the reponse function $R^{(n)}$ will be reflected in the corresponding properties of $\chi^{(n)}$.

CC-0. In Public Domain. Gurukul Kangri Collection, Haridwar

Digitized by Arya Samaj Foundation Chennai and eGangotri

We now restrict ourselves to the area of nonlinear refraction and absorption in the semiconducting crystals duly irradiated by lasers. The total induced polarization can be expressed as

$$P(\omega)=\varepsilon_0\chi(\omega)E(\omega)=\varepsilon_0[\chi^{(1)}+\chi^{(3)}|E|^2+\ \ldots\ ]E(\omega), \tag{4}$$

where $E(\omega)$ is the Fourier transform of the electric field $E(t)$ of the pump laser. We also assume that the medium is centrosymmetric in nature such that the nonlinear optical susceptibilities of even orders (viz., $\chi^{(2)}$, $\chi^{(4)}$, . . .) vanish under parity considerations. Nonlinearity expressed by (4) can have its origin in different types of mechanisms like (i) band nonparabolicity (Khan *et al* 1980), (ii) intensity-dependent free electron-hole pair generation (Jain 1982), (iii) interband transition saturation (Wherrett and Higgins 1982a), (iv) coherent radiation-exciton interaction (Sen 1982), etc.

While addressing ourselves to the question of developing a generalized dispersion relation in nonlinear optics, we have considered $\chi(\omega)$ to be intensity-dependent and given by

$$\chi(\omega)=\frac{G_1}{X+i\gamma}\left(1+\frac{A|E|^2}{X^2+\gamma^2}\right)^{-1}. \tag{5}$$

Equation (5) can be regarded as a model representation of $\chi(\omega)$ irrespective of its origin. The symbols G_1, A, X and γ have been defined in terms of the material parameters of the crystals in table 1. It can be shown without much difficulty that the usage of table 1 leads one to obtain the correct expression for $\chi(\omega)$ for both the models (iii) and (iv) discussed in the preceding paragraph. This equation yields the various odd-ordered optical susceptibility components only if the excitation intensity $I(=\frac{1}{2}\varepsilon_0\eta_0 c|E|^2)$ is

Table 1. Definition of terms used in equation (5).

Parameter	Wherrett and Higgins (1982b)[a]	Sen (1984)[b]
G_1	$\left\|\frac{e\varepsilon\cdot\mathbf{p}_{cv}}{m\omega}\right\|^2\frac{1}{\hbar\pi^2}\int_0^\infty k^2\mathrm{d}k$	$\frac{N\mu^2}{\varepsilon_0\hbar}\|\psi_1(0)\|^2$
A	$4T_1T_2^{-1}\|ep_{cv}/(m\omega_g\hbar)\|^2$	$\mu^2\|\psi_1(0)\|^2/4\hbar^2$
X	$\omega_{cv}(k)-\omega$	$(\omega_1-\Omega_r)-\omega$
γ	T_2^{-1}	γ_r

[a]equations (12) and (19); [b]equations (17) and (18).

$\left|\frac{e\varepsilon\cdot\mathbf{p}_{cv}}{m\omega}\right|$ is the transition dipole moment where ε is the radiation polarization and $\mathbf{p}_{cv}$ is the momentum matrix element. m is the electron rest mass. $|\mu|$ is the magnitude of the transition dipole moment and $|\psi_1(0)|$ corresponds to the 1*s* Wannier-Mott exciton wave function. T_1 and T_2 are the population relaxation life time and dephasing time, respectively. $\omega_{cv}(k)=\omega_g+\hbar k^2/2m_r$ with ω_g being the band-gap frequency and m_r is the electron-hole pair reduced mass. ω_1 is the excitonic effect incorporated band-gap frequency, γ_r is the renormalized damping constant due to the self-energy of the excited pair state while Ω_r appears due to the Stark broadening of the band edge.

CC-0. In Public Domain. Gurukul Kangri Collection, Haridwar

Digitized by Arya Samaj Foundation Chennai and eGangotri

considerably small such that $A|E|^2 \ll (X^2+\gamma^2)$ whence (5) reduces to

$$\chi(\omega)=\frac{G_1}{X+i\gamma}-\frac{G_1A|E|^2}{(X^2+\gamma^2)(X+i\gamma)}+\ \ldots\ +\frac{(-1)^nG_1A^n|E|^{2n}}{(X^2+\gamma^2)^n(X+i\gamma)} \tag{6}$$

with $n=0,1,2,3,\ldots$ For $A|E|^2 \gtrsim (X^2+\gamma^2)$, the present model breaks down. From (6), it can be immediately recognized that the first term corresponds to $\chi^{(1)}(\omega)$ while the second one yields $\chi^{(3)}(\omega)$ and so on. The response function $R^{(2n+1)}(t)$ can be obtained by taking the inverse Fourier transform of (6) as

$$R^{(2n+1)}(t)=(-1)^n\int_{-\infty}^{+\infty}G_1A^n|E|^{2n}\exp(-i\omega t)/[(X^2+\gamma^2)^n(X+i\gamma)]\mathrm{d}\omega \tag{7}$$

where we have taken

$$\chi^{(2n+1)}(\omega)=\frac{(-1)^nG_1A^n|E|^{2n}}{(X^2+\gamma^2)^n(X+i\gamma)}.$$

Before proceeding further with $R^{(2n+1)}(t)$, one has to check whether $\chi^{(2n+1)}(\omega)$ is a causal function or not. For $t<0$, $R^{(2n+1)}(t)$ must be evaluated in the upper half-plane where $\exp(-i\omega t)$ is bounded. It can be easily shown that $R^{(1)}(t)$ has no singularity in the upper half of the complex ω-plane and hence it vanishes. $R^{(3)}(t)$ and other higher-order response functions have poles in both the lower and upper half-planes. But at $t<0$, $E=0$ such that the integrands disappear. This leads one to conclude that the generalized response function $R^{(2n+1)}(t)$ as well as $\chi^{(2n+1)}(t)$ satisfy the principle of causality.

We now attempt to establish the validity of the nonlinear K-K relations in obtaining nonlinear refraction from the knowledge of nonlinear absorption and vice-versa in terms of complex

$$\chi^{(2n+1)}(\omega)\ (=\chi_r^{(2n+1)}(\omega)+i\chi_i^{(2n+1)}(\omega)).$$

From (6) and (7), one can find

$$\chi_r^{(2n+1)}(\omega)|E|^{2n}=\frac{(-1)^nA^n|E|^{2n}G_1X}{(X^2+\gamma^2)^{n+1}} \tag{8a}$$

and

$$\chi_i^{(2n+1)}(\omega)|E|^{2n}=\frac{(-1)^{n+1}A^n|E|^{2n}G_1\gamma}{(X^2+\gamma^2)^{n+1}}. \tag{8b}$$

While applying K-K relations to the third-order nonlinear optical susceptibility under certain approximations, Miller *et al* (1981) found the results to agree well with experimental observations. Thus we first examine the correctness of equation (8) for $n=1$ in obtaining $\chi_r^{(3)}$ from the knowledge of $\chi_i^{(3)}$ and vice-versa. We obtain

$$\frac{1}{\pi}\mathrm{P.V.}\int_{-\infty}^{\infty}\frac{\chi_i^{(3)}(\omega')\mathrm{d}\omega'}{\omega'-\omega}=(\tfrac{3}{2}+\tfrac{1}{2}X^2/\gamma^2)\,\chi_r^{(3)}(\omega) \tag{9a}$$

CC-0. In Public Domain. Gurukul Kangri Collection, Haridwar

Digitized by Arya Samaj Foundation Chennai and eGangotri

and

$$-\frac{1}{\pi}\text{P.V.}\int_{-\infty}^{+\infty}\frac{\chi_r^{(3)}(\omega')\mathrm{d}\omega'}{\omega'-\omega}=\tfrac{1}{2}(1+X^2/\gamma^2)\,\chi_i^{(3)}(\omega). \tag{9b}$$

From equations (9), it may be noted that under near band-gap resonant transitions with $X^2 \ll \gamma^2$, approximate K-K dispersion relations can be established for the nonlinear regime and may be regarded as the mathematical expression of the approximation taken by Miller *et al* (1981). The applicability of K-K relations in nonlinear optics is thus severely restricted within a very narrow frequency spectrum ($X^2 \ll \gamma^2$). This has stimulated our interest in developing a generalized dispersion relation which can be employed in the study of nonlinear optical effects over a broad frequency spectrum.

We proceed along a line similar to that followed usually to derive K-K relations in linear optics and arrive at the generalized K-K relations applicable to nonlinear optical susceptibility of any arbitrary order. It is well known that K-K relations are obtainable by using a Cauchy integral formula under the causal limit. Consequently, these relations are restricted only to analytic response functions. Although $\chi^{(2n+1)}(\omega)|E|^{2n}$ is causal it does not satisfy the Cauchy-Reimann conditions of analyticity. It is due to this non-analyticity of $\chi^{(2n+1)}(\omega)|E|^{2n}$ that exact K-K relations could not be obtained resulting in (9). To avoid this shortcoming, we define a new function

$$\chi'^{(2n+1)}(\omega)=(X^2+\gamma^2)^n\chi^{(2n+1)}(\omega) \tag{10}$$

which is causal and satisfies the Cauchy-Reimann conditions for analyticity as well. The application of Cauchy integral formula to this function finally leads to the following relations:

$$(X'^2+\gamma^2)^n\,\chi_r^{(2n+1)}(\omega')=\frac{1}{\pi}\text{P.V.}\int_{-\infty}^{\infty}\frac{(X^2+\gamma^2)^n\,\chi_i^{(2n+1)}(\omega)\mathrm{d}\omega}{(\omega-\omega')} \tag{11a}$$

and

$$(X'^2+\gamma^2)^n\,\chi_i^{(2n+1)}(\omega')=-\frac{1}{\pi}\text{P.V.}\int_{-\infty}^{\infty}\frac{(X^2+\gamma^2)^n\,\chi_r^{(2n+1)}(\omega)\mathrm{d}\omega}{(\omega-\omega')} \tag{11b}$$

where X' represents X with ω being replaced by ω'. For $n=0$, (11) yields

$$\chi_r^{(1)}(\omega')=\frac{1}{\pi}\text{P.V.}\int_{-\infty}^{\infty}\frac{\chi_i^{(1)}(\omega)\mathrm{d}\omega}{(\omega-\omega')} \tag{12a}$$

and

$$\chi_i^{(1)}(\omega')=-\frac{1}{\pi}\text{P.V.}\int_{-\infty}^{\infty}\frac{\chi_r^{(1)}(\omega)\mathrm{d}\omega}{(\omega-\omega')}. \tag{12b}$$

Equations (12) are the well known K-K dispersion relations in linear optics. For $n=1$, we obtain the dispersion relations for the complex third-order susceptibility $\chi^{(3)}$ and so on for $n=2, 3, \ldots$

CC-0. In Public Domain. Gurukul Kangri Collection, Haridwar

Digitized by Arya Samaj Foundation Chennai and eGangotri

3. Results and discussion

Equations (11) are applicable over an arbitrarily chosen frequency spectrum although the pump power has to be restricted within a certain limit such that the condition $A|E|^2 \ll (X^2+\gamma^2)$ is satisfied. The validity of (11) can be tested by applying these to the well-known phenomena of nonlinear optical effects in solids as well as in plasmas. As an example, we consider the phenomena of nonlinear refraction and absorption under low power resonant excitation regime in direct-gap semiconductors like InSb, GaAs, GaSb and InAs where the coherent radiation-exciton interaction model has been employed (Sen 1984, 1986). One finds (Sen 1984, equation (22))

$$\chi_i^{(3)}(\omega) = -\frac{N\mu^4|\psi_1(0)|^4}{\varepsilon_0\hbar^3} \quad \frac{\gamma_r}{[(\omega-\omega_{gr})^2+\gamma_r^2]^2}. \tag{13a}$$

Subsequently, one may use this equation in (11a) choosing $\omega-\omega_{gr}=X$ and $\gamma_r=\gamma$ to obtain

$$\chi_r^{(3)}(\omega) = \frac{N\mu^4|\psi_1(0)|^4}{\varepsilon_0\hbar^3} \quad \frac{\omega-\omega_{gr}}{[(\omega-\omega_{gr})^2+\gamma_r^2]^2}. \tag{13b}$$

Equation (13b) is exactly identical with that obtainable from (19) of Sen (1984). The results obtained by using the expression for $\chi^{(3)}(\omega)$ of the interband transition saturation model (Wherrett and Higgins 1982b) also lead one to the same conclusion and confirms the validity of (11) in the study of nonlinear dispersion in semiconducting crystals. The same equations can also be successfully employed in correlating the nonlinear magneto-absorption and magneto-refraction studied earlier (Sen 1983, 1986). Quite interestingly, the nonlinear plasma dispersion arising due to the relativistic complex oscillatory electron fluid velocity depending upon various powers of the pump intensity is another important area where (11) can be employed satisfactorily.

It may be inferred that (11) are valid for all such kinds of nonlinear optical processes for which the nonlinearity resembles with the form obtainable from (5) irrespective of the nature of its origin. However, equation (11) is restricted to the study of nonlinear refraction and absorption in solids duly irradiated by moderately low power lasers. The possibility of extending the present formulations to two-photon absorption and nonlinear wave-wave coupling will be the subject matter of a future publication.

4. Conclusions

It may be noted that the model relations represented by (11) can be regarded as the appropriate dispersion relations dealing with nonlinear optical properties of centrosymmetric solids and plasmas. This may be of immense help in the study of nonlinear refraction and absorption processes which are the origins of a class of nonlinear phenomena like optical bistability, optical phase conjugation, laser pulse shaping, etc.

CC-0. In Public Domain. Gurukul Kangri Collection, Haridwar

Digitized by Arya Samaj Foundation Chennai and eGangotri

Acknowledgments

The authors are indebted to Professor R K Singh and Dr S Guha for constant encouragement. PS acknowledges financial support from CSIR, New Delhi.

References

Ducuing J 1977 in *Nonlinear optics* (eds) P G Harper and B S Wherrett (London: Academic) p. 11
Flytzanis C 1975 in *Quantum electronics: A treatise* (eds) H Rabin and C L Tang (New York: Academic) Vol. 1, Part A, p. 9
Jain R K 1982 *Opt. Engg.* **21** 199
Khan M A, Kruse P W and Ready J F 1980 *Opt. Lett.* **5** 261
Landau L D and Lifshitz E M 1959 *Electrodynamics of continuous media* (Reading, Mass: Addison-Wesley) p. 260
Miller D A B, Seaton C T, Prise M E and Smith S D 1981 *Phys. Rev. Lett.* **47** 197
Sen P K 1982 *Solid State Commun.* **43** 141
Sen P K 1983 *J. Phys.* **C16** 2603
Sen P K 1984 *Phys. Status Solidi* **B124** 117
Sen P K 1986 *Phys. Rev.* **B33** 4038
Wherrett B S and Higgins N A 1982a *Proc. R. Soc. London* **A379** 67
Wherrett B S and Higgins N A 1982b *J. Phys.* **C15** 1741
Wooten F 1972 *Optical properties of solids* (New York: Academic)
Yariv A 1975 *Quantum electronics* (New York: John Wiley) 2nd ed.

CC-0. In Public Domain. Gurukul Kangri Collection, Haridwar

Digitized by Arya Samaj Foundation Chennai and eGangotri

CC-0. In Public Domain. Gurukul Kangri Collection, Haridwar

Digitized by Arya Samaj Foundation Chennai and eGangotri

Pramāṇa – J. Phys., Vol. 28, No. 6, June 1987, pp. 669–673. © Printed in India.

Electronic contribution to electric field gradient in dilute alloys

K V K NAIR and N V NAIR
Department of Physics, Mahatma Gandhi College, Trivandrum 695 004, India

MS received 25 November 1985; revised 2 March 1987

Abstract. A simple relation for calculating the electronic contribution to the electric field gradient in dilute alloys of transition metals is reported and is compared with the conduction electron charge shift model. The dependence of the field gradient on the *s* and *d* electrons and the difference in radii between the host and the probe atoms is considered for calculating the field gradient. It is found that the *d* electrons are the major contributors to the field gradient.

Keywords. Electric field gradient; electronic contribution; transition metals.

PACS No. 76·80

1. Introduction

Measurement of electric field gradient (EFG) in metals using Mössbauer spectroscopy has been a field of active research for the past several years and theoretical calculations on the EFG have gained considerable attention in recent years. All the relevant charges contributing to the EFG are considered to be external to the nucleus. The field gradient in most cases is found to be amplified by the atomic electrons bounded by the nucleus. Theoretical calculations on the enhancement of the EFG by bound electrons have been done by Sternheimer (1966), Foley *et al* (1954) and Das and Bersohn (1956). The field gradient at the nucleus is written in the form:

$$\text{eq} = (1-\gamma_\infty)\text{eq}^{\text{ext.}} + (1-R)\text{eq}^{\text{local}}. \tag{1}$$

The first term of (1) represents the field gradient arising from electrons and ions outside the atom or ion where the interacting nucleus resides, enhanced by the factor $(1-\gamma_\infty)$, where γ_∞ is the Sternheimer antishielding factor. Contributions to the field gradient due to the non-spherical unfilled orbitals of the atom are taken as $(1-R)\text{eq}^{\text{local}}$, R being the Sternheimer shielding factor, and represents the second term of (1). Equation (1) cannot be used as such to metallic systems and ionic solids (Beri *et al* 1978). The field gradient due to the lattice ions has been calculated considering the crystalline solids as an array of point ionic charges Ze situated at the lattice sites, where Z is taken to be the valence of the metal ion. The so-called ionic contribution (eq^{ion}) written as $(1-\gamma_\infty)\,\text{eq}^{\text{latt.}}$ is now used as the first term. Contributions from non-spherical electronic charge are presumed to represent an additional field gradient corresponding to the

CC-0. In Public Domain. Gurukul Kangri Collection, Haridwar

Digitized by Arya Samaj Foundation Chennai and eGangotri

second term and are called the electronic contribution (eq^{el}). The expression now used to represent the electric field gradient is:

$$eq^{total} = (1-\gamma_\infty)\, eq^{latt.} + eq^{el}. \tag{2}$$

For hexagonal close-packed structure with lattice constants a and c, Das and Pomerantz (1961) have deduced the lattice contribution to the EFG, using the point ion lattice sum method, given by,

$$eq^{latt.} = \frac{eZ}{a^3}\left[0{\cdot}0065 - 4{\cdot}3584\left(\frac{c}{a} - 1{\cdot}633\right)\right], \tag{3}$$

which is valid over a range of c/a from 1·55 to 1·9. Additional corrections to the model, by including point quadrupoles in addition to monopoles at ion sites, have been suggested by Taylor and Hygh (1963) and Das and Ray (1969), but did not result in any significant changes of $eq^{latt.}$ in the cases studied. Microscopic calculations on the electronic contribution to the EFG based on various methods such as orthogonal plane wave and augmented plane wave methods have been reported by Pomerantz and Das (1960), Mohapatra *et al* (1972) and others, a detailed review of which is given by Kaufmann and Vianden (1979). Based on experimental results an empirical correlation was proposed by Raghavan *et al* (1975), according to which the electronic contribution is proportional to the ionic contribution and the proportionality constant varies from -2 to -5. This correlation is found to be applicable in certain cases and deviations from this have also been noticed in several cases (Krusch and Forker 1980; Vianden 1983; Ernst *et al* 1979; Verma *et al* 1981). Ernst *et al* (1979) suggested different proportionality constants having both positive and negative signs for different groups elements. Bodenstedt and Perscheid (1978) proposed a model called the conduction electron charge shift model for calculating the EFG. According to the model, the EFG is given by:

$$eq^{total}_{probe} = (1-\gamma_\infty)[eq - eq^{P}(Z_{eff}) + eq^{P}(Z'_{eff})], \tag{4}$$

where,

$$eq = eq^{ion} - \tfrac{1}{6}eq^{-}_{hp}(1+\delta) - \tfrac{1}{6}eq^{-}_{el}(1-\delta) \tag{5}$$

$$eq^{P} = \frac{Z_{eff}e}{4\pi\varepsilon_0 a^3}4 \quad (1+\delta) - (1-\delta)\frac{\frac{1}{2}\left(\frac{c}{a}\right)^2 - \frac{1}{3}}{\left\{\frac{1}{3} + \frac{1}{4}\left(\frac{c}{a}\right)^2\right\}^{5/2}}, \tag{6}$$

where $eq^{ion} = (1-\gamma_\infty)\, eq^{latt.}$ is the ionic contribution to the EFG, eq^{-}_{hp} and eq^{-}_{el} are respectively the EFG's at the nucleus of the probe atom due to the conduction electron charge clouds in the hexagonal plane and the charge clouds in between the hexagonal planes, a and c are the lattice constants of the host lattice, Z_{eff} is the effective charge of the host atom, Z'_{eff} is the effective charge of the probe atom, ε_0 is the permittivity of free

CC-0. In Public Domain. Gurukul Kangri Collection, Haridwar

Digitized by Arya Samaj Foundation Chennai and eGangotri

space and δ is the charge shift, calculated using the formula

$$\delta = \frac{\frac{c}{a} - \left(\frac{8}{3}\right)^{1/2}}{Z_{\text{eff}}^2 e^2 \left(\frac{8}{3}\right)^{1/2}} \frac{36\varepsilon_0 a^4}{\frac{1}{6}(-2S_{13}+S_{12}+S_{11})+S_{33}-S_{13}}, \tag{7}$$

where, S_{ij}'s are the compliance constants of the host lattice calculated from the known values of elastic constants. But the free parameter Z'_{eff} has to be adjusted so as to make the calculated values agree with the experimental results. It is also found that $Z'_{\text{eff}}/Z_{\text{eff}} = 0{\cdot}75$, as suggested by Bodenstedt and Perscheid does not hold good in many cases. Recently, Bodenstedt (1985) used the Thomas-Fermi model for only group IIb hosts and the values obtained do not agree with experimental results. Chandra and Verma (1985) modified the charge shift model to suit pure systems containing groups IIIb and IVb hcp metals. But, so far, no successful formula for calculating the electronic part of the EFG for dilute impurity alloys has evolved. In this paper a simple relation which can be used to calculate eq^{el} in dilute impurity alloys of transition metals is reported.

2. Theoretical calculation of electronic contribution to the EFG

The total electronic contribution to the EFG (eq^{el}) in metals is composed of the contributions from the electrons of the probe atom in the host lattice, and the electrons in the lattice. Hence it depends on the electronic structure of both the probe and the host atoms and on the nature of the lattice. The distribution of ions and electrons of the host in the lattice controls the distribution of electrons in the probe atom which totally depends on the type of the lattice and the electronic structure of both the probe and the host atoms. This causes the electrons in the probe to occupy sites so that their potential energy is a minimum in the lattice. Hence it is assumed that the non-spherical distribution of electrons of a particular kind which produces the EFG at the probe nucleus depends on the difference between the number of electrons of that kind in the probe and the host and their distribution in the lattice. There will be an additional contribution because of the strain in the lattice caused by the difference in size of the host and the probe atoms which produces a small distortion of the host lattice from its natural structure.

In the case of transition metals the electronic contribution to the EFG is due to the *d* and *s* electrons and the size difference between the probe and host atoms. The *d* electron contribution is written as $K_1(Z_{dh}-Z_{dp})$, where Z_{dh} and Z_{dp} are the number of *d* electrons in the host and probe atoms respectively and K_1 is a constant. The contribution from the *s* electrons is taken as $K_2(Z_{sh}-Z_{sp})$, Z_{sh} and Z_{sp} being the number of *s* electrons in the host and probe atoms and K_2, a constant, which depends upon the nature and distribution of ions in the lattice. The contribution due to the distortion of the host lattice is taken as $K_3(r_h-r_p)$, r_h and r_p being the radii of the host and probe and K_3, a constant. Thus the effective electronic contribution to the EFG is

$$\text{eq}^{\text{el}} = K_1(Z_{dh}-Z_{dp}) + K_2(Z_{sh}-Z_{sp}) + K_3(r_h-r_p) \tag{8}$$

CC-0. In Public Domain. Gurukul Kangri Collection, Haridwar

Digitized by Arya Samaj Foundation Chennai and eGangotri

Table 1. Values of electronic contribution to the EFG calculated using equation (8) and the conduction electron charge shift model

System	$*eq^{el}_{calc.}$ (10^{17}V/cm^2)	$eq^{el}_{exp.}$ (10^{17} V/cm^2) I	II	$**eq^{el}_{calc.}$ (10^{17} V/cm^2)	Z'_{eff}/Z_{eff}
FeSc	+1	+1·085	..	−1·465	0·75
FeZr	+4·5	+2·983	−3·606	−2·686	6·25
FeRu	−1·5	..	−1·38	−1·255	0
FeTi	−2	..	−0·963	−1·008	1
IrCo	−5	..	−3·069	−3·207	4
IrRe	−6	..	−6·24	−6·268	2·57
IrRu	−11	+0·065	−5·725	−7·018	0·25
IrTi	−11·5	+4·583	−8·537	−9·503	3·75
IrHf	−6	+9·756	−13·284	−13·97	2·75
TaHf	+4	+3·28	−8·38	−9·88	1·25
TaZr	+5	+2·7	−6·37	−6·995	2
RuHf	+5	+4·596	−6·554	−5·77	2
RuZr	+6	+3·762	−5·228	−3·96	3·5
AuZr	−30	+15·93	−19·99	−19·836	6·25
AuRu	−11·5	−0·88	−7·84	−10·806	0·25
AuHf	−17·5	+12·475	−18·175	−19·677	2·5

*eq^{el} calculated using equation (8).

**eq^{el} calculated using the conduction electron charge shift model.

I and II refer to values of eq^{el} obtained assuming positive and negative signs to the EFG, in systems for which sign is not determined experimentally.

Experimental values are taken from Vianden (1983).

where the constants K_1, K_2 and K_3, calculated from experimental results, are respectively 3·5, 10 and 0·5. Using (8) eq^{el} for various systems have been calculated and compared with the experimental values obtained using the data available in the literature (Vianden 1983). The values are given in table 1 and there is good agreement between the experimental and calculated values both in magnitude and sign. It is also found that the *d* electrons are the major contributors to eq^{el}. It is also observed (Nair and Vijayakumaran Nair 1986) that when the number of *d* electrons is less than two eq^{el} is positive, when it is equal to two the sign of eq^{el} may be positive or negative and when the number exceeds two, eq^{el} is negative. Equation (8) agrees well with this systematic variation in the sign of eq^{el} with the number of *d* electrons. Calculations using the conduction electron charge shift model have also been done and the values obtained are also entered in table 1 and compared with those obtained using the relation reported (equation (8)). It is found that the value of Z'_{eff}/Z_{eff} has to be very large for agreement with experimental results in majority of the systems, when the charge shift model is used.

3. Conclusions

A successful relation for calculating the electronic contribution to the EFG is arrived at by taking into account the difference in the number of *s* electrons, *d* electrons, and the

CC-0. In Public Domain. Gurukul Kangri Collection, Haridwar

Digitized by Arya Samaj Foundation Chennai and eGangotri

radii of the host and probe atoms. It is found that the d electrons are the major contributors to the EFG. The constants K_1, K_2 and K_3 appearing in (8) are the same for all the systems, which shows that the relation can be applied in the case of any dilute impurity alloy of transition metals. The large value of K_2 appears to imply that the anti-shielding effect is contained in it. The relation agrees well with the value of eq^{el} obtained using the available experimental results.

References

Beri A C, Lee T, Das T P and Sternheimer R M 1978 *Hyperfine Interact.* **11** 509
Bodenstedt E 1985 *Hyperfine Interact.* **24–26** 521
Bodenstedt E and Perscheid B 1978 *Hyperfine Interact.* **5** 291
Chandra S and Verma H C 1985 *Phys. Status. Solidi* **B131** K73
Das T P and Bersohn R 1956 *Phys. Rev.* **102** 733
Das T P and Pomerantz M 1961 *Phys. Rev.* **123** 2070
Das K C and Ray D K 1969 *Phys. Rev.* **187** 777
Ernst H, Hagn E, Zech E and Eska G 1979 *Phys. Rev.* **B19** 4460
Foley H M, Sternheimer R M and Tyeko D 1954 *Phys. Rev.* **93** 734
Kaufmann E N and Vianden R J 1979 *Rev. Mod. Phys.* **51** 161
Krusch K and Forker M 1980 *Z. Phys.* **B37** 225
Mohapatra N C, Singal C M, Das T P and Jena P 1972 *Phys. Rev. Lett.* **29** 456
Nair N V and Vijayakumaran Nair K 1986 *Phys. Rev.* **B33** 6025
Pomerantz M and Das T P 1960 *Phys. Rev.* **119** 70
Raghavan R S, Kaufmann E N and Raghavan P 1975 *Phys. Rev. Lett.* **34** 1280
Sternheimer R M 1966 *Phys. Rev.* **146** 140
Taylor T T and Hygh E H 1963 *Phys. Rev.* **129** 1193
Verma H C, Chappert J and Rao G N 1981 *Hyperfine Interact.* **11** 45
Vianden R 1983 *Hyperfine Interact.* **15/16** 189, 1081

CC-0. In Public Domain. Gurukul Kangri Collection, Haridwar

Digitized by Arya Samaj Foundation Chennai and eGangotri

CC-0. In Public Domain. Gurukul Kangri Collection, Haridwar

Digitized by Arya Samaj Foundation Chennai and eGangotri

Pramāṇa – J. Phys., Vol. 28, No. 6, June 1987, pp. 675–688. © Printed in India.

X-ray, electrical conductivity, magnetic and infrared studies of the system $Co_{2-x}Ge_{1-x}Fe_{2x}O_4$

PRABHA NATHWANI and V S DARSHANE
Chemistry Department, Institute of Science, Bombay 400 032, India

MS received 25 December 1986

Abstract. X-ray, electrical conductivity, magnetic hysteresis and IR studies for the system $Co_{2-x}Ge_{1-x}Fe_{2x}O_4$ were carried out. All the compounds, $0 \leqslant x \leqslant 1$, showed cubic symmetry. X-ray intensity calculations, magnetic hysteresis measurements and IR studies indicated the presence of Ge^{4+} at tetrahedral, Co^{2+} at octahedral and Fe^{3+} at both the sites. The activation energy and threshold frequency decreased with increasing value of x. The compounds with $x \leqslant 0{\cdot}5$ are p-type and those with $x \geqslant 0{\cdot}75$ are n-type semiconductors. Magnetic hysteresis indicated that all the compounds are ferrimagnetic except for $x = 0$ which is antiferromagnetic. The shapes of χ/χ_i vs T plots, high H_c values and J_R/J_s ratios showed that all the compounds except $x = 0$ exhibit single-domain behaviour. Curie temperature, T_c increased with increasing Fe^{3+} ions. The probable ionic configuration for the system is suggested as $Ge^{4+}_{1-x}Fe^{3+}_x[Co^{2+}_{2-x}Fe^{3+}_x]O^{2-}_4$.

Keywords. Spinel; electrical conductivity; mobility; magnetic hysteresis; coerecive force; threshold frequency; cation distribution.

PACS No. 70

1. Introduction

Oxidic spinels show interesting structural, electrical and magnetic properties. In these compounds the properties are controlled by the nature of the ions, their charge and site distribution amongst tetrahedral and octahedral sites. Several workers (Landolt-Börnstein 1970; Jain and Darshane 1983; Kulkarni *et al* 1985) have reported the solid solutions of ferrites by substituting suitable ions at tetrahedral and octahedral sites.

The compound Co_2GeO_4 possesses a normal spinel structure (Romeijn 1953), while $CoFe_2O_4$ is inverse (Jonker 1959) or partly inverse (Prince 1956; Sawatzky *et al* 1968, 1969). The ionic configuration of $CoFe_2O_4$, therefore, requires further investigation. This paper gives the results of our studies on the system $Co_{2-x}Ge_{1-x}Fe_{2x}O_4$ by x-ray, electrical conductivity, magnetic hysteresis and IR spectroscopic studies to arrive at the probable ionic configuration. Recently it has been pointed out (Radhakrishnamurty and Nanadikar 1979; Nagarajan and Radhakrishnamurty 1981) that magnetic hysteresis and initial susceptibility studies at various temperatures can help to distinguish between multi-domain, single-domain and super-paramagnetic behaviour. Therefore, an attempt has been made to use such studies to determine coercive force, Curie temperature and the magnetic domain behaviour of the compounds of the system.

CC-0. In Public Domain. Gurukul Kangri Collection, Haridwar

Digitized by Arya Samaj Foundation Chennai and eGangotri

2. Materials and methods

2.1 *X-ray analysis*

Different compositions of the system $Co_{2-x}Ge_{1-x}Fe_{2x}O_4$ ($x = 0{\cdot}0$, $0{\cdot}25$, $0{\cdot}50$, $0{\cdot}75$ and $1{\cdot}0$) were prepared by mixing high purity oxides, CoO (prepared from Co_3O_4), GeO_2 and Fe_2O_3 in acetone using appropriate molar proportions. The unreacted oxide mixture (after homogenizing) of each composition was subjected to TG analysis (using MOM derivatograph) upto 1273 K. The loss in weight in all the compositions of the system was negligible ($<0{\cdot}03\%$) suggesting that the compounds were sufficiently stoichiometric. The pellets were prepared using 2% solution of polyvinyl acetate as a binder. To remove the binder, the pellets were slowly heated at 773 K for 20 hr and fired at 1173 K, sintering temperature, for 100 hr. The samples were cooled in air at 50 K per hour.

X-ray diffraction patterns were taken on a diffractometer (Siemens D-500, Kristalloflex) with a microprocessor controller, using CuK_α radiation with Ni filter. The x-ray patterns of all the compositions indicate formation of single spinel phase. To measure the intensity, the areas under different $\{hkl\}$ peaks were determined and values obtained in relation to the peak area for 311 reflection which was taken as 100. To ensure the reliability of the method, the specimens were subjected to x-ray diffractometry twice and after correcting for background a mean value of area was taken (reproducible within 2%). To calculate the relative integrated intensity, I, of a given $\{hkl\}$ reflection, the following formula (Bürger 1960) was used.

$$I = |F_{hkl}|^2 \cdot P \cdot \frac{1 + \cos^2 2\theta}{\sin^2\theta \cdot \cos\theta}, \tag{1}$$

where F is the structure factor, P is the multiplicity factor and the term

$$\frac{1 + \cos^2 2\theta}{\sin^2\theta \cdot \cos\theta} = L_p$$

which is the Lorentz-polarization factor. The atomic scattering powers for various ions were taken from literature (International tables 1959).

To determine the cation distribution and its variation with the composition, the intensity ratios (I_{440}/I_{422}, I_{220}/I_{440}, I_{422}/I_{400}, I_{311}/I_{422} and I_{220}/I_{400}) for different possible models of cation distribution were calculated as the reflections 220, 311, 400, 422 and 440 are sensitive to cation distribution at both the sites (Bertaut 1950; Weil *et al* 1950). These were then compared with the observed intensity ratios. The maximum standard deviation in the observed intensity ratios was $\pm 0{\cdot}02$.

2.2 *Electrical conductivity*

The DC resistivity was measured using LCR Marconi bridge. The end faces of each pellet were coated with a thin layer of conducting silver paste and the resistivity measured from room temperature to 773 K using a two-probe technique. Thermoelectric coefficient was measured from room temperature to 573 K. The sign of the thermoelectric coefficient value was designated as positive if the cold end was positive indicating *p*-type of semiconduction.

CC-0. In Public Domain. Gurukul Kangri Collection, Haridwar

Digitized by Arya Samaj Foundation Chennai and eGangotri

The IR spectra were recorded on a spectrophotometer (Perkin-Elmer 683) from 4000–200 cm^{-1}.

2.3 *Magnetic measurements*

The magnetic hysteresis loops at room temperature (300 K) and at liquid nitrogen temperature (80 K) for all the ferrimagnets were taken on alternating current electromagnet-type loop tracer (Likhite *et al* 1965). The saturation magnetization (σ_s) at 300 K and 80 K was also measured on a digital multimeter.

Initial susceptibility studies were made from room temperature to 873 K for all the compounds except $x=0$, using a field of 0·5 Oe by a double coil method (Radhakrishnamurty and Likhite 1970). From the plots of χ/χ_i vs T, the Curie temperature (T_c) of the compounds were determined.

3. Results and discussion

3.1 *X-ray analysis*

The results of x-ray analysis are given in table 1. All the compounds of the system are cubic. The lattice constant increases from Co_2GeO_4 ($a=8{\cdot}29$ Å) to $CoFe_2O_4$ (8·38 Å). These values are in good agreement with the values reported earlier (Romeijn 1953; Blasse and Fast 1963). The increase in lattice constant is due to the replacement of smaller Ge^{4+} ion by comparatively bigger Fe^{3+} ion in the tetrahedral site (Shannon and Previtt 1970) $Ge^{4+} \rightarrow 0{\cdot}53$ Å and $Fe^{3+} \rightarrow 0{\cdot}63$ Å. The cation distribution at two sites in the system has been arrived at by x-ray intensity calculations. The observed and calculated intensity ratios for the compound $Co_{1{\cdot}5}Ge_{0{\cdot}5}FeO_4$ using different models are summarized in table 2. It is seen that the model with Ge^{4+} at A-site, Co^{2+} at B-site and Fe^{3+} equally distributed between A- and B-sites shows better agreement. This site occupancy is in agreement with the site preference energy data (Miller 1959).

3.2 *Electrical conductivity*

The room temperature resistivity values (ρ_{RT}) of all the compounds of the system vary between 10^6 and 10^7 ohm cm^{-1}. High resistivity values indicate that the elements with only one oxidation state are present at B-site (Verwey *et al* 1951). The activation energy (ΔE) vary between 0·88 eV and 0·43 eV (table 1). The electrical resistivity-temperature behaviour obeys Wilson's law, $\rho=\rho_0 \exp(\Delta E/KT)$, indicating the semiconducting nature of all the compounds (figure 1).

The plot of thermo-emf (ΔV) developed across the compounds against the temperature difference (ΔT) is given in figure 2. Table 1 shows that the compounds with $x \leqslant 0{\cdot}5$ are p-type semiconductors while the compounds with $x \geqslant 0{\cdot}75$ show n-type behaviour. Thermoelectric coefficient values (α) vary between $+278$ and -129 μV/K (table 1).

The electrical conductivity, σ, is related to the number of charge carriers, p, and their mobility μ at room temperature by the relation:

$$\sigma = p \cdot e \cdot \mu, \qquad (2)$$

CC-0. In Public Domain. Gurukul Kangri Collection, Haridwar

Digitized by Arya Samaj Foundation Chennai and eGangotri

Table 1. Lattice constant (a), activation energy (ΔE) and thermoelectric coefficient (α) values for the system $Co_{2-x}Ge_{1-x}Fe_{2x}O_4$.

Compounds	a (Å)	ΔE (eV)	α ($\mu V/K$)
Co_2GeO_4	8·29	0·88	+278
$Co_{1·75}Ge_{0·75}Fe_{0·5}O_4$	8·31	0·74	+107
$Co_{1·5}Ge_{0·5}FeO_4$	8·35	0·66	+80
$Co_{1·25}Ge_{0·25}Fe_{1·5}O_4$	8·37	0·58	−24
$CoFe_2O_4$	8·38	0·43	−129

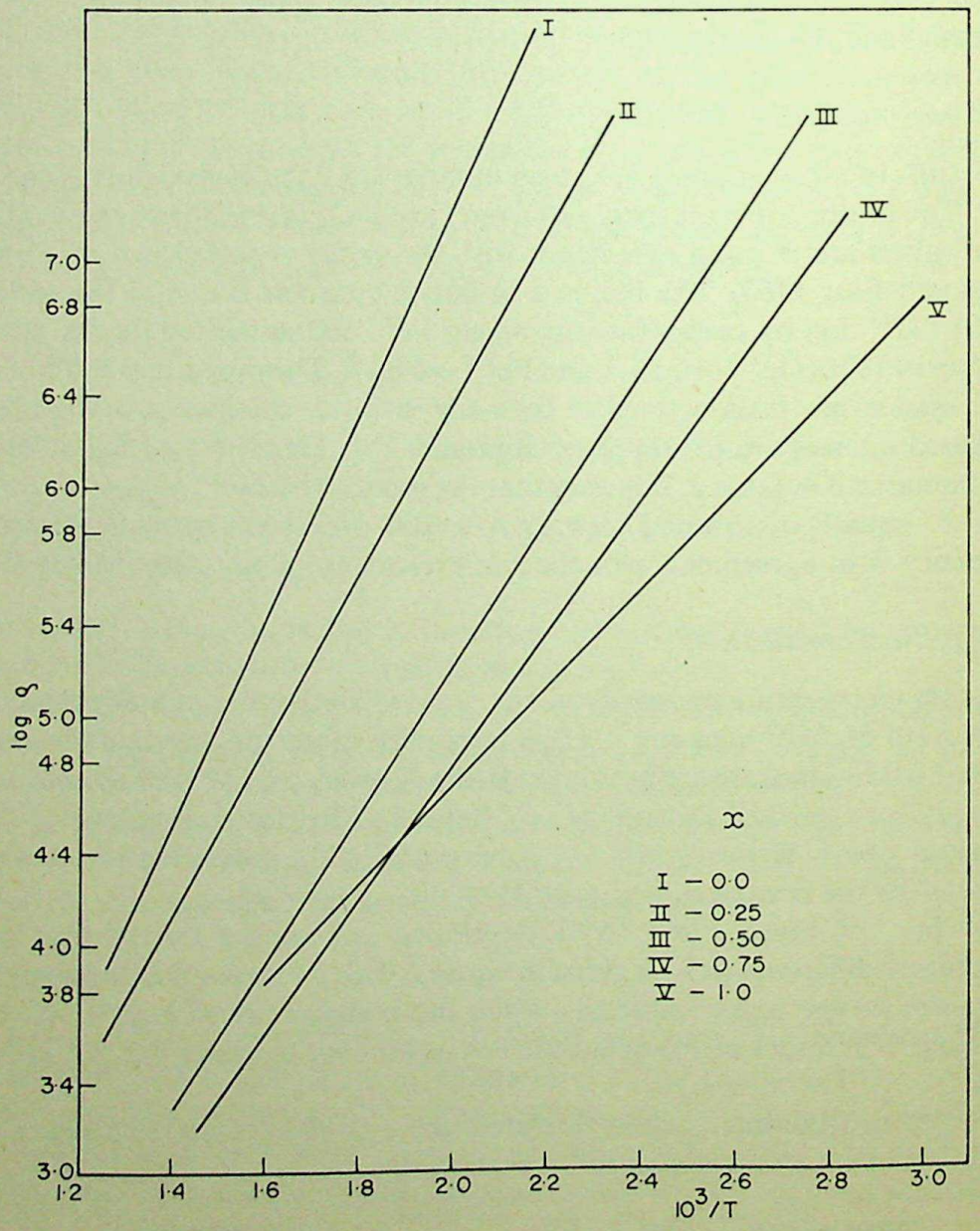

Figure 1. Plot of $\log \rho$ vs $10^3/T$ for the system $Co_{2-x}Ge_{1-x}Fe_{2x}O_4$.

CC-0. In Public Domain. Gurukul Kangri Collection, Haridwar

Digitized by Arya Samaj Foundation Chennai and eGangotri

Table 2. Comparison of intensity ratios for $Co_{1\cdot5}Ge_{0\cdot5}FeO_4$.

		I_{440}/I_{422}		I_{220}/I_{440}		I_{422}/I_{400}		I_{311}/I_{422}		I_{220}/I_{400}	
A-site	B-site	Obs.	Cal.	Obs.	Cal.	Obs.	Cal.	Obs.	Cal.	Obs.	Cal.
Co^{2+}	$Ge^{4+}_{0\cdot5}Fe^{3+}$ $Co^{2+}_{0\cdot5}$		4·83		0·55		0·43		10·23		1·16
$Fe^{3+}_{0\cdot5}Co^{2+}_{0\cdot5}$	$Ge^{4+}_{0\cdot5}Fe^{3+}_{0\cdot5}$ Co^{2+}		5·15		0·52		0·38		10·81		1·02
$Ge^{4+}_{0\cdot5}Fe^{3+}_{0\cdot5}$	$Co^{2+}_{1\cdot5}Fe^{3+}_{0\cdot5}$	4·00	4·05	0·62	0·61	0·61	0·60	8·50	8·70	1·50	1·48
$Ge^{4+}_{0\cdot5}Co^{2+}_{0\cdot5}$	$Co^{2+}Fe^{3+}$		3·83		0·65		0·68		8·24		1·69
$Ge^{4+}_{0\cdot25}Co^{2+}_{0\cdot75}$	$Co^{2+}_{0\cdot75}Fe^{3+}$ $Ge^{4+}_{0\cdot25}$		4·28		0·60		0·54		9·17		1.40

CC-0. In Public Domain. Gurukul Kangri Collection, Haridwar

Digitized by Arya Samaj Foundation Chennai and eGangotri

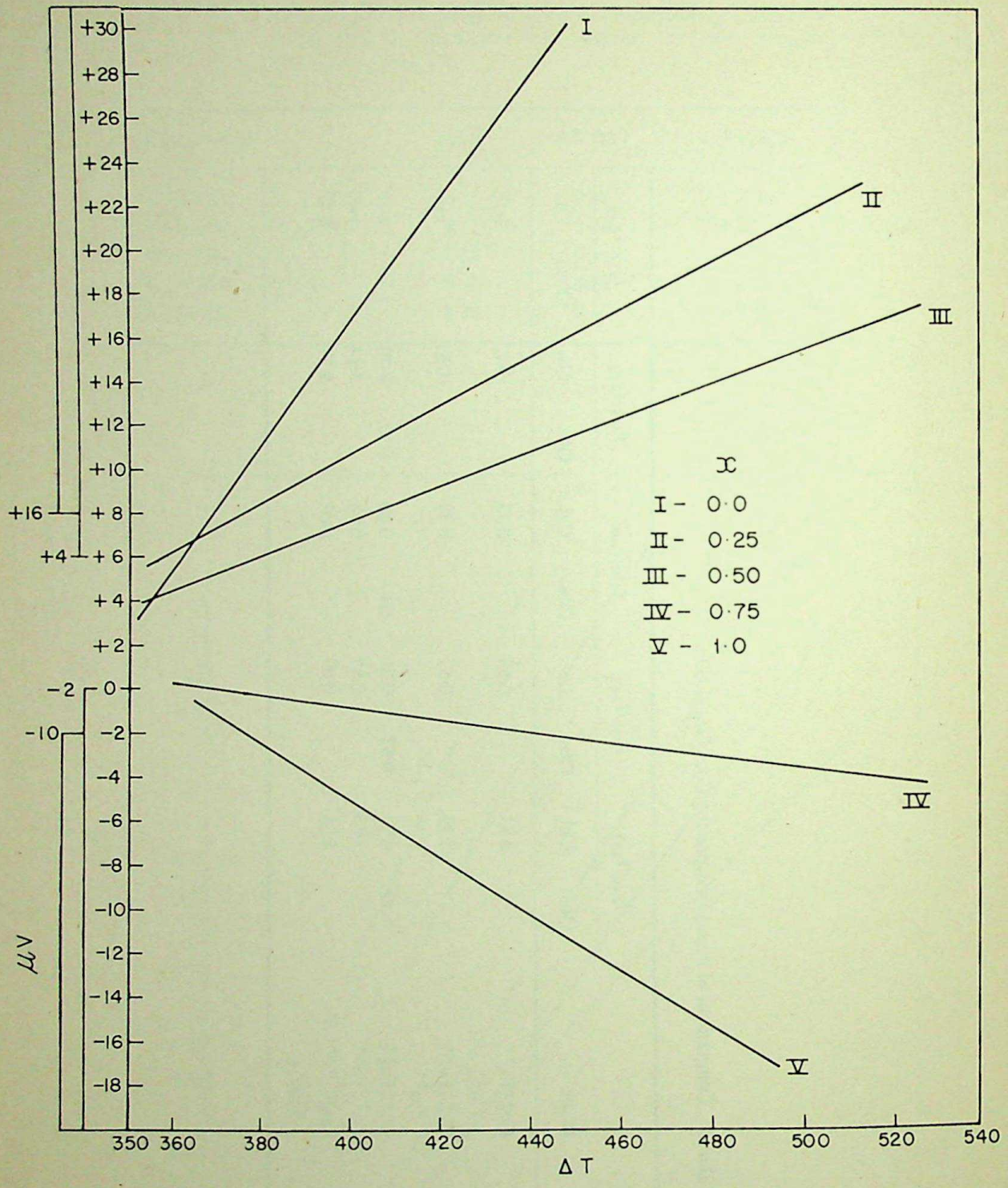

Figure 2. Plot of μV vs ΔT for the system $Co_{2-x}Ge_{1-x}Fe_{2x}O_4$.

where e is the electric charge. Taking the average unit cell volume as $(8{\cdot}34)^3$, the value of hole concentration would be 10^{22} per cc and the mobility value is 10^{-9} cm^2/V-sec. It has also been calculated using the formula (Heikes and Johnston 1957):

$$\mu = \frac{ed^2 v \exp(-\Delta E/KT)}{KT}, \tag{3}$$

CC-0. In Public Domain. Gurukul Kangri Collection, Haridwar

Digitized by Arya Samaj Foundation Chennai and eGangotri

where ΔE is the activation energy, K, the Boltzman constant, d, the jump length and ν, the lattice frequency. The mobility value comes to 10^{-9} cm^2/V-sec. Infrared studies indicated the presence of two strong absorption bands at around 400 and 600 cm^{-1}. However, the band at 600 cm^{-1} being stronger than 400 cm^{-1} was considered for calculating the lattice frequency in (3).

All the compounds of the system possess low mobility, and it increases exponentially with increasing temperature following the relationship:

$$\mu = \mu_0 \exp(-\Delta E/KT), \tag{4}$$

where μ_0 is a constant representing the mobility at $T = \infty$. In the case of low mobility semiconductors and its exponential temperature dependence, the charge carriers are localized to a particular site and electrical conduction involves the hopping of charge carriers from one site to another during lattice vibrations. Thus, mobility shows exponential temperature dependence.

From table 1, it is seen that the activation energy decreases from Co_2GeO_4 (0·88 eV) to $CoFe_2O_4$ (0·43 eV) as the concentration of Ge^{4+} decreases and that of Fe^{3+} increases. On substituting Ge^{4+} ions by Fe^{3+} ions in the crystal lattice, activation energy decreases due to the fact that completely filled Ge^{4+} (d^{10}) orbitals have much lower energy, i.e., they are very stable and they are more contracted than the Fe^{3+} d-orbitals. Also, as the concentration of Fe^{3+} increases in the lattice, the mobility of charge carriers increases resulting in a gradual decrease in the activation energy.

In the present system $Co_{2-x}Ge_{1-x}Fe_{2x}O_4$, the cobalt-rich compounds are p-type and the iron-rich compounds are n-type semiconductors. The p-type semiconduction for the compounds $x \leqslant 0{\cdot}5$ can be attributed to $Co^{2+} + Co^{3+}$ pair formation. Very small concentration of Co^{3+} must be present in the lattice, otherwise compounds would have shown an insulating nature. The presence of Co^{3+} could not be detected by x-ray analysis as its concentration was very small. The value of thermoelectric coefficient (α) goes on decreasing with the decrease in concentration of Co^{2+} at the B-site as the number of charge carriers decreases.

The compounds $x \geqslant 0{\cdot}75$ show n-type behaviour. In these compounds a slight oxygen deficiency is suspected due to the ability of Fe_2O_3 to lose oxygen when heated at elevated temperatures (Kulkarni *et al* 1985). This oxygen nonstoichiometry will give rise to some Fe^{2+} ions so as to maintain the electrical neutrality. Thus the following hopping mechanism is expected

$$Fe^{2+} + Fe^{3+} \rightleftharpoons Fe^{3+} + Fe^{2+}.$$

Thus we have small polaron-hopping charge carriers. As the concentration of Fe^{3+} increases in the compounds, the hopping process increases. Thus we have both the types of charge carriers in these compounds and the observed thermoelectric coefficient (α) results from the compensating effect of p-type and n-type charge carriers. The sign of α is positive for the samples with excess of Co^{2+} and is negative for the samples with excess of Fe^{3+} (Jonker 1959).

CC-0. In Public Domain. Gurukul Kangri Collection, Haridwar

Digitized by Arya Samaj Foundation Chennai and eGangotri

Table 3. Saturation magnetization (σ_s), coercine force (H_c), remanance ratio (J_R/J_s), magnetic moment (n_B) and Curie temperature (T_c) values for the system $Co_{2-x}Ge_{1-x}Fe_{2x}O_4$.

	H_c (Oe)		J_R/J_s		σ_s (emu/g)		n_B ($\mu\beta$)		T_c (K)
Compound	300 K	80 K	300 K	80 K	300 K	80 K	Obs.	Cal.	
Co_2GeO_4	—	—	—	—	—	—	—	—	—
$Co_{1\cdot75}Ge_{0\cdot75}Fe_{0\cdot5}O_4$	113	338	0·36	0·48	23·4	36·5	1·63	5·25	442
$Co_{1\cdot5}Ge_{0\cdot5}FeO_4$	94	188	0·21	0·30	39·5	59·1	2·59	4·50	516
$Co_{1\cdot25}Ge_{0\cdot25}Fe_{1\cdot5}O_4$	150	410	0·37	0·63	58·8	65·8	2·82	3·75	638
$CoFe_2O_4$	223	265	0·43	0·50	55·9	70·9	2·98	3·00	785

3.3 *Magnetic properties*

All the compounds of the system except for $x=0$ show the magnetic hysteresis loops at 300 K as well as at 80 K (figure 3). This indicates that they are all ferrimagnetic in nature. The coercive force (H_c), remanance ratio (J_R/J_s), saturation magnetization (σ_s), magnetic moment (n_B) and ferrimagnetic Curie temperature (T_c) have been listed in table 3. The magnetic moment is calculated from the σ_s value at 80 K by using the relation

$$n_B = \frac{\sigma_s \times \text{molecular weight}}{5585}. \tag{5}$$

The Curie temperature is determined from χ/χ_i vs T plot (figure 4). The observed n_B values obtained by using equation (5) are compared with the calculated n_B values on the basis of spin-only moments (table 3).

It has been observed that in the case of $CoFe_2O_4$ the observed and calculated magnetic moments are very close to each other ($n_B = 2{\cdot}98$ μB and $3{\cdot}00$ μB respectively). As the concentration of Fe^{3+} decreases and that of Ge^{4+} increases the observed n_B values are lower than the calculated n_B values. The observed low magnetic moments can be explained in terms of the non-collinear spin arrangement.

The simple Neél model of parallel and antiparallel moments cannot account for the observed magnetic data (Neél 1948). Such behaviour (low values of n_B than expected) has also been observed by many others on zinc containing ferrites. This has been explained by using various models such as: (a) the occupation of B-sites by diamagnetic ions like Zn^{2+} or Ge^{4+} (Gorter 1954; Guilland 1951); (b) the development of a paramagnetic cluster (Gilleo 1960; Ishikawa 1962); and (c) the occurrence of non-collinear spin structures (Yafet and Kittel 1952; Nowick 1969; Iyons *et al* 1962). Pettit and Forester (1971) have indicated that the non-collinear magnetic structure plays an important part in the explanation of this behaviour in the oxidic spinel system $Co_{1-x}Zn_xFe_2O_4$. The canting in this system has been interpreted in terms of a uniform Yafet-Kittel triangular type magnetic ordering of spins at the B-sublattice. Thus, considering the Yafet-Kittel model, we can also explain the variation observed in n_B values for the germanium-rich compounds of the present system.

CC-0. In Public Domain. Gurukul Kangri Collection, Haridwar

Digitized by Arya Samaj Foundation Chennai and eGangotri

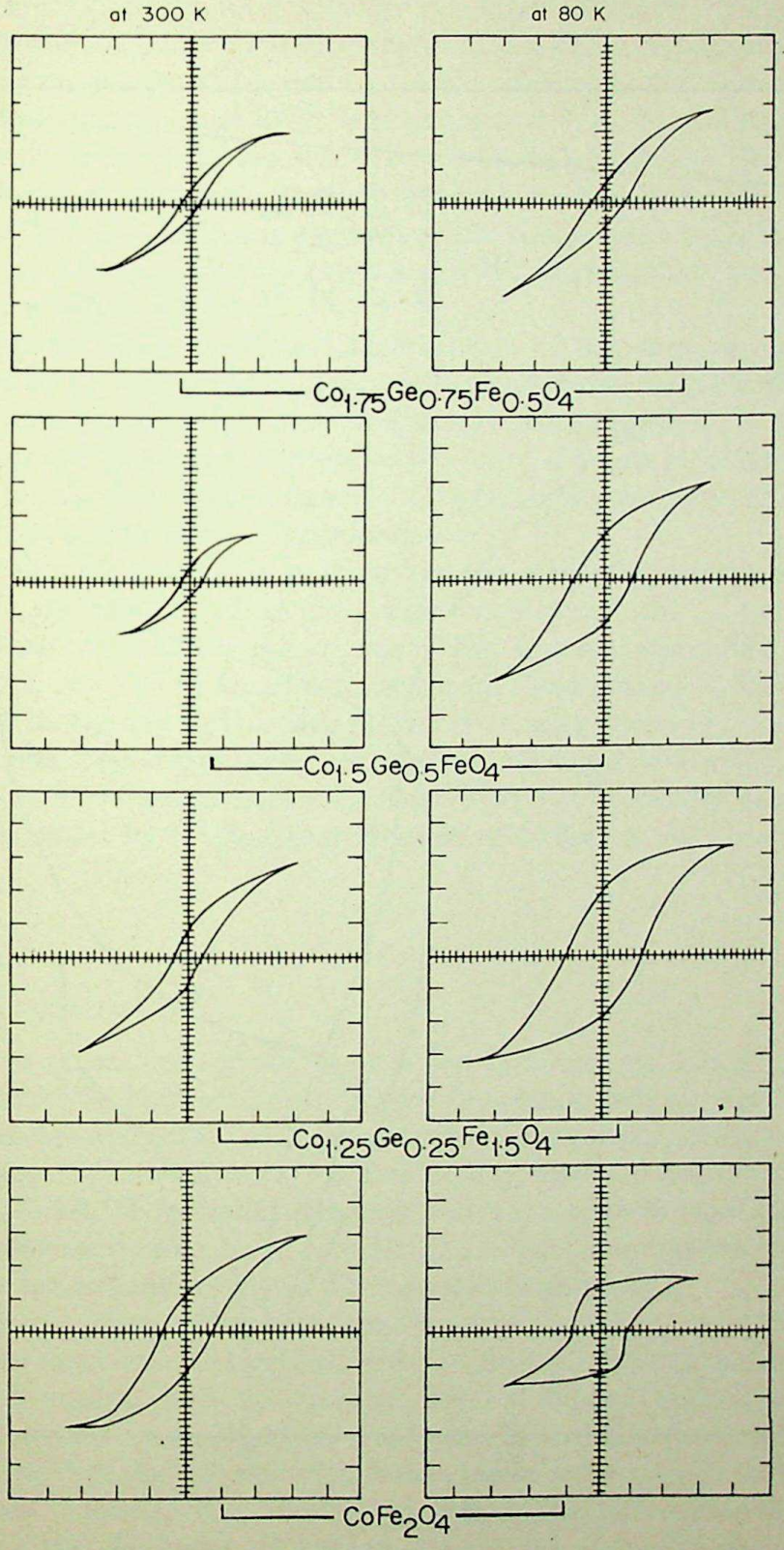

Figure 3. Hysteresis loops for the compounds of the system $Co_{2-x}Ge_{1-x}Fe_{2x}O_4$.

CC-0. In Public Domain. Gurukul Kangri Collection, Haridwar

Digitized by Arya Samaj Foundation Chennai and eGangotri

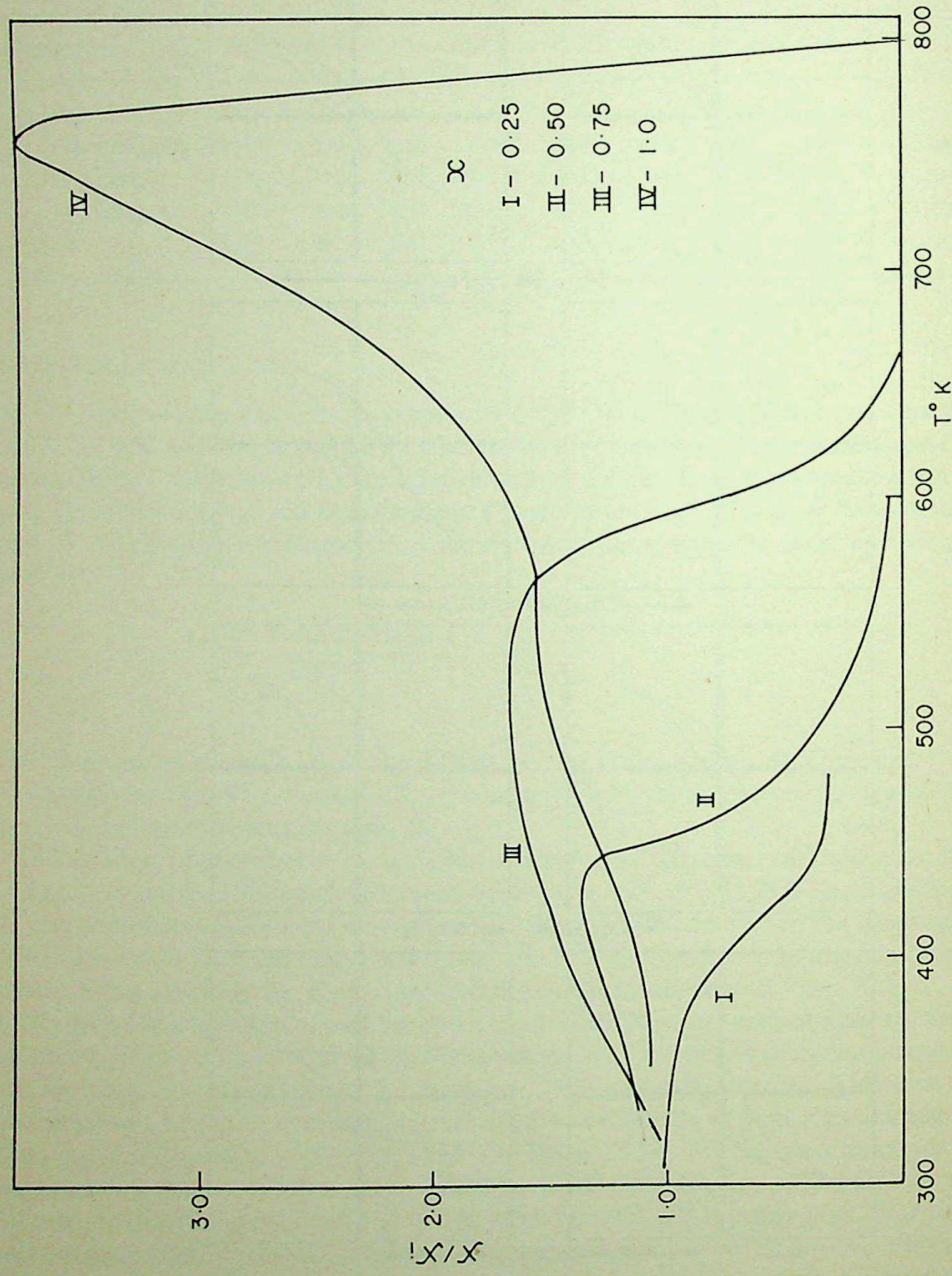

Figure 4. Plot of χ/χ_i vs T for the system $Co_{2-x}Ge_{1-x}Fe_{2x}O_4$.

CC-0. In Public Domain. Gurukul Kangri Collection, Haridwar

Digitized by Arya Samaj Foundation Chennai and eGangotri

From the magnetic hysteresis loops (figure 3) it is seen that all compounds (except $x=0$) possess high values of coercive force (H_c) which may be due to the presence of anisotropy in these compounds. Further it is observed that the higher values of H_c at 80 K may be due to decrease in thermal vibrations. This increase in H_c with decreasing temperature can also be attributed to a rapid increase in the anisotropy constant on cooling (Takahashi and Fine 1972). A large increase in H_c on cooling to liquid nitrogen temperature (80 K) is indicative of single-domain (SD) behaviour (Rao and Keer 1982). $CoFe_2O_4$ shows a constricted (square) hysteresis loop at 80 K. The squareness of the loop decreases as the temperature increases. The compound Co_2GeO_4 did not give any hysteresis loop at an applied field of 4 K gauss indicating that the magnetic ordering temperature is below 80 K.

The remanance ratios (J_R/J_s) are listed in table 3. There is a considerable increase in the values at 80 K. According to Berkotwitz and Schuele (1959), if there is a marginal increase in the value of J_R/J_s at a low temperature as compared with room temperature, multi-domain (MD) grains are present. However, if a considerable increase in J_R/J_s value is obtained, then single-domain (SD) grains may be present. This suggests the presence of SD grains in our compounds.

From the shapes of the χ/χ_i vs T curves, the magnetic domain behaviour can be decided. The χ/χ_i values first increase with temperature and then suddenly becomes zero just before the Curie temperature. The Curie temperature (T_c) for all the compounds (except $x=0$) are determined from these curves. T_c values are found to increase with increasing Fe^{3+} concentration, probably due to the strengthening of the AB interactions. The shape of the curves (figure 4) suggests that the samples contain single-domain (SD) states of grains (Dunlop 1969). The absence of multi-domain (MD) grains is supported by the fact that Hopkinson's effect is not observed (Hopkinson 1889).

3.4 *Infra-red spectra*

As mentioned earlier, all the compounds show two strong bands at about 600 and 400 cm^{-1} (figure 5). The band positions for the compounds Co_2GeO_4 and $CoFe_2O_4$ are in good agreement with those reported earlier (Preudhomme and Tarte 1971; White and De Angelis 1967; Waldron 1955). The band positions and the threshold frequency are listed in table 4. The threshold frequency for the electronic transition is found to be decreasing with increasing Fe^{3+} concentration. This is in agreement with the trend observed for the activation energy (ΔE) as seen from table 1.

Tarte and coworkers (Tarte and Preudhomme 1963; Tarte and Collongues 1964) have observed that in normal ferrites, both the absorption bands depend on the nature of octahedral cations and do not significantly depend upon the nature of the tetrahedral ions. However, Waldron (1955) and Hafner (1961) attributed the band ν_1 around 600 cm^{-1} to the intrinsic vibrations of tetrahedral complexes and the band ν_2 around 400 cm^{-1} to that of octahedral complexes. The difference in the band position is because of the difference in the Fe^{3+}-O^{2-} distances for the octahedral and tetrahedral complexes.

Around 320 cm^{-1} a small band ν_3 with low intensity appeared for compounds with $x=0$ and $x=0{\cdot}25$. With the decrease in Co^{2+} concentration at the B-site, this band is found to be disappearing (table 4 and figure 5). The band ν_2 is due to octahedral

CC-0. In Public Domain. Gurukul Kangri Collection, Haridwar

Digitized by Arya Samaj Foundation Chennai and eGangotri

Table 4. IR bands and threshold frequencies for the system $Co_{2-x}Ge_{1-x}Fe_{2x}O_4$.

Compound	Absorption bands (cm^{-1}) ν_1	ν_2	ν_3	Threshold frequency (cm^{-1})
Co_2FeO_4	678 (s)	425 (s)	323 (m)	1050 ± 50
$Co_{1.75}Ge_{0.75}Fe_{0.5}O_4$	645 (s)	413 (s)	312 (m)	940 ± 50
$Co_{1.5}Ge_{0.5}FeO_4$	585 (s)	413 (s)	—	880 ± 50
$Co_{1.25}Ge_{0.25}Fe_{1.5}O_4$	585 (s)	410 (s)	—	820 ± 50
$CoFe_2O_4$	585 (s)	410 (s)	—	790 ± 50

s—high intensity, m—medium intensity.

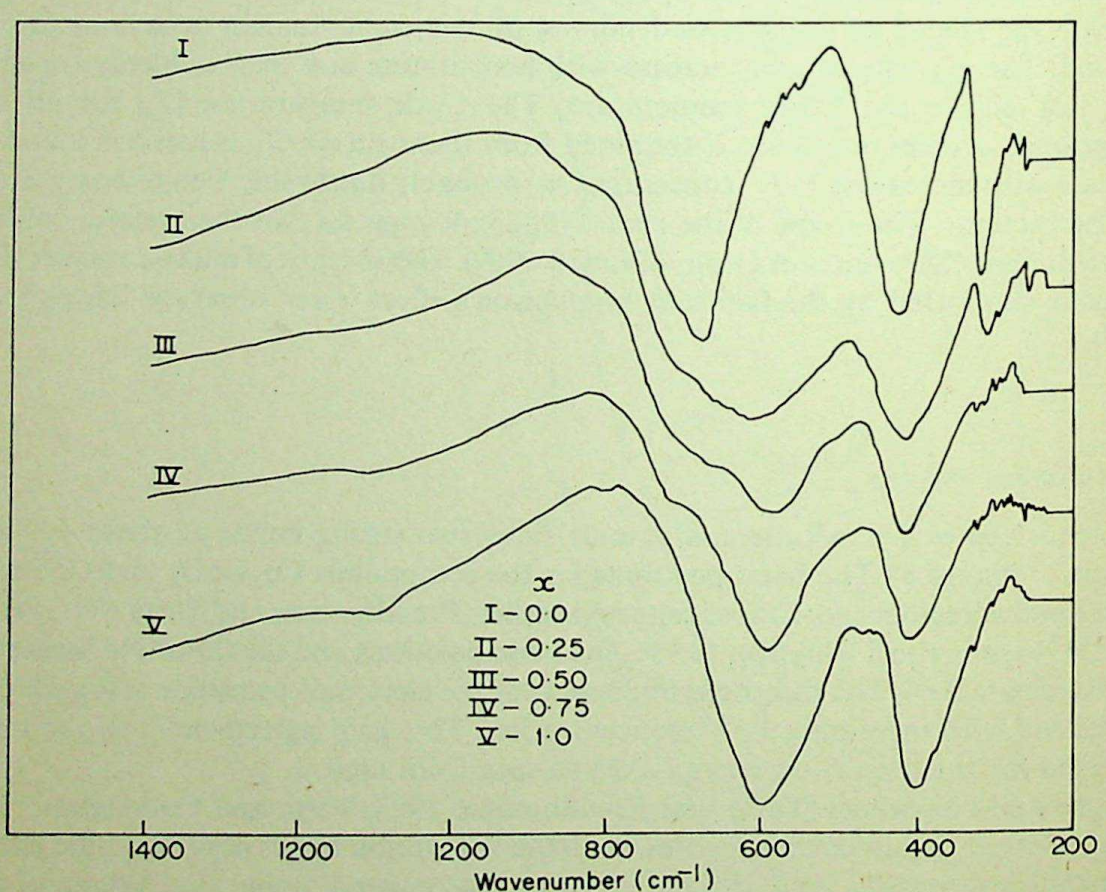

Figure 5. IR spectra of the system $Co_{2-x}Ge_{1-x}Fe_{2x}O_4$.

complexes, so the small band ν_3 around ν_2 may also be coming from octahedral complexes. This band ν_3 is assigned to the Co^{2+}-O^{2-} octahedral complexes. As the concentration of Co^{2+} at the octahedral site decreases, the intensity of ν_3 band also decreases and finally the band disappears (Josyulu and Sobhanadri 1981).

CC-0. In Public Domain. Gurukul Kangri Collection, Haridwar

Digitized by Arya Samaj Foundation Chennai and eGangotri

The presence of Fe^{2+} ions in the ferrites causes a shoulder or splitting of the absorption band (Murthy *et al* 1978). In the case of our compounds, both the bands do not show any shoulder or splitting indicating the absence of Fe^{2+} ions.

Thus, from x-ray, electrical, magnetic and IR studies, we suggest the probable cation distribution for the system $Co_{2-x}Ge_{1-x}Fe_{2x}O_4$ as $Ge^{4+}_{1-x}Fe^{3+}_{x}$ $[Co^{2+}_{2-x}Fe^{3+}_{x}]O^{2-}_{4}$.

Acknowledgements

One of the authors (PN) is thankful to UGC, New Delhi for a fellowship. The other author (VSD) thanks UGC, New Delhi for financial support.

References

Berkowitz A E and Schuele W J 1959 *J. Appl. Phys.* **30** 134 Suppl.
Bertaut E F 1950 *Compt. Rend.* **230** 213
Blasse G and Fast 1963 *Phillips Res. Rep.* **18** 393
Bürger M J 1960 Crystal structure analysis (New York: John Wiley) 46
Dunlop D J 1969 *Philos. Mag.* **19** 329
Gilleo M A 1960 *J. Phys. Chem. Solids* **13** 33
Gorter E W 1954 *Phillips Res. Rep.* **9** 1
Guilland G 1951 *J. Phys. Rad.* **12** 239
Hafner S 1961 *Z. Kristallogr.* **115** 331
Heikes R R and Johnston W D 1957 *J. Chem. Phys.* **26** 582
Hopkinson J 1889 *Philos. Trans. R. Soc. (London)* **A180** 443
International tables for x-ray crystallography 1959 Vol. IV (Birmingham: Kynoch Press)
Ishikawa Y 1962 *J. Phys. Soc. Jpn* **17** 1877
Iyons D H, Kalpan T A, Dwight K and Menyuk N 1962 *Phys. Rev.* **126** 540
Jain P S and Darshane V S 1983 *Pramāṇa–J. Phys.* **20** 7
Jonker G H 1959 *J. Phys. Chem. Solids* **9** 165
Josyulu O S and Sobhanadri J 1981 *Phys. Stat. Sol.* **A65** 479
Kulkarni J A, Muraleedharan K, Srivastava J K, Marathe V R, Darshane V S, Murty C R K and Vijayraghavan R 1985 *J. Phys.* **C18** 2593
Landolt-Börnstein 1970 *Magnetic oxides and related compounds* (Berlin: Springer) Vol. 3/4b
Likhite S D, Radhakrishnamurty C and Sahasrabudhe P W 1965 *Rev. Sci. Instrum.* **36** 1558
Miller A 1959 *J. Appl. Phys.* **30** (suppl.) 24
Murthy V R K, Chitra Sankar S, Reddy K V and Sobhanadri J 1978 *Indian J. Pure Appl. Phys.* **16** 79
Nagarajan R and Radhakrishnamurty C 1981 *Bull. Mater. Sci.* **3** 217
Neél L 1948 *Ann. Phys. (Paris)* **3** 137
Nowick I 1969 *J. Appl. Phys.* **40** 872
Pettit G A and Forester D W 1971 *Phys. Rev.* **B4** 3912
Preudhomme J and Tarte P 1971 *Spectrochim. Acta* **A27** 961
Prince E 1956 *Phys. Rev.* **102** 674
Radhakrishnamurty C and Likhite S D 1970 *Earth Planet. Sci. Lett.* **7** 389
Radhakrishnamurty C and Nanadikar N G 1979 *Pramāna–J. Phys.* **13** 413
Rao Venkatesh and Keer H V 1982 *Pramāna–J. Phys.* **19** 103
Romeijn F C 1953 *Phillips Res. Rep.* **8** 304, 321
Sawatzky G H, Van der Woude F and Morrish A H 1968 *J. Appl. Phys.* **39** 1204
Sawatzky G H, Van der Woude F and Morrish A H 1969 *Phys. Rev.* **187** 747
Shannon R D and Previtt C T 1970 *Acta Crystallogr.* **B26** 1076
Takahashi Masatake and Fine Morris E 1972 *J. Appl. Phys.* **43** 4205

CC-0. In Public Domain. Gurukul Kangri Collection, Haridwar

Digitized by Arya Samaj Foundation Chennai and eGangotri

Tarte P and Collongues R 1964 *Ann. Chim.* (*France*) **9** 135
Tarte P and Preudhomme J 1963 *Acta Crystallogr.* **16** 227
Verwey E J W, Braun P B, Gorter E W, Romeijn F C and Van Santen J H 1951 *Z. Phys. Chem.* **198** 6
Waldron R D 1955 *Phys. Rev.* **99** 1727
Weil L, Bertaut E F and Bochirol L 1950 *J. Phys. Rad.* **11** 208
White W B and De Angelis B A 1967 *Spectrochim. Acta* **A23** 985
Yafet Y and Kittel C 1952 *Phys. Rev.* **87** 290

CC-0. In Public Domain. Gurukul Kangri Collection, Haridwar

Digitized by Arya Samaj Foundation Chennai and eGangotri

Pramāṇa – J. Phys. Vol. 28, No. 6, June 1987, pp. 689–697. © Printed in India.

Unified study of alkaline earth metal

SURATNA DAS and A SARKAR
Physics Department, Presidency College, Calcutta 700073, India

MS received 4 August 1986; revised 31 March 1987

Abstract. A comprehensive unified study of fcc alkaline earth metal Ca, Sr and the bcc phase of Sr and Ba has been made. Properties studied include equilibrium lattice parameter, total crystal energy, second order elastic constants, pressure derivative of the second order elastic constants and phonon spectrum in the symmetry direction. The results obtained show an overall agreement with experiment. The results partially reproduced the experimentally observed phonon-crossover in Ba, and this has been found as the many-body effect in lattice dynamics.

Keywords. Pseudopotential; unified study; phonon frequency; alkaline earth metal; second-order elastic constants; calcium; strontium; barium.

PACS Nos 62·20; 63·30

1. Introduction

Numerous theoretical studies on simple, noble and transition metals have been made but relatively few attempts have been made on alkaline earth metals. The cubic alkaline earth metals Ba, Ca and Sr are divalent. Under the normal condition of pressure and room temperature, Ca and Sr exhibit an fcc structure whereas Ba exhibits a bcc structure; however Ca and Sr also exhibit a bcc phase (Pearson 1958) at high temperature. These metals give rise to similar physical properties. Thus understanding their physical properties from a microscopic theory is of interest.

From band-structure calculation (Vasvari *et al* 1967; Johansen 1969; Johansen and Mackintosh 1970; Jan and Skriver 1981) it has been observed that below the Fermi level the electronic band structure of these metals lies in close proximity to the Fermi level. However the electronic wavefunction at the Fermi level contains an admixture of the *d*-band character.

Due to lack of experimental information on the solid state properties the theoretical study of lattice mechanical properties of these metals is scanty. This is because of the difficulty in growing large single crystals of these metals. Recently Stassis and his collaborators (Stassis *et al* 1983; Mizuki *et al*.1985; Mizuki and Stassis 1985) have been able to grow the single crystal and measure the phonon frequencies of fcc Ca, bcc Sr and Ba. The experimental results of lattice dynamics of these metals present the following interesting features. (i) There is a phonon-softening near zone-boundary (100) along with phonon-anomalies in the experimental phonon-dispersion in Ca (Stassis *et al* 1983). (ii) In the measured dispersion curves for Ba (Mizuki *et al* 1985) it has been found

CC-0. In Public Domain. Gurukul Kangri Collection, Haridwar

Digitized by Arya Samaj Foundation Chennai and eGangotri

that at room temperature along (q00), the frequencies of the longitudinal branch for q between 0·2 and 0·8 are found to be lower than those of the transverse branch resulting in a phonon cross-over around $q=0{\cdot}8$. (iii) The experimental phonon-dispersion (Mizuki and Stassis 1985) curves for bcc Sr showed that the frequencies of the longitudinal branch along (q00) direction are slightly above those of the transverse branch. However the phonon-frequency for single crystal fcc Sr has not been measured.

In the following, we present a brief survey of the existing literature. As mentioned earlier due to lack of experimental data, there are only a few studies based on the microscopic theory of these metals. Dagens (1976, 1977) applied his resonant model potential (RMP) to Ca and calculated the pseudopotential form-factor, the total energy and elastic modulus. However Upadhaya and Animalu (1977) applied their rare earth metal model potential (REMMP), which is an extension of the transition metal model pseudopotential (Animalu 1973), to rare earth metals but no study was made by them on the alkaline earth metals. Recently Moriarty (1983) calculated the phonon spectra of fcc Ca and Sr, from a first principle generalized pseudopotential theory which accounts for the full effects of d-band hybridization. The results obtained agree with experimental data to within 10%. On the other hand there exist several calculations (Animalu 1967; Sharma 1981; Moriarty 1972, 1973, 1977, 1982, 1983) on phonon-dispersion curves of bcc Ba. All the calculations have been performed within the framework of the pseudopotential theory of metals. The phonon frequencies, calculated by Animalu (1967) and Sharma (1981), using local pseudopotentials, are substantially higher than the measured value. Furthermore in both these studies (Animalu 1967; Sharma 1981) the phonon frequencies of the L (q00) branch were higher than those of the T(q00) branch. Moriarty (1972, 1973, 1977, 1982, 1983) calculated the zone boundary frequencies along some high-symmetry directions, using a generalized pseudopotential approach which incorporates the effect of hybridization of the free electron states to the d-states. The results obtained, however, are better than those obtained by Animalu (1967) and Sharma (1981), but are higher than the experimental values and fail to reproduce the observed peculiarity.

On the other hand no first principle calculations of the dispersion curves of bcc Sr are available for a detailed comparison with experimental results. However, pseudopotential calculations were performed by Animalu (1967), using a local pseudopotential, except for the T(qq0) branch and the calculated frequencies are substantially higher than the experimental values and finally the calculation fails to explain the features observed in the experimental results.

In this paper we present a unified study of fcc Ca and Sr, and that of bcc Sr and Ba by using simple metal model potential (SMMP).

The success of SMMP in explaining lattice mechanics of alkali and simple metals has already been established (Das 1981; Sarkar 1981; Sen 1982). Recently SMMP with a slight modification has been able to fairly explain the lattice mechanics of lead (Pb) (Sarkar and Sen 1986) and the noble metals (Sarkar 1985). These studies encouraged us to apply SMMP in alkaline earth metals Ca, Sr and Ba. The objective of the present paper is to investigate how far SMMP is applicable to alkaline earth metals and also to point out its limitation. We have used the focal form of the Heine-Abarenkov (1964) model pseudopotential which is the most popular SMMP. The properties studied include equilibrium lattice parameter, total crystal energy, second order elastic (s.o.e.) constants, phonon frequencies and pressure derivative of elastic constants.

CC-0. In Public Domain. Gurukul Kangri Collection, Haridwar

Digitized by Arya Samaj Foundation Chennai and eGangotri

2. Theory

The Heine-Abarenkov model potential in its local form is given by,

$$V(r) = Ze^2U/r_c; \qquad r \leqslant r_c,$$
$$= -Ze^2/r; \qquad r > r_c.$$

The Fourier transform of the potential $V(r)$ is given by

$$V(q) = -(4\pi Ze^2/\Omega_0 q^2)\,[(1+U)\cos(qr_c) - U\sin(qr_c)/qr_c)] \times$$
$$[\exp(-\eta/2(q/2K_F)^2)],$$

where r_c and U are the two parameters of the model, η is an arbitrary convergence-parameter and the total energy is independent of η.

For a metallic solid, the dynamical matrix D can be expressed as the sum of the three terms,

$$D = D^C + D^E + D^R,$$

D^C represents the contribution of the direct Coulomb interaction between the ions and can be evaluated by the standard method (Kellerman 1940), D^E corresponds to the ionic interaction via the conduction electrons and D^R represents a repulsive interaction due to core-wave function which has been neglected in the present study. The contribution of the second-order term to the dynamical matrix in the framework of the second-order perturbation theory is given by

$$D^E_{\alpha\beta}(q) = 2\left(\sum_{\bar{G}} F_{|\bar{G}+\bar{K}|}(\bar{G}+\bar{q})_\alpha(\bar{G}+\bar{q})_\beta - \sum_{\bar{G}}{}' F_G G_\alpha G_\beta\right),$$

where $\bar{G}$ is a reciprocal lattice vector and F_G the energy wave number characteristics is given by,

$$F_G = \Omega_0 G^2/(8\pi e^2)\cdot|V_G|^2[1-\varepsilon(G)]/\varepsilon(G),$$

where Ω_0 is the volume/ion, and $\varepsilon(\bar{G})$ the dielectric function which describes the conduction electron screening; here we have used Taylor's dielectric function (Taylor 1978) which satisfied the consistency condition of pseudopotential (Sen *et al* 1981, 1983).

In making a unified study of metals with second-order local pseudopotential theory one has to face a problem that the second-order elastic constants obtained by the method of homogeneous deformation theory do not agree with those obtained from long-wave theory (Sen *et al* 1981, 1983), where the consistency condition of the energy expression of the pseudopotential theory is equivalent to the statement that the static and dynamic elastic constants must be the same. The fact that the two elastic constants do not agree indicates that the dynamical matrix does not correctly reproduce the slope of the dispersion curve in the long-wave limit. Thus it is evident that the dynamical matrix demands a modification. In fact this modification of the dynamical matrix is important and crucial in the unified study.

In the following results obtained by Sen *et al* (1981, 1983) will be summarized where the correction to the s.o.e. constants and dynamical matrix is to be shown. It is to

CC-0. In Public Domain. Gurukul Kangri Collection, Haridwar

Digitized by Arya Samaj Foundation Chennai and eGangotri

be noted that the expressions used for the mentioned properties have been taken as the standard expression (Sen *et al* 1980).

The elastic constants obtained by the two methods do not agree and the difference in values of the individual elastic constants is given by

$$C_{11}-C_{11}^{L}=C_{12}-C_{12}^{L}=\Delta;\quad C_{44}=C_{44}^{L},$$

where C_{11}'s are elastic constants in homogeneous deformation theory and C_{11}^{L}'s are that of long wave theory, and

$$\Delta=\sum_{G}{}'\Omega^{2}\cdot\left(\frac{\partial^{2}F_{G}}{\partial\Omega_{sc}^{2}}+\frac{2\partial^{2}F_{G}}{\partial\Omega\partial\Omega_{sc}}\right),$$

Ω being the volume/ion, F_G is the well-known energy-wave number characteristics and Ω_{sc} means differentiation w.r.t. atomic volume occurring in K_F in the band structure energy and $\partial/\partial\Omega$ means differentiation w.r.t. atomic volume other than Ω_{sc} i.e., w.r.t. the volume occurring explicitly in E_{bs} (band-structure energy) and the volume occurring in the reciprocal lattice vector G. Hence following Sen *et al* (1981, 1983) we get in the long wave limit

$$D_{\alpha\beta}^{ext}(\bar{K})|_{k\to 0}=\sum_{G}\left[\frac{\partial^{2}F_{G}}{\partial\Omega_{sc}^{2}}\Omega^{2}K_{\alpha}K_{\beta}-\frac{\partial F_{1G+K1}\Omega}{\partial\Omega_{sc}}\cdot((\bar{G}+\bar{K})_{\alpha}K_{\beta}\right.$$

$$\left.+(\bar{G}+\bar{K})_{\beta}K_{\alpha})\right]$$

$$=\sum{}'\Omega^{2}\left(\frac{\partial^{2}F_{G}}{\partial\Omega_{sc}^{2}}+2\frac{\partial^{2}F_{G}}{\partial\Omega_{sc}\partial\Omega}\right)K_{\alpha}K_{\beta}=\Delta K_{\alpha}K_{\beta}.$$

Hence the extra term in the dynamical matrix will contribute to the long-wave elastic constants and the extra contribution to the elastic constants is given by

$$C_{11}^{ext}=C_{12}^{ext}=\Delta\quad\text{and}\quad C_{44}^{ext}=0.$$

It is to be noted here that in the analysis, Sen *et al* (1981, 1983) have shown that inclusion of the consistency condition in the second-order theory simulates a part of the third-order effect which is essentially a many-body effect.

3. Results and discussion

The equilibrium lattice constants are fitted by using the equilibrium condition of the lattice and pseudopotential parameters of the proposed unified study are chosen as the best fit parameters. The results of various static properties calculated for the alkaline metals (Ca, Sr and Ba) along with their pseudopotential parameter are shown in tables 1 and 2 which also include available experimental results and a comparison with theoretical results obtained from other calculations. Figures 1 to 4 show the phonon-dispersion curves for Ca, fcc Sr, bcc Sr and bcc Ba respectively in the symmetry

CC-0. In Public Domain. Gurukul Kangri Collection, Haridwar

Digitized by Arya Samaj Foundation Chennai and eGangotri

Table 1. Table of pseudopotential parameter and calculated static properties.

Metals	Pseudopotential parameters		Half the lattice constants (a.u)	Total crystal energy (Ryd)	s.o.e. constants (10^{12} dynes cm^2)			Pressure derivative of s.o.e. constants		
	r_c (a.u)	U			C_{11}	C_{12}	C_{44}	dc_{11}/dp	dc_{12}/dp	dc_{44}/dp
Ca (fcc)	3·80	−1·164	5·32 (5·32[b])	−1·49 (−1·46[b])	0·1863 (0·278[a])	0·1771 (0·1823[a])	0·1509 (0·163[a])	5·32	4·40	4·22
Sr (fcc)	2·80	−0·70	5·79 (5·79[b])	−1·374 (−1·36[b])	0·1888	0·1473	0·1180	3·92	4·164	3·745
Sr (bcc)	3·80	−1·08	4·604 (4·604)[c]	−1·384	0·121	0·179	0·168	5·16	3·21	3·57
Ba (bcc)	3·20	−0·84	4·734 (4·734)[c]	−1·312 (−1·262)[b]	0·121	0·167	0·163	4·8	2·91	3·32

[a] Stassis *et al* (1983); [b] Kittel (1970); [c] Pearson (1958).

Table 2. Contribution of consistency condition (Δ) in elastic of Ca.

Values	C_{11}	C_{12}	C_{44}
(a) Calculated (present)	0·1863	0·1771	0·1509
(b) Δ	0·04	0·04	0·00
(c) Total	0·2263	0·2171	0·1509
(d) Calculated[a]	0·2780	0·1823	0·1630

[a] Stassis *et al* (1983).

direction. A comparison of the calculated and experimental values is also given in the figures.

The difficulties in obtaining experimental data have been mentioned earlier. In fact for all the metals no experimental data for their s.o.e. constants and pressure derivative of s.o.e. constants have yet been reported. The results obtained for Ca are compared with those calculated by Stassis *et al* (1983). It is interesting to note that the values of s.o.e. constants from the present study show a marked difference with that calculated by Stassis *et al* (1983), who used the long wave theory. The apparent discrepancy is due to the effect of consistency condition (see Sen *et al* 1981, 1983). If we subtract from the calculated value of s.o.e. constants the extra contribution to the s.o.e. constants, arising due to the consistency condition the results show a gross agreement with that of Stassis *et al* (1983). But no such analysis can be carried out for the s.o.e. constants for bcc Sr and Ba. Mizuki *et al* (1985) and Mizuki and Stassis (1985) have reported a calculation of s.o.e. constants from their force constant modes; however their results are misleading because they have quoted exactly the same table of values for force constants and s.o.e. constants for both the metals (Sr and Ba).

CC-0. In Public Domain. Gurukul Kangri Collection, Haridwar

Digitized by Arya Samaj Foundation Chennai and eGangotri

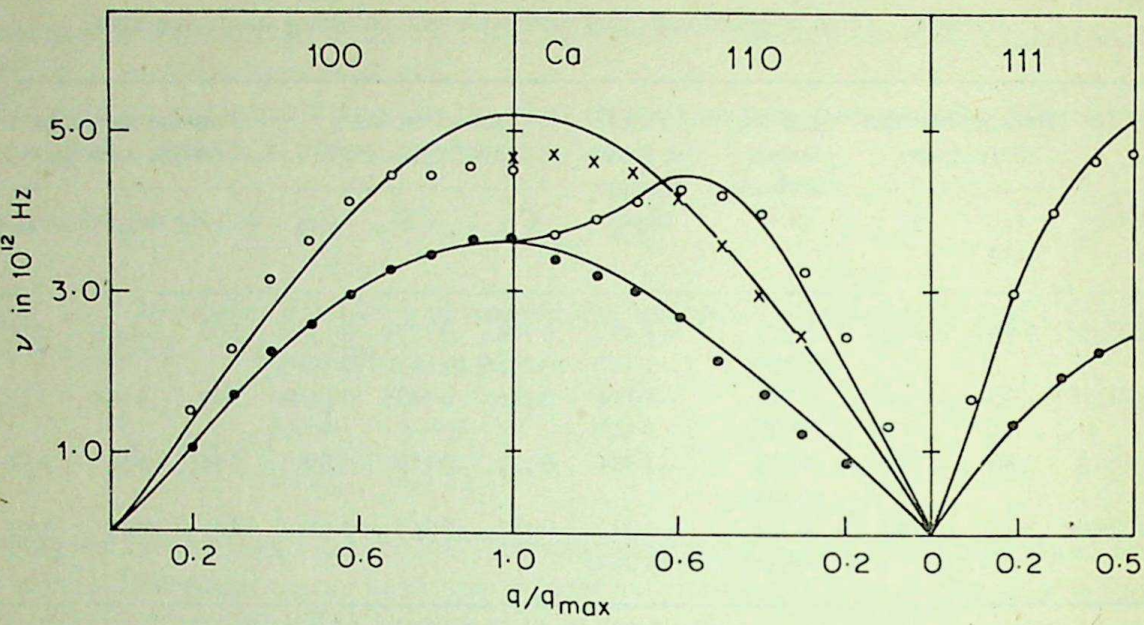

Figure 1. Phonon dispersion curves for fcc Ca at room temperature. — corresponds to the present study. Experimental points are taken from Stassis *et al* (1983) and are indicated by ○, ● and × for the longitudinal and two transverse branches respectively.

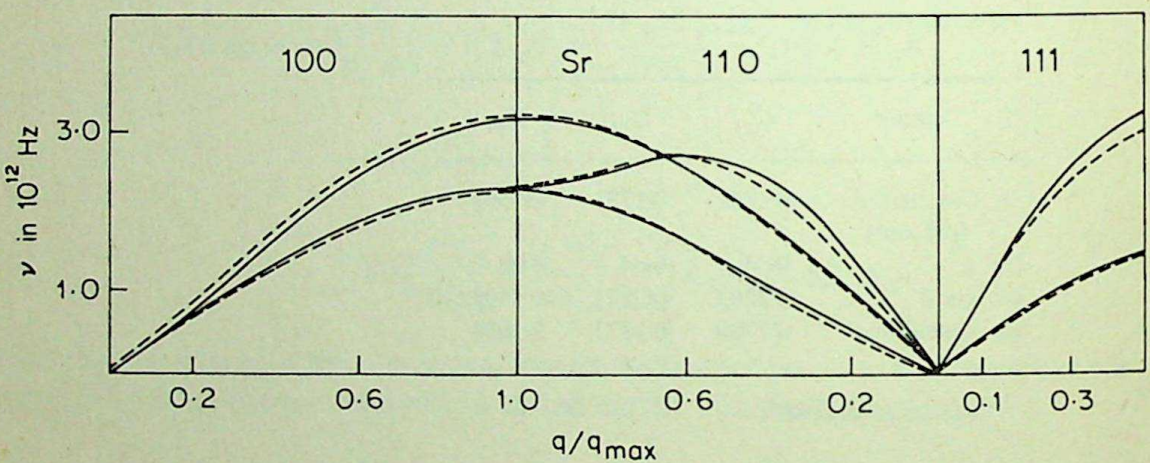

Figure 2. Phonon dispersion curves for fcc Sr at room temperature. — corresponds to the present study; – – – represents the experimental results on polycrystalline specimen (quoted from Moriarty 1983).

We have calculated the corresponding polycrystalline elastic constants from the s.o.e. constants obtained using a reliable averaging scheme (Middya *et al* 1984). The polycrystalline elastic constants of the metals (excepting fcc Sr) obtained have been compared with experimental results as also with the calculated values of Dagens (1977) in table 3. The calculated crystal energy agrees with experimental results (Kittel 1976) for all the metals excluding bcc Sr. No experimental data are available for bcc Sr, which is known to exist at a high temperature between 830 K and its melting point 1040 K.

Figures 1 and 2 show the calculated phonon frequencies for fcc Ca and Sr. As far as phonon dispersion is concerned this simple model gives good results for the metals. It is to be noted that for Ca, the calculated phonon frequencies compare well with the single crystal experimental results (Stassis *et al* 1983). However no such direct comparison can be given for fcc Sr. No experimental results have yet been reported for single crystal fcc

CC-0. In Public Domain. Gurukul Kangri Collection, Haridwar

Digitized by Arya Samaj Foundation Chennai and eGangotri

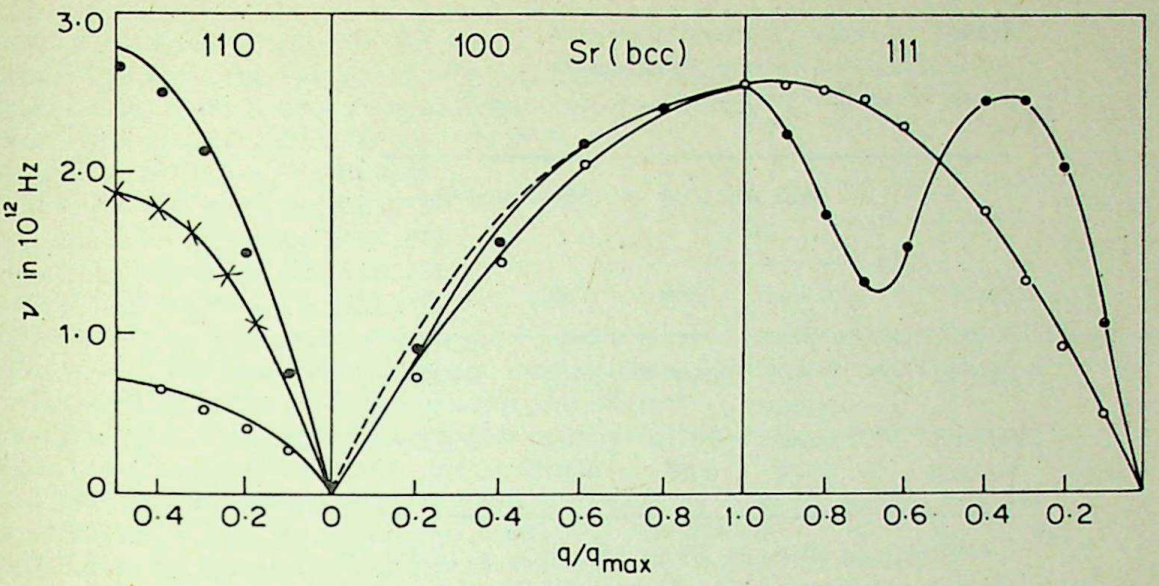

Figure 3. Phonon dispersion curves for bcc Sr at 930 K. — corresponds to the present study and – – – phonon curves indicates the present study excluding the consistency condition. Experimental points are taken from Mizuki and Stassis (1985) and are indicated by ○, ● and × for the longitudinal and two transverse branches respectively.

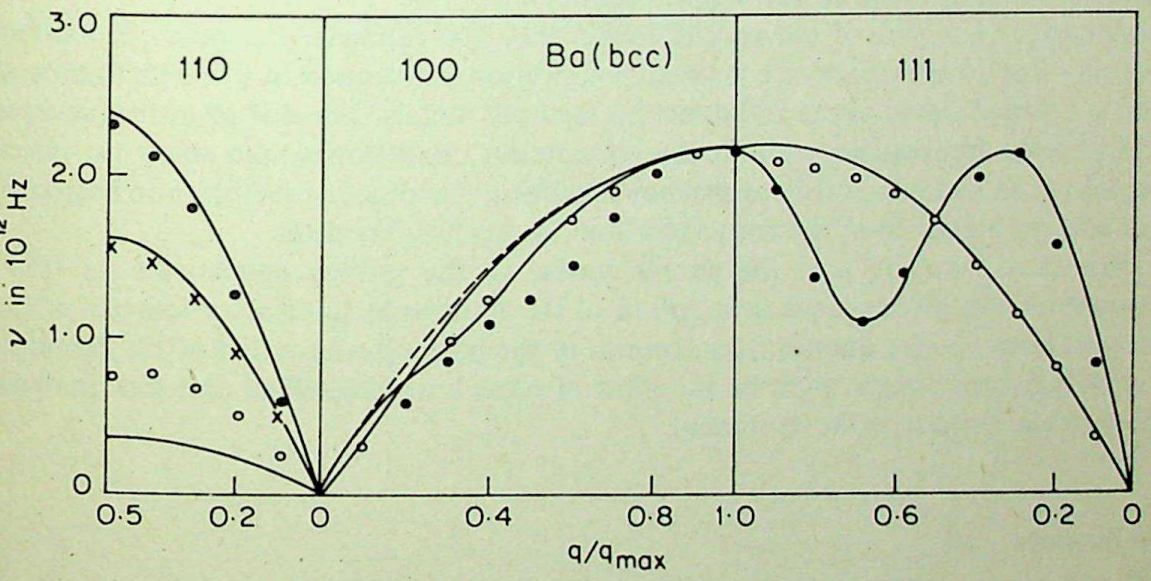

Figure 4. Phonon dispersion curves for bcc Ba 300 K, — corresponds to the present study, – – – phonon curves indicates the present study excluding the consistency condition. Experimental points are taken from Mizuki *et al* (1985) and indicated by ○, ● and × respectively for the longitudinal and two transverse branches respectively.

Sr. However we have compared the calculated phonon spectra with the experimental dispersion curve obtained from polycrystalline results (quoted from Moriarty 1983).

Figure 3 shows the calculated phonon frequencies for bcc Sr and the results obtained have been found to be in good agreement with experimental values. Even, from the point of view of unified study the present calculation gives a good account of the phonon-dispersion of this metal along with its peculiarities mentioned in the earlier section. Figure 4 shows the calculated phonon-dispersion curve for bcc Ba. Although the results show good agreement, it reproduces the observed phonon cross-over

CC-0. In Public Domain. Gurukul Kangri Collection, Haridwar

Digitized by Arya Samaj Foundation Chennai and eGangotri

Table 3. Calculated polycrystalline elastic constants and corresponding experimental values. (10^{12} dynes/cm^2).

	Bulk modulus (B)		Shear modulus (G)	
Metals	Calc.	Expt	Calc.	Expt.
Ca (fcc)	0·1802 0·1968[e]	0·1870[a]	0·1041	0·075[b]
Sr (bcc)	0·160	0·1184[c]	0·033	0·0533
Ba (bcc)	0·152	0·105[d]	0·09	0·05

[a] Vaidya and Kennedy (1970); [b] Smith *et al* (1957); [c] Koster and Franz (1961); [d] Koster (1947); [e] Dagens (1976).

partially. The calculated results show that the phonon-crossover is at $q = 0{\cdot}3$ in the 100 direction whereas experiment shows it upto $q = 0{\cdot}8$. Thus a partial success for the qualitative agreement of calculated results can be claimed over the existing theoretical calculation mentioned in the earlier section.

A careful analysis of the results reveal that the calculated phonon crossover is entirely due to the effect of consistency condition mentioned in § 2. The figures also show a dotted curve in the 100 direction for both metals. The dotted curves represent the phonon frequencies without the consistency condition which show no phonon crossover, in fact minus the consistency condition the longitudinal phonon frequencies are always higher than the transverse one in the 100 direction.

We thus conclude that the simple model in the unified spirit with its best fit parameter can give a good description of the lattice-mechanical properties of these metals; however the quantitative account of the phonon-anomalies of Ba demands a careful analysis which might be the effect of some non-local effect and this analysis is now in the process of development.

References

Animalu A O E 1967 *Phys. Rev.* **161** 445
Animalu A O E 1973 *Phys. Rev.* **B8** 3542
Dagens L 1976 *J. Phys.* **F6** 1801
Dagens L 1977 *J. Phys.* **F7** 1167
Das S K 1981 *Studies on the lattice dynamical and related properties of metals*, Ph.D. thesis, Calcutta University
Harrison W A 1966 *Pseudopotentials in the theory of metals* (New York: W A Benjamin)
Heine V and Abarenkov I 1964 *Philos. Mag.* **9** 453
Jan J P and Skriver H L 1981 *J. Phys.* **F11** 805
Johansen G 1969 *Solid State Commun.* **7** 731
Johansen G and Mackintosh A R 1970 *Solid State Commun.* **8** 121
Kellerman E W 1940 *Philos. Trans. R. Soc. (London)* **A238** 513
Kittel C 1976 *Introduction to solid state physics*, (New Delhi: Wiley Eastern) 5th ed.
Köster W 1947 *Z. Metallk.* **39** 1

CC-0. In Public Domain. Gurukul Kangri Collection, Haridwar

Digitized by Arya Samaj Foundation Chennai and eGangotri

Köster W and Franz H 1961 *Met. Rev.* **6** 1
Middya T, Sarkar A and Sengupta S 1984 *Acta Phys. Pol.* **A66** 561
Mizuki J, Chen Y, Ho K M and Stassis C 1985 *Phys. Rev.* **B32** 666
Mizuki J and Stassis C 1985 *Phys. Rev.* **B32** 8372
Moriarty J A 1972 *Phys. Rev.* **B6** 4445
Moriarty J A 1973 *Phys. Rev.* **B8** 1338
Moriarty J A 1977 *Phys. Rev.* **B16** 2537
Moriarty J A 1982 *Phys. Rev.* **B26** 1754
Moriarty J A 1983 *Phys. Rev.* **B28** 4818
Pearson W B 1958 *A handbook of lattice spacing and structure of metals and alloys* (London: Pergamon)
Sarkar A 1985 Pseudopotential studies of some simple and non-simple metals including a study of polycrystalline metals, Calcutta University (Unpublished)
Sarkar S K 1981 *Unified studies of ionic solids and metals*, Ph.D. thesis, Calcutta University
Sarkar A and Sen D 1986 *Pramana – J. Phys.* **26** 231
Sen D 1982 *Unified study and effective interaction in metals*, Ph.D. thesis, Calcutta University
Sen D, Sarkar S K, Roy D and Sengupta S 1981 *Phys. Rev.* **B24** 876
Sen D, Sarkar S K, Sengupta S and Roy D 1980 *Acta. Phys. Pol.* **A57** 73
Sen D, Sarkar S K, Sengupta S and Roy D 1983 *Phys. Status Solidi* **B115** 593
Sharma K S 1981 *Phys. Status. Solidi* **B108** K101
Smith J F, Carlson C E and Spedding F H 1957 *Trans. AIME* **209** 1212
Stassis C, Zaretsky J, Misemor D K, Skriver H L, Harmann B N and Nicklow R M 1983 *Phys. Rev.* **B27** 3303
Taylor R 1978 *J. Phys.* **F8** 1699
Upadhaya J C and Animalu A O E 1977 *Phys. Rev.* **B15** 1867
Vaidya S N and Kennedy G C 1970 *J. Phys. Chem. Solids* **27** 637
Vasvari B, Animalu A O E and Heine V 1967 *Phys. Rev.* **154** 535

CC-0. In Public Domain. Gurukul Kangri Collection, Haridwar

Digitized by Arya Samaj Foundation Chennai and eGangotri

CC-0. In Public Domain. Gurukul Kangri Collection, Haridwar

Digitized by Arya Samaj Foundation Chennai and eGangotri

Pramāṇa – J. Phys., Vol. 28, No. 6, June 1987, pp. L699–L703. © Printed in India.

Constraint on unstable photino mass from a superlight gravitino

TANMOY BHATTACHARYA and PROBIR ROY
Tata Institute of Fundamental Research, Homi Bhabha Road, Bombay 400 005, India

MS received 13 February 1987

Abstract. The known lower bound on the unstable photino mass gets invalidated by a gravitino lighter than 10^{-3} eV. Nevertheless, general bounds can be derived by feeding early universe constraints from the primary abundance of He^4 and the extant lower bound on the gravitino mass into the lifetime for the decay photino → photon + gravitino. The mass-range $O(100)$ eV to $O(1)$ MeV is excluded.

Keywords. Unstable photino; gravitino; supersymmetry.

PACS Nos 14·80; 11·30; 98·80

Interaction characteristics and constraints from the early universe can form a cogent combination in restricting the masses of certain weakly interacting elementary particles. Take the photino $\tilde{\gamma}$ for instance. This spin 1/2 neutral Majorana particle is the superpartner of the photon in supersymmetric (Bagger and Wess 1983) gauge theories. Since such supersymmetry is known to be broken* in nature, the photino must be massive. Photinos with energies below the threshold for producing charged superparticles are very weakly interacting and consequently hard to detect. Nevertheless, there exist laboratory limits on the process $e^+e^- \to \gamma\tilde{\gamma}\tilde{\gamma}$ constraining the photino not to be too light unless the selectron exchanged in the process is too heavy (Haber and Kane 1985). On the other hand, too heavy a selectron reduces $\tilde{\gamma}\tilde{\gamma}$ creation/annihilation cross-sections to such an extent that the photino decouples too soon in the early universe; consequently the critical density is adversely affected. The trade-off between these two requirements takes place for a photino mass $m_{\tilde{\gamma}}$ higher than** 2 GeV and lower than $O(10^2)$ eV. Therefore the mass of a stable photino cannot lie between these two values (Goldberg 1983; Krauss 1983). Unfortunately, for unstable photinos no such reliable bounds exist and this is the problem that we address here.

R-parity, a generally accepted good quantum number in supersymmetric theories, dictates stability for the lightest supersymmetric particle (LSP). Thus, in case $\tilde{\gamma}$ is not the LSP, it is likely to be unstable. Could the sneutrino $\tilde{\nu}$, the scalar superpartner of the neutrino, be lighter than $\tilde{\gamma}$ thereby allowing the rapid decays $\tilde{\gamma} \to \nu\tilde{\nu}^*, \bar{\nu}\tilde{\nu}$? This is unlikely for photino masses of our interest since data from τ-decay imply (Kane and

---

* The yet unseen selectron $\tilde{e}$, which is the scalar superpartner of the electron, is known to weigh more than 23 GeV (Gladney *et al* 1983).

** This number can be pushed upto about 5 GeV by considering the cosmological constraints on photino-quark interactions and using an experimental lower limit of 70 GeV on the mass of the exchanged squark.

CC-0. In Public Domain. Gurukul Kangri Collection, Haridwar

Digitized by Arya Samaj Foundation Chennai and eGangotri

Rolnick 1983) that $m_{\tilde{\nu}_\tau} + m_{\tilde{\nu}_l}(l = e, \mu) > m_\tau$. Therefore we shall assume the nonexistence of such a decay mode at any substantial level.

Now suppose a superlight† gravitino $\tilde{G}$ is the LSP. Then the predominant decay mode of the photino is $\tilde{\gamma} \to \gamma\tilde{G}$ and this is what we consider. The only other possible competing decay mode is $\tilde{\gamma} \to \gamma +$ axino where the axino is the superpartner of the invisible axion. This was assumed to be the main photino decay channel by Kim *et al* (1984). From the requirement of the thermalization of the decay photon into the background radiation of the universe, they claimed to derive a lower bound of 4 MeV on $m_{\tilde{\gamma}}$ for a value $\sim 10^9$ GeV of the Pecci-Quinn symmetry-breaking scale. Later, this bound was pushed up to 150 MeV by Sarkar and Cooper (1984) by considering the primordial abundance of deuterium. *However, all these bounds get invalidated in the presence of a superlight gravitino.* This is because the characteristic partial lifetime $\tau(\tilde{\gamma} \to \gamma +$ axino) for $m_{\tilde{\gamma}} = O(1)$ MeV is in the vicinity of 10^7 sec. This cannot compete with $\tau(\tilde{\gamma} \to \gamma\tilde{G})$ which we show (figure 1) to be† $\lesssim 10^2$ sec in the region of interest.

The gravitino $\tilde{G}$ is the spin 3/2 Majorana superpartner of the graviton. The $\tilde{\gamma}\gamma\tilde{G}$ vertex can be easily obtained by supersymmetrization of the interaction which bends light in a gravitational field. To the lowest order, it is described in terms of the EM structure tensor $F_{\mu\nu}$, the photino field λ and the gravitino Rarita-Schwinger field ψ_ρ as

$$L_{\text{eff}} = -i(\pi G_N/8)^{1/2}\bar{\lambda}\gamma^\rho[\gamma^\mu, \gamma^\nu]\psi_\rho F_{\mu\nu}, \tag{1}$$

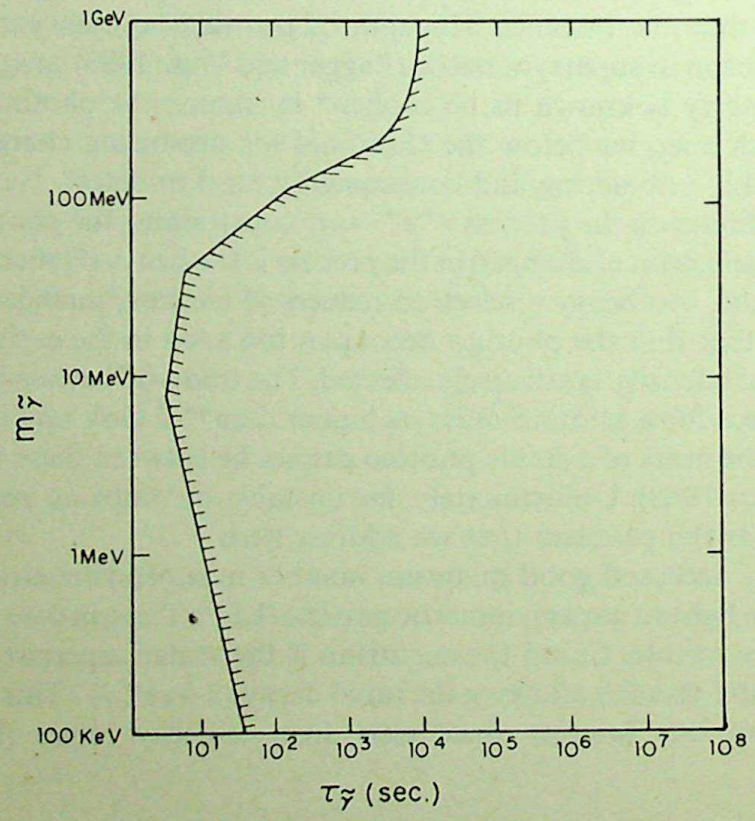

Figure 1. Allowed and forbidden regions in the plot of $m_{\tilde{\gamma}}$ vs $\tau_{\tilde{\gamma}}$

†The value of $m_{3/2}$ is theoretically wide open if the Kähler potential is logarithmic as in no-scale supergravity theories.

CC-0. In Public Domain. Gurukul Kangri Collection, Haridwar

Digitized by Arya Samaj Foundation Chennai and eGangotri

where G_N is Newton's constant. From (1) the partial lifetime for the decay $\gamma \to \gamma\tilde{G}$ may be computed to be

$$\tau(\tilde{\gamma} \to \gamma\tilde{G}) = 6G_N^{-1} m_{3/2}^2 \, m_{\tilde{\gamma}}^{-5} (1 + 3m_{3/2}^2 \, m_{\tilde{\gamma}}^{-2})^{-1} (1 - m_{3/2}^2 \, m_{\tilde{\gamma}}^{-2})^{-3}. \quad (2)$$

In (2) $m_{3/2}$ is the mass of the gravitino which is unknown but has a very weak lower limit, namely (Fayet 1986) $2{\cdot}3 \times 10^{-6}$ eV from a laboratory search for the reaction $e^+e^- \to \gamma\tilde{\gamma}\tilde{G}$. Thus gravitinos could very well be[††] superlight. It should be emphasized that (2) has been derived just from general relativity and supersymmetry without any model-dependent assumptions.

The decay of a photino into a photon and such a superlight gravitino is possible at a cosmologically acceptable rate, but there is a caveat. The resulting excess of photons should not affect the post-nucleosynthesis abundance of natural elements in the universe to an extent that would conflict with observation. This problem has been investigated in detail by Salati *et al* (1986). For $m_{\tilde{\gamma}} > 150$ GeV, the strongest upper bound on the photino lifetime $\tau_{\tilde{\gamma}}$ comes from the avoidance of excessive photofission of deuterium. This rules out photino lifetimes much in excess of 10^3–10^4 sec. For $m_{\tilde{\gamma}} < 150$ MeV, on the other hand, the major factor is the excessive entropy generation by the decay photons leading to an overproduction of He^4. The primordial He^4: H mass-fraction Y_P, deduced (Kunth and Sargent 1984) from observation to be 0·25, should not be exceeded. In consequence, a large region in the $m_{\tilde{\gamma}}$ vs $\tau_{\tilde{\gamma}}$ plot gets ruled out. The consolidated effect of these restrictions has been shown (Salati *et al* 1986) in figure 1 for $Y_P = 0{\cdot}25$.

Despite the severity of the above constraints, it is evident from figure 1 that low photino masses with low lifetimes are still allowed since such shortlived photinos have little effect on Y_P. Thus $m_{\tilde{\gamma}}$ could still be much less than 150 MeV. How does one really bound it from below? This can be done for a photino decaying primarily into a photon and a gravitino since $\tau_{\tilde{\gamma}}$ can then be replaced by the right side of (2). By folding the constraints of figure 1 with (2), one is led to the $m_{3/2}$ vs $m_{\tilde{\gamma}}$ plot of figure 2. Now $m_{3/2} > 2{\cdot}3 \times 10^{-6}$ eV restricts $m_{\tilde{\gamma}}$ to be more than 1 MeV.

How reliable is the use of the results of Salati *et al* (figure 1) in the present context? One may question the two following assumptions that they made: (i) they assumed three* species of stable ultralight 2-component neutrinos. (ii) The ratio Ω_B of baryon density to the critical density was taken to be not less than 0·02 $(H/50\ \mathrm{km\,sec^{-1}\,mpc^{-1}})^2$ which means a present-day baryon to photon number-density ratio $n_B/n_\gamma \gtrsim 1{\cdot}4 \times 10^{-10}$. Firstly, a stable superlight gravitino, weighing less than 10^{-2} eV, is likely to stay in equilibrium in the early universe sufficiently long to act in effect as a fourth species of 2-component neutrino (Fayet 1983). Secondly, the analysis (Yang *et al* 1984) leading to $n_B/n_\gamma \gtrsim 1{\cdot}4 \times 10^{-10}$, from the kinetics of $D + He^3$ formation, is not believable in the presence of a non-relativistic photoemitting photino; it is safer to use $n_B/n_\gamma \gtrsim 5 \times 10^{-11}$ directly from observation, i.e. the lower bound 0·01 $(H/50\ \mathrm{km\,sec^{-1}\,mpc^{-1}})^2$ on Ω_B.

[††]This is nevertheless long compared to the time ($\sim$1 sec) for the neutron to proton ratio "freezing out" modulo β-decay.

* The photino is equivalent to a fraction of a neutrino species since it acts like a neutrino when it is highly relativistic and not so at all when it is very nonrelativistic.

CC-0. In Public Domain. Gurukul Kangri Collection, Haridwar

Digitized by Arya Samaj Foundation Chennai and eGangotri

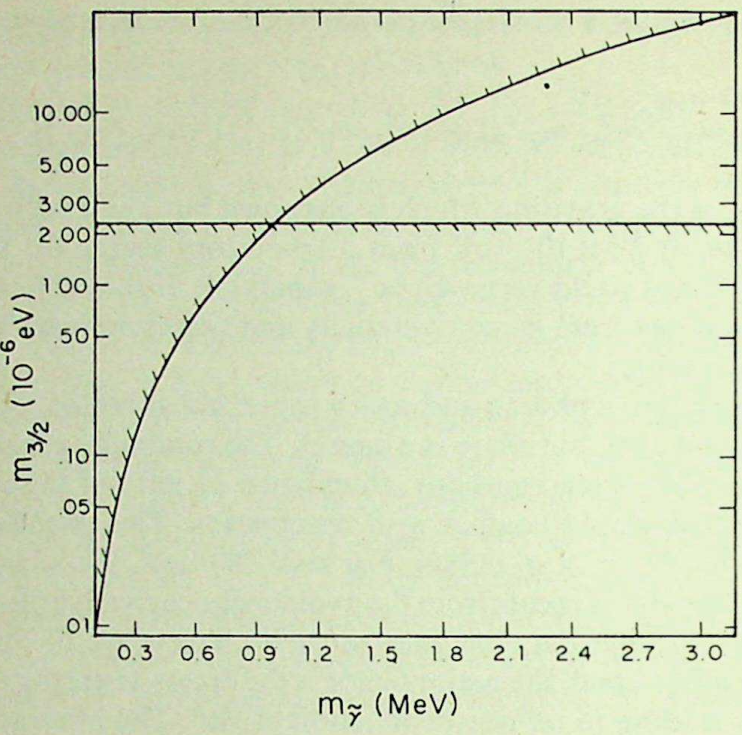

Figure 2. Allowed and forbidden regions in the $m_{3/2}-m_{\tilde{\gamma}}$ plot.

What would be the effect of the above changes? The explicit dependence of Y_P on the number N_ν of stable ultralight neutrino species and on the baryon to photon number density ratio at nucleo-synthesis $(n_B/n_\gamma)_{NS}$ is known (equation (41) of Sarkar 1985). The increase in N_ν from three to four with Y_P unchanged implies a change $\Delta \ln (n_B/n_\gamma)_{NS} = -13/11$ from the value used by Salati *et al.* We can obtain a crude order of magnitude estimate of the effect this has on the photino lifetime constraint by making three drastic assumptions. (a) All photinos are taken to decay more or less instantaneously when $\tau_{\tilde{\gamma}}$ equals the expansion time of the universe. (b) The decay photons get degraded in energy to a uniform temperature through processes such as double Compton scattering. (c) The bulk of the photinos decay after nucleosynthesis, as ought to be the case if Y_P is taken at the absolute upper limit of 0·255. It is then straightforward to estimate

$$1+0{\cdot}6\, m_{\tilde{\gamma}}\, \tau_{\tilde{\gamma}}^{1/2} (g^*)^{-1/4} \frac{n_{\tilde{\gamma}}}{n_\gamma} \lesssim c\, \frac{(n_B/n_\gamma)_{NS}}{n_B/n_\gamma}. \tag{3}$$

In (3) g^* is the degeneracy factor or effective number of relativistic degrees of freedom, being 43/4 for a completely nonrelativistic photino and 50/4 for an ultrarelativistic one. Further, c is the proportionality constant which accounts for photon reheating at the e^+e^- annihilation era.

On using (3), we find a reduction of the upper bound in the paper of Salati *et al* by a factor ~ 16. Feeding that into (2), our lower bound on $m_{\tilde{\gamma}}$ gets increased by a factor $\sim 1{\cdot}8$. Of course, our simplifying assumptions (in particular (c)) could be wrong and the true upper bound on $\tau_{\tilde{\gamma}}$ could even be somewhat smaller. But since $m_{\tilde{\gamma}} \propto \tau_{\tilde{\gamma}}^{-1/5}$, the actual numerical effect of various astrophysical uncertainties on the photino mass lower bound is not expected to be significant. Thus we can safely say that $m_{\tilde{\gamma}} > O(1)$ MeV.

CC-0. In Public Domain. Gurukul Kangri Collection, Haridwar

Digitized by Arya Samaj Foundation Chennai and eGangotri

Such a constraint obviously cannot apply if $\tau_{\tilde{\gamma}}$ exceeds the age of the universe. However, in that case there is a very small upper bound on the photino mass from critical density considerations (Sciama 1982). This is since the photino-electron cross-section is comparable to the neutrino-electron one. Thus the $\tilde{\gamma}$ number-density should be similar to that of the neutrinos. Then the requirement on the density of the universe in terms of the known Hubble constant and the age of the universe allows only photino masses less than $O(10^2)$ eV. The decay into a photon and a gravitino of such a low-mass photino with a lifetime $\sim 10^{24}$ sec has been advocated (Sciama 1982, 1984) as a possible source of ultraviolet photons which can ionize the galactic halo.

Finally, our conclusion is that the mass-range $O(10^2)$ eV to $O(1)$ MeV is excluded for a quasistable photino decaying mainly via $\tilde{\gamma}\rightarrow\gamma\tilde{G}$. These are the best bounds on the unstable photino mass with a superlight gravitino. As $m_{3/2}$ increases, these remain valid but may get superseded by stronger bounds from the decay $\tilde{\gamma}\rightarrow\gamma+$axino. The supercession region 10^{-3} to 10^{-2} eV is made imprecise by the model-dependence of the latter through the Peccei-Quinn symmetry breaking scale and the domain number (number of inequivalent vacua) of the universe. Other bounds on the unstable photino mass involve (Grivaz 1986) assumptions on the selectron mass and are not as general as our statement.

We thank S Sarkar for helpful discussions.

References

Bagger J and Wess J 1983 *Supersymmetry and supergravity*, (Princeton: University Press)
Fayet P 1983 *Phys. Rep.* **105** 21
Fayet P 1986 *Phys. Lett.* **B175** 471
Gladney L *et al* 1983 *Phys. Rev. Lett.* **51** 2253
Goldberg H 1983 *Phys. Rev. Lett.* **50** 1419
Grivaz J F 1986 *Proc. XXIII Intl. Conf. High Energy Physics* (ed.) S Loken (Singapore: World Scientific) (in press)
Haber H and Kane G 1985 *Phys. Rep.* **117** 75
Kane G and Rolnick W 1983 *Nucl. Phys.* **B217** 1706
Kim J E, Masiero A and Nanopoulos D V 1984 *Phys. Lett.* **B139** 346
Krauss L 1983 *Nucl. Phys.* **B227** 556
Kunth D and Sargent W L W 1984 *Astrophys. J.* **294** 1
Salati P, Delbouurgo-Salvado P D and Audouze J 1987 *Astron. Astrophys.* **173** 1
Sarkar S 1985 *Superstrings, supergravity and unified theories* (eds) G Furlan, R Iengo, Q Shafi and J Pati (Singapore: World Scientific)
Sarkar S and Cooper A 1984 *Phys. Lett.* **B148** 347
Sciama D 1982 *Phys. Lett.* **B118** 327
Sciama D 1984 *Phys. Lett.* **B137** 169
Yang J *et al* 1984 *Astrophys. J.* **281** 493

CC-0. In Public Domain. Gurukul Kangri Collection, Haridwar

Digitized by Arya Samaj Foundation Chennai and eGangotri

CC-0. In Public Domain. Gurukul Kangri Collection, Haridwar

Digitized by Arya Samaj Foundation Chennai and eGangotri

Pramāṇa–J. Phys, Vol. 28, No. 6, June 1987, pp. L705–707. © Printed in India.

Observation of inverse a.c. Josephson effect in bulk Y-Ba-Cu-O possessing high T_c

A K GUPTA, S K AGARWAL, B JAYARAM, ANURAG GUPTA and A V NARLIKAR

National Physical Laboratory, Hillside Road, New Delhi 110 012, India

MS received 14 May 1987

Abstract. Microwave-induced d.c. voltage due to inverse a.c. Josephson effect has been observed across bulk samples of Y-Ba-Cu-O. Variation of the d.c. voltage with small external magnetic field and temperature has been investigated. Our results indicate that weakly coupled superconducting grains exist up to 230 K.

Keywords. High temperature superconductivity; yttrium-barium-copper-oxide; Josephson tunnelling.

PACS No. 74·70

It is well known that a d.c. voltage is induced across unbiased Josephson junctions by applied microwave radiations due to inverse a.c. Josephson effect (Langenberg *et al* 1966; Chen *et al* 1972). The d.c. voltage could be either discretely quantized or continuously varying. It is affected by applied external magnetic field and varies with microwave power. The continuously varying induced d.c. voltages have also been observed across bulk granular superconductors (Warman *et al* 1971; Saxena *et al* 1974; Yu and Saxena 1975).

We have observed microwave-induced d.c. voltage across several unbiased bulk samples of Y-Ba-Cu-O possessing high superconducting critical temperature. The samples are in the form of strips of dimensions 10 mm × 2 mm × 1 mm. The samples were prepared by direct oxide mixing technique described elsewhere (Jayaram *et al* 1987a). Typical resistance transition curve is as shown in figure 1. As may be seen the onset of superconductivity is at 91 K and the resistance becomes zero at 83 K.

For the microwave studies the samples are mounted inside an X-band wave guide and are irradiated with highly stabilized phase-locked microwave radiations having a stability of one part in 10^9 over a period of 2 hr. The d.c. voltage is measured using a high impedance nanovoltmeter. Correction for thermal e.m.f. is applied to each measurement. The overall uncertainty in the measurement of the induced voltage is $\pm 0{\cdot}1\ \mu V$ which is mainly due to variation in the thermal e.m.f.

Figure 2 shows the variation of the microwave-induced d.c. voltage at liquid nitrogen temperature as a function of the microwave power. The lower curve shows the effect at zero magnetic field while the upper curve shows the effect at the finite magnetic field which is produced by passing a current of 250 mA in a single turn coil wound on the outer surface of the wave guide. The change in the magnitude of the induced voltage by the application of such a small magnetic field confirms that the induced voltage is due to Josephson effect between the weakly coupled superconducting grains of the sample.

CC-0. In Public Domain. Gurukul Kangri Collection, Haridwar

Digitized by Arya Samaj Foundation Chennai and eGangotri

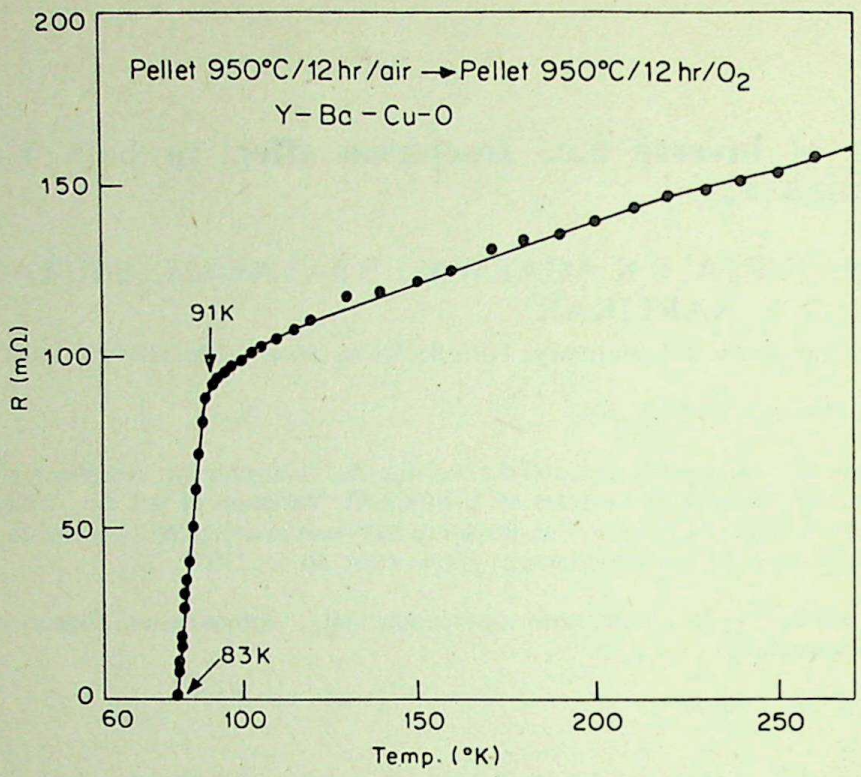

Figure 1. Resistive transition curve for the sample $Y_1Ba_2Cu_3O_{9-y}$.

The temperature variation of the microwave induced d.c. voltage for a fixed value of the microwave power is shown in figure 3. As the temperature is increased the induced voltage decreases, becomes constant at 150 K and disappears at 230 K. These results clearly indicate that weakly coupled superconducting grains are

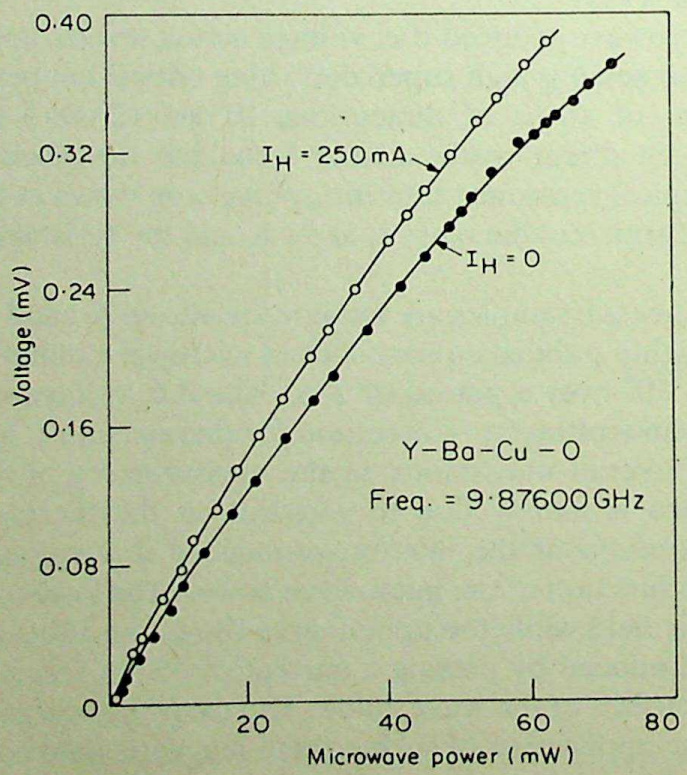

Figure 2. Variation of microwave-induced voltage as a function of microwave power at liquid nitrogen temperature.

CC-0. In Public Domain. Gurukul Kangri Collection, Haridwar

Digitized by Arya Samaj Foundation Chennai and eGangotri

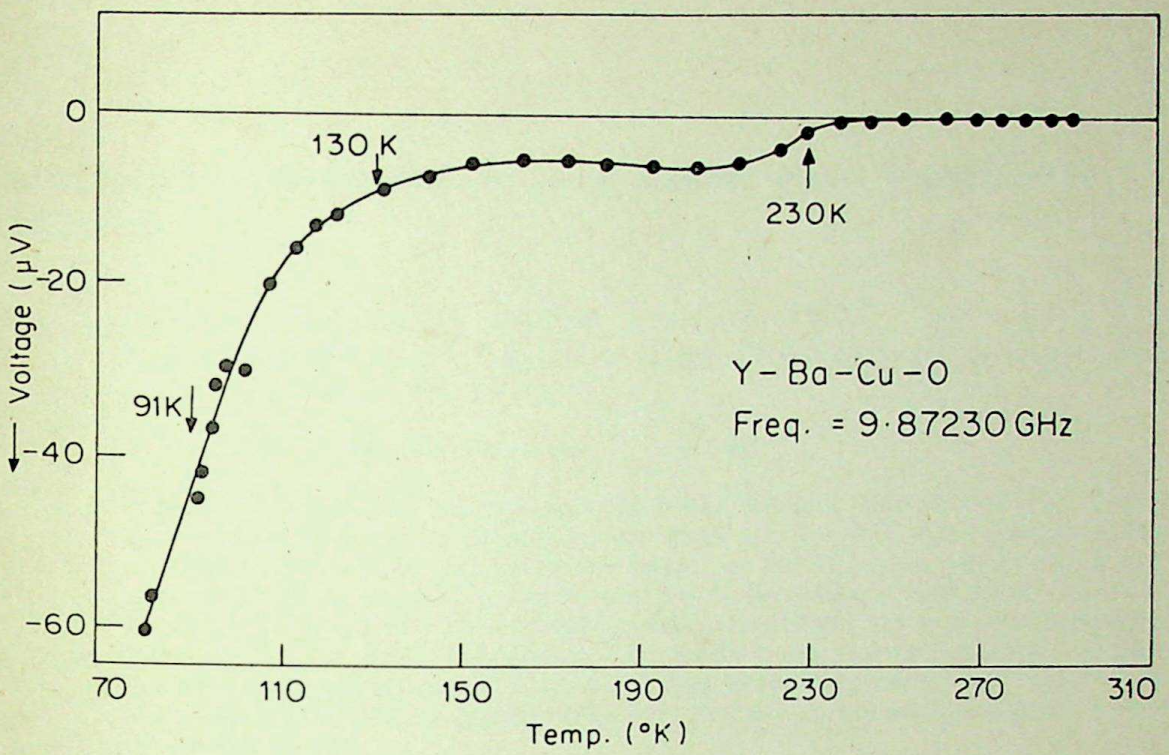

Figure 3. Temperature variation of the microwave-induced voltage for a fixed microwave power.

present in these samples up to as high a temperature as 230 K which are however not detected by resistive studies. In this context, it is interesting to mention that in a different series of samples reported elsewhere (Jayaram *et al* 1987b), the possibility of superconducting transition occurring above 230 K had been manifested by resistive studies. Their detailed inverse Josephson effect studies are currently in progress which will be reported later.

The authors thank Prof. S K Joshi for his interest and encouragement.

References

Chen J T, Todd R J and Kim Y W 1972 *Phys. Rev.* **B5** 1843
Jayaram B, Agarwal S K, Gupta A and Narlikar A V 1987a Jpn. *J. Appl. Phys.* (submitted)
Jayaram B, Agarwal S K, Gupta A and Narlikar A V 1987b *Solid State Commun.* (submitted)
Langenberg D N, Scalpino D J, Taylor B N and Eck R E 1966 *Phys. Lett.* 20, 563
Saxena A M, Crow J E and Strongin M 1974 *Solid State Commun.* **14** 799
Warman J, Jahn M T and Kao Y H 1971 *J. Appl. Phys.* **42** 5194
Yu M L and Saxena A M *IEEE Trans. Mag.* **MAG-11** 674

CC-0. In Public Domain. Gurukul Kangri Collection, Haridwar

Digitized by Arya Samaj Foundation Chennai and eGangotri

CC-0. In Public Domain. Gurukul Kangri Collection, Haridwar

Digitized by Arya Samaj Foundation Chennai and eGangotri

Pramāṇa – J. Phys, Vol. 28, No. 6, June 1987, pp. L709–712. © Printed in India.

Endothermic quasicrystalline-to-crystalline phase transition in Al_6CuMg_4

M K SANYAL, V C SAHNI and G K DEY*

Nuclear Physics Division, *Physical Metallurgy Division, Bhabha Atomic Research Centre, Bombay 400 085, India

MS received 20 March 1987; revised 27 April 1987

Abstract. Electron microscopic and differential scanning calorimetric (DSC) studies have been performed to investigate the phase transitions in the rapidly solidified Al_6CuMg_4 alloy system. We present evidence, for the first time, that an *endothermic* quasicrystalline to crystalline transition occurs in this system around 340°C. This is an unexpected feature—for conventional wisdom would lead one to expect exothermic behaviour as was seen in $Al_{86}Mn_{14}$—and points to the fact that stability of certain quasicrystalline phases may be much larger than hitherto expected. Some comments on the recently reported large quasicrystal for the Al_6CuLi_3 system are also made in the light of our observation.

Keywords. Quasicrystals; phase transition; thermal-study.

PACS Nos. 61·55; 64·70; 65·40

Since the discovery of quasicrystalline phase with 532 symmetry in Al-Mn system by Shechtman *et al* (1984), a variety of other quasicrystals have been reported. Sastry *et al* (1986) produced a new quasicrystalline alloy, Al_6CuMg_4, which is an important member of a class (Ramachandrarao *et al* 1985) of quasicrystalline solids. More recently this class of quasicrystalline solids has also been predicted on the basis of quantum structural diagrams (Villars *et al* 1986). In this communication we report a study on the quasicrystalline to crystalline phase transitions in this system. Our study has interesting implication concerning the stability of the quasicrystalline phase.

The stoichiometric compound (Al_6CuMg_4) was prepared by melting constituent elements in pure form (99·99%) under argon atmosphere in a graphite crucible. Ribbon samples, of about 5 mm width and 30 μm thickness, for the present study were obtained by rapid solidification using the usual melt spinning method. The quasicrystalline character of these samples was confirmed (Dey *et al* 1986) by transmission electron microscopy (TEM) observations. Bright field electron micrograph showing the morphology of the icosahedral domains and selected area diffraction pattern showing five-fold symmetry are presented in figures 1a and 1b respectively. All other diffraction patterns were obtained from the same nodule at the expected angles characteristic of the $m\bar{3}\bar{5}$ point group. The three-fold pattern is shown in figure 3a.

Three DSC measurements were performed: one on the original crystalline material (out of which quasicrystalline ribbons were prepared), the second on as-grown quasicrystalline phase and the third on quasicrystal samples which were in situ heated to 400°C and then cooled to 30°C before the DSC scans were made. The

CC-0. In Public Domain. Gurukul Kangri Collection, Haridwar

Digitized by Arya Samaj Foundation Chennai and eGangotri

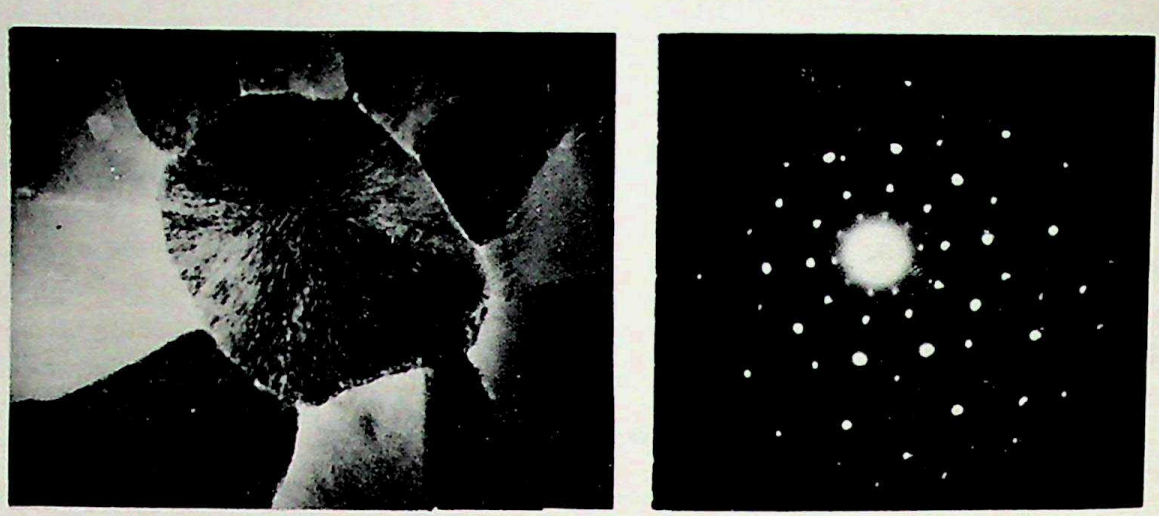

Figure 1. (a). The bright field electron micrograph is displayed showing the grain morphology. (**b**) Electron diffraction pattern exhibiting five-fold symmetry.

results for these three measurements are identified by the symbols I, II and III respectively and are displayed in figure 2. We performed the measurements several times with different portions of materials to confirm the repeatability of the results. All the DSC measurements were done on Mettler TA3000 thermal analysis system and the system was calibrated with pure indium. Further the DSC runs were conducted with two different heating rates viz 10 K/minute as well as 30 K/minute and it was confirmed that identical features were shown by both kinds of runs. In figure 2, however, only the results for 30 K/minute heating rate have been displayed.

Above 400°C, the results for all the three are similar, in that there is a strong endothermic peak at 474·9°C and the enthalpy change is 230·92 J/g. However, below 360°C the spectra are very different as shown in figure 2. While for the original crystalline material (I), the heat out vs temperature shows no peaks and for the as-grown quasicrystalline phase (II) we see a broad endothermic structure

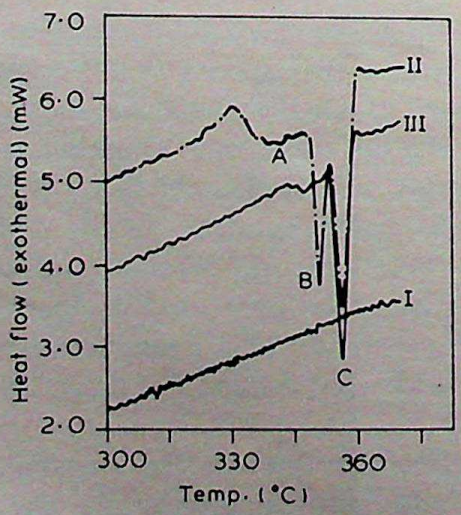

Figure 2. As-recorded DSC data (I) for original crystalline material (10 mg of sample), (II) for as-grown quasicrystalline phase (5 mg of sample) and (III) for in-situ annealed quasicrystalline sample.

CC-0. In Public Domain. Gurukul Kangri Collection, Haridwar

Digitized by Arya Samaj Foundation Chennai and eGangotri

around 340·06°C followed by two sharp peaks at 351·01°C and 356·45°C respectively. These are designated as A, B, C in figure 2 and the enthalpy changes associated with these peaks are 2·2, 1·47 and 2·5 J/g respectively. For the quasicrystalline samples first heated to 400°C (III), there is only a sharp endothermic peak at 356·45°C coinciding with the peak C of II, and neither the broad structure A nor the peak B is seen.

It was observed that arresting a phase, from a region between the two peaks A and B, at room temperature is not possible. If the as-grown quasicrystalline sample was kept at peak A (340°C) for a few minutes, and then the subsequent DSC scan through higher temperature (above 340°C) did not show the presence of peak B. In view of this finding the electron diffraction pattern of the quasicrystalline sample, which was heat-treated at 340°C for one hour, was recorded and compared with that of the as-grown quasicrystalline sample (refer figure 3). In figure 3a the three-fold pattern for the as-grown quasicrystalline phase is shown and in figure 3b we display the pattern of the heat-treated quasicrystalline sample. As can be seen from a comparison of figures 3a and 3b the separation of spots in (3a) is related to the 'golden ratio', while those in (3b) exhibit a periodicity, which confirms crystallization. This is analogous to what was observed (Chen *et al* 1985) in the case of $Al_{86}Mn_{14}$, wherein a broad exothermic structure (below 680 K) precedes a sharp exothermic peak at 780 K and an icosahedral to crystalline transformation can be brought about by annealing the samples at 650 K for 30 minutes (or at 700 K for 20 minutes). So we believe that A and B are both associated with the quasicrystalline to crystalline transition. Peak C is connected with a reversible (polymorphic) crystalline phase transition. This was confirmed through the following experiment. The as-grown quasicrystalline samples were first in situ heated to 400°C and then DSC runs were performed at a cooling rate of 30 K/min. It was found that peak C reappears (as an exothermic peak) at the same temperature confirming the reversibility of this transition.

In conclusion, we have found that quasicrystalline to crystalline phase transition in Al_6CuMg_4 system is an *endothermic* process as compared to exothermic crystallization in the Al-Mn system. This indicates that Al_6CuMg_4 forms a stabler quasicrystal than the Al-Mn system. Better stability of this alloy system was

Figure 3. Electron diffraction pattern (a) for quasicrystalline phase and (b) for annealed sample as detailed in the text.

CC-0. In Public Domain. Gurukul Kangri Collection, Haridwar

Digitized by Arya Samaj Foundation Chennai and eGangotri

predicted on the basis of quantum structural diagram (Villars *et al* 1986) and the result of this communication confirms that prediction. Our observation suggests that, by judicious choice of cooling rate, it should be possible to grow large-sized quasicrystals, akin to what has been found possible (Dubost *et al* 1986) in the Al_6CuLi_3 system. Subsequent x-ray diffraction study (details will be published separately) of this quasicrystalline to crystalline transition shows that the transformed crystalline phase is not the same as that of the equilibrium alloy phase. Although both the crystalline phases have the space group of Im3-T_h^5, their atomic positional parameters are different.

We thank L Varshney for valuable advice on DSC measurements. It is a pleasure to acknowledge valuable conversation with S Banerjee and S B Ota.

References

Chen H S, Chen C H, Inoue A and Krause J T 1985 *Phys. Rev.* **B32** 1940
Dey G K, Savatia R T and Banerjee S 1986 *Proc. Int. Conf. on Metallic and Semiconducting Glasses, Hyderabad* (to be published by Trans. Tech. Publ., Switzerland)
Dubost B, Lang J M, Tanaka M, Sainfort P and Audier M 1986 *Nature (London)* **324** 48
Ramachandrarao P and Sastry G V S 1985 *Pramana-J. Phys.* **25** L225
Sastry G V S, Rao V V, Ramachandrarao P and Anantharaman T R 1986 *Scr. Metall.* **20** 191
Shechtman D, Blech I, Gratias D and Cahn J W 1984 *Phys. Rev. Lett.* **53** 1951
Villars P, Phillips J C and Chen H S 1986 *Phys. Rev. Lett.* **57** 3085

CC-0. In Public Domain. Gurukul Kangri Collection, Haridwar

Digitized by Arya Samaj Foundation Chennai and eGangotri

Pramāṇa – J. Phys, Vol. 28, No. 6, June 1987, pp. L713–719. © Printed in India.

Electromagnetic response of a single phase Y-Ba-Cu-O compound superconducting in the 90 K range

V NAGARAJAN, P L PAULOSE, A K GROVER, S K DHAR and E V SAMPATHKUMARAN

Tata Institute of Fundamental Research, Homi Bhabha Road, Bombay 400 005, India

MS received 6 May 1987

Abstract. The results of x-ray diffraction, electrical resistance, DC and AC magnetization studies on two specimens of compositions $Y_{2\cdot1}Ba_{3\cdot9}Cu_6O_{14-\delta}$ and $Y_{1\cdot8}Ba_{4\cdot2}Cu_6O_{14-\delta}$ are presented. Our studies confirm that $La_3Ba_3Cu_6O_{14}$ type orthorhombic phase is responsible for superconductivity in the 90 K range. The heat treatment that yields high quality samples with sharp transition in electrical resistance as well as in AC magnetic susceptibility measurements is described. Magnetic response just below T_c is found to be sensitive to the measuring field.

Keywords. High temperature superconductivity; Y-Ba-Cu-O system; Electromagnetic response.

PACS No. 74·70

The discovery of superconductivity by Wu *et al* (1987) above the boiling point of liquid nitrogen in a multiphase Y-Ba-Cu-O system has stimulated intense activity everywhere. This result was confirmed and improved upon (Ganguly *et al* 1987a; Sampathkumaran *et al* 1987; Umarji *et al*. 1987; G V Subba Rao, Private Communication; S K Malik, Private Communication) and the phase that superconducts in the multiphase system was identified independently by several groups (Ganguly *et al* 1987b; Dhar *et al* 1987; Cava *et al* 1987; Beno *et al* 1987). In the course of our work towards isolating the single phase compound, we had synthesized and investigated the compounds belonging to the series $Y_{1-x}Ba_xCuO_y$ (Dhar *et al* 1987). On the basis of the correlation between the strength (as well as sharpness) of the diamagnetic response and the x-ray diffraction intensities of a particular set of lines, we arrived at the conclusion that the superconducting (T_c = 90 K) phase has the orthorhombic $La_3Ba_3Cu_6O_{14}$ type structure (Er-Rakho *et al* 1981). In this communication, we present the details of electrical resistance and magnetization measurements on a few specimens, close to the single phase composition, further characterizing the behaviour of the phase superconducting in the 90 K range. Extremely sharp transitions in the AC susceptibility and electrical resistance data have been observed for a particular heat treatment of our specimens. We think that this information is of technological importance.

The samples $Y_{2\cdot1}Ba_{3\cdot9}Cu_6O_y$ and $Y_{1\cdot8}Ba_{4\cdot2}Cu_6O_y$ (where $y = 14-\delta$) were prepared by a solid state reaction procedure. The stoichiometric amounts of Y_2O_3 (> 99%), CuO (> 99%) and $BaCO_3$ (AR grade) were thoroughly mixed in a medium of acetone and presintered at 700°C in air overnight. The presintered materials were then heated at 900°C for 2 days in air, with a few intermediate grindings. One portion of the reacted mixture for each sample was pelletized by

CC-0. In Public Domain. Gurukul Kangri Collection, Haridwar

Digitized by Arya Samaj Foundation Chennai and eGangotri

applying a pressure of about 4 tons and the pellet annealed at 900°C for 15 hr in a continuous flow of oxygen gas (hereafter referred to as oxygen-annealed specimen). The other portion of the reacted mixture was further heated at 900°C in oxygen atmosphere overnight prior to pelletizing. This pellet was also subsequently heated at 900°C for 15 hr (hereafter referred to as oxygen-presintered specimen).

The x-ray diffraction patterns obtained using CuK_α radiation for both the compositions are shown in figure 1. The oxygen-annealed and oxygen-presintered specimens at the same composition give nearly identical x-ray patterns. The majority of the sharp lines could be identified (Dhar *et al* 1987) with the $La_3Ba_3Cu_6O_{14}$ type (Er-Rakho *et al* 1981) distorted tetragonal structure. It has since been confirmed independently by several groups that the splitting visible in several of the intense lines corresponds to the orthorhombic nature (see, for instance, Schuller *et al* 1987). We find that the set of extra lines (marked by crosses in figure 1) belong to Y_2BaCuO_5 phase in the case of $Y_{2.1}Ba_{3.9}Cu_6O_y$ specimen, whereas they arise from $BaCuO_2$ type phase in $Y_{1.8}Ba_{4.2}Cu_6O_y$ specimen. Therefore, the perfect single phase compound could be synthesized at a composition intermediate between the above two specimens. This is consistent with many recent reports (Ganguly *et al* 1987b; Cava *et al* 1987; Beno *et al* 1987) which give the stoichiometry as $YBa_2Cu_3O_{6.85}$.

DC electrical resistance measurements were performed on all the specimens by the conventional four-probe method. The detailed AC susceptibility and DC magnetization studies were carried out only on oxygen-presintered $Y_{2.1}Ba_{3.9}Cu_6O_y$ specimen.

Figure 2 shows AC susceptibility data in the oxygen-presintered specimen at stoichiometry $Y_{1.8}Ba_{4.2}Cu_6O_y$. The inset shows the temperature variation of AC susceptibility and resistance values on the same expanded scale. The rapid increase in diamagnetic response sets in at a temperature slightly lower (~ 2 K) than the fall in resistance values. It is satisfying to note that the width of the transition (defined as the variation from 10 to 90% value) in AC susceptibility and resistance data is very small (~ 2 K). The zero resistance state is obtained at 89 K and the mid-point is at 90 K.

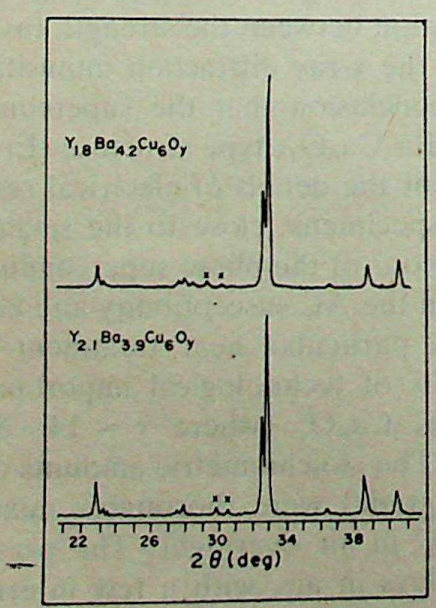

Figure 1. X-ray diffraction patterns of the specimens $Y_{1.8}Ba_{4.2}Cu_6O_y$ and $Y_{2.1}Ba_{3.9}Cu_6O_y$.

CC-0. In Public Domain. Gurukul Kangri Collection, Haridwar

Digitized by Arya Samaj Foundation Chennai and eGangotri

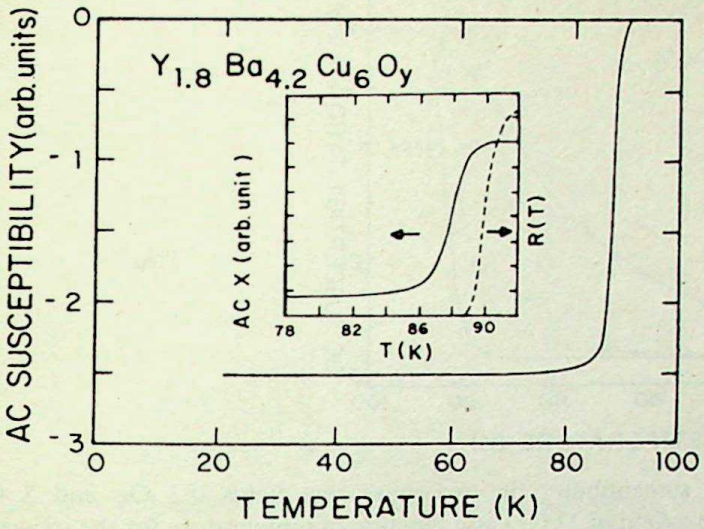

Figure 2. AC susceptibility (χ) in the temperature interval 20–100 K for the specimen $Y_{1\cdot8}Ba_{4\cdot2}Cu_6O_y$. Inset shows AC χ as well as the resistance data in the temperature interval 78–92 K for the same specimen.

Figure 3 displays the resistance data normalized to the 300 K value for the oxygen-presintered $Y_{2\cdot1}Ba_{3\cdot9}Cu_6O_y$ specimen. The zero resistance temperature, mid-point and 10 to 90% width values are 89 K, 90·5 and 2 K respectively. These values are the same as in oxygen-presintered $Y_{1\cdot8}Ba_{4\cdot2}Cu_6O_y$ specimen, thereby characterizing the parameters underlying the superconducting phase in two specimens. The inset of figure 3 affords a comparison of resistance behaviour near the transition in oxygen-presintered and oxygen-annealed specimens at the same composition. The latter shows higher zero resistance temperature (90 K). However, the comparison of the AC susceptibility data shows that in the oxygen-annealed specimen the transition is not only somewhat broadened but also shows a kink (see figure 3 in Dhar *et al* 1987) during the rapid fall. Similar differences have also been observed in the AC susceptibility response of the oxygen-presintered and oxygen-annealed specimens at composition $Y_{1\cdot8}Ba_{4\cdot2}Cu_6O_y$.

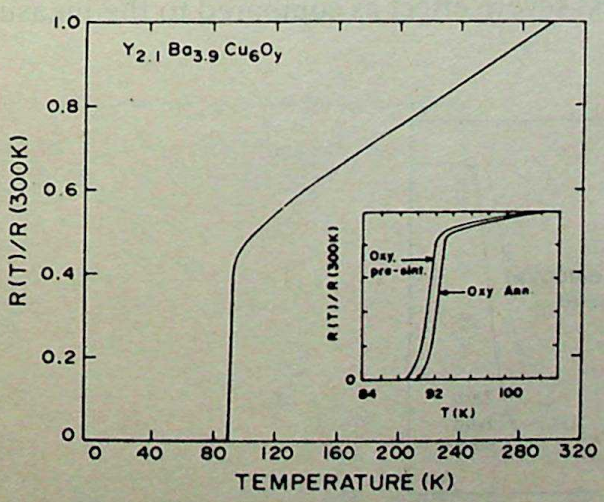

Figure 3. Resistance (4·2–300 K) normalized to the 300 K value for the oxygen presintered specimen of the sample $Y_{2\cdot1}Ba_{3\cdot9}Cu_6O_y$. Inset shows the difference in the resistance data for the oxygen-presintered and oxygen-annealed specimens of the same composition.

CC-0. In Public Domain. Gurukul Kangri Collection, Haridwar

Digitized by Arya Samaj Foundation Chennai and eGangotri

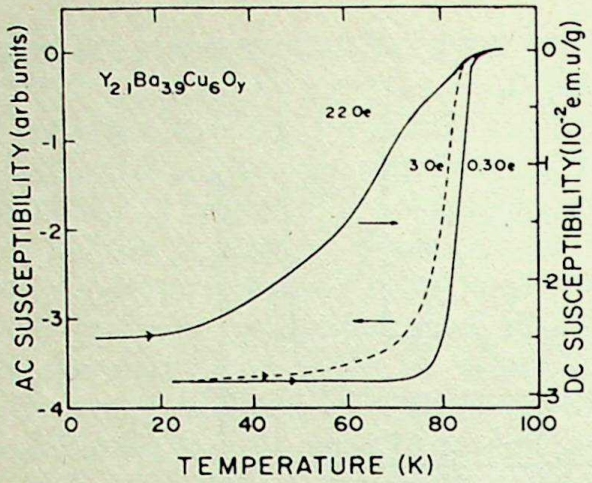

Figure 4. AC susceptibility (in two measuring fields 0·3 Oe and 3 Oe) and DC susceptibility (in a field of 22 Oe) as a function of temperature for the oxygen-presintered specimen of $Y_{2\cdot1}Ba_{3\cdot9}Cu_6O_y$.

These results imply that presintering the reaction product in oxygen atmosphere yields more homogeneous specimens.

Figure 4 shows the temperature variation of DC susceptibility measured in a field of 22 Oe and the AC susceptibility data recorded in fields of ~ 0·3 Oe (r.m.s.) and ~ 3·0 Oe (r.m.s.) at 320 Hz in $Y_{2\cdot1}Ba_{3\cdot9}Cu_6O_y$ (oxygen presintered specimen). The sample was first cooled down to the lowest temperature in earth's magnetic field and the measurements were made during the warm-up cycles. The different curves of figure 4 vividly show the sensitivity of the width of the transition in susceptibility data to the strength of the measuring field. Similar effect has also been seen recently by Ray Chaudhary *et al* (1987). Figure 5 contains the comparison of AC susceptibility data recorded in the same measuring field (~ 1 Oe r.m.s.) for specimen cooled down to the lowest temperature in the nominal zero field and 60 Oe field values. As earlier, the data were recorded during the warm-up cycle with the field on. The two curves of figure 5 demonstrate that as far as the widths of the transition in AC susceptibility data are concerned, the presence of steady DC magnetic field has less severe effect as compared to the measuring field.

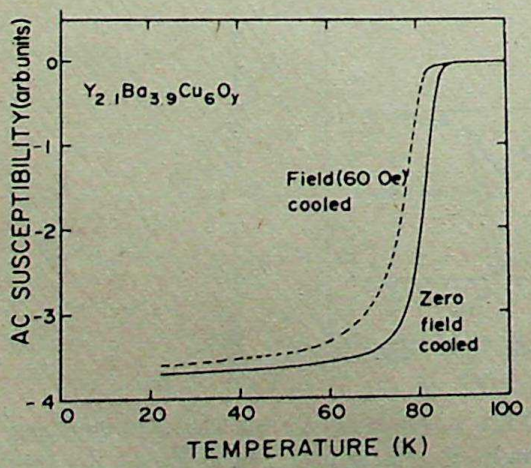

Figure 5. AC susceptibility of the oxygen-presintered specimen of the composition $Y_{2\cdot1}Ba_{3\cdot9}Cu_6O_y$ in the presence of DC field (60 Oe) as well as in the absence of this field.

CC-0. In Public Domain. Gurukul Kangri Collection, Haridwar

Digitized by Arya Samaj Foundation Chennai and eGangotri

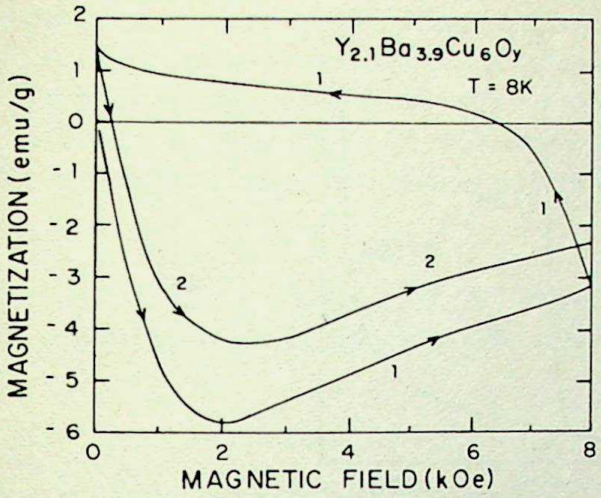

Figure 6. Magnetic hysteresis curve (measured up to a field of 8 kOe) for the oxygen-presintered specimen of $Y_{2\cdot1}Ba_{3\cdot9}Cu_6O_y$.

Figure 6 shows the magnetization versus field plot obtained at 8 K in oxygen-presintered $Y_{2\cdot1}Ba_{3\cdot9}Cu_6O_y$ specimen by cycling the field upto 8 kOe. The sample was cooled down to 8 K in nominal zero field before performing the measurements, the numbers labelling the curves in figure 6 connote the sequence of the cycling. The general shape and the hysteritic behaviour of the plot imply the irreversible type II nature of the specimen. The minimum in M versus H is observed at ~ 2 kOe field, this value is comparable to that observed earlier in oxygen-annealed multiphase specimen at composition $Y_{1\cdot2}Ba_{0\cdot8}CuO_4$ (see figure 5 in Paulose *et al* 1987). The magnitude of the magnetization value at the minimum position in the case of $Y_{2\cdot1}Ba_{3\cdot9}CuO_y$ is about 4 times the corresponding value in $Y_{1\cdot2}Ba_{0\cdot8}CuO_4$ (cf. figure 6 with figure 5 in Paulose *et al* 1987). This fact is qualitatively consistent with the ratio of the fractions of the superconducting phase present at the two compositions (Dhar *et al* 1987). Figure 7 depicts M versus H data at 8 K in $Y_{2\cdot1}Ba_{3\cdot9}CuO_y$ on an expanded scale. In this specimen, the deviation from linearity in M versus H behaviour sets in above 600 Oe whereas in the multiphase $Y_{1\cdot2}Ba_{0\cdot8}CuO_4$ a linear response could not be observed even below 50 Oe.

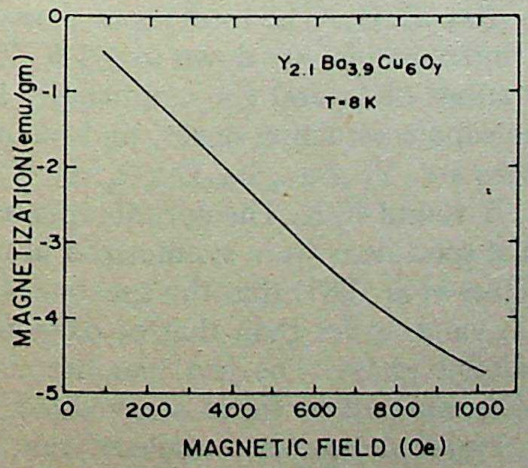

Figure 7. Magnetization as a function of the applied magnetic field at 8 K for the oxygen-presintered specimen of the $Y_{2\cdot1}Ba_{3\cdot9}Cu_6O_y$.

CC-0. In Public Domain. Gurukul Kangri Collection, Haridwar

Digitized by Arya Samaj Foundation Chennai and eGangotri

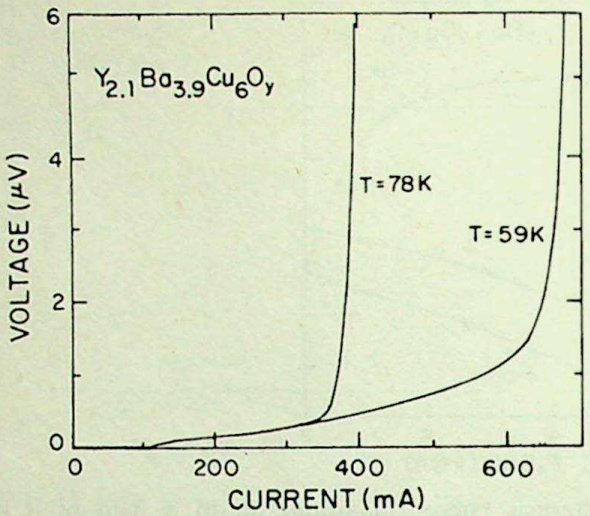

Figure 8. Current versus voltage characteristic of the oxygen-presintered specimen of $Y_{2\cdot1}Ba_{3\cdot9}Cu_6O_y$ at two temperatures.

Figure 8 presents the current versus voltage characteristics at 59 K and 78 K. It is interesting to note that the sample remains superconducting only upto 120 mA at both the temperatures; this corresponds to the critical current density of < 10 A/cm^2. Above this current value, the sample acquires a small finite resistance. At further higher value of current, which depends upon the temperature, another jump in resistance value is seen. The two-step increase in resistance value is curious, such a behaviour has not been observed in La-based compounds superconducting in the 30 K range (Grover *et al* 1987).

It is being increasingly argued (see, for instance, Müller *et al* 1987; Razavi *et al* 1987) that the response of the high T_c ceramic superconductors to the electromagnetic fields is analogous to that expected in granular superconducting materials. Most of the magnetic properties described above, like the dependence of the AC susceptibility on the measuring field, the difference in the DC field dependence of the AC susceptibility and the DC susceptibility etc., can be explained in terms of the collective behaviour of clusters containing loops of coupled superconducting grains (Ebner and Stroud 1985).

As a final remark, we may state here the results of various substitutional studies attempted on the stoichiometry of $Y_{2\cdot1}Ba_{3\cdot9}CuO_y$. The total replacement of Ba by Ca and Sr resulted in the absence of superconductivity down to 4·2 K. The partial replacement of Ba by small concentrations of Sr and Ca significantly lowers the superconducting T_c. For instance, the superconducting onset, mid-point and zero resistance temperature for two specimens are: $Y_{1\cdot8}Ba_{3\cdot6}Sr_{0\cdot6}Cu_6O_y$: 96 K, 85 K and 82 K and $Y_{1\cdot8}Ba_{3\cdot6}Ca_{0\cdot6}Cu_6O_y$: 90 K, 72 K and 46 K. The partial replacement of Y by La also lowers T_c. All substitutional specimens were synthesized in the oxygen atmosphere. We had earlier found (Dhar *et al* 1987) that the specimens heated in air had a tetragonal structure with T_c value lower than that of oxygen-annealed specimens giving rise to the orthorhombic phase. The fact that the air-annealed specimens are deficient in oxygen as compared to those synthesized in oxygen atmosphere, may imply that the oxygen deficiency stabilizes the tetragonal structure. When this manuscript was at a final stage, we came to know the work of Schuller *et al* (1987), reporting systematic high temperature x-ray diffraction studies

CC-0. In Public Domain. Gurukul Kangri Collection, Haridwar

Digitized by Arya Samaj Foundation Chennai and eGangotri

in the single phase specimens of $YBa_2Cu_3O_7$. These authors find the existence of a tetragonal to orthorhombic structural phase transition above 700 K. The authors also report that samples quenched from high temperatures giving rise to tetragonal phase have a lower T_c than those of slow-cooled specimens crystallizing in the orthorhombic structure. Our results (Dhar *et al* 1987) independently support these ideas.

The authors would like to thank Prof. R. Vijayaraghavan for his keen interest, support and encouragement throughout the course of this work.

References

Cava R J, Batlogg B, van Dover R B, Murphy D W, Sunshine T, Siegrisr T, Remeika J P, Rietman E A, Zahurak S and Espinosa G P 1987 *Phys. Rev. Lett.* **58** 1676

Beno M A, Soderholm L, Capone D W, Hinks D G, Jorgensen J D, Schuller I K, Segre C V, Zhang K and Grace J D 1987 *Appl. Phys. Lett.* (submitted)

Dhar S K, Paulose P L, Grover A K, Sampathkumaran E V and Nagarajan V 1987 *J. Phys.* **F** (in press)

Ebner C and Stroud A 1985 *Phys. Rev.* **B31** 1541

Er-Rakho L, Michel C, Provost J and Raveau B 1981 *J. Solid State Chem.* **37** 151

Ganguly P, Raychaudhuri A K, Sreedhar K and Rao C N R 1987a *Pramana—J. Phys.* **27** L229

Ganguly P, Mohanram R A, Sreedhar K and Rao C N R 1987b *Pramana—J. Phys.* **28** L321

Grover A K, Dhar S K, Paulose P L, Nagarajan V, Sampathkumaran E V, and Nagarajan R 1987 *Solid State Commun.* (submitted)

Müller K A, Takashige M and Bednorz J G 1987 *Phys. Rev. Lett.* **58** 1143

Paulose P L, Nagarajan V, Grover A K, Dhar S K and Sampathkumaran E V 1987 *J. Phys.* **F** (in press)

Raychaudhuri A K, Sreedhar K, Rajeev K P, Mohanram R A, Ganguly P and Rao C N R 1987 *Philos. Mag. Lett.* (submitted)

Razavi F S, Koffyberg F P and Mitrovic B 1987 *Phys. Rev.* **B35** 5323

Sampathkumaran E V, Paulose P L, Grover A K, Nagarajan V and Dhar S K 1987 *Curr. Sci.* **56** 252

Schuller I K, Hinks D G, Beno M A, Capone D W, Soderholm L, Locquet J P, Bruynseraede Y, Segre C U and Zhang K 1987 *Solid State Commun.* (in press)

Umarji A M, Gopalakrishnan I K, Yakhmi J V, Gupta L C, Vijayaraghavan R and Iyer R M 1987 *Curr. Sci.* **56** 250

Wu M K, Ashburn J R, Torng C J, Hor P H, Meng R L, Gao L, Huang Z J, Wang Y Q and Chu C W 1987 *Phys. Rev. Lett.* **58** 908

CC-0. In Public Domain. Gurukul Kangri Collection, Haridwar

Digitized by Arya Samaj Foundation Chennai and eGangotri

CC-0. In Public Domain. Gurukul Kangri Collection, Haridwar

Digitized by Arya Samaj Foundation Chennai and eGangotri

Pramāṇa

journal of physics

Volume 28, January–June 1987

SUBJECT INDEX

Foreword 433

A-15 superconductors
Transformation kinetics of A-15 superconductors formed by solid state reactions 529

Absorption
Kramers-Kronig type of dispersion relation in nonlinear optics 661

Absorption edge
Photoacoustic determination of energy band gap of semiconductors 293

Absorption spectra
Transient excited singlet state absorption in Rhodamine 6G 59

Accelerating motion
Production of tachyons and antiparticles in extended manifolds of general relativity 379

Aging effects
Effects of various ambient-aging processes in chopped and non-chopped optical films 277

Alkali halide mixed crystals
X-ray diffraction and colour centre studies on RbCl-RbBr mixed crystals 81

Alkaline earth metal
Unified study of alkaline earth metal 689

Amino acids
Theoretical study of ^{14}N pure quadrupole resonance in amino acids 45

Analytic representation
Analytic representation for ^{3}He form factors 117

Anisotropic model
Nonsingular cosmological models with torsion determined by vacuum polarization of quantum fields 241

Anisotropy
Thermodynamic properties of molecular fluid mixtures of hard ellipsoids 343

Antiferromagnet
Periodic density redistribution of parametrically excited spin waves in an antiferromagnet 603

Antiferromagnets
Magnetic properties and peculiarity of magnetic states in dilute antiferromagnets $Mn_{1-x}Zn_xF_2$ 602

Antiparticle
Production of tachyons and antiparticles in extended manifolds of general relativity 379

Antisymmetrized
Electron impact excitation of hydrogen and helium in Coulomb-projected Born methods 167

Approximation scheme
Near perpendicular propagation of ion cyclotron modes in a deuterium-hydrogen-oxygen fusion plasma 181

Arbitrary curved space-time
Local quantum statistics in arbitrary curved space-time 355

As-Sb-Se glasses
Low temperature elastic behaviour of As-Sb-Se and Ge-Sb-Se glasses 471

Band gap energy
Photoacoustic determination of energy band gap of semiconductors 293

Barium
Unified study of alkaline earth metal 689

Binary liquids
The dielectric constant of the binary liquid system *n*. heptane + methanol near its critical temperature 269

Binary mixture
Thermodynamic properties of molecular fluid mixtures of hard ellipsoids 343

Black hole
Production of tachyons and antiparticles in extended manifolds of general relativity 379

Boltzmann gas
Spin waves in paramagnetic Boltzmann gases 601

Boron monosulphide
Isotope shift studies in the spectrum of boron monosulphide 159

Boson fluid
Microscopic theory of soliton propagation in a mixture of two boson fluid films 361

Calcium
Unified study of alkaline earth metal 689

Cation distribution
X-ray, electrical conductivity, magnetic and infrared studies of the system $Co_{2-x}Ge_{1-x}Fe_{2x}O_4$ 675

Canonical gravity
A Lagrangian basis for Ashtekar's reformulation of canonical gravity L429

CC-0. In Public Domain. Gurukul Kangri Collection, Haridwar

Digitized by Arya Samaj Foundation Chennai and eGangotri

Cerium solid
Stabilization of valence fluctuations in the cerium solid by the time-dependent collision approach 299
Chopped films
Effects of various ambient-aging processes in chopped and non-chopped optical films 277
Chou-Yang model
Chou-Yang model and predictions for high-energy pion-deuteron scattering 607
Classical microscopic
Equations of motion approach
Heavy-ion fusion cross-section calculations in classical microscopic equations of motion approach 41
Classical spinning particles
The generalized Pauli-Lubanski vector for massless spinning particles in arbitrary space-time dimensions 233
Coercive force
X-ray, electrical conductivity, magnetic and infrared studies of the system $Co_{2-x}Ge_{1-x}Fe_{2x}O_4$ 675
Coexistence
Theoretical studies on magnetic superconductors 565
Collective excitation mode
Collective excitation modes in the intermediate and superconducting states of doped and undoped indium and lead 205
Colour centres
X-ray diffraction and colour centre studies on RbCl-RbBr mixed crystals 81
Constrained density method
On the direct determination of constrained pure state one-electron density matrices: II. A modified algorithm and its applications 51
Constrained variational calculations
On the direct determination of constrained pure state one-electron density matrices: II. A modified algorithm and its applications 51
Continuous flow cryostat
Precise lattice parameter measurements in CsCl-Br solid solutions between room temperature and 90°K by powder X-ray diffraction 73
Continuum dissolution
Relativistic extension of the Hohenberg-Kohn theorem 633
Cosmological models
Nonsingular cosmological models with torsion determined by vacuum polarization of quantum fields 241
Coulomb projection
Electron impact excitation of hydrogen and helium in Coulomb-projected Born methods 167
Critical capacitance
The dielectric constant of the binary liquid system *n*. heptane + methanol near its critical temperature 269
Critical exponents
The dielectric constant of the binary liquid system *n*. heptane + methanol near its critical temperature 269
Critical phenomena
The dielectric constant of the binary liquid system *n*.heptane + methanol near its critical temperature 269
Critical temperature
The dielectric constant of the binary liquid system n. heptane + methanol near its critical temperature 269
Curved space-time with torsion
Nonsingular cosmological models with torsion determined by vacuum polarization of quantum fields 241

Debye-Waller factor
X-ray diffraction and colour centre studies on RbCl-RbBr mixed crystals 81
Decay widths
Relativistic effects on meson spectra 131
deSitter universe
Kerr-Newman metric in deSitter background 109
Diamond anvil cell
High pressure techniques at low temperatures 435
Dielectric tensor
Near perpendicular propagation of ion cyclotron modes in a deuterium-hydrogen-oxygen fusion plasma 181
Diffraction
Precession photography of fibres: Prediction of patterns 415
Diffusion
Transformation kinetics of A-15 superconductors formed by solid state reactions 529
Direct density method
On the direct determination of constrained pure state one-electron density matrices: II. A modified algorithm and its applications 51
Disorder
Disorder in superconductors—a study on $Cu_2Mo_6S_8$ 547
Disordered conductors
Low-temperature resistance fluctuation in disordered conductors 471
Residual conductance fluctuations of tiny disordered conductors 593
Disordered magnets
Disordered magnets 600
Disordered metals
Quantum interference of electrons in disordered metals 592

CC-0. In Public Domain. Gurukul Kangri Collection, Haridwar

Digitized by Arya Samaj Foundation Chennai and eGangotri

Dispersion curves
Phonon dispersion curves of transition metals using modified general tensor force model 287
Dispersion relation
Near perpendicular propagation of ion cyclotron modes in a deuterium-hydrogen-oxygen fusion plasma 181
Distorted wave
Electron impact excitation of hydrogen and helium in Coulomb-projected Born methods 167
2-D scalar field model
Existence of quantum soliton of ϕ^6-like field theories in $1+1$ dimensions 87
2-D scalar field theories
Some remarks on the finiteness of soliton mass L95
Dynamic disorder
Resistivity of metallic systems with a strong dynamic disorder 509
Experimental study of resistivity of metallic materials with dynamic disorder 594

Effective action
Nonsingular cosmological models with torsion determined by vacuum polarization of quantum fields 241
Elastic behaviour
Low temperature elastic behaviour of As-Sb-Se and Ge-Sb-Se glasses 471
Elastic scattering
Modifications in high energy higher order Born approximation 387
Electric field gradient
Theoretical study of ^{14}N pure quadrupole resonance in amino acids 45
Electronic contribution to electric field gradient in dilute alloys 669
Electrical conductivity
X-ray, electrical conductivity, magnetic and infrared studies of the system $Co_{2-x}Ge_{1-x}Fe_{2x}O_4$ 675
Electrical properties
High pressure techniques at low temperatures 435
Electro-magnetic response
Electro-magnetic response of a single phase Y-Ba-Cu-O compound superconducting in the 90 K range L713
Electrohydrodynamics
Flexoelectric origin of oblique-roll electrohydrodynamic instability in nematics L311
Electromagnetic fields
Kerr-Newman metric in deSitter background 109
Electromagnetic generation
Electromagnetic generation of ultrasound in metals at low temperatures 483
Electron
Modifications in high energy higher order Born approximation 387
Electron acoustic double layer
Weak electron acoustic double layers in a multi-component plasma 399
Electron fluid
Electron fluid and quasiparticles in the quantum Hall effect 596
Electron impact excitation
Electron impact excitation of hydrogen and helium in Coulomb-projected Born methods 167
Electron quantum interference
Quantum interference of electrons in disordered metals 592
Electronic contribution
Electronic contribution to electric field gradient in dilute alloys 669
Emission band spectrum
Isotope shift studies in the spectrum of boron monosulphide 159
Enhancement of superconductivity
Theoretical studies on magnetic superconductors 565
Equation of motion approach
Heavy-ion fusion cross-section calculations in classical microscopic equations of motion approach 41
Equation of state
Thermodynamic properties of molecular fluid mixtures of hard ellipsoids 343
Equivalent potentials
Equivalent potentials for a nonsymmetric non-local interaction 325
Excess free energy
Thermodynamic properties of molecular fluid mixtures of hard ellipsoids 343
Exchange potential
Electron impact excitation of hydrogen and helium in Coulomb-projected Born methods 167
Excited singlet state absorption
Transient excited singlet state absorption in Rhodamine 6G 59
Excitons
Quenching of excitations in an impure molecular crystal 653
Extended supersymmetry
Superconformal transformations of $N=2$, $D=4$, SSYM 9

Fermi-Breit approximation
Relativistic effects on meson spectra 131
Few body problem
Calculation of geometrical coupling coefficients for the hyperspherical harmonics approach 645
Fibre
Precession photography of fibres: Prediction of patterns 415

CC-0. In Public Domain. Gurukul Kangri Collection, Haridwar

Digitized by Arya Samaj Foundation Chennai and eGangotri

Films
Microscopic theory of soliton propagation in a mixture of two boson fluid films 361
Flexoelectricity
Flexoelectric origin of oblique-roll electrohydrodynamic instability in nematics L311
Fluorescence spectra
Transient excited singlet state absorption in Rhodamine 6G 59
Fractional free volume
Temperature invariance of S_0-parameter of polymers 195
Fusion cross-section
Heavy-ion fusion cross-section calculations in classical microscopic equations of motion approach 41
Fusion plasma
Near perpendicular propagation of ion cyclotron modes in a deuterium-hydrogen-oxygen fusion plasma 181

Gauge symmetry
Supersymmetric $SU_C(4) \times SU_L(2) \times SU_R(2)$ and spontaneous breakdown of symmetries 621
Gaussian detector response
Implementation and comparative study of random sequences for nonlinear least square data fitting 97
Ge-Sb-Se glasses
Low temperature elastic behaviour of As-Sb-Se and Ge-Sb-Se glasses 471
General relativity
A Lagrangian basis for Ashtekar's reformulation of canonical gravity L429
Generalized extended diffusion models
Interpolation model for molecular reorientation in gases and liquids 367
Geometrical structure coefficients
Calculation of geometrical coupling coefficients for the hyperspherical harmonics approach 645
Global optimization
Implementation and comparative study of random sequences for nonlinear least square data fitting 97
Grain boundaries
Transformation kinetics of A-15 superconductors formed by solid state reactions 529
Gravitino
Constraint on unstable photino mass from a superlight gravitino L699
Gribov-Lipatov relation
Phenomenological structure functions and Gribov-Lipatov relation 23
Gruneisen parameter
Temperature invariance of S_0-parameter of polymers 195

Hadron-nucleus scattering
Chou-Yang model and predictions for high-energy pion-deuteron scattering 607
Hard ellipsoid
Thermodynamic properties of molecular fluid mixtures of hard ellipsoids 343
^{3}He form factors
Analytic representation for ^{3}He form factors 117
Heat capacity
Temperature invariance of S_0-parameter of polymers 195
Heavy fermions
Superconductive states 599
Helium
Electron impact excitation of hydrogen and helium in Coulomb-projected Born methods 167
Study of the two-domain processing structure in the superfluid ^{3}He-B 590
Helium atom
Modifications in high energy higher order Born approximation 387
Helium crystal
Roughening (faceting) transitions on the helium crystal-superfluid interface 591
High pressure techniques
High pressure techniques at low temperatures 435

High temperature superconductivity
High-temperature superconductivity in the 100 K region in perovskite-related oxides of the Ln-Ba-Cu-O (Ln = Y or La) system L229
Identification of the high-temperature superconducting phase in the Y-Ba-Cu-O system as the perovskite $YBa_2Cu_3O_{7+\delta}$ L321
An "EPR" study of $YBa_2Cu_3O_7$ and related high-temperature superconductors L425
Observation of inverse a.c. Josephson effect in bulk Y-Ba-Cu-O possessing high T_c L705
Electro-magnetic response of a single phase Y-Ba-Cu-O compound superconducting in the 90 K range L713
Hybrid orbitals
Theoretical study of ^{14}N pure quadrupole resonance in amino acids 45
Hydrogen
Electron impact excitation of hydrogen and helium in Coulomb-projected Born methods 167

Hydrogen atom
Modifications in high energy higher order Born approximation 387
Hyperspherical harmonics method
Calculation of geometrical coupling coefficients for the hyperspherical harmonics approach 645

CC-0. In Public Domain. Gurukul Kangri Collection, Haridwar

Digitized by Arya Samaj Foundation Chennai and eGangotri

Indium
Collective excitation modes in the intermediate and superconducting states of doped and undoped indium and lead 205
Infrared line shapes
Interpolation model for molecular reorientation in gases and liquids 367
Instrumentation
High pressure techniques at low temperatures 435
Intensity addition
Refinement of twinned crystal data 409
Interference factor
Phonon dispersion curves of transition metals using modified general tensor force model 287
Intermediate valence
Stabilization of valence fluctuations in the cerium solid by the time-dependent collision approach 299
Interpolation model
Interpolation model for molecular reorientation in gases and liquids 367
Ion cyclotron wave
Near perpendicular propagation of ion cyclotron modes in a deuterium-hydrogen-oxygen fusion plasma 181
Isotope shifts
Isotope shift studies in the spectrum of boron monosulphide 159

Jahn-Teller polarons
Electron fluctuating distortion interaction in the new high T_c superconductors L317
Josephson effect
Josephson voltage standard at National Physical Laboratory, New Delhi 517
Josephson tunnelling
Observation of inverse a.c. Josephson effect in bulk Y-Ba-Cu-O possessing high T_c L705

Kerr-Newman metric
Kerr-Newman metric in deSitter background 109
Knight shift
Nuclear magnetic resonance studies in rare earth ternary phosphides 583
Kramers-Kronig dispersion relation
Kramers-Kronig type of dispersion relation in nonlinear optics 661

Lagrangian formulation
A Lagrangian basis for Ashtekar's reformulation of canonical gravity L429
Lambda-scattering
Slope parameter and scaling functions and Gribov-Lipatov relation 35
Lattice constants
X-ray diffraction and colour centre studies on RbCl-RbBr mixed crystals 81
Layered structure
Layered structure of superfluid ^{4}He at supercritical motion 589
Lead
Collective excitation modes in the intermediate and superconducting states of doped and undoped indium and lead 205
Least square data fitting
Implementation and comparative study of random sequences for nonlinear least square data fitting 97
Lennard-Jones potential
Heavy-ion fusion cross-section calculations in classical microscopic equations of motion approach 41
Linac design calculation
Design studies of a 100 MeV proton linear accelerator 257
Local quantum statistics
Local quantum statistics in arbitrary curved space-time 355
Low temperature elasticity
Low temperature elastic behaviour of As-Sb-Se and Ge-Sb-Se glasses 471
Low temperatures
High pressure techniques at low temperatures 435
Electromagnetic generation of ultrasound in metals at low temperatures 483
Phase transition studies of paramagnetic crystals at low temperatures 573
Low-temperature resistance fluctuation
Low-temperature resistance fluctuation in disordered conductors 503

Magnetic hysteresis
X-ray, electrical conductivity, magnetic and infrared studies of the system $Co_{2-x}Ge_{1-x}Fe_{2x}O_4$ 675
Magnetic phenomena
High pressure techniques at low temperatures 435
Magnetic properties
Magnetic properties and peculiarity of magnetic states in dilute antiferromagnets $Mn_{1-x}Zn_xF_2$ 602
Magnetic superconductors
Theoretical studies on magnetic superconductors 565
Massless particles
Semiclassical approximation for relativistic potentials 1

CC-0. In Public Domain. Gurukul Kangri Collection, Haridwar

Digitized by Arya Samaj Foundation Chennai and eGangotri

Mechanical properties
High pressure techniques at low temperatures 435
Metallic systems
Resistivity of metallic systems with a strong dynamic disorder 509
Mixed phases
Refinement of twinned crystal data 409
Mixed valence
Stabilization of valence fluctuations in the cerium solid by the time-dependent collision approach 299
Mobility
X-ray, electrical conductivity, magnetic and infrared studies of the system $Co_{2-x}Ge_{1-x}Fe_{2x}O_4$ 675
Mobility edge
Low-temperature resistance fluctuation in disordered conductors 503
Modified N/D method
Analytic representation for ^{3}He form factors 117
Molecular crystal
Quenching of excitations in an impure molecular crystal 653
Molecular rotations
Interpolation model for molecular reorientation in gases and liquids 367
Mössbauer spectra
High pressure techniques at low temperatures 435
Multicomponent plasma
Weak electron acoustic double layers in a multicomponent plasma 399

Nb_3Sn
Transformation kinetics of A-15 superconductors formed by solid state reactions 529
Nelson-Riley extrapolation scheme
Precise lattice parameter measurements in CsCl solid solutions between room temperature and 90°K by powder X-ray diffraction 73
Nematic liquid crystals
Flexoelectric origin of oblique-roll electrohydrodynamic instability in nematics 311
New variables
A Lagrangian basis for Ashtekar's reformulation of canonical gravity L429
Non-local interaction
Equivalent potentials for a nonsymmetric nonlocal interaction 325
Nonlinear optical susceptibility
Kramers-Kronig type of dispersion relation in nonlinear optics 661
Nonlinear refraction
Kramers-Kronig type of dispersion relation in nonlinear optics 661
Nonstationary phenomena
Nonstationary phenomena in Si MOSFETs in the quantum Hall effects 595
Nuclear magnetic resonance
Nuclear magnetic resonance studies in rare earth ternary phosphides 583
Nuclear structure
Calculation of geometrical coupling coefficients for the hyperspherical harmonics approach 645
Nucleon-nucleon potential
Heavy-ion fusion cross-section calculations in classical microscopic equations of motion approach 41

Oblique roll instability
Flexoelectric origin of oblique-roll electrohydrodynamic instability in nematics L311
Occupation number
Theoretical study of ^{14}N pure quadrupole resonance in amino acids 45
Off-shell effect
Off-shell variation in the binding energy of triton 247
Off-shell variation
Off-shell variation in the binding energy of triton 247
Omega transformation
Structural instability and superconductivity in niobium-titanium alloys 555
Optical films
Effects of various ambient-aging processes in chopped and non-chopped optical films 277
Ordering
Transformation kinetics of A-15 superconductors formed by solid state reactions 529
$^{16}O + ^{16}O$ reaction
Heavy-ion fusion cross-section calculations in classical microscopic equations of motion approach 41

Paramagnetic crystals
Phase transition studies of paramagnetic crystals at low temperatures 573
Pattern prediction
Precession photography of fibres: Prediction of patterns 415
Pauli-Lubanski vector
The generalized Pauli-Lubanski vector for massless spinning particles in arbitrary space-time dimensions 233
PbTe films
Frozen photoconductivity in PbTe films 604
Penalty function method
On the direct determination of constrained pure state one-electron density matrices: II. A modified algorithm and its applications 51

CC-0. In Public Domain. Gurukul Kangri Collection, Haridwar

Digitized by Arya Samaj Foundation Chennai and eGangotri

Periodic density distribution
Periodic density redistribution of parametrically excited spin waves in an antiferromagnet 603
Phase equilibria
High pressure techniques at low temperatures 435
Phase method
Equivalent potentials for a nonsymmetric nonlocal interaction 325
Phase transition
Phase transition studies of paramagnetic crystals at low temperatures 573
Endothermic quasicrystalline-to-crystalline phase transition in Al_6CuMg_4 L709
Phonon drag effect
Phonon drag effect in three- and two-dimensional electron systems 489
Phonon frequency
Unified study of alkaline earth metal 689
Photoacoustic spectroscopy
Photoacoustic determination of energy band gap of semiconductors 293
Photoconductivity
Frozen photoconductivity in PbTe films 604
Polarizable point ion model
A three-body force shell model calculation of Schottky defect formation energies of ionic crystals with CsCl structure 217
Polymer
Temperature invariance of S_0-parameter of polymers 195
Precession method
Precession photography of fibres: Prediction of patterns 415
Proton linear accelerator
Design studies of a 100 MeV proton linear accelerator 257
Proximity effect
Structural instability and superconductivity in niobium-titanium alloys 555
Pseudo-random sequences
Implementation and comparative study of random sequences for nonlinear least square data fitting 97
Pseudopotential
Unified study of alkaline earth metal 689
Pseudosymmetry
Refinement of twinned crystal data 409

Quadrupole coupling constant
Theoretical study of ^{14}N pure quadrupole resonance in amino acids 45
Quantization
Semiclassical approximation for relativistic potentials 1
Quantum Hall effect
Electron fluid and quasiparticles in the quantum Hall effect 596
Nonstationary phenomena in Si MOSFET's in the quantum Hall effects 595
Quasi-random sequences
Implementation and comparative study of random sequences for nonlinear least square data fitting 97
Quasicrystals
Endothermic quasicrystalline-to-crystalline phase transition in Al_6CuMg_4 L709
Quasiparticles
Electron fluid and quasiparticles in the quantum Hall effect 596
Quenching
Quenching of excitations in an impure molecular crystal 653

Radial wavefunction
Equivalent potentials for a nonsymmetric nonlocal interaction 325
Radiation correction
Supersymmetric $SU_C(4) \times SU_L(2) \times SU_R(2)$ and spontaneous breakdown of symmetries 621
Radio frequency quadrupole-Alvarez combinations
Design studies of a 100 MeV proton linear accelerator 257
Raman line shapes
Interpolation model for molecular reorientation in gases and liquids 367
Raman spectra
High pressure techniques at low temperatures 435
Random search
Implementation and comparative study of random sequences for nonlinear least square data fitting 97
Rare earth ternary phosphides
Nuclear magnetic resonance studies in rare earth ternary phosphides 583
Regularizations
Some remarks on the finiteness of soliton mass L95
Relativistic
Relativistic extension of the Hohenberg-Kohn theorem 633
Relativistic meson spectra
Relativistic effects on meson spectra 131
Relativistic potentials
Semiclassical approximation for relativistic potentials 1
Residual conductance fluctuations
Residual conductance fluctuations of tiny disordered conductors 593
Residual resistance
Low-temperature resistance fluctuation in disordered conductors 503

CC-0. In Public Domain. Gurukul Kangri Collection, Haridwar

Digitized by Arya Samaj Foundation Chennai and eGangotri

Resistivity
Resistivity of metallic systems with a strong dynamic disorder 569
Experimental study of resistivity of metallic materials with dynamic disorder 594
Structural instability and superconductivity in niobium-titanium alloys 555
Rhodamine 6G
Transient excited singlet state absorption in Rhodamine 6G 59
Rigid shell model
A three-body force shell model calculation of Schottky defect formation energies of ionic crystals with CsCl structure 217
Roughening transitions
Roughening (faceting) transitions on the helium crystal-superfluid interface 591
Rubidium halides
X-ray diffraction and colour centre studies on RbCl-RbBr mixed crystals 81

S_0-parameter
Temperature invariance of S_0-parameter of polymers 195
SU(2) × U(1) theory
Tree-level breaking of SU(2) × U(1) in general SUGRA theories 15
Saito potential
Equivalent potentials for a nonsymmetric nonlocal interaction 325
Scale breaking
Phenomenological structure functions and Gribov-Lipatov relation 23
Schottky defect energy
A three-body force shell model calculation of Schottky defect formation energies of ionic crystals with CsCl structure 217
Screening
Electron impact excitation of hydrogen and helium in Coulomb-projected Born methods 167
Second critical field
Theoretical studies on magnetic superconductors 565
Second order elastic constants
Unified study of alkaline earth metal 689
Semiclassical approximation
Semiclassical approximation for relativistic potentials 1
Shell model density
Density of nucleons in heavy nuclei 641
Sinai fluctuations
Low-temperature resistance fluctuation in disordered conductors 503
Single-ion species
Weak electron acoustic double layers in a multi-component plasma 399
Slope parameter
Slope parameter and scaling of differential cross-section of Λ-p scattering 35
Solid solutions
Precise lattice parameter measurements in CsCl-Br solid solutions between room temperature and 90° K by powder X-ray diffraction 73
Solitons
Existence of quantum soliton for ϕ^6-like field theories in 1 + 1 dimensions 87
Some remarks on the finiteness of soliton mass L95
Microscopic theory of soliton propagation in a mixture of two boson fluid films 361
Spinel
X-ray, electrical conductivity, magnetic and infrared studies of the system $Co_{2-x}Ge_{1-x}Fe_{2x}O_4$ 675
Spin glasses
Disordered magnets 600
Spin waves
Spin waves in paramagnetic Boltzmann gases 601
Spin-lattice relaxation
Nuclear magnetic resonance studies in rare earth ternary phosphides 583
Spontaneous symmetry breakdown
Tree-level breaking of SU(2) × U(1) in general SUGRA theories 15
Stochastic quantization
Equivalence of stochastic quantization to field theories from supersymmetry 617
Strontium
Unified study of alkaline earth metal 689
Structural distortion
Electron-fluctuating distortion interaction in the new high T_c superconductors L317
Structural instability
Structural instability and superconductivity in niobium-titanium alloys 555
Structure function
Phenomenological structure functions and Gribov-Lipatov relation 23
Superconducting devices
Josephson voltage standard at National Physical Laboratory, New Delhi 517
Superconductive systems
Investigations of UBe_{13} of other compounds of Be and U in normal and superconductive states 599
Superconductivity
Collective excitation modes in the intermediate and superconducting states of doped and undoped indium and lead 205
Electron-fluctuating distortion interaction in the new high T_c superconductors L317

CC-0. In Public Domain. Gurukul Kangri Collection, Haridwar

Digitized by Arya Samaj Foundation Chennai and eGangotri

Josephson voltage standard at National Physical Laboratory, New Delhi 517
Structural instability and superconductivity in niobium-titanium alloys 555
Unusual superconductivity and its physical properties 597
Superconductivity of the twinning plane 598
Superconductors
Disorder in superconductors—a study on $Cu_2Mo_6S_8$ 547
Superconformal symmetry
Superconformal transformation of the $N=2$, $D=4$, SSYM 9
Supercritical motion
Layered structure of superfluid ^{4}He at supercritical motion 589
Superfluid ^{4}He
Layered structure of superfluid ^{4}He at supercritical motion 589
Supergravity
Tree-level breaking of $SU(2)\times U(1)$ in general SUGRA theories 15
Supersymmetry
Equivalence of stochastic quantization to field theories from supersymmetry 617
Supersymmetric $SU_C(4)\times SU_L(2)\times SU_R(2)$ and spontaneous breakdown of symmetries 621
Constraint on unstable photino mass from a superlight gravitino L699
Survival amplitude
On the short-time behaviour of quantum unstable systems 335

Tachyon
Production of tachyons and antiparticles in extended manifolds of general relativity 379
Taylor expansion
On the short-time behaviour of quantum unstable systems 335
Tensor elements
Near perpendicular propagation of ion cyclotron modes in a deuterium-hydrogen-oxygen fusion plasma 181
Tensor force
Phonon dispersion curves of transition metals using modified general tensor force model 287
Thermal properties
High pressure techniques at low temperatures 435
Thermal study
Endothermic quasicrystalline-to-crystalline phase transition in Al_6CuMg_4 L709
Three-body force shell model
A three-body force shell model calculation of Schottky defect formation energies of ionic crystals with CsCl structure 217
Three-dimensional electron system
Phonon drag effect in three- and two-dimensional electron systems 489
Threshold frequency
X-ray, electrical conductivity, magnetic and infrared studies of the system $Co_{2-x}Ge_{1-x}Fe_{2x}O_4$ 675
Ti-Nb system
Structural instability and superconductivity in niobium-titanium alloys 555
Time-dependent collision
Stabilization of valence fluctuations in the cerium solid by the time-dependent collision approach 299
Torsion
Nonsingular cosmological models with torsion determined by vacuum polarization of quantum fields 241
Transition metals
Phonon dispersion curves of transition metals using modified general tensor force model 287
Electronic contribution to electric field gradient in dilute alloys 669
Triple-well potential
Existence of quantum soliton for ϕ^6-like field theories in $1+1$ dimensions 87
Triton binding energy
Off-shell variation in the binding energy of triton 247
True lattice parameters
Precise lattice parameter measurements in CsCl solid solutions between room temperature and 90 K by powder x-ray diffraction 73
Twinned structures
Refinement of twinned crystal data 409
Twinning plane
Superconductivity of the twinning plane 598
Two-dimensional electron system
Phonon drag effect in three- and two-dimensional electron systems 489
Two-domain structure
Study of the two-domain processing structure in the superfluid ^{3}He-B 590
Two-ion species
Weak electron acoustic double layers in a multicomponent plasma 399

Ultrasonic attenuation
Collective excitation modes in the intermediate and superconducting states of doped and undoped indium and lead 205
Ultrasound in metals
Electromagnetic generation of ultrasound in metals at low temperatures 483
Umklapp processes
Phonon dispersion curves of transition metals using modified general tensor force model 297

CC-0. In Public Domain. Gurukul Kangri Collection, Haridwar

Digitized by Arya Samaj Foundation Chennai and eGangotri

Unified study
Unified study of alkaline earth metal 689
Unitarity bound
Slope parameter and scaling of differential cross-section of Λ-*p* scattering 35
Unstable particles
On the short-time behaviour of quantum unstable systems 335
Unstable photino
Constraint on unstable photino mass from a superlight gravitino L699
Upper critical field
Structural instability and superconductivity in niobium-titanium alloys 555

Valence fluctuations
Stabilization of valence fluctuations in the cerium solid by the time-dependent collision approach 299
Variational collapse
Relativistic extension of the Hohenberg-Kohn theorem 633
Voltage standard
Josephson voltage standard at National Physical Laboratory, New Delhi 517
Volume expansivity
Temperature invariance of S_0-parameter of polymers 195

Ward-Takahashi identities
Equivalence of stochastic quantization to field theories from supersymmetry 617
Wave group velocity
Near perpendicular propagation of ion cyclotron modes in a deuterium-hydrogen-oxygen fusion plasma 181

Y-Ba-Cu-O system
Electro-magnetic response of a single phase Y-Ba-Cu-O compound superconducting in the 90°K range L713
$YBa_2Cu_3O_7$
Identification of the high-temperature superconducting phase in the Y-Ba-Cu-O system as the perovskite $YBa_2Cu_3O_{7\pm\delta}$ L321
An "EPR" study of $YBa_2Cu_3O_7$ and related high-temperature superconductors L425
Yttrium-barium copper oxides
High-temperature superconductivity in the 100 K region in perovskite-related oxides of the Ln-Ba-Cu-O (Ln = Y or La) system L229
Observation of inverse a.c. Josephson effect in bulk Y-Ba-Cu-O possessing high T_c L705

AUTHOR INDEX

Agarwal S K
see Gupta A K L705
Agrawalla K N
Analytic representation for ^{3}He form factors 117
Alekseevskii N E
Investigations of UBe_{13} of other compounds of Be and U in normal and superconductive states 599

Altshuler B L
Residual conductance fluctuations of tiny disordered conductors 593
Anurag Gupta
see Gupta A K L705
Ateequddin Mohd.
see Srinivas K 81

Atre M V
The generalized Pauli-Lubanski vector for massless spinning particles in arbitrary space-time dimensions 233

Babkin A V
Roughening (faceting) transitions on the helium crystal-superfluid interface 591
Bandyopadhyay Tapas
Implementation and comparative study of random sequences for nonlinear least square data fitting 97
Bashkin E P
Spin waves in paramagnetic Boltzmann gases 601

CC-0. In Public Domain. Gurukul Kangri Collection, Haridwar

Digitized by Arya Samaj Foundation Chennai and eGangotri

Batra V K
see Gupta A K 517
Bazhan A N
Magnetic properties and peculiarity of magnetic states in dilute antiferro- magnets $Mn_{1-x}Zn_xF_2$ 602
Betigeri M G
Design studies of a 100 MeV proton linear accelerator 257
Bhat S V
An 'EPR' study of $YBa_2Cu_3O_7$ and related high temperature superconductors L425
Bhatt P V
see Patel L K 109
Bhattacharyya Sankar P
see Das Kalyan K 51
Bhattacharyya Tanmoy
Constraint on unstable photino mass from a superlight gravitino L699
Bhuyan B
Supersymmetric $SU_C(4) \times SU_L(2) \times SU_R(2)$ and spontaneous breakdown of symmetries 621
Biswas A C
Microscopic theory of soliton propagation in a mixture of two boson fluid films 361
Borovik-Romanov A S
Study of the two-domain processing structure in the superfluid ^{3}He-B 590
Buchbinder I L
Nonsingular cosmological models with torsion determined by vacuum polarization of quantum fields 241
Bujarbarua S
see Goswami K S 399
Bunkov Yu M
see Borovik-Romanov A S 590

Chaddah P
Disorder in superconductors—a study on $Cu_2Mo_6S_8$ 547
Chakrapani G
see Venkateswarlu Putcha 59
Chandra K
see Gupta A K 517
Chaturvedi S
Equivalence of stochastic quantization to field theories from supersymmetry 617
Chaudhuri K D
see Joshi V V 205
Choudhury D K
Phenomenological structure functions and Gribov-Lipatov relation 23

Darshane V S
see Prabha Nathwani 675
Das Kalyan K
On the direct determination of constrained pure state one-electron density matrices: II. A modified algorithm and its applications 51
Das Tapan K
Calculation of geometrical coupling coefficients for the hyperspherical harmonics approach 645
Datta S N
Relativistic extension of the Hohenberg-Kohn theorem 633
see Priyadarshy S 653
De Tushar Baran
see Das Tapan K 645
Deb S K
Interpolation model for molecular reorientation in gases and liquids 367
Deo B B
see Bhuyan B 621
Desai H S
see Suja K 387
Dey G K
see Sanyal M K L709
Dhar S K
see Nagarajan V L713
Dmitriev V V
see Borovik-Romanov A S 590
Dutta Roy S K
Phase transition studies of paramagnetic crystals at low temperatures 573

Edel'man V S
see Pudalov V M 595

Feigel'man M V
Disordered magnets 600
Fomin I A
see Borovik-Romanov A S 590

Gaidukov Yu P
see Vasil'ev A N 483
Ganesan V
Precise lattice parameter measurements in CsCl-Br solid solutions between room temperature and 90 K by powder X-ray diffraction 73
Ganguly P
High-temperature superconductivity in the 100 K region in perovskite-related oxides of the Ln-Ba-Cu-O (Ln = Y or La) system L229
Identification of the high-temperature superconducting phase in the Y-Ba-Cu-O system as the perovskite $YBa_2Cu_3O_{7\pm\delta}$ L321
see Bhat S V L425
Gantmakher V F
Resistivity of metallic systems with a strong dynamic disorder 509
Experimental study of resistivity of metallic materials with dynamic disorder 594
George M C
see Venkateswarlu Putcha 59

CC-0. In Public Domain. Gurukul Kangri Collection, Haridwar

Digitized by Arya Samaj Foundation Chennai and eGangotri

Ghosh B
see Dutta Roy S K 573
Girirajan K S
see Ganesan V 73
Godre S S
Heavy-ion fusion cross-section calculations in classical microscopic equations of motion approach 41
Gopal E S R
see Jayalaxmi Y 269
see Ramaseshan S 435
Low temperature elastic behaviour of As-Sb-Se and Ge-Sb-Se glasses 471
Gor'kov L P
Unusual superconductivity and its physical properties 597
Goswami K S
Weak electron acoustic double layers in a multicomponent plasma 399
Grover A K
see Nagarajan V L713
Guha S
see Jayalaxmi Y 269
Gupta A K
Josephson voltage standard at National Physical Laboratory, New Delhi 517
Observation of inverse a.c. Josephson effect in bulk Y-Ba-Cu-O possesing high T_C L705
Gurin V S
see Trofimenko A P 379

Jagadish R
Electron-fluctuating distortion interaction in the new high T_c superconductors L317
Theoretical studies on magnetic superconductors 565
Jagannath H
see Venkateswarlu Putcha 59
Jayalaxmi Y
The dielectric constant of the binary liquid system *n*.heptane + methanol near its critical temperature 269
Jayaram B
see Gupta A K L705
Joshi V V
Collective excitation modes in the intermediate and superconducting states of doped and undoped indium and lead 205
Joshipura S Anjan
Tree-level breaking of SU(2) × U(1) in general SUGRA theories 15

Kapoor A K
see Chaturvedi S 617
Karekar R N
see Vijaya K 277
Kataria N D
see Gupta A K 517
Kaul R K
Some remarks on the finiteness of solition mass L95
Keshishev K O
see Babkin A V 591
Khan Priyotosh
see Das Kalyan K 51
Khlustikov I N
Superconductivity of the twinning plane 598
Khmel'nitskii D E
see Altshuler B L 593
Kopeliovich D B
see Babkin A V 591
Krishna Kishore G
see Murty B V R R K 45
Krylov I P
Frozen photoconductivity in PbTe films 604
Kulesko G I
see Gantmakher V F 509, 594
Kulikov I
see Pronin P 355
Kumar C N
Existence of quantum soliton for ϕ^6-like field theories in 1 + 1 dimensions 87
Kumar N
Low-temperature resistance fluctuation in disordered conductors 503

Laha U
see Sett G C 325
Lakshminarayana G
see Sheila Gopal 159

Madhusudana N V
Flexoelectric origin of oblique–roll electrohydrodynamic instability in nematics L311
Mahna Satish Kumar
Phonon dispersion curves of transition metals using modified general tensor force model 287
Mehta R Mayank
Superconformal transformations of the $N=2$, $D=4$, SSYM 9
Menon V J
On the short-time behaviour of quantum unstable systems 335
Miahnahri A
see Venkateswarlu Putcha 59
Mishra V
A three-body force shell model calculation of Schottky defect formation energies of ionic crystals with CsCl structure 217
Misra A K
see Choudhury D K 23

CC-0. In Public Domain. Gurukul Kangri Collection, Haridwar

Digitized by Arya Samaj Foundation Chennai and eGangotri

Misra S P
Relativistic effects on meson spectra 137
Mohan Ram R A
see Ganguly P L321
Mohanty S
see Mohapatra J K 35
Mohapatra J K
Slope parameter and scaling of differential cross-section of Λ-*p* scattering 35
Mukharsky Yu M
see Borovik-Romanov A S 590
Mukherjee A
see Joshipura S Anjan 15
Mukundan T S
see Gopal E S R 471
Murty B V R R K
Theoretical study of ^{14}N pure quadrupole resonance in amino acids 45
Mythili R
see Singh P 257

Nagarajan V
Electro-magnetic response of a single phase Y-Ba-Cu-O compound superconducting in the 90 K range L713
Naik S
see Misra S P 137
Nair K V K
Electronic contribution to electric field gradient in dilute alloys 669
Nair N V
see Nair K V K 669
Narlikar A V
see Gupta A K 517, L705
Transformation kinetics of A-15 superconductors formed by solid state reactions 529
Natarajan N S
see Gupta A K 517
Nayak S N
see Mohapatra J K 35

Odintsov S D
see Buchbinder I L 241
Om Prakash
see Ram R S 293

Panda A R
see Misra S P 137
Pandey A N
see Ram R S 293
Parida B K
see Kumar C N 87
Parida M K
see Agrawalla K N 117
see Patel Sunachand 607
Parshin A Ya
see Babkin A V 591
Parthasarathy G
see Ramaseshan S 435
Patel L K
Kerr-Newman metric in deSitter background 109
Patel Sunachand
Chou-Yang model and predictions for high-energy pion-deuteron scattering 607
Paulose P L
see Nagarajan V L713
Petrov S V
see Bazhan A N 602
Philip J
see Gopal E S R 471
Pitaevskii L P
Layered structure of superfluid ^4He at supercritical motion 589
Pojarkov Ya B
see Krylov I P 604
Pokrovsky V L
Electron fluid and quasiparticles in the quantum Hall effect 596
Prabha Nathwani
X-ray, electrical conductivity, magnetic and infrared studies of the system 675
Priyadarshy S
Quenching of excitations in an impure molecular crystal 653
Pronin P
Local quantum statistics in arbitrary curved space-time 355
Pudalov V M
Nonstationary phenomena in Si MOSFET's in the quantum Hall effects regime 595
Puri R K
see Vijaya K 277

Radhakrishnan T S
Structural instability and superconductivity in niobium-titanium alloys 555
Raghunathan V A
see Madhusudana N V L311
Rai D K
see Singh C S 167
Rajaraman R
see Kaul R K L95
Ram R S
Photoacoustic determination of energy band gap of semiconductors 293
Ramaseshan S
High pressure techniques at low temperatures 435
Rao C N R
see Ganguly P L229, L321
see Bhat S V L425

CC-0. In Public Domain. Gurukul Kangri Collection, Haridwar

Digitized by Arya Samaj Foundation Chennai and eGangotri

Rao D Krishna
see Murty B V R R K 45
Rao Yerneni V
see Venkateswarlu Putcha 59
Ratan Lal
Stabilization of valence fluctuations in the cerium solid by the time-dependent collision approach 299
Raychaudhuri A K
see Ganguly P L229
Reddy R R
see Sharma B K 195
Roy Probir
see Bhattacharya Tanmoy L699

Sahni V C
see Sanyal M K L709
Sampathkumaran E V
see Nagarajan V L713
Samuel Joseph
A Lagrangian basis for Ashtekar's reformulation of canonical gravity L429
Sandhya Bhakay-Tamhane
Refinement of twinned crystal data 409
Sanyal M K
Endothermic quasicrystalline-to-crystalline phase transition in Al_6CuMg_4 L709
Sanyal S P
see Mishra V 217
Sarkar A
see Suratna Das 689
Sarkar P K
see Bandyopadhyay Tapas 97
Sathish S
see Gopal E S R 471
Satyanandam G
see Murty B V R R K 45
Semenchinsky S G
see Pudalov V M 595
Sen P
Kramers-Kronig type of dispersion relation in nonlinear optics 661
Sen P K
see Sen P 661
Sequeira A
see Sandhya Bhakay-Tamhane 409
Sett G C
Equivalent potentials for a nonsymmetric non-local interaction 325
Sharda S Koppar
see Patel L K 109
Sharma B K
Temperature invariance of S_0-parameter of polymers 195
Sharvin Yu V
Quantum interference of electrons in disordered metals 592
Sheila Gopal
Isotope shift studies in the spectrum of boron monosulphide 159
Singh A K
Thermodynamic properties of molecular fluid mixtures of hard ellipsoids 343
Singh C S
Electron impact excitation of hydrogen and helium in Coulomb-projected Born methods 167
Singh P
Design studies of a 100 MeV proton linear accelerator 257
Singh R K
see Mishra V 217
Singh U N
see Singh A K 343
Sinha K P
see Jagadish R L317, 565
Sinha S K
see Singh A K 343
Sirdeshmukh D B
see Srinivas K 81
Smirnov A I
Periodic density redistribution of parametrically excited spin waves in an antiferromagnet 603
Soni K Sanjeev
see Joshipura S Anjan 15
Sood A K
see Deb S K 367
Spivak B Z
see Altshuler B L 593
Sreedhar K
see Ganguly P L229
Srinivas K
X-ray diffraction and colour centre studies on RbCl-RbBr mixed crystals 81
Srinivasan V
see Chaturvedi S 617
Suja K
Modifications in high energy higher order Born approximation 387
Sumathy K R
see Madhusudana N V L311
Sundaramoorthy M
Precession photography of fibres: Prediction of patterns 415
Suratna Das
Unified study of alkaline earth metal 689

Talapov A L
see Pokrovsky V L 596
Talukdar B
see Sett G C 325
Teplinsky V M
see Gantmakher V F 509, 594

CC-0. In Public Domain. Gurukul Kangri Collection, Haridwar

Digitized by Arya Samaj Foundation Chennai and eGangotri

Thakur J
Semiclassical approximation for relativistic potentials 1
Tomar V S
see Gupta A K 517
Trofimenko A P
Production of tachyons and antiparticles in extended manifolds of general relativity 379

Ullah Nazakat
Density of nucleons in heavy nuclei 641

Vani V C
see Jayalaxmi Y 269
Vasil'ev A N
Electromagnetic generation of ultrasound in metals at low temperatures 483

Venkateswarlu Putcha
Transient excited singlet state absorption in Rhodamine 6G 59
Venugopal Chandu
Near perpendicular propagation of ion cyclotron modes in a deuterium-hydrogen-oxygen fusion plasma 181
Vijaya K
Effects of various ambient-aging processes in chopped and non-chopped optical films 277
Vijayaraghavan R
Nuclear magnetic resonance studies in rare earth ternary phosphides 583

Waghmare Y R
see Godre S S 41

Yasin Md
Off-shell variation in the binding energy of triton 247

Zavaritsky N V
The phonon drag effect in three- and two- dimensional electron systems 489

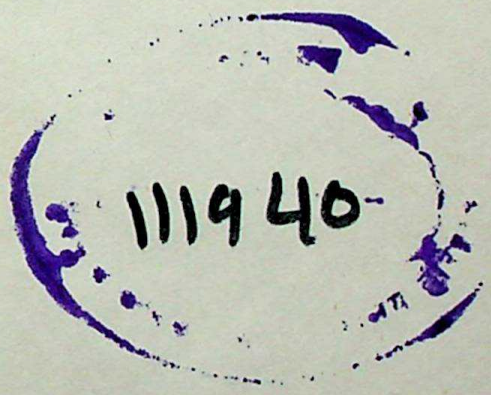

CC-0. In Public Domain. Gurukul Kangri Collection, Haridwar

Digitized by Arya Samaj Foundation Chennai and eGangotri

CC-0. In Public Domain. Gurukul Kangri Collection, Haridwar

Digitized by Arya Samaj Foundation Chennai and eGangotri

CC-0. In Public Domain. Gurukul Kangri Collection, Haridwar

Digitized by Arya Samaj Foundation Chennai and eGangotri

CC-0. In Public Domain. Gurukul Kangri Collection, Haridwar

Digitized by Arya Samaj Foundation Chennai and eGangotri

CC-0. In Public Domain. Gurukul Kangri Collection, Haridwar